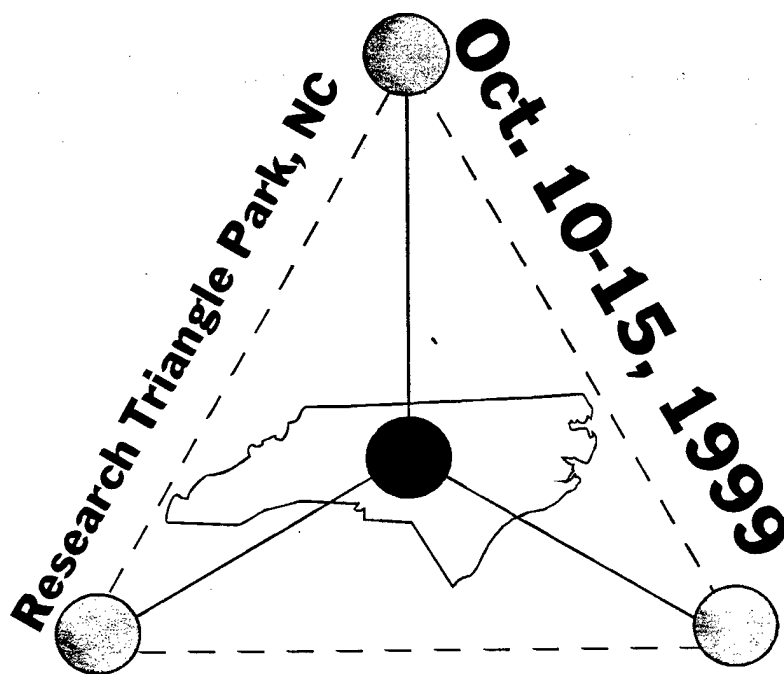


# Silicon Carbide and Related Materials - 1999

Part 1



## ICSCRM '99

Editors:

**Calvin H. Carter, Jr., Robert P. Devaty  
and Gregory S. Rohrer**

**tto**

**TRANS TECH PUBLICATIONS**

Approved for Public Release  
Distribution Unlimited

**Silicon Carbide and  
Related Materials – 1999  
Part 1**

**DISTRIBUTION STATEMENT A**  
Approved for Public Release  
Distribution Unlimited

**DTIC QUALITY INSPECTED 4**

**20000706 025**



# **Silicon Carbide and Related Materials - 1999**

## **Part 1**

### **ICSCRM'99**

**Proceedings of the International Conference on Silicon  
Carbide and Related Materials - 1999  
Research Triangle Park, North Carolina, USA  
October 10-15, 1999**

*Editors:*

**Calvin H. Carter, Jr., Robert P. Devaty  
and Gregory S. Rohrer**

---

**Copyright © 2000 Trans Tech Publications Ltd, Switzerland**  
**ISBN 0-87849-854-0 (2-Vol. Set)**

Volumes 338 – 342 of  
*Materials Science Forum*  
ISSN 0255-5476

***Distributed in the Americas by***

Trans Tech Publications Inc  
PO Box 699, May Street  
Enfield, New Hampshire 03748  
USA

Phone: (603) 632-7377  
Fax: (603) 632-5611  
e-mail: [ttp@ttp.net](mailto:ttp@ttp.net)  
Web: <http://www.ttp.net>

***and worldwide by***

Trans Tech Publications Ltd  
Brandrain 6  
CH-8707 Uetikon-Zuerich  
Switzerland

Fax: +41 (1) 922 10 33  
e-mail: [ttp@ttp.net](mailto:ttp@ttp.net)  
Web: <http://www.ttp.net>

Printed in the United Kingdom  
by Hobbs the Printers Ltd,  
Totton, Hampshire SO40 3WX

## **Silicon Carbide and Related Materials - 1999**

### **ICSCRM '99 Sponsors**

**NASA Glenn Research Center**

**Air Force Research Laboratory, Materials and Manufacturing Directorate**

**Office of Naval Research**

**Director of Defense Research and Engineering**

### **Corporate Sponsors**

**Cree, Inc.**

**Charles & Colvard, Inc.**

**ABB Semiconductors**

**Sterling Semiconductor, Inc.**

**ATMI, Inc.**

**Epigress, AB**

**Aixtron, AG**

**Northrop Grumman**

**Siemens, AG**

**EMCORE, Inc.**

**General Electric Corporate R & D**

**Litton Airtron**

**II-VI Incorporated**

## **ICSCRM '99 Committee Chairpersons**

### **General Chairman**

**C.H. Carter, Jr., Cree, Inc., USA**

### **Program Committee Chairmen**

**W.J. Choyke, University of Pittsburgh, USA**

**D.J. Larkin, NASA Glenn Research Center, USA**

### **Publication Committee Chairmen**

**R.P. Devaty, University of Pittsburgh, USA**

**G.S. Rohrer, Carnegie Mellon University, USA**

### **Treasurer**

**R. Hopkins, Northrop Grumman (retired) , USA**

## **ICSCRM '99 Committees**

### **International Steering Committee**

<b>C.H. Carter, Jr.</b>	<b>Cree, Inc., USA</b>
<b>W.J. Choyke</b>	<b>University of Pittsburgh, USA</b>
<b>R. Hopkins</b>	<b>Northrop Grumman, USA (retired)</b>
<b>E. Janzén</b>	<b>Linköping University, Sweden</b>
<b>H. Matsunami</b>	<b>Kyoto University, Japan</b>
<b>B. Monemar</b>	<b>Linköping University, Sweden</b>
<b>G. Pensl</b>	<b>University of Erlangen-Nürnberg, Germany</b>
<b>L. Rea</b>	<b>Air Force Research Laboratory/MLMP, USA</b>
<b>D. Stephani</b>	<b>Siemens AG, Germany</b>
<b>C.E.C. Wood</b>	<b>Office of Naval Research, USA</b>
<b>S. Yoshida</b>	<b>Saitama University, Japan</b>

### **Program Committee**

<b>W.J. Choyke</b>	<b>University of Pittsburgh, USA</b>
<b>D.J. Larkin</b>	<b>NASA Glenn Research Center, USA</b>
<b>R.P. Devaty</b>	<b>University of Pittsburgh, USA</b>
<b>G.S. Rohrer</b>	<b>Carnegie Mellon University, USA</b>
<b>A. Burk</b>	<b>Cree, Inc., USA</b>
<b>P. Neudeck</b>	<b>NASA Glenn Research Center, USA</b>
<b>J. Palmour</b>	<b>Cree, Inc., USA</b>
<b>B. Monemar</b>	<b>Linköping University, Sweden</b>
<b>G. Pensl</b>	<b>University of Erlangen-Nürnberg, Germany</b>
<b>H. Matsunami</b>	<b>Kyoto University, Japan</b>
<b>S. Yoshida</b>	<b>Saitama University, Japan</b>
<b>R. Madar</b>	<b>CNRS, France</b>

## Preface

These volumes contain written versions of papers which were presented at the International Conference on Silicon Carbide and Related Materials 1999 (ICSCRM'99), held October 10-15, 1999 in Research Triangle Park, North Carolina. Over 650 participants from 25 countries attended the conference. This attendance was the highest in the conference series to date.

This record attendance and the large number of papers submitted attest to the rapidly increasing interest in wide bandgap semiconductors in both academic and industrial communities. Contained in the two volumes of these proceedings are 401 papers, 19 of which were invited. They document our present understanding of the many topics of interest, such as the growth of bulk crystals, the growth of epitaxial layers, theoretical approaches, materials characterization, device processing and design, fabrication and characterization of electronic and optoelectronic devices, some with outstanding performance.

The success of the conference was due in large part to the labor of many people on the various committees as well as the generous support of four U.S. Government and thirteen industrial sponsors. We wish to thank the students from the University of Pittsburgh (Song Bai, Oleg Shigiltchoff, and Yevgeniy Shishkin) and Carnegie Mellon University (S.-Y. Ha, T. Jang, T. Kuhr, and E. Sanchez) for their hard work in getting the papers organized and reviewed. We also wish to thank the students from the University of South Carolina for helping the session chairpersons and handling the microphones for questions during the conference. Finally, we thank the staff of the North Carolina State University Department of Continuing Education for their hard work in organizing the conference, especially Connie McElroy-Bacon, Cindy Allen and Dee Dee Coon.

The next conference will be held in October, 2001 in Tsukuba, Japan. Prof. S. Yoshida of Saitama University will chair the Organizing Committee, Prof. H. Matsunami of Kyoto University will chair the International Steering Committee and Prof. S. Nakashima of Miyazaki University will chair the Sponsor Committee. We wish the organizers of the next conference much success.

Durham, Pittsburgh, October 1999

Calvin H. Carter, Jr.

Robert P. Devaty

Gregory S. Rohrer

## OVERVIEW

### PART 1:

<b>Chapter 1:</b>	<b>SiC Bulk Growth .....</b>	<b>1</b>
<b>Chapter 2:</b>	<b>SiC Epitaxy and Thin Film Growth.....</b>	<b>123</b>
	2.1 Homoepitaxial Growth .....	125
	2.2 Heteroepitaxy and Thin Film Growth .....	241
<b>Chapter 3:</b>	<b>Physical Properties of SiC.....</b>	<b>333</b>
	3.1 Surfaces and Interfaces .....	335
	3.2 Structure.....	431
	3.3 Optical Properties .....	545
	3.4 Electrical Properties.....	703
	3.5 Magnetic Resonance .....	785
	<b>Author Index.....</b>	<b>xxxix</b>
	<b>Keyword Index .....</b>	<b>liii</b>

### PART 2:

<b>Chapter 4:</b>	<b>Processing of SiC.....</b>	<b>829</b>
	4.1 Polishing .....	837
	4.2 Doping and Implantation .....	849
	4.3 Contacts and Etching.....	981
	4.4 Oxides and Other Dielectrics.....	1065
	4.5 Micromachining.....	1141
<b>Chapter 5:</b>	<b>SiC Devices .....</b>	<b>1153</b>
	5.1 Surveys.....	1155
	5.2 Unipolar Devices .....	1167
	5.3 Bipolar Devices.....	1319
	5.4 Sensors .....	1431
<b>Chapter 6:</b>	<b>Growth of III-Nitrides and Related Materials.....</b>	<b>1451</b>
<b>Chapter 7:</b>	<b>Physical Properties of III-Nitrides .....</b>	<b>1531</b>
	7.1 Surfaces and Interfaces .....	1533
	7.2 Structure.....	1549
	7.3 Optical and Electrical Properties .....	1561
<b>Chapter 8:</b>	<b>III-Nitrides: Processing and Devices.....</b>	<b>1607</b>
	<b>Author Index.....</b>	<b>1659</b>
	<b>Keyword Index .....</b>	<b>1673</b>

## Table of Contents

Sponsors .....	v
Committees .....	vi
Preface .....	ix
Overview .....	x

### **PART 1:**

#### **Chapter 1: SiC Bulk Growth**

##### **Status of Large Diameter SiC Crystal Growth for Electronic and Optical Applications**

D. Hobgood, M. Brady, W. Brixius, G. Fechko, R. Glass, D. Henshall, J. Jenny, R. Leonard, D. Malta, St.G. Müller, V. Tsvetkov and C.H. Carter, Jr. ....	3
--	---

##### **Large Diameter PVT Growth of Bulk 6H SiC Crystals**

D.W. Snyder, V.D. Heydemann, W.J. Everson and D.L. Barrett .....	9
--	---

##### **Progress in SiC Bulk Growth**

M. Anikin, O. Chaix, E. Pernot, B. Pelissier, M. Pons, A. Pisch, C. Bernard, P. Grosse, C. Faure, Y. Grange, G. Basset, C. Moulin and R. Madar .....	13
---	----

##### **Generation and Properties of Semi-Insulating SiC Substrates**

S. Wang, A. Powell, J. Redwing, E. Piner and A. W. Saxler .....	17
---	----

##### **Vanadium-free Semi-insulating 4H-SiC Substrates**

W.C. Mitchel, A. Saxler, R. Perrin, J. Goldstein, S.R. Smith, A.O. Evwaraye, J.S. Solomon, M. Brady, V. Tsvetkov and C.H. Carter, Jr. ....	21
---	----

##### **Numerical Simulation of SiC Boule Growth by Sublimation**

R. Madar, M. Pons, J.-M. Dedulle, E. Blanquet, A. Pisch, P. Grosse, C. Faure, M. Anikin and C. Bernard .....	25
---	----

##### **Global Numerical Simulation of Heat and Mass Transfer during SiC Bulk Crystal PVT Growth**

M. Selder, L. Kadinski, F. Durst, T.L. Straubinger, D. Hofmann and P.J. Wellmann .....	31
--	----

##### **An Analytical Study of the SiC Growth Process from Vapor Phase**

D.I. Cherednichenko, Y.I. Khlebnikov, I.I. Khlebnikov, S.I. Soloviev and T.S. Sudarshan .....	35
--	----

##### **Growth Rate Control in SiC-Physical Vapor Transport Method Through Heat Transfer Modeling and Non-Stationary Process Conditions**

T.L. Straubinger, M. Bickermann, M. Grau, D. Hofmann, L. Kadinski, S.G. Müller, M. Selder, P.J. Wellmann and A. Winnacker .....	39
--	----

##### **Experimental and Theoretical Analysis of the Thermal Conductivity of SiC Powder as Source Material for SiC Bulk Growth**

St.G. Müller, J. Fricke, D. Hofmann, R. Horn, O. Nilsson and B. Rexer .....	43
---	----

##### **Seed Surface Preparation for SiC Sublimation Growth**

B. Pelissier, C. Moulin, E. Pernot, M. Anikin, P. Grosse, C. Faure, B. Ferrand, M. Couchaud, G. Basset and R. Madar .....	47
--	----



**Single Crystal Growth of 6H-SiC on Saw-Damaged Substrate by Sublimation****Method**

S. Okada, T. Nishiguchi, T. Shimizu, M. Sasaki, S. Oshima and S. Nishino ..... 51

**Thermal Decomposition Cavities in Physical Vapor Transport Grown SiC**

E.K. Sanchez, V.D. Heydemann, D.W. Snyder, G.S. Rohrer and M. Skowronski ..... 55

**Initial Stage of Crystallization in the Growth of Silicon Carbide on Substrate with Micropipes**

I.I. Khlebnikov, D.I. Cherednichenko, Y. Khlebnikov and T.S. Sudarshan ..... 59

**Nucleation of Dislocations during Physical Vapor Transport Growth of Silicon Carbide**

E.K. Sanchez, V.D. Heydemann, D.W. Snyder, G.S. Rohrer and M. Skowronski ..... 63

**Plastic Deformation and Residual Stresses in SiC Boules Grown by PVT**

S. Ha, G.S. Rohrer, M. Skowronski, V.D. Heydemann and D.W. Snyder ..... 67

**Digital X-Ray Imaging of SiC PVT Process: Analysis of Crystal Growth and Powder Source Degradation**

P.J. Wellmann, M. Bickermann, D. Hofmann, L. Kadinski, M. Selder, T.L. Straubinger and A. Winnacker ..... 71

**SiC Single Crystal Growth Rate Measurement by *in-Situ* Observation using the Transmission X-Ray Technique**

N. Oyanagi, S. Nishizawa, T. Kato, H. Yamaguchi and K. Arai ..... 75

**Role of Temperature Gradient in Bulk Crystal Growth of SiC**

C. M. Balkas, A. A. Maltsev, M. D. Roth and N. K. Yushin ..... 79

**Pressure Effect in Sublimation Growth of Bulk SiC**

Y. Kitou, W. Bahng, S. Nishizawa, S. Nishino and K. Arai ..... 83

**Study of Nitrogen Incorporation in 6H-SiC Single Crystals Grown by PVT**

D. Schulz, K. Irmscher, J. Dolle, W. Eiserbeck, T. Müller, H.-J. Rost, D. Siche, G. Wagner and J. Wollweber ..... 87

**Evaporation Behavior of SiC Powder for Single Crystal Growth - An Experimental Study on Thermodynamics and Kinetics**

A. Pisch, A. M. Ferrara, C. Chatillon, E. Blanquet, M. Pons, C. Bernard, M. Anikin and R. Madar ..... 91

**Considerations on the Crystal Morphology in the Sublimation Growth of SiC**

P. Råback, R. Yakimova, M. Syväjärvi, T. Iakimov, R. Nieminen and E. Janzén ..... 95

**Shape of SiC Bulk Single Crystal Grown by Sublimation**

S. Nishizawa, Y. Kitou, W. Bahng, N. Oyanagi, M. N. Khan and K. Arai ..... 99

**Enlargement of SiC Single Crystal: Enhancement of Lateral Growth using Tapered Graphite Lid**

W. Bahng, Y. Kitou, S. Nishizawa, H. Yamaguchi, M. N. Khan, N. Oyanagi, K. Arai and S. Nishino ..... 103

**Top-seeded Solution Growth of Bulk SiC: Search for Fast Growth Regimes**

B.M. Epelbaum, D. Hofmann, M. Müller and A. Winnacker ..... 107

**Controlled Growth of Bulk 15R-SiC Single Crystals by the Modified Lely Method**

N. Schulze, D. Barrett, M. Weidner and G. Pensl ..... 111

**Crystal Growth of 15R-SiC Boules by Sublimation Method**

T. Nishiguchi, S. Okada, M. Sasaki, H. Harima and S. Nishino ..... 115

**Growth of 3C SiC Single Crystals from Convection Dominated Melts**

J. Wollweber, V. Chévrier, D. Siche and Th. Duffar ..... 119

**Chapter 2: SiC Epitaxy and Thin Film Growth****2.1 Homoepitaxial Growth****An Overview of SiC Growth**

H. Matsunami ..... 125

**Fast SiC Epitaxial Growth in a Chimney CVD Reactor and HTCVD Crystal****Growth Developments**A. Ellison, J. Zhang, W. Magnusson, A. Henry, Q. Wahab, J.P. Bergman,  
C. Hemmingsson, N.T. Son and E. Janzén ..... 131**Morphology Control for Growth of Thick Epitaxial 4H SiC Layers**

J. Zhang, A. Ellison and E. Janzén ..... 137

**Vertical Hot-Wall Type CVD for SiC Growth**

K. Takahashi, M. Uchida, M. Kitabatake and T. Uenoyama ..... 141

**LPCVD Growth and Structural Properties of 4H-SiC Epitaxial Layers**

H. Tsuchida, I. Kamata, T. Jikimoto and K. Izumi ..... 145

**3-D Computational Modeling of SiC Epitaxial Growth in a Hot Wall Reactor**

W. Ji, P. M. Lofgren, C. Hallin and C.-Y. Gu ..... 149

**3-D Thermal and Flow Modeling of Hot Wall Epitaxial Chemical Vapor Deposition****Reactors, Heated by Induction**

P. M. Lofgren, C. Hallin, C.-Y. Gu and W. Ji ..... 153

**The Development of Resistive Heating for the High Temperature Growth of  $\alpha$ -SiC using a Vertical CVD Reactor**E. Eshun, C. Taylor, N. Fama Diagne, J. Griffin, M.G. Spencer, I. Ferguson,  
A. Gurary and R. Stall ..... 157**Initial Results on Thick 4H-SiC Epitaxial Layers Grown Using Vapor Phase Epitaxy**

L.B. Rowland, G.T. Dunne and J.A. Freitas, Jr. .... 161

**High Growth Rate Epitaxy of Thick 4H-SiC Layers**

M. Syväjärvi, R. Yakimova, H. Jacobsson, M.K. Linnarsson, A. Henry and E. Janzén ..... 165

**Competitive Growth between Deposition and Etching in 4H-SiC CVD Epitaxy****Using Quasi-Hot Wall Reactor**M. Kushibe, Y. Ishida, H. Okumura, T. Takahashi, K. Masahara, T. Ohno, T. Suzuki,  
T. Tanaka, S. Yoshida and K. Arai ..... 169**Multi-Wafer VPE Growth and Characterization of SiC Epitaxial Layers**H.D. Nordby, Jr., M.J. O'Loughlin, M.F. MacMillan, A.A. Burk, Jr.  
and J.D. Oliver, Jr. .... 173**Homoepitaxy of Silicon Carbide Using the Single Precursor 1,3-Disilabutane**

S. Y. Lee, K.-W. Lee and Y. Kim ..... 177

<b>Supersonic Seeded Beam Assisted Growth of Epitaxial Silicon Carbide</b> K.D. Jamison, M.L. Kempel, R.L. Woodin, J.D. Shovlin, D. Beck, Q. Li and M.E. Kordesch .....	181
<b>4H-SiC Substrate Orientation Effects on Hydrogen Etching and Epitaxial Growth</b> B.E. Landini and G.R. Brandes .....	185
<b>4H-SiC (11<math>\bar{2}</math>0) Epitaxial Growth</b> T. Kimoto, T. Yamamoto, Z.Y. Chen, H. Yano and H. Matsunami .....	189
<b>Homoepitaxial Growth of 6H SiC on Single Crystalline Spheres</b> K. Christiansen, S. Christiansen, H.P. Strunk and R. Helbig .....	193
<b>Morphological Stability of 6H-SiC Epitaxial Layer on Hemispherical Substrates Prepared by Chemical Vapor Deposition</b> S. Nishino, Y. Nishio, Y. Masuda, Y. Chen and C. Jacob .....	197
<b>Growth of SiC on 6H-SiC {01<math>\bar{1}</math>4} Substrates by Gas Source Molecular Beam Epitaxy</b> S. Nakamura, T. Hatayama, T. Kimoto, T. Fuyuki and H. Matsunami .....	201
<b>Molecular Beam Epitaxial Growth of Heteropolytypic and Low-Dimensional Structures of SiC</b> A. Fissel, U. Kaiser, B. Schröter, J. Kräußlich, H. Hobert and W. Richter .....	205
<b>Thermodynamical Consideration of the Epitaxial Growth of SiC Polytypes</b> A. Fissel .....	209
<b>Mechanisms of SiC(111) Step Flow Growth</b> P. J. Stout .....	213
<b>Mechanism of Various Defects Formation in Epitaxial Layer Prepared by Sublimation Epitaxy</b> T. Furusho, K. Matsumoto, H. Harima and S. Nishino .....	217
<b>Investigation of 3C-SiC Epitaxial Layers Grown by Sublimation Epitaxy</b> D.V. Davydov, A.A. Lebedev, A.S. Tregubova, V.V. Kozlovski, A.N. Kuznetsov and E.V. Bogdanova .....	221
<b>Growth of SiC and GaN on Porous Buffer Layers</b> M. Mynbaeva, N.S. Savkina, A.S. Tregubova, M.P. Scheglov, A.A. Lebedev, A. Zubrilov, A. Titkov, A. Kryganovski, K. Mynbaev, N. Seredova, D. Tsvetkov, S. Stepanov, A. Cherenkov, I. Kotousova and V. Dmitriev .....	225
<b>4H-SiC Layers Grown by Liquid Phase Epitaxy on 4H-SiC Off-Axis Substrates</b> N. Kuznetsov, A. Morozov, D. Baumann, V. Ivantsov, V. Sukhoveev, I. Nikitina, A. Zubrilov, S. Rendakova, V. Dmitriev, D. Hofman and P. Masri .....	229
<b>Temperature Gradient Effect on SiC Epitaxy in Liquid Phase</b> M. N. Khan, S. Nishizawa, W. Bahng and K. Arai .....	233
<b>Micropipe Healing in Liquid Phase Epitaxial Growth of SiC</b> R. Yakimova, M. Syväjärvi, S. Rendakova, V. Dmitriev, A. Henry and E. Janzén .....	237
 <b>2.2 Heteroepitaxy and Thin Film Growth</b>	
<b>Growth of CVD Thin Films and Thick LPE 3C SiC in a Specially Designed Reactor</b> A. Leycuras .....	241

<b>Lateral Epitaxial Overgrowth and Pendeo Epitaxy of 3C-SiC on Si Substrates</b> S. E. Sadow, G. Carter, B. Geil, T. Zheleva, G. Melnychuck, M.E. Okhuysen, M. S. Mazzola, R.D. Vispute, M. Derenge, M. Ervin and K. Jones .....	245
<b>Selective Epitaxial Growth of Silicon Carbide on Patterned Silicon Substrates Using Hexachlorodisilane and Propane</b> C. Jacob, M.-H. Hong, J. Chung, P. Pirouz and S. Nishino .....	249
<b>The APD Annihilation Mechanism of 3C-SiC Hetero-Epilayer on Si(001) Substrate</b> Y. Ishida, T. Takahashi, H. Okumura, T. Sekigawa and S. Yoshida .....	253
<b>Improvement of 3C-SiC Surface Morphology on Si(100) by Adding HCl Using Atmospheric CVD</b> Y. Chen, Y. Masuda, C. Jacob, T. Shirafuji and S. Nishino .....	257
<b>Carbonization on (100) Silicon for Heteroepitaxial Growth of 3C-SiC</b> H. Shimizu and T. Ohba .....	261
<b>Growth of 3C-SiC/Si Multilayer Heterostructures by Supersonic Free Jets</b> Y. Ikoma, T. Endo, T. Tada, F. Watanabe and T. Motooka .....	265
<b>Formation of High Quality SiC on Si(100) at 900°C using Monomethylsilane Gas-Source MBE</b> H. Nakazawa, M. Suemitsu and S. Asami .....	269
<b>Growth and Characterization of N-Doped SiC Films from Trimethylsilane</b> J. Chen, A.J. Steckl and M.J. Loboda .....	273
<b>The Effect of Ge on the Structure &amp; Morphology of SiC Films Grown on (111) Si Substrates</b> W.L. Sarney, L. Salamanca-Riba, P. Zhou, C. Taylor, M.G. Spencer, R.D. Vispute and K.A. Jones .....	277
<b>In Situ Monitoring of the Effect of Ge on the SiC Growth on (111)Si Surfaces</b> T. Wöhner, Th. Stauden, J.A. Schaefer and J. Pezoldt .....	281
<b>Structural Investigations of the Nucleation and Growth of SiC during Rapid Thermal Conversion of (111)Si</b> V. Cimalla, W. Attenberger, J.K.N. Lindner, B. Stritzker and J. Pezoldt .....	285
<b>The Influence of Foreign Atoms on the early Stages of SiC Growth on (111)Si</b> J. Pezoldt, P. Masri, M. Rouhani Laridjani, M. Averous, T. Wöhner, J.A. Schaefer, Th. Stauden, G. Ecke, R. Pieterwas and L. Spieß .....	289
<b>Studies of the Initial Stages of Silicon Carbide Growth Using Molecular Hydrocarbon and Methyl Radical Gas Species</b> J.S. Gold, J.S. Lannon, Jr., V.L. Tolani, K.S. Ziemer and C.D. Stinespring .....	293
<b>Carbonization of SIMOX Substrates for Fabrication of Single-Crystal SiC-on-Insulator</b> S. Harada, M. Arita, Y. Ikoma and T. Motooka .....	297
<b>SOL Thinning Effects on 3C-SiC on SOI</b> N. Planes, H. Möller, J. Camassel, Y. Stoemenos, L. Falkovski, M. Eickhoff and G. Krötz .....	301
<b>Low Temperature Growth of 3C-SiC on Silicon for Advanced Substrate Development</b> M.E. Okhuysen, M. S. Mazzola and Y.-H. Lo .....	305

### **Epitaxial Growth of $\beta$ -SiC on Ion-Beam Synthesized $\beta$ -SiC: Structural Characterization**

- A. Romano-Rodríguez, A. Pérez-Rodríguez, C. Serre, J.R. Morante, J. Esteve, M.C. Acero, R. Kögler, W. Skorupa, M. Östling, N. Nordell, S. Karlsson and J. Van Landuyt ..... 309

### **Growth of Single Crystalline 3C-SiC and AlN on Si using Porous Si as a Compliant Seed Crystal**

- D. Purser, M. Jenkins, D. Lieu, F. Vaccaro, A. Faik, M.-A. Hasan, H.J. Leamy, C. Carlin, M.R. Sardela Jr., Q. Zhao, M. Willander and M. Karlsteen ..... 313

### **The Growth and Characterization of 3C-SiC/SiN<sub>x</sub>/Si Structure**

- K.C. Kim, C.I. Park, K.S. Nahm and E.-K. Suh ..... 317

### **The Diffusion Coefficient of Silicon in Thin SiC Layers as a Criterion for the Quality of the Grown Layers**

- V. Cimalla, Th. Wöhner and J. Pezoldt ..... 321

### **Plasma Enhanced Chemical Vapor Deposition and Characterization of Hydrogenated Amorphous SiC Films on Si**

- Y. Wang, J. Lin, Z.C. Feng, S.J. Chua and C.H.H. Alfred ..... 325

### **Thin Films of $\alpha$ -Si<sub>1-x</sub>C<sub>x</sub>:H Deposited by PECVD: The R.F. Power and H<sub>2</sub> Dilution Role**

- R.J. Prado, M.C.A. Fantini, M.H. Tabacniks, I. Pereyra and A.M. Flank ..... 329

## **Chapter 3: Physical Properties of SiC**

### **3.1 Surfaces and Interfaces**

#### **Surface Composition of 4H-SiC as a Function of Temperature**

- K.W. Bryant and M.J. Bozack ..... 335

#### **Stacking Rearrangement on SiC Surfaces: A Possible Seed for Polytype Heterostructure Growth**

- U. Starke, J. Bernhardt, J. Schardt, A. Seubert and K. Heinz ..... 341

#### **Atomic Structure of 6H-SiC(0001)-(2x2)<sub>c</sub>**

- J. Bernhardt, A. Seubert, M. Nerding, U. Starke and K. Heinz ..... 345

#### **Ab Initio Calculation on Clean and Oxygen Covered 6H-SiC(0001) Surfaces:**

##### **( $\sqrt{3} \times \sqrt{3}$ )R30° Reconstruction**

- W. Lu, P. Krüger and J. Pollmann ..... 349

#### **Photo-Emission Electron Microscopy (PEEM) of Cleaned and Etched 6H-SiC(0001)**

- J.D. Hartman, K. Naniwae, C. Petrich, V. Ramachandran, R.M. Feenstra, R.J. Nemanich and R.F. Davis ..... 353

#### **High Resolution Electron Energy Loss Spectroscopy of $\sqrt{3} \times \sqrt{3}$ 6H-SiC(0001)**

- K. Takahashi, M. Uchida and M. Kitabatake ..... 357

#### **In-Situ RHEED Analysis During $\alpha$ -SiC Homoepitaxy on (0001)Si- and (0001)C-Faces by Gas Source Molecular Beam Epitaxy**

- T. Hatayama, T. Fuyuki, S. Nakamura, K. Kurobe, T. Kimoto and H. Matsunami ..... 361

<b>(10<math>\bar{1}</math>0)- and (11<math>\bar{2}</math>0)-Surfaces in 2H-, 4H- and 6H-SiC</b> E. Rauls, Z. Hajnal, P. Deák and Th. Frauenheim .....	365
<b>Theory of Structural and Electronic Properties of Cubic SiC Surfaces</b> J. Pollmann, P. Krüger and W. Lu .....	369
<b>Characterization of Anisotropic Step-Bunching on As-Grown SiC Surfaces</b> M. Syväjärvi, R. Yakimova, T. Iakimov and E. Janzén .....	375
<b>Observation of Macrostep Formation on the (0001) Facet of Bulk SiC Crystals</b> N. Ohtani, M. Katsuno, T. Aigo, H. Yashiro and M. Kanaya .....	379
<b>Silicate Monolayers on the Hexagonal Surfaces of 4H- and 6H-SiC</b> J. Bernhardt, J. Schardt, U. Starke and K. Heinz .....	383
<b>Electronic and Atomic Structure of an Ordered Silicate Adlayer on Hexagonal SiC</b> M. Hollering, N. Sieber, F. Maier, J. Ristein, L. Ley, J.D. Riley, R.C.G. Leckey, F. Leisenberger and F. Netzer .....	387
<b>Photoemission Study of the Silicate Adlayer Reconstruction on Si-terminated 6H-SiC (0001)</b> N. Sieber, M. Hollering, J. Ristein and L. Ley .....	391
<b>Initial Oxidation of the Si-terminated 6H-SiC(0001) 3x3 Surface</b> F. Amy, Y.-K. Hwu, C. Brylinski and P. Soukiassian .....	395
<b>XPS Analysis of SiO<sub>2</sub>/SiC Interface Annealed in Nitric Oxide Ambient</b> H.-F. Li, S. Dimitrijević, D. Sweatman and H.B. Harrison .....	399
<b>Surface Studies on Thermal Oxidation on 4H-SiC Epilayer</b> A. Koh, A. Kestle, S.P. Wilks, P.R. Dunstan, C.J. Wright, M. Pritchard, G. Pope, P.A. Mawby and W.R. Bowen .....	403
<b>Quantified Conditions for Reduction of ESO Contamination During SiC Metalization</b> G.Y. McDaniel, S.T. Fenstermaker, D.E. Walker, Jr., W.V. Lampert, S.M. Mukhopadhyay and P.H. Holloway .....	407
<b>Thermal Annealing Effect on TiN/Ti Layers on 4H-SiC: Metal-Semiconductor Interface Characterization</b> D. Defives, O. Durand, F. Wyczisk, J. Olivier, O. Noblanc and C. Brylinski .....	411
<b>A Surface/Interfacial Structural Model of Pd Ultra-thin Film on SiC at Elevated Temperatures</b> W.J. Lu, D.T. Shi, T.R. Crenshaw, A. Burger and W.E. Collins .....	415
<b>Study of a Clean Surface of <math>\alpha</math> - SiC and its Metallization Process by Cu, Au and Ni Using STM and Electron/Photon Spectroscopies</b> M. Iwami, M. Hirai, M. Kusaka, I. Mihara, T. Saito, M. Yamaguchi, T. Morii and M. Watanabe .....	419
<b>Monolayer Growth Modes of Re and Nb on the Polar Faces of 4H-SiC</b> K.W. Bryant and M.J. Bozack .....	423
<b>Group-III Adsorption and Bond Stacking on SiC(111) Surfaces</b> U. Grossner, J. Furthmüller and F. Bechstedt .....	427

### 3.2 Structure

<b>Characterization of SiC Using Synchrotron White Beam X-Ray Topography</b>	
M. Dudley and X. Huang .....	431
<b>Growth of Low Micropipe Density SiC Wafers</b>	
A. Powell, S. Wang and G. Brandes .....	437
<b>Investigation of the Origin of Micropipe Defect</b>	
A. Okamoto, N. Sugiyama, T. Tani and N. Kamiya .....	441
<b>Analysis on the Formation and Elimination of Filamentary and Planar Voids in Silicon Carbide Bulk Crystals</b>	
D. Hofmann, M. Bickermann, W. Hartung and A. Winnacker .....	445
<b>Origin of the Internal Stress Around the Micropipe of 6H-SiC Single Crystal</b>	
T. Kato, H. Ohsato and T. Okuda .....	449
<b>Structural Investigation on the Nature of Surface Defects Present in Silicon Carbide Wafers Containing Varying Amount of Micropipes</b>	
M. Shamsuzzoha, S. E. Sadow, T.E. Schattner, L. Jin, M. Dudley, S.V. Rendakova and V.A. Dmitriev .....	453
<b>In-Situ Observation of SiC Bulk Single Crystal Growth by X-Ray Topography</b>	
T. Kato, N. Oyanagi, H. Yamaguchi, Y. Takano, S. Nishizawa and K. Arai .....	457
<b>X-Ray Topographic Study of SiC Crystal at High Temperature</b>	
H. Yamaguchi, Na. Oyanagi, T. Kato, Y. Takano, S. Nishizawa, W. Bahng, S. Yoshida and K. Arai .....	461
<b>Synchrotron White Beam Topography Studies of 2H SiC Crystals</b>	
M. Dudley, W. Huang, W.M. Vetter, P. Neudeck and J.A. Powell .....	465
<b>Synchrotron White Beam X-Ray Topography and Atomic Force Microscopy Studies of a 540R-SiC Lely Platelet</b>	
W.M. Vetter, M. Dudley, W. Huang, P. Neudeck and J.A. Powell .....	469
<b>X-Ray Characterization of 3 Inch Diameter 4H and 6H-SiC Experimental Wafers</b>	
T.A. Kuhr, W.M. Vetter, M. Dudley and M. Skowronski .....	473
<b>Origin of Threading Dislocation Arrays in SiC Boules Grown by PVT</b>	
S. Ha, N.T. Nuhfer, M. De Graef, G.S. Rohrer and M. Skowronski .....	477
<b>Structural Characterization of Silicon Carbide Etched by Using a Combination of Ion Implantation and Wet Chemical Etching</b>	
T. Henkel, G. Ferro, S. Nishizawa, H. Pressler, Y. Tanaka, H. Tanoue and N. Kobayashi .....	481
<b>Polytype and Defect Control of Two Inch Diameter Bulk SiC</b>	
M. Sasaki, H. Shiomi, H. Harima and S. Nishino .....	485
<b>Correlation of EBIC and SWBXT Imaged Defects and Epilayer Growth Pits in 6H-SiC Schottky Diodes</b>	
C.M. Schnabel, M. Tabib-Azar, P.G. Neudeck, S.G. Bailey, H.B. Su, M. Dudley and R.P. Raffaele .....	489
<b>Investigation of Low Angle Grain Boundaries in Modified-Lely SiC Crystals by High Resolution X-Ray Diffractometry</b>	
M. Katsuno, N. Ohtani, T. Aigo, H. Yashiro and M. Kanaya .....	493

<b>Structural, Electrical and Optical Properties of Bulk 4H and 6H p-Type SiC</b> E.V. Kalinina, A.S. Zubrilov, N.I. Kuznetsov, I.P. Nikitina, A.S. Tregubova, M.P. Shcheglov and V.Ya. Bratus' .....	497
<b>High Order X-Ray Diffraction and Internal Atomic Layer Roughness of Epitaxial and Bulk SiC Materials</b> G. Xu and Z.C. Feng .....	501
<b>4H-SiC CVD Epitaxial Layers with Improved Structural Quality Grown on SiC Wafers with Reduced Micropipe Density</b> E.V. Kalinina, A. Zubrilov, V. Solov'ev, N. Kuznetsov, A. Hallen, A. Konstantinov, S. Karlsson, S. Rendakova and V. Dmitriev .....	505
<b>Structural and Optical Studies of Low-Doped n-6H SiC Layers Grown by Vacuum Sublimation</b> N.S. Savkina, A.A. Lebedev, A.S. Tregubova and M.P. Scheglov .....	509
<b>Stacking Fault Energy of 6H-SiC and 4H-SiC Single Crystals</b> M.-H. Hong, A.V. Samant and P. Pirouz .....	513
<b>Deformation Tests on 4H-SiC Single Crystals between 900°C and 1360°C and the Microstructure of the Deformed Samples</b> J.L. Demenet, M.-H. Hong and P. Pirouz .....	517
<b>Void Shapes in the Si (111) Substrate at the Heteroepitaxial Thin Film / Si Interface</b> J. Jinschek, U. Kaiser and W. Richter .....	521
<b>Defect Characterization in 3C-SiC Films Grown on Thin and Thick Silicon Top Layers of SIMOX</b> M.-H. Hong, J. Chung, F. Namavar and P. Pirouz .....	525
<b>Structural Characteristics of 3C-SiC Films Epitaxially Grown on the Si/Si<sub>3</sub>N<sub>4</sub>/SiO<sub>2</sub> System</b> S. Zappe, H. Möller, G. Krötz, M. Eickhoff, W. Skorupa, E. Obermeier and J. Stoemenos .....	529
<b>Illusion of New Polytypes</b> U. Kaiser, A. Chuvilin and W. Richter .....	533
<b>Microstructural, Optical and Electronic Investigation of Anodized 4H-SiC</b> S. Zangoie, P.O.Å. Persson, J.N. Hilfiker, L. Hultman, H. Arwin and Q. Wahab .....	537
<b>Characterization of Polycrystalline SiC Grown on SiO<sub>2</sub> and Si<sub>3</sub>N<sub>4</sub> by APCVD for MEMS Applications</b> C.-H. Wu, C.A. Zorman and M. Mehregany .....	541

### 3.3 Optical Properties

<b>Theory of Below Gap Absorption Bands in n-Type SiC Polytypes; Or, How SiC Got Its Colors</b> W.R.L. Lambrecht, S. Limpijumnong, S. Rashkeev and B. Segall .....	545
<b>Absorption Bands Associated with Conduction Bands and Impurity States in 4H and 6H SiC</b> S.G. Sridhara, S. Bai, O. Shigiltchoff, R.P. Devaty and W.J. Choyke .....	551



<b>Determination of the Polarization Dependence of the Free-Carrier-Absorption in 4H-SiC at High-Level Photoinjection</b>	
V. Grivickas, A. Galeckas, P. Grivickas and J. Linnros .....	555
<b>Bandstructure and Transport Properties of 4H- and 6H-SiC: Optically Detected Cyclotron Resonance Investigations</b>	
B.K. Meyer, D.M. Hofmann, D. Volm, W.M. Chen, N.T. Son and E. Janzén .....	559
<b>Hole Effective Masses in 4H SiC Determined by Optically Detected Cyclotron Resonance</b>	
N.T. Son, P.N. Hai, W.M. Chen, C. Hallin, B. Monemar and E. Janzén .....	563
<b>Differential Absorption Measurement of Valence Band Splittings in 4H SiC</b>	
S.G. Sridhara, S. Bai, O. Shigiltchoff, R.P. Devaty and W.J. Choyke .....	567
<b>Anisotropic Dielectric Function Properties of Semi-Insulating 4H-SiC Determined from Spectroscopic Ellipsometry</b>	
M. Kildemo, M.B. Mooney, P.V. Kelly, C. Sudre and G.M. Crean .....	571
<b>Optical Characterization of 4H-SiC by Variable Angle of Incidence Spectroscopic Ellipsometry</b>	
O.P.A. Lindquist, H. Arwin, U. Forsberg, J.P. Bergman and K. Järrendahl .....	575
<b>Isotope Effects on the Raman Spectrum of SiC</b>	
S. Rohmfeld, M. Hundhausen, L. Ley, N. Schulze and G. Pensl .....	579
<b>Disappearance of the LO-Phonon Line in the UV-Raman Spectrum of 6H-SiC</b>	
R. Püsche, S. Rohmfeld, M. Hundhausen and L. Ley .....	583
<b>Selectively Resonant Raman Spectra of Folded Phonon Modes in SiC</b>	
T. Tomita, S. Saito, M. Baba, M. Hundhausen, T. Suemoto and S. Nakashima .....	587
<b>Raman Spectral Profiles of Folded Longitudinal Modes in SiC under Off-Resonant Condition</b>	
S. Nakashima, H. Harima, T. Tomita and T. Suemoto .....	591
<b>Raman Spectroscopy on Biaxially Strained Epitaxial Layers of 3C-SiC on Si</b>	
S. Rohmfeld, M. Hundhausen, L. Ley, C.A. Zorman and M. Mehregany .....	595
<b>Characterization of 3C-SiC/SOI Deposited with HMDS</b>	
N. Planes, P. Aboughé-Nzé, M. Ravetz, S. Contreras, P. Vicente, T. Chassagne, B. Fraisse, J. Camassel, Y. Monteil and S. Rushworth .....	599
<b>Raman Imaging Characterization of Electric Properties of SiC Near a Micropipe</b>	
H. Harima, T. Hosoda and S. Nakashima .....	603
<b>Carrier Density Evaluation in P-Type SiC by Raman Scattering</b>	
H. Harima, T. Hosoda and S. Nakashima .....	607
<b>Shallow Nitrogen Donor States in 4H-SiC Investigated by Photothermal Ionization Spectroscopy</b>	
C.Q. Chen, J. Zeman, F. Engelbrecht, C. Peppermüller, R. Helbig and G. Martinez .....	611
<b>Characterization of Silicon Carbide using Raman Spectroscopy</b>	
J.C. Burton, F.H. Long, Y. Khlebnikov, I. Khlebnikov, M. Parker and T.S. Sudarshan .....	615
<b>Photoluminescence Study of CVD Layers Highly Doped with Nitrogen</b>	
U. Forsberg, A. Henry, M.K. Linnarsson and E. Janzén .....	619

<b>Low Temperature Photoluminescence of <math>^{13}\text{C}</math> Enriched SiC-Crystals Grown by the Modified Lely Method</b>	
H. Sadowski, C. Peppermüller, N. Schulze, M. Laube, G. Pensl and R. Helbig .....	623
<b>Sub-<math>\mu\text{m}</math> Scale Photoluminescence Image of SiC and GaN at a Low Temperature</b>	
M. Yoshimoto, M. Goto, J. Saraie, T. Kimoto and H. Matsunami .....	627
<b>Vanadium-Related Center in 4H Silicon Carbide</b>	
B. Magnusson, Mt. Wagner, N.T. Son and E. Janzén .....	631
<b>Spectroscopic Investigation of Vanadium Acceptor Level in 4H and 6H-SiC</b>	
V. Lauer, G. Brémond, A. Souifi, G. Guillot, K. Chourou, R. Madar and B. Clerjaud .....	635
<b>Photoluminescence and DLTS Measurements of 15 MeV Erbium Implanted 6H and 4H SiC</b>	
Y. Shishkin, W.J. Choyke, R.P. Devaty, N. Achtziger, Th. Opfermann and W. Witthuhn .....	639
<b>Electronic States of Vacancies in 3C- and 4H-SiC</b>	
A. Zywiets, J. Furthmüller and F. Bechstedt .....	643
<b>Pseudo-Donors in SiC</b>	
T. Egilsson, I.G. Ivanov, A. Henry and E. Janzén .....	647
<b>Metastability of a Hydrogen-Related Defect in 6H-SiC</b>	
A. Henry, T. Egilsson, I.G. Ivanov and E. Janzén .....	651
<b>Optical Characterization of Lattice Damage and Recovery in Ion-Implanted and Pulsed Excimer Laser Irradiated 4H-SiC</b>	
D. Sands, P.H. Key, M. Schlaf, C.D. Walton, C.J. Anthony and M.J. Uren .....	655
<b>Microscopic Probing of Raman Scattering and Photoluminescence on C-Al Ion Co-Implanted 6H-SiC</b>	
Z.C. Feng, S.J. Chua, Z.X. Shen, K. Tone and J.H. Zhao .....	659
<b>Confocal Raman Microprobe of Lattice Damage in <math>\text{N}^+</math> Implanted 6H-SiC</b>	
N. Mestres, F. Alsina, F.J. Campos, J. Pascual, E. Morvan, P. Godignon and J. Millán .....	663
<b>Ion Beam Induced Change in the Linear Optical Properties of SiC</b>	
E.K. Williams, D. Ila, D.B. Poker, D.K. Hensley and D. J. Larkin .....	667
<b>Free Carrier Diffusion Measurements in Epitaxial 4H-SiC with a Fourier Transient Grating Technique: Injection Dependence</b>	
P. Grivickas, J. Linnros and V. Grivickas .....	671
<b>Time-Resolved Photoluminescence Study of Bound and Free Excitons in 4H SiC</b>	
G. Pozina, J.P. Bergman, C. Hemmingsson and E. Janzén .....	675
<b>Optical Lifetime Measurements in 4H SiC</b>	
Y. Shishkin, R.P. Devaty and W.J. Choyke .....	679
<b>Optical Characterization of 4H-SiC <math>\text{p}^+\text{n}^+\text{n}^+</math> Structures Applying Time- and Spectrally Resolved Emission Microscopy</b>	
A. Galeckas, J. Linnros and B. Breitholtz .....	683
<b>Electroluminescence from Implanted and Epitaxially Grown pn-Diodes</b>	
F.H.C. Carlsson, L. Storasta, C. Hemmingsson, J.P. Bergman and E. Janzén .....	687

**Avalanche Breakdown Electroluminescence in Silicon Carbide Light Emitting****Diodes**

S. Aboujja, C. Carlone, A. Houdayer, P.F. Hinrichsen and J.-P. Charles ..... 691

**Photon Emission Mechanisms in 6H and 4H-SiC MOSFETs**

C. Banc, E. Bano, T. Ouisse, S. Scharnholz, U. Schmid, W. Wondrak and E. Niemann ..... 695

**Non-Contact Photovoltage Measurements in SiC**

Y. Koshka and M. S. Mazzola ..... 699

**3.4 Electrical Properties****Ionization Energies and Electron Mobilities in Phosphorus- and Nitrogen-Implanted 4H-Silicon Carbide**

M.A. Capano, J. A. Cooper, Jr., M.R. Melloch, A. Saxler and W.C. Mitchel ..... 703

**MicroRaman and Hall Effect Study of n-Type Bulk 4H-SiC**

M. Chafai, J. Jiménez, E. Martin, W.C. Mitchel, A. Saxler and R. Perrin ..... 707

**Electrical Properties of 3C-SiC Grown on Si by CVD Method using  $\text{Si}_2(\text{CH}_3)_6$** 

Y. Masuda, Y. Chen, H. Matsuura, H. Harima and S. Nishino ..... 711

**Electrical and Physical Behavior of SiC Layers on Insulator (SiCOI)**

E. Hugonnard-Bruyère, F. Letertre, L. Di Cioccio, H.J. von Bardeleben, J.L. Cantin, T. Ouisse, T. Billon and G. Guillot ..... 715

**Theoretical Treatments of Band Edges in SiC Polytypes at High Carrier Concentrations**

U. Lindefelt and C. Persson ..... 719

**A Theoretical Study of Electron Drift Mobility Anisotropy in n-Type 4H- and 6H-SiC**

E. Velmre and A. Udal ..... 725

**Theoretical Calculation of the Electron Hall Mobility in n-Type 4H- and 6H-SiC**

H. Iwata and K.M. Itoh ..... 729

**Hall Scattering Factor and Electron Mobility of 4H SiC: Measurements and Numerical Simulation**

G. Rutsch, R.P. Devaty, W.J. Choyke, D.W. Langer, L.B. Rowland, E. Niemann and F. Wischmeyer ..... 733

**Hall Mobility of the Electron Inversion Layer in 6H-SiC MOSFETs**

N.S. Saks, S.S. Mani, A.K. Agarwal and V.S. Hegde ..... 737

**Application and Improvement of the Spreading Resistance Method for p-Type 6H-SiC**

T. Gebel, D. Panknin, R. Riehn, S. Parascandola and W. Skorupa ..... 741

**Theoretical Study of Carrier Freeze-Out Effects on Admittance Spectroscopy and Frequency-Dependent C-V Measurements in SiC**

A.V. Los, M.S. Mazzola and S.E. Sadow ..... 745

**On the Existence of Deep Levels of the Acceptors Ga and In and of the Potential Double Acceptors Zn and Cd in SiC**

N. Achtziger, J. Grillenberger, M. Uhrmacher and W. Witthuhn ..... 749

<b>Correlation between DLTS and Photoluminescence in He-implanted 6H-SiC</b>	
T. Frank, G. Pensl, S. Bai, R.P. Devaty and W.J. Choyke .....	753
<b>Observation of Deep Levels in SiC by Optical-Isothermal Capacitance Transient Spectroscopy</b>	
S. Kobayashi, S. Imai, Y. Hayami, M. Kushibe, T. Shinohe and H. Okushi .....	757
<b>Improved Measurements of High-Field Drift Velocity in Silicon Carbide</b>	
I.A. Khan and J.A. Cooper, Jr. ....	761
<b>A Full Band Monte Carlo Study of High Field Carrier Transport in 4H-SiC</b>	
H.-E. Nilsson, E. Bellotti, K.F. Brennan and M. Hjelm .....	765
<b>Electron Saturated Vertical Velocities in Silicon Carbide Polytypes</b>	
V.I. Sankin and A.A. Lepneva .....	769
<b>High Temperature Effects on the Terahertz Mobility of Hot Electrons in 3C-SiC and 6H-SiC</b>	
E.W.S. Caetano, E.F. Bezerra, V. Lemos, V.N. Freire, E.F. da Silva, Jr. and J.A.P. da Costa .....	773
<b>Electron Beam Induced Current Investigation of High-Voltage 4H Silicon Carbide Diodes</b>	
J. Österman, A. Hallén, M. Jargelius, U. Zimmermann, A. Galeckas and B. Breitholtz .....	777
<b>Measurement of Charge Carrier Lifetime Temperature-Dependence in 4H-SiC Power Diodes</b>	
A. Udál and E. Velmré .....	781

### 3.5 Magnetic Resonance

<b>Donors and Acceptors in SiC - Studies with EPR and ENDOR</b>	
J.-M. Spaeth .....	785
<b>ESR Spectrum of Nitrogen in 6H SiC in the Ground and Excited States</b>	
E.N. Kalabukhova and S.N. Lukin .....	791
<b>Dopant-Related Complexes in SiC</b>	
A. Gali, J. Miró, P. Deák, R.P. Devaty and W.J. Choyke .....	795
<b>The Spatial Distribution of the Electronic Wave Function of the Shallow Boron Acceptor in 4H- and 6H-SiC</b>	
A. v. Duijn-Arnold, J. Mol, R. Verberk, J. Schmidt, E.N. Mokhov and P.G. Baranov .....	799
<b>The Electronic Structure of the Be Acceptor Centers in 6H-SiC</b>	
A. v. Duijn-Arnold, J. Schmidt, O.G. Poluektov, P.G. Baranov and E.N. Mokhov .....	805
<b>Electron Paramagnetic Resonance of the Scandium Acceptor in 4H and 6H Silicon Carbide</b>	
S. Greulich-Weber, M. März, J.-M. Spaeth, E.N. Mokhov and E.N. Kalabukhova .....	809
<b>ESR Study of Delamination in H<sup>+</sup> Implanted Silicon Carbide</b>	
E.A. Chowdhury, T. Seki, T. Izumi, H. Tanaka and T. Hara .....	813
<b>Vacancies and Their Complexes with H in SiC</b>	
P. Deák, A. Gali, B. Aradi, N.T. Son, E. Janzén and W.J. Choyke .....	817

**The Carbon Vacancy Pair in 4H and 6H SiC**

N.T. Son, P.N. Hai, A. Shuja, W.M. Chen, J.L. Lindström, B. Monemar and E. Janzén ..... 821

**Electron Spin Resonance in Neutron-Irradiated n-type 6H-Silicon Carbide**

S. Kanazawa, I. Kimura, M. Okada, T. Nozaki, I. Kanno, S. Ishihara and M. Watanabe ..... 825

**Author Index** .....xxxix**Keyword Index** .....liii**PART 2:****Chapter 4: Processing of SiC****Physics of SiC Processing**

G. Pensl, V.V. Afanas'ev, M. Bassler, T. Frank, M. Laube and M. Weidner ..... 831

**4.1 Polishing****Polishing and Surface Characterization of SiC Substrates**

W.J. Everson, D.W. Snyder and V.D. Heydemann ..... 837

**Comparison of Mechanical and Chemomechanical Polished SiC Wafers Using Photon Backscattering**

W.C. Mitchel, J. Brown, D. Buckanan, R. Bertke, K. Malalingham, F.D. Orazio, Jr., P. Pirouz, H.-J. R. Tseng, U.B. Ramabadran and B. Roughani ..... 841

**Damage-Free Surface Modification of Hexagonal Silicon Carbide Wafers**

T.C. Chandler, Jr., M.B. Lari and T.S. Sudarshan ..... 845

**4.2 Doping and Implantation****Nuclear Transmutation Doping of Phosphorus into 6H-SiC**

S. Tamura, T. Kimoto, H. Matsunami, M. Okada, S. Kanazawa and I. Kimura ..... 849

**Radiation Defects and Doping of SiC with Phosphorus by Nuclear Transmutation Doping (NTD)**

H. Heissenstein, H. Sadowski, C. Peppermüller and R. Helbig ..... 853

**Relationship between Donor Activation and Defect Annealing in 6H-SiC Hot-Implanted with Phosphorus Ions**

T. Ohshima, A. Uedono, H. Itoh, M. Yoshikawa, K. Kojima, S. Okada, I. Nashiyama, K. Abe, S. Tanigawa, T. Frank and G. Pensl ..... 857

**Hot-Implantation of Phosphorus Ions into 4H-SiC**

S. Imai, S. Kobayashi, T. Shinohe, K. Fukuda, Y. Tanaka, J. Senzaki, H. Tanoue, N. Kobayashi and H. Okushi ..... 861

<b>Electrical Characteristics and Surface Morphology for Arsenic Ion-Implanted 4H-SiC at High Temperature</b>	
J. Senzaki, K. Fukuda, S. Imai, Y. Tanaka, N. Kobayashi, H. Tanoue, H. Okushi and K. Arai .....	865
<b>Damage Evolution in Al-implanted 4H SiC</b>	
A. Hallén, P.O.Å. Persson, A.Yu. Kuznetsov, L. Hultman and B.G. Svensson .....	869
<b>Excimer Laser Annealing of Ion-Implanted 6H-Silicon Carbide</b>	
Y. Hishida, M. Watanabe, K. Nakashima and O. Eryu .....	873
<b>High Concentration Doping of 6H-SiC by Ion Implantation: Flash versus Furnace Annealing</b>	
D. Panknin, H. Wirth, W. Anwand, G. Brauer and W. Skorupa .....	877
<b>Consequences of High-Dose, High Temperature Al<sup>+</sup> Implantation in 6H-SiC</b>	
J. Stoemenos, B. Pécz and V. Heera .....	881
<b>Al and Al/C High Dose Implantation in 4H-SiC</b>	
J.M. Bluet, J. Pernot, T. Billon, S. Contreras, J.F. Michaud, J.L. Robert and J. Camassel .....	885
<b>Channeled Implants in 6H Silicon Carbide</b>	
M.S. Janson, A. Hallén, P. Godignon, A.Yu. Kuznetsov, M.K. Linnarsson, E. Morvan and B.G. Svensson .....	889
<b>Damage Reduction in Channeled Ion Implanted 6H-SiC</b>	
E. Morvan, N. Mestres, F.J. Campos, J. Pascual, Anders Hallén, M.K. Linnarsson and A.Yu. Kuznetsov .....	893
<b>Ion Beam Induced Nanocrystallization of SiC</b>	
A. Höfgen, V. Heera, A. Mücklich and W. Skorupa .....	897
<b>High Temperature Implant Activation in 4H and 6H-SiC in a Silane Ambient to Reduce Step Bunching</b>	
S.E. Sadow, J. Williams, T. Isaacs-Smith, M. Capano, J.A. Cooper, M.S. Mazzola, A.J. Hsieh and J.B. Casady .....	901
<b>Characterization of Implantation Layer in (1100) Oriented 4H- and 6H-SiC</b>	
M. Satoh, Y. Nakaike, K. Uchimura and K. Kuriyama .....	905
<b>Electrical and Structural Properties of Al and B Implanted 4H-SiC</b>	
Y. Tanaka, N. Kobayashi, H. Okumura, R. Suzuki, T. Ohdaira, M. Hasegawa, M. Ogura, S. Yoshida and H. Tanoue .....	909
<b>Secondary Defect Distribution in High Energy Ion Implanted 4H-SiC</b>	
T. Ohno and N. Kobayashi .....	913
<b>Coimplantation Effects of (C and Si)/Ga in 6H-SiC</b>	
Y. Tanaka, N. Kobayashi, M. Hasegawa, M. Ogura, Y. Ishida, S. Yoshida, H. Okumura and H. Tanoue .....	917
<b>Improved Annealing Process for 6H-SiC p<sup>+</sup>-n Junction Creation by Al Implantation</b>	
M. Lazar, L. Ottaviani, M.L. Locatelli, D. Planson, B. Canut and J.P. Chante .....	921
<b>Characteristics of n-p Junction Diodes Made by Double-Implantations into SiC</b>	
J.B. Tucker, E.M. Handy, M.V. Rao, O.W. Holland, N. Papanicolaou and K.A. Jones .....	925

<b>Reactivation of Hydrogen-Passivated Aluminum Acceptors in p-type SiC</b> C. Hülsen, N. Achtziger, U. Reislöhner and W. Witthuhn .....	929
<b>Formation of Passivated Layers in p-Type SiC by Low Energy Ion Implantation of Hydrogen</b> N. Achtziger, C. Hülsen, M.S. Janson, M.K. Linnarsson, B.G. Svensson and W. Witthuhn .....	933
<b>Metal-Contact Enhanced Incorporation of Deuterium in 4H- and 6H-SiC</b> M.K. Linnarsson, A. Li. Spetz, M.S. Janson, L.G. Ekedahl, S. Karlsson, A. Schöner, I. Lundström and B.G. Svensson .....	937
<b>Transient-Enhanced Diffusion of Boron in SiC</b> M. Laube and G. Pensl .....	941
<b>Selective Doping of 6H-SiC by Diffusion of Boron</b> S.I. Soloviev, Y. Gao, I.I. Khlebnikov and T.S. Sudarshan .....	945
<b>Ab Initio Study of Intrinsic Point Defects and Dopant-Defect Complexes in SiC: Application to Boron Diffusion</b> M. Bockstedte and O. Pankratov .....	949
<b>Beryllium Implantation Doping of Silicon Carbide</b> T. Henkel, Y. Tanaka, N. Kobayashi, S. Nishizawa and S. Hishita .....	953
<b>Ion-Channeling Studies of Interfaces and Defect Properties in Silicon Carbide</b> W. Jiang and W.J. Weber .....	957
<b>Formation of Precipitates in 6H-SiC after Oxygen Implantation and Subsequent Annealing</b> B. Pécz, O. Klettke, G. Pensl and J. Stoemenos .....	961
<b>Microstructural Evolution of Radiation-Induced Defects in Semi-Insulating SiC During Isochronal Annealing</b> W. Puff, A.G. Balogh and P. Mascher .....	965
<b>Vacancy-Type Defects in Proton-Irradiated 6H- and 4H-SiC: A Systematic Study with Positron Annihilation Techniques</b> W. Puff, A.G. Balogh and P. Mascher .....	969
<b>Deep Centres Appearing in 6H and 4H SiC after Proton Irradiation</b> A.A. Lebedev, D.V. Davydov, A.M. Strel'chuk, A.N. Kuznetsov, E.V. Bogdanova, V.V. Kozlovski and N.S. Savkina .....	973
<b>Radiation-Induced Conductivity and Simultaneous Photoconductivity Suppression in 6H-SiC under 17 MeV Proton Irradiation</b> H. Amekura, N. Kishimoto and K. Kono .....	977

### 4.3 Contacts and Etching

<b>Study of Contact Formation by High Temperature Deposition of Ni on SiC</b> K. Robbie, S.T. Jemander, N. Lin, C. Hallin, R. Erlandsson, G.V. Hansson and L. D. Madsen .....	981
<b>Ohmic Contact Formation on n-Type 6H-SiC using NiSi<sub>2</sub></b> T. Nakamura, H. Shimada and M. Satoh .....	985

<b>Lowering the Annealing Temperature of Ni/SiC for Ohmic Contacts under N<sub>2</sub> Gas, and Application to a UV Sensor</b> T. Toda, Y. Ueda and M. Sawada .....	989
<b>Adhesion and Microstructure of Ni Contacts to 3C-SiC</b> S.C. Kang and M.W. Shin .....	993
<b>Low Resistance Ohmic Contacts to n-SiC Using Niobium</b> T.N. Oder, J.R. Williams, K.W. Bryant, M.J. Bozack and J. Crofton .....	997
<b>A Comparison of Single- and Multi-Layer Ohmic Contacts Based on Tantalum Carbide on n-Type and Osmium on p-Type Silicon Carbide at Elevated Temperatures</b> T. Jang, G. Rutsch, B. Odekirk and L.M. Porter .....	1001
<b>Improved Ohmic Contacts to 6H-SiC by Pulsed Laser Processing</b> K. Nakashima, O. Eryu, S. Ukai, K. Yoshida and M. Watanabe .....	1005
<b>Al/Si Ohmic Contacts to p-Type 4H-SiC for Power Devices</b> L. Kassamakova, R. Kakanakov, I. Kassamakov, N. Nordell, S. Savage, E.B. Svedberg and L.D. Madsen .....	1009
<b>Searching for Device Processing Compatible Ohmic Contacts to Implanted p-Type 4H-SiC</b> Y. Luo, F. Yan, K. Tone, J.H. Zhao and J. Crofton .....	1013
<b>Structural and Morphological Characterization of Al/Ti-Based Ohmic Contacts on p-Type 4H-SiC Annealed under Various Conditions</b> K.V. Vassilevski, K. Zekentes, G. Constantinidis, N. Papanicolaou, I.P. Nikitina and A.I. Babanin .....	1017
<b>Thermal Stability in Vacuum and in Air of Al/Ni/W Based Ohmic Contacts to p-Type SiC</b> S. Liu, G. Potts and J. Scofield .....	1021
<b>A UHV Study of Ni/SiC Schottky Barrier and Ohmic Contact Formation</b> A. Kestle, S.P. Wilks, P.R. Dunstan, M. Pritchard, G. Pope, A. Koh and P.A. Mawby .....	1025
<b>Fermi Level Pinning and Schottky Barrier Characteristics on Reactively Ion Etched 4H-SiC</b> B.J. Skromme, E. Luckowski, K. Moore, S. Clemens, D. Resnick, T. Gehoski and D. Ganser .....	1029
<b>Real-Time Assessment of Overlayer Removal on 4H-SiC Surfaces: Techniques and Relevance to Contact Formation</b> N.V. Edwards, L.D. Madsen, K. Robbie, G.D. Powell, K. Järrendahl, C. Cobet, N. Esser, W. Richter and D.E. Aspnes .....	1033
<b>Pre-Growth Treatment of 4H-SiC Substrates by Hydrogen Etching at Low Pressure</b> K. Masahara, Y. Ishida, H. Okumura, T. Takahashi, M. Kushibe, T. Ohno, T. Suzuki, T. Tanaka, S. Yoshida and K. Arai .....	1037
<b>SiC <i>In Situ</i> Pre-Growth Etching: A Thermodynamic Study</b> E. Neyret, L. Di Cioccio, E. Blanquet, C. Raffy, C. Pudda, T. Billon and J. Camassel .....	1041
<b>The Effect of in Situ Surface Treatment on the Growth of 3C-SiC Thin Films on 6H-SiC Substrate - An X-Ray Triple Crystal Diffractometry and Synchrotron X-Ray Topography Study</b> J. Chaudhuri, J.T. George, J.H. Edgar, Z.Y. Xie and Z. Rek .....	1045



### **Dry Etching and Metallization Schemes in a GaN/SiC Heterojunction Device Process**

E. Danielsson, C.-M. Zetterling, M. Östling, S.K. Lee, K. Linthicum, D.B. Thomson, O.-H. Nam and R.F. Davis ..... 1049

### **Demonstration of Deep (80 $\mu\text{m}$ ) RIE Etching of SiC for MEMS and MMIC Applications**

D.C. Sheridan, J.B. Casady, E.C. Ellis, R.R. Siergiej, J.D. Cressler, R.M. Strong, W.M. Urban, W.F. Valek, C.F. Seiler and H. Buhay ..... 1053

### **Reactive Ion Etching in $\text{CF}_4/\text{O}_2$ Gas Mixtures for Fabricating SiC Devices**

M. Imaizumi, Y. Tarui, H. Sugimoto, J. Tanimura, T. Takami and T. Ozeki ..... 1057

### **Electrochemical C-V Profiling of p-Type 6H-SiC**

M. Kayambaki and K. Zekentes ..... 1061

## **4.4 Oxides and Other Dielectrics**

### **Electrically Active Traps at the 4H-SiC/ $\text{SiO}_2$ Interface Responsible for the Limitation of the Channel Mobility**

M. Bassler, V.V. Afanas'ev, G. Pensl and M. Schulz ..... 1065

### **Anomalous High Density of Interface States Near the Conduction Band in $\text{SiO}_2$ /4H-SiC MOS Devices**

M.K. Das, B.S. Um and J.A. Cooper, Jr. .... 1069

### **Effect of Post-Oxidation-Annealing in Hydrogen on $\text{SiO}_2$ /4H-SiC Interface**

S. Suzuki, K. Fukuda, H. Okushi, K. Nagai, T. Sekigawa, S. Yoshida, T. Tanaka and K. Arai ..... 1073

### **Process Dependence of Inversion Layer Mobility in 4H-SiC Devices**

D. Alok, E. Arnold and R. Egloff ..... 1077

### **Controlled Thermal Oxidation of Sacrificial Silicon on 4H-SiC Epilayer**

A. Koh, A. Kestle, P.R. Dunstan, M. Pritchard, S.P. Wilks, G. Pope and P.A. Mawby ..... 1081

### **Ozone Treatment of SiC for Improved Performance of Gas Sensitive Schottky Diodes**

S. Zangooie, H. Arwin, I. Lundström and A.L. Spetz ..... 1085

### **Reliability and Degradation of Metal-Oxide-Semiconductor Capacitors on 4H- and 6H-Silicon Carbide**

M. Treu, R. Schörner, P. Friedrichs, R. Rupp, A. Wiedenhofer, D. Stephani and H. Ryssel ..... 1089

### **SiC Devices with ONO Stacked Dielectrics**

L.A. Lipkin and J.W. Palmour ..... 1093

### **The Effect of Si:C Source Ratio on $\text{SiO}_2$ /SiC Interface State Density for Nitrogen Doped 4H and 6H-SiC**

G.Y. Chung, C.C. Tin, J.H. Won and J.R. Williams ..... 1097

### **Channel Doped SiC-MOSFETs**

S. Ogino, T. Oikawa and K. Ueno ..... 1101

**Anisotropy of Inversion Channel Mobility in 4H- and 6H-SiC MOSFETs on (11 $\bar{2}$ 0) Face**

H. Yano, T. Hirao, T. Kimoto, H. Matsunami, K. Asano and Y. Sugawara ..... 1105

**MOSFET Performance of 4H-, 6H-, and 15R-SiC Processed by Dry and Wet Oxidation**

H. Yano, T. Kimoto, H. Matsunami, M. Bassler and G. Pensl ..... 1109

**Interface Trap Profiles near the Band Edges in 6H-SiC MOSFETs**

N.S. Saks, S.S. Mani and A.K. Agarwal ..... 1113

**Characterization of SiC MOS Structures Using Conductance Spectroscopy and Capacitance Voltage Analysis**

E.Ö. Sveinbjörnsson, M. Ahnoff and H.Ö. Ólafsson ..... 1117

**Mobility in 6H-SiC n-Channel MOSFETs**

C.J. Scozzie, A.J. Lelis and F.B. McLean ..... 1121

**Effects of Oxidation Conditions on the Concentration of Carbon Dangling Bonds in Oxidized 6H-SiC**

P.J. Macfarlane and M.E. Zvanut ..... 1125

**Effects of Steam Annealing on Electrical Characteristics of 3C-SiC Metal-Oxide-Semiconductor Structures**

M. Yoshikawa, K. Kojima, T. Ohshima, H. Itoh, S. Okada and Y. Ishida ..... 1129

**Atomic-Scale Engineering of the SiC-SiO<sub>2</sub> Interface**

S.T. Pantelides, G. Duscher, M. Di Ventra, R. Buczko, K. McDonald, M.B. Huang, R.A. Weller, I. Baumvol, F.C. Stedile, C. Radtke, S.J. Pennycook, G. Chung, C.C. Tin, J.R. Williams, J. Won and L.C. Feldman ..... 1133

**Comparison of High-Temperature Electrical Characterizations of Pulsed-Laser Deposited AlN on 6H- and 4H-SiC from 25 to 450°C**

A.J. Lelis, C.J. Scozzie, F.B. McLean, B.R. Geil, R.D. Vispute and T. Venkatesan ..... 1137

**4.5 Micromachining****Molding-based Thin Film Patterning Techniques for SiC Surface Micromachining**

X. Song, S. Guo, C.A. Zorman, C.-H. Wu, A.A. Yasseen and M. Mehregany ..... 1141

**Bulk Micromachining of Polycrystalline SiC Using Si Molds Fabricated by Deep Reactive Ion Etching**

N. Rajan, C.A. Zorman and M. Mehregany ..... 1145

**Preliminary Investigation of SiC on Silicon for Biomedical Applications**

G.E. Carter, J.B. Casady, J. Bonds, M.E. Okhuysen, J.D. Scofield and S. E. Sadow ..... 1149

## Chapter 5: SiC Devices

### 5.1 Surveys

<b>SiC and GaN High-Voltage Power Switching Devices</b>	
T.P. Chow .....	1155
<b>Electrical Impact of SiC Structural Crystal Defects on High Electric Field Devices</b>	
P.G. Neudeck .....	1161

### 5.2 Unipolar Devices

<b>Performance and Reliability Issues of SiC-Schottky Diodes</b>	
R. Rupp, M. Treu, A. Mauder, E. Griebel, W. Werner, W. Bartsch and D. Stephani .....	1167
<b>Designing, Physical Simulation and Fabrication of High-Voltage (3.85 kV) 4H-SiC Schottky Rectifiers Processed on Hot-Wall and Chimney CVD Films</b>	
Q. Wahab, A. Ellison, J. Zhang, U. Forsberg, E. Duranova, A. Henry, L. D. Madsen and E. Janzén .....	1171
<b>Influence of Epitaxial Growth and Substrate Induced Defects on the Breakdown of High-Voltage 4H-SiC Schottky Diodes</b>	
Q. Wahab, A. Ellison, C. Hallin, A. Henry, J. Di Persio, R. Martinez and E. Janzén .....	1175
<b>A 2.8 kV, 2 V Forward Drop JBS Diode with Low Leakage</b>	
F. Dahlquist, J.-O. Svedberg, C.-M. Zetterling, M. Östling, B. Breitholtz and H. Lendenmann .....	1179
<b>3.6 kV 4H-SiC JBS Diodes with Low RonS</b>	
Y. Sugawara, K. Asano and R. Saito .....	1183
<b>Fabrication and Testing of 1,000V-60A 4H-SiC MPS Diodes in an Inductive Half-Bridge Circuit</b>	
K. Tone, J. H. Zhao, M. Weiner and M. Pan .....	1187
<b>Large Contact Ti/4H-SiC Schottky Diodes Fabricated Using Standard Silicon Processing Techniques</b>	
C. Sudre, M. Mooney, C. Leveugle, J. O'Brien and W.A. Lane .....	1191
<b>Optical Beam Induced Current Analysis of High-Voltage 4H-SiC Schottky Rectifiers</b>	
T. Tsuji, R. Asai, K. Ueno and S. Ogino .....	1195
<b>Effect of Plasma Etching and Sacrificial Oxidation on 4H-SiC Schottky Barrier Diodes</b>	
D.J. Morrison, A.J. Pidduck, V. Moore, P.J. Wilding, K.P. Hilton, M.J. Uren and C.M. Johnson .....	1199
<b>4H-SiC Device Scaling Development on Repaired Micropipe Substrates</b>	
T.E. Schattner, J.B. Casady, M.C.D. Smith, M.S. Mazzola, V. Dmitriev, S.V. Rentakova and S.E. Sadow .....	1203
<b>Design and Characterization of a SiC Schottky Diode Mixer</b>	
J. Eriksson, F. Ferdos, H. Zirath and N. Rorsman .....	1207

<b>Breakdown Voltage Improvement of 4H-SiC Schottky Diodes by a Thin Surface Implant</b>	
V. Khemka, K. Chatty, T.P. Chow and R.J. Gutmann .....	1211
<b>DC and Pulse Characterizations of (600V) 6H-SiC Schottky Diode Breakdown</b>	
A. Torres, O. Flament, O. Musseau and T. Billon .....	1215
<b>6H-SiC Schottky Barrier Diodes with Nearly Ideal Breakdown Voltage</b>	
G. Brezeanu, M. Badila, J. Millan, P. Godignon, M.L. Locatelli, J.P. Chante, A. Lebedev and V. Banu .....	1219
<b>Lateral Current Spreading in SiC Schottky Diodes using Field-Plate Edge Termination</b>	
Q. Zhang, V. Madangarli, M. Tarplee and T.S. Sudarshan .....	1223
<b>Characterization of Schottky Contact on p-type 6H-SiC</b>	
K. Kamimura, S. Okada, H. Ito, M. Nakao and Y. Onuma .....	1227
<b>Computer Simulation of p-Type SiC Schottky Diode using ATLAS</b>	
M. Tarplee, V. Madangarli, Q. Zhang, P. Palmer and T.S. Sudarshan .....	1231
<b>Schottky Barrier Characteristics of 3C-SiC Epilayers Grown by Low Pressure Chemical Vapor Deposition</b>	
Y. Ishida, T. Takahashi, H. Okumura, T. Sekigawa and S. Yoshida .....	1235
<b>Characterization of Au Schottky Contacts on p-Type 3C-SiC Grown by Low Pressure Chemical Vapor Deposition</b>	
K. Kojima, M. Yoshikawa, T. Ohshima, H. Itoh and S. Okada .....	1239
<b>Static and Dynamic Characteristics of 4H-SiC JFETs Designed for Different Blocking Categories</b>	
P. Friedrichs, H. Mitlehner, R. Kaltschmidt, U. Weinert, W. Bartsch, C. Hecht, K.O. Dohnke, B. Weis and D. Stephani .....	1243
<b>Power Density Comparison between Microwave Power MESFET's Processed on Conductive and Semi-Insulating Wafer</b>	
O. Noblanc, C. Arnodo, C. Dua, E. Chartier and C. Brylinski .....	1247
<b>Surface Induced Instabilities in 4H-SiC Microwave MESFETs</b>	
K.P. Hilton, M.J. Uren, D.G. Hayes, P.J. Wilding, H.K. Johnson, J.J. Guest and B.H. Smith .....	1251
<b>Characterization of SiC MESFETs on Conducting Substrates</b>	
P.Å. Nilsson, A.M. Saroukhan, J.-O. Svedberg, A. Konstantinov, S. Karlsson, C. Adås, U. Gustafsson, C. Harris, N. Rorsman, J. Eriksson and H. Zirath .....	1255
<b>Fabrication, Characterization, and Modeling of SiC MESFETs</b>	
N. Rorsman, J. Eriksson and H. Zirath .....	1259
<b>Physical Simulations on the Operation of 4H-SiC Microwave Power Transistors</b>	
R. Jonsson, Q. Wahab and S. Rudner .....	1263
<b>Properties of Transmission Lines on Various SiC Substrates</b>	
A.S. Royet, B. Cabon, T. Ouisse and T. Billon .....	1267
<b>High Temperature, High Current, 4H-SiC Accu-DMOSFET</b>	
R. Singh, S.-H. Ryu and J.W. Palmour .....	1271
<b>4H-SiC Self-Aligned Implant-Diffused Structure for Power DMOSFETs</b>	
A.V. Suvorov, L.A. Lipkin, G.M. Johnson, R. Singh and J.W. Palmour .....	1275

<b>Nitrogen vs. Phosphorus as Implant Species for High-Voltage Lateral RESURF MOSFETs on 4H-SiC</b>	
K. Chatty, S. Banerjee, T.P. Chow and R.J. Gutmann .....	1279
<b>Effect of Off-Angle from Si (0001) Surface and Polytype on Surface Morphology of SiC and C-V Characteristics of SiC MOS Structures</b>	
K. Fukuda, S. Suzuki, J. Senzaki, R. Kosugi, K. Nagai, T. Sekigawa, H. Okushi, S. Yoshida, T. Tanaka and K. Arai .....	1283
<b>Accumulation-Mode SiC Power MOSFET Design Issues</b>	
Y. Wang, C. Weitzel and M. Bhatnagar .....	1287
<b>Progress Towards a Manufacturable SiC Mixed Analog-Digital Integrated Circuit Technology</b>	
D. Brown, D. McGrath, M. Nielsen, N. Krishnamurthy, J.W. Kretchmer and M. Ghezzi .....	1291
<b>Rugged Power MOSFETs in 6H-SiC with Blocking Capability up to 1800V</b>	
R. Schörner, P. Friedrichs, D. Peters, H. Mitlehner, B. Weis and D. Stephani .....	1295
<b>Influence of Post-Oxidation Annealing on Electrical Characteristics in 6H-SiC MOSFETs</b>	
T. Ohshima, M. Yoshikawa, H. Itoh, K. Kojima, S. Okada and I. Nashiyama .....	1299
<b>Effect of Boron Implantation on 6H-SiC N-MOSFET Interface Properties</b>	
P. Godignon, X. Jordà, M. Vellvehi, S. Berberich, J. Montserrat and L. Ottaviani .....	1303
<b>Investigation of Lateral RESURF, 6H-SiC MOSFETs</b>	
A.K. Agarwal, N.S. Saks, S.S. Mani, V.S. Hegde and P.A. Sanger .....	1307
<b>Highly Durable SiC nMISFET's at 450°C</b>	
W.J. Zhu, X.W. Wang and T.P. Ma .....	1311
<b>SiC MISFETs with MBE-grown AlN Gate Dielectric</b>	
C.-M. Zetterling, M. Östling, H. Yano, T. Kimoto, H. Matsunami, K. Linthicum and R.F. Davis .....	1315

### 5.3 Bipolar Devices

<b>Steady-State and Transient Forward Current-Voltage Characteristics of 5.5 kV 4H-Silicon Carbide Diodes at High and Superhigh Current Densities</b>	
N.V. Dyakonova, P.A. Ivanov, V.A. Kozlov, M.E. Levinshtein, J.W. Palmour, S.L. Rumyantsev and R. Singh .....	1319
<b>Current Voltage Characteristics of High-Voltage 4H Silicon Carbide Diodes</b>	
U. Zimmermann, A. Hallén and B. Breitholtz .....	1323
<b>Dynamic Avalanche and Trapped Charge in 4H-SiC Diodes</b>	
M. Domeij, B. Breitholtz, D. Åberg, A. Martinez and P. Bergman .....	1327
<b>Comparison of Nitrogen and Phosphorus Implanted, Planar, High-Voltage 4H-SiC Junction Rectifiers</b>	
K. Chatty, V. Khemka, T.P. Chow and R.J. Gutmann .....	1331
<b>Dynamic and Steady-State Description of Incomplete Ionization in 4H-SiC Power Diodes under Turn-Off</b>	
A. Martinez and U. Lindefelt .....	1335

### **Simulation and Fabrication of High-Voltage 4H-SiC Diodes with Multiple Floating Guard Ring Termination**

D.C. Sheridan, G. Niu, J.N. Merrett, J.D. Cressler, C. Ellis, C.C. Tin and R.R. Siergiej ..... 1339

### **Transient Characterization of SiC P-N Diode**

N. Keskar, K. Shenai and P.G. Neudeck ..... 1343

### **Formation of Deep pn Junctions by MeV Al- and B-Ion Implantations into 4H-SiC and Reverse Characteristics**

N. Miyamoto, A. Saitoh, T. Kimoto, H. Matsunami, Y. Hishida and M. Watanabe ..... 1347

### **Defect Modeling and Simulation of 4H-SiC P-N Diode**

N. Keskar, K. Shenai and P. Neudeck ..... 1351

### **6H-SiC Diodes with Cellular Structure to Avoid Micropipe Effects**

M. Badila, G. Brezeanu, J.P. Chante, M-L. Locatelli, J. Millan, P. Godignon,  
A. Lebedev, P. Lungu and V. Banu ..... 1355

### **A Closed-Form Analytical Solution of 6H-SiC Punch-Through Junction Breakdown Voltages**

J. Wang, B.W. Williams, S.E. Madathil and M.M. Desouza ..... 1359

### **Study of the Breakdown Voltage of Protected or Non-Protected 6H-SiC Bipolar Diodes by OBIC Characterisation**

K. Isoird, L. Ottaviani, M.L. Locatelli, D. Planson, C. Raynaud, P. Bevilacqua and  
J.P. Chante ..... 1363

### **Al/C/B Co-Implanted High-Voltage 4H-SiC PiN Junction Rectifiers**

J.B. Fedison, Z. Li, V. Khemka, N. Ramungul, T.P. Chow, M. Ghezze,  
J. W. Kretchmer and A. Elasser ..... 1367

### **6.2kV 4H-SiC pin Diode with Low Forward Voltage Drop**

Y. Sugawara, K. Asano, R. Singh and J.W. Palmour ..... 1371

### **Theoretical and Experimental Study of 4H-SiC Junction Edge Termination**

X. Li, K. Tone, L. H. Cao, P. Alexandrov, L. Fursin and J. H. Zhao ..... 1375

### **Monte Carlo Simulation of 4H-SiC IMPATT Diodes**

V. Gruzinskis, Y. Luo, J.H. Zhao, M. Weiner, M. Pan, P. Shiktorov and E. Starikov ..... 1379

### **Demonstration of High Performance Visible-Blind 4H-SiC Avalanche Photodiodes**

F. Yan, Y. Luo, J.H. Zhao, C. Dries and G. Olsen ..... 1383

### **2600 V, 12 A, 4H-SiC, Asymmetrical Gate Turn Off (GTO) Thyristor Development**

A. Agarwal, S.-H. Ryu, R. Singh, O. Kordina and J.W. Palmour ..... 1387

### **Factors Influencing the Design and Performance of 4H-SiC GTO Thyristors**

J.B. Fedison, T.P. Chow, M. Ghezze, J.W. Kretchmer and M.C. Nielsen ..... 1391

### **4H-SiC Gate Turn-Off Thyristor Designs for Very High Power Control**

P.B. Shah, B.R. Geil, K.A. Jones, T.E. Griffin and M.A. Derenge ..... 1395

### **Fabrication and Characterization of 4H-SiC GTOs and Diodes**

L. Fursin, K. Tone, P. Alexandrov, Y. Luo, L. Cao, J. Zhao, M. Weiner and M. Pan ..... 1399

### **100 kHz Operation of SiC Junction Controlled Thyristor (JCT) Switches Used in an All-SiC PWM Inverter**

S. Seshadri, W.B. Hall, J.C. Kotvas and P.A. Sanger ..... 1403

### **SiC-Power Rectifiers**

R. Held, M. Füllmann and E. Niemann ..... 1407

<b>Comparison of 5 kV 4H-SiC N-Channel and P-Channel IGBTs</b>	
J. Wang, B.W. Williams, S.E. Madathil and M.M. Desouza .....	1411
<b>Design and Simulations of 5000V MOS-Gated Bipolar Transistor (MGT) on 4H-SiC</b>	
Y. Tang, N. Ramungul and T.P. Chow .....	1415
<b>TCAD Evaluation of Double Implanted 4H-SiC Power Bipolar Transistors</b>	
K. Adachi, C.M. Johnson, S. Ortolland, N.G. Wright and A.G. O'Neill .....	1419
<b>Operation of a 2500V 150A Si-IGBT/SiC Diode Module</b>	
H. Lendenmann, N. Johansson, D. Mou, M. Frischholz, B. Åstrand, P. Isberg and C. Ovren .....	1423
<b>High-Power P-Channel UMOS IGBT's in 6H-SiC for High Temperature Operation</b>	
S.-H. Ryu, R. Singh and J.W. Palmour .....	1427

## 5.4 Sensors

<b>High Temperature 4H-SiC FET for Gas Sensing Applications</b>	
S.M. Savage, A. Konstantinov, A.M. Saroukhan and C.I. Harris .....	1431
<b>High Temperature Gas Sensors Based on Catalytic Metal Field Effect Transistors</b>	
H. Svenningstorp, L. Unéus, P. Tobias, I. Lundström, L.-G. Ekedahl and A. L. Spetz .....	1435
<b>SiC-Based Gas Sensor Development</b>	
G.W. Hunter, P.G. Neudeck, M. Gray, D. Androjna, L.-Y. Chen, R.W. Hoffman, Jr., C.C. Liu and Q.H. Wu .....	1439
<b>Fabrication of SiC Hydrogen Sensor by Pd-Implantation</b>	
C.I. Muntele, D. Ila, E.K. Williams, D.B. Poker, D.K. Hensley, D.J. Larkin and I. Muntele .....	1443
<b>Epitaxial 6H-SiC Layers as Detectors of Nuclear Particles</b>	
A.A. Lebedev, N.S. Savkina, A.M. Ivanov, N.B. Strokan and D.V. Davydov .....	1447

## Chapter 6: Growth of III-Nitrides and Related Materials

<b>GaN Quantum Dots on Sapphire and Si Substrates</b>	
H. Morkoç, M.A. Reshchikov, A. Baski and M.I. Nathan .....	1453
<b>Achievement of MBE-Grown GaN Heteroepitaxial Layer with (0001) Ga-Polarity and Improved Quality by In Exposure</b>	
T. Ide, M. Shimizu, X.-Q. Shen, S. Hara, H. Okumura and T. Nemoto .....	1459
<b>Crack-Free, Single-Crystal GaN Grown on 100 mm Diameter Silicon</b>	
H.M. Liaw, R. Venugopal, J. Wan, R. Doyle, P. Fejes, M.J. Loboda and M.R. Melloch .....	1463
<b>3C-SiC Pseudosubstrates for the Growth of Cubic GaN</b>	
P. Aboughé-Nzé, T. Chassagne, D. Chaussende, Y. Monteil, F. Cauwet, E. Bustarret, A. Deneuve, G. Bentoumi, E. Martinez-Guerrero, B. Daudin and G. Feuillet .....	1467
<b>Lateral- and Pendeo-epitaxial Growth and Defect Reduction in GaN Thin Films</b>	
R.F. Davis, O.-H. Nam, T.S. Zheleva, T. Gehrke, K.J. Linthicum and P. Rajagopal .....	1471

**Pendeoepitaxy of GaN and InGaN LEDs on SiC**

- H.S. Kong, J. Edmond, K. Doverspike, D. Emerson, G. Bulman, K. Haberern,  
H. Dieringer and D. Slater ..... 1477

**Comparison of Different Epitaxial Lateral Overgrowth GaN Structures using SiO<sub>2</sub>  
and Tungsten Mask by Cathodoluminescence Microscopy and Micro-Raman  
Spectroscopy**

- F. Bertram, T. Riemann, D. Rudloff, J. Christen, A. Kaschner, A. Hoffmann and  
K. Hiramatsu ..... 1483

**High Quality GaN on Si(111) Using (AlN/GaN)<sub>x</sub> Superlattice and Maskless ELO**

- H. Lahèche, V. Bousquet, M. Laügt, O. Tottereau, P. Vennéguès, B. Beaumont and  
P. Gibart ..... 1487

**Pendeo-Epitaxy<sup>TM</sup> Process for Aluminum Gallium Nitride Thin Films on Silicon  
Carbide Substrates via Metalorganic Chemical Vapor Deposition**

- T. Gehrke, K.J. Linthicum, P. Rajagopal, E.A. Preble, E.P. Carlson, B.M. Robin and  
R.F. Davis ..... 1491

**Reduction of Defects on GaN and AlGaN by In-Doping in Metalorganic Vapor  
Phase Epitaxy**

- T. Kachi, K. Itoh, K. Tomita and H. Tadano ..... 1495

**Comparison of AlGaN and GaN Grown on Various Substrates: Step Flow Growth  
on LiGaO<sub>2</sub> at Low Growth Temperature**

- S. Kang, W.A. Doolittle, S. R. Stock and A.I S. Brown ..... 1499

**Pulsed Laser Deposition: A Novel Growth Technique for Wide-Bandgap  
Semiconductor Research**

- R.D. Vispute, R. Enck, A. Patel, B. Ming, R.P. Sharma, T. Venkatesan, C.J. Scozzie,  
A. Lelis, F.B. McLean, T. Zheleva and K.A. Jones ..... 1503

**Investigation into the Film Growth of AlN on SiC by Low Pressure Chemical  
Vapour Deposition**

- V. Williams, E. Pernot, E. Ramberg, E. Blanquet, J.M. Bluet and R. Madar ..... 1507

**AlN Epitaxial Films Grown by ECR Plasma Assisted Metalorganic Chemical Vapor  
Deposition under Controlled Plasma Conditions in Afterglow Region**

- K. Yasui, S. Hoshino and T. Akahane ..... 1511

**Silicon Carbide Substrates for Epitaxial Growth of Aluminium Nitride by Chloride-  
Transport Process**

- D.D. Avrov, S.I. Dorozhkin, A.O. Lebedev, V.P. Rastegaev and Yu.M. Tairov ..... 1515

**Low-Energy-Ion-Assisted Reactive Sputter Deposition of Epitaxial AlN Thin Films  
on 6H-SiC**

- S. Tungasmita, P.O.Å. Persson, K. Järrendahl, L. Hultman and J. Birch ..... 1519

**Pulsed Laser Deposition of Oriented Aluminum Nitride Thin Films and Their  
Application**

- J. Meinschien, F. Falk and H. Stafast ..... 1523

**State of Art of c-BN Growth Physics: Substrate Effect**

- P. Masri, E. Guiot, V. Mortet, M. Rouhani Laridjani and M. Averous ..... 1527



## Chapter 7: Physical Properties of III-Nitrides

### 7.1 Surfaces and Interfaces

#### Adsorption and Desorption of Hydrogen on Ga-rich GaN(0001)

Y. Yang, V.J. Bellitto, B.D. Thoms, D.D. Koleske, A.E. Wickenden and R.L. Henry ..... 1533

#### Extremely Efficient Electron Stimulated Desorption of Hydrogen from GaN(0001)

V.J. Bellitto, B.D. Thoms, D.D. Koleske, A.E. Wickenden and R.L. Henry ..... 1537

#### The Reaction of Oxygen with GaN(0001)

B.D. Thoms, V.J. Bellitto, Y. Yang, D.D. Koleske, A.E. Wickenden and R.L. Henry ..... 1541

#### Observation of Cubic GaN/AlN Heterointerface Formation by RHEED in Plasma-Assisted Molecular Beam Epitaxy

H. Okumura, T. Koizumi, Y. Ishida, S.-H. Cho, X.-Q. Shen and S. Yoshida ..... 1545

### 7.2 Structure

#### Analysis of Dislocation Densities and Nanopipe Formation in MBE-Grown AlN-Layers

D.G. Ebling, L. Kirste, M. Rattunde, J. Portmann, R. Brenn, K.W. Benz and K. Tillmann ..... 1549

#### Correlation between Optical and Structural Properties of Thick GaN Films Grown by Direct Reaction of Ga and NH<sub>3</sub>

K.S. Nahm, S.H. Yang, S.H. Ahn and E.-K. Suh ..... 1553

#### Improved Electron Emission from Defective Diamond Film Deposited by CVD Method

Y. Show, T. Matsukawa, H. Ito, M. Iwase and T. Izumi ..... 1557

### 7.3 Optical and Electrical Properties

#### Theory of Impurities and Defects in III-Nitrides: Vacancies in GaN and Related Materials

C.G. Van de Walle ..... 1561

#### Nonabrupt Interface Related Exciton Energy Shifts in GaN/Al<sub>x</sub>Ga<sub>1-x</sub>N Quantum Dots

J.R. Filho, V. Lemos, J.S. de Sousa, G.A. Farias and V.N. Freire ..... 1567

#### Radiative Recombination in InGaN/GaN Multiple Quantum Wells

J.P. Bergman, B. Monemar, G. Pozina, B.E. Sernelius, P.O. Holtz, H. Amano and I. Akasaki ..... 1571

#### Impact of Epitaxial Lateral Overgrowth on the Recombination Dynamics in GaN Determined by Time Resolved Micro-Photoluminescence Spectroscopy

J. Holst, A. Kaschner, A. Hoffmann, I. Broser, P. Fischer, F. Bertram, T. Riemann, J. Christen, K. Hiramatsu, T. Shibata and N. Sawaki ..... 1575

<b>Structured Ultrafast Carrier Drift Velocity in Photoexcited Zincblende GaN</b>	
C.G. Rodrigues, A.R. Vasconcellos, R. Luzzi, V. Lemos and V.N. Freire .....	1579
<b>Characterization of Thick GaN Layers Using Guided Optical Waves</b>	
D. Ciplys, R. Rimeika, M.A. Khan, J.W. Yang, R. Gaska and M.S. Shur .....	1583
<b>Polarization Memory in Band Edge Luminescence from Free Standing Gallium Nitride</b>	
M.E. Kompan, S.D. Raevki, I.N. Safronov, I.Yu. Shabanov and Yu.V. Zhilyaev .....	1587
<b>Enhancement of UV-Sensitivity in GaN/GaAs Heterostructures by Si-Doping</b>	
M. Lisker, H. Witte, A. Krtschil, J. Christen, D.J. As, B. Schöttker and K. Lischka .....	1591
<b>Resonant Raman Scattering and the Emission Process in Zincblende-In<sub>x</sub>Ga<sub>1-x</sub>N</b>	
V. Lemos, E. Silveira, J.R. Leite, A. Tabata, R. Trentin, T. Frey, D.J. As, D. Schikora and K. Lischka .....	1595
<b>A Comparison of Aluminum Nitride Freely Nucleated and Seeded on 6H-Silicon Carbide</b>	
J.H. Edgar, L.H. Robins, S.E. Coatney, L. Liu, J. Chaudhuri, K. Ignatiev and Z. Rek .....	1599
<b>Low Frequency Noise in n-GaN with High Electron Mobility</b>	
S.L. Rumyantsev, D.C. Look, M.E. Levinshtein, M. Asif Khan, G. Simin, V. Adivarahan, R.J. Molnar and M.S. Shur .....	1603

## Chapter 8: III-Nitrides: Processing and Devices

<b>Role of Alloy Fluctuations in InGaN-Based LEDs and Laser Diodes</b>	
S. Nakamura .....	1609
<b>Influence of Annealing Conditions on Dopant Activation of Si<sup>+</sup> and Mg<sup>+</sup> Implanted GaN</b>	
A. Suvkhanov, N. Parikh, I. Usov, J. Hunn, S. Withrow, D. Thomson, T. Gehrke, R.F. Davis and L.Ya. Krasnobaev .....	1615
<b>Ohmic Contact Formation on Silicon-Doped Gallium Nitride Epilayers by Low Temperature Annealing</b>	
S. Prakash, L.S. Tan, K.M. Ng, A. Raman, S.J. Chua, A.T.S. Wee and S.L. Lim .....	1619
<b>Time-Resolved Photoluminescence Measurements of InGaN Light-Emitting Diodes</b>	
M. Pophristic, F.H. Long, C. Tran and I.T. Ferguson .....	1623
<b>GaN PIN Photodiodes Grown on Sapphire and SiC Substrates</b>	
G.M. Smith, M.F. Chriss, F.D. Tamweber, K.S. Boutros, J.S. Flynn and D.M. Keogh .....	1627
<b>Temperature Dependent Performance of GaN Schottky Diode Rectifiers</b>	
X.A. Cao, G.T. Dang, A.P. Zhang, F. Ren, S.J. Pearton, C.-M. Lee, C.-C. Chuo, J.-I. Chyi, G.C. Chi, J. Han, S.N.G. Chu and R.G. Wilson .....	1631
<b>Monte Carlo Simulation of Gunn Effect and Microwave Power Generation at 240 GHz in n<sup>+</sup>-n<sup>-</sup>-n<sup>+</sup> GaN Structures</b>	
J.H. Zhao, V. Gruzinskis, M. Weiner, M. Pan, P. Shiktorov and E. Starikov .....	1635
<b>DC and Large-Signal RF Performance of Recessed Gate GaN MESFETs Fabricated by the Photoelectrochemical Etching Process</b>	
W.S. Lee, K.W. Chung and M.W. Shin .....	1639

**Improved 10-GHz Operation of GaN/AlGa<sub>N</sub> HEMTs on Silicon Carbide**

S.T. Sheppard, K. Doverspike, M. Leonard, W.L. Pribble, S.T. Allen and

J.W. Palmour ..... 1643

**Characterization of AlGa<sub>N</sub>/Ga<sub>N</sub> HEMT Devices Grown by MBE**

T.W. MacElwee, J.A. Bardwell, H. Tang and J.B. Webb ..... 1647

**A Comparative Study of n-p Ga<sub>N</sub>/SiC Heterojunction and p-n 6H-SiC  
Homojunction Diodes**

J. Vacas, H. Lahèche, T. Monteiro, C. Gaspar, E. Pereira, C. Brylinski and

M.A. di Forte-Poisson ..... 1651

**Electrical Characteristics of 6H-SiC/Ga<sub>N</sub> Isotype n-n Heterojunctions**

N.I. Kuznetsov, A.E. Nikolaev, Yu.V. Melnik and I.P. Nikitina ..... 1655

**Author Index** ..... 1659**Keyword Index** ..... 1673

# Chapter 1

## SiC Bulk Growth

## Status of Large Diameter SiC Crystal Growth for Electronic and Optical Applications

D. Hobgood, M. Brady, W. Brixius, G. Fechko, R. Glass, D. Henshall,  
J. Jenny, R. Leonard, D. Malta, St.G. Müller, V. Tsvetkov and C. Carter, Jr.

Cree Research, Inc., 4600 Silicon Drive, Durham, NC 27703, USA

**Keywords:** Absorption, Defects, Micropipe, Purity, Resistivity, Substrate, Thermal Conductivity

**Abstract.** The realization of the full potential of semiconductor SiC for electronic and optical applications is critically dependent on the production of large diameter SiC single-crystals of high crystalline quality and controlled impurity content. In this paper, recent empirical results reflecting the current state of the art of SiC bulk growth are presented. Recent progress in monocrystalline SiC bulk crystal growth is characterized by the attainment of: substrate diameters up to 100-mm; residual impurities in the  $10^{15}\text{cm}^{-2}$  range; thermal conductivity approaching 5.0 W/cmK; near colorless 6H-SiC at crystal diameters up to 75-mm; and micropipe densities as low as  $1.1\text{ cm}^{-2}$  over an entire 50-mm diameter 4H-SiC wafer. The implication of these results for silicon carbide electronic devices operating at high power densities is discussed. Additionally, the recent interest in SiC for the production of a unique near colorless gemstone material, moissanite, increases the demand for high quality SiC bulk material.

**Introduction.** Within the last several years SiC semiconductor device technology for electronic and optoelectronic applications has made tremendous progress resulting primarily from the commercial availability of SiC substrates of ever increasing diameter and quality. Examples of current state of the art devices exploiting the unique electrical and thermophysical properties of silicon carbide include [1]: high brightness blue and green InGaN-based LEDs which take full advantage of the electrical conductivity of the SiC substrate by employing a conductive AlGaIn buffer layer; microwave MESFETs on semi-insulating 4H-SiC substrates with power densities as high as 4.6 W/mm at 3.5 GHz and total CW output power of 80W at 3.1 GHz from a single chip; 8.6 kV p-i-n diodes fabricated on high quality SiC epitaxial layers; thyristors conducting 12 A at 6.5 V with 2600 V blocking voltage; and GaN/AlGaIn HEMTs fabricated on semi-insulating SiC substrates with power density of 6.9 W/mm at 10 GHz. Throughout the technical evolution of semiconductor SiC, the fabrication of SiC crystals exhibiting the desired electrical and crystalline properties has played a central role in the realization of the full potential of this important semiconductor material. In this paper, we give an overview of the current state of the art of bulk SiC growth by highlighting recent advances in the fabrication of large diameter SiC crystals of improved quality.

**Diameter Enlargement.** 6H and 4H-SiC single crystals are grown using the technique of physical vapor transport (PVT) via seeded sublimation. This technique has been recently reviewed [2] and is currently the preferred method for the bulk growth of monocrystalline SiC. Production volumes of 6H and 4H-polytypes are now available at diameters up to 50-mm. Increasing the wafer diameter is crucial for reducing the cost of SiC devices through economies of scale and the use of Si or GaAs device fab equipment. SiC substrate development has been characterized by the continuous increase in crystal diameter from less than 25-mm in the early part of this decade to crystals with diameters up to 75-mm, first announced in 1997 [3]. Early R&D prototype 75-mm diameter wafers suffered from excessive low-angle grain boundaries,

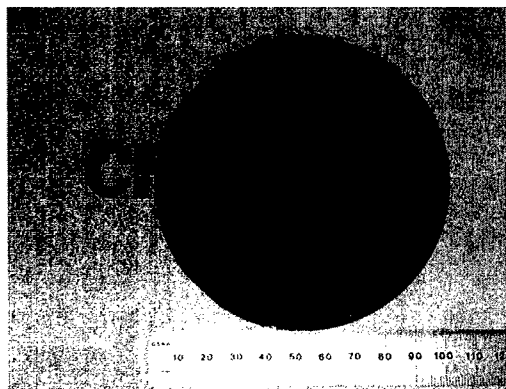


Figure 1. 100-mm diameter 6H-SiC wafer grown by physical vapor transport.

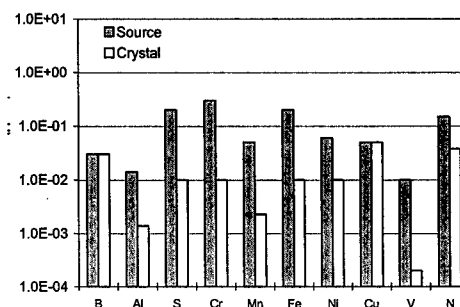


Figure 2. Impurity concentration (ppmw) vs. element in bulk SiC.

near the wafer periphery [3]. This problem has been circumvented in the intervening years allowing for the first time the extension of the PVT technique to the fabrication of fully single-crystal substrates with diameters up to 100-mm, as shown in Figure 1. Crack-free growth of large diameter SiC crystals requires increased attention to system design and optimization of the thermal distribution in the growth environment to minimize excessive mechanical and thermoelastic stresses [2]. This significant development in wafer enlargement represents a major step toward bringing SiC to parity with III-V compound semiconductors, such as GaAs, in available wafer area for device fabrication.

**Crystal Purity.** The electrical behavior of SiC substrates is intimately connected with the purity of the as-grown crystals. The maximum attainable resistivity in undoped n-type crystals is limited

Table 1. Thermal Conductivity

Crystal	direction	n (cm <sup>-3</sup> )	W/cmK
4Hn	a	5.00E+15	4.9
4Hn	c	5.00E+15	3.9
4Hn	c	2.00E+18	3.3
4Hn	c	S.I.	3.3
6Hn	a	3.50E+17	3.8
6Hn	c	3.50E+17	3.2
6Hn	c	1.50E+18	3.0
6Hp	a	1.40E+16	4.0

principally by residual nitrogen in the growth environment, while that for undoped p-type crystals is limited by residual boron. Reduction of boron content in SiC is particularly difficult since it exhibits a transfer coefficient of near unity [4]. The extent to which these impurities dominate the electrical behavior of undoped SiC crystals grown by PVT is largely a function of the purity of source materials and the cleanliness of the growth system. Fig 2 shows the results of quantitative analysis of source material and as-grown crystals based on secondary ion mass spectroscopy, neutron activation analysis, and glow discharge mass spectroscopy.

These results show that concentrations of nitrogen and boron in bulk crystals can be reduced to mid  $10^{15} \text{ cm}^{-3}$ . In material of the highest purity, elemental metallic impurities typically exhibit concentrations less than or equal to 0.01 ppmwt and transfer coefficients less than unity. For heat dissipation in high power density device structures, the thermal conductivity of the substrate is a critical parameter. Thermal conductivity (Table 1) in bulk SiC samples shows a significant dependence on the impurity content of the sample and the crystallographic direction of heat flow.

In bulk crystals exhibiting low residual impurity content, thermal conductivity approaches 5 W/cmK for heat flow directions transverse to the c-axis. This value is close to that determined by Slack for Lely-grown samples [5]. However, an appreciable reduction in heat conduction parallel to the c-direction is observed, consistent with previous results [6].

**Crystallographic Perfection.** In parallel with efforts to enlarge crystal diameter, efforts have been directed toward improvement in overall crystal perfection. These improvements have focussed on reduction of stress, reduction in micropipe density, and the elimination of low angle boundaries. The significant overall quality improvement of 75-mm diameter 4H- and 6H-SiC wafers is illustrated in Figure 3 where the reduction of stress birefringence in recent wafers is compared to

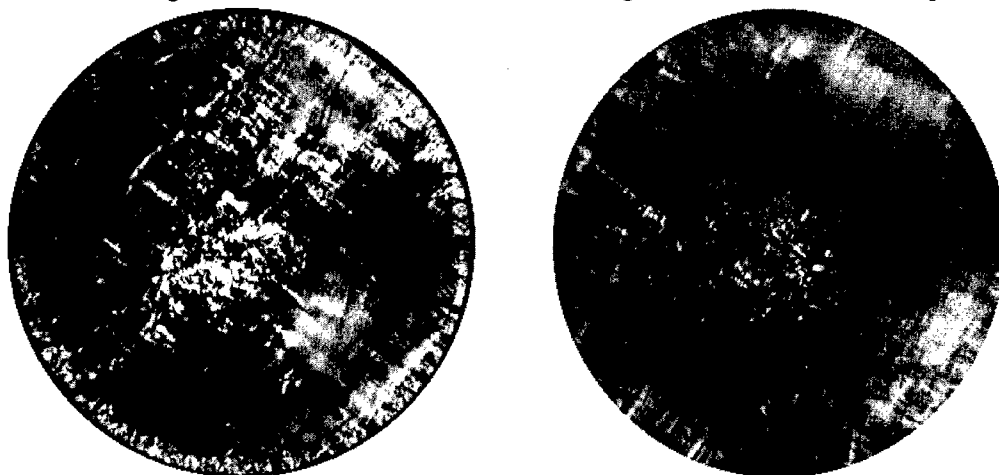
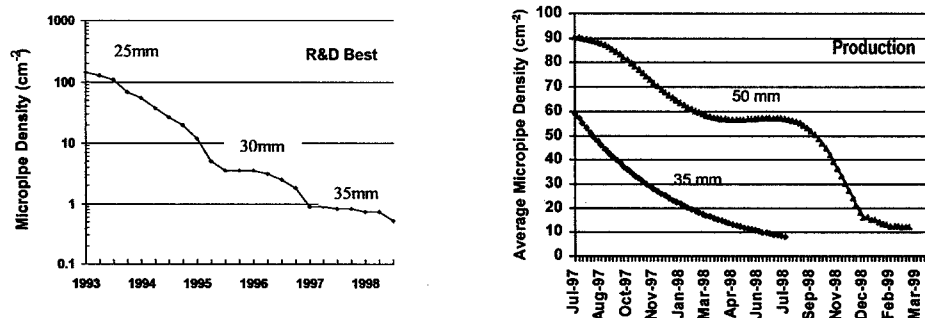


Figure 3. Quality improvement of 75-mm 4H-SiC substrates as indicated by stress birefringence: a) early R&D wafer, b) recent wafer.

earlier 75-mm wafers. Micropipe defects occurring to varying extent in all SiC wafers produced to date are seen by many as preventing the commercialization of many types of SiC devices, especially high current power devices. The dislocation content of micropipes is indicated by the existence of growth spirals originating from micropipes, characteristic stress patterns around micropipes visible in stress birefringence [7] and by the results of synchrotron white beam X-ray topography (SWBXT) experiments [8] and their interpretation based on kinematical diffraction theory [9]. Mounting evidence supports the Frank-model of hollow dislocation cores which allows a quantitative correlation of the micropipe radius with the Burgers vector of a screw dislocation associated with the pipe [10]. Regardless of the various fundamental and technological reasons for micropipe formation, we have identified empirically several mechanisms or combination of mechanisms causing micropipes in SiC boules grown by the seeded sublimation method. Our investigations have resulted in a steady decrease in the micropipe density over the past several years (Figure 4) indicating that micropipes may be totally eliminated in the next few years. The analysis of KOH etched 4H-SiC wafers from low micropipe density 4H-SiC boules has determined micropipe free material at a diameter of 25-mm and densities as low as  $1.1 \text{ cm}^{-2}$  for an entire 50-mm

diameter wafer (Figure 5), suitable for the production of large area devices. Concomitant with the growth of large diameter crystals is the tendency of the crystal to form low angle boundaries near the crystal periphery which occur under non-optimized process conditions. In SiC substrates, low angle boundaries are visible as linear crystallographic features extending radially inward from the wafer edge and generally following low-index crystal planes. They may sometimes extend through the entire thickness of the wafer.

Figure 4. a) Plot of micropipe density vs. year for "best" SiC wafers produced at Cree; b) reduction in production micropipe average over time for 4H-SiC wafers at Cree.



Recent work has resulted in a dramatic reduction in these defects to  $< 3$  with a length of  $< 3$  mm each for production 50-mm wafers, while they are totally eliminated in our current R&D wafers up to diameters of 100-mm (Figure 6). Superimposed on the micropipe distribution in etched wafers is an additional distribution of shallow etch pits at densities typically in the  $10^4$  cm<sup>-2</sup> range, associated with the general dislocation background in the wafer. The radial distribution of etch pits across the crystal diameter exhibits a characteristic W-pattern (Figure 7). This spatial variation is consistent with predictions of the radial dependence in resolved shear stress stemming from excess thermoelastic stresses during growth [2,11]. These results strongly suggest that thermal stress plays a key role in the generation of dislocations during SiC growth.

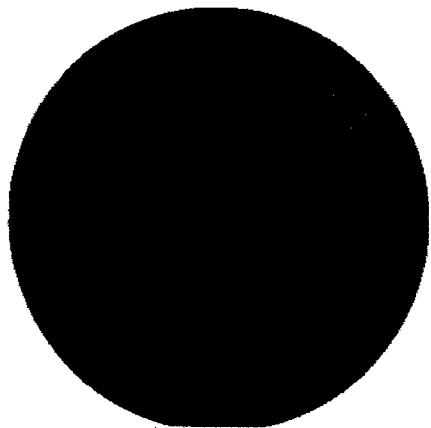


Figure 5. 50-mm diameter KOH-etched 4H-SiC wafer with micropipe density of  $1.1 \text{ cm}^{-2}$ .

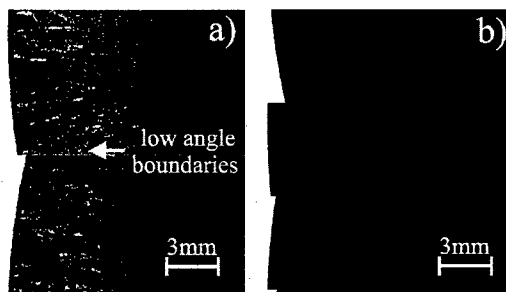


Figure 6. Elimination of low angle boundaries in large diameter SiC substrates: a) early wafer, b) current wafer.



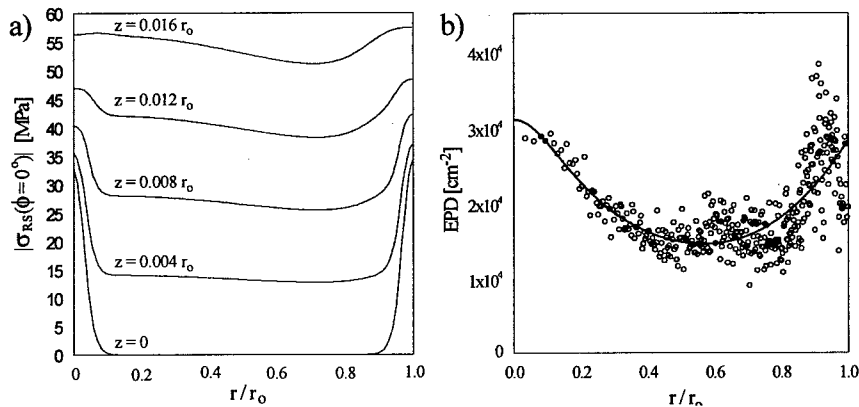


Figure 7. a) Radial dependence of the resolved shear stress in the (0001)<1120> glide direction as a function of distance from the growth interface ( $z=0$ ); b) Radial variation of the local etch pit density within areas of  $949\mu\text{m} \times 714\mu\text{m}$  on a 6H-SiC wafer.

**SiC for Optical Applications: Moissanite.** Up to the present, SiC crystal growth has focused almost exclusively on the fabrication of SiC crystals targeted toward electronic devices. However, additional interest in silicon carbide has arisen recently for purely optical applications. This interest stems from the similarities in refractive index, dispersion, mechanical hardness, and thermal conductivity, between silicon carbide and diamond, which suggest the utility of silicon carbide as a unique gemstone material (moissanite). Moissanite, like diamond, is characterized by its broad

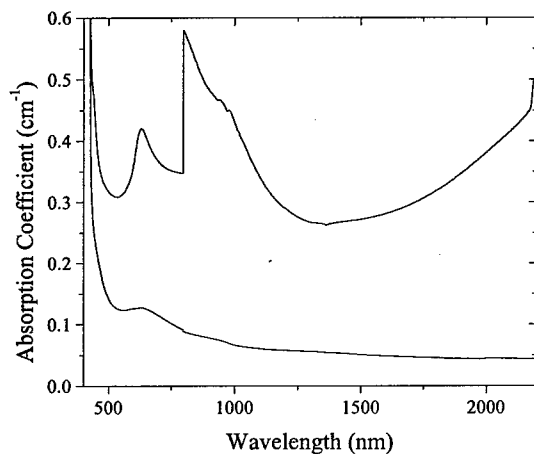


Figure 8. Absorption spectra at 293K comparing conventional 6H-SiC (upper curve) and near colorless Moissanite (lower curve).

transparency over the visible spectrum, optical brilliance, and resistance to chemical and abrasive attack. Recent advances at Cree have allowed the fabrication of monocrystalline moissanite in a near colorless form at crystal diameters up to 75-mm. Figure 8 shows absorption spectra for near colorless moissanite compared to conventional 6H-SiC. Conventional 6H-SiC exhibits large absorption bands in the visible region at energies below the band edge. These absorption bands give rise to the characteristic green color observed in n-type 6H-SiC [12]. The origin of the bands is attributed to interband transitions from states near the conduction band edge to states in higher lying conduction bands [13]. [The large offset in the absorption

spectrum (upper curve) near 800 nm is an artifact associated with a detector change in the

spectrometer at this wavelength.] By contrast, near colorless moissanite exhibits a broad transparency associated with a relatively featureless absorption spectrum. The implications of this development for the manufacture of bulk SiC crystals for the gemstone industry are clearly significant when it is realized that the materials volume associated with the manufacture of cubic zirconia alone is estimated to be approximately 440 metric tons per year. Semiconductor SiC for the electronics industry is expected to benefit greatly from this parallel development of high quality SiC crystals for the gemstone industry.

**Summary.** Recent progress in the development of the PVT technique for SiC bulk growth at our laboratories has led to substrate diameters up to 100-mm, residual impurities in the  $10^{15}$  cm<sup>-2</sup> range, thermal conductivity approaching 5.0 W/cmK in bulk crystals, near colorless 6H-SiC at crystal diameters up to 75-mm, and micropipe densities as low as 1.1 cm<sup>-2</sup> over 50-mm diameter 4H-SiC wafers. These advances help to position SiC for an exciting future and provide a sound foundation for the realization of the full potential of SiC for high power density electronic devices, optoelectronic devices of high brightness, and SiC materials applications requiring low optical absorption.

**Acknowledgements.** This work was funded in part by DARPA/AFRL, contract F33615-95-C-5426 and AFRL Agreement No. F33615-98-2-5433. The authors wish to thank Prof. W.J. Choyke, Univ. of Pittsburgh, and Dr. M. Kellam of Charles & Colvard, Inc., for their insightful discussions.

#### References.

- [1] C.H. Carter, Jr., V.F. Tsvetkov, R.C. Glass, D. Henshall, M. Brady, St. G. Müller, O. Kordina, K. Irvine, J.A. Edmond, H.-S. Kong, R. Singh, S.T. Allen, and J. W. Palmour, *Matls. Sci. and Eng.* **B61-62** (1999), p.1.
- [2] St. G. Müller, R.C. Glass, H.M. Hobgood, V.F. Tsvetkov, M. Brady, D. Henshall, J.R. Jenny, D. Malta, and C.H. Carter, Jr., *American Assoc. of Crystal Growth*, Tucson, AZ, (1999).
- [3] V. Tsvetkov, R. Glass, D. Henshall, D. Asbury, and C.H. Carter, Jr., *Matl. Sci. Forum* **264-268** (1998), p. 3.
- [4] R.C. Glass, G. Augustine, V. Balakrishna, H.M. Hobgood, R. H. Hopkins, J. Jenny, M. Skowronski, and W. J. Choyke, *Inst. Phys. Conf. Ser. No. 142* (1996), p. 37.
- [5] G.A. Slack, *J. Phys. Chem. Solids* **34** (1973), p. 321.
- [6] L.A. Burgemeister, W. von Munch, E. Pettenpaul, *J. Appl. Phys.* **50** (1979), p. 5790.
- [7] St. G. Müller, R. Eckstein, W. Hartung, D. Hofmann, M. Kolbl, G. Pensl, E. Schmitt, E.J. Schmitt, A.-D. Weber, and A. Winnacker, *Mat. Sci. Forum*, **264-268** (1998), p.33.
- [8] W. Si, M. Dudley, R. Glass, V. Tsvetkov, C. Carter, Jr., *J. Elect. Matl.*, **26** (1997), p. 128.
- [9] X.R. Huang, M. Dudley, W.M. Vetter, W. Huang, W. Si, and C.H. Carter, Jr., *J. Appl. Crystallography*, **32** (1999), p. 516.
- [10] F.C. Frank, *Acta Cryst.*, **4** (1950), p. 497.
- [11] A.S. Jordan, R. Caruso, A.R. von Neida, *Bell Syst. Tech. J.* **59** (1980), p. 593.
- [12] E. Biedermann, *Solid State Comm.* **3** (1965), p. 343.
- [13] W.R.L. Lambrecht, S. Limpijumnong, S.N. Rashkeev, and B. Segall, *Matl. Sci. Forum* **264-268** (1998), p. 271.

## Large Diameter PVT Growth of Bulk 6H SiC Crystals

D.W. Snyder, V.D. Heydemann, W.J. Everson and D.L. Barrett

II-VI Incorporated, 375 Saxonburg Blvd, Saxonburg, PA 16056, USA

**Keywords:** Micropipe, Polytype, Purity, PVT, Sublimation Growth, Substrates

**Abstract:** Within the past year we have grown SiC boules and produced wafers of 25, 35, 41, 50, 75 and 100 mm diameter in custom-designed physical vapor transport (PVT) furnaces. By synthesizing high purity SiC source material, controlling defect introduction during growth initiation, and optimizing hot zone geometry, we have increased the monocrystalline area in 50 to 100 mm substrates and have reduced micropipe densities in our 35 mm and 41 mm substrates to below  $300 \text{ cm}^{-2}$ .

### Introduction

We report here on the physical vapor transport (PVT) growth of SiC boules up to 100 mm diameter, Figure 1, and our continuing efforts to improve the quality of 6H SiC substrates. Our technical approach has focused on the following efforts:

- The synthesis of ultra-high purity SiC source material and improvements in purity of graphite hot zone components.
- Seeding / nucleation studies to suppress defect generation in the early stages of boule growth and to control boule polytype.
- Designed experiments and finite element (FE) modeling to optimize interface shape, to scale-up the PVT hot zone design, and to minimize the thermo-elastic stress during crystal growth and cooldown.

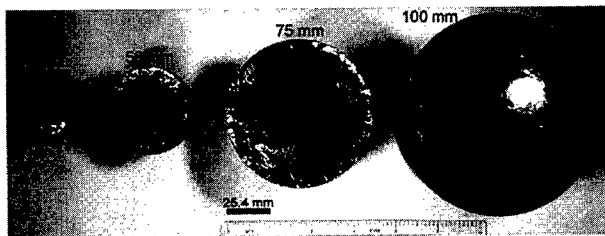


Fig. 1: PVT growth of 6H SiC boules with 25, 50, 75 and 100 mm diameter.

### PVT Furnace Design and Operation

SiC was grown in three identical physical vapor transport growth systems (Fig. 2). The PVT reaction chamber consisted of a water-cooled jacket of concentric quartz tubes flanged to a vacuum system and a high purity gas supply system. The vacuum system used a turbomolecular pump to evacuate the growth chamber to below  $1 \times 10^{-7}$  torr, and a rotary pump with a computer controlled throttle valve. The gas supply system handled ultrahigh purity argon as an inert gas, and nitrogen as an n-type dopant. The growth chamber contained the graphite reaction crucible inside a graphite susceptor that was thermally insulated by carbon foam [1].

The furnaces, inductively heated by a 25 kW, 10 kHz rf generator, provided a maximum crucible temperature exceeding  $2500^\circ\text{C}$ . The coil design and thermal insulation were optimized to reduce the operating power to approximately 12 kW during growth. The top and bottom of the growth crucible were monitored using pyrometers to measure the approximate temperature of the seed crystal / boule and the SiC source, respectively.

An automated process control system provided precise, stable, repeatable control of crucial process parameters (e.g. furnace pressure, crucible temperatures, temperature gradient, rf heating power and induction coil position).



Seed crystal temperature ( $T_{\text{seed}}$ ):	2100 - 2200°C
Axial temperature gradient ( $\Delta T$ ):	10 - 30°C/cm
Argon pressure ( $p_{\text{Ar}}$ ):	5 - 30 torr
Average growth rate:	0.3 - 1.4 mm/h

Fig. 2: Custom designed II-VI Incorporated PVT furnaces currently produce boules up to 100 mm in diameter.

### Purity Improvements of SiC Source and Hot Zone Materials

Impurities are a major source of defect generation during PVT boule growth [2, 3] and control the electrical properties of SiC substrates. We used GDMS to evaluate the purity of source materials, halogen purified graphite hot zone materials, and halogen purified porous carbon, Table 1, that were commercially available at the start of this program. Improvements in halogen purification resulted in a 2- to 3-fold reduction in impurities in the graphite used in the hot zone construction. Porous carbon, which exhibits a high impurity content was eliminated from the design.

The highest levels of impurities detrimental to the quality of the SiC boules, (e.g. B, N, P, Ti, V) were found in the SiC source powders. High purity SiC source material was synthesized using high purity silicon and graphite in modified PVT systems in a 600 torr argon atmosphere at temperatures from 2100-2500°C. Two silicon and two graphite sources were used to synthesize SiC and evaluate the purity, grain size, and processability of the resulting SiC powder. The synthesized SiC exhibited a dramatic reduction, more than two orders of magnitude in some cases, in the concentrations of impurities (Table 2). The current synthesis process yields material that exhibits lower impurities concentration than commercially available CVD SiC.

Table 1: Impurity levels of graphite used in hot zone construction; and grain size, relative, sublimation rates, approximate costs and impurity levels of commercial and in-house synthesized SiC source material..

Material	Grain size ( $\mu\text{m}$ )	Relative transport rate	Approx. cost (\$/kg)	Element Concentration (GDMS ppm wt.)					
				B	N	Al	P	Ti	V
Graphite 1	—	—	—	0.2	50	0.08	0.1	0.01	0.01
Graphite 2	—	—	—	0.04	—	0.05	0.05	0.01	0.005
Porous Graphite	—	—	—	0.6	20	0.15	0.1	1.7	1.2
High purity Acheson - S1	500-1500	0.68	5	1.6	700	80	2	50	70
High purity Acheson - S2	7	0.91	150	12	1000	1.8	35	1.5	0.5
Ultra-high purity Acheson - S3	100	0.83	150	0.5	9000	7.8	0.05	4.7	0.03
CVD	1000-4000	0.79	3000	0.9	22000	0.3	0.1	6	0.1
II-VI Synthesis - 1998	1000	0.96	120	0.2	300	1.2	0.04	4.3	2.3
II-VI Synthesis - 1999	1000	1.00	200	0.01	3300	0.15	0.05	1.1	1.3

### Seeding, Nucleation, and Defect Studies

Three primary sources for defects in SiC boule are: 1) propagation of defects present in the seed crystal, 2) propagation of macropipes from the backside of the seed, and 3) defects which nucleate during growth at the seed/boule interface or in the boule due to polytype inclusions, secondary phase inclusions, and high stress levels.

The quality and size of seed crystals have been continuously improved through process improvements and by fabricating the highest quality boule material into seeds for subsequent growth. The mechanism for formation of macrodefects originating from the back surface of the seed crystal and propagating into the boule has been investigated [4]. A dense carbon layer applied to the backside of the seed crystal as a protective coating has been shown to effectively inhibit the generation of macrodefects [4].

We have evaluated defect nucleation during seeding and the effect of seed face polarity by a controlled set of experiments in which the growing boule was simultaneously nucleated on both the carbon and silicon faces in dual seed experiments. For this purpose, on-axis 6H SiC wafers were polished (0.25  $\mu\text{m}$  diamond), and diced in half. The two half wafers were mounted side by side on the same crucible lid, one half exhibiting the (0001) Si-face as a growth surface ("Si-face seed"), the other half exhibiting the (000 $\bar{1}$ ) C-face ("C-face seed"). Both half wafers were simultaneously overgrown [1, 5].

Fig. 3(c) shows a vertical section parallel to the c-axis of a boule grown at a seed crystal temperature of 2100°C. In this boule, initially 6H polytype nucleated on both the 6H C-face seed (left half) and on the 6H Si-face seed (right half). During the growth run, the C-face region expanded radially along the growth direction overgrowing the simultaneously nucleated Si-face region and eliminated it by competitive growth. This result was reproduced several times. These observations suggest that growth on the C-face appears to be energetically favored under these growth conditions. The dual seed experiments were used to determine the temperature ranges for stable growth of the 6H and 4H polytype, and to investigate the impact of growth face polarity and seed temperature on the size and density of inclusions and voids. In our experiments, the material grown on C-face seeds exhibits a smoother surface morphology than material grown on Si-face seeds. Macrodefects appear to terminate during long runs (duration >18 h) in the material grown on C-face seed crystals at a higher rate than in material grown on Si-face seeds.

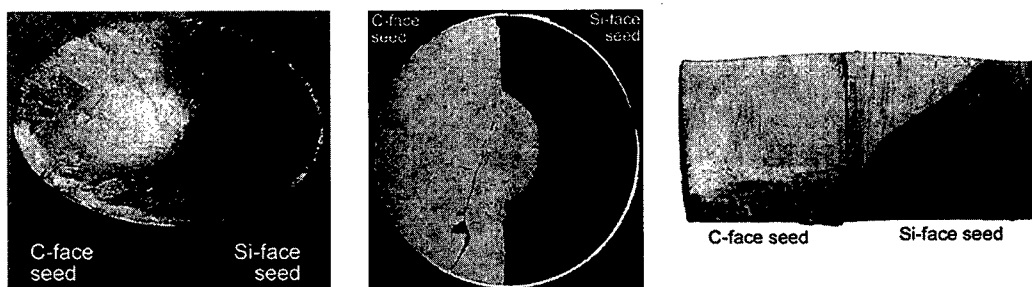


Fig. 3: Dual seed boule growth experiments:

(a) Boule grown by dual seed method. Note the different surface morphology of material grown on Si- and C-face seed.

(b) Radial slice showing differences in dopant incorporation for C-face and Si-face growth.

(c) Axial boule slice parallel to the growth direction (c-axis) showing preferential growth on carbon face seed.

### Growth Process Optimization and Reactor Modeling

The PVT process is being optimized using a combination of designed experiments and numerical simulation. Statistically designed experiments have been used to evaluate the effect of key process parameters on the sublimation transport and the resulting material quality.

Our in-house finite element (FE) crystal growth simulation program for thermal, and thermal stress simulations was modified to include electromagnetic induction heating calculations to analyze key design and processing issues associated with the scale-up of the PVT hot zone. The software is computationally highly efficient due to the use of a unique "net flux" radiation model based on a unit-sphere projection technique and an optimized induction heating algorithm. The model uses input process parameters (including coil current, frequency, coil position relative to the hotzone, graphite component dimensions and location, materials properties, size and position of SiC source and boule) to compute the axial and radial temperature distribution, and thermoelastic stresses thus enabling a wide range of hot zone design modifications to be evaluated quickly. The numerical simulation results were validated by a set of designed experiments, and helped to implement significant improvements of the hot zone and crucible design, and optimize the process parameters for the growth of large diameter SiC boules.

As an example, the inductive heating and calculated temperature distribution for a hot zone used to produce 35 mm substrates is illustrated in Fig. 4. Note the radial gradients present in the boule during growth. Fig. 4(d) shows the thermal stresses due to mismatch in thermal expansion coefficient (TEC)

between the crucible lid and boule. For this early design, the high stresses near the base of the boule, indicated by dark contrast, correlated with crack formation in our SiC boules. Modification of lid design and use of a graphite grade closely matched to the TEC of SiC minimized this cracking problem.

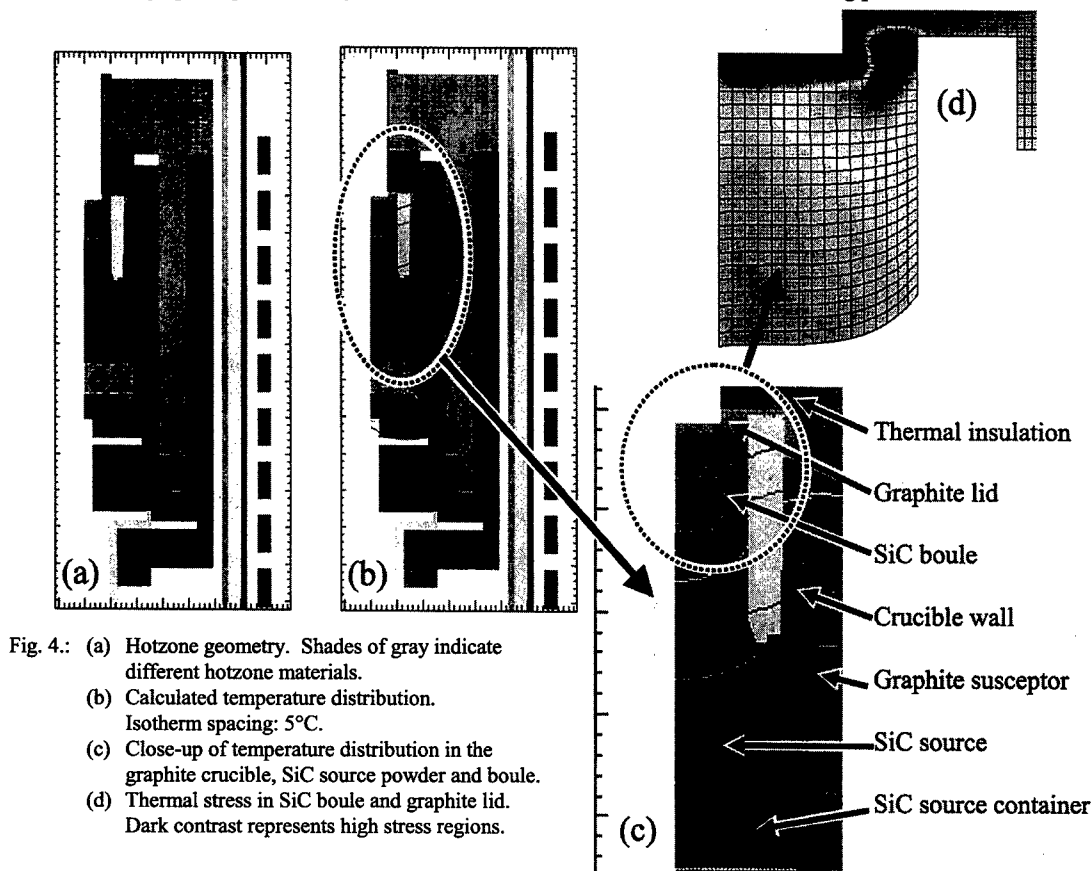


Fig. 4.: (a) Hotzone geometry. Shades of gray indicate different hotzone materials.  
 (b) Calculated temperature distribution. Isotherm spacing: 5°C.  
 (c) Close-up of temperature distribution in the graphite crucible, SiC source powder and boule.  
 (d) Thermal stress in SiC boule and graphite lid. Dark contrast represents high stress regions.

### Summary

We have developed a PVT furnace design and process to produce boules that yield 35 and 50 mm substrates that consistently exhibit micropipe densities less than 300 cm<sup>-2</sup>. A source synthesis process has been developed which produces SiC powder comparable in purity to commercially available CVD grown SiC powders. We have scaled up the furnace hot zone to grow boules 100 mm in diameter and have fabricated 75 mm and 100 mm wafers. Designed experiments and PVT process simulation are being used to reduce the density of grain boundaries and residual stress in large diameter substrates.

### References:

- [1] V. D. Heydemann, N. Schulze, D. L. Barrett, G. Pensl, *Appl. Phys. Lett.* **69** (1996), p. 3728
- [2] G. Augustine, H. McD. Hobgood, V. Balakrishna, G. Dunne, R. H. Hopkins, *phys. stat. sol. (b)* **202** (1997), p. 137
- [3] R. C. Glass, D. Henshall, V. F. Tsvetkov, C. H. Carter, Jr., *phys. stat. sol. (b)* **202** (1997), p. 149
- [4] E. Sanchez, presented at Electronic Materials EMC 99, to be published in *J. Electron. Mat.*
- [5] V. D. Heydemann, N. Schulze, D. L. Barrett, G. Pensl, *Diamond Rel. Mat.* **6** (1997), p. 1262

## Progress in SiC Bulk Growth

M. Anikin<sup>1</sup>, O. Chaix<sup>1</sup>, E. Pernot<sup>1</sup>, B. Pelissier<sup>1</sup>, M. Pons<sup>2</sup>, A. Pisch<sup>2</sup>,  
C. Bernard<sup>2</sup>, P. Grosse<sup>3</sup>, C. Faure<sup>3</sup>, Y. Grange<sup>3</sup>, G. Basset<sup>3</sup>, C. Moulin<sup>3</sup> and  
R. Madar<sup>1</sup>

<sup>1</sup> LMGP, UMR 5628 (INPG/CNRS), BP 46, FR-38402 St. Martin d'Hères, Cedex, France

<sup>2</sup> LTPCM, UMR 5614 CNRS/INPG/UJF, BP 75, FR-38402 Saint Martin d'Hères, Cedex, France

<sup>3</sup> LETI-CEA Grenoble, 17 rue des Martyrs, FR-38054 Grenoble, Cedex 9, France

**Keywords:** 4H and 6H-SiC sublimation growth, Crystal Shape, Defects, In Situ Etching

**Abstract** 4H and 6H-SiC ingots with diameter up to 30 mm have been grown by the Modified Lely Method with *in situ* etching. The original source design allowed us to maintain an excess of Si above the growing crystal to decrease defect density.

**Introduction** Growth of large ingots with a low defect density is the most important problem of SiC technology. An important factor affecting defect formation is the ingot shape which depends on the design of the crucible assembly and growth conditions. A change of design allows one to grow the crystals with convex, concave or flat "as grown" surface. It is important to notice, that the change of ingot shape during the growth can cause additional defects.

Our work was focused on the growth of crystals with flat "as grown" surface, because on one hand, this shape seems to be the best one from a commercial point of view (maximum yield for a given diameter) and on the other hand it allows one to obtain wafers with a uniform radial doping and to minimize the density of low angle grain boundaries. To grow such crystals with flat surfaces we have decreased the radial component of the growth rate taking into account the information obtained by numerical simulation of the process. In these conditions the enlargement of the crystals was quite small and their shape was close to cylindrical.

**Experimental details** 6H and 4H crystals with diameters up to 30 mm have been grown by the Modified Lely Method with « in situ » sublimation etching. [1-3, 5]. An experimental set up with RF heating and graphite crucible was used. The crucible was wrapped by graphite felt for thermal insulation and the whole assembly was placed inside a water cooled quartz reactor. The growth temperature (measured on the top of graphite lid) was about 2200°C and the argon pressure was about 2 Torr. Under these experimental conditions we obtained 4H and 6H single crystals with a thickness of about 10 mm. The growth rate was between (1.1- 1.3) mm/h.

The SiC source powder (Fig 1) was loaded both between a dense graphite crucible and a graphite thin-walled inner cylinder (as in the design of the Lely Method) and inside of the inner cylinder. This allowed us to reduce the influence of the leakage of Si and reaction of Si from the main central source with the walls to maintain excess of Si over the seed.

The seed was fixed at the top. The distance between source and seed was 15-20 mm. The temperature gradient within the growth cell was changed during the growth process. The inversion of the temperature gradient resulted in a etching of the seed. The temperatures of the top and the bottom of the crucible were measured by pyrometers.

## Results and discussion

**In situ etching** The growth at a relatively low temperature was always observed with a positive temperature gradient even at a high argon pressure (650 Torr). To suppress nucleation at a low temperature, which would result in undesirable crystal generation, we started the growth process with a reverse temperature gradient. At about 1800°C, sublimation etching of the seed was observed

when the Si pressure over the substrate was maintained close to equilibrium over SiC. To obtain SiC surfaces with a regular step structure it was necessary to eliminate the loss of Si from the seed surface which can result in carbon-rich and low-quality surface. Material supply from the source at the periphery reduced the influence of the Si leakage from the growth cell. Control of the temperature gradient and argon pressure became important factors to obtain high quality SiC surface. An increase in the reversed temperature gradient as well as in the temperature, increased the etching rate but, in the same time, the probability of the seed carbonization increased. At a too low argon pressure, less than 50 Torr, the seed surface became heavily step-bunched. Sometimes, even a carbonization of the seed surface was observed. After etching the sign of temperature gradient was changed and pressure increased to start the growth at slow rate.

The influence of *in situ* etching conditions and the initial stage of the growth on the defect formation have been investigated. A system of pyramidal holes [1, 2] was found at the interface. The size and the shape of holes depended on the conditions of etching and were greatly affected by seed orientation. Optimization of etching and the initial stage of the growth allowed the reduction of both the number and the size of holes. Defects were usually found at the periphery of the seed only. It is important to notice that the ingots where the pyramidal holes were not found by SEM contained pinholes.

**Shape** Both temperature distribution over the growing crystal and temperature distribution in the source affect the crystal shape. Our design of the crucible assembly, with a hole in the middle for temperature measurements and the seed fixed on the graphite lid resulted in to lower temperature in the middle of the seed than at the periphery. If the material transport is uniform over the surface of the seed, the lower surface temperature results in a higher growth rate. On the other hand the temperature distribution in the source is nonuniform too. This is due to the presence of the hole for temperature measurements and the relatively low heat conductivity of the powder. Furthermore temperature distribution can be changed during the growth.

Crystals were grown in conjunction with a mixture of 6H and 15R polytype poly-SiC at the periphery of the ingot. The change of the growth cell geometry allowed the growth of crystals with convex, concave and flat "as grown" surface. The wafers with uniform radial doping (Fig.2) were obtained. This confirms that flat growth front shape was not changed during the growth process.

To realize good polytype replication over entire ingot, the 8° off axis 4H-SiC wafers were used as seeds. This allowed us to achieve stable step-flow growth as in the case of CVD homoepitaxy. Step-flow growth enabled us to improve interface seed-ingot quality. We have used the (0001) C face for 4H growth and (0001)Si face for 6H growth.

**Morphology** Examining the ingot morphology was a useful way of assessing the crystal quality. Morphology of the ingots is greatly affected by C/Si ratio in vapor phase. The crystals with low defect density exhibited specular, smooth "as-grown" surface. Such crystals were grown at low C/Si ratio which was achieved by an original design of the source and good closure of the crucible. Material supply from the source at the periphery allowed to suppress the reaction of Si from the main source in the middle of the crucible with graphite walls and the losses of Si, which would have increased the C/Si ratio. The vapor transport is controlled by the main source in the middle. Graphitization of the source at the periphery resulted in fast degradation of the main source and then to a degradation the morphology and quality of the crystals. Microinclusions could be found in the grown crystals in this case (Fig.3).

**Macrodefects** Macrodefects were often present in the crystals grown at temperature higher than 2300°C [4,1-3]. These are holes with enlargement at the end, which start at the interface holder-seed and can penetrate deep in the growing crystal. Formation of these defects are explained by a local sublimation of the seed and then of the growing ingot. This is due to the temperature gradient created in the crystal during the growth. Lower growth temperature and lower temperature gradient with optimization of seed attachment technique allowed to achieve the growth of ingots without macrodefects.



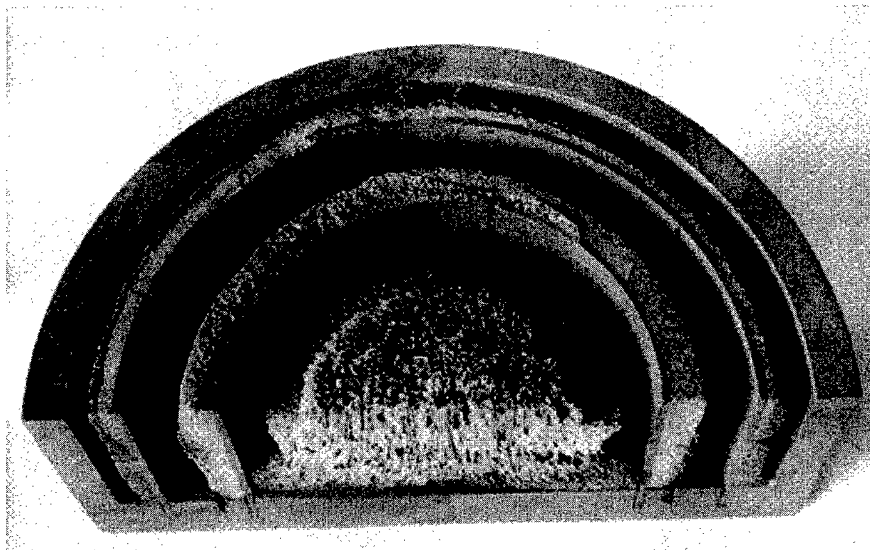


Fig.1 SiC source after 6H growth process

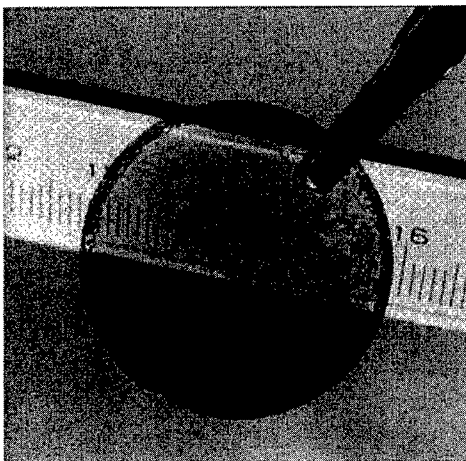


Fig.2 4H-SiC wafer

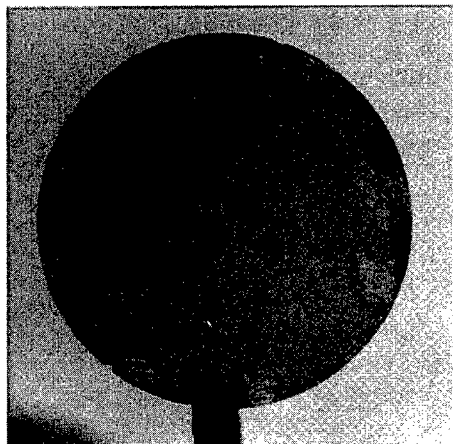


Fig.3 4H-SiC wafer with inclusions

**X-ray topography** Ingots and wafers have been studied by white beam synchrotron topography at the ESRF (ID19 beam line). To investigate growth process in ingots, section topography has been realized by inserting a narrow collimating slit (200  $\mu\text{m}$ ) in front of the crystal to reduce the X-ray beam. We recorded horizontal section perpendicular to the c-axis at different positions in the crystal. Fig.4a shows an horizontal section taken at the center of a 25 mm diameter 4H-SiC boule. All the border of the sample is highly misoriented and small crystallites in this region diffract as small spots on the topograph. The middle of the topograph exhibits dark lines coming from local

misorientations. Several sections indicate that these misorientations are perpendicular to the  $[11\bar{2}0]$  directions. Dark lines appear 2 mm under the seed and do not change a lot up to the top of the crystal.

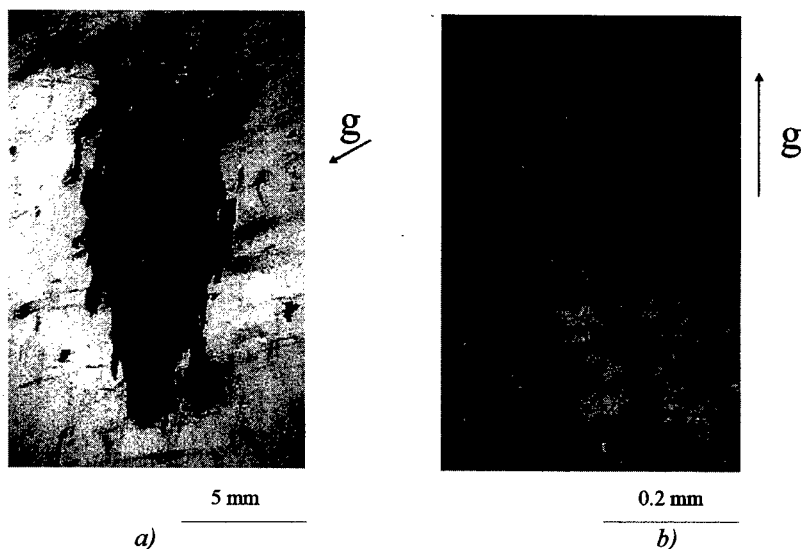


Fig. 4: *a)* a white beam synchrotron horizontal section topograph ( $200\mu\text{m}$ ) of a 4H-SiC ingot. *b)* a white beam synchrotron reflection topograph (00012 reflection) recorded from a (0001) 4H-SiC wafer.  $2\theta_{\text{bragg}} = 45^\circ$ . Sample-film distance = 20 cm.

Wafers have been investigated by white beam synchrotron reflection topography. Topographies taken at different Bragg angles and at different crystal-film distances indicate that the borders of wafers are highly curved. But, for several wafers, the center present a good structural quality. Fig.4b shows a part of a topograph of a 4H-SiC wafer. The diffraction vector is parallel to the  $c$ -axis. So it is easy to observe screw dislocations along this axis. Contrasts appearing as comets are associated with the strain field around dislocations. An 8 mm diameter region in the center of the crystal exhibits low dislocations density less than  $10^4\text{cm}^{-2}$ . In this region, we did not observe any topographic contrast coming from micropipes.

Average pinholes density in our crystals was less than  $100\text{cm}^{-2}$ . This was shown by observation after etching in molten KOH and confirmed by synchrotron white beam X-ray topography (SWBXT)

**Acknowledgements** The authors gratefully acknowledge the support of the French Ministry of Education and Research, the French Ministry of Industry and the European Brite Euram Program (Contract BRPR- CT98-0812-JESICA).

## References

- [1] M.M.Anikin, R.Madar, A.Rouault, I.Garçon, L. Di Cioccio, J.L.Robert, J.Camassel and J.M.Bluet, Inst. Phys.Conf.Ser.N 142, Chapter 1, presented ISCRM-95, Kyoto, Japan, IOP Publishing Ltd (1996), 33.
- [2] M.Anikin, R.Madar, Mat.Sci.and Eng.B46(1997)278.
- [3] R.Madar, M.Anikin, K.Chourou, M.Labeau, M.Pons, E.Blanquet, J.M.Dedulle, C.Bernard, S.Milita, J.Baruchel, Diam. Rel. Mat. 6(1997)1249.
- [4] R.A.Stein, Physica B 185(1993)211.)
- [5] M.Anikin, K.Chourou, R.Madar et al., Mat. Sci. Eng. B56(1999) accepted for publication.

## Generation and Properties of Semi-Insulating SiC Substrates

Shaoping Wang<sup>1</sup>, Adrian Powell<sup>1</sup>, Joan Redwing<sup>2</sup>, Eddie Piner<sup>2</sup> and  
Adam W. Saxler<sup>3</sup>

<sup>1</sup> ATMI, Inc, 7 Commerce Dr., Danbury, CT 06810, USA

<sup>2</sup> Epitronics, Inc., 21002 North 19th Av., Suite 5, Phoenix, AZ 85027, USA

<sup>3</sup> AFRL/MLPO, Bldg 651, 3005 P St., Wright-Patterson AFB, OH 45433, USA

**Keywords:** GaN Device on SI-SiC, Resistivity, Semi-insulating (SI), SiC Substrates

**Abstract:** Semi-insulating SiC crystals were grown by sublimation Physical Vapor Transport technique and semi-insulating 6H-SiC substrate wafers up to 2" in diameter were fabricated. Resistivity measurement and high temperature Hall measurement results showed that a large segment of a SiC boule grown in this process was semi-insulating. To evaluate these SI SiC substrates, GaN thin films and device structures were grown on the semi-insulating SiC substrates and device characterization results are presented.

### Introduction

SiC has emerged as the most advanced wide bandgap semiconductor for high frequency, high power, high temperature electronics. A key requirement for many devices and circuits, such as those operating at microwave frequencies, is the use of semi-insulating (SI) or insulating substrates that exhibit low dielectric loss and reduced device parasitics. A SI substrate is defined as having a resistivity greater than  $10^5 \Omega \cdot \text{cm}$ . The high resistivity permits easy isolation of epitaxial layers or devices from the substrate. In addition, it enables the use of simple device and circuit topologies which do not require complex and expensive isolation techniques. Therefore, superior performance of the SI SiC-based devices can be realized.

Semi-insulating SiC bulk crystals can be grown by sublimation physical vapor transport technique [1-6] and commercial semi-insulating SiC substrates are already available from limited suppliers. However, these commercial semi-insulating SiC substrates are very expensive. The availability of affordable semi-insulating SiC substrates will greatly accelerate the commercialization of superior SiC devices and circuits for both military and commercial applications. We believe that the most important factor limiting the production of affordable semi-insulating SiC substrates is the low yield of semi-insulating materials from each SiC boule produced. One way to achieve affordable semi-insulating SiC substrates that are comparable to regular SiC substrates is to drastically increase the yield of the semi-insulating growth process so that the majority of the boule produced is semi-insulating.

### Growth of SI SiC

In a recent research program <sup>a</sup> aiming at developing a sublimation growth process for SI SiC substrates for GaN devices, we demonstrated a high yield semi-insulating 6H-SiC sublimation growth process. The SI SiC crystals were grown via an ATMI proprietary growth process utilizing ultra high purity SiC source materials. As a result, semi-insulating SiC wafers with

room temperature resistivities larger than  $10^5$  ohm.cm and sizes up to 2" in diameter have been fabricated. Transmission optical and cross-polarizer pictures of a 1.8" diameter SI-SiC wafer are shown in Figure 1(a) and (b), respectively. On the cross-polarizer picture, the dark areas of

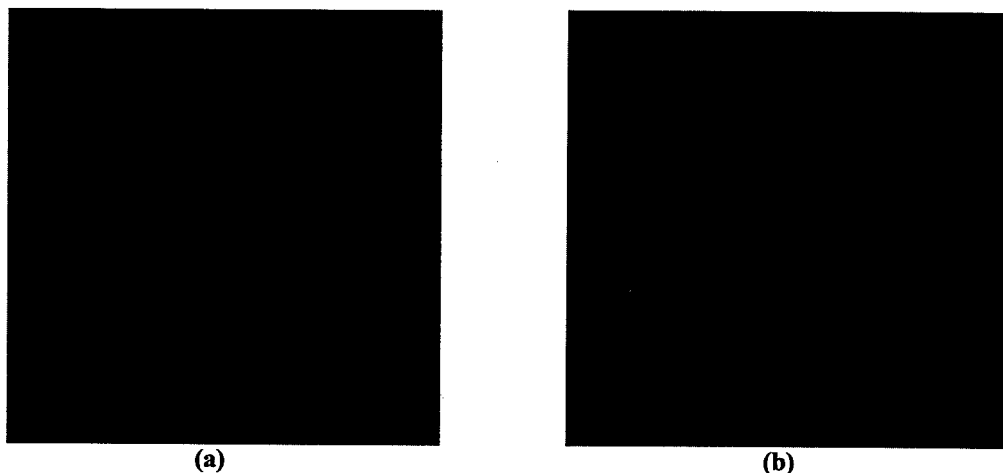


Figure 1. Semi-insulating SiC wafer of 1.8" in diameter produced at ATMI: (a) Optical microscope image and (b) Cross-polarizer image showing good single crystal area in the wafer.

the crystal wafer correspond to the good single crystal area and the light areas correspond to materials of poorer quality, where high densities of micropipes, grain boundaries and other defects can be found.

#### Electrical Characterization of SI SiC

Electrical resistivity of the SI SiC wafers was measured by using various techniques including Eddy current measurement (Lehigh), high temperature resistivity measurement and high temperature Hall measurement. The critical aspect of our semi-insulating growth process is the high yield of semi-insulating wafers from each boule. This is illustrated by the two sets of high temperature Hall measurement data obtained from two sample SiC wafers (wafer #1 and #15) taken from the same boule shown in Figure 2(a) and (b)<sup>b</sup>. The extrapolated room temperature resistivities of these two wafers are higher than  $10^8$  ohm.cm, i.e. they are semi-insulating. Since high temperature Hall measurement is destructive, a Lehigh system was used to measure resistivities of the remaining wafers from this boule. It was found that the resistivities of all the wafers between the two SI SiC wafers are all above the limit to which a Lehigh system can measure (5000 ohm.cm). All these measurements seem to indicate that a large segment of this boule (wafers #1-#15) is semi-insulating. This result is significant because it demonstrates that many SI wafers can be obtained from a single boule.<sup>c</sup> Thus, the cost of production of these SI SiC wafers will be reduced significantly.

<sup>b</sup> These Hall measurements were carried out at Wright-Patterson Air Force Research Laboratory.

<sup>c</sup> Wafers are available through Sterling Semiconductor, Inc., 22660 Executive Drive, Suite 101, Sterling, VA 20166

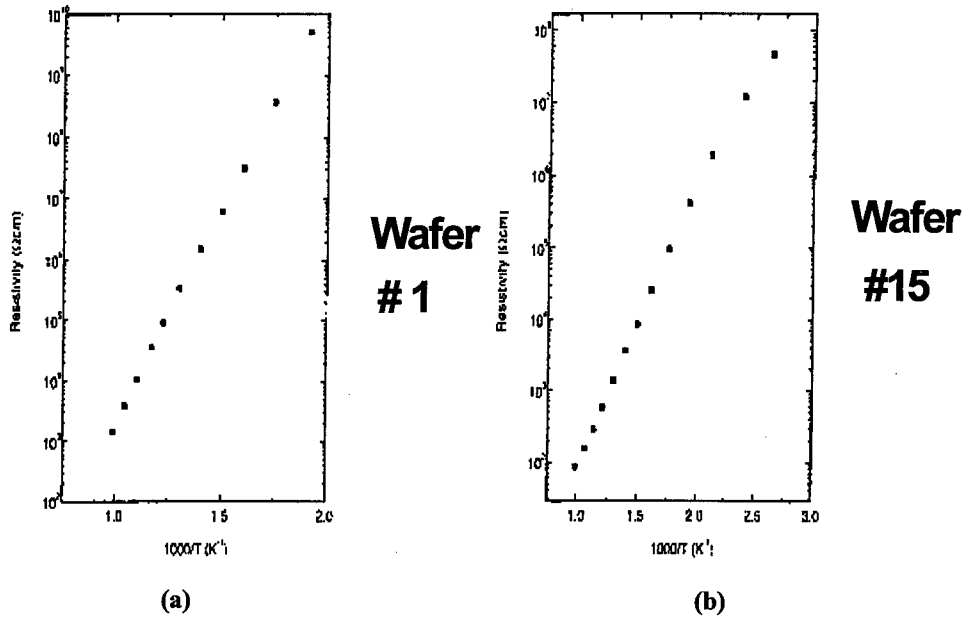


Figure 2. Resistivity versus temperature for ATMI SI-SiC substrates.

#### GaN Thin Films and Device Structures on SI SiC Substrates

For these semi-insulating substrates to be considered commercially viable, a number of further tests must be passed. The most important of these is the deposition of high quality epitaxial films. As an example, GaN thin films and AlGaIn/GaN/SiC high electron mobility transistor (HEMT) structures [7] have been grown by MOCVD on these SI SiC substrates as well as other substrates. Figure 3 shows the RF-power measurement results at 2GHz from a GaN HEMT

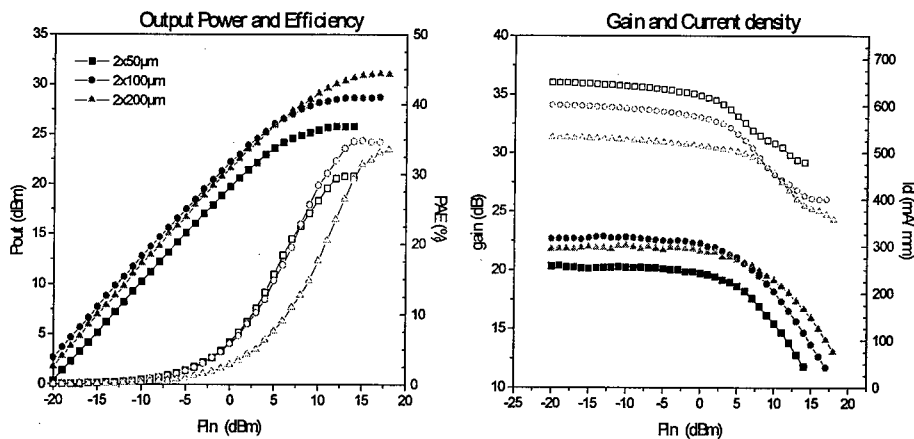


Figure 3. RF-power measurement at 2GHz from a GaN HEMT structure grown on an ATMI SI SiC substrate. A power output density of 3.8 W/mm from a 100μm size HEMT device is obtained.

structure. Note that an output power density of 3.8W/mm from a 100 $\mu$ m size HEMT device was achieved. The GaN epitaxial layer quality on these SI-SiC substrates, characterized by both double-crystal X-ray diffraction and mobility measurements, is similar to that obtained from regular n-type SiC wafers. All these results suggest that the SI SiC substrate wafers produced at ATMI are suitable for GaN RF devices.

### Summary

Semi-insulating SiC crystals were grown by sublimation Physical Vapor Transport technique and a high yield semi-insulating growth process for 6H-SiC wafers up to 2" in diameter was demonstrated. Evaluations of the quality of GaN epitaxial layers and the performance of AlGaIn/GaN HEMT device structures made on the SI SiC suggest that these SI-SiC substrates are suitable for high frequency device applications.

### Acknowledgement

This research was funded by the U.S. government through a BMDO contract: DASG60-98-C-0025. We want to acknowledge the following people who made important contributions to this work: Dr. W.C. Mitchel of U.S. Air Force Research Laboratory at Wright-Patterson AFB for allowing us to use his high temperature Hall measurement equipment, and A. Vescan, A. Wieszt, R. Dietrich and H. Leier of Research and Technology at Daimler-Chrysler for fabricating and testing the AlGaIn/GaN HEMT structures.

### References:

- [1] Y. M. Tairov, and V. F. Tsvetkov, J. Crystal Growth, **43**, (1978), p. 209.
- [2] G. Ziegler, P. Lanig, D. Theis and C. Weyrich, IEEE Trans. Electron Dev. ED-30, (1983), p. 227.
- [3] R. F. Davis, C. H. Carter and C. F. Hunter, U. S. Patent 4,866,005, (1989).
- [4] D. L. Barrett, R. G. Seidensticker, W. Gaida, R. H. Hopkins and W. J. Choyke, J. Crystal Growth, **109**, (1991), p. 17.
- [5] R.C. Glass, G. Augustine, V. Balakrishna, H. McD. Hobgood, R.H. Hopkins, J. Jenny, M. Skowronski, and W.J. Choyke, Silicon Carbide and Related Materials, 1995, Proceeding of the Sixth International Conference, Kyoto, Japan, (1995), p. 37.
- [6] H. McD. Hobgood, R.C. Glass, G. Augustine, R.H. Hopkins, J. Jenny, M. Skowronski, W.C. Mitchel and M. Roth, Appl. Phys. Lett. **66** (1995), p. 1364.
- [7] G.J. Sullivan, J.A. Higgins, M.Y. Chen, J.W. Yang, Q. Chen, R.L. Pierson, and B.T. McDermott, Electronics Lett., vol. 34, no. 9 (1998) p. 922.

## Vanadium-free Semi-insulating 4H-SiC Substrates

W.C. Mitchel<sup>1</sup>, Adam Saxler<sup>1</sup>, Ronald Perrin<sup>1</sup>, Jonathan Goldstein<sup>1</sup>,  
S.R. Smith<sup>1</sup>, A.O. Ewwaraye<sup>2</sup>, J.S. Solomon<sup>1</sup>, M. Brady<sup>3</sup>, V. Tsvetkov<sup>3</sup> and  
C.H. Carter, Jr.<sup>3</sup>

<sup>1</sup> Materials and Manufacturing Directorate, Air Force Research Laboratory, 3005 P Street, Suite 6,  
Wright-Patterson AFB, OH 45433-7707, USA

<sup>2</sup> University of Dayton, 300 College Park, Dayton, OH 45469-0170, USA

<sup>3</sup> Cree Research, Inc., 4600 Silicon Drive, Durham, NC 27703, USA

**Keywords:** 4H-SiC, Admittance Spectroscopy, Hall Effect, Physical Vapor Transport, Semi-Insulating Material

**Abstract:** We report the demonstration of semi-insulating bulk 4H-SiC without the use of vanadium doping. Single crystal boules were grown by the physical vapor transport method and sliced into wafers. The semi-insulating material was examined with temperature dependent Hall effect, optical admittance spectroscopy, optical absorption and secondary ion mass spectrometry. The material was insulating at room temperature and was not measurable until near 300°C where the resistivity was  $4 \times 10^7 \Omega \cdot \text{cm}$ . The thermal activation energy is 1.1 eV as determined by temperature dependent Hall effect. Optical admittance spectroscopy detected the 1.1 eV level but did not observe any response in the band around 1.6 eV where the vanadium donor response has previously been detected. Vanadium was below the  $10^{15} \text{ cm}^{-3}$  detection limit of our SIMS system. The identity of the defect responsible for the 1.1 eV level has not been identified.

### Introduction

Semi-insulating SiC substrates are required for high power microwave transistors made from both SiC and GaN. Vanadium doping has been the only reported method for producing bulk semi-insulating SiC that is very nearly insulating at room temperature [1,2]. In vanadium doped material the Fermi level is pinned at the vanadium donor level which is located near mid gap at 1.6 eV in 4H and 1.5 eV in 6H-SiC. This results in material that is virtually insulating at room temperature and maintains a resistivity in excess of  $10^7 \Omega \cdot \text{cm}$  at temperatures up to as high as 450°C. However, for a variety of reasons alternatives to vanadium doping are desirable. Due to differences in the segregation coefficients of vanadium and residual impurity shallow donors and acceptors such as nitrogen, and boron or aluminum, it is difficult to maintain a constant compensation ratio throughout a long boule. This can lead to a low yield of semi-insulating material if the starting material is not of the highest purity. Vanadium also acts as a trap and limits the lifetime and mobility of the material. We report here on a study of vanadium-free semi-insulating bulk 4H-SiC.

### Experimental Details

The samples were all fabricated from 4H-SiC crystals grown at Cree Research facilities by the sublimation vapor transport (SVT) technique[3]. Several samples were grown using Cree's standard semi-insulating SVT technique. The vanadium-free sample was grown using a new technique. Square samples approximately 0.75 cm on a side were cut for van der Pauw transport measurements. Ohmic contacts were formed by annealing Ta/Au contacts at 925°C in forming gas

for two minutes. Hall effect and resistivity measurements were made at temperatures up to 750°C. Schottky contacts for optical admittance spectroscopy (OAS) experiments were unannealed aluminum dots. Ohmic contacts were made on the back side by annealing nickel at 950°C for ten minutes in forming gas prior to the deposition of the aluminum film. The OAS measurements were made with an HP4274A multifrequency LCR meter at 100 kHz. Optical absorption measurements were made with a Cary model 5E spectrophotometer.

## Results

We have examined several 4H-SiC samples to determine the deep levels responsible for the semi-insulating properties. Semi-insulating SiC samples are virtually insulating at room temperature and

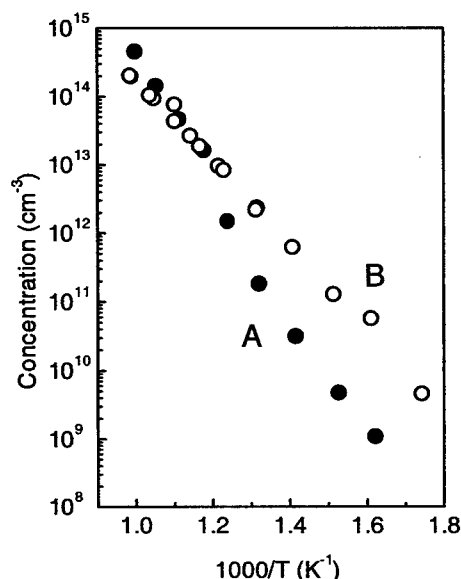


Fig. 1:  $n$  vs  $1000/T$  for semi-insulating 4H-SiC samples.

In addition to TDH measurements we have made Optical Admittance Spectroscopy (OAS) measurements of the semi-insulating samples in Fig. 1 and others. Typical results are shown in Figs. 2 and 3. Sample A shows a conductance onset very close to 1.6 eV with several other peaks between there and the bandgap at 3.2 eV, while sample B has a weak but clearly visible response near 1 eV. The OAS results of sample B are compared with those of another sample in Fig. 3. The TDH results for sample C were similar to those of sample B in that the activation energy was near 1.1 eV. In

the resistivities cannot be measured with our transport system, the maximum resistivity that can be measured is around  $10^{12} \Omega \cdot \text{cm}$  under the best of conditions. These samples do not start to conduct until temperatures around 350°C. Fig. 1 shows the results of our temperature dependent Hall effect (TDH) experiments on two semi-insulating 4H-SiC samples where we have plotted the carrier concentration versus inverse temperature. The resistivities of these two samples at 620 K were  $4 \times 10^8$  and  $6 \times 10^6 \Omega \cdot \text{cm}$  respectively. The two samples have different activation energies,  $E_a = E_C - 1.5$  eV for sample A and  $E_a = E_C - 1.1$  eV for sample B. The activation energy  $E_C - 1.5$  eV is within experimental error of the vanadium donor level in 4H-SiC, which we find from TDH measurements to be  $1.6 \pm 0.1$ , while the 1.1 eV level of sample B has not yet been identified but has been observed in both semi-insulating and conducting SiC samples[4]. The activation energies were determined by fitting  $\ln(nT^{-1.5}) = A - B(E_a/kT)$ .

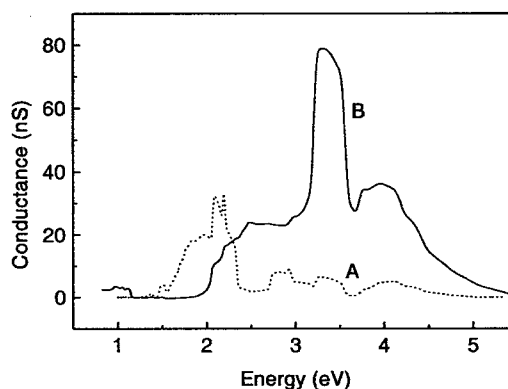


Fig. 2: Optical Admittance spectroscopy results for the two samples in Fig. 1.



sample C both the OAS response due to the 1.1 eV level and the peaks at and above 1.5 eV due  $V_d$  are clearly visible, while the  $V_d$  response is absent from sample B, suggesting the absence of vanadium.

To further investigate the role of vanadium in these samples, we performed optical absorption experiments. Neutral vanadium,  $V^{4+}(3d^1)$ , has an intracenter absorption spectra in the 1300 to 1400 nm range [5]. These spectral lines were observed in both samples A and C, as well as all other semi-insulating samples we investigated that contained vanadium were not observed in sample B. Secondary Ion Mass Spectrometry (SIMS) measurements were made on the samples as well. Vanadium is a common impurity in bulk SiC and was detected in both samples A and C in the mid  $10^{16} \text{ cm}^{-3}$  range. However, it was below the detection limit ( $\approx 10^{15} \text{ cm}^{-3}$ ) in sample B.

The detection limit for vanadium in SiC is estimated to be approximately  $1 \times 10^{15} \text{ cm}^{-3}$ . We were able to detect trace amounts of Ti as well as oxygen in sample B. The detection limit for Ti is  $1 \times 10^{16} \text{ cm}^{-3}$ , we do not have standards for oxygen at this time but we estimate the detection limit to be around mid  $10^{16} \text{ cm}^{-3}$ . No other impurities were above the detection limits for this sample.

## Discussion

The results presented above show that the Fermi level in semi-insulating 4H-SiC can be pinned at one of two levels, either the  $V_d$  level or the 1.1 eV level and that both levels can exist simultaneously, in sample C for example. Sample B is the only sample we have measured that did not have an OAS response in the region around 1.5 eV and is also the only semi-insulating SiC sample where vanadium was below the SIMS detection limit. These results and the optical absorption results discussed above demonstrate that it is highly unlikely that the defect responsible for the 1.1 eV level involves vanadium. It is not likely that it is the vanadium acceptor level[6] or a complex defect involving vanadium, as some of the present authors previously suggested[7]. The absence of impurities other than oxygen and titanium in sample B suggests that the defect is either related to one of these two impurities or is intrinsic in nature. At present we do not have a positive identification of this defect.

## Conclusions

We have found two separate activation energies for semi-insulating 4H SiC from TDH and OAS experiments. The level at  $E_C - 1.6 \text{ eV}$  is the donor level of substitutional vanadium. The level at  $E_C - 1.1 \text{ eV}$  has been observed in vanadium free material and is at present unidentified. We have observed for the first time vanadium-free semi-insulating 4H-SiC.

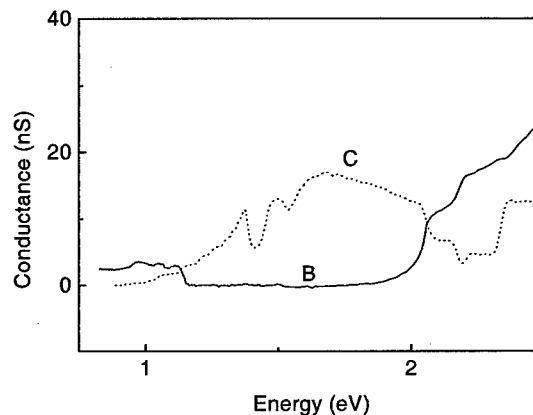


Fig. 3: OAS results for two samples showing 1.1 eV activation energy from TDH experiments.

**Acknowledgments:** The authors are pleased to acknowledge the assistance of Mr. Robert Leese, Mr. R. Bertke, Mr. Shawn Davidson and Mr. G. Landis. Work of SRS and JSS was supported in part by Air Force Contract F33615-95-C-5445.

### References

- [1] H. McD. Hobgood, R. C. Glass, G. Augustine, R. H. Hopkins, J. Jenny, M. Skowronski, W. C. Mitchel and M. Roth, *Appl. Phys. Lett.* **66** (1995), pp. 1364-1366.
- [2] W. C. Mitchel, R. Perrin, J. Goldstein, M. Roth, M. Ahoujja, S. R. Smith, A. O. Evwaraye, J. S. Solomon, G. Landis, H. McD. Hobgood, G. Augustine, and V. Balakrishna, *Mat'ls Sci. Forum*, **264-268** (1998), pp. 545-548.
- [3] R. C. Glass, D. Henshall, V. F. Tsvetkov, and C. H. Carter, Jr., *phys. stat. sol. (b)* **202** (1997) pp. 149-162.
- [4] W. C. Mitchel, R. Perrin, J. Goldstein, M. Roth, S. R. Smith, J. S. Solomon, A. O. Evwaraye, H. McD. Hobgood, G. Augustine and V. Balakrishna, 1998 IEEE Semiconducting and Insulating Materials Conference, ed. Zuzanna Liliental-Weber and Carla Miner, (IEEE, Piscataway, NJ, 1999) pp. 283-286.
- [5] J. Schneider, H. D. Muller, K. Maier, W. Wilkening, F. Fuchs, A. Dörnen, S. Leibenzeder, and R. Stein, *Appl. Phys. Lett.* **56** (1990), pp. 1184-1186.
- [6] Norbert Achtziger and W. Witthuhn, *Appl Phys Lett* **71** (1997), pp. 110-112.
- [7] A. O. Evwaraye, S. R. Smith and W. C. Mitchel, *J. Appl. Phys.* **79** (1996), pp. 7726-7730.

For correspondence, please contact W. C. Mitchel at [william.mitchel@afrl.af.mil](mailto:william.mitchel@afrl.af.mil)

## Numerical Simulation of SiC Boule Growth by Sublimation

Roland Madar<sup>1</sup>, Michel Pons<sup>2</sup>, Jean-Marc Dedulle<sup>1</sup>, Elisabeth Blanquet<sup>2</sup>,  
Alexander Pisch<sup>2</sup>, Philippe Grosse<sup>3</sup>, Christian Faure<sup>3</sup>, Michail Anikin<sup>1</sup> and  
Claude Bernard<sup>2</sup>

<sup>1</sup> LMGP - UMR 5628 (CNRS/INPG), Domaine Universitaire, BP 46, FR-38402  
St. Martin d'Hères Cedex, France

<sup>2</sup> LTPCM-UMR 5614 (CNRS/INPG-UJF), Domaine Universitaire, BP 75, FR-38402  
Saint Martin d'Hères Cedex, France

<sup>3</sup> LETI-CEA Grenoble, 17 rue des Martyrs, FR-38054 Grenoble Cedex 9, France

**Keywords:** Modeling, Numerical Simulation, SiC, Sublimation Growth

**Abstract :** The silicon carbide SiC semiconductor material is proving today, from intense scientific and industrial development, its potential to replace and outperform silicon in several or all electronic devices for high power, high frequency and high temperature applications.

However, at present, the material quality still remains an obstacle to a commercial breakthrough of a SiC technology and the improvement of the structural properties together with the increase of the available size of SiC wafers are key areas of research and development in this field.

The continuing improvement of the quality of crystals obtained by the seeded sublimation growth technique, the so-called "Modified Lely Method", observed so far are mainly the results of extensive experimental work. However, different computational tools have allowed to obtain important additional information to the wide experimental knowledge.

The phenomena involved in the sublimation growth process are quite complex, they include heat transfer by electromagnetic heating, radiation, conduction and convection, multicomponent gaseous species transport and gas surface chemistry.

An accurate modeling of the sublimation growth process needs a code taking into account all these phenomena. Our modeling work is too recent to propose such a code as a black box. However, some parts of it like magnetic and thermal modeling coupled with simple chemical models have reached maturity.

In this presentation we will mainly describe the kind of information which may be routinely obtained with this simulation tool with special emphasis on the shape control of the growing ingot.

### Introduction

Silicon carbide SiC has many remarkable properties which make it a very promising semiconductor material for the production of high temperature, high frequency and high power electronic devices. However the manufacturing of such devices requires the availability of good quality wafers. In the case of SiC main polytypes 4H and 6H there are still some problems related to crystal size and defects that hinder the commercial utilization of this material.

This work deals with the numerical modeling of the crystal growth of silicon carbide ingots by high temperature sublimation, technique which is also known as physical vapor transport and historically referred to as the "Modified Lely Method". In this process polycrystalline SiC at the source sublimates at high temperature and low pressure and the resulting gases travel through natural transport mechanisms to the cooler seed where crystallization takes place. The growth occurs in a closed graphite crucible usually heated by electromagnetic induction.

### General trends

During the last ten years, significant progress has been made on the modeling of this sublimation process [1-10]. Different computational tools have been set up and have helped in providing additional information to experimental knowledge. Since experiments have shown that in this method the growth is mainly controlled by the temperature distribution, it is quite natural that the calculation of the temperature field inside the crucible was the first step of this modeling approach.

Global heat transfer generated by induction heating and including conduction, convection and radiation as well as the heat of crystallization and sublimation at the interface were studied. We must point out that some high temperature thermal data, principally emissivity and conductivity of polycrystalline SiC source powder, are still under study [11-12] and that their accurate knowledge still remains a challenge and is essential for realistic simulations. Moreover, during the sublimation growth of crystal of significant length, the temperature distribution inside the cavity changes owing to an increase of the crystal size, deposition on the crucible walls and modifications of the volume, porosity and properties of the SiC powder.

Once determined, the thermal field into the cavity allows the calculation of the supersaturation which is the driving force for the growth. This driving force may be estimated by equilibrium thermodynamics calculations. This approach is quite relevant in this case since sublimation growth of SiC occurs close to equilibrium conditions due to the high temperature and slow mass transport rates. These thermodynamic calculations provide information on the partial pressures of the gaseous species and on the nature of the solid phases.

However, the simulation of only the heat transfer and the equilibrium calculations do not directly allow the determination of the growth rate and shape of the crystal, both characteristics which may be measured experimentally and compared with the simulation results in order to check the validity of the modeling. In order to target such questions, mass transport is needed. It certainly depends on the temperature distribution but also on the diffusion of gaseous species, convection and reactivity at the interfaces.

Knowing the temperature field, we have used a coupled mass-transport equilibrium approach which offers some advantages such as the availability of reliable data for a large variety of chemical systems. Moreover the linking of thermodynamic databases, thermochemical and mass transport calculations offer a modeling route avoiding the need to write out the appropriate chemical reactions. Indeed, the lack of kinetic data at high temperature has been up to now the bottleneck in applying kinetic calculations as an alternative route for the modeling of the sublimation growth process.

In fact, an accurate modeling and simulation of this growth process needs a software taking into account a multitude of highly coupled phenomena: fluid mechanics, convective, conductive and radiative heat transfer, electromagnetic, multicomponent species transport, homogeneous and heterogeneous thermochemical equilibrium and finally thermal and transport databases.

So even the most ambitious researcher can model the process only partially. However, some parts of this modeling work like magnetic and thermal modeling coupled with simplified chemical models have reached maturity and may be already extremely useful for the development of the process. Firstly, it gives some insight on what is happening in the system for a given set of experimental conditions and secondly it may be used for a first evaluation of the effect of changes of the system design without the need of making them.

After a brief recall of the main features of our process modeling approach [13], we will illustrate with some recent examples this dual aspect of the modeling contribution to the sublimation growth process development.

## Physical models

- **Thermodynamic modeling:** The thermodynamic calculations were carried out by minimization of the total free energy of the Si-C-Ar system in the temperature range 2300-3000K. The thermodynamic data came from the recent work of P. Rocabois et al. [14]. A self-consistent set of data was generated for the gaseous molecules from a literature review, measurements and heat capacity and entropy calculations using recent results on molecular structures, vibrational frequencies and electronic spectra. Nine gaseous species in addition to argon ( $\text{Si}_1$ ,  $\text{Si}_2$ ,  $\text{Si}_3$ ,  $\text{C}_1$ ,  $\text{C}_2$ ,  $\text{C}_3$ ,  $\text{SiC}$ ,  $\text{Si}_2\text{C}$ ,  $\text{SiC}_2$ ) and three condensed phases ( $\text{SiC}\beta$ , Si and C graphite) were considered. The parameters introduced in the calculations were the temperature, the crucible volume and the initial quantities of argon and solid silicon carbide at the source.

- **Induction heating and temperature distribution:** Electromagnetodynamics must be coupled with heat transfer, especially radiative heat transfer within the growth cavity. In our code, the radiation model is tightly coupled to the fluid transport, conjugate heat transfer and chemistry models to ensure energy conservation. These calculations make use of the materials database which include the electrical and the thermal conductivity of crucible and insulation material, the source and the boule material properties, the gas species and associated reactivity data, the induction frequency and the current density.

- **Multicomponent fluid transport:** The fluid transport model is based on the low pressure kinetic theory of gases. Transport coefficients such as viscosity, conductivity, specific heat, diffusivity and thermodiffusion coefficients are calculated as local functions of temperature, pressure and composition. The Stefan-Maxwell formulation for diffusive transport ensures complete mass conservation of all species in the system.

For the modified-Lely method with graphite crucible, within the range of investigated experimental parameters, we have verified that the natural convective transport of heat and of chemical species can be neglected when compared to diffusive transport and conductive heat [2].

- **Gas and surface chemistry:** A comprehensive capability must be available to simulate multi-step gas and surface chemistry. Large sets of multi-step reactions or thermodynamic equilibrium must be handled in the code. The surface chemistry is treated by doing a complete reaction-diffusion balance at the surface to obtain the surface concentration of species. The heat release from the gas/surface reactions are included in the model.

## Selected simulation results

The thermal field and concentration distributions of the main reactive species in the cavity and on the surface of the growing crystal are the keys parameters determining the growth rate at any point of the surface and therefore the shape of the crystallization front. In situ observations and measurements of the ingots characteristics as the growth proceeds are extremely difficult and most of the information on the growth process is obtained by ex situ examinations, trying to correlate the shape of the crystal and its defects density to the growth conditions.

So, the first question concerns the possibility to reproduce by simulation the crystal shape evolution experimentally observed in relation with variation of one or more process parameter without modification of the crucible design. We will discuss only the influence of the argon partial pressure and of the crystal growth progress on the thermal field and on the resulting shape of the growing crystal. The modeling has been undertaken on the basis of the experimental configuration of the reactor and in the range of parameters described in the reference [13].

### - Influence of the argon partial pressure

For the chosen set of experimental conditions, the partial pressures of the reactive species are constant ( $P(r)=660$  Pa, calculated at thermodynamic equilibrium). In the example given in figure 1, the argon pressure was varied from 133 to 2660 Pa. In the first case, the contribution of argon can be considered negligible, while, in the second case, it represents the major part of the total pressure. This has a strong effect on the boundary conditions for both evaporation and condensation on the seed and leads to a modification of the crystal shape.

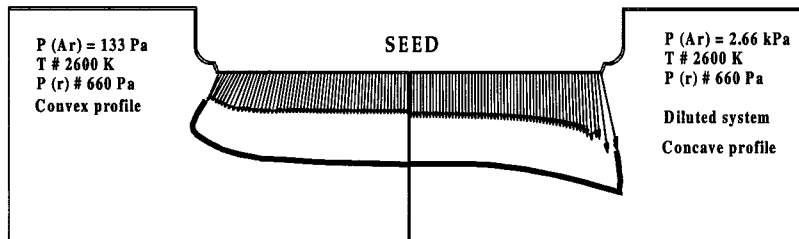


Fig. 1 : Influence of the argon partial pressure at the beginning of the growth process

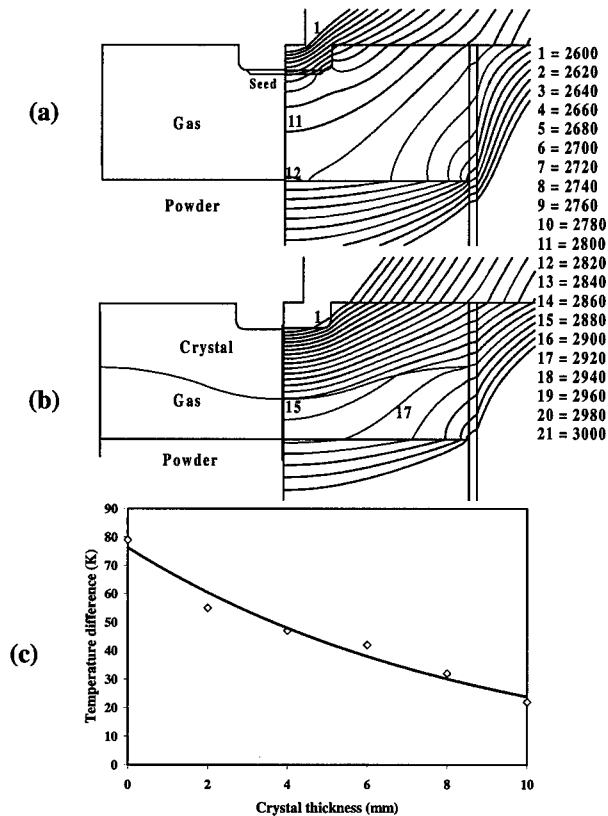


Fig. 2 : Influence of the crystal thickness on the thermal field (a) and (b) and on the axial temperature difference in the cavity.

### - Influence of the growing crystal

Many simulations have been made at the beginning of the growth process. Nevertheless, it is also important to simulate the evolution of the temperature field as the growth proceeds. In fact, during the growth process, the distance between the crystal and the powder varies. The shape of the reaction chamber is modified and we must take into account the variation of the electrical and thermal conductivities of the SiC powder due to its sintering. An example of the evolution of the thermal field inside the reaction chamber as the crystal grows is given in figure 2.

### - Influence of a crucible design modification

The second question deals with the ability of the simulation tools to predict the influence of any modification of the crucible design on the thermal field inside the reaction chamber. We will discuss one example, the influence of the modification of the size of the hole on the graphite lid (figure 3). The simulation of the variation of the axial temperature gradients as function of the diameter of the hole at the backside of the seed crystal is shown in figure 3. The thermal gradient can be strongly increased by increasing the hole diameter.

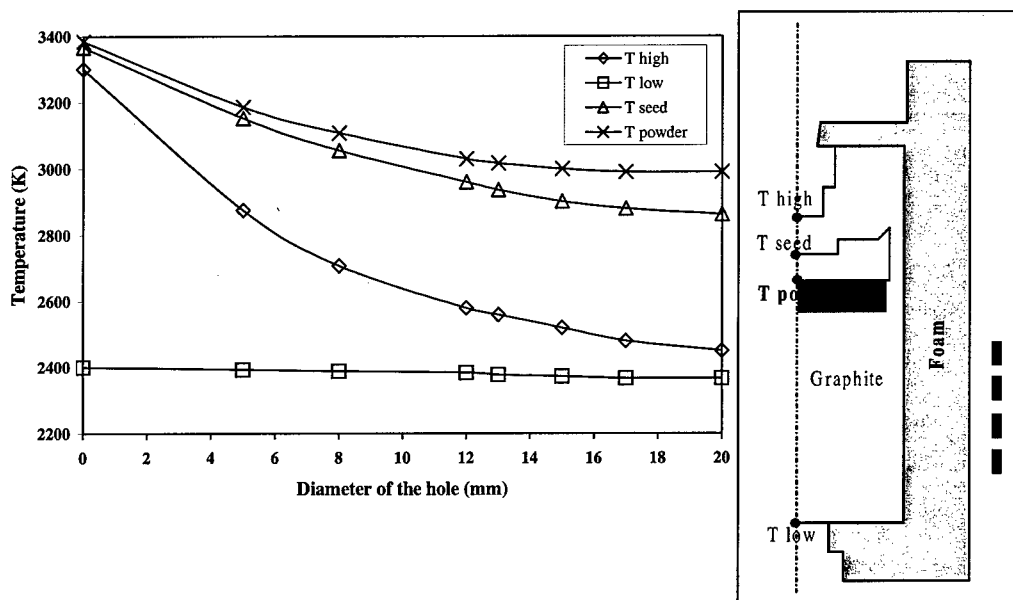


Fig. 3 : Influence of the diameter of the hole used for pyrometric measurements on the temperature of the different part of the reactor along the symmetry axis

### Conclusion

A detailed modelling of SiC crystal growth by the modified Lely method has been set up by combining mass transfer and local thermochemical equilibrium calculations. This tool may be used routinely to understand the evolution of crystal shape resulting from a variation of the process parameters and as a useful guide in the optimization of the reactor design. To illustrate the first point, we have shown that for a given geometry and temperature profile, the initial growth shape curvature of the single crystal can vary with argon pressure. This is mainly due to the initial boundary conditions at the SiC powder sublimation surface.

This shows the importance of a macroscopic description of the growth process, but a detailed knowledge of the specific surface reaction that control the crystallographic texture, the microstructure and the defect/impurity incorporation is still needed. All these issues are critical for controlling crystal properties and processing leading to a complete understanding of the basic mechanisms of SiC growth.

### Acknowledgements

The authors gratefully acknowledge the support of the French Ministry of Education and Research, the French Ministry of Industry and the European Brite Euram Program (Contract BRPR-CT98-0815- JESICA)

### References

- [1] D. Hofmann, M. Heinze, A. Winnacker, F. Durst, L. Kadinski, P.Kaufmann, Y. Makarov, M. Schäfer, J. Crystal Growth, 146 (1995) 214.
- [2] M. Pons, E. Blanquet, J.M. Dedulle, I. Garcon, R. Madar, C. Bernard, J.Electrochem. Soc., 143 (1996) 3727.
- [3] R.C. Glass, D. Henshall, V.F. Tsvetkov, C.H. Carter, MRS Bull., 3(1997) 30.
- [4] S. Yu Karpov, Yu N. Makarov, M.S. Ram, Phys. Stat. Sol. (b), 202 (1997) 201.
- [5] P. Raback, R. Nieminen, R. Yakimova, M. Tuominen, E. Janzen,, Mat. Sci.Forum, 264-268 (1998) 65.
- [6] R. Eckstein, D. Hofmann, Y. Makarov, St.G. Muller, G. Pensl, Mat. Res.Symp. Proc, 423 (1996) 215.
- [7] Yu E. Egorov, A.O. Galyukov, S.G. Gurevich, Yu N. Makarov, E.N. Mokhov,M.G. Ramm, M.S. Ramm, A.D. Roenkov, A.S. Segal, Yu A. Vodakov, A.N.Vorob'ev, A.I. Zhmakin, Mat.Sci. Forum, 264-268 (1998) 61.
- [8] D. Hofmann, R. Eckstein, M. Kolbl, Yu N. Makarov, St.G. Muller, E.Schmitt, A.Winnacker, R. Rupp, R. Stein, J. Volkl, J. Crystal Growth, 174 (1997) 669.
- [9] SiC-Sim, Cape Simulations, Inc., Newton, Ma 02181, USA, 1997.
- [10] M. Pons, M. Anikin, J.M. Dedulle, R. Madar, K. Chourou, E. Blanquet,C. Bernard, Surf. Coat. Technol., 94-95 (1997) 279.
- [11] St.G. Muller, R. Eckstein, J. Fricke, D. Hofmann, R. Hofmann, R. Horn, H. Mehling, O. Nilsson, Mat. Sci. Forum, 264-268 (1998) 623.
- [12] O. Nilsson, H. Mehling, R. Horn, J. Fricke, R. Hofmann, St.G. Muller, R. Eckstein,, D. Hofmann,, High press. High Temp., 29 (1997) 73.
- [13] M.Pons, M Anikin, K. Chourou, J.M. Dedulle, R. Madar, E. Blanquet, A. Pisch, C. Bernard, P. Grosse, C. Faure, G. Basset, and Y. Grange, Mater. Science & Engineering B 56 (1999) in press
- [14] P. Rocabois, C. Chatillon, C. Bernard, F. Genet , High Temp. High Press., 27-28 (1995/96) 25



## Global Numerical Simulation of Heat and Mass Transfer during SiC Bulk Crystal PVT Growth

M. Selder<sup>1</sup>, L. Kadinski<sup>1</sup>, F. Durst<sup>1</sup>, T. Straubinger<sup>2</sup>, D. Hofmann<sup>2</sup> and  
P. Wellmann<sup>2</sup>

<sup>1</sup> Institute of Fluid Mechanics, University of Erlangen-Nürnberg, Cauerstr. 4,  
DE-91058 Erlangen, Germany

<sup>2</sup> Department of Materials Science, University of Erlangen-Nürnberg, Martensstr. 7,  
DE-91058 Erlangen, Germany

**Keywords:** Global Heat Transfer, Mass Transfer, Numerical Modeling, Physical Vapor Transport,  
SiC Bulk Growth

**Abstract.** Modeling results of a global heat and mass transfer analysis of the SiC bulk growth process in an inductively heated PVT reactor are presented. The modeling approach is summarized and its reliability is shown by comparing experimental data to simulation results. The temporal evolution of the temperature gradients at the crystal surface during the growth process is analyzed and related to the radial growth rate distribution. The species fluxes at the surface of the source are investigated.

### 1 Introduction

The preparation of SiC bulk crystals is usually performed by the modified Lely method in the inductively heated growth reactor [1]. As monitoring of the growth process by experimental means is limited by the process conditions and the reactor design, the mathematical modeling of the growth process is considered to be an important tool to overcome the present difficulties in the SiC wafer production (high defect densities, small crystal size, small growth rates). The simulation of the global heat transfer problem has been studied in the last years and has proved its importance in the optimization of the reactor design. By comparing experimental data to numerical results, different authors have shown the reliability of their modeling approach [2, 3].

In this paper we present modeling results of a global heat and mass transfer analysis of the SiC bulk growth process. The modeling route is summarized, and its reliability is shown. The relation between temperature gradients at the crystal/gas interface and the radial growth rate distribution is discussed, and the sublimation process at the porous SiC source is analyzed.

### 2 Experimental Set-up

A schematic model of an axisymmetric PVT growth reactor designed for the production of SiC bulk crystals is shown in Fig. 1. By inductive heating (induction frequency:  $f = 10$  kHz; induction power:  $6 \text{ kW} < P < 12 \text{ kW}$ ) temperatures between 2200 K and 2600 K are established inside the growth cell. The temperature level can be monitored experimentally by optical pyrometers (temperatures  $T_t$ ,  $T_b$ ), the detailed temperature distribution inside the growth cell can be determined numerically. Chemical species which are subliming from the hot porous SiC source are transported to the cold end of the growth cell (location of seed) by diffusion and advection. The growth process can be analyzed after growth by an interface demarcation technique [4] or during growth by x-ray imaging [5].

### 3 Modeling Approach

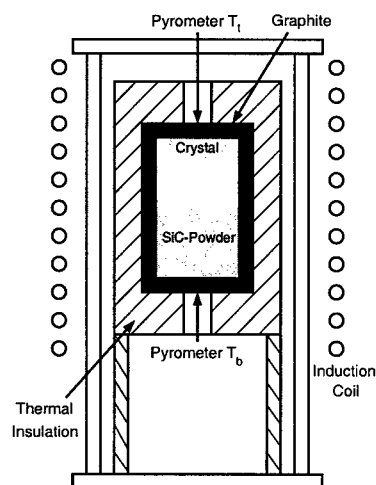


Fig. 1. Scheme of the inductively heated SiC growth reactor.

The prerequisite for the simulation of heat and mass transfer problems is the solution of the inductive heating problem which is described by the Maxwell Equations for axisymmetric geometries and harmonic electromagnetic fields. The Joule heat sources are calculated as function of the electric field and the electrical conductivities of the respective materials [2].

The transport processes inside the growth reactor are described by the coupled set of equations for mass, momentum, energy and chemical species [6]. Heat transfer by convection, conduction and radiation is accounted for in the model. The radiation modeling uses grey-diffuse, viewfactor based heat exchange between all internal boundaries of the reactor [7].

The vapor phase is assumed to consist of the three reactive species Si, Si<sub>2</sub>C and SiC<sub>2</sub> which are diluted in Ar. Diffusion processes are modeled using the Wilke approximation, transport properties of the gas phase are calculated as functions of the gas phase composition. We assume that the chemical species do not undergo any homogeneous chemical reactions. Heterogeneous chemical processes take place at the crystal surface, source and container side wall [8].

The transport equations are solved by the Finite Volume code FASTEST-CVD which is described in the references [2, 6, 7, 8]. The algorithm is based on block-structured non-orthogonal grids and uses the multigrid-technique to speed up convergence. The block structured discretization serves as basis for distinguishing between fluid and solid regions.

The vapor phase is assumed to consist of the three reactive species Si, Si<sub>2</sub>C and SiC<sub>2</sub> which are diluted in Ar. Diffusion processes are modeled using the Wilke approximation, transport properties of the gas phase are calculated as functions of the gas phase composition. We assume that the chemical species do not undergo any homogeneous chemical reactions. Heterogeneous chemical processes take place at the crystal surface, source and container side wall [8].

### 4 Modeling of the Growth process

We checked the reliability of our modeling approach by comparing calculated growth rates to experimental data. For three different coil positions the growth rate evolution in the center

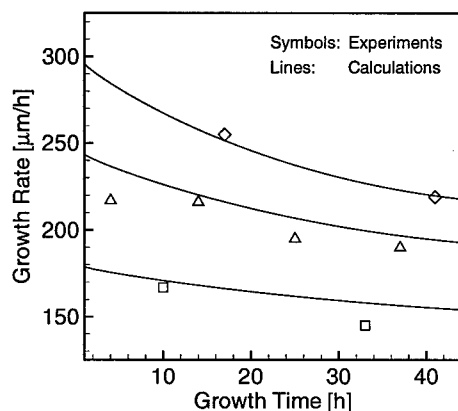


Fig. 2. Measured and computed growth rates for three different coil positions.

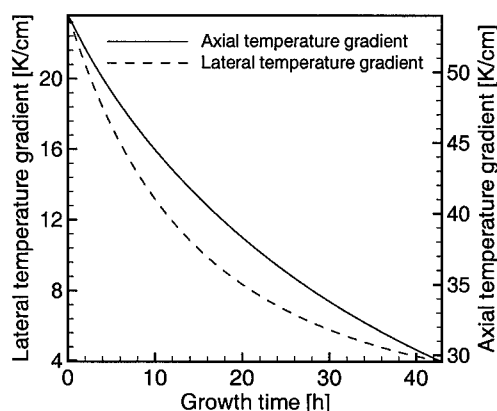


Fig. 3. Temperature gradients at the crystal/gas interface.

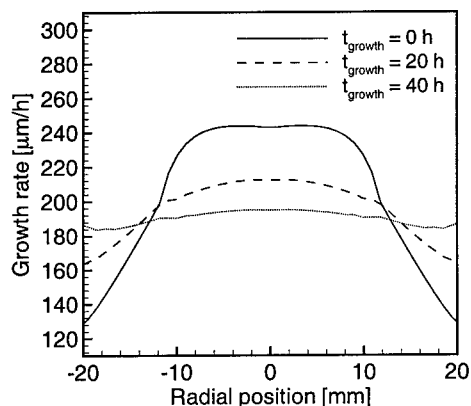


Fig. 4. Radial distribution of the calculated growth rate for three different points in time.

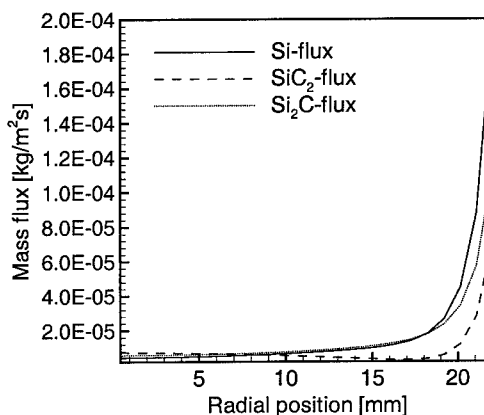


Fig. 5. Mass fluxes of species (Si,  $\text{SiC}_2$ ,  $\text{Si}_2\text{C}$ ) leaving the SiC-source.

of the crystal was monitored (Fig. 2). For each of the three configurations the correspondence between experiment and simulation is very good: The absolute value of the growth rate as well as the growth rate dependence on growth time are reproduced correctly. The further simulations discussed in this section correspond to the middle curve in Fig. 2.

The calculated evolution of the axial and lateral temperature gradient at the crystal/gas interface is shown in Fig. 3. The axial gradient is monitored at the symmetry axis, the lateral gradient in the middle between symmetry axis and side wall. The high values of both gradients at the beginning of the growth run can be considered as main reasons for a variety of defects; the lateral gradient causes a strong radial non-uniformity of the growth rate. In particular the lateral gradient is decreasing during the growth run. As a result thereof, the radial growth rate distribution is smoothed out with increasing crystal length (Fig. 4).

The conditions at the source/gas interface are similar to the conditions at the crystal/gas interface. The radial temperature gradient results in non-uniformly distributed species fluxes leaving the source. The distribution at the beginning of the growth run is shown in Fig. 5. Resulting from the strong radial dependence of the species fluxes the source material will be consumed particularly at the side of the porous source while the powder in the middle of the growth cell will sublime only very weakly.

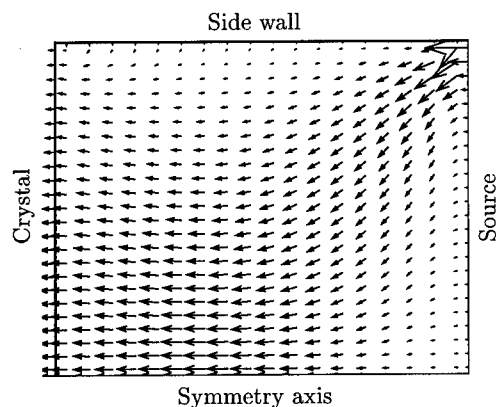


Fig. 6. Flow field inside the growth cell.

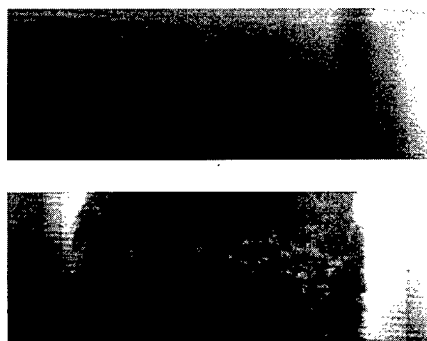


Fig. 7. X-ray images of the SiC source material before (upper image) and after a growth run. The powder orientation corresponds to Fig. 1.

The flow field in the growth cell is determined by the species fluxes at the source/gas and crystal/gas interfaces. This is due to the advective Stefan flow resulting from diffusive fluxes at solid/gas interfaces [9] and can be seen in Fig. 6 where the flow field at the beginning of the growth run is shown. This figure shows in another way that significant species fluxes at the source are only present in the corner between source and side wall, the non-uniformity of the growth rate is also obvious.

The conclusions drawn from the calculations are confirmed by x-ray imaging of the porous source material (Fig. 7). While at the beginning of the growth run the SiC source material gives rise to a homogeneous contrast, after the growth process graphitization of the source material is observed in the vicinity of the graphite crucible (bright regions). This is due to the Si-rich fluxes leaving the source at the side wall (compare to Fig. 5). The dark contrast of the core part indicates a compression of the SiC powder due to sublimation in outer parts and recrystallization in the colder central part.

## 5 Conclusions

A modeling approach for the simulation of global heat and mass transfer during SiC bulk crystal growth was introduced and verified by comparing calculated results to experimental data. The evolution of the radial growth rate distribution was determined and related to the temperature gradients at the crystal/gas interface. Similar considerations were performed for the processes at the source/gas interface; calculated species fluxes at the source were compared to x-ray images of the porous source material.

## Acknowledgement

Financial support by the Bavarian Science Foundation (contract 176/96) and the Deutsche Forschungsgemeinschaft (contracts Du 101/47 and Wi 393/9) is gratefully acknowledged.

## References

- [1] Y.M. Tairov, V.F. Tsvetkov, *Journal of Crystal Growth* 43 (1978) 209.
- [2] M. Selder, L. Kadinski, F. Durst, T. Straubinger, D. Hofmann, *Mat. Sci. Eng.* B61–62 (1999) 93.
- [3] M. Pons, E. Blanquet, J. M. Dedulle, I. Garcon, R. Madar, C. Bernard, *J. Electrochem. Soc.* 143 (1996) 3727.
- [4] R. Eckstein, D. Hofmann, Y. Makarov, St.G. Müller, G. Pensl, E. Schmitt, A. Winnacker, *Mat. Res. Soc. Proc.* 423 (1996) 215.
- [5] P. Wellmann, M. Bickermann, M. Grau, D. Hofmann, T. Straubinger, A. Winnacker, *Mat. Res. Soc. Proc.* 572 (1999).
- [6] F. Durst, L. Kadinski, M. Perić, M. Schäfer, *Journal of Crystal Growth* 125 (1992) 612–626.
- [7] T. Bergunde, M. Dauelsberg, L. Kadinski, Y. Makarov, V. Yuferev, D. Schmitz, G. Strauch, H. Jürgensen, *Journal of Crystal Growth* 180 (1997) 660–669.
- [8] M. Selder, L. Kadinski, Yu. Makarov, F. Durst, P. Wellmann, T. Straubinger, D. Hofmann, S. Karpov, M. Ramm, *accepted for publication in Journal of Crystal Growth*.
- [9] A.S. Segal, A.N. Vorob'ev, S.Yu. Karpov, Yu.N. Makarov, E.N. Mokhov, M.G. Ramm, M.S. Ramm, A.D. Roenkov, Yu.A. Vodakov, A.I. Zhmakin, *Mat. Sci. Eng.* B61–62 (1999) 40.

## An Analytical Study of the SiC Growth Process from Vapor Phase

D.I. Cherednichenko, Y.I. Khlebnikov, I.I. Khlebnikov, S.I. Soloviev and  
T.S. Sudarshan

Department of Electrical and Computer Engineering, University of South Carolina,  
Columbia, SC 29208, USA

**Keywords:** Analytical Model, SiC Growth, Velocity of Growth

**Abstract.** A kinetic model of bulk SiC growth has been developed. In order to calculate the velocity of growth, Frenkel's model of vapor condensation has been used. It is shown that the dynamics of growth is very sensitive to instabilities of the processes in the crucible.

**1. Introduction.** There are a few analytical models for the calculation of the dynamics of SiC single crystal growth [1-4]. For crystals growing from the vapor phase, models are based on the law of mass conservation. However, there are severe difficulties in calculating the mass transport rate in the growth cell and the condensation conditions on the seed surface, in order to estimate the velocity of growth. It is relatively easy to find the molecular flux for growth in vacuum from the Hertz-Knudsen's equation [1,2]. When the SiC crystals are grown in the atmosphere of an inert gas (i.e., argon), the calculation of mass flow becomes more complicated because diffusion flow of the vapor must be taken into account [3,4]. In the above case, the stationary diffusion equation has been used to calculate mass transport intensity between the source material and the growth front. However, experimental results show that the velocity of growth is not constant, but rather varies during the growth process. The variations in velocity may originate from instability in the growth cell, or from an interaction between the vapor species and the graphite walls of the crucible, which result in a change in the crystallization conditions. All of these factors can affect the rate of crystal growth. Formulating models that enable one to estimate the weight of each factor in the crystallization process is important for developing a global model of SiC crystal growth [5,6].

**2. Vapor composition and transport phenomena.** A detailed thermodynamic analysis of vapor composition in the 1500 – 3150 K temperature range is given in [7]. It is shown that within the typical temperature range for SiC crystal growth (2500-2700 K), the total pressure of the vapor is approximately 1.53-11.83 Torr, with a particle concentration of  $5.9 \cdot 10^{15}$  -  $4.3 \cdot 10^{16} \text{ cm}^{-3}$  ( $C_V = P/k \cdot T_V$ , where  $T_V$  is evaporation temperature). At these temperatures, carbon atoms exist in the gas phase only as a component of the molecules of  $\text{Si}_2\text{C}$ ,  $\text{SiC}_2$  and  $\text{SiC}$ . As a result of dissociative chemical reactions, the carbon atoms remaining in the solid phase accumulate in the source zone during the entire growth run.

Mass transport in a closed system may be stimulated by diffusion, convection, and chemical reactions at the location of phase transformation (Stefan flux). An estimation of the gas-dynamics parameters suggests that convection does not take place in low pressure argon atmosphere and at a temperature difference between source and seed less than 50K, and for certain crucible geometry. Heat and mass transport are carried out only by the diffusion of vapor components in argon [4,5].

The effective diffusion coefficient of the vapor has been evaluated as  $D = \sum_i D_{iA} \cdot \eta_i$  (where  $\eta_i = P_i / \sum_i P_i$  is the partial fraction of the vapor constituents). The binary diffusion coefficient for

vapor species in gas,  $D_{IA}$ , depends on the average thermal velocity and the free path of molecules and can be determined from the Chapman-Enskog formula [8]. At an argon pressure of 10 Torr and a temperature of 2600 K, the effective diffusion coefficient is  $90 \text{ cm}^2/\text{s}$ . For this value of the diffusion coefficient, the velocity of a vapor front in the gas phase  $V_f \cong D/L$ , is 9 cm/s and the average time of flight of the species from the source material to the seed,  $\tau \cong L^2/D$ , is 0.1s ( $L < 5 \text{ cm}$  is a typical source-crystal distance). For a closed system at the equilibrium condition, the time of flight can be considered as the lifetime of a vapor species in the system. During this time, a migrating particle might be incorporated into the growing crystal or return to the source, maintaining equilibrium conditions in the growth cell. We disregarded the boundary layer effect because there is no convection flow in the gas [5], and the "non-hydrodynamic" layer [9] near the surface of the phase transformation does not significantly influence the growth conditions due to the diffusion mass transfer.

At the same time, if any local fluctuations in the pressure (density) or composition occur in the gas phase, the time taken for this fluctuation to be transmitted to any point in the growth cell (response time) is very short,  $\tau_r = \eta/P$ . For the dynamic viscosity of argon at  $2.2 \cdot 10^{-4}$  poises (argon pressure of 10 Torr), the response time is  $1.65 \cdot 10^{-8} \text{ s}$ . This means that the vapor pressure near the growing surface almost instantaneously responds to any possible instability in the crucible. Thus, in order to describe the vapor phase near the growing surface, the diffusion equation can be replaced by the kinetic equation. The dynamic of vapor phase formation above the growing surface can be determined by (the initial vapor concentration in the crucible  $C=0$  at  $t=0$ ):

$$C(t) = \left[ \int_0^t C_V(t) \cdot \exp(t/\tau) \cdot dt / \tau \right] \cdot \exp(-t/\tau), \quad (1)$$

where  $C_V(t) = C_0 + C_f(t)$  is vapor concentration in the crucible ( $C_0$  is the average concentration,  $C_f(t)$  is the fluctuation of the vapor concentration). The effective flow of the chemical species from the vapor to the growing surface can be estimated as  $F(t) = (F_V - F_S) \cong U \cdot C(t) \cdot \alpha(t)/4$  where  $F_V(t)$  is the vapor flux to the growing surface;  $F_S(t)$  is the re-evaporation flux;  $\alpha(t) = (1 - C_S(t)/C(t))$  is the supersaturation;  $C_S$  is the concentration of the re-evaporated vapor from the growing surface. Considering the vapor to be an ideal gas and evaluating the vapor pressure as a function of the evaporation energy  $P = A \cdot \exp(-W/R \cdot T)$  (for SiC  $W = 135.6 \text{ kcal/mol}$  [4]), the supersaturation may be written as  $\alpha(t) = W \cdot \Delta T / R \cdot T^2$ , where  $\Delta T(t) = T_V(t) - T_S(t)$  is the difference of the temperatures in the crucible ( $T_S$  is the temperature at the growing surface). An estimation made from heat balance calculation at the surface of crystallization showed that for a small temperature difference between the source and seed, the temperature of the growth front could be approximated as a linear function of the time of growth  $T_S(t) = T_{S0} + \beta \cdot t$  (where  $\beta = \Delta T/t_G$ ,  $t_G$  is the time of growth run).

**3. The velocity of growth.** The classical theory of condensation uses only macroscopic parameters such as surface energy, density, temperature, and supersaturation. In order to estimate the influence of surface processes on the growth dynamics, we will use Frenkel's model of condensation [10]. This theory takes into account atomic processes such as the migration and collisions of atoms on the surface, an atom's lifetime on the surface in adsorbed stage, interaction energy during collision, etc. According to this model, as a result of the collision between two individual atoms, a pair (doublet) of atoms is formed. This doublet may accept additional atoms forming a higher-order complex. In the meantime, it has been shown that the rate of generation of condensation centers,  $dG/dt$ , is determined by the rate of the formation of doublets, even if dissociation of large complexes takes place [11]:

$$\frac{dG}{dt} = \frac{\omega}{2} \cdot n_1^2, \quad (2)$$

where  $G = \sum_{i=2}^{\infty} n_i$  is the surface density of two-dimensional centers of condensation;  $\omega = 4D_s / \sqrt{\pi}$  is the collision factor ( $D_s \cong a^2 \cdot \nu \cdot \exp(-W_D/R \cdot T_s)$  is the surface diffusion coefficient,  $W_D \cong W/4$  is the activation energy of diffusion,  $a \cong (\Omega)^{1/3}$ ,  $\Omega \cong M/N_A \cdot \rho$  is the molecular volume (for SiC:  $M = 41$ ,  $\rho = 3.2 \text{ g/cm}^3$ ,  $N_A$  is Avogadro's number);  $\nu$  is the frequency of atomic vibration;  $n_1 = F \tau_A$  is the surface concentration of adsorbed chemical species;  $\tau_A = \exp(W_S/RT)/\nu$  is the lifetime of the particles at the condensed stage;  $W_S \cong W/2$  is the desorption energy.

The velocity of growth can be found as a function of the generation rate of condensation centers and the molecular volume,  $\Omega$ :

$$V = \frac{dG}{dt} \cdot \Omega = F \cdot \Omega \cdot \varepsilon / 2 \quad (3)$$

The parameter  $\varepsilon = 2 \cdot X_s^2 \cdot n_1 \cdot \exp(-W_C/R \cdot T_s) / \sqrt{\pi}$  is the sticking coefficient, where  $X_s^2 = D_s \cdot \tau_A$  is the surface diffusion length;  $W_C$  is the activation energy of chemical reaction between atoms during collision (for SiC  $W_C = 15.6 \text{ kcal/mol}$ ).

**4. Calculation and analysis.** Experimental observations show that both graphitization and re-crystallization of the source material take place during SiC bulk crystal growth. Therefore, the mass, structure, a composition, thermal and diffusion property of the source material changes during the growth process. As a result, the temperature and the concentration of the chemical species in the vapor will also change. Instability within the growth cell will have a strong influence on the dynamics of the crystal growth process. We can assume that the characteristic time of these processes is equal to the sublimation time of the source material,  $\tau_v$ . Considering that the granules of powder have an average initial radius,  $R_0$ , and evaporate simultaneously at temperature  $T_v$ , we

have  $\tau_v \cong \sqrt[3]{4\pi/3} \cdot \int_0^{R_0} \exp[(W \cdot \xi - 2\gamma \cdot \Omega \cdot N_A)/R \cdot T_v \cdot \xi] \cdot d\xi / \omega_s$  (where  $\omega_s \cong 10^5 \text{ cm/s}$  is the velocity

of sound in solids;  $\sigma \cong 3000 \text{ erg/cm}^2$  is the surface energy. It is important to note that the characteristic time is a function of the granules' radius and the evaporation temperature. In a temperature range 2600-3000 K and for  $R_0 = (10^{-3} - 3 \cdot 10^{-1}) \text{ cm}$ , the characteristic time is approximately in a range from one to 284 hours.

According to Equation (3) for  $\alpha \cong 0.1$  ( $T_v = 2600 \text{ K}$ ) and a stable growth condition (no fluctuation in crucible), the velocity of growth is  $V \cong 0.1 \text{ cm/h}$  and the sticking parameter is  $\varepsilon = 0.039$ . If the temperature fluctuation is approximated as a periodic function  $T_v = T_{v0} + \Delta T_f \sin(2\pi t/\tau_f)$ , then it is possible to estimate the sensitivity of the growth process to the temperature fluctuation in the growth cell. For example, if the amplitude of temperature fluctuation is  $\Delta T_f \cong 2.5 \text{ K}$  (correspondingly, the change in concentration of the vapor is 2.5% (when  $\Delta C \cong 4 \cdot 10^{14}$ )), we can see that at the final stage of growth the velocity can be negative (curve 2 Fig.1 (left)). This result indicates that re-evaporation of the crystal is possible at this stage of growth. With the increase of the amplitude of fluctuation, the re-evaporation process can occur at earlier stages of growth (curve 3,4 Fig.1 (left) and curve 3,4 Fig. 1 (right)).

Approximating the source depletion as a function of the characteristic time,  $\tau_v$ ,  $C_v(t) = C_{v0} \exp(-t/\tau_v)$ , it is possible to show that the dynamic of growth is very sensitive to the

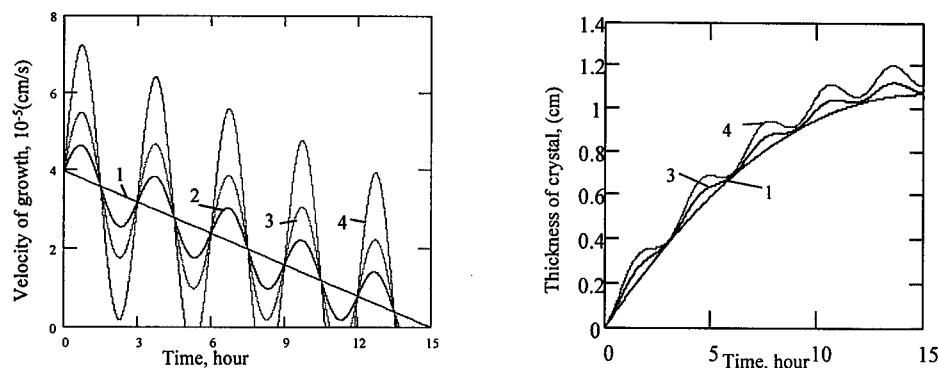


Fig.1 Time dependence of velocity of growth (left) and crystal thickness (right) at different amplitude of temperature fluctuation,  $\Delta T$ : 1 – 0; 2 – 2.5; 3 – 5.0; 4 – 10.0

radius of the source powder grains. Aside from other reasons, the graphitization of the growing crystal surface could be one of the additional reasons for defect generation in the crystal volume. When the temperature of the growth front approaches the evaporation temperature, supersaturation in the vapor decreases to zero and, as a result, the growth process terminated.

## References

- [1] T. Kaneko. Growth kinetic of vapor-growth SiC. J. of Crystal Growth. V.128. (1993), p. 354-357.
- [2] S.Yu. Karpov, Yu.N. Makarov, M.S. Ramm, Analytical model of silicon carbide growth under free-molecular transport conditions, J. of Crystal Growth, V.169 (1996), p. 491-495.
- [3] Yu.M. Tairov, V.F. Tsvetkov. Investigation of kinetic and thermal condition of Silicon Carbide epitaxial layer growth from the vapor phase. J. of Crystal Growth, V.469 (1979) p. 403-409.
- [4] S.K. Lilov and I.Y. Yanchev. Peculiarities of Silicon Carbide Crystal Growth under the Diffusion Mechanism of Vapor Transfer. Advanced Materials for Optics and Electronics. V.1, (1992), p. 203-207.
- [5] M. Pons, E. Blanquet. J. M. Garcon, R. Madar, and C. Bernard. Thermodynamic Heat Transfer and Mass Transport Modeling of the Sublimation Growth of Silicon Carbide Crystals. J. Electrochem. Soc. V.143, No.11, (1996), p. 3727-3735.
- [6] St.G. Müller, R. Eckstein, D. Hofmann, L. Kadinski, P. Kaufman, M. Kölbl, E. Schmitt. Modeling of the PVT-SiC Bulk Growth Process Taking into Account Global Heat Transfer, Mass Transport and Heat of Crystallization and Results on its Experimental Verification. Materials Science Forum, V. 264-268, (1998), p. 57-60.
- [7] S.K. Lilov. Study of the equilibrium processes in the gas phase during silicon carbide sublimation. Materials Science and Engineering, B21 (1993), p. 65-69.
- [8] E.L. Cussler. Diffusion (Mass transfer in fluid systems), Cambridge University Press. (1984).
- [9] S.I. Anisimov, J.A. Imas, G.V. Romanov, and U.V. Khodyko. High-Energy Radiation Action on Metals. Nauka Press, Moscow (1970).
- [10] G. Zinsmeister. A contribution to Frenkel's theory of condensation. Vacuum, V.16, N10, (1966), p. 529-535.
- [11] G. Zinsmeister. Theory of thin film condensation. Thin Solid Films, 2 (1968), p. 497-507.



## Growth Rate Control in SiC-Physical Vapor Transport Method Through Heat Transfer Modeling and Non-Stationary Process Conditions

T.L. Straubinger<sup>1</sup>, M. Bickermann<sup>1</sup>, M. Grau<sup>1</sup>, D. Hofmann<sup>1</sup>, L. Kadinski<sup>2</sup>,  
S.G. Müller<sup>1</sup>, M. Selder<sup>2</sup>, P.J. Wellmann<sup>1</sup> and A. Winnacker<sup>1</sup>

<sup>1</sup>Department of Materials Science 6, University of Erlangen-Nürnberg, Martensstr. 7,  
DE-91058 Erlangen, Germany

<sup>2</sup>Department of Fluid Mechanics, University of Erlangen-Nürnberg, Cauerstr. 4,  
DE-91058 Erlangen, Germany

**Keywords:** Heat Transfer, Mass Transport, Non-Stationary Process

**Abstract.** The growth velocity determined by an one dimensional diffusion dominated transport model turns out to be proportional to the difference of the partial pressures at source and crystal surface (= driving force) and reciprocal proportional to a diffusive transport resistance.

For verification we have investigated the growth rate as a function of growth temperature, position of induction heating coil and carrier gas pressure for several growth runs. Contrary to the conventional procedure of performing single stationary experiments for each parameter set we have applied non stationary process conditions by varying one of these parameters with time. This allowed us to measure the growth rate for different parameter sets out of one crystal.

The thermal data used were determined from pyrometrical measurements on the top and bottom of the crucible during the experiments and were combined with simulations of the 2-dimensional heat transfer in the assembly. The latter allowed us to obtain the temperatures (source, crystal) inside the reaction chamber which were not assessable by direct measurements.

### Introduction

Despite recent success in the growth of SiC bulk crystals by the physical vapor transport (PVT) growth process [1], i.e. considerable defect reduction, a further understanding of the underlying transport mechanisms is necessary. Numerical modeling of the PVT process [2,3] and it's verification by non stationary experiments is believed to play a key role for improving the SiC crystal growth.

### Theory

In order to describe the mass transfer through the vapor phase we used a 1-DIM theory [4] which focuses on diffusive transport. The mass flow is proportional to a driving force  $U_v$  (difference of partial saturation pressures at source and crystal) and reciprocal proportional to a diffusive resistance  $R_{D,v}$ . [Tab.1]

To evaluate the theoretical growth rate the system pressure  $p_{tot}$ , the distance between source and crystal surface  $d_{CS}(t)$  and the temperatures  $T_s / T_C(t)$  have to be determined.

According to theory [Tab.1] the growth rate should have the following dependence on these parameters. The rate should increase with rising global temperature, rising temperature difference between source and crystal, decreasing system pressure and decreasing distance source-crystal.

$$\text{Formula for Theoretical Growth Rate: } v_G = \frac{M_{\text{SiC}}}{\rho_{\text{SiC}}} \sum_v \frac{U_v}{R_{D,v}} = \frac{M_{\text{SiC}}}{\rho_{\text{SiC}}} \sum_v (p_v^{s,s} - p_v^{c,s}) \cdot \left( \frac{R\tilde{T}d_{sc}}{D_{Ar,v}} \right)^{-1}$$

$$\text{Driving Force: } U_v = p_v^{s,s} - p_v^{c,s} = p_0 \cdot \left( e^{\frac{\Delta H_v}{k_B T_s}} - e^{\frac{\Delta H_v}{k_B T_c}} \right)$$

$$\text{Diffusion Resistance: } R_{D,v} = \frac{R\tilde{T}d_{sc}}{D_{v,Ar}}$$

$$\text{Diffusion Constant: } D_{v,Ar} = \frac{(const.)\tilde{T}^{3/2} \left( \frac{1}{M_v} + \frac{1}{M_{Ar}} \right)^{1/2}}{P_{Ar} s_{av}}$$

Tab.1:  $v_G$  is the growth rate,  $v$  indicates the two gas species  $\text{Si}_2\text{C}$  and  $\text{SiC}_2$ ,  $M_v$  is the molar mass,  $\rho_{\text{SiC}}$  is the density of Silicon Carbide,  $p_v^{i,s}$  are the saturation pressures and  $T_i$  the temperatures at source ( $i=S$ ) and crystal ( $i=C$ ),  $R_{D,v}$  is the diffusive resistance,  $\tilde{T}$  represents an average temperature,  $d_{sc}$  is defined as distance crystal-source,  $D_{v,Ar}$  is the binary diffusion coefficient in Argon,  $p_{\text{tot}}$  is the system pressure and  $s_{av}$  is an average cross section of  $\text{Si}_2\text{C}/\text{SiC}_2$  in Argon.

### Experiments

For verification of the theory we performed experiments with non stationary process conditions in a conventional PVT reactor [4,5]. For all runs we used 6H Si/C-face orientated seed wafers with a MPD of about  $200\text{cm}^2$  and a diameter of 30mm. The temperature on top of the crucible was set to  $2100^\circ\text{C} \dots 2300^\circ\text{C}$  while the system pressure was varied between 10 and 50mbar.

During the experiments we measured the system pressure  $p_{\text{tot}}$  and the temperature  $T_i$  on top of the crucible by an optical pyrometer. The crystals were vertically cut in order to obtain the experimental growth rate  $v_G(t)$  and the distance crystal-source  $d_{cs}(t)$  through the intentionally introduced doping striations [6].

Since the thermal conditions inside the chamber were not accessible by direct measurement we used a 2-DIM heat transfer program [7] to determine the temperatures of the crystal and source as a function of crystal length and temperature on top of the crucible (=top pyrometer).

### Results and Discussion

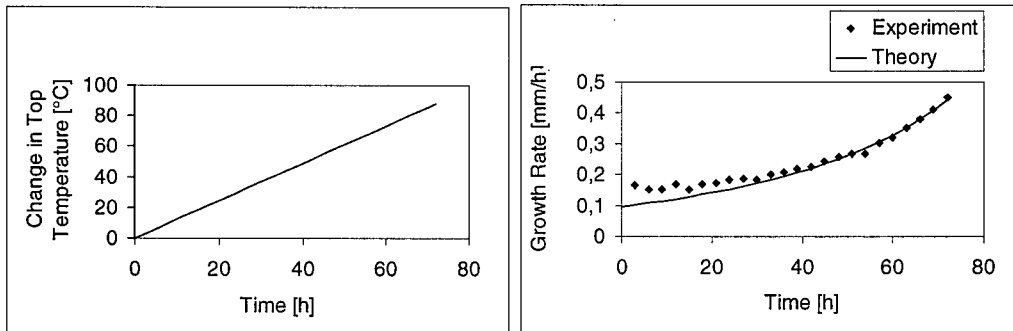


Fig.1: PVT-Experiment with rising temperature.

a. Measured temperature on top of crucible versus time.

b. Corresponding experimental and theoretical growth rate versus time.

Fig.1 shows an experiment with linear rising top [Fig.1a] and bottom temperature. The progression of the experimental growth rate [Fig.1b, dots] corresponds very well with theory [Fig.1b, line]. The growth rate increases because of increasing driving forces  $U_v$  and corresponding decreasing diffusion resistances  $R_{D,v}$  [Tab.1]. Since the growth rate does not deviate from theory during the run we conclude that degradation of the powder or mass transfer limitation by heat transfer play a minor role for the vapor transport in our case.

In a run with an additional falling temperature sequence [Fig.2a] the growth rate is also reproduced by theory [Fig.2b]. The difference between  $v_G(t=0)$  and  $v_G(t=60h)$  at equal  $T_i$  is attributed to the different values for  $T_C$  and  $d_{CS}$  due to crystal growth.

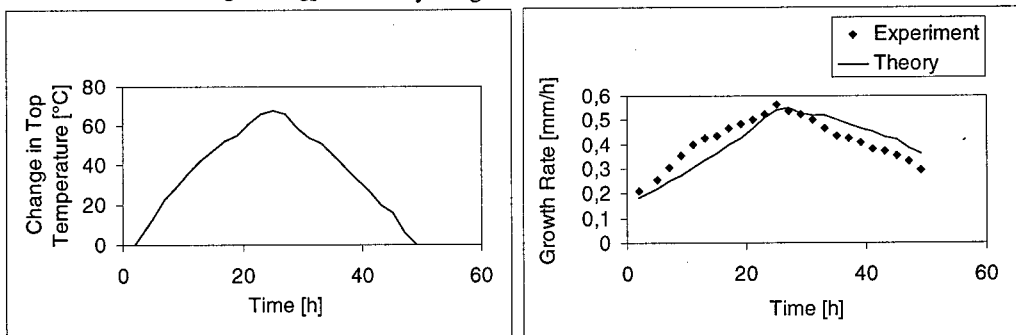


Fig.2: PVT-Experiment with rising/falling temperature.

- Measured temperature on top of crucible versus time.
- Corresponding experimental and theoretical growth rate versus time.

In the experiment described in Fig.3 the pressure was changed linearly in the range from 45mbar to 15mbar [Fig.3a]. The change in  $v_{G,ex}$  through modification of  $T_i/T_C/T_S$  (efficiency of isolation is depending on the system pressure),  $p_{tot}$  and  $d_{CS}$  (growing crystal) is well described by theory [Fig.3b] and again no deviation according to change of the SiC powder and/or heat transfer limitation is observed.

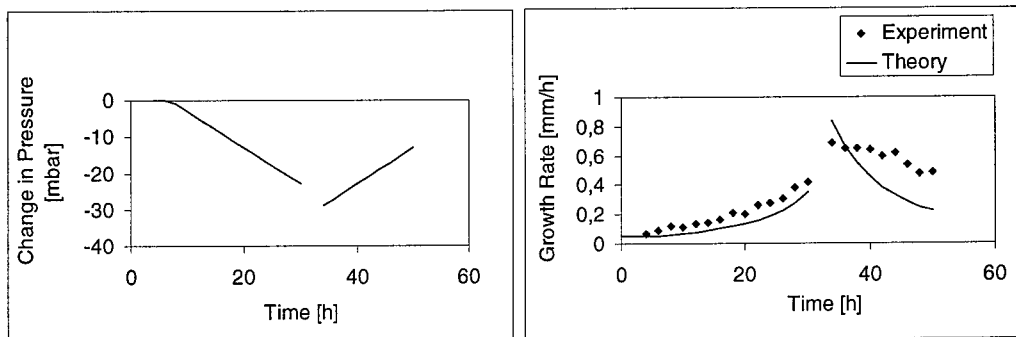


Fig.3: PVT-Experiment with variable system pressure.

- Measured system pressure versus time.
- Corresponding experimental and theoretical growth rates versus time.

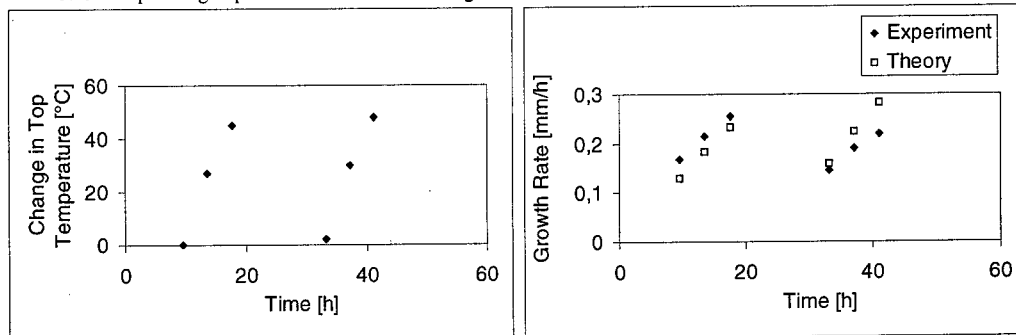


Fig.4: PVT-Experiment with varying coil positions (-2cm, 0, +2cm, -2cm, 0, +2cm). Growth rates were measured after rearrangement of the thermal equilibrium.

- Measured temperature on top of the crucible versus time.
- Corresponding experimental and theoretical growth rates versus time.

During one experiment we have changed the relative position of the coil and the crucible in equidistant steps. Fig.4 shows that the temperature ( $T_1$ ) depends linearly on the position of the coil. Since the growth rate also rises linearly [Fig.4b], only the temperatures between crystal and powder surfaces seem to be crucial for the growth rate. If the mass transfer inside the powder would be the limiting factor the transport rate should rather decrease with a higher coil position because the average powder temperature drops at a higher coil position.

For low defect generation and homogeneous doping incorporation a constant growth rate over the entire PVT process time is desirable.

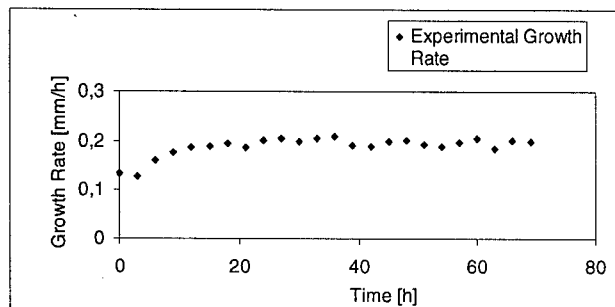


Fig.5 shows an experiment where  $v_G$  could be stabilized by the use of a suitable geometry in which increasing  $T_C$  and decreasing  $d_{CS}$  compensated each other. The increase during the first 5 hours is caused by the stabilization of the powder and crystal surface inside the thermal field.

Fig.5: Experimental growth rate of an experiment with a new crucible geometry, constant power, top temperature and system pressure.

### Conclusions/Summary

We have shown that the parameter field of our PVT process is in the diffusive dominated transport range. The 1-DIM theory can be used to predict the approximate growth rate for given process conditions ( $p$ ,  $T$ , coil, geometry). Temperature distribution and the variations inside the powder during an experiment have no significant influence on the transport rate.

The PVT-process with a specially designed crucible geometry, fixed power and system pressure results in a growth rate which is nearly constant after stabilization during the first 5 hours.

### Acknowledgements

This work has been supported by the Bayrische Forschungsförderung (contract No.176196) and the Deutsche Forschungsgemeinschaft (contract No.W:39319).

### References

- [1] C.H. Carter, Jr., V.F. Tsvetkov, D. Henshall, O. Kordina, K. Irvine, R. Singh, S.T. Allen and J.W. Palmour, *Mat. Sci. Eng. B*, 1999.
- [2] D. Hofmann, M. Heinze, A. Winnacker, F. Durst, L. Kadinski; P. Kaufmann, Y. Makarov and M. Schäfer, *J. Cryst. Growth*, 146, 214-219, 1995.
- [3] M. Pons, M. Anikin, K. Chourou, J.M. Dedulle, R. Madar, E. Blanquet, A. Pisch, C. Bernard, P. Grosse, C. Faure, G. Basset and Y. Grange, *Mat. Sci. Eng. B*, 1999.
- [4] St.G. Müller, "Herstellung von Siliziumkarbid im Sublimationsverfahren", Shaker Verlag, 60-91, 1998.
- [5] R.C. Glass, D. Henshall, V.F. Tsvetkov, and C.H. Carter, Jr., *Phys. Stat. Sol. (b)* 202, 149-162, 1997.
- [6] R. Eckstein, D. Hofmann, Y. Makarov, St.G. Müller, G. Pensl, E. Schmitt and A. Winnacker, *Mat. Res. Soc. Symp. Proc.* 423, 215-220, 1996.
- [7] M. Selder, L.Kadinski, F. Durst, T. Straubinger and D. Hofmann, *Mat. Sci. Eng.*, 1999.

## Experimental and Theoretical Analysis of the Thermal Conductivity of SiC Powder as Source Material for SiC Bulk Growth

St.G. Müller<sup>1,2</sup>, J. Fricke<sup>3</sup>, D. Hofmann<sup>2</sup>, R. Horn<sup>3</sup>, O. Nilsson<sup>3</sup> and B. Rexer<sup>2</sup>

<sup>1</sup> Cree Research, Inc., 4600 Silicon Drive, Durham, NC 27703, USA

<sup>2</sup> Department of Materials Science 6, University of Erlangen-Nürnberg, Martensstr. 7,  
DE-91058 Erlangen, Germany

<sup>3</sup> Bavarian Center for Applied Energy Research (ZAE Bayern), Am Hubland,  
DE-97074 Würzburg, Germany

**Keywords:** Numerical Modeling, Powder, Theory, Thermal Conductivity

**Abstract:** The availability of accurate thermal conductivity data for all types of materials used inside a reactor for SiC bulk growth is the basis of a realistic numerical heat transfer model as a tool for further process optimizations. Measurements of the thermal conductivity of synthesized SiC powder as a possible source material for SiC bulk growth are reported as a function of pressure and temperature. For the extrapolation of experimental data to high temperature regimes not accessible by measurements, a theoretical model was developed. Based on the structural analysis of the powder and without introducing fitting parameters good agreement between theory and experiment was found.

### Introduction

Within the last several years SiC based device technology involving electronic applications for high power, high temperatures, chemical harsh environments and intense radiation has made tremendous progress. The commercial availability of high quality SiC substrates is essential for the development of the full potential of this technology. The growth of SiC boules by the seeded sublimation method has proven to be an efficient technique for the industrial production of these wafers [1,2]. With the demand for even further quality improvements and increasing wafer diameters this growth technology has to face future challenges. In order to achieve this goal, more and more crystal growth research groups are beginning to utilize the possibilities of numerical simulation of heat- and mass-transfer during growth for process improvements [2,3,4]. A key issue for the numerical calculations is the availability of accurate thermal conductivity data for all types of materials used in the growth system. While experimental data of the high temperature thermal conductivity of monocrystalline SiC was reported recently [5], to our knowledge no equivalent experimental study on the SiC-powder used as source material for SiC bulk growth is available. Owing to a lack of this data, in early publications related to the simulation of SiC bulk growth [6] the thermal conductivity of monocrystalline SiC was used to represent the thermal conductivity of SiC powder. It has become clear that this assumption leads to completely different calculated temperature profiles inside the growth crucible [7]. This paper is devoted to an accurate description of the actual thermal conductivity of the SiC powder.

### Experiment

The thermal conductivity of synthesized SiC-powder [8] was measured with the transient hot-wire-method [9]. For this purpose a platinum wire was placed within a SiC powder sample, serving simultaneously as heating element and as temperature sensor. For times  $t > 0$  a constant electrical heating power was provided. The thermal conductivity within the temperature range of 300-1462K under a argon atmosphere of 10 mbar and at 300K within a pressure range of 0.0024-985 mbar (air) was extracted from the measurement by fitting the analytical solution of the Fourier equation to the characteristic time dependency of the temperature increase at the wire (Fig.1).

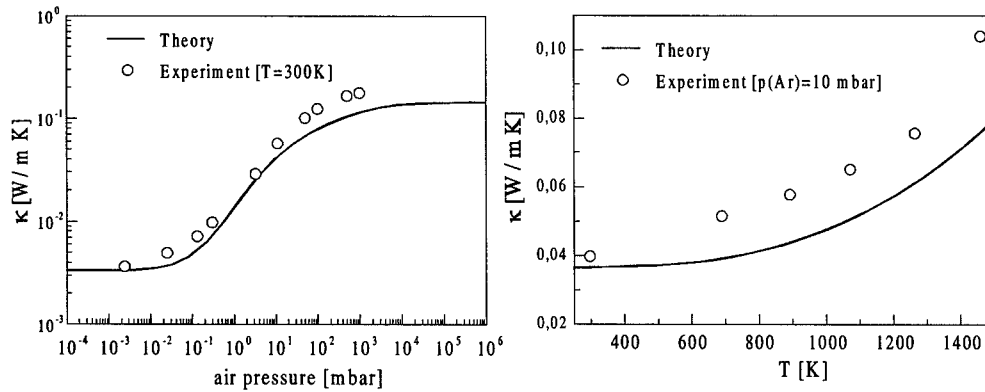


**Figure 1:** Thermal conductivity  $\kappa$  of SiC-powder as a function of pressure (air,  $T = 300$  K) and temperature (argon atmosphere, 10 mbar). The pressure dependence can be attributed to the Smoluchowski-effect [13] and the increase with temperature indicates the dominance of heat transfer by radiation.

### Theory

For the necessary extrapolation of experimental data to the high temperature regimes of SiC bulk growth ( $\sim 2300$ - $2800$  K [2]) not directly accessible by the measurements, a theoretical model was developed. The basis of the calculations is the description of the powder as a network of thermal resistances representing the different heat transfer mechanisms inside the powder:

- Conduction dominates within the single grains, between the contact points of adjacent grains and within the gas-phase of the powder pores
- Radiation dominates within the powder pores

With small local temperature differences inside the powder it is possible to account for the radiation by a proper definition of a radiative thermal conductivity [10] inside the pores. This allows the combined heat transfer mechanisms to be described by a network of thermal resistances. While the following description of this model will stress the relevant theoretical assumptions, further details can be found in [7,11].

Important input parameters for the calculations are the powder-porosity and the grain size of the particles as obtained from a structural analysis of the powder (average grain diameter:  $45 \mu\text{m}$ ). The measured high porosity of  $\Pi = V_{\text{gas}}/V_{\text{powder}} = 65$ - $70\%$  is connected to a very inhomogeneous pore structure. For a more realistic description of this structure we define subsets of smaller pores of 1<sup>st</sup> order (total volume  $V_1$ ) as they are present in a relatively close packed configuration ( $\Pi \leq 40\%$ ) and larger pores of 2<sup>nd</sup> order ( $V_2$ ) for  $\Pi > 40\%$  with  $V_{\text{gas}} = V_1 + V_2$  (Fig. 2). For the description of the heat transfer between adjacent powder grains the actual contact points are replaced by a simplified model geometry. Hereby, the effective contact area is a function of porosity and surface roughness. For  $\Pi > 40\%$  the powder is simulated as a regular, periodic grid with branches made out of close packed areas with pores of 1<sup>st</sup> order ( $\Pi_{1\text{st}} = V_1/(V_{\text{powder}} - V_2) \equiv 40\%$ ), while the porosity of the grid itself due to the larger 2<sup>nd</sup> order pores in between is given by  $\Pi_{2\text{nd}} = V_2/V_{\text{powder}} = (\Pi - \Pi_{1\text{st}})/(1 - \Pi_{1\text{st}})$ . The final calculation of the thermal conductivity is done in two steps:

1. For the description of the thermal conductivity  $\kappa_{1\text{st}}$  within the close packed areas, the heat transfer flow is considered as 1D process along parallel lines between adjacent grains. For this purpose the inside of a powder grain, the contact area and the 1<sup>st</sup> order pore between two grains is divided into geometrical segments with characteristic thermal resistances. The resistances are combined by analogy to resistances in an electrical circuit, while additionally a numerical factor is introduced to account for the spreading of the heat from the contact area within the grains [12].

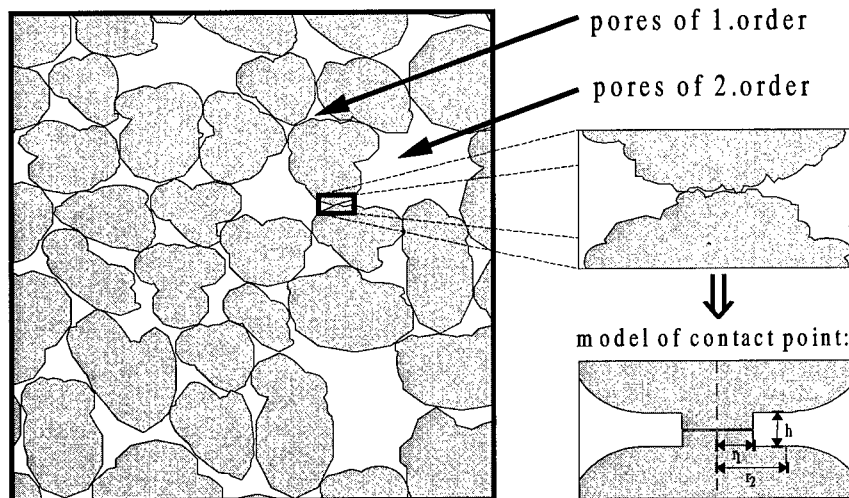


**Figure 2:** Schematic cross-section of the powder structure with smaller 1<sup>st</sup> order and larger 2<sup>nd</sup> order pores and the simplified model geometry for the contact points between adjacent grains.

2. The total thermal conductivity is now calculated from the thermal resistances of the regular, periodic grid with "solid" parts with the thermal conductivity  $\kappa_{1st}$  and the gaseous parts representing the pores of 2<sup>nd</sup> order.

#### Comparison between theory and experiment

Contrary to the case of monocrystalline SiC [5], the effective thermal conductivity of SiC powder significantly increases with temperature. This behavior, as well as the strong dependency of theoretical results on the porosity and the emissivity of the powder, is related to the dominant heat transfer mechanism of radiation towards higher temperatures. This is most significant in a direct comparison of theoretical results with and without considering radiation (Fig.3). Keeping all theoretical approximations in mind and without introducing any fitting parameters, good agreement was found between theory and experiment (Fig.1). The pressure dependence of the thermal conductivity can be attributed to the *Smoluchowski-effect* [13]. The limiting values at low and high pressures are determined by the thermal conductivity of the solid and the gas phase.

#### Conclusion

Experimental data of the thermal conductivity of synthesized SiC powder as a possible source material for SiC bulk growth was reported as a function of pressure and temperature. A theoretical model was developed for the extrapolation to high temperature regimes with the flexibility to consider different growth pressures. Good agreement was found between theory and experiment, stressing the relevance of heat transfer by radiation inside the powder pores. It is important to notice, that the effective thermal conductivity of SiC powder is up to two orders of magnitude lower than of monocrystalline SiC in typical SiC growth regimes, leading to completely different calculated temperature profiles inside the growth crucible, if these values are used for the description of the SiC source material in the numerical heat transfer simulations of SiC bulk growth [7]. By applying the presented concepts to the description of the SiC source material during different growth times, one has to keep in mind, that sintering

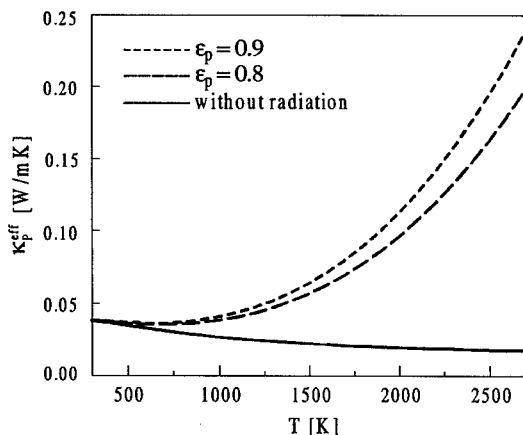


**Figure 3:** Comparison of theoretical results of the effective thermal conductivity of SiC powder with and without considering radiation and the effect of the emissivity  $\epsilon_p$  of the grains.

processes can lead to structural changes. A possible powder graphitization can be taken into account within the presented theoretical network model by adding specified graphite layers to the powder particles.

#### Acknowledgements

This work was financially supported by the Bundesministerium für Bildung und Wissenschaft (BMBF) (FKZ: 03 M 2746)

#### References

- [1] C.H. Carter, Jr., V.F. Tsvetkov, R. C. Glass, D. Henshall, M. Brady, St.G Müller, O. Kordina, K. Irvine, J.A. Edmond, H-S. Kong, R. Singh, S.T. Allen, J.W. Palmour, 2<sup>nd</sup> European Conference on SiC and Related Materials, Montpellier, Sept. 2-4 (1998), to be published in Mat. Sci. Eng.
- [2] St.G. Müller, R.C. Glass, H.M. Hobgood, V.F. Tsvetkov, M. Brady, D. Henshall, J.R. Jenny, D. Malta, C.H. Carter, ACCGE-11, Tuscon Arizona 1999, to be published in J. Cryst. Growth.
- [3] D. Hofmann, R. Eckstein, M. Kölbl, Y. Makarov, St.G. Müller, E. Schmitt, A. Winnacker, R. Rupp, R. Stein, J. Völkl, J. Cryst. Growth 174 (1997) 669-674.
- [4] M. Pons, M. Anikin, J.M. Dedulle, R. Madar, K. Chourou, E. Blanquet, C. Bernard, Surf. Coat. Tech. 94-95 (1997) 279-284.
- [5] St.G. Müller, R. Eckstein, J. Fricke, D. Hofmann, R. Hofmann, R. Horn, H. Mehling, O. Nilsson, Mat. Sci. For. 264-268 (1998) 623-626.
- [6] D. Hofmann, M. Heinze, A. Winnacker, F. Durst, L. Kadinski, P. Kaufmann, Y. Makarov, M. Schäfer, J. Cryst. Growth 146 (1995) 214-219.
- [7] Stephan Müller, Herstellung von Siliziumkarbid im Sublimationsverfahren, Shaker Verlag, Aachen 1998.
- [8] St.G. Müller, R. Eckstein, R.F.P. Grimbergen, D. Hofmann, B. Rexer, Mat. Sci. For. 264-268 (1998) 425-428.
- [9] J.J. Healy, J.J. de Groot, J. Kestin, Physica 82C (1976) 392-408.
- [10] J.P. Holman, Heat Transfer, McGraw-Hill, New York (1990).
- [11] E.L. Kitanin, V.V. Ris, M.S. Ramm, A.A. Schmidt, Mat. Sci. Eng. B 55(3) (1998) 174-183.
- [12] G.N. Dulnev, Y.P. Zarichniy, Heat conductivity of mixtures and composite materials, Energia Publ., Leningrad (1974).
- [13] P. Zehner, E.-U. Schlünder, Chemie-Ingenieur-Technik 44 (1972) 1303-1308.

Send correspondence to:

Stephan Müller, FAX: (919) 313-5454, e-mail: stephan\_mueller@cree.com



## Seed Surface Preparation for SiC Sublimation Growth

B. Pelissier<sup>1</sup>, C. Moulin<sup>2</sup>, E. Pernot<sup>1</sup>, M. Anikin<sup>1</sup>, P. Grosse<sup>2</sup>, C. Faure<sup>2</sup>,  
B. Ferrand<sup>2</sup>, M. Couchaud<sup>2</sup>, G. Basset<sup>2</sup> and R. Madar<sup>1</sup>

<sup>1</sup>LMGP, UMR 5628 INPG/CNRS, BP 46, FR-38402 St. Martin d'Hères Cedex, France

<sup>2</sup>LETI-CEA Grenoble, 17 rue des Martyrs, FR-38054 Grenoble Cedex 9, France

**Keywords:** Ex-Situ Seed Preparation, In Situ Sublimation Etching, Step Flow Growth, Sublimation Growth

**Abstract :** The seed surface preparation for SiC sublimation growth has been investigated. Two methods have been developed to prepare and improve the seed surface contribution during the growth initiation:

- An in-situ sublimation etching of the seed is performed.
- The seed surface is prepared by ex-situ polishing and chemical and ozone cleaning.

Both methods promote a better lateral growth mechanism, and then promote the preferred step flow growth mechanism. This results in a better crystalline quality of the crystals in terms of mosaicity, polytype stability and micropipe density.

### I) Introduction

In 1978 the invention of the seeded sublimation growth technique, the so-called "Modified Lely Method", opened the path to the production of large area SiC wafers. However, at present, the material quality still remains an obstacle to a commercial breakthrough of SiC technology. The improvement of the structural properties and an increase of the available size of SiC wafers are key areas of research and development in this field. The seed surface quality has a major influence on the initiation of SiC sublimation growth. A contaminated or damaged surface will lead to defects which propagate into the growing ingot. This results in a high pinhole density and the formation of inclusions. In order to optimize the seed/ingot interface, a number of treatment methods for seed surface preparation have been investigated.

The experimental setup used for the whole study has been previously described [1].

### II) The in situ sublimation etching

To remove the damaged and contaminated surface layer, and to initiate lateral growth, Anikin proposed in situ sublimation etching [2]. This technique has been optimised to obtain a calibrated sequence of temperature and pressure as a function of time which improves the reproducibility of the early stages of SiC growth. The etching sequence is as following :

-At the beginning of the growth process, under atmospheric pressure of argon, the temperature is raised to Tise (temperature of in-situ etching) while the temperature gradient is inverted (seed temperature > source temperature).

-Then the pressure is decreased down to Pise (pressure of in-situ etching), while temperature is maintained to Tise. The pressure remains at Pise during Dise (duration time of in-situ etching).

-Finally, the argon pressure is increased to atmospheric level and the temperature gradient is slowly established in accordance to the growth conditions.

According to the model Matsunami et al proposed for CVD growth [3], the average step size on the surface must remain close to the lattice parameter to allow for the step flow growth mechanism. If the steps are too high, the step flow is not homogeneous and structural defects such as inclusions of other polytypes are more likely to be formed. The influence of the parameters Tise, Pise and Dise on the step height have been investigated, on the C-face and Si-face on both 4H and 6H seeds. The experimental samples were pieces of off-axis seeds. On-axis seeds like Lely crystals don't allow to obtain a continuous step structure. The step

structure has been observed by Scanning Electron Microscopy (SEM) and the step height has been measured by Atomic Force Microscopy (AFM).

The steps height on the surface depends exponentially on temperature but also on pressure and etching duration time. In addition, if the Si pressure over the seed is too low, carbonisation of the SiC surface is observed for elevated temperature ( $T_{\text{ise}} = 2000^\circ\text{C}$ ) and low pressure ( $P_{\text{ise}} < 50\text{Torr}$ ).

At high temperature ( $T_{\text{ise}} = 2000^\circ\text{C}$ ) and for a short duration  $D_{\text{ise}} = 3\text{min}$ , the etching is very efficient and all the surface defects have been removed. The surface is very regular but the steps height RMS value measured by AFM is  $757 \text{ \AA}$  for  $P_{\text{ise}} = 50\text{Torr}$  and  $306 \text{ \AA}$  for  $P_{\text{ise}} = 150 \text{ Torr}$  (Fig. 1). The etching is too strong to initiate a good step flow mechanism.

As etching efficiency strongly depends on temperature, a lower temperature allows to obtain smaller steps. A compromise between etching depth and step height has been found in a parametric study: At  $T_{\text{ise}} = 1800^\circ\text{C}$  /  $P_{\text{ise}} = 50 \text{ Torr}$  /  $D_{\text{ise}} = 10\text{min}$ ., the step height value is  $52 \text{ \AA}$  (Fig. 2).

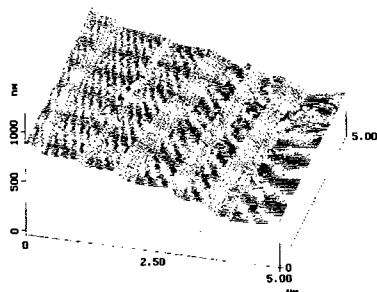


Fig. 1 : AFM image ( $5\mu\text{m} \times 5\mu\text{m}$ ) of a heavily etched 6H Si-face.

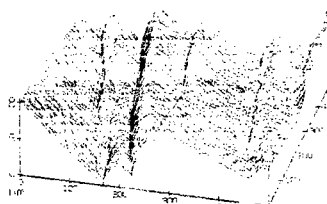


Fig. 2 : AFM image ( $0.5\mu\text{m} \times 0.5\mu\text{m}$ ) of a smooth etched 6H Si-face

The influence of the duration  $D_{\text{ise}}$  has been studied. An Increase of the etching duration  $T_{\text{ise}}$  results in an increase in step size. At  $T_{\text{ise}} = 1800^\circ\text{C}$  /  $P_{\text{ise}} = 50 \text{ Torr}$  /  $D_{\text{ise}} = 1\text{min}$ , we observed no significant step structure on the surface. The etching duration is too short to achieve the required removal of material. In opposite, for  $D_{\text{ise}} = 20\text{min}$ , the step height is almost twice as large as for 10min duration.

In all cases we found that the steps are higher on the Si-face than on the C-face. For example, at  $T_{\text{ise}} = 1850^\circ\text{C}$  /  $P_{\text{ise}} = 150 \text{ Torr}$  and  $D_{\text{ise}} = 10\text{min}$  the step height is  $350 \text{ \AA}$  on the Si-face (Fig. 3) and  $120 \text{ \AA}$  on the C-face (Fig. 4), respectively, for a 6H seed.

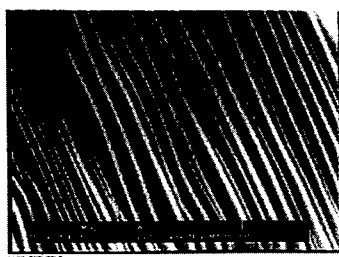


Fig. 3 : SEM image of a 6H Si-face after thermal in-situ etching

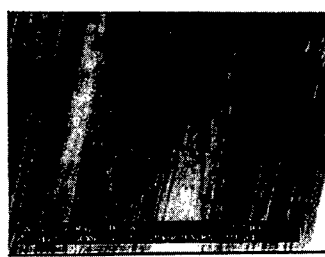


Fig. 4 : SEM image of a 6H C-face after thermal in-situ etching

For 4H substrates, we observed that the minimum temperature necessary to reveal any observable step structure is higher than for 6H. A working point has been found for 4H at  $1825^\circ\text{C}$  /  $150 \text{ Torr}$  /  $10\text{min}$  with similar consideration like in the 6H study.

### III) Ex situ surface preparation process

To prepare and improve the start of growth, two points have been developed. Both of them intend to promote a better lateral growth mechanism. The 4H-SiC seeds under study are  $8^\circ$  off axis. Optical microscopy and micromap (Michelson interference microscope) were used to observe the seed surface.

The seed preparation includes a first step of polishing. The roughness measured by micromap on a 4H-SiC C-face reaches a value of 1 to 2 Å RMS. Possible preferential nucleation due to irregular surface features can be avoided.

A chemical treatment is then performed in order to remove contamination from the seed surface. The first chemical treatment ( $\text{H}_2\text{O}_2 + \text{H}_2\text{SO}_4$ ) forms a thin oxide layer which is subsequently removed after an acid etch ( $\text{HF} + \text{HNO}_3$ ). This is followed by an UV ozone cleaning (Jelight model 42-220). The analysis of the seed surface by AES indicates solely silicon, oxygen and carbon. Figures 5a and 5b show the distribution of these elements versus sputter time (directly proportional to depth) after chemical treatment, respectively before and after the ozone cleaning; the characteristic lines of Si-O, Si-C and C-(O,H) bondings have been separated. AES indicates, The contaminated carbon layer is significantly reduced by the ozone cleaning: 40% of C-graphite bonding instead of 60% without ozone cleaning. All the samples contain a silicon oxide layer. Under this layer, a stoichiometric Si/C ratio of 1 is observed. This silicon oxide layer is supposed to act as a protective layer during the initial heat-up and then to desorb from the seed surface at elevated temperature.

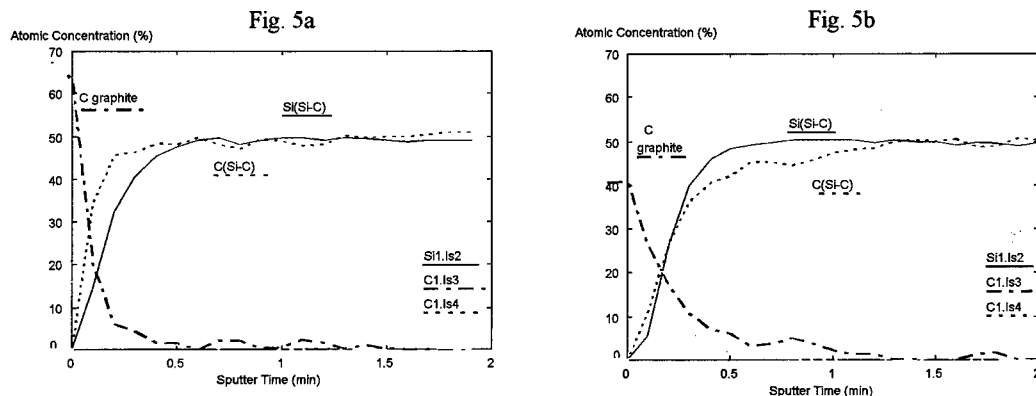


Fig. 5 : Analysis of the seed surface by Auger Electron Spectroscopy after chemical treatment, before ozone cleaning (Fig5a) and after ozone cleaning (Fig5b)

After this ex-situ preparation, great care must be taken during the initial steps of the growth process in terms of the optimization of the pressure and temperature history to avoid the deterioration of the ex-situ prepared surface. Figure 6 shows the seed surface observed by optical microscopy after process interruption during the heat-up. The best surface morphology was achieved at lower temperature value for the increase of the argon pressure, and a higher pressure during the heat-up. If the temperature corresponding to the outgassing is too high, silicon rich species in the vapor can condense on the seed surface. This leads to silicon-like droplets that probably correspond to the dark circle visible in figure 6a. If the pressure is too low during the heat-up, nucleation of undesired polytypes such as 3C inclusions can occur [4]. This can also lead to the premature graphitization of the source powder: the Si/C ratio of the gaseous species is larger than 1 for low temperature [5]. To avoid the sublimation of the source powder at these temperatures, argon is introduced in the growth chamber at a pressure of 600 Torr.

The roughness of the seed surface corresponding to Fig 6b has been determined by micromap measurements after process interruption at  $1200^\circ\text{C}$ , 300Torr (during the heat-up). It agreed exactly with the roughness value after polishing ( $\text{RMS}=2 \text{ \AA}$ ,  $P\text{-}V=50 \text{ \AA}$ ) showing no deterioration of the seed surface.

Fig. 6a

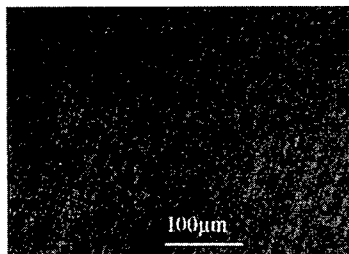


Fig. 6b

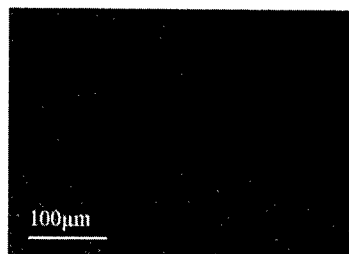


Fig. 6: Optical microscopy observation of the seed surface after heat-up interruption.  
Fig 6a: 1450°C, 50 or 300 Torr and Fig 6b: 1200°C, 300 Torr.

Before the growth process, the SiC powder is heated under vacuum and then sintered inside the PVT reactor at high temperature value and atmospheric argon pressure. This preparation step leads to the formation of more homogeneous steps on the seed surface compared to the results obtained with non-sintered powder (see Figs 7). The process has been interrupted once the growth temperature was achieved and just before decreasing the pressure for crystal growth (interruption at 2050°C, 300Torr). Most likely the source exhibits a more homogeneous sublimation behaviour when it is sintered: sintering leads to more homogeneous grain size and hence, reduces significantly the influence of grain size on evaporation rate.

Fig. 7a

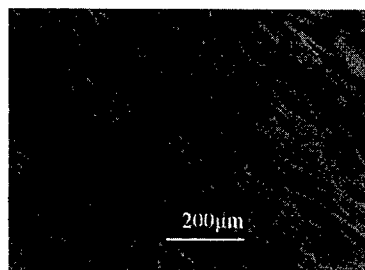


Fig. 7b

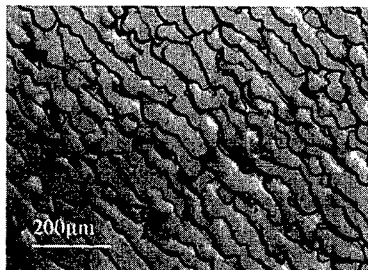


Fig. 7: Optical microscopy observation of the seed surface after process interruption.  
Fig7a: non sintered source powder      Fig. 7b: sintered source powder

This seed surface preparation has significantly improved the quality of the boules, especially in terms of a reduction of mosaïcicity: double crystal X-ray diffraction mapping shows misoriented domains with 60 arcsec misorientation. Misorientation was typically 300 arcsec before introducing this method.

#### Acknowledgements

The authors gratefully acknowledge the support of the French Ministry of Education and Research, the French Ministry of Industry and the European Brite Euram Program (BRPR-CT980815-JESICA).

#### References :

- [1] K.Chourou, M.Anikin, J.M.Bluet, V.Lauer, G.Guillot, J.Camassel, S.Juillaguet, O.Chaix, M.Pons and R.Madar, Materials Science Forum, vol 264-268 (1998), pp 17-20.
- [2] M. Anikin, R. Madar, A. Rouault, I. Garçon, L. Di Cioccio, J.L. Robert, J. Camassel, J.M. Bluet, Inst. of Phys. Conf. Ser., vol 142 (1996), pp 33-36..
- [3] H. Matsunami, Y Ueda and S. Nishino, Mater. Res. Soc. Symp. Proc, vol 162 (1990), pp 397-407.
- [4] Y.M.Tairov and V.F.Tsvetkov, Journal of Crystal Growth, vol 43 (1978), p 209.
- [5] V.F.Tsvetkov, D.N.Henshall, M.F.Brady and R.C.Glass, C.H.Carter, Mat.Res.Soc.Symp.Proc, Vol.512 (1998), pp 89-99.

## **Single Crystal Growth of 6H-SiC on Saw-Damaged Substrate by Sublimation Method**

S. Okada, T. Nishiguchi, T. Shimizu, M. Sasaki, S. Oshima and S. Nishino

<sup>1</sup> Department of Electronics and Information Science, Kyoto Institute of Technology, Matsugasaki, Sakyo-ku, Kyoto, 606-8585, Japan

**Keywords:** Defects, Micropipe, Polytype, Saw-Damage, Sublimation Method

**Abstract** There are various defects such as micropipes and polycrystals in SiC bulk crystals grown by the sublimation method. It is important to confirm the mechanism of defect formation. So sublimation growth of 6H-SiC crystal was carried out on the SiC substrate which was intentionally damaged by a diamond embedded blade. The surface of the growth layer and the interface of the damaged region was observed and characterized.

### **Introduction**

The bulk growth of SiC advances remarkably in recent years. However, to apply SiC wafer to the device, the problem of defects such as micropipes is still remained. It is reported that the micropipe defect is formed when inhomogeneous stress is applied to the seed crystal [1-4]. However, there are many origins for micropipe formation [5-8]. So it is important to investigate the origin of defects.

In order to make a long boule of bulk SiC, source material has to be charged many times during sublimation growth. At the beginning of each growth run, polycrystals often grow, partly on the previously grown surface of the bulk SiC. When the polycrystalline region was removed by a grinding tool made of a diamond-embedded disk and growth re-commenced, damage-free SiC grew on the saw-damaged surface. This technique is important to obtain a long boule of bulk SiC without any intermingling polycrystalline material. It is interesting to investigate how single crystal SiC grows on the saw-damaged surface. To study this new mechanism, we intentionally induced mechanical damage on the substrate by a diamond-blade, and characterized the cross section of the bulk SiC. In this paper, we will report the results observed at the interface of the damaged region and discuss this new mechanism.

### **Experiments**

Sublimation growth of SiC crystal was carried out in a quartz tube with a water-cooled jacket. The crucible was heated by a r.f. generator at a frequency of 300 kHz in Ar atmosphere. Temperature of the bottom and the cap of the crucible ( $T_b$ ,  $T_s$ ) were measured by optical pyrometers. Growth conditions for conventional sublimation growth were given below. The source material was abrasive SiC powder with an average particle size of 1 mm. The substrates were Acheson crystals or 6H-SiC wafers which were cut from bulk crystals made by the sublimation method. Distance between the top of the source SiC and the substrate was 10-20 mm. Inner and outer diameter of the crucible were 24 mm and 32 mm, respectively. The length of the crucible was

75 mm. The growth pressure was 50-100 Torr.  $T_b$  and  $T_s$  were 2300-2400 °C and 2200-2300 °C, respectively.

To observe the defect formation from the damaged region, a 6H-SiC substrate was intentionally damaged by a diamond embedded blade which rotated at 3000 rpm. In this manner, the width and the depth of the groove created on the substrate were 0.6 mm and 0.8 mm, respectively, as shown in Fig.1. Bulk SiC of about 10 mm long with 24 mm in diameter was grown and sliced vertically along the growth direction. The surface morphology of the substrate and the grown layer was carefully characterized by optical microscopy (OM) in the Nomarski mode and transmission mode as well as by fluorescence optical microscopy (FOM), Raman spectroscopy and PL measurement.

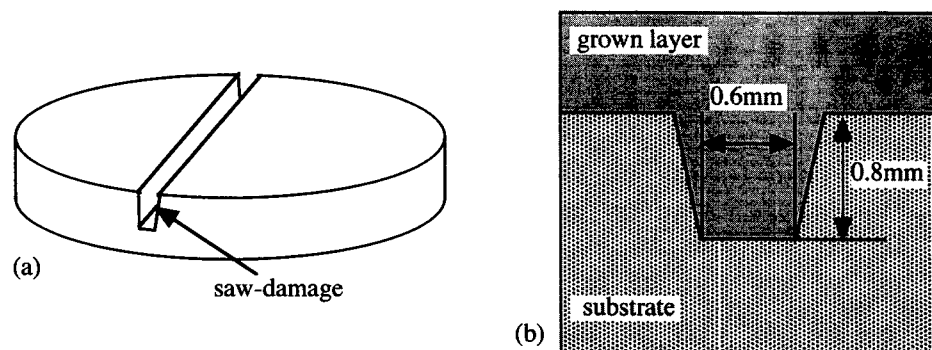


Fig.1 Illustration of the saw-damaged substrate (a), and the substrate and the grown layer (b).

## Results and discussion

The saw-damage created on the substrate was observed by OM in the Nomarski mode as shown in Fig.2. The damaged region has an irregularity of a few  $\mu\text{m}$ , and was very rough. The blade rotated at high speed, so the temperature of the contact region with the substrate became high. Therefore, great stresses seemed to exist. However, when the crystal growth of SiC was carried out for 6 hours, SiC crystal of 6 mm length was grown. The surface of the grown layer was smooth as shown in Fig.3. It is supposed that large defects such as polishing scratches on the substrate differ

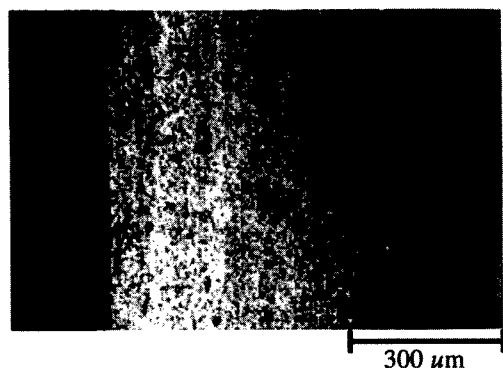


Fig.2 The saw-damage created on the substrate.

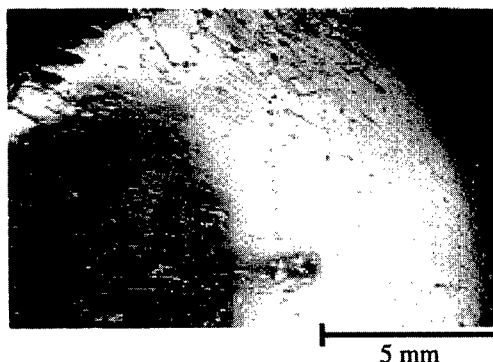


Fig.3 The surface of grown layer on the saw-damaged substrate.

from the micropipe and heal up gradually as the sublimation growth is carried out.

But, it is supposed that new defects may be created from saw-damage. therefore, bulk SiC was sliced vertically along the growth direction and polished. The interface between the grown layer and the blade-damaged substrate was clearly observed by OM in the transmission mode as shown in Fig.4. Micropipes penetrated from the damaged substrate to the grown layer. However, new defects were not created in the grown layer. The reason why the different color is seen at the interface indicates that the impurity density by the filling of the source material is high and it is irrelevant to the stress. The growth rate in the groove was 1.5 times higher than in the flat area (undamaged area) until the groove was filled. The grown layer was single crystalline as determined by X-ray diffraction. PL image of the whole cross section at liquid nitrogen temperature (77 K) was homogeneous, which indicated no polytype inclusion in the grown layer. When the polytype of this area was characterized by Raman spectroscopy, the peaks of TO phonon of 6H-SiC ( $768\text{ cm}^{-1}$ ,  $789\text{ cm}^{-1}$  and  $798\text{ cm}^{-1}$ ) were observed in the damaged area or above it as shown in Fig.5. When the photoluminescence spectra was measured at liquid nitrogen temperature, the peak as shown in Fig.6 was observed, no change of polytype was detected in this area. It is supposed that a shift of the grown layer depends on the impurity density. Normally, the substrate surface should be clean and smooth enough to prevent unwanted defect formation and origin of other polytypes. Our result seems to contradict this statement. We suppose that the mechanically damaged layer was quickly healed at higher temperature before the growth commenced.

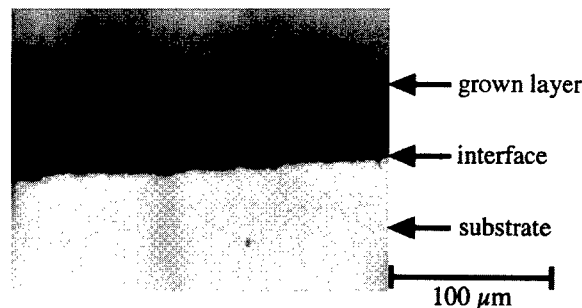


Fig.4 The interface between the grown layer and the substrate.

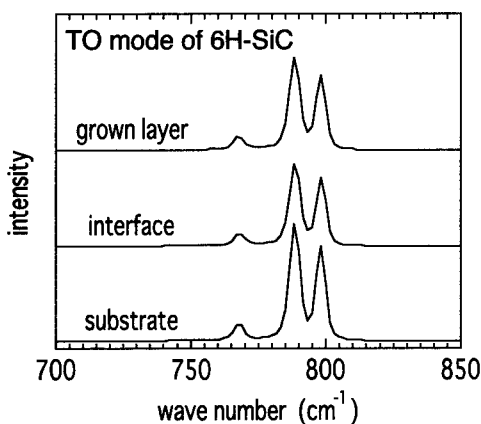


Fig.5 A comparison between the substrate and the grown layer measured by Raman scattering.

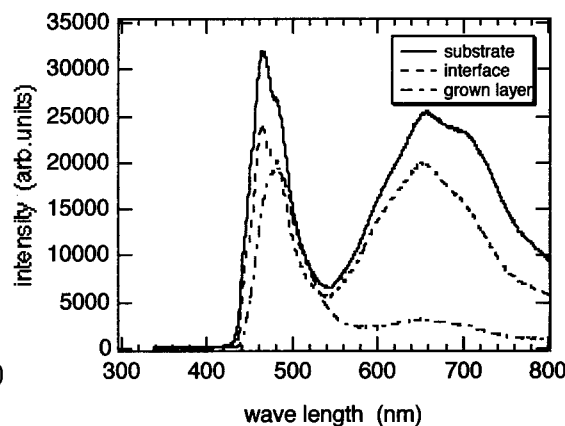


Fig.6 Photoluminescence spectra at liquid nitrogen temperature.

## Conclusions

Sublimation growth of 6H-SiC crystals was carried out on a SiC substrate which was intentionally damaged by a diamond embedded blade. The surface of the grown layer was smooth. Micropipes penetrated from the damaged substrate to the grown layer. However, new defects were not created in the grown layer. The grown layer was single crystalline. No change of polytype was detected in the damaged area. Therefore, it is beneficial that the polycrystalline region on the previously grown surface of the bulk SiC is removed by a grinding tool made of diamond embedded disk and growth is re-commenced.

## Acknowledgements

This work was partially supported by a Grant-in-Aid for Science Research No. 0945001 from the Ministry of Education, Science and Culture, Japan and FED, NEDO Japan, and Ion Engineering Institute (Osaka, Japan).

## References

- [1] V.Dmitriev, S.Rendakova, N.Kuznetsov, N.Savkina, M.Rastegaeva, M.Mynbaeva, and A. Morozov, ECSCRM98, Montpellier, France.
- [2] S.V.Rendakova, I.P.Nikitina, A.S.Tregubova, and V.A.Dmitriev, J.Electronic Materials 27,(1998)292.
- [3] I.Khlebnikov, T.S.Sudarshan, V.Madargarli, and M.A.Capano, Mat.Res.Soc.Symp.Proc. vol.483, (1998)123.
- [4] I.Khlebnikov, V.P.Madargarli, M.A.Khan, and T.S.Sudarshan, Silicon Carbide, III-Nitrides and Related Materials part1(Trans Tech publications)(1997)167.
- [5] V.D.Heydeman, E.K.Sanchez, G.S.Rohre, and M.Skoronski, Mat.Res.Soc.Symp.Proc.vol.483, (1998)295.
- [6] K.Chourou, M.Anikin, J.M.Bluet, V.Lauer, G.Guillot, J.Camassel, S.Juillanguet, O.Chaix, M.Pons and R.Madar,Silicon Carbide, III-Nitrides and Related Materials part1(Trans Tech publications)(1997)17.
- [7] M.Anikin, M.Pons, K.Chourou, O.Chaix, J.M.Bluet, V.Lauer, and R.Madar, Silicon Carbide, III-Nitrides and Related Materials part1(Trans Tech publications)(1997)45.
- [8] V.F.Tsvetkov, S.T.Allen, H.S.Kong and C.H.Carter, Jr Silicon Carbide and Related Materials (Institute of Physics Publishing)(1995)17.



## Thermal Decomposition Cavities in Physical Vapor Transport Grown SiC

E.K. Sanchez<sup>1</sup>, V.D. Heydemann<sup>2</sup>, D.W. Snyder<sup>2</sup>, G.S. Rohrer<sup>1</sup> and  
M. Skowronski<sup>1</sup>

<sup>1</sup>Department of Materials Science and Engineering, Carnegie Mellon University, 5000 Forbes Ave,  
Pittsburgh, PA 15213, USA

<sup>2</sup>II-VI Incorporated, 375 Saxonburg Blvd, Saxonburg, PA 16056, USA

**Keywords:** Physical Vapor Transport Growth, Pinholes, PVT, Sublimation Growth

**Abstract:** The relationship between the formation of thermal decomposition cavities and seed mounting in physical vapor transport grown silicon carbide was investigated. Experimental results indicate that voids exist in the attachment layer between the single crystal seed and graphite crucible lid. These voids lead to the formation of cavities in the seed and grown boule by local decomposition of the seed, transport of silicon bearing species across the void and the deposition of silicon on, and diffusion into, the porous graphite lid. The application of a diffusion barrier on the seed crystal backside is shown to suppress the formation of thermal decomposition cavities.

### Introduction

It is well known that hollow tubes form along the c-axis of SiC crystals during physical vapor transport (PVT) growth [1,2]. These defects intersect the surface of (0001) oriented wafers sliced from such boules and limit the usable area of the substrate. It has been argued by the authors that these defects can be divided in two separate classes, micropipes and thermal decomposition cavities (TDC) [3]. The TDCs, also called macrodefects, have been observed by several authors [4-6]. They have noted that thermal decomposition cavities originate at the interface between the SiC seed and the graphite seed holder. Vodakov *et al.* [5] proposed that thermal decomposition cavities form through a recrystallization process, in which SiC is transported across small gaps or liquid droplets at the holder/SiC interface. Similarly, Anikin *et al.* [6] suggested that they form by localized sublimation from the back of the relatively hot seed to a relatively cool graphite seed holder. More recently several authors have stated that voids in the carbonized sucrose attachment layer at the seed crystal/crucible lid interface are responsible for thermal decomposition cavities [7,8]. Tuominen *et al.* [7] have suggested that backside evaporation can be diminished by maintaining the system near the equilibrium silicon vapor pressure. Chourou *et al.* [8] have stated that TDCs can be removed by using a mechanical mount instead of carbonized sucrose. They have also observed that the depth of TDCs can be decreased by reducing the growth temperature. This paper has two goals. First it provides evidence for the mechanism by which voids in the attachment layer create cavities. Second, it demonstrates that cavity formation can be suppressed by controlling the homogeneity of the attachment layer.

### Experimental

On-axis (0001) 6H-SiC plates, produced by the Lely method [9], were used as seeds for all of the growth experiments. The experiments were carried out in a PVT growth apparatus similar to those described in the literature [2]. The source powder, 1-2 mm grain size high purity Acheson powder, was produced by Elektroschmelzwerk Delfzijl, Netherlands. Two different techniques were used for seed mounting; attachment with carbonized sucrose and a mechanical mount. For the first method sucrose is placed on a graphite crucible lid and melted at a temperature of 200°C. The Lely

seed is then placed on top of the melted sucrose, and a small force is applied to it. The attachment layer is baked to 400 °C while the seed is still under load. This results in a carbonized attachment layer. The second method is accomplished by pressing the seed crystal against the lid with a graphite disk and support sleeve.

During each growth run the system is heated in stages to about 1200 °C at a pressure below  $3 \times 10^{-4}$  torr. The system is then backfilled with ultra high purity argon to a pressure of 650 torr. The temperature is gradually increased to the growth temperature of 2300 °C, at a rate of 24°C/min. The duration of individual growth experiments ranged from 15 minutes to 14 hours. The pressure in the growth chamber was maintained at 650 torr during short growth runs to minimize transport of the vapor species. This resulted in slow growth rates of approximately 0.05 mm/hr. For longer growth runs, the pressure is lowered to between 10 to 20 torr. Here, the growth rates were between 0.2 mm/hr and 6mm/hr.

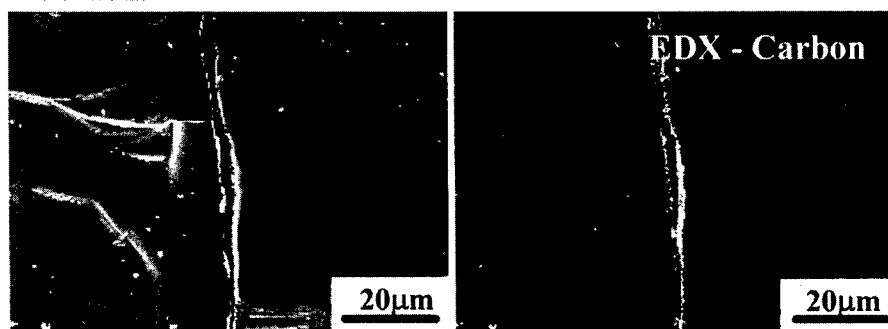
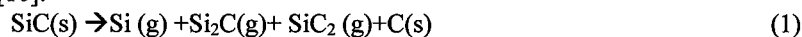


**Fig. 1** Cross-sectional image of a thermal decomposition cavity in a 6H SiC crystal grown by physical vapor transport.

Samples for energy dispersive x-ray (EDX) and Auger electron spectroscopy (AES) were cleaved open in order to avoid chemical contamination due to cutting and polishing. Scanning electron microscopy (SEM) and EDX images were obtained at an accelerating voltage of 25 kV on a Philips XL-30 microscope. AES was performed on a scanning Auger spectrometer at an accelerating voltage of 3 kV. Optical transmission images of axial slices from PVT grown SiC were obtained by cutting boules along the c-axis and polishing with diamond paste.

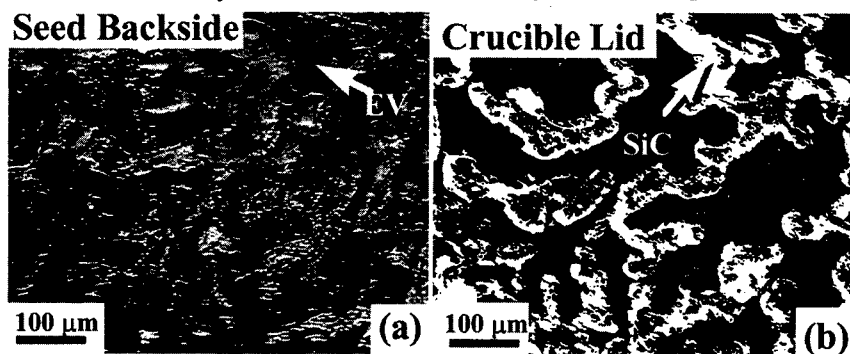
### Results and Discussion

Fig. 1 shows a SEM and EDX image of a cleaved surface of a PVT boule grown at 2300 °C and a pressure of 10 torr. The section of the seed was located approximately 4 mm from the seed/crucible lid interface. A tubular void running almost vertically is apparent in both images. The bright areas in the carbon EDX image indicate that the cavity walls have a higher carbon concentration than the SiC matrix. The silicon EDX image (not shown) was in agreement. This result was additionally supported by Auger spectroscopy on the same cleaved sample. The Auger spectrum inside the cavity revealed only carbon while the spectrum taken outside the cavity indicated the presence of silicon, carbon and oxygen. One possible explanation for the observed concentration of carbon in the cavities is local sublimation of the SiC matrix. During PVT growth, SiC sublimates and releases mainly Si, Si<sub>2</sub>C and SiC<sub>2</sub> as vapor. Since the vapor is silicon rich, carbon is left behind [10]:



Due to the axial temperature gradient in PVT growth, it is expected that material from the hot seed will transport across voids in the carbonized attachment layer to the cooler lid. An estimate of this

transport rate was obtained by growing on a seed with an intentional gap between the seed crystal and the graphite lid. The lower limit for the transport rate across the intentional gap was 0.5 mm/hour [3]. This is on the same order of magnitude as the typical crystal growth rates in PVT. In the fashion described above, a Lely seed was mounted on the lid with sucrose. It was then annealed at 2300 °C, 10K/cm, 10 torr, for 15 minutes. Following growth, the seed was removed from the crucible lid, and the backside inspected. Fig. 2(a), an optical image taken in reflection, shows a section of the backside of the seed, and Fig. 2(b), the corresponding area on the graphite crucible (mirrored). There is a one to one relationship between the dark, topographically lower areas on the seed, and the bright, topographically higher areas on the cap. The crucible lid was analyzed with powder x-ray diffraction. Indexing the resulting peaks indicated the presence of graphite and SiC. Based on these observations, it can be concluded that the bright portions on the seed backside are areas where the attachment layer created a bond between the lid and seed. The dark areas on the seed backside show signs of sublimation and correspond to the voids which existed in the attachment layer. Here the seed has locally sublimed, vapor has been transported



**Fig. 2** Optical images of (a) the backside of the seed crystal and (b) the corresponding area of the graphite lid. Dark regions in both images are topographically lower than light regions. The arrow shows where SiC has been deposited on the lid directly under the evaporated region of the seed, EV.

across the void and deposited on the lid as polycrystalline SiC.

The lid shown in Fig. 2 was fractured along the growth direction and analyzed with EDX. The EDX results indicate the presence of silicon in the graphite lid, up to 200 μm from the mounting surface. The intensity of this silicon signal is comparable to that of SiC. If cavities are to form at voids in the attachment layer then the silicon rich vapor has to be dissipated into the growth system. It is possible that the silicon species diffuses through the porous graphite lid.

The above observations provide an insight to how the formation of TDCs can be suppressed. It suggests that the key to the prevention of TDCs is the existence of a continuous diffusion barrier on the seed backside. To test this, a Lely platelet was cut in half. One half had the backside painted with photoresist of approximately 15 μm thickness and cured at 120°C for 5 min. It was then heated in vacuum ( $<3 \times 10^{-4}$  torr) to a temperature of 1200°C, utilizing a temperature ramp rate of 400°C/h [11]. The resulting carbon layer was smooth and contained no visible cracks or voids. Using the carbonized sucrose method, this seed and an unprotected seed crystal were mounted side by side on the same crucible lid. Both crystals were overgrown simultaneously in the same PVT growth experiment (2300°C, 10 K/cm, 20 torr) for 14 hours. An axial slice parallel to the growth direction was cut from the boule revealing both seed crystals.

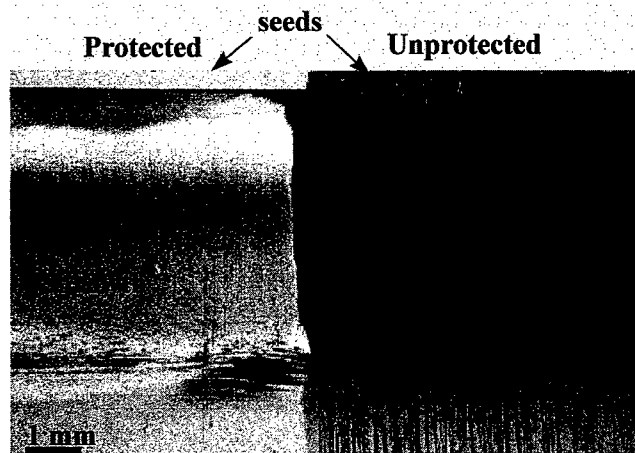


**Fig. 3** Transmission optical microscopy image of a cross sectional slice along the c-axis of a dual seed growth. The seed crystal on the left has been protected by the application of a thin continuous film of graphite on the seed backside.

An optical image of the slice in transmitted light is shown in Fig. 3. The protected seed is transparent with no signs of backside decomposition. The seed crystal that was not protected contains thermal decomposition cavities propagating through it. It is apparent that the continuous graphite film on the backside of the protected seed has suppressed the local evaporation, while the TDCs in the unprotected seed are seen to originate at the seed/lid boundary. Further work on optimization of this method is in progress.

#### Conclusions

Experimental observations support the proposed mechanism for the formation of thermal decomposition cavities during the PVT growth of SiC. Voids in the sucrose attachment layer have been shown

to cause local evaporation of the seed crystal backside. Energy dispersive x-ray analysis and Auger electron spectroscopy support this by indicating that the walls of these cavities are decorated with carbon. The vapor released during sublimation was transported across the cavities and along the axial temperature gradient. The vapor either recrystallized on the exposed graphite surface of the lid, or partially diffused into it. A continuous, void-free carbon protection layer applied to the backside of the seed crystal helped to suppress the formation of thermal decomposition cavities at the interface between the seed crystal and the graphite lid.

#### Acknowledgments

This work was supported by the Commonwealth of Pennsylvania through the Ben Franklin Technology Center (Grant # 98W.CM00562R-1) and the National Science Foundation (Grant # DMR.9903702).

#### References

- [1] Yu. M. Tairov and V.F. Tsvetkov, *J. Cryst. Growth*, **43** (1978), p. 209.
- [2] D. L. Barrett, R. G. Seidensticker, W. Gaida, R. H. Hopkins, and W. J. Choyke, *J. Cryst. Growth*, **109** (1991), p. 17.
- [3] E. K. Sanchez, V. Heydemann, T. Kuhr, G. S. Roher, M. Skowronski, *J. Elec. Mater.* (1999), submitted.
- [4] R. A. Stein, *Physica*, **185b** (1993), p. 211.
- [5] Yu. A. Vodakov, A. D. Roenkov, M. G. Ramm, E. N. Mokhov, and Yu. N. Makarov, *Phys. Stat. Sol. (b)*, **202** (1997), p. 177.
- [6] M. Anikin, M. Pons, K. Chourou, O. Chaix, J. M. Bluet, V. Lauer, and R. Madar, *Materials Science Forum*, **264-268** (1998), p. 45.
- [7] M. Tuominen, R. Yakimova, A. Vehanen, E. Janzen, *Mat. Sci. Eng.*, **B57** (1999), p. 229.
- [8] K. Chourou, M. Anikin, J. M. Bluet, J. M. Dedulle, R. Madar, M. Pons, E. Blanguet, C. Bernard, P. Grosse, C. Faure, G. Basset, Y. Grange, *Mat. Sci. Eng. B*, **B61** (1999), p. 82.
- [9] J.A. Lely, *Ber. Dt. Ker. Ges.*, **32** pp. (1955), p. 229.
- [10] J. Drowart, G. De Maria, M. G. Inghram, *J. Chem. Phys.*, **29** (1958), p. 1015.
- [11] C. Thomas, C. Taylor, J. Griffen, M. G. Spencer, K. Kornegay, M. Capano, S. Rendakova, *Spring MRS 1999 proceedings*, in print.

## Initial Stage of Crystallization in the Growth of Silicon Carbide on Substrates with Micropipes

I. Khlebnikov, D. Cherednichenko, Y. Khlebnikov and T.S. Sudarshan

Department of Electrical and Computer Engineering, University of South Carolina,  
Columbia, SC 29208, USA

**Keywords:** Dendrite, Micropipe, Planar Defects, Silicon Carbide Growth, Transition Layer

**Abstract.** Defect generation and the kinetics of the initial stage of crystallization have been studied. The influence of silicon liquid phase on the transition layer structure has been investigated. The micropipe stability during the process of growth has been examined. The conditions of defect reproduction from the seed into the bulk have been determined.

**1. Introduction.** The initial stage of crystallization on the seed during PVT bulk SiC growth occurs during non-equilibrium conditions, when all the process parameters are changing. The transition process of establishing stationary conditions initiates such negative processes as the replication of seed micropipes, polytype inheritance, polytype transformation, and the generation of dislocations. Investigation of defect formation in the transition layer between the seed and the growing crystal is the focus of this paper.

**2. Experiment.** Using the modified Lely technique, bulk crystals were grown in a reactor with flexible temperature control in the crystallization zone during the growth process. Temperature control was facilitated by two pyrometers simultaneously measuring crucible surface temperature at different locations. Temperature, crucible position, gas pressure, flow rate and gas composition in the growth zone are fully computer controlled. The growth process was investigated under the following conditions: growth temperature of 2270-2770 K, argon pressure of 1-760 Torr, temperature difference between source and seed from 1-100 K, source to seed distance of 1-5 cm, and boule diameter of 1-2 inches. Specially synthesized polycrystalline SiC was used as source material. The presence of silicon droplets within planar defects have been studied by EDAX microprobe and micro-Raman spectroscopy.

**3. Results and Discussion.** The transition layer thickness and the density of defects primarily depends upon the kinetics of crystal growth during the transition stage, and to a lesser extent, the seed quality. Within the transition layer, all types of defects are inherited from the seed and may transform through annihilation, multiplication, or new defect generation. The majority of defects generated within the transition layer (see Fig.1 optical micrograph of a boule slice along *c*-axis taken in the transmission mode) can be enumerated as follows: *C and Si inclusions, carbon dendrites, planar defects, and micropipes.*

The micropipe density at the origin of the transition layer depends on the kinetic process parameters (temperature, pressure, etc.) during initial layer growth, the original seed micropipe density, and the quality of the seed's surface preparation. Variation of the  $V_C/V_A$  ratio ( $V_C$  is the normal growth velocity component and  $V_A$  is the tangential component) has the most significant effect on the number of micropipes propagating from the seed to the transition layer. We determined that with  $V_C/V_A \approx 1/6$ , the quantity of micropipes propagating from the seed into the bulk crystal abruptly decreased. Micropipe density at the end of the transition layer is determined by the

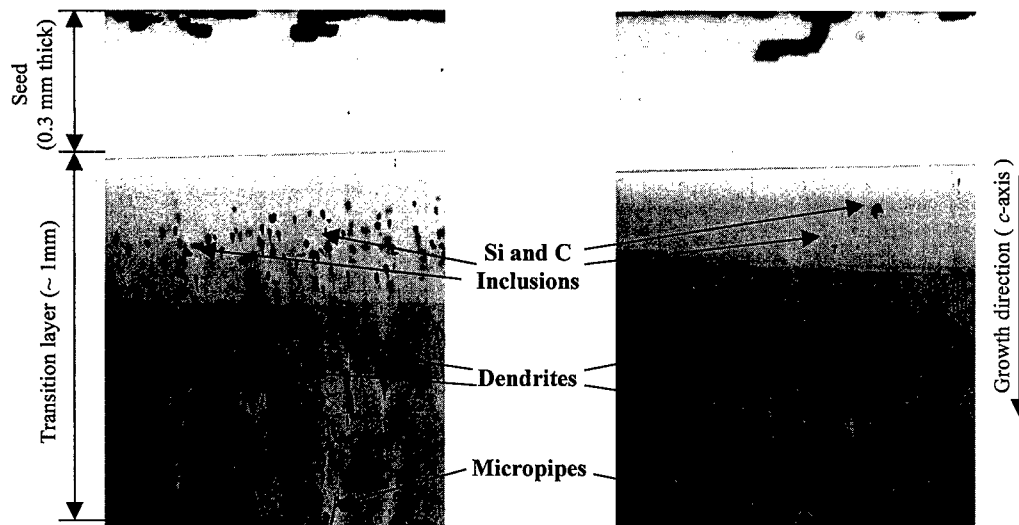


Figure 1. Defect generation within the transition layer.

quantity of the inclusions, dendrites, planar defects, and may greatly exceed the micropipe density in the seed. We observed the generation of a large number of micropipes on dendrites, as micropipes developed from practically all dendrite branches. It was noted that increasing the concentration of excess silicon in the source material increased the defect density and thickness of the transition layer. However, decreasing the duration of the transition process, the thickness of the transition layer is reduced and the defect density within it increased.

Because the seed already contains a certain number of micropipes and screw dislocations, at high temperatures a hollow core may spontaneously be generated in the center of dislocations as soon as the dislocations free enthalpy,  $G$ , becomes less than or equal to zero [1]. Taking into account that in the center of a dislocation the material deviates from Hooke's law, the general thermodynamic condition under which the hollow cores are stable has been formulated in Ref. [2].

$$\frac{dG}{dr} = 2\pi\gamma \cdot \left( \frac{r}{r_c} - U(r) \cdot \frac{r}{\gamma} + 1 \right) \leq 0, \quad (1)$$

where  $r_c = \Omega \cdot \gamma / \Delta\mu$ ,  $\Delta\mu$  is the difference in thermodynamic potential, characterizing supersaturation;  $\Omega$  is the volume of the molecule ( $\Omega = M/N_A \cdot \rho$ ,  $M = 41$ ,  $\rho = 3.2$  g/cm for SiC and  $N_A$  is Avogadro's number);  $\gamma \cong 10^{-16} \cdot G / 4 \cdot a_0$  [3] is the surface energy ( $3.929 \cdot 10^3$  erg/cm<sup>2</sup>), ( $G = 4.4 \cdot 10^{12}$  dyn/cm<sup>2</sup> is the Young modulus, and  $a_0 \cong (\Omega)^{1/3} \cong 2.8 \cdot 10^{-8}$  cm) is the lattice constant (in the equilibrium position).

To estimate the bulk strain energy of the dislocation core  $U(r) = dE(r)/dr/2\pi \cdot r$ , the linear energy density in the dislocation core was approximated by the function  $E(r) = \mu \cdot b^2 \cdot \ln(1 + (r^2/r_h^2))/8\pi$  [4]. Here  $\mu$  is the shear modulus,  $b$  is the Burgers vector (for 6H SiC:  $\mu = 1.9 \cdot 10^{12}$  dyn/cm<sup>2</sup>,  $b_0 = 15.2 \cdot 10^{-8}$  cm, and  $b = n \cdot b_0$  for super-dislocation, where  $n \geq 4$  [5]). The function  $E(r)$ , containing the Hooke's radius  $r_h = (\mu b^2 / 8\pi^2 \cdot U_0)$ , takes into account the deviation from Hooke's law, and also excludes the singularity at the center of dislocation ( $r \cong 0$ ). Here,  $U_0$  is the specific strain energy in the center of the dislocation. The specific strain energy cannot be greater than the specific latent heat of melting  $U_0 \leq \Delta H_M$  [2].

Since SiC does not have a molten phase, we suggest that the core energy density can be estimated based on the maximum crystal strength,  $\sigma_M$ .

$$U_0 = \sigma_M \cdot \Lambda / \Omega \quad (2)$$

where  $\sigma_M = G/6 \cdot \eta$  is the pressure of atomic interaction in a solid lattice (molecular pressure) [6],  $\eta = 2$  is the Gruneisen's parameter, and  $\Lambda$  is the activated volume of lattice distortion.

The value of  $\Lambda$  can be estimated by the maximum atom displacement from the equilibrium position,  $\Delta a$ , that the lattice is able to withstand without plastic deformation:  $\Delta a = \beta/2g \cong a_0/12\eta = 1.359 \cdot 10^{-9}$  cm. Here, the parameters  $\beta$  and  $g$  are the elastic force constant and the inharmonic constant of atom oscillation. Both of these constants are in the expansion of the quasi-elastic force of the atom interaction in a solid,  $\Delta F = -\beta \cdot \xi + g \cdot \xi^2$ , where  $\xi = (a - a_0)$  is the amplitude of the atom displacement. The approximate value of the ratio  $\Lambda/\Omega$  is 1.2. For this value, the strain energy density for the single dislocation is  $U_0 \cong 1.9 \cdot 10^{11}$  erg/cm<sup>3</sup>. If the vapor saturation ratio is  $\alpha_0 \cong 1.1$ , our estimations show that as in Ref. [5] the screw dislocations with Burgers vector of  $b_0 = 15.2$  Å are stable and do not have visible open cores. Hence the dislocations with  $b_0 = 15.2$  Å, initially present in the seed, would propagate into the bulk crystal as a dislocation without open core. On the other hand, all microcopies are found to lie along the lines of super-dislocation with Burgers vector of  $n \cdot b_0$ , where  $n$  is greater than or equal to 4 [5]. For  $b = 9 \cdot b_0$  the equilibrium radius of the hollow core of dislocation (pipe) is  $4.5 \cdot 10^{-6}$  cm ( $r_p \cong 30 \cdot b_0$ ).

Experimental observations indicate that the radius of some pipes could be larger than  $4.5 \cdot 10^{-6}$  cm indicating that there are additional factors that will instigate the development of a hollow core with a larger radius. These factors include the capillary effect in a pipe, the temperature distribution, and the thermal tension in the vicinity of the pipe. Estimations show that at SiC growth conditions, the value of thermal tension is comparatively small ( $\sigma \leq 10^7$  dyn/cm<sup>2</sup>) to have such a remarkable influence on the specific energy in the area of dislocation. It is possible to show that with increasing temperature, the supersaturation decreases very quickly around a pipe. When the supersaturation is reduced to zero, the pipe radius asymptotically approaches the maximum value  $r_M = 2 \cdot \gamma \cdot \Omega \cdot N_A \cdot T_V / W(T_V - T_S)$ , where  $W$  is the activation energy of the sublimation process (for SiC,  $W = 135.6$  kcal/mol [7]),  $T_V$  is the temperature of the source material, and  $T_S$  is the temperature of the pipe surface. For example, if  $T_V = 2600$  K and the temperature of the pipe surface is in the range (2590 – 2598 K), the radius of the pipe changes from 0.024 to 0.12 μm.

Using the distance measured between steps on the spirals of growth (magnified image of spirals in vicinity of micropipe is shown in lower right corner of Fig.2), the supersaturation in the vicinity of the pipe is three times smaller than the supersaturation above the defect-free surface. Consequently, the temperature in the pipe must be several degrees higher than on the defect-free surface. This condition is especially possible during the initial stage of crystallization when the temperature difference is  $\Delta T \geq 100$ . In this case the total supersaturation is increased and the partial pressure of silicon can significantly exceed its saturated pressure in vapor [7]. As a result the liquid phase of silicon will condense on the growth front affecting the process of defect formation. An analysis of our experimental results shows that under the above experimental conditions, there is a tendency for micropipe stability and micropipe penetration from the seed to the bulk. On the other hand, when the tangential component of growth is much

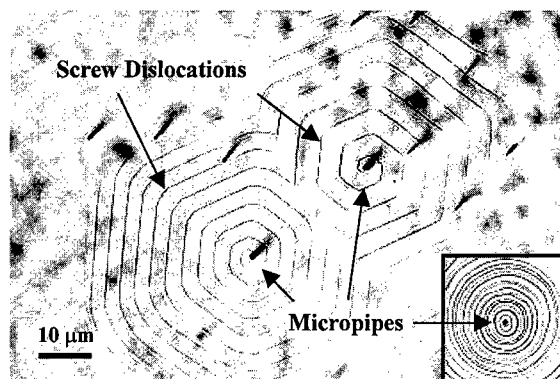


Figure 2. Micropipes are the open core of screw dislocations.

higher than the normal component, the micropipes lose stability and are terminated. Also, we found that the micropipes tended to follow the direction of growth.

The appearance of secondary phase inclusions (mainly carbon, since convection may take place) occurs when the Si/C ratio is shifted to the Si side at the initial stage of transition layer crystallization (high temperature gradient, etc.). As a result, liquid phase Si is condensed on the growing surface and on the graphite parts of the crucible. The interaction of liquid silicon with the graphite crucible results in the erosion of graphite and the saturation of liquid phase silicon by non-soluble carbon particles (the solubility of carbon in silicon is very low even at these temperatures). Increasing the percentage of silicon in the source material enhances erosion and increases the number of inclusions. These observations suggest that the transport of non-soluble carbon particles by silicon liquid phase to the growing surface is probable.

It is known that dendrites grow from the liquid phase due to the accumulation of non-soluble impurities on the growing surface. Formation of large quantities of dendrites at this stage of growth again indicates the existence of a condensed liquid phase.

Formation of planar defects is usually observed at the end of the transition layer, when stationary conditions of crystal growth are established. At this time, the temperature of growth reaches the maximum value, and temperature gradients are reduced. The rate of liquid phase condensation is reduced because the Si/C ratio decreases. The liquid film on the growing surface becomes depleted, and at some point, splits into separate droplets. Anisotropy of the surface tension deforms the liquid phase islands in accordance with crystallographic orientation. Constitutional supercooling disturbs the uniformity of the growth front with the formation of shaped voids or encapsulated solution which, during crystal growth, is dispersed by the diffusion process [9].

**4. Conclusion.** Large temperature difference ( $\Delta T > 100$  °C) at the initial stage of crystallization creates a high supersaturation in the vapor phase and as a result a liquid phase forms at the growth front. EDAX and micro-Raman analyses confirm presence of Si within planar defects and in the bulk crystal close to the seed region. Thermodynamic analysis shows that dislocations with Burgers vector  $b_0 = 15.2$  Å will propagate into the bulk crystal without open core formation. Open cores will be generated from dislocations with Burgers vector  $b \geq 4 b_0$ .

## References

- [1] D. Kuhlmann-Wilsdorf, "Theory of melting," *Phys. Rev.*, V.140, N5A, (1965), p. 1599- 1610
- [2] B.Van Der Hoek, J.P. Van Der Eerden and P.Bennema, "Thermodynamical stability condition for the occurrence of hollow cores caused by stress of line and planar defects," *Journal of Crystal Growth*, 56 (1982), p. 621-632.
- [3] W.W. Mullins "Metal Surface: Structure, Energetics and Kinetics" Metals Park, Ohio, (1962), p. 17-66
- [4] J. Heindle, W.Dorsch, H.P.Strunk, St.G.Muller, R. Eckshtein, D. Hofman, and A.Winnacker, "Dislocation Content of Micropipes in SiC", *Phys. Rev. Letters*, V.80, N4, (1998), p. 740-741.
- [5] J. Giocondi, G.S. Rohrer, M. Skowronski, V. Balakrishna, G. Augustine, H.M. Hobgood, and R.H. Hopkins. "The Relationship between Micropipes and Screw Dislocation in PVT Growth 6H-SiC", *MRS Symposium Proceedings V.423*. San Francisco, CA, USA, (1996), p.539-544.
- [6] A.I. Burshtain, "Molekylarnaya Fizika". Part 2. Novosibirsk, (1975).
- [7] S.K.Lilov and I.Y.Yanchev. "Peculiarities of Silicon Carbide Crystal Growth under the Diffusion Mechanism of Vapor Transfer. *Advanced Materials for Optics and Electronics*." V.1, (1992), p. 203-207.
- [8] S. K. Lilov, "Study of the equilibrium processes in the gas phase during silicon carbide sublimation. *Materials Science and Engineering*," B21 (1993), p. 65-69.
- [9] E.K. Sanchez, V.D. Heydemann, G.S. Rohrer, et. al. "Structural Characterization of SiC Crystals Grown by Physical Vapor Transport." *Silicon Carbide, III-Nitrides and Related Materials*, Sweden, (1997), p. 433.



## Nucleation of Dislocations during Physical Vapor Transport Growth of Silicon Carbide

E.K. Sanchez<sup>1</sup>, V.D. Heydemann<sup>2</sup>, D.W. Snyder<sup>2</sup>, G.S. Rohrer<sup>1</sup> and  
M. Skowronski<sup>1</sup>

<sup>1</sup> Department of Materials Science and Engineering, Carnegie Mellon University, 5000 Forbes Ave,  
Pittsburgh, PA 15213, USA

<sup>2</sup> II-VI Incorporated, 375 Saxonburg Blvd, Saxonburg, PA 16056, USA

**Keywords:** Nucleation, Physical Vapor Transport, Screw Dislocation, Sublimation Growth, Threading Dislocations

**Abstract:** Two possible nucleation mechanisms for threading edge and screw dislocations during the physical vapor transport growth of SiC have been investigated. First, growth over intentionally deposited carbon inclusions led to an edge and screw dislocation density orders of magnitude higher than the surrounding crystal. Second, seeds with mechanical polishing damage have been shown to lead to a dislocation density nearly three orders of magnitude higher than seeds that were hydrogen etched. A new linear step source has been observed and correlated with an increase in the dislocation density.

### Introduction

It has recently been shown that single Burgers vector screw dislocations aligned along the [0001] direction limit silicon carbide (SiC) device performance [1]. Even though they may not be as detrimental to a device as super screw dislocations (micropipes) [2], their densities are much higher, on the order of  $10^4/\text{cm}^2$  [3,4]. Their formation mechanism is still not fully understood. Considering the magnitude of the Burgers vector (1.5 nm in 6H-SiC), it is unlikely that they form by plastic deformation [5]. It is more probable that screw dislocations are a grown-in defect. Several authors have suggested that the seed surface quality can be a factor in the generation of defects [6,7]. Super screw dislocations have been observed to start at second phase inclusions (carbon or silicon) [3,8]. Dudley *et al.* [6] have taken this observation further and proposed a mechanism in which second phase inclusions act as the nucleation sites for screw dislocations. A second factor is surface polishing; Powell *et al.* [7] have shown that surface polishing in chemical vapor deposition of SiC can lead to growth pits. This paper will focus on the nucleation of screw dislocations on second phase inclusions and mechanically polished surfaces during physical vapor transport (PVT) growth of SiC.

### Experimental

All experiments used basal plane (0001) 6H SiC Lely platelets as seeds. A wet oxidation treatment ( $1100 \pm 50^\circ \text{C}$ , for a half hour in  $\text{H}_2\text{O}$  saturated  $\text{O}_2$ ) was used to determine the surface polarity. Two sets of experiments were carried out. In the first set, only seeds with virgin surfaces were used. However, the virgin surfaces contained carbon deposits ranging from 10 to 500  $\mu\text{m}$  in size. In addition, carbon deposits were intentionally produced by placing small spots of melted sucrose on the seed surface and annealing at high temperature. The second set of experiments used seeds with different surface finishes. All seeds were first polished with 0.5  $\mu\text{m}$  diamond paste. One was left as polished and used as a control; a second was polished using 30  $\mu\text{m}$  diamond paste to introduce severe mechanical damage. The last two seeds underwent a hydrogen etch for 15 minutes under a flow of hydrogen and nitrogen at 1600  $^\circ\text{C}$  [9]. In each run, two seeds (a hydrogen etched seed and a mechanically polished seed) were attached to the same lid and grown on simultaneously.

Seed surfaces were cleaned using a standard RCA cleaning and mounted to the crucible lid using the carbonized sucrose method [10]. Growth experiments were carried out in a physical vapor transport

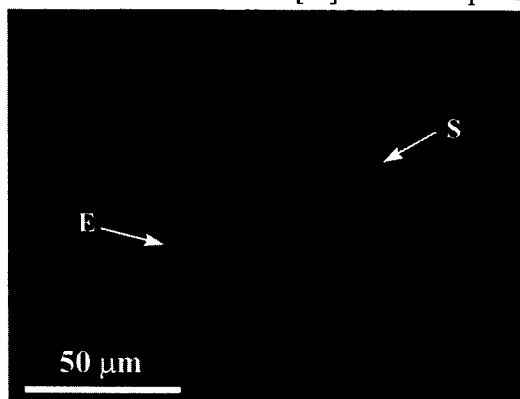


Fig 1. Optical image of a KOH etched surface. Dislocations are revealed on top of carbon precipitates. E is an edge dislocation, S is a screw dislocation.

system similar to those described in literature [11]. The source material used was grade B-hp from H.C. Starck. Prior to growth, the system was evacuated to a pressure below  $3 \times 10^{-7}$  torr. It was then heated in stages to about 1200 °C at a pressure below  $1 \times 10^{-4}$  torr. The system was then backfilled with ultra high purity argon to a pressure of 650 torr and the temperature was gradually increased to the growth temperature of 2300 °C, at a rate of 24°C/min. The seeds with carbon deposits were grown on at 650 torr for time periods ranging from 5 to 30 minutes. For the polished seeds, the system pressure was slowly decreased to 10 torr and held for 1 hour. Contact mode atomic force microscopy (AFM) was carried out using standard  $\text{Si}_3\text{N}_4$  probes and contact forces in the 0.1 to 5 nN range.

Scanning electron microscopy (SEM) and energy dispersive x-ray (EDX) images were obtained on a Philips XL-30 microscope under an accelerating voltage of 25 kV. To reveal dislocation etch pits, the crystals were etched in molten KOH at 500°C for 3-8 minutes.

## Results

The first set of experiments was conducted to test the effect of surface deposits on the nucleation of dislocations. After growth, AFM was carried out on the seeds followed by etching in molten KOH. AFM scans revealed a screw dislocation density of  $2 \times 10^5/\text{cm}^2$  in areas above carbon inclusions. Fig. 1 shows an optical image, after etching, of the areas directly above a carbon deposit. Two types of etch pits are distinguishable: the small round etch pits labeled with E, and the larger faceted pits labeled with S. Smaller pits are most likely due to threading edge dislocations and the larger pits are most likely screw dislocations lined along the [0001] direction [12]. The density of larger pits above the carbon inclusions is  $8 \times 10^5/\text{cm}^2$ ; this agrees well with screw dislocation density observed by AFM. In contrast, the density of screw dislocations in the rest of the crystal is only  $10^4/\text{cm}^2$ , nearly two orders of magnitude less than above the precipitate. The threading edge dislocations had a density of  $10^7/\text{cm}^2$  above the precipitate and a density of  $5 \times 10^5/\text{cm}^2$  in the rest of the crystal. This correlation indicates that surface deposits play a role in the generation of dislocations in SiC. One possible mechanism to explain the formation of dislocations above a precipitate has been suggested by Dudley *et al* [6]. When surface carbon deposits are overgrown, misorientations are created as growth fronts from opposite sides of the inclusion meet. Another possible mechanism involves

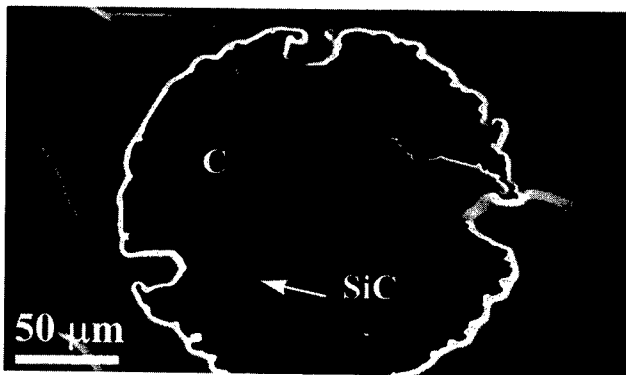


Fig 2. SEM micrograph of a carbon precipitate (C). SiC marks the location of one of the many SiC growth islands.

the nucleation of SiC islands on a second phase deposit. Individual islands are expected to be misoriented with respect to one another and, when they coalesce, this misorientation can be accommodated by dislocations. A key step in the process is the nucleation of SiC on carbon precipitates. The initial stages of the overgrowth of carbon deposits were investigated with SEM.

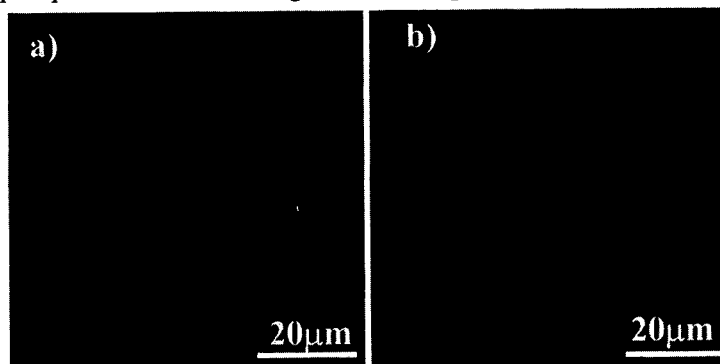


Fig 3. AFM images of a KOH etched (a) crystal grown on a hydrogen etched seed, and (b) a crystal grown on an industry polished seed.

Fig. 2 is an SEM image of a carbon deposit on a SiC seed after a 5 minute growth at 2300 °C, 10 °C/cm, and 650 torr. EDX indicates that the small islands (labeled SiC) have the same silicon and carbon concentration as the rest of the crystal. AFM on the surface of an island revealed that the surfaces are atomically flat. These observations suggest that

nucleation of SiC islands has occurred on top of a carbon deposit.

The second set of experiments was conducted to test the effect of surface finish. Following growth, the seeds were characterized by AFM to determine the screw dislocation density and were then KOH etched to reveal both screws and threading edge dislocations. SiC was grown simultaneously on a seed polished with 30 μm diamond grit and on a hydrogen etched seed, mounted side by side. The polished seed had a screw dislocation density of  $10^6/\text{cm}^2$  while the hydrogen etched sample had a screw dislocation density of less than  $10^3/\text{cm}^2$ . The results for the hydrogen etched and fine grit polished samples are shown in Fig. 3a and 3b, respectively. In Fig. 3a, two etch pits can be seen at the top of the image. The total etch pit density on this crystal was about  $10^4/\text{cm}^2$ . Fig. 3b shows a line of etch pits, along the left side of the image. This is interpreted as dislocations arranged in a greater density along a scratch left behind by polishing. The density of total etch pits on this crystal is  $3.5 \times 10^7/\text{cm}^2$ , three orders of magnitude higher than the hydrogen etched sample. This provides evidence that polishing leaves behind damage in the crystal that leads to dislocation nucleation during PVT growth. It further suggests that hydrogen etching helps to remove this damage.

An AFM image of a SiC growth surface is shown in Fig. 4. This image was taken after etching in KOH for 5 minutes at 500 °C. The image reveals a linear step source, 30 μm long, aligned along the  $\langle 11\bar{2}0 \rangle$  direction. Several screw dislocations (etch pits where steps end) and several threading edge dislocations (isolated etch pits) are also revealed in close proximity to the linear step source. These linear step sources were observed on all surfaces formed by short growth treatments. All of the observed lines have a Burgers vector in the  $[0001]$  direction, making them step sources. Taking a Burgers circuit around the one in Fig. 4, reveals a height difference of 3 nm or two 6H lattice cells. These linear step sources are 3 to 30 μm in length and have been seen to rise above the surface as linear hills to heights of 7 nm or fall below the surface as narrow trenches to

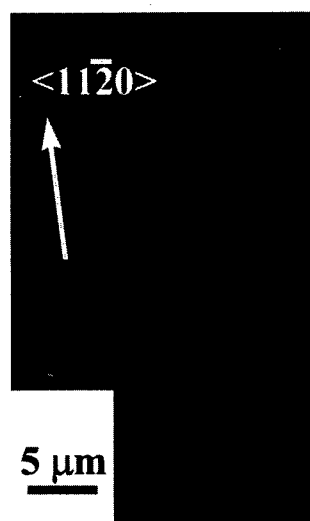


Fig 4. AFM image of a KOH etched linear step source.

depths of 3 nm. Laue x-ray revealed that they are all orientated along  $\langle 11\bar{2}0 \rangle$  directions. It is interesting that there is a direct correlation between these lines and both threading edge and screw dislocations. Examining several of these sources reveals that both edge dislocations and screw dislocations decrease in density as you move radially away from the linear step source. Edge dislocations decrease from  $10^6/\text{cm}^2$ , within 10  $\mu\text{m}$  of the line sources, to  $10^4/\text{cm}^2$  at 80  $\mu\text{m}$  from the line. Screw dislocations decrease from  $5 \times 10^5/\text{cm}^2$ , near the lines, to less than  $10^3/\text{cm}^2$  at 40  $\mu\text{m}$  away from the linear sources. This suggests that there is a mechanistic link between the formation of these linear step sources and dislocations. Further work is in progress to determine the exact nature of this step source. However, we speculate that this could be a stacking fault along one of the pyramidal planes, similar to those described by Heindl *et al.* [13]. Since they all align along  $\langle 11\bar{2}0 \rangle$  directions, it is most likely a stacking fault on either the  $\{10\bar{1}1\}$  or  $\{10\bar{1}2\}$  pyramidal planes.

### Conclusions

The seed surface quality before growth has a direct relation to the dislocation density in the PVT grown material. Second phase precipitates on the seed growth surface lead to the nucleation of both screw dislocations and threading edge dislocations. This formation appears to tie into the nucleation of SiC islands on top of second phase material. There is also a direct relationship between the surface polish and dislocation density. Hydrogen etching has been shown to remove this damage and in turn lower the dislocation density. When the surface of a seed is cleaned and the damage removed, the major step source is related to a newly discovered defect. Long narrow defects aligned along the  $\langle 11\bar{2}0 \rangle$  directions act as step sources and are correlated to elevated populations of both threading edge and screw dislocations.

### Acknowledgments

This work was supported by the Commonwealth of Pennsylvania through the Ben Franklin Technology Center (Grant # 98W.CM00562R-1) and the National Science Foundation (Grant # DMR.9903702).

### References

- [1] P. G. Neudeck, W. Huang, M. Dudley, *Mat. Res. Soc. Symp. Proc.*, **483** (1998), p. 285.
- [2] P. G. Neudeck, J. A. Powell, *IEEE Electron Device Lett.*, **15** (1994), p. 63.
- [3] R. C. Glass, D. Henshall, V. F. Tsvetkov, C. H. Carter, Jr., *Phys. Stat. Sol. (b)*, **202** (1997), p. 149.
- [4] J. Takahashi, N. Ohtani, M. Kanaya, *J. Cryst. Growth*, **167** (1996), p. 596.
- [5] P. Pirouz, *Mat. Res. Soc. Symp. Proc.*, **512** (1998), p. 113.
- [6] M. Dudley, X. R. Huang, W. Huang, *App. Phys. Lett.*, **75** (1999), p. 784.
- [7] J. A. Powell, D. J. Larkin, *Phys. Stat. Sol. (b)*, **202** (1997), p. 529.
- [8] D. Hofmann, E. Schmitt, M. Bickermann, M. Kolbl, P. J. Wellmann, A. Winnacker, *Mat. Sci. Eng.*, **B61** (1999), p. 48.
- [9] V. Ramachandran, M. F. Brady, A. R. Smith, R. M. Feenstra, D. W. Greve, *J. Elec. Mat.*, **27** (1998), p. 308.
- [10] E. K. Sanchez, V. Heydemann, T. Kuhr, G. S. Rohrer, M. Skowronski, *J. Elec. Mat.* (1999), submitted.
- [11] D. L. Barret, R. G. Seidensticker, W. Gaida, R. H. Hopkins, W. J. Choyke, *J. Cryst. Growth*, **109** (1991), p. 17.
- [12] J. Takahashi, M. Kanaya, Y. Fujiwara, *J. Cryst. Growth*, **135** (1994), p. 61.
- [13] J. Heindl, H. P. Strunk, V. D. Heydemann, G. Pensl, *Phys. Stat. Sol. (b)*, **202** (1997), p. 251.

## Plastic Deformation and Residual Stresses in SiC Boules Grown by PVT

S. Ha<sup>1</sup>, G.S. Rohrer<sup>1</sup>, M. Skowronski<sup>1</sup>, V.D. Heydemann<sup>2</sup> and D.W. Snyder<sup>2</sup>

<sup>1</sup>Department of Materials Science and Engineering, Carnegie Mellon University, 5000 Forbes Ave, Pittsburgh, PA 15213, USA

<sup>2</sup>II-VI Incorporated, 375 Saxonburg Blvd, Saxonburg, PA 16056, USA

**Keywords:** Bulk Crystal Growth, Physical Vapor Transport, Plastic Deformation, Residual Stresses, Thermoelastic Stress

### Abstract

The thermoelastic stress distribution in growing 6H SiC crystals was simulated using a two dimensional finite element model. Based on the calculated stress distribution, possible plastic deformation of the material was postulated. High resolution x-ray diffraction (HRXRD) was used to detect the net deformation and residual stresses in the grown crystals. The results were in agreement with the postulated plastic deformation.

### Introduction

One of the outstanding issues in SiC technology is the optimization of the bulk crystal growth process. Of particular interest is the relationship between growth conditions and the structural quality of boules. In recent years, several research groups have employed mathematical modeling to study this subject. Advanced models have been developed for simulating the global temperature distribution and growth rate by accounting for major features of the physical vapor transport (PVT) process such as heat generation by electromagnetic induction, heat transfer by conduction, convection, and radiation, mass transport, and chemical reactions [1-4].

Tsvetkov *et al.* [5] discussed the effect of thermal stress developed in growing or cooling crystals. They applied a one dimensional model in order to estimate the resolved shear stress in the basal plane glide systems due to an axial temperature gradient. They estimated that the stress in a 50 mm diameter crystal can be in the range of 0.1~100 GPa and concluded that this mechanism can be the main source of the basal plane dislocations.

In this study, we describe a two dimensional model of thermoelastic stresses in growing 6H SiC crystals which involves both an axial and a radial temperature distribution. The effect of stress distribution on the plastic deformation of SiC boules and the possible mechanisms of the deformation are considered.

### Finite Element Modeling

The distribution of various stress components was modeled using the ANSYS software package, employing the finite element method. The assumed growth conditions are illustrated schematically in Fig. 1. The cylindrical crystal grows downward. Heat is injected from the growth surface of the crystal (the bottom and lateral faces of the cylinder) and extracted through the radiation window at the top of the seed. Because of the geometry, an axisymmetric model along the growth

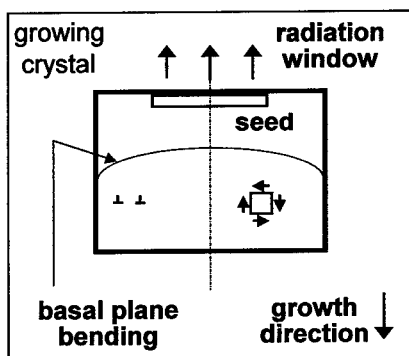


Fig. 1 Schematic showing the growth condition, the shear stress direction, edge dislocations involved, and the bending of the basal plane.

direction (the [0001] direction) was used. With this assumption, the 3-D cylindrical problem can be simplified into a 2-D rectangular problem. Three normal and one shear component ( $\sigma_{rr}$ ,  $\sigma_{\theta\theta}$ ,  $\sigma_{zz}$ ,  $\sigma_{rz}$ ) out of the six independent 3-D stress components can be non-zero.

The growth surface of the crystal is allowed to move freely. The possible interaction between growing crystal and the crucible side wall was neglected for simplicity. Two opposite extreme boundary conditions were considered on the top face. It is set free to move in the first case and restricted not to bend vertically in the second case. These can be considered as conditions for two different seed mounting methods, simple mechanical and rigid glue mounting. In an actual growth with a glue mounted seed, the condition will not be as rigid as the second case and will be between the two extreme cases.

One of the difficulties in the analysis is that the necessary material properties are not known at temperatures of the PVT growth process. Inoue and Kurachi [6] reported the anisotropic thermal expansion behavior of 6H single crystal from 850 °C to 2100 °C. We extrapolated their experimental data to the modeling temperature. The complete set of room temperature elastic constants was reported by Kamitani *et al.* [7]. Their temperature dependence was studied by Li and Bradt [8] and Samant *et al.* [9], but the highest temperatures used were only 1000 °C and 1300 °C, respectively. Thus, in this study, we applied the room temperature values for approximation.

### Stress Distribution

In Fig. 2, a typical temperature distribution in a growing crystal is shown. The left side represents the center axis (the symmetry axis) and the right side is the crystal periphery. The diameter is 50 mm and the aspect ratio of crystal height to diameter is 0.25 in the case. Since the heat is extracted through a window over the center portion of the top face, the region is coldest during growth. In this particular case, the average axial temperature gradient along the symmetry axis is 80 °C/cm and the average radial temperature gradient at the top face 30 °C/cm. The cold temperature at the center of the top face is 2200 °C.

The resultant thermoelastic stress components due to temperature distribution of Fig. 2 are shown in Fig. 3, where (A~D) are for the case of mechanical mounting and (a~d) glue mounting method. The absolute maximum values of all the components are increased greatly when the displacement constraint due to glue mounting is considered. The distribution of each component is also influenced. This is especially true for the shear component, where a negative shear stress becomes dominant.

The normal stress components are tensional in the center of crystal and compressive in the outer edge as clearly shown in the case of mechanical mounting. The radial and tangential components are dominant. This can be expected since the center of crystal is cooler than the outer edge during growth. The effect is more pronounced in the region close to the top face where the radial temperature gradient is larger. For the glue mounting, the region where the compressive radial and tangential normal stresses are maximum moves from the outer edge to the center of the bottom face and the axial normal stress increases much more than the other components. These changes appear to be exaggerated and due to the simplified boundary conditions used. In an actual growth, as mentioned above, the glue mounting is not expected to be as firm as assumed by the model. The crystal periphery is also bounded by the crucible wall and can interact with it.

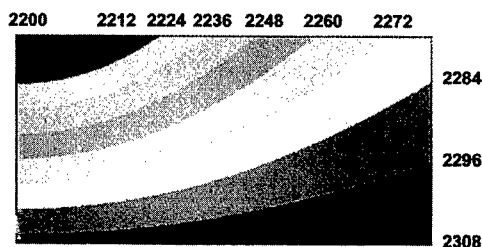


Fig. 2 A typical temperature profile in a growing crystal. (unit: °C)

### Crystal Response and HRXRD Measurements

The negative shear stress will cause the basal plane edge dislocations of the type shown in Fig. 1 to glide toward the center of crystal. The accumulation of such dislocations will cause the basal plane to bend to a shape as indicated, which is concave to the growth direction. The critical resolved shear stress for the glide system was reported to be 5 MPa at 1300 °C by Samant *et al.* [9]. The value is expected to be even smaller at the growth temperature. Thus, the magnitude of calculated shear stress appears to be large enough to activate the basal plane dislocation glide.

In addition to the shear component, crystal can deform in response to the normal stresses. From the distribution of normal stresses in Fig. 3, we suggest that the central region expands plastically during growth. If this plastic expansion occurs and relieves a certain amount of elastic stress at the growth temperature and if it isn't reversed and removed fully during cooling, the resultant plastic strain will be frozen into the boule after cooling and act as the source of residual stresses. The stress state after cooling will be opposite of that during growth, i.e. the periphery of crystal is expected to be under tension while the center be under compression. The plastic expansion is expected to occur by the slip of threading edge dislocations in the prism planes. The slip system  $\langle 11\bar{2}0 \rangle \{1100\}$  has been reported active in PVT grown hexagonal SiC [10].

HRXRD mapping along diameters of the boules was used to capture the plastic deformation frozen in the crystals as well as the residual elastic strains. The crystals were sectioned horizontally in slabs thick enough to prevent bending due to residual stresses. The total orientation change of the basal plane along a boule diameter was typically in the range of 100–2000 arc seconds (Fig. 4). The shape of bending was consistent with the calculated shear stress direction as shown in Fig. 1. Continuous reduction of the c-lattice spacing was observed along the radii of crystals from the center to the edge, which is consistent with the expected residual normal stress that is tensional along the radial and tangential direction and compressive along the axial direction. The amount of strain at the edge compared to the center was typically  $(-0.006) \sim (-0.002) \%$  (Fig. 5).

### Acknowledgements

This work was supported in part by the Commonwealth of Pennsylvania through the Ben Franklin Technology Center (Grant No. 98W.CM00562R-1) and by National Science Foundation (Grant No. DMR.9903702).

### References

- [1] M. Pons, M. Anikin, K. Chourou, J. M. Dedulle, R. Madar, E. Blanquet, A. Pisch, C. Bernard, P. Grosse, C. Faure, G. Basset, Y. Grange, Mater. Sci. Eng. **B61-62** (1999), p. 18.
- [2] P. Råback, R. Yakimova, M. Syväjärvi, R. Nieminen, E. Janzén, *ibid.*, p. 89.
- [3] M. Selder, L. Kadinski, F. Durst, T. Straubinger, D. Hofmann, *ibid.*, p. 93.
- [4] M. S. Ramm, E. N. Mokhov, S. E. Demina, M. G. Ramm, A. D. Roenkov, Yu. A. Vodakov, A. S. Segal, A. N. Vorob'ev, S. Yu. Karpov, A. V. Kulik, Yu. N. Makarov, *ibid.*, p. 107.
- [5] V. F. Tsvetkov, D. N. Henshall, M. F. Brady, R. C. Glass, C. H. Carter, Jr., Mat. Res. Soc. Symp. Proc. **512** (1998), p. 89.
- [6] Z. Inoue, Y. Kurachi, Proc. of the Int. Symp. on Ceramic Components for Engines (KTK Scientific, Tokyo, 1983), p. 519.
- [7] K. Kamitani, M. Grimsditch, J. C. Nipko, C.-K. Loong, M. Okada, I. Kimura, J. Appl. Phys. **82** (1997), p. 3152.
- [8] Z. Li, R. C. Bradt, Int. J. High Technology Ceramics **4** (1988), p. 1.
- [9] A. V. Samant, W. L. Zhou, P. Pirouz, phys. stat. sol. (a) **166** (1998), p. 155.
- [10] S. Ha, N. T. Nuhfer, G. S. Rohrer, M. De Graef, M. Skowronski, in this proceedings, p. 477

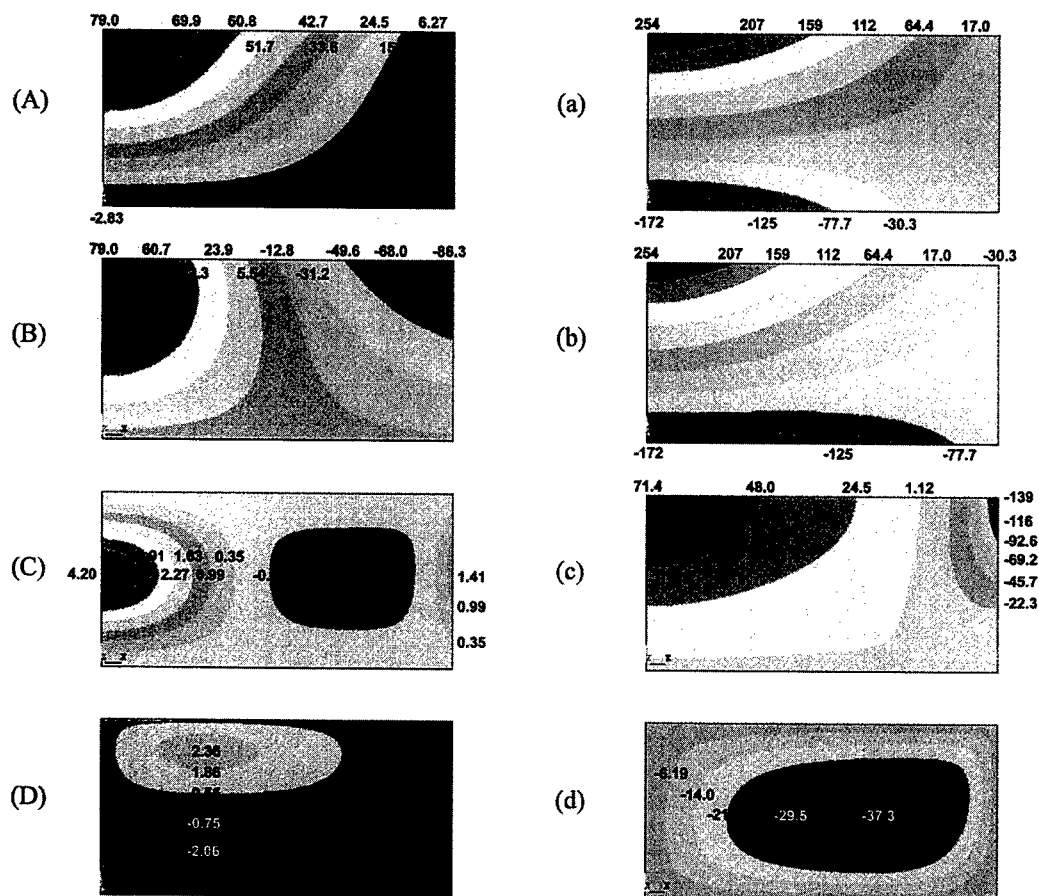


Fig. 3 Distribution of four non-zero stress components in the crystals during PVT growth for the two cases of mounting practice; (A~D) mechanical mounting, (a~d) glue mounting (unit: MPa)

(A, a) radial normal stress  $\sigma_{rr}$

(B, b) tangential normal stress  $\sigma_{\theta\theta}$

(C, c) axial normal stress  $\sigma_{zz}$

(D, d) shear stress  $\sigma_{rz}$

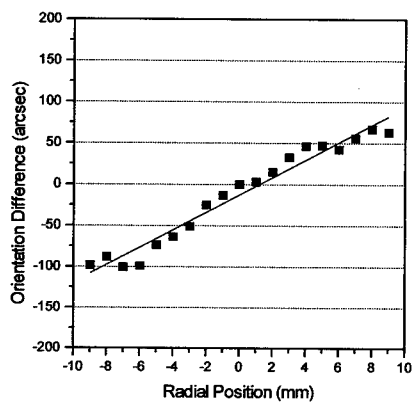


Fig. 4 Orientation difference of the basal plane along a crystal diameter with respect to the center position

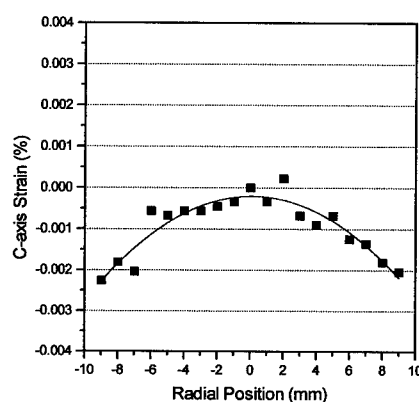


Fig. 5 The variation of strain of the c-lattice spacing along a crystal diameter due to the residual stress



## Digital X-Ray Imaging of SiC PVT Process: Analysis of Crystal Growth and Powder Source Degradation

P.J. Wellmann<sup>1</sup>, M. Bickermann<sup>1</sup>, D. Hofmann<sup>1</sup>, L. Kadinski<sup>2</sup>, M. Selder<sup>2</sup>,  
T.L. Straubinger<sup>1</sup> and A. Winnacker<sup>1</sup>

<sup>1</sup> Department of Materials Science 6, University of Erlangen-Nürnberg, Martensstr. 7,  
DE-91058 Erlangen, Germany

<sup>2</sup> Institute of Fluid Mechanics, University of Erlangen-Nürnberg, Cauerstr. 4,  
DE-91058 Erlangen, Germany

**Keywords:** PVT Process, SiC Powder, X-Ray Imaging

**Abstract.** Using digital x-ray imaging during silicon carbide (SiC) physical vapor transport process the SiC crystal growth as well as SiC powder source degradation have been monitored online. Using digital image processing we have (i) extracted from the x-ray shots the shape of the crystal growth interface, (ii) determined the crystal growth rate and (iii) analyzed the evolution of the SiC source material by determining its density as a function of progressing process time. The underlying sublimation and crystallization effects are discussed.

### Introduction

The physical vapor transport (PVT) method is presently the most promising growth technique for SiC bulk crystals [1-5] for commercial applications. However, up to now high process temperatures ( $T = 2100^{\circ}\text{C} \dots 2400^{\circ}\text{C}$ ) and the use of closed graphite crucibles have limited the observation and control of SiC crystal growth process. For a better understanding of the PVT SiC growth process it would be advantageous to monitor the evolution of the SiC crystal length and growth interface as well as the evolution of the SiC source material online during growth.

### Experiments

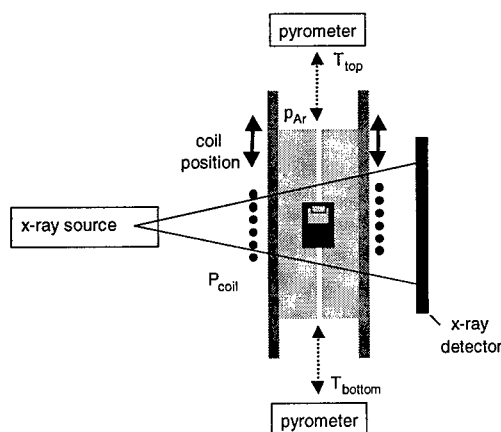


Fig. 1. PVT setup with attached x-ray imaging system.

In order to visualize the SiC crystal growth process we have developed a digital x-ray imaging technique. The system is based on a high resolution and high speed x-ray detector based on image plates and digital recording [6] (see Fig. 1). By x-ray exposure an image of the graphite crucible interior (SiC seed/crystal and SiC source material) is transferred to the x-ray detector (Fig. 1). The total image capture time including data processing and storage is less than 1min and allows an online monitoring and control of the PVT growth process. The main difficulty associated with imaging the ongoing processes inside the graphite crucible are major image distortions due to x-ray absorption by the inductive heating coil. Applying hardware image processing by moving the coil for a short time and distance during x-ray exposure we were

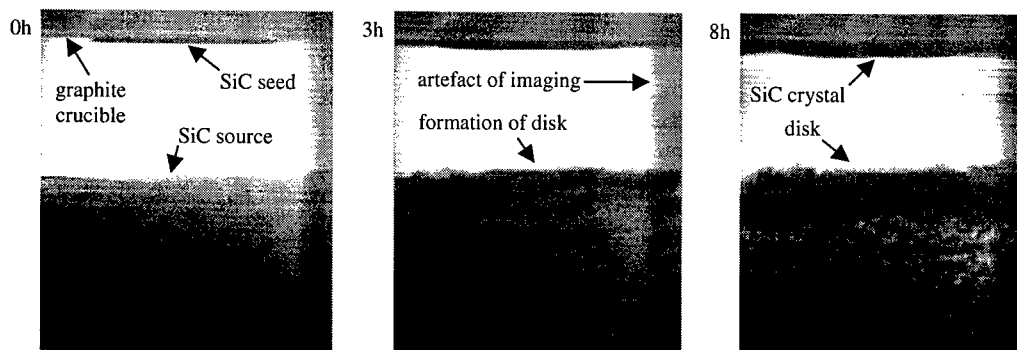


Fig. 2. Sequence of x-ray images taken online during PVT SiC crystal growth. Partial view of growing SiC crystal, gas room and top of SiC powder source. The indices 0h, 3h and 8h represent the actual growth time.

able to extract an unperturbed image of the growing SiC crystal and degrading SiC source material. Further details have been described in [7].

6H and 4H SiC bulk crystals have been grown in the PVT setup illustrated in Fig. 1. Our standard process uses (0001) Si- and C-face oriented 6H and 4H SiC seed wafers with a diameter of 30mm ... 40mm and micropipe density of  $<200\text{cm}^{-2}$ . The temperature is usually set to about  $2100^{\circ}\text{C}$  ...  $2300^{\circ}\text{C}$  with argon as carrier gas. The growth process is started by lowering the argon pressure from 800mbar to about 10mbar ... 50mbar and takes typically 60h ... 72h.

### X-ray imaging - experimental results

Fig. 2 shows a series of 4 x-ray images of the graphite crucible interior taken online during PVT growth. The graphite walls as well as the SiC crystal and the SiC source material are clearly resolved with a spatial resolution of approximately  $100\mu\text{m}$ . The flat surface of the SiC seed at the beginning of the growth process (index 0h in Fig. 2) illustrates the low imaging distortion level of our x-ray system.

In a different growth run (not shown) the shape of the growth interface (convex/concave) determined by the x-ray imaging technique has been compared with the growth interface determined from intentionally introduced doping striations [3] and showed an overall matching; the x-ray method, however, being superior due to its non-destructive nature.

The crystal growth interface (Fig.2; 0h, 3h, 8h) evolves with a flat area in the central part which is favorable for low defect generation and turns into convex in the outer part of the original seed area. Outside the seed area a concave growth interface evolves; in this part polycrystalline growth of various polytypes and orientations is observed. The flat growth interface in the central part of the crystal is a consequence of an optimized temperature field in the graphite crucible interior. Using numerical modeling we minimized the radial temperature variation over the seed area to less than 15K. The computer code we used took into account RF-heating of the crucible and heat transfer by conduction, radiation and convection.

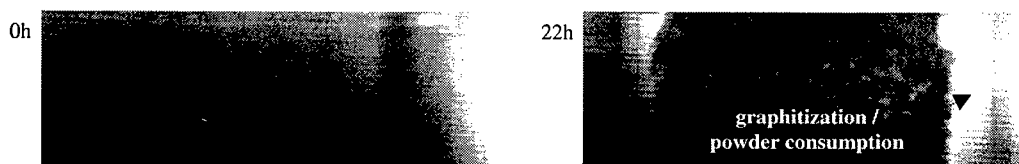


Fig. 3. Sequence of x-ray images taken online during PVT SiC crystal growth. Partial view of SiC source core. The indices 0h and 22h represent the actual growth time.

In Fig. 5 we have plotted the volume of the growing SiC crystal including the polycrystalline parts and its time derivative, the volume growth rate. The crystal volume evolves linearly with time; the corresponding length growth rate is about 250 $\mu\text{m}/\text{h}$ .

In the case of the evolution of the SiC source material two striking features are visible in Fig. 2 and Fig. 3: (i) the formation of a compressed disk-like structure at the source top in the initial phase of growth (about first 5h, Fig. 2) and (ii) graphitization/consumption of the SiC source which starts next to the hot graphite walls and proceeds into the core of the crucible (22h, Fig. 3).

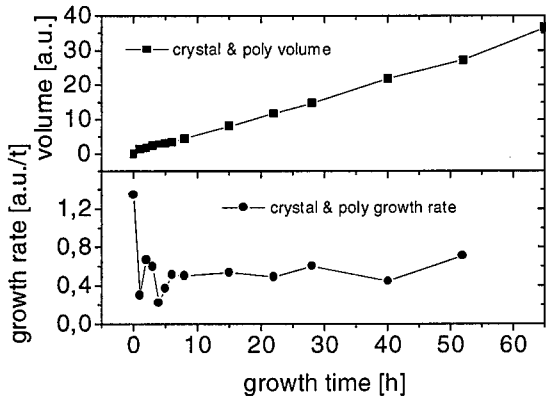


Fig. 4. Evolution of crystal volume and crystal volume growth rate.

growth process (homogeneous SiC powder, dashed line in Fig. 4). During formation of the disk-like structure at the SiC source top in the initial phase of the growth process (first 5h) a compression of the density of about factor two is observed. Remarkable is that the density of the SiC source core part increases only by 10% ... 20% over growth time. However, the morphology of the core part undergoes striking changes. In Fig. 2 and Fig. 3 the evolution of a spotty image pattern is observed in the SiC source core part (sequence 0h  $\rightarrow$  3h  $\rightarrow$  8h  $\rightarrow$  22h). In order to minimize their surface energy large SiC powder grains grow due to sublimation and crystallization processes at the expense of smaller ones. At the same time hollow channels evolve between the powder grains. As a consequence the average density of the core part remains almost constant over PVT process time.

#### Analysis of PVT growth process

SiC crystal growth by the PVT process is usually carried out in a growth regime where crystal

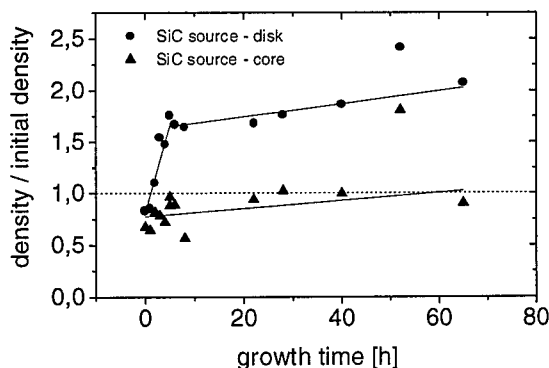


Fig. 5. Evolution of density of SiC source top (disk-like structure) and core part.

An analysis of the image contrast of Fig. 2 allowed us to extract the density  $\rho$  of the SiC source material as a function of growth time. The image contrast of the growing SiC crystal served as reference ( $\rho(\text{SiC-crystal})=3.21\text{g}/\text{cm}^3$ ). Fig. 4 shows the evolution of the disk-like structure and core part of the SiC source in arbitrary units. For a better comparison the data have been normalized to the nominal density of the SiC powder at the beginning of the

growth is limited by (i) kinetics (sublimation/crystallization at source/crystal), by (ii) diffusion of the SiC-containing gas species or by (iii) heat transfer limitations due to crystallization energy. It can be shown in an analytical mathematical approach [8] that a constant growth rate with time as observed in our case (Fig. 4) is indicating a limitation by kinetics and/or diffusion. Heat transfer limitation due to crystallization causes a decreasing growth rate with process time. Such effects were observed in our lab in the case of high growth rates (i.e.  $>500\mu\text{m}/\text{h}$ ). Growth

experiments carried out with a varying carrier gas pressure support that mass transfer limitation by diffusion dominated. The growth rate increased by a factor of two when decreasing the system pressure by a factor of three and returned to its initial value when setting the pressure as at the beginning.

Numerical modeling of the temperature field of the graphite crucible interior exhibited an average temperature gradient of about 40K/cm in the core of the SiC source and 110K/cm in the disk-like area. However, the temperature gradient dropped to only 1K/cm at the top of the SiC source and rose again to 50K/cm in the vicinity of the SiC crystal growth interface. The large temperature gradient inside the SiC source (40K/cm ... 110K/cm) is responsible for mass transfer from the source core to the top. The strong decrease at the top from about 110K/cm to 1K/cm causes a "jam" of the vapor transport and is responsible for the formation of the condensed disk-like structure. However, numerical modeling of the mass transfer [9] from source to seed indicates the existence of a two to three times larger SiC gas flow in the vicinity of the graphite crucible wall as compared to sublimation from the central part of the disk-like structure. Although the formation of the disk-like structure is believed to have a stabilizing effect on the growth process in terms of defect generation - a well defined needlelike top area serves as SiC source - it is possible that the high SiC gas flow close to the side walls (=graphitization area in Fig. 3/22h) carries carbon particles which could be responsible for the formation of the well known carbon inclusions in PVT grown SiC crystals [10].

In conclusion, digital x-ray imaging was used as a tool to investigate the ongoing processes during PVT growth of SiC single crystals. The evolution of the volume SiC crystal growth rate and the SiC source morphology and density were analyzed. The formation of a growth stabilizing disk-like structure of the SiC source was observed in the initial phase of the process. The SiC source could supply a higher mass transfer. Mass transfer limitation by diffusion between SiC source and SiC crystal is found to be dominant in the presented experiments.

### Acknowledgements

This work has been supported by the Deutsche Forschungsgemeinschaft (contract No. Wi393/9 and Du101/47).

### References

- [1] Y.M. Tairov and V.F. Tsvetkov: *J.Cryst.Growth* 43, 209, 1978.
- [2] G. Ziegler, P. Lanig, D. Theis and C. Weyerich: *IEEE Trans. Electron. Devices* 30, 277, 1983.
- [3] R. Eckstein, D. Hofmann, Y. Makarov, St.G. Müller, G. Pensl, E. Schmitt and A. Winnacker: *Mat. Res. Soc. Symp. Proc.* 423, 215-220, 1996.
- [4] D. Hofmann, R. Eckstein, M. Kölbl, Y. Makarov, St.G. Müller, E. Schmitt, A. Winnacker, R. Rupp, R. Stein and J. Völkl: *J.Cryst.Growth* 174, 669-674, 1997.
- [5] C.H. Carter, Jr., V.F. Tsvetkov, D. Henshall, O. Kordina, K. Irvine, R. Singh, S.T. Allen and J.W. Palmour: *Mat.Sci.Engr.* B61/62, 1999.
- [6] M. Thoms, H. Burzlaff, A. Kinne, J. Lange, H. von Seggern, R. Spengler and A. Winnacker: *Mater.Sci.Forum* 107 (1), 228-231, 1995.
- [7] P.J. Wellmann, M. Bickermann, M. Grau, D. Hofmann, T.L. Straubinger and A. Winnacker: *Mat. Res. Soc. Symp. Proc.*, Vol.572, 1999.
- [8] St.G. Müller: thesis, University of Erlangen-Nürnberg, 1998.
- [9] M. Selder, L. Kadinski, F. Durst, T. Straubinger, D. Hofmann, P. Wellmann: paper presented at the ICSCRM'99 conference, 1999, p. 31
- [10] D. Hofmann, E. Schmitt, M. Bickermann, P.J. Wellmann and A. Winnacker: *Mat.Sci.Engr.* B61-62, 48-53, 1999.

## SiC Single Crystal Growth Rate Measurement by *In-Situ* Observation using the Transmission X-Ray Technique

Naoki Oyanagi<sup>1</sup>, Shin-ichi Nishizawa<sup>2</sup>, Tomohisa Kato<sup>2</sup>, Hiroataka Yamaguchi<sup>2</sup>  
and Kazuo Arai<sup>2</sup>

<sup>1</sup>R&D Association for Future Electron Devices (FED), UPR Ultra-Low-Loss Power Device Technology Research Body, c/o Elerotechnical Laboratory, 1-1-4 Umezono, Tsukuba, Ibaraki, 305-8568, Japan

<sup>2</sup>Electrotechnical Laboratory, UPR Ultra-Low-Loss Power Device Technology Research Body, 1-1-4 Umezono, Tsukuba, Ibaraki, 305-8568, Japan

**Keywords:** Growth Rate, *In-Situ* Observation, Sublimation Growth, Transmission X-Ray Technique

**Abstract:** The growth rate of SiC bulk single crystal by sublimation was measured in real time by using the transmission X-ray technique. The growth rate obtained by transmission X-ray intensity corresponds to the growth rate measured by nitrogen marker. The growth rate increases as the growth temperature increases and as pressure decreases. While taking into account the pressure balance between the surrounding pressure and vapor pressures of seed and source, the growth rate can be calculated by mass flux from source to seed.

### Introduction

Since modified Lely method has developed [1], the SiC bulk crystal quality gradually improves every year. But it has observed many defects by X-ray topography [2]. Therefore the SiC power device performance has not been enough. Growth rate is one of the important factors, which determine the grown crystal quality. From this point of view, the crystal growth rate is studied related to the heat and mass transport phenomena [3-6]. Until now, there has been no such information on the growth rate measurement during the growth in real time. In this study, we succeeded in the growth rate measurement of the grown crystal during the growth by measuring the intensity of X-ray in transmission geometry.

### Experiment

6H-SiC crystals have been grown by the modified Lely method. The Acheson crystal, such as the seed crystal, fixed the graphite crucible lid. The source material was abrasive SiC powder with an average grain size of 80  $\mu\text{m}$ . The distance between the source and the seed crystal was about 15mm. The crystal growth is carried out for 2-8hours. To avoid the scattering and absorption by source abrasive powder, the inner cone tube was installed in the crucible. The crucible was put into a water-cooled stainless chamber and it was heated by RF induction

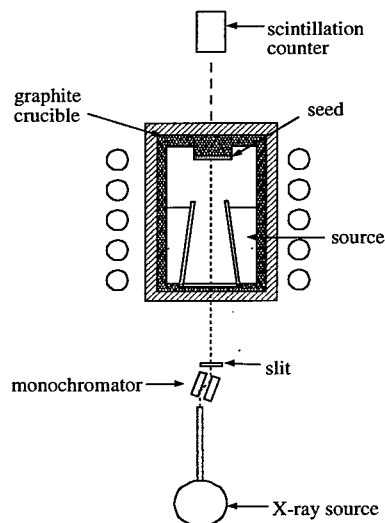


Fig.1 Scheme of experimental method

with a frequency of 20 kHz. The growth pressures  $P_0$  were 1 to 100 torr and the graphite crucible lid temperatures were 2000°C to 2300°C.

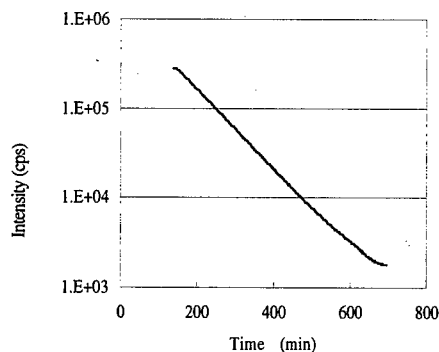
During the growth, an X-ray beam was transmitted from the bottom to the top of a crucible through the grown crystal and the intensity was measured directly by the scintillation counter, which was set on the top of a crucible. X-ray beam was limited through the monochromator and with a slit width of 1mm. The crystal growth rate is calculated by the following equation

$$d\ln(I)/dt = -\mu(dx/dt) \cdot \dots \cdot (1)$$

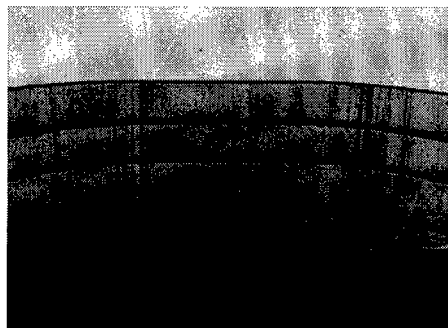
where  $I$ ,  $\mu$ ,  $t$  and  $x$  are X-ray intensity, linear absorption coefficient, time and thickness of the grown crystal respectively. The growth rate was also measured by  $N_2$  gas marking and compared with the growth rate by a transparent X-ray intensity measurement.

## Result and Discussion

### 1. Real time measurement by the transmission X-ray technique



(a) Time dependence on X-ray intensity

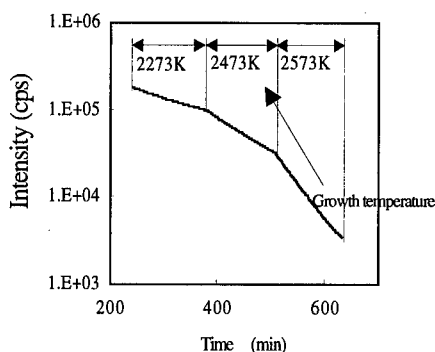


(b) Cross section photograph

Fig.2 Crystal growth at 2200°C constant

Fig.2 (a) shows the time dependence of x-ray intensity when the graphite lid temperature was constant. As crystal grows, the transmission intensity decreases because of the absorption of grown crystal. In Fig.2 (a), the X-ray intensity was uniformly decreased for 8 hours. Fig.2 (b) shows the cross section photograph with the  $N_2$  marker every 2 hours.  $N_2$  lines were laid with same interval in the crystal. Therefore growth rate was constant for 8 hours without any influence of time dependent parameter.

Fig.3 shows a typical result of the X-ray transmission intensity measurement with varying growth temperature. It was caught to change the growth rate at each temperature. As the growth temperature increases, the intensity decreases rapidly. It means that the growth rate increases as the growth temperature increases. The growth rate was also measured using  $N_2$  marker at each growth temperature. Fig.4 compares the growth rate calculated by X-ray



intensity and optical microscope measurement with  $N_2$  line markers. There is a good agreement between the

growth rate calculated by X-ray intensity and that of optical microscope measurement with  $N_2$  line markers. It was confirmed that the real time measurement of growth rate by the transmission X-ray technique provides reliable results.

## 2. Growth rate

Fig.5 shows the effects of graphite lid temperature and pressure on the growth rate. The crystal growth rate depends not only on the temperature but also pressure. As the growth temperature increases, the crystal growth rate also increases. Moreover the growth rate at 100torr was lower than that of 10torr, because the diffusion coefficients differ from each growth pressure. On the other hand, the growth carried out at 1torr, the growth rate seems to be independent of the temperature. In fig.6, the grown crystal surface temperature  $T_c$  is higher than the graphite lid temperature  $T_s$ . And the source surface temperature  $T_F$  is higher than the crystal surface temperature  $T_c$ . By taking into account  $T_c$  and  $T_F$ , which are obtained by numerical simulation, equilibrium vapor pressure related to each surface temperature, were estimated. And growth rate was re-calculated with the mass flux of each chemical species described by the following equation

$$G = (M/\rho)(D/RT)((P_F - P_c)/L) \cdot \cdot \cdot (2)$$

Where  $M$ ,  $\rho$ ,  $D$ ,  $R$  and  $L$  are molecular weight, density, diffusion coefficient, gas constant and the distance between the source and the seed respectively.  $P_F$ ,  $P_c$  are the vapor pressure at the seed and the source surface.

### 1) Case 1 ( $P_F, P_c < P_0$ )

When the surrounding pressure  $P_0$  is larger than the sublimation pressure  $P_F$ , growth rates depend on  $(P_F - P_c)$  and diffusion coefficient. For the growth at 10 and 100 Torr, the calculated crystal growth rates were in good agreement with experimental results.

### 2) Case 2 ( $P_F, P_c > P_0$ )

When surrounding pressure  $P_0$  is smaller than sublimation pressure  $P_F$ , the growth rate is different from the previous case. Namely this might be due to

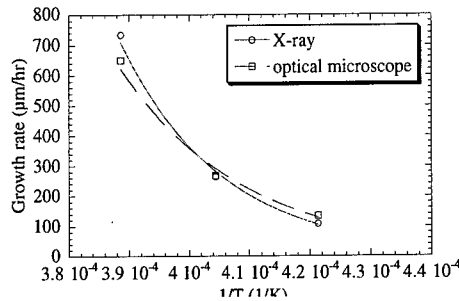


Fig.4 Comparison of X-ray growth rate measurement with Optical microscope measurement

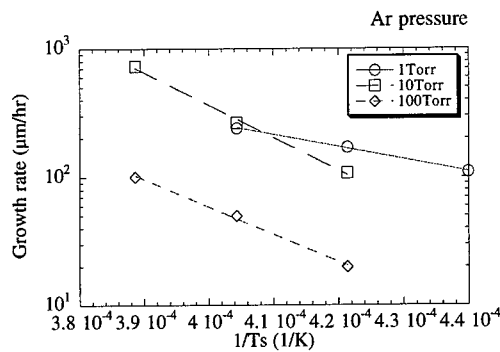


Fig.5 Temperature dependence on growth rate

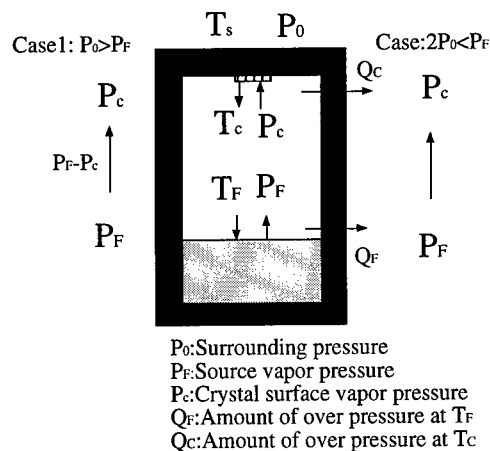


Fig.6 The model of growth rate by gas transport

the reason that the vapor pressure of sublimated species in the crucible is greater than the growth pressure ( $\approx 1$  torr). The amount of sublimated species above the surrounding will escape to the outside of the crucible. By replacing  $P_F$  and  $P_C$  in Eq. (2) by  $P_F - Q_F$  and  $P_C - Q_C$  respectively, the recalculated growth rate was in good agreement with the experimental results. As a result, the growth rate has smaller dependence on the growth temperature at 1 torr compared with that of 10 and 100 torr. It is suggested that the vapor pressure of the sublimated species must be given consideration in order to optimize the surrounding gas pressure.

### Conclusion

The growth rate of the SiC bulk single crystal by sublimation was measured in real time by the transmission X-ray technique. The growth rate increases as growth temperature increase, and as pressure decreases. In the case of high pressure, the growth rate can be calculated with sublimated vapor pressure and diffusion coefficient. In the case of low pressure, pressure balance between inside and outside the crucible must be considered. Considering the loss, which is equal to the amount of over pressure, the crystal growth rate can be calculated with vapor pressure at the seed and the source surface.

### Acknowledgement

This work was carried out by the Ultra-Low Loss Power device Project under the management of the R&D Association for Future Electron Devices (FED) as a part of the Ministry of International Trade and Industry (MITI) R&D of Industrial Science and Technology Frontier Program supported by New Energy and Industrial Technology Development Organization (NEDO).

### Reference

- [1] Yu. M. Tairov, V. F. Tsvetkov, J. Crystal Growth 43 (1978) 209
- [2] H. Ymaguchi S. Nishizawa, W. Bahng, K. Fukuda, S. Yoshida, K. Arai, Y. Takano, Mat. Sci. & Eng., B61-62 (1999) 221.
- [3] A.S. Segal, A.N. Vorob'ev, S.Yu. Karpov, Yu.N. Makarov, E.N. Mokhov, M.G. Ramm, M.S. Ramm, A.D. Roenkov, Yu.A. Vodakov, A.I. Zhmakin, Material Science and Engineering B61-62 (1999) 40-43
- [4] H.J. Rost, D.Siche, J.Dolle, W. Eiserbeck, T.Muller D.Schulz, G.Wagner, Material Science and Engineering B61-62 (1999) 68-72
- [5] D. Hofmann, M. Bickermann, R.Eckstein, M. Kolbl, St.G. Muller, E. Schmitt J. Crystal Growth 198 /199 (1999) 1005-1010
- [6] P. Raback, R. Yakimova, M. Syajarvi, R. Nieminen, E. Janze'n, Material Science and Engineering B61-62 (1999) 89-92

Correspond to N.Oyanagi: FAX: +81-298-54-3397, E-mail: noyanagi@etl.go.jp



## Role of Temperature Gradient in Bulk Crystal Growth of SiC

Cengiz M. Balkas, Andrei A. Maltsev, Matthew D. Roth and  
Nikolay K. Yushin\*

Sterling Semiconductor, Inc, 22660 Executive Drive, Suite 101, Sterling, VA 20166, USA

**Keywords:** Activation Energy, Bulk Crystal Growth, Enlargement, Growth Rate, Mass-Transport, Sublimation, Temperature Distribution, X-Ray

**Abstract** The effects of axial and radial components of temperature gradient on the silicon carbide (SiC) bulk crystal growth were investigated. It was shown that the growth rate is a linear function of an axial temperature gradient in the growth chamber. In addition preliminary information relating radial temperature gradient to boule diameter enlargement is also presented. The grown crystals were analyzed by optical microscopy and X-ray diffraction.

### Introduction

Bulk crystal growth of SiC via sublimation/re-condensation method has been under investigation for more than 20 years; starting with Tairov's work [1]. In spite of the abundance of publications (See [2-7] for example) some aspects of the bulk growth are still unclear in the open literature. The effect of temperature distribution on the crystal growth is one of such topics. It should be emphasized that sublimation growth of SiC crystal takes place under conditions of relatively high temperatures. The temperature profile inside the crystal growth chamber in most cases is very complex. Due to the complicated nature of the temperature distribution, the experimental investigation of the effect of the temperature on the crystal growth was performed separately for two independent components: (1) a vertical, or axial gradient and (2) radial gradient. More specifically, our aim was to clarify the role of the axial temperature gradient in the temperature dependence of the growth rate, as well as its radial component in the boule diameter enlargement. Although the experimental data were collected mainly from 6H-polytype growth runs, 4H-SiC boules were also grown during the course of this study.

### Experimental

The main components of the experimental set-up were the growth chamber, vacuum assembly, power supply, optical pyrometers, and a computerized control system. Crystal growth was accomplished on 6H [0001] seeds. The growth rate,  $G$ , is defined as the increase in boule length per unit time. Growth rate was analyzed as an exponential function of the inverse growth temperature,  $T_{\text{growth}}$ . Commercial statistical analysis software was used for the analyses of the data. Results revealed the following Arrhenius-like dependence:  $G(T) \propto \exp(-B/T_{\text{growth}})$  where  $B = (7.2 \pm 1.2) \cdot 10^4$ , K. Figure 1 presents a set of data confirming this dependence also found in many publications with some spread in the activation energy values. Analysis of existing data (from the present study as well as from literature [1-9]) shows that the value of  $B$  corresponds to the energy of SiC evaporation. The spread in the values of the activation energy is due to the fact that the evaporation rate of SiC source powder relates to source polytype, grain shape and surface condition, contamination, and other uncontrolled parameters that may change from one experiment to another.

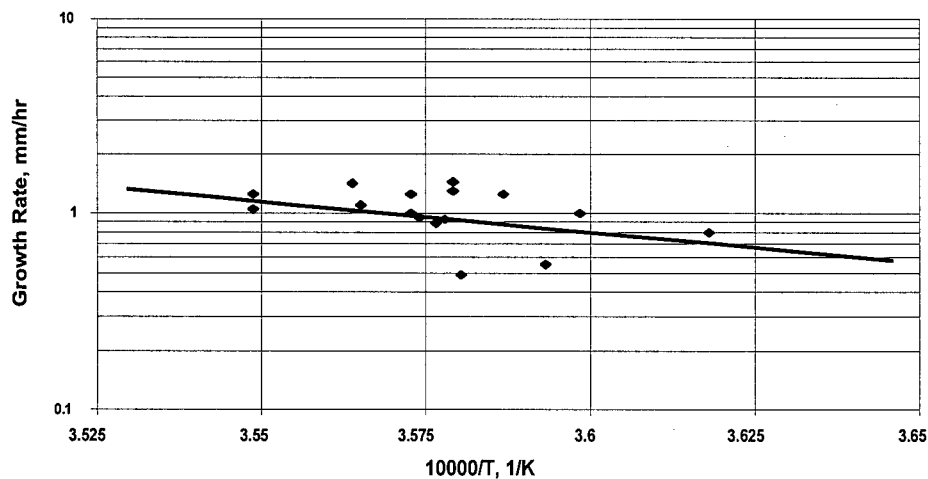


**Figure 1.** Growth rate versus inverse temperature,  $10^4/T$

Our analysis showed also that the  $G(T)$  is a linear function of  $\Delta T$ , that is the difference of the temperature, measured on top of the growth assembly, ( $T_{top}$ ) and the temperature measured on the bottom ( $T_{bot}$ ). Figure 2 illustrates the data to support this conclusion.

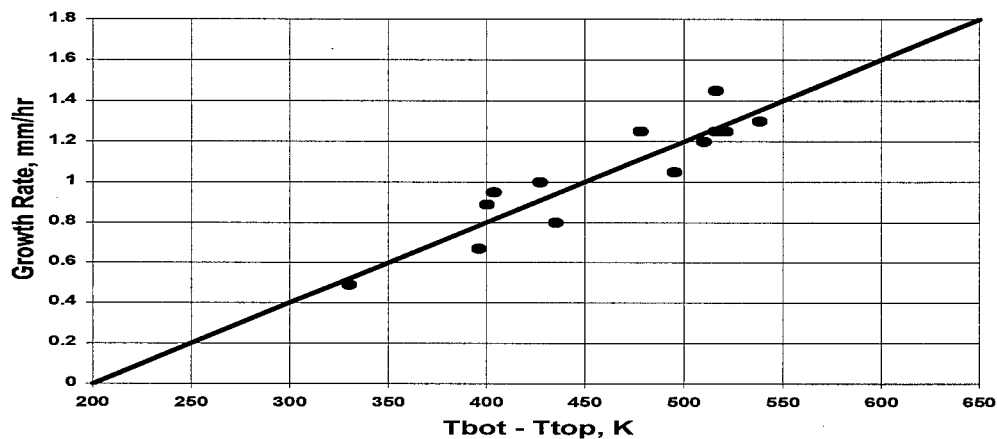


**Figure 2.** Growth rate versus difference of temperature  $\Delta T$ , K

The temperature  $T_{top}$  differs from the actual seed temperature  $T_{seed}$  by a value of  $\Delta_1$ , that is,  $T_{top} = T_{seed} - \Delta_1$ . Likewise, the temperature  $T_{bottom}$  is read at some distance from the source therefore  $T_{bot} = T_{source} - \Delta_2$ . Thus,  $\Delta T = T_{bot} - T_{top} = T_{source} - T_{seed} + (\Delta_1 - \Delta_2)$ . One can find the value of  $(\Delta_1 - \Delta_2)$  by extrapolating the  $G(\Delta T)$  to zero. If the temperature of seed  $T_{seed}$  is equal to the source temperature  $T_{source}$ , the mass transport is absent and  $G(\Delta T) = 0$ . The linear approximation of  $G(T)$  ( $G(\Delta T) = a + b \Delta T$  with  $a = -0.8 \pm 0.2$ , mm/hr and  $b = 0.004 \pm 0.001$ , mm/K hr) intersects the horizontal axis

at  $\Delta T = 200$  K (See Figure 2). Therefore, one may approximate  $(\Delta_1 - \Delta_2) = 200$  K. Figure 2 now may be re-plotted as a function of the temperature gradient,  $(T_{\text{source}} - T_{\text{seed}}) / d$ , where  $d$  is the source-seed distance. It is worth mentioning that the crystal quality strongly correlates with the growth rate. The important task is to optimize the growth conditions (such as inert gas pressure, radial gradient etc.) in such way that the highest crystalline quality is achieved at increased axial temperature gradients.

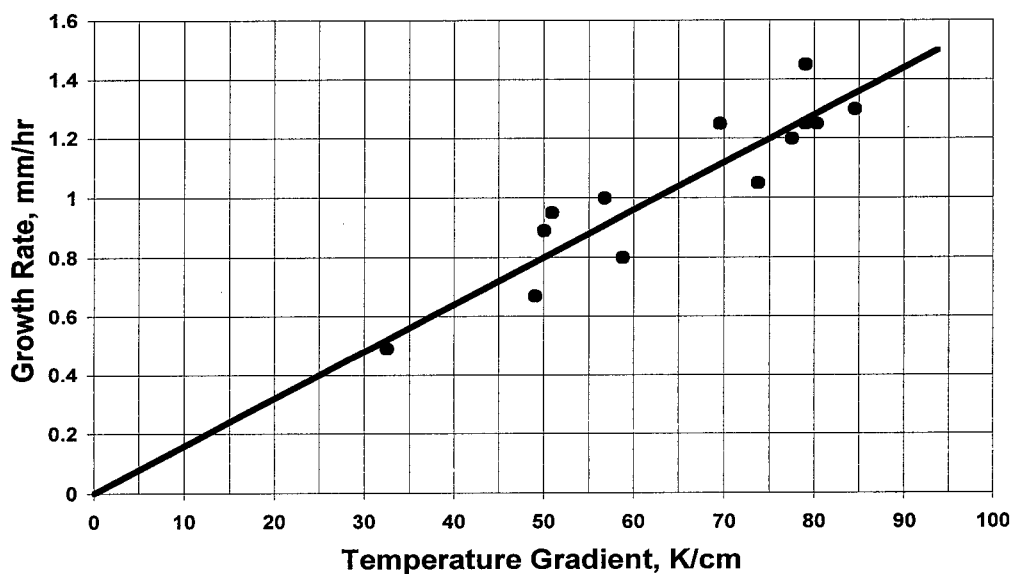


Figure 3. Growth rate versus axial temperature gradient.

It is clear that the axial temperature gradient contributes to growth along the primary growth direction (in this case [0001]). However, it is much more complicated to define the role of the radial temperature gradient in the crystal growth process. The appropriate choice of the radial gradient can provide conditions to grow SiC crystal boules up to 3" in diameter starting with seeds of  $\sim 1 \text{ cm}^2$ . Figure 4 shows a photographic image of a 2" Sterling wafer expanded from a Lely crystal and the X-ray diffraction rocking curve map measured over a 5x5 grid. Expansion was achieved over several successive growth runs.

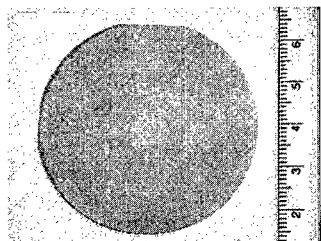
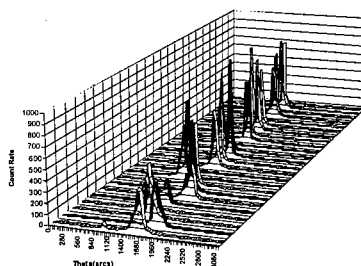


Figure 4. (a) A 6H, 2"- Sterling wafer expanded from a Lely crystal



(b) 25 point X-ray rocking curve map of the wafer shown in (a)

### Discussion

The experimental data indicate that the growth rate is a linear function of  $\Delta T$  and exponential function of the inverse temperature. As such the growth rate can be described by a complex function of temperature,  $F(T)$ . If the temperature,  $T$  and temperature gradient,  $\Delta T$  are independent components of the formula one may use the following expression:

$$G(T) = F(T) = A(P, S, t) \Delta T \exp(-U/RT), \quad (1)$$

where  $G(T)$  is the growth rate,  $R$  is the gas constant,  $R=8.314 \text{ JK}^{-1}\text{mol}^{-1}$ ,  $\Delta T$  is the difference of the temperature on the seed and source and,  $U$  is the activation energy,  $A(P, S, t)$  is a constant defined by the inert gas pressure  $P$ , the effective source surface area  $S$ , and the duration of the growth run  $t$ . The mass transport of the SiC species from source to the seed is controlled by diffusion of the species from hot zone to cool zone. The Arrhenius exponent appears in the above expression due to the activation energy needed for SiC sublimation. Thus, the model described by Eq.1 correlates sublimation of the SiC species from the source (the exponential part), the species transport from seed along the temperature gradient ( $\Delta T$  component), and the crystal growth is governed by  $A$ .

The role of radial gradient can be correlated to the growth anisotropy along different crystallographic directions as a reason for the crystal boule enlargement. It is well known (See for example [10]) that the SiC growth rate in orthogonal direction exceeds the rate along the [0001] axis. It means that the SiC crystal, under equilibrium conditions (i.e. zero temperature gradient), would have a tendency to grow in a direction perpendicular to the hexagonal axis [0001]. In any case, the preferable growth in orthogonal direction (lateral growth) can participate in the crystal boule enlargement together with a radial gradient.

In summary, the present analysis demonstrates the influence of temperature and temperature gradient on sublimation growth of SiC. In particular, effect on the growth rate and crystal area expansion. The results clearly show the importance of using precise temperature profiles, stabilization and control in bulk growth of SiC boules.

### Acknowledgement

This work was supported in a part by SBIR Projects # N00014-98-C-0176 (*BMDO/IST-managed by ONR*) and F33615-98-C-5422 (*BMDO/TOI-managed by AFRL*).

### References:

- [1] Yu. M. Tairov and V. F. Tsvetkov, *J. Cryst. Growth*, **43** (1978), p. 209.
- [2] V. F. Tsvetkov, R. Glass, D. Henshall, D. Asbury, and C. H. Carter, Jr., *Materials Science Forum*, **264**, (1998), p. 3.
- [3] Yu. A. Vodakov, A. D. Raenkov, M. G. Ramm, E. N. Mokhov, and Yu.N. Makarov, *Phys.Stat.Solidi*, **B202** (1997), p. 177.
- [4] M. Anikin and R. Madar, *Material Science and Engineering*, **B46** (1997), p. 278.
- [5] G. Augustine, H. McD. Hobgood, V. Balakrishna, G. T. Dunne, R. H. Hopkins, R. N. Thomas, W. A. Doolittle, and A. Rohatgi, *Materials Science Forum*, **264** (1998), p. 9.
- [6] P. Raback, R. Nieminen, R. Yakimova, M. Tuominen, and E. Janzen, *Materials Science Forum*, **264** (1998), p. 65.
- [7] A. A. Maltsev, A. Yu. Maksimov, N. K. Yushin, *Inst.Phys.Conf.Ser.* **142-1** (1996), p. 41.
- [8] L.J. Kroko, *J.Electrochem.Soc.*, **112** (1966) p. 801.
- [9] Yu.M. Tairov, V.F. Tsvetkov, S.K. Lilov, G.K. Safaraliev, *J.Cryst. Growth*, **36** (1976), p 147.
- [10] J. Takahashi and J. Ohtami, *Phys.Stat.Sol.* **b202** (1997) p. 163.

## Pressure Effect in Sublimation Growth of Bulk SiC

Yasuo Kitou<sup>1</sup>, Wook Bahng<sup>2</sup>, Shin-ichi Nishizawa<sup>2</sup>, Shigehiro Nishino<sup>3</sup> and  
Kazuo Arai<sup>2</sup>

<sup>1</sup>R&D Association for Future Electron Devices (FED), UPR Ultra-Low-Loss Power Device  
Technology Research Body, 1-1-4 Umezono, Tsukuba, Ibaraki, 305-8568, Japan

<sup>2</sup>UPR, Electrotechnical Laboratory, 1-1-4 Umezono, Tsukuba, Ibaraki, 305-8568, Japan

<sup>3</sup>UPR, Kyoto Institute of Technology, Matsugasaki, Sakyo-ku, Kyoto, 606-8585, Japan

**Keywords:** Al, C/Si Ratio, Crystal Defect, Growth Pressure, Growth Rate, Impurity Incorporation, SIMS, Sublimation Growth

**Abstract:** The effect of growth pressure on the impurity incorporation as well as on the crystal quality was investigated in sublimation growth of a bulk SiC single crystal. The growth pressure was varied within the range of 1-100 Torr and it was found that many voids or precipitates were generated in the grown crystals and the Aluminum (Al) impurity incorporation increased during the Si-face growth when the growth pressure decreased. The pressure effect on the Al impurity incorporation with the change of step structure was discussed.

### Introduction

Silicon carbide (SiC) is a promising semiconductor material because of its wide band gap, large thermal conductivity, high saturated electron drift velocity and high breakdown voltage. With these properties of SiC we can expect the realization of high performance devices operating at high power, high temperature and high frequency.

Although two inchs wafers in diameter are available, the quality and size of the wafers are not satisfactory. SiC ingots of single crystals for producing SiC wafers have been grown by sublimation method (modified Lely method) [1]. To improve the quality of SiC ingots, it is necessary to understand fundamental processes of sublimation growth. Growth pressure is one of the important parameters, that can specifically control growth rate [1]. In this work, we focused on the growth pressure and examined its effect on the impurity incorporation as well as on the crystal quality.

### Experiments

Bulk SiC single crystal was grown in a cylindrical graphite crucible with carbon thermal insulator. The crucible was heated in a water-cooled double quartz tube by RF induction coil. An Acheson 6H (0001) single crystal with Si-face was used as a seed crystal and commercial SiC abrasive as the source powder. The source powder was not treated with acid cleaning or baking. Al, Fe, and Ti were the major impurities in the source powder. The concentrations of Al, Ti were in the order of several tens ppm and that of Fe was around a thousand ppm. High purity graphite was used as the crucible and the impurity level in it was less than a ppm. The temperatures of the top and bottom of the crucible were measured as seed and source temperature by an optical pyrometer giving 2200°C and 2280°C respectively. The growth pressure was controlled with an automatic

program controller. High purity Ar gas was supplied constantly and the flow rate was 200 sccm. The pressure was changed within one growth run to eliminate the variations of the other conditions. Figure 1 shows the profile of the growth pressure, which was varied within the range of 1-100Torr while the temperature of the top of the crucible was kept constant.

The crystal quality was characterized by observing the cross-sectional sample which was sliced parallel to the growth direction.

Both sides of the sliced sample were polished and observed by optical microscope. Impurity concentrations in grown crystals were analyzed by secondary ion mass spectroscopy (SIMS) and fluorescence X-ray spectroscopy.

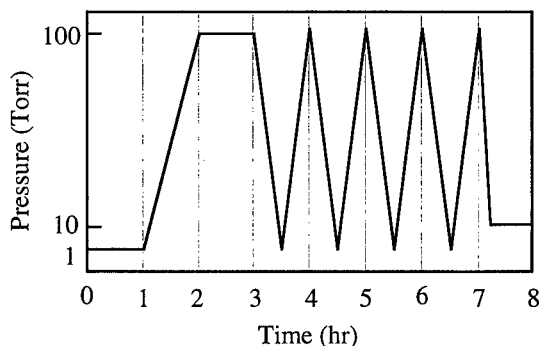


Fig.1 The profile of growth pressure

## Results and Discussion

### Crystal Defects

Figure 2 shows the cross-sectional transmission optical micrograph of the grown crystal. Five white lines were observed corresponding to the five replicate region grown at 100Torr. The regions grown at both 1Torr and 10Torr produced a dark violet color although the region at 1 Torr was darker than that at 10 Torr. In the region grown at 1Torr, many black particles of 5-20  $\mu\text{m}$  were observed and were shown to be pits on the surface (indicated by white arrows in figure 3(b)). These pits are voids or precipitates and correspond to the black particles in figure 2 and 3(a). Therefore, this means that these defects can be easily generated at lower pressure. The white diffused spots were also observed in the region grown at 1Torr as shown in figure 3(a) when the configuration of a polarizer and an analyzer was close to that of crossed Nicol. The white contrast was clearly different from the black particles and we speculate that these are the distorted or misoriented crystal grains of SiC. It should be noted that the generation of micropipes from these defects was not observed. Further analysis is necessary for the identification of these defects.

In our growth conditions, the growth rate increased as the growth pressure decreased and the growth rate varied 1-0.1mm/hr within the pressure range of 1-100Torr. It was reported that the pinhole and etch pit densities increased with the increase of the growth rate [2]. Thus it is suggested that the growth rate has an effect on the generation of defects that were observed in figure 2 and 3.

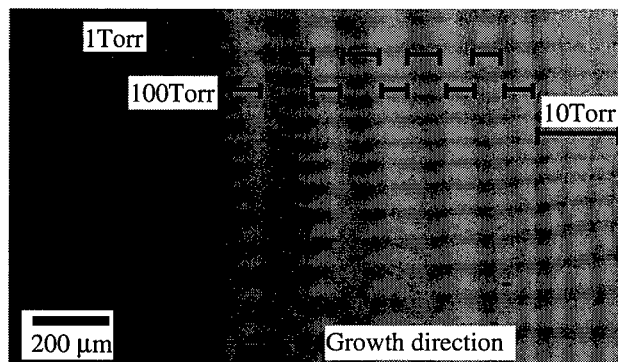


Fig.2 Cross-sectional transmission optical micrograph of the grown crystal.

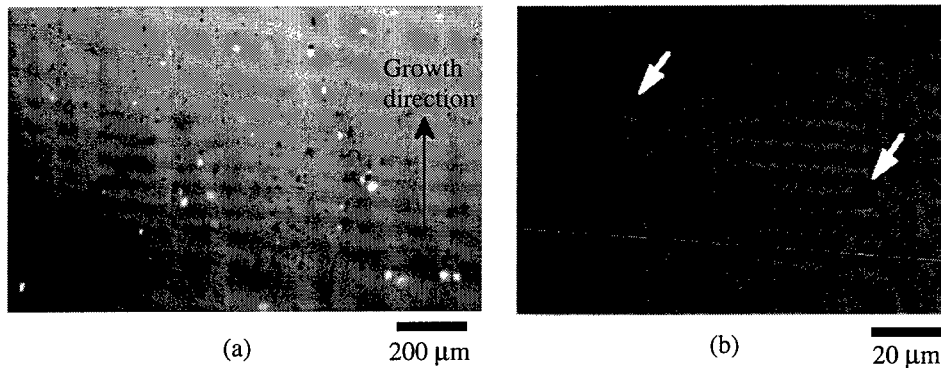


Fig.3 Optical micrograph of the region grown at 1 Torr.  
(a) transmission polarized image. (b) magnified reflection image.

#### Impurity Incorporation

Impurity concentrations of grown crystals were analyzed by fluorescence X-ray spectroscopy. The green crystal grown on the C-face as well as the dark violet crystal grown on the Si-face were analyzed to examine the difference between them. It was found that the crystal grown on the Si-face contained much more Al than that on the C-face. The concentrations of Fe and Ti were almost the same in both the Si-face and the C-face growth. SIMS analysis (Fig.4) revealed that the darker regions grown on the Si-face at lower pressure contained more Al than the regions grown at higher pressure while the B concentration was almost the same. These results are consistent with the report [3] that focuses on the relationship between color and the Al impurity. The results show that the Al incorporation is mainly influenced by the growth pressure.

In the similar growth experiments as shown in figure 2, we found that some polycrystalline grains showed the same pattern of figure 2, but the color was green. This means that crystals grown on near to the C-face incorporates nitrogen impurity more at lower pressure growth. It seems that the impurity concentration increases with the decrease of the growth pressure and/or with the increase of the growth rate. However it has been reported that the nitrogen incorporation dose not depend on the growth rate [4] and another report stated that the nitrogen concentration in the ingots diminished when the growth rate increased [1]. These reports suggest that the impurity incorporation is not directly related to the growth rate, otherwise our result strongly suggest that the growth pressure influences the impurity incorporation.

Although the reason of variation of the Al

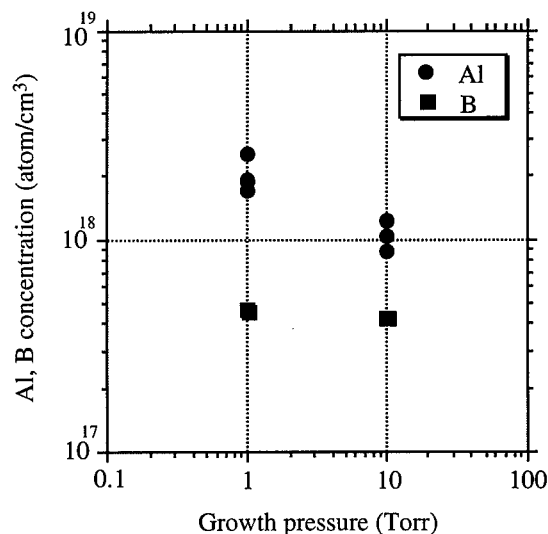


Fig.4 Dependence of Al,B concentration on growth pressure (grown on Si-face)

impurity incorporation was explained by the hermeticity of graphite crucible [2], the mechanism of the pressure effect is not clear. In step-controlled epitaxy, off-angle of the substrate has an effect on the impurity incorporation [5]. This would explain that the number of steps with dangling bonds determines the impurity incorporation. The polytypic dependence of impurity incorporation in sublimation growth was explained by the growth surface morphology [6]. We suggest that the step structure is changed by the growth pressure since it is possible that the flux of gas species and the nucleation on the surface increase when the growth pressure decreases. Consequently, an increase of the step density could enhance the impurity incorporation. As another consideration, we tried to apply a "site-competition epitaxy" model reported in CVD growth [7] to the sublimation growth. Our calculations showed that C/Si ratio was constant within the total pressure range of 1-100 Torr. It appeared that the "site-competition epitaxy" model could not explain the pressure effect on the impurity incorporation within our experimental setup.

There may be an effect of the impurity incorporation on the generation of the defects at lower pressure. From the technological viewpoint, the growth pressure is a parameter that not only directly determines the growth rate but also the crystal quality.

### Conclusions

The effect of growth pressure on the impurity incorporation as well as on the crystal quality was investigated in sublimation growth of a bulk SiC single crystal. It was found that many voids or precipitates were generated in grown crystals and the Al impurity incorporation increased during the Si-face growth when the growth pressure decreased. It is suggested that the Al impurity incorporation is related to the change of the step structure caused by the growth pressure.

### Acknowledgement

This work was performed under the management of FED as a part of the MITI NSS Program (R&D of Ultra-low-Loss Power Device Technologies) supported by NEDO.

### References

- [1] Yu.M. Tairov and V.F. Tsvetkov, *J. Crystal Growth* **52** (1981) 146.
- [2] S. I. Dorozhkin, D. D. Avrov, V. P. Rastegaev and Y. M. Tairov, *Mater. Sci. Eng.* **B46** (1997) 296.
- [3] N. Sugiyama, A. Okamoto, and T. Tani, *Inst. Phys. Conf. Ser. No.142* (1996) p489.
- [4] K. Onoue, T. Nishikawa, M. Katsuno, N. Ohtani, H. Yashiro and M. Kanaya, *Jpn. J. Appl. Phys.* **35** (1996) 2240.
- [5] T. Yamamoto, T. Kimoto and H. Matsunami, *Mater. Sci. Forum* **264-268** (1998) p.111.
- [6] N. Ohtani, M. Katsuno, J. Takahashi, H. Yashiro, M. Kanaya and S. Shinoyama, *Mater. Sci. Forum* **264-268** (1998) p49.
- [7] D. J. Larkin, P. G. Neudeck, J. A. Powell, and L. G. Matus, *Appl. Phys. Lett.* **65** (1994) 1659.

Corresponding author: Yasuo Kitou Fax: +81-298-54-3397, E-mail: kitou@etl.go.jp



## Study of Nitrogen Incorporation in 6H-SiC Single Crystals Grown by PVT

D. Schulz, K. Irmscher, J. Dolle, W. Eiserbeck, T. Müller, H.-J. Rost, D. Siche,  
G. Wagner and J. Wollweber

Institut für Kristallzüchtung, Max-Born-Str. 2, DE-12489 Berlin, Germany

**Keywords:** 6H Polytype, Nitrogen Concentration, Seed Orientation, Sublimation Bulk Growth

### Abstract

The incorporation of nitrogen during single crystal growth of silicon carbide via the vapour phase has been studied in the concentration range of  $3 \cdot 10^{17} \text{ cm}^{-3} \leq c_N \leq 3 \cdot 10^{19} \text{ cm}^{-3}$ . The nitrogen concentration was measured by secondary ion mass spectrometry (SIMS) and the net doping concentration by capacitance-voltage measurements (CV). In general with increasing the ratio  $N_2/(N_2+Ar)$  the nitrogen concentration in the crystals also increases resulting in a function of the square root of nitrogen partial pressure. Furthermore the influence of the seed orientation on the nitrogen level was investigated.

### Introduction

Electronic materials require definite impurity levels for their technical use. In general the concentration of foreign elements in a crystal has to be as low as possible, whereas dopants are used to adjust the electronic properties. In 6H-silicon carbide n-type conductivity is most often achieved by introduction of nitrogen replacing carbon atoms.

Although the nitrogen concentration can be adjusted in chemical vapour deposition by using site competition epitaxy quite well [1], there is still a lack of understanding for the sublimation technique, which is mainly due to the strong coupling of growth parameters. Therefore the present work focuses on the nitrogen concentration in dependence of the nitrogen partial pressure.

### Experimental

Different experiments have been performed in order to study the incorporation of nitrogen during single crystal growth of silicon carbide via the vapour phase. This growth technique is commonly referred to as modified Lely method (MLM). The details of the equipment used in this investigation has been described elsewhere [2]. Main control parameters are the growth temperature,  $2100^\circ\text{C} \leq T_{\text{seed, source}} \leq 2400^\circ\text{C}$ , the applied total pressure,  $1 \cdot 10^2 \text{ Pa} \leq p \leq 5 \cdot 10^3 \text{ Pa}$ , and the temperature difference. This difference between the measuring points at the top and at the bottom of the growth assembly is only a rough estimate of the actual temperature gradient in front of the growing interface. Usually the crucible is made of graphite and therefore it is easy to control the amount of nitrogen that is incorporated into the growing crystal by adding certain amounts of nitrogen to the inert gas ambient.

6H single crystals of 1" diameter have been grown on 6H-seeds of (0001)Si and (0001)C orientation. The nitrogen partial pressure was varied in the range of  $0 \leq [N_2/(N_2+Ar)] \leq 0.3$ . In order to minimize changes of different growth runs, experiments have been done using a dual-seed method, because crystal growth at high temperatures often suffers from reproducibility [3].

### Results and discussion

In a first growth experiment the nitrogen concentration dependent on the nitrogen partial pressure was investigated. Several nitrogen to argon ratios have been used and these ratios have been adjusted repeatedly for the determination of the growth time effect. A 6H single crystal was grown on both the (0001)Si as well as the (0001)C face although on the C-face polytype inclusions were often observed.

The nitrogen concentration measured by SIMS was in the range from  $4 \cdot 10^{18} \text{ cm}^{-3}$  to  $3 \cdot 10^{19} \text{ cm}^{-3}$ . In Fig. 1 data are presented.

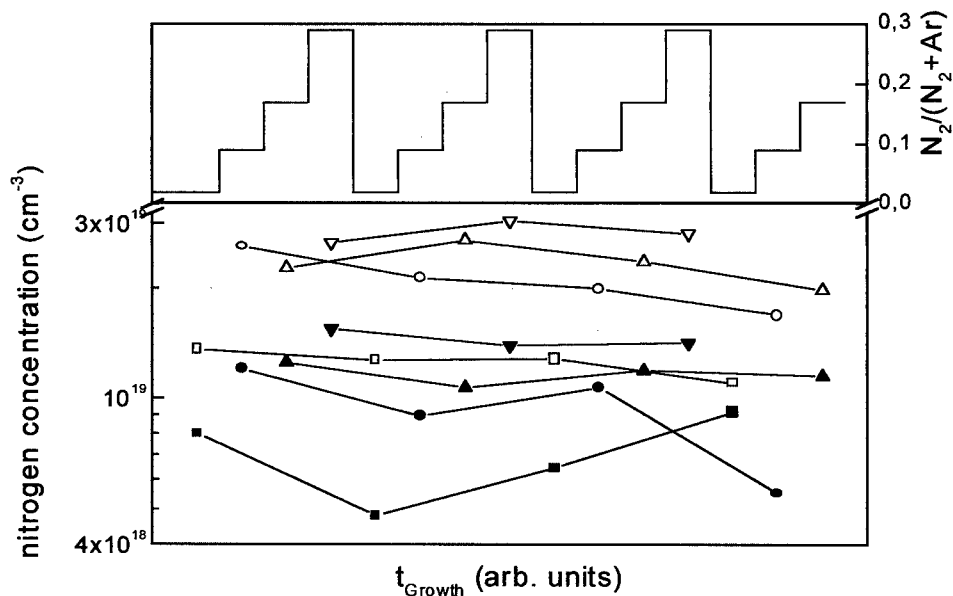


Fig. 1: Nitrogen concentration and  $N_2/(N_2+Ar)$  ratio as a function of growth time, solid symbols for (0001)Si and open symbols for (0001)C

On the (0001)C face more nitrogen is incorporated than on the (0001)Si face. This is due to the fact, that nitrogen replaces for the carbon atom. Commonly nitrogen incorporation is believed to occur at step sites of the growing surface because step flow is the dominant growth mechanism [5]. The surface consists of several bilayers and consequently it is assumed, that the impurity is preferentially incorporated to the topmost layer. The nitrogen concentration in the C-face grown crystal is twice as high that grown on the Si-face. With growth time there is a slight decrease in concentration, which can be attributed to the increasing interface temperature and therefore the change in the Si/C ratio. The growth rate was approximately constant for the undoped regions and strongly dependent on the supply of nitrogen to the growth atmosphere. In case of intentional doping the growth rate decreases by a factor of 2. The nitrogen content in the crystal is roughly proportional to the square root of its partial pressure [4]. However a fit of the data in the high concentration range shows that the exponent is somewhat lower than 0.5 suggesting a complex adsorption mechanism for nitrogen on silicon carbide surfaces during sublimation growth (fig. 2).

A second set of experiments was done in the nitrogen concentration range below  $4 \cdot 10^{18} \text{ cm}^{-3}$ . During these growth runs the nitrogen partial pressure was either kept constant to evaluate the axial and radial distribution or varied as in the previous experiments.

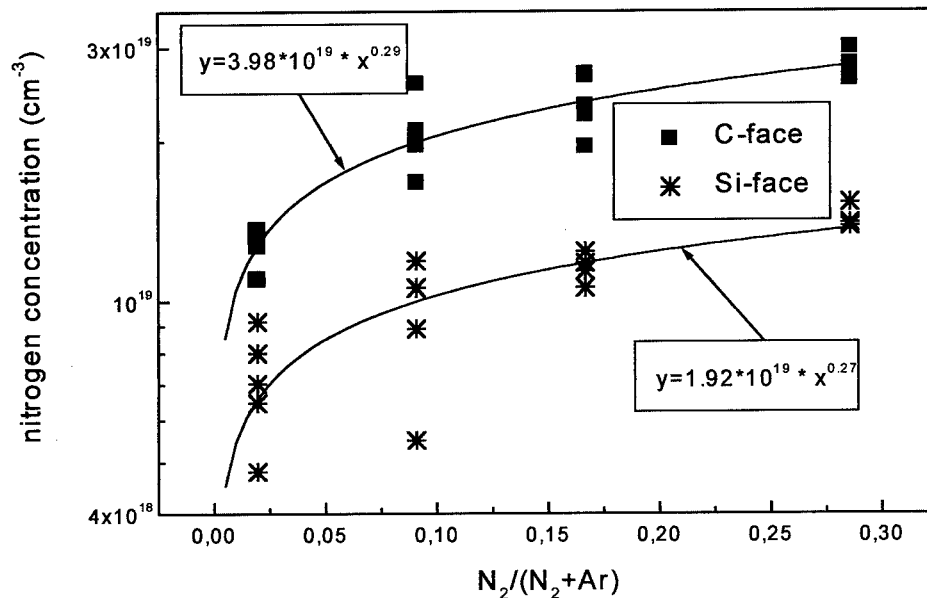


Fig. 2: Nitrogen concentration versus nitrogen to argon ratio, 6H single crystal growth on (0001)Si and (0001)C face, SIMS analysis

The data measured by SIMS reveal a change in concentration with crystal length and therefore with growth time (fig. 3). Good agreement was found between SIMS and C-V data, which gave a similar decrease in nitrogen concentration. Although a relatively high correlation of 0.92 has been found, the C-V always yields lower values. However this may be explained by the error limit of the two methods applied, which is in the range of 10% for the absolute values. Compensation effects can be excluded, since the level of background impurities is well below  $1 \cdot 10^{17}$  cm<sup>-3</sup> [6].

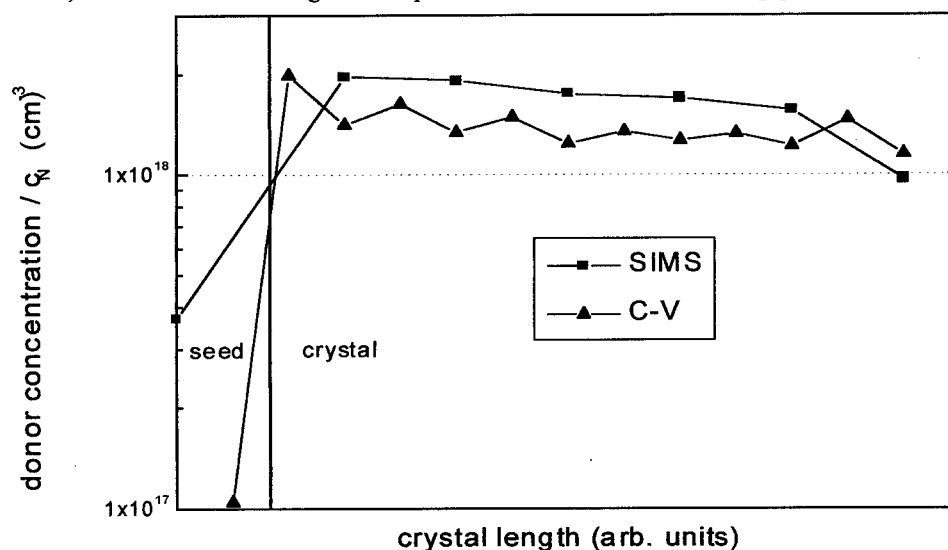


Fig. 3: Axial distribution of nitrogen along the c-axis in 6H-SiC

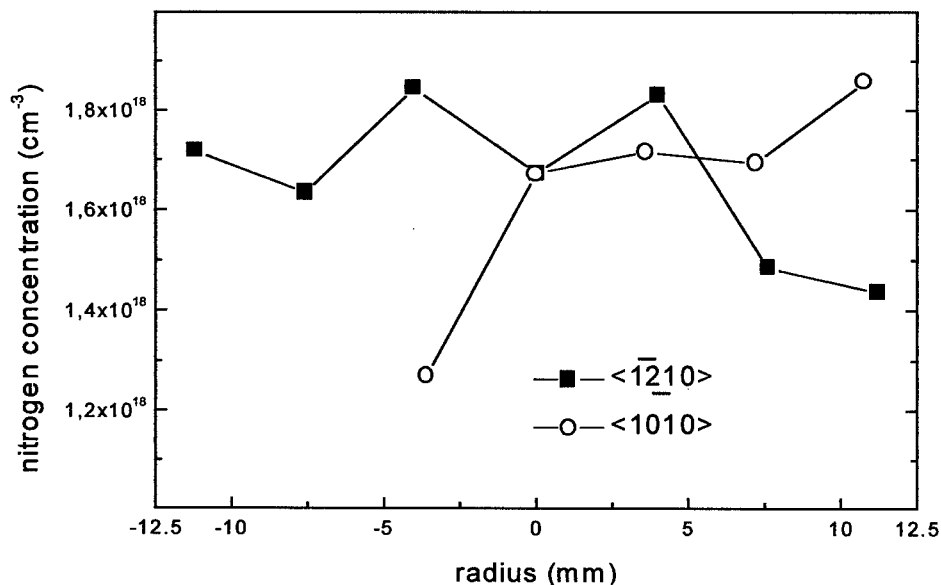


Fig. 4: Radial distribution of nitrogen measured across a (0001)-wafer (SIMS)

The radial nitrogen distribution was measured perpendicular to the c-axis on several wafers. The maximum value of all wafers is  $2.1 \cdot 10^{18} \text{ cm}^{-3}$  and the minimum one  $1.04 \cdot 10^{18} \text{ cm}^{-3}$  indicating that the variation across the radius and with growth time is quite low. As an example one wafer is shown exhibiting a standard deviation of 10.8 % (fig. 4).

### Conclusions

C-V measurements are in good agreement with SIMS analysis in terms of nitrogen in the concentration range  $3 \cdot 10^{17} \text{ cm}^{-3} \leq c_N \leq 5 \cdot 10^{18} \text{ cm}^{-3}$ . Highly homogeneous 6H-SiC wafers can be produced by the sublimation technique with a standard deviation lower than 16% for the whole crystal.

### Acknowledgement

The authors would like to acknowledge the support by Dr. D. Stephani from the Siemens AG. This work was financially supported by the Bundesministerium für Bildung und Forschung under the project number 01M2952B1.

### References

- [1] D.J. Larkin, Inst. Conf. Phys. Ser., **142** (1996), p. 23-28
- [2] D. Schulz, G. Wagner, J. Doerschel, J. Dolle, W. Eiserbeck, T. Müller, H.J. Rost, D. Siche and J. Wollweber, Mater. Sci. Engineer. B, **61-62** (1999), p. 86-88
- [3] V.D. Heydemann, N. Schulze, D.L. Barrett and G. Pensl, Appl. Phys. Lett., **69** (1996), p. 3728-3730
- [4] J.A. Lely, Ber. Dt. Keram. Gesellsch., **32** (1955), p. 229-231
- [5] J. Takahashi, N. Ohtani and M. Kanaya, Jpn. J. Appl. Phys., **34** (1) (1995), p. 4694-4698
- [6] D. Schulz, G. Wagner, J. Dolle, K. Irmscher, T. Müller, H.J. Rost, D. Siche and J. Wollweber, J. Cryst. Growth, **198/199** (1999), p. 1024-1027

## Evaporation Behavior of SiC Powder for Single Crystal Growth- An Experimental Study on Thermodynamics and Kinetics

Alexander Pisch<sup>1</sup>, Ana Maria Ferraria<sup>1</sup>, Christian Chatillon<sup>1</sup>,  
Elisabeth Blanquet<sup>1</sup>, Michel Pons<sup>1</sup>, Claude Bernard<sup>1</sup>, Michail Anikin<sup>2</sup> and  
Roland Madar<sup>2</sup>

<sup>1</sup> LTPCM-UMR 5614 (CNRS/INPG-UJF), Domaine Universitaire, BP 75,  
FR-38402 Saint Martin d'Hères, Cedex, France

<sup>2</sup> LMGP - UMR 5628 (CNRS/INPG), Domaine Universitaire, BP 46,  
FR-38402 St. Martin d'Hères, Cedex, France

**Keywords:** Evaporation Coefficient, High Temperature Mass Spectrometry, Vaporization

**Abstract :** The vaporization behavior of SiC has been analyzed by high temperature mass spectrometry with single and multiple Knudsen effusion cells. The vaporization of SiC is kinetically hindered and can be described by evaporation coefficients. These coefficients have been determined for the four major gas species: Si<sub>1</sub>(g), Si<sub>2</sub>C(g), SiC<sub>2</sub>(g) and Si<sub>2</sub>(g) in the temperature range from 1700°C to 2050°C. Metallic Ta in contact with SiC reacts to TaC. The evaporation coefficients are slightly higher in the presence of Ta and the vaporization is less time dependent which could explain literature information on higher growth rates in the presence of Ta in the PVT process.

### Introduction

Semiconducting SiC is a promising material for high temperature and power device applications. However, the lack of large area substrates of good quality with low defect densities are the major drawback for a further development. The standard growth procedure to obtain SiC single crystals is the physical vapor transport (PVT) process by the modified Lely method [1]. Highly pure SiC powder is sublimated in a semi-closed graphite crucible under Ar atmosphere and recondensed on a seed crystal. The temperature range of the sublimation is 2400°C-2650°C with a typical gradient of 10°C/mm towards the single crystal surface. Because of the high temperature conditions, direct measurement or control of the process conditions inside the crucible is difficult. Numerical modeling of the sublimation is therefore the only way to provide additional information to the experimental knowledge. During the last 5 years, significant progress has been made in this field (see e.g. a recent review by Pons et al. [2]). Such a modeling effort is primarily motivated by the need of a better control of the local temperature field inside the crucible, an environment of strong thermal radiation. The computed temperature distribution can help to quantitatively obtain the growth history in relation to process parameters and geometry. Global heat transfer phenomena are mainly studied and must include conduction, convection, radiation and induction heating as well as the heats of crystallization and sublimation at the crystal-vapor and the source-vapor interfaces. Nevertheless the simple simulation of heat transfer alone does not directly allow the determination of the growth rate and the shape of the growing crystal. This can only be achieved by combining mass transfer to local thermodynamic equilibrium or kinetic calculations for a given temperature distribution inside the growth cavity. In order to obtain good quantitative agreement, the precision of the underlying material properties, especially the thermal conductivity of all reactor material parts as well as the vaporization and condensation behavior of the SiC source powder is crucial.

The vaporization of silicon carbide possesses several peculiarities. The thermodynamic data for Si - C solid and gaseous species have been critically assessed recently [3]. Si<sub>1</sub>(g), Si<sub>2</sub>C(g), SiC<sub>2</sub>(g), Si<sub>2</sub>(g) and C<sub>3</sub>(g) has been identified as main gas species present over solid SiC at high temperature. For temperatures below 2700°C, the evaporation of SiC is not congruent, i.e. the powder loses

more Si than C leading to an aging of the source and graphitization [4,5]. A second point to mention is the fact that one never reaches the equilibrium pressure given by theoretical calculations using the optimized thermodynamic data. The vaporization is always retarded due to kinetic barriers. These kinetic barriers - or hindered vaporization reactions - can be evaluated by introducing evaporation and condensation coefficients in the Hertz-Knudsen flows at the surface of the SiC crystal. These coefficients are usually determined by thermogravimetry or torsion-effusion experiments as summarized for SiC in [6] and thus they correspond to the total vaporization rate as referred to the maximum rate at equilibrium.

The purpose of this study is the determination of the evaporation coefficients of  $\text{Si}_1(\text{g})$ ,  $\text{Si}_2\text{C}(\text{g})$ ,  $\text{SiC}_2(\text{g})$  and  $\text{Si}_2(\text{g})$  by high temperature mass spectrometry as a function of temperature. The experimental evidence in the literature that the presence of tantalum could lead to higher growth rates is verified by the same technique and the results will be discussed.

## Experimental

The vaporization behavior of SiC+C, SiC+Ta+C and SiC+TaC+C powder mixtures has been studied by conventional single and multiple Knudsen effusion cells. Most of the quantitative results have been achieved in the multiple cell configuration, the single cell was only used for qualitative experiments. The cells themselves have been made of high purity dense graphite (SGL TECHNIC S.A., purity IG11) with an inner diameter/height of 16 mm and an orifice opening varying from 1.5 to 3 mm for a lid thickness of 1 or 2 mm. The high purity SiC powder (NORTON purity HP 100F) has a standard grain size of 100  $\mu\text{m}$ . The grain size of TaC (ALFA, 99.5%) was in the order of 325 mesh. For the cells with tantalum, a piece of metallic foil has been added along the cell walls. The SiC and C materials used in this study are identical with the ones used in the single crystal growth by the physical vapor transport method [2]. The molecular flow coming from the cells has been analyzed by high temperature mass spectrometry. Details of the complete experimental setup as well as the measuring procedure are given elsewhere [7,8]. Four graphite cells are symmetrically packed inside a tantalum holder and heated by resistance heating. The temperature of the effusion cells has been varied stepwise in the range from 1700°C to 2050°C. The temperature measurement has been performed by a monochromatic pyrometer through a long hole drilled in the bottom part of the tantalum block. Standard corrections are made for the window transmission.

Identification of the gaseous species in the vapor cell was made by analyzing the ionization efficiency curves and the isotopic distribution of the ions. Every load (SiC+C, SiC+Ta+C and SiC+TaC+C) has been measured twice in the given temperature interval with a total heating time of 3h per run at high temperature (30 min per temperature for 4 cells and 4 analyzed species, total measuring time 8h) to monitor additionally the aging behavior of the powder mixtures. The shape of the crystals as well as the chemical composition of the remaining powder after the two runs have been analyzed by scanning electron microscopy coupled to EDX.

The calculation of evaporation coefficients for powder samples is based on earlier work by Whitman [9] and Motzfeld [10]:

$$P_{\text{eq}} = (1 - sC/Ak\alpha) P_m \quad (1)$$

with  $s$ : orifice area,  $C$ : Clausing coefficient,  $A$ : vaporization cross section,  $P_{\text{eq}}$ ,  $P_m$ : equilibrium/measured pressure and  $k$ : coefficient equal to the ratio of the effective vaporization area  $A'$  of the porous solid to the cross section  $A$  of the cell. For powders,  $k$  is normally within the range  $1 < k < 3.29$  [11]. Usually, for different experiments conducted with different orifice sizes,  $P_{\text{eq}}$  can be deduced by extrapolation and  $1/k\alpha$  is calculated from the slope [10]. In the case of multiple cells, the  $\alpha$  or  $k\alpha$  values can be determined directly from the ionic intensity ratios between two cells

with different orifices. More details on the calculation procedure and the theoretical background are given in [5].

## Results and Discussion

The measured  $k\alpha$  values for  $\text{Si}_1(\text{g})$ ,  $\text{Si}_2\text{C}(\text{g})$ ,  $\text{SiC}_2(\text{g})$  and  $\text{Si}_2(\text{g})$  for the mixtures  $\text{SiC}+\text{C}$  and  $\text{SiC}+\text{TaC}+\text{C}$  are summarized and compared to literature values in table 1. For all species, the temperature dependence in the measured temperature range are within the experimental scatter and therefore a mean value has been calculated.

**Table 1:** Measured values of the evaporation coefficient  $k\alpha$  as compared to literature data.

Mixture	Gas species	$k\alpha$ (1 <sup>st</sup> run / 2 <sup>nd</sup> run)	Reference
SiC+C	$\text{Si}_1(\text{g})$	0.052 / 0.019	this work
		0.033 - 0.038	[3]
	$\text{Si}_2\text{C}(\text{g})$	0.010 - 0.050	[3]
	$\text{SiC}_2(\text{g})$	0.080 / 0.020	this work
		0.017 - 0.067	[3]
SiC+TaC+C	$\text{Si}_1(\text{g})$	0.077 / 0.070	this work
	$\text{Si}_2\text{C}(\text{g})$	0.010 / 0.025	this work
	$\text{SiC}_2(\text{g})$	0.079 / 0.077	this work
	$\text{Si}_2(\text{g})$	0.010 / 0.040	this work

For the  $\text{SiC}+\text{C}$  powder mixture, the determined  $k\alpha$  values are in good agreement with the values reported by Rocabois et al. [3]. A noticeable difference is however observed between the two runs. The values in the first run are distinctively higher than those in the second run which means that the pressures are getting smaller in time for a given temperature. The analysis of the remaining powder reveals that the shape of the grains did not change. No sintering is observed but the surface of the grains has a higher carbon content. The diffusion of Si atoms towards the grain surface seems therefore to be a supplementary limiting step in the vaporization process. A calculation of  $k\alpha$  for  $\text{Si}_2(\text{g})$  was not possible. The values are close to the intrinsic limit of the method ( $k\alpha < 10^{-4}$ ) leading to negative calculated values without any physical meaning. By plotting the logarithm of the ionic intensity as a function of  $1/T$  a distinct change of the slope proportional to an enthalpy change is observed at a temperature around 1950°C. Two explanations are possible: a phase transformation of the SiC powder ( $\alpha$  to  $\beta$ ) with different vaporization behavior or the faster vaporization of the species compared to their diffusion through the bulk material. Because the enthalpy of transformation from  $\alpha$  to  $\beta$  is rather small [12] the expected change in slope should also be small which is not the case. Therefore the second explanation is favored. The calculated enthalpies of vaporization from the lower temperature values are in reasonable agreement with the literature data [12].

In the case of the  $\text{SiC}+\text{TaC}+\text{C}$  mixture, the  $k\alpha$  values are slightly higher. The most notable difference is the behavior in time. Even after 2 complete runs, the vaporization coefficients for the different species remain constant or even increase. TaC is known to be non-stoichiometric with a homogeneity range of a few percent. This homogeneity range could have an influence on the vaporization behavior at the SiC-TaC interface due to the capacity of TaC to absorb C up to

saturation. This stabilizes the vaporization and leads to higher growth rates in the PVT process as already observed in the literature [13]. The behavior in the SiC+Ta+C mixture is similar but time retarded due probably to the prior formation of TaC (the Ta foil turned yellow which is the characteristic color for TaC).

### Conclusion

The vaporization behavior of SiC has been studied by high temperature mass spectrometry from 1700°C to 2050°C. The main species identified in the gas phase are Si<sub>1</sub>(g), Si<sub>2</sub>C(g), SiC<sub>2</sub>(g) and Si<sub>2</sub>(g). The vaporization coefficients  $\alpha$  have been determined. The vaporization is kinetically hindered and the theoretical equilibrium pressures are never achieved. The vaporization of SiC is not congruent. The values for  $\alpha$  decrease with time due to the graphitization of the SiC grains. The influence of a tantalum addition has been investigated. The evaporation coefficients are slightly higher and the vaporization is less time dependent. These coefficients can now be included in coupled thermodynamic/mass transport calculations to simulate the SiC bulk growth process by the PVT method for better quantitative agreement.

### Acknowledgements

The authors gratefully acknowledge the support of the French Ministry of Education and Research, the French Ministry of Industry and the European Brite Euram Program (Contract BRPR-CT98-0815- JESICA)

### References

- [1] Yu.M. Tairov and V.F. Tsvetkov, *J. Cryst. Growth*, **43** (1978), p. 209.
- [2] M.Pons, M. Anikin, K. Chourou, J.M. Dedulle, R. Madar, E. Blanquet, A. Pisch, C. Bernard, P. Grosse, C. Faure, G. Basset, and Y. Grange Mater. Science & Engineering B, **56**, (1999), p. 18.
- [3] P. Rocabois, C. Chatillon, C. Bernard, F. Genet, *High Temp. High Press.*, **27-28** (1995/96), p. 25.
- [4] R.N. Ghoshtagore, *Solid-State Electronics* **9** (1966), p. 178.
- [5] R.G. Behrens, G.H. Rinehart in "Characterization of High Temperature Vapors and Gases" Ed. J. Hastie, NBS Special Publication, Gaithersburg FL, (1979), p. 125.
- [6] P. Rocabois, C. Bernard and C. Chatillon, *High Temp. High Press.*, **31** (1999), p. 413.
- [7] P. Rocabois, C. Chatillon and C. Bernard, *Rev. Int. Hautes Temp. Réfr.* **28** (1992/93), p. 37.
- [8] P. Morland, C. Chatillon and P. Rocabois, *High Temp. Sci.* **37** (1997), p. 167.
- [9] C.I. Whitman, *J. Chem. Phys.* **20** (1952), p. 161.
- [10] K. Motzfeld, *J. Phys. Chem.* **59** (1955), p. 139.
- [11] P. Rocabois, C. Chatillon and C. Bernard, *J. Amer. Ceram. Soc.* **79** (1996), p. 1351.
- [12] "Janaf Thermochemical Tables", Ed. M.W. Chase et al. 3rd edition, The American Institute of Physics, New-York (1985)
- [13] E.N. Mokhov, S.E. Demina, M.G. Ramm, S.Yu. Karpov, Yu.N. Makarov, M.S. Ramm A.D. Roenkov, A.S. Segal, Yu.A. Vodakov and A.N. Vorob'ev, *Mater. Science & Engineering B*, **56**, (1999), in press



## Considerations on the Crystal Morphology in the Sublimation Growth of SiC

P. Råback<sup>1</sup>, R. Yakimova<sup>2,3</sup>, M. Syväjärvi<sup>2</sup>, T. Iakimov<sup>3</sup>, R. Nieminen<sup>4</sup>  
and E. Janzén<sup>2</sup>

<sup>1</sup> Center for Scientific Computing, Box 405, FIN-02101 Espoo, Finland

<sup>2</sup> Department of Physics and Measurement Technology, Linköping University,  
SE-581 83 Linköping, Sweden

<sup>3</sup> Okmetic AB, Box 255, SE-17824 Ekerö, Sweden

<sup>4</sup> Laboratory of Physics, Helsinki University of Technology, Box 1100, FIN-02015 Hut, Finland

**Keywords:** Crystal Growth, Instability, Mass Transport, Shape Evolution, Simulation

**Abstract** In this paper the shape evolution of SiC source and seed is studied with simulations. Some basic geometries and temperature distributions are investigated. Also the condition for stable growth is discussed.

### Introduction

The controlling of the crystal shape is important in the sublimation growth of SiC. The shape affects the stress distribution and defect formation in the growing crystal. It may also influence the local growth rate and thereby cause morphological instability.

In this paper we use simulations to study the growth morphology from a macroscopic point of view. The growth profile is assumed to be defined by the mass transport which is obtained by solving the diffusion equation coupled with equilibrium chemistry [1]. Calculations are performed for some elementary geometries with predefined temperature distributions. The seed is colder than the source which generates a flux from the source to the seed. This flux defines the local growth and sublimation rates. In the calculations we assume equilibrium with condensed SiC and carbon at the source and equilibrium with condensed SiC at the seed. In the gas phase only the three main species are considered; SiC<sub>2</sub>, Si<sub>2</sub>C and Si.

### Growth Shape

In an ideal case the source and seed are horizontal and their temperatures are uniform. This makes the problem essentially one-dimensional; thus the crystal grows evenly and the source is uniformly consumed. In practice one-dimensional mass transport may be broken either by geometry or by temperature distribution. If the size of the seed is smaller in radius than the cavity, the growth at the seed edges is favored, as shown in Fig. 1. Large fluxes at the edges is an intrinsic property of the Laplace equation. Even if the size of the source is reduced correspondingly the edge effect remains, and is also seen at the source.

The source and the seed do not have to be horizontal. Large boules have been grown using vertical sources. The smaller the source-to-seed distance the more the growth is favored at the seed edge as shown in Fig. 2. Even growth may be nearly reproduced if the temperature of the source depends linearly on the axial coordinate as depicted in Fig. 3. When the height of the source is reduced growth near the edges increases.

The seed and the source do not need to be planar. Fig. 4 shows the mass flux for cylindrical and spherical seeds. In all the cases the horizontal source is at constant temperature. The

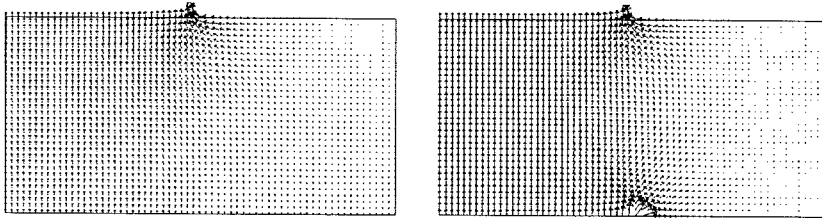


**Fig.1.** Mass flux resulting from a smaller seed at the top. On the left the source at the bottom is large and in the right it is of the same size with the seed.

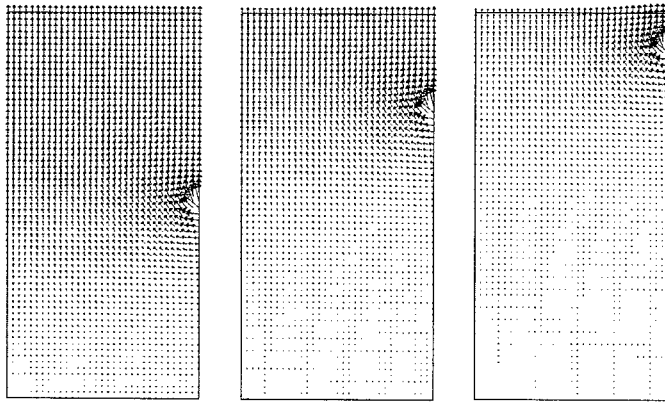


**Fig.2.** Mass flux in three different cases with varying source height ( $R$ ,  $1.5R$  and  $1.8R$ ). In each case the seed at the top and the source on the right have uniform temperatures.

growth rate over the seed surface varies with position and therefore the shape of the crystal changes with time. If the seed and source have uniform temperatures only some specific shapes will be maintained. The axial and spherical symmetries have this property. The latter geometry is, however, not practical to implement.

Sometimes it may be even desirable that the shape is not maintained. For example, the crystal diameter may be increased by a convex growth front [2]. Fig. 5 presents the flux arising from linear temperature distributions for the seed. If the temperature is lower at the center the growth front will eventually turn convex and correspondingly, if the temperature is lower at the edge the growth front will become concave.

The calculations show that the ideal one-dimensional growth may be broken either by temperature distribution or by geometry. However, for each geometry there exists a temperature profile that leads to even growth. For example, the edge effect on a small seed may be canceled by a carefully tuned temperature distribution.

Consider the case with a small seed. If the temperature difference is constant the growth rate has the maximum value at the seed edge and decays closely exponentially to the origin. This suggests that a uniform growth rate might result from an exponential temperature profile

$$T_c(r) = T_s - \Delta T_0 \left( 1 + a \frac{e^{br/R} - 1}{e^b - 1} \right). \quad (1)$$

The dimensionless parameters  $a \approx 0.4$  and  $b \approx 3.0$  were found with manual iterations. The original and transformed fluxes are shown in Fig. 6. The delicate tuning of the temperature profile is very difficult. This is a strong argument for simple, one-dimensional designs.

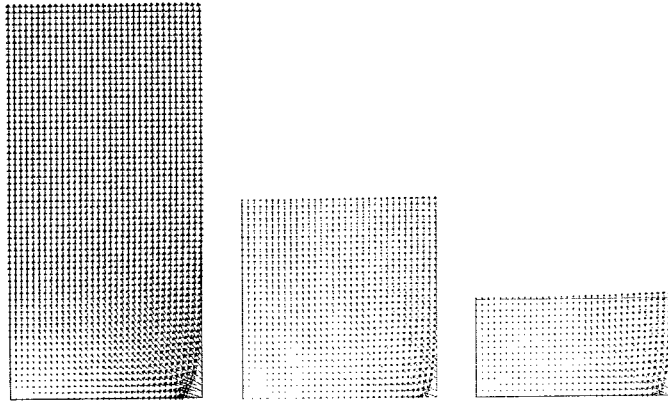


**Fig.3.** Mass flux in three different cases with varying source height ( $2R$ ,  $R$  and  $R/2$ ). In each case the seed at the top has a constant temperature and the source on the right has a linear temperature distribution.

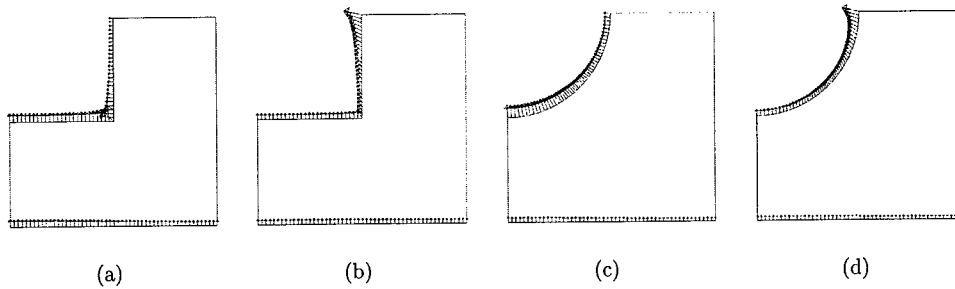


**Fig.4.** Mass flux at the active surfaces with cylindrical and spherical seeds. In (a) and (c) the temperature over the seed is constant and in (b) and (d) it depends linearly on  $z$ .

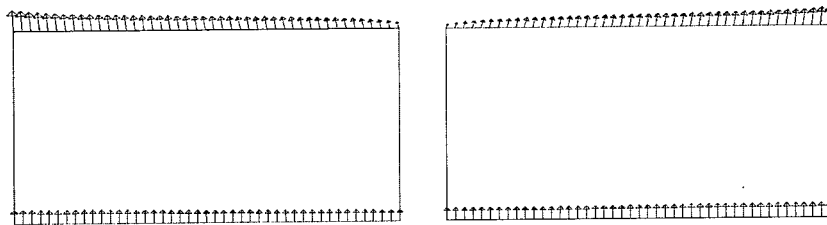


**Fig.5.** Mass flux with linear temperature distributions. The temperature of the source is constant and the temperature difference is  $\Delta T_0(2 + r/R)$  on the left and  $\Delta T_0(3 - r/R)$  on the right.

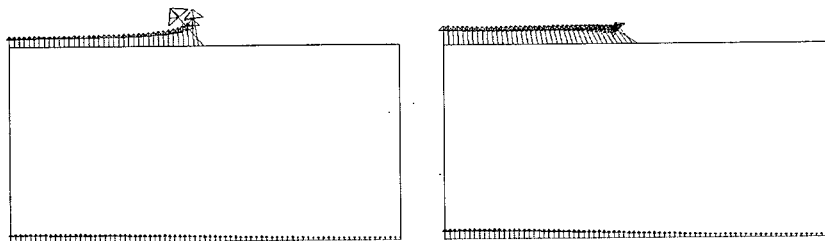


**Fig.6.** Mass flux at analytical temperature distributions. On the left the temperature difference is constant and on the right it is obtained from  $\Delta T_0(1 + a(e^{br/R} - 1)/(e^b - 1))$ , where  $a = 0.4$  and  $b = 3.0$ .

## Growth Stability

The previous examples show the mass fluxes resulting from continuous temperature profiles and reactive surfaces. Fluctuations in temperature or shape may, however, lead to growth instability.

Using simple analytical formulas [3] we may speculate what happens when a step is imposed on the crystal surface. In order to have stable growth, the trailing part must catch up with the step. This happens if the temperature gradient inside the seed is larger than the one between the seed and source. This leads to a condition for the thermal conductivity of the seed  $\kappa_c$ . The condition for stable sublimation is that the temperature gradient within the source  $\kappa_s$  is smaller than the one between the source and seed. Combining these requirements we obtain

$$\kappa_c < \frac{4\epsilon}{2-\epsilon} \sigma_{SB} T^3 L < \kappa_s, \quad (2)$$

where  $\epsilon$  is the emissivity and  $L$  the source-to-seed distance. This rough condition tells that in the one-dimensional case stable growth and stable sublimation are not simultaneously possible because always  $\kappa_s \leq \kappa_c$ . Usually the condition for stable sublimation is much more difficult to meet which may be seen in the degradation of the source material. We were able to reproduce the instability of the source using a novel level-set method. In the simulations numerical fluctuations was the seed for positive feedback resulting to holes and islands being created in the source.

## Conclusions

The simulations could explain some experimental observations relating temperature profiles, size and location of seed and source as well as their shapes. There are however some simplifications that limit the accuracy of the model. The walls are assumed to be inert which is an extreme case. In reality this is not quite true because the graphite may act as a carbon source or amorphous SiC may start to grow on the walls. Also the surface diffusion and the growth mechanism may have a damping effect on the growth shape. Thus, the growth shape is not as pronounced as suggested by the calculations.

## References

- [1] P. Råback, R. Nieminen, R. Yakimova, M. Tuominen, and E. Janzén, *Mat.Sci.Forum*, 264–268 (1998), p. 65.
- [2] M. Anikin, M. Pons, K. Chourou, O. Chaix, J. M. Bluet, V. Lauer, and R. Madar, *Mat.Sci.Forum*, 264–268 (1998), p. 45.
- [3] P. Råback, R. Yakimova, M. Syväjärvi, R. Nieminen, and E. Janzén, *Mat.Sci.Eng.*, B 61–62 (1999), p. 89.

Corresponding author: Peter Råback, E-mail: raback@csc.fi, Fax: +358 9 457 2302

## Shape of SiC Bulk Single Crystal Grown by Sublimation

Shin-ichi Nishizawa<sup>1</sup>, Yasuo Kitou<sup>2</sup>, Wook Bahng<sup>1</sup>, Naoki Oyanagi<sup>2</sup>,  
Muhammad Nasir Khan<sup>1</sup> and Kazuo Arai<sup>1</sup>

<sup>1</sup> Electrotechnical Laboratory, UPR Ultra-Low-Loss Power Device Technology Research Body,  
1-1-4 Umezono, Tsukuba, Ibaraki, 305-8568, Japan

<sup>2</sup> Advanced Power Devices Laboratory, R&D Association of Future Electron Device, UPR Ultra-  
Low-Loss Power Device Technology Research Body, c/o Electrotechnical Laboratory,  
1-1-4 Umezono, Tsukuba, Ibaraki, 305-8568, Japan

**Keywords:** Crystal Shape, Numerical Simulation, Sublimation Growth, Temperature Gradient

### Abstract

Numerical simulation of sublimation SiC bulk single crystal growth was performed. Electromagnetic and temperature fields in a growth furnace were analyzed numerically. The relation between grown crystal shape and temperature distribution in a growth cavity was discussed. It is pointed out that the crystal shape has a close relationship with temperature distribution. By modifying the crucible design and temperature distribution in a growth cavity, it is possible to enhance the enlargement of grown crystal, and also possible to keep grown surface flat.

### Introduction

In order to realize the power devices with SiC, it is necessary to develop a large and high quality SiC bulk crystal. With respect to the crystal enlargement in a diameter, Koga, et.al. reported the degree of extension in the a-axis of the grown crystal[1]. Madar, et.al. discussed it with taking account of the nucleation steps[2]. In order to grow high quality crystal, it was suggested that grown surface should be kept flat[3]. It was also suggested that temperature distribution in a grown crystal affects its quality[4,5]. Furthermore, sublimation growth is time-dependent and closed process. So, it is important to understand the phenomena, which occurred in a crucible. From these points of view, a lot of works have done by numerical simulation[6-9]. However, there are still problems that must be solved. In this paper, the temperature distribution in a growth cavity (space between crystal and source) was analyzed numerically and compared with experiment. The correlation between crystal shape and temperature distribution in a growth cavity was obtained. It is pointed out that it is possible to control the grown crystal shape by modifying the temperature distribution in a growth cavity.

### Numerical Simulation

The configuration of numerical modeling was based on the conventional RF induction-heating furnace that we used in our experiments. Experimental conditions were described in ref [10-13]. With taking account of the grown crystal shape during experiments, electromagnetic and thermals field were analyzed for each time step by finite element method. It means that temperature distribution in a growth cavity was analyzed with taking account of grown crystal shape at each time step. Temperature at the top of graphite crucible was monitored as correlation parameter

between simulation and experiment. Since convective heat and mass transfer could be neglected in our experimental conditions, the equation for momentum transfer was not considered. Numerical procedures were described in detail elsewhere[7].

## Results and Discussions

### Heat transfer in a growth cavity

With respect to the heat transfer in a growth cavity which is a gas region in a crucible, (a)both radiation and conduction transfer, (b)radiation transfer without conduction, and (c)conduction transfer without radiation, were considered. Temperature distribution of case (a) is similar to that of case (b), and differs from case (c). It is confirmed that radiation transfer is dominant in a growth cavity. But conductive transfer still has a weak effect on the temperature distribution. Then both radiation and conduction transfer were considered in the following discussions.

### Shape of Grown Crystal

Fig.1 shows the numerical results of temperature distribution in a growth cavity with conventional crucible at each time step. During the experiment, the temperature at the top of graphite crucible, which was measured by pyrometer, was kept constant. But the temperature distribution in a growth cavity changed as crystal grew. In the experiment, single crystal enlarged rapidly

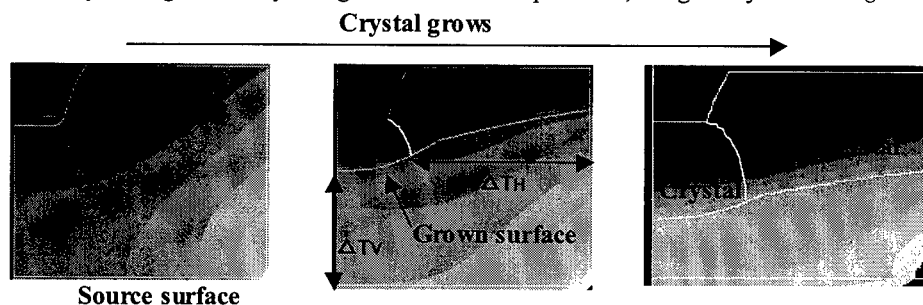


Fig.1 Numerical results of temperature distribution in a growth cavity with conventional crucible at each time step

in diameter at the initial stage. This enlargement, however, slacked as crystal grew. Furthermore, a crystal growth rate decreased as crystal grew in experiments. Fig.2 shows a numerical results of the vertical temperature difference ( $\Delta T_v$ ) between grown surface and source surface at the center of crucible, and horizontal temperature difference ( $\Delta T_h$ ) between the rim of single crystal region on the grown surface and the crucible at the same vertical position, during the growth. There is a correlation between a crystal diameter and the temperature differences in a cavity. As

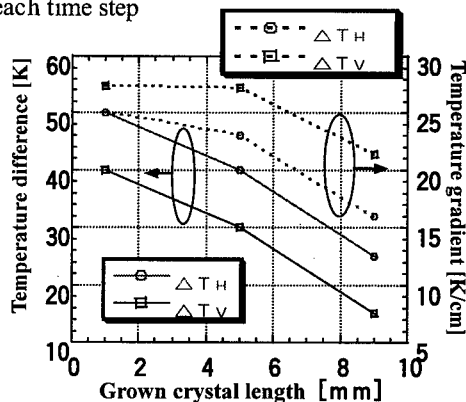


Fig.2 Numerical results of vertical and horizontal temperature differences in a growth cavity

crystal grew, horizontal temperature difference decreased, and enlargement slacked gradually in experiments. For the enlargement, it is necessary to keep a large temperature difference and a large temperature gradient parallel to a-axis. Furthermore, as crystal grew, the vertical temperature difference decreased. This is the reason for decreasing the growth rate in experiment.

#### *Design for rapid enlargement*

Bhang, et.al. proposed to use a taper-lid crucible to achieve a rapid enlargement. They discussed the suppression of re-sublimation of grown crystal to backwards by taper-lid. Fig.3 shows the temperature distribution in a growth cavity with taper-lid crucible, and Table 1 shows the comparison of temperature difference between taper-lid and convectional crucibles. From these results, it was shown that taper-lid not only suppresses re-sublimation, but also makes large horizontal temperature difference, and enhances the growth in diameter. These effects make rapid enlargement possible.

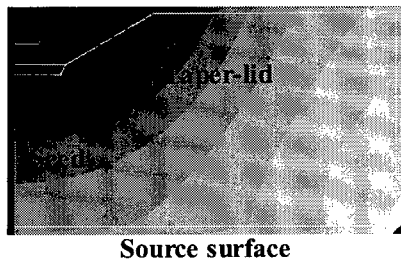


Fig.3 Temperature distribution in a growth cavity with taper-lid crucible

Table 1 Comparison of temperature difference for conventional and taper-lid crucible

	$\Delta TH$	$\Delta TV$
Conventional crucible	30K	50K
Taper-lid crucible	60K	55K

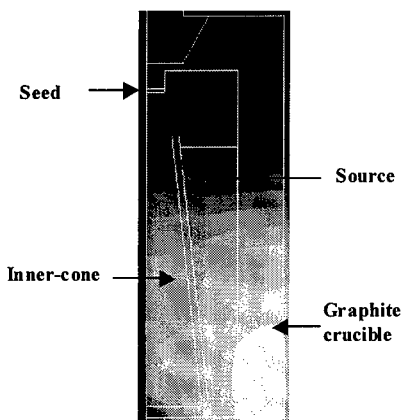


Fig.4 Temperature distribution of inner-cone crucible

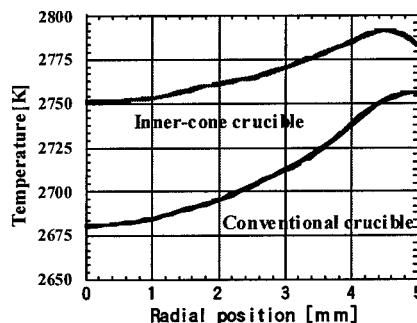


Fig.5 Temperature distribution on the seed surface of both conventional and inner-cone crucible

### *Design for flat grown surface*

Fig.4 shows the temperature distribution with inner-cone crucible, and Fig.5 shows the temperature distribution on the seed surface of both conventional and inner-cone crucible. The temperature uniformity of inner-cone crucible was much better than that of conventional crucible. Then it might be possible to get flat grown surface with inner-cone crucible. This effect was confirmed by the experiment[12,13].

### **Conclusion**

Temperature distribution in a growth cavity was analyzed numerically and compared with experiment. The correlation between grown crystal shape and temperature distribution in a growth cavity was obtained. It is concluded that it is possible to control the grown crystal shape by modifying the temperature distribution in a growth cavity.

### **Acknowledgement**

This work was performed under the management of FED as a part of the MITI NSS Program (Ultra-Low Loss Power Device Technology Project) supported by NEDO and also supported by NEDO as Short Term International Joint Research on the Prevention of Global Warming. The author, S.N, thanks Dr.M.Pons for his help on numerical simulation.

### **References**

- 1)K.Koga, Y.Ueda, T.Nakata, T.Yamaguchi and T.Niina, Shinku, 30,(1987)886. (in Japanese)
- 2)R.Madar, M.Anikin, K.Chourou, L.Labeau, M.Pons, E.Blanquet, J.M.Dedulle, C.Bernard, S.Milita and J.Baruchel, Diamond and Related Materials, 6,(1997)1249.
- 3)M.Anikin, K.Chourou, M.Pons, J.M.Bluet, R.Madar, P.Grosse, C.Faure, G.Basset and Y.Grange, Mat.Sci.&Eng., B61(1999)73.
- 4)M.S.Ramm, E.N.Mokhov, S.E.Demina, M.G.Ramm, A.D.Roenkov, Yu.A.Vodakov, A.S.Segal, A.N.Vorob'ev, S.Yu.Karpov, A.V.Kulik and Yu.N.Makarov, Mat.Sci.&Eng.,B46(1997)107.
- 5)M.Pons, E.Blanquet, J.M.Dedulle, R.Madar and C.Bernard, Mat.Sci.&Eng.,B46(1997)308.
- 6)D.Hofmann, M.Heinze, A.Winnacker, F.Durst, L.Kadinski, P.Kaufmann, Y.Makarov and M.Schafer, J.Crystal Growth, 146(1995)214.
- 7)M.Pons, E.Blanquet, J.M.Dedulle, I.Garcon, R.Madar and C.Bernard, J.Electrochem.Soc., 143,(1996)3723.
- 8)D.Hofmann, R.Eckstein, M.Kolbl, Y.Makarov, St.G.Muller, E.Schmitt, A.Winnacker, R.Rupp, R.Stein and J.Volkl, J.Crystal Growth, 174(1997)669.
- 9)M.Selder, K.Kadinski, F.Durst, T.Straubinger and D.Hofmann, Mat.Sci.&Eng.,B46(1997)93.
- 10)W.Bahng, Y.Kitou, S.Nishizawa, K.Arai and S.Nishino, in this conference, p. 103
- 11)H.Yamaguchi, S.Nishizawa, W.Bhang, N.Oyanagi, T.Kato, S.Yoshida, K.Arai, Y.Machitani and T.Kikuchi, in this conference, p. 461
- 12)N.Oyanagi, S.Nishizawa, T.Kato, H.Yamaguchi and K.Arai, in this conference, p. 75
- 13)T.Kato, N.Oyanagi, H.Yamaguchi, Y.Takano, S.Nishizawa, K.Arai, in this conference, p. 457



## Enlargement of SiC Single Crystal: Enhancement of Lateral Growth using Tapered Graphite Lid

Wook Bahng<sup>1,2</sup>, Yasuo Kitou<sup>1</sup>, Shin-ichi Nishizawa<sup>2</sup>, Hirotaka Yamaguchi<sup>2</sup>,  
Muhammad Nasir Khan<sup>2</sup>, Naoki Oyanagi<sup>1</sup>, Kazuo Arai<sup>2</sup>  
and Shigehiro Nishino<sup>3</sup>

<sup>1</sup> R&D Association for Future Electron Devices (FED), UPR Ultra-Low-Loss Power Device  
Technology Research Body, 1-1-4 Umezono, Tsukuba, Ibaraki, 305-8568, Japan

<sup>2</sup> UPR, Electrotechnical Laboratory, 1-1-4 Umezono, Tsukuba, Ibaraki, 305-8568, Japan

<sup>3</sup> UPR, Kyoto Institute of Technology, Matsugasaki, Sakyo-ku, Kyoto, 606-8585, Japan

**Keywords:** Cone-Shaped Platform, Lateral Growth, Polycrystals, PVT Growth, Rapid Enlargement, Single Crystal, Taper Angle

**Abstract.** We investigated the rapid enlargement of SiC single crystal during physical vapor transport growth by enhancing the lateral growth. The degrees of enlargement of the single crystals grown on the newly developed graphite lid were larger than those of crystals grown on the conventional one. Using a cone-shaped platform, the polycrystals grown around the single crystal could assist the lateral growth of single crystal. There was no significant difference between the central region and the enlarged region as far as the micropipe density was considered. The dependence of the broadening angle ( $\beta$ ) of the single crystal on the taper angle ( $\theta$ ) of the cone-shaped platform was also investigated and an optimum angle at a given growth condition was found.

### Introduction

Recent research on silicon carbide (SiC) single crystal growth has shown great improvement, especially, on the reduction of micropipe density [1]. However, the size is insufficient and it is difficult to enlarge the single crystal until now. Rapid enlargement of the single crystal is an important technology for the realization of commercial SiC-based electronic devices. Physical vapor transport (PVT) growth systems using rf-induction heating have a radial temperature gradient as well as axial one. This radial temperature gradient is a driving force for enlargement of single crystal. Attempts to enlarge the diameter of single crystal ingot by controlling the lateral temperature gradient had been reported [2]. In PVT growth of SiC single crystals, a crucible larger than the seed crystal is used in order to enlarge the single crystal ingots. Single crystal grows in conjunction with polycrystals, started simultaneously when a larger crucible than the seed crystal diameter is used. Therefore, it is necessary to control the growth rates of both the single crystal and the polycrystal for enlargement of the single crystal. Tairov [3] reported that an optimum ratio of the growth rate of single crystal ( $V_s$ ) and that of polycrystal ( $V_p$ ) is 0.95~0.98 ( $V_p/V_s$ ). Another method is making a platform, which is slightly higher than the graphite lid surface [4]. In ref. [4], it was suggested that the single crystal could be enlarged due to the rotation and the combination of these polycrystals into single crystal.

In this report, rapid enlargement of the single crystal using the modified graphite lid has been investigated. The shape of the platform was modified to a truncated cone, expecting that the growth

of the single crystal could be assisted by polycrystals. Various taper angles of the cone were examined in order to verify the influence on the enlargement of single crystal.

### Experiment

SiC single crystals were grown by the PVT method. A graphite crucible was heated by rf-induction. The temperatures of the top and the bottom side of graphite crucible were measured by an optical pyrometer. The typical growth temperature of the seed was 2200°C, and the temperature difference ( $T_{\text{bottom}} - T_{\text{top}}$ ) was varied in the range of 50~100°C. The typical growth pressure was 10 torr. The temperature of the crucible and the pressure of the chamber were controlled automatically during growth. 6H-SiC crystals grown by the PVT method as well as the Acheson method were used as seed crystals.

We have modified the structure of the platform on the graphite lid surface. The graphite lid that has been used generally and a newly modified one were schematically illustrated in Fig. 1 (a) and (b), respectively. The newly developed graphite lid has a cone-shaped platform whose tip was truncated for seed attachment. Its characteristic is that the wall of the platform has an inclined angle with respect to the surface of the graphite lid. Various inclined angles *i.e.*, taper angles ( $\theta$ ) were examined in order to clarify the dependence of the broadening angle on it. The grown crystals were sliced perpendicular to the growth direction for KOH etching characterization and parallel for observation of the enlargement of the crystal. A polarizing optical microscope was used for observation of defects and shapes of the grown crystals.

### Results and Discussion

Lateral growth of the single crystal is restricted by polycrystals grown around the single crystal when crystals were grown using a graphite lid without a platform. In the case of the conventional platform, the height of the platform should be determined considering the parameters related to specific growth systems as well as the temperature profile in the crucible. Using a high platform is advantageous because the single crystal grown on a seed rarely collide with the polycrystal, which has been considered a cause of the stress in the grown ingot [5]. In the sublimation method, SiC is re-crystallized in the region of relatively low temperature, while sublimed in the high temperature region. The growth and the sublimation of

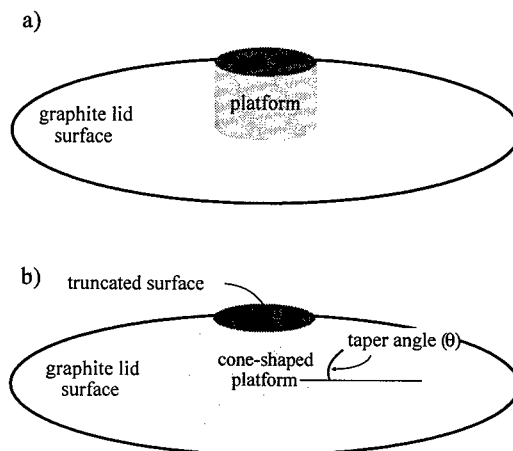


Fig. 1 Schematic diagrams of the graphite lids for the SiC single crystal growth with (a) a conventional platform and (b) a modified one.

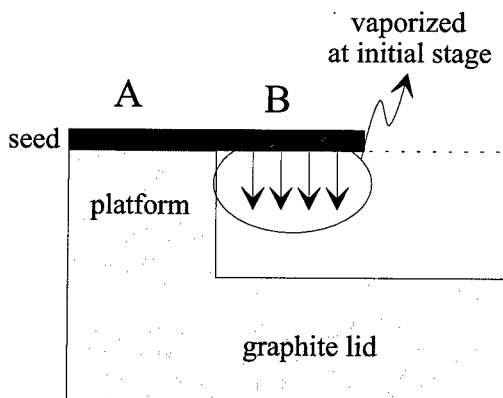


Fig. 2 Schematic diagram of sublimation process of seed at initial stage.

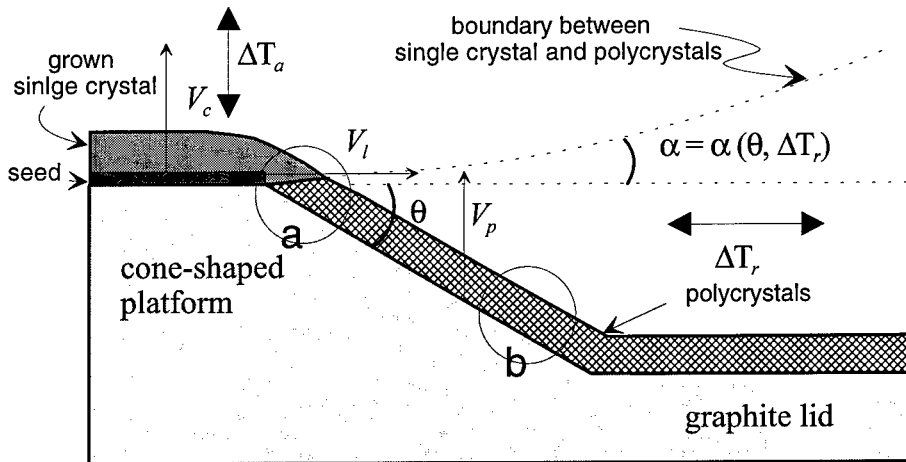


Fig. 3 Schematic mechanism of crystal growth on the cone-shaped platform. The  $\alpha$  is an angle of the single crystal's boundary with respect to basal plane of SiC which is the growth plane of the present work.

SiC occur at the same time even in the seed crystal. The temperature of the seed is higher than that of the lid. Therefore, the side edge of seed is likely to sublime. The ultimate situation is illustrated in Fig. 2. The size of the seed crystal is larger than that of the platform. The main difference of the region B from the region A is the existence of gap between the seed and the graphite lid. The region B is easier to vaporize than to re-crystallize. As a result, the region B is totally eliminated at the initial growth stage. It was also confirmed experimentally using in-situ X-ray topography [6]. Therefore, the difficulties for enlarging the single crystal in diameter during growth still remained because the temperature of the single crystal is higher than that of the polycrystals. It implies that it needs an additional parameter besides the radial temperature gradient in order to realize the rapid enlargement of the single crystal.

Both the axial and the lateral growth of the single crystal occur at the same time as that of polycrystals [Fig. 3]. The growth rate along the axial direction is the growth rate of the basal plane ( $V_c$ ) at a given axial temperature gradient ( $\Delta T_a$ ). The growth rates of polycrystals are also depending on  $\Delta T_a$ , but slightly different with  $V_c$  because the growth is mixed in the crystallographic planes. The growth rates of polycrystals are almost the same all around the graphite lid. The lateral growth rate ( $V_l$ ) of the single crystal mainly depends on the radial temperature gradient ( $\Delta T_r$ ), and its maximum might be a growth rate of the planes perpendicular to the basal plane, *i. e.* (1100)

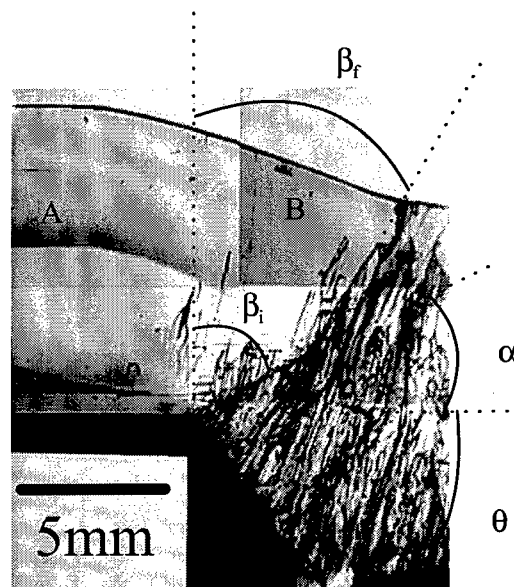


Fig. 4 A cross section of the crystal grown on modified platform.

and/or  $(1\bar{1}20)$ , at a given  $\Delta T_r$ . The real lateral growth rate will have a value lower than the growth rate of  $(1\bar{1}00)$  or  $(11\bar{2}0)$  planes, because the growth is restricted by the polycrystals. The polycrystals grown on a tapered plane would form a same shape as that of the initial platform. At the initial stage, the polycrystals in the region near the seed crystal edges (marked a in Fig. 3) grow rapidly up to the seed height and then act as a platform for the growing single crystal. While the polycrystals grown in the lower region (marked b in Fig. 3) keep almost the same initial cone shape. Consequently, the enlargement of the single crystal could be continued by the assist of polycrystals. For the extreme case of  $\Delta T_a \sim 0$ ,  $\Delta T_r > 0$ , more rapid enlargement of the single crystal can be expected. The optimum taper angle ( $\theta$ ) would be  $\tan\theta = V_l/V_p$  for  $\alpha = 0$ . More precise analysis and control of the parameters such as  $\Delta T_a$ ,  $\Delta T_r$ , and the flux of each vapor species are needed in order to grow ingots with low  $\alpha$ .

A typical cross sectional photograph of a crystal grown on a graphite lid with a cone-shaped platform is shown in Fig. 4. It was sliced parallel to the growth direction and the sliced plane is a  $(11\bar{2}0)$  plane. The dark line lying perpendicular to the growth direction is the boundary between the first and second growth run possibly due to the high incorporation of impurities such as N, Al, and B at the initial stage of the second growth run. It clearly shows that the single crystal grown on cone-shaped platform enlarged rapidly. The angle  $\beta$  ( $=90^\circ - \alpha$ ) is considered as a degree of single crystal enlargement or broadening. The initial broadening angle ( $\beta_i$ ) was larger than the final angle ( $\beta_f$ ). This is due to the decrease of the lateral temperature gradient as the crystal growth proceeds [7]. In addition, we could not find any distinguishable difference between the region A and B through the KOH etching. The effect of the taper angle on the enlargement of ingots was also investigated. In our experimental setup, the maximum broadening angles were achieved with taper angles in the range of 30 to 50° [8].

## Conclusion

Using a cone-shaped platform, the growth of polycrystals was controlled gradually, which serves as a platform for single crystal enlargement. Consequently, the lateral growth of the single crystal, which was driven by the radial temperature gradient, was much improved. We have also confirmed that the degree of enlargement was influenced by the taper angle. The enlargement of SiC single crystals could be improved and easily controlled by a tapered platform.

## Acknowledgement

This work was performed under the management of FED as a part of the MITI NSS Program (R&D of Ultra-Low Loss Power Device Technologies) supported by NEDO.

## References

- [1] N. Schulze, D. L. Barrett and G. Pensl, *Appl. Phys. Lett.*, **72** (1998) 1632.
- [2] A. R. Powell, S. Wang, G. Fechko and G. R. Brandes, *Mater. Sci. Forum* **264-268** (1998), p.13.
- [3] Yu. M. Tairov, *Mater. Sci. Eng.* **B29** (1995) 83.
- [4] S. Milita, R. Madar, J. Bruchel and A. Mazuelas, *Mater. Sci. Forum* **264-268** (1998), p.29.
- [5] A. S. Bakin, S. I. Dorozhkin, A. O. Lebedev, B. A. Kirillov, A. A. Ivanov and Yu. M. Tairov, *J. Cryst. Growth*, **198/199** (1999) 1015.
- [6] H. Yamaguchi, N. Oyanagi, T. Kato, Y. Takano, S. Nishizawa, W. Bahng, S. Yoshida and K. Arai, this conference, p. 461
- [7] S. Nishizawa, Y. Kitou, W. Bahng, N. Oyanagi, M. Nasir Khan and K. Arai, this conference, p. 99
- [8] W. Bahng, Y. Kitou, S. Nishizawa, H. Yamaguchi, M. Nasir Khan, N. Oyanagi, K. Arai and S. Nishino, this conference, p. 103

Corresponding author (Wook Bahng): Fax. +81 (298) 54-3397, e-mail: bahng@etl.go.jp

## Top-seeded Solution Growth of Bulk SiC: Search for Fast Growth Regimes

B.M. Epelbaum, D.Hofmann, M. Müller and A. Winnacker

Department of Materials Science 6, University of Erlangen-Nürnberg, Martenstr. 7,  
DE-91058 Erlangen, Germany

**Keywords:** Bulk Crystals, Silicon Carbide, Solution Growth, Top-seeded Growth Method

**Abstract.** Top-seeded solution growth of bulk SiC has been accomplished in an argon atmosphere at 100-120 bar with the use of pure silicon melt solvent. Supersaturation in the growth system was shown to be dependent not only on temperature gradient but on the kinetics of the heterogeneous reaction between solid carbon and silicon melt as well. Thick epitaxial layers and boules 20-25 mm in diameter and up to 20 mm in length were grown using different container arrangements. Growth stability and material quality are discussed in context of growth conditions.

### Introduction

Liquid-phase epitaxy (LPE) of SiC yields high quality crystalline material, sometimes even superior to one produced by physical vapour transport (PVT) growth [1], but only a little work has been done so far on the growth of bulk SiC crystals from solutions. We report the first results on the adaptation of top-seeded solution growth (TSSG) for bulk SiC growth. The emphasis of this work was the search on rapid growth regimes.

### Principle of Reaction TSSG

The scheme of TSSG as applied in our research for SiC growth is shown in Fig.1. Silicon melt is held in the high-purity graphite crucible at temperature 1900-2400°C under the overpressure of 100-120 bar of argon, that is sufficient for effective suppression of melt evaporation [2]. Thick-walled crucible dissolves partially and graphite reacts with the Si melt until the reaction-formed SiC barrier makes the process very slow (reaction choking). Once the surface of the graphite becomes covered with SiC, it can be considered as a nutrient. SiC seed is fixed on a holder at the top of the melt. Since the crucible bottom is placed in a hotter region, solution saturated in the hot 'feed end' becomes supersaturated in the cooler 'growth end' enabling seeded crystal growth.

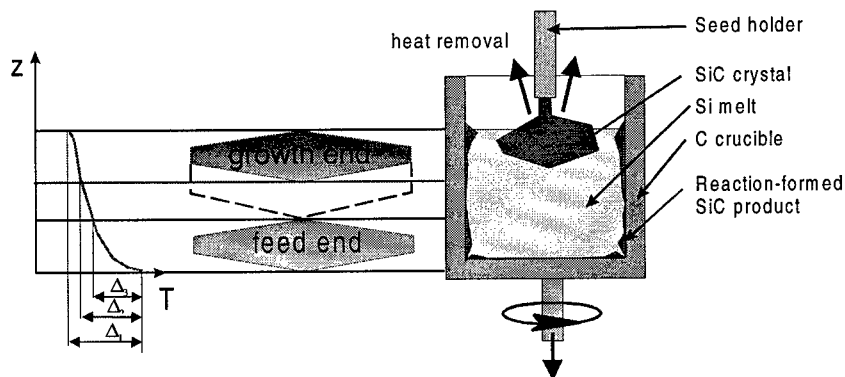


Fig. 1 Schematic of Reaction TSSG

The distinguishing feature of the TSSG method here, is that the only suitable crucible material (carbon) is highly reactive to the silicon melt solute and only due to the reaction choking the integrity of the crucible unit can be kept at an acceptable level. Thus, an acting supersaturation is produced not only by temperature gradients but it is also affected by the complicated kinetics of heterogeneous reaction between liquid silicon and solid carbon. The impact of this feature on the growth process is rather distinct. Following the classification of Elwell and Scheel [3], we would like to introduce therefore the applied method as *Reaction TSSG* in order to stress the dual origin of supersaturation in our system.

### Formation and dissolution of SiC nutrient

At the feed end, silicon melt saturation with carbon includes two conceptually independent processes: heterogeneous reaction of formation of SiC  $\text{Si}_{\text{melt}} + \text{C}_{\text{solid}} = \text{SiC}_{\text{solid}}$  (1) and dissolution of  $\text{SiC}_{\text{solid}}$  in the silicon melt. Let us first consider the case of dissolution of a large flat SiC source (represents an idealised hot crucible wall) in terms of boundary layer theory. The situation is shown schematically in Fig. 2. As it is typical of liquid metals, the thermal diffusivity  $K/\rho C_p$  for liquid silicon is much higher than the mass diffusivity  $D$ . This is manifested in four-order disparity of Schmidt and Prandtl numbers (about 50 and 0.05 correspondingly, see for details [2]). The thermal boundary layer is sufficiently thicker than the mass boundary layer, leaving an undersaturated region near the hot nutrient crystal even if the hot surface itself is in equilibrium. By this means dissolution proceeds smoothly and it is enhanced in direct proportion to the separation between the mass transfer profile and the temperature profile, since this is a measure of undersaturation. Thus, dissolution of a bulk SiC nutrient is dependent on melt dynamics and can be readily controlled by forced melt convection.

The case at the  $\text{C}_{\text{solid}} - \text{Si}_{\text{melt}}$  interface (true hot crucible wall) differs from that of at  $\text{SiC}_{\text{solid}} - \text{Si}_{\text{melt}}$  because of the complex nature of reaction (1) in which no continuous product layer is generally formed. There are two conflicting interpretations for the mechanism of this reaction presented in the existing literature. Most of researches [4,5] reported on continuous product layer between carbon and silicon and diffusion-limited growth mechanism. The other mechanism is 'solution-precipitation' as proposed in [6] as well as in [7]. Detailed discussion on this problem is out of the scope of our paper, but it should be particularly emphasised that our observations support definitely the second model in which the reaction product splits from graphite surface leading to the interface limited reaction directly between silicon and carbon. We found an additional SiC layer composed by rounded particles about 100 nm in size in between unreacted graphite and faceted recrystallized layer. Hence in the first stage the reaction product is a very fine particulate SiC. Carbon solubility  $C(r)$  at small particles is enhanced according Gibbs-Thomson equation:

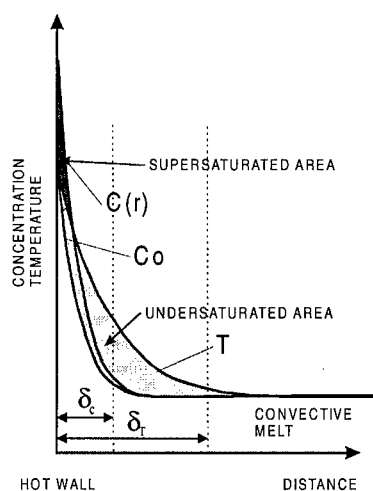


Fig.2 Schematic diagram illustrating the formation of supersaturated area in the reaction zone near the crucible hot wall

$$C(r) = C^0 \exp\left(\frac{2\gamma \cdot V_m}{rRT}\right)$$

where  $C_0$  is the equilibrium solubility for a flat interface,  $\gamma$  is the interfacial energy,  $V_m$  is the molar volume of SiC and  $r$  is the particle radius.

This brings supersaturated region into existence and causes quick growth of relatively large faceted crystals in the adjacent melt layer, see Fig.2. Further development of the process depends strongly on the melt flow pattern near the reaction surface. When it favours the accumulation of precipitated particles on the reaction surface, the reaction process slows down because of lack of silicon and finally becomes diffusion-controlled. Otherwise, when melt flow carries the material away from the reaction surface, some remote sinks are produced. This situation brings about quick dissolution of the graphite. In both cases dissolution is not regular, it is accompanied by fluctuations in carbon concentration and formation of loose (parasitic) SiC sediment. All this must be given proper weight in designing the container unit for solution growth of SiC.

### Crystal growth experiments

Crystal growth experiments were directed toward exploring of TSSG method as one of the most feasible for the active control of supersaturation. Saturation control was achieved by means of forced melt convection inside of the growth container of particular shape including mobile and stationary parts. The design objective of the container unit was to arrange three definite zones: a main one of uniform temperature and carbon concentration around the seed crystal (1) should be located inside an auxiliary growth zone (2), which include crucible walls overgrown with SiC. A feeding zone (3) with dissolving graphite surfaces was separated from zone 2 with buffering SiC baffle in order to suppress concentration fluctuations caused by irregular dissolution of graphite nutrient. Current structure of the furnace system allows crucible downwards lowering at closely controllable rates in the range of 1-100 mm/day and crucible rotation up to 200 rpm.

Two main types of arrangement for different seed shape and orientation were designed and tested: the first one was intended for a flat vicinal (0001) substrates 30-35 mm in diameter and the second one for a rod-like 3x3 mm<sup>2</sup> seeds. In both cases 6H PVT grown material was used for seed preparation. In the first arrangement smooth single crystalline layers 20-60  $\mu$ m in thickness were grown at growth rate 10-15  $\mu$ m/h. Micropipes in PVT seed were completely overgrown. Attempts to produce layers thicker than 100  $\mu$ m were mainly unsuccessful because of the development of characteristic growth instability. After coalescence of growth steps, the surface became covered with hexagonal columns and monocrystalline growth was disturbed after 100-150  $\mu$ m of growth.

In the second arrangement bulk boules 20-25 mm in diameter and up to 20 mm in length have been grown at growth rates 5-15 mm/day, Fig.3. Such a high pulling rates were achievable only for pulling direction taken within (0001) plane (mainly seeds oriented along <1100> directions were used). The growth interface was composed by numerous faces those build re-entrant edges. It is shown experimentally that graphite dissolution rate can be easily varied in a wide range up to 0.5 kg/m<sup>2</sup>h. This ensures effective carbon transport to crystal growing at linear rates of the same order of magnitude as during PVT growth.

All fast grown samples had a number of flat silicon inclusions. Many of inclusions were of definite geometric shapes. Monocrystalline growth was preserved within first 3-5 mm from the seed, the last part of a boule was always polycrystalline. Distribution of the inclusions was very nonuniform: peripheral part was almost free of inclusions, whereas the central area was highly defective.

Characterisation of grown layers and bulk samples were made with the use of optical microscopy and X-ray diffractometry. Crystals grown at temperatures higher than 1900 C belong to 6H polytype only. No micropipes were observed in solution-grown material. Layer quality as revealed by rocking curves method is rather high (FWHM for the (0006) reflection is about 30 arcsec). Crystallinity of

the inclusion-free parts separated from the bottom (polycrystalline) part of bulk samples was of the same order. Upper (monocrystalline) part had a mosaic structure.

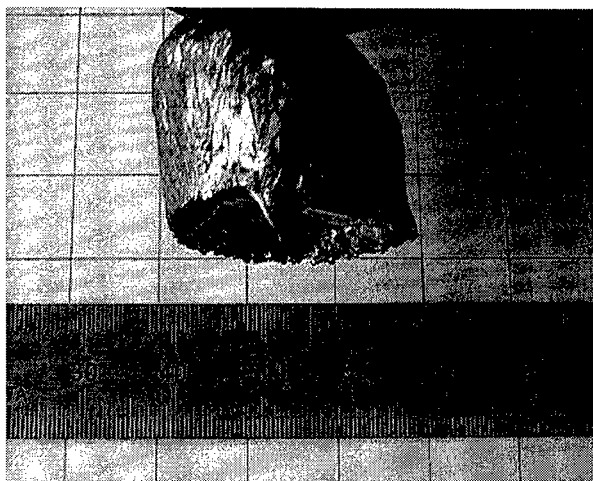


Fig.3 As-grown SiC boule

#### General remarks

High-pressure Reaction TSSG is likely the most controllable and adaptable method for solution growth of SiC which has been explored so far. It allows to overcome easily the problem of low carbon solubility in pure silicon melt and has great potentiality for process design. The feasibility of 'fast solution growth' has been demonstrated, but crystal quality is still poor in comparison with 'thick' epitaxial layers because of insufficient process stability. More complete understanding of the reaction between solid carbon and silicon melt and factors affecting growth stability such as melt convection are required for further advancement of SiC solution growth.

#### References

- [1] V. Dmitriev and A. Cherenkov, J. of Crystal Growth 128(1993), 343
- [2] D. Hofmann, M. Müller, A. Materials Science & Engineering B61-62 (1999)
- [3] Elwell D., Scheel H.J., *Crystal growth from high temperature solutions*, Academic press, London, 1975
- [4] W.P. Minnear, J. Am. Ceram. Soc., 65 (1982) No.1, 10
- [5] H. Zhou., R.N. Singh, J. Am. Ceram. Soc., 78 (1995) No.9, 2456
- [6] T. Hase, H. Suzuki, J. Nucl. Mater., 59 (1976) 42
- [7] J.N. Ness, T.F. Page, J. Mater. Sci., 21 (1986) 1377



## Controlled Growth of Bulk 15R-SiC Single Crystals by the Modified Lely Method

Norbert Schulze, Donovan Barrett, Michael Weidner and Gerhard Pensl

Institute of Applied Physics, University of Erlangen-Nürnberg, Staudtstr. 7/A3,  
DE-91058 Erlangen, Germany

**Keywords:** 15R-SiC, Boron Acceptor, Defect Centers, DLTS, Hall Effect, Stoichiometry, Sublimation Growth

**Abstract.** A near-thermal-equilibrium process has been used to grow 15R-SiC bulk single crystals by the modified Lely method. The 15R-SiC growth can only be stabilized if stoichiometric SiC source material is used. Crystals grown on the Si-face at temperatures between 2150°C and 2180°C are free of inclusions of different polytypes and without micropipes. The incorporation of nitrogen and boron depends on the polarity of the seed crystal face. Three deep defect centers ( $W_1$ ,  $W_2$ ,  $W_3$ ) have been observed by deep level transient spectroscopy (DLTS) in 15R-SiC crystals.

### Introduction

The 15R silicon carbide (SiC) polytype is gaining considerable attention as a potential candidate for the fabrication of MOS devices [1,2]. Several papers about the growth of 15R-SiC epitaxial layers [1,3] and 15R-SiC Lely platelets [4] have been published, however, no successful experiments are reported in the literature on the controlled growth of 15R-SiC bulk single crystals by the modified Lely method. Under special growth conditions and based on the "near-thermal-equilibrium" process described in [5], the controlled growth of micropipe-free 6H-SiC boules has been achieved, whereas polytype inclusions and micropipes could not completely be avoided regarding the 4H- and 15R-SiC polytype [6]. In this paper, we report on sublimation growth experiments, which result in the reproducible growth of high-quality 15R-SiC single crystals.

### Experimental

SiC bulk single crystals have been grown by sublimation physical vapor transport (PVT) (or so-called modified Lely method). The growth system used as well as the preparation of the graphite parts, the source material, and the seed prior to the growth run are described in [7]. All growth experiments reported in this letter have been conducted according to the near-thermal-equilibrium process [5]. The source temperature, the seed temperature and the argon pressure inside the growth cell have been established to  $T_{\text{source}} = 2100^\circ\text{C} - 2300^\circ\text{C}$ ,  $T_{\text{seed}} = 2100^\circ\text{C} - 2280^\circ\text{C}$  and  $p_{\text{Argon}} = 1 \text{ mbar} - 820 \text{ mbar}$ , respectively. Si powder has been added to the SiC source material in the range of 0% to 10%. The exact course of the growth process is described elsewhere [5]. The average thermal gradient inside the growth cell has been kept at 5 K/cm or below during the entire process to avoid the formation of micropipes [5]. We used 15R-SiC Lely platelets grown by the original Lely method as seed crystals. In order to be able to investigate the influence of the polarity of the seed face on the growing crystal, we used two seed crystals exposing opposite faces (Si-/C-face) during each run ("dual-seed method" [7]). The growth faces have been prepared with on-axis orientation relative to the c-axis.

Low temperature photoluminescence (LTPL) and microprobe Raman spectroscopy measurements were employed to detect the particular polytypes of the grown crystal. Electrically active

defects were detected by Hall effect and deep level transient spectroscopy (DLTS). Secondary ion mass spectrometry was used to determine the content of boron (B) and nitrogen (N).

## Results and Discussion

**15R-SiC growth.** Fig. 1 shows a transmission light image of the cross section parallel to the *c*-axis of a crystal resulting from a growth experiment, which was performed without addition of Si powder to the SiC source material ( $T_{\text{seed}} = 2150^\circ\text{C}$ ,  $T_{\text{source}} = 2150^\circ\text{C} - 2180^\circ\text{C}$ ,  $p_{\text{Argon}} = 5 \text{ mbar} - 800 \text{ mbar}$ ). The two 15R-SiC seed crystals providing opposite faces (Si-face: left part; C-face: right part) are clearly visible at the bottom of this picture. Macrodefects are formed in the gap between the two seeds. The significant result of this growth experiment is documented on the left part of the image. On the Si-face of the seed, a 15R-SiC single crystal is grown, which covers the entire area of the seed and is fully extended over the crystal length. No polytype inclusions can be identified in the bulk of this crystal. Investigations of wafers cut perpendicular to the *c*-axis and treated in molten KOH at  $450^\circ\text{C}$  for 15 min. reveal no etch pits which can be attributed to micropipes. These results can only be obtained using a stoichiometric SiC source material (without addition of Si).

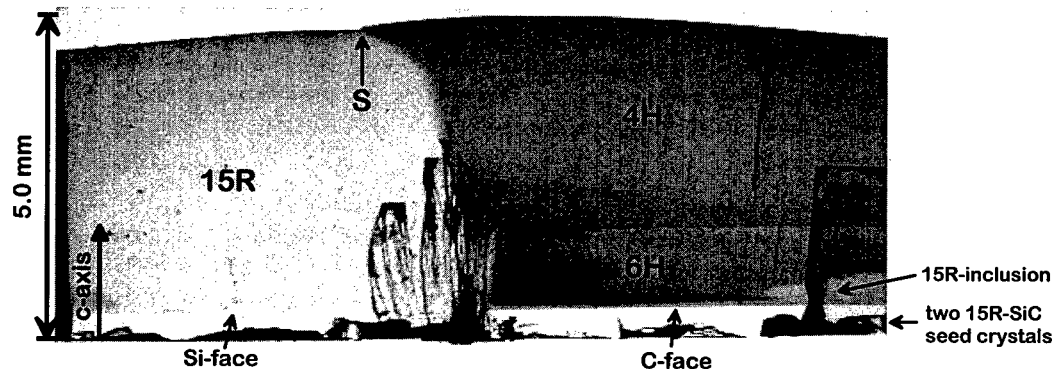


Fig.1. Transmission light image of a cross section parallel to the *c*-axis of a crystal grown by a near-thermal-equilibrium process without Si powder addition to the SiC source material. Arrow S indicates a step line at the surface of the crystal.

The crystal grown on the C-face of the 15R-SiC seed (see Fig. 1, right part) shows polytype changes; the 15R-SiC growth starts directly on the C-face. Then, a change to the 6H-SiC polytype locally occurs after a differing growth period. Finally, the 4H-SiC growth is homogeneously stabilized over the entire seed area; this polytype occupies the largest volume.

We performed several growth experiments in the temperature range between  $2100^\circ\text{C}$  and  $2300^\circ\text{C}$ . Stable 15R-SiC growth is only possible, if the seed temperature is adjusted in the range of  $T_{\text{seed}} = 2150^\circ\text{C}$  to  $2180^\circ\text{C}$ . Table 1 summarizes all essential parameters for the growth of bulk 15R-SiC single crystals.

As can be observed in Fig. 1 towards the end of the crystal (upper part), the 15R-SiC crystal is partially overgrown by the 4H-SiC polytype. This situation is observed in all our growth experiments using two seed crystals with opposite faces. Arrow S in Fig. 1 indicates a step line at the surface of the crystal. The facet of the 4H-SiC crystal is about 0.5 mm higher than the facet of the

Table 1. Essential growth parameters for the stable growth of 15R-SiC single crystals

seed polytype	15R-SiC
seed face polarity	Si-face
seed orientation	on-axis
Si addition to the source	0%
seed temperature	$2150^\circ\text{C} - 2180^\circ\text{C}$
temperature gradient	$\leq 5 \text{ K/cm}$
argon pressure	1 mbar - 820 mbar

15R-SiC crystal meaning that the growth rate of 15R-SiC is slightly smaller than that one of the 4H-SiC polytype. The same overgrowth of 15R-SiC occurs, if 6H-SiC is the topmost polytype on the seed exposing the C-face. This repression of 15R-SiC can be avoided by using only one seed (Si-face). In this case, the 15R-SiC single crystal area spreads out suppressing the polycrystalline part surrounding the edges with progressive crystal height as known for the growth of 4H- and 6H-SiC (see e.g. [8]). We succeeded in growing 15R-SiC boules of 20 mm in diameter and 10 mm in length. The achieved maximum growth rate is equal to 0.25 mm/h.

**Hall effect characterization.** 15R-SiC single crystals grown on both the Si-face and the C-face were electrically characterized by Hall effect measurements. The incorporation of nitrogen donors on the C-face is higher by a factor of two than on the Si-face. In contrast, the incorporation of boron acceptors is higher by a factor of two on the Si-face than on the C-face, which has additionally been confirmed by SIMS analysis. All unintentionally doped crystals are n-type. The total concentration

of nitrogen donors and of boron acceptors (compensation) are in the range of  $N(N) = 5 \cdot 10^{17} \text{ cm}^{-3}$  to  $5 \cdot 10^{18} \text{ cm}^{-3}$  and  $N(B) = 1 \cdot 10^{17} \text{ cm}^{-3}$  to  $1 \cdot 10^{18} \text{ cm}^{-3}$ , respectively.

The maximum of the electron Hall mobility  $\mu_H(\text{max})$  of the investigated 15R-SiC samples ( $> 300 \text{ cm}^2/\text{Vs}$ ) is comparable to the one of the 4H-SiC polytype and significantly higher than the one of the 6H-SiC polytype (ca.  $200 \text{ cm}^2/\text{Vs}$ ) [6].

**DLTS characterization.** Since no investigations on deep defect centers in 15R-SiC are reported in the literature, DLTS measurements have been conducted on as-grown 15R-SiC crystals. Nickel Schottky contacts ( $\varnothing=0.4 \text{ mm}$ ) were evaporated on the polished surface of 15R-SiC samples.

Fig. 2 shows a normalized DLTS

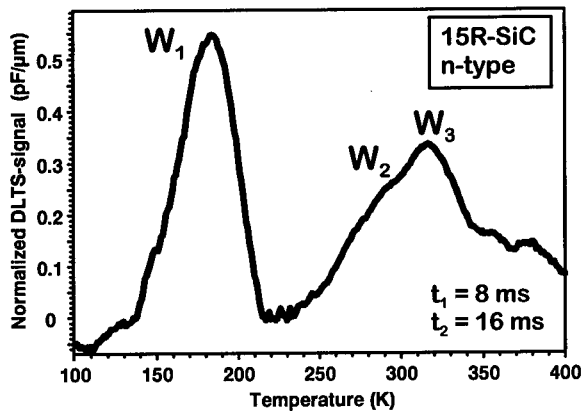


Fig. 2. Normalized DLTS signal as a function of temperature (time window ( $t_1 / t_2$ )). The spectrum is taken on as-grown 15R-SiC. Three distinguishable peaks are denoted by  $W_1$ ,  $W_2$  and  $W_3$ . Results of the analysis of  $W_1$  and  $W_3$  are given in Table 2.

spectrum for one time window ( $t_1 = 8 \text{ ms} / t_2 = 16 \text{ ms}$ ). Three peaks denoted by  $W_1$ ,  $W_2$  and  $W_3$  can be distinguished in the DLTS spectrum.

A quantitative analysis of the energy position and the concentration of the respective defect centers was conducted for  $W_1$  and  $W_3$ ;  $W_2$ , located on the shoulder of the  $W_3$  peak, cannot be used for an Arrhenius evaluation. The temperature position of the peak  $T$ , the ionization energy  $\Delta E$  and the concentration  $C$  of de-

Table 2. Peak temperature position  $T$ , concentration  $C$  and ionization energy  $\Delta E$  of defect centers  $W_1$  and  $W_2$  in as-grown 15R-SiC as identified by DLTS (see Fig. 2).  $\Delta E$  is listed for two different dependencies of the capture cross section  $\sigma$  on the temperature  $T$ . The last column lists known defect centers in 6H-SiC which show similar ionization energies to  $W_1$  and  $W_3$ , respectively.

	$T$ [K]	$C$ [ $10^{15} \text{ cm}^{-3}$ ]	$\Delta E$ [meV]	energetically comparable de- fects in 6H-SiC
$W_1$	185	( $1.5 \pm 0.1$ )	( $275 \pm 15$ ) ( $\sigma \sim T^0$ ) ( $305 \pm 15$ ) ( $\sigma \sim T^{-2}$ )	$E_{1/2}$ [9]
$W_3$	315	( $1.2 \pm 0.1$ )	( $530 \pm 15$ ) ( $\sigma \sim T^0$ ) ( $590 \pm 15$ ) ( $\sigma \sim T^{-2}$ )	$Z_{1/2}$ [9]

fect centers  $W_1$  and  $W_3$  are summarized in Table 2.  $\Delta E$  is listed for two different temperature dependencies of the capture cross section  $\sigma$ .

At the present, the microscopic structure and chemical nature of centers  $W_1$  and  $W_{2/3}$  are not known. However, the energy positions in the band gap are comparable to centers  $E_{1/2}$  and  $Z_{1/2}$  in the 6H-SiC polytype, which has an almost equivalent band gap energy ( $\approx 3\text{eV}$ ). Further investigations are necessary to clarify whether  $W_1$  and  $W_{2,3}$  are qualitatively of the same defect type like the  $E_{1/2}$ - and  $Z_{1/2}$ -center, respectively.

### Summary

We have demonstrated the growth of 15R-SiC single crystals without micropipes and polytype inclusions. Stable 15R-SiC growth requires a stoichiometric SiC source material and a 15R-SiC seed crystal exposing its Si-face. The ratio of nitrogen and boron incorporation on the C-face to the one on the Si-face is 2 and  $\frac{1}{2}$ , respectively. The maximum value of the electron Hall mobility determined for 15R-SiC samples ( $> 300\text{ cm}^2/\text{Vs}$ ) is comparable to the corresponding value for 4H-SiC samples and significantly higher than for 6H-SiC samples (ca.  $200\text{ cm}^2/\text{Vs}$ ). Three defect centers  $W_1$ ,  $W_{2/3}$  are detected by DLTS investigations.

### Acknowledgment

The authors would like to thank C. Peppermüller and H. Sadowski for the LTPL measurements, M. Laube for the SIMS analysis, M. Baßler for the thermal oxidation of the seeds, and S. Rohmfeld and M. Hundhausen for the Raman spectroscopy measurements. The support of this work by the German Science Foundation (Sonderforschungsbereich 292) is gratefully acknowledged.

### References

- [1] R. Schörner, P. Friedrichs, D. Peters, and D. Stephani, IEEE Electron. Dev. Lett. Vol. 20 (1999), pp. 241.
- [2] V.V. Afanasev, M. Baßler, G. Pensl, and M. Schulz, phys. stat. sol. (a) Vol. 162 (1997), pp. 321.
- [3] T. Kimoto, A. Itoh, and H. Matsunami, phys. stat. sol. (b) Vol. 202 (1997), pp. 247.
- [4] D.L. Barrett and R.B. Campbell, J. Appl. Phys Vol. 38 (1967), pp. 53.
- [5] N. Schulze, D.L. Barrett, and G. Pensl, Appl. Phys. Lett. Vol. 72 (1998), pp. 1632.
- [6] N. Schulze, D.L. Barrett, G. Pensl, S. Rohmfeld and M. Hundhausen, Mater. Sci. and Engineering B, Vols. 61-62 (1999), pp. 44.
- [7] V.D. Heydemann, N. Schulze, D.L. Barrett, and G. Pensl, Appl. Phys. Lett. Vol. 69 (1996), pp. 3728.
- [8] V.D. Heydemann, N. Schulze, D.L. Barrett and G. Pensl, Diamond Relat. Mater. Vol. 6 (1997), pp. 1262.
- [9] T. Dalibor, G. Pensl, H. Matsunami, T. Kimoto, W.J. Choyke, A. Schöner, and N. Nordell, phys. stat. sol. (a) Vol. 162 (1997), pp. 199.

## Crystal Growth of 15R-SiC Boules by Sublimation Method

T. Nishiguchi<sup>1</sup>, S. Okada<sup>1</sup>, M. Sasaki<sup>1</sup>, H. Harima<sup>2</sup> and S. Nishino<sup>1</sup>

<sup>1</sup> Kyoto Institute of Technology, Matsugasaki, Sakyo-ku, Kyoto, 606-8585, Japan

<sup>2</sup> Department of Applied Physics, Osaka University, Yamadagaoka 2-1, Suita,  
Osaka 565-0871, Japan

**Keywords:** 15R-SiC, Crystal Growth, Polytype, Sublimation Method

**Abstract.** Recently much attention is being paid to 15R-SiC for application in MOSFET devices. But there are few reports about 15R-SiC boule growth. SiC boules have been grown by the sublimation method, and this technique has produced high quality crystals of 6H-SiC and 4H-SiC. In this paper, single crystal growth of 15R-SiC using the sublimation method on 15R-SiC and 6H-SiC substrates is discussed. The polytype of the grown crystal was determined by Raman spectroscopy. A close relationship between the substrate temperature and the 15R-SiC growth was observed. To obtain 15R-SiC boules without inclusion of other polytypes, the substrate temperature must be kept below 2000°C. The use of a 15R-SiC substrate is important for the growth of 15R-SiC boules. Growth on the (11 $\bar{2}$ 0) plane of 15R-SiC is also useful for 15R-SiC growth.

### 1. Introduction

SiC is suitable for power devices and MOSFETs. Particularly, 4H-SiC is used for MOSFET because of its isotropic mobility. In 6H-SiC, the mobility is anisotropic. However, in 4H-SiC, the channel mobility is too low because of a high density of surface states at the SiO<sub>2</sub>/SiC interface. Recently, it has been reported that 15R-SiC is suitable for MOSFET [1], since the mobility of 15R-SiC is isotropic and its channel mobility is larger than in the case of 6H-SiC or 4H-SiC. But it has not been well studied due to the lack of 15R-SiC substrate. It is necessary to establish suitable growth conditions for 15R-SiC boules and to avoid mixed polytype growth. In the present paper, the parameters for 15R-SiC growth using the sublimation method are discussed.

### 2. Experiment

Sublimation growth was achieved using a quartz tube reactor with a water-cooled jacket under argon atmosphere at reduced pressure of 200 Torr. Substrates used were (0001) plane (Si-face), (000 $\bar{1}$ ) plane (C-face) and (11 $\bar{2}$ 0) plane of 15R-SiC and 6H-SiC produced by the Acheson method or the Lely method. Some substrates were obtained by cutting boules previously produced by the sublimation method. The source material was abrasive SiC powder. The distance between substrate and source was approximately 15 mm. The crucible (inside diameter of 24 mm, height of 70 mm) was surrounded by graphite felt to prevent heat dissipation. The crucible was heated externally by RF induction with a frequency of 300 kHz. The temperatures at the top (Ts) and the bottom (Tb) of the crucible were measured by an optical pyrometer. Ts and Tb were approximately 1800~2300°C and 2300~2600°C, respectively. To examine the polytype along the growth direction, several wafers were produced by cutting 10 mm-long SiC boules parallel to the growth direction. Raman spectroscopy was used to confirm the polytype. Photoluminescence (PL) images of whole wafers were taken.

### 3. Results and Discussion

#### (1) Growth on 6H-SiC

Growth experiments using both faces of 6H-SiC were conducted at  $T_s=1850\sim 2160^\circ\text{C}$ . The growth rate was  $0.1\sim 1.8\text{ mm/h}$ . The run duration was approximately  $1\sim 4\text{ hours}$ , and the boules were grown several times after recharging the source material. In this manner,  $10\text{ mm}$ -long SiC boules were obtained. The polytype of each layer was confirmed by Raman spectroscopy. 15R-SiC occasionally grew in a small region on 6H-SiC substrates. The Si-face appeared to be slightly favorable for growing 15R-SiC. Temperatures below  $2000^\circ\text{C}$  were also favorable.

#### (2) Growth on the (000 $\bar{1}$ ) plane (C-face) of 15R-SiC

Growth parameters for 6H-SiC boule growth have been previously established in our laboratory [2, 3]. Initially, the same conditions ( $T_s=2100\sim 2140^\circ\text{C}$ ,  $T_b=2280\sim 2320^\circ\text{C}$ ) that were used for 6H-SiC growth were used for 15R-SiC growth experiments. The growth rate was  $0.5\sim 1.5\text{ mm/h}$ . Three polytypes were produced: 15R-, 6H- and 4H-SiC. 4H-SiC grew less frequently than the other two polytypes. These three polytypes often grew alternately along the growth direction as shown in Fig.1. However, 15R-SiC did not grow during some growth runs. Under these conditions, it was not possible to obtain an entire boule of pure 15R-SiC. The relationship between the substrate temperature and the polytype of the grown crystal is shown in Fig.2. Based on Knippenberg's report on the relationship of the yield of SiC polytypes and growth temperature [4], it appeared that 15R-SiC grew well around  $2450^\circ\text{C}$ . The second set of experiments was conducted at  $T_s=2150\sim 2240^\circ\text{C}$ . Growth rates of  $0.3\sim 1.5\text{ mm/h}$  were observed. The result was

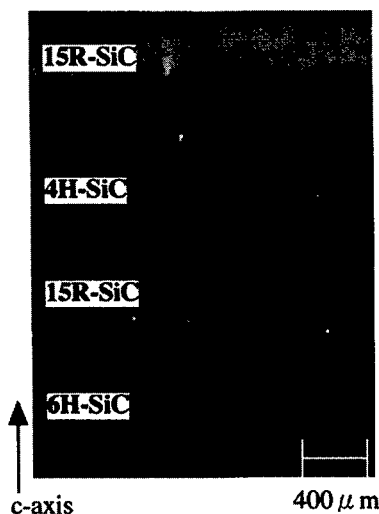


Fig.1 PL image of grown layer at room temperature.  
(sample cut parallel to the c-axis)

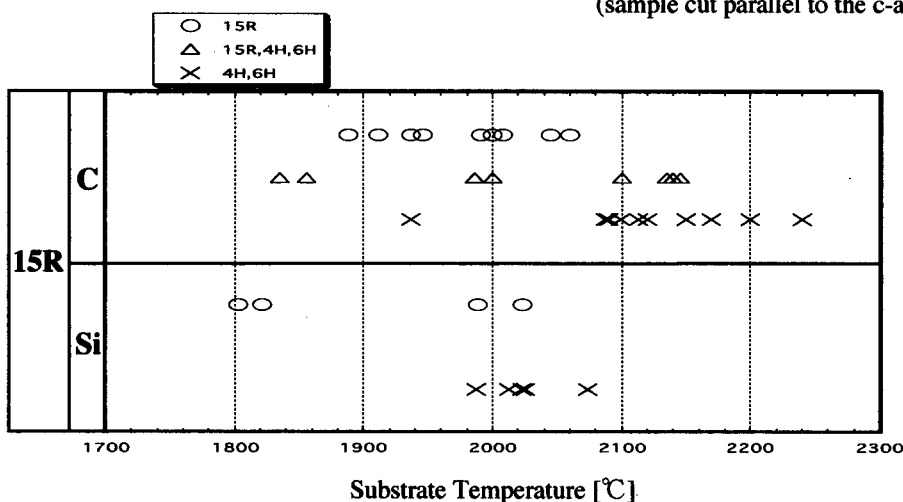


Fig.2 Relationship between the substrate temperature and grown polytype. The upper and lower column correspond to the growth on the C-face and on the Si-face of 15R-SiC substrates, respectively. Each point represents the polytypes that grew at the corresponding substrate temperature.

contrary to our expectations and only 6H-SiC grew. It appears that 6H-SiC is more stable than 15R-SiC at higher temperatures. It is also possible that the grown 15R-SiC crystal transformed to 6H-SiC at high temperature as demonstrated by Bootsma, et al. [5] and Jepps, et al. [6]. Therefore the growth temperature was reduced to  $T_s=1840\sim2060^\circ\text{C}$ . The observed growth rates were 0.1~1.7 mm/h. Under these conditions, primarily 15R-SiC was obtained. However, if the growth rate was greater than 1.0 mm/h, the growth of 15R-SiC became unstable and only 6H-SiC or a mixture of 15R-SiC and 6H-SiC grew. From the viewpoint of polytype control, crystal quality, and high growth rate, a suitable growth rate for 15R-SiC would be 0.4~0.5 mm/h.

### (3) Growth on the (0001) plane (Si-face) of 15R-SiC

Growth experiments were conducted under almost the same conditions as for the C-face of 15R-SiC. The growth temperature was  $T_s=1800\sim2080^\circ\text{C}$ , and the growth rate was 0.2~1.5 mm/h. The relationship between the substrate temperature and the polytype of the grown crystal is shown in Fig.2. Though there are fewer sample points, the result was almost the same as in the growth experiments on the C-face. That is, at low temperature below  $2000^\circ\text{C}$ , and at a low growth rate, 15R-SiC grows stably. There are a lot of factors which influence the polytype of the grown crystal, e.g. the growth temperature, the degree of supersaturation, the polarity of the growth surface, the presence of impurities etc.. It is not easy to determine the polytypes based only on the growth temperature, since the stacking energy of each bi-layer along c-axis is almost identical in most polytypes [7]. However, in our experiments, a close relationship between the substrate temperature and the 15R-SiC growth is observed. At high growth temperatures, even if a 15R-SiC substrate was used, the growth of 15R-SiC could not be stabilized. When  $T_s$  was lower than approximately  $2000^\circ\text{C}$ , 15R-SiC was obtained on both C-face and Si-face of 15R-SiC substrates. Thus it can be concluded that the temperature for stable growth of 15R-SiC is lower than that of 6H-SiC and 4H-SiC. Additionally, the use of a 15R-SiC substrate is critical for reproducibly obtaining 15R-SiC.

### (4) Growth on the (1120) plane of 15R-SiC and 6H-SiC

The substrate used in this experiment was a (1120) oriented wafer containing both polytypes of 15R-SiC and 6H-SiC side by side. A two hour growth was performed at  $T_s=2150^\circ\text{C}$ . As noted previously, at this high temperature, 15R-SiC did not grow on the (0001) and (000 $\bar{1}$ ) plane (c-plane). But on the (1120) plane (a-plane), the polytype of the grown layer was the same as that of the substrates, and 15R-SiC grew on the 15R-SiC substrates. Fig.3 shows the cross section of this sample in transmitted light microscopy. As noted previously, a low growth temperature was required to grow 15R-SiC on the c-plane. However, in the growth on the a-plane, 15R-SiC grew at higher temperatures. Comparing this result with Knippenberg's report [4], it appears that he

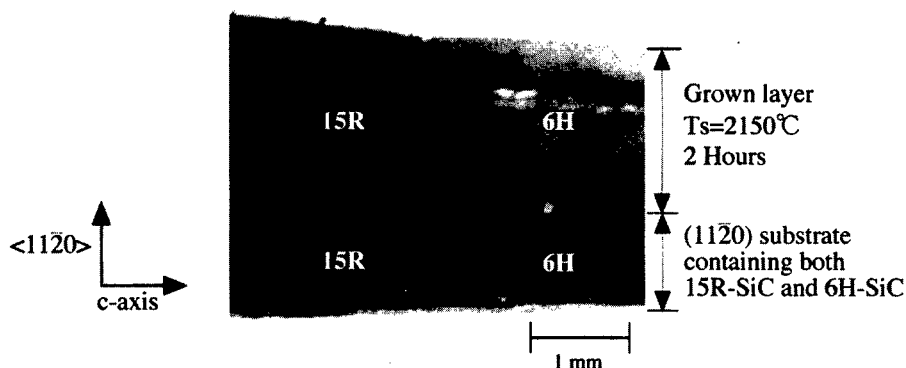


Fig.3 Cross section of a crystal grown on the (1120) plane in transmitted light microscopy. The dark area is 15R-SiC and the bright area is 6H-SiC. The polytype of grown layer is determined by the substrate.

describes the growth on the a-plane, since the Lely method was used. Knippenberg's publication does not describe the results of growth on the c-plane. In the case of growth on the a-plane, our results agree with Knippenberg's papers which report 15R-SiC grows even at high temperature. But in the case of the growth on the c-plane, temperatures below 2000°C are essential. The optimum growth conditions for 15R-SiC is shown in Table 1.

Table 1: Optimum growth conditions for 15R-SiC

Substrate		Substrate Temperature	Growth Rate
15R	(000 $\bar{1}$ ) C	1890~2060°C	0.1~0.5 mm/h
	(0001) Si	1800~2020°C	0.2~0.4 mm/h
	(11 $\bar{2}$ 0)	2070~2150°C	0.5~1.0 mm/h

#### 4. Conclusions

In order to achieve stable growth of 15R-SiC on the c-plane, it was very important to keep the substrate temperature below 2000°C. 15R-SiC was reproducibly obtained on 15R-SiC substrate under these conditions. Sometimes 15R-SiC grew at temperatures above 2000°C, but it was not possible to obtain a crystal of 15R-SiC without any inclusion of other polytypes at temperatures higher than 2060°C. We think that 15R-SiC is stable more at a lower temperature than 6H-SiC and 4H-SiC. When 15R-SiC was used as a substrate, it became easier to grow 15R-SiC on both C-face and Si-face. There appeared to be little difference between growth on the C-face and on the Si-face. On 6H-SiC substrates, it was difficult to grow 15R-SiC, even though the growth conditions were the same as for 15R-SiC substrate. Therefore, using a 15R-SiC substrate is essential for growing large boules of 15R-SiC. Growth of 15R-SiC on the a-plane may take place at higher temperature (~2100°C) in agreement with Knippenberg's results obtained from investigation of Lely crystals.

#### Acknowledgements

This work was partially supported by a Grant-in-Aid for Science Research No.0945001 from the Ministry of Education, Science and Culture, Japan and FE, NEDO Japan, and Ion Engineering Institute (Osaka, Japan).

#### References:

- [1] R.Schörner, P.Friedrichs, D.Peters, and D.Stephani, IEEE Electron. Device Letters, **20** (1999), p. 241.
- [2] N.Takanaka, S.Nishino and J.Saraie, Inst. Phys. Conf., **142** (1996), p. 49.
- [3] M.Sasaki, Y.Nishio, S.Nishino, S.Nakashima and H.Harima, Materials Science Forum, **264-268** (1998), p. 41.
- [4] W.F.Knippenberg, Philips Research Reports, **18** (1963), p. 161.
- [5] G.A.Bootsma, W.F.Knippenberg and G.Verspui, J. Crystal Growth, **8** (1971), p. 341.
- [6] N.W.Jepps and T.F.Page, in "Crystal Growth and Characterization of Polytype Structures", ed: P.Krishna (Pergamon Press: Oxford), **7** (1983), p. 259.
- [7] Y.M.Tairov and V.Tsvetkov, in "Crystal Growth and Characterization of Polytype Structures", ed: P.Krishna (Pergamon Press: Oxford), **7** (1983), p. 111.



## Growth of 3C SiC Single Crystals from Convection Dominated Melts

J. Wollweber<sup>1</sup>, V. Chévrier<sup>1,2</sup>, D. Siche<sup>1</sup> and Th. Duffar<sup>2</sup>

<sup>1</sup>Institut für Kristallzüchtung im Forschungsverbund Berlin e.V., Max-Born-Str. 2,  
DE-12489 Berlin, Germany

<sup>2</sup>CEA Commissariat à l'Énergie Atomique Grenoble, 17 rue des Martyrs,  
FR-38054 Grenoble, Cedex 9, France

**Keywords:** 3C Polytype, Bulk Material, Forced Convection, Solution Growth

### Abstract

Bulk material of 3C-SiC was grown using a conventional Floating Zone arrangement with aspects of the THM process. Feeding and growing part were made of graphite or sintered SiC rods for the first runs. Silicon has been used as solvent. High temperature gradients in the molten zone and in the vicinity of the growth interface can be assumed because of the applied induction heating. Marangoni and electrodynamic convection give rise to complete mixing of the molten zone consequently. The influence of complete mixing on the transport rate from feeding rod to the growing rod has been studied. The observed average growth rates in the  $0.1\text{--}0.4\text{ mm h}^{-1}$  range were comparable to the corresponding values of vapour growth. Diffusion is not a limiting factor for the growth rate in this system.

### Introduction

There has been essential progress in SiC single crystal growth from the vapour phase during the last years. Wafers of 4H and 6H polytype are commercially available up to 2" in diameter. Unfortunately, the problems of micropipe defects and of stable bulk growth of other polytypes like 3C are not solved.

The alternative growth from silicon solutions is restricted to the epitaxial layer growth today. The low growth rate is caused by the low solubility of carbon in silicon. By addition of rare earth elements and Sc the solubility was increased by a factor 1.5, but the electronic properties could be influenced undesirable. Crucible material, suitable for mixed melts, can hardly be found.

Otherwise, solution growth has advantages. Lower growth temperatures can be used, the theory of convective processes is well developed and the growth of the 3C polytype is possible.

Gillissen and von Münch [2] used already the Floating Zone - method in combination with iodine transport agent in a closed silica ampoule to prevent the evaporation loss of silicon by the iodine back transport.

### Experimental Procedure

To overcome the problem concerning the low solubility, the application of a very efficiently mixed melt solution is suggested. This efficient mixing can be obtained by forced convection in the RF-heated zone of a crucible free Floating Zone - growth equipment. The convective flow velocities are in the range of some  $\text{cm s}^{-1}$  [1]. It is assumed that without kinetic limitation in the dissolving region (source) the transport rate depends only on the velocity of the melt solution in such a system.

With the goal to prove the assumed high transport rates in our experiments a conventional FZ - method was utilized (Fig. 1).

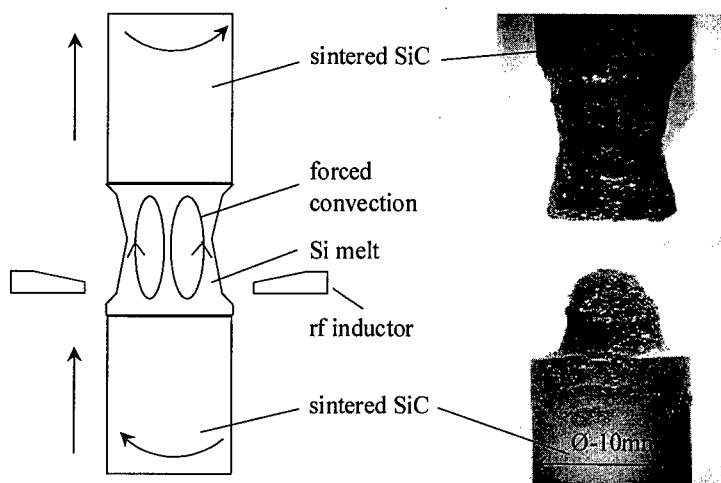


Fig.1: Conventional FZ - method arrangement; growth result: dissolved (bottom) and grown (top) rod

The arrangement consists of two rods ( $\varnothing=10\text{mm}$  or  $14\text{mm}$ , length=  $50\text{mm}$ ) made of graphite (SGL) or sintered silicon carbide (HALSIC) without single crystalline seed. A cylinder of solid silicon ( $h=7\text{mm}$ ,  $\varnothing=10\text{mm}$  or  $14\text{mm}$ ) was attached between the rods and molten by means of a RF-inductor („pancake“ inductor,  $3\text{MHz}$ ). After homogenisation for  $30\text{ min}$  the system was pulled up ( $0.02\text{-}0.5\text{ mmh}^{-1}$ ). During growth the temperatures have been controlled for a constant value in the  $1450\text{-}1700^\circ\text{C}$  range with a pyrometer. The growth ambient was  $\text{Ar}+\text{N}_2(0.25\text{vol}\%)$  under atmospheric pressure. It was observed that nitrogen stabilized the 3C polytype. No essential silicon loss could be observed within the time of  $72\text{ hours}$ .

### Results and Discussion

It was shown that the growth conditions are more stable using sintered SiC rods. The reason is the lower dependence of the wetting angle on the temperature in comparison to graphite. The stability of the zone geometry is quite low using graphite rods up to a total run off.

The occurrence of the 3C-SiC polytype has to be expected for the applied temperatures. In fact, 3C-SiC could be found in the whole grown volume (Fig. 2). The polytype was proven by cathodoluminescence (CL) on selected areas in the vicinity of the seed and at the end of the boules (Fig. 3).

The grown 3C-SiC boules were polycrystalline large grains with  $\varnothing=7\text{mm}$ , length=  $4\text{-}13\text{mm}$  and  $\varnothing=11\text{mm}$ , length=  $3\text{-}4\text{mm}$ . The average growth rates in the  $0.1\text{-}0.4\text{ mmh}^{-1}$  range were comparable to the rates of vapour growth.



Fig. 2: Growth interface of polycrystalline 3C-SiC crystal,  $\varnothing \sim 10\text{mm}$ , top view (see Fig. 1)

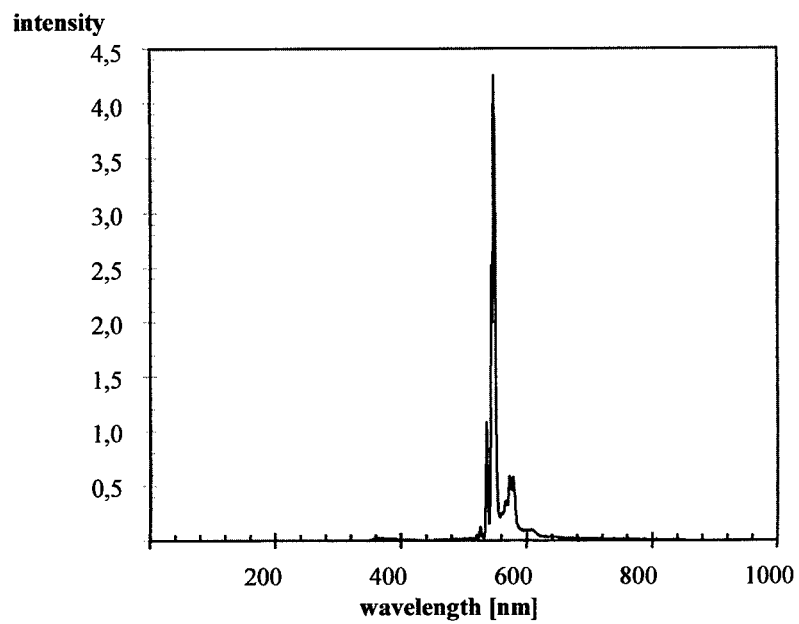


Fig. 3: CL spectrum of 3C-SiC measured at the growth interface of polycrystalline 3C-SiC crystal (see Fig. 2)

The grown boules were not dense at the end. Constitutional supercooling could be the reason for this phenomenon because fluctuations of the RF-coupling behaviour between inductor and molten zone were often revealed by observing the fluctuations of the luminosity. In this connection it should be taken into account that the constitutional supercooling is decreased by the high temperature gradients on the one side but otherwise the supersaturation is high as.

Temperature measurements on the surface of the molten zone are quite difficult because of the overheating in the thin skin of induction [1,3]. So we tried to stabilise the RF-power using the luminosity as compensator signal for the power controller [4]. The stability of the RF-power seems to be increased essentially. This was the prerequisite to start the growth on monocrystalline seeds.

#### **Acknowledgement**

We wish to thanks our colleagues for the helpful collaboration, especially:

D. Schulz	-	permanent discussion
Dr. J. Doerschel	-	SEM/PL/EDX investigations
V. Lange, M. Imming	-	Slice preparation

#### **References**

- [1] J. Bohm, A. Lüdge, W. Schröder, Crystal growth by floating zone melting, in Handbook of Crystal Growth, vol. 1a, 45-65, ed. by Hurle, D.T.J., North-Holland (1993)
- [2] K. Gillessen, W. von Münch, J. Cryst. Gr., vol. 19 (1973) p. 263-268
- [3] D. Schulz, J. Wollweber, N. Darowski, W. Schröder, Cryst. Res. Technol., vol. 32 (1) (1997) p.61-68
- [4] J. Wollweber, V. Chevrier, Final Report, IKZ Berlin-CEA/DTA/CEREM Grenoble (contract: B-4046)

## Chapter 2

# SiC Epitaxy and Thin Film Growth

## An Overview of SiC Growth

Hiroyuki Matsunami

Department of Electronic Science and Engineering, Kyoto University,  
Yoshidahonmachi, Sakyo, Kyoto, 606-8501, Japan

**Keywords:** Bulk Growth, Doping, Epitaxial Growth, Heteroepitaxy, Homoepitaxy, Step Bunching, Step-Controlled Epitaxy

### Abstract

An overview of SiC crystal growth mainly for device application is given. Bulk growth including recent development is briefly reviewed. Epitaxial growth involving both heteroepitaxy and homoepitaxy is described. The concept of step-controlled epitaxy to obtain high-quality homoepitaxial layers is introduced, and the step bunching peculiar to this method is discussed. Doping characteristics during homoepitaxial growth is described. New techniques for production of SiC epitaxial layers are introduced. Finally, a future prospect in crystal growth is given.

### 1. Introduction

The potential of silicon carbide (SiC) for electronic devices has been recognized for a long time. However, the difficulty to grow large and high-quality SiC crystals without polytype mixing has prevented its applications. One innovation in bulk crystal growth with controlled polytypes utilizing seeded sublimation has triggered the feasibility of SiC devices [1]. Nowadays, 2-inch wafers of 6H- and 4H-SiC are commercially available. In addition, the success to grow high-quality epitaxial layers on off-axis SiC{0001} at rather low temperatures around 1500°C, named "step-controlled epitaxy"[2], utilizing step-flow growth has increased remarkable attention to SiC. This technique gave an epoch-making breakthrough to get high-quality material enough for device applications. Since then, many prototype devices have been demonstrated, and some of them are now being realized as vital devices.

In this paper, an overview of SiC growth is given using some of historical aspects. Bulk growth, heteroepitaxy and homoepitaxy are reviewed. The details on step-controlled epitaxy together with step bunching are discussed. Control of doping level during homoepitaxial growth is explained. Trials for production-oriented SiC epitaxial growth are introduced. Finally, a future prospect of SiC crystal growth is given.

### 2. Bulk Crystal Growth

Bulk single crystal growth has been carried out by seeded-sublimation using thermal decomposition and recrystallization of source SiC at temperatures above 2000°C [1]. The polytype of bulk single crystals depends on the growth temperature, reactor pressure and surface polarity. For production of high-quality bulk single crystals with a single polytype, optimization of conditions, such as controlling nucleation, composition and thermal geometry, is strongly needed [3]. Usually 6H- or 4H-SiC bulk crystals are grown on the {0001} faces of 6H- or 4H-SiC seed crystals. Defects named 'micropipes' often appear along <0001>, which are a cause of concern for device applications. The reduction of micropipes has been strongly required, and efforts to eliminate micropipes have been continued steadily. The number of micropipes has been decreased, and now it becomes  $0.5\text{cm}^{-2}$  in a research level. In spite of recent efforts, SiC wafers still contain a high density of elemental screw and edge dislocations with an order of  $10^4$ - $10^5\text{cm}^{-2}$ .

With regard to expanding the diameter, growth of a bulk crystal exceeding 75mm has been reported [3]. The lowest doping concentration is in the  $10^{15}$ - $10^{16}\text{cm}^{-3}$  range [3,4]. The conductivity of n- and p-types can be

controlled by adding impurities to the source material. Wafers of low-resistivity ( $10^{-3} \Omega \text{ cm}$ ) through insulator ( $10^{15} \Omega \text{ cm}$ , 4H-SiC) are available [3].

Bulk crystal growth by seeded sublimation on other crystal faces rather than {0001} has been tried, which has realized micropipe-free boule growth [5]. However, stacking faults in the basal plane prohibit the growth of high-quality crystals. 6H-SiC grown on [1-100] has a high density of stacking faults ( $10^3\text{-}10^4 \text{ cm}^{-1}$ ), whereas 6H-SiC on [11-20] and 4H-SiC on [1-100] and [11-20] contain much lower density, by one or two orders of magnitude [6].

### 3. Epitaxial Growth of SiC by Chemical Vapor Deposition

#### 3.1 Heteroepitaxial growth of 3C-SiC on Si

Growth of 3C-SiC ( $\beta$ -SiC) has been extensively studied using Si substrates with a large diameter. After the success in reproducible growth utilizing carbonization of Si before CVD proposed by the author's group [7], many studies have been done up to today. Most of the works have been done at around  $1300^\circ\text{C}$  in a cold-wall atmospheric-pressure CVD reactor. Although single crystalline 3C-SiC is grown on Si, the grown layer has a lot of plane defects (stacking faults). Nowadays, 3C-SiC with 150mm in diameter can be available by alternating supply of source gases in a hot-wall low-pressure CVD reactor (at around  $1000^\circ\text{C}$ ) after carbonization of Si [8]. Trials of the growth using a low-pressure CVD reactor has given different growth mechanism and atomically flat surface morphology [9].

Conduction types can be controlled by impurity doping during growth. The undoped carrier concentration is in the range of  $1\text{-}5 \times 10^{16} \text{ cm}^{-3}$ . Electron mobilities over  $500 \text{ cm}^2/\text{Vs}$  are obtained for  $5 \mu\text{m}$ -thick epitaxial layers with a carrier concentration of  $3.2 \times 10^{16} \text{ cm}^{-3}$ .

#### 3.2 Homoepitaxial growth of $\alpha$ -SiC

In spite of many efforts for homoepitaxial growth of  $\alpha$ -SiC, there had been a serious problem of polytype mixing. Growth temperatures as high as  $1800^\circ\text{C}$  have been applied to achieve homoepitaxy of 6H-SiC [10]. After the innovation of high-quality epitaxial growth on off-axis 6H-SiC{0001} at around  $1500^\circ\text{C}$  utilizing step-flow growth [2], realization of SiC devices has been strongly accelerated. Crystal growth is usually carried out in a horizontal quartz reactor.  $\text{SiH}_4$  and  $\text{C}_3\text{H}_8$  are used as source gases and  $\text{H}_2$  as a carrier gas.  $\text{N}_2$  is used for n-type doping, and trimethylaluminum (TMA) or  $\text{B}_2\text{H}_6$  are for p-type doping. Both (0001)Si and (000-1)C faces of 6H- and 4H-SiC wafers are used, and an off-angle of  $3.5\text{-}8^\circ$  toward  $\langle 11\text{-}20 \rangle$  is required to get high-quality homoepitaxial layers at rather low temperatures. SiC substrates put on a SiC-coated graphite susceptor are heated by rf induction. The growth temperature is typically  $1500\text{-}1600^\circ\text{C}$ .

### 4. Step-controlled Epitaxy [11]

#### 4.1 Growth features

On on-axis 6H-SiC substrates, the grown layer shows a smooth surface with a mosaic pattern separated by

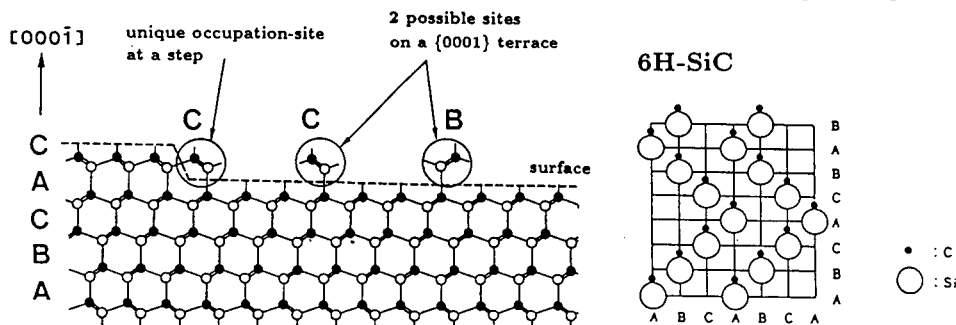


Fig.1 Model for step-flow growth and two-dimensional nucleation in the case of growth on 6H-SiC(0001).

groove boundaries on the (0001)Si face, and a roughened surface by island growth on the (000-1)C face. Both are revealed as twinned 3C-SiC by RHEED analysis. In contrast, the grown layer on off-axis substrates shows a specular smooth surface, which is revealed as 6H-SiC. The difference of crystal growth can be explained as follows.

When the concentration of chemical species adsorbed on a substrate surface reaches critical supersaturation, nucleation occurs on the surface. On on-axis {0001} faces, since the terrace width is wide, crystal growth occurs through two-dimensional nucleation on terraces. As the stacking order of 6H-SiC substrate is ABCACB..., nucleation occurs following either the orders of ABC..., or ACB.... The grown layer becomes twinned 3C-SiC, since the stable polytype is cubic at a low substrate temperature of 1500°C, and two possible stacking orders can be available as shown in Fig.1. On the contrary, on off-axis {0001} faces, since the terrace width becomes narrow, adsorbed species can reach steps easily. The incorporation of chemical species is uniquely determined by chemical bonds at the steps as in Fig.1. Thus, homoepitaxy can be achieved even at low substrate temperatures through step-flow growth inheriting the stacking order of the substrate.

From the growth rate dependence on the C/Si ratio in the source gas, crystal growth is governed by the supply of Si-related chemical species. The growth rate between 1200 and 1600°C gives a small activation energy of 2.8kcal/mole, which can be explained by a stagnant layer model applied for Si-related species [12].

On off-axis substrates with an off-angle toward <1-100>, stripe-type morphology caused by step bunching appears during long-time growth. And so the off direction toward <11-20> should be taken for high-quality thick epilayers. The feature of step-controlled epitaxy can be applied for any other polytypes such as 4H- and 15R-SiC.

#### 4.2 Critical condition for step-controlled epitaxy

Using a simple surface diffusion model based on the BCF theory and experimental results for various off-angles, critical conditions for step-flow growth in 6H-SiC was obtained as shown in Fig.2 [13]. The ordinate of the figure shows the growth rate implying the flux supply. A higher growth rate (or higher flux supply) and lower off-angle are allowed for step-flow growth at higher growth temperatures. At 1800°C, step-flow growth is achieved with a moderate growth rate of 6  $\mu$ m/h using a very small off-angle of 0.2°, corresponding almost a growth on an on-axis substrate. Whereas at a low temperature of 1200°C, larger off-angles more than 5° are needed to realize homoepitaxy of 6H-SiC with a growth rate of 1  $\mu$ m/h.

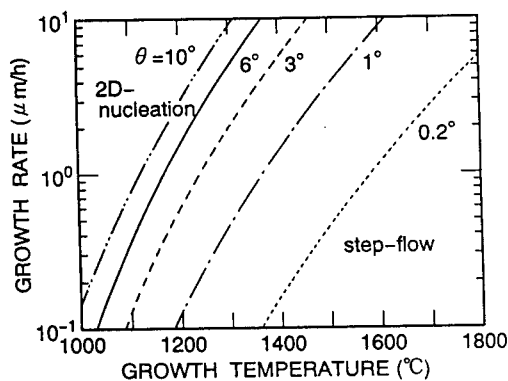


Fig.2 Critical growth conditions in 6H-SiC CVD.

#### 4.3 Step bunching

By atomic force microscopy and cross-sectional electron microscopy, step structures of 6H- and 4H-SiC

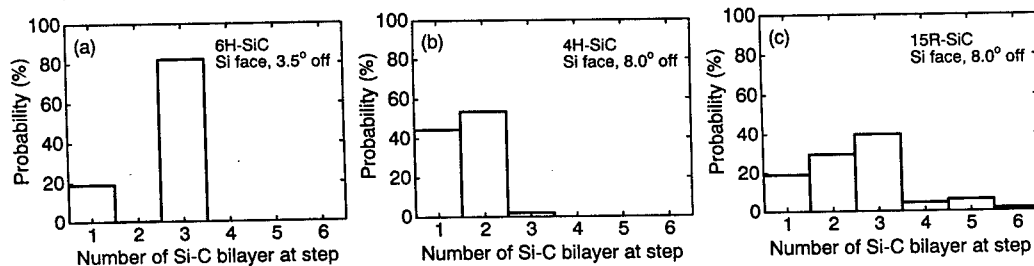


Fig.3 Histograms of step height for (a) 6H-SiC, (b) 4H-SiC, and (c) 15R-SiC (0001) epilayers.



epilayers grown on off-axis substrates have been studied [14]. An epilayer on a 6H-SiC (0001)Si face with an off-angle of  $5^\circ$  yields apparent step bunching (macro steps) with a terrace width of 220-280nm. Each macrostep is composed of a number of micro steps. On a (000-1)C face, however, the surface is rather flat with micro steps but no macro steps. 4H-SiC epilayers have similar step structures with a 110-160nm terrace width.

A histogram of step height obtained from detailed AFM analysis for various epitaxial layers is shown in Fig.3 as an example (The total number of examined steps was 40-70) [15]. On  $3.5^\circ$  off-axis 6H-SiC, 81% of steps was composed of 3 Si-C bilayer height, and 19% has single SiC bilayer height. On  $8^\circ$  off-axis 4H-SiC, steps with 2 bilayer height are the most dominant (54%) and steps with single bilayer height shows the second highest (44%). In the case of  $8^\circ$  off-axis 15R-SiC, steps with 2 and 3 bilayer height inherent to this polytype are the most dominant, 29% and 40%, respectively. Step bunching can be explained by a model taking account of different step velocities for each Si-C bilayer caused by the surface energy difference. Thus, step bunching in SiC epitaxial growth may be correlated with the peculiar stacking sequence of each polytype, and can be called "polytype-induced macro step formation".

On a Si face with  $3.5^\circ$  off-angle, the average terrace widths were 12.4nm for 6H-SiC, and 16.8nm for 4H-SiC. The difference in the average terrace widths between 6H- and 4H-SiC, in spite of the same off-angle, probably originates from the difference in surface energies between polytypes. Supersaturation occurs easier on wider terraces, leading to 3C-SiC nucleation. In this sense, 4H-SiC showing wider terraces may have a disadvantage of relatively high nucleation on terraces. Substrates with larger off-angles are effective in 4H-SiC growth (Commercially available 4H-SiC substrates have  $8^\circ$  off-angle). On the other hand, C faces show much narrower average terrace width (4-5nm). For some applications, the growth on a C face is recommended, although the growth window to get a specular surface is tight.

### 5. Doping control

Unintentionally-doped epilayers show n-type conductivity with a donor concentration of  $10^{14}$ - $10^{15}\text{cm}^{-3}$  depending on the C/Si ratio in the source gas. The higher C/Si ratio leads to the lower donor concentration which is explained by "site-competition epitaxy" [16]. The high C-atom coverage on a growing surface prevents the incorporation of N atoms into SiC, which work as donors by substituting at C sites. On a Si face, the donor concentration can be remarkably decreased by increasing the C/Si ratio: the lowest value is  $5 \times 10^{13}$ - $1 \times 10^{14}\text{cm}^{-3}$  as shown in Fig.4. In contrast, on a C face, the donor concentration is not sensitive to the C/Si ratio.

N-type conductivity can be controlled by  $\text{N}_2$  doping during CVD. The donor concentration is increased proportionally with the  $\text{N}_2$  flow rate in the wide range on both Si and C faces. The incorporation of Al and B atoms, which substitute at Si sites, is enhanced under C-rich conditions on a Si face. The electron mobility at room temperature vs. the electron concentration is shown in Fig.5 for epilayers of 4H- and 6H-SiC. 4H-SiC

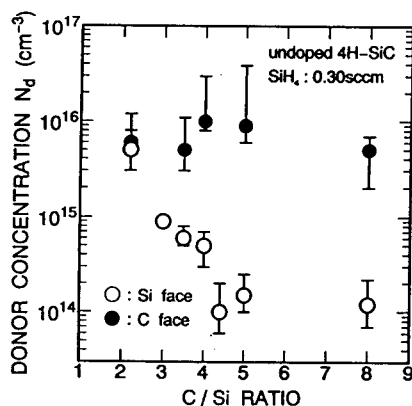


Fig.4 C/Si ratio dependence of donor concentration for undoped 4H-SiC epilayers.

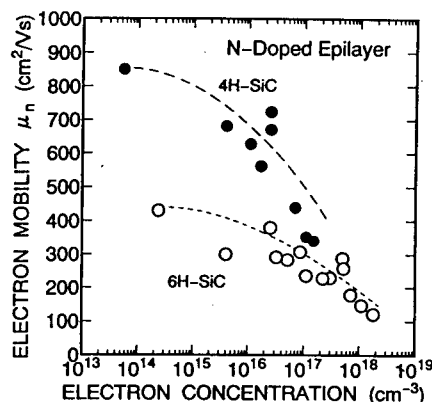


Fig.5 Electron mobility vs. carrier concentration for n-type 4H- and 6H-SiC epilayers.

epilayers exhibit two times higher electron mobility than 6H-SiC epilayers. The highest values of electron mobility are  $851\text{cm}^2/\text{Vs}$  ( $n=6\times 10^{13}\text{cm}^{-3}$ ) for 4H-SiC and  $431\text{cm}^2/\text{Vs}$  ( $n=2\times 10^{14}\text{cm}^{-3}$ ) for 6H-SiC.

## 6. New techniques -approach for production

Horizontal hot-wall reactors have been proposed for the growth of high-power device material: thick layers of low doping and good morphology [17]. Growth on substrates of 35mm and 51mm in diameter have been tried at around  $1600^\circ\text{C}$ . The grown layers showed n-type and the intrinsic background doping was in the low  $10^{14}\text{cm}^{-3}$  range. The uniformity of thickness and doping was less than 4% and 7-11%, respectively for epilayers of around  $50\mu\text{m}$  thickness grown with a rate of  $3\text{-}5\mu\text{m/h}$ . Epitaxial layers thicker than  $150\mu\text{m}$  have been grown in a hot-wall type reactor [18]. A vertical hot-wall reactor, named chimney reactor, has been applied for thick epitaxial growth [19]. Mirror-like 4H-SiC epitaxial layers with growth rates of  $10\text{-}30\mu\text{m/h}$  were obtained in the temperatures of  $1750\text{-}1900^\circ\text{C}$ . The doping level was  $5\text{-}7\times 10^{15}\text{cm}^{-3}$  range.

A unique planetary SiC-CVD reactor for multi-wafer epitaxial growth has been designed for atmospheric and reduced pressure operation at temperatures up to and exceeding  $1600^\circ\text{C}$  [20]. Specular epitaxial layers have been grown at growth rates of  $3\text{-}5\mu\text{m/h}$ , and the thickest layer was  $42\mu\text{m}$ . The minimum unintentional doping was  $1\times 10^{15}\text{cm}^{-3}$  with an electron mobility of  $1000\text{cm}^2/\text{Vs}$ . Intrawafer thickness and doping uniformities of 4 and 7% have been obtained on 35mm diameter, and 3% thickness uniformity on 50mm diameter.

A vertical cold-wall reactor for a single wafer has been used to grow SiC with high purity and crystal quality [21]. The process temperature was up to  $1600^\circ\text{C}$  using rf heating of a bell-jar-like graphite susceptor with a flat pancake coil. The susceptor and attached sample holder are usually rotated with a speed of 800rpm to stabilize the gas flow. A background impurity level below  $10^{14}\text{cm}^{-3}$  (p-type) was obtained with a growth rate of  $5\text{-}6\mu\text{m/h}$ . The thickness uniformity was within 5% across the 35mm diameter.

A new trial to obtain thick epitaxial layers with a very high growth rate has been demonstrated by using a concept of high-temperature CVD [22]. This feature is particularly important in the power device field for large device sizes which require large quantity of high-quality substrates. Growth rates of  $10\text{-}500\mu\text{m/h}$  have been demonstrated at temperatures between  $1800\text{-}2300^\circ\text{C}$ . Applying this technique to the growth of SiC boule has been started.

## 7. Future prospect

So far, concerned with epitaxial growth, off-axis SiC{0001} wafers with several degrees have been employed for homoepitaxial growth. SiC{0001} wafers, however, contain micropipes along <0001>, which tend to be replicated from substrates to epitaxial layers. Since micropipes affect significantly the device performance, they are thought to be a particularly serious threat for large-scale production of SiC devices. To avoid extending of micropipes into epilayers, SiC homoepitaxial growth on (1-100) and (11-20) is promising, since those faces are parallel to <0001> and do not have a micropipe in a plane. In the epitaxial growth on (11-20) and (1-100), the presence of misfit attributed to the doping difference between the epitaxial layer and the substrate has brought a wide FWHM of X-ray diffraction [23]. In the epitaxial growth on (11-20), the C/Si ratio dependence of impurity incorporation is between the cases on Si- and C-faces [24].

4H-SiC epitaxial growth on 4H-SiC substrates with the (11-20) faces has been successfully carried out [25]. An extremely smooth surface can be obtained on (11-20) without macro steps (step bunching), large triangular defects and carrot-like defects, which are quite often observed in epilayers on the (0001) face. The surface roughness is as small as  $0.18\text{nm}$ . A typical surface defect is a small elongated shallow depression. The surface defect area defined by the ratio of defective area to the total area is as small as 0.010%, whereas it is 0.16% for epilayers on the (0001) face with an off-angle of  $8^\circ$ .

The epitaxial growth on (11-20) becomes very important, since the small channel mobility in the (0001) face of 4H-SiC can be dramatically improved by using the (11-20) face [26].

### Summary

An overview of SiC crystal growth was given for bulk and epitaxial growth. The feature of step-controlled epitaxy was described together with an inherent problem of step bunching. Trials for production-oriented crystal growth techniques were introduced.

### Acknowledgement

The author is indebted to Dr. T.Kimoto for completing this article. The work done in the author's group has been supported by a Grant-in Aid for Specially Promoted Research, No. 09102009, from the Ministry of Education, Science, Sports and Culture of Japan.

### References

- [1] Yu.M.Tairov and V.F.Tsvetkov, *J. Crystal Growth* 43(2) (1978), p.209.
- [2] N.Kuroda, K.Shibahara, W.S.Yoo, S.Nishino, and H.Matsunami, *Ext. Abstr. 19th Conf. on Solid State Devices and Mater.* (1987), p.227.
- [3] V.Tsvetkov, R.Glass, D.Henshall, D.Asbury, and C.H.Carter, Jr., *Mater. Sci. Forum* 264-268 (1998), p.3.
- [4] G.Augstine, H.McD.Hobgood, V.Balakrishna, G.T.Dunne, R.H.Hopkins, R.N.Thomas, W.A.Doolittle, and A.Rohatgi, *Mater. Sci. Forum* 264-268 (1998), p.9.
- [5] J.Takahashi, M.Kanaya, and Y.Fujiwara, *J. Cryst. Growth* 135 (1994), p.61.
- [6] J.Takahashi, N.Ohtani, M.Katsuno, and S.Shinoyama, *Mater. Sci. Forum* 264-268 (1998), p.25.
- [7] H.Matsunami, S.Nishino, and H.Ono, *IEEE Trans. Electron Devices*, ED-28 (1981), p.1235.
- [8] K.Yagi and H.Nagasawa, *Mater. Sci. Forum* 264-268 (1998), p.191.
- [9] Y.Ishida, T.Takahashi, H.Okumura, S.Yoshida, and T.Sekigawa, *Jpn. J. Appl. Phys.* 36 (1997), p.6633.
- [10] V.J.Jennings, A.Sommer, and H.Chang, *J. Electrochem. Soc.* 113 (1966), p.728.
- [11] H.Matsunami and T.Kimoto, *Mater. Sci. and Eng. R20* (1997), p.125.
- [12] T.Kimoto, H.Nishino, W.S.Yoo, and H.Matsunami, *J. Appl. Phys.* 73 (1993) p.726.
- [13] T.Kimoto and H.Matsunami, *J. Appl. Phys.* 75 (1994), p.850.
- [14] T.Kimoto, A.Itoh, and H.Matsunami, *Appl. Phys. Lett.* 66 (1995), p.3645.
- [15] Z.Y.Chen, N.Onojima, T.Kimoto, and H.Matsunami, submitted to *Jpn. J. Appl. Phys.*
- [16] D.J.Larkin, *phys. stat. sol. (b)* 202 (1997), p.305.
- [17] O.Kordina, A.Henry, E.Janzen, and C.H.Carter, Jr., *Mater. Sci. Forum* 264-268 (1998), p.97.
- [18] O.Kordina, K.Irvine, J.Sumakeris, H.S.Kong, M.J.Paisley, and C.H.Carter, Jr., *Mater. Sci. Forum* 264-268 (1998), p.107.
- [19] A.Ellison, J.Zhang, J.Peterson, A.Henry, P.Bergman, Y.Makarov, S.Elvstrom, A.Vehanen, and E.Janzen, *Abstracts of ECSCRM'98* (1998), p.25.
- [20] A.A.Burk, Jr., M.J.O'Loughlin, and S.S.Mani, *Mater. Sci. Forum* 264-268 (1998), p.83.
- [21] R.Rupp, A.Wiedenhof, P.Friedrichs, D.Peters, A.Schomer, and D.Stephani, *Mater. Sci. Forum* 264-268 (1998), p.89.
- [22] O.Kordina, C.Hallin, A.Ellison, A.S.Bakin, I.G.Ivanov, A.Henry, R.Yakimova, M.Tuominen, A.Vehanen, and E.Janzen, *Appl. Phys. Lett.* 69 (1996), p.1456.
- [23] C.Hallin, A.Ellison, I.G.Ivanov, A.Henry, N.T.Son, and E.Janzen, *Mater. Sci. Forum* 264-268 (1998), p.123.
- [24] T.Yamamoto, T.Kimoto and H.Matsunami *Mater. Sci. Forum* 264-268 (1998), p.111.
- [25] T.Kimoto, T.Yamamoto, Z.Y.Chen, H.Yano, and H.Matsunami, *this conf. Proc.*, p. 189
- [26] H.Yano, T.Hirao, T.Kimoto, H.Matsunami, K.Asano, and Y.Sugawara, *this conf. Proc.*, p. 1105

## Fast SiC Epitaxial Growth in a Chimney CVD Reactor and HTCVD Crystal Growth Developments

A. Ellison<sup>1</sup>, J. Zhang<sup>1</sup>, W. Magnusson<sup>2</sup>, A. Henry<sup>1,2</sup>, Q. Wahab<sup>1</sup>,  
J.P. Bergman<sup>1,2</sup>, C. Hemmingsson<sup>3</sup>, N.T. Son<sup>1</sup> and E. Janzén<sup>1</sup>

<sup>1</sup> IFM, Linköping University, SE-581 83 Linköping, Sweden

<sup>2</sup> ABB Corporate Research, SE-721 78 Västerås, Sweden

<sup>3</sup> Okmetic AB, c/o Linköping University, SE-581 83 Linköping, Sweden

**Keywords:** Chimney, CVD, Defect Density, Growth Process, High Resistivity, HTCVD, Purity, Vertical Hot-Wall Reactor

**Abstract.** The epitaxial growth of SiC is investigated in a CVD process based on a vertical hot-wall, or "chimney", reactor geometry. Carried out at increased temperatures (1650 to 1850 °C) and concentrations of reactants, the growth process enables epitaxial rates ranging from 10 to 50 µm/h. The growth rate is shown to be influenced by two competing processes: the supply of growth species in the presence of homogeneous gas-phase nucleation, and, the etching effect of the hydrogen carrier gas. The quality of thick (20 to 100 µm) low-doped 4H-SiC epitaxial layers grown at rates ranging between 10 and 25 µm/h are discussed in terms of thickness uniformity, surface morphology and purity. The feasibility of high voltage Schottky rectifiers ( $V_{BR}$  from 2 to ~3.8 kV) on as-grown chimney CVD epilayers is reported.

In a second part, recent developments of the High Temperature Chemical Vapor Deposition (HTCVD) technique for SiC crystal growth are described. Using pure gases ( $\text{SiH}_4$  and  $\text{C}_2\text{H}_4$ ) as source material and growth temperatures of 2100-2300 °C, this technique enables at present growth rates ranging from 0.4 to 0.8 mm/h. 6H and 4H-SiC crystals of thickness up to 7 mm and diameters up to 40 mm have been grown. We report micropipe densities of ~80 cm<sup>-2</sup> over areas of 0.5 cm<sup>2</sup> in 35 mm diameter 4H-SiC wafers sliced from HTCVD grown crystals. Undoped wafer demonstrators exhibit semi-insulating behavior with a bulk resistivity higher than  $7 \cdot 10^9 \Omega \text{ cm}$  at room temperature.

### 1. Introduction

State-of-the-art silicon carbide (SiC) device structures are currently essentially grown by Chemical Vapour Deposition (CVD) techniques, as demonstrated by small-area microwave components and power rectifiers exceeding the performances and capabilities of their GaAs and Si counter-parts. The availability of substrates with increasing diameter and quality [1] is in turn triggering higher demands on the epitaxial process, namely in terms of throughput. In a first part of this paper, we present a CVD process enabling growth of 4H-SiC epilayers with deposition rates ranging from 10 to 50 µm/h. Carried out in a chimney reactor, a geometry by principle well suited for both increased capacity and growth temperatures, this process enables a material quality comparable to the one of more established SiC CVD techniques for growth rates ranging up to ~25 µm/h.

In a second part of this paper, we report the development of a seeded vapor phase growth technique, generically described as High Temperature CVD (HTCVD) [2, 3]. Carried out at temperatures ranging from 2100 to 2300 °C and using gas precursors (silane and ethylene diluted in a helium carrier gas), the HTCVD method is essentially a CVD technique. However, the thermal environment and the growth rates achievable in this technique are to a large extent closer to the conventional physical vapor transport (PVT) method which is today used for the commercial fabrication of SiC wafers. We here report the main results of the HTCVD process and the related structural and electrical properties of 4H wafer demonstrators.

## 2. Epitaxial growth results: the chimney CVD reactor

The chimney reactor uses a vertical, symmetric, hot-wall geometry where the process gases are introduced at the bottom of the reaction cell. The reactants (silane and ethylene), mixed in a pure hydrogen carrier gas, are hence distributed upwards through a vertical channel formed by a rectangular opening in a SiC-coated susceptor [3]. The typical growth temperatures range from 1650 to 1850 °C. Although the chimney geometry offers a fully symmetric structure with respect to the gas flow profile, the substrates (4H, 8° off-axis) were in this stage mounted only along one side of the vertical channel.

### 2.1 Rate determining steps and uniformity

The growth process is here first described in a small-scale system where a susceptor without tapering was used. As shown in Fig. 1, when the  $C_2H_4$  flow rate is increased at fixed silane supply, the growth rate first increases sharply for C/Si ratios ranging between 0.1 and 0.4, then saturates at a nearly constant value. At the growth temperature used here, no significant difference is observed whether growth is carried out on C- or Si-face substrates (Fig. 1). This indicates that the growth regime becomes Si-supply limited for C/Si ratios higher than ~0.4, a result similar to the one reported for one order of magnitude lower growth rates in a cold-wall CVD process carried out at 1500 °C [4]. Because a Si-supply limited regime is obtained at C/Si ratios higher than 0.4, the leading parameter controlling the growth rate is expected to be the silane feed rate. Under otherwise optimal conditions, increasing the  $SiH_4$  flow rate or partial pressure, while keeping a constant C/Si, enables indeed a growth rate variation between 10 and 50  $\mu\text{m/h}$  (Fig. 2).

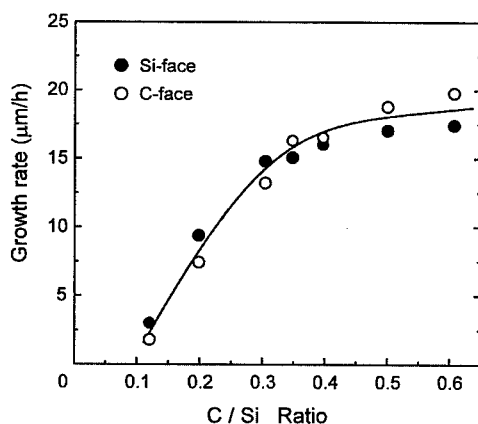


**Fig. 1** Growth rate dependence on C/Si ratio at a fixed  $SiH_4$  flow rate of 12.2 ml/min at 1730 °C and 210 mbar. The closed and open circles refer to mean growth rates with a carrier flow of 3.4 l/min, on Si-face and C-face off-axis substrates, respectively.

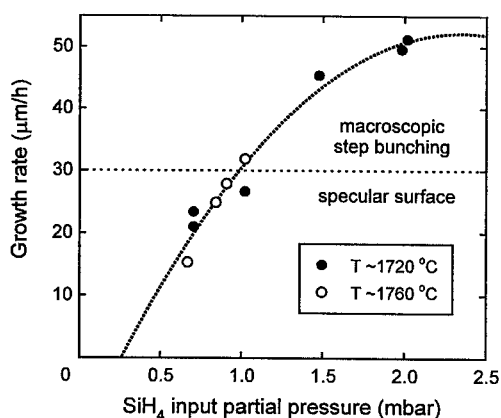


**Fig. 2** Growth rate dependence on input silane partial pressure at fixed C/Si = 0.55. The horizontal line at 30  $\mu\text{m/h}$  represents the upper growth rate limit within which, 30 to 80  $\mu\text{m}$  thick Si-face epilayers with specular surface morphology have been obtained under otherwise optimized conditions.

At a given supply of source gases, the most important parameter determining both the growth rate and the surface morphology is the process temperature. The reciprocal temperature dependence plotted in Fig. 3 reveals that growth can proceed within two main regimes: in the 1650 to 1775 °C temperature range, the growth rate increases with an apparent activation energy of ~44 kcal/mol, whereas higher growth temperatures lead to a decrease of the growth rate. Within this second regime, the net growth rate is reduced by an enhanced competing hydrogen etching of the growing SiC surface, as further discussed in [5]. Within the first regime, the activation energy is surface polarity independent (Fig. 3), indicating that surface kinetics are not the main rate limiting step in the present system. Being one order of magnitude higher than the one reported in Si mass-transport limited cold-wall CVD [4], this activation energy shall relate to a process limiting the supply of Si-vapor in the gas-phase. Further,

experimental results [5] indicate that the homogeneous nucleation of the silane precursor into  $\text{Si}_x$  clusters or droplets at the entrance of the susceptor mainly accounts for this rate limiting step. In particular, we experimentally determined the clusters evaporation process to be thermally activated with an apparent activation energy close to  $\sim 56$  kcal/mol [5]. At C/Si ratios higher than 0.4 (Fig. 1), the growth rate becomes essentially Si-species supply limited (Fig. 2) where higher growth temperatures increase the release of Si vapor from the  $\text{Si}_x$  clusters (Fig. 3). In turn, lower temperatures can introduce retarding effects in the gas phase nucleation chemistry, which will affect the growth rate uniformity. As shown by the arrows in Fig. 3, with decreasing temperature, the deposition uniformity is indeed observed to gradually shift from *depletion* towards an *increase* of the growth rate along the gas flow direction. Within this latter case, homogeneous nucleation thus plays a similar role to the "cold-finger" effect encountered in horizontal cold-wall CVD reactors, by acting as a reservoir for the reactants, which are gradually released from the nucleated clusters as they pass through the susceptor. This reduces depletion effects until sufficiently high temperatures ( $\sim 1750$  °C in Fig. 3), and growth rates, in turn enhance the hydrocarbon consumption. Within this depletion regime, the uniformity is improved with decreased growth pressures or increased carrier flows [5], an approach which remains meaningful in the chimney system as long as the corresponding etching rate does not noticeably influence the growth rate. N-type epilayers over 100  $\mu\text{m}$  thick with a thickness uniformity of 5% have been grown at 23  $\mu\text{m}/\text{h}$  in a small scale susceptor. Although this uniformity is one of the best reached for thick epilayers in a small scale susceptor, it corresponds to the ones obtained under optimised conditions for relatively thinner epilayers (30-40  $\mu\text{m}$ ), which demonstrates the stability of the growth process. Results in an upscaled system show that the thickness uniformity is noticeably improved (5% or less over 35 mm wafers, Fig. 4).

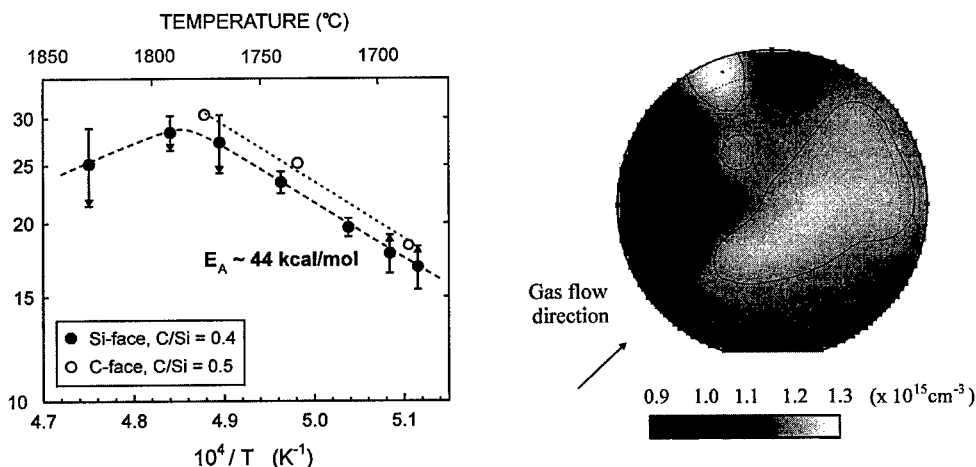


**Fig. 3** Growth rate dependence on temperature for Si-face (closed circles) and C-face (open circles) off-axis 4H epilayers. The closed circles denote the mean growth rate along a 35 mm length from the leading edge and the error bar the corresponding standard deviation. The arrows are pointed upwards for an epilayer thickness increasing along the gas flow direction, and downwards in the opposite case.

**Fig. 4** Doping map of an intentionally doped 32  $\mu\text{m}$  thick epilayer grown at 16  $\mu\text{m}/\text{h}$  on a Si-face 35 mm diameter substrate. The doping and the thickness uniformity are better than 5 % as determined by non destructive PL and FTIR measurements, respectively.

## 2.2 Material properties: morphology, doping and device characteristics

**Morphology** The device application driven need of specular epitaxial layers of thickness exceeding 50  $\mu\text{m}$ , requires that the stability of the step-flow mode is kept throughout the growth. Under the increased reactant concentrations used in the present process, surface roughening is observed to depend more on

epilayer thickness and growth conditions than on the growth rate ( $R \leq 30 \mu\text{m/h}$  in Fig. 1). As presented in [6], surface roughening effects are enhanced under too C-rich conditions or low temperatures. The best surface morphology is reached under growth conditions where the thickness uniformity is controlled by depletion of the reactants along the gas flow direction and a weak  $\text{H}_2$  etching. Under these conditions, stable growth without macroscopic step-bunching is achieved, with step heights on Si-face epilayers (thickness up to  $80 \mu\text{m}$ ) ranging from 0.5 to 2 nm [6]. In the absence of macroscopic step bunching or preferential  $\text{H}_2$  etching at e.g. screw dislocations, epilayers grown at rates ranging from 15 to  $25 \mu\text{m/h}$  are mainly characterized by growth pits related to the initial growth stages. In upscaled susceptors with improved thermal and flow distributions, preliminary optimizations enable at present surface defect free areas of  $\frac{1}{2} \text{cm}^2$ .

**Purity and doping** The lowest n-type doping realised at growth rates up to  $25 \mu\text{m/h}$  are in our research reactor of  $\sim 6 \cdot 10^{13} \text{cm}^{-3}$  and  $\sim 4 \cdot 10^{14} \text{cm}^{-3}$  on Si- and C-face 4H layers, respectively, as determined both by CV and PL measurements. In a well conditioned system, SIMS measurements indicate that the concentrations of impurities, such as Ti, V, B or Al, are all below detection limits (high  $10^{13} \text{cm}^{-3}$  for e.g. boron). Characterization of Si-face epilayers grown at temperatures up to  $\sim 1800^\circ\text{C}$  (either undoped or intentionally doped in the  $10^{15} \text{cm}^{-3}$  range) by DLTS reveals a low concentration of Ti and the  $Z_1$  electron traps, typically between  $1.6$  to  $7 \cdot 10^{12} \text{cm}^{-3}$  and  $0.5$  to  $2 \cdot 10^{13} \text{cm}^{-3}$ , respectively. Under intentional n-type doping levels from the mid  $10^{14}$  to  $10^{19} \text{cm}^{-3}$ , the nitrogen incorporation in the chimney process increases exponentially with temperature, as long as the growth regime is reactant supply limited. This result differs from the one reported by other groups [e.g. 7] and is here related to the decrease of the effective C/Si ratio with the enhanced evaporation of  $\text{Si}_x$  clusters. In the presence of additional site competition effects influenced by the depletion of the hydrocarbon precursor, achieving doping uniformity lower than 5% (Fig. 4) requires attention to be paid to the uniformity of the gas flow pattern and susceptor temperature distribution.

**Schottky device characteristics.** In order to assess the breakdown behavior of as-grown chimney epilayers, Schottky structures were processed on a  $42 \mu\text{m}$  thick,  $\sim 5 \cdot 10^{14} \text{cm}^{-3}$  layer (growth rate  $20 \mu\text{m/h}$ ). As presented in [8], the measured breakdown voltages ranged from 2 up to 3.85 kV, with an increasing yield for smaller diameter devices. The typical leakage current densities at 1 and 2 kV were as low as  $10^{-6}$  and  $10^{-5} \text{A/cm}^2$  for diodes with diameter ranging from 0.3 to 1 mm.

### 3. SiC crystal growth developments in High Temperature CVD

#### 3.1 Main aspects of the HTCVD growth process

The HTCVD system is based on an inverted vertical open reactor geometry where the process gases are distributed upwards, through an axis-symmetric heating zone, to a seed-crystal holder [2,3]. Achieving growth rates of interest for crystal growth applications requires substantially increased feed rates of the precursor gases. As in the chimney reactor, in a first phase, *condensation* of the silane precursor by-products into  $\text{Si}_x$  clusters takes place in the entrance of the hot-zone. Within the inert helium carrier gas ambient,  $\text{Si}_x$  clusters can further chemically interact with the  $\text{C}_2\text{H}_4$  precursor or its by-products, leading to a thermally more stable  $\text{Si}_x\text{-C}_y$  clusters mixture [5]. The axial temperature distribution in the growth chamber is thus established so that, in a second phase, as the clusters pass through a heating zone, their temperature is raised high enough to favor their *sublimation*. The release of part or all of the Si- and C-containing vapor species into the gas phase thereby provides the driving force for the crystallization at the seed holder, maintained at a lower temperature. The actual HTCVD process may thus conveniently be interpreted as a Gas Fed Sublimation (GFS) process, where the source material is directly synthesized from pure gases and subsequently evaporated into active species transported by e.g. the carrier gas to the SiC seed crystal.

Within a lower temperature range, the growth rate is therefore partially limited by the evaporation of  $\text{Si}_x\text{-C}_y$  clusters, with activation energies of the order of 95 kcal/mol [3]. Optimizing the temperature distribution and minimizing the interaction with the graphite environment [5] has enabled to lower this activation energy to  $\sim 60$  kcal/mol. In the higher temperature range ( $T \sim 2200^\circ\text{C}$ ) a smoother temperature dependence of the growth rate is obtained, which can be ascribed to a mass-transport controlled regime

where the growth rate is influenced by the temperature gradient applied to the seed holder. The growth of up to 7 mm thick 6H-SiC crystals on Si-face Lely seeds with an average growth rate of 0.45 mm/h has previously been reported [3]. As in PVT growth, stable growth of the 4H polytype is in our process found to require C-face seeds, preferably of the 4H polytype. The optimization of the growth process for larger area 4H seeds enables at present growth rates ranging from 0.5 to 0.8 mm/h. Crystals of length about  $\frac{1}{2}$  cm and diameter up to 40 mm have been grown, from which three to five useful wafers can be sliced (Fig. 5).

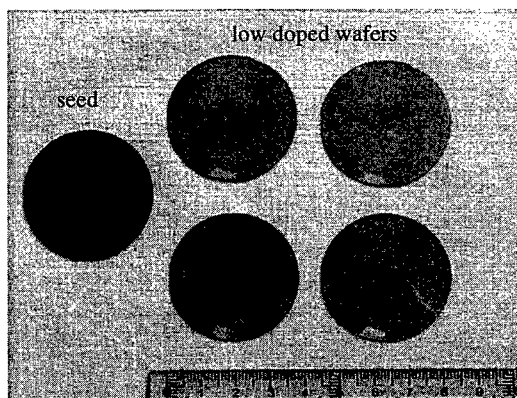


Fig. 5 38 mm diameter low doped wafers (right) sliced from a crystal grown at 0.6 mm/h on a 4H  $n^+$  seed (left).

### 3.2 Structural and electrical properties of 4H wafer demonstrators

**Polytype stability** Owing to the high growth rates and temperatures involved in the process, the parameters affecting the polytype stability are somewhat similar to the ones reported in seeded sublimation growth. In HTCVD, successful growth of 4H crystals requires attention to be paid to the initial stages of the growth, to possible process instabilities related to the growth temperature control or the precursors supply rate, and to the gas phase stoichiometry. In particular, the use of too low gas feed C/Si ratios favors an unwanted 4H to 6H polytype transformation during the first millimeter of the growth. This may be related to the observation that the deviation from stoichiometry and the silicon content in SiC polytypes decreases with increasing hexagonality [9].

**Structural characterization** Issues relating to the defect density and structural quality of the grown material have recently been addressed. Micropipe defect mapping of double side polished wafers was performed by optical microscopy under polarised light using magnifications of 100 to 400 and verified by selective KOH etching. In substrates sliced from 4H crystals grown at rates ranging from 0.5 to 0.6 mm/h, we have observed mainly three types of hollow-core defects, which we do not relate directly to re-crystallisation processes. The first ones are small diameter ( $\varnothing < 1 \mu\text{m}$ ) micropipes lying nearly parallel to the c-axis that can be related hollow-core super-screw dislocations [10]. The second ones are oblique micropipes [10] with a diameter of the order of  $1 \mu\text{m}$ . These can be isolated within a small region of the crystal, however they are often clustered with local densities, ranging in the worst cases above  $1000 \text{ cm}^{-2}$  as measured over areas of  $1 \text{ mm}^2$ . The formation mechanisms associated to such micropipes may be associated to the entrapment of obstacles introduced by system instabilities or by the condensation of Si-droplets on the growing surface. The third type of hollow defects are basal plane defects (not related to secondary evaporation) and occur preferentially under higher thermal gradients and Si-rich growth conditions. Although these results are preliminary, and the defects mentioned above occur in various extent in our process, we have been able to grow 5 mm thick crystals leading to 35 mm diameter substrates having areas slightly larger than  $\frac{1}{2} \text{ cm}^2$  with an averaged micropipe density of  $80 \text{ cm}^{-2}$  (Fig. 6). Regions with low defect density exhibit a good crystal quality with X-ray diffraction (0004) rocking curves having a FWHM of  $22''$ , recorded over an area of  $15 \text{ mm}^2$ .

**Purity and electrical properties** The residual doping in 4H-SiC is p-type like, mainly due to the boron acceptor with an atomic concentration typically in the mid  $10^{15} \text{ cm}^{-3}$  range, as determined by SIMS measurements. At growth rates above 0.4 mm/h, the incorporation of nitrogen on C-face seeds can range down to the low  $10^{15} \text{ cm}^{-3}$  levels. Resistivity measurements using annealed Ni contacts were performed on wafers prepared from undoped crystals. The contact resistance was estimated by the Cox-Strack method and the bulk resistivity was determined from the slope of the I-V characteristics measured in the 100-700 V range. At room temperature, the extrapolated resistivity is higher than  $7 \cdot 10^9 \Omega \text{ cm}$  in the



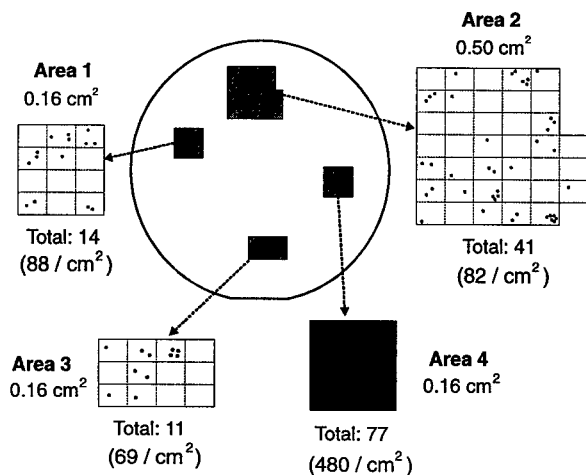


**Fig. 6** Micropipe distribution over a 35 mm 4H wafer (95% of the surface) sliced from the top of a 4 mm thick crystal grown at 0.55 mm/h. The averaged density of micropipes and basal plane defects is of  $\sim 450 \text{ cm}^{-2}$  over the full wafer, with areas having micropipe density less than  $80 \text{ cm}^{-2}$ , the largest one being of  $\sim 0.5 \text{ cm}^2$ .

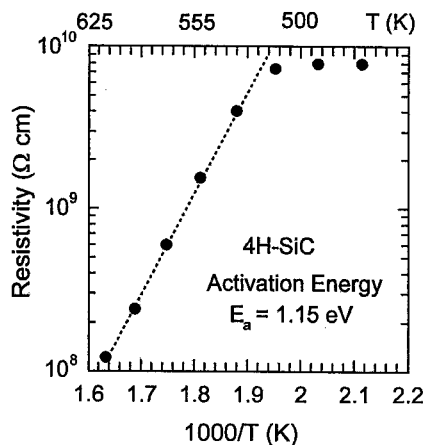


**Fig. 7** Resistivity measured on a 30 mm 4H wafer sliced from an undoped crystal with vanadium concentration below SIMS detection limit.

regions of good crystalline quality (Fig. 7), which is comparable to the values reported in [10] for V-doped SiC. Here, although a linear fit over the high temperature range yields an activation energy of about 1.15 eV (Fig. 7), a value very close to the 1.18 eV given in [10], the high resistivity of undoped HTCVD wafers may not be related to a vanadium deep level, but possibly to an intrinsic defect or complex: SIMS measurements carried out on this specific wafer showed a residual vanadium concentration lower than  $10^{13} \text{ cm}^{-3}$ .

### Acknowledgements

The authors wish to thank Mr. J. Peterson, B. Magnusson, P.-O. Narfgren, L. Storasta and Dr. E. Sörman for their valuable contributions. This work was supported by Okmetic, ABB Corporate Research, the SSF-SiCEP programme, NUTEK and the European Union (Brite Euram contract No. BRPR-CT98-0815 and TMR Marie Curie contract No. ERBFMBICT960728).

### References

- [1] V. Tsvetkov, R. Glass, D. Henshall, D. Asbury and C. H. Carter, Jr., *Mat. Sci. Forum* Vol. 264-268 (1998), pp. 3-8.
- [2] O. Kordina, C. Hallin, A. Ellison, A.S. Bakin, I.G. Ivanov, A. Henry, R. Yakimova, M. Tuominen, A. Vehanen and E. Janzén, *Appl. Phys. Lett.*, Vol 69(10) (1996) pp. 1456-1458.
- [3] A. Ellison, J. Zhang, J. Peterson, A. Henry, Q. Wahab, J. P. Bergman, Y. N. Makarov, A. Vorob'ev, A. Vehanen and E. Janzén, *Mat. Sci. Eng.* Vol. B61-62 (1999), pp. 113-120.
- [4] H. Matsunami and T. Kimoto, *Mat. Science. Eng.* R20, No. 3 (1997), pp. 125-166.
- [5] A. Ellison, PhD thesis, Diss. No. 510 Linköping University, Linköping, Sweden (1999).
- [6] J. Zhang, A. Ellison and E. Janzén, these proceedings, p. 137
- [7] T. Yamamoto, T. Kimoto and H. Matsunami, *Mat. Sci. Forum* Vols 264-268 (1998), pp. 111-114.
- [8] Q. Wahab, A. Ellison, J. Zhang, U. Forsberg, E. Duranova, A. Henry and E. Janzén, these proceedings.
- [9] Y. M. Tairov and V. F. Tsvetkov, in "Growth and characterisation of polytypic crystals", Ed. by P. Krishna, Pergamon Press, London (1983), pp. 111-161.
- [10] G. Augustine, D. McD. Hobgood, V. Balakrishna, G. Dunne and R. H. Hopkins, *phys. stat. sol. (b)* 202 (1997), pp. 137-148.

## Morphology Control for Growth of Thick Epitaxial 4H SiC Layers

J. Zhang, A. Ellison and E. Janzén

Dept. of Physics and Measurement Technology, Linköping University,  
SE-581 83 Linköping, Sweden

**Keywords:** Chimney CVD, Morphology, SiC Epitaxy, Step Bunching, Surface Roughness

### Abstract

A study of morphology control is conducted on 4H SiC Si- and C-face epilayers grown in a chimney CVD reactor. The macroscopic step-bunching and the defect evolution processes with increasing epilayer thickness are investigated in order to achieve smooth surface morphology for thick epilayers of 30 – 120  $\mu\text{m}$ . The growth temperature and input precursor concentrations are observed to have strong impact on the surface morphology.

### 1. Introduction and background

4H SiC has shown great potential for high-power and high-temperature electronics applications. For high-voltage devices, low-doped thick epilayers are required. A smooth surface of the active layer is essential for the compatibility with device processing and for ensuring device performance. Generally the morphological defects can be classified as substrate related or as induced during the epitaxial growth. The former includes micropipes, dislocations and polishing related defects on the substrate surface and the latter mainly refers to pit-like defects and macroscopic step-bunching. With the continuous progress in both bulk and epitaxial SiC growth, specular epilayers with reduced defect density have been obtained [1, 2, 3]. The further investigation of common or special morphological defects and surface imperfections emerged in thick (30 – 120  $\mu\text{m}$ ) and low-doped (low  $10^{13}$  to low  $10^{16}$   $\text{cm}^{-3}$ ) epilayers is of interest from both the technological (high voltage device application) and the scientific (surface kinetics and growth mechanism) point of view.

### 2. Experimental

The epitaxial growth was performed in a small-scale chimney reactor (vertical hot-wall CVD) in the temperature range of 1650 – 1850  $^{\circ}\text{C}$ , with 10%  $\text{SiH}_4$  and 10%  $\text{C}_2\text{H}_4$  diluted in  $\text{H}_2$  as precursor gases and Pd-Ag purified  $\text{H}_2$  as carrier gas, which is described in more detail in [4]. Growth rates of 15 – 50  $\mu\text{m}/\text{h}$  and background N-doping of low  $10^{13}$  to low  $10^{16}$   $\text{cm}^{-3}$  are obtained in this system. Good morphology is achieved with growth rates up to 30  $\mu\text{m}/\text{h}$ . In order to study how the surface roughness and the localized defects evolve with the epilayer thickness, a set of two successive growth runs were performed at 1815  $^{\circ}\text{C}$  and 180 mbar, with *sample1* grown for 15min and *sample2* regrown on *sample1* for 1h. The surface morphology was investigated on each sample. The  $\text{H}_2$  and  $\text{SiH}_4$  flows were 3.2 l/min and 14.79 ml/min, respectively, and the C/Si ratio was 0.3. Both Si- and C-face substrates, cut 8 $^{\circ}$  off-axis towards the [11  $\bar{2}$  0] direction, have been used in this investigation.

Normaski Differential Interference Contrast Microscopy (NDIC) and Atomic Force Microscopy (AFM) with a nanoscope III from Digital Instruments were used to characterize the surface morphology. The surface roughness was estimated by the averaged macrostep height measured by an Alpha Step 500 Surface Profiler from Tencor Instruments, using a scan range of 500  $\mu\text{m}$  and scan rate of 20  $\mu\text{m}/\text{s}$ . The epilayer thickness was determined with Fourier Transform Infrared Spectrometry (FTIR) or by the observation of contrast difference of the cleaved cross section of the epilayers using either NDIC or Secondary Electron Microscopy (SEM).

### 3. Results and discussion

#### 3.1 Macroscopic step-bunching and Surface roughness

Step-bunching is well recognized on epilayers grown on off-oriented substrates. In SiC it is observed that 4H Si-face epilayers tend to form microscopic steps of 4 Si-C bilayer height while C-face epilayers are dominated by steps of 1 Si-C bilayer height [5]. More severe step-bunching occurs on thicker epilayers, leading eventually to macroscopic hill-valley morphology (rough surface), as depicted in Fig. 1(a) for a 74  $\mu\text{m}$  epilayer grown at 25  $\mu\text{m/h}$ . The inter-valley distance was 200 ~ 400 nm with the macrostep height of ~ 4 nm, as obtained by AFM section analysis. The systematic increase in surface roughness with increased thickness is represented by the plot of the surface roughness versus thickness in Fig. 2 for Si-face epilayers grown at two temperatures with C/Si ratio of 0.3 – 0.4. A high growth temperature is critical to avoid formation of macroscopic step-bunching under the growth conditions used here. At the low temperature range (1650 – 1750  $^{\circ}\text{C}$ ), the surface roughness increases drastically with increasing thickness, whereas at higher growth temperatures (1750 – 1850  $^{\circ}\text{C}$ ), the epilayer surface remains smooth with thickness up to 80  $\mu\text{m}$ , which is also shown by the AFM surface plot in Fig. 1(b). At a fixed growth temperature and C/Si ratio, the macroscopic step-bunching becomes more pronounced with increased input precursor partial pressure, as illustrated in Fig. 3. Our experimental results also suggest that an increased  $\text{SiH}_4$  flow under otherwise identical conditions, i.e. a decreased C/Si ratio, results in smoother surface.

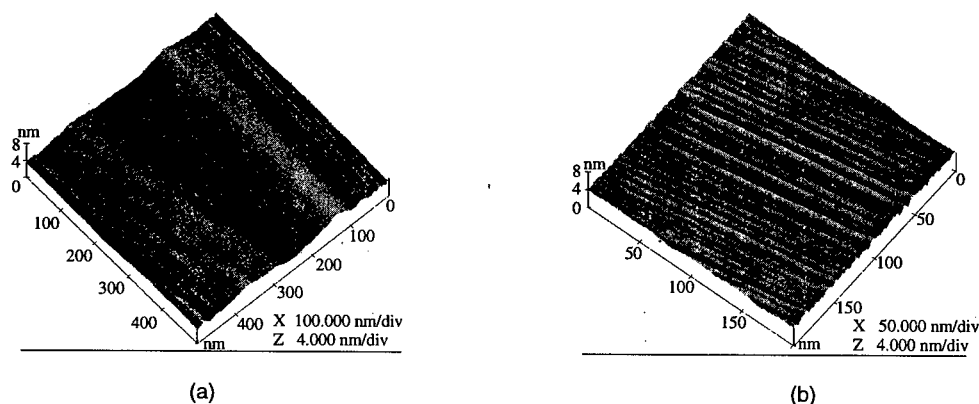


Fig. 1 (a) AFM surface plot of a 74  $\mu\text{m}$  epilayer with macroscopic step-bunching, grown at 1710  $^{\circ}\text{C}$ ; (b) AFM surface plot of an 80  $\mu\text{m}$  epilayer with smooth surface, grown at 1810  $^{\circ}\text{C}$ .

Step-bunching does occur on very thick C-face epilayers as well (see Fig. 2), but to much less extent, compared with Si-face epilayers grown under similar conditions. This result is consistent with the smaller height of microsteps (1 Si-C bilayer) on C-face compared with that of Si-face epilayers (4 Si-C bilayer), as discussed in [5], where 3.5 $^{\circ}$  off-oriented substrates were used.

In the step-flow controlled epitaxy, a smooth surface is maintained by the lateral step advancement through incorporation of growth species at the kink sites. However, inherent bunching of elementary steps occurs as a result of minimization of surface free energy [5]. As the Si-face exhibits higher free energy than the C-face [6], step-bunching is expected to be more enhanced on the Si-face. Once step-bunching has occurred, it continues with increasingly higher speed during the growth, as the lateral step growth rate is inversely proportional to the step height [5]. Step-bunching is strongly affected by growth parameters. Conditions that increase surface diffusion length of the growth species, such as higher substrate temperature or lower C/Si ratio [5], are expected to result in less step-bunched surface. A high incident flux of growth species as a consequence of the high precursor partial pressure leads to decreased diffusion length, thereby increasing step-bunching.

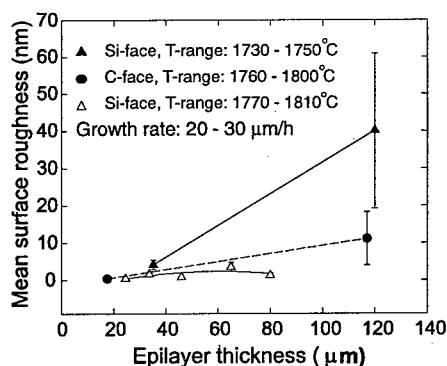


Fig. 2 Plot of the mean surface roughness as a function of epilayer thickness for both Si- and C-face samples.

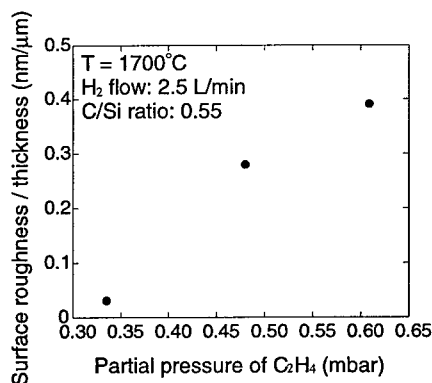


Fig. 3 Surface roughness normalized to epilayer thickness plotted as a function of the partial pressure of  $\text{C}_2\text{H}_4$  at constant C/Si ratio.

### 3.2 Morphological defects: formation and evolution

The morphological defects in the chimney grown Si-face epilayers are either related to preferential  $\text{H}_2$  etching (etch pits) or induced by obstacles during the epitaxial growth (growth pits). The typical etch pits are illustrated in Fig. 4. Molten KOH etching revealed that these defects were induced by  $\text{H}_2$  preferential etching at screw dislocations [4]. Noteworthy are the etch stripes observed at the down-step end of the pits. The AFM section analysis (Fig. 4(b)) of an etch pit reveals it as an irregularly shaped hole with a depth of  $\sim 80$  nm and an extension of 10  $\mu\text{m}$ . The etch stripes are revealed as ditches of  $\sim 20$  nm in depth and 200 nm in width. These etch pits are typically observed under the combination of low temperatures (1650 – 1750  $^\circ\text{C}$ ) and high C/Si ratios ( $> 0.5$ ). Under these conditions homogeneous gas phase nucleation is facilitated [4], giving rise to less amount of available vapour growth species and the  $\text{H}_2$  preferential etching at screw dislocations may therefore be favoured.

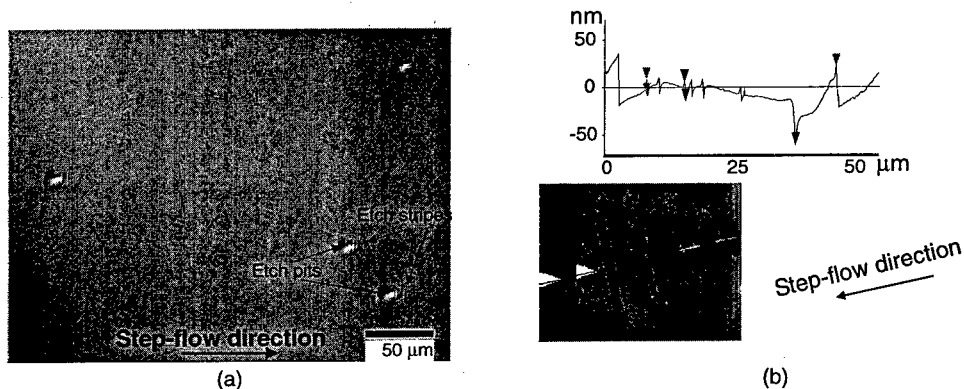


Fig. 4 Etch pits observed under conditions of low temperature and high C/Si ratio. The epilayer thickness is 46  $\mu\text{m}$ . (a) NDIC photograph; (b) AFM section analysis of an etch pit and the associated etch stripes.

The growth pits, classified as wavy and half-moon pits in [4], are more frequently observed on epilayers grown at high temperatures and low C/Si ratio. These defects were not associated with hexagonal etch pits after molten KOH etching. Fig. 5 (a) and (b) display the defects observed in the same area of the successively grown epilayers: *sample1* and *sample2*, respectively. It is shown that almost all the defects observed in *sample1* are also present in *sample2*, but with increased size and have developed to wavy pits, as a consequence of the enlargement of defects with the step-flow of the epitaxial growth. The pit density is essentially the same under the conditions leading to the formation of wavy pits. These wavy pits didn't give negative impact on the device characteristics in the investigated cases, and Schottky

diodes with breakdown voltage higher than 3.5 kV have been fabricated on our chimney-grown Si-face epilayers.

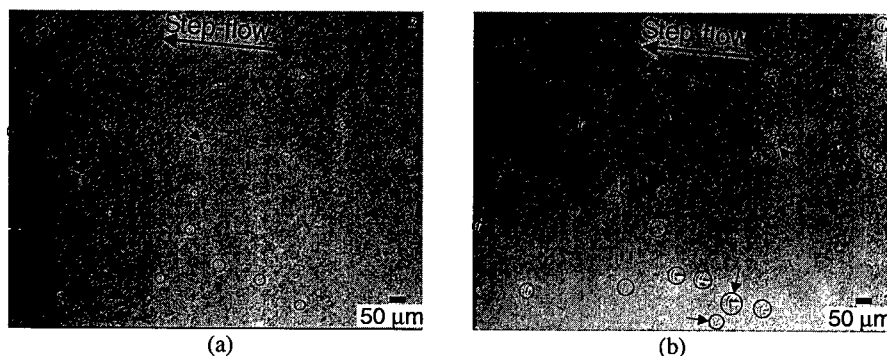


Fig. 5 NDIC photographs for the two epilayers successively grown at 1815 °C and 180 mbar. (a) *sample1* with thickness of 6 μm; (b) *sample2* with thickness of 27 μm. The common defects on the both samples are marked in circles, whereas defects observed only in one of the samples are pointed out with additional arrows.

One explanation for the unchanged density of wavy pits is that most of them are formed during the initial growth of the low-doped epilayer on the high-doped substrate. On the other hand, as the surface starts to become wavy with thickness under these growth conditions, the observation of any additional small defects becomes more difficult due to the surface waviness. At still higher temperatures, with the absence of H<sub>2</sub> preferential etching, surface diffusion is enhanced and the step-flow growth mode is more stable, resulting in half-moon pits (not shown here) from the smooth overgrowth at the obstacles.

#### 4. Conclusion

Increased macroscopic step-bunching with increasing thickness is observed on both Si- and C-face epilayers, with more pronounced effect on the Si-face. Careful adjustment of the growth conditions has enabled to minimize the step-bunching even on Si-face epilayers with thickness up to 80 μm. Increased growth temperature and SiH<sub>4</sub> flow while maintaining low precursor supersaturation lead to smoother surface morphology. The growth conditions dominated by either a stable step-flow growth mode or preferential H<sub>2</sub> etching determines the formation of etch pits or growth pits. Most of the growth pits are formed during the initial growth, possibly from the substrate-epilayer interface. The etch pits are related to preferential hydrogen etching at screw dislocations.

#### References

- [1] J. A. Powell and D. J. Larkin, *phys. stat. sol. (b)* 202 (1997), p. 529
- [2] C. Hallin, F. Owman, P. Mårtensson, A. Ellison, A. Konstantinov, O. Kordina and E. Janzén, *J. Cryst. Growth* 181 (1997), p. 241
- [3] O. Kordina, K. Irvine, J. Sumakeris, H. S. Kong, M. J. Paisley and C. H. Carter, Jr., *Materials Science Forum* 264-268 (1998), p. 107
- [4] A. Ellison, Doctoral thesis: Silicon Carbide Growth by high temperature CVD techniques, Dissertation No. 599, Linköping University, Sweden (1999)
- [5] T. Kimoto, Doctoral thesis: Step-Controlled Epitaxial Growth of α-SiC and Device Applications, Kyoto University, Japan (1995)
- [6] E. Pearson, T. Takai, T. Halicioglu and W. A. Tiller, *J. Cryst. Growth* 70 (1984), p. 33

Correspondence: Tel: +46 13 28 57 16, Fax: +46 13 14 23 37, e-mail: jizha@ifm.liu.se

## **Vertical Hot-Wall Type CVD for SiC Growth**

Kunimasa Takahashi, Masao Uchida, Makoto Kitabatake and  
Takeshi Uenoyama

Advanced Technology Research Laboratories, Matsushita Electric Industrial Co. Ltd.,  
Hikaridai 3-4, Seika-cho, Kyoto, 619-0237, Japan

**Keywords:** Epitaxial Growth, Pulse Doping, Pulse Valve, Vertical Hot-Wall Type CVD

**Abstract:** We propose new methods of SiC growth and doping; "Vertical hot-wall type CVD" for higher growth rate and lower background impurity, and "Pulse doping" for well-controlled doped layer. The CVD reactor was equipped with a graphite crucible in which the substrate was set surface-down. High growth rate of  $15 \mu\text{m/hr}$  was obtained at  $1700^\circ\text{C}$ . The background impurity concentration of the undoped epitaxial layer was less than  $10^{14} \text{cm}^{-3}$ . A pulse valve, which could open and close within very short period less than  $10 \mu\text{s}$ , was used to supply the dopant gases. Carrier concentrations of the doped layers were precisely controlled, and abrupt doping profiles were achieved by "Pulse doping".

### **1. Introduction**

The epitaxial growth of SiC is fundamental and principal for the SiC device processes. High performance SiC power devices require thick active layers with low background impurity.[1,2] Therefore, it is desirable that high quality SiC epitaxial layers are achieved with high growth rate. Moreover, it is necessary to precisely control the carrier concentrations and the profiles of the doped layers. In this study, we investigated the technologies of SiC growth and doping based on new concepts; "Vertical hot-wall type CVD" for higher growth rate and lower background impurity, and "Pulse doping" for well-controlled doped layer.

### **2. Experimental**

#### **2.1. Vertical Hot-Wall Type CVD**

Figure 1 shows a schematic drawing of the "Vertical hot-wall type CVD" reactor used in this study. The reactor was equipped with a crucible made of graphite in the quartz chamber. Out side of the crucible was surrounded by the heat insulators made of carbon felt. The substrate was set surface-down in the crucible heated by a radio frequency induced current. The source gases ( $\text{SiH}_4$  and  $\text{C}_3\text{H}_8$ ) and carrier gas ( $\text{H}_2$ ) flowed in from the bottom of the crucible and out from the top in consideration of the buoyancy of the gas flow in the high temperature region above  $1600^\circ\text{C}$ . These geometric features improved the uniformity of the gas flow on surface of the substrate. Moreover, the gases passed through the heated crucible before reaching the substrate, so that the gases on the substrate were efficiently cracked into the elements. Additionally, the hot-wall system inhibited the impurity contamination from the wall of the chamber.

## 2.2. Pulse Doping

In conventional doping process, the dopant gases are introduced into the reactor during the epitaxial growth, and the dopant gas flow is controlled by mass flow controller.[2,3] However, it is hard to precisely control a small dopant gas flow, especially less than  $10^{-1}$  sccm, to form the lower doped layer by the conventional doping method. Furthermore, the instability of the dopant gas flow makes it difficult to form an abrupt doping profile.

A new doping method, "Pulse doping", was developed using a pulse valve (solenoid valve) consists of actuator assembly, nozzle, and plunger for sealing against the nozzle. The valve is actuated by passing a current pulse through a solenoid, exerts a magnetic force on a ferromagnetic core material. The valve can open and close within very short period less than  $10 \mu\text{s}$ . The period of the valve open (on period) and the period of the valve close (off period) are separately controlled. The  $\text{N}_2$  gas as n-type dopant was injected into the reactor through the pulse valve. The primary pressure of the regulated  $\text{N}_2$  gas was fixed at  $1 \text{ kgf/cm}^2$ . The supply of small dopant gas injected into the reactor is controlled by varying on period.

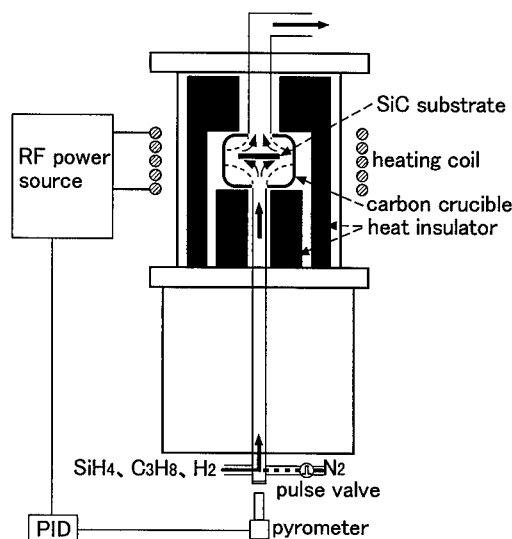


Fig. 1. Schematic drawing of the "Vertical hot-wall type CVD" reactor

## 3. Results and Discussion

### 3.1. Epitaxial Growth

Commercially available 6H- and 4H-SiC(0001) off-axis wafers were used for the substrates. Prior to introduction into the reactor, the substrates were wet-oxidized at  $1100^\circ\text{C}$  for 3 hours, then the  $400 \text{ \AA}$  oxide was removed by the buffered hydrofluoric acid solution. The treated substrate was set in the crucible, and the reactor was evacuated below  $10^{-6}$  Torr. The  $\text{H}_2$  carrier gas (2 slm) flow was introduced, and then the temperature was raised to the growth temperature. The growth temperature of the substrate measured by an optical pyrometer was typically  $1600^\circ\text{C}$ . The pressure in the reactor was kept at 700 Torr during the growth. The epitaxial growth was initiated by introducing  $\text{SiH}_4$  and  $\text{C}_3\text{H}_8$  with  $\text{H}_2$  carrier gases into the reactor. The typical flow rates of  $\text{SiH}_4$  and  $\text{C}_3\text{H}_8$  were both 3 sccm with the C/Si ratio of 3.

It was confirmed that the growth of SiC epitaxial layer by the "Vertical hot-wall type

CVD" was proceeded by "step-controlled epitaxy" in the substrate temperature range between 1400 and 1700°C. The epitaxial layer had mirror-like surface with step-bunching ( $\sim 100$  nm width and  $\sim 10$  nm height observed by AFM) [4] without any particles and voids. The impurity of the undoped layer was evaluated by C-V measurement. From this result, the impurity concentration was estimated to be less than  $10^{14} \text{ cm}^{-3}$ .

Figure 2 shows a temperature dependence of growth rates on 6H-SiC(0001) Si face. The growth rate of SiC increased with increasing temperature. As shown in Fig.2, it was confirmed that the highest growth rate of  $15 \mu\text{m/hr}$  was obtained at 1700°C. The influence of  $\text{SiH}_4$  supply on the growth rate was also investigated. At a constant  $\text{C}_3\text{H}_8$  flow rate (3 sccm), the growth rate rose almost linearly with increasing  $\text{SiH}_4$  flow rate. For example, the growth rate of  $10 \mu\text{m/hr}$  at  $\text{SiH}_4$  flow rate of 9 sccm was obtained even at 1600°C.

### 3.2. Pulse Doping

The doped layers formed by "Pulse doping" are described in this section. The conditions of the epitaxial growth were same as the typical conditions described in § 3.1. The n-type doped layers (thickness of about  $1 \mu\text{m}$ ) were formed on the undoped epitaxial layers. Figure 3 shows carrier concentration of the n-type doped layers of 6H-SiC as a function of the on period. The off period was fixed at 4ms, and the on period was varied around  $100 \mu\text{s}$ . Almost 250 pulses per second of dopant gas were supplied to the substrate surface. It was found that the carrier concentration increased with increasing the on period. This result suggests that wide range control of n-type doping (from  $10^{15}$  to  $10^{18} \text{ cm}^{-3}$ ) is achieved by this new doping method.

The doping profile (high doped layer of  $10^{19} \text{ cm}^{-3}$ ) formed by "Pulse doping" was analyzed by SIMS. Rapid increase of dopant density up to  $10^{19} \text{ cm}^{-3}$  from  $10^{16} \text{ cm}^{-3}$  was observed within  $200 \text{ \AA}$  (transition layer). Moreover, the dopant-density profile in the doped layer was

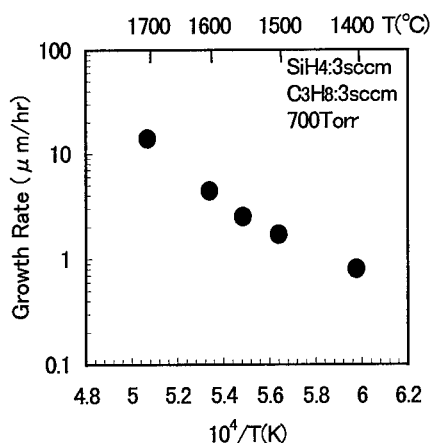


Fig. 2. Temperature dependence of growth rates on 6H-SiC(0001) Si faces

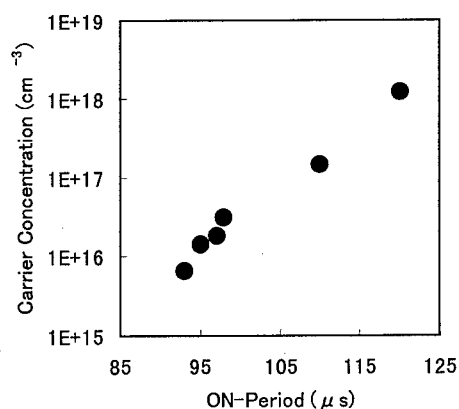
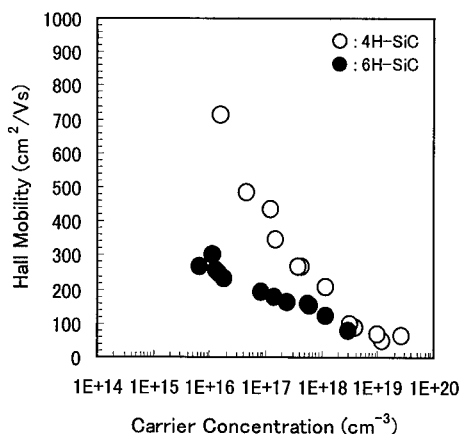


Fig. 3. Carrier concentration as a function of on period with off period 4 ms.



completely constant. The transition layer formed by the conventional doping method was about 500 Å. Abrupt doping profile with thin transition layer, which is required to form a high performance FET, was achieved by "Pulse doping".

The mobilities and carrier concentrations of the doped layer of 6H- and 4H-SiC were investigated. The mobilities and carrier concentrations of the doped layer were measured by Hall effect measurement at room temperature. Figure 4 shows Hall mobility vs. carrier concentration of the n-type doped layers of 6H- and 4H-SiC. The typical mobilities of 6H- and 4H-SiC are 300 cm<sup>2</sup>/Vs on  $n=1.11 \times 10^{15}$  cm<sup>-3</sup> and 711 cm<sup>2</sup>/Vs on  $n=1.60 \times 10^{16}$  cm<sup>-3</sup>, respectively. These obtained mobilities were almost equal to those reported previously.[5]



**Fig. 4.** Hall mobility vs. carrier concentration of 6H- and 4H-SiC

#### 4. Conclusion

We proposed new technologies of SiC growth and doping; "Vertical hot-wall type CVD" for higher growth rate and lower impurity, and "Pulse doping" for well-controlled doped layer. High quality films were achieved with high growth rate of 15 μm/hr, and the background impurity of the undoped layer was less than 10<sup>14</sup> cm<sup>-3</sup>. Carrier concentrations of the doped layers were precisely controlled, and abrupt doping profiles were achieved by "Pulse doping".

#### Acknowledgements

Part of this work was supported by NEDO (New Energy and Industrial Technology Development Organization) Japan.

#### References

- [1] O. Kordina, C. Hallin, A. Ellison, A. S. Bakin, I. G. Ivanov, A. Herry, R. Yakimova, M. Touminen, A. Vehanen, and E. Janzen, Appl. Phys. Lett. 69 (1996) p.1456.
- [2] O. Kordina, K. Irvine, J. Sumakeris, H. S. Kong, M. J. Paisely, and C. H. Carter, Jr., Mater. Sci. Forum, Vols.264-268 (1998) p.107.
- [3] A. A. Burk, Jr., and L. B. Rowland, Phys. Stat. Solid. (b) 202 (1997) p.263.
- [4] T. Kimoto, A. Itoh, and H. Matsunami, Appl. Phys. Lett. 66 (1995) p.3645.
- [5] A. Itoh, H. Akita, T. Kimoto, and H. Matsunami, Appl. Phys. Lett. 65 (1994) p.1400.

## LPCVD Growth and Structural Properties of 4H-SiC Epitaxial Layers

H. Tsuchida, I. Kamata, T. Jikimoto and K. Izumi

Yokosuka Research Laboratory, Central Research Institute of Electric Power Industry,  
2-6-1 Nagasaka, Yokosuka, Kanagawa, 240-0196, Japan

**Keywords:** Crystal Bending, LPCVD, Rocking Curve, Schottky Diodes, Thick Layers

### Abstract

Thick 4H-SiC epitaxial layers have been grown in a vertical LPCVD reactor with a radiantly-heated susceptor. High growth rates exceeding 10  $\mu\text{m/hr}$  are achieved in the reactor with mirror-like morphology. Structural properties of 4H-SiC epitaxial layers have been characterized by high-resolution XRD. Rocking curve maps taken before and after epitaxial growth show that epitaxial growth in the reactor improves greatly crystal bending and achieves narrow FWHMs of rocking curves for epitaxial layers. The electrical performance of epitaxial layers has been demonstrated on high-voltage Schottky diodes.

### Introduction

To develop high-voltage SiC devices with large handling current for power electric transmission and distribution systems, it is necessary to obtain a thick epitaxial layer with high purity and high crystallographic perfection. Growth of high-quality SiC epitaxial layers is realized through step-controlled epitaxy in cold-wall and hot-wall CVD reactors [1-5], and advanced growth techniques to achieve higher growth rates (10-100  $\mu\text{m/hr}$ ) with low background doping have been reported [6, 7]. At present, however, several kinds of crystallographic imperfection including crystal bending and domain structure exist in SiC wafers. Further improvement in crystallographic perfection of epitaxial layers is an important technical subject. In an earlier report [8], it was found that crystal bending and mosaicity of epitaxial layers are inherited from the substrates while crystal bending is strongly affected by substrate's backside preparations. In this paper, we report on the results of growing thick 4H-SiC epitaxial layers using a vertical low-pressure (LP) CVD reactor and on the improvements in crystal bending associated with the epitaxial growth process.

### Epitaxial growth and characterization methods

4H-SiC epitaxial layers were grown in a vertical reactor consisting of a water-cooled quartz tube, a cylindrical graphite hot-wall and a wedge-shaped graphite susceptor as shown in Fig. 1. Epitaxial growth was performed using the  $\text{H}_2+\text{SiH}_4+\text{C}_2\text{H}_2$  system with upward gas stream. Commercial 4H-SiC(0001) 8° off wafers were purchased. The reactor can process 2x2-inch wafers, though we used quarter sections of 1.38-inch wafers or sections (approximately 17x17  $\text{mm}^2$ ) of 2.00-inch wafers as substrates in this experiment. The substrates are mounted on each sloped susceptor face. The susceptor is placed inside the hot-wall. The greater part of the susceptor surface was in-situ coated by SiC by a preliminary growth run. In this reactor configuration, induction current flows only in the hot-wall, and the substrate and the susceptor are heated by radiation from the hot-wall. Therefore, the temperature of the susceptor is cooler than that of the hot-wall, and the susceptor surface is further coated by SiC during the growth run.

Nomarski differential interference contrast optical microscopy, SEM, AFM, C-V measurement, and XRD were used to characterize the epitaxial layers. Evaporated Au- or Ni-Schottky contacts were employed for C-V measurements. XRD measurements were made using the Philips X'Pert-MRD system equipped with a 4-crystal monochromator. X-ray  $\omega$ -rocking curves for (0004) reflection were obtained where the x-ray incident plane was kept parallel to the [1T00] and the [1120] directions, respectively. The curvatures of crystal bending along the [1T00] and [1120] directions were determined respectively by correlation between the peak-shifts of the rocking curve and the measured positions parallel to the x-ray incident plane. The presence of 3C-SiC inclusions in epitaxial layers was checked by x-ray  $2\theta/\omega$  scanning using an analyzer crystal.

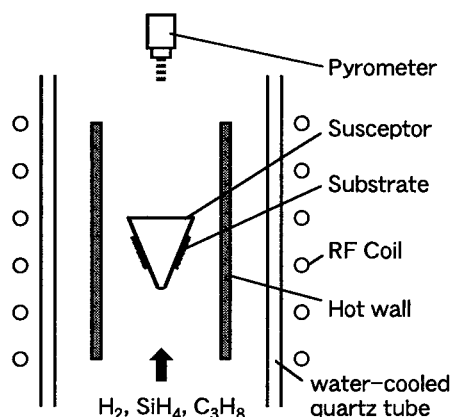


Fig. 1. Schematic drawing of the vertical LPCVD reactor.

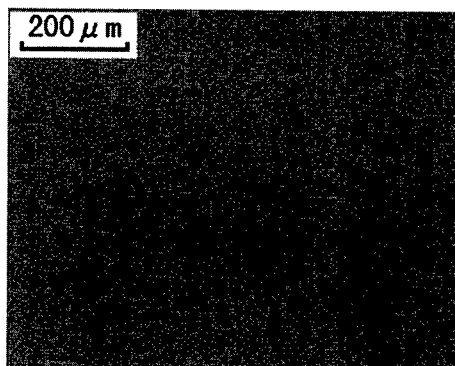


Fig. 2. Interference contrast optical micrograph of a 63  $\mu\text{m}$ -thick epitaxial layer grown at 10.4  $\mu\text{m/hr}$ .

### Results and discussions

Epitaxial growth was performed under reduced pressures between 25 to 75 Torr at 1500-1600 °C. The temperature was measured for the susceptor top by a pyrometer as shown in Fig. 1. We apply high  $\text{SiH}_4$  flow rates up to 30 sccm under a hydrogen flow rate of 10 slm. Growth rates of up to 11  $\mu\text{m/hr}$  were obtained without any evidence of 3C-SiC inclusions on x-ray  $2\theta/\omega$  scanning. In preliminary growth runs, background doping was p-type with net carrier density ranging from mid  $10^{14}$  to mid  $10^{15} \text{ cm}^{-3}$ . Unintentional p-type dopants might have originated from graphite parts used in the reactor. Reduction of the p-type background doping was achieved through testing graphite parts purchased from different suppliers, choosing the lower C/Si ratio of source gases and increasing the total pressure. Although combinations of a high C/Si ratio and a low total pressure still yield p-type layers, background doping becomes n-type for low C/Si ratios and total pressures above 50 Torr. The n-type background doping is changed from mid  $10^{14}$  to high  $10^{15} \text{ cm}^{-3}$  for C/Si ratios from 0.7 to 0.4.

Morphology of the epitaxial layers was also influenced by the C/Si ratio, and a high C/Si ratio (around 1.0) resulted in large steps as high as 10-20 nm. Decreasing the C/Si ratio could inhibit the large steps. Figure 2 shows an interference contrast optical micrograph of a 63  $\mu\text{m}$ -thick layer. The layer was grown at 10.4  $\mu\text{m/hr}$ . The input C/Si ratio was 0.7, and the net carrier density was determined as  $4 \times 10^{14} \text{ cm}^{-3}$  (n-type) by C-V measurement. The optical micrograph shows a mirror-like morphology without Si-droplets, although AFM measurement revealed long-range shallow wave structures (typically 3-8  $\mu\text{m}$  in period and 1-4 nm high).

Rocking curve maps were taken before and after epitaxial growth to evaluate crystal bending. The rocking curves of as-received wafers exhibited large peak-shifts for the measured positions parallel to the x-ray incident plane due to crystal bending corresponding to curvature radius of 3-20 m [Fig. 3(a)]. On the other hand, rocking curve maps along the [1T00] direction and the [1120] direction measured after epitaxial growth exhibited small peak-shifts and high intensities [Fig. 3(b) and 3(c)]. The remarkable reduction of the peak-shifts means that crystal bending can be improved by epitaxial growth in our reactor. Although resulting curvatures showed large wafer-to-wafer variations, an improvement in crystal bending was always confirmed after epitaxial growth, and usually curvature radius of crystal bending along the [1T00] was better than that along the [1120]. Rocking curves taken from the backside of the substrate also showed small peak-shifts, indicating that crystal bending of the substrate was released during epitaxial growth. Improving on crystal bending will allow growth of epitaxial layers under a reduced stress in the basal plane. In our best case, the curvature radius of crystal bending along the [1T00] direction was 621 m and that along the [1120] direction was 304 m for a 25  $\mu\text{m}$ -thick layer. Note that the sample was mounted on the susceptor using a built-in sample holder (slide-mount). We do not use any glue or clips to hold substrates. In this experiment, the slide-mount sample holder was touching on periphery of the sample along the gas stream during epitaxial growth. The crystal bending after epitaxial growth should be influenced by the design of sample holder.

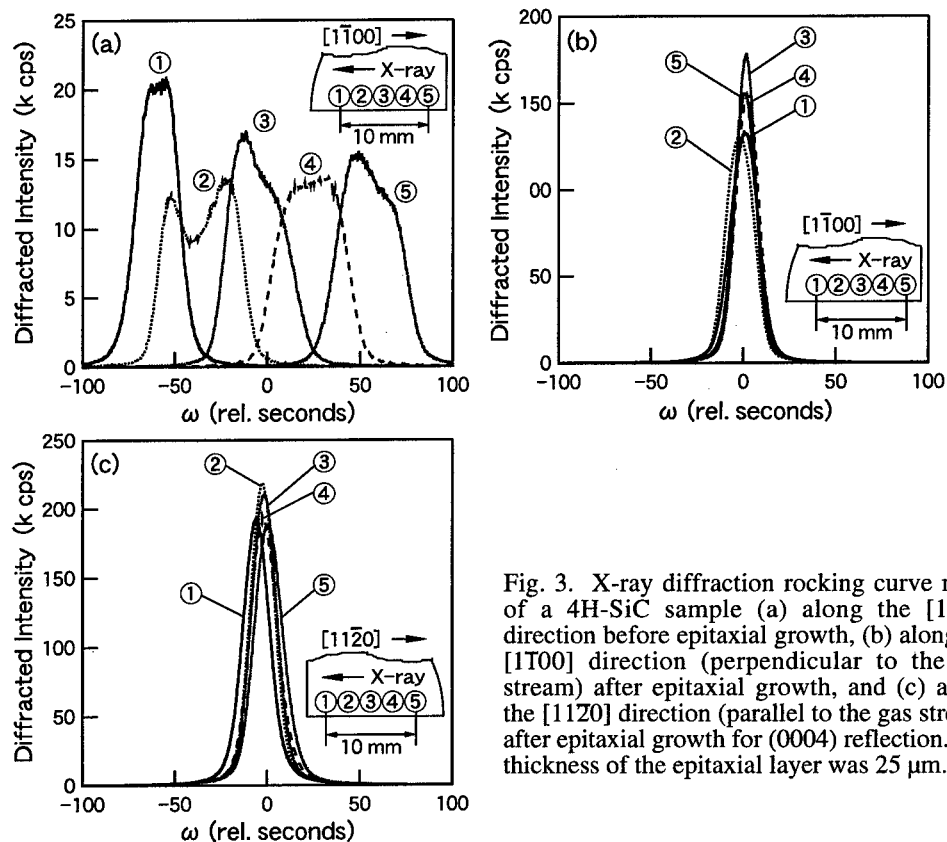


Fig. 3. X-ray diffraction rocking curve maps of a 4H-SiC sample (a) along the  $[1\bar{1}00]$  direction before epitaxial growth, (b) along the  $[1\bar{1}00]$  direction (perpendicular to the gas stream) after epitaxial growth, and (c) along the  $[11\bar{2}0]$  direction (parallel to the gas stream) after epitaxial growth for (0004) reflection. The thickness of the epitaxial layer was 25  $\mu\text{m}$ .

Crystal bending is also strongly affected by substrate's backside preparations as previously reported [8]. In conventional reactors, inductive heating is applied to a susceptor, and samples are placed on the susceptor. Therefore, the temperature of the samples becomes cooler than that of the susceptor. This temperature gradient leads to unnecessary SiC depositions on the substrate's backside when a SiC-coated susceptor is used. On the other hand, in our reactor, the temperature of the substrate is slightly higher than that of the susceptor surface behind the substrate because the substrate and the susceptor are heated by radiation from the hot-wall. This inverse temperature gradient can be confirmed by the phenomenon that the substrate's backside is sublimated during heating and the sublimated SiC deposits on the susceptor surface behind the substrate. Consequently, a smooth backside surface of the substrate can be obtained even after a long growth run. We suppose that the heat distribution around the substrate, as well as sample holding design in the reactor, are factors behind the improvement in crystal bending. Furthermore, the wafers showing rocking curves with heavily split peaks yielded smaller improvements on curvatures. This indicates that the crystal bending of epitaxial layers is also dependent on the crystallographic structure of purchased wafers. It is known that commercial SiC wafers contain a high density of edge dislocations and low angle boundaries (edge dislocation walls) with burgers vector in  $\langle 11\bar{2}0 \rangle$  directions [9, 10]. The rocking curve with split peaks suggests that the wafer contained subgrains separated by low angle boundaries. Further correlation is needed to estimate the impact of subgrain structures in the substrates on the magnitude of crystal bending after epitaxial growth in the reactor.

The improvement in crystal bending resulted in a sharpening of each rocking curve. Figure 4 shows high-resolution rocking curves recorded using a Ge(440) 4-crystal monochromator ( $\Delta\omega = 5''$ ) and Ge(220) triple bounce analyzer ( $\Delta 2\theta = 12''$ ). The 25  $\mu\text{m}$ -thick layer exhibited extremely narrow rocking curves. At the best point, the FWHMs for a beam size of  $1 \times 2.5 \text{ mm}^2$  were 5.2'' and 8.5'' for scanning where the x-ray incident plane was kept parallel to the  $[1\bar{1}00]$  direction and the  $[11\bar{2}0]$  direction, respectively. For a beam size of  $2 \times 5 \text{ mm}^2$ , the rocking curves became wider and the FWHMs were 7.7'' and 10.0'' where the incident plane was parallel to the  $[1\bar{1}00]$  direction and

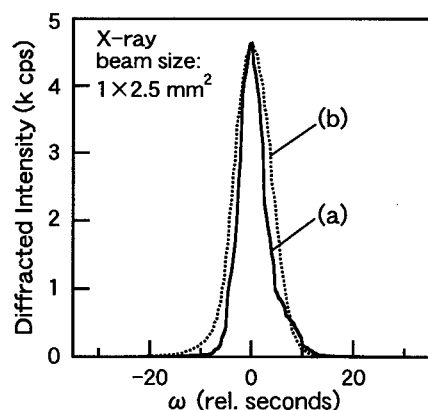


Fig. 4. High-resolution x-ray rocking curves of a 25  $\mu\text{m}$ -thick 4H-SiC epitaxial layer for (0004) reflection. The x-ray incident plane is parallel to (a) the [1100] and (b) the [1120] directions.

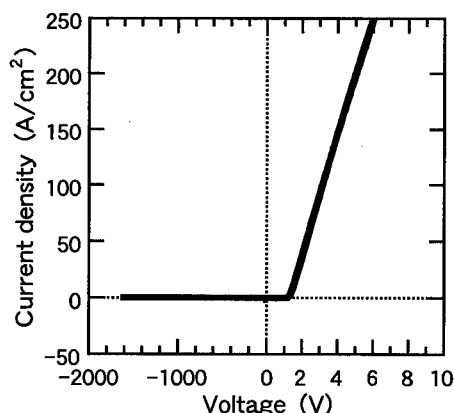


Fig. 5. I-V characteristics of a Ni/4H-SiC Schottky diode (0.5 mm  $\phi$ ) using a 43  $\mu\text{m}$ -thick n<sup>+</sup> epitaxial layer.

the [1120] direction, respectively. Owing to that fine  $\omega$ -rocking curves are sensitive to crystal bending, the FWHMs for each scan are influenced by magnitude of crystal bending of the sample. For example, a crystal bending with a curvature radius of 100 m spreads x-ray about  $\pm 3.5^\circ$  in angle for (0004) reflection where the incident x-ray beam width is 1 mm. The sharpening of each rocking curve associated with epitaxial growth can be explained by the changes in crystal bending. The difference in FWHMs for each scan direction corresponds to the result that crystal bending along the [1100] direction was better than that along the [1120] direction as shown in Fig. 3.

The 0.5 mm  $\phi$  Ni/4H-SiC Schottky diode with n-type substrate ( $8 \times 10^{18} \text{ cm}^{-3}$ ) and n<sup>+</sup> layer (45  $\mu\text{m}$ -thick,  $3 \times 10^{15} \text{ cm}^{-3}$ ) showed a blocking voltage of 1600 V as shown in Fig. 5, even no edge terminations were processed. The layer was grown at 7.5  $\mu\text{m/hr}$ . The leakage current at 1000 V was less than  $5 \times 10^{-7} \text{ A/cm}^2$ . The forward voltage drop at 100  $\text{A/cm}^2$  was 3.3 V, and the corresponding specific on-resistance was 18  $\text{m}\Omega\text{cm}^2$ . We have also obtained an over 2000 V Ni-Schottky diode using a 73  $\mu\text{m}$ -thick p<sup>+</sup> layer. The electrical performances of the preliminary diodes encourage growth of thick epitaxial layers with a high growth rate in the reactor for high-voltage SiC devices.

## Conclusions

We have demonstrated growth of thick 4H-SiC epitaxial layers in a vertical hot-wall LPCVD reactor with an inner susceptor configuration. Thick epitaxial layers with low background doping and mirror-like morphology have been obtained under high growth rates exceeding 10  $\mu\text{m/hr}$ . We found that crystal bending can be improved greatly by the epitaxial growth process in the reactor, and narrow FWHMs of rocking curves for epitaxial layers are obtained.

## References

- [1] T. Kimoto, A. Itoh, and H. Matsunami, *Phys. Stat. Sol. (b)* **202** (1997) 247.
- [2] D.J. Larkin, *Phys. Stat. Sol. (b)* **202** (1997) 305.
- [3] A.A. Burk Jr., M.J. O'Loughlin, and H.D. Nordby Jr., *J. Cryst. Growth* **200** (1999) 458.
- [4] R. Rupp, Yu.N. Makarov, H. Behner, and A. Wiedenhofer, *Phys. Stat. Sol. (b)* **202** (1997) 281.
- [5] O. Kordina, C. Hallin, A. Henry, J.P. Bergman, I. Ivanov, A. Ellison, N.T. Son, and E. Janzén, *Phys. Stat. Sol. (b)* **202** (1997) 321.
- [6] K.G. Irvine, R. Singh, M.J. Paisley, J.W. Palmour, O. Kordina, and C.H. Carter Jr., *Mat. Res. Soc. Symp. Proc.* **512** (1998) 119.
- [7] A. Ellison, J. Zhang, J. Peterson, A. Henry, Q. Wahab, J.P. Bergman, Y.N. Makarov, A. Vorob'ev, A. Vehanen, and E. Janzén, *Mater. Sci. and Engineer.* **B61-62** (1999) 113.
- [8] A. Ellison, H. Radamson, M. Tuominen, S. Milita, C. Hallin, A. Henry, O. Kordina, T. Tuomi, R. Yakimova, R. Mader, and E. Janzén, *Diamond and Related Materials* **6** (1997) 1369.
- [9] J. Takahashi, N. Ohtani, and M. Kanaya, *J. Cryst. Growth* **167** (1996) 596.
- [10] M. Dudley, S. Wang, W. Huang, C.H. Carter Jr., V.F. Tsvetkov, and C. Fazi, *J. Phys. D: Appl. Phys.* **28** (1995) A63.

### 3-D Computational Modeling of SiC Epitaxial Growth in a Hot Wall Reactor

Wei Ji<sup>1</sup>, Peter M. Lofgren<sup>1,2</sup>, Christer Hallin<sup>1,3</sup> and Chun-Yuan Gu<sup>1</sup>

<sup>1</sup>ABB Corporate Research, SE-721 78 Västerås, Sweden

<sup>2</sup>Faxén Laboratory, Royal Institute of Technology, SE-100 44 Stockholm, Sweden

<sup>3</sup>IFM, Linköping University, SE-581 83 Linköping, Sweden

**Keywords:** CVD, Epitaxial Growth, Hot-Wall, Numerical Simulation

**Abstract.** A three-dimensional computational model for chemical vapor deposition (CVD) of silicon carbide (SiC) in a hot wall reactor is developed, where the susceptor is tapered with a rectangular cross-section. The present work focuses on the advection-diffusion-reaction process in the susceptor. The precursors are propane and silane, and the carrier gas is hydrogen with mass fraction higher than 98%. Computed growth rates under different system pressures and precursor concentrations are compared with the experimental data measured on samples grown in the Linköping CVD reactor. The gas composition distribution and the growth rate profile are shown. Dependence of the growth rate on precursor concentrations is investigated.

## 1 Introduction

Silicon carbide (SiC) is a promising material in micro-electronics and also in a variety of other applications due to its excellent properties as large bandgap, high thermal conductivity, and high temperature and corrosion resistances [1]. One of the promising techniques to grow epitaxial SiC is to use a hot wall CVD reactor heated by an RF coil reducing needed heating power [2].

In this work, a three-dimensional computational model for epitaxial growth of SiC in a tapered susceptor with rectangular cross-section is developed. It is an extension of our previous two-dimensional axisymmetric model [3]. This work focuses on the advection-diffusion-reaction problem, while the flow and heat transfer are solved from the model developed by Lofgren et al. [4]. The Linköping Chemical Vapor Deposition (CVD) reactor [2] is studied, where the carrier gas is hydrogen ( $H_2$ ), and the precursors are silane ( $SiH_4$ ) and propane ( $C_3H_8$ ).

## 2 Model Formulation

The mass transport equation takes into account the ordinary diffusion, thermal diffusion, and production/destruction of gas species due to chemical reactions. A body-fitted coordinate system is introduced for the tapered geometry of the susceptor. Influence of the axial diffusion on the predicted results is verified by including it as source term in the equation. The reaction mechanisms for gas phase and surface deposition are taken from [5, 6]. The commercial Fortran package Chemkin [7] and Surface Chemkin [8] are used in incorporating chemical kinetics into the model. Detailed description of the model and the formulas are given in [9].

## 3 Results

Most of the results shown here are for the *reference case* [9].

### 3.1 Gas composition

Fig. 1 shows the mole fraction distributions just above the susceptor floor for the species:  $C_2H_2$ ,  $C_2H_4$ ,  $Si$  and  $SiH_2$ , which are the most significant to the growth [3]. The concentration of  $C_2H_4$  decreases quickly after its peak value near the susceptor entrance, partly due to the depletion by the deposition of  $SiC$  on the floor, and also due to the consumption by the gas decomposition to produce  $C_2H_2$ . The silicon contributors have higher mole fractions than that of carbon contributors, indicating that the deposition is most likely carbon limited.

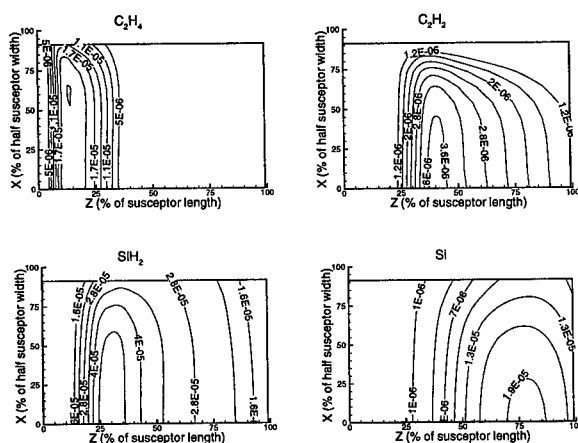


Fig. 1. Mole fraction contours of  $C_2H_4$ ,  $C_2H_2$ ,  $SiH_2$ , and  $Si$  just above the susceptor floor.

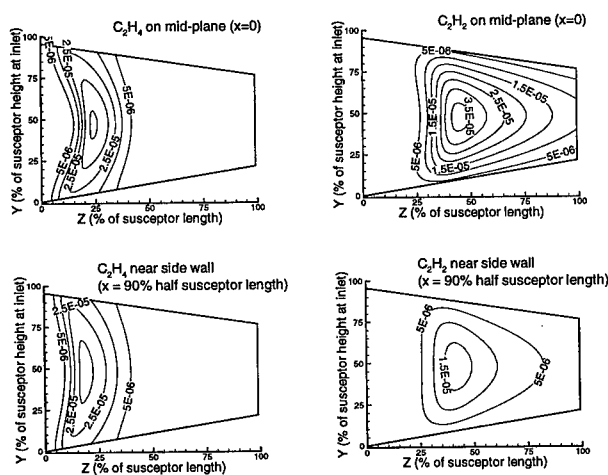


Fig. 2. Mole fraction contours of  $C_2H_4$  and  $C_2H_2$  in vertical planes at different  $x$  locations.

In fig. 2, mole fraction contours on vertical planes are shown for the carbon species. The mole fraction profiles at different spanwise locations are similar. Near the entrance of the susceptor where the species begin to form, the mole fractions close to the top and bottom walls are higher than that in the center region, the deposition is chemical reaction controlled. In the downstream region of the susceptor, the concentration boundary layers are formed, mainly due to the depletion of the gas species at the deposition walls, indicating that the deposition is diffusion mass transport limited.

### 3.2 Growth rate

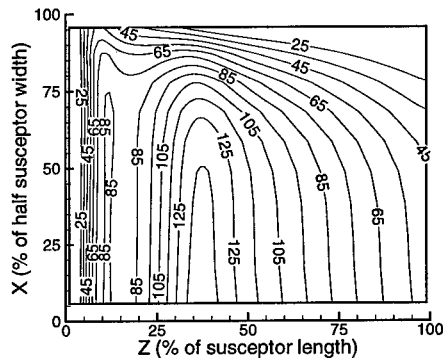


Fig. 3. Growth rate contour on susceptor floor.

Contour of the growth rate on the susceptor floor is shown in fig. 3. The first peak of the growth rate is at about 12% of the susceptor length, where  $C_2H_4$  has the highest mole fraction; and the second one is at about 37% of the susceptor length, where  $C_2H_2$  has the highest mole fraction, see fig. 1, demonstrating that  $C_2H_4$  and  $C_2H_2$  are the largest carbon contributors to the  $SiC$  growth.

Fig. 4 shows the calculated growth rates from different models (stated in the plot) compared to the experimental data. The predicted growth rate is slightly higher by using the Ho's model [6]. In comparison with the two-dimensional axisymmetric model [3], the three-dimensional model predicts higher growth rate peak and stronger depletion effect. The difference of the susceptor configurations: circle cross-section in the two-dimensional model and the rectangular cross-section in the three-dimensional model, is thought to be the reason why the growth rate profiles are different [9]. Comparing to the measured data, the model predicts the right level of the growth rate.

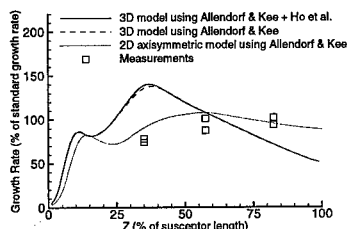


Fig. 4. Comparison between experimental and predicted growth rates.

Dependence of  $SiC$  deposition on precursor concentrations is shown in fig. 5. A common feature is found from the two plots in the figure, that as long as the input  $C/Si$  below 1.7, the deposition rates are independent of the input silane concentration, or follow the trend of propane, representing a carbon limited deposition; after input  $C/Si$  exceeds the value of 1.7, the situation becomes opposite, especially in the downstream region of the susceptor. These findings were also partly reported from other model study [5] and the experiments [10, 11, 12].

## 4 Summary

The Linköping CVD reactor [2] for the epitaxial growth of  $SiC$  is studied, where the carrier gas is hydrogen and precursors are propane and silane. The predicted growth rates along the



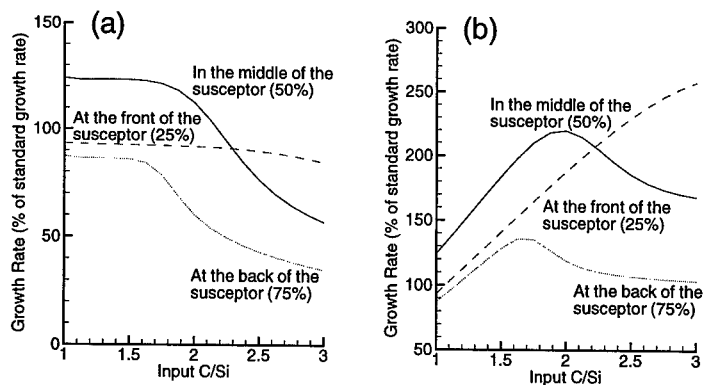


Fig. 5. Dependence of growth rate on input C/Si ratio. For calculations in (a), the inlet volume flux of  $C_3H_8$  was kept constant at  $2\text{ ml/min}$ , while the volume flux of  $SiH_4$  was changed. For calculations in (b), the inlet volume flux of  $SiH_4$  was kept constant at  $6\text{ ml/min}$ , while the volume flux of  $C_3H_8$  was changed. ( $1873\text{ K}$ ,  $300\text{ mbar}$ ).

middle line of the susceptor floor are fairly close to the measured data.

For a case with input  $C/Si = 1$ , a concentration boundary layer for  $C_2H_2$  is demonstrated which indicates that the deposition process is carbon mass transport limited. A critical value of 1.7 for input  $C/Si$  is found for the studied system, below the value the deposition is carbon limited, otherwise the process may be silicon controlled, at least for the growth in the downstream region of the susceptor.

## References

- [1] H. Morkoc, S. Strite, G. B. Gao, M. E. Lin, B. Sverdlov, and M. Burns, *J. Appl. Phys.*, **76**, (1994), p. 1363.
- [2] O. Kordina, A. Henry, E. Janzén, and C. H. Carter Jr. In *Silicon Carbide, III-Nitrides and Related Materials*, G. Pensl, H. Morkoc, B. Monemar, and E. Janzén, Editors, volume 264-268 of *Mat Sci Forum*, Trans Tech Publications Ltd., Switzerland, (1998), p. 97.
- [3] P. M. Lofgren, W. Ji, C. Hallin, and C.-Y. Gu, To be published in *J. Electrochem. Soc.*, (1999).
- [4] P. M. Lofgren, C. Hallin, C.-Y. Gu, and W. Ji, Submitted to *Int. Conf. on Silicon Carbide, and Related Materials, ICSCRM '99*, (1999).
- [5] M. D. Allendorf and R. J. Kee, *J. Electrochem. Soc.*, **138**, (1991), p. 841.
- [6] P. Ho, M. E. Coltrin and W. G. Breiland, *J Phys Chem*, **98**, (1994), p. 10138.
- [7] R. J. Kee, F. M. Rupley, E. Meeks, and J. A. Miller, Technical Report SAND96-8216, Sandia National Laboratories, Albuquerque (NM) and Livermore (CA) USA, (1996).
- [8] M. E. Coltrin, R. J. Kee, F. M. Rupley, and E. Meeks, Technical Report SAND96-8217, Sandia National Laboratories, Albuquerque (NM) and Livermore (CA) USA, (1996).
- [9] W. Ji, P. M. Lofgren, C. Hallin, and C.-Y. Gu, To be submitted to *J. Electrochem. Soc.*, (1999).
- [10] J. M. Harris, H. C. Gatos, and A. F. Witt, *J. Electrochem. Soc.*, **118**, (1971), p. 338.
- [11] P. E. R. Nordquist, G. Kelner, M. L. Gipe, and P. H. Klein, *Mat Lett*, **8**, (1989), p. 209.
- [12] C. Hallin, I. G. Ivanov, T. Egilsson, A. Henry, O. Kordina, and E. Janzén, *J. Crystal Growth*, **183**, (1998), p. 163.

### 3-d Thermal and Flow Modeling of Hot Wall Epitaxial Chemical Vapor Deposition Reactors, Heated by Induction

Peter M. Lofgren<sup>1,2</sup>, Christer Hallin<sup>1,3</sup>, Chun-Yuan Gu<sup>1</sup> and Wei Ji<sup>1</sup>

<sup>1</sup> ABB Corporate Research, SE-721 78 Västerås, Sweden

<sup>2</sup> Faxén Laboratory, Royal Institute of Technology, SE-100 44 Stockholm, Sweden

<sup>3</sup> IFM, Linköping University, SE-581 83 Linköping, Sweden

**Keywords:** CVD, Epitaxial Growth, Hot-Wall, Numerical Simulation

**Abstract.** A three dimensional computational model for temperature and flow predictions in hot wall chemical vapor deposition (CVD) reactors, heated by induction, is presented. It includes heating by a Radio Frequency (RF) coil, flow and heat transfer. Thermal radiation is modeled by a modified Monte Carlo method. Model predictions are compared to full scale experiments at Linköping CVD reactor for epitaxial growth of silicon carbide (SiC). Both streamwise and spanwise temperature gradients are well predicted, with the temperature maximum location shifted slightly upstream compared to the measured. Additionally, the model succeeds in predicting a recirculation zone just downstream of the susceptor. It is demonstrated how thermal gradients can be greatly reduced by simple geometrical changes.

## 1 Introduction

Silicon carbide (SiC) is a very promising semiconductor for high-power and high-temperature applications, due to large bandgap, high thermal conductivity and other desirable characteristics, see [1]. The most successful method for SiC active layer fabrication is Chemical Vapor Deposition (CVD). Several CVD techniques compete, where the hot-wall technique, using a hollow reactor that decreases needed heating power, is very promising. Good wafer morphology, few defects and high growth rates require very low temperature gradients as well as smooth laminar flow conditions. With computational models, incorporating CVD reactor physics, this can be achieved.

A three dimensional computational model for temperature and flow predictions in hot wall CVD reactors, heated by induction, is presented. It includes heating by a Radio Frequency (RF) coil, flow and heat transfer, with thermal radiation modeled by a modified Monte Carlo method. The model has been applied to epitaxial growth of silicon carbide (SiC) in the Linköping hot wall CVD reactor.

## 2 Experiments

The hot wall CVD reactor in Linköping, described in [2], runs at 300 mbar with hydrogen as carrier gas and propane and silane as precursors [3, 4]. The temperature is measured with a pyrometer focused on the susceptor surface, calibrated by melting silicon pieces. By stepwise increase of the process temperature and controlling when spatially distributed silicon pieces are melting, an experimental temperature gradient map is constructed. Recirculation zones downstream the susceptor are detected by soot deposition on the quartz tube.

### 3 Numerical Simulation

The numerical model, originally in two dimensions [3], solves the induced heat in conducting solids by applying the Maxwell equations and Ohm's law. Since the precursors are well diluted in the carrier gas, the dilute mixture approach [5, 6] is used, solving the Navier-Stokes and the energy equations. Internal thermal radiation is solved by a modified Monte Carlo method, where the gas mixture is assumed transparent.

#### 3.1 Comparison to experiments

A temperature comparison on the susceptor floor between experiments and predictions, for 300 mbar, is presented in fig. 1. Solid lines (—) show the predicted temperature at the symmetry line and dashed lines (- -) denote the predicted temperature close to the susceptor side-wall. Centerline measurements are squares ( $\square$ ) and measurements close to the side walls, diamonds ( $\diamond$ ). The simulation seems to predict the correct streamwise temperature slopes, but fails somewhat in predicting the temperature maximum location, possibly caused by a somewhat upstream-shifted coil position in the simulation geometry compared to the experimental setup. However, by incorporating the uncertainty in the experimental values, the prediction still works well. Spanwise, the temperature decreases about 1% from the centerline to the position close to the wall for simulation compared to somewhat less than 1% for experiments.

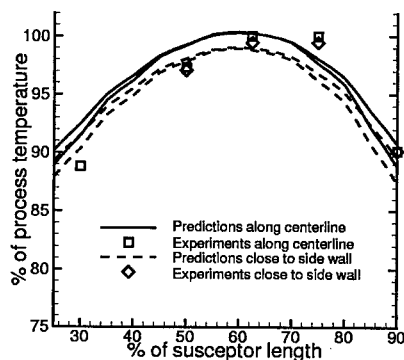


**Fig. 1.** Comparison between predicted and experimental temperature distributions on the susceptor floor at 300 mbar. Solid lines (—) show the predicted temperature at the symmetry line and dashed lines (- -) denote the predicted temperature close to the susceptor side-wall. Centerline measurements are squares ( $\square$ ) and measurements close to the side walls, diamonds ( $\diamond$ ).

As the hot susceptor gases meet the downstream cold gases within an enlarged flow area, strong buoyancy effects force the hot flow to rise against the quartz tube ceiling, creating a recirculation zone. The phenomena is shown by streamlines from the numerical simulation in fig. 2A, appearing experimentally as a soot pattern forming on the quartz tube after a while, see fig. 2B.

#### 3.2 Temperature field

The model predicts the temperature field in the whole reactor, including all solids. In fig. 3A the field at the symmetry plane is presented, showing that in the susceptor the flow contains a cold 'finger'. In the susceptor graphite, the temperature exceeds the process temperature.

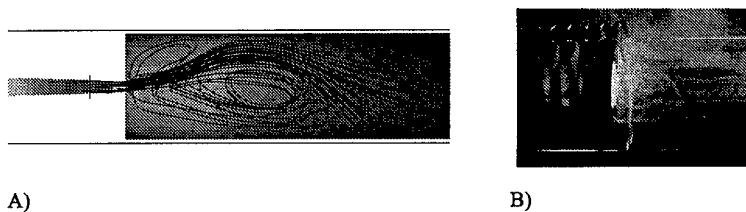


**Fig. 2.** A recirculation zone just downstream of the susceptor shown by A) streamlines from a numerical simulation B) a soot pattern forming on the quartz tube during the experiments.

Downstream of the susceptor, the buoyancy effect is visible through the asymmetric temperature field with hot gases striving upwards. Fig. 3B shows the large temperature gradients in the insulation. The left part of the figure, at 30% of the susceptor length, shows the cold gas in the center of the susceptor, not appearing at 60%, shown in the right part of the figure.

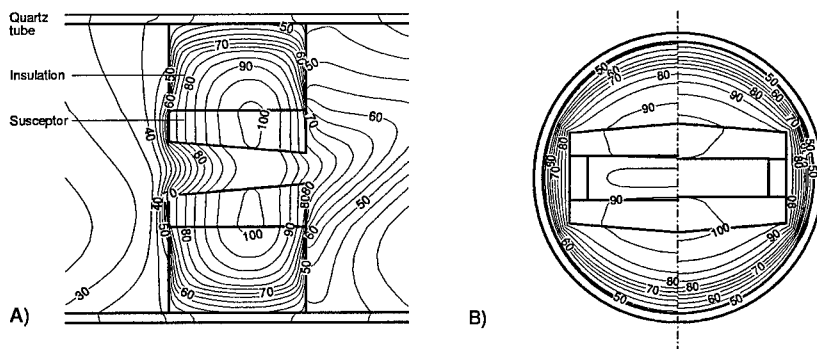


**Fig. 3.** Temperature field as percentage of the process temperature for A) the symmetry plane and B) two axial planes, to the left at 30% of the susceptor length and to the right at 60%.

### 3.3 Process Improvement

One of the keys to success in CVD technology is small or no temperature gradients at all in the growth area. There are many possibilities for reducing thermal gradients, e.g. by optimizing the coil configuration, redesigning the susceptor or changing its material thickness. Here it is demonstrated that by these simple geometrical changes, temperature gradients can be greatly reduced, see fig. 4. For this optimized case, temperatures vary less than  $\pm 1\%$  over more than half of the susceptor length, compared to the variation between about 92 and 100% of the process temperature for the standard case over the same length, see fig. 1. In the same way, the model can be used reducing spanwise temperature gradients and improving flow conditions. Incorporating the chemistry model by Ji et al. [7], growth rate and growth conditions can be predicted.

## 4 Conclusions

It is clearly demonstrated that three dimensional thermal and flow modeling can successfully be used in the development of greatly improved hot-wall CVD reactors. By simple changes in the

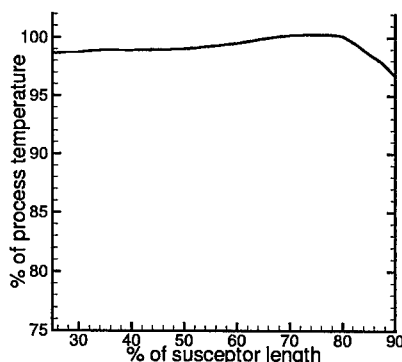


Fig. 4. Predicted temperature distribution along the centerline on the susceptor floor for optimized reactor configuration.

reactor configuration, such as coil configuration and susceptor design, temperature gradients in the susceptor can be greatly reduced. Recirculation zones can be detected by simulation, and removed by smoother flow conditions. By incorporating a chemistry model, growth rate and growth conditions can be predicted, see Ji et al. [7].

## 5 Acknowledgements

The authors greatly acknowledge Dr. Y. Liu at ABB Corporate Research for valuable ideas and support. Electromagnetic field calculations are performed by Opera-3d [8] and flow and heat transfer by CFX 4.2 [9, 10].

## References

- [1] H. Morkoc, S. Strite, G. B. Gao, M. E. Lin, B. Sverdlov and M. Burns, *J. Appl. Phys.*, **76**, (1994), p. 1363.
- [2] O. Kordina, A. Henry, E. Janzén and C. H. Carter Jr. In *Silicon Carbide, III-Nitrides and Related Materials*, G. Pensl, H. Morkoc, B. Monemar and E. Janzén, Editors, volume 264-268 of *Mat Sci Forum*, Trans Tech Publications Ltd., Switzerland, (1998), p. 97.
- [3] P. M. Lofgren, W. Ji, C. Hallin and C.-Y. Gu, To appear in *J. Electrochem. Soc.*, (1999).
- [4] C. Hallin, I. G. Ivanov, T. Egilsson, A. Henry, O. Kordina and E. Janzén, *J. Crystal Growth*, **183**, (1998), p. 163.
- [5] C. R. Kleijn, *Computational Modeling in Semiconductor Processing*, chapter Chemical Vapor Deposition Processes, Editor M. Meyyappan, Artech House, London, (1995).
- [6] M. Pons, E. Blanquet, J. M. Dedulle, I. Garcon, R. Madar and C. Bernard, *J. Electrochem. Soc.*, **143**, (1996), p. 3727.
- [7] W. Ji, P. M. Lofgren, C. Hallin and C.-Y. Gu, To be presented at *Int. Conf. on Silicon Carbide, and Related Materials, ICSCRM '99*, (1999), p. 149
- [8] *Opera-3d*, Vector Fields, Oxford, United Kingdom, (1998).
- [9] *CFX-4.2: Solver*, AEA Technology, Oxfordshire, United Kingdom, (1997).
- [10] *CFX-4.2: Radiation*, AEA Technology, Oxfordshire, United Kingdom, (1997).

## The Development of Resistive Heating for the High Temperature Growth of $\alpha$ -SiC using a Vertical CVD Reactor

Ebenezer Eshun<sup>1</sup>, Crawford Taylor<sup>1</sup>, N.Fama Diagne<sup>1</sup>, James Griffin<sup>1</sup>,  
M.G. Spencer<sup>1</sup>, Ian Ferguson<sup>2</sup>, Alex Gurary<sup>2</sup> and Rick Stall<sup>2</sup>

<sup>1</sup> Materials Science Research Center of Excellence, Howard University,  
Washington, DC 20059, USA

<sup>2</sup> EMCORE Corporation, 349 Elizabeth Avenue, Somerset, NJ 08873, USA

**Keywords:** Background Doping, CVD, Filament Lifetime, Homoepitaxial Growth, Resistive Heating

**Abstract.** The rapid development of high quality silicon carbide (SiC) epitaxy and substrates has resulted in the SiC technology developing into a production process. Epitaxial growth over large areas, require increased temperature uniformity, which is better achieved with resistive heating relative to RF heating. In this work, we report on our progress in the development of resistive heating for a vertical Chemical Vapor Deposition (CVD) reactor. We have developed a usable resistive heating system for growing  $\alpha$ -SiC, which requires temperatures in excess of 1500°C. We have designed a He purge system to purge the vicinity of the filament with He during growth, and have been able to achieve filament lifetimes of 30 hours at 1500°C. Using this system, we have grown "state of the art"  $\alpha$ -SiC at 1580°C and higher (1680°C), with backgrounds between  $6 \times 10^{14} \text{ cm}^{-3}$  to  $5 \times 10^{15} \text{ cm}^{-3}$  at 1580°C, p-type. We have also grown n-type device layers using nitrogen.

### INTRODUCTION

Silicon carbide (SiC) has long been known to have excellent physical and electronic properties, which should allow production of electronic devices that can operate at significantly higher temperatures and power levels than devices produced from Si and GaAs[1]. These important properties include high breakdown fields (>5 times that of Si), wide bandgap energy (>2 times that of Si), higher carrier saturation velocity (>2 times that of Si) and high thermal conductivity (>3 times that of Si) [2]. The success of SiC for high temperature and high power electronic applications is dependent upon the ability to reproducibly attain quality SiC epitaxial layers. This includes the ability to produce in-situ, both n-type and p-type epitaxial layers with doping profiles ranging from extremely low doped epitaxial layers for high voltage devices to degenerately doped layers for minimizing parasitic resistances[3]. In the epitaxial growth of SiC, high temperatures in excess of 1500°C are required. High voltage bipolar devices require thick, low doped epitaxial layers with long carrier lifetimes, which are most conveniently grown by Chemical Vapor Deposition (CVD) [4]. In this paper, we discuss the development of resistive heating for the growth of  $\alpha$ -SiC using a vertical CVD reactor equipped with a rotating disk. The advantage of resistive heating over RF heating is the uniformity of heating over large areas which is important for

growing high quality, uniform epitaxial layers for SiC devices as well as lower cost, footprint and maintenance.

### RESISTIVE HEATING DEVELOPMENT

The reactor used for this study is an EMCORE Corporation vertical CVD system, which is equipped with a high speed rotating disk. It consists of a double walled, water-cooled vertical chamber, made out of stainless steel. The sample sits on a graphite susceptor, which is placed on a graphite cup. The sample is heated with a resistive graphite filament, which is located inside the graphite cup. The reactant gases used during growth of SiC include Silane ( $\text{SiH}_4$ ) and Propane ( $\text{C}_3\text{H}_8$ ), with Hydrogen as a carrier gas.

Hydrogen is also used as the shroud with a flow rate of 28slm, which is required for flow stability in the reactor during growth, at a rotation speed of 750 rpm. The presence of large volumes of Hydrogen results in etching of the hot graphite filament, thus presenting a lifetime reduction problem. Studies indicate that filament failure is likely to occur after 5% reduction in the filament cross sectional area. In order to increase the filament lifetime, hydrogen must be eliminated or the partial pressure of hydrogen in the vicinity of the filament must be reduced. Also, a reduction in the temperature difference between the filament and the substrate will enhance the filament lifetime. If hydrogen is eliminated, filament failure will be determined by carbon evaporation, and it is predicted for our geometry that, filament lifetimes of over 1000 Hours at a filament temperature of 2000°C can be achieved.

The interior of the cup is purged with Helium during growth, which reduces the partial pressure of Hydrogen in the cup. By this method, we have been able to achieve filament lifetimes of 30 hours at 1500°C.

### GROWTH EXPERIMENTS

For the growth of  $\alpha$ -SiC, the substrates of choice are (0001)  $\alpha$ -SiC substrates with the polished growth surface tilted at angles between 3° and 8° from the basal plane. This tilt angle ensures that "step-flow" homoepitaxial growth occurs and that good morphology is obtained [5]. We have optimized the growth parameters including growth temperature, chamber pressure, reactant gas flows, growth rates, carrier gas flows, dopant gas flows and rotation speed. In our system a shroud flow of 21-30 slm is required to stabilize the reactor, typical growth parameters can be found in our previous paper [6]. Pure nitrogen is used as the n-type dopant source, we flow nitrogen between 15sccm to 60sccm to achieve doping between  $5 \times 10^{15} \text{cm}^{-3}$  and  $5 \times 10^{17} \text{cm}^{-3}$ .

### RESULTS AND DISCUSSIONS

Fig. 1 shows a plot of the filament temperature as a function of the filament lifetime. This indicates a decrease in lifetime as temperature increases implying an increase in the hydrogen etching of the filament. In the characterization of our epitaxial layers, the most important electrical method we use is Capacitance-Voltage (CV) measurements, which gives us information about background doping levels, doping profiles, doping uniformity across the wafer, breakdown voltages and epitaxial thickness. Surface morphology is analyzed with an Optical Microscope and Atomic Force Microscope. Fig. 2 shows the background doping

profile for a  $\alpha$ -SiC (6H) sample, while fig. 3 shows a plot of the doping variation across the sample (1.5cm square) showing a bowing profile as expected.

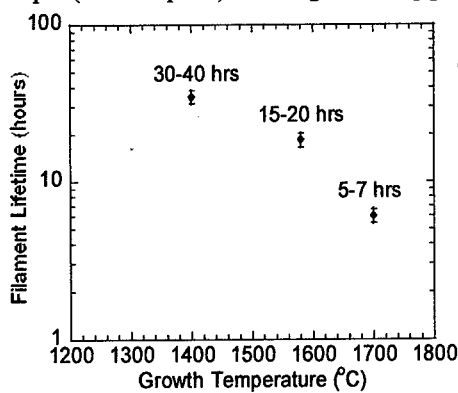


Fig. 1: A plot showing filament temperature as a function of filament lifetime.

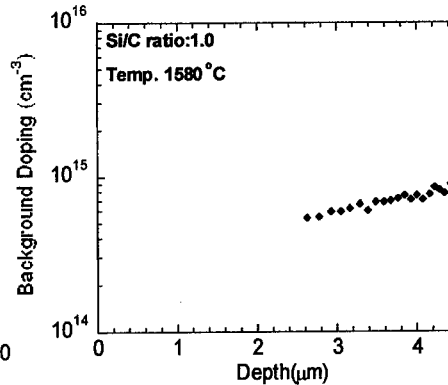


Fig. 2: Background doping profile for a 6H sample.

This profile shows very low background between  $6 \times 10^{14} \text{ cm}^{-3}$  and  $5 \times 10^{15} \text{ cm}^{-3}$  at  $1580^\circ\text{C}$ , p-type without the use of SiC coated parts. We have calibrated our reactor for growing n-type device layers. N-type calibration was done by flowing nitrogen with the reactant gases. CV and Secondary Ion Mass Spectroscopy (SIMS) measurements were then used to characterize the epitaxial layers for doping concentrations as shown in fig. 4. Experiments are underway to fully calibrate the reactor for p-type doping.

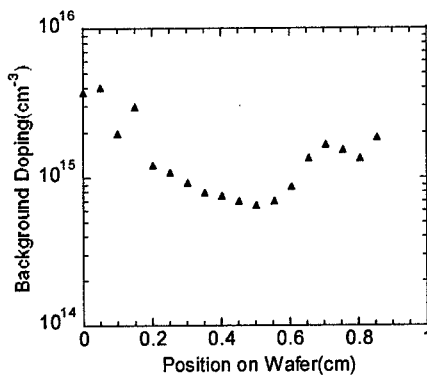


Fig. 3: Doping variation across wafer.

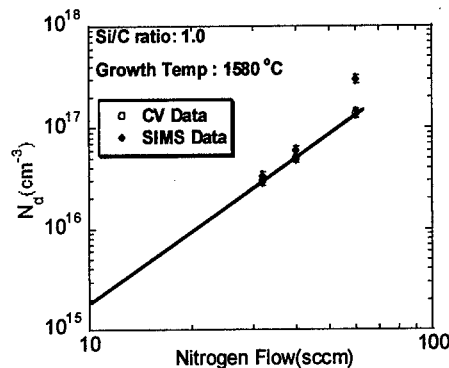


Fig. 4: Calibration plot showing CV results and SIMS results. The straight line is a fit to the CV data for doping device layers.



CV measurements were done with Al Schottky diodes by electron beam evaporation of Al dots onto the epi surface, no edge termination was used.

## CONCLUSION

We have developed a usable resistively heated vertical CVD reactor for the growth of SiC. Filament lifetimes of up to 30 hours have been achieved at 1500°C. These lifetimes are due to the fact that we have not been able to totally eliminate hydrogen in the vicinity of the filament. We have grown "state of the art"  $\alpha$ -SiC epi layers with this reactor, with a growth rate of 5  $\mu\text{m/hr}$ . We have achieved very low background doping (p-type  $\sim 6 \times 10^{14} \text{ cm}^{-3}$  at 1580°C) without the use of SiC coated parts. The high temperature capability of resistive heating has enabled us to perform growth experiments at elevated temperatures (1680°C). We have successfully grown high quality n-type device layers.

## ACKNOWLEDGEMENTS

The authors acknowledge the support of the MURI on Manufacturable Power Switching Devices, contract manager John Zolper and the Office of Naval Research (ONR). The work with EMCORE Corporation was supported by contract numbers N00014-99-C-0357 (Colin Wood) and F33615-99-C-5413 (Adam Saxler).

## REFERENCES

- [1] J.W Palmour, J.A Edmond, H.S. Kong and C.H Carter, Jr., in *Amorphous and Crystalline Silicon Carbide IV*, C.Y Yang, M.M Rahman and G.L Harris, Springer-Verlag(1992) p289-297
- [2] P. G Neudeck, in *Inst. Phys. Conf. Ser. No 141: Chapter 1* (1995) p1-6
- [3] D.J Larkin, P. G Neudeck, J.A Powell and L.G Matus, in *Inst. Phys. Conf. Ser. No 137: Chapter 1* (1993) p51-54
- [4] O. Kordina, C.Hallin, R.C. Glass, A. Henry, Mandeep Singh, L.O. Björketun and E. Janzén, in *Growth and Characterization of SiC Power Device Material*, (Linköping Studies in Science and Technology. Dissertations No. 352 1994) pp. 47
- [5] H. Matsunami et al., in *Amorphous and Crystalline Silicon Carbide*, edited by G.L Harris and C.Y.W Yang, (Springer Proceedings in Physics 1989, Vol.34) pp. 34-39
- [6] Ebenezer Eshun, Crawford Taylor, M. G. Spencer, Kevin Kornegay, Ian Ferguson, Alex Gurary and Rick Stall, *Homo-Epitaxial And Selective Area Growth Of 4h And 6h Silicon Carbide Using A Resistively Heated Vertical Reactor*, presented at the 1999 MRS Spring Meeting, San Francisco, CA, 1999

## Initial Results on Thick 4H-SiC Epitaxial Layers Grown Using Vapor Phase Epitaxy

L.B. Rowland<sup>1</sup>, G.T. Dunne<sup>1</sup> and J.A. Freitas, Jr.<sup>2</sup>

<sup>1</sup> Sterling Semiconductor, Inc, 22660 Executive Drive, Suite 101, Sterling, VA 20166, USA

<sup>2</sup> Naval Research Laboratory, Code 6877, Washington, DC 20375, USA

**Keywords:** Epitaxy, Tantalum Carbide

### Abstract

Epitaxial layers of 4H-SiC of up to 120 micron thickness have been grown by vapor phase epitaxy using a tantalum carbide-coated susceptor surrounded by graphite foam. Background doping levels due to N and Al impurities were in the low  $10^{15} \text{ cm}^{-3}$  range. The electrical and optical properties of these layers are comparable to those grown using conventional vapor phase epitaxy.

### Introduction

Silicon carbide (SiC) is a crucial material for the future of the power electronics industry. This is primarily because of its high thermal conductivity, saturated electron velocity, and breakdown field relative to silicon (Si). These superior properties allow us not only to extend the voltage range of a certain type of device but also give us considerable speed advantages for the same type of device in SiC when compared to Si. Thick epitaxial layers with the proper doping and thickness for SiC devices are not commercially available for breakdown voltages  $> 5 \text{ kV}$ . These devices are needed for high power motor drives as well as for power transmission for electrical utilities. Initial results from our effort to develop these thick epitaxial 4H-SiC layers are described herein.

### Experimental

Heavily doped n-type 4H-SiC substrates cut  $8^\circ$  off (0001) towards  $\langle 11\bar{2}0 \rangle$  were used as starting material. The experimental apparatus used for thick SiC epitaxial layers is drawn schematically in Figure 1. SiC wafers were placed on a tantalum carbide (TaC) -coated graphite susceptor that was inductively heated. TaC coated reactor components have been used with some success in conventional vapor phase epitaxy (VPE) [1]. Graphite foam and graphite felt were used to enclose the susceptor to help maintain a uniform temperature. Epitaxial layers were grown using  $\text{SiH}_4$ ,  $\text{C}_3\text{H}_8$ , and  $\text{H}_2$  at 700 torr at  $1650 \pm 50^\circ\text{C}$ . Layers were grown for short periods of time ( $< 1 \text{ hr}$ ) to measure growth rate and effects of dopant flow and gas-phase stoichiometry on growth rate and doping. On these layers, doping and thickness were obtained using 1 MHz capacitance-voltage (CV) measurements using a mercury probe. Thickness of cleaved SiC wafer pieces for thicker layers was measured by scanning electron microscopy (SEM) in cross-section. Low temperature photoluminescence (PL) was performed at 6 K using a He-Cd laser as excitation source [2].

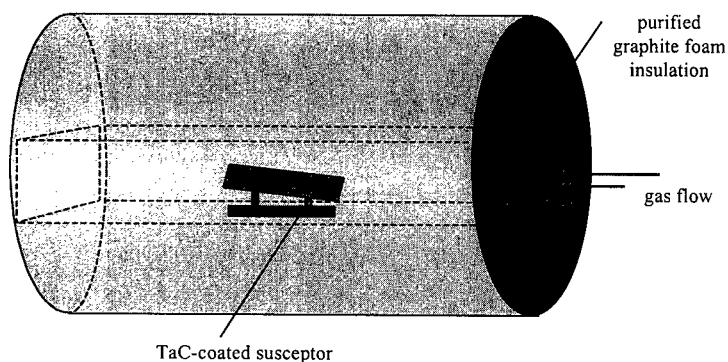


Figure 1: Growth configuration used in the thick epitaxial 4H-SiC work.

## Results and Discussion

Initial work focused on minimizing background doping density in order to achieve doping levels of  $10^{15} \text{ cm}^{-3}$  or below. Figure 2 shows the residual doping density as a function of propane flow for runs performed using this configuration. The doping densities were measured by CV measurements on films about 3 microns thick. Relatively thin films were used to help obtain rapid feedback of characterization data. The transition from n-type to p-type background doping occurred for low  $10^{15} \text{ cm}^{-3}$  doping and a Si/C gas source input ratio of 3.3. This ratio is much higher than that seen by either conventional VPE (0.17-1.0) or hot-wall CVD (typically 0.25). We believe that the graphite foam was etched by the  $\text{H}_2$  flow and transported free carbon in the form of hydrocarbons to the diffusion boundary layer above the substrate. This is consistent with observations of doping behavior using uncoated graphite susceptors [3].

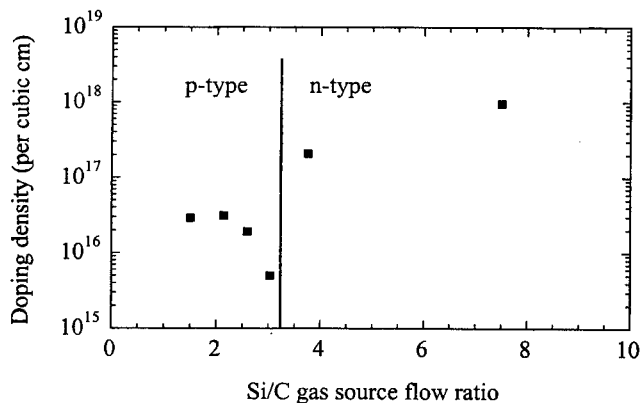


Figure 2: Background doping level of epitaxial layers grown with graphite foam surrounding TaC-coated susceptor as a function of Si/C input gas source ratio. All layers grown with Si/C less than 3.1 were p-type, while all layers grown with Si/C greater than 3.1 were n-type.

In order to demonstrate the feasibility of this technique, a 120 micron-thick epitaxial layer of 4H-SiC was grown using the configuration shown in Figure 1. This layer was grown at a growth rate of 3.7 microns/hour using silane and propane at 700 torr in 22 slm hydrogen carrier gas at approximately 1600°C. This layer was intentionally doped n-type using 0.10 sccm  $\text{N}_2$  during growth. The doping density from CV measurements was  $9 \times 10^{15} \text{ cm}^{-3}$ . This epitaxial layer is shown in cross section in Figure 3. The substrate appears darker in the figure due to its higher doping level (i.e., there are more electrons to be emitted as secondary electrons in the more heavily doped layer).

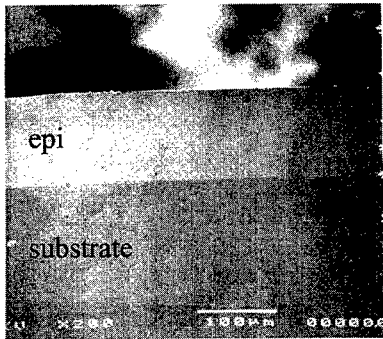


Figure 3: Cross-sectional scanning electron micrograph of 120  $\mu\text{m}$  thick 4H-SiC epitaxial layer. Secondary electron contrast occurs because of doping difference between epitaxial layer and substrate.

Figure 4 shows the surface morphology of this 120 micron-thick epitaxial layer after growth. Surface scratches are present but at a very low density. In general, most of the wafer has this morphology, but near the edges and near micropipes, triangular defects extend in the down-step  $[11\bar{2}0]$  direction [4]. These defects, known as tetrahedral pits or triangular defects, are due to formation of 3C-SiC on the wafer surface [5]. An example of this defect is shown in Figure 5.

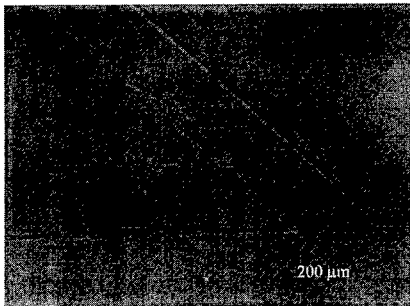


Figure 4: Surface morphology of central region of 120  $\mu\text{m}$  thick 4H-SiC epitaxial layer. Surface scratches are evident but not present at a high density. Dark splotches near center of micrograph are artifact of camera and not part of the epitaxial layer.

This defect can be used to estimate the thickness of the epitaxial layer. At the end of growth, the length of the defect and the off-angle of the substrate can be used to estimate the thickness of the epitaxial layer. This of course assumes that the defect formed at the beginning of growth. From these defects, we obtain a thickness of about 120 microns, which correlates with the cross-sectional SEM analysis (shown in Figure 3).

Figure 6 shows the photoluminescence spectrum from near the 4H-SiC band edge for this 120 micron thick layer. While the nitrogen related peaks  $P_0$  and  $Q_0$  constitute the dominant features in the spectrum in Figure 6 (indicating the sample is almost assuredly n-type) there is evidence of an Al related feature between  $P_0$  and  $Q_0$  indicating a low level of p-type compensation in the film. This would be expected given a transition from n- to p-type in background doping in the low  $10^{15} \text{ cm}^{-3}$  range.

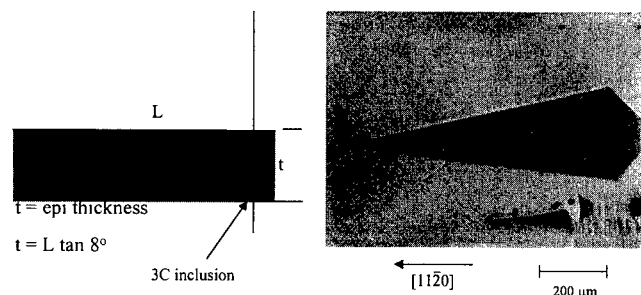


Figure 5: Tetrahedral defect in 120 micron thick 4H-SiC epitaxial layer grown by VPE.

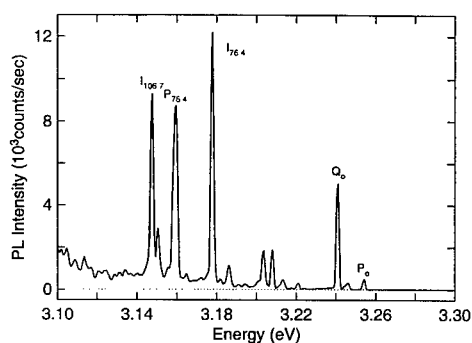


Figure 6: Near band-edge photoluminescence spectrum of 120-micron thick epitaxial 4H-SiC layer. The presence of intrinsic peaks and the relatively low luminescence intensity from Al bound excitons (energy is approximately 3.245 eV, or between  $P_0$  and  $Q_0$  in the Figure) indicates the high purity of this epitaxial layer.

### Summary

In this work, we have demonstrated 120 micron-thick 4H-SiC epitaxy intentionally doped to levels below  $1 \times 10^{16} \text{ cm}^{-3}$ . The electrical and optical properties of these layers were comparable with much thinner layers grown by conventional SiC epitaxy. Further work will focus on reducing impurities in graphite foam to achieve reproducible doping levels in the range usable for high-voltage diodes ( $>5 \text{ kV}$ ).

This work was sponsored by Air Force contract F33615-98-C-5424 (Tom Kensky, contract monitor).

### References

1. A. A. Burk, Jr., M. J. O'Laughlin, and H. D. Nordby, Jr., *J. Cryst. Growth* 200 (1999), p. 458.
2. M.W. Russell, J.A. Freitas, Jr., W.J. Moore, and J.E. Butler, *Adv. Mater. for Optics and Electronics* 7 (1997), p. 195.
3. K. Rottner and R. Helbig, *J. Cryst. Growth* 144 (1994), p. 258.
4. A. A. Burk, Jr. and L. B. Rowland, *J. Cryst. Growth* 167 (1996), p. 586.
5. A. Konstantinov, C. Hallin, O. Kordina, and E. Janzen, *J. Appl. Phys.* 80 (1996), p. 5704.

## High Growth Rate Epitaxy of Thick 4H-SiC Layers

M. Syväjärvi<sup>1</sup>, R. Yakimova<sup>2</sup>, H. Jacobsson<sup>1</sup>, M.K. Linnarsson<sup>3</sup>,  
A. Henry<sup>1</sup> and E. Janzén<sup>1</sup>

<sup>1</sup> Department of Physics and Measurement Technology, Linköping University,  
SE-581 83 Linköping, Sweden

<sup>2</sup> also Okmetic AB, Box 255, SE-17824 Ekerö, Sweden

<sup>3</sup> Department of Solid State Electronics, Royal Institute of Technology, Electrum 229,  
SE-16440 Stockholm, Sweden

**Keywords:** Doping, Epitaxy, Purity, Semi-Insulating

### Abstract

Sublimation epitaxy for fabrication of thick 4H-SiC layers has been studied with respect to surface morphology, structural quality, and purity. The surface morphology of thick (50-100  $\mu\text{m}$ ) epilayers is smooth, even though the growth rate was 100  $\mu\text{m}/\text{h}$ . These surfaces are obtained within a parameter window for morphological stability. The structural perfection is confirmed by high-resolution X-Ray diffraction measurements and the epilayer quality is improved compared with the substrate. The limitation in purity is dependent mainly on the purity of the SiC source material. The growth system purity, mainly graphite and Ta parts of the growth crucible, is also of major importance. Results from intentional doping for high-resistive, semi-insulating and p-type material are presented.

### Introduction

Advancement in epitaxy by chemical vapor deposition (CVD) [1,2] demonstrate the potential of SiC for electronics. Some device applications require thick layers. Epitaxy is demanding since substrate defects (e.g. micropipes, domains, etc) together with imperfections created during growth disturb the growth stability. In an unstable growth process, the epilayer quality will degrade with increasing layer thickness. A smooth surface morphology, which together with structural perfection and high-purity material, is a requirement for device-quality epilayers, becomes a crucial factor for thick layers. Thick CVD grown epilayers have been demonstrated [3]. However, these layers require long deposition time due to low growth rate of the technique ( $<5 \mu\text{m}/\text{h}$ ). Sublimation epitaxy is a suitable technique for high growth rates. To date, however, high-quality 4H-SiC layers with low residual doping grown by this method have not been reported.

We will demonstrate 4H-SiC epilayers grown with high growth rates (100  $\mu\text{m}/\text{h}$ ) showing structural improvement as compared with the substrate quality. The results are obtained when growth parameters for the sublimation epitaxy technique are selected within a window for morphological stability and at these conditions the surfaces have no visible defects besides micropipes inherited from the substrate. We will show that by controlling the growth environment purity, a reduction in impurity incorporation is achieved.

### Experimental

Epitaxial growth by sublimation has been studied for a long time, e.g. see [4,5]. The method is technologically simple, low cost, environmentally friendly and can easily be up-scaled. We have grown 4H-SiC layers with a growth rate of 100  $\mu\text{m}/\text{h}$  on 4H-SiC wafers (diameter 35 mm) off-oriented  $8^\circ$  in  $[11\bar{2}0]$  direction. Our growth

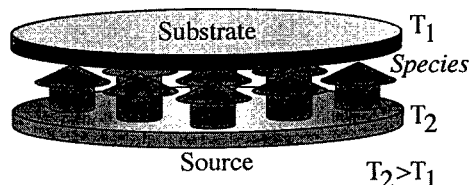


Fig. 1. Schematic view of the principle for growth by sublimation epitaxy.

configuration consists of a polycrystalline SiC source and a SiC substrate separated with a spacer [6], Fig. 1. By applying a temperature gradient with higher temperature at the source, Si and C-containing species are sublimed from the source and deposited on the cooler SiC substrate. Source to substrate distance is short (1-3 mm). To avoid graphitization, Ta (99.8% purity) was placed at the crucible bottom [6]. The epilayer surface morphology was characterized with optical microscopy using Nomarski differential interference contrast (NDIC). The structural quality was assessed from high-resolution X-Ray diffraction measurements. Low-temperature photoluminescence (PL) measurements were performed as well. Vanadium, boron and aluminium impurity concentrations were obtained from SIMS measurements.

### Results and discussion

Since good surface morphology is crucial for device fabrication, much attention was given to this issue. SiC epitaxy on off-axis surfaces usually proceeds via step-flow growth [2] and typical morphological features like shallow pits, scratches, elongated grooves, and triangular shaped defects may appear [7]. The latter two are especially important to avoid since they affect device performance [8]. Disregarding micropipes and screw dislocations (determined by KOH etching) inherited from the substrate, we obtained featureless epilayer surfaces by selecting conditions for stable growth within a parameter window for morphological stability. Although the growth proceeds via step-flow growth, macrosteps have not been resolved using NDIC microscopy. The parameter window is given by initial growth rate ramp-up, growth rate, temperature gradient, source to substrate distance, and substrate surface orientation. These parameters are discussed as follows and essential details for our results are shown in Table 1.

At the initial stages of growth, morphological disturbances may appear. In the beginning of our process, to avoid defect formation, the growth rate was increased slowly by 5-15  $\mu\text{m/h}$  per minute until the rate of 100  $\mu\text{m/h}$  was reached. During growth rate ramp-up, the substrate surface may improve since both sublimation and nucleation occur [4]. By this, polishing damages are reduced. A too slow growth rate ramp-up lead to formation of morphological disturbances. There is an upper limit of the growth rate below which growth disturbances are not likely to occur [6]. We have found that a growth rate up to 100  $\mu\text{m/h}$  is suitable for reproducible results for avoiding the features. The supersaturation is important for preferred growth mechanism and polytype stability. Competing growth mechanisms to step-flow growth may give rise to defects. Important factors for the supersaturation in sublimation epitaxy are growth temperature and temperature gradient. Our temperature gradient is  $<10^\circ\text{C/cm}$  as measured on top and bottom of the crucible. Smaller temperature gradients are beneficial for the structural quality [9] and for suppression of graphitization [10]. Our results were obtained with an upper temperature of  $1775^\circ\text{C}$ . High-quality epitaxial layers were only achieved on  $8^\circ$  off-oriented surfaces. In case of  $3.5^\circ$  off-orientation, inclusions of other polytypes could appear. Another important factor for growth stability is source to substrate separation. The morphology roughened at a separation larger than 4 mm due to larger influence from the graphite wall on growth species transported from source to substrate. Instead of a direct flux mass transfer from source to the growing epilayer, species are reacting with the graphite causing unstable growth behaviour. The morphology of thick layers grown under optimized conditions is remarkably good considering layer thickness (50-100  $\mu\text{m}$ ) and growth rate (100  $\mu\text{m/h}$ ). The thickness variations over 32 mm are less than 5% expressed as  $\sigma/\text{mean}$ .

The smooth surfaces are accompanied by a high structural quality. In fact, we observed direct proof that the epilayer structural quality improved compared with the substrates as evident from  $\omega$ -rocking curve measurements, Fig. 2. The substrate rocking curve shape is broad and superposition of several peaks indicate many misoriented domains whereas the epilayer rocking curve shape is more symmetric and much more

TABLE 1. Parameters used for sublimation epitaxy of SiC.

Growth parameter	Range of used values
Substrate off-orientation	$8^\circ$ in $[11\bar{2}0]$
Substrate temperature	$1775^\circ\text{C}$
Temperature gradient	$<10^\circ\text{C/cm}$
Argon pressure	$<1$ mbar
Source to substrate separation	1 mm
Growth rate ramp-up	5-15 ( $\mu\text{m/h}$ )/min
Growth rate	100 $\mu\text{m/h}$
Growth duration	30-60 min

narrow. This shows that different orientations of domains in the substrate have merged into one with one major orientation. Other domains giving rise to broadening of the substrate rocking curve have been suppressed. By growth of sufficiently thick (50-100  $\mu\text{m}$ ) epilayers, substrate domain structure misorientation is diminished and an overall improvement occurs. In  $2\theta-\omega$  measurements, the epilayer  $2\theta-\omega$  diffraction curve was more narrow compared with the substrate. Thus strain from the substrate is reduced in the epilayer which would be explained by improved domain structure and crystallinity.

Structural improvement might be a consequence of step-flow growth mechanism. Since substrate surfaces are off-oriented, nucleation takes place at the wafer edge opposite to the step-flow direction. As epilayer thickness increases, domains at the edge from where steps start, partly or completely overtake domains in down-step direction by increased domain sizes.

A series of seven samples was grown to study conditions for improved purity. The effect of graphite and Ta was investigated. Al and B concentrations in purified and unpurified graphite parts, source material, and grown epilayers were measured using SIMS, Table 2. Sample 1 was grown using un-purified graphite and shows a higher Al level than samples 2-4 which were grown using purified graphite (other conditions similar). For the latter samples the Al concentration decreases for each run whereas the B concentration stays constant. We observed, also when using source material with higher B concentration, that the B incorporation is almost unity from source to grown material. Thus the B concentration in epilayers is very sensitive to the B concentration in the source. As seen in Table 2, higher Al concentrations than given by source and graphite can be detected in the epilayers. This is most probably due to the Ta foil in which Al was detected. Using more pure Ta or Ta converted to TaC will very likely reduce this contribution. Sample 5 was grown without Ta in a high-purity graphite crucible. The Al concentration drastically decreased compared with samples 1-4. For samples 6 and 7 (high purity graphite crucible was used), the Ta surface was slightly converted prior to growth. The Al concentration in these samples are also drastically reduced. With improving purity control (samples 1 to 7) the Al level has been reduced about two orders of magnitude.

The layers grown at optimized conditions are n-type with carrier concentration  $N_D-N_A \sim 1-2 \times 10^{15} \text{ cm}^{-3}$  as obtained by C-V measurements. A low residual impurity level is supported by appearance of phonon replicas of free excitons in low-temperature PL measurements, Fig. 3.

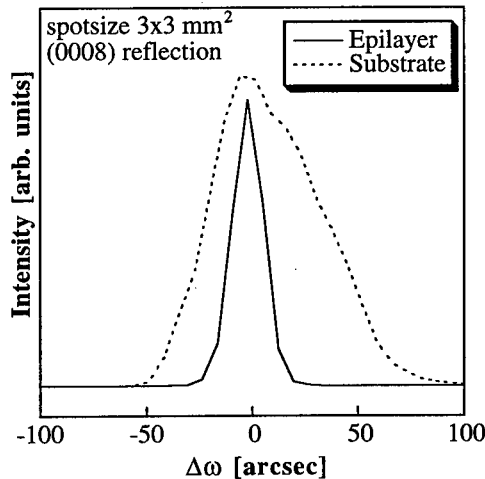


Fig. 2.  $\omega$ -rocking curve measurements from a substrate and the epilayer grown on the same substrate; layer thickness 100  $\mu\text{m}$ . The FWHM values are 60" and 20" for the substrate and epilayer, respectively.

TABLE 2. SIMS results for Al and B concentrations using same source for all epilayers, an unpurified graphite crucible for sample 1, and a purified graphite crucible for samples 2-7. Layer thicknesses 50  $\mu\text{m}$ ; b=background level ( $5 \times 10^{14} \text{ cm}^{-3}$  for B and Al) in the SIMS system.

	B	Al
Sample 1 (Ta)	$3 \times 10^{15}$	$1 \times 10^{17}$
Sample 2 (Ta)	$3 \times 10^{15}$	$6 \times 10^{15}$
Sample 3 (Ta)	$3 \times 10^{15}$	$2 \times 10^{16}$
Sample 4 (Ta)	$3 \times 10^{15}$	$3 \times 10^{16}$
Sample 5 (no Ta)	$3 \times 10^{15}$	$4 \times 10^{15}$
Sample 6 (TaC)	$3 \times 10^{15}$	$2 \times 10^{15}$
Sample 7 (TaC)	$3 \times 10^{15}$	$1.5 \times 10^{15}$
Source	$3 \times 10^{15}$	$< 1 \times 10^{15}$
Unpurified graphite	$2 \times 10^{15}$	$1-10 \times 10^{15}$
Purified graphite	$4 \times 10^{15}$	$< 1 \times 10^{15}$
Ta	b	yes



The fact that free exciton related luminescence is observed at low temperatures together with high PL intensity, indicates high-quality material. When impurity concentration or number of crystal imperfections become too large, free excitons will form bound excitons or recombine non-radiatively. With improving epilayer quality, the probability for free excitons to recombine radiatively will increase.

Results from our studies on intentional doping for high-resistive/semi-insulating thick layers show that the resistivity influenced by compensation of N with B is  $6 \times 10^4 \Omega\text{cm}$  (p-type) at room temperature where the B concentration is  $\sim 3 \times 10^{16} \text{ cm}^{-3}$ . Additional vanadium doping for semi-insulating behaviour shows that the V concentration is between  $2\text{--}3 \times 10^{16} \text{ cm}^{-3}$ . The material is not yet semi-insulating, probably due to impurities in the V source. The doping has not been observed to degrade the surface morphology or structural quality. Preliminary results from intentional doping with Al show that at  $2 \times 10^{19} \text{ cm}^{-3}$  the shallow level is predominately occupied. The samples are free of stress associated with high doping.

### Summary

Thick (50–100  $\mu\text{m}$ ) 4H-SiC layers have been grown by sublimation epitaxy with a growth rate of 100  $\mu\text{m/h}$ . Surfaces are specular and featureless regarding typical defects in SiC epitaxy. The structural quality is high and has even considerably improved as compared with the substrate. This shows that, at proper growth conditions, step-flow growth mechanism is stable which is important for growth of thick high-quality epilayers. Control of purity in graphite parts, source material and Ta (TaC) parts are necessary for growth of high-purity SiC using sublimation epitaxy. The net carrier concentration is  $< 2 \times 10^{15} \text{ cm}^{-3}$ . Intentional doping studies show that high-resistive material is reproducibly achieved using N and B.

### Acknowledgement

This work was supported by the SSF program SICEP and Lennanders Foundation.

### References

- [1] O. Kordina, C. Hallin, A. Henry, J.P. Bergman, I. Ivanov, A. Ellison, N.T. Son, and E. Janzén, *Phys. Stat. Sol. (b)* **202** (1997) p. 321.
- [2] T. Kimoto, A. Itoh, H. Matsunami, *Phys. Stat. Sol. (b)* **202** (1997) p. 247.
- [3] O. Kordina, K. Irvine, J. Sumarekis, H.S. Kong, M.J. Paisley, and C.H. Carter, Jr, *Mat. Sci. Forum* **264-268** (1998) p. 107.
- [4] Yu.A. Vodakov, E.N. Mokhov, M.G. Ramm, and A.D. Roenkov, *Krist. und Tech.* **14** (1979) p. 729.
- [5] E.N. Mokhov, I.L. Shulpina, A.S. Tregubova, and Yu.A. Vodakov, *Crystal Res. Tech.* **16** (1981) p. 879.
- [6] M. Syväjärvi, R. Yakimova, M. Tuominen, A. Kakanakova-Georgieva, M.F. MacMillan, A. Henry, Q. Wahab, and E. Janzén, *J. Crystal Growth* **197** (1999) p. 155.
- [7] J.A. Powell and D.J. Larkin, *Phys. Stat. Sol. (b)* **202** (1997) p. 529.
- [8] T. Kimoto, N. Miyamoto, and H. Matsunami, *Mat. Sci. Eng. B*, in press (1999).
- [9] D. Hofmann, S.Yu. Karpov, Yu.N. Makarov, E.N. Mokhov, M.G. Ramm, M.S. Ramm, A.D. Roenkov, and Yu.A. Vodakov, *Inst. Phys. Conf. Ser.* **142** (1996) p. 29.
- [10] Yu.A. Vodakov, A.D. Roenkov, M.G. Ramm, E.N. Mokhov, and Yu.N. Makarov, *Phys. Stat. Sol. (b)* **202** (1997) p. 177.

Correspondence; Phone: +46 13 285708; Fax: +46 13 142337; E-mail: msy@ifm.liu.se

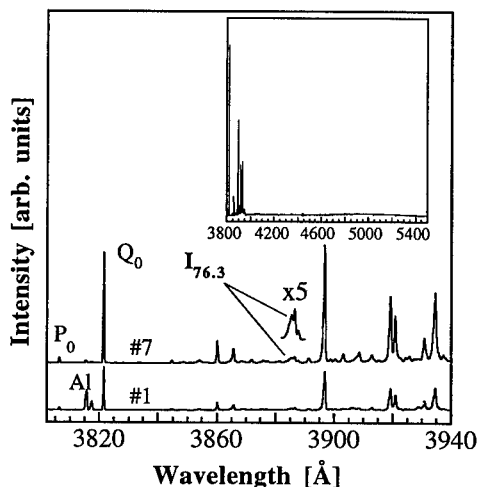


Fig. 3. Low-temperature (2K) PL from samples 1 and 7 showing decreasing Al signal and increasing luminescence intensity with improved growth conditions #1→#7 as well as phonon replica from the free exciton. The PL intensities have been shifted for distinction between the luminescence from the samples. No donor-acceptor pair luminescence is observed (insert).

## Competitive Growth between Deposition and Etching in 4H-SiC CVD Epitaxy Using Quasi-Hot Wall Reactor

M. Kushibe<sup>1</sup>, Y. Ishida<sup>2</sup>, H. Okumura<sup>2</sup>, T. Takahashi<sup>2</sup>, K. Masahara<sup>1</sup>,  
T. Ohno<sup>1</sup>, T. Suzuki<sup>1</sup>, T. Tanaka<sup>1</sup>, S. Yoshida<sup>2</sup> and K. Arai<sup>2</sup>

<sup>1</sup> Advanced Power Devices Laboratory, UPR Ultra-Low-Loss Power Device Technology Research Body, 1-1-4 Umezono, Tsukuba, Ibaraki, 305-8568, Japan

<sup>2</sup> R&D Association for Future Electron Devices, UPR Ultra-Low-Loss Power Device Technology Research Body, Eletrotechnical Laboratory, 1-1-4 Umezono, Tsukuba, Ibaraki, 305-8568, Japan

**Keywords:** Deposition Rate, Surface Modification, Temperature Dependence

### ABSTRACT

Deposition temperature dependence of deposition rate is studied quantitatively in 4H-SiC CVD under hydrogen atmosphere in the temperatures range from 1470 to 1720 °C. When process temperature is higher than 1620 °C, etching rate is comparative to the growth rate and reduction of deposition rate occurs. At 1720 °C, etching rate was so large as 33 µm/hr and large amount of source gas supply was required to attain deposition. The reduction of deposition rate is simply deduced from etching rate observed in hydrogen atmosphere. The maximum deposition rate for samples with mirror surface increases with deposition temperature. High growth rate of about 30 µm/hr is obtained when deposition temperature is 1720 °C. However, etching rate is suggested to be larger than the maximum epitaxial growth rate when deposition temperature is higher than 1800 °C due to the large temperature dependence of etching rate.

### INTRODUCTION

For the realization of high power devices of SiC, a few tens of microns thick epitaxial-layer is required. Conventionally, 4H-SiC is deposited in the temperature range between 1400 to 1600 °C and growth rate is around 5 µm/hr [1]. To attain higher growth rate and to improve the quality of SiC epitaxial layers, higher growth temperatures are considered to be preferable. To obtain quite high growth rate of a few hundreds µm/hr, deposition of SiC at over 2000 °C is reported [2]. CVD in that temperature range is, however, considered to suffer from controllability and reproducibility of epitaxial layer properties such as thickness. Due to the high temperature, gas phase reaction is inevitable. Degradation of carbon susceptor is unavoidable. In addition etching rate of SiC is quite large in hydrogen atmosphere in that temperatures range causing difficulty for preparation of the surface condition of the substrate before the deposition [3].

In this work, we tried to attain larger growth rate of 4H-SiC by adopting slightly higher growth temperature than conventional CVD. We investigated the maximum growth rate in this temperature range. The effect of etching on growth rate is investigated quantitatively.

### EXPERIMENTAL

A quasi-hot wall type reactor is developed to attain higher temperature in CVD. The reactor is equipped with a RF-heated carbon cover put several mm above a RF-heated susceptor to heat wafer from both sides. The system has two pyrometers. One is set at the top of the reactor to observe the temperature of the susceptor from surface side. The other one is set at the bottom of the reactor to reveal the backside temperature of the susceptor. The growth temperature is determined by the top pyrometer just at the beginning of the deposition. Backside pyrometer is used to ensure the temperature observed from surface side.

The (0001) Si-face 4H-SiC wafers are used for this study. They are miscut by 8 degree toward

$\langle 11\bar{2}0 \rangle$ . Deposition temperature was varied from 1470 to 1740 °C. The process pressure was varied from 2 to 760 Torr. The standard pressure was 20 Torr as the surface morphology of the wafers was excellent after thermal etching at this pressure in preliminary experiment. Carrier gas was  $H_2$  and source gases were  $SiH_4$  and  $C_3H_8$ . C/Si supply ratio was 3 for standard conditions. Deposition layer was grown for 30 min. For etching process, wafer was kept at process temperature for 30 to 50 min in  $H_2$  ambient.

Deposition rate and etching rate were determined by the weight difference of wafers measured before and after the process. Surface morphology of the epitaxial layers was observed by Nomarski differential interference contrast microscope.

## RESULTS AND DISCUSSIONS

Source gas flow rate dependence of deposition rate is shown in fig. 1. Deposition temperature is 1470, 1620 and 1720 °C. Open marks represent mirror surface samples and closed marks represent rough surface samples. No flow of  $SiH_4$  corresponds to the etching as there supplied no source gases. When process temperature is 1470 °C, etching rate is 1  $\mu m/hr$ . When 0.4 sccm of  $SiH_4$  and  $C_3H_8$  are supplied, deposition rate of SiC reaches 5  $\mu m/hr$ . Deposition rate of SiC increases with  $SiH_4$  flow rate until it reaches 1.2 sccm, then it decreases. When  $SiH_4$  flow rate is smaller than 0.8 sccm, surface of sample is mirror. The utmost deposition rate for the sample with mirror surface is about 8  $\mu m/hr$ . When process temperature is 1620 °C, etching rate is 10  $\mu m/hr$ . At this temperature, deposition rate of SiC is as small as 0.4  $\mu m/hr$  for 0.4 sccm  $SiH_4$  supply due to the reduction of deposition presumably caused by the etching. Deposition rate of SiC increases with the increase of  $SiH_4$  flow rate and reaches about 20  $\mu m/hr$  when  $SiH_4$  flow rate is 2 sccm. For high process temperature of 1720 °C, the etching rate is as large as 33  $\mu m/hr$ . When  $SiH_4$  flow rate is smaller than 1.6 sccm, deposition does not occur. The flow rate of 1.6 sccm is a large enough value to attain high deposition rate of nearly 20  $\mu m/hr$  when deposition temperature is 1620 °C. Only when quite large flow rate of  $SiH_4$  is adopted, deposition occurs. The largest deposition rate for samples with mirror surface is, however, larger than 30  $\mu m/hr$  owing to the high deposition temperature.

Temperature dependence of competition between deposition and etching is shown in fig. 2. Closed marks represent the temperature dependence of etching rate. Open marks represent the temperature dependence of deposition rate at constant  $SiH_4$  flow rate of 1.6 sccm. At the higher etching temperature, the etching rate is larger. When etching temperature is larger than 1600 °C, the increase of etching rate is drastic. Growth rate decreases with increasing deposition temperature. Above 1600 °C, decrease of deposition rate with temperature is clear. When deposition temperature is higher than 1680 °C, etching overcomes deposition and deposition does

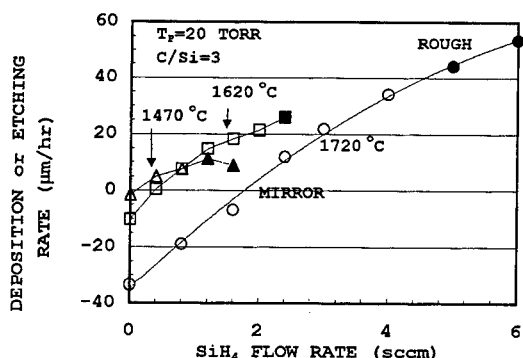


Fig. 1 Deposition rate dependence on  $SiH_4$  flow rate

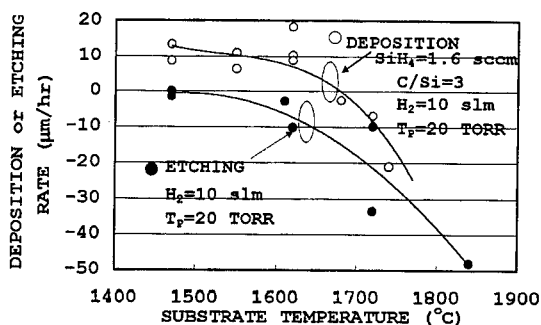


Fig. 2 Competition of deposition and etching at various deposition temperatures

not occur. For temperatures higher than 1680 °C, similar to the etching case, the higher deposition temperature, the larger the etching rate. Increase of etching rate and decrease of deposition rate show similar temperature dependence suggesting that decrease of deposition is mainly originated from the increase of etching.

These results indicate that higher temperature is preferable for higher growth rate but they also indicate that effect of etching is quite serious at higher deposition temperature.

If there is no etching, deposition rate is expected to be proportional to the  $\text{SiH}_4$  flow rate. In fig. 3, the etching rate is added to measured deposition rate depicted in fig. 1. If we assume that the etching is a simple additional effect to the deposition, "deposition rate + etching rate" is considered to be "genuine" deposition rates, which should be observed if there is no etching.

Open marks represent samples with mirror surface and closed mark represent samples with rough surface.

"Deposition rate + etching rate" increases proportionally with  $\text{SiH}_4$  flow rate irrespective of deposition temperature. When  $\text{SiH}_4$  flow rate nearly reaches the maximum value for mirror surface samples, the deposition rate tends to level off from the proportional line between deposition rate and  $\text{SiH}_4$  flow. From this simple result, the origin of the decrease of deposition rate with rise of temperature can be attributed to the increase of etching rate as far as when mirror surface samples are obtained. These relations also suggest that no synergetic effect occurred between etching and deposition though they are competitive in this temperature range.

In fig. 4, pressure dependence of deposition rate is shown. When the pressure is higher than 100 Torr, there is almost no etching and deposition rates are almost proportional to  $\text{SiH}_4$  flow rate. Below 20 Torr, no deposition occurs

when  $\text{SiH}_4$  flow rate is lower than a certain threshold value. Deposition rate is however almost proportional to  $\text{SiH}_4$  flow rate when it is higher than the threshold values. These results indicate that the etching affects the deposition more when deposition pressure is low, suggesting the importance of the desorption mechanism of some species from SiC surface.

The temperature dependence of the maximum deposition rate for mirror surface samples is shown in fig. 5. By using higher deposition temperature, mirror surface samples are obtained at

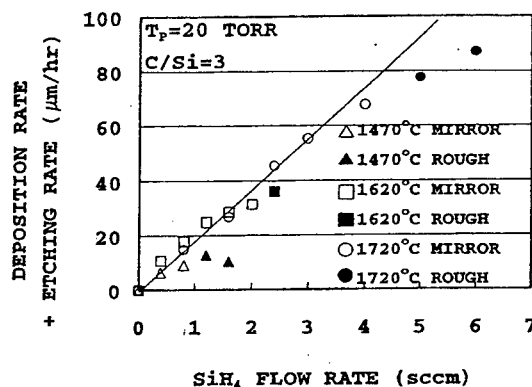


Fig. 3 "Deposition rate + etching rate" dependence on  $\text{SiH}_4$  flow rate. Line indicates the proportional relation "Deposition rate + Etching rate" and between  $\text{SiH}_4$  flow rate.

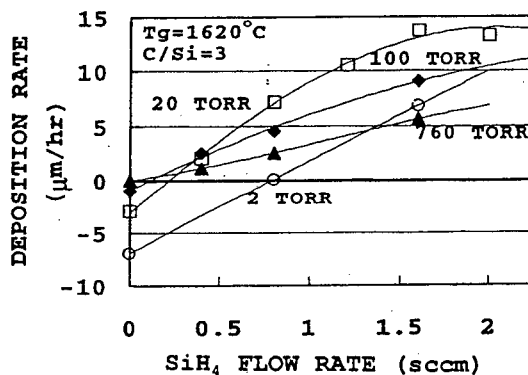


Fig. 4 Pressure dependence of deposition rate

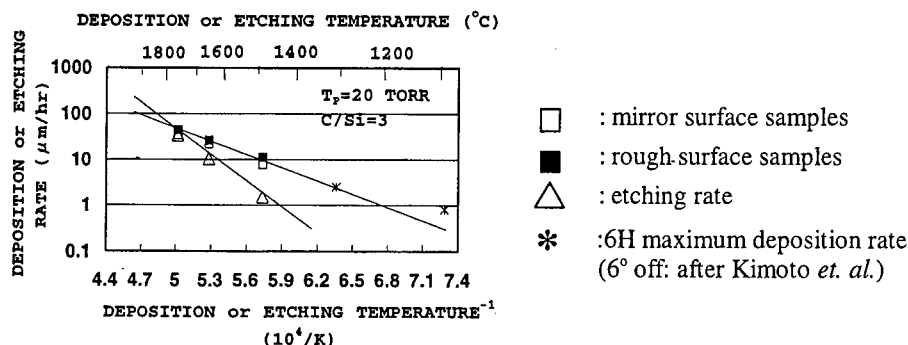


Fig. 5 Comparison of temperature dependence between deposition and etching

larger deposition rate. The largest deposition rate with mirror surface is as high as about 30  $\mu\text{m/hr}$ . The maximum deposition rate for step flow mode epitaxy reported by Kimoto *et. al.* [4] is also plotted in the figure for comparison. When deposition temperature is higher than 1300 °C, the maximum deposition rate decreases exponentially with temperature. This result suggests that the dominant factor that determines the temperature dependence of deposition is the same in this temperatures range. Temperature dependence of etching rate is also plotted in fig. 5. The dependence of etching is larger than that of maximum deposition rate. The etching rate is suggested to be larger than the maximum deposition rate when deposition temperature is higher than 1800 °C. The mechanism of deposition might be different when temperature is higher than 1800 °C.

## SUMMARY

Competition between growth and etching was studied quantitatively in 4H-SiC CVD under hydrogen atmosphere in the temperature range between 1470 and 1720 °C. At higher temperature, etching rate increases and deposition rate decreases corresponding to the increase of etching rate. Etching rate is comparative to the growth rate when growth temperature is higher than 1620 °C. Large source gas supply is required to attain deposition at 1720 °C. With the increase of the deposition temperature, however, maximum growth rate for mirror surface sample increases. The largest growth rate, of about 30  $\mu\text{m/hr}$ , was obtained at 1720 °C.

The hypothetical deposition rate obtained by adding observed deposition rate and etching rate is proportional to the  $\text{SiH}_4$  flow rate irrespective of the deposition temperature, suggesting that deposition and etching can be dealt with separately without considering the synergetic effect though they are competitive in this temperature range. When deposition temperature is higher than 1800 °C, etching rate is suggested to be larger than the maximum epitaxial growth rate and the mechanism of deposition might differ from that in the temperature range of this work.

**Acknowledgement** This work was performed under the management of FED as a part of the MITI NSS Program (R&D of Ultra-Low-Loss Power Devices Technologies) supported by NEDO.

## References

- [1] R. Rupp *et. al.*, Mater. Sci. Forum, **264-268** (1998), p. 89
- [2] O. Kordina *et. al.*, Appl. Phys. Lett., **29** (1996), p. 1456
- [3] J.A. Powell *et. al.*, Mater. Sci. Forum, **264-268** (1998), p. 421
- [4] T. Kimoto *et. al.*, J. Appl., Phys. **75** (1994), p. 850

## Multi-Wafer VPE Growth and Characterization of SiC Epitaxial Layers

H.D. Nordby, Jr.<sup>1</sup>, M.J. O'Loughlin<sup>1</sup>, M.F. MacMillan<sup>2</sup>, A.A. Burk, Jr.<sup>1\*</sup>  
and J.D. Oliver, Jr.<sup>1</sup>

<sup>1</sup> Northrop Grumman Advanced Technology Laboratories, PO Box 1521, MS 3K13,  
Baltimore, MD 21203, USA

<sup>2</sup> Northrop Grumman Science and Technology Center, Pittsburgh, PA 15235, USA

**Keywords:** Epitaxial Growth, Growth Rate, Multi-Wafer Reactor, Production

### Abstract

Current results are presented for SiC epitaxial growths employing a 7x2" SiC-VPE reactor. For growths on 2-inch SiC diameter substrates, the dopant concentration and layer thickness uniformity is typically  $\pm 5\%$  (standard deviation/mean). For the seven wafers within a run, the interwafer uniformity has been improved to approximately  $\pm 7\%$  for dopant concentration and  $\pm 3\%$  for layer thickness. Data will be presented which exhibit interrun (run-to-run) variation, for both thickness and doping, within  $\pm 10\%$  of the desired values. Also, preliminary results of investigations into higher growth rates (5.0 to 9.5  $\mu\text{m/hr}$ ) and thick epitaxial layers are presented.

### Introduction

High-frequency, high-power static induction transistors (SITs) and metal semiconductor field effect transistors (MESFETs) have been demonstrated with performance exceeding that available from both silicon and gallium arsenide transistors [1,2,3]. For the production of these SiC based devices, a multi-wafer SiC VPE reactor has been developed in collaboration with Aixtron, AG [4]. The reactor, based on the design of Frijlink and coworkers [5], features full planetary motion and, as currently configured, is capable of simultaneous, high quality epitaxy on seven, two-inch diameter substrates. Aluminum and boron impurity levels of less than mid  $10^{14}$  atoms/cm<sup>3</sup> have been measured by SIMS. At silicon-to-carbon (Si/C) ratios normally employed, background n-type doping levels are less than  $1 \times 10^{15}$  cm<sup>-3</sup>, and room temperature mobilities as high as 1000 cm<sup>2</sup>/Vs are routinely obtained [6].

Previously, to achieve satisfactory uniformity and to reduce run-to-run variability for pre-production layers, it was necessary to modify many of the original reactor components [6]. Currently, the start of production has significantly increased the number of wafers required with the specifications that all epitaxial layers must be within  $\pm 10\%$  of target values for both dopant concentration and thickness. Additional reactor modifications which

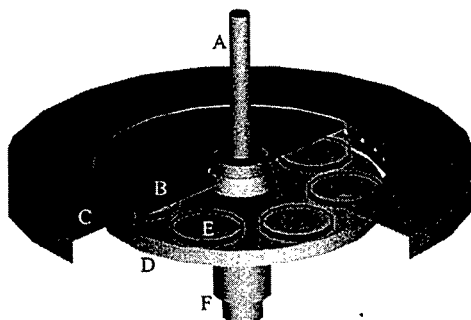


**Fig. 1:** Stylized cross section of VPE reactor. A) Gas Injector, B) Ceiling, C) Gas Collector, D) Susceptor, E) Wafer Holder, F) Rotation Axis

\* Current Address: Cree Research, Durham, NC 27703

have allowed these production specifications to be realized will be summarized. Also, in an attempt to better utilize the production reactor and to further expand its processing envelope, preliminary investigations into higher growth rates, 5.0 to 9.5  $\mu\text{m/hr}$ , and thick epitaxial layers were conducted.

### Experiment

The VPE reactor used to grow the SiC epitaxial layers discussed within has been described in detail elsewhere [3,6,7]. A cross sectional view of the reactor is shown in Fig. 1.

Detailed conditions for SiC epitaxial layer growth in this reactor have been previously reported [6]. The production growths reported in this study were performed at reduced pressure, susceptor temperatures of  $\sim 1600^\circ\text{C}$ , growth rates of  $\sim 3 \mu\text{m/hr}$ , and Si/C around 0.88. The mass of each wafer was measured with an analytical balance, both before and after growth, to determine average epitaxial layer thickness, growth rate, and wafer-to-wafer uniformity. All epitaxial layers were characterized by capacitance versus voltage (CV) measurements [8]. CV measurements were performed at regular intervals along one radius of each wafer. Rotating wafers have been found to be highly axially symmetric making the measurement of one radius sufficient.

Also, a preliminary study into growth rates as high as 9.5  $\mu\text{m/hr}$  and epitaxial layers thicker than 25  $\mu\text{m}$  was performed. The layers for this investigation were grown under similar conditions to those above. Higher growth rates were accomplished by increasing the precursor flows (silane and propane) while keeping all other process parameters constant. Thick epitaxial layers were then grown at the higher growth rate conditions and characterized using CV measurements, low temperature photoluminescence (PL), and FTIR thickness mapping [9].

### Results

Three levels of epitaxial uniformity were examined; intra-wafer uniformity, inter-wafer (or intrarun) uniformity, and inter-run (run-to-run) uniformity.

Previous reductions of susceptor and component induced inhomogeneity [6,7] have reduced the intra-wafer dopant concentration and thickness uniformities (standard deviation divided by the mean) for 2-inch diameter wafers to 4.7% and 5.2% respectively. However, the inter-wafer (wafer-to-wafer within a run) uniformity had only been reduced to 10% at best. With typical inter-wafer standard deviations ranging from 11 to 18%, at least one-third of the wafers were falling outside the  $\pm 10\%$  specifications for production epitaxial layers.

By replacing the original graphite foam gas collector (C in Fig. 1) with a molybdenum one with smaller perforations, the inter-wafer thickness uniformity improved to approximately 3%. This is thought to be due to increased flow symmetry resulting from an increased pressure drop across the interface between the growth region and the gas collector. The time evolution of inter-wafer uniformity is presented in Fig. 2. The molybdenum gas collector was installed at point A on that chart. It is evident that the improvement in thickness uniformity was not matched by a corresponding improvement in dopant

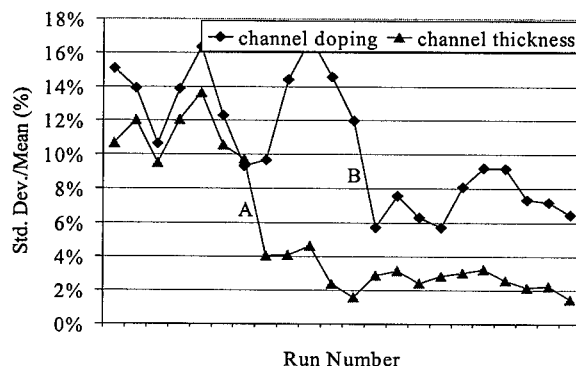


**Fig. 2:** Inter-wafer uniformity for 22 runs. A new gas collector was installed at A. Susceptor hardware was rearranged at B to improve the temperature balance.

concentration uniformity. The dopant concentration of the individual wafers still exhibited a systematic distribution, *i.e.* the highest doped position was opposite the lowest doped position. The highest doped position correlated with the hottest side of the susceptor. By rearranging the susceptor hardware to improve the temperature balance (point B in Fig. 2), the dopant concentration uniformity was reduced to 7%. Most of the remaining non-uniformity is randomly distributed and arises from small differences in local temperature due to variations in; emissivity of components, thermal contact between wafer and satellite, satellite levitation, *etc.* An overlay of the dopant profiles at five positions along the radius of each of seven wafers in a single run is presented in Fig. 3. For the run represented by that figure, both the thickness and dopant concentration uniformity at  $2 \times 10^{17} \text{ cm}^{-3}$  are approximately 5%. At  $1 \times 10^{16} \text{ cm}^{-3}$  the dopant concentration uniformity is 7%.

Having demonstrated good uniformity on a 2-inch diameter wafer and for each wafer in a run, the remaining obstacle to high yield production epitaxy is interr run variation. The improvements effected to decrease the interwafer variation also permitted better control of run-to-run variation. In fact, after point B (Fig. 2), corresponding to improved gas collector geometry and susceptor temperature uniformity, the average absolute deviation from target values were 2.8% for dopant and 3.6% for thickness.

Once the  $\pm 10\%$  uniformity production specifications were achieved, higher growth rates were investigated to make the reactor more efficient and provide the ability to grow thick epitaxial layers in a multi-wafer production reactor. As a preliminary attempt to increase the growth rate, only the precursor flows, which were adjusted for a Si/C ratio of approximately 0.95, were increased while all other process parameters were held constant. The growth rate was found to increase linearly with increasing precursor flow through the entire range of the existing silane mass flow controllers. Fig. 4 illustrates the affect that input silane flow has on growth rate. The linearity of the growth rate as a function of silane concentration indicates that even at these high silane flow rates, the reaction is still silicon diffusion limited. This is made possible by high ceiling temperatures which avoid silicon supersaturation [8]. The maximum growth rate

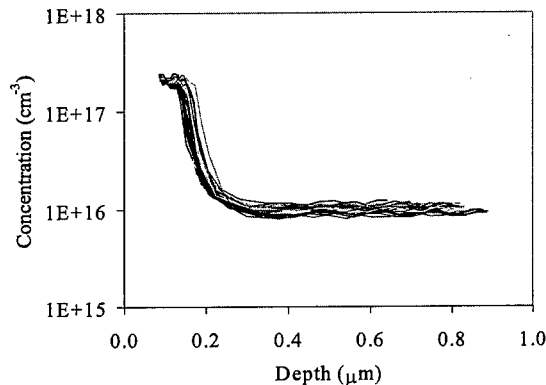


Fig. 3: An overlay of the CV dopant profile measured along the radius of each of seven wafers in a run.

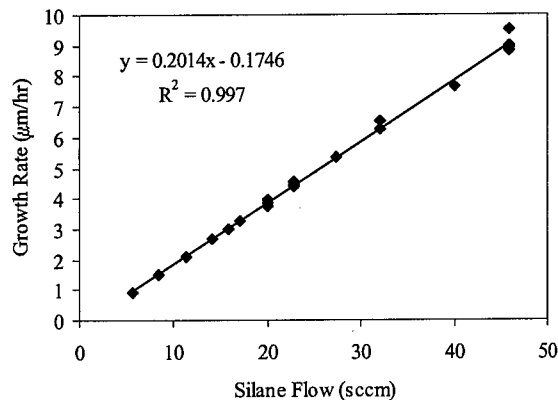
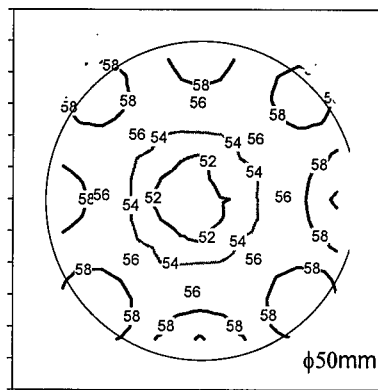


Fig. 4: The linear dependence of growth rate on input silane flow



achieved was 9.5  $\mu\text{m/hr}$ . All layers grown at the higher rates were specular and had an overall thickness uniformity of 3.1%.

Next, attempts were made to grow thick epitaxial layers using the higher growth rates. Fig. 5 shows the FTIR thickness contour map for a 57  $\mu\text{m}$  layer with 3.9% thickness uniformity grown at 9.5  $\mu\text{m/hr}$ . This wafer was intentionally doped with nitrogen to a concentration of  $5 \times 10^{14} \text{ cm}^{-3}$ , but at that low concentration the dopant uniformity was only 18.5%. Fig. 5 also shows that the thick layer exhibits the typical radial thickness distribution due to wafer holder rotation. PL and lifetime measurements were made on this sample. The PL spectrum was typical of SiC, however, the measured lifetime of 57 ns was very low. Growth conditions were not optimized to maximize lifetime.



**Fig. 5:** The FTIR thickness map for a 57  $\mu\text{m}$  layer with a 3.9% thickness uniformity.

### Conclusions

Sufficient uniformity has been demonstrated for SiC epitaxy on seven at-a-time two-inch diameter wafers for high yield in production. Intra-wafer uniformity of approximately 5% can be routinely achieved on two-inch diameter wafers. The most significant improvement has been the reduction of inter-wafer uniformity to 3% for thickness and 7% for dopant concentration. The combination of good intra-wafer and inter-wafer uniformity has been coupled with better control of run-to-run variation such that a very high percentage of epitaxial layers meet stringent production specifications. Also, results show that greater than 50  $\mu\text{m}$  thick layers can be grown at growth rates as high as 9.5  $\mu\text{m/hr}$  with thickness uniformity of 4%.

### References

1. S. Sriram, G. Augustine, A. A. Burk, Jr., R.C. Glass, H. M. Hobgood, P. A. Orphanos, L.V. Rowland, T. J. Smith, C. D. Brandt, M. C. Driver, and R. H. Hopkins, *IEEE Electron Device Lett.*, **EDL-17**, (1996) p. 369.
2. R. R. Siergiej, S. Sriram, R. C. Clarke, A. K. Agarwal, C. D. Brandt, A. A. Burk, Jr., T. J. Smith, A. Morse, and P. A. Orphanos, *Tech. Digest Int. Conf. SiC and Rel. Mat'95*, (Kyoto, Japan 1995), p. 321.
3. A. A. Burk, Jr., M. J. O'Loughlin, R. R. Siergiej, A. K. Agarwal, S. Sriram, R. C. Clarke, M. F. MacMillan, V. Balakrishna, and C. D. Brandt, *J. Solid State Electronics*, accepted for publication.
4. Aixtron Inc. Kackerstr. 15-17, D-52072 Aachen, Germany.
5. P. M. Frijlink, *J. Crystal Growth*, **93**, (1988) p. 207.
6. A. A. Burk, Jr., M. J. O'Loughlin, and H. D. Nordby, Jr., *J. Crystal Growth*, **200**, (1999) p. 458-466.
7. A. A. Burk, Jr., M. J. O'Loughlin, and S. S. Mani, in *Silicon Carbide, III-Nitrides, and Related Materials*, Materials Science Forum, **264-268**, (Switzerland 1998), p. 83-88.
8. M. J. O'Loughlin, H.D. Nordby, Jr., and A. A. Burk, Jr., 1999 MRS Spring Meeting, San Francisco, April 5-9.
9. M. F. MacMillan, P. O. Narfgrén, A. Henry, and E. Janzen, in *Silicon Carbide, III-Nitrides, and Related Materials*, Materials Science Forum, **264-268**, (Switzerland 1998), p. 645-648.

The authors gratefully acknowledge Gil Rykiel, Rick Prola, Ollie Gildow, and Rich Siergiej for their assistance in reactor modifications, epitaxial growth, and characterization. We would also like to thank Professor Jim Choyke at University of Pittsburgh for performing the low temperature PL and lifetime measurements.

Corresponding authors: [howard\\_nordby@cree.com](mailto:howard_nordby@cree.com) and [james\\_d\\_oliver@md.northgrum.com](mailto:james_d_oliver@md.northgrum.com)

## Homoepitaxy of Silicon Carbide Using the Single Precursor 1,3-Disilabutane

Sung Yong Lee, Kyung-Won Lee and Yunsoo Kim

Advanced Materials Division, Korea Research Institute of Chemical Technology,  
Yusong, PO Box 107, Taejeon, 305-600, Korea

**Keywords:** Chemical Vapor Deposition, Homoepitaxy, Single Precursors

**Abstract** Homoepitaxial growth of SiC thin films by chemical vapor deposition using the single source 1,3-disilabutane has been carried out at the low temperatures of 900-1100 °C in an ultrahigh vacuum chamber equipped with reflection high energy electron diffraction. The structure and morphology of the films have been found to be strongly affected by the growth temperature. The films grown on on-axis 6H-SiC(0001) substrates at temperatures between 900 and 1100 °C had only the 3C-SiC(111) structure, but those grown on vicinal (3.5° off-oriented) 6H-SiC(0001) substrates produced the 3C-SiC structure at temperatures below 1000 °C and the 6H-SiC structure at temperatures between 1000 and 1100 °C, while on vicinal (8° off-oriented) 4H-SiC(0001) the films had the 4H-SiC structure even at 900 °C.

### Introduction

Silicon carbide (SiC) has been studied for high power and high temperature electronic device applications due to its high thermal conductivity, wide band gap and many superior physical and electronic properties. There have been many studies of homoepitaxial growth of SiC for the past ten years or so since it results in higher quality films than heteroepitaxial growth. Most heteroepitaxial growth of SiC has been carried out by conventional chemical vapor deposition (CVD) using two source chemicals (e.g., SiH<sub>4</sub> or Si<sub>2</sub>H<sub>6</sub> for silicon and C<sub>2</sub>H<sub>4</sub> or C<sub>3</sub>H<sub>8</sub> for carbon) in the temperature range 1400-1800 °C [1,2]. SiC crystallizes in many polytypes, and generally, 3C-SiC is known as the low temperature polytype owing to its higher probability of appearance at low temperatures. Because many defects are created during the film growth of the 3C-SiC, many people have concentrated on homoepitaxial growth of 6H- and 4H-SiC and have made efforts to decrease the growth temperature using various methods and techniques. It has been reported that 6H- and 4H-SiC can be grown homoepitaxially on off-oriented substrates at temperatures of 1400-1500 °C by the step flow mechanism [3,4]. It is important, however, to further decrease the growth temperature (because growth at high temperatures is usually accompanied by more impurity incorporation and interdiffusion of dopants across the interfaces in the case of multilayer films) and to reduce the number of steps in the CVD process for device applications. There have been a few studies of heteroepitaxial growth using single sources but we could hardly find any studies of homoepitaxial growth using them. 1,3-disilabutane, which is nontoxic, fairly volatile, and inert in air, was successfully employed in growing heteroepitaxial films of 3C-SiC on Si substrates at the relatively low temperatures of 900-1000 °C [5,6]. We consider it to be a proper candidate among many single sources for SiC homoepitaxy.

### Experimental

Homoepitaxial growth of SiC thin films has been carried out in an ultrahigh vacuum (UHV) chamber equipped with a quadrupole mass analyzer (QMA) for measurement of residual gases in

the chamber and a reflection high energy electron diffraction (RHEED) for in situ analysis of the surface structures of the films. The base pressure of the system was below  $3 \times 10^{-9}$  Torr. On-axis and vicinal 6H- and 4H-SiC wafers oriented  $3.5^\circ$  and  $8^\circ$ , respectively, toward the  $\langle 11\bar{2}0 \rangle$  direction were obtained from Cree Research, Inc. These wafers were cut to the size  $5 \times 7 \text{ mm}^2$ . The substrates were chemically etched in a 10 % HF solution for 10 min to remove the oxide layer, rinsed in deionized water, and immediately loaded into the growth system. To obtain clean surfaces, these substrates were held at 400-500 °C for 4-6 h and heated at 1100 °C for 1-3 min under UHV conditions just before introducing the precursor.

### Results and Discussion

The effect of temperature on the film growth on on-axis 6H-SiC(0001) substrates was investigated at temperatures between 900 and 1100 °C and pressure of  $1 \times 10^{-6}$  Torr. Fig. 1 shows the RHEED patterns and the scanning electron microscopy (SEM) images of the films grown at 900, 1000 and 1100 °C, respectively, for 2 h. The RHEED patterns of the films grown at low temperatures show diamond-hatched shapes consisting of extra spots indicative of poor crystallinity, which probably arises from twin and double positioning boundary (DPB) defects. These incoherent twin boundaries occur when 3C-SiC(111) is grown on Si(111) or on-axis 6H-SiC(0001) because two different orientations rotated  $60^\circ$  from each other are present [7-9]. As the growth temperature was increased, the extra spots of the RHEED patterns changed into streaks indicating fewer of these

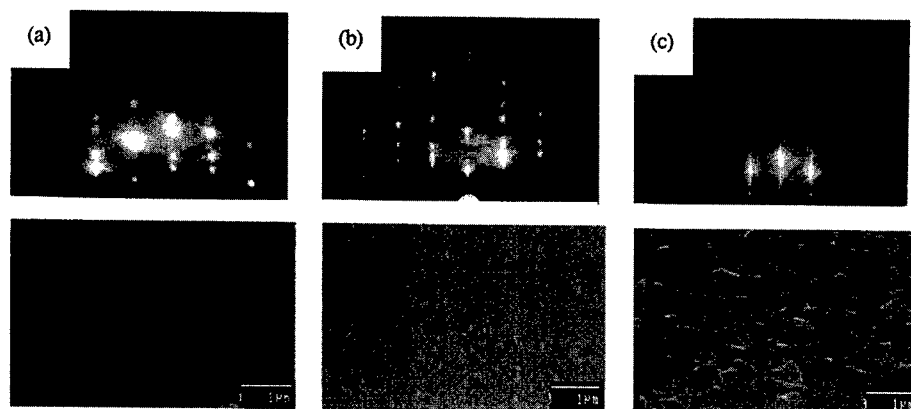


Fig. 1. RHEED patterns and SEM images of 3C-SiC films grown on on-axis SiC(0001) substrates at various temperatures: (a) 900, (b) 1000, and (c) 1100 °C.

defects and an improvement of the surface morphology. The SEM images also show that surface smoothness and uniformity improved with the growth temperature. These results are similar to previous ones carried out by molecular beam epitaxy (MBE) at temperatures between 1000 and 1500 °C [2].

It has generally been known that the density and orientation of the surface steps determine the resultant SiC polytype [3,4]. When few steps are present, most of the adsorbed species can not reach the step sites, and they start three-dimensional nucleation on terraces irrespective of the substrate polytype and commonly form the 3C polytype. On the other hand, it is possible to induce nucleation of the adsorbed species exclusively at the step sites by using substrates with the step-to-step distance smaller than the diffusion length for a given source flux and temperature. Thus, these steps serve as a template for SiC growth, and the stacking sequence of the 6H (or 4H) polytype is preserved by means of a special type of two-dimensional growth mode referred to as the step flow mechanism. Fig. 2 shows the RHEED pattern, SEM image, high resolution transmission electron

microscopy (HRTEM) image, and transmission electron diffraction (TED) pattern taken from the film that was grown for 2 h on a vicinal 4H-SiC(0001) cut off  $8^\circ$  toward  $\langle 11\bar{2}0 \rangle$  at  $900^\circ\text{C}$  and  $1 \times 10^{-6}$  Torr. The RHEED pattern similar to that of a clean substrate prior to growth strongly indicates that the film has grown epitaxially. This assertion was confirmed by the cross-sectional HRTEM which also shows a stacking fault around the interface. The step flow growth competes with the three-dimensional nucleation which results in the cubic structure according to the source flux and/or growth rate. The former is more prevalent than the latter when the source flux is decreased because the probability of three-dimensional nucleation is decreased. Although the average terrace width at the surface of the film is increased to 30 nm by step bunching, it is thought that the film has been homoepitaxially grown even at  $900^\circ\text{C}$  by step flow mechanism owing to the growth rate as low as 6-10 nm/h or by the characteristics of the single source, 1,3-disilabutane. With increasing the growth rate, the films formed show rougher morphology and increase in the number of stacking faults. Meanwhile the film grown on vicinal ( $3.5^\circ$  off-oriented) 6H-SiC exhibited the cubic structure at  $900^\circ\text{C}$  and the hexagonal structure in the temperature range 1000-1100  $^\circ\text{C}$ . It is inferred that this result arises from the higher step density of the  $8^\circ$  off-oriented substrate compared with that of the  $3.5^\circ$  off-oriented 6H-SiC substrate. The addition of the carrier gas,  $\text{H}_2$ , to 1,3-disilabutane increased the growth rate up to 50-100 nm/h. It is believed that hydrogen reacts with carbon impurities from residual gases which play the role of three-dimensional nucleation sites, removes them and keeps the surfaces clean. Thus it suppresses the probability of three-dimensional nucleation and enhances the step flow growth. It has resulted in the increase of the growth rate. In the case of  $3.5^\circ$  off-oriented 6H-SiC, hydrogen addition caused surface reconstruction to the  $(3 \times 3)$  structure and did not make the island growth take place in spite of increase in the growth rate. The RHEED pattern and SEM image of the films are not illustrated here. It has been known that surface mobility of adatoms is enhanced on the surface of the  $(3 \times 3)$  structure that has a smaller number of dangling bonds for bonding to the adatoms [10,11]. Thus, the step flow growth may easily be carried out.

In summary, we have shown that homoepitaxy of 4H- and 6H-SiC can be accomplished at much lower temperatures than previously possible by employing the single precursor 1,3-disilabutane.

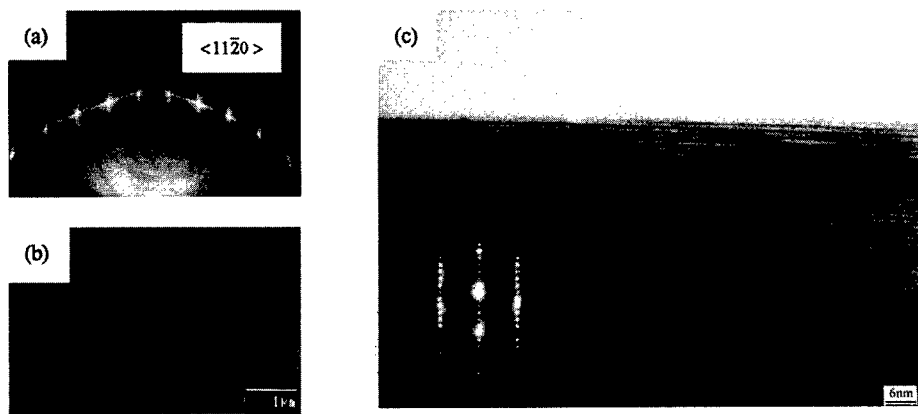


Fig. 2. (a) RHEED pattern, (b) SEM image, and (c) typical cross-sectional TEM image of the film grown on  $8^\circ$  off-oriented 4H-SiC(0001) at  $900^\circ\text{C}$ . The inset of (c) shows a selected area electron diffraction pattern indicative of the 4H-SiC structure.

**Acknowledgment**

The authors are grateful to the Ministry of Information and Communication and the Ministry of Science and Technology of Korea for the financial support.

**References**

- [1] H. Matsunami and T. Kimoto, *Mat. Sci. Eng.*, **R(20)** (1997) 125.
- [2] R. S. Kern, K. Järrendahl, S. Tanaka, and R. F. Davis, *Phys. Stat. Sol. (b)*, **202** (1997) 379.
- [3] N. Kuroda, K. Shibahara, W. S. Yoo, S. Nishino, and H. Matsunami, *Extended Abstracts, 19th Conf. On Solid State Devices and Materials, Tokyo* (1987) 227.
- [4] H. S. Kong, J. T. Glass, and R. F. Davis, *J. Appl. Phys.*, **64** (1988) 2672.
- [5] K.-W. Lee, K.-S. Yu, J.-H. Boo, Y. Kim, T. Hatayama, T. Kimoto, and H. Matsunami, *J. Electrochem. Soc.*, **144** (1997) 1474.
- [6] K.-W. Lee, K.-S. Yu, and Y. Kim, *J. Cryst. Growth*, **179** (1997) 153.
- [7] I. H. Khan and R. N. Summergrad, *Appl. Phys. Lett.*, **11** (1967) 12.
- [8] H. S. Kong, B. L. Jiang, J. T. Glass, G. A. Rozgonyi, and K. L. More, *J. Appl. Phys.*, **63** (1988) 2645.
- [9] L. B. Rowland, R. S. Kern, S. Tanaka, and R. F. Davis, *Appl. Phys. Lett.*, **62** (1993) 3333.
- [10] R. Kaplan, *Surf. Sci.*, **215** (1989) 111.
- [11] S. Tanaka, R. S. Kern, and R. F. Davis, *Appl. Phys. Lett.*, **65** (1994) 2851.

## Supersonic Seeded Beam Assisted Growth of Epitaxial Silicon Carbide

K.D. Jamison<sup>1</sup>, M.L. Kempel<sup>1</sup>, R.L. Woodin<sup>1</sup>, J.D. Shovlin<sup>1</sup>, D. Beck<sup>2</sup>, Q. Li<sup>2</sup>  
and M.E. Kordesch<sup>2</sup>

<sup>1</sup> Extreme Devices, 101 W. 6th St., Suite 200, Austin, TX 78701, USA

<sup>2</sup> Department of Physics and Astronomy, Ohio University, Athens, OH 45701, USA

**Keywords:** Crystal Growth, Doping, Seeded Supersonic Molecular Beam, Silicon Carbide

**Abstract** Devices fabricated from silicon carbide (SiC) have the potential to fulfill many of the required properties of next generation high performance electronics. Presently, commercial SiC substrates are available in the 6H and 4H polytypes but will contain defects such as micropipes and high etch pit densities. Homoepitaxial growth on these substrates can result in improved material quality. Unfortunately, present growth processes may result in epilayers containing mixed phase polytypes and high background dopant levels. An innovative silicon carbide growth process based on pulsed seeded supersonic molecular beam deposition enables homoepitaxial SiC films to be deposited at lower growth temperatures which improves quality and potentially reduces the cost of production devices. Development and performance of a multiple beam reactor capable of depositing doped, epitaxial SiC films up to 2" diameter is described. Deposition rates, film quality and doping levels are discussed.

**Introduction** Development of alternative semiconductor materials for electronic devices is of interest because silicon and gallium arsenide cannot currently meet some of the power, frequency, temperature and speed requirements of the next generation of electronic devices. Silicon carbide (SiC) has many of the required properties such as wide bandgap, high breakdown field and physical strength that make it attractive for many of these applications [1,2]. There are now commercially available SiC substrates in the 6H and 4H polytypes. As substrate quality continues to improve, more efforts will be made to fabricate devices from this material.

**Supersonic Molecular Beams** Supersonic molecular beams were originally suggested as a replacement for effusive gas sources where the supersonic jet of gas travels through a nozzle in the intended beam direction of the effusion source. Using supersonic gases removes the effusion constraint (Knudsen number >1) on the mean free path of the molecular beam. The advantages of this approach are beam intensities on the order of 1000 times those available from effusive sources, extremely long mean free path, and narrow energy spread in the beam as a result of cooling of the gas by isentropic expansion [3-7]. This concept is illustrated in Fig. 1.

The technology for "nozzle" beam sources depends on the ratio of pressures before and after the expansion, and the mean free path of the molecules in the source (before the expansion). The gas in the source chamber is undergoing hydrodynamic flow, i.e. a dense, continuum flow such as for a liquid. When the gas flow passes through the nozzles, the gas expands, and the forward velocity of the gas is increased due to a local reduction in the enthalpy of the gas (i.e. conversion into translational kinetic energy in the beam direction). The dense flow in the nozzle allows energy

transfer through collisions. As the gas expands into the low pressure region the gas evolves to molecular flow. Here the number of collisions available for energy transfer is greatly reduced and the physical parameters of the beam are "frozen". The beam parameters are usually expressed in terms of the Mach number, and the terminal Mach number reached by the beam in the low density, molecular flow regime. An illustration of a supersonic beam is given in Fig. 2.

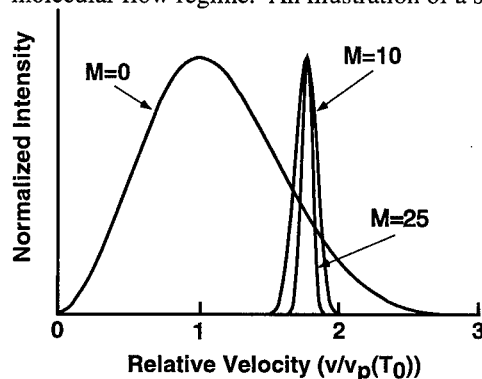


Fig. 1. Beam energy narrowing for three Mach numbers. Velocity is normalized to  $v_p(T_0)$ , the peak velocity at  $M=0$ . Adapted from Ref. 7.

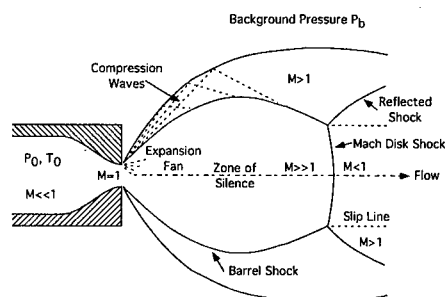


Fig. 2. Illustration of a supersonic beam flow. The supersonic beam is in the "zone of silence." Adapted from Ref. 5.

The continuum flow of the high density beam in the nozzle allows a special method for achieving beam energies beyond those available from thermal velocities. In a mixture of two gases, if there are enough collisions in the expansion process to maintain energy and momentum equilibrium between the two gases, the mixture will have a uniform temperature and velocity after expansion. If a small amount of heavy gas is mixed (seeded) with a light gas, the heavy species will attain the velocity of the light gas, but have a kinetic energy increase by the mass ratio of the two species. For hydrogen and helium, the terminal velocities are  $\sim 2.96 \times 10^5$  cm/sec and  $1.77 \times 10^5$  cm/sec respectively. Molecules of interest for silicon carbide epitaxy seeded in these beams would obtain the kinetic energies given in Table 1. As can be seen in Table 1, chemically significant energy can be imparted to seed molecules in a supersonic expansion. This can allow deposition at lower substrate temperatures than in traditional reactors where reactant activation is only via interaction with the hot substrate.

Table 1 Kinetic energy of seed gases in supersonic beams of hydrogen and helium.

Carrier Gas	Silane (eV)	Propane (eV)	Ethane (eV)	Trimethyl aluminum (eV)	Nitrogen (eV)
Hydrogen	1.45	2.00	1.36	3.27	1.27
Helium	0.52	0.71	0.49	1.17	0.46
Argon	0.052	0.071	0.048	0.12	0.045

A diagram of the apparatus used for these experiments is shown in Fig. 3 [8]. A third pulsed valve is used to add dopants. To ensure that the pressure in the growth chamber remains below 0.1 Torr during deposition, the chamber is pumped by a 450 l/s turbomolecular pump which is backed by a 30 CFM roughing pump. The chamber has a base pressure of  $< 1 \times 10^{-8}$  Torr. The supersonic beams were created using General Valve series 9 pulsed valves having a 0.5 mm aperture. The substrate temperature was kept at 1230°C during growth using a PBN/PG heater and measured by a W/Re thermocouple in contact with the sample surface. The system can maintain a pressure well below

0.1 Torr necessary for the supersonic beam to strike the sample using a 2Hz pulse rate with the pulsed valves opened for ~3 milliseconds per pulse.

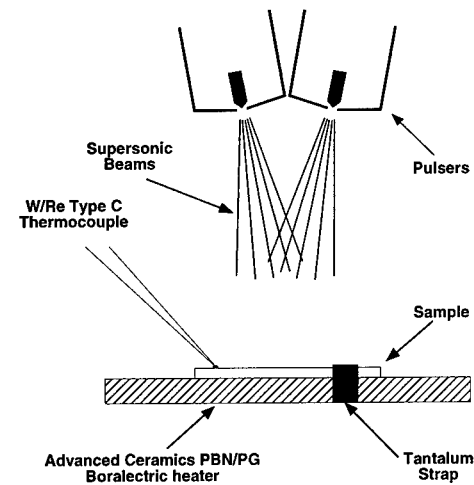


Fig. 3. Seeded supersonic deposition system showing two of the pulsed valves.

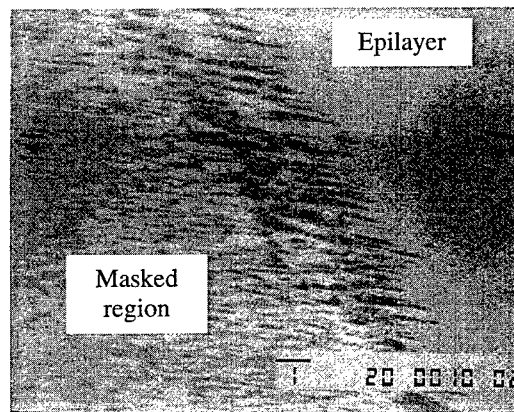


Fig. 4. Epitaxial film grown on 6H SiC with  $H_2$  carrier gas. The bar indicates 1  $\mu m$ .

**Epitaxial SiC Deposition** SiC films were deposited on both Si  $\langle 100 \rangle$  and the 6H surface of SiC at 1230°C. All growth on silicon resulted in three dimensional domain growth. Growth on SiC using hydrogen as the seed gas resulted in high quality epitaxial growth, while growth on SiC using helium as the carrier gas yielded poor three-dimensional growth. A micrograph of an epitaxial SiC film grown on SiC is shown in Fig. 4. Changes in the source gas pressure did not significantly change the crystal quality but did slightly increase the growth rate due to more reactive growth gases striking the crystal per unit time. It is important to note that using this technique, high quality homoepitaxial films of SiC (as determined by scanning electron microscopy and X-ray diffraction measurements) are obtained at a substrate temperature of 1230°C, substantially lower than the standard growth temperatures reported in the literature. Macroscopic growth rate is 1  $\mu m/hr$ . These results demonstrate that the kinetic energy given to the growth gases in the supersonic beams enables high quality crystal growth at lower growth temperatures.

**Doping** Molecular nitrogen is used as the n-type dopant and trimethylaluminum (aluminum) as the p-type dopant. SiC films were grown using beams of 0.5% silane and 0.5% propane in hydrogen and doped using supersonic beams of nitrogen (0.05%) and trimethylaluminum (TMA, 0.74%) seeded in various carrier gases. The nitrogen is seeded in the hydrogen carrier gas by pre-mixing the gases in a pressurized cylinder then introducing the gas mixture through the pulsed valve. The TMA is seeded by passing the carrier gas over the TMA, which is kept at a constant temperature (with a constant vapor pressure) in a bath. Table I shows the energy of the dopant beams using hydrogen, helium and argon carrier gases.

Secondary Ion Mass Spectrometry (SIMS) results for aluminum doped samples grown at three different beam energies are shown in Fig. 5. This SIMS data show the dependence of the doping level on the energy of the dopant. Using the same percentage of trimethylaluminum, we find a doping level of  $\sim 1 \times 10^{17}/cc$  using a hydrogen carrier gas, a doping level of  $\sim 1 \times 10^{16}/cc$  using a helium carrier gas and a doping level of  $5 \times 10^{15}/cc$  using an argon carrier gas. Notice the logarithmic dependence of the dopant concentration as a function of energy. This behavior is typical of a rate-controlled process where the rate is essentially governed by an activation barrier.



For n-type doping using molecular nitrogen, no dependence of the dopant level on the dopant energy is observed. This may be due to the relatively low kinetic energy of the nitrogen molecules combined with a high reaction activation barrier. The activation barrier could be either a surface reaction or the high dissociation energy of molecular nitrogen (9.9eV).

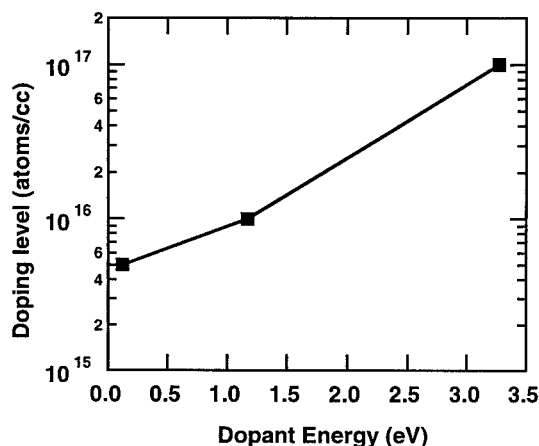


Fig. 5. Dependence of doping concentration in SiC vs the dopant precursor kinetic energy for trimethylaluminum as the p-type dopant precursor.

**Summary** High quality SiC homoepitaxial films are deposited at substrate temperatures of 1230°C using a seeded supersonic beam deposition system. Further, it is possible to vary the dopant concentration in SiC during growth by changing the kinetic energy of the arriving dopant molecules. This was done without changing the growth species flow rate, growth temperature, or dopant flow rate. It should therefore be possible to construct a seeded supersonic SiC growth system that uses seeded supersonic beams to dope the crystal at different concentrations without changing other growth parameters. Deposition at lower temperature should reduce defects and improve film quality.

**Acknowledgements** This work supported by the Ballistic Missile Defense Organization through grants monitored by the Defense Special Weapons Agency (Grant Nos. DSWA01-96-C-0113 and DSWA01-97-C-0149) and the Office of Naval Research (Grant Nos. N00014-96-1-0782 and -1060).

#### References

- [1] J.B. Casady and R.W. Johnson, *Solid State Electronics* **49** (1996) p. 1409.
- [2] P.G. Newdeck, *J. Elec. Mat.* **24** (1995) p. 283.
- [3] L. Abad, D. Bermejo, V.J. Herrero, J. Santos, and I. Tanarro, *Rev. Sci. Instrum.* **66** (1995) p. 3826.
- [4] D.B Atkinson and M.A. Smith, *Rev. Sci. Instrum.* **66** (1995) p. 4170.
- [5] D.R. Miller, in *Atomic and Molecular Beam Methods*, edited by G. Scoles (Oxford University Press, Oxford, 1988), Vol 1.
- [6] K.A. Brown, S.A. Ustin, L. Lauhon, and W. Ho, *J. Appl. Phys.* **79** (1996) p. 7667.
- [7] J.B. Anderson and J.B. Fenn, *Phys. Fluids*, **8** (1965) p. 780.
- [8] K.D. Jamison, M.L. Kempel, V.W. Ballarotto and M.E. Kordesch, *J. Vac. Sci. Technol. A* **16** (1998) p. 1327.

Please direct correspondence to R.L. Woodin, woodin@extremedevices.com.

## 4H-SiC Substrate Orientation Effects on Hydrogen Etching and Epitaxial Growth

B.E. Landini and G.R. Brandes

ATMI, Inc, 7 Commerce Dr., Danbury, CT 06810, USA

**Keywords:** Epitaxial Growth, Hydrogen Etching, Step Height, Substrate Orientation

**Abstract** H<sub>2</sub> etching and epitaxial growth were performed on 4H-SiC (0001) substrates offcut 8° towards either  $\langle 1\bar{1}00 \rangle$  or  $\langle 11\bar{2}0 \rangle$ . As-received surfaces possessed no discernable step structure. H<sub>2</sub> etched surfaces possessed step edges parallel to the offcut direction and step heights of typically 1-2 Si-C bilayers, although larger step heights were observed on both orientations using variable etch conditions. Epilayers were smooth regardless of the pre-growth H<sub>2</sub> etch used, provided there was minimal substrate polishing damage. No large-scale step bunching or rough growth was observed on epilayers grown on either orientation for thicknesses up to 15 µm. AFM revealed epilayer step heights of typically 1 and 2 Si-C bilayers, the largest step heights remaining within 5-6 bilayers for the thickest layers on both orientations.

### Introduction

Substrate crystalline orientation plays a critical role in determining the quality of epitaxial SiC grown by chemical vapor phase epitaxy. It was found that an offcut of several degrees from the (0001) plane promoted high quality homoepitaxial growth via lateral (step flow) growth from the surface steps created by the offcut [1]. Increasing the offcut angle from 4° to 8° reduced the density of triangular 3C-SiC inclusions in 4H-SiC epilayers [2]. Most of the work in SiC epitaxy has focused on SiC substrates offcut towards the  $\langle 11\bar{2}0 \rangle$  crystalline direction. Recent work found that 4H-SiC epilayers with smooth morphologies and controlled doping could be grown on substrates offcut 8°  $\rightarrow \langle 1\bar{1}00 \rangle$  [3]. In this paper we report the results of investigations of the surface morphology and step structure progressing from H<sub>2</sub> etching through increasing epilayer thicknesses for epilayers grown on 4H-SiC substrates offcut 8° from (0001) towards both the  $\langle 11\bar{2}0 \rangle$  and the  $\langle 1\bar{1}00 \rangle$  crystalline directions.

### Experimental

SiC etching and epilayer growth were performed on 4H-SiC substrates offcut  $8^\circ \pm 1^\circ$  from (0001) towards either  $\langle 1\bar{1}00 \rangle$  or  $\langle 11\bar{2}0 \rangle$ . H<sub>2</sub> etching and growth occurred in a quartz water-cooled low-pressure vapor phase epitaxial growth system. Growth was performed using dilute SiH<sub>4</sub> and CH<sub>4</sub> with an H<sub>2</sub> carrier gas. The H<sub>2</sub> flow rate used for etching was identical to that used for growth. Growth and etching were performed at 100 Torr at temperatures of 1475 - 1500 °C. Film morphology was characterized using Nomarski diffraction interference optical microscopy, and film thickness was measured in cross section using a scanning electron microscope. A

Digital Instruments Nanoscope atomic force microscope (AFM) was used in tapping mode to examine fine surface features and to measure root mean square (rms) roughness.

### Results and Discussion

AFM analysis of as-received substrate surfaces revealed randomly-oriented polishing scratches, with no observable step structure on either substrate orientation. After 15 minutes of  $H_2$  etching at 1500 °C, shallow scratches were removed and surface steps were observed on both orientations (Figure 1). The appearance of steps with  $H_2$  etching is consistent with other work [4]. The step edge direction was parallel to the offcut direction on both orientations. The step structure on the  $\langle 11\bar{2}0 \rangle$  - offcut surface after  $H_2$  etching was somewhat less regular compared to the more parallel step structure observed on the  $\langle 1\bar{1}00 \rangle$  -offcut surface. The etched surfaces were smooth, and the AFM data revealed step heights of typically 1 and 2 Si-C bilayers for both substrate orientations.

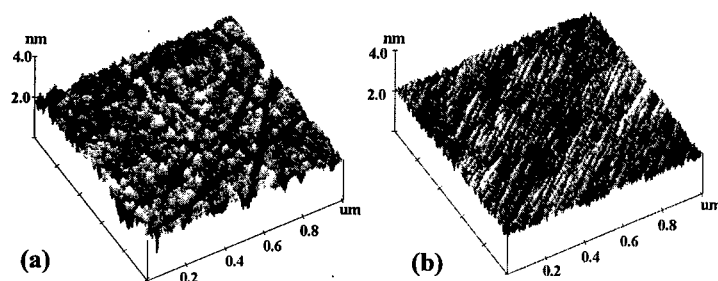


**Figure 1.** AFM analysis of 4H-SiC substrates offcut  $8^\circ \rightarrow \langle 1\bar{1}00 \rangle$   
(a) As received  
(b) After  $H_2$  etching.  
Images show  $1 \times 1 \mu m^2$  areas and 2 nm/div height scales.

Different step structures were observed using variable  $H_2$  etch conditions. In general, higher etch temperatures and longer etch times produced smaller step heights and lower rms values on both offcut direction surfaces. On both surfaces, the longer and hotter etches more readily revealed subsurface polishing and other substrate damage, producing rougher epilayer morphologies on more highly damaged substrates. If the substrate had minimal polishing damage, the epilayers exhibited small step heights even when the  $H_2$  pre-growth etch produced large steps. For example, a  $H_2$  etch produced large steps and an rms roughness of 0.87 nm on a  $\langle 1\bar{1}00 \rangle$  - offcut substrate. A 1.5  $\mu m$  thick film grown using a different sample from the same substrate and the identical pre-growth etch possessed the typical smaller steps and an rms of 0.14 nm. The same trend was observed on the  $\langle 11\bar{2}0 \rangle$  -offcut surface, where the  $H_2$  etched surface possessed an rms of 0.44 nm, while the 1.5  $\mu m$  thick epilayer grown using those etch conditions had an rms of 0.16 nm.

Smooth epitaxial surface morphologies were obtained using identical growth conditions for epilayers grown on both substrate offcut orientations for thicknesses up to 15  $\mu m$ , the thickest layer attempted. A low density of 3C-SiC triangular inclusions was observed mainly on the wafer periphery for epilayers grown on both orientations. No degradation in epilayer surface morphology, rough three dimensional growth, or large-scale step bunching was observed using Nomarski microscopy and variable area AFM on both orientations, unlike previous work using 6H-SiC substrates offcut  $\leq 4^\circ \rightarrow \langle 1\bar{1}00 \rangle$  [5,6]. AFM revealed smooth surfaces and a step formation for epilayers grown on both substrate orientations. The step edge direction for films

grown on both substrate orientations was parallel to the offcut direction, consistent with step flow growth theory [1]. As observed on  $H_2$ -etched surfaces, films grown on substrates offcut towards  $\langle 1\bar{1}00 \rangle$  displayed more distinct, parallel, and regular steps compared to the steps on films grown on  $\langle 11\bar{2}0 \rangle$ -offcut substrates (Figure 2). The parallel steps observed on  $\langle 1\bar{1}00 \rangle$  offcuts and the irregular (zig-zag) steps observed on  $\langle 11\bar{2}0 \rangle$  offcuts are consistent with proposed 6H-SiC surface models [6], although we observe no macroscopic step bunching on either orientation. Epilayers in this work typically possessed rms values less than 1 nm for 400  $\mu m^2$  scan areas for films grown on both substrate orientations.

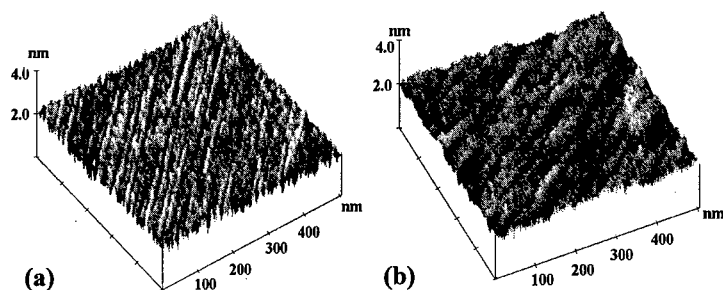


**Figure 2.** AFM analysis of 5  $\mu m$  4H-SiC epilayers grown on substrates offcut  $8^\circ \rightarrow$

(a)  $\langle 1\bar{1}00 \rangle$ , rms 0.14 nm  
(b)  $\langle 11\bar{2}0 \rangle$ , rms 0.13 nm. Images show 500 x 500  $nm^2$  areas and 2 nm/div height scales.

The raw AFM data was used to generate comparative histograms of step heights for the various films. Figure 3 shows a histogram of the step heights for a 5  $\mu m$  thick epilayer grown on a substrate offcut  $8^\circ \rightarrow \langle 1\bar{1}00 \rangle$ . Taking probe tip effects into account, a correlation between the measured step height and the number of Si-C bilayers in the step was determined (Figure 3 inset). Uncounted single bilayer steps, bypassed due to the 1 nm lateral probe tip displacement, were determined from Laue measurement of the offcut angle. The most common step height for both 3 and 5  $\mu m$  thick films, each set of films grown during the same growth run, was 0.5 nm (1-2 Si-C bilayers) for both substrate orientations. Steps of four Si-C bilayers were also observed, but with less frequency than observed for epilayers grown on 4H-SiC (0001) offcut  $3.5^\circ \rightarrow \langle 11\bar{2}0 \rangle$  [7]. Step bunching is attributed [7] to the minimization of the surface free energy during growth, although minimal surface defects and proper gas flow ratios may help reduce step bunching [8].

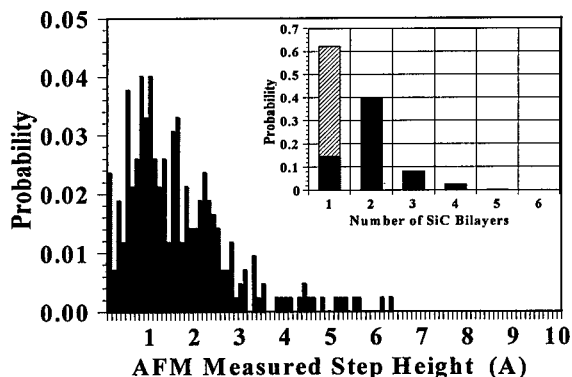


**Figure 3.** Distribution of measured (AFM) step heights from a 5  $\mu m$  thick epilayer grown on a 4H-SiC substrate offcut  $8^\circ \rightarrow \langle 1\bar{1}00 \rangle$ . Inset: Distribution of step heights obtained by converting the raw AFM data into number of Si-C bilayers at a step. The hatched bar corresponds to calculated uncounted single bilayers (see text).

Thicker films tended to display additional low-scale superstructure, but low rms values were retained on both orientations. The AFM scan and accompanying step height distribution of a 15  $\mu\text{m}$  thick film grown on a substrate offcut  $8^\circ \rightarrow \langle 1\bar{1}00 \rangle$  is shown in Figure 4. There is a slightly wider distribution of step heights compared to thinner films. The most common step heights are 1 and 2 Si-C bilayers, and the largest step heights remain within 5 and 6 bilayers. The 15  $\mu\text{m}$  thick film grown on the  $\langle 11\bar{2}0 \rangle$ -offcut substrate possessed step heights up to 4 bilayers. Both films were smooth, possessing average (3 random measurements) rms values on 400  $\mu\text{m}^2$  areas of 0.77 and 0.68 nm for the  $\langle 1\bar{1}00 \rangle$  and  $\langle 11\bar{2}0 \rangle$  offcuts, respectively.

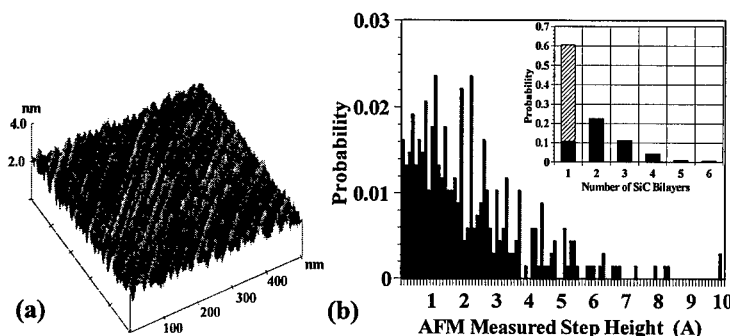


**Figure 4.** 15  $\mu\text{m}$  thick 4H-SiC epilayer grown on a substrate offcut  $8^\circ \rightarrow \langle 1\bar{1}00 \rangle$ . (a) AFM analysis, 500x500  $\text{nm}^2$  area, 2.0 nm/div height scale (b) Step height distribution calculated from AFM data and measured offcut angle.

### Summary

The surface structure of  $\text{H}_2$ -etched surfaces and epilayers grown on 4H-SiC (0001) substrates offcut  $8^\circ$  towards  $\langle 11\bar{2}0 \rangle$  and  $\langle 1\bar{1}00 \rangle$  was investigated. As-received substrate surfaces possessed no discernable step structure.  $\text{H}_2$  etching of both surfaces resulted in surface step edges parallel to the offcut direction, with the smoothest etched surfaces possessing step heights of 1 and 2 Si-C bilayers. Epilayers on both orientations remained smooth for thicknesses up to 15  $\mu\text{m}$  with more regular and parallel steps on the  $\langle 1\bar{1}00 \rangle$ -offcut surface. Large scale step bunching was not observed on either orientation, and step heights remained  $\leq 6$  Si-C bilayers on the thickest films.

**Acknowledgements** This work was supported in part by NASA (NAS3-97095), by the U.S. Air Force (F33615-97-C-2771), and by BMDO/IST (F33615-95-C-2514, managed by the U.S. Air Force).

### References

- [1] N. Kuroda, K. Shibahara, W. S. Woo, S. Nishino, and H. Matsunami, Ext. Abstr. The 19<sup>th</sup> Conf. On Solid State Devices and Materials (Tokyo, 1987) p. 227.
- [2] J. A. Powell and D. J. Larkin, Phys. Stat. Solidi B 202 (1997), p. 529.
- [3] B. E. Landini and G. R. Brandes, Appl. Phys. Lett. 74 (1999), p. 2632.
- [4] C. Hallin *et al.*, J. Crystal Growth 181 (1997), p. 241.
- [5] H. S. Kong, J. T. Glass, and R. F. Davis, J. Appl. Phys. 64 (1988), p. 2672.
- [6] T. Ueda, H. Nishino, and H. Matsunami, J. Crystal Growth 104 (1990), p. 695.
- [7] T. Kimoto, A. Itoh, and H. Matsunami, Appl. Phys. Lett. 66 (1995), p. 3645.
- [8] O. Kordina *et al.*, Appl. Phys. Lett. 69 (1996), p. 1456, and references therein.

## 4H-SiC (11 $\bar{2}$ 0) Epitaxial Growth

T. Kimoto, T. Yamamoto, Z.Y. Chen, H. Yano and H. Matsunami

Department of Electronic Science and Engineering, Kyoto University,  
Yoshidahonmachi, Sakyo, Kyoto, 606-8501, Japan

**Keywords:** (11 $\bar{2}$ 0), Chemical Vapor Deposition, Deep Levels, Homoepitaxial Growth, X-Ray Diffraction

**Abstract** Homoepitaxial growth on micropipe-free 4H-SiC(11 $\bar{2}$ 0) substrates has been systematically investigated. In contrast to step-bunched surface on conventional off-axis (0001) epilayers, the (11 $\bar{2}$ 0) epilayers exhibit very smooth morphology with a surface roughness of 0.18 nm. An X-ray diffraction analysis revealed that lattice-mismatch strain between n<sup>-</sup>epilayers and n<sup>+</sup>substrates can be reduced by introducing n-type buffer layers. The lowest donor concentration of unintentionally doped epilayers is  $1 \times 10^{14} \text{ cm}^{-3}$ . Three electron traps located at  $E_c - 0.27$ , 0.32, and 0.66 eV have been detected with a total trap concentration as low as  $3.8 \times 10^{12} \text{ cm}^{-3}$ .

### 1. Introduction

Nowadays, 4H- and 6H-SiC(0001) wafers with several degree off-angles have exclusively been employed for SiC homoepitaxy as well as device fabrication. Drawbacks of this face include micropipe penetration from substrates and probable 3C-SiC inclusions in epilayers, both of which severely degrade device performance. Growth on SiC(11 $\bar{2}$ 0) faces, perpendicular to the *c*-axis, has advantages such as the absence of micropipes and perfect polytype replication [1]. However, only a few investigations on 4H-SiC [2] or 6H-SiC [2-4] homoepitaxy on (11 $\bar{2}$ 0) have been reported, where the quality of epilayers is somewhat poor compared to the standard (0001) epilayers. In this paper, the authors present successful 4H-SiC homoepitaxy on (11 $\bar{2}$ 0), utilizing buffer layers to minimize lattice-mismatch strain caused by the doping difference between epilayers and substrates. Doping control, deep level analysis, fabrication of Schottky diodes are systematically investigated.

### 2. Experiments

Epitaxial growth was performed by atmospheric-pressure CVD in a cold-wall horizontal reactor [5]. Source gases were SiH<sub>4</sub> and C<sub>3</sub>H<sub>8</sub> with a Pd-cell purified H<sub>2</sub> carrier gas. The n-type 4H-SiC(11 $\bar{2}$ 0) substrates with a doping concentration in the  $10^{18} \text{ cm}^{-3}$  range were prepared from [000 $\bar{1}$ ] grown ingots at Nippon Steel Corp. The 4H-SiC(1 $\bar{1}$ 00) and 8° off-axis (0001) substrates were placed side by side on an SiC-coated susceptor for comparison. Typical growth temperature and growth rate were 1500°C and 2.5  $\mu\text{m/h}$ , respectively.

Epilayers were characterized by Nomarski microscope, AFM (Atomic Force Microscopy), X-ray diffraction, photoluminescence (PL), *C-V*, and ICTS (Isothermal Capacitance Transient Spectroscopy) measurements on Ni/4H-SiC Schottky structure.

### 3. Results and discussion

Under a typical growth condition at 1500°C, the growth rate on (11 $\bar{2}$ 0) (2.5  $\mu\text{m/h}$ ) was nearly

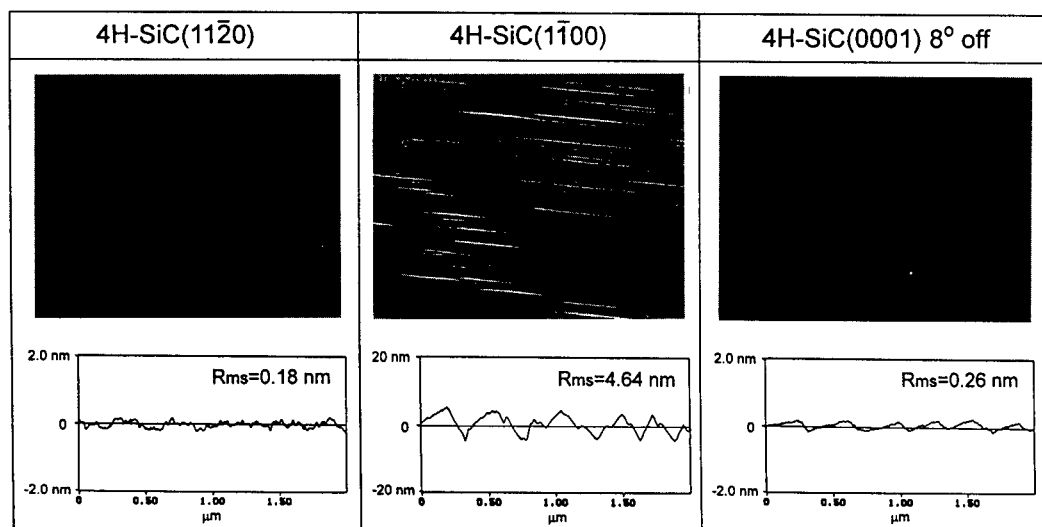


Fig.1 Nomarski photographs and AFM height profiles for ( $11\bar{2}0$ ), ( $1\bar{1}00$ ), and off-axis (0001) 4H-SiC epilayers.

identical to that on off-axis (0001). The temperature dependence of growth rate is small, and the Arrhenius plot of growth rate yielded the same activation energy of 3 kcal/mol as that obtained on off-axis (0001), indicating that growth is diffusion-controlled on both faces. Figure 1 shows Nomarski photographs and height profiles obtained by an AFM analysis for 7.5  $\mu\text{m}$ -thick 4H-SiC epilayers grown on various faces. Epilayers on ( $11\bar{2}0$ ) substrates exhibited excellent surface morphology without any triangular- or "carrot"-shaped defects. Growth on ( $1\bar{1}00$ ), however, resulted in a high density of "elongated surface defects", probably due to stacking fault formation during CVD. From molten KOH etching experiments, the stacking fault density was estimated to be  $10^2 \text{ cm}^{-1}$  for ( $11\bar{2}0$ ) and  $10^3\text{--}10^4 \text{ cm}^{-1}$  for ( $1\bar{1}00$ ) epilayers. In contrast to epilayers on off-axis (0001) where step-flow growth does occur, no step bunching and wavy surface structures were observed on ( $11\bar{2}0$ ), leading to a very small surface roughness of 0.18 nm. The surface defect area, defined as the ratio of defective area to the total area, was much smaller for the ( $11\bar{2}0$ ) epilayers (0.010 %) than that for the (0001) epilayers (0.16 %).

Figure 2 depicts the X-ray rocking curve ( $\omega$  scan), sensitive to lattice tilt and crystal bending, at the ( $11\bar{2}0$ ) peak ( $2\theta=60.05^\circ$ ) obtained from 9  $\mu\text{m}$ -thick undoped 4H-SiC( $11\bar{2}0$ ) epilayers and a substrate. The epilayer directly grown on a substrate exhibited considerable broadening of the diffraction peak with splitting (FWHM=161 arcsec), which has never been observed for off-axis (0001) grown epilayers. Similar degradation of epilayer quality has been pointed out in 4H-SiC( $11\bar{2}0$ ) and ( $1\bar{1}00$ ) growth by hot-wall CVD [2]. This peak broadening may originate from a lattice-mismatch caused by the doping difference between an  $n^-$ -type epilayer and an  $n^+$ -type substrate [2]. By introducing a 1.2  $\mu\text{m}$ -thick  $n$ -type buffer layer, the FWHM of rocking curve could be improved to 45 arcsec, being even smaller than a substrate (49 arcsec).

The C/Si ratio dependence of donor concentration for unintentionally doped epilayers on various substrates is represented in Fig.3. The doping concentration on ( $11\bar{2}0$ ) is sensitive to the C/Si ratio, and is located in between that on (0001) Si and ( $000\bar{1}$ ) C faces. Similar tendencies were

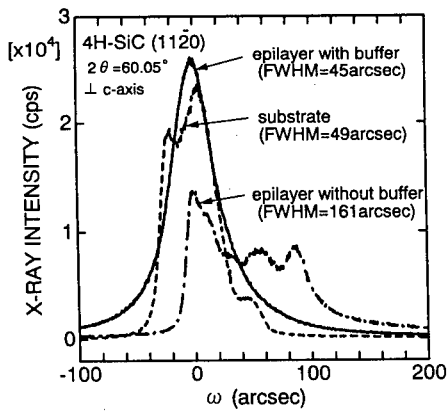


Fig.2 X-ray rocking curves for a 4H-SiC(11 $\bar{2}$ 0) substrate and epilayers with or without a buffer layer.

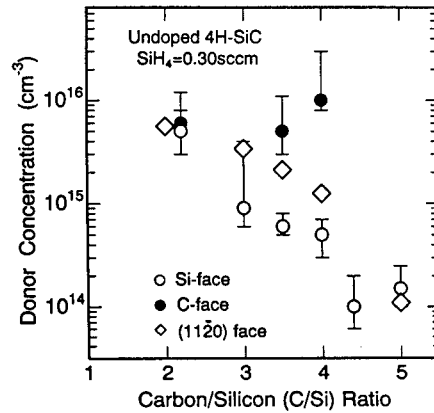


Fig.3 C/Si ratio dependence of background doping concentration for epilayers on various substrates.

observed in intentional N and Al doping [6]. The lowest net donor concentration determined by  $C-V$  measurements on (11 $\bar{2}$ 0) epilayers is  $1.1 \times 10^{14} \text{ cm}^{-3}$ . In spite of the C-rich CVD condition ( $C/Si=5$ ) to produce this high-purity material, surface morphology was still excellent, suggesting a wide growth window on the (11 $\bar{2}$ 0) face.

In low-temperature PL measurements, well-resolved peaks due to the neutral nitrogen donor bound excitons and free excitons were observed. The free exciton peaks survived even at 290 K, indicating high-purity of the epilayers. Hall effect measurements revealed electron mobilities of  $680\text{--}750 \text{ cm}^2/\text{Vs}$  at room temperature for epilayers with a carrier concentration of  $10^{16} \text{ cm}^{-3}$ .

Wide range scans of both temperature (120–420 K) and transient time ( $10^{-6}\text{--}10^4 \text{ s}$ ) in ICTS measurements on high-purity epilayers ( $N_d=1 \times 10^{14} \text{ cm}^{-3}$ ) enabled very high-resolution detection in the energy range from  $E_c-0.1 \text{ eV}$  down to about  $E_c-1.4 \text{ eV}$  (close to midgap). The authors detected three kinds of electron traps located at  $E_c-0.27$ ,  $E_c-0.32$ , and  $E_c-0.66 \text{ eV}$  (assuming temperature-independent capture cross section), trap parameters of which are shown in Table 1. The deepest trap can be regarded as the “ $Z_1$  center”, and the two shallower traps may be the same as “ $ID_3$ ” and “ $ID_4$ ” centers reported for ion-implanted 4H-SiC epilayers [7]. Thus, the origins of three kinds of traps may be intrinsic defect complexes including vacancies [7]. It should be noted, however, that the total trap concentration is as low as  $3.8 \times 10^{12} \text{ cm}^{-3}$  (with the  $\lambda$  effect correction) and is favorably compared to that observed from 4H-SiC(0001) epilayers [5].

The Ti and Ni barrier heights on 4H-SiC(11 $\bar{2}$ 0) were determined to be 1.21 eV and 1.73 eV, respectively, by  $I-V$ ,  $C-V$ , and internal photoemission (IPE) measurements. These barrier heights are situated in between the values on Si and C faces for each metal. Finally, Ni/4H-SiC Schottky barrier

Table 1 Trap parameters of defect centers observed in as-grown 4H-SiC(11 $\bar{2}$ 0) epilayers.

Center	Activation Energy	Capture Cross Section	Concentration
$ID_3$	0.27 eV	$4 \times 10^{-16} \text{ cm}^2$	$3.1 \times 10^{11} \text{ cm}^{-3}$
$ID_4$	0.32 eV	$1 \times 10^{-15} \text{ cm}^2$	$6.4 \times 10^{11} \text{ cm}^{-3}$
$Z_1$	0.66 eV	$4 \times 10^{-15} \text{ cm}^2$	$2.8 \times 10^{12} \text{ cm}^{-3}$



diodes with field plate termination were fabricated on both (11 $\bar{2}$ 0) and (0001) epilayers. The donor concentration of 8~10  $\mu\text{m}$ -thick drift layers was  $3\sim 5 \times 10^{15} \text{ cm}^{-3}$ , and the diode size was 300  $\mu\text{m}$  in diameter. Although the authors have not yet observed significant differences in ideality factor (1.02~1.05), on-resistance (4~6  $\text{m}\Omega\text{cm}^2$ ), and breakdown voltage (800~1000 V) between (11 $\bar{2}$ 0) and (0001) Schottky diodes, the leakage current of (11 $\bar{2}$ 0) diodes is lower as shown in Fig.4. The average leakage current at -100 V was  $2 \times 10^{-7} \text{ A/cm}^2$  for (11 $\bar{2}$ 0) and  $1 \times 10^{-6} \text{ A/cm}^2$  for (0001) diodes. This difference might be ascribed to superior surface flatness and/or much lower screw dislocation density of (11 $\bar{2}$ 0) epilayers.

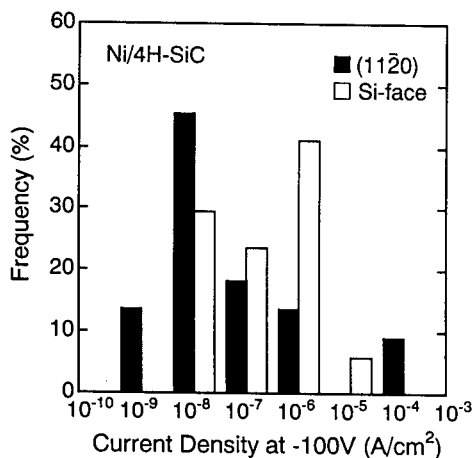


Fig.4 Histograms of leakage current density for Ni/4H-SiC Schottky diodes processed on (11 $\bar{2}$ 0) and 8° off-axis (0001) epilayers.

#### 4. Conclusions

4H-SiC has been homoepitaxially grown on micropipe-free 4H-SiC(11 $\bar{2}$ 0) substrates by CVD. The (11 $\bar{2}$ 0) epilayers showed very smooth morphology with a surface roughness of 0.18 nm and a surface defect area of 0.010%. Effects of n-type buffer layers have been presented to minimize lattice-mismatch strain between n $^+$ -epilayers and n $^+$ -substrates. The lowest donor concentration of unintentionally doped epilayers is  $1 \times 10^{14} \text{ cm}^{-3}$ . ICTS measurements revealed three electron traps located at  $E_c - 0.27$ , 0.32, and 0.66 eV with a total trap concentration as low as  $3.8 \times 10^{12} \text{ cm}^{-3}$ . The Ni/4H-SiC(11 $\bar{2}$ 0) Schottky barrier diodes exhibited lower leakage current density than the (0001) diodes. The present study together with attractive MOS interface properties [8] has demonstrated that micropipe-free 4H-SiC(11 $\bar{2}$ 0) epilayers with proper buffer layers are a promising alternative for high-power SiC device applications.

#### Acknowledgments

The authors would like to thank Nippon Steel Corporation for supplying 4H-SiC (11 $\bar{2}$ 0) and (1 $\bar{1}$ 00) wafers. This work was partially supported by a Grant-in-Aid for Specially Promoted Research, No.09102009, from the Ministry of Education, Science, Sports and Culture, Japan, and Toyota High-Tech Research Grant Program.

#### References

- [1] J.Takahashi and N.Ohtani, *phys. stat. sol. (b)* **202**(1997), p.163.
- [2] C.Hallin, A.Ellison, I.G.Ivanov, A.Henry, N.T.Son, and E.Janzen, *Mat. Sci. Forum* **264-268**(1998), p.123.
- [3] J.A.Powell and H.A.Will, *J. Appl. Phys.* **44**(1973), p.5177.
- [4] A.A.Burk, Jr., D.L.Barrett, H.M.Hobgood, R.R.Siergiej, T.T.Braggins, R.C.Clarke, G.W.Eldridge, C.D.Brandt, D.J.Larkin, J.A.Powell, and W.J.Choyke, *Silicon Carbide and Related Materials* (IOP, Bristol, 1994), p.29.
- [5] H.Matsunami and T.Kimoto, *Mat. Sci. & Eng. R20*(1997), p.125.
- [6] T.Yamamoto, T.Kimoto, and H.Matsunami, *Mat. Sci. Forum* **264-268**(1998), p.111.
- [7] T.Dalibor, G.Pensl, H.Matsunami, T.Kimoto, W.J.Choyke, A.Schoner, and N.Nordell, *phys. stat. sol. (a)* **162**(1997), p.199.
- [8] H.Yano, T.Hirao, T.Kimoto, H.Matsunami, K.Asano, and Y.Sugawara, *presented in this conference*, p. 1105

## Homoepitaxial Growth of 6H SiC on Single Crystalline Spheres

K. Christiansen<sup>1</sup>, S. Christiansen<sup>2</sup>, H.P. Strunk<sup>2</sup> and R. Helbig<sup>1</sup>

<sup>1</sup> Institute of Applied Physics, University of Erlangen-Nürnberg,  
Staudtstr. 7/A3, DE-91058 Erlangen, Germany

<sup>2</sup> Institute of Material Science-Microcharacterization, University of Erlangen-Nürnberg,  
Cauerstr. 6, DE-91058 Erlangen, Germany

**Keywords:** Chemical Vapor Deposition, Growth Anisotropy, Non-Planar Substrates, Transmission Electron Microscopy

**Abstract:** Growth of homoepitaxial layers has been performed by chemical vapor deposition on 6H SiC spheres ground from modified Lely crystals. We used such a sphere as substrate which provides naturally all crystallographic orientations in order to obtain an overview over the homoepitaxial growth in different directions. From scanning electron micrographs we could determine 6 pronounced crystallographic bands running from the (0001) Si pole to the (000 $\bar{1}$ ) C pole along  $\langle 1\bar{1}0x \rangle$  directions. Around the (0001) Si and (000 $\bar{1}$ ) C poles smooth growth planes have developed. The bands show a stair-like character consisting of treads and risers with surface normals parallel to the  $\langle 1\bar{1}00 \rangle$ - and  $\langle 11\bar{2}0 \rangle$ -directions, respectively. Between the bands a rough topology consisting of terraces is observed. Concerning the growth rates of the different directions we find the  $\langle 11\bar{2}0 \rangle$  as the fastest, followed by  $\langle 1\bar{1}00 \rangle$ . The (000 $\pm 1$ ) planes grow slowest.

### Introduction

Up to now all SiC-electronic devices were realized using homoepitaxial layers grown on SiC substrates, because the crystallographic and electrical properties of the substrates materials are not satisfying. Therefore the understanding of the epitaxial growth process e.g. on substrates with various orientations is important for the use of SiC for electronic devices. To maintain polytype purity of the homoepitaxial layers on SiC, substrates with orientations slightly off  $\langle 000\pm 1 \rangle$  are generally utilized. A few other miscut directions (e.g.  $\langle 1\bar{1}00 \rangle$ ,  $\langle 11\bar{2}0 \rangle$ ) have been tested also [1,2]. It is, however, desirable in view of the tendency to produce SiC devices on mesa-structured substrates of various shapes (and thus local substrate orientations) to obtain an overview on the epitaxial growth in a large range of orientations. Up to now all investigations used substrates with certain miscuts, surface orientations or structured substrates providing a small number of different surface directions. In this contribution, we investigate by means of microscopical techniques the homoepitaxial growth by chemical vapor deposition (CVD) on a 6H SiC sphere that naturally provides all crystallographic orientations at a time.

### Experimental

We have used for our experiments 6H SiC spheres with a diameter between 3.5mm and 5mm which were ground from modified Lely single crystals. In order to mark crystallographic orientations and terminations of the poles we oxidized the spheres (wet oxidation, 12h, 1373K). The resulting oxide layers have different thickness as dependent on the local orientation, which therefore can easily be discriminated by the respective interference colors [3]. The oxide shows a sixfold symmetry in

thickness that allows distinction of the  $\langle 11\bar{2}0 \rangle$  directions as well as the (0001) Si- and (000 $\bar{1}$ ) C-face.

Taking this information on orientations we cut the spheres in two symmetrically equivalent hemispheres. Two experiments are conducted (c.f. Fig. 1): (1) one sphere is cut along the c-axis, (2) one sphere is cut perpendicular to the c-axis in the equator plane. The hemispheres can easily be positioned inside the CVD reactor (good heat coupling to the susceptor) for subsequent epitaxy (the oxide is removed before the CVD process, of course). Layer growth is conducted at 1550°C for 4h with  $C_3H_8$  and  $SiH_4$  as precursor gases and  $H_2$  as carrier gas. These growth conditions have lead to homoepitaxial layers on flat (000 $\pm 1$ ) substrates (growth rate  $\sim 2\mu m/h$ ) with good crystallographic and electrical quality (detailed in [4]).

For electron and optical microscope investigations we prepared slices (thickness 100 $\mu m$ ) from the hemispheres for a cross sectional view on the epilayer-substrate-interface. The high resolution transmission electron microscope (HRTEM) specimens were prepared from these slices by conventional mechanical grinding and dimpling followed by ion milling with  $Ar^+$  at liquid nitrogen temperatures to electron transparency. Electron microscopy has been performed using a Philips CM300UT microscope operated at 300keV.

## Results and Discussion

The SEM micrograph in Fig. 2 shows a hemisphere cut along the c-axis after growth for 4 hours. As for the oxide, the epilayer topology varies with orientation. We again obtain a sixfold symmetry on the sphere that results in three pronounced crystallographic bands (marked with the solid lines on the hemisphere in Fig. 2). Comparing the oxidized sphere with the sphere with an epitaxial layer we can determine the orientation of the bands, which run from the (0001) Si pole to the (000 $\bar{1}$ ) C pole along  $\langle 1\bar{1}0 \rangle$  directions. A zoom in on one of the  $\langle 1\bar{1}0 \rangle$ -bands is shown in Fig. 3a. The band consists of steps with an increasing step spacing towards the (000 $\pm 1$ )-poles (c.f. Fig. 1, Fig. 3a). Using the picture of a stair we observe risers and treads. The treads have a surface

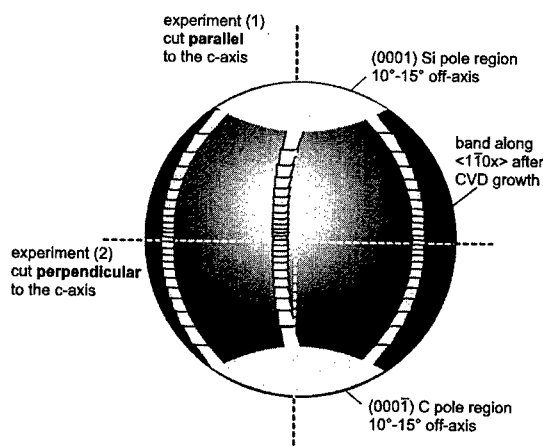


**Fig. 1:** Scheme of the sphere with the cutting planes of the two experiments and with the pole regions and pronounced crystallographic bands along  $\langle 110 \rangle$  after the CVD growth.

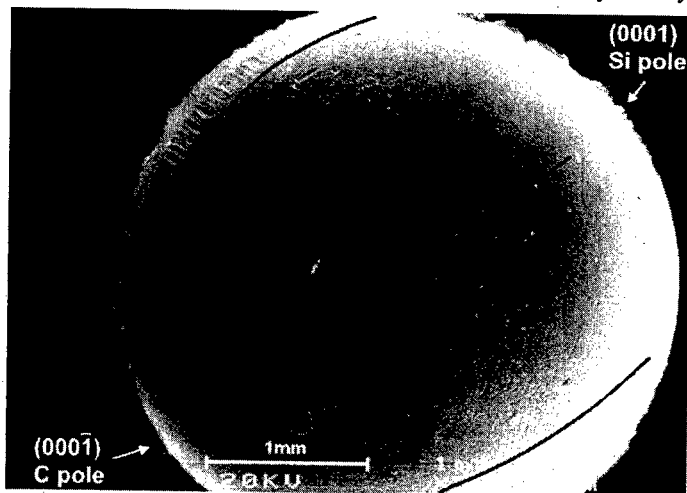


**Fig. 2:** 6H SiC hemisphere after growth for 4h, three pronounced bands along the  $\langle 110 \rangle$  directions from the (0001) Si pole to the (000 $\bar{1}$ ) C pole can be distinguished. Scanning electron micrograph.

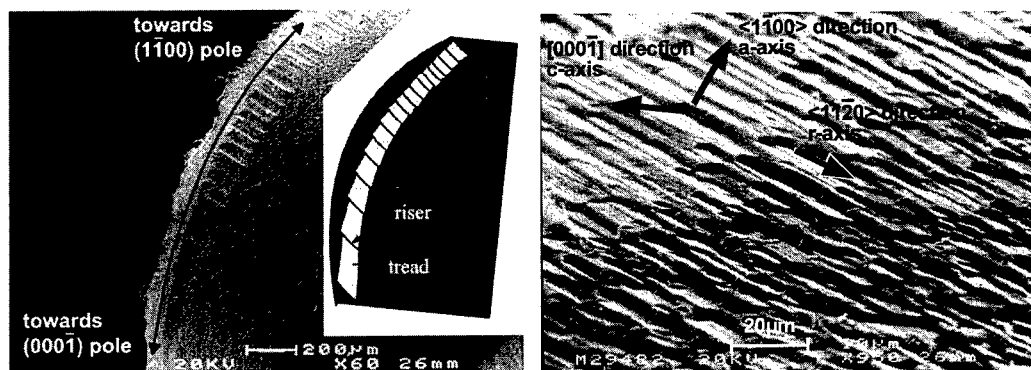


**Fig. 3a:**  $\langle 1\bar{1}0 \rangle$  band in higher magnification showing the stairlike character of the bands. The length of the treads decreases towards the  $\langle 1\bar{1}0 \rangle$  pole. Scanning electron micrograph.

**Fig. 3b:** Edge of one band (close to  $\langle 1\bar{1}0 \rangle$  pole) showing the lateral overgrowth of the terraces in  $\langle 11\bar{2}0 \rangle$  directions. Scanning electron micrograph.

normal parallel to the c-axis ( $(0001)$  Si or  $(000\bar{1})$  C orientation, depending on the hemisphere), the risers show a surface normal parallel  $\langle 1\bar{1}00 \rangle$  directions (a-axis) and the rims of the bands are oriented towards  $\langle 11\bar{2}0 \rangle$ . Towards the poles the treads increase in size and transform into a large smooth region around the poles (Fig. 4). Between these bands we observe a rough topology consisting of terraces, all with  $(000\pm 1)$ -top facets, respectively, and lateral extension parallel to the  $\langle 11\bar{2}0 \rangle$ -directions. We interpret the shape and orientation of the terraces and steps as step bunching growth. This growth mode is known for flat  $\langle 000\pm 1 \rangle$  6H SiC substrates to occur during off-axis epilayer growth [5]. The macroscopic risers on the hemispheres are oriented towards  $[1\bar{1}00]$ . The risers height increases towards the  $(1\bar{1}00)$  poles. We observe between the steps on the band lateral overgrowing the terraces next to the band. A comparison of two spheres with different growth times under otherwise identically growth conditions shows that the band width increases laterally with longer growth times. The shape of the steps is triangular with the basis of the triangles oriented towards the  $(000\pm 1)$ , respectively (c.f. Fig. 3b).

Taking all this information into account we can infer a hierarchy in growth velocities:  $\langle 11\bar{2}0 \rangle > \langle 1\bar{1}00 \rangle > [000\pm 1]$ . Obviously, the  $(0001)$  Si and  $(000\bar{1})$  C directions are the directions with the slowest growth velocities, the  $\langle 1\bar{1}00 \rangle$  directions grow faster, as obvious from the step formation.

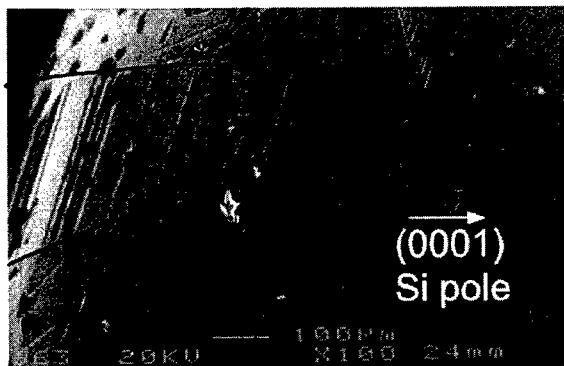


**Fig. 4:** Transformation of a band oriented towards  $\langle 1\bar{1}0 \rangle$  (marked by the solid lines) into the smooth region on the  $(0001)$  Si pole. Scanning electron micrograph.

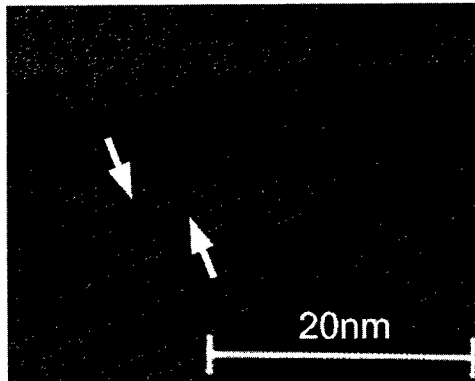


**Fig. 5:** HRTEM cross section micrograph. Deviations from the prominent 6H stacking sequence (marked by arrows) in the epilayer near the  $\langle 1\bar{1}00 \rangle$  pole.

The  $\langle 11\bar{2}0 \rangle$  directions have the highest growth velocity. This hierarchy in growth velocities results in the broad and stepped appearance of the bands (due to lateral overgrowth of terraces in  $\langle 11\bar{2}0 \rangle$  directions). Besides these three preferred hierarchical epitaxial orientations no other crystallographic orientations are particularly fast in growth.

HRTEM investigations (c.f. Fig. 5) of the epilayer near the pole reveal a highly increased number of deviations from the prominent 6H stacking sequence as compared to epilayers grown on flat  $(000\pm 1)$  substrates. These stacking faults have an average spacing of 20-50nm. The terraces in this region, however, have an average spacing of 2-5 $\mu$ m. We interpret the stacking faults as nuclei of terraces forming in the early stages of epitaxial growth on the sphere.

### Concluding discussion

We have conducted two experiments of CVD homoepitaxy on hemispheres of 6H SiC. This enables us to investigate the CVD growth on all crystallographic orientations. We observe (i) smooth surfaces around the  $(000\pm 1)$  pole regions until an off-axis angle of 10°-15° away from the pole, and (ii) 6 pronounced bands running from the  $(0001)$  Si pole to the  $(000\bar{1})$  C pole along  $\langle 1\bar{1}0x \rangle$  directions consisting of steps perpendicular to the  $\langle 1\bar{1}0x \rangle$  and  $\langle 0001 \rangle$  directions. Homoepitaxy on orientations far away from the  $(000\pm 1)$  directions seems to be more difficult even on the bands along the  $\langle 1\bar{1}0x \rangle$  directions as may be concluded from the high density of growth-induced deviations from the prominent 6H stacking sequence. These form between coalescing terraces and reduce the crystallographic and electrical quality of the epilayer. From the rough topology (terraces) between the bands and the poles we deduce that, for epilayer growth, no further favored crystallographic orientation is available in addition to the  $(000\pm 1)$  and  $\langle 1\bar{1}00 \rangle$  directions.

Taking all information from these experiments comprising the growth anisotropy in all crystallographic orientation we infer a hierarchy in growth velocities. Growth in  $\langle 11\bar{2}0 \rangle$  direction is the fastest, followed by  $\langle 1\bar{1}00 \rangle$ . The  $(000\pm 1)$  planes grow slowest.

**Acknowledgments.** Thanks are to Norbert Schulze for providing the modified Lely crystals and to Jörg Lottes for sample preparation. This work was supported by the Sonderforschungsbereich 292 of the Deutsche Forschungsgemeinschaft.

### References:

- [1] N. Nordell, S. Karlsson, A.O. Konstantinov, *Mater. Sci. For.* Vols. **264-268** (1998), p. 131
- [2] A. Henry, I.G. Ivanov, T. Egilsson, C. Hallin, A. Ellison, O. Kordina, U. Lindefelt, E. Janzén, *Diamond Rel. Mat.* **6** (1997), p. 1289
- [3] K. Christiansen, R. Helbig, *J. Appl. Phys.* **79** (1996), p.3275
- [4] K. Christiansen, T. Dalibor, R. Helbig, S. Christiansen, H.P. Strunk, *Mater. Sci. For.* Vols. **264-268** (1998), p. 135
- [5] T. Kimoto, A. Itoh, H. Matsunami, T. Okano, *J. Appl. Phys.* **81** (1997), p. 3494

## Morphological Stability of 6H-SiC Epitaxial Layer on Hemispherical Substrates Prepared by Chemical Vapor Deposition

S. Nishino, Y. Nishio, Y. Masuda, Y. Chen and Chacko Jacob

Faculty of Engineering & Design, Kyoto Institute of Technology,  
Matsugasaki, Sakyo-Ku, Kyoto 606-8585, Japan

**Keywords:** 6H-SiC, CVD, Homoepitaxial Growth, Morphology

**Abstract :** In this study, homoepitaxial growth was carried out by atmospheric pressure CVD using a  $\text{Si}_2\text{Cl}_6 + \text{C}_3\text{H}_8$  gas system. Hemispherical substrates of 6H-SiC were used for a better understanding of the stable growth on the substrate having a miscut angle. The substrates have a miscut angle of  $0^\circ$  to  $15^\circ$  toward  $\langle h k l \rangle$  directions. Sixfold patterns were observed on the Si-face and the C-face after the epitaxial growth. However, the pattern direction had different orientations. On the Si-face the rough surface extended along the  $\langle 1\bar{1}00 \rangle$  direction, while on the C-face the rough surface extended along the  $\langle 11\bar{2}0 \rangle$  direction. Extremely smooth surface morphology is observed when the substrate is tilted toward  $\langle 1\bar{1}00 \rangle$  direction on the C-face. The growth mechanism is discussed.

### Introduction

In homoepitaxial growth of SiC, step-controlled epitaxial method is widely known, where the wafers that are tilted several degrees from the (0001) faces to  $\langle 11\bar{2}0 \rangle$  are used.[1] This method is a key technology to realize a SiC device and so the surface morphology should be studied in detail. To obtain much more information about morphological stability on the tilted substrate, a hemispherical substrate was used. The surface morphology depended strongly on the polarity of the substrate, off-angle of the substrate and temperature as already reported.[2-5] In this report, surface stability of the epilayer on a hemispherical substrate is discussed.

### Experiments

The hemisphere was made of commercial SiC off-axis substrates ( $3.5^\circ$ ,  $8^\circ$  toward  $\langle 11\bar{2}0 \rangle$ ) and Lely substrates (on-axis) by using a dimpl grinder for the preparation of TEM samples. The surface of the spherically polished substrate was not smooth as of a commercial wafer. However, it was sufficient smooth to observe morphological stability of the epilayers. The diameter of the hemisphere was 15 mm with an off-axis angle from the (0001) and (000 $\bar{1}$ ) basal planes of  $0^\circ$ - $15^\circ$ . By using those substrates, the morphological stability of the epilayer in various direction  $\langle h k l \rangle$  could be investigated. In this study homoepitaxial growth was carried out by atmospheric pressure CVD. The substrates were placed on a SiC-coated graphite susceptor and inductively heated by a RF generator at a frequency of 300 kHz. The SiC epilayers were grown using  $\text{Si}_2\text{Cl}_6$  (hexachlorodisilane:HCDS) and  $\text{C}_3\text{H}_8$  (5% in  $\text{H}_2$ ). The growth rate on conventional flat substrates was  $1.5 \mu\text{m/h}$ . The growth conditions were as follows: flow rate of HCDS  $\sim 0.3 \text{ sccm}$ , flow rate of  $\text{C}_3\text{H}_8 \sim 0.2\text{-}2.0 \text{ sccm}$ , flow rate of  $\text{H}_2 \sim 3.0 \text{ slm}$  as carrier gas, growth temperature  $\sim 1400\text{-}1600^\circ\text{C}$ , growth time  $\sim 60\text{-}660 \text{ min}$ . The growth profiles consisted of two steps: an etching step with  $\text{H}_2$  at  $1500^\circ\text{C}$  for 10 min. and a CVD step for the epitaxial growth. The surface morphologies of the epilayer were observed by a Nomarski microscope and Scanning Electron Microscope (SEM). The polytype of the epilayers was characterized by photoluminescence and Raman spectroscopy.

### Results and Discussion

In this system, the activation energy of SiC growth was about 7.90 kcal/mol in the temperature range from 1400 to 1550 °C. The growth rate was limited by the flow rate of Si<sub>2</sub>Cl<sub>6</sub> similar to the SiH<sub>4</sub>+C<sub>3</sub>H<sub>8</sub> system [4]. The surface morphology depended on growth temperature, the C/Si ratio of the reaction gases and the off-axis of the substrate. To investigate the morphological stability of the epilayer, the C/Si ratio was chosen using 3.5 degree off-axis substrate(Si-face). Smooth surface of epilayer was obtained by the C/Si ratio of 10 on the flat substrate.

Figure 1(a) shows the surface morphology of the epilayer on the Si-face observed by optical microscopy. The central part of the hemisphere was rough and 3D nucleation was observed. The rough area seems to be hexagonal shape and is located off-center in this figure, because the hemisphere was made on a 3.5° off-axis substrate. The dark regions start from an edge of the hexagonal shaped area and extends along  $\langle 1\bar{1}00 \rangle$  direction. These dark regions were rather smooth and consisted of "step flow growth"[4]. Beside the dark areas, the surface shows "kink growth". However, it is gradually inclined, and so the reflected light in the microscope was small. Figure 1 (b) shows the morphology of the epilayer on C-face. Dark and rough regions extend along  $\langle 11\bar{2}0 \rangle$ . Dark regions make rather wide bands. The mid white regions between those bands are along the  $\langle 1\bar{1}00 \rangle$  direction and show smooth surface.

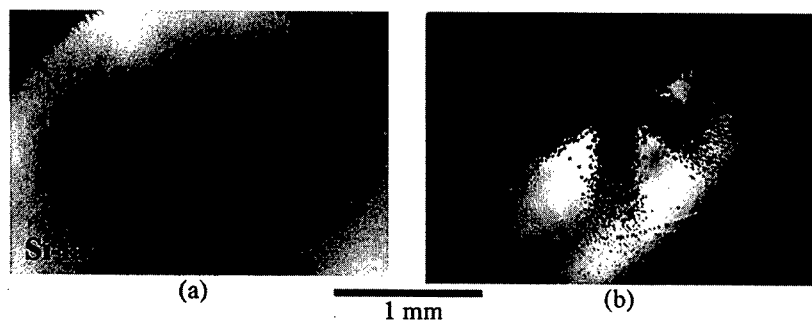


Fig.1 Optical microscopy image a) epilayer on the Si-face. The sixfold dark region extends along the  $\langle 1\bar{1}00 \rangle$  direction and is rough and the white region in the central part is rough. b) epilayer on the C-face. Sixfold dark pattern extends along  $\langle 11\bar{2}0 \rangle$  and the white region along  $\langle 1\bar{1}00 \rangle$  is smooth. Stripes in the circle are the image of the filament in the optical microscope.

Figure 2 shows the PL image of the epilayer on Si-face and C-face taken at liquid nitrogen temperature under the fluorescent optical microscope. It is easy to identify the polytype by observing the color distribution of the epilayer. The dark area was along  $\langle 1\bar{1}00 \rangle$  directions and the white area was along  $\langle 11\bar{2}0 \rangle$  directions for the epilayer growth on Si-face as shown in Fig.2(a). The dark area was 3C-SiC and the white area was 6H-SiC as confirmed by PL measurement. The sixfold white zone is observed along  $\langle 11\bar{2}0 \rangle$  after the epilayer growth on the C-face as shown in Fig.2(b). This zone is rough and 3C-SiC hillocks were observed. However, the dark area was very smooth from almost the top to periphery of the circle. It is interesting to compare the morphology between the epilayers on different polarity substrates. Rough surface extended along  $\langle 1\bar{1}00 \rangle$  for the Si-face. However, it extended along  $\langle 11\bar{2}0 \rangle$  for the C-face.

Surfaces of interest were enlarged for Si-face and C-face as shown in Fig.3. The epilayer along the  $\langle 1\bar{1}00 \rangle$  directions showed "step flow growth" and a stepped pattern is observed easily as shown in Fig.3(a). However, the rest of the area showed "kink growth". These patterns have already been reported[4]. However, the smooth surface on the C-face along  $\langle 1\bar{1}00 \rangle$  directions as shown in Fig.3(b) needs to be emphasized. The top of the hemisphere

was extremely rough. However, once this area was inclined towards the  $\langle 1\bar{1}00 \rangle$  direction, an extremely smooth surface appeared. Kimoto et. al. explained a mechanism of the step bunching along  $\langle 1\bar{1}00 \rangle$  by considering different dangling bonds at the step[4]. He also confirmed steps on C-face consisted one bilayer. In our case, the smooth surface of the epilayer on the C-face was observed along  $\langle 1\bar{1}00 \rangle$  directions. This can be related with the dangling bonds at the steps toward the  $\langle 1\bar{1}00 \rangle$  directions, because of the dangling bonds at

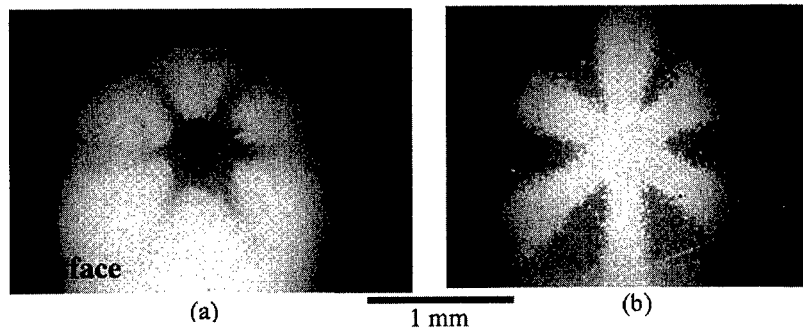


Fig.2 PL image taken at liquid nitrogen temperature. a) epilayer on the Si-face. Sixfold dark regions extends along the  $\langle 1\bar{1}00 \rangle$  directions and are rough. The white regions were smooth. b) epilayer on the C-face. Sixfold white pattern extends to  $\langle 11\bar{2}0 \rangle$  and dark regions along the  $\langle 1\bar{1}00 \rangle$  are smooth.

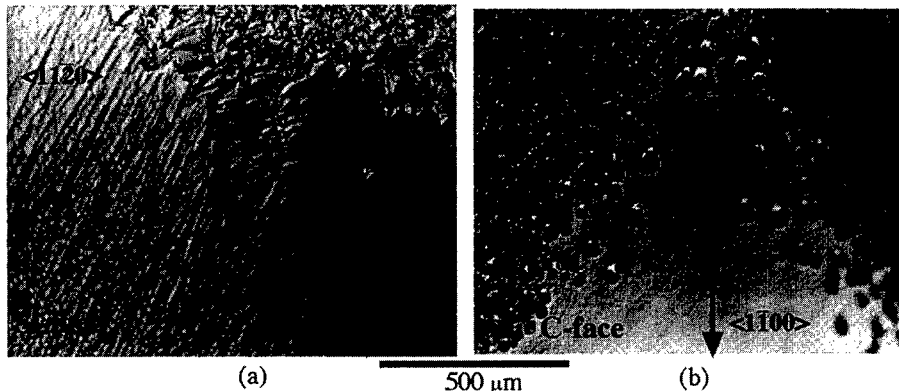


Fig.3 Optical microscopy image a) epilayer on the Si-face. Step flow growth is observed along  $\langle 1\bar{1}00 \rangle$  as shown by the arrow, and kink growth observed along  $\langle 11\bar{2}0 \rangle$ . The upper part in the figure is near the on-axis region and rough. b) epilayer on the C-face. Two sides along  $\langle 11\bar{2}0 \rangle$  are extremely rough and the area between those two is smooth, and the direction is  $\langle 1\bar{1}00 \rangle$  as shown by the arrow.

the edge, which consists of one bilayers. The steps are Si terminated as shown in Fig.4(a)[4]. Our CVD parameters were adjusted to the Si-face. So Si terminated steps may be favorable for a smooth surface. However, in case of the C-face tilted towards the  $\langle 11\bar{2}0 \rangle$  direction, the terrace is terminated by C atoms and the step edge is terminated by one Si atom and one C atom as shown in Fig.4(b)[6]. The rough surface along the  $\langle 11\bar{2}0 \rangle$  on the C-face may be related to those number of dangling bonds and the anisotropy of the lateral growth rate[4,5]. This difference will be explained by the difference of bonding energy. It is well known that the window of CVD parameters is narrow for smooth epilayer growth on the C-face. However, we could obtain a mirror-like surface on the C-face tilted long  $\langle 1\bar{1}00 \rangle$  direction



without special adjustment of the CVD parameters. In our system a mirror-like surface was obtained for more than 3 hour growth, that gives a thickness of about 4.5  $\mu\text{m}$ . To obtain a flat and mirror-like surface of the epilayer on the C-face tilted to  $\langle 1\bar{1}00 \rangle$  direction is favorable.

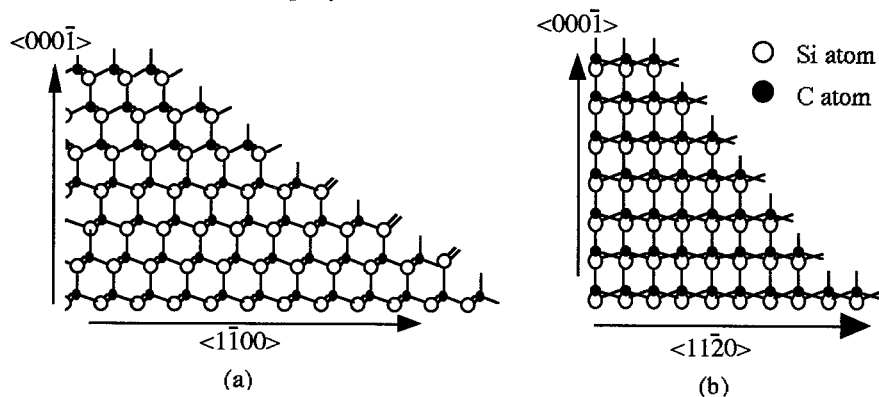


Fig. 4 Bonding configuration of 6H-SiC along  $\langle 1\bar{1}00 \rangle$  and  $\langle 11\bar{2}0 \rangle$  directions.  
a) step consists of Si atoms, b) step consists of C atoms and Si atoms.

PL spectra were also measured to confirm the polytype of epilayers using He-Cd laser as excitation light source at 11 K. The epilayer on the on-axis region of the Si-face showed 3C-SiC as the dominant polytype. However, it showed 6H-SiC as the dominant one along  $\langle 11\bar{2}0 \rangle$  when the off-axis angle was increased. Ti related peaks appeared at the wavelength of 433 nm and 445 nm. [3] In case of C-face, PL spectra of epilayer on on-axis showed overlapped spectra of 3C-SiC and 6H-SiC. However, the spectra showed 6H-SiC as the dominant one (main peak at around 470 nm) along  $\langle 1\bar{1}00 \rangle$  as off-axis was increased. Polytype of the epilayer along the  $\langle 1\bar{1}00 \rangle$  and  $\langle 11\bar{2}0 \rangle$  was also characterized by Raman spectroscopy and the results confirm the PL measurement.

### Conclusion

Morphological stability of the epilayer on 6H-SiC was studied using hemispherical substrate. A sixfold symmetrical pattern was observed on both Si-face and C-face. However, rough surface directions were different on both faces. Mirror-like surfaces were obtained on the epilayer on the Si-face with an off-angle along  $\langle 11\bar{2}0 \rangle$  directions. However, the direction of mirror-like surface for the C-face was along  $\langle 1\bar{1}00 \rangle$ . Flat and mirror-like surfaces are expected once we use (000 $\bar{1}$ ) C-face tilted more than 2° off towards  $\langle 1\bar{1}00 \rangle$ . This orientation of the substrate may be useful for device application.

### References

- [1] N.Kuroda, K.Shibahara, W.S.Yoo, S.Nishino and H.Matsunami, Extended Abstracts of the 19th Conf. on Solid State Devices and Materials, Tokyo (1987) 227.
- [2] S.Nishino, K.Takahashi, Y.Kojima and J.Saraie, Springer Proceedings in Physics, vol.56, Amorphous and Crystalline Silicon Carbide III, (1992)363.
- [3] S.Nishino, T.Miyanagi, and Y.Nishio, Mat. Sci. For. vol.264-268 (1998) pp.139-142.(Trans Tech Publications, Switzerland)
- [4] T.Kimoto, and H.Matsunami, Inst.Phys.Conf.Ser.No.137:Chap 3. pp.55-58 (1994:IOP Publishing Ltd.)
- [5] N.Nordel, S.Karlsson, and A.O.Konstantinov, Mat. Sci. For. vol.264-268 (1998) pp.131-134.(Trans Tech Publications, Switzerland)
- [6] T.Yamamoto, T.Kimoto, and H.Matsunami, Mat. Sci. For. vol.264-268 (1998) pp.111-114.(Trans Tech Publications, Switzerland)

## Growth of SiC on 6H-SiC {01 $\bar{1}4$ } Substrates by Gas Source Molecular Beam Epitaxy

Shun-ichi Nakamura<sup>1</sup>, Tomoaki Hatayama<sup>2</sup>, Tsunenobu Kimoto<sup>1</sup>,  
Takashi Fuyuki<sup>2</sup> and Hiroyuki Matsunami<sup>1</sup>

<sup>1</sup>Department of Electronic Science and Engineering, Kyoto University, Yoshidahonmachi, Sakyo,  
Kyoto, 606-8501, Japan

<sup>2</sup>Graduate School of Material Science, Nara Institute of Science and Technology,  
Takayama 8916-5, Ikoma, Nara, 630-0101, Japan

**Keywords:** {01 $\bar{1}4$ } Face, GSMBE, RHEED, XTEM

**Abstract** Growth of SiC was carried out on 6H-SiC {01 $\bar{1}4$ } substrates using gas source molecular beam epitaxy (GSMBE). The reflection high-energy electron diffraction (RHEED) pattern showed a mixture of 6H-SiC {01 $\bar{1}4$ } and 3C-SiC (001) patterns, when grown at 850 °C. Structural analysis using cross-sectional transmission electron microscopy (XTEM) revealed that randomly-oriented silicon islands of high density exist near the surface, and that the very surface of the islands is 3C-SiC, which should be aligned to the substrate crystal orientation, since a 3C-SiC (001) pattern was observed in RHEED.

### 1. Introduction

Among all SiC polytypes, cubic SiC (3C-SiC) is the only one isotropic polytype and is considered to have the highest electron mobility. Due to the lack of 3C-SiC wafering technology, heteroepitaxial growth of 3C-SiC has been carried out mainly on silicon (Si) substrates. However, the large differences of lattice constant and thermal expansion coefficient have resulted in single crystals with high-density defects, which has been a large obstacle to characterization and device application of 3C-SiC on Si.

To overcome this lattice mismatch problem, growth of 3C-SiC on  $\alpha$ -SiC has been carried out using 6H- or 15R-SiC {0001} substrates, with which 3C-SiC {111} is lattice-matched. Our group had found that 3C-SiC (001) is lattice-matched with 6H-SiC {01 $\bar{1}4$ } [1], which corresponds to 54.7°-inclined from {0001}, and reported an observation of 3C-SiC (001) spot patterns using reflection high-energy electron diffraction (RHEED) during gas source molecular beam epitaxy (GSMBE) on 6H-SiC (01 $\bar{1}4$ ) [2]. However, structural analysis of the grown layers has not been carried out. In this paper, the authors discuss further trial on growth and the structural analysis using cross-sectional transmission electron microscopy (XTEM).

### 2. Experimental

Growth was carried out in the same GSMBE apparatus as used in the previous work [2]. Source gases were Si<sub>2</sub>H<sub>6</sub> and C<sub>2</sub>H<sub>2</sub>, and were alternately supplied. The same growth condition as the previous work (Si<sub>2</sub>H<sub>6</sub>: 0.20 sccm, C<sub>2</sub>H<sub>2</sub>: 0.06 sccm, growth temperature: 850 °C, substrate: 6H-SiC (01 $\bar{1}4$ )) somehow resulted in a very dark Si ring pattern. Under a more C-rich condition (Si<sub>2</sub>H<sub>6</sub>: 0.06 sccm, C<sub>2</sub>H<sub>2</sub>: 0.06 sccm), the RHEED pattern showed a mixture of 6H-SiC {01 $\bar{1}4$ } and 3C-SiC (001) as illustrated in Fig. 1 after 1-hour growth for both (01 $\bar{1}4$ ) and (01 $\bar{1}4$ ) substrates. The RHEED pattern did not change after longer growth. For (01 $\bar{1}4$ ), the diffraction from 3C-SiC (001) was more dominant, while the pattern from 6H-SiC (01 $\bar{1}4$ )

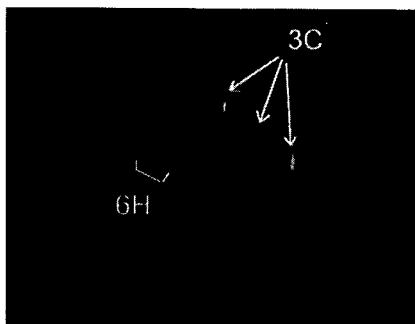


Fig. 1 RHEED pattern at 850 °C

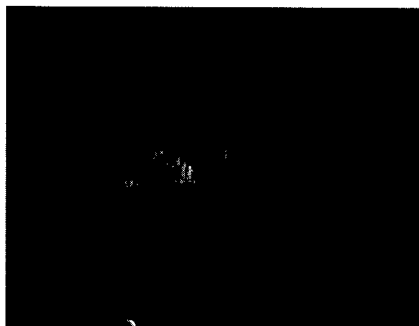


Fig. 2 RHEED pattern at 960 °C

still remained. Moreover, a higher growth temperature (960 °C) resulted in a streaky 6H-SiC (01 $\bar{1}$ 4) pattern as shown in Fig. 2, implying homoepitaxial growth of 6H-SiC at a lower temperature, by more than 100 °C, than reported for chemical vapor deposition [3].

### 3. Results and Discussion

XTEM observation was done for a sample in the previous work with a dominant 3C-SiC (001) RHEED pattern. Figure 3 shows lattice images near the interface between the substrate and grown layer. Black and white stripes corresponding to the stacking order of 6H-SiC were observed in the substrate. In the grown layer some regions showed these stripes, while the

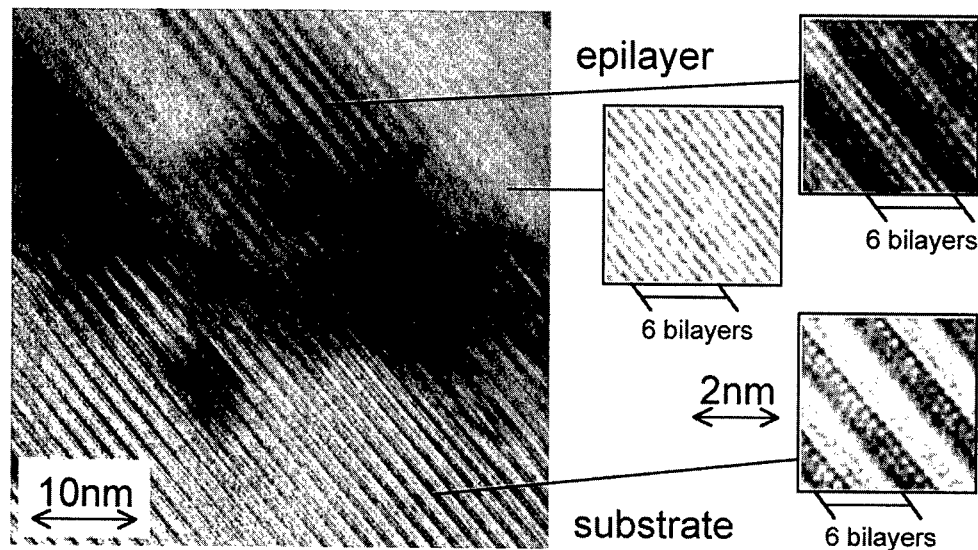


Fig. 3 XTEM lattice image near the interface

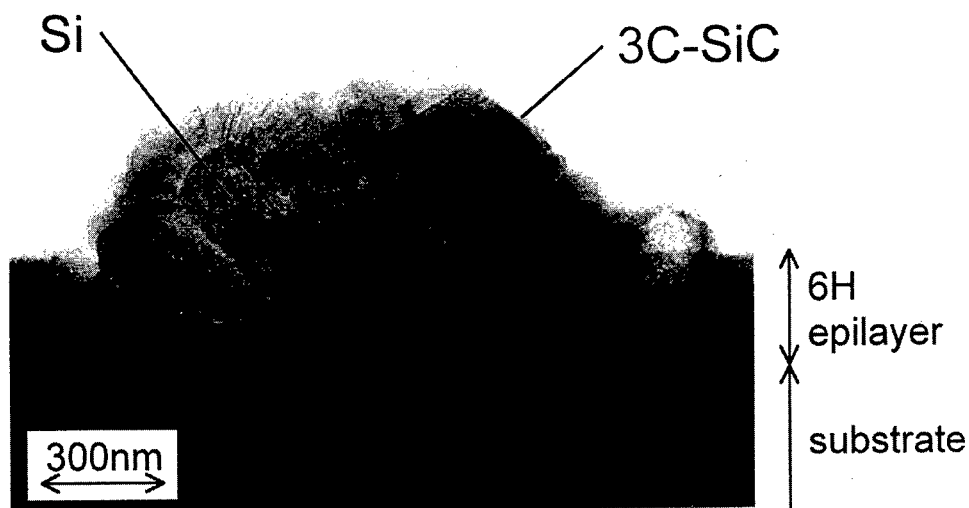


Fig. 4 XTEM image near the surface

other did not. Detailed electron diffraction confirmed that the both regions with and without stripes were 6H-SiC. Indeed, specimen tilting during XTEM observation changed the regions with stripes to those without stripes, and vice versa. Therefore, the grown layer should be 6H-SiC. The cause of the dark area in Fig. 3 is not clear yet, but probably strain near the interface.

Near the surface, a high density of large islands was observed as shown in Fig. 4. Figure 5 shows the electron diffraction from an island: a pattern of Si  $\langle 110 \rangle$  overlapping a pattern of SiC. More detailed electron diffraction confirmed that these islands were randomly-oriented Si

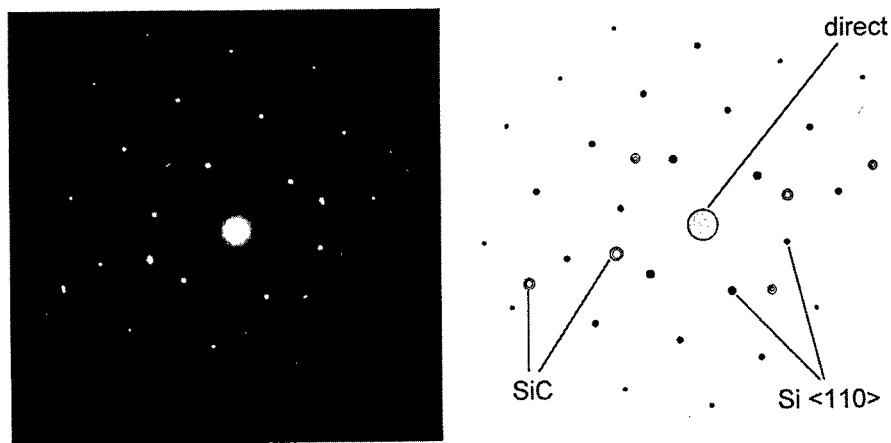


Fig. 5 Electron diffraction from an island near the surface

whose very surface was SiC, probably due to carbonization of Si. Thus, the RHEED pattern of 3C-SiC in the previous work should be from SiC on the surface of these Si islands; as they blocked off the electron beam, the pattern of 6H-SiC was not observed. Also, existence of 3C-SiC on the surface of the Si islands should have prevented the appearance of the Si ring pattern [4].

In our new trial, similar islands were observed, though much smaller and of much lower density, probably due to lower  $\text{Si}_2\text{H}_6$  gas flow rate and to shorter growth time. Since these islands did not disappear after dipping into a solution of hydrofluoric and nitric acid, their surface should be coated with SiC. The mixture of 3C- and 6H-SiC patterns may come from the same mechanism: the pattern of 6H-SiC from the substrates, with the pattern of 3C-SiC from the surface of Si islands, whose density in this case was not so high as to block off the electron beam completely. However, it should be noted that those patterns of 3C-SiC were spotty and not ring-like, indicating that the surface 3C-SiC layers should be aligned to the substrate crystal orientation. RHEED observation indicated that 3C-SiC  $\langle 110 \rangle$  were parallel to 6H-SiC  $\langle 11\bar{2}0 \rangle$  or  $\langle 01\bar{1}\bar{8} \rangle$ . Although the reason of this orientation relation is not clear yet, this phenomenon may be useful for the growth of single crystalline 3C-SiC: deposition of Si ultrathin film on the whole 6H-SiC  $\{01\bar{1}4\}$  substrate, followed by complete carbonization, may produce single crystalline 3C-SiC.

#### 4. Conclusion

Growth of SiC was carried out on 6H-SiC  $\{01\bar{1}4\}$  substrates using GSMBE. The RHEED pattern showed a mixture of 6H-SiC  $\{01\bar{1}4\}$  and 3C-SiC (001) patterns when grown at  $850^\circ\text{C}$ , while a streaky 6H-SiC  $\{01\bar{1}4\}$  pattern when grown at  $960^\circ\text{C}$ . Structural analysis using XTEM revealed that randomly-oriented silicon islands of high density exist near the surface, and that the very surface of the islands is 3C-SiC, which should be aligned to the substrate crystal orientation, since a 3C-SiC (001) pattern was observed in RHEED. Although the reason of the orientation relation between 3C-SiC coating layers and 6H-SiC substrates is not clear yet, this phenomenon may be useful for the growth of single crystalline 3C-SiC.

#### Acknowledgment

This work is partly supported by a Grant-in-Aid for Specially Promoted Research, No. 09102009, by the Ministry of Education, Science, Sports and Culture in Japan, and partly by a project of Kyoto University Venture Business Laboratory (KU-VBL). The authors would like to thank Nippon Steel, Co. for supplying 6H-SiC  $\{01\bar{1}4\}$  substrates, and Dr. Tetsuyuki Okano at Matsushita Technoresearch, Inc. for the XTEM observation.

#### References

- [1] W. S. Yoo, and H. Matsunami, Jpn. J. Appl. Phys. **30** (1991) p.545.
- [2] T. Yoshinobu, H. Mitsui, I. Izumikawa, T. Fuyuki and H. Matsunami, Appl. Phys. Lett. **60** (1992) p.824.
- [3] A. Yamashita, W. S. Yoo, T. Kimoto and H. Matsunami, Jpn. J. Appl. Phys. **31** (1992) p.3655.
- [4] T. Yoshinobu, H. Mitsui, Y. Tarui, T. Fuyuki and H. Matsunami, J. Appl. Phys. **72** (1992) p.2006.

## Molecular Beam Epitaxial Growth of Heteropolytypic and Low-Dimensional Structures of SiC

A. Fissel<sup>1</sup>, U. Kaiser<sup>1</sup>, B. Schröter<sup>1</sup>, J. Kräußlich<sup>2</sup>, H. Hobert<sup>3</sup> and W. Richter<sup>1</sup>

<sup>1</sup> Institut für Festkörperphysik, Friedrich Schiller Universität Jena, Max-Wien-Platz 1,  
DE-07743 Jena, Germany

<sup>2</sup> Institut für Optik und Quantenelektronik, Friedrich-Schiller-Universität Jena, Max-Wien-Platz 1,  
DE-07743 Jena, Germany

<sup>3</sup> Institut für Physikalische Chemie, Friedrich Schiller Universität Jena, Max-Wien-Platz 1,  
DE-07743 Jena, Germany

**Keywords:** Growth Conditions, Heterostructures, MBE, Polytype

**Abstract:** Epitaxial growth experiments to realize SiC heteropolytypic structures have been performed in two different ways by solid-source molecular beam epitaxy depending on substrate orientation. In the first way, on on-axis substrates, 4H/3C/4H-SiC(0001) structures have been grown by first nucleating a few monolayers thick 3C-SiC layer at lower temperatures ( $T < 1500$  K). In a second step, 4H-SiC has been grown on top of the 3C-SiC layer under carbon-rich conditions and low supersaturations at higher  $T$  (1600 K). 3C-SiC layers grown on well-prepared surfaces at low supersaturations were found to be free of double-position boundaries in a large scale (some  $\text{mm}^2$ ). The 3C-SiC layers grow pseudomorphic with respect to the substrate for both 6H- and 4H-SiC. Furthermore, a second way is opened to grow multi-heterostructures consisting of 4H/3C- or 6H/3C-stacking sequences by first nucleating 3C-SiC selectively on the terraces of well-prepared off-axis  $\alpha$ -SiC(0001) substrates at low  $T$  ( $< 1300$  K). Next, the SiC layers were grown further in a step-flow growth mode at high  $T$  and conditions corresponding to a low supersaturation (Si-rich). In this way also smaller (1D-wires) structures were obtained on the terraces of the hexagonal material in the initial stage of growth. The number of these wires was found to be strongly dependent on the substrate temperature and the off-angle. As revealed by electron channeling, Raman and photoluminescence spectroscopy, many wire-like regions consisting of 3C-SiC were found within the hexagonal SiC layer material after the subsequent layer growth on the C-face of  $\alpha$ -SiC(0001), indicating a simultaneous step-flow growth of the cubic and hexagonal material.

### 1. Introduction

The growth of SiC-heteropolytypic structures is a challenge for future new applications of the semiconductor material SiC, such as resonant tunneling or other heterojunction devices. Moreover, it offers the potential of increasing flexibility in the design of electronic structures in SiC-based electronics. However, no suitable heterostructures has been obtained so far because of the high defect level resulting from the heteropolytypical growth and, moreover, because the growth of such structures demands definite nucleation and growth conditions for each of the polytypes forming the structure. We report about different growth studies of SiC on  $\alpha$ -SiC(0001) suitable to realize polytypic hetero- or nanostructures. The growth experiments have been performed by means of solid-source molecular beam epitaxy at temperatures ranging from 900 to 1300 °C. Different experiments have been performed by varying the substrate temperature, supersaturation, the Si/C ratio and the substrate off-angle. The experimental conditions have been described in detail elsewhere [1]. The obtained structures have been investigated by transmission electron microscopy (TEM), electron channeling (EC) patterns, Raman and photoluminescence (PL) spectroscopy.

### 2. Results

#### 2.1. Surface preparation

To obtain an accurate epitaxial growth and, moreover, to get sharp heteropolytypic interfaces it is

necessary to use well prepared and ordered surfaces. Therefore, after plasma-etching and wet chemical treatment [2], the substrates have been prepared in situ by sublimation etching at high temperature (1600 K) in a Si-flux. Whereas no ordered step structure has been found after ex situ preparation, a well-developed step structure has been obtained after this treatment, with steps typically of 2-6 monolayers (ML) in height in case of 6H-SiC and of 1-4 ML in case of 4H-SiC. Afterwards a SiC-buffer layer has been grown at the same temperature and conditions suitable to realize a step-flow growth mode also on nominal on-axis substrates [3]. The final step morphology mostly consists of steps one unit cell in height.

## 2.2. Growth on on-axis substrates

The most serious problem in the growth of SiC-heterostructures is the occurrence of incoherent twin (double-position) boundaries (DPB) when 3C-SiC is involved. Recently, we have already [4] demonstrated that the growth of 3C-SiC was found to be significantly improved by an alternating supply of Si and C at medium temperatures (T) (1425 K) on on-axis  $\alpha$ -SiC(0001). The size of DPB domains was found to be increased to some hundreds  $\mu\text{m}$  in diameter. This already demonstrated the importance of adatom mobility and supersaturation (S) conditions for the growth of single domain films. A further improvement of the 3C-SiC layer quality on  $\alpha$ -SiC has been achieved by a further decrease of S and the improvement of surface quality. In this way single domain 3C-SiC was obtained on  $\alpha$ -SiC(0001) in dimensions on the order of a mm also for layers only on the order of nm thick as demonstrated in Fig.1. The 3C-SiC in the other domain was found to be only associated with surface imperfections (scratches). This indicates a coherent nucleation of 3C-SiC in one orientation at low S and on well-ordered surfaces. Furthermore, as already demonstrated recently for the growth of 3C-SiC on 6H-SiC(0001) [5], the 3C-layers grow also pseudomorphic on 4H-SiC. That means, there is no difference in the in-plane lattice constant between the cubic layer and the hexagonal substrate material, whereas the difference in the lattice constant in the growth direction was  $\Delta c/c = -1.3 \times 10^{-3}$  in case of 3C/4H-SiC(0001) as shown in Fig.2.

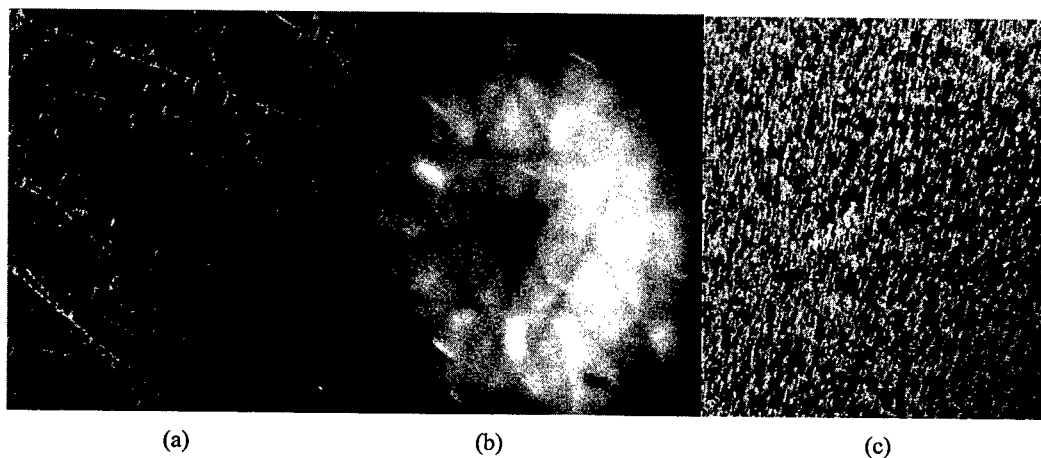


Fig.1: EC contrast micrograph (400x400  $\mu\text{m}$ ) of 3C-SiC layers grown by MBE on on-axis 4H-SiC(0001) at a growth rate of 30 nm/h at 1525 K (a) and 1475 K (c) (lighter parts represent the other cubic domain); (b) corresponding EC pattern of the single-domain layer.

Growing SiC at 1600 K under C-rich conditions results in the homogeneous formation of 4H-SiC across a region of on the order of a  $\mu\text{m}$  on top of the 3C-SiC layer (Fig.3). The preferential formation of 4H-SiC at low S and C-rich conditions has been already suggested from estimations within the framework of nucleation theory [6]. The C-rich conditions can easily be checked by the occurrence of the C-rich  $\sqrt{3} \times \sqrt{3}$  superstructure formed in the initial stage of graphitization process [7]. Further changes of the polytypic structure in one growth cycle have also been tried. However, in this way no more than two changes, such as 3C/4H/3C/4H/3C/4H-SiC(0001), have been achieved so far.

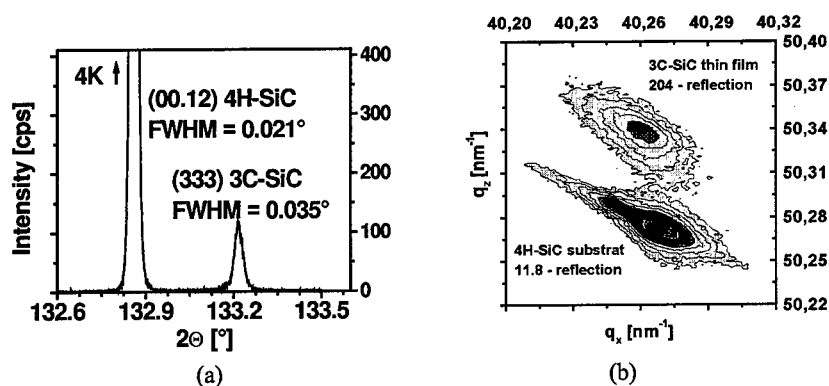


Fig.2: (a)  $\Theta$ - $2\Theta$  scan of a 3C-SiC layer on 4H-SiC(0001); (b) X-ray reciprocal space mapping of a 3C-SiC layer grown on on-axis 4H-SiC(0001) by MBE at  $T = 1500$  K and a rate of 30 nm/h.

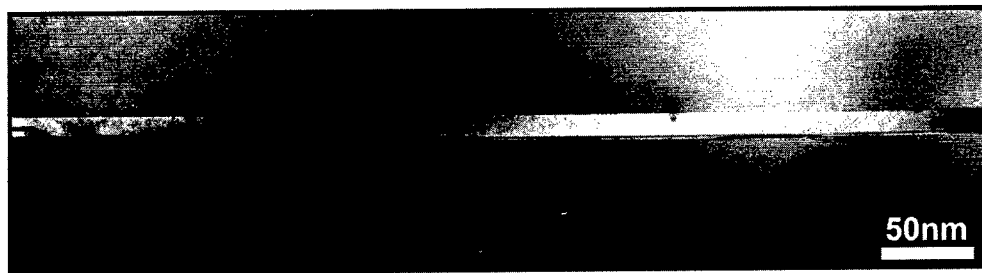


Fig.3: Cross sectional transmission electron micrograph of a 4H/3C/4H-SiC-(0001) heterostructure grown at 1500 K (3C-SiC) and 1600 K (4H-SiC) by MBE.

### 2.3. Growth on off-axis substrates

On off-axis substrates, a lower temperature of 1300 K was used to form a 3C-SiC growth. A careful growth by nucleation of 3C-islands on the terraces and a subsequent further growth of some monolayers at higher temperatures (1550 K) resulted in the formation of wire-like regions of 3C-SiC on the terraces of  $\alpha$ -SiC(0001) as demonstrated in Fig.4. Depending on the off-angle either nucleation takes place on each of the terraces (low off-angle) (Fig 4c) or only on some larger ones ( $>1^\circ$ ) at the present growth conditions. During further growth at high temperatures (1600 K) and Si-rich conditions, wire-like regions were found within the hexagonal layer material (4a,b). These wires consist of 3C-SiC as revealed by EC, Raman and PL spectroscopy. The 3C-SiC formed by nucleation at defects (scratches) and grown on the terraces are clearly distinguished by its intensity and shape, as demonstrated in Fig. 4b. This indicates a simultaneous growth of both hexagonal and cubic parts and demonstrates that a SiC heteropolytypic structure has been realized via step-flow growth mode. The photoluminescence spectrum (Fig.5) taken from such a structure at 4.2 K and an excitation wavelength of 325 nm shows in comparison to the 4H-SiC substrate one additional strong peak at 427.2 nm, and two small peaks at 643.5 nm and 646.2 nm, resp.. The peak at 427.2 nm corresponds well to the  $L_1$  peak found for other 4H-SiC materials under certain conditions [8], whereas the two small peaks may be associated with the 3C-SiC parts of the polytypic structure [9].

### 3. Summary

SiC-heterostructures consisting of a hexagonal and cubic polytype have been grown by two different methods. On well-oriented substrates, at first 3C-SiC is nucleated at lower temperatures and then further grown in a second step at low supersaturation. Layers nearly free of double-position boundaries has been obtained in this way. On the 3C-SiC layer, 4H-SiC was nucleated and grown at C-rich conditions. On off-axis substrates, 3C-SiC has been nucleated at even lower temperatures (or



higher supersaturations). At certain conditions (off-axis angle) a selective nucleation occurs. In a second step, the layers were grown further by a step-flow of both the hexagonal and cubic materials. As a result of the growth process a multi-heterostructure has been formed consisting of many cubic and hexagonal lamellae. 3C-SiC wire-like low-dimensional structures were formed on the terraces in the initial stage of step-flow.

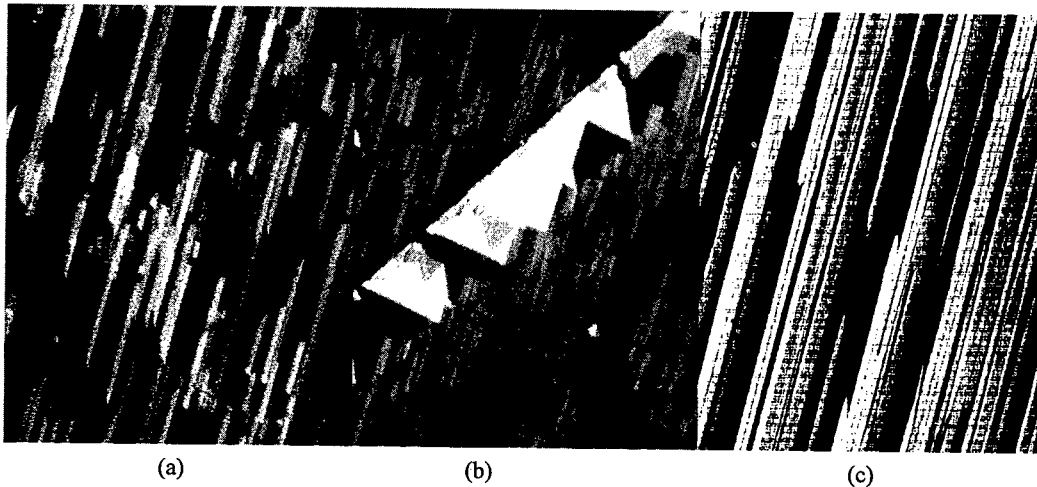


Fig.4: EC contrast micrograph (40x40  $\mu\text{m}$ ) of (a) 1.6  $\mu\text{m}$  thick SiC film grown on 3.5° off-axis 4H-SiC(0001) C-face at 1600 K; (b) 1.6  $\mu\text{m}$  thick SiC film grown on 3.5° off-axis 4H-SiC C-face at 1550 K and (c) 3C-SiC nucleation on 0.9° off-axis 6H-SiC(0001) at 1500 K (light parts correspond to 3C-SiC).

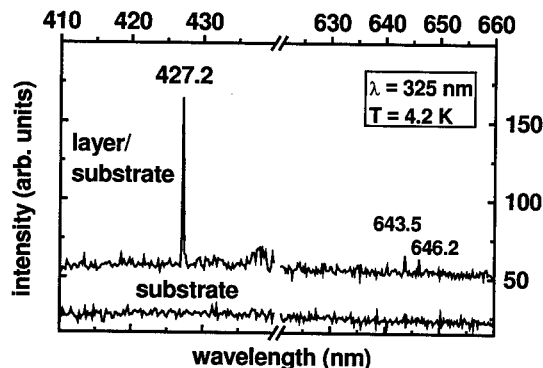


Fig.5: Photoluminescence spectra of a 4H-SiC(0001) substrate and of a 1.6  $\mu\text{m}$  thick SiC layer grown by MBE on the C-face of a 3.5° off-axis 4H-SiC(0001) substrate obtained with an excitation wavelength of 325 nm at 4.2 K.

The authors like to acknowledge the support of this work by the Deutsche Forschungsgemeinschaft (SFB 196, project A03).

## References

- [1] A. Fissel et al., J. Cryst. Growth, **154** (1995), p. 72.
- [2] E. Ducke et al., Inst. Phys. Conf. Ser., **142** (1996), p. 609.
- [3] A. Fissel et al., Adv. Sol. State Phys., **38** (1999), p. 87.
- [4] A. Fissel et al., Mater. Sci. Eng. B, **61-62** (1999), p. 139.
- [5] A. Bauer, Mater. Sci. Technol. B, **61-62** (1999), p. 179.
- [6] A. Fissel, J. Cryst. Growth (submitted).
- [7] A. Fissel et al., J. Electron. Mater., **28** (1999), p. 206.
- [8] Ch. Haberstroh et al., J. Appl. Phys., **76** (1994), p. 509.
- [9] W.J. Choyke and L. Patrick, Phys. Rev. B, **4** (1971), p. 1843.

## Thermodynamical Consideration of the Epitaxial Growth of SiC Polytypes

A. Fissel

Institut für Festkörperphysik, Friedrich Schiller Universität Jena, Max-Wien-Platz 1,  
DE-07743 Jena, Germany

**Keywords:** Growth Conditions, MBE, Nucleation, Polytype, Polytypism, Sublimation, Thermodynamics

**Abstract:** The growth of certain SiC polytypes by molecular beam epitaxy (MBE) under near equilibrium conditions, such as low rates and high temperatures, was analyzed within the framework of classical nucleation theory. It has been demonstrated that the formation of certain polytypes in the nucleation stage is due to an interplay between their differences in the surface and formation energy as well as the growth conditions. Based on these considerations, it was obtained that the formation of a polytype in the nucleation stage is established by a set of growth parameters: substrate temperature, Si/C-ratio and C-flux. The obtained results agree very well with experimental findings based on sublimation bulk-growth experiments as well as with results obtained recently by MBE.

### 1. Introduction

The growth of heteropolytypic structures makes it possible to build devices from heterostructures consisting of one semiconducting material only by different stacking of atomic SiC layers in [0001] direction. In this context, thin epitaxial SiC-films on SiC(0001) substrates with definite layer structure are of interest. The growth of such heteropolytypic structures, however, is a big challenge because it demands definite nucleation conditions for each of the polytypes forming the structure. However, despite the fact that many effects will be discussed regarding their influence on the polytype formation and stabilization, a conclusive theory is still missing. Therefore, it is not so clear in the moment what are really the mechanisms responsible for the polytype formation and, moreover, why under special growth conditions only one certain polytype occurs and others not. Therefore, it is of interest generally to estimate conditions stabilizing the growth of a certain SiC polytype. These conditions should be applicable in principle for both bulk growth and epitaxial layer growth methods of SiC, because both are based on a vapor phase deposition process and the mechanisms of the growth process in both methods are comparable.

Therefore, it was the purpose of this work to analyze the epitaxial growth conditions of SiC quantitatively from the point of view of nucleation within the classical nucleation theory. The use of the classical nucleation theory to characterize the MBE growth process is justified especially because of the large critical nucleus size occurring under the selected near equilibrium growth conditions (low rates, high substrate temperatures). For the presented analysis were considered especially the Si/C-ratio, the supersaturation, the heat of SiC formation and surface energy. Moreover, it is known from literature that among the SiC polytypes there are small differences in the formation energy as well as in the surface free energy. It will be demonstrated that the preferential occurrence of certain SiC polytypes in the nucleation stage can be explained already taking the influence of these small differences on the nucleation energy into account.

### 2. Results

The thermodynamical considerations of SiC polytype growth were performed within the framework of classical nucleation theory. The free energy  $\Delta G^*$  of formation of a stable nucleus on a (111) or

(0001) surface can be expressed in case of two-dimensional (2D) homogeneous nucleation by [1]:

$$\Delta G_2^* = b^4 \sigma^2 / \Delta \mu \quad (1),$$

where  $\sigma$  - surface energy,  $b$  - first neighbor distance corresponding to the in-plane lattice constant and  $\Delta \mu = kT \ln(p/p_0)$  - difference in the chemical potential between the solid and the gas phase. In case of heteropolytypic 2D-nucleation the following equation is valid [1]:

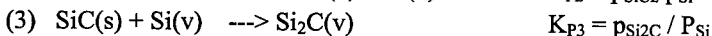
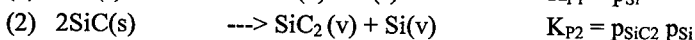
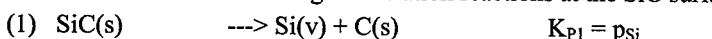
$$\Delta G_2^* = b^4 \sigma_i^2 / [\Delta \mu - b^2 (\sqrt{3}/2) (\sigma_i + \sigma_s - \sigma_l)] \quad (2),$$

where  $\sigma_s$ ,  $\sigma_i$  and  $\sigma_l$  are the free energy of the substrate surface, of the layer/substrate interface and of the layer surface, respectively. The ratio  $p/p_0$  corresponds to the supersaturation ( $S$ ) ratio, where  $p$  and  $p_0$  are the vapor pressures above the substrate (corresponding to the supply) and the equilibrium vapor pressure, respectively.

$S$  at the surface is determined by the equilibrium partial pressures of  $\text{SiC}_2$  and  $\text{Si}_2\text{C}$ :

$$S = p_C / (p_{\text{Si}_2\text{C}} + 2p_{\text{SiC}_2}) \quad (3),$$

in accordance to the following dissociation reactions at the SiC surface:



where v and s refers to the vapor and solid phase, respectively. The partial pressures of the carbon bearing species are a strong function of temperature but also of the given Si vapor pressure (that corresponds to the Si supply) above the surface in accordance with the reactions given above. Therefore, the supersaturation ratio can not be controlled independently concerning Si and C.

The equilibrium constants  $K_{Pi}$  of the reactions can be calculated by means of the isobaric-isothermal potential  $\Delta G_T^R(i)$  of the reaction:

$$-RT \ln K_p = \Delta G_T^R \quad (4),$$

where  $R$  is the universal gas constant. The chemical potential  $\Delta G_T^R$  is given by the known thermodynamical relation:

$$\Delta G_T^R = n \sum_E \Delta H_{f,298.15}^0 + 298 \int_{298}^T c_p dT - T [s_{298}^0 - 298 \int_{298}^T \Delta c_p / T dT] - n \sum_A \Delta H_{f,298.15}^0 + 298 \int_{298}^T c_p dT - T [s_{298}^0 - 298 \int_{298}^T \Delta c_p / T dT] \quad (5),$$

where  $n$  - number of moles of the component,  $\Delta H_{f,298.15}^0$  - formation enthalpy of the component at 298 K (standard),  $c_p$  - specific heat,  $T$  - temperature in K and  $s_{298}^0$  - entropy at 298 K (standard) of the component. E and A stand for the reaction products and starting components, respectively.

The partial pressures of  $\text{Si}_2\text{C}$  and  $\text{SiC}_2$  can be calculated, for example, using the relations presented by Tsvetkov et al. [2] for the 6H-SiC polytype:

$$p_{\text{Si}_2\text{C}} = 2.85 \times 10^2 \exp(-1.79 \times 10^4 / T) \times p_{\text{Si}} = K_{P3} p_{\text{Si}}$$

$$p_{\text{SiC}_2} = 9.41 \times 10^{28} \exp(-14.35 \times 10^4 / T) / p_{\text{Si}} = K_{P2} / p_{\text{Si}}$$

However, as already suggested by Tairov and Tsvetkov [3], these partial pressures are not equal for the different SiC polytypes. They have already found that the vapor phase above 3C-SiC, for example, is enriched with silicon more than that above 4H-SiC, and attributed this effect to the different heat of formation of 3C- and 4H-SiC.

To quantify the differences in the vapor pressures between the polytypes, we have to consider that the chemical potential of reaction is mainly determined by the heat of formation of the participating components, that means also by the heat of SiC formation. Therefore, a different heat of SiC formation results also in a different equilibrium constant, and, therefore, in different partial pressures of  $\text{Si}_2\text{C}$  and  $\text{SiC}_2$  at constant temperature. In accordance to the heat of formation of 6H- and 3C-SiC, respectively, presented in Tab.1 and to the reactions (2) and (3) given above, in case of 3C-SiC, the partial pressures of  $\text{Si}_2\text{C}$  and  $\text{SiC}_2$  calculated for 6H-SiC have been corrected by a factor of  $\exp[(\Delta H_{f,298.15}^0(3\text{C-SiC}) - \Delta H_{f,298.15}^0(6\text{H-SiC})) / RT]$  and a factor of  $\exp[(2 \times 1.3 \text{ kJ/mol}) / RT]$ , respectively. It should be noted that the difference in the formation energy between the polytypes is comparable to those obtained for the difference in the free lattice energy [4]. Therefore, an increase in temperature should result in an increase of the difference [4]. The same procedure has been applied to 4H-SiC using the corresponding value in Table 1. As a result of the corrections, the

equilibrium partial pressures of the carbon bearing species are larger in case of 3C-SiC, while the corresponding ones in case of 4H-SiC are lower in comparison to 6H-SiC.

Tab.1: Some thermodynamic properties of the most common SiC polytypes

SiC-Polytype	in-plane lattice constant (nm)	Surface energy (J/m <sup>2</sup> )	Heat of formation (kJ/mol)
3C	0.3083 [5]	1.742 [6]	- 64 [3]
6H	0.3082 [5]	1.767 [7]	- 65.3 [3]
4H	0.3078 [5]	1.8 [7]	- 66.6 [3]

The calculated data of supersaturation ( $S$ ) at 1600 K and a carbon supply corresponding to a vapor pressure of  $4 \cdot 10^{-5}$  Pa are given in Fig.1 for 3C-, 6H- and 4H-SiC as function of the Si supply. Generally, a strong change in  $S$  is seen from these curves by varying the Si flux. At a certain Si flux (corresponding to more C-rich condition) a maximum in  $S$  occurs. Moreover, the higher equilibrium vapor pressures of Si<sub>2</sub>C and SiC<sub>2</sub> lead to the lowest  $S$  above the 3C-SiC surface during the growth.

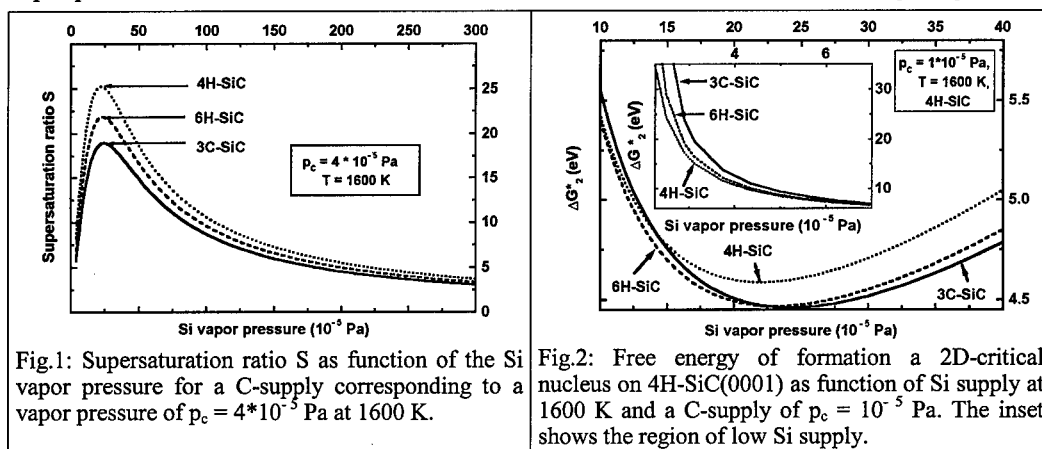


Fig.1: Supersaturation ratio  $S$  as function of the Si vapor pressure for a C-supply corresponding to a vapor pressure of  $p_c = 4 \cdot 10^{-5}$  Pa at 1600 K.

Fig.2: Free energy of formation a 2D-critical nucleus on 4H-SiC(0001) as function of Si supply at 1600 K and a C-supply of  $p_c = 10^{-5}$  Pa. The inset shows the region of low Si supply.

From the data of  $S$  calculated for the three polytypes and the surface energies given in Tab.1, the energy necessary to form a 2D-critical nucleus on the most common SiC substrates has been estimated using Eqn.1 and Eqn.2. Despite the uncertainty in the absolute values, the differences in the surface energy were obtained by calculations [6] and confirmed experimentally also at higher temperatures [7]. In Fig.2, the results are plotted as function of the Si vapor pressure for the nucleation on the Si-face of 4H-SiC(0001) at  $T = 1600$  K and a C-flux corresponding to  $10^{-5}$  Pa. From these plots it is clearly seen that under C-rich conditions the formation of 4H-SiC is favored, whereas with an increase in the Si-supply 3C-SiC becomes more stable in the nucleation stage. This demonstrates that despite the higher surface energy, the nucleation energy of 4H is lower than that of 3C at certain growth conditions, such as low  $S$  and more C-rich gas phase. Moreover, it is interesting to note that within a small region of Si supply the 6H-SiC polytype also should exist preferentially in the nucleation stage, what we have never obtained experimentally so far.

Increasing  $S$  by an increase of the C-supply, the 3C-SiC polytype is clearly the dominant polytype within a large range of Si supply (Fig.3), whereas at C-rich conditions no SiC polytype is clearly preferred. This should result in a frequently change of the stacking sequences. The preferential occurrence of 3C-SiC at larger supersaturations and Si-excess agrees very well with many epitaxial growth experiments, like CVD and MBE [8], performed at  $T < 2000$  K. The situation does not change considering the nucleation on 6H-SiC or 3C-SiC. However, at this point it should be also emphasized that at extreme conditions, those corresponds to very low supersaturations and a very high Si-supply (however, still below Si clustering), the calculations indicate that under these conditions 6H-SiC should be again preferred in the nucleation stage, as demonstrated in Fig.4. Such conditions are comparable for example to an heteroepitaxial growth on silicon.

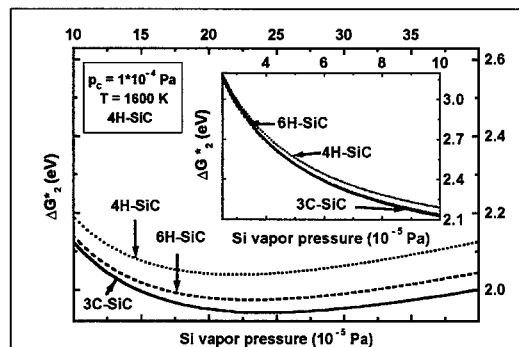


Fig. 3: Free energy of nucleation on 4H-SiC(0001) at 1600 K and a C-supply of  $p_c = 10^{-4}$ .

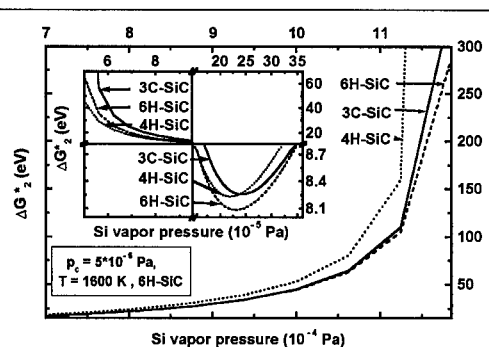


Fig. 4: Free energy of nucleation on 6H-SiC(0001) at 1600 K and a C-supply of  $p_c = 5 \cdot 10^{-6}$  Pa.

The underlying conditions for the presented estimations compare to conditions (low T, lower rates) applicable to the solid-source MBE growth. Therefore, to demonstrate the applicability of the model presented, conditions comparable to sublimation growth experiments have also been considered. At growth conditions of  $T = 2400$  K and  $p_c = 50$  Pa, the preferential nucleation of 4H on 4H-SiC(0001)

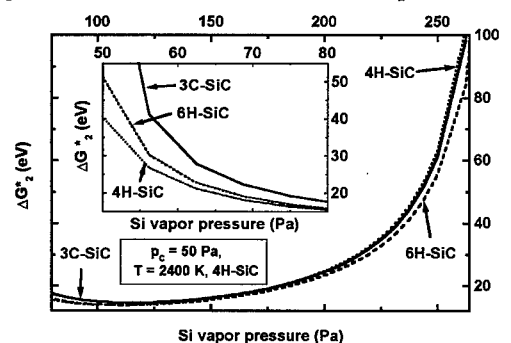


Fig. 5: Free energy of nucleation on 4H-SiC(0001) at 2400 K and a C-supply of  $p_c = 50$  Pa

also corresponds to C-rich conditions, whereas Si-rich conditions result in the preferential formation of 6H-SiC (Fig. 5). An increase in C-supply (or  $S$ ) results in the preferential formation of 3C-SiC within a large range of Si supply, whereas no polytype is preferred at C-rich conditions. The same result was obtained in principle for the nucleation on 6H- and 3C-SiC, too. To explain the preferential occurrence of the 4H-SiC polytype on the C-face within the nucleation model, the strong relaxation of the C-face has to be considered. It is clearly evident from the present estimations that such an effect results in a strong preference of 4H-SiC on the C-face of any kind of SiC polytype.

### 3. Conclusions

In summary, it has been demonstrated that the growth of different polytypes can be explained within the framework of modified nucleation theory. In such a way, it is possible also to estimate quantitatively the growth conditions stabilizing the formation of a certain polytype, which become more accurate if more precise thermodynamic data of the different polytypes are available.

*The author wishes to thank Profs. H. Duncken, F. Bechstedt, and W. Richter for helpful and fruitful discussions, and the University of Jena for partly supporting this work.*

### References

- [1] I. Markov, R. Kaischew, Thin Solid Films, **32** (1976), p. 163.
- [2] V.F. Tsvetkov et al., Inst. Phys. Conf. Ser., **142** (1996), p. 17.
- [3] Yu.M. Tairov and V.F. Tsvetkov, Prog. Cryst. Growth Character., **7** (1983), p. 111.
- [4] A. Zywitz et al., Phys. Rev. B, **54** (1996), p. 1791.
- [5] A. Bauer et al., Phys. Rev. B, **57** (1998), p. 2647.
- [6] J. Furthmüller, private communication.
- [7] R. Yakimova et al., Mater. Sci. Forum, **264-268** (1998), p. 159.
- [8] A. Fissel et al., Adv. Solid State Physics, **38** (1999), p. 87.; J. Electron. Mater., **28** (1999), p. 204.

## Mechanisms of SiC(111) Step Flow Growth

Phillip J. Stout

CFD Research Corporation, Cummings Research Park, 215 Wynn Drive,  
Huntsville, AL 35805, USA

**Keywords:** Computational Modeling, Hexagonal Stacking, Monte Carlo, Polytype, Step Bunching, Surface Kinetics

**ABSTRACT:** Aspects of step flow growth for various SiC(111) polytypes are described using a dangling bond formulation of a surface kinetics model. Differences in the dangling bond dispersion at the step riser "growth" sites are used to predict the variability in the step flow growth rates with flow direction. Step flow growth on a (111) plane in  $\langle 1120 \rangle$  directions is faster than growth in  $\langle 1100 \rangle$  directions. There is also step flow growth rate variability among the  $\langle 1100 \rangle$  directions as a consequence of the characteristic triangular and hexagonal morphologies seen when growing SiC(111). Step bunching is shown to be due in part to the growth rate variability of  $\langle 1100 \rangle$  directions and the hexagonal stacking content in the  $\alpha$ -SiC polytype.

### I. INTRODUCTION

SiC has been recognized as a good candidate for devices required to operate in harsh environments such as high temperature and high radiation. [1] The adoption of SiC in these devices is hindered, in part, by the difficulty in single crystal growth of device quality SiC with high reliability and large area. Other problems encountered during step flow growth of SiC are defect formation, step bunching, and polytype uniformity.

This paper focuses on mechanisms or microscopic processes which affect SiC(111) step flow growth. First, an overview of a Monte Carlo (MC) model is given. Then, the MC model is used to describe the microscopic processes which affect characteristics of SiC step flow growth such as triangular and hexagonal morphologies, anisotropy of step flow growth direction, increase in growth rate with off-axis angle, and step bunching.

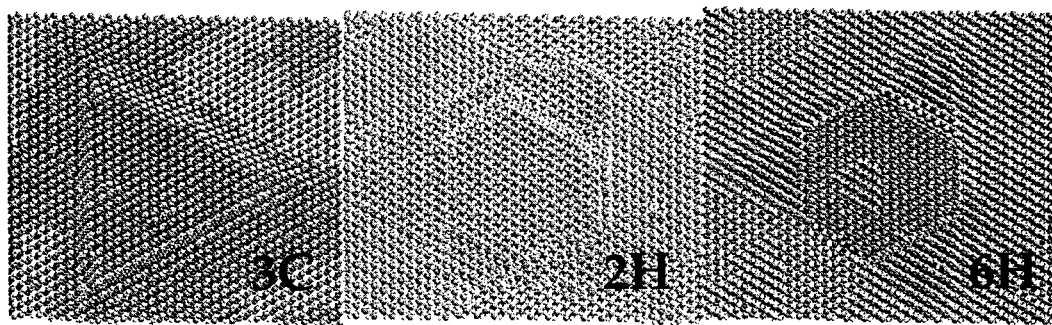


Figure 1 MC model predicted morphology after growth on a 4 BL high circular mesa structure on SiC(111).

### II. MONTE CARLO MODEL: DANGLING BOND FORMULATION

A dangling bond formulation of a Monte Carlo (MC) model of crystal growth [2] is used to describe mechanisms which affect the step flow growth of polytypes of SiC(111). The model predicts macroscopic morphological features of SiC growth based only on fundamental microscopic processes occurring on the surface and in the bulk of the film. The three-dimensional MC model retains the entire lattice structure, tracks

the bond dispersion across the crystal lattice, and the surface reactions and adatom movement are a function of the bond dispersion across the surface. Indirectly, surface sites at step risers are high probability growth sites when compared to surface sites at step terraces. Surface sites at step risers have more than one bond available for growth whereas surface sites on the terrace have only one.

The crystal lattice can be zincblende, wurzite, or a mixture of face centered cubic (fcc) and hexagonal close packed (hcp) stacking of close-packed planes. Allowing combinations of cubic and hexagonal stacking enables the crystal lattice in the MC model to represent polytypes found in SiC.

The factors which effect bond dispersion and site occupancy in the model are growth plane orientation, polytype of crystal lattice, and surface roughness. An adatom will have a larger diffusion length on a flat (111) plane where it will have one nearest neighbor and a lower reactivity versus a flat (100) plane where the adatom will have two nearest neighbors and a higher reactivity with the surface. Polytypes differ from each other in their stacking sequence. Cubic and hexagonal stacking of adjacent bilayers (BLs) leads to different atom positions and different bond dispersion at the steps between the BL especially at step riser sites. Finally, surface roughness affects near atom occupancy and bond availability which can impact adatom surface movement. A rougher surface will have more surface sites for an adatom to hop to than a smooth surface. However, a rougher surface will have more surface sites with greater than one available bond which may reduce the diffusion length of the adatom.

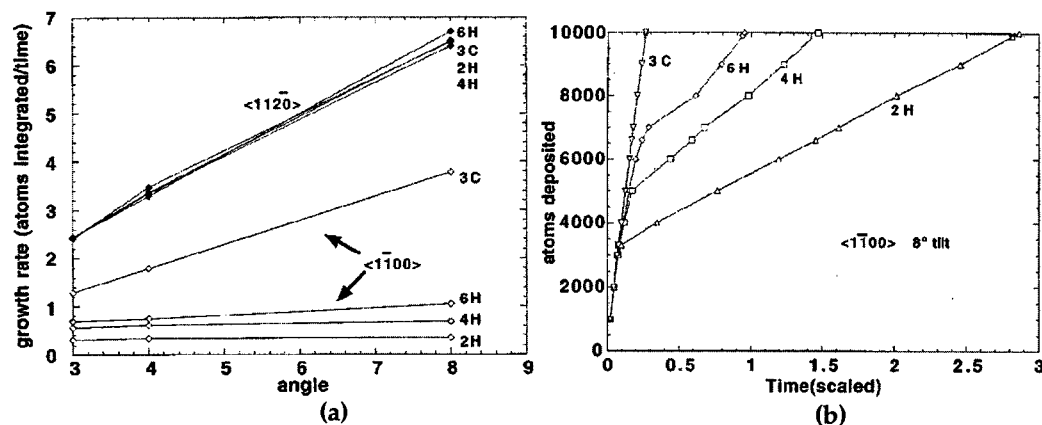


Figure 2 (a) Relative growth rate versus off-axis angle. Growth is faster for step flow growth in  $\langle 1120 \rangle$  directions than  $\langle 1100 \rangle$  directions. (b) Number of atoms deposited on a surface tilted  $8^\circ$  from the  $[0001]$  axis in a  $\langle 1100 \rangle$  direction versus time for different SiC polytypes.

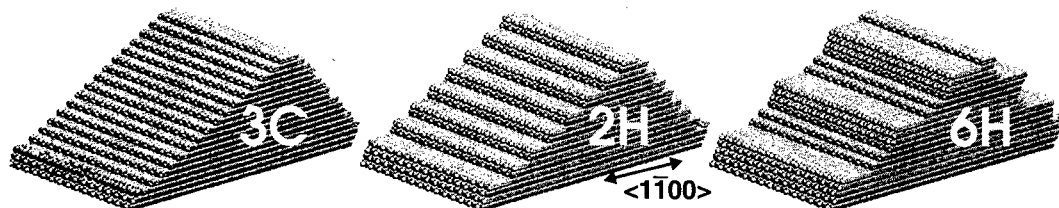


Figure 3 Step bunching resulting from step flow in  $\langle 1100 \rangle$  directions for different polytypes.

### III. TRIANGULAR AND HEXAGONAL MORPHOLOGIES

Results of the MC model for 3C, 6H, and 2H-SiC(111) growth on a circular mesa four BLs high on a  $60 \times 60 \times 30$  lattice mesh are shown in Fig. 1. The growth precursors are  $\text{CH}_4$  and  $\text{SiH}_4$ , and the ratio of  $\text{CH}_4$  to  $\text{SiH}_4$  flux to the surface is one. Only Si-C bonds are allowed in the lattice. The simulation ended after 2999 atoms integrated into the crystal lattice. The results reflect experimental observations [3]. The model predicts the triangular morphology typical of  $\beta$ -SiC (3C) and the hexagonal morphology indicative of  $\alpha$ -SiC (2H, 6H).

Triangular islands are a result of faceting at (111) planes. The hexagonal morphology seen in  $\alpha$ -SiC is a consequence of the hexagonal stacking content in the bilayer stacking sequence.

For a zincblende or wurzite lattice when a BL grows on the (111) plane in a surface kinetic dominated growth process the BL forms a triangle. At the edges of the triangle each atom at the step riser has only a single available bond assuming a perfect crystal lattice (i.e., no surface reconstruction). The triangular morphology results for both hexagonal and cubic stacking of BLs.

The orientation of the atomic hexagonal rings formed by the atoms on the (111) plane can be reversed (rotated  $180^\circ$ ) depending on the type of stacking between BLs. Two adjacent BLs with cubic stacking preserve the orientation of the atomic hexagonal ring. Two adjacent BLs with hexagonal stacking reverse the orientation of the atomic hexagonal ring. Reversing the atomic hexagonal ring also reverses the orientation of a triangular island forming on the surface. The consequence of having triangular islands of BLs of reversing orientations growing on each other is the formation of hexagonal morphologies. The hexagon forms since a triangular island growing on and rotated  $180^\circ$  with respect to a triangular island under it will have its corners "clipped" off. That is, if the direction of growth of a step is perpendicular to one of the sides of a triangular structure formed under it, the growing step will slow at the step forming the triangle edge.

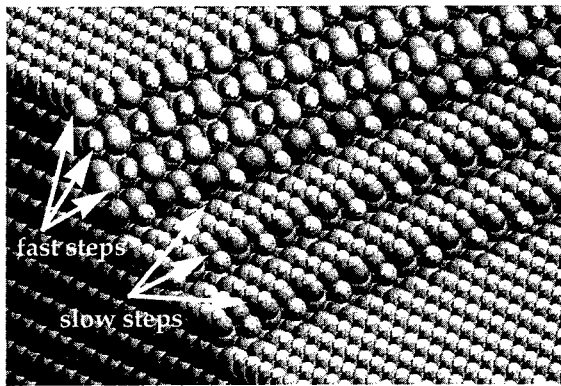


Figure 4 Atomic configuration of a step bunch on 6H-SiC(0001) with a C face.

#### IV. GROWTH OFF-AXIS FROM VICINAL PLANE

Much of the SiC growth is done off-axis to preserve the stacking order of the BLs thereby preserving the polytype of the wafer. For example, growth on a 6H-SiC(111) wafer off-axis 1 to 3 degrees results in 6H-SiC film growth [4,5], but growth on-axis yields film of mixed polytype with twinned 3C-SiC the typical result [3].

The MC model was used to explore step-flow growth behavior on an off-axis {0001} vicinal plane. Growth was started initially on a staircase structure (Fig. 3) with a lattice mesh of  $330 \times 30 \times 30$  sites. Due to periodic boundary conditions for adatom movement a stair case descends from either side of a center point. Results of the model for relative growth rate versus off-axis angle for two directions and four different polytypes are shown in Fig. 2(a). The model predicts (i) an increase in the growth rate with increasing off-axis angle, (ii) polytypes of SiC(111) off-axis in  $\langle 11\bar{2}0 \rangle$  directions achieves faster growth rates than  $\langle 1\bar{1}00 \rangle$  directions, and (iii) growth rate for a surface off-axis in a  $\langle 11\bar{2}0 \rangle$  direction is insensitive to polytype but the growth rate is sensitive to polytype for a surface off-axis in a  $\langle 1\bar{1}00 \rangle$  direction.

Model predictions (i) and (ii) agree with experiment. As observed experimentally [3], increasing the tilt off-axis toward  $[11\bar{2}0]$  from a {0001} vicinal plane increases the growth rate if the growth mechanism is dominated by atom incorporation at step riser kink sites. In the MC model, increasing the tilt angle increases the ratio of step riser sites to terrace sites. Growth is more rapid on a step at a riser site than a terrace site. The increased ratio of high growth sites to low growth sites increases the growth rate.

Experimentally Kimoto, et. al. have shown that lateral growth rate (growth across a terrace from a step) on 6H-SiC is about three orders of magnitude higher than the vertical growth rate at temperatures higher than  $1400^\circ\text{C}$ , although the lateral growth rate decreases at low temperatures. Also, the lateral growth rate is



observed to be anisotropic on 6H-SiC with the fastest growth direction on a {0001} surface in the  $[11\bar{2}0]$  direction and the slowest in the  $[1\bar{1}00]$  direction. In the MC model the characteristic triangular growth morphology is the main reason for the varying growth rates with off-axis direction seen in Fig. 2(a). Steps at a characteristic triangular edge have only one bond available for growth per atom at the step and as a consequence do not grow as rapidly as steps oriented in other directions. Any step-flow growth in a  $\langle 1\bar{1}00 \rangle$  equivalent direction is either toward a "triangle point" or a "triangle edge". In contrast any step-flow growth in a  $\langle 11\bar{2}0 \rangle$  characteristic direction will form steps that are not at a triangle edge.

Step bunching explains why the MC model predicts slower step flow growth in the  $\langle 1\bar{1}00 \rangle$  directions for  $\alpha$ -SiC (2H,4H,6H) than 3C-SiC. For step flow growth in  $\langle 1\bar{1}00 \rangle$  directions there are "fast" flowing steps which flow toward a characteristic triangle point, and "slow" flowing steps which flow toward a characteristic triangle edge. If a fast flowing step encounters a slow flowing step under it the growth rate will be limited by the growth of the slower flowing step. For 3C-SiC the orientation of the triangle never reverses so all the steps flowing in one direction are slowed while all the steps flowing in the opposite direction continue to flow. For  $\alpha$ -SiC however the orientation of the characteristic triangle reverses periodically in the stacking order. As a result a "fast" flowing step will encounter a step under it which has a slower growth rate.

Fig. 2(b) is a plot of the number of atoms deposited on a surface off-axis  $8^\circ$  from a {0001} vicinal plane in a  $\langle 1\bar{1}00 \rangle$  direction versus time for different polytypes. The growth rate transition seen in Fig. 2(b) (2H, 4H, 6H) are due to two growth regimes. The first growth rate is due to all steps on the surface flowing, but primarily the fast flowing steps. The second slower growth rate is due to step bunching as fast flowing steps bunch up at slow moving steps and growth is limited by growth of slow moving steps.

The step bunching seen in Fig. 3 is due to hexagonal BL stacking content causing the triangular morphology characteristic of 2D growth to change orientation. The bunching is periodic with the repeated pattern polytype dependent. For 2H-SiC or (11)-SiC in Zhdanow notation (in Zhdanow notation the two numbers in the parenthesis indicate the BL period of the two characteristic triangle orientations) the alternating fast-slow step flow pattern results in all steps bunched two BLs high. For 6H-SiC (or (33)-SiC) the fast-fast-fast-slow-slow step flow pattern results in the three fast flowing steps bunching up at the first slow step and the other two slow steps isolated from the 4 BL high step bunch. 3C-SiC shows no step bunching due to hexagonal stacking since all of its BL stacking is cubic. A closer look at a step bunch for 6H-SiC is shown in Fig. 4. The chemical makeup along the step bunch is not the same for each BL step. The variation in the chemical makeup of the bunch will have consequences on the chemical reactivity of Si and C atoms at the step riser.

## V. CONCLUDING REMARKS

A dangling bond formulation of a MC model was applied to the growth of 3C, 2H, 4H, and 6H-SiC(111). The model predicts the (111) plane faceting seen in  $\beta$ -SiC (3C) and the hexagonal structures seen when growing on  $\alpha$ -SiC (2H,4H,6H). The sensitivity of the reaction probability to the number of available bonds at a particular lattice site allows the model to predict the triangular and hexagonal morphologies. The model predicts faster step flow growth rates for  $\langle 11\bar{2}0 \rangle$  directions compared to  $\langle 1\bar{1}00 \rangle$  directions and the variability of the step flow growth rate between  $\langle 1\bar{1}00 \rangle$  directions. The model illustrates a possible step bunching mechanism. The hexagonal stacking content found in  $\alpha$ -SiC reverses the flow direction of "fast" and "slow" moving steps in  $\langle 1\bar{1}00 \rangle$  directions causing faster flowing steps to bunch up at slower moving steps.

**ACKNOWLEDGMENTS:** This work was supported by the NASA Lewis Research Center (NAS3-97062).

## REFERENCES

- [1] S. Nakashima, H. Matsunami, S. Yoshida, and H. Harima, eds., *Inst. Phys. Conf. Ser. No. 142* (Institute of Physics Publishing, Philadelphia), Chapter 4 (1996)
- [2] P. Stout, *J. Vac. Sci. Technol. A* 16(6), pp. 3314-3327 (1998).
- [3] T. Kimoto and H. Matsunami, *J. Appl. Phys.* 76 (11), pp. 7322-7327 (1994).
- [4] J. A. Powell, D.J. Larkin, L.G. Matus, W.J. Choyke, and J.L. Bradshaw, L. Henderson, M. Yoganathan, J. Yang, N.P. Pirouz, *Appl. Phys. Lett.* 56 15, pp. 1442-1444, (1990).
- [5] L. B. Rowland, R. S. Kern, S. Tanaka, and R. F. Davis, *J. Mater. Res.* 8 11 pp. 2753-2756 (1993).

Correspondence: [www.cfdrc.com](http://www.cfdrc.com), 256 726 4800, 256 726 4806 (fax)

## Mechanism of Various Defects Formation in Epitaxial Layer Prepared by Sublimation Epitaxy

T. Furusho<sup>1</sup>, K. Matsumoto<sup>1</sup>, H. Harima<sup>2</sup> and S. Nishino<sup>1</sup>

<sup>1</sup> Kyoto Institute of Technology, Matsugasaki, Skayo-ku, Kyoto, 606-8585, Japan

<sup>2</sup> Department of Applied Physics, Osaka University, Yamadagaoka 2-1, Suita,  
Osaka 565-0871, Japan

**Keywords:** Micropipe, Raman Spectroscopy, Small Angle Grain Boundaries, Sublimation Epitaxy, Sublimation Method, X-Ray Diffraction

### abstract

SiC epi-layer was grown by CST(Close space technique). The feature of CST is that crystal growth is carried out in quasi-equilibrium. Epi-layers were characterized by X-Ray diffraction, Raman spectroscopy and KOH etching. The crystal quality of the epi-layers was very high. After KOH etching, it was determined that micropipes in the epi-layer were caused by the substrate. The epi-layers were characterized by Raman spectroscopy. Though p-type source material was used to grow the epi-layers, the epi-layer was n-type.

### Introduction

SiC is suitable for high power devices because of its wide-bandgap and high thermal conductivity. To make a SiC device having high breakdown voltage, thick epitaxial layers are needed. In conventional CVD method ( in which silane and propane are normally used), epitaxial growth rate is about 3  $\mu$ m/h. From an industrial point of view, rapidly grown thick epi-layers are required. Sublimation epitaxy(CST) has been demonstrated to grow thick epi-layers at higher growth rate [1-3]. Quality of the epi-layer was influenced significantly by pressure during growth and polarity of the substrate. In this report, we focus on the formation mechanism of defects in the epi-layer.

### Experiment

3C-SiC polycrystalline plates of semiconductor grade (MUHSIC:Admap Ltd.) were used as SiC source material while 4H-SiC(0001) substrates of commercially obtained wafers inclined 8° off towards <11 $\bar{2}$ 0> were used as substrates. Size of the substrate was 5mm x 5mm. In order to have an accurate spacer height between source and substrate, a graphite spacer with a square opening size of 4 mm x 4 mm was used. The source and substrate were set in a graphite crucible. The crucible was thermally shielded by graphite foam. A vertical quartz tube cooled by an air-fan was used as the reaction tube. The experiments were carried out in Ar atmosphere. The crucible in the reaction tube was heated by an rf generator at a frequency of about 45kHz. Typical growth conditions were as follows: growth temperature of source material (T<sub>g</sub>) 1900-2100°C, temperature gradient (grad T) 3.7°C/mm, growth pressure (P) 0.3-100Torr, distance ( $\Delta$ X) between source and substrate 1.5 mm. The surface morphology of the epi-layer was observed by optical microscopy (OM) in the Nomarsky mode. Crystallinity and purity of the epi-layer were characterized by X-ray diffraction and Raman spectroscopy.

### Result

Attention was paid to the temperature gradient to obtain a high growth rate. In order to get a high temperature gradient, that is to say, to prevent an eddy current around the crucible wall, slits were made in the upper part of crucible. A temperature gradient of about 8°C/mm and a high growth

rate were obtained when this type of crucible was used. But the surface morphology of epi-layers grown in the crucible with slits was rougher than that grown in the crucible with no slits. This was probably caused by high growth rate and high temperature gradient. In the range of the growth pressure in this experiment, epitaxial growth is carried out in the diffusion transfer limited stage. If the growth pressure is above about 1Torr, epitaxial growth is carried out in the diffusion transfer limited stage. If the pressure is below 1Torr, epitaxial growth is carried out in the surface reaction limited stage[4]. The substrate temperature used in the crucible with slits was the same as that used in the case of the crucible without slits. But the source temperature was different in each case. As the temperature is higher, the pressure of molecules is higher and supersaturation is higher, too. Therefore the reaction space is in a stage of non-equilibrium and the crystal quality of the epi-layer decrease. Since CST crystal growth is supposed to be carried out in quasi-equilibrium, the use of non-equilibrium affects the surface morphology. Therefore, other ways need to be developed to get high growth rate and high crystal quality.

Fig.1 shows the dependence on FWHM of X-ray diffraction of the growth pressure. FWHM of Si (111) face is 0.041 degrees in our X-ray diffraction apparatus. And this width is the minimum width capable of analysis by our X-ray diffraction apparatus. The number on the figure between the substrate FWHM and the epi-layer FWHM is the difference between the two numbers. As the growth pressure is lower, the difference is larger. When the growth pressure is 10 and  $3.0 \times 10^{-6}$  Torr, the difference is 0.012 degrees and this is the largest. Therefore it may be concluded that as growth pressure is reduced, the crystal quality of the epi-layer is better. Besides, it is observed that the FWHM of the epi-layer depends on that of the substrate. Therefore to get a high quality epi-layer, a high quality substrate is needed. At a growth pressure of 10Torr, the FWHM of epi-layer is 0.042 degrees which is almost the same of that of Si. So the crystal quality of this epi-layer is very high.

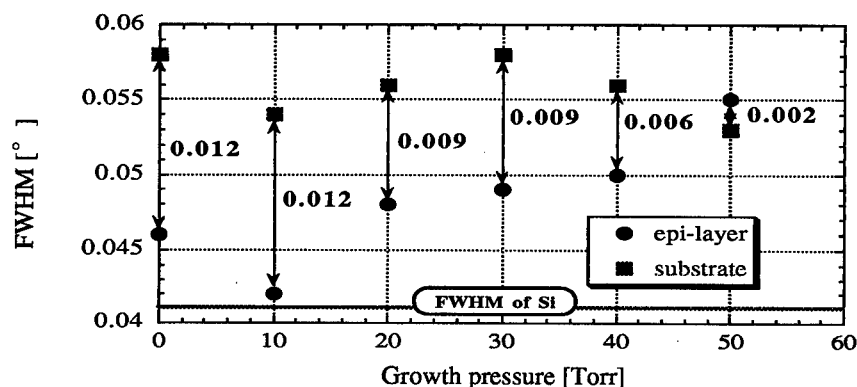


Fig.1 FWHM of X-Ray diffraction dependence on growth pressure

Fig.2 is the picture of the surface morphology of the boundary between the epi-layer and the substrate. This picture was taken after KOH etching. The etching time was four minutes and the temperature of KOH was 500°C. It can be observed that there are two types of etch pits. Large etch pits are caused by micropipes and small ones are caused by the crystal dislocations. A number of etch pits continue from the substrate to the epi-layer in one line. These etch pit lines are caused by small angle grain boundaries in the substrate. If there is a small angle boundary in a crystal, there are many crystal dislocation and these are continuous. So when the sample which has the small angle boundary is etched, many etch pits appear continuously like one line. Because the etch pit line continues from the substrate to the epi-layer, we believe that the etch pit line on the epi-layer are caused by small angle grain boundaries in the substrate. Therefore a high quality substrate which has no crystal dislocations is needed to obtain a high quality epi-layers.

Fig.3 is the Raman spectra of the epi-layer grown using p-type source. Usually, polycrystalline 3C-SiC plates was used to grow the n-type epi-layer. To grow the p-type epi-layer, a p-type single crystal 6H-SiC wafer was used. This wafer was divided into 6x6mm size and was used as source material. The growth temperature and the pressure was the same of the n-type growth. The growth temperature of source material was about 2000°C and pressure was 0.3-50 Torr. Fig.3(a) shows TA Raman spectra of the epi-layer grown by the p-type source material and the p-type 4H-SiC. The doping level of this p-type wafer source was  $1.1 \times 10^{19}/\text{cm}^3$ . The feature of the p-type Raman spectrum in TA mode is that the base line lifts a bit in comparison with that of n-type.[5][6]. In LO mode the spectrum becomes like a delta function and if the carrier concentration varies, the spectrum hardly shifts right or left. The only variation in the LO spectrum is the value of the FWHM in changing with carrier concentration[5][6]. In Fig. 3, the Raman spectrum of the p-type wafer is shown as a reference for a p-type spectrum. In comparing the spectrum of the p-type wafer and that of epi-layer grown by p-type source material, it can be observed that the epi-layer does not become p-type. Carrier concentration of this samples was  $3.3 \times 10^{17}/\text{cm}^3$  and  $2.4 \times 10^{17}/\text{cm}^3$  on Raman measurement. Assuming that these samples were n-type, we made Schottky diodes on these samples. From CV measurement of these, the donor density was  $4.7 \times 10^{18}/\text{cm}^3$  and  $2.3 \times 10^{18}/\text{cm}^3$ . Therefore the acceptor density must be  $4 \times 10^{18}/\text{cm}^3$  and  $2 \times 10^{18}/\text{cm}^3$  and to make a p-type epi-layer, the donor concentration(that is nitrogen) must be reduced.

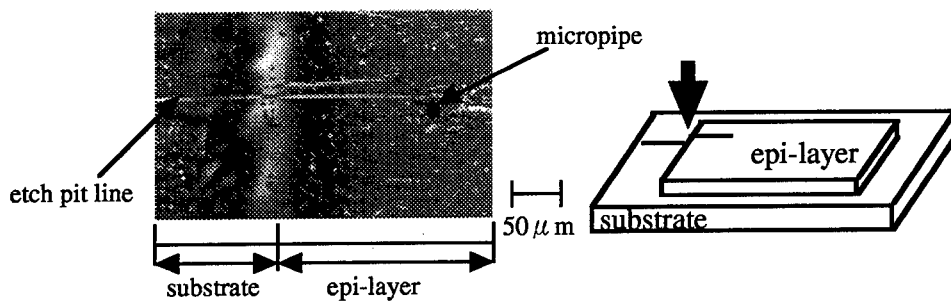


Fig.2 Surface morphology of the epi-layer after KOH etching

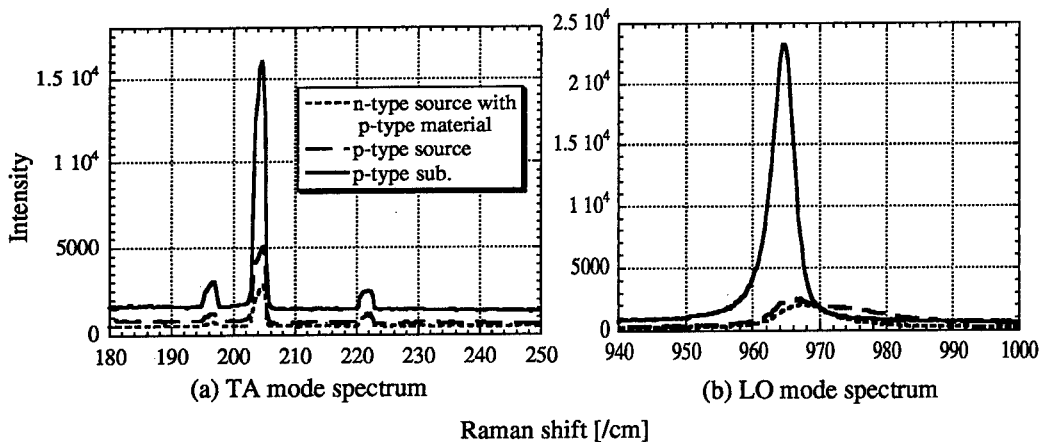


Fig.3 Raman spectra of the epi-layer using p-type source material

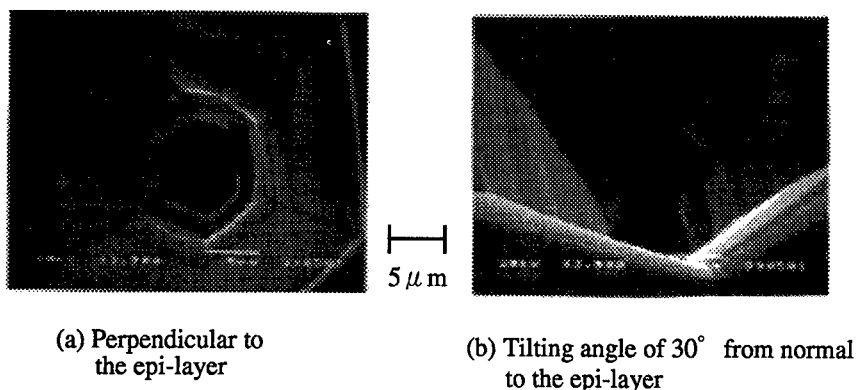


Fig.4 SEM image of micropipe defect

To study the defect distribution between the substrate and epi-layer, we observed micropipe defects that appeared on epi-layer after etching with molten KOH. The micropipe defects were observed by SEM and two SEM image are shown in Fig.4. Fig.4(a) is an image which was taken perpendicular to the epi-layer and Fig.4(b) is an image which was taken at a tilting angle of 30° from normal to the epi-layer. Concentric hexagonal shapes are observed in this micropipe. Several steps are also seen in this micropipe. By simple calculation, the height of this micropipe defect was 46.2  $\mu\text{m}$ . The thickness of this epi-layer was 14.7  $\mu\text{m}$ , so it can be seen that the micropipe defect originated from the substrate.

### Conclusions

SiC epi-layer grown by CST was characterized by XRD, Raman spectroscopy, KOH etching, and SEM. To make a high quality (defect free) epi-layer, micropipe free, low defect density substrates are needed. And if the quality of the substrate is good, high quality epi-layers like Si are obtained.

This work was partially supported by a Grant-in-Aid for Science Research No.0945001 from the Ministry of Education, Science and Culture, Japan and FED, NEDO Japan, and Ion Engineering Institute (Osaka, Japan).

### References

- [1] T.Yoshida, Y.Nishio, S.K.Lilov and S.Nishino, Silicon Carbide, III-Nitrides and Related Materials, part-1 (Trans Tech Publications) (1997), 155.
- [2] S.Nishino, T.Yoshida, K.Matsumoto, S.K.Lilov and Y.Nishio. Mat. Res. Soc.Symp.Proc.vol.483, (1988) 307
- [3] S.Nishino, K.Matsumoto, Y.Chen and Y.Nishio. Materials Science and Engineering B61-62 (1999) 121
- [4] S.K.Lilov, Journal of Crystal Growth 46, (1979) pp269-273
- [5] H.Harima, T.Hosoda and S.Nakashima, Abstract on 1999 International Conference on SiC and Related Materials, No.113 p. 603
- [6] S.Nakashima and H.Harima, Proceedings of 15th International Conference on Raman Spectroscopy Pittsburgh, USA (1996) p932

## Investigation of 3C-SiC Epitaxial Layers Grown by Sublimation Epitaxy

D.V. Davydov<sup>1</sup>, A.A. Lebedev<sup>1</sup>, A.S. Tregubova<sup>1</sup>, V.V. Kozlovski<sup>2</sup>,  
A.N. Kuznetsov<sup>1</sup> and E.V. Bogdanova<sup>1</sup>

<sup>1</sup> A.F. Ioffe Physico-Technical Institute, Russian Academy of Sciences,  
Polytekhnicheskaya st. 26, RU-194021 St.-Petersburg, Russia

<sup>2</sup> St. Petersburg State Technical University, Polytekhnicheskaya 29,  
RU-194251 St. Petersburg, Russia

**Keywords:** Carbon Vacancy, Deep Centers, DLTS, Proton Irradiation, Sublimation Heteropolytype Epitaxy, X-Ray Topography

**Abstract.** The objective of the present work was to prepare 3C-SiC epilayers on base of 6H-SiC substrate and to study epilayer's parameters. Heteroepitaxy was carried out using sublimation epitaxy (SE) in an open system. The presence of 3C-SiC layer in the prepared structures was confirmed by X-ray diffraction. Parameters of Schottky diodes prepared on base of this epilayers were investigated by capacitance-voltage characteristics and DLTS. Also it was investigated influence of proton irradiation and annealing on epilayers Nd-Na value and deep centres concentration.

**Introduction.** Owing to its high carrier mobility, cubic silicon carbide (3C-SiC) is object of particular commercial interest. At the same time, 3C substrates are practically not produced at all. Therefore, epitaxial 3C-SiC layers are commonly grown by heteroepitaxy on silicon substrates [1, 2].

**Growth condition.** In the present work an epitaxial 3C-SiC layer was grown by sublimation heteroepitaxy in an open growth system. The growth was conducted on the (0001)Si face of a 6H-SiC substrate produced by the Lely method. No impurities were introduced purposefully in the process of growth. The growth conditions leading to 6H - 3C transformation of polytype in sublimation epitaxy were studied in [3,4].

**Experimental.** X-ray topography demonstrated that the structural perfection of the layer is determined by the twin structure. Figure 1 presents a topograph of the 4-5  $\mu\text{m}$  thick 3C-SiC layer studied. Twins of two types with a rotation of  $180^\circ$  appear in the topography as regions with black and white contrast. As can be seen from fig.1, epitaxial layer contains twins with high area of about  $5\text{mm}^2$ .

Schottky diodes 300  $\mu\text{m}$  in diameter were fabricated on the layer by magnetron sputtering of nickel. A study of their capacitance-voltage characteristics demonstrated a uniform doping of the layer to a depth of 1  $\mu\text{m}$ . The net donor concentration in the layer under study was  $\text{Nd-Na} = 2 \cdot 10^{16} \text{ cm}^{-3}$ .

The parameters of deep centres were determined by capacitance (C-DLTS) and current (i-DLTS) spectroscopes. DLTS spectra were studied in temperature range 85-350 K. Applied reverse voltage during measurement was 6 V. For recharging of the traps, applied voltage was periodically decreased down to zero. Duration of the recharging pulses was 5 ms. A study of DLTS spectra revealed a single deep centre in the upper half of the forbidden gap with ionisation energy  $E_c - 0.62$  eV. The concentration of this centre was  $N_t = 9.8 \cdot 10^{14} \text{ cm}^{-3}$ .

**Irradiation.** Also it were investigated parameters of deep levels arisen in 3C-SiC layers after proton irradiation. Irradiation was made at cyclotron MGC-20. Proton energy was 8 MeV, irradiation dose  $1 \cdot 10^{14} \text{ cm}^{-2}$ . On Fig.2 it is shown C-U characteristics before and after irradiation and after



Fig.1. X-ray topograph of the 3C-SiC epilayer (Bragg's reflection  $(311)_{3C}$ ,  $\text{CuK}_\alpha$  - radiation).

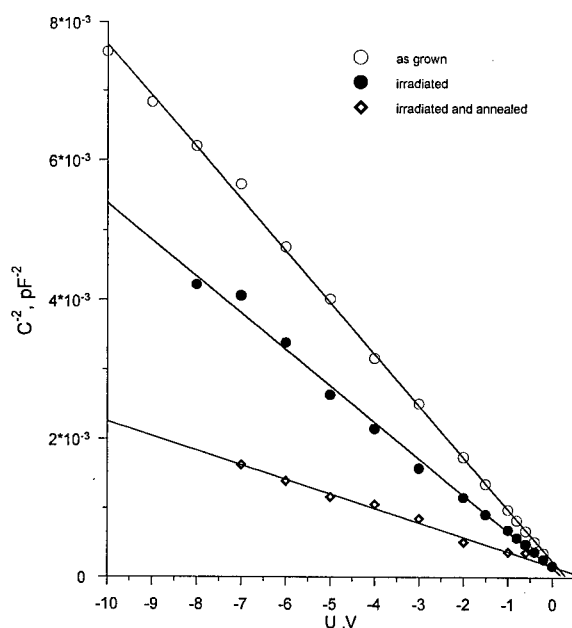


Fig.2. C-U characteristics of the Schottky diodes fabricated on the investigated layer

annealing at 650 K. After irradiation we did not see any new deep centres above presented in epilayer before irradiation. Nd-Na value and concentration of deep centre are presented in the Table.

As shown in table, irradiation and annealing leads to increasing of the Nd-Na value, and this increasing was on one order of magnitude more than increasing of concentration of detected deep level. This, possible, shows that the irradiation (above increasing of detected deep centre concentration) leads to arising new deep centres of donor and acceptor nature, which we can not detect by our DLTS measurements. These centres

can be in upper half of forbidden gap, if they recharge not in temperature range

85-350 K, or in lower half of forbidden gap. In this case difference in concentrations of irradiation induced donor and acceptor centres determined increasing of Nd-Na value. Increasing of Nd-Na value after annealing can take place, if new acceptor centres annealed out and concentration of donor-like centres did not strongly change.

Table. Concentration of impurities in investigated 3C-SiC epilayers.

Sample	Nd-Na, cm <sup>-3</sup>	Deep centre concentration, cm <sup>-3</sup>
as grown	$2 \cdot 10^{16}$	$9.8 \cdot 10^{14}$
irradiated	$2.8 \cdot 10^{16}$	$5 \cdot 10^{15}$
irradiated and annealed at 650 K	$7.14 \cdot 10^{16}$	$5 \cdot 10^{15}$

**Discussion.** An Arrhenius temperature dependence is shown in Fig. 3 for the centre discovered in this work. The same figure presents Arrhenius dependencies for the centres T3 [1] and SCE2 [2], previously found in layers grown by gas-phase epitaxy on silicon substrates. It can be seen that all the three curves have close parameters and are presumably related to a single centre. Possibly, this centre is a carbon vacancy, since one of the factors governing the transformation of the polytype is elevated pressure of silicon vapour in the growth cell [5]. Moreover, the ionisation energy of the discovered centre is the closest to the ionisation energy of the carbon vacancy calculated theoretically in [6].

Also previously it was found that the Si/C ratio is not the same in different polytypes - it increases with increasing degree of hexagonality, being equal to 1.046, 1.022, and 1.001 for 3C, 6H, and 4H, respectively [7]. Data on diffusion and solubility of impurities in different SiC polytypes [5] also indicate that concentrations of Vc vacancies in these polytypes are different and its maximum concentration is in 3C SiC. Theoretical analysis of this experimental data is given in [8]. Our data on proton irradiation also confirm that this centre may be intrinsic defect.

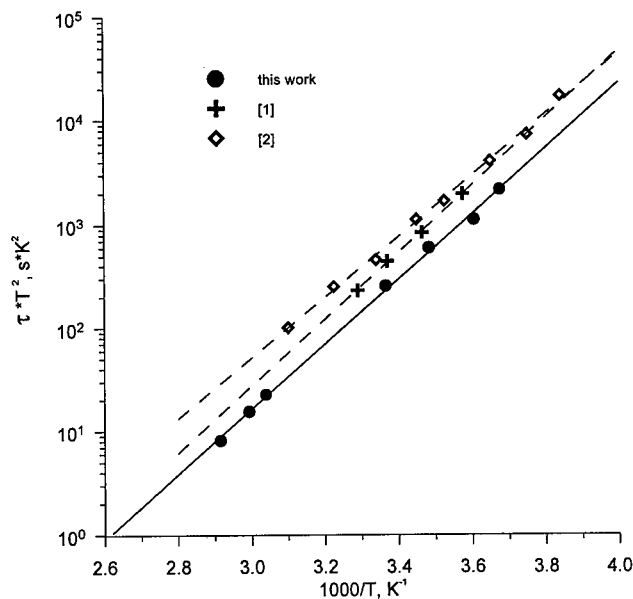


Fig.3. Arrhenius plots for the trap observed in this work



**Summary.** The experiments we carried out indicate that by sublimation epitaxy it is possible to obtain a low-doped n-type 3C-SiC layer on 6H-SiC substrate. Schottky diodes prepared on base of this epilayers has enough good electrical characteristics. DLTS measurements indicate one deep centre, concentration of which increased after proton irradiation. It is possible to connect this level with intrinsic defect, i.e. carbon vacancy. So, it seems reasonable to suggest that after optimisation of the technological conditions used, it would be possible to produce, because of high electron mobility in 3C-SiC, small size microwave devices (e.g. MESFET) on base of such epilayers.

**References.**

- [1] K. Zekentes, M. Kayambaki, and G. Constantinidis, Appl. Phys. Lett. **66**(1995), p.3015.
- [2] P. Zhou, M. G. Spenser, G. L. Harris, and K. Fekade, Appl. Phys. Lett. **50** (1987) , p.1384.
- [3] A. N. Andreev, A. S. Tregubova, M. P. Scheglov, A. L. Syrkin, V. E. Chelnokov, Mater. Sci. Eng. **B 46** (1997), p.141.
- [4] A. A. Lebedev, N. S. Savkina, A. M. Strel'chuk, A. S. Tregubova, M. P. Scheglov, Mater. Sci. Eng. **B 46** (1997), p.168.
- [5] Yu.A.Vodakov, G.A.Lomakina, E.N.Mokhov, Sov.Phys.Solid State  $\Phi$ TT **24** (1982), p.780.
- [6] L. Wenchang, Z. Kaiming, and X. Xibe, J. Phys. Condens. Matter **5** (1993), p.891.
- [7] N.N.Sorokin, Yu.M.Tairov, V.F.Tsvetkov, M.A.Chernov, Sov. Phys.Crystallogr. **28** (1983), p.539.
- [8] A.A.Lebedev, Semiconductors **33** (1999), p.769.

## Growth of SiC and GaN on Porous Buffer Layers

M. Mynbaeva<sup>1</sup>, N. Savkina<sup>1</sup>, A. Tregubova<sup>1</sup>, M. Scheglov<sup>1</sup>, A. Lebedev<sup>1</sup>,  
A. Zubrilov<sup>1</sup>, A. Titkov<sup>1</sup>, A. Kryganovski<sup>1</sup>, K. Mynbaev<sup>1</sup>, N. Seredova<sup>2</sup>,  
D. Tsvetkov<sup>2</sup>, S. Stepanov<sup>2</sup>, A. Cherenkov<sup>2</sup>, I. Kotousova<sup>2</sup>  
and V.A. Dimitriev<sup>1,3</sup>

<sup>1</sup> Ioffe Institute, RU-194021 St.-Petersburg, Russia

<sup>2</sup> Crystal Growth Research Center, RU-124021 St. Petersburg, Russia

<sup>3</sup> TDI, Inc., 8660 Dakota Drive, Gaithersburg, MD 20877, USA

**Keywords:** Defect Density, Epitaxial Growth, Porous Substrate, Stress Reduction

### Abstract

In this paper, we describe a novel technique, which shows a high potential for defect densities and stress reduction in SiC and GaN, both epitaxial and bulk. This technique is based on nanometer scale epitaxial lateral overgrowth (NELOG) method, which employs porous substrate materials. This technique does not require any mask and may be easily scaled for large area substrates.

SiC layers were grown on porous SiC by sublimation sandwich method. Porous SiC substrates were formed by surface anodization of SiC commercial wafers.

GaN layers were overgrown by hydride vapour phase epitaxy on porous GaN. Porous GaN was formed by anodization of single crystal GaN layers grown previously on SiC substrates.

Epitaxial layers grown on porous buffer layers were investigated in terms of crystal structure, residual stress, and optical properties.

### Introduction

Defect density and stress reduction in bulk and epitaxial materials is the main issue of SiC and GaN technology. Recently, significant dislocation density reduction has been achieved in GaN materials using epitaxial lateral overgrowth (ELOG) approach [1,2]. Improvement of device performance by ELOG has been demonstrated for lasers and transistors. However, the ELOG method allows one to reduce defect density in local areas only. The method requires precise mask alignment and use of advanced lithography techniques. Mask material may serve as a source of GaN contamination during the epitaxial overgrowth. In this paper, we describe a novel epitaxial overgrowth technique, which does not require any mask. The idea of the method is to overgrow pores formed on the surface and in the bulk of an initial substrate. Usually, porous, formed in semiconductor materials, have size ranging from 10 to 50 nm. The proposed technique deals with lateral overgrowth of these pores, so we call this technique "nanometer scale epitaxial lateral overgrowth" or NELOG method. The method can be easily scaled for large area substrates. We demonstrate the method for both SiC and GaN.

### Experimental procedure and results

SiC epitaxial layers were grown on porous SiC by sublimation sandwich method [3]. Porous SiC substrates were formed by surface anodization of 6H-SiC commercial wafers. The anodization was done on polished (0001)Si face 6H-SiC substrate. The anodization procedure was similar to the process, which has been recently developed for porous GaN [4]. Thicknesses of porous SiC layers ranged from 1 to 10 microns. Pore size was in nanometer scale. Interface between porous SiC and non-porous SiC was abrupt. Typical surface morphology of porous SiC measured by atomic force microscope (AFM) is shown in Fig. 1a.

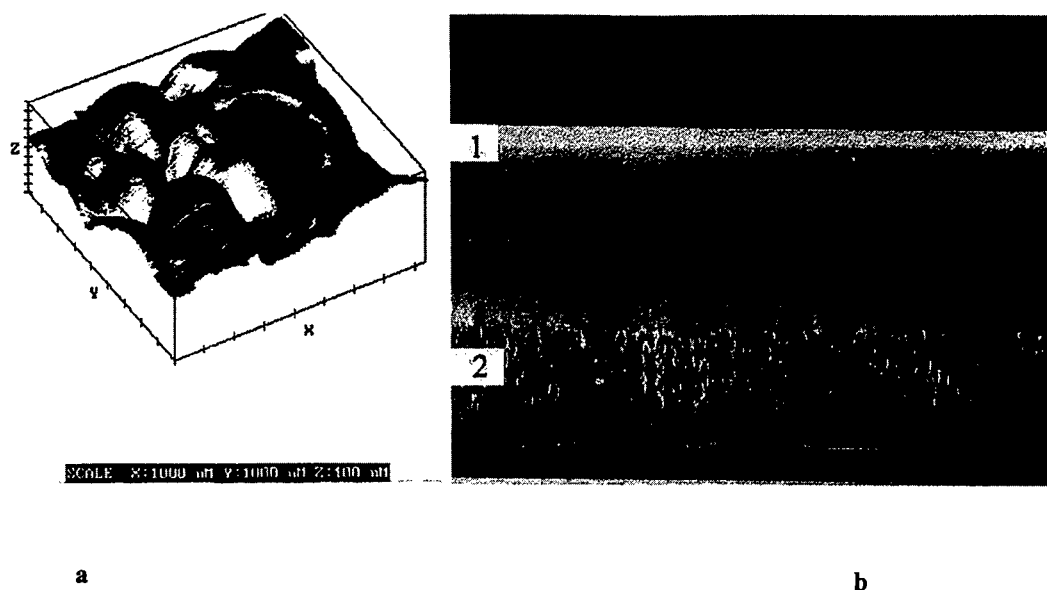


Figure 1. Scanning AFM image of porous surface (a) and scanning electron microscopy (SEM) image (b) of cleaved surface of 12  $\mu\text{m}$  thick SiC layer (1) grown on porous SiC layer (2).

Sublimation epitaxial growth of silicon carbide on porous SiC was done at 2000°C. Growth procedure was described in details elsewhere [5]. Growth rate was 10-20  $\mu\text{m/hr}$ . Thickness of the epitaxial layers was about 11-13 microns (Fig. 1b).

The surface of overgrown material was uniform and flat without any traces of porous structure (Fig. 2). The PL measurements showed that the grown material is of the same polytype as the initial 6H-SiC substrate. The position of exciton related peak was characteristic for 6H-SiC. Intensity of broad PL band at 550 nm was much lower than that for SiC layers grown on usual SiC substrate indicating a reduction of deep level concentration in SiC grown on porous substrate. X-ray measurements detected an improvement of crystal structure of SiC layer grown on porous material. The full width at a half maximum of x-ray rocking curve for (00012) reflection for  $\omega$ -2 $\Theta$ -scan ranged from 10 to 15 arc sec and from 8 to 12 arc sec for SiC layers grown on standard and porous substrates, respectively. X-ray topography indicated that size of defect-related stressed areas in SiC layer grown on porous SiC is smaller than that for initial substrate. Density of defects in SiC layer grown on porous buffer was estimated to be a few times less than that for SiC layer grown on the same substrate without porous buffer layer. X-ray topography showed that in some areas of the sample, the dislocation density was reduced from the  $10^4 \text{ cm}^{-2}$  to low  $10^3 \text{ cm}^{-2}$  range. The reduction of defect-related stress leads to the narrowing of the x-ray diffraction rocking curves.

GaN layers were overgrown by hydride vapour phase epitaxy (HVPE) on porous GaN. Porous GaN material was formed by anodization of single crystal GaN layers, grown previously on SiC substrate. The HVPE method and properties of GaN grown on SiC by HVPE are described elsewhere [6]. Pore size was in nanometer scale range. Figure 3 clearly shows that GaN layer overgrows the pores formed in GaN substrate material. Thickness of overgrown GaN layers ranged from 2 to 70 microns (Fig. 4).

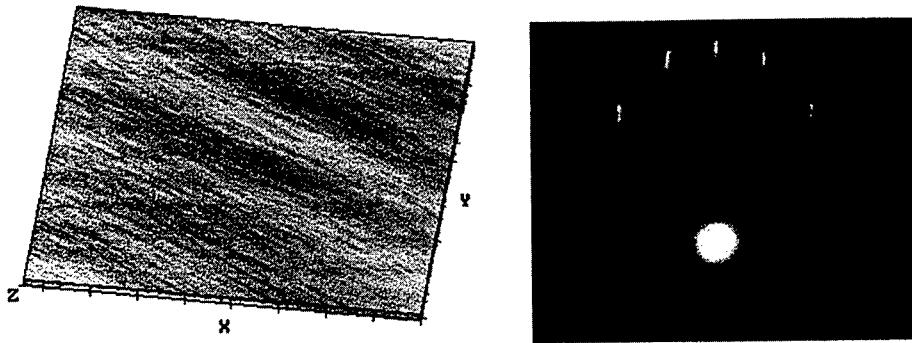


Figure 2. AFM surface image (a) and RHEED image (b) for SiC layer grown on porous SiC.

SCALE X:1000 nm Y:1000 nm Z:100 nm

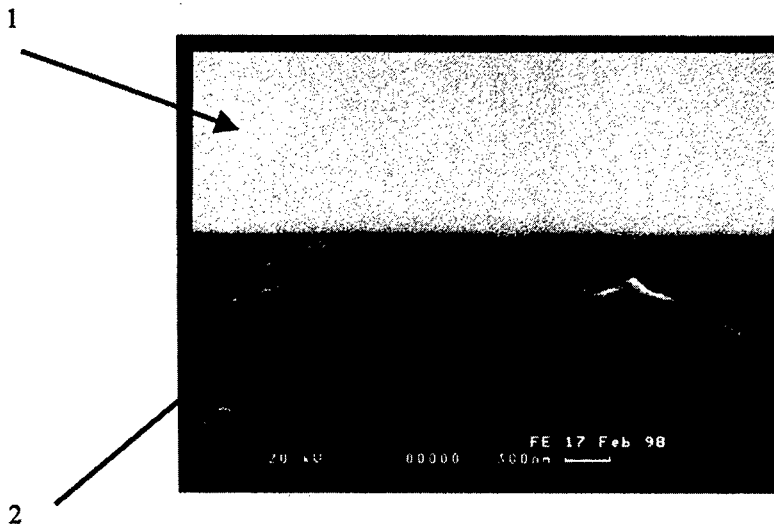


Figure 3. SEM image of GaN layer overgrown on porous GaN: 1 – GaN layer, 2 – porous GaN substrate material.

It was shown that GaN layers overgrown on porous GaN have good surface morphology and high crystalline quality (Fig. 4). X-ray and Raman measurements indicated that the stress in the layers grown on porous GaN was reduced down to 0.1-0.2 GPa, while the stress in the layers grown directly on 6H-SiC substrates remains at its usual level of about 1 GPa. Results of stress-reduction measurements in single crystal GaN layers grown on porous GaN are discussed elsewhere [7]. We propose porous GaN to be used as buffer layer for stress-reduced GaN device structures and bulk material.

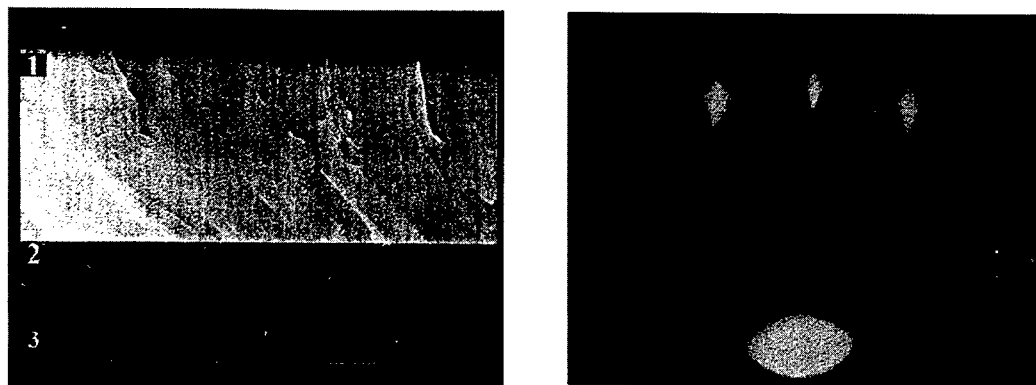


Figure 4. SEM image (left) of cleaved surface of 11  $\mu\text{m}$  thick GaN layer (1) grown on porous GaN layer (2) formed on SiC substrate (3). RHEED (right) for GaN layer grown on porous GaN.

### Conclusions

SiC and GaN epitaxial layers were grown on porous SiC and GaN, respectively. Material quality was improved by using porous substrates. Much more research is necessary to optimize parameters of porous materials and overgrown layers.

### Acknowledgments

This work at Ioffe Institute was supported by INTAS projects 96-0254, 96-1031 and 98-2141.

### References

- [1] Y.Kato, S.Kitamura, K.Hiramatsu, N.Sawaki, *J. Cryst. Growth*, **144** (1994), p. 133.
- [2] S.Nakamura, M.Senoh, S.Nagahama, N.Iwasa, T.Yamada, T.Matsushita, H.Kiyoku, Y.Sugimoto, T.Kozaki, H.Umemoto, M.Sano, K.Chocho, *J. Cryst. Growth*, **189/190** (1998), p.820.
- [3] M.Anikin, A.Lebedev, S.Pyatko, A.Syrkin, A.Strel'chuk, *Mater Sci. Eng.*, **B 11** (1992), p. 113.
- [4] M.Mynbaeva, D.Tsvetkov, *Inst. Phys. Conf. Ser.*, **155** (1997), p. 365.
- [5] N.S.Savkina, A.A.Lebedev, D.V.Davydov, A.M.Strel'chuk, A.S.Tregubova, M.A.Yagovkina, *Abstr. 2nd European Conf.SiC and Rel. Mat.*, (Sept.2-4, 1998, Montpellier, France), p.135.
- [6] Yu.Melnik, I.Nikitina, A.Zubrilov, A.Sitnikova, Yu.Musikhin, V.Dmitriev, *Inst. Phys. Conf. Ser.*, **142** (1995), p. 863.
- [7] M. Mynbaeva, D. Tsvetkov, S. Stepanov, A. Cherenkov, A. Titkov, A. Kryzhanovskii, I. Kotousova, A. Zubrilov, V. Ratnikov, V. Davydov, N. Kuznetsov, K. Mynbaev and V. Dmitriev, *MRS Internet J., Nitride Semiconductors*, **4** (1999) 14.

## 4H-SiC Layers Grown by Liquid Phase Epitaxy on 4H-SiC Off-Axis Substrates

N. Kuznetsov<sup>1</sup>, A. Morozov<sup>2</sup>, D. Bauman<sup>2</sup>, V. Ivantsov<sup>1</sup>, V. Sukhoveev<sup>2</sup>,  
I. Nikitina<sup>1</sup>, A. Zubrilov<sup>1</sup>, S. Rendakova<sup>3</sup>, V.A. Dimitriev<sup>3</sup>, D. Hofman<sup>4</sup>  
and P. Masri<sup>5</sup>

<sup>1</sup> A.F. Ioffe Institute, PhysTech, WBG Research Group, RU-194021 St. Petersburg, Russia

<sup>2</sup> Crystal Growth Research Center, RU-124021 St. Petersburg, Russia

<sup>3</sup> TDI, Inc., 8660 Dakota Drive, Gaithersburg, MD 20877, USA

<sup>4</sup> University of Erlangen-Nürnberg, DE-91058 Erlangen, Germany

<sup>5</sup> Université Montpellier 2, Place E. Bataillon, FR-34095 Montpellier Cedex 5, France

**Keywords:** Background Doping Concentration, Electric Carrier Diffusion Length, Liquid Phase Epitaxy

**Abstract** We investigated properties of undoped 4H-SiC epitaxial layers grown on 4H-SiC substrates by liquid phase epitaxy (LPE). Vertical dipping version of LPE method was employed. Growth was carried out from Si-based melt contained in graphite crucible in the temperature range from 1550 to 1700°C. Growth rate and layer thickness ranged from 0.1 to 1 micron per hour and 1 to 9 microns, respectively. Crystal quality of grown material was evaluated by x-ray diffraction and photoluminescence (PL). Background doping concentration and minority carrier diffusion lengths were measured.

**Introduction** Liquid phase epitaxy was the first method to demonstrate a number of SiC devices on earlier stages of silicon carbide development [1] including high temperature field effect and bipolar transistors, thyristors, blue and violet light emitting diodes. Recently it has been shown that defect density in SiC layers grown by LPE can be significantly reduced in comparison with that in the substrate materials [2,3,4]. SiC pn structures with stable operation at high breakdown current were demonstrated [5]. Due to low defect density and relatively large minority carrier diffusion length, LPE grown SiC layers were proposed to be used as base regions for large area high-power SiC devices [6]. Most of these results were obtained on 6H-SiC LPE grown structures. In this paper, we report on properties of undoped 4H-SiC epitaxial layers grown by LPE.

**Experiment and results** 4H-SiC epitaxial layers were grown on 4H-SiC (0001) 8 degrees off-axis commercial substrates. Epitaxial deposition was done on the (0001)Si face of the substrate. Both n-type and p-type substrates were used. Growth processes were performed on production-type reactor NIKA-S. Vertical dipping version of LPE process in temperature gradient field was employed [7]. Inductively heated growth zone was modified to accept 2-inch diameter SiC wafers. Growth zone parts including crucible were machined from extra high-purity graphite. Si-based melt was used as a solvent [8]. Samples were rotated during the growth. Growth temperature ranged from 1550 to 1700°C.

Thickness of grown layers was measured using both (1) scanning electron microscopy and (2) luminescent optical microscopy at 77 and 300 K. Growth rate depending on substrate temperature varied from 0.1 to 1 micron per hour. Thicknesses of the grown layers ranged from 1 to 9 microns.

Surface of the grown material was investigated by optical and electron microscopy, reflectance high-energy electron diffraction (RHEED), and atomic force microscopy. Surface morphology exhibits a high degree of step bunching, which is typical for epitaxial layers grown by LPE on off-oriented substrates [9].

Crystal structure of grown layers was investigated by x-ray diffraction. The layers were found to be 4H-SiC. The full width at a half maximum of  $\omega$ -2 $\theta$ -scan x-ray rocking curve for (0004)

reflection ranged from 10 to 20 arc sec. Photoluminescence measurements confirmed that grown layers have 4H polytype structure (Fig. 1).

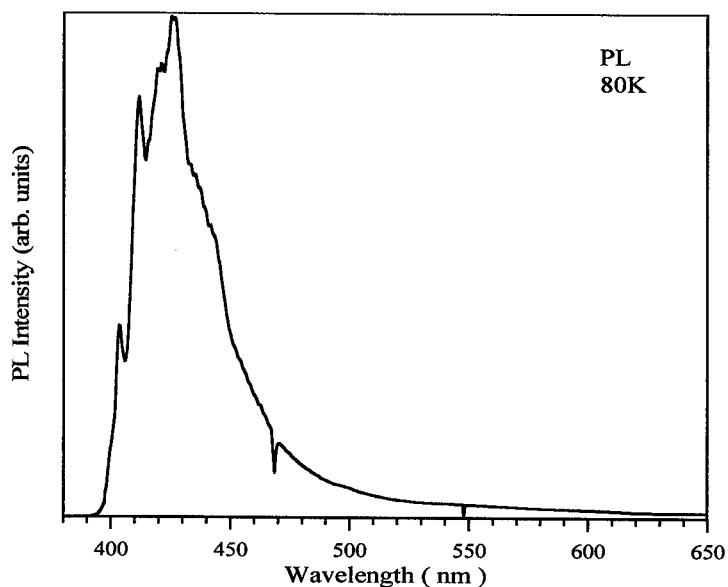


Figure 1. Photoluminescence spectrum measured at 80 K for undoped 4H-SiC layer grown on p-type 4H-SiC substrate. Layer thickness is 8 microns. Concentration  $N_d - N_a$  is  $1 \times 10^{17} \text{ cm}^{-3}$ .

Concentration of uncompensated electrically active donors,  $N_d - N_a$ , in these epitaxial layers was estimated using capacitance-voltage characteristics of Schottky barriers formed by vacuum thermal evaporation of high purity Ni. It was found that the  $N_d - N_a$  concentration depends on ambient gas in reaction chamber (Fig. 2). High donor concentration measured for SiC layers grown in He probably was due to low purity of He gas.

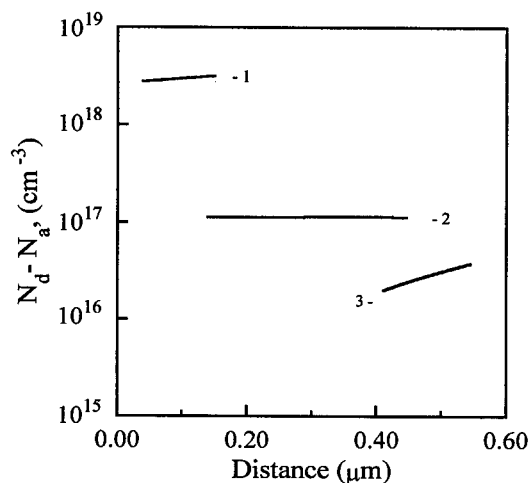


Figure 2. Concentration  $N_d - N_a$  measured for 4H-SiC layers grown in He ambient gas (1), in Ar ambient gas (2) and in vacuum of  $5 \times 10^{-4} \text{ Pa}$  (3).

The minimum concentration  $N_d - N_a$  of  $2 \times 10^{16} \text{ cm}^{-3}$  was measured for 4H-SiC epitaxial layer grown in a vacuum. Growth in a vacuum is unstable due to rapid melt evaporation and LPE growth of SiC layers must be developed for ambient pressure more than 100 Torr. We believe that background doping concentration may be reduced by coating of graphite parts by high purity silicon carbide and use of gases with higher purity.

Minority carrier diffusion length,  $L_p$ , in grown 4H-SiC layer was measured using electron beam induced current (EBIC) technique. The measurements were performed on Schottky barriers formed on layer surfaces and pn junctions formed between n-layer and p-type substrates. It was found that  $L_p$  value ranged from 0.6 micron for the layer with  $N_d - N_a$  concentration of  $1 \times 10^{17} \text{ cm}^{-3}$  to 1.2 micron for the layer with  $N_d - N_a$  concentration of  $5 \times 10^{16} \text{ cm}^{-3}$ . We may expect that  $L_d$  value will increase further for LPE grown 4H-SiC layers with lower background doping concentration leading to epitaxial materials suitable for high-power switching devices.

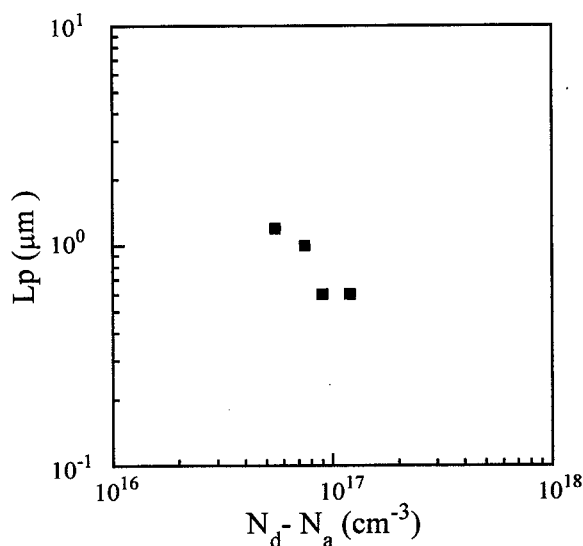


Figure 3. Minority carrier diffusion length measured by EBIC technique for 4H-SiC layers with different  $N_d - N_a$  concentrations.

Pn junctions formed between n-layer and p-substrate were investigated using 300  $\mu\text{m}$  diameter mesa-structures formed by reactive ion etching. Current-voltage (I-V) characteristics of these pn junctions were measured in a temperature range from 300 to 600 K. Exponential dependence of forward current on applied voltage with non-ideality factor,  $\eta$ , of 2.0 (Fig. 4a) measured in the whole temperature range indicates that current flow mechanism may be described by Shockley - Noyce - Sah's theory. The reverse I-V characteristics showed an abrupt breakdown at voltages around 300 V. The breakdown field was estimated to be  $3 \times 10^6 \text{ V/cm}$ .

Electroluminescence spectra of substrate-layer pn junction (Fig. 4b) contain an edge peak related to exciton recombination and peak related to carrier recombination on donor-acceptor pairs. At 300 K, the exciton peak situated at 391 nm (3.17 eV). Shockley - Noyce - Sah current flow mechanism and intense exciton luminescence from undoped 4H-SiC layers indicated a high quality of grown material and relatively low defect density at the substrate-layer interface.



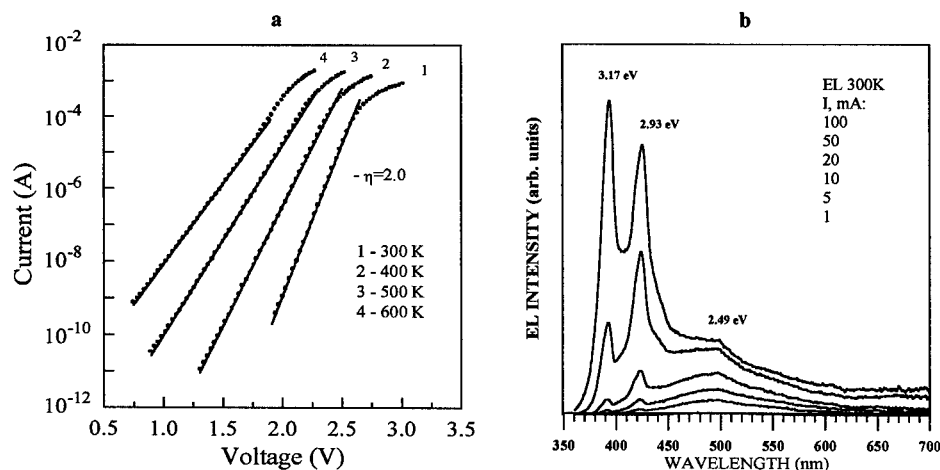


Figure 4. Current-voltage characteristics (a) and electroluminescence (b) for 4H-SiC pn junction formed between n-type LPE layer and p-type substrate. Concentration  $N_d-N_a$  in 4H-SiC layer is  $1 \times 10^{17} \text{ cm}^{-3}$ . Layer thickness is  $8.7 \text{ }\mu\text{m}$ . Concentration  $N_a-N_d$  in 4H-SiC substrate is  $5 \times 10^{17} \text{ cm}^{-3}$ .

**Conclusions** Undoped 4H-SiC layers were grown on off-axis 4H-SiC substrates by dipping LPE technique. Si-based melt contained in graphite crucible was used as a solvent for SiC. Growth rate depending on growth temperature ranged from 0.1 to  $1 \text{ }\mu\text{m/hr}$ . Thickness of the layers was controlled from 2 to 9 microns. The minimum  $N_d-N_a$  concentration of  $2 \times 10^{16} \text{ cm}^{-3}$  was obtained for SiC grown in vacuum. For Ar gas ambient, the minimum  $N_d-N_a$  concentration in SiC layers was about  $9 \times 10^{16} \text{ cm}^{-3}$ . Minority carrier (hole) diffusion length measured at room temperature using EBIC method ranged from 0.6 to 1.2 micron for layers with  $N_d-N_a$  concentration  $1 \times 10^{17} \text{ cm}^{-3}$  and  $5 \times 10^{16} \text{ cm}^{-3}$ , respectively. Future research will be focused on background concentration reduction and surface improvement.

**Acknowledgments** We would like to thank V. Soloviev for EBIC measurements and N. Seredova for PL measurements. This work was supported by INTAS grants # 96-0254 and # 96-1031, and NATO grant # SfP-971979.

## References

- [1] V. Dmitriev, *Physica*, **B 185** (1993), p. 440.
- [2] R. Yakimova, M. Tuominen, A.S. Bakin, J.-O. Fornall, A. Vehanen, and E. Janzen, *Inst. Phys. Conf. Ser.*, **142** (1996), p. 101.
- [3] M. Muller, M. Bickermann, D. Hofmann, A.-D. Weber and A. Winnacker, *Material Science Forum*, **264-268** (1998), p. 69.
- [4] S.V. Rendakova, I.P. Nikitina, A.S. Tregubova, and V.A. Dmitriev, *J. Electron. Materials*, **27** (1998), p.292.
- [5] S. Rendakova, V. Ivantsov, and V. Dmitriev, *Material Science Forum*, **264-268** (1998), p.163.
- [6] V.E. Chelnokov, A.L. Syrkin, V.A. Dmitriev, *Diamond and Related Materials*, **6** (1997), p. 1480.
- [7] M. Ikeda, K. Koga, Y. Matsushita, Y. Ueda, T. Tanaka, *J. Appl. Phys.* **50** (1979), p. 8215.
- [8] V. Dmitriev, in: *Properties of Silicon Carbide*, ed. G.L. Harris (London, 1995), pp. 214.
- [9] S. Rendakova, N. Kuznetsov, N. Savkina, M. Rastegaeva, A. Andreev, M. Minbaeva, and V. Dmitriev, *Mat. Res. Soc. Symp. Proc.*, **512** (1998), p. 131.

## Temperature Gradient Effect on SiC Epitaxy in Liquid Phase

Muhammad Nasir Khan, Shin-ichi Nishizawa, Wook Bahng and Kazuo Arai

Electrotechnical Laboratory, UPR Ultra-Low-Loss Power Device Technology Research Body,  
1-1-4 Umezono, Tsukuba, Ibaraki, 305-8568, Japan

**Keywords:** Growth Rate, Liquid Phase Epitaxy, Surface Morphology, Temperature Gradient

**Abstract.** Epitaxial growth of 6H-SiC was carried out on 6H-SiC Acheson seed crystals in the silicon melt using closed carbon crucible. The growth was carried out in the temperature range 1500-1700 °C. The geometry was specific one, such that epitaxial layer growth occurred simultaneously on both faces of seed crystal under similar growth conditions. We have measured the growth rate and studied the surface morphology of these grown layers. The temperature gradient within the melt seems to play a dominant role in the growth mechanism in liquid phase and also results in a better surface morphology of the grown layers.

### Introduction

Silicon carbide is technologically an important material for the realization of high performance electronic devices, which can be operated, in extremely harsh conditions, such as high frequency, high temperatures and high power [1-2]. Research on materials preparation for the above realization has been carried out from different angles over the past few years. Although wafers of SiC with diameter of more than 50 mm prepared by usual physical vapor transport method are commercially available, but the active region required to fabricate electronic devices on these wafers is restricted by different defects present in these wafers. The defects of serious concern are micropipes and dislocations. The density of these defects has been on gradual decrease over the past few years of active research, but to fabricate the electronic devices commercially are still in vain.

SiC growth is carried out by different methods but preparation of the semiconductor materials in the past for device fabrication had proved the liquid phase growth as an appealing one because the growth in this process is carried out close to equilibrium conditions [3]. Thus, it is a viable growth method for production of high quality material. Therefore, growth of SiC from liquid phase might be utilized both for epitaxial and bulk crystal growth.

SiC research in our laboratory started with large diameter single crystal growth by sublimation method. But the intrinsic deficiencies in this method such as reduced controllability of chemical vapor content, degradation of source material, high heat release during crystallization and the defect formation, especially voids, micropipes and macrodefects are considered closely related to the vapor phase growth. Therefore, research on alternative SiC growth techniques / variants were performed. Growth of SiC from liquid phase using silicon based melts, as solvent for carbon was one of them. Liquid phase crystallization offers principle advantages, e.g. better control of the concentration field along the solid - liquid interface either by forced / natural convection. It was also considered as a possible tool to close the defects such as micropipes existing in the commercial SiC wafers as well as the one grown in our own laboratory. In the first phase, epitaxial layers were grown on the Acheson seed crystals to test the experimental facility to be used for LPE purpose. Until now different experimental setups have been used for the growth of SiC epitaxy in liquid phase and all of these were limited to the growth on any one face of the seed crystal. In our setup the geometrical configuration of the seed within the vertical crucible was such that growth occurred simultaneously on both faces of the same seed under the same growth conditions.

In this article we report on the liquid phase epitaxy of 6H-SiC Acheson seed crystals at different temperatures in a closed vessel. The difference of the growth rate and surface morphology is discussed in the light of temperature gradient occurring within the melt during LPE growth and is compared with the results of earlier studies.

### Experimental

Epitaxial growth of SiC layers on 6H-SiC Acheson seed crystals in Si melt has been investigated in a specific geometry to evaluate the growth rate and surface morphology with the process conditions, such as growth temperature, temperature gradient or substrate properties. Graphite crucibles with 24-mm inner diameter and with variable length were used in the experiments. The seed crystals below average quality but polished on both Si and C faces up to 1  $\mu\text{m}$  diamond slurry were set from the bottom of the crucible both in vertical and horizontal geometry with the help of a carbon lid. The crystals were set in such a way that growth occurred simultaneously on both the faces under similar growth conditions. The crucible was filled with pure powder of silicon and was closed with a carbon lid. The heating was performed with a 200 kHz - rf generator. Growth temperature was measured on lower and top end of the crucible with pyrometers. Experiments were performed in the temperature range 1500 -1700  $^{\circ}\text{C}$  for 1 hour in Ar at atmospheric pressure. Growth takes place due to the mass transport from the crucible acting as C-source to the seed in the established temperature gradient. The process was finished by a slow cool down step to avoid cracking of SiC crystals in the re-solidification process of the melt. The substrates with the grown layers were separated from the solidified structure by etching in a mixture of  $\text{HNO}_3$  and HF. The growth rate was measured by measuring the thickness of these layers by a mechanical micrometer gauge and an optical microscope on a perpendicular cut.

### Results & Discussion

The growth mechanism and surface morphology in liquid phase are greatly influenced by a number of parameters such as, seed crystal configuration, polarity, off and on axis orientations and the temperature gradient. We tried to fix some of these parameters except for the seed crystal position, which were set vertical and horizontal from the bottom of the crucible in order to know the effect of temperature gradient. Growth was carried out for the same temperature and duration for the two geometries. The grown epitaxial layers are of 6H polytype transparent greenish, and free of inclusions. We have measured the growth rate of these layers grown simultaneously on the two faces of the same seed. The temperature dependence of the growth rates on Si and C - faces for the seed set horizontal and vertical from the bottom of the crucible is shown in Figs.1 (a) and (b) respectively. We have observed variations in the growth rate for vertical and horizontal geometries. Further the growth rate on C- face is higher than Si - face for both cases. The growth rate agrees well to the earlier literature data [4]. From Arrhenius plot of the temperature dependencies of growth rates, the apparent activation energies calculated for growth processes are 55.54 and 23.80 kcal/mole for Si and C-faces of the seed set horizontally. The activation energies have higher values of 113.75 and 62.74 kcal/mole for Si and C-faces of the seed set vertically. These values are higher than the one typically reported for liquid diffusion [5] and is an indication of the complex structures of species within the solvent.

The apparent difference in the growth rate on Si and C -faces can be attributed to the low surface energy of the C- face, as nucleation densities on the two faces are different. Since nucleation preferably takes place on the surface with low surface free energy. The nucleation rate is higher on C-face compared to Si one. This has been observed earlier in CVD growth where for 6H-SiC the growth rate is higher on C - face compared to the Si face [6]. The difference in growth rate between the vertical and horizontal geometry can be attributed to temperature gradient. The temperature gradient has a value of 3-10  $^{\circ}\text{C}/\text{cm}$  on crystal surface in the vertical geometry compared to the horizontal one where it is almost nil on seed crystal surfaces for the same growth temperature. The temperature gradient increases the rate of flow of solution past the crystal surface, which is parallel to the flow direction in vertical geometry. It also evens out the distribution of solute over the crystal

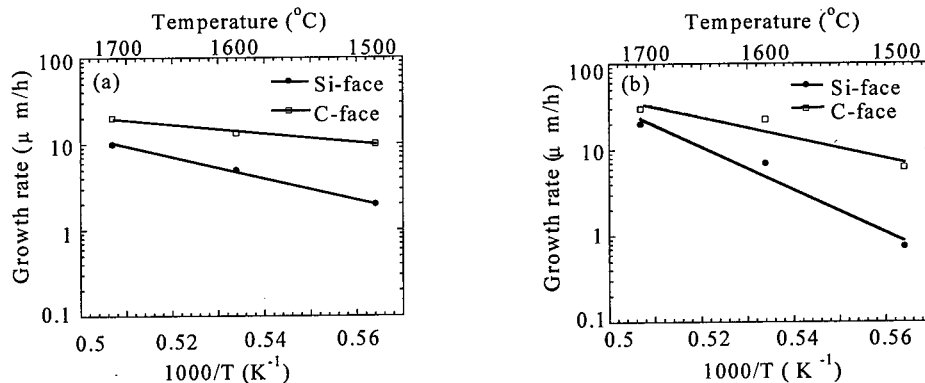


Fig. 1: Temperature dependence of the growth rate: (a) seed set horizontal (b) set vertical from the bottom of the crucible

surfaces resulting in a uniform and stable growth in the vertical geometry.

For surface morphology studied by polarizing optical microscope, various features have been observed with respect to growth temperature and seed crystal geometry. Surface appearance in liquid phase epitaxy depends on substrate orientation, solvent composition and thickness. The layers grown on the basal planes are generally irregular composed of many growth steps due to spontaneous nucleation and inhomogeneous growth at the initial stage. The layers grown on off oriented substrates are relatively smooth and show regular wavy pattern. The wave density depends on the solvent composition indicating that the ratio of the normal and tangential growth is different at different growth conditions [7].

In our case spiral growth is dominant on Si-face and step formation on C-face of all the seed crystals. These spiral and steps, which are smaller at low growth temperature converts to larger and macro steps as the growth temperature increases. Further the step sizes on C-face and Si-face morphology are quite different for the two geometries at the same growth temperature. We correlate these observations to the different growth mechanism occurring during the epitaxial growth [3]. Spiral mechanism is favored when supersaturation is below certain transitional supersaturation because nucleation above this point is two-dimensional and further higher supersaturation on the seed crystals faces results in unstable growth. At low growth temperature we have found some circular depression close to spiral, which we think are caused by Si melt droplets. Figure 2(a) shows Si and C-faces for seed set horizontal from the bottom of crucible at the growth temperature of 1700 °C. We have observed domain like features on Si face. These domains are smooth and are separated from one another. Under this type of growth regime, the opportunity for the defect formation is high as step moves across one another, island thus formed contact one another at a slightly different angles and localized thermodynamic and kinetic variations are easy to be formed. Fig 2(b) shows optical micrographs for the Si and C - faces of seed crystal set vertical from the bottom of crucible at the same growth temperature. One can see the wavy pattern on the Si-face and anisotropic step formation on the C-face. The C-faces morphology is almost the same for two geometries, except it is rough and the steps are smaller and more perturbed on C - face of the substrate set horizontal. As mentioned above the temperature gradient plays a dominant role for the growth mechanism and surface morphology. The gradient helps the melt flow across crystal surfaces to spread uniformly and isotropically in vertical geometry. Further the geometry itself provides a low wetting angle (solvent /crystal contact) a prerequisites for homogeneously grown materials. In horizontal geometry the solvent does not float out but remains as drop with an angle of contact between liquid and crystal resulting in a different growth mechanism as can be seen by comparing the optical micrographs for the two geometries. No significant change was observed for placing seed crystal at the bottom of crucible or higher in the melt in horizontal geometry. Further, no appreciable change

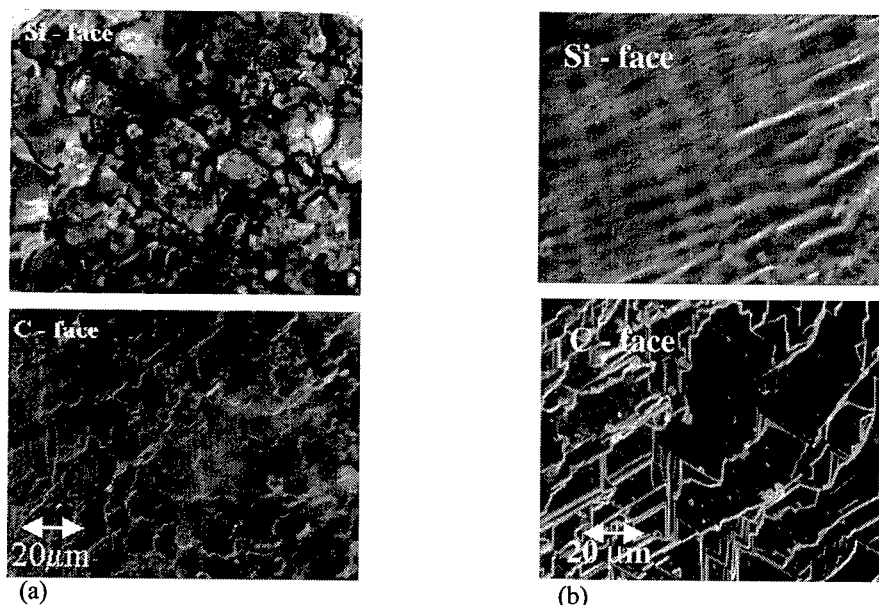


Fig. 2: Optical micrographs for the Si and C- faces of the same seed after LPE at 1700 °C (a) seed set horizontal (b) seed set vertical from the bottom of the crucible

in results was observed for the seed crystal polarity in the up down directions at the same position. In practice, the environmental conditions for growth in our system are such that convection is present in the solvent and the motion generally varies in both magnitude and geometry with time during the growth cycle. Finally, as growth occurs simultaneously on the two faces of the same seed crystal under similar growth condition and a growth rate as high as 20~30 μm/h have been achieved by this method. In this regard we consider that rapid recovery of defects such as micropipes and cracks within the seed can also be done by this method. The work for defect recovery studies by this method is in progress and will be presented later.

#### Acknowledgement

This study was supported by the Proposal-Based New Industry Creative Type Technology R&D Promotion Program from the New energy and Industrial Technology Development Organization (NEDO) of Japan.

#### References

- [1] R. Yakimova, M. Tuominen, A.S. Bakin, J. O. Fornell, A. Vehanen and E. Janzén, *Inst. Phys. Conf. Ser. No 142* (1996), 101.
- [2] S.V. Rendakova, I. P. Nikitina, A. S. Tregubova and V. A. Dmitriev, *J. Elect. Mater.* **27** (1998), 292.
- [3] M. Müller, M. Bickermann, D. Hofmann, A. -D. Weber and A. Winnacker, *Mater. Sci. Forum* **264-286** (1998), 69.
- [4] A. Suzuki, M. Ikeda, N. Nagao, H. Matsunami and T. Tanaka, *J. Appl. Phys.* **47** (1976), 4546.
- [5] M. A. Wright, *J. Electrochem. Soc.* **112** (1965), 1114.
- [6] T. Kimoto, H. Nishino, W. S. Yoo, and H. Matsunami, *J. Appl. Phys.* **73** (1993), 726.
- [7] A. Kakanakova, Georgieva, T. Paskova, R. Yakimova, C. Hallin, M. Syväjärvi, E. P. Trifonova, M. Surtchev and E. Janzén, *Mater. Sci. & Engg.*, **B46** (1997), 345.

## Micropipe Healing in Liquid Phase Epitaxial Growth of SiC

R. Yakimova<sup>1</sup>, M. Syväjärvi<sup>1</sup>, S. Rendakova<sup>2</sup>, V.A. Dimitriev<sup>2,3</sup>, A. Henry<sup>1</sup>  
and E. Janzén<sup>1</sup>

<sup>1</sup>Department of Physics and Measurement Technology, Linköping University,  
SE-581 83 Linköping, Sweden

<sup>2</sup>TDI, Inc., 8660 Dakota Drive, Gaithersburg, MD 20877, USA

<sup>3</sup>Howard University, MSRCE, Washington, DC, USA

**Keywords:** Interfacial Energy, Liquid Phase Epitaxy, Micropipe Filling, SiC Wafers

### Abstract

In this study we demonstrate the feasibility of micropipe reduction in SiC commercial wafers by using liquid phase epitaxial (LPE) growth. We have studied the stability of the micropipe healing by performing hot KOH etching and growing thick (40-50  $\mu\text{m}$ ) layer with sublimation epitaxy at temperature higher than that used for the LPE growth. Experimental evidences have been collected by means of different techniques and a phenomenological model for micropipe healing is proposed.

### Introduction

Wide energy bandgap, high thermal conductivity, high saturated electron drift velocities, and high breakdown electric field make silicon carbide (SiC) a candidate of choice for high-temperature, high-speed, high frequency, and high-power applications. SiC is also hard, chemically stable, and resistant to radiation damage. It has been found superior to both Si and GaAs for the development of novel electronic structures, including hybrid GaN/SiC devices. Due to the phase equilibrium in the Si-C system, SiC can not be grown from a stoichiometric melt because it sublimates before melting. This naturally limits the application of melt growth techniques and thus the growth rate. Typical growth rates for the bulk growth of SiC are in the range of 0.5 to 2.0 mm/hour [1]. The technique commonly exploited is seeded sublimation growth based on the method proposed by Tairov and Tsvetkov [2]. One critical issue in SiC bulk crystal growth is the generation of microchannels, termed micropipes, penetrating virtually the whole boule. Since 1995, a significant progress has been made in the sublimation growth technology, resulting in better understanding of micropipe formation mechanisms and demonstrating reduction of micropipe density down to a few pipes per square centimeter [3]. However, these are just selected wafers showing the feasibility of solving the micropipe problem but not proving it in marketing of SiC wafers today. For high voltage, high power vertical devices the needed active area may be on the order of several  $\text{cm}^2$  and that restricts the usable area of the wafer if it contains micropipes, while for other type of devices this problem may be not so detrimental but still undesirable. It is of interest to look for alternatives of micropipe reduction even as a temporary solution until the fundamental problems in the boule growth of SiC are solved. In 1995 we [4] first demonstrated that micropipes existing in the substrates can be healed during subsequent liquid phase epitaxial growth. Recently, TDI, Inc. (USA) has developed a method for filling micropipes in commercial wafers by using liquid phase epitaxy (LPE) [5]. However, there are many questions to be answered regarding micropipe filling process, e.g. what is the mechanism of micropipe healing, what is the role of the liquid phase, are micropipes closed or filled, is the healing stable or metastable, etc.

In this study, we show evidence that micropipe healing during LPE is a thermodynamically stable and irreversible process independently of the subsequent thermal treatment. An attempt is made to elucidate the phenomenon from a fundamental point of view and to motivate the practical interest in the results.

We have employed several growth and characterization techniques: liquid phase epitaxy [5,6], sublimation sandwich epitaxy [7], KOH etching, optical microscopy, scanning electron microscopy (SEM) and cathodoluminescence (CL) imaging.

### Results and discussion

From earlier investigations micropipe closing has been demonstrated for epitaxial layers grown on 6H-SiC on-axis substrates. In Fig. 1 two micropipes emerging from the substrate are not observed on the surface of the epilayer grown by LPE [4]. Instead a spiral has appeared. This effect was also observed for 6H-SiC off-axis substrates. The layer thicknesses range from 50 to 100  $\mu\text{m}$ .

We studied commercial 4H-SiC wafers, Si-face,  $8^\circ$  off, on which the micropipes were mapped prior to LPE. Fig. 2 shows an optical micrograph illustrating (a) the surface appearance after LPE [5] filling of a micropipe present in a 4H-SiC substrate; (b) the pipe is also seen as filled on the back side of the substrate by focusing below the surface.

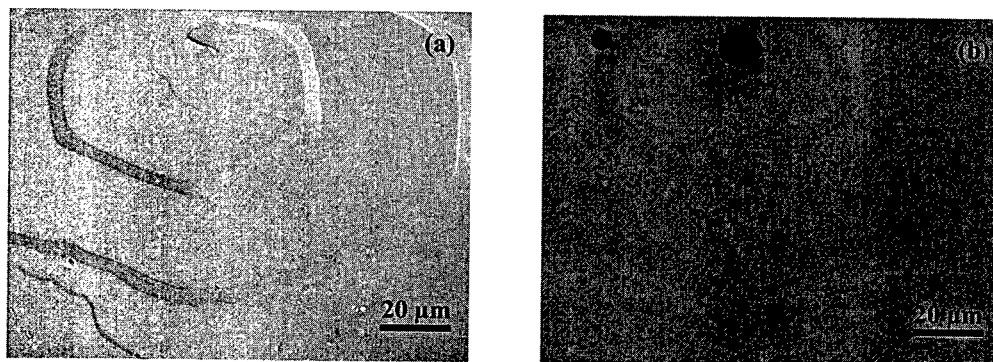


Fig. 1. Optical micrographs taken from a 6H-SiC LPE layer with filled micropipes: (a) in reflected light and focused on the surface and (b) transmission light focused below the layer surface.

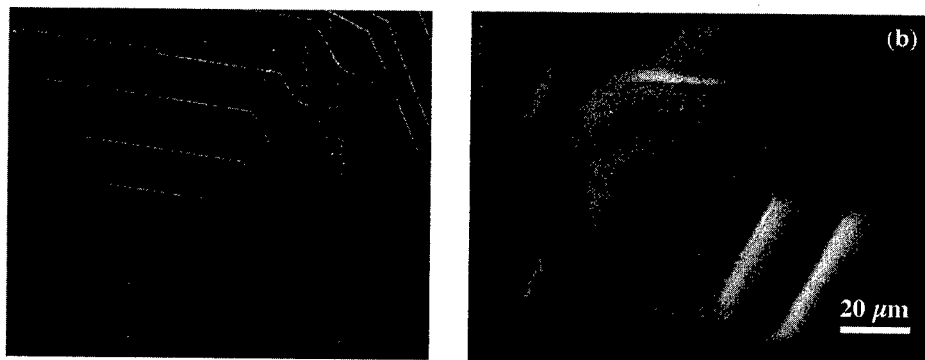


Fig. 2. An optical micrograph of a filled micropipe: (a) top view of a 4H-SiC LPE layer; the micropipe is terminated by a spiral growth and (b) the same micropipe viewed from the backside of the substrate.

After the LPE growth of about 0.1  $\mu\text{m}$  - 5  $\mu\text{m}$  thick layers, most micropipes were not optically detectable but spirals or some cellular patterns were seen. The latter appeared on micropipes with rather large diameter ( $>5 \mu\text{m}$ ). These patterns were better resolved with SEM in secondary electron (SE) and CL modes, suggesting that several blocks have grown together inside the channel (Fig. 3). The white contrast in the SE image (Fig. 3a) indicates a presence of grown material while the darker contrast in the CL image (Fig. 3b) can suggest a structure different from the surrounding SiC material. Micropipes at the periphery of the wafer remain open more frequently. This may be related to stress concentrated at that area and thus not optimal LPE growth.

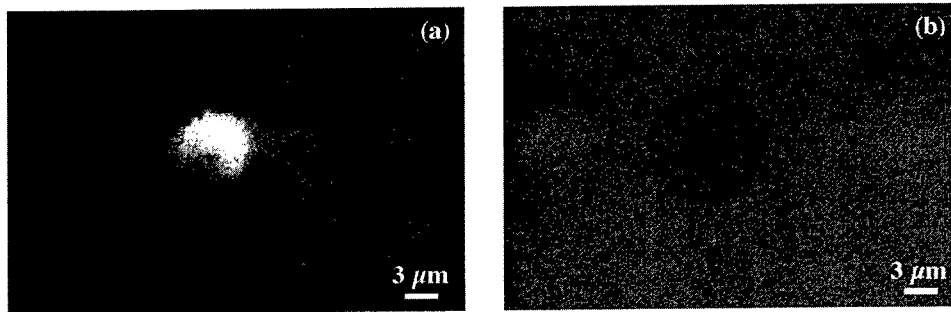


Fig. 3. SE (a) and CL (b) images from a filled micropipe; acceleration voltage 15kV.

LPE is a technique which provides growth conditions close to thermodynamic equilibrium and the driving force needed to achieve growth is small. The latter means that the epitaxial layers grow at low supersaturation. In sublimation growth of SiC the supersaturation is much higher and temperature fluctuations may easily result in a local deviation from optimal growth conditions and micropipe formation. This is not expected in the LPE growth. The growth on off-oriented substrate is given by step flow mechanism which is not supposed to yield micropipes under optimal growth conditions but generally can not terminate micropipes propagating from the substrate. This is clearly demonstrated in the CVD and sublimation epitaxial growth. From our experimental observations it follows that during LPE favorable conditions exist for growth inside micropipes which are commonly believed to be hollow dislocation cores [8]. The strain field around a dislocation with large Burgers vector contains a high energy that can be minimized by removing the crystalline material around the dislocation line and creating a new surface in the form of a hollow tube. Simulation [9] predicts that a thermodynamically stable hollow core may be closed if a large enough supersaturation is applied. As pointed out earlier our experimental conditions do not provide high supersaturation and thus the mechanism of micropipe filling must have another explanation. We base our model on the following findings: (i) the interfacial energy between the crystal (micropipe wall) and the liquid feeding phase is low [6,10], so that growth can occur even if the driving force for crystallization is low; (ii) micropipes contain screw dislocations and the wall surface is probably stepped [6]. Finally we observe growth hillocks and spirals at the locations of former micropipes. Thus it appears to be energetically easy to start growth inside a micropipe during LPE and this results in a stable micropipe healing. During growth the substrate is placed on top of the liquid solvent across which a temperature gradient is applied. Due to capillary effect the solvent penetrates into micropipe channels and depending on the surface tension stops up to a certain level. The solution in contact with the crystal becomes supersaturated and the growth starts at the most favorable nucleation sites, e.g. steps provided by dislocations.

The stability of the micropipe healing was tested by growing a layer by sublimation epitaxy at about 1800°C on top of the LPE layer. Inspection under reflected light, transmitted light and crossed polarizer modes did not show any indications of micropipes propagating from the substrate. This was confirmed by KOH etching. It was observed that at the location of former micropipes dislocation etch pits appeared, and we did not observe traces of Si in closed micropipes. Furthermore, on cross-sectional samples it was observed that micropipes terminate close to the substrate/LPE layer interface. Fig. 4 shows the number of terminated micropipes below the surface of a polished sublimation epitaxy layer

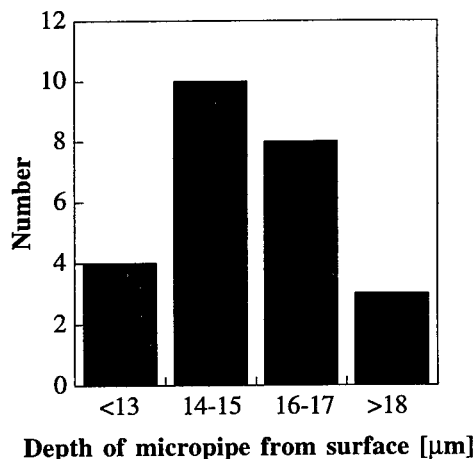


Fig. 4. Number of terminated micropipes below the sublimation epitaxy layer.



grown on a 5  $\mu\text{m}$  thick LPE layer. At this thickness the LPE layer surfaces are rough which affected the morphology of the subsequently grown sublimation epitaxy layer. The sublimation epitaxy layer was polished down to about 20  $\mu\text{m}$  to make microscopy investigation possible. The data in Fig. 4 were collected by using transmission light microscopy and focussing at the terminated micropipe below the surface. The scattering of the data is within the measurement accuracy.

Another interesting observation in this study is that the surface morphology of 30-50  $\mu\text{m}$  thick layers grown by sublimation epitaxy is featureless under optical microscopy examination, when being grown on the as-grown initial surface of a 0.1  $\mu\text{m}$  thick LPE layer. The structural quality as assessed by high resolution X-ray diffraction (HRXRD) is considerably better in the sublimation epi-layer. Fig. 5 shows the  $\omega$ -rocking curves taken from substrate with a LPE layer (broad peak) and after a sublimation epitaxy layer has been grown on top (narrow peak). This finding suggests a perspective for growing device structures directly on LPE grown materials free of micropipes.

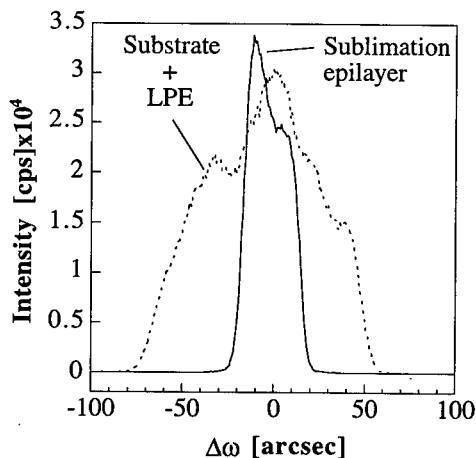


Fig. 5. Representative  $\omega$ -scans showing improvement of structural quality after sublimation epitaxy on a LPE layer grown on a commercial 4H-SiC wafer.

### Summary

Liquid phase epitaxy is a capable technique to considerably (>50% including peripheral region) reduce micropipes in commercial SiC wafers. The yield might depend on the layer thickness which on its turn determines the surface morphology. The process is stable and irreversible under subsequent thermal treatment. No polytype dependence is observed. A model to explain the phenomenon is proposed.

### Acknowledgement

The SSF SICEP program, NUTEK, Brite-Euram Contract BRPR-CT98-0815 (DG12-GZMM) and Okmetic AB are gratefully acknowledged for support. The authors would like to thank A. Kakanakova-Georgieva, Tungasmita Sukkaneste and H. Jacobsson for SEM/CL and HRXRD measurements.

### References

- [1] V.A. Dmitriev and M.G. Spencer in "SiC Materials and Devices" Ser. Semiconductors and Semimetals, eds. R.K. Willardson and E.R. Weber, Academic Press 52 (1998) p. 28
- [2] Y.M. Tsirov and V.F. Tsvetkov, J. Cryst. Growth 43 (1978), p. 209.
- [3] C.H. Carter, Jr., V.F. Tsvetkov, R.C. Glass, D. Henshall, St.G. Muller and M. Brady, MRS Spring Meeting 1999, 5-9 April 1999, San Francisco, Symposium T, Abstracts p. 308.
- [4] R. Yakimova, M. Tuominen, A. S. Bakin, J. O. Fornell, A. Vehanen, and E. Janzén, Proc. Int. Conf. on Silicon Carbide and Related Materials (1995), Inst. Phys. Conf. Ser. 142 (1996) p. 101.
- [5] S. Rendakova and V. Dmitriev, reported at the MRS Spring Meeting, April 5-9, 1999, San Francisco, California.
- [6] M. Syväjärvi, R. Yakimova, H.H. Radamson, N.T. Son, Q. Wahab, I.G. Ivanov and E. Janzén, J. Cryst. Growth 197 (1999) p. 147.
- [7] M. Syväjärvi, R. Yakimova, M. Tuominen, A. Kakanakova-Georgieva, M.F. MacMillan, A. Henry, Q. Wahab and E. Janzén, J. Cryst. Growth 197 (1999) p. 155.
- [8] J. Heindl, H.P. Strunk, V.D. Heydemann and G. Pensl, Phys. Stat. Solidi (a) 162 (1997) p. 251.
- [9] Liu G.Zh., J.P. van der Eerden and P. Bennema, J. Cryst. Growth 58 (1982) p. 152.
- [10] M. Syväjärvi, R. Yakimova and E. Janzén, J. Electrochem. Soc. 146 (1999) p. 1565.

## Growth of CVD Thin Films and Thick LPE 3C SiC in a Specially Designed Reactor

André Leycuras

Centre de Recherche sur l'Hétéroépitaxie et ses Applications, CNRS,  
Rue Bernard Grégory, FR-06560 Valbonne, France

**Keywords:** CVD and LPE Reactor for SiC, Hot Wall Resistive Heating Reactor

### Abstract

A hot wall internal furnace reactor has been designed and built to meet the requirements of CVD or LPE growth of SiC on 2 inches diameter. The substrates can be heated up to 1800°C, the temperature rise rate is 75°C/sec between 20 and 1400°C, the operating pressure is between  $10^3$  and a few  $10^5$  Pascal, and the power consumption is 4 kW at  $5 \cdot 10^3$  Pascal at a hydrogen flow rate of  $8 \text{ slm}^{-1}$ . All the parameters of the 3C SiC/Si growth have not yet been optimized but uniform thickness layers with very good surface morphology and 200arcsec FWHM rocking curves have been obtained at a growth rate of  $10 \mu\text{m h}^{-1}$ . First results in LPE Si solvent in this reactor are encouraging.

### Introduction

SiC physical properties make this material very interesting for high power, high frequency and high temperature devices. The problems concerning SiC for its use in mass production come from its price and from its crystalline defects. The use of a low price substrate like Si can be a good approach if the crystalline quality of the SiC layer can be improved up to the level which is required for a specific application. The quality of standard SiC/Si layers is sufficient for many sensors. For electronic applications the density of defects must be much lower and the quality of the material has to be improved for instance by epitaxial lateral overgrowth (ELO). A new LPE approach is also proposed in this paper. This paper relates an attempt to grow high quality thick SiC layers starting from Si substrates and with a very simple and cheap CVD reactor.

### The Hot Wall CVD Reactor

The use of Si as well as other quasi transparent substrates poses the problem of heating at low pressure since no or little thermal radiation is absorbed by the substrate and no gas conduction can transfer the heat from the hot substrate holder to the substrate. Direct Joule heating of Si substrates is possible but only doped samples. A good solution for heating transparent materials under a vacuum is to put them in a hot wall reactor, this geometry which has been adopted here, insures a radiation equilibrium between the sample and the wall and hence an efficient heating. The low pressure inside the wall allows a laminar flow, a high gas velocity for sharp doping transitions, high purity and no thermal convection. The walls are heated by resistors which allow the use of radiation shields to minimize the heat losses.

The wall is a horizontal rectangular graphite tube for 2 inches wafers. The wall is tightly connected to the precursors and carrier gases entrance while a neutral gas flows between the wall and the water cooled stainless steel reactor tube. All the parts inside the reactor are made out of pure

refractory and inert materials which have very low vapor pressure at the working temperatures. The maximum temperature can be in excess of 2000°C but in practice, above 1800°C the lifetime expectancy of the resistors decreases rapidly. At 1500°C the power consumption is 4kW at  $5 \cdot 10^3$  Pascal and under a hydrogen flow rate of  $8 \text{ slm}^{-1}$ , the temperature rise rate is 75°C/sec between 20°C and 1400°C, the operating pressure is between  $10^3$  and a few  $10^5$  Pascal.

For a good thickness uniformity, the substrate holder rotates at a speed of 2 rotations per second. This is sufficient even during the carbonization step which is very rapid because the temperature rise rate is 75°C/s.

### 3C SiC CVD Growth

The SiC/Si growth conditions in this reactor are very similar to those in other reactors and follow the same two steps procedure : carbonization at medium temperature and growth at high temperature. The carbonization step consists of a high temperature rise rate from 600 to 1200°C in 8 sec under a high propane partial pressure <sup>[1]</sup>. The growth conditions are 1400°C,  $5 \cdot 10^3$  Pascal and Si/C=1. Very shiny layers are obtained at growth rates of  $10 \mu\text{m h}^{-1}$  and a thickness of 20  $\mu\text{m}$ . The surface has the shape of a diffraction lattice due to equal width steps  $\sim 2 \mu\text{m}$  wide and perpendicular to the of direction of the  $4^\circ$  off of the (100) substrate <sup>[2]</sup> (Fig.1). Hence the layer is shiny at the 0 order i.e. at normal incident and it decomposes the light at other orientations. On 2 mm thick substrates cracks appear on the layers at thicknesses above 8  $\mu\text{m}$ . The cracks are almost exclusively oriented perpendicularly to the steps which suggests that the role of the disorientation is not only to prevent antiphase domains but also to favorize the relaxation of the layer's stress in this direction. On usual 300  $\mu\text{m}$  thick substrates no cracks appear on the layers because the substrates can bend. The thickness non uniformity of the layers is about 5% but it can probably be lowered by following theoretical simulations results <sup>[3]</sup>. The best crystalline quality has been measured by DCXRD rocking curve with a FWHM of 200 arcsec.

This value as all the other parameters of the growth have not yet been optimized and the growth conditions will probably be improved. in the near future thanks to the constant progress in the prototype of the reactor.

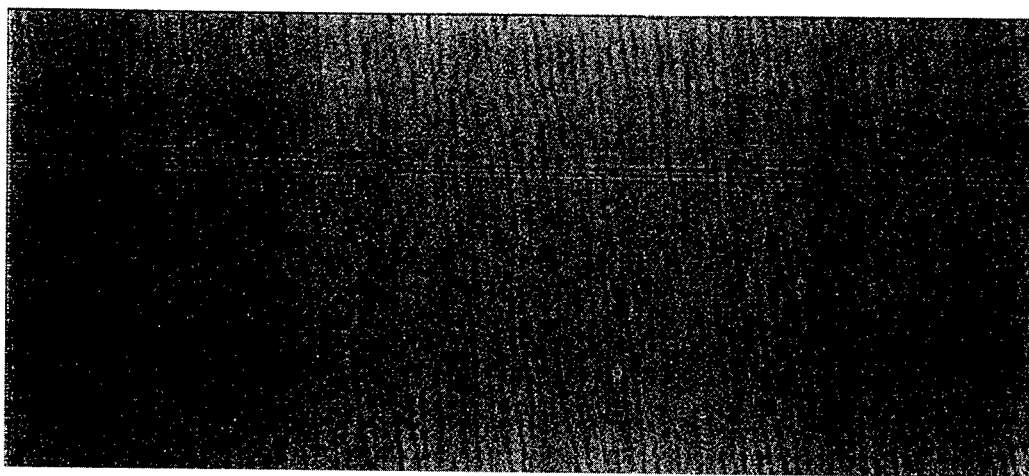


Fig.1: Optical microscope view of a 16  $\mu\text{m}$  thick 3C SiC layer grown by CVD on a 2mm thick Si(100)  $4^\circ$  off substrate. The mean width of the steps is 2  $\mu\text{m}$ . The area of the view on the layer is  $160 \times 70 \mu\text{m}^2$ . Cracks do not appear on this view, they are perpendicular to the steps and their mean distance is 2 mm.

The quality of these 3C SiC layers is probably sufficient for many applications like sensors for which the electronic properties of the layer do not play an essential role. For electronic applications the density of defects in 3C SiC must be lowered by 2 to 3 orders of magnitude. Several ways have been followed to tend toward this goal but so far, none of these techniques has led to a significant breakthrough for the production of high quality monocrystalline and large area wafers of this material. Attempts to grow thick 3C SiC layers from SiC/Si layers by LPE in the present reactor have shown interesting growth features which could pave the way to the production of high quality thick 3C SiC layers.

### 3C SiC/ Si and LPE

The quality of LPE grown materials is generally very good mainly because this method is close to the thermodynamic equilibrium. In the case of SiC the solvent can be Si though it evaporates rapidly. It is at once the solvent and the source of Si. The source of C is generally the graphite crucible itself<sup>[4]</sup>. The other approach which has been followed here uses the SiC layer as a crucible, the melt Si substrate as the solvent and the propane as the C precursor. The top and the bottom of the hot wall can be heated at different temperatures to create a thermal gradient through the liquid Si. The figure 2 shows the optical micro graph of the surface of a LPE layer grown with the SiC layer (seed) cooler than the Si bath on top of it, the thickness of the layer is 10  $\mu\text{m}$  on top of the 2  $\mu\text{m}$  original CVD layer. The scale is the same as in fig.1 so that the steps are 6 to 7 times broader. By transparency cubic structures are seen on the other side of the layer on the right side of the figure. This is more visible on Fig.3 which is taken at the same place but focused through the layer on its back side and still better on the direct view of Fig.4. These cubic crystals grow on the surface which is hotter than the liquid Si. The LPE growth on both side of the initial SiC layer has been made possible because liquid Si was present on both side of this layer.

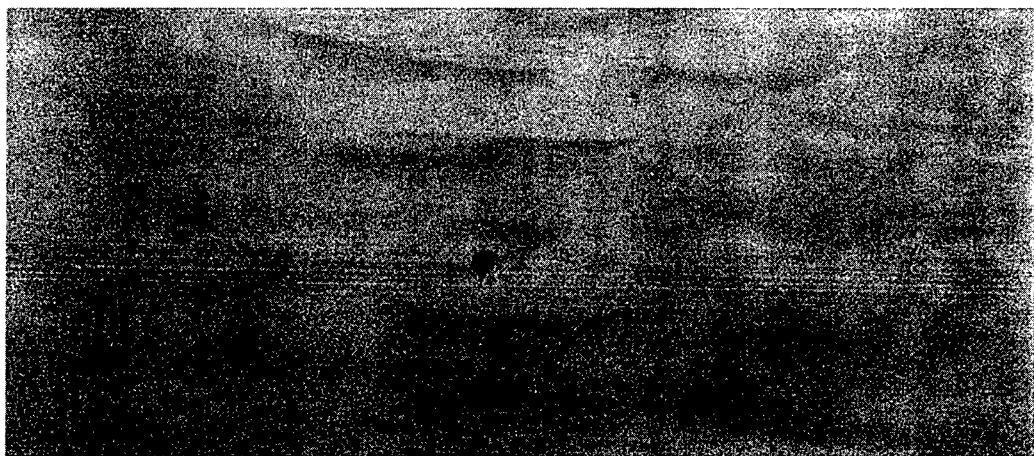


Fig.2 Optical microscope view of a 12  $\mu\text{m}$  thick 3C SiC layer grown by LPE on a 2  $\mu\text{m}$  thick SiC (100) 4° off CVD layer. The mean width of the steps is  $\approx 12\mu\text{m}$ . The area on the layer is  $160 \times 60 \mu\text{m}^2$ .

In the case where liquid Si is present only on the low temperature side of the SiC layer, very regular cubic SiC crystals are grown and the quality of these cubes is very good ( $10^6$  dislocations. $\text{cm}^{-2}$ ) as it has been observed by TEM and also by AFM as in Fig.5. By inverting the sign of the gradient it is possible to enlarge their top and make them coalesce as it is seen in Fig.4. As in the case of ELO the enlarged part of the cubes contains very few dislocations. Hence the process could lead to high quality thick SiC layers without the technological steps needed in ELO.

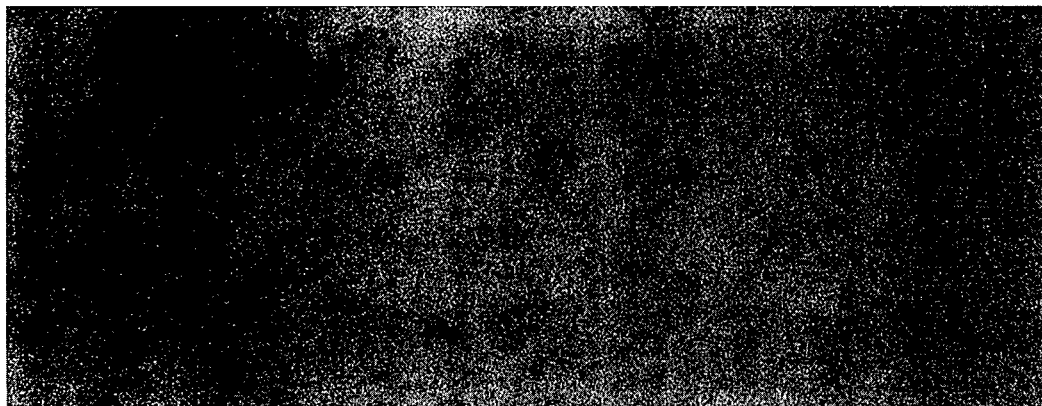


Fig.3: Optical microscope view of the same 3C SiC layer as in fig.2, but focused on its back side through the layer. The square features are better seen on fig.4. The scale is the same as in fig.2.

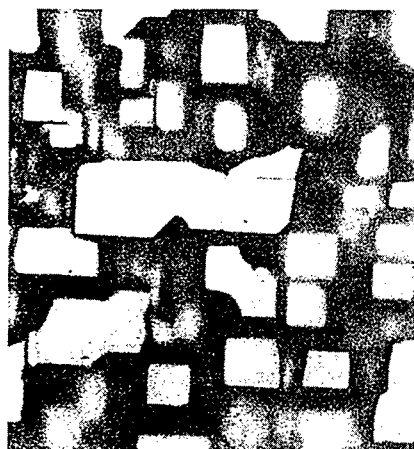


Fig.4: Optical microscope top view of a LPE 3C SiC layer. The area of the view on the layer is  $80 \times 80 \mu\text{m}^2$

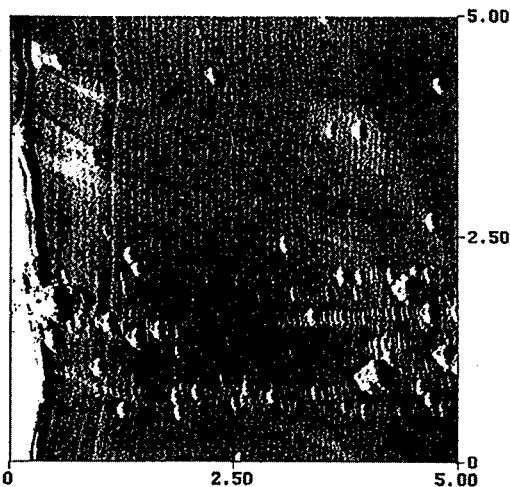


Fig.5: AFM view of one of the LPE grown 3C SiC crystals shown in fig.4. The lines correspond to the steps due to the  $4^\circ$  off of the layer. The spots are Si droplets. The scale is in micrometers.

### Conclusion

A new reactor has been built in view to grow SiC either by classical CVD or by a modified LPE technique. The LPE approach on CVD SiC could lead to the production of high quality 3C SiC crystals of large dimensions without the technological step necessary in the ELO technique.

### References

- [1] A.J. Steckl and J.P.Li, IEEE Trans. Elect. Devices, **39** (1992), p.64
  - [2] K. Shibahara, S. Nishino, and H. Matsunami, Appl. Phys. Lett. **50** (1990), p.18
  - [3] J. Xu and X.J. Cheng, Jour. of Crystal Growth, **193** (1998), p.636
  - [4] V. Ivantsov and V. Dmitriev, Mater. Sci. Forum, **264-268** (1998), p. 73
- Fax: (33) 493958361, E. mail: al@crhea.cnrs.fr

## Lateral Epitaxial Overgrowth and Pendeo Epitaxy of 3C-SiC on Si Substrates

S.E. Sadow<sup>1</sup>, G.E. Carter<sup>1</sup>, B. Geil<sup>2</sup>, T. Zheleva<sup>2</sup>, G. Melnychuck<sup>1</sup>,  
M.E. Okhuysen<sup>1</sup>, M.S. Mazzola<sup>1</sup>, R.D. Vispute<sup>3</sup>, M. Derenge<sup>2</sup>, M. Ervin<sup>2</sup>  
and K.A. Jones<sup>2</sup>

<sup>1</sup> Emerging Materials Res., Dept. Electrical & Computer Eng.,  
Mississippi State, MS 39762-9571, USA

<sup>2</sup> Sensors and Electron Devices Directorate, Army Research Laboratory,  
2800 Powder Mill Road, Adelphi, MD 20783-1197, USA

<sup>3</sup> Center for Superconductivity Research, University of Maryland, College Park, MD 20742, USA

**Keywords:** 3C-SiC, Heteroepitaxy, LEO, Pendeo, TEM

**Abstract** Lateral Epitaxial Overgrowth (LEO) experiments on 3C-SiC were conducted on patterned substrates. Due to the high CVD growth temperatures required for high-quality single-crystal 3C-SiC, dielectric mask materials with higher thermal stability than SiO<sub>2</sub> were used. Experiments were performed with amorphous Si<sub>3</sub>N<sub>4</sub> deposited via PECVD and AlN, deposited both by PLD and MOCVD. These masks were deposited and patterned on (100) Si substrates containing a 4 µm 3C-SiC epitaxial layer grown using a standard 3C-SiC growth process. Single crystal 3C-SiC was regrown in the mask window regions. However, polycrystalline 3C-SiC nucleated on the mask stripes for the growth conditions studied. Pendeo epitaxy (PE) was performed on the same material where the 3C-SiC epilayer was etched to form 3C-SiC stripes on a (100) Si substrate. It appears that Pendeo epitaxy was achieved with lateral and vertical growth on the 3C-SiC columns having been observed.

### Introduction

Cubic silicon carbide (i.e., 3C-SiC) has been grown epitaxially on both (100) and (111) Si substrates for many years [1,2]. While this work has resulted in single crystal 3C-SiC on Si substrates, the high degree of lattice mismatch (>20%) has resulted in films with a high level of defects, mostly twinning defects for 3C-SiC grown on (100) Si. Lateral Epitaxial Overgrowth in the GaN wide bandgap system has been successful where growth temperatures of approximately 1000 °C permit the use of SiO<sub>2</sub> as a dielectric mask to achieve selective growth of GaN on 6H-SiC substrates [3] as well as on sapphire substrates [4]. 3C-SiC on Si LEO was performed by one group whereby carbonization of the Si substrate was performed directly through a SiO<sub>2</sub> mask at growth temperatures of 950 and 1000 °C [5]. This initial 3C-SiC LEO work utilized HCL to suppress nucleation of 3C-SiC on the SiO<sub>2</sub> mask. Unfortunately, the low growth temperatures used resulted in poor 3C-SiC crystal quality as pointed out in the literature. A 3C-SiC LEO process, whereby higher temperature masks would permit sufficient growth temperatures to be used to achieve high-quality 3C-SiC crystal growth, is the next logical step towards achieving high-quality good single crystalline 3C-SiC films on low-cost, large-area Si substrates. This paper discusses our initial research towards this objective.

### Patterned 3C-SiC on Si Substrates for LEO

Both Si<sub>3</sub>N<sub>4</sub> and AlN are high quality electronics grade dielectric films with melting points in excess of 3C-SiC CVD growth temperatures (~1350°C). Using PECVD (in the case of Si<sub>3</sub>N<sub>4</sub>), and PLD and MOCVD (in the case of AlN) high-quality films were deposited on 3C-SiC on (100) Si substrates. The 3C-SiC on Si seed layer was grown using a standard 3C-SiC CVD growth process that has been described in detail elsewhere [6]. The salient features of the 3C-SiC growth are a SiC-coated graphite susceptor temperature of 1310°C in a H<sub>2</sub> carrier gas flow of 3 slm with silane and

propane (each 3% in UHP  $H_2$ ) precursor gas flows of 10 sccm each. A film of an approximate thickness of 4  $\mu m$  was grown during a 2 hour CVD experiment. Characterization of the seed layer process has been adequately described elsewhere and indicates that a single crystal film with numerous twinning defects results (this will be shown later in this paper in the characterization section). Directly on the 3C-SiC seed layer the dielectric films were deposited with a thickness of between 1000 and 1500 Å. These films were then patterned into 4 sets of stripe/window widths of 5/5, 6/4, 7/3 and 8/2  $\mu m$ , respectively. The films were patterned using standard photolithographic processes and an ion milling tool. To ensure that the seed layer was completely free of any dielectric mask material, the ion mill was permitted to mill a very shallow portion of the 3C-SiC seed layer. Prior to loading of the substrates into the CVD reactor a standard solvent clean in an ultrasonic cleaner was performed to prepare the seed crystal in the window region for CVD growth.

### LEO Experiments

LEO experiments were performed at various times (5, 10, 30, 16 and 120 minutes) on substrates patterned with both  $Si_3N_4$  and AlN dielectric films in an effort to measure the vertical and lateral growth rates. The LEO experiments were conducted under the following conditions: 1285°C growth temperature, 3 slm  $H_2$  carrier flow, and 7 sccm flow of both silane and propane precursors. No carbonization step was necessary since a high-quality 3C-SiC seed layer was already grown. In order to assess the affect of 3C-SiC growth on the seed layer, control samples were placed in the reactor adjacent to the patterned substrates. These control substrates were also 4  $\mu m$  films of 3C-SiC on Si but did not contain a patterned substrate. Two-theta XRD scans comparing the seed layer with a control sample after LEO growth were made. It was noted that high-quality 3C-SiC resulted during these experiments.

Figure 1 shows a cleaved sample after LEO growth on both  $Si_3N_4$  and AlN patterned substrates. Initial experiments indicated that not only did 3C-SiC regrowth occur in the window regions, as is clearly evident in this figure, but that lateral growth might have occurred. Unfortunately, TEM studies which will be described next proved that lateral growth was not achieved but rather the direct nucleation on the stripe areas was responsible for observations made during SEM studies.

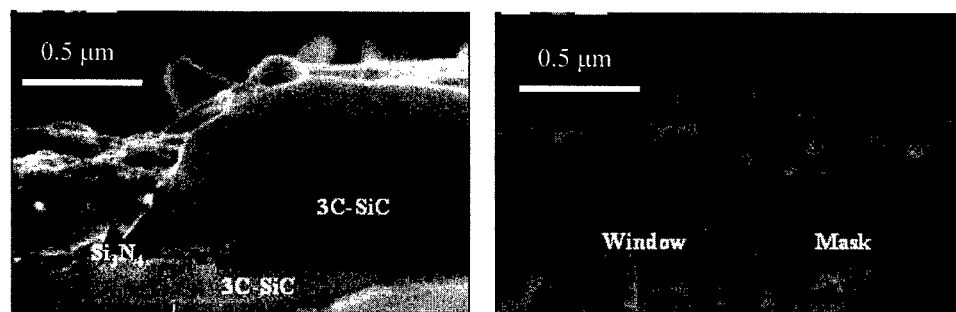


Figure 1 SEM characterization data from (a) 60 min 3C-SiC LEO growth on  $Si_3N_4$  patterned substrate and (b) 10 min 3C-SiC LEO growth on AlN patterned substrate. Note 3C-SiC regrowth has occurred in the window regions but also on the mask itself.

### TEM Characterization of LEO-3C-SiC/Si with $Si_3N_4$ and AlN masks

TEM studies were performed on four samples : i) 3C-SiC/Si (001) with a  $Si_3N_4$  mask (30 min growth); ii) 3C-SiC/Si with a  $Si_3N_4$  mask (10 min growth); iii) 3C-SiC/Si with an AlN mask (30 min growth) and iv) 3C-SiC/Si with an AlN mask (10 min growth). TEM observations revealed that in all four samples the regions over the masks, as well as over the windows, are continuously covered with the 3C-SiC film after 30 min of growth (see Fig. 2), and after ten minutes of growth,

as well (not shown). From the regrown 3C-SiC material, particularly after only 10 minutes of regrowth, the existence of lateral fronts over the mask regions which are not coalesced was expected. Instead, the  $\text{Si}_3\text{N}_4$ , as well as AlN mask, were covered with 3C-SiC. Thus, there is a vertical growth within the windows regions, as well as over the masked regions, indicating no selectivity during growth. The surface of the 3C-SiC over the mask is very rough, compared to that for the regrown 3C-SiC from the windows regions after 10 min. of growth. TEM reveals a morphology which is typical for the 3D island growth, and after ten minutes of growth the 3C-SiC islands over the mask have achieved coalescence to a film thickness of  $\sim 0.2\mu\text{m}$ . TEM micrographs and SAD patterns from 3C-SiC within the window regions (area A) and from 3C-SiC regions over the mask (area B) after 30 minutes regrowth are shown in Fig. 2. SAD patterns clearly reveal the difference in crystallographic quality in the above two regions. Region A, over the window, shows single crystal 3C-SiC which is epitaxially oriented with respect to the Si substrate surface, where  $(001)3\text{C-SiC} \parallel (001)\text{Si}$ . Despite epitaxial growth and single-crystal SAD, these volumes of regrown 3C-SiC exhibit high density of defects, with predominant defects being twins and stacking faults, typical for zinc-blende material. Part of these micro-twin boundaries continue from the 3C-SiC seed layer, but part of them originate at the 3C-SiC homoepitaxial interface (see Fig. 2). Volume B, above the mask, reveal misorientation in the  $[1-10]$  SAD pattern, originated from neighboring 3C-SiC grains of different orientation, resulting in a polycrystalline diffraction pattern.

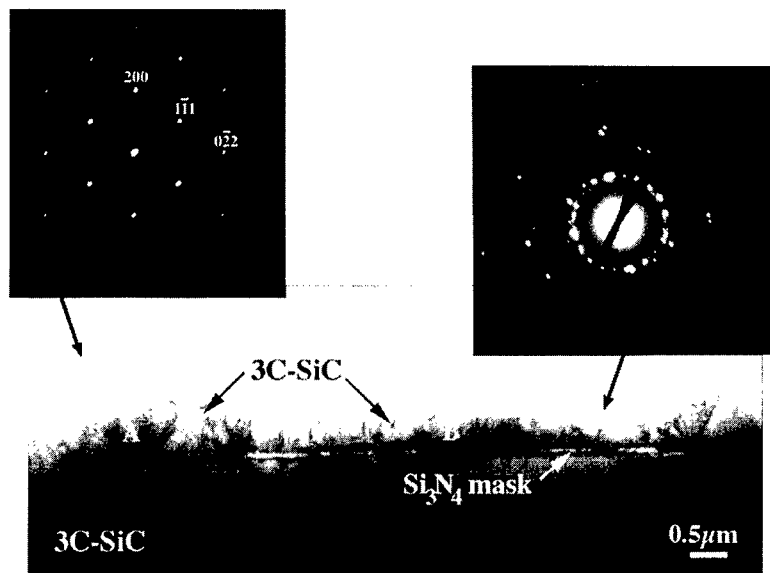


Figure 2 Cross-section TEM micrograph of 30 min  $\text{Si}_3\text{N}_4$  LEO experiment. 3C-SiC has nucleated in window and on mask region. Selected area electron diffraction also shown indicating single crystal material in the window regions and polycrystalline on the mask.

The fact that the thickness of the regrown 3C-SiC from the windows regions is two-to-four times larger, reveals that the vertical growth rate from these regions is up to four times higher, as compared to that over the mask, due to the higher sticking coefficient of the Si and C species to the 3C-SiC (001) surface compared to that to the amorphous  $\text{Si}_3\text{N}_4$  surface. Similar results are obtained from TEM of 3C-SiC material regrown over AlN mask after 10 and 30 minutes of growth. Overall, analysis of the TEM data leads to a conclusion that lateral growth is not achieved and the selective growth process needs optimization. This means that the growth process of the LEO-3C-SiC material needs further optimization as it seems that the growth rate is too fast so that there is not enough time for the incoming species to attach to the appropriate crystallographic sites with the corresponding



potential minima. The growth process could be slowed down via different approaches : possibly either via reduction of the flow rates, or temperature reduction, or a slight change in the geometry could also be helpful. The selectivity could also be improved by appropriate surface treatment before 3C-SiC regrowth, such as the use of HCL to suppress nucleation on the dielectric mask [3].

### Pendeo epitaxy (PE) of 3C-SiC

Pendeo epitaxy (PE) of 3C-SiC was conducted on the same 3C-SiC on Si substrate as used for the LEO results reported earlier. Using the same geometry as for LEO, the 3C-SiC layer was etched in an RIE system to form 3C-SiC stripes and Si window regions. For 3 slm  $H_2$  carrier flow wiskers indicative of 3D island growth resulted indicating a super saturated growth condition. The experiment was repeated with 4.5 slm  $H_2$  carrier flow and a uniform film resulted (see Fig. 3). Significant  $H_2$  etching of the exposed Si material in the window regions occurred, indicating that direct nucleation on the Si surface did not, at least initially, occur. 3C-SiC bridges across the exposed Si regions are evident, indicating that lateral growth may have been achieved. TEM experiments are planned to ascertain whether or not Pendeo epitaxy was in fact achieved.

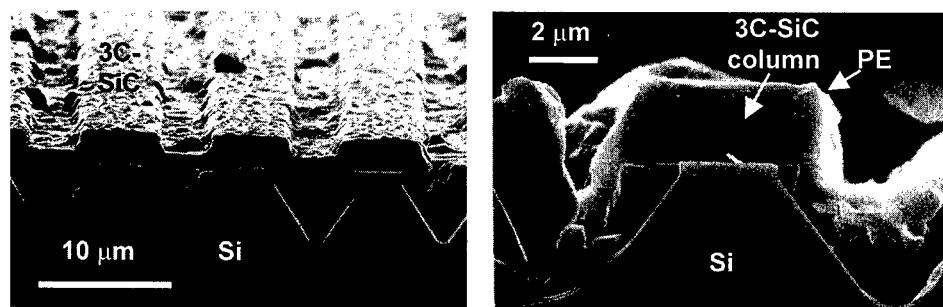


Figure 5 SEM image of Pendeo epitaxy (PE) sample (a) after 5 min PE regrowth with 3 slm  $H_2$  carrier flow and (b) after 30 min PE regrowth with 4.5 slm  $H_2$  carrier flow.

### Summary

A preliminary investigation of LEO of 3C-SiC on (100) Si was performed whereby several dielectric masks were studied in an attempt to achieve lateral overgrowth. The high temperatures and the highly reactive SiC CVD environment resulted in poor mask stability leading to a lack of growth selectivity. Research is continuing whereby HCL will be used to suppress nucleation on the dielectric mask. Pendeo epitaxy of 3C-SiC was conducted on Si substrates for the first time with very promising results: indication is that Pendeo epi was achieved. TEM characterization is underway to confirm this observation.

### References

- [1] J. A. Powell, L. G. Matus, M. A. Kuczmarski, *J. Electrochem. Soc.* **134** 1558 (1987)
- [2] H. Matsunami, "Progress in SiC Epitaxy-present and future," *Inst. Phys. Conf. Ser.* No **137**:Chp 1 (1994).
- [3] T. Zheleva, O.H. Nam, M. Bremser, and R.F. Davis, *Appl. Phys. Lett.*, **71**, 2472 (1997).
- [4] H. Marchand, J.P. Ibbetson, P.T. Fini, P. Kosodoy, S. Keller, S. DenBaars, J.S. Speck and U.K. Mishra, *Materials Internet J.-Nitride Semiconductor Res.*, **3**, 3 (1998).
- [5] J.H. Edgar, Y. Gao, J. Chaudhuri, S. Cheema, S.A. Casalnuovo, P.W. Yip, M.V. Sidorov, *JAP* **84** (1) (1998).
- [6] S.E. Saddow, M.E. Okhuysen, M.S. Mazzola, M. Dudley, X.R. Huang, W. Huang and M. Shamsuzzoha, *Mater. Res. Soc. Proceedings Vol.* **535**, 107-112 (1998).

## Selective Epitaxial Growth of Silicon Carbide on Patterned Silicon Substrates Using Hexachlorodisilane and Propane

Chacko Jacob<sup>1</sup>, Moon-Hi Hong<sup>2</sup>, Juyong Chung<sup>2</sup>, Pirouz Pirouz<sup>2</sup> and Shigehiro Nishino<sup>1</sup>

<sup>1</sup> Department of Electronics and Information Science, Kyoto Institute of Technology, Matsugasaki, Sakyo-ku, Kyoto, 606-8585, Japan

<sup>2</sup> Department of Materials Science and Engineering, Case Western Reserve University, 10900 Euclid Ave., Cleveland, OH 44106, USA

**Keywords:** HCDS, Lateral Overgrowth, Low Temperature Epitaxy, Selective Epitaxy, TEM, TMA

**Abstract:** To improve the quality of heteroepitaxially grown 3C-SiC on Si, a selective epitaxial growth approach has been developed. An oxide mask was used and almost perfect selectivity was obtained at high temperatures (~1350°C). However, the oxide mask began to peel off at temperatures above ~1250°C, resulting in damaged masks. In order to lower the temperature for epitaxial growth, trimethylaluminium (TMA) was used and epitaxial films successfully grown at 1250°C. Using this approach, selective epitaxial growth and lateral overgrowth was demonstrated at 1250°C. The use of hydrogen chloride as an in-situ etchant was critical to this process.

### Introduction

The rapid development of 6H- and 4H-SiC substrates has resulted in the progress of device development in these materials. However, the absence of high quality 3C-SiC bulk substrates has practically pushed 3C-SiC off the development map. While homoepitaxial growth of 3C-SiC has not developed, heteroepitaxial growth of 3C-SiC on Si [1] and other substrates [2] has indicated the promise of high mobility devices, etc. [3]. Nevertheless, the high density of interfacial defects (misfit dislocations, voids) as well as other defects (threading dislocations) result in the growth of lower quality material. Various approaches are being tried to overcome this problem. One of the most promising is the use of selective epitaxial growth on patterned substrates followed by epitaxial lateral overgrowth. The successful demonstration of this technique recently in GaN growth [4] has spurred interest in this technique. However, there are only a handful of reports on the application of selective epitaxy to the growth of 3C-SiC.

The earliest work in selective epitaxy was done by Joyce and Baldrey in growing Si [5]. Continuous advances resulted in a better understanding of the technique in the mid-80's. The main factors affecting selective epitaxy were temperature of growth, choice of mask material, orientation of windows, mask to window ratio, influence of an etchant (e.g. HCl), quality of the mask material, etc. [6]. Edgar *et al* [7] report that a limiting factor is the oxide as well as the duration of growth. For long growth times, it was difficult to suppress the unwanted nucleation on the oxide. Nishino *et al* [8] also reported that the use of HCl aided the process of selective epitaxy.

### Experimental procedures

Patterned silicon (001) substrates were used. A SiO<sub>2</sub> layer (~0.7 µm) was used as the mask and conventional lithographic techniques used to create a patterned surface. The features ranged in size from a few microns to 100 microns. The windows are of different shapes mostly oriented along the [110] directions. The substrates were cleaned by blowing with dry nitrogen. No additional ex-situ cleaning was performed, as it appeared to increase nucleation on the mask surface, thereby reducing the selectivity.

A horizontal atmospheric pressure chemical vapor deposition reactor was used. Source gases were hexachlorodisilane (HCDS) and propane. Hydrogen (3 slm) was used as the carrier gas. Hydrogen chloride gas was used as an etchant to suppress the unwanted nucleation on the mask as well as for in-site cleaning of the substrate. The HCDS bubbler was maintained at a temperature of 10°C. At this temperature, HCDS has a vapor pressure of 1.3 torr. Hydrogen (henceforth referred to as bubbling hydrogen) was bubbled through the HCDS to transport it to the reactor. Changing the propane flow through the reactor varied the ratio of C/Si, while the Si concentration was kept constant. The substrates were placed on a silicon carbide coated graphite susceptor and the reactor was heated by RF induction. For each run, an unpatterned Si(001) substrate was placed alongside the patterned substrate to compare the effects of patterned growth with regular growth.

Parameters that were studied include the size of the window, C/Si ratio, temperature of growth, HCl content, influence of ex-situ cleaning of the substrate as well as in-situ cleaning using hydrogen. The surface morphology of the grown films was analyzed using optical microscopy and scanning electron microscopy (SEM). Micro-Raman spectroscopy was also used to analyze various features. Surface morphology was analyzed using Atomic Force Microscopy. Films grown on unpatterned substrates were studied using Reflection High Energy Electron Diffraction (RHEED) to determine whether they were single crystalline. Due to the small size of the window areas, x-ray diffraction could not be used to determine if the film growing in the window regions was single crystalline or not. Transmission electron microscopy (TEM) was done to further analyze the selectively grown SiC films.

## Results and Discussion

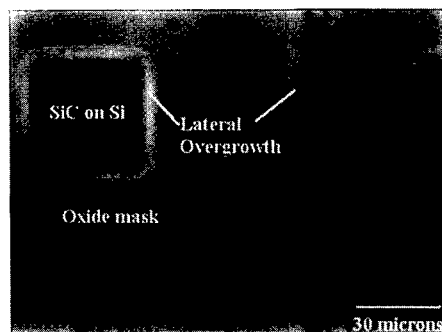


Fig.1: Selective epitaxial growth at 1250°C

Selective growth was demonstrated in films grown at 1350°C and below (Fig.1). The selectivity improved at lower temperatures (~1250°C). Initially, the films grow vertically and once they reach the top of the window, they expand laterally. When thinner films are examined by cross-sectional scanning electron microscopy (SEM), it is seen that initially, the SiC is growing within the window. Limited nucleation occurs on the mask. This issue is dealt with further in a later section. The ratio of the window to mask is critical in determining whether the films growing laterally meet each other and form a continuous film or not as well as in controlling the polycrystalline nucleation on the mask. Some deposition occurs on the oxide surface in the form of large, spherical (3-5  $\mu\text{m}$  diameter) polycrystals. Using micro-Raman spectroscopy, they were identified as 3C-SiC deposits. In masked areas that were smaller than about ~15  $\mu\text{m}$ , polycrystalline SiC deposits were rarely observed. Their density depended on i) temperature of growth, ii) size of the mask area, iii) cleaning techniques employed, and iv) HCl concentration.

Micro-Raman spectroscopy indicates that SiC grows in the window area and then spreads out laterally over the mask. No SiC signal was detected from areas on the mask that did not have any SiC overgrowth. The SiC signals from within the window regions are strong and the TO and LO phonon peaks were detected. But the signal from the region that is laterally overgrown is rather weak, as the film is thin in that region. Further work will be done on thicker films.

The addition of hydrogen chloride to the reaction improves the selectivity. Fewer SiC particles are formed on the oxide mask, though they are larger in size. Additionally, there is a decrease in the growth rate. As the HCl concentration increases from 0 sccm to 10 sccm, the growth rate decreases from about 2.3  $\mu\text{m}/\text{hour}$  to 1.3  $\mu\text{m}/\text{hour}$ . The addition of HCl also influences the facetting of the laterally growing interface.

Transmission Electron Microscopy (TEM) demonstrated that under optimum conditions single-crystalline SiC was growing selectively in the window region (Fig. 2). However, the SiC had a columnar structure. Some evidence for the bending of the defects as well as a reduction in defect density is visible in Fig.2. Lateral overgrowth was observed though the overgrowth was incomplete and coalescence had not yet occurred.

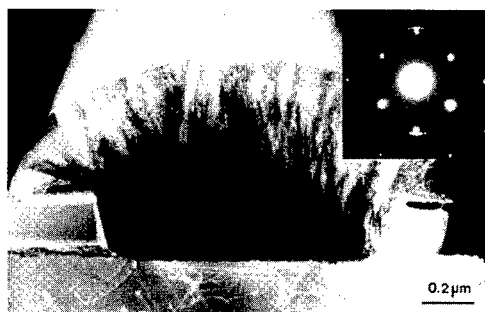


Fig.2. High magnification DF image of SiC in the window region with the beginning of lateral overgrowth.

One of the main problems was the integrity of the oxide masking layer. Initially, the lateral overgrowth process was hampered by the peeling off of the oxide. SiC was growing under the peeled off oxide but there was no real overgrowth. Heating experiments revealed that the oxide would maintain its integrity up to temperatures of about 1250°C. Above that, the oxide was unstable for long term growth. At 1350°C, the oxide began to peel off within 5-10 minutes (Fig. 3).

Attempts were made to lower the growth temperature to 1250°C. But the deposit was polycrystalline (Fig. 4a). However, the addition of 0.05 sccm of trimethylaluminium (TMA) during the growth step resulted in single crystalline SiC at 1250°C (Fig. 4b). This is a promising approach to obtain selective epitaxial growth at lower temperatures while retaining the oxide mask integrity. Another approach would be to use a different mask that is stable up to 1350°C and has a closer thermal expansion coefficient to the silicon substrate. The use of a nitride mask is a possibility. Another option would be to use other sources for lower temperature growth.

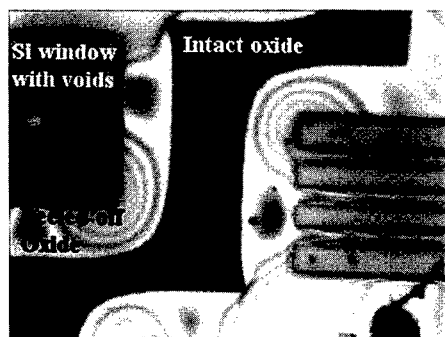


Fig. 3 Oxide peeling off when heated in argon to 1350°C for 10 minutes

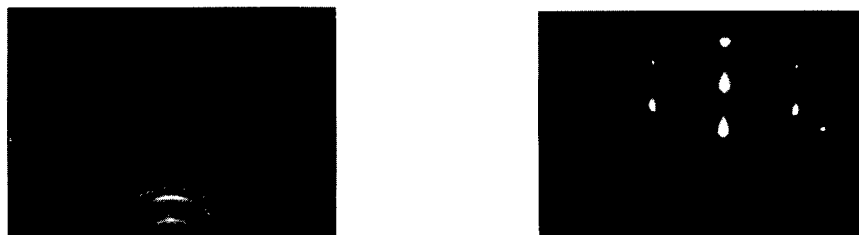


Fig. 4 RHEED pattern of a) growth at 1250°C without TMA. b) Growth at 1250°C with TMA

### Conclusions

Epitaxial growth was performed on a selectively masked Si(001) substrate. Perfect selectivity and lateral overgrowth were demonstrated at 1350°C. TEM analysis demonstrates the high defect density at the interface of the SiC growing directly in the window area. However, there is some evidence of defects bending over as the film begins to grown laterally over the oxide mask. Additionally, the oxide mask peeled off at temperatures above 1250°C and so the epitaxial growth temperature was reduced by the addition of TMA. The use of a lower temperature growth system and/or a more suitable mask (e.g. nitride) will be needed to get high quality, large area selectively grown epitaxial films.

### References

- [1] S. Nishino, J. A. Powell, and H. A. Will, Appl. Phys. Lett. 42 (1983), p. 460
  - [2] J. D. Parsons, Mat. Res. Soc. Symp. Proc. (Pittsburgh, PA:MRS) 97 (1987) p. 271
  - [3] C. Jacob, C-H. Wu, M. Mehregany and P. Pirouz, Transactions of the 3<sup>rd</sup> International High Temperature Conf., (Albuquerque, NM), Vol.1 (1996), p. II-9
  - [4] T.S. Zheleva, O-H Nam, M. D. Bremser and R. F. Davis, Appl. Phys. Lett. 71 (17) (1997), p.2472
  - [5] B. D. Joyce and J. A. Baldrey, Nature Vol. 195 (1962), p. 485
  - [6] L. Jastrzebski, J. Cryst. Growth 63 (1983), p. 493
  - [7] J. H. Edgar, Y. Gao, J. Chaudhari, S. Cheema, S. A. Casalnuovo, P. W. Yip and M. V. Sidorov, J. Appl. Phys. 84 (1) (1998), p. 201
  - [8] S. Nishino, H. Tanaka, K. Takahashi and J. Saraie, Amorphous and Crystalline Silicon Carbide IV, Eds. C. Y. Yang, M. M Rahman and G. L. Harris, (Springer Verlag: Berlin, 1992), p. 411
- For correspondence, please contact Chacko Jacob.  
E-mail. [chacko@dj.kit.ac.jp](mailto:chacko@dj.kit.ac.jp); Tel. (+81) 75 724 7438; Fax. (+81) 75 724 7400

## The APD Annihilation Mechanism of 3C-SiC Hetero-Epilayer on Si(001) Substrate

Y. Ishida<sup>1</sup>, T. Takahashi<sup>1</sup>, H. Okumura<sup>1</sup>, T. Sekigawa<sup>1</sup> and S. Yoshida<sup>2</sup>

<sup>1</sup> UPR Ultra-Low-Loss Power Device Technology Research Body, Eletrotechnical Laboratory,  
1-1-4 Umezono, Tsukuba, Ibaraki, 305-8568, Japan

<sup>2</sup> Saitama University, 255, Shimo-Ohkubo, Urawa, Saitama 338-8570, Japan

**Keywords:** 3C-SiC, APCVD, APDs Annihilation Mechanism, Growth Mode, LPCVD, Simulation

**ABSTRACT.** Heteroepitaxial layers of 3C-SiC on Si(001) without antiphase domains (APDs), which can hardly be obtained by atmospheric pressure chemical vapor deposition (APCVD), can be obtained by low-pressure chemical vapor deposition method (LPCVD) despite using on-axis Si(001) substrate. LPCVD is different from APCVD in the growth mode, i.e., three dimensional (3D) island growth in APCVD and step-flow growth in LPCVD. This difference is attributed to the difference of the main Si species to carry Si atoms onto the grown surface. Based on these results, we propose a new APD annihilation model taking account of the difference in the main Si species and the confirmation of this model is demonstrated by the cellular automata (CA) simulation.

### 1. INTRODUCTION

3C-SiC heteroepitaxial growth on Si substrates is very attractive because of the possibility of obtaining large area SiC crystals at low cost. Recently, we have developed the 3C-SiC growth method by low-pressure chemical vapor deposition (LPCVD) using a silane-propane-hydrogen reaction gas system and succeeded in obtaining atomically flat surfaces without protrusions and antiphase domains (APDs) [1, 2], which can hardly be obtained by atmospheric pressure chemical vapor deposition (APCVD). In the case of LPCVD, the flow rates of SiH<sub>4</sub>, C<sub>3</sub>H<sub>8</sub> and H<sub>2</sub> carrier gases were 0.8 sccm, 1.33 sccm and 8 slm. The atomic ratio of Si/C was 0.2 and the growth rate was 0.31 nm/s. The growth temperature was 1420 K and the pressure was kept at 10 Torr. Details of the carbonization and the growth by LPCVD have been described elsewhere [1]. For APCVD, the flow rates of SiH<sub>4</sub>, C<sub>3</sub>H<sub>8</sub> and H<sub>2</sub> carrier gases were 3.0 sccm, 2.23 sccm and 8 slm, respectively, and the growth temperature was 1520 K. The Si/C ratio was 0.45 and the growth rate was 0.81 nm/s.

With regard to obtaining atomically flat surfaces by LPCVD, the growth mechanism has been discussed in terms of the difference of the growth mode, three dimensional (3D) island growth in APCVD and step-flow growth in LPCVD. This difference in the growth mode is attributed to the difference of the main Si species to carry Si atoms onto the grown surface, i.e., SiH<sub>2</sub> radicals for APCVD and SiH<sub>4</sub> for LPCVD [3, 4]. However, the reason why APD-free crystals can be obtained by LPCVD method and not by APCVD method have not been clarified yet. In this report, we study the APD annihilation mechanism of 3C-SiC on Si(001) by computer simulation and show the difference of the APD annihilation process between LPCVD and APCVD cases.

## 2. THEORETICAL MODEL and COMPUTER SIMULATION

There are Si-Si bonds or C-C bonds at antiphase boundaries (APBs) of SiC crystals. If a C-C bond occur preferentially compared with a Si-Si bond or the contrary case occurs at APB, the APB may propagate along  $\langle 111 \rangle$  direction and annihilate at the cross point of two APBs, as shown in Fig 1. This has been really observed by transmission electron microscope (TEM) [5]. By this model, however, the difference between APCVD case and LPCVD case can not be explained, i.e., APDs do not annihilate if not using misoriented Si substrates in APCVD case, while in LPCVD case, APDs disappear despite using on-axis Si(001) substrates when 3C-SiC epilayers are grown over 5  $\mu\text{m}$  thick [2]. The difference in the crystal structures of grown epilayers between LPCVD and APCVD can be mainly caused by the difference of the growth mode i.e., the difference of the main Si species to carry Si atoms onto the grown surface. Therefore, we propose the model taking account of the difference of the main Si species. There are three sites where atoms can adsorb as illustrated in Fig. 2. In the model, we assumed the sticking coefficient of the in-plane site (IS) equal to 1 and set that of the edge-site (ES) and the terrace site (TS) to  $\alpha$  ( $0 < \alpha < 1$ ). We can express the difference of main Si species by changing  $\alpha$ , i.e., more reactive  $\text{SiH}_2$  radical corresponds to large  $\alpha$  and less reactive  $\text{SiH}_4$  corresponds to small  $\alpha$ . We also assume that C-C bonds occur preferentially at APB.

Based on these assumptions, the direction of APBs propagation results in following. If the species adsorb at IS or TS, APBs propagate along  $\langle 111 \rangle$  direction. On the other hand, if the species adsorb at ES earlier than they adsorb at IS, APBs propagate along  $\langle 110 \rangle$  direction as shown in Fig. 3.

In order to make the validity of this model clear, we used the cellular automata (CA) method, which is a computer simulation that tries to emulate the way the laws of nature are supposed to work in nature. The CA method is more suitable than other simulation methods, e.g.,

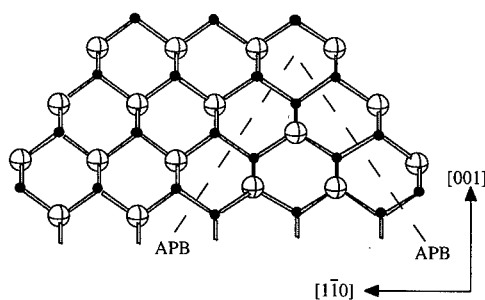


Fig. 1. A model for the annihilation of APD at the cross point of two APBs.

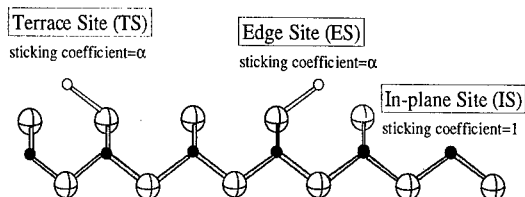


Fig. 2. Schematic drawing of the lattice sites where Si atoms can adsorb.

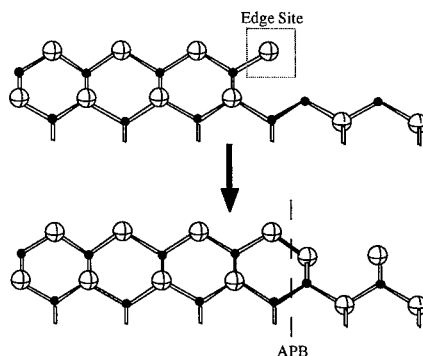


Fig.3. Schematic diagram of APB propagation when a Si atom adsorb at ES.

molecular dynamics and Monte Carlo for a large system which contains more than 10000 atoms inside[6]. The computational cell in our calculation includes 10000 atoms in a layer on a two-dimensional  $100 \times 100$  lattice points. We applied periodic boundary conditions to the four  $\{110\}$  boundary planes.

### 3. RESULTS and DISCUSSION

Figure 4 shows the calculated results for the change of root-mean-square roughness (RMS) with the number of growth layers. The figure shows that larger  $\alpha$  values result in the slower smoothing speed of surfaces. This is in good agreement with our experimental results, i.e., the surfaces of APCVD epilayers are rough while those of LPCVD epilayers are smooth [3]. Figure 5(a) shows the snapshot of the surface structure for  $\alpha=0.01$  after growth of 62 layers. Surface steps are parallel to  $\langle 110 \rangle$  direction. This means that the growth mode is the step-flow in this case. The surface structure of the snapshot shown in Fig. 5(b), which is at  $\alpha=0.5$  and after growth of 169 layers, reveals many 3D islands. These results indicate that the growth mode changes from step-flow growth to 3D island growth with increasing  $\alpha$  value owing to the increase of an adsorption probability at TS.

The number of layers required for annihilation of APDs is shown in Fig. 6. The number required increases with increasing  $\alpha$  value because an adsorption probability at ES becomes large with  $\alpha$ . The required number of layers for  $\alpha=0.9$  is about 1800 layers, which corresponds to 3C-SiC epilayers of 250 nm thick. However, this result does not coincide with the fact that APD free epilayer could not be obtained in APCVD case, though  $\alpha=0.9$  is larger than the sticking coefficient of  $\text{SiH}_2$  radical reported [7], which is main species in APCVD case. Regarding the disagreement, two reasons can be pointed out. One is the problem of used  $100 \times 100$  lattice size for simulation. Since APB is considered to propagate along  $\langle 111 \rangle$  direction when an APD annihilates, the minimum number of layers corresponding to about half size of an

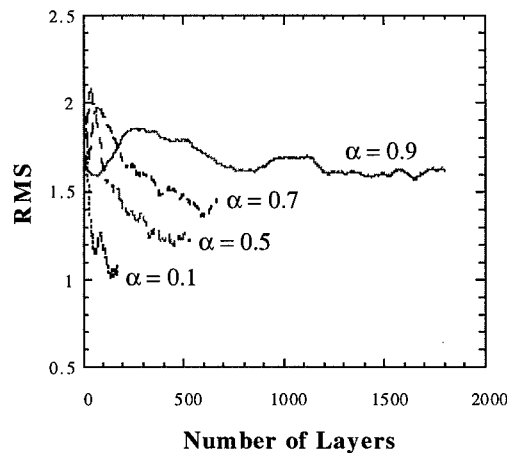


Fig.4. The change of RMS of the surface roughness with the number of growth layers.

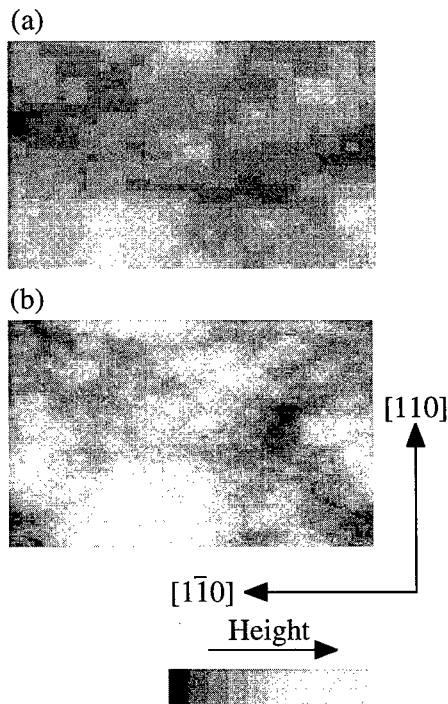


Fig.5. Snapshots of the surface structure: (a)  $\alpha=0.01$  and after growth of 62 layers; (b)  $\alpha=0.5$  and after growth of 169 layers.



APD length is required to annihilate the antiphase domain. Therefore, initial size of an APD is important, though the size is limited by a computer resource. The lattice size we used was not large enough to emulate the real growth of epilayers. The other is the influence of twins. Bahng *et al.* have pointed out the possibility that the annihilation of APDs is interrupted at twin boundaries [8]. The existence of twin is not considered in our model. Although our model is short of quantitative precision, the result obtained from the simulation based on our model is in good agreement with the tendency of our experiments, i.e., annihilation of APDs occurs at thinner thickness in LPCVD case compared with APCVD case. Our proposed model is considered to be qualitatively appropriate.

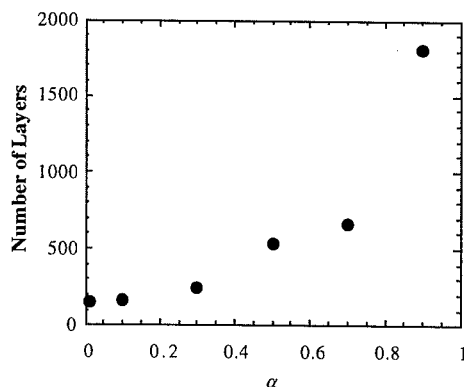


Fig.6. The number of layers required for annihilation of APDs.

#### 4. CONCLUSION

We have proposed the APD annihilation model of 3C-SiC hetero-epilayer on Si(100) substrate. Generally, Si-Si bonds occur preferentially compared with C-C bonds or the contrary case occurs at APB, and APB propagates along  $\langle 111 \rangle$  direction. If the Si species adsorb at ES earlier than they adsorb at IS, APBs propagate along  $\langle 110 \rangle$  direction. The effect on the difference of main species is taken in our model by changing the sticking coefficient ( $\alpha$ ) of each adsorbed site. It was found that surface becomes rough with increasing  $\alpha$  value at TS and the number of layers required to annihilate APDs increases with increasing  $\alpha$  value at ES. These results qualitatively coincided with experimental results, which confirm the validity of our model proposed.

#### 5. REFERENCES

- [1] Y. Ishida, T. Takahashi, H. Okumura, S. Yoshida and T. Sekigawa : Jpn. J. Appl. Phys. **36** (1997) 6633.
- [2] T. Takahashi, Y. Ishida, H. Okumura, S. Yoshida and T. Sekigawa : Materials Science Forum. **264-268** (1998) 207.
- [3] Y. Ishida, T. Takahashi, H. Okumura, S. Yoshida and T. Sekigawa : Materials Science Forum. **264-268** (1998) 183.
- [4] Y. Ishida, T. Takahashi, H. Okumura, S. Yoshida and T. Sekigawa : Fall Meeting of Japanese Applied Physics (1996) 8a-ZK-8. (in Japanese)
- [5] M. Kitabatake and J. E. Greene : Jpn. J. Appl. Phys. **35** (1996) 5261.
- [6] Stephen Wolfram, *Cellular Automata and Complexity, Collected Papers* (Addison-Wesley, Reading, MA, 1994).
- [7] L-S. Hong, S. Misawa, H. Okumura and S. Yoshida: Inst. Phys. Conf. Ser. No.137 (1994), p. 239.
- [8] W. Bahng, H. Matsuhata, T. Takahashi, Y. Ishida, H. Okumura, S. Yoshida, H. Sawada and H. Ichinose: Eleventh International Conference on Microscopy of Semiconducting Materials (1999) F5.

## Improvement of 3C-SiC Surface Morphology on Si(100) by Adding HCl using Atmospheric CVD

Y. Chen, Y. Masuda, C. Jacob, T. Shirafuji and S. Nishino

Department of Electronics & Information Science, Faculty of Engineering & Design,  
Kyoto Institute of Technology, Matsugasaki, Sakyo-Ku, Kyoto 606-8585, Japan

**Keywords:** 3C-SiC/Si, AFM, Anti-Phase Domain, Heteroepitaxial Growth, Surface Morphology

**Abstract:** 3C-SiC films have been grown on carbonized Si(100) using HMDS at 1350°C. The surfaces of SiC films were very rough and a number of ridges were observed. The ridges were distributed over the surface probably along [110] and  $\bar{1}\bar{1}0$  directions. The surface of the carbonization layer at 1350°C for 3min was characterized by AFM. The AFM result revealed many voids or grooves existing in carbonized layer. we think the reason of ridge growth results from the existence of grooves, because the CVD growth is controlled by diffusion process at the high temperature of 1350°C, a high supersaturation of source gas occurred at knees of inhomogeneity of grooves. The growth rate at knees of grooves was very high so that many ridges appeared on the surface of SiC films. By adding appropriate amount HCl gas to CVD process, ridges can be removed due to a high HCl supersaturation at knees of grooves and the surface of SiC films became flatter compared with the growth using HMDS alone.

### Introduction

SiC possesses large energy gap, high electron mobility, high breakdown field, high saturation drift velocity, temperature stability and chemical inertness. These excellent physical properties make 3C-SiC a promising material for high-temperature microsensors and microactuators. Due to large lattice mismatch(about 20%) and thermal expansion coefficients mismatch(8%) between 3C-SiC and Si, defects such as misfit dislocations, anti-phase boundaries (APBs) and anti-phase domains (APDs) exist in the 3C-SiC films. For SiC heteroepitaxy, APCVD method has been widely used. However, it is known that problems exist in the APCVD epilayers, such as nonuniform thickness and rough surface of epilayers, to result in poor electrical properties of the SiC films.

We had reported the growth of single crystalline 3C-SiC films on Si(100) using  $\text{Si}_2(\text{CH}_3)_6 + \text{H}_2$  gases by APCVD[1-2]. In this work, we place emphasis on the improvement on the surface morphology by adding HCl to the growth process.

### Experiments

3C-SiC films were grown on on-axis Si(100) substrates in an air-cooled quartz tube(ID: 50mm) with horizontal geometry and heated by rf induction. The source gas was  $\text{Si}_2(\text{CH}_3)_6$  (HMDS) and the carrier gas was  $\text{H}_2$  with a flow rate of 2.5 slm. HMDS flow rate was controlled by bubbling  $\text{H}_2$  through the liquid HMDS. The deposition procedure consisted of three processes,

which were in-situ etching by HCl, carbonization process and single crystal growth at 1350°C. The deposition times were 5min and 1 hour. After finishing the carbonization, the propane was shut off and the deposition process was initiated by introducing HMDS at a flow rate of 0.5sccm and adding HCl simultaneously. The films were characterized by XRD and the only presented SiC (200) peak. The growth rates monitored by intensity variation of reflected He-Ne laser did not change significantly by addition HCl to the CVD process. Epilayers with and without HCl addition were compared. The resulting film surfaces were all mirror-like. The morphology and microstructure of SiC films were characterized by Nomarski optical microscopy, X-ray diffraction (XRD) and atomic force microscopy (AFM).

## Results and discussion

The microstructures of the film surfaces for 1 hour growth characterized by AFM are shown in Fig.1. As shown in Fig.1a, with no HCl addition, the surface was very rough and a

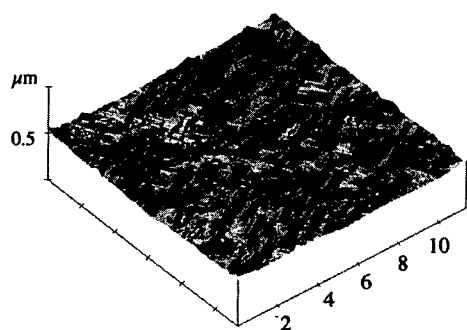


Fig.1a

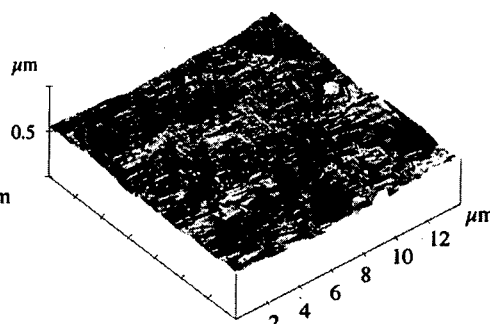


Fig.1b

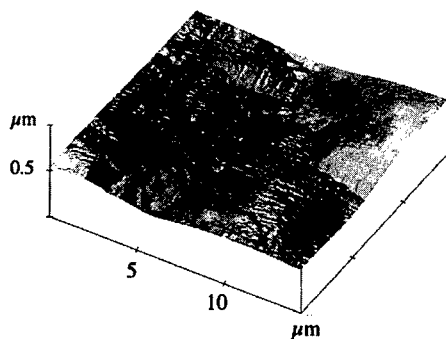


Fig.1c

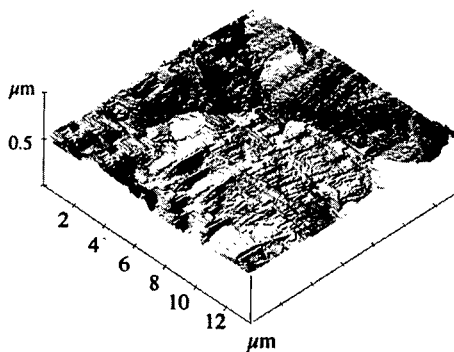


Fig.1d

Fig.1 The microstructures of the SiC surface morphologies on Si(100)

- a). without adding HCl;    b). with adding 1sccm HCl  
c). with adding 2sccmHCl; d). with adding 4.2sccm HCl

number of ridges were observed. The size of ridges are about 1.3μm in length and 0.2μm in width and 0.04μm in height. The ridges were distributed over the surface probably along [110] and  $\bar{1}\bar{1}0$  directions. The morphologies of the epilayer grown on (100) substrate for 1 hour growth by adding HCl are shown in Fig.1b-d. Growth using HMDS(0.5sccm)+ HCl (1sccm) at 1350°C produced the

profile of the film surface shown in Fig.1b. The density of ridges diminished and the boundaries of domain-like boundary could be observed. They may be APDs. When HCl gas was increased to 2 sccm, the film surface became flatter than with 1sccm HCl as shown in Fig. 1c. The boundaries could be observed as in the case of addition of 1sccm HCl. As shown in Fig. 1d, when HCl was increased further up to 4.2sccm, the film surface became rough and pits appeared on the surface.

Based on these facts, we believe that the appearance of ridges probably results from the  $\{111\}$  faceted pits, which are one of the major defects in the carbonization process[3]. The surface of the carbonized layer at 1350°C for 3min by AFM is shown in Fig.2, where many voids exist. The control of the void formation will be investigated farther. Rough square and rectangular pits exist in the carbonized layer with hills and valleys. In general, carbonization is normally performed in a hydrocarbon atmosphere, a very thin epitaxial SiC layer is formed by the consumption of Si atoms in the substrate and a lot of hollow pits with  $\{111\}$  planes present in the carbonized substrate. In most cases a continuous SiC film covers the voids but a careful investigation by AFM revealed that some voids emerge at the surface of carbonized layer, particularly in the valley part of the carbonized layer as shown in Fig. 2. The carbonized layer consists of peaks and grooves as revealed by the section analysis of AFM. When the SiC CVD growth occurs on such a carbonized layer, since the CVD growth is controlled by diffusion process at the high temperature of 1350°C, the knee of the inhomogeneity on the  $\{111\}$  faceted pits is highly supersaturated, while supersaturation was low in the groove of the pit. As a result, pronounced ridges occurred at the boundaries of the pit walls, similar to those in the growth of Si epitaxial layers on the Si substrate[4]. These ridges are oriented in  $\langle 110 \rangle$  directions, identical to the pit edges.

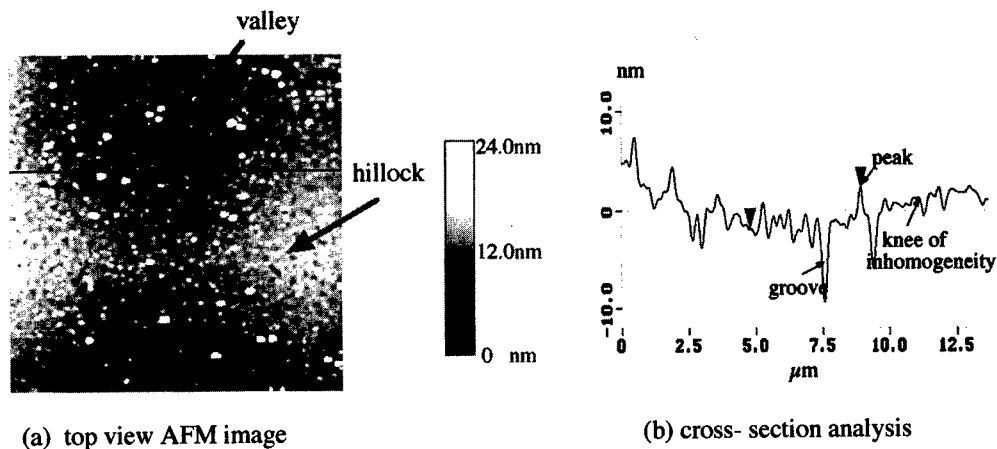


Fig.2. The top view AFM image with cross-section analysis of the carbonization layer on Si(100) for 3min at 1350°C

Fig.3 shows the surfaces of SiC films of AFM images with 0sccm and with 2sccm HCl addition for 5min growth. As shown in Fig.3a, a number of small ridges appear on the surface along  $[110]$  and  $\bar{[110]}$  directions. However, when 2sccm HCl was added, the density of the ridges decreased and the size of the ridges became smaller. since the ridge growth can be suppressed by the high supersaturation of HCl at the knee of inhomogeneity, the ridges on the SiC surface can be diminished, and so the surface of SiC films becomes flatter.

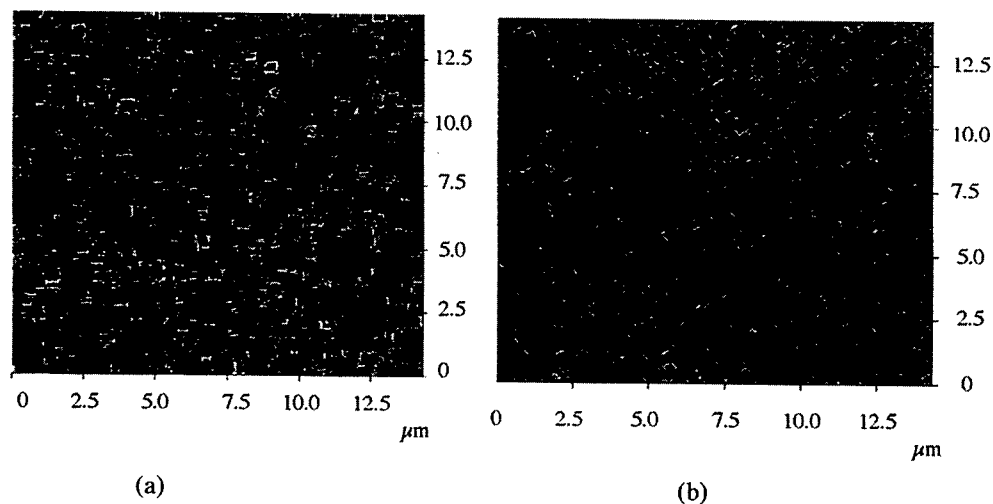


Fig.3. The top view AFM images of SiC films on Si(100) after 5min growth at 1350°C  
(a) with no HCl addition, (b) with 2sccm HCl addition

Above results indicate that the growth using HMDS+HCl at 1350°C occurs by competing processes of etching and growth. The growth rate at the knee of inhomogeneity is high but the ridges are etched faster due to the higher HCl supersaturation as compared with the base of groove. At the base of groove, the growth rate is low but the etching rate is also very low. Eventually, the etching is faster so that a lot of etch pit occur on the surface and the film surface becomes rough. The ridges on the films disappear by adding the proper amount of HCl and the film surface becomes flatter, but the APBs and APDs still exist in the films. The sizes of APDs seem to be wider compared with the growth using HMDS alone. With increasing growth time, the APDs become more larger and the resulting surface of SiC films can be improved after adding the proper amount of HCl.

## Conclusion

Based on AFM analysis, the ridge growth on the SiC surface maybe result from the rough carbonization layer with peaks and voids or grooves. In a diffusion controlled case, the knee of inhomogeneity has a supersaturation of source gas so that the ridges can be created in the surface of SiC films. By the addition of proper HCl, SiC films grow on the carbonized layer at 1350°C, and inhomogeneity. It is valid to add appropriate of HCl to the CVD process for improvement of 3C-SiC surface morphology on Si(100) at high temperature.

## References:

- [1] K. Takahasi, S. Nishino, J. Saraie, J. Electrochem. Soc. 139(1992) 3565-3571
- [2] Y. Chen, K. Matsumoto, Y. Nishio, T. Shirafuji, S. Nishino, 2nd European Conference on Silicon Carbide and Related Materials, Montpellier, France, Materials Science and Engineer, B(56) (1999)
- [3] J. P. Li and A. J. Steckl, J. Electrochem. Soc. 142 (1995) 634-641
- [4] J. Bloem and L. J. Giling, Current Topics in Material Science, Volume 1, edited by E. Kaldis, North-holland Publishing Company, 1978, Chemical vapour deposition of silicon, p300-303

## Carbonization on (100) Silicon for Heteroepitaxial Growth of 3C-SiC

Hideki Shimizu and Takaomi Ohba

Department of Technology, Aichi University of Education,  
Hirosawa, Igaya-cho, Kariya, Aichi 448-8542, Japan

**Keywords:** Carbonization, Desorption, Epitaxial Growth, Plasma-Assisted CVD, Substrate Bias, Substrate Temperature, Surface Defects

**Abstract:** To reproducibly obtain the single-crystalline 3C-SiC film on (100)Si, a carbonization process has been carefully investigated. Prior to carbonization, Si surfaces are covered with carbon sources by holding the temperature of the Si substrate at the range of hydrogen desorption temperature so that covering Si surface with amorphous carbon films prevents the Si atoms from blowing out from surface defects on Si and the reproducible carbonized layers were obtained. Si surfaces are covered with amorphous carbon films at 600°C which are crystallized by out-diffusion of Si atoms at the carbonization temperature, with increasing the carbonization time. At substrate temperatures below 1000 °C the substrate bias is an effective tool for supplying carbon sources.

### 1. Introduction

Heteroepitaxial growth of 3C-SiC on Si substrate has been a promising method for obtaining large area 3C-SiC. Due to the large mismatch in lattice constant and thermal expansion coefficient between 3C-SiC and Si, considerable efforts were devoted to improving the film quality. Recently many workers have pointed out an importance of carbonization, preparations for Si surfaces prior to growing and an initial growth step[1-3]. A single-crystalline 3C-SiC film on (100)Si was grown at relatively low substrate temperature by AC-plasma assisted CVD [4]. However, the films sometimes included a twin crystal and a polycrystal. In this work, to reproducibly obtain the single-crystalline 3C-SiC film on (100)Si, we have paid careful attention to the carbonization process.

### 2. Experimental Procedures

Carbonization on Si was carried out at the substrate temperature between 700°C and 1100°C by using  $C_3H_8$  gas. (100)Si wafer ( $20 \times 20 \text{ mm}^2$ ) was degreased in acetone and dipped in 12%-HF solution and was immediately set on graphite susceptor in AC plasma-assisted CVD system [5]. After evacuating the system up to  $2 \times 10^{-6}$  Torr by a turbo molecular pump,  $H_2$  was introduced up to 60 Torr and a hydrogen plasma was excited at a room temperature.  $C_3H_8$  diluted to 5% in  $H_2$  at flow rate of 5 sccm were passed through the hydrogen plasma and supplied to the Si substrate prior to heating-up the Si substrate. The heating-up of the Si substrate was examined in two different ways as shown in Figure 1. Type I is the way of heating the Si substrate up to the carbonization temperature at a heating rate of 10-20°C/sec. Type II is the way of keeping the Si substrate at 600°C (L-type:L) or 750°C (H-type:H) for 5 or 10 min, before heating up to carbonization temperature. The microstructures of the films were examined by a reflection electron diffraction (RED) and the thickness of the films was measured by an ellipsometer. Ellipsometric measurements in this work were carried out under the conditions as follows. The wavelength of the incident beam was 6328 Å and the incident angle was 45 degree. In this condition, the ellipsometric measurement data ( $\Delta$ ,  $\Psi$ ) for optical stable thermal oxide film (900Å) was measured during 2 hours and standard deviations of  $\Delta$  and  $\Psi$  were 0.02 degree and 0.01 degree. The beam spot size was about 1 mm in diameter. 100 points in the area of 10 mm x 10 mm of the sample were measured. Simple one layer model was applied to the analysis in this work. An optical constant (n, k) of the Si substrate for the ellipsometric analysis was used by

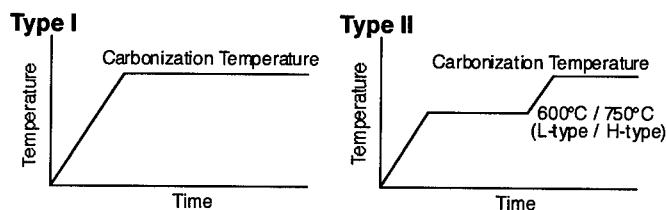


**Figure 1.** Temperature program for carbonization process. L-type and H-type indicates 600°C and 750°C in the substrate temperature held prior to heating up to carbonization temperature.

measuring  $\Delta$  and  $\Psi$  of the Si substrate after cleaning. An average  $\Delta$  and  $\Psi$  were 179.21 degree and 35.13 degree respectively. From these values, the optical constant ( $n, k$ ) of the Si substrate was decided as  $n=4.119$  and  $k=0.154$ . The standard deviation of  $\Delta$  and  $\Psi$  in the 100 points of the Si substrate were 0.088 degree and 0.053 degree respectively. The Si substrate after HF treatment was stable in the air for 1 hour because the standard deviation of  $\Delta$  and  $\Psi$  for the Si substrate were 0.02 degree and 0.02 degree for 1 hour after HF treatment.

### 3. Result and Discussion

Figure 2 shows changes in measured  $\Delta$  and  $\Psi$  values and the results of RED patterns of the films deposited by Type I and Type II respectively. Theoretical lines in these figures were calculated by using simple one layer model on Si. Typical RED patterns of the films deposited in this work are shown in Figure 3. For samples deposited below 950 °C by Type I, ones which showed streaks originated from a (100)Si surface in the RED pattern had the  $\Delta$  values of greater than that of the Si substrate and others which showed a halo in the RED pattern had the  $\Delta$  values of less than that of the Si substrate. The changes in the  $\Psi$  values are supposed to show a roughness of Si surface because of including 3D spots in the Si streaky pattern. No films on Si are deposited below 950 °C except the films deposited above ten min with plasma. For samples deposited at 1000 °C by Type I, the RED patterns showed a halo, a halo with diffused spots originated from single domain 3C-SiC, diffused spots or diffused spots with satellite spots originated from a twin phase. Consequently, the  $\Delta$  and  $\Psi$  values extremely change. For samples deposited at 1100 °C by Type I, the RED patterns showed diffused spots originated from single domain 3C-SiC or diffused spots with satellite spots originated from the twin phase as shown in Figure 3 (e) and the  $\Delta$  and  $\Psi$  values approach the theoretical line for 3C-SiC single-crystal ( $n=2.65$ ,  $k=0$ ). From these results, it is supposed that  $C_3H_8$  starts to be thermally decomposed from 950°C and Si atoms blow out abruptly from surface defects on Si at 1000° C. The blowing out of Si atoms from surface defects on Si at greater than 1100°C must be superior to the thermal decomposition of  $C_3H_8$  so that the films deposited on Si often include twin crystals. It is suggested that even if carbon is supplied enough, the blowing out of Si atoms from surface defects on Si takes place at temperatures of greater than 1000°C and reproducible carbonized layers are not obtained by using type I.

It has been well known that the Si surfaces dipped in HF solution are terminated by hydrogen and the Si surfaces are stable. An desorption of hydrogen from Si surfaces deposited by an epitaxial growth using  $SiH_4$  is observed at the range of the temperature from 425 °C to 675 °C [6]. Therefore, to prevent Si atoms from blowing out from surface defects on Si, the Si surface prior to the carbonization are expected to be covered with carbon sources from the plasma by using Type II. 600°C (L) and 750°C (H) in the substrate temperature were examined to cover Si surfaces with amorphous carbon films. To decompose  $C_3H_8$  at low substrate temperature of 600°C and 750°C, the carbonization process by Type II was carried out by using the plasma. For samples deposited at 1000 °C by Type II, the RED patterns showed a halo, characteristic for an amorphous film deposited on Si. The  $\Delta$  and  $\Psi$  values were almost in the region of less than those of Si substrate where extinction coefficient ( $k$ ) is zero, except sample deposited by L-type with substrate bias (LB) whose  $\Delta$  and  $\Psi$  values lay on theoretical line of a-C film ( $n=2.95$ ,  $k=0.42$ )[7]. As compared with the results of Type I, these results suggest that amorphous carbon films cover the Si surfaces and prevent Si atoms from blowing out from surface defects on Si. For samples deposited at 1050 °C by Type II, the RED patterns

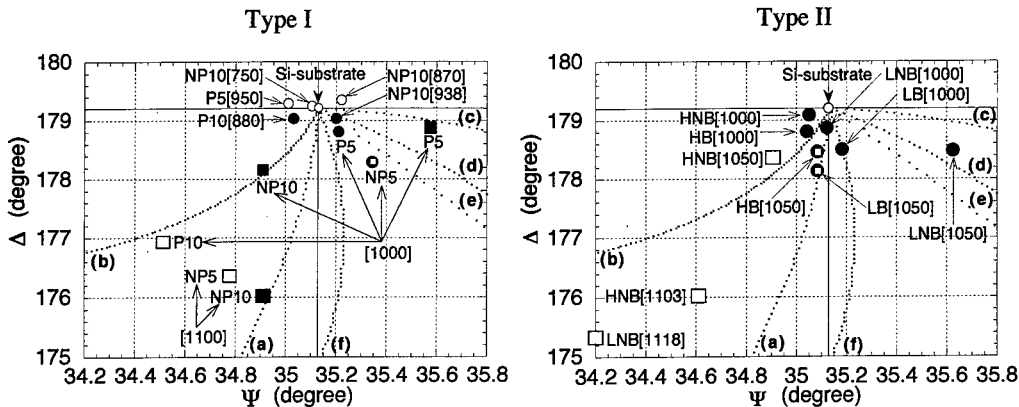


**Figure 2.** Changes in measured  $\Delta$  and  $\Psi$  values and the results of RED patterns of the films deposited by Type I and Type II. Theoretical lines indicate (a)  $n=2.65$ ,  $k=0$  for 3C-SiC, (b)  $n=3.6$ ,  $k=0$ , (c)  $n=4.1$ ,  $k=1$ , (d)  $n=3.6$ ,  $k=1$ , (e)  $n=2.86$ ,  $k=1.73$  for graphite, (f)  $n=2.95$ ,  $k=0.42$  for a-C respectively and one dot indicates  $2\text{\AA}$ .

○: Si-streak, ●: halo, ◐: halo and 3C-SiC diffused spot, □: 3C-SiC diffused spot, ■: 3C-SiC diffused spot with 3C-SiC satellite spot.

P and NP indicate with and without plasma and continuous numbers indicate carbonization time. H and L indicate H-type and L-type respectively. B and NB indicate with and without substrate bias. Continuous number in the bracket indicate carbonization temperature. A carbonization time is 10 min in Type II.

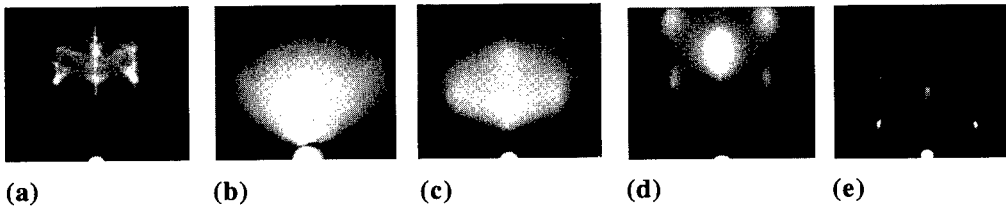


**Figure 3.** Typical RED patterns of the films in this work. (a), (b), (c), (d) and (e) indicate Si-streak, halo, 3C-SiC diffused spot with faint Si-streak, 3C-SiC diffused spot and 3C-SiC spot with satellite spot respectively.

showed diffused spots originated from single domain 3C-SiC with faint streaks originated from the Si surfaces and the  $\Delta$  and  $\Psi$  values lay on theoretical line of 3C-SiC single crystal ( $n=2.65$ ,  $k=0$ ), except that the RED pattern of the films deposited under L-type without substrate bias showed a halo. Consequently, the 3C-SiC films deposited at  $1050\text{ }^{\circ}\text{C}$  consist of islands[3]. For samples deposited at  $1100\text{ }^{\circ}\text{C}$  by Type II, the RED patterns showed diffused spots originated from single domain 3C-SiC. Therefore, single-crystalline 3C-SiC film without twin crystalline phase is grown even at  $1100^{\circ}\text{C}$  by using Type II. From these results, L-type and substrate bias seem to be more effective action for covering the Si surface with carbon than H-type.

The  $\Delta$  and  $\Psi$  values in Figure 2 are the average of 100 points in the area of  $10\text{ mm} \times 10\text{ mm}$ . Then, assuming that a value (D) divided the product of the standard deviation of  $\Delta$  and  $\Psi$  for the sample by that for the Si substrate indicates surface roughness of the sample, changes in the D values as a function of the substrate temperature are shown in Figure 4. The D values of the films deposited by Type II much lower than those by Type I. Therefore, It is confirmed that Type II is reproducible carbonization process.

Changes in the  $\Delta$  and  $\Psi$  values of the films deposited under the L-type as a function of the carbonization time are shown in Figure 5. The  $\Delta$  and  $\Psi$  values of the films deposited at  $950\text{ }^{\circ}\text{C}$  were in amorphous carbon region where the  $\Delta$  values are less than those of the Si substrate and the  $\Psi$  values are greater than those of the Si substrate. The  $\Delta$  and  $\Psi$  value decrease with increasing the



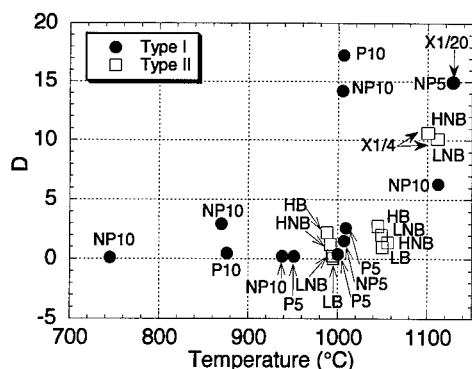


**Figure 4.** Changes in the D values as a function of the substrate temperature.

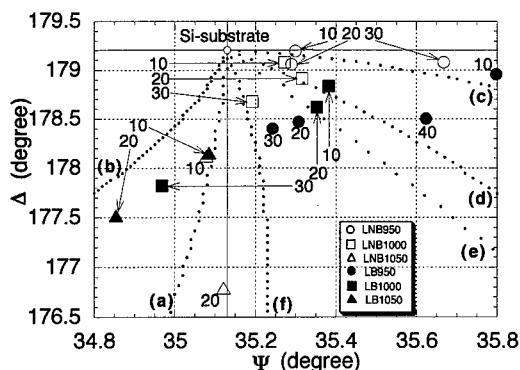


**Figure 5.** Changes in the  $\Delta$  and  $\Psi$  values of the films deposited under the L-type as a function of the carbonization time. the number in figure indicate carbonization time.

deposition time. For higher deposition time (30 min for LNB and 40 min for LB), the  $\Delta$  value become saturated and the  $\Psi$  value increases. The  $\Delta$  and  $\Psi$  values of the films deposited at 1000 °C decrease with increasing the deposition time and approach crystal region. For higher annealing times (30 min) the films become 3C-SiC single-crystal. The films deposited at 1050 °C were 3C-SiC single crystal and the thickness increases with increasing deposition time. These results suggest that the Si surfaces are covered with amorphous films at 600 °C (L-type) and the amorphous carbon films are crystallized by out-diffusion of Si atoms at the carbonization temperature with increasing the carbonization time. At substrate temperatures below 1000 °C the substrate bias seems to be an effective tool for supplying carbon sources.

#### 4. Conclusion

To reproducibly obtain the single crystalline 3C-SiC film on (100)Si, the carbonization process has been carefully investigated. It is suggested that even if carbon is supplied enough, the blowing out of Si atoms from surface defects on Si takes place at temperatures of greater than 1000 °C and reproducible carbonized layers are not obtained by using type I. It is suggested that Si surfaces are covered with carbon sources prior to the carbonization by holding the temperature of the Si substrate at the range of hydrogen desorption temperature so that the reproducible carbonized layer is obtained by using type II. To supply carbon sources to Si surfaces, the plasma and the substrate bias have an effect on decomposition of  $C_3H_8$  at low substrate temperature. From the result that the 3C-SiC films consist of islands, the optimum conditions for a high density of the nucleus generation have to be find out to reproducibly obtain good carbonization layer for heteroepitaxial growth of 3C-SiC

#### References

- [1] H. Nagasawa and Y. Yamaguchi, J. Cryst. Growth, **115**(1991), p.612.
  - [2] T. Yoshinobu, H. Mitsui, T. Fuyuki, Y. Tarui and H. Matsunami, J. Appl. Phys., **72** (1992), p.2006.
  - [3] T. Takaoka, H. Saito, Y. Igari and I. Kusunoki, Materials Science Forum, **Vols. 264-268** (1998), pp.203-206
  - [4] H. Shimizu and M. Shiga, Materials Science Forum, **Vols. 264-268** (1998), pp. 211-214
  - [5] H. Shimizu, Inst. phys. Conf. Ser., **142**(1996), pp.161-164
  - [6] C. Michael Greenlie and Michael Liehr, Appl. Phys. Lett., **Vol. 64**(1994), p.31.
  - [7] N. Savvides, J. Appl. Phys., **59**(1986), p.4133.
- Phone : 0566-26-2485 , Fax : 0566-26-2485, E-mail : hksimizu@aecc.aichi-edu.ac.jp

## Growth of 3C-SiC/Si Multilayer Heterostructures by Supersonic Free Jets

Y. Ikoma, T. Endo, T. Tada, F. Watanabe and T. Motooka

Department of Materials Science and Engineering, Kyushu University,  
6-10-1 Hakozaki, Higashiku, Fukuoka, 812-8581, Japan

**Keywords:** 3C-SiC/Si/3C-SiC/Si(100),  $\text{CH}_3\text{SiH}_3$ , Si/3C-SiC/Si(100),  $\text{Si}_3\text{H}_8$ , Supersonic free jet CVD

**Abstract.** We have investigated growths of 3C-SiC/Si multilayer heterostructures on Si(100) by supersonic free jet CVD.  $\text{CH}_3\text{SiH}_3$  and  $\text{Si}_3\text{H}_8$  gas jets were used for 3C-SiC and Si layer growth, respectively. The crystal quality of Si layers on 3C-SiC/Si(100) was found to strongly depend on the 3C-SiC surface roughness. Polycrystalline Si was grown on rough 3C-SiC layers with a thickness of 9 nm, while epitaxial Si was grown by using ultrathin ( $\approx 3$  nm) 3C-SiC layers with smooth surfaces. Epitaxial 3C-SiC/Si/3C-SiC/Si(100) heterostructures were successfully obtained on ultrathin 3C-SiC/Si(100).

### Introduction

Silicon carbide (SiC) is one of promising semiconductor materials due to the large band gap (2.2~3.3 eV). Among many polytypes of SiC, cubic SiC (3C-SiC) has a wide gap (2.2 eV) and is the only polytype which can be epitaxially grown on Si(100) substrates in spite of the large lattice mismatch (20%). Since 3C-SiC/Si(100) has a much larger conduction band offset ( $\approx 0.6$  eV) than that of  $\text{Si}_{1-x}\text{Ge}_x$  [1, 2], it may become an important material system for application of double-barrier resonant tunneling diodes (DBRTDs) to Si microelectronic devices [3]. In spite of many studies of heteroepitaxial growth of 3C-SiC on Si substrates, relatively little work has been done for growth of Si on 3C-SiC films [4, 5].

Recently, we have developed a new CVD method using pulsed supersonic free jets for ultrathin film growth by adjusting the pulse width and numbers [6,7]. In this study, we have investigated epitaxial growth of Si/3C-SiC/Si(100) and 3C-SiC/Si/3C-SiC/Si(100) heterostructures by supersonic free jet CVD of  $\text{CH}_3\text{SiH}_3$  and  $\text{Si}_3\text{H}_8$ .

### Experimental

The growth chamber was equipped with turbomolecular and mechanical pumps and had a base pressure of  $\sim 10^{-8}$  Torr. The details are described elsewhere [6,7]. Si(100) wafers were cleaned by the conventional RCA method. The substrates were introduced into the chamber immediately after being dipped in aqueous 5% HF solution. Electronic grade  $\text{CH}_3\text{SiH}_3$  and He-diluted 4%  $\text{Si}_3\text{H}_8$  were used for 3C-SiC and Si growth, respectively. These gases were introduced into the chamber using a General Valve with a nozzle diameter of 0.8 mm. The source pressure of the valve was 760 Torr at room temperature. The pulse frequency was set at 10 Hz. The pulse widths were 130  $\mu\text{s}$  for  $\text{CH}_3\text{SiH}_3$  and 140  $\mu\text{s}$  for  $\text{Si}_3\text{H}_8$ . The distance between the substrate and valve is approximately 20 cm. At first, the Si substrate was heated at 900 °C and 3C-SiC layer was formed by irradiating

$\text{CH}_3\text{SiH}_3$  jets. The thickness and surface roughness of the 3C-SiC films were proportional to the  $\text{CH}_3\text{SiH}_3$  pulse number up to 18000 at the substrate temperature of 900 °C [7]. Subsequently, the substrate temperature was decreased to 700 °C and Si layer was grown by irradiating  $\text{Si}_3\text{H}_8$  jets onto the 3C-SiC layer. In case of 3C-SiC/Si/3C-SiC layer growth, the substrate was heated again at 900 °C and  $\text{CH}_3\text{SiH}_3$  jets were supplied after growing Si/3C-SiC/Si(100) structure. The obtained samples were mainly characterized by cross-sectional transmission electron microscopy (XTEM).

### Results and discussions

Figure 1 shows the XTEM bright-field image and diffraction pattern of the sample grown by 3000 pulse irradiation of  $\text{CH}_3\text{SiH}_3$  and  $\text{Si}_3\text{H}_8$  jets. The diffraction pattern indicates that 3C-SiC film is epitaxially grown on Si(100), while polycrystalline Si is grown on 3C-SiC. From the bright-field image, the thicknesses of 3C-SiC and surface Si are 9 and 30 nm, respectively. The surface Si layer forms polycrystalline islands and includes planar defects. This can be attributed to the fact that the interface between the 3C-SiC and Si layers are rough with a root-mean-square (RMS) roughness of 0.9 nm measured by the AFM images of  $5 \times 5 \mu\text{m}^2$  scan [7]. There exists a {111} faceted pit with a size of 80 nm near the interface in the Si substrate.

When the  $\text{CH}_3\text{SiH}_3$  pulse number was reduced to 900 and the  $\text{Si}_3\text{H}_8$  pulse number was increased to 4500, it was found that single-crystal Si was epitaxially grown on 3C-SiC/Si(100). Figure 2 shows the XTEM dark-field image and diffraction pattern of the sample. The diffraction spots indicate that the surface Si layer is epitaxially grown on 3C-SiC and includes {111} twins. The thicknesses of the 3C-SiC and Si layers are 3 and 60 nm, respectively. Although there exists {111} planar defects in the surface Si layer, the crystal quality is much improved. This improvement can be attributed to the reduction of the 3C-SiC surface roughness since RMS roughness of the 3C-SiC layer decreased to 0.4 nm at  $\text{CH}_3\text{SiH}_3$  pulse number of 900 [7].

We grew the 3C-SiC/Si/3C-SiC/Si(100) structures using ultrathin ( $\leq 3$  nm) 3C-SiC for the bottom layer and the dependence of the morphology of the top 3C-SiC on the middle Si layers was examined. The middle Si layer was predominantly composed of islands when it was grown by  $\text{Si}_3\text{H}_8$  jets of 1800 pulses, and thus no further SiC growth was attempted. The top 3C-SiC layer was inhomogeneously grown on the middle Si layer at the  $\text{Si}_3\text{H}_8$  pulse number of 3000, whereas continuous 3C-SiC layer was formed at 6000 pulses of  $\text{Si}_3\text{H}_8$  jets. Figure 3 shows XTEM bright-field image and diffraction pattern of the samples grown by 6000 pulses of  $\text{CH}_3\text{SiH}_3$  jets irradiation after 600 pulses of  $\text{CH}_3\text{SiH}_3$  jets and 6000 pulses of  $\text{Si}_3\text{H}_8$  jets. The bright-field image shows that the trilayer is clearly formed on the Si(100). The thicknesses of the bottom 3C-SiC, middle Si and top 3C-SiC layers are 3, 80 and 12 nm, respectively. Although the diffraction pattern shows that each layer is epitaxially grown on Si(100), the top 3C-SiC layer is rough due to the roughness of the middle Si layers.

Although the SiC/Si multilayer can epitaxially grow on Si(100) using ultrathin 3C-SiC, the middle Si layer is too thick to apply it in DBRTDs. The high-resolution TEM observations of Si/3C-SiC/Si(100) indicates that there exist transition regions with a thickness of  $\approx 1$  nm at the both interface between 3C-SiC and Si in addition to misfit dislocations in 3C-SiC layer [8]. It is necessary to utilize pseudomorphic growth of very thin ( $\approx 1$  nm) 3C-SiC films in order to fabricate epitaxial 3C-SiC/Si multilayer formations.



Fig. 1 XTEM bright-field image and diffraction pattern obtained from the sample grown by 3000 pulses of  $\text{CH}_3\text{SiH}_3$  and  $\text{Si}_3\text{H}_8$ .



Fig. 2 XTEM dark-field image and diffraction pattern of the sample grown by 900 and 4500 pulses of  $\text{CH}_3\text{SiH}_3$  and  $\text{Si}_3\text{H}_8$ , respectively.



Fig. 3 XTEM bright-field image and diffraction patterns of the sample grown by 600/6000/6000 pulse irradiations of  $\text{CH}_3\text{SiH}_3/\text{Si}_3\text{H}_8/\text{CH}_3\text{SiH}_3$  gas jets.

### Conclusion

We have investigated the growth of 3C-SiC/Si multilayer heterostructures by supersonic free jets of  $\text{CH}_3\text{SiH}_3$  and  $\text{Si}_3\text{H}_8$ . The crystal quality of Si layers on 3C-SiC was affected by the 3C-SiC surface roughness. Polycrystalline Si was grown on rough 3C-SiC films with a thickness of  $\sim 9$  nm. Epitaxial Si/3C-SiC/Si(100) and 3C-SiC/Si/3C-SiC(100) heterostructures were achieved using ultrathin ( $\approx 3$  nm) 3C-SiC films. It is essential to grow very thin ( $\approx 1$  nm) 3C-SiC films in order to fabricate DBRTDs using 3C-SiC/Si multilayers.

### Acknowledgment

The authors gratefully appreciate the help of Per Persson at Linköping University, Sweden for high-resolution TEM observation.

### References

- [1] H. C. Liu, D. Landheer, M. Buchanan, and D. C. Houghton, *Appl. Phys. Lett.* **52** (1988) 1809.
- [2] K. Ismail, B. S. Meyerson, and P. J. Wang, *Appl. Phys. Lett.* **59** (1991) 973.
- [3] E. R. Brown, in *Heterostructures and Quantum Devices* (Academic Press, 1994) p. 305.
- [4] Q. Wahab, L. Hultman, I. P. Ivanov, M. Willander, and J-E. Sundgren, *J. Mater. Res.* **10** (1995) 1349.
- [5] L-O. Björketun, L. Hultman, O. Kordina, and J-E. Sundgren, *J. Mater. Res.* **13** (1998) 2632.
- [6] Y. Ikoma, T. Endo, F. Watanabe, and T. Motooka, *J. Vac. Sci. Technol. A* **16** (1998) 763.
- [7] Y. Ikoma, T. Endo, F. Watanabe, and T. Motooka, *Jpn. J. Appl. Phys.* **38** (1999) L301.
- [8] Y. Ikoma, T. Endo, F. Watanabe, and T. Motooka (unpublished).

## Formation of High Quality SiC on Si(100) at 900°C using Monomethylsilane Gas-Source MBE

H. Nakazawa<sup>1</sup>, M. Suemitsu<sup>1</sup> and S. Asami<sup>2</sup>

<sup>1</sup> Research Institute of Electrical Communication, Tohoku University,  
Katahira 2-1-1, Aoba-ku, Sendai, 980-8577, Japan

<sup>2</sup> Department of Electronics Engineering, Sendai National College of Technology,  
Kitahara 1, Aoba-ku, Sendai, Japan

**Keywords:** Gas-Source Molecular Beam Epitaxy, Monomethylsilane, Si Outdiffusion, Surface Hydrogen

**Abstract** We have conducted a systematic series of 3C-SiC/Si(100) gas-source MBE experiments using monomethylsilane (MMS:  $\text{H}_3\text{Si-CH}_3$ ), and have obtained growth-temperature and MMS-pressure dependences of the grown film. As a result, an optimum growth temperature was found to exist for each pressure, which decreased with decreasing pressure. The low temperature degradation of the film is related to residual surface hydrogen termination as suggested from  $\text{H}_2$ -temperature-programmed-desorption observations from MMS-adsorbed Si(100) surfaces. The high temperature degradation is understood by the onset of Si outdiffusion from the substrate into the film. A balance between these two competing processes accounts for the presence of the optimum growth temperature and its pressure dependence as well.

### 1. Introduction

Heteroepitaxy of SiC on Si has been a hot issue in SiC epitaxy since it forms a solution to overcome the problem of micropipes in present SiC wafers. SiC/Si heteroepitaxy at high temperatures, however, suffers from the formation of voids in the Si substrate at the SiC/Si interface as well as dislocations in the grown SiC films [1]. Lowering the SiC growth temperature, therefore, is of crucial importance in fabricating devices using SiC/Si heterostructures. In the conventional methods, however, growth below 1000°C resulted in unwanted incorporation of Si microcrystals in the film, which has determined the lower limit of the growth temperature. This has been understood by insufficient decomposition of C-source molecules at low temperatures, which causes insufficient formation of Si-C bonds in the film. In this respect, monomethylsilane ( $\text{H}_3\text{Si-CH}_3$ ; MMS) has attracted much attention in that the molecule already contains a Si-C bond in itself and has the same stoichiometry as of SiC crystal. Recent low pressure CVD experiments using MMS have successfully grown 3C-SiC films on Si(100) at 900-1000°C [2,3]. With an aim of elucidating its growth kinetics in more detail, we have conducted in this study a systematic series of 3C-SiC/Si(100) gas-source MBE growth experiments using MMS, and have obtained the growth-temperature ( $T$ ) and the MMS-pressure ( $P$ ) dependences of the grown film quality. Based on the results, the role of surface hydrogen in the growth kinetics will also be discussed.

### 2. Experimental

Experiments were made in an aluminum-alloy ultrahigh vacuum chamber, whose base pressure is  $\sim 5.0 \times 10^{-10}$  Torr. Samples were boron-doped Si(100) ( $\rho = 8.5\text{-}11.5 \Omega \cdot \text{cm}$ ) wafers, which were cut to  $5 \times 35 \text{ mm}^2$ . The sample preparation is identical to the one used in our previous study [3]. Monomethylsilane (99.999 %) was used as the source gas. The film quality was evaluated with atomic force microscopy (AFM), Fourier transform infrared spectroscopy (FTIR), x-ray diffraction (XRD), Auger electron spectroscopy (AES), and scanning electron microscopy (SEM). To obtain information on the surface hydrogen atoms, a temperature programmed desorption measurement (TPD) was carried out on a MMS/Si(100) surface.

### 3. Results and discussion

Figure 1 shows the temperature dependence of the root-mean-square (RMS) roughness of the

grown film, averaged from  $100 \times 100 \text{ nm}^2$  AFM scans. It indicates a presence of a minimum for each MMS pressure  $P$ . As  $P$  is reduced from  $2.0 \times 10^{-4}$  to  $5.0$  or to  $2.5 \times 10^{-5}$  Torr, the optimum temperature  $T_{\text{opt}}$  lowers from  $1100$  to  $900^\circ\text{C}$ . Simultaneously, the minimum value of the RMS also decreases, indicating the improvement of the surface morphology as a result of reduced  $P$ . Equivalently, the pressure dependence of the RMS for each temperature has a minimum, and the optimum pressure  $P_{\text{opt}}$  lowers as  $T$  decreases. This result indicates that there exists a set of optimum  $T$  and  $P$  ( $T_{\text{opt}}$ ,  $P_{\text{opt}}$ ) values for the surface morphology and that  $T_{\text{opt}}$  is an increasing function of  $P_{\text{opt}}$ .

FTIR measurements were conducted to evaluate the crystallinity of the grown films. The insert in Fig.1(b) shows the FTIR spectrum obtained from a SiC film grown at  $T=900^\circ\text{C}$  and  $P=5.0 \times 10^{-5}$  Torr. The spectrum presents a sharp transverse-optical (TO) phonon absorption peak at  $795 \text{ cm}^{-1}$ , whose position and the symmetrical lineshape indicates the presence of a high quality SiC crystal. In Fig.1 (b), the full width at half maximum (FWHM) of this TO line is plotted as a function of growth temperature. The dotted line in the figure indicates the boundary between the single- and the poly-crystalline growth of the film as determined by XRD. The FWHM behaves quite similarly as the RMS in Fig.1(a). The FWHM presents a minimum for each pressure and the optimum temperature lowers with decreasing  $P$ . Concurrently, the minimum FWHM value decreases, indicating an improvement of the grown film crystallinity with decreasing  $P$ . The chemical composition of the grown film, as obtained from AES, was also closest to the stoichiometry at the optimum condition [4]. Otherwise, it deviated to Si-rich compositions both at high and low temperatures.

To understand the growth kinetics that yields the optimum growth conditions, we investigated the desorption species from a MMS-adsorbed Si (100) surface by using scan-mass TPD. For a mass range of  $m/e=2-50$ , the only TPD spectrum that showed a peak ( $300 < T < 1000^\circ\text{C}$ ) was for  $m/e=2$ , which corresponds to  $\text{H}_2$  molecule desorption. No other desorptions were observed, species such as  $\text{CH}_x$  ( $m/e=12-16$ ),  $\text{SiH}_x$  ( $m/e=28-32$ ), or  $\text{SiH}_x\text{CH}_y$  ( $m/e=40-46$ ). I.e., none of the surface Si and C adatoms generated by the MMS adsorption desorb from the surface during growth, but they are all incorporated into the growing SiC film. Figure 2 shows the  $\text{H}_2$ -TPD spectrum. It consists of the  $\beta_1$  peak, the hydrogen desorption from Si monohydrides (SiH), and a new high-temperature peak at around  $870^\circ\text{C}$ , which we named  $\delta$  peak. The  $\delta$  peak is understood to arise from the hydrogen desorption from surface  $\text{CH}_x$  ( $x \leq 3$ ) groups [5], based on a comparison with the  $\text{H}_2$ -TPD from a hydrogenated diamond surface, whose  $\text{CH}_2$  desorption presents a peak at almost identical temperatures ( $852-897^\circ\text{C}$ ) [6-8].

The appearance of the  $\delta$  peak at  $870^\circ\text{C}$  can be related to the degradation of the SiC film grown at  $T < 900^\circ\text{C}$ . The lower curves in Figs.1(a) and 1(b) are the reproduction of the  $\delta$  peak shown in Fig.2. The rapid increase of the RMS(Fig.1(a)) and FWHM(Fig.1(b)) for  $T < 900^\circ\text{C}$  coincides with the peak temperature of the  $\delta$  peak, which suggests surface hydrogen termination as the main cause for the low-temperature degradation of the SiC film. The hydrogen termination may impede the MMS adsorption and its subsequent dissociation on the surface, and may thereby disturb the complete formation of 3C-SiC crystals. Based on this scheme, the observed degradation at higher  $P$  ( $2.0 \times 10^{-4}$  Torr) for a fixed  $T$  (i.e.  $900^\circ\text{C}$ ) is explained by an increased hydrogen coverage during high-pressure growth. The presence of the surface  $\text{CH}_x$  phase can partly be attributed to a surface segregation of the  $\text{CH}_x$  species during growth, which is evidenced from our AES depth profile measurements [4]. This  $\text{CH}_x$  surface segregation in turn accounts for the Si-rich chemical composition in the bulk of the film grown at low temperatures.

The degradation at high temperatures, on the other hand, is understood by the occurrence of Si outdiffusion into the film. Figure 3 presents the SEM image from the SiC surface grown at  $T=1200^\circ\text{C}$  and  $P=2.0 \times 10^{-4}$  Torr. The observed dark spots beneath the surface features are identified as voids in the Si substrate at the SiC/Si interface [1,9,10]. These voids are formed by Si outdiffusion from the Si substrate into the SiC film during growth. When the growth temperature was reduced to  $T=1000^\circ\text{C}$  under the same  $P$ , no voids were observed. The degradation and the Si-rich composition of the SiC film grown at high temperatures, are therefore best understood in terms of the enhanced Si outdiffusion into the film.

The degradation by reducing the MMS pressure can also be explained by Si outdiffusion. Figure 4 shows the SEM images from surfaces grown at (a)  $2.5 \times 10^{-5}$  Torr and (b)  $5.0 \times 10^{-5}$  Torr at  $T=1000^\circ\text{C}$ . The square spots observed in Fig.4(a), which corresponds to the Si voids at the SiC/Si interface, are not observed in Fig.4(b). This indicates that the degradation of the film at reduced MMS pressures is caused by Si outdiffusion into the film, which has been accelerated by the decreased deposition rate as a result of the  $P$  reduction.

Having found that the grown film degradation can be caused by both, surface hydrogen termination and Si outdiffusion, we now understand the presence of the optimum growth condition as to be caused by a balance between the two processes (Fig.5). These two are competing with each other; increasing  $T$  reduces the H termination while it enhances the Si outdiffusion, and increasing  $P$  enhances the H termination while it reduces the Si outdiffusion. The degradation at high- $T$ , low- $P$  regime, therefore, is dominated by the Si outdiffusion mechanism while the one at low- $T$ , high- $P$  regime is dominated by the H termination mechanism. The boundary between the two regimes defines the optimum growth condition ( $T_{\text{opt}}, P_{\text{opt}}$ ), along which  $T_{\text{opt}}$  is an increasing function of  $P_{\text{opt}}$ .

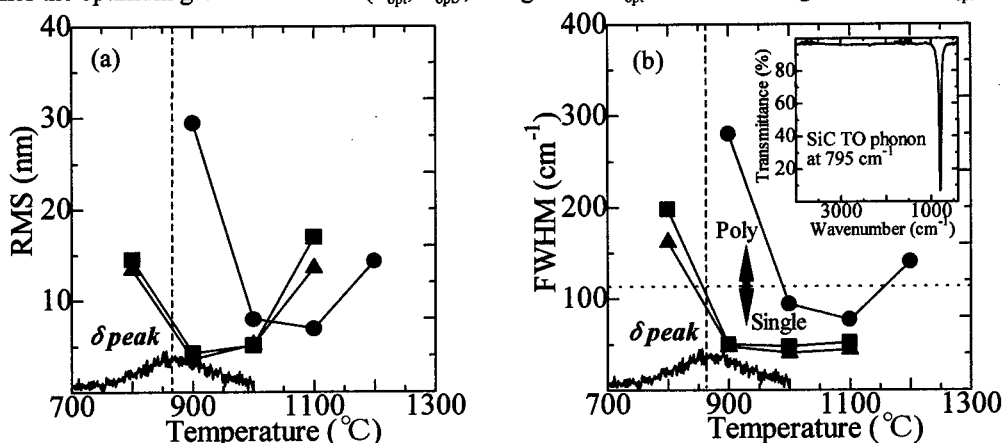


Fig.1 Growth-temperature dependence of (a) AFM root-mean-square roughness of the film surfaces and (b) full width at half maximum of the SiC TO phonon line, for  $P=2.0 \times 10^{-4}$  Torr ( $\bullet$ ),  $5.0 \times 10^{-5}$  Torr ( $\blacktriangle$ ), and  $2.5 \times 10^{-5}$  Torr ( $\blacksquare$ ). The insert in (b) is an FTIR spectrum from a SiC film at  $T=900^\circ\text{C}$ ,  $P=5.0 \times 10^{-5}$  Torr.

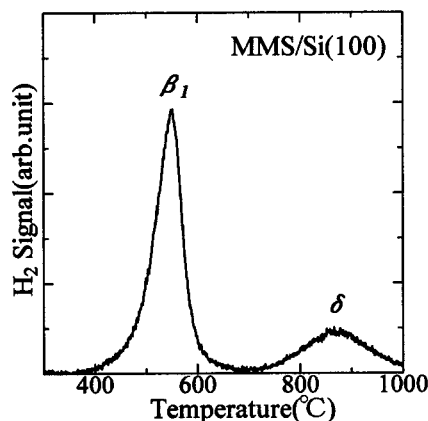


Fig.2  $\text{H}_2$ -TPD spectrum from MMS/Si(100) surface adsorbed at room temperature.

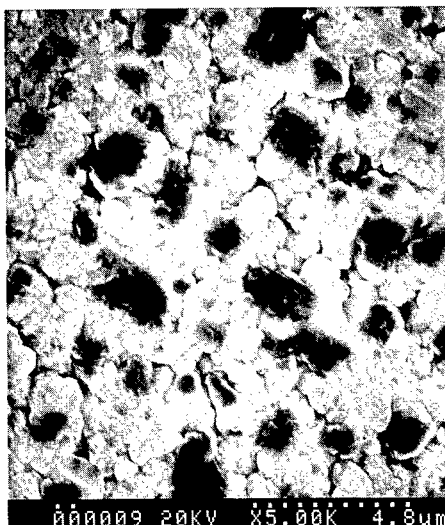


Fig.3 SEM image from a film surface grown at  $T=1200^\circ\text{C}$ ,  $P=2.0 \times 10^{-4}$  Torr.



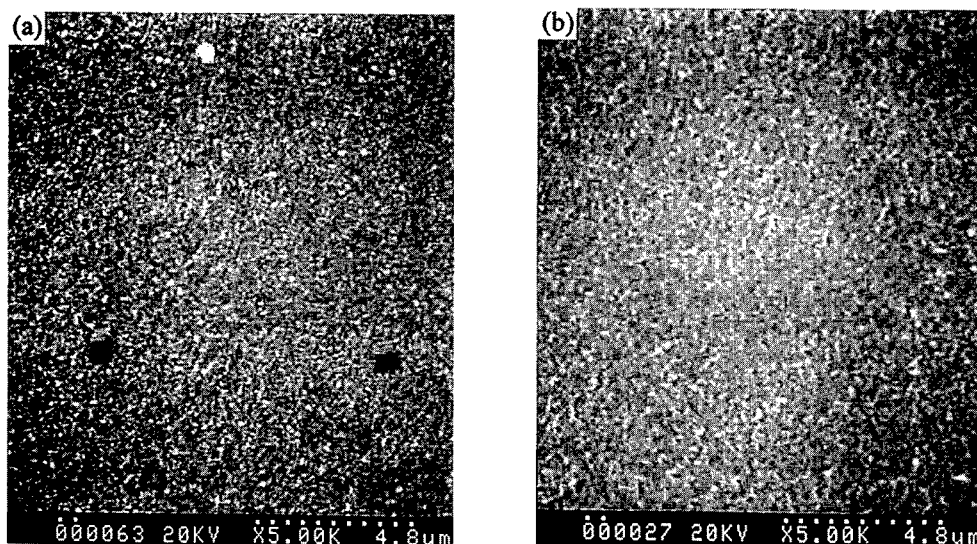


Fig.4 SEM images from film surfaces grown at  $T=1000^{\circ}\text{C}$  for (a) $P=2.5\times 10^{-5}$  Torr and (b) $5.0\times 10^{-5}$  Torr.

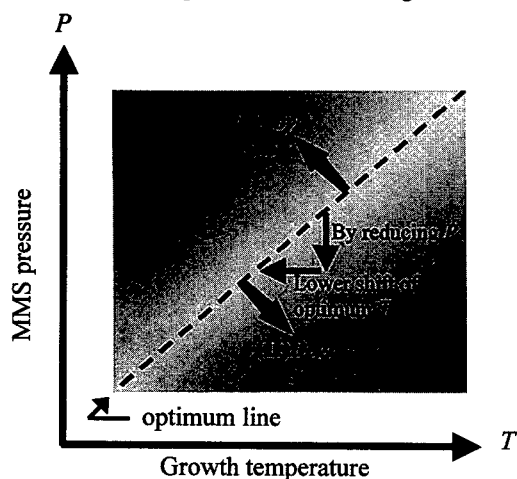


Fig.5 Growth-temperature and MMS pressure dependence of the SiC film quality

#### 4. Conclusion

We conducted a systematic series of 3C-SiC/Si(100) gas-source MBE experiments using MMS, and clarified that there exists an optimum growth temperature for the film quality for each given MMS pressure. From a comparison between the  $\text{H}_2$ -TPD spectrum from the MMS-adsorbed Si(100) surface and the temperature dependence of the film quality, it was found that the degradation of the film quality at low  $T$  is due to the surface hydrogen termination. On the other hand, the degradation at high  $T$  or low  $P$  was understood by SEM observations to be caused by Si outdiffusion into the film.

#### References

- [1] N. Sonoda, Y. Watari, Y. Sun and T. Miyasato, Jpn. J. Appl. Phys. 35(1996) p.L1655.
- [2] Y. Oshita, J. Electrochem. Soc. 142(1995), p.1002.
- [3] G. Krötz, W. Legner, G. Müller, H. W. Grueninger, L. Smith, B. Leese, A. Jones and S. Rushworth, Mat. Sci. and Eng. B29(1995), p.154.
- [4] H. Nakazawa, M. Suemitsu and S. Asami, accepted in Thin Solid Films.
- [5] H. Nakazawa and M. Suemitsu, accepted in Appl. Surf. Sci.
- [6] C. Su and J. -C. Lin, Surf. Sci. 406(1998), p.149.
- [7] A. V. Hamza, G. D. Kubiak and R. H. Stulen, Surf. Sci. 237(1990), p.35.
- [8] Y. L. Yang, L. M. Struck, L. F. Sutcu and M. P. D'Evelyn, Thin Solid Films 225(1993), p.203.
- [9] Y. Ikoma, T. Endo, F. Watanabe and T. Mottoka, J. Vac. Sci. Technol. A612(1998), p.763.
- [10] I. Kusunoki, M. Hiroi, T. Sato, Y. Igari and S. Tomoda, Appl. Surf. Sci. 45(1990), p.171.

E-mail: nakazawa@bunshi.riec.tohoku.ac.jp, FAX: +81-22-217-5484

## Growth and Characterization of N-Doped SiC Films from Trimethylsilane

J. Chen<sup>1</sup>, A.J. Steckl<sup>1,2</sup> and M.J. Loboda<sup>2</sup>

<sup>1</sup> Nanoelectronics Laboratory, University of Cincinnati, Cincinnati, OH 45221-0030, USA

<sup>2</sup> Dow Corning Corporation, Midland, MI 48686-0994, USA

**Keywords:** CVD, Hall Effect Measurement, N<sub>2</sub> doping, Trimethylsilane

**ABSTRACT:** Nitrogen-doped 3C-SiC films grown by chemical vapor deposition on Si (111) substrates using trimethylsilane (SiC<sub>3</sub>H<sub>9</sub>) have been investigated. The structure of the SiC films is studied by X-Ray diffraction, reflection-mode FTIR. The surface and interface of the grown films were examined by SEM. The effects of N<sub>2</sub> flow rate on the electrical properties of the 3C-SiC films were investigated by Hall effect measurement over a range of temperatures. The highest electron mobility measured at 300 K is 104 cm<sup>2</sup>/V·s with a corresponding carrier concentration of 2×10<sup>17</sup> cm<sup>-3</sup>. The electron carrier concentration in trimethylsilane grown SiC films can be readily controlled by the flow rate of N<sub>2</sub>.

### 1. INTRODUCTION

SiC is a promising material for microelectronic devices and MEMS to be used in extreme conditions such as high power, high temperature, high frequency, high radiation and highly corrosive environments. Current price and wafer size of commercially available SiC substrates limit the number of applications being pursued by industry. Heteroepitaxy of SiC on Si is an attractive alternative to obtain large area SiC pseudo-substrates at low cost. We have been pursuing the use of the novel organosilane precursor trimethylsilane (3MS-SiC<sub>3</sub>H<sub>9</sub>) as a low cost approach to develop large area 3C-SiC pseudo-substrates [1-2]. This gas is commercially available and relatively safe to handle. Films grown by CVD from 3MS [2] show that crystalline SiC can be obtained on Si(111) at growth temperatures as low as 1100°C. Our previous results show that the chemical and structural properties of SiC films grown using 3MS are similar to those grown at higher temperatures using the SiH<sub>4</sub>/C<sub>3</sub>H<sub>8</sub>/H<sub>2</sub> gas system. In this work we studied the effect of *in-situ* N<sub>2</sub> doping on the structural and electrical transport properties of the SiC films using XRD, FTIR and Hall effect measurements.

### 2. EXPERIMENTAL

Nitrogen-doped SiC films were grown on 3 inch p-type Si(111) substrates with a resistivity of 150-300 Ω-cm. The 3MS purity is 99% (with ~1% toluene). A thin buffer layer was first formed using propane at 1300°C and atmospheric pressure. The propane flow rate was 10 sccm for the carbonization process. In the subsequent SiC growth, 40 sccm 3MS was utilized. H<sub>2</sub> was used as the carrier gas, while N<sub>2</sub> was used as the dopant source. The H<sub>2</sub> flow rate was 2 slm during carbonization and 1 slm during growth. N<sub>2</sub> flow rates from 0.1 to 20 sccm were used during both carbonization and growth. The growth temperature and working pressure were 1200°C and 4 Torr during all 3MS growth, respectively. The crystallinity of the SiC films was characterized by XRD. The SiC film surfaces and interfaces were checked by SEM. The incorporation of N in SiC was investigated by reflection-mode FTIR. Electrical properties of grown SiC films were investigated using Hall effect measurements with a magnetic field up to 1.2 T and a temperature range from 77 to 720 K. Electrical contacts were made by depositing Ni on the four corners of the sample and annealing at 900°C for 10 min. The quality of the electrical contacts was evaluated by checking the linearity of their I-V relation. The magnetic field was set at 1 T for all Hall effect measurements.

### 3. RESULTS AND DISCUSSIONS

The XRD spectrum of a 3C-SiC film grown using 10 sccm  $N_2$  at 1200°C for 3 min is shown in Fig. 1. A Si (111) peak at 28.4° and a SiC (111) peak at 35.6° are observed. No other SiC crystal orientations were detected. The FWHM of SiC (111) peak is 0.233°, which is 1.75 times that of the Si (111) peak. The FWHM values of N-doped SiC films are similar to those of films without  $N_2$  doping. This indicates that  $N_2$  doping does not significantly affect the SiC crystal structure by the incorporation of N atoms. The insert in Fig. 1 shows an SEM cross-sectional image of the N-doped SiC/Si. Voids in the Si substrate are clearly observable. The growth rate for this sample was 0.6  $\mu\text{m}/\text{min}$ . In general, the SiC growth rate is in the range of 0.3-0.6  $\mu\text{m}/\text{min}$  at 40 sccm 3MS and 1200°C, which is much higher than those typically obtained from the  $\text{SiH}_4/\text{C}_3\text{H}_8/\text{H}_2$  gas system.

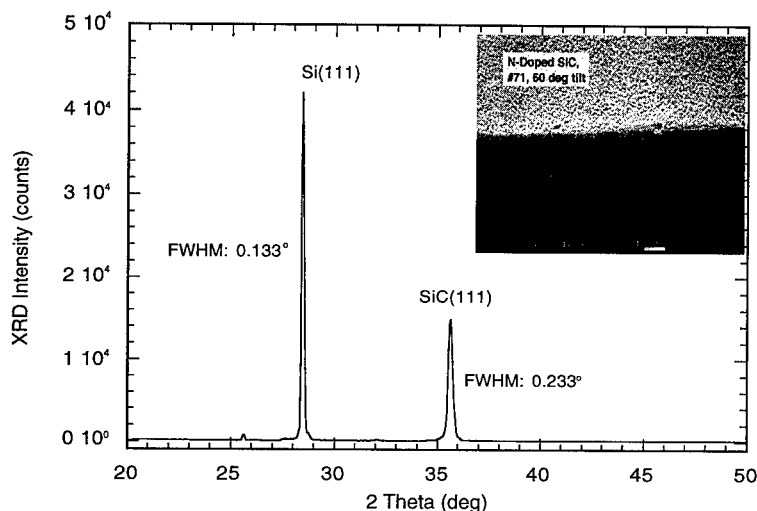


Fig. 1 XRD and SEM of N-doped SiC/Si(111) grown from 3MS at 1200°C.

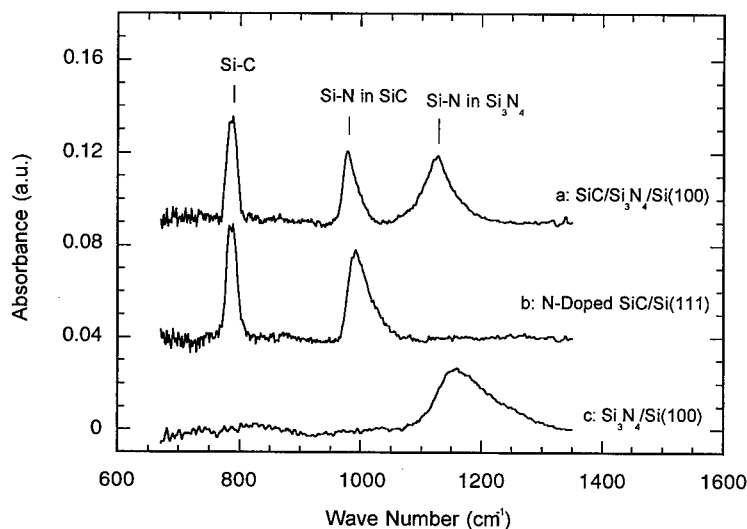


Fig. 2 Reflection-mode FTIR: (a) SiC grown on  $\text{Si}_3\text{N}_4/\text{Si}$  (100) at 1200°C and 40 sccm SCB; (b) SiC grown on Si (111) at 1200°C, 40 sccm 3MS and 0.1 sccm  $N_2$  doping; (c)  $\text{Si}_3\text{N}_4/\text{Si}$  (100) substrate for SiC growth.

Reflection-mode FTIR was used to study the chemical structure of N-doped SiC. In Fig. 2a and 2b, the peaks at  $\sim 785\text{ cm}^{-1}$  are due to the Si-C stretching vibration. The peak at  $\sim 1159\text{ cm}^{-1}$  in Fig. 2c should be assigned to Si-N bond vibration in  $\text{Si}_3\text{N}_4$  layer, as is the peak at  $\sim 1128\text{ cm}^{-1}$  in Fig. 2a. The peaks at 980-990  $\text{cm}^{-1}$  in Fig. 2a and 2b can be reasonably assigned to Si-N bonds

formed by N atoms occupying C vacancy sites in the SiC lattice. This possibility is much more likely than that of N atoms occupying Si sites and forming N-C bonds, due to the large difference of N and Si atomic radii. In addition, the C-N bond vibration peaks (in tertiary amine) are reported to be at  $\sim 1350$  and  $\sim 2800$   $\text{cm}^{-1}$ . [3] Furthermore, we have observed a monotonic increase in the 980  $\text{cm}^{-1}$  peak intensity with increasing  $\text{N}_2$  flow rate during growth. This indicates that an increasing number of N atoms were incorporated in the C vacancies of the SiC lattice, generating an increasing number of electrons as shown in the following Hall effect measurements.

The electron mobility and carrier concentration of SiC films grown with 3MS are shown in Fig. 3 as a function of  $\text{N}_2$  flow rate. Line (a) shows that by varying the  $\text{N}_2$  flow rate from 0.1 to 20 sccm, the net electron carrier concentration changed from just above  $1 \times 10^{17} \text{ cm}^{-3}$  to nearly  $1 \times 10^{20} \text{ cm}^{-3}$ . The  $\text{N}_2$  doping efficiency during SiC growth with 3MS is similar to that obtained with  $\text{SiH}_4/\text{C}_3\text{H}_8$  in the same C:Si ratio of 3 on Si [4] and on 6H SiC [5]. Curve (b) shows the effect of the  $\text{N}_2$  flow rate on the mobility. Increasing the doping level decreases the mobility from 104  $\text{cm}^2/\text{V}\cdot\text{s}$  for an electron carrier concentration of  $2 \times 10^{17} \text{ cm}^{-3}$  to 2  $\text{cm}^2/\text{V}\cdot\text{s}$  when the electron density is  $7 \times 10^{19} \text{ cm}^{-3}$ .

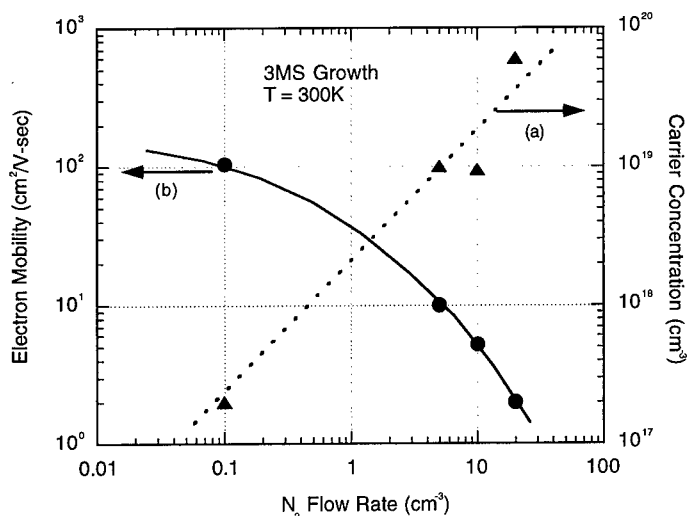


Fig. 3. Electron mobility and carrier concentration as a function of  $\text{N}_2$  flow rate for 3MS grown SiC.

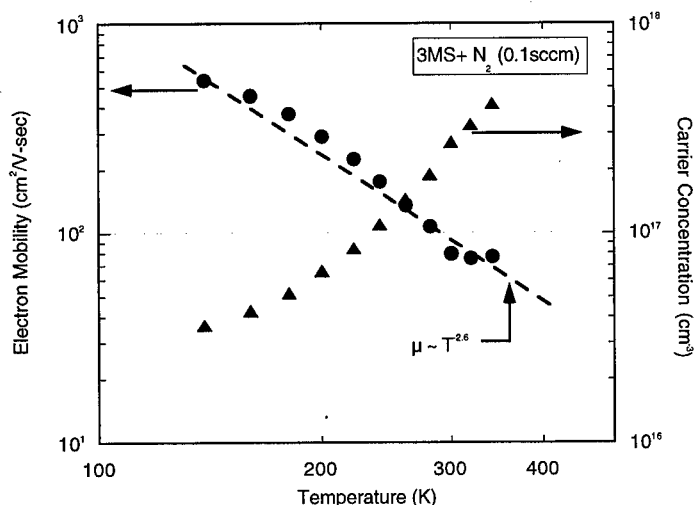


Fig. 4. Temperature dependence of electron mobility and carrier concentration of 3C-SiC films grown from 3MS with *in-situ*  $\text{N}_2$  doping. Dashed line shows  $\mu \propto T^{-2.6}$  curve fit.

Fig. 4 shows the temperature dependence of electron mobility and carrier concentration in a SiC film grown with 0.1 sccm  $N_2$  at 1200°C. The Hall electron mobility increases monotonically with decreasing temperature over the range measured. At 139 K, the electron mobility of the SiC film is 538.2  $cm^2/V\cdot s$  and it decreases to 76.6  $cm^2/V\cdot s$  at 342 K. The corresponding carrier concentrations are  $3.63 \times 10^{16}$  and  $4.15 \times 10^{17} cm^{-3}$ , respectively. The mobility decreases with a  $T^{-n}$  dependence, with  $n = 2.6$ . This temperature dependence is probably due to lattice scattering. Similar results have been suggested by Suzuki et al. [4] for  $SiH_4/C_3H_8$ -grown SiC films, where they measured a value of  $n = 2 - 2.2$ .

Fig. 5 shows the relationship between electron mobility and carrier concentration at room temperature for SiC films grown from 3MS with *in-situ*  $N_2$  doping. The trend of increasing electron mobility with decreasing carrier concentration is reproduced for the 3MS grown SiC films. The trend is comparable to that obtained by Matsunami's group [6] and by Powell et al. [7] on 3C-SiC films grown with the  $SiH_4/C_3H_8/H_2$  gas system. So far, the best result measured at 300 K from 3MS grown SiC films is a mobility of 104  $cm^2/V\cdot s$  with a carrier concentration of  $2 \times 10^{17} cm^{-3}$ . By reducing the electron carrier concentration, significantly higher electron mobility should be obtained.

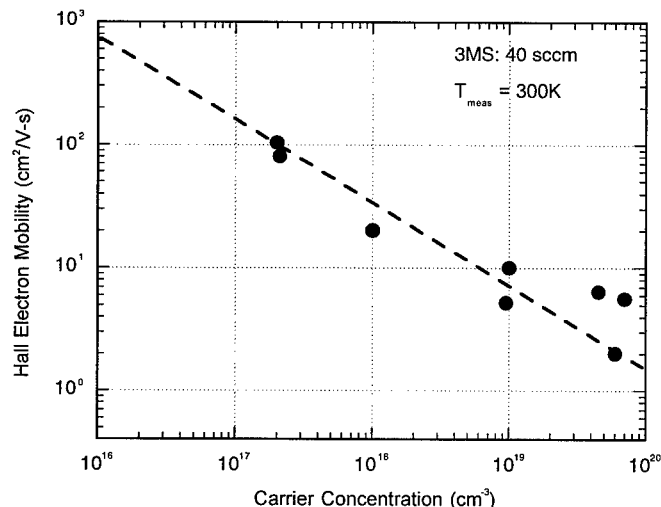


Fig. 5. Electron mobility versus carrier density measured at 300 K from SiC films grown with 3MS on Si(111).

#### 4. SUMMARY

We have grown and characterized N-doped SiC films grown on Si (111) substrates. The 3MS grown SiC films can be readily doped over a wide range with  $N_2$ . FTIR study indicates that N atoms occupy the C vacancies in the SiC lattice. A mobility of 104  $cm^2/V\cdot s$  has been obtained at 300 K from a 3MS grown SiC film. 3MS is an appealing precursor for 3C-SiC growth given its ability to provide a safe and simple growth process compare with conventional silane precursors.

#### 5. REFERENCES

- [1] A. J. Steckl, C. Yuan, J. P. Li and M. J. Loboda, *Appl. Phys. Lett.*, **63**, (1993), 3347.
- [2] S. Madapura, A. J. Steckl and M. Loboda, *J. Electrochem. Soc.* **146**, (1999), 76.
- [3] *Infrared Spectroscopy: Its Use in Coating Industry*, Federations of Societies of Paint Technology, Philadelphia, 1969, p40.
- [4] A. Suzuki, A. Uemoto, M. Shigeta, K. Furukawa and S. Nakajima, *Appl. Phys. Lett.*, **49**, (1986), 450.
- [5] H. Matsunami, *US-Japan conference on Wide Bandgap Technology*, Arlington, VA (1998).
- [6] H. Matsunami, in *Amorphous and Crystalline Silicon Carbide and Related Materials II*, M. M. Rahman, C. Y.-W. Yang, G. L. Harris, Editors, V 43, Springer Proceedings in Physics, Berlin (1989), p. 2.
- [7] J. A. Powell, L. G. Matus, and M. A. Kuczmarski, *J. Electrochem. Soc.* **134**, (1987), 1558.

## The Effect of Ge on the Structure & Morphology of SiC Films Grown on (111) Si Substrates

W.L. Sarney<sup>1</sup>, L. Salamanca-Riba<sup>1</sup>, P. Zhou<sup>2</sup>, C. Taylor<sup>2</sup>, M.G. Spencer<sup>2</sup>,  
R.D. Vispute<sup>3</sup> and K.A. Jones<sup>4</sup>

<sup>1</sup>Dept. of Materials & Nuclear Engineering, University of Maryland, College Park, MD 20742, USA

<sup>2</sup>Materials Science Research Center of Excellence, Howard University,  
Washington, DC 20059, USA

<sup>3</sup>Center for Superconductivity Research, University of Maryland, College Park, MD 20742, USA

<sup>4</sup>U.S. Army Research Laboratory, Adelphi, MD 20783, USA

**Keywords:** Cubic SiC, Polytypism, Substrate Growth

### ABSTRACT

Due to the lack of isomorphism and the large lattice and thermal expansion coefficient mismatch, SiC films grown on Si are usually low quality and grow three dimensionally. To stabilize the growth front we grew several SiC films on Si (111) substrates with GeH<sub>4</sub> flow rates ranging from 0 – 50 sccm in a MOCVD reactor at 1000°C. SiC films grown with GeH<sub>4</sub> flow rates at or below 15 sccm consist of amorphous and/or small polycrystalline grains. Samples grown with GeH<sub>4</sub> flow rates at or exceeding 20 sccm consist of crystalline 3C grains, and have a single crystalline initial layer followed by a heavily twinned crystalline layer. The initial layer consists of up to 80 nm of high quality single crystal 3C SiC, which could possibly be used as a buffer layer for either cubic nitride growth or for further SiC growth without Ge.

### INTRODUCTION

The expense and small available size of SiC substrates motivates the investigation of alternative substrates or the use of buffer layers for cubic nitride and SiC film growth. We attempted to optimize MOCVD growth of 3C SiC/Si (111). The temperatures usually required to grow crystalline SiC on any substrate approach the melting point of Si (1687 K), so lower than optimum temperatures must be used. Surfactants have improved the quality of other large lattice mismatched systems. Since Ge is a large atom with a lower surface energy than either Si or SiC, we expected it to effectively segregate to the surface as a surfactant, and help compensate for the deleterious effects caused by our very low growth temperature of 1000° C. In this work, we find that an initial nucleation layer of high quality crystalline 3C SiC results for SiC grown with GeH<sub>4</sub> flow rates of 20 sccm – 50 sccm.

### EXPERIMENT

Several SiC films with GeH<sub>4</sub> flow rates ranging from 0 – 50 sccm were grown at 1000° C on (111) Si substrates in a commercial vertical rotating disk CVD reactor for two minutes. The C<sub>3</sub>H<sub>8</sub> and SiH<sub>4</sub> flow rates were 50 sccm and 30 sccm, respectively. The substrates were carbonized at 700 Torr in a C<sub>3</sub>H<sub>8</sub> environment as described by Nishino and Li [1-2]. Characterization techniques included X-ray diffraction, transmission electron microscopy (TEM), and atomic force microscopy (AFM). The TEM samples were prepared using tripod polishing and ion milling, and were observed in a JEOL 4000 FX operated at 300 kV.

### RESULTS

TEM images of samples grown with GeH<sub>4</sub> flow rates at and below 15 sccm show that the films consist of an amorphous matrix with small crystallites having a preferred orientation with respect to

the substrate. The crystallite size within the amorphous matrix increases and the preferred orientation improves with increasing  $\text{GeH}_4$  flow rate.

Samples grown with  $\text{GeH}_4$  flow rates at or exceeding 20 sccm have an initial layer of up to 80 nm of reasonably high quality 3C SiC. The thickest layers of high quality 3C SiC are obtained for

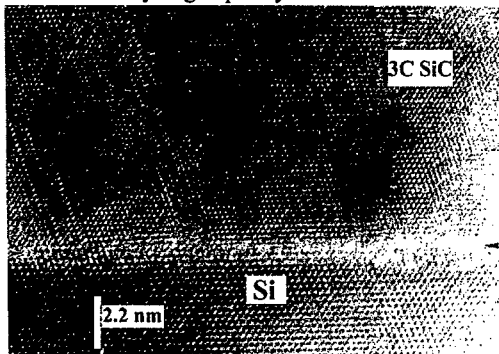


Fig. 1a. High resolution image of SiC/Si interface from a sample grown with 20 sccm  $\text{GeH}_4$ .

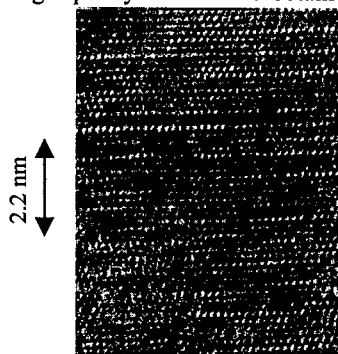


Fig. 1c. High resolution image of twinned 3C SiC region.

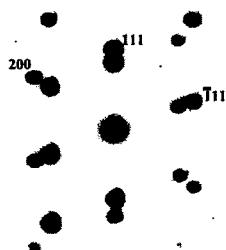


Fig 1b.  $(1\bar{1}0)$  diffraction pattern of region seen in Fig. 1a.

films grown with  $\text{GeH}_4$  flow rates between 20 – 30 sccm. The single crystalline nature of the initial layer is confirmed by the high resolution TEM image of the SiC/Si interface (Fig. 1a), and the diffraction pattern taken using a selected area aperture centered over the SiC/Si interface (Fig. 1b).

For all films grown with a  $\text{GeH}_4$  flow rate of at least 20 sccm, the initial layer abruptly terminates and is followed by a thicker layer of heavily twinned crystalline 3C SiC with the morphology shown in Fig. 1c. The fringes look deceptively similar to those typically seen for 6H SiC samples. Figure 2 shows diffraction patterns from samples grown with  $\text{GeH}_4$  flow rates from 20 sccm to 50

sccm  $\text{GeH}_4$ , and include contributions from the Si substrate, the initial single crystalline 3C region, and the twinned 3C region. The (111),  $(\bar{1}\bar{1}1)$ , and (200) spots are labeled as sets where the outer spot corresponds to the SiC film and the inner spot to the Si substrate. These patterns (Fig. 2) show the same set of spots as Fig 1b plus several additional spots. Some of these spots arise from twinning, for example, spot A (Fig. 2) is the twin of the  $(\bar{1}\bar{1}1)$  spot, and spot C is the twin of the (200) spot about the  $[111]$  direction. Additional spots arise from multiple diffraction from twins along the beam direction. For example, spot B is due to diffraction from the  $(\bar{1}\bar{1}1)$  spot and its corresponding twin across the (111) plane, and has indices of  $(2/3\ 2/3\ 2/3)$  in terms of the reciprocal lattice of the matrix [3].

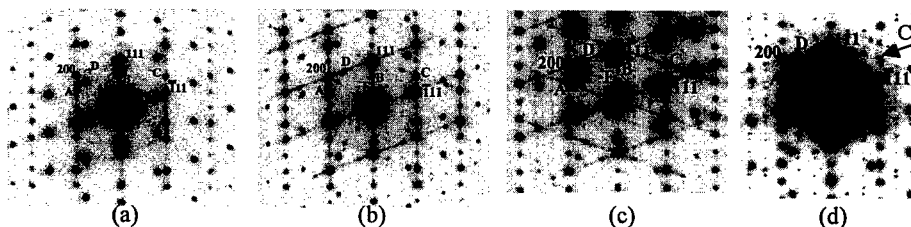
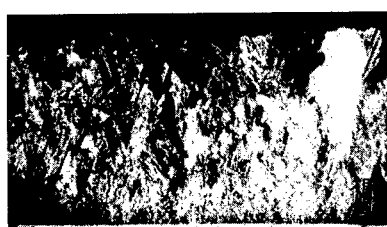


Fig. 2. Diffraction patterns from samples grown with  $\text{GeH}_4$  flow rates of (a) 20 sccm, (b) 30 sccm, (c) 40 sccm, and (d) 50 sccm.

Misidentifying twinned 3C regions (Fig 1c), for 6H SiC is an easy and common mistake [4]. The lattice fringes have the zig-zag appearance of 6H SiC and several of the additional spots in the diffraction patterns shown in Fig. 2 could correspond to 6H spots. For example, multiple diffraction spot B could correspond to 6H SiC, since the interplanar lattice spacing for (0004) 6H SiC and (2/3 2/3 2/3) 3C SiC are the same. Similarly, multiple diffraction spot E, having indices (1/3 1/3 1/3), is at the position of the (0002) spot for 6H SiC. Careful analysis of the diffraction patterns (Fig. 2) reveal that the top layer (Fig. 1b), is indeed 3C SiC. The greatest evidence is that the "6H spots" disappear when we tilt along the (111) axis, indicating that they rely on the existence of other spots, which do not lie along the (111) axis.

The diffraction patterns in Fig. 2 show that twinning occurs across the entire {111} family of planes. For example, spot D corresponds to the twin of the  $(\bar{1}\bar{1}\bar{1})$  spot across the  $(\bar{1}11)$  twin plane. This spot and several others become more distinct with increasing  $\text{GeH}_4$  flow rate. The diffraction patterns (Fig. 2) show that higher  $\text{GeH}_4$  flow rates leads to more twins along the {111} family of planes in addition to the (111) surface. Multiple diffraction increases with the number of twinned regions, which even further increases the number of visible spots.

Dark field images were obtained for (111) and  $(\bar{1}\bar{1}\bar{1})$  two-beam conditions for each sample. Images from the samples grown with  $\text{GeH}_4$  flow rates of 20 and 40 sccm are shown in Fig. 3(a)-3(d).

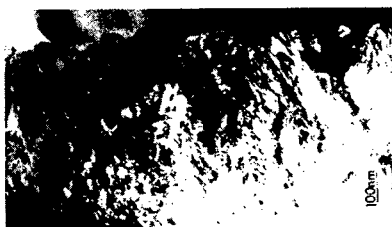


a



b

Fig 3(a-b) (111) DF images with two beam condition of samples grown with  $\text{GeH}_4$  flow rates of (a) 20 sccm and (b) 40 sccm Ge.



c



d

$(\bar{1}\bar{1}\bar{1})$  DF images with two beam condition of samples grown with  $\text{GeH}_4$  flow rates of (c) 20 sccm and (d) 40 sccm Ge.

The grain sizes in the twinned regions increase with increasing  $\text{GeH}_4$  flow rate, which is confirmed by AFM and x-ray diffraction, as discussed below. Almost the entire film is visible in the (111) two beam images for samples grown with 20 and 30 sccm Ge, therefore most of the regions in these two films have the (111) growth spot in common and most of the twins are across the (111) twin plane. The invisibility of some regions in the  $(\bar{1}\bar{1}\bar{1})$  two beam condition confirms that twinning across the (111) plane is present for all samples and increases with increasing  $\text{GeH}_4$  flow rate. Larger invisible regions exist in the (111) two-beam image of the film grown with 40 sccm Ge than in the film grown with 20 sccm Ge. These invisible regions do not have the (111) growth spots in common, and therefore result from twinning across other {111} planes. We find that twinning over the entire {111} family, including the (111) plane, increases with increasing  $\text{GeH}_4$  flow rate.

Phi and  $\theta$ -2 $\theta$  scans were taken for samples grown with a  $\text{GeH}_4$  flow rate of at least 20 sccm. Twinning along the {111} family of planes does not introduce twin spots or change the film's properties along the growth direction, so the scans do not change appearance with changing  $\text{GeH}_4$  flow



rates. The  $\theta$ -2 $\theta$  scans show that the samples are well oriented along the  $\langle 111 \rangle$  growth direction. The phi-scans show two sets of three peaks corresponding to the (022) reflections, each set having peaks every  $120^\circ$  and being rotated  $60^\circ$  with respect to the other set. Therefore, we see a total of six peaks, which is expected for material twinned across the (111) plane. AFM images (Fig. 4) show that the surface roughness initially decreases with increasing  $\text{GeH}_4$  flow rates up to 20 sccm, and then increases with the  $\text{GeH}_4$  flow rate for samples grown with flow rates of and above 20 sccm. Samples grown with  $\text{GeH}_4$  flow rates of 0, 10 and 15 sccm contain larger amorphous regions, which would tend to be smoother than the crystalline regions.

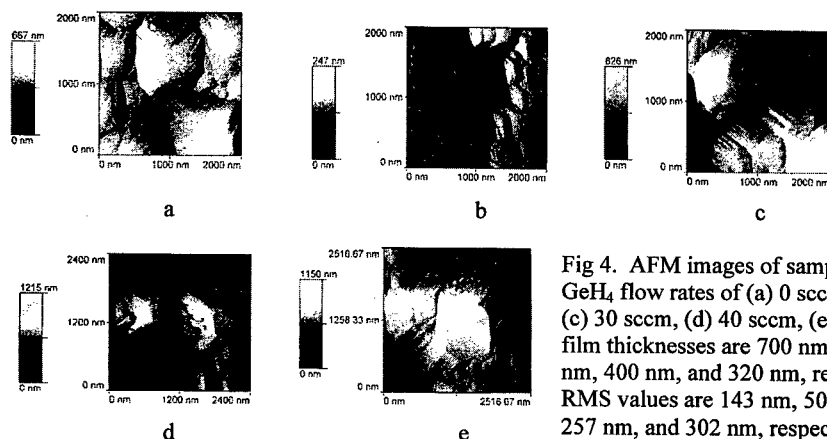


Fig 4. AFM images of samples grown with  $\text{GeH}_4$  flow rates of (a) 0 sccm, (b) 20 sccm, (c) 30 sccm, (d) 40 sccm, (e) 50 sccm. The film thicknesses are 700 nm, 660 nm, 640 nm, 400 nm, and 320 nm, respectively. The RMS values are 143 nm, 50 nm, 177 nm, 257 nm, and 302 nm, respectively.

## CONCLUSION

We find that adding Ge in the form of  $\text{GeH}_4$  to the reactant gases in a MOCVD reactor allows crystalline growth of 3C SiC on (111) Si substrates for a low growth temperature of  $1000^\circ\text{C}$ . We repeatedly obtain an initial layer of up to approximately 80 nm of single crystalline 3C SiC for samples grown with  $\text{GeH}_4$  flow rates between 20 sccm and 50 sccm. The remainder of the film consists of a thick region of heavily twinned 3C SiC. The initial layer may be suitable as a buffer layer for further SiC or nitride film growth. We plan to optimize this growth process and obtain the thickest possible single crystalline 3C SiC layer, which may be used as a cheaper and larger wafer alternative to the currently available 3C SiC substrates.

## ACKNOWLEDGEMENTS

The authors acknowledge the financial support and technical collaboration with the U.S. Army Research Laboratories. This project is funded by MRCP Army Grant No. DAAL 019523530.

## REFERENCES

- [1] S. Nishino, J.A. Powell, and H.A. Will, *Appl. Phys. Lett.* **460** (1983), p. 42.
- [2] J.P. Li, A.J. Stecki, *J. Electrochemical Soc.* **142** (1995), p. 624.
- [3] W.L. Sarney, L. Salamanca-Riba, P. Zhou, M.G. Spencer, C. Taylor, R.D. Vispute, and K.A. Jones, *Journal of Electronic Materials*, in press.
- [4] W.L. Sarney, L. Salamanca-Riba, P. Zhou, M.G. Spencer, C. Taylor, R.P. Sharma, and K.A. Jones, *Mat. Res. Soc. Symp. Proc.* **572** (1999), p.339.

## CORRESPONDENCE

Please direct all correspondence to [wsarney@eng.umd.edu](mailto:wsarney@eng.umd.edu).

## In Situ Monitoring of the Effect of Ge on the SiC Growth on (111)Si Surfaces

T. Wöhner<sup>1,2</sup>, Th. Stauden<sup>1</sup>, J.A. Schaefer<sup>2</sup> and J. Pezoldt<sup>1</sup>

<sup>1</sup> Institut für Festkörperelektronik, TU Ilmenau, Postfach 100 565, DE-98684 Ilmenau, Germany

<sup>2</sup> Institut für Physik, TU Ilmenau, Postfach 100 565, DE-98684 Ilmenau, Germany

**Keywords:** Carbonization, Germanium, Heteroepitaxy, In Situ Monitoring, SiC Growth, Spectroscopic Ellipsometry

**Abstract** 3C-SiC was grown by carbonization on (111)Si by solid source molecular beam epitaxy at 750°C. The use of additional Ge deposition before or during carbonization leads to a lowering of the SiC growth rate in a different way at the beginning of the growth process, which was obtained by real time spectroscopic ellipsometry and real time RHEED. Ge is mainly incorporated at the SiC/Si interface and causes an increase of the SiC grain diameter independent on the incorporation method.

### Introduction

For an effective and optimal process adjustment monitoring techniques are necessary which can be applied for a wide variety of deposition methods. This is especially important in the case of heteroepitaxial growth where a great variety of different factors have to be controlled. Different methods are valid to study these ongoing processes which should be monitored *in situ* in real time. *In situ* monitoring techniques are important for reproducibility and feedback of growth processes. For this reason we used *in situ* reflection high energy electron diffraction (RHEED) and *in situ* spectroscopic ellipsometry (SE) to study the SiC growth on Si with and without additional Ge deposition at UHV conditions to determine the influence of Ge on the early stages of SiC nucleation and growth.

RHEED and SE are very fast and sensitive methods to films less than one monolayer in thickness. Therefore they are established to monitor processes of growing films. RHEED gives information about the crystal structure and the morphology at the sample surface. Applying SE to growing SiC films on Si, we obtain information about the nucleation and the growth of surface roughness, film thickness and SiC/Si interface width [1, 2]. On the other hand SE can be easily applied to deposition processes independent on the pressure.

The present work shows our first results on the effect of Ge atoms on the SiC growth on (111)Si. RHEED and SE data of the grown SiC layers with and without Ge are compared. Changes of the nucleation and of the growth behaviour are observed in the presence of Ge. We obtained differences in the time dependence of the SE data which are related to a lowering of the SiC growth rate. In principle the surface roughness decreases and the grain diameter increases if Ge is incorporated into the heterointerface.

### Experimental

In our experiments the carbonization process was performed with and without additional Ge during the carbonization with evaporated C in a solid source molecular beam epitaxy (SSMBE) growth of SiC at 750°C substrate temperature. We used (7x7) (111)Si substrate surfaces, which were applied to two different methods of Ge deposition before and during carbonization of Si. Three samples were prepared with the following process steps: a) carbonization without Ge (sample MC103); b) carbonization with Ge, sample MC104: 3ML Ge on Si (ML with respect to the Si surface), 200s annealing at 750°C before carbonization; sample MC105: 3ML Ge during carbonization. The Ge deposition time (225s) was calibrated by RHEED oscillations. The calibration of the C flux ( $2 \times 10^{13} \text{ cm}^{-2} \text{ s}^{-1}$ ) was ob-

tained using the deposition time of the maximum intensity of the C induced ( $\sqrt{3}\times\sqrt{3}$ )R30° surface reconstruction, which corresponds to approximately 1ML C deposition on (111)Si [3]. The process was monitored by *in situ* RHEED and by *in situ* SE in real time. The rotating analyser ellipsometer has a wavelength range between 250 ... 850 nm. The angle of incidence was set to 72.6°. Spectra of  $\Psi$  and  $\Delta$  as a function of wavelength were successively measured in parallel mode using a photodiode array (spectral resolution: 0.61nm). The time interval of one measured spectra was about 10s to get a satisfactory signal to noise ratio. The final sample surfaces were investigated *ex situ* by atomic force microscopy (AFM) and X-ray photoelectron spectroscopy (XPS). The AFM images were obtained in contact mode with a  $1\times 1\mu\text{m}^2$  scan area. XPS spectra of the Si2p, C1s, O1s, Ge2p and Ge3d core levels were taken using Mg and AlK $\alpha$  X-ray sources.

### Results and Discussion

A Si-Ge intermixing was observed after deposition of Ge onto (111)Si by real time SE. The ellipsometric  $\Psi$  and  $\Delta$  spectra of Ge deposition before carbonization (sample MC104) could be well interpreted using a three layer optical model (0.5nm mixture: 20%Ge / 80%voids, 0.6nm Si<sub>0.65</sub>Ge<sub>0.35</sub>, 0.3nm Si<sub>0.85</sub>Ge<sub>0.15</sub>) on (111)Si substrate. The optical parameters of the Ge/voids mixture were calculated using effective medium approximation (EMA). The observed intermixing of Si and Ge is in agreement with Ikeda e.a. [5] and Jeong e.a. [6]. Wedler e.a. [4] found intrinsic stress during Ge growth on Si at the first few monolayers. This effect causes an energy shift of the E<sub>g</sub>' transition at 3.32 eV of the dielectric function of the Si substrate [7]. A similar effect on the dielectric function was obtained by Si-Ge intermixing [8]. In our case the best fit was obtained with the model taking into account only the intermixing of Ge and Si.

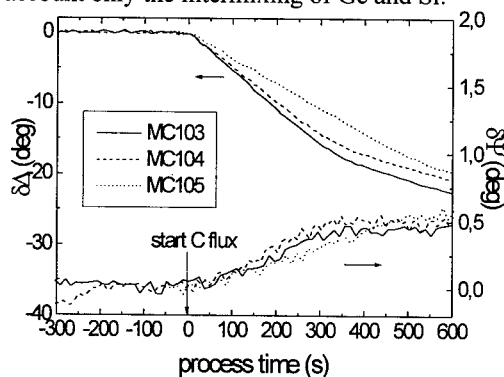


**Fig. 1** Real time SE of the carbonization process without Ge (MC103) and with Ge before (MC104) and during (MC105) carbonization,  $\delta\Psi$  and  $\delta\Delta$  as function of process time

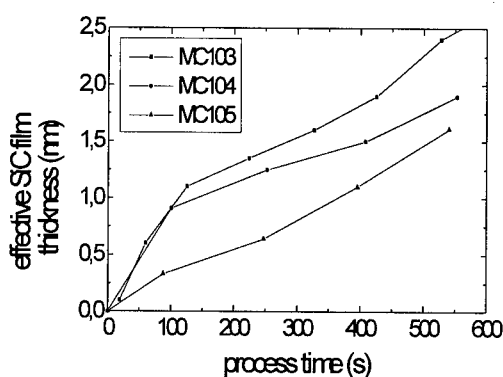


**Fig. 2** Effective SiC film thickness as function of process time, fitted from SE data (Fig.1) using the introduced two optical models (see text)

Fig.1 shows the ellipsometric signals  $\delta\Delta(t)=\Delta(t)-\Delta(t=0)$  (left axis) and  $\delta\Psi(t)=\Psi(t)-\Psi(t=0)$  (right axis) of samples MC103-105 as a function of process time  $t$ . The wavelength of  $\Psi$  and  $\Delta$  is set to 400nm to get maximum sensitivity on the growth process. A different time dependence of the SE data is observed and demonstrates the influence of Ge atoms on the early stages of the SiC film growth. Furthermore, the differences between the SE data of MC104 and MC105 suggest different effects of the two applied methods of Ge incorporation on the growth kinetics.

An interpretation of the received SE data was obtained by fitting the data using an optical model. To obtain consistent results within one experiment different optical models for the growth process with and without Ge have to be used. This reflects the change in the growth process. The models were: a) two layer model (SiC/void mixture, c-Si/void mixture) on (111)Si without Ge; b) three layer model (SiC/Ge/void mixture, Si<sub>x</sub>Ge<sub>1-x</sub>, c-Si/void mixture) on (111)Si with Ge. Model a) is

similar to that which was successfully applied in [1, 2] to fit the *in situ* ellipsometric spectra of SiC films grown on Si. Fig.2 shows the fit results of the effective SiC film thickness (product of the layer thickness and the SiC fraction of the upper layer of both introduced models) as a function of process time. This is reflected by the time dependence of  $\delta\Delta$  (Fig.1), which is very sensitive to the increase of the effective SiC film thickness.

**Carbonization without Ge (MC103):** The behaviour of the effective SiC film thickness of this process has a typical time dependence, which we observed at other C fluxes [1, 2]. At the beginning of the process the SiC growth is limited by the C-Si reaction at the Si surface. Nucleation and growth of crystallites takes place. This is evident by the observed strong increase of the effective film thickness with the highest growth rate (Fig.2, until 100s). Above 100s, the growth is limited process by Si outdiffusion from the substrate, which corresponds with the observed lowering of effective film thickness increase and growth rate.

**Ge deposition before carbonization (MC104):** At the beginning (until about 100s) the process has approximately the same growth rate compared to the process without Ge. An explanation is given by the observed Si-Ge intermixing, exhibiting a partly uncovered Si surface. We calculated a  $\approx 20\%$  Ge coverage on Si using the ratio of the effective film thickness maximum in the reaction limited time interval (at about 100s) between the samples MC103 and MC104, when we assume 0% Ge coverage on MC103. Above 100s, the effective film thickness increase is lower compared to MC 103. This could be caused by the observed SiGe formation near the SiC/Si interface and the small Ge coverage on the Si surface, which reduce the Si outdiffusion and therefore lower the growth rate.

**Ge deposition during carbonization (MC105):** Ge deposition on the Si surface during the carbonization limits the C-Si reaction and reduces the effective film thickness increase and the growth rate even at the beginning of the process. Si-Ge intermixing during SiC growth was observed by real time SE and reduces the Si outdiffusion. We can not exclude Ge incorporation into SiC crystallites during carbonization with additional Ge deposition, which could influence the growth rate. After shut off the Ge deposition (225s) the effective film thickness increases comparably to the process without Ge (MC103), which suggests an equal growth rate.

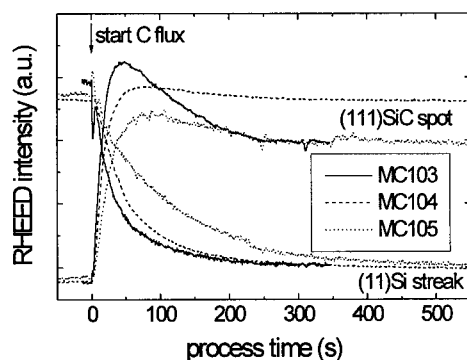


**Fig. 3** Real time RHEED of the carbonization process with and without Ge (see Fig.1), intensity of the (11)SiC spot and (11)SiC spot as function of process time

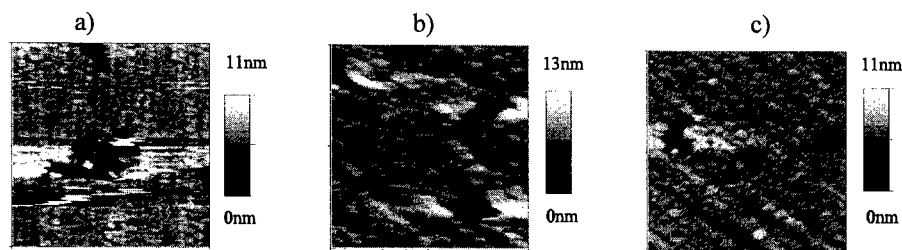
Referring to the different time behaviour of the effective film thickness, Ge incorporation before or during carbonization has to be distinguished. However, the time behaviour of both processes with Ge seems to be adjusted above 600s.

Fig.3 shows the decreasing RHEED intensity of the (11)SiC streak and the increasing RHEED intensity of the (11)SiC spot of samples MC103-105 as a function of process time. The largest intensity increase of the (11)SiC spot is seen at the process without Ge. The intensity increase is smaller when Ge is deposited before carbonization. Ge deposition during carbonization strongly reduces this intensity increase. These observations correlate with the results observed by real time SE.

Ex situ AFM investigations on the final sample surfaces (Fig. 4a-c) show a nonclosed surface on each sample, which supports the used optical models to fit the SE data. The observed increase of the grain diameter is in agreement with [9].

The surface morphology of MC104 and MC105 is very similar.

Ex situ XPS investigations on the final sample surfaces of MC104 and MC105 are affected by the topography. The spectra of the Ge2p and the Ge3d core levels show an equal intensity of Ge-Ge



**Fig.4** AFM images ( $1 \times 1 \mu\text{m}^2$ ) of the final surfaces of the samples: a) MC103, b) MC104, c) MC105

bonds on both samples, which indicates a similar Ge incorporation at the SiC/Si interface. However, a higher intensity of Ge-O bonds on MC104 was observed. The Ge-O bonds are located at the sample surface. For our opinion the Si surface between the SiC crystallites is covered by small Ge clusters. But this was not seen by RHEED. Furthermore, the Si2p core level shows a higher intensity of Si-C bonds on MC104. From this follows a larger SiC coverage on MC104, which supports the SE fit results of the effective film thickness (Fig.2).

### Conclusion

In the case of additional Ge deposition, carbonization of (111)Si leads to a lowering of the increase of effective SiC film thickness within the investigated interval of process time (until 600s). This is connected with a lowering of the growth rate. Reasons are reductions of the C-Si reaction probability and of the Si outdiffusion from the substrate in the presence of additional Ge at the surface. Referring to a different increase of the effective film thickness, the applied methods of Ge deposition before or during carbonization has to be distinguished. The difference between both methods is the partly uncovered Si surface before carbonization due to the observed Si-Ge intermixing at the Si subsurface. This increases the C-Si reaction probability at the beginning of the process. Furthermore, the Ge incorporation into the Si subsurface leads to the observed increase of the SiC grain diameter.

### Acknowledgement

This work was supported by DFG under contract Pe 624/2-1,2.

### References

- [1] T. Wöhner, T. Stauden, V. Cimalla, G. Eichhorn, J.A. Schaefer, J. Pezoldt, MRS Symp. Proc. 569 (1999), p.95.
- [2] T. Wöhner, V. Cimalla, Th. Stauden, J.A. Schaefer, J. Pezoldt, E-MRS, Spring Meeting 1999, Symposium P, PII.6, to be published.
- [3] V. Cimalla, Th. Stauden, G. Ecke, F. Scharmann, G. Eichhorn, J. Pezoldt, Appl.Phys.Lett. 73, 24 (1998), p.3542.
- [4] G. Wedler, J. Walz, T. Hesjedal, E. Chilla, R. Koch, Surf.Sci. 402-404 (1998), p.290.
- [5] A. Ikeda, K. Sumitomo, T. Nishioka, T.Yasue, T. Koshikawa, Y. Kido, Surf.Sci. 385 (1997), p.200.
- [6] S. Jeong, A. Oshiyama, Surf.Sci. 436 (1999), p.L666.
- [7] H. Lee, E.D. Jones, Appl.Phys.Lett. 68 (1996), p.3153.
- [8] A.R. Heyd, S.A. Alterovitz, E.T. Croke, MRS Symp. Proc. 358 (1995), p.993.
- [9] K.Zekentes, T.Tsagaraki, Mater.Sci.Eng. B61-62 (1999), p.169.

## Structural Investigations of the Nucleation and Growth of SiC during Rapid Thermal Conversion of (111)Si

V. Cimalla<sup>1,2</sup>, W. Attenberger<sup>3</sup>, J.K.N. Lindner<sup>3</sup>, B. Stritzker<sup>3</sup> and J. Pezoldt<sup>1</sup>

<sup>1</sup> Institut für Festkörperelektronik, TU Ilmenau, Postfach 100 565, DE-98684 Ilmenau, Germany

<sup>2</sup> Foundation for Research and Technology Hellas, Microelectronic Research Group,  
PO Box 1527, GR-71110 Heraklion/Crete, Greece

<sup>3</sup> Institut für Physik, Universität Augsburg, Universitätsstrasse 1, DE-86135 Augsburg, Germany

**Keywords:** Carbonization, Growth Model, Heteroepitaxy, Transmission Electron Microscopy

**Abstract** The influence of the process conditions (heating rate, propane concentration and substrate temperature) on the initial growth of SiC on silicon was investigated by transmission electron microscopy, atomic force microscopy and reflection high energy electron diffraction. The results obtained are summarized in a model.

### Introduction

The carbonization of Si substrates prior to the growth as a separate process or during the heating cycle is a common method in the formation of heteroepitaxial SiC layers on Si. In conjunction with the heteroepitaxy of III-nitrides or diamond revitalized the interest in this technique to create a pseudosubstrate. Since the first work was published in 1959 [1] the conversion of Si into SiC with a C containing precursor has been studied intensively by several groups. However, up to now this process is not fully understood and different growth and morphological models of the conversion process can be found [2-7]. The aim of this work is to give a contribution for a better understanding of the structural and morphological evolution during the conversion of Si into SiC under chemical vapour deposition conditions. For this reason we studied the nucleation and growth behaviour in dependence on the heating rate, the C<sub>3</sub>H<sub>8</sub> concentration and substrate temperature in a rapid thermal processing reactor.

### Experimental

The conversion process was carried out in a home made rapid thermal chemical vapour deposition (RTCVD) reactor described in [8]. The RTCVD system allows an accurate adjustment of the heating rate ( $\pm 3 \text{ K s}^{-1}$ ), the holding temperature ( $\pm 0.5 \text{ K}$ ) and the process time ( $\pm 0.2 \text{ s}$ ) [9]. The carbonization of (111)Si was carried out by using C<sub>3</sub>H<sub>8</sub> diluted in 1000 sccm H<sub>2</sub>. The C<sub>3</sub>H<sub>8</sub> concentration was adjusted between 0.01% and 0.3%, the holding temperature between 1100°C and 1330°C, heating ramps between 20 and 200 K s<sup>-1</sup> and holding times in the range from 0 to 120 s. 0 s and negative holding times in Fig. 1 represent an interruption of the heating-up cycle at a lower temperature and an immediate cooling down. Depending on the heating rate the effective process time is 1 ... 3 s [10]. A detailed description of the process steps of the conversion including *ex situ* and *in situ* cleaning of the samples can be found in [10].

The thickness measurements, the structural and morphological investigations of the samples were carried out by using ellipsometry, atomic force microscopy (AFM), reflection high energy electron diffraction (RHEED) and cross-sectional transmission electron microscopy (XTEM), respectively.

### Results and Discussion

In dependence on the growth conditions we found three different growth kinetics (Fig. 1). Every type is correlated with a distinct morphological evolution. With the C<sub>3</sub>H<sub>8</sub> concentration, which has the most important influence, they can be classified as (a) quasi-two dimensional growth, (b) Stranski-

Krastanov like growth and (c) three dimensional growth.

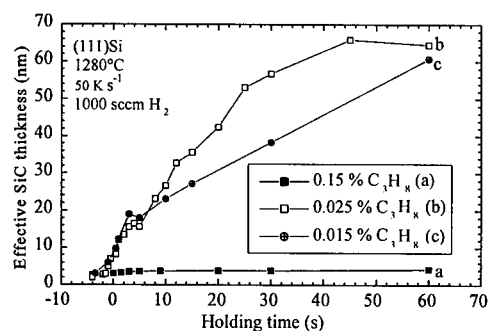


**Fig.1** Growth kinetics at 1280°C, 50 K s<sup>-1</sup> at C<sub>3</sub>H<sub>8</sub> concentrations of (a) 0.15%, (b) 0.025% and (c) 0.015% in 1000 sccm H<sub>2</sub>.

ous initial layer allows an epitaxial lateral growth and the high secondary nucleation density rapidly seals off the diffusion paths for Si entirely. The resulting layer was single domain [11] with a saturation thickness of 3...5 nm. These layers showed no morphological defects at all. The final state of such a layer as observed by RHEED, AFM and XTEM is represented in Fig.2.

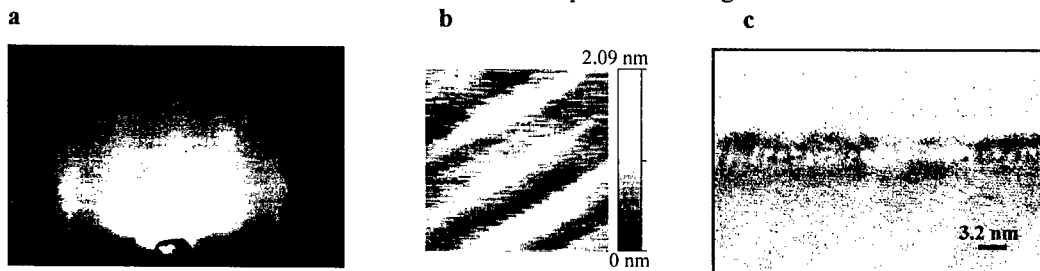


**Fig.2** RHEED (a), AFM (1×1 μm<sup>2</sup>) (b) and XTEM (c) pattern obtained from a (111)Si sample converted at 1280°C/0.15% C<sub>3</sub>H<sub>8</sub> at 50 K s<sup>-1</sup> and 10 s holding time.

#### Case B: Stranski-Krastanov like growth and saturation

At intermediate C<sub>3</sub>H<sub>8</sub> concentrations (0.02 ... 0.1%, Fig. 1, curve (b)) a similar thin initial layer was detected by RHEED, AFM, XTEM and ellipsometric investigations. Fig.3 represents a XTEM micrograph of a sample after 0 s conversion process at 1280°C/60s/ 0.025% C<sub>3</sub>H<sub>8</sub>/50 K s<sup>-1</sup> was interrupted during the heating-up phase at 1190°C. The thin and closed initial layer on the top of the Si substrate is evident as a small dark band. This is surprising, because since the critical temperature of SiC formation using C<sub>3</sub>H<sub>8</sub> in a H<sub>2</sub> environment was found to be between 1050 ... 1100°C [10]. Consequently, if the hydrocarbon concentration is high enough the Si surface will be immediately covered with SiC by quasi-two dimensional growth.

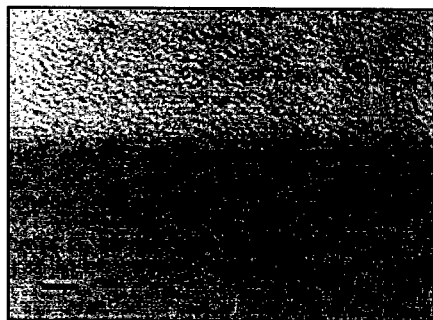


**Fig.3** XTEM micrograph of a sample with a process interruption at 1190°C/0.025% at 50 K s<sup>-1</sup> and 0 s holding time.

#### Case A: quasi-two dimensional growth

For C<sub>3</sub>H<sub>8</sub> concentrations above 0.1% a thin initial SiC layer is formed already during the heating-up phase (Fig. 1, curve (a)). The existence of a SiC layer with a finite thickness for a holding time < 0 s was confirmed by RHEED investigations. Large diffuse and elongated spots corresponding to SiC without any Si related diffraction spots were found. In addition, the recorded AFM patterns were smooth and featureless with a roughness close to the values obtained for the virgin (111)Si wafer. Although apparently closed, the thin initial layer does not act as a complete diffusion barrier. This results in secondary nucleation with a density proportional to the hydrocarbon flux. The homogeneous

As in case A the initial layer allows Si diffusion to the surface leading to secondary nucleation. However, the lower hydrocarbon concentration causes a decreased secondary nucleation density. Consequently, and in contrast to case A, not all diffusion paths are sealed off by

these secondary nuclei. This stimulates the local Si transport inducing the formation of voids in the substrate adjacent to the layer. The fast growth around the voids leads to an enhanced defect formation. Also in this case the diffusion paths will be sealed and the saturation sets in, however, after longer processing times and at higher layer thickness. These converted layers have shown rotational twins. RHEED, AFM and XTEM pattern of the final state are shown in Fig.4.

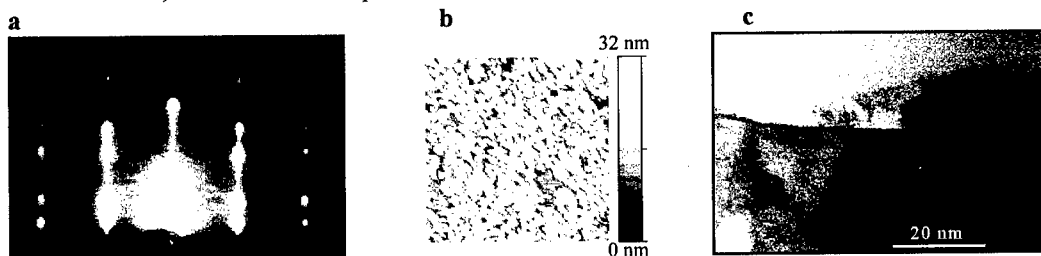


**Fig.4** RHEED (a), AFM ( $1 \times 1 \mu\text{m}^2$ ) (b) and XTEM (c) pattern obtained from a (111)Si sample converted at  $1280^\circ\text{C}/0.025\% \text{C}_3\text{H}_8$  at  $50 \text{ K s}^{-1}$  and 10 s holding time.

#### *Case C: Three dimensional growth*

At  $\text{C}_3\text{H}_8$  concentrations below 0.02% we could not observe the formation of an initial layer, the SiC growth sets in with a three dimensional nucleation. This region is characterized by the growth of separated high islands (Fig.5) and results in very rough surfaces and interfaces. This lead to a smaller effective thickness of the grown layer compared to the 0.025% case. The morphology of the grown islands can be explained by the transport of Si atoms from the surrounding uncovered substrate surface to the regions where the initial nucleation occurs. As a consequence the uncovered surface between the islands is sinking with respect to the virgin surface. At the island periphery, steps, kinks and non-parallel areas are formed preventing a parallel epitaxy of SiC during the lateral growth (Fig.6). As a result the original single-crystalline early SiC crystal is found on a pedestal while the lateral growing part shows misorientations and polycrystalline portions. The trenches between the islands allow an unlimited Si transport to the surface even at longer processing times. This behaviour is similar to the nucleation behaviour observed during the conversion of Si into SiC by using a solid carbon source under ultra high vacuum conditions [12]. As a consequence of this growth behaviour within our experimental conditions no saturation of the growth kinetics could be detected (Fig.1, curve (c)).

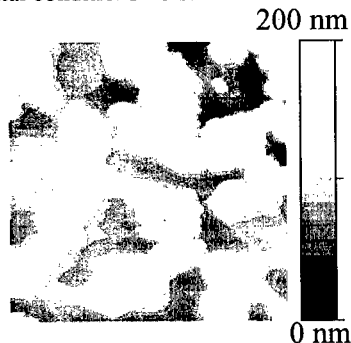


**Fig.5** AFM of the sample carbonized at  $1280^\circ\text{C}/0.015\%/75 \text{ K s}^{-1}$  and 1 s holding time ( $5 \times 5 \mu\text{m}^2$ ).

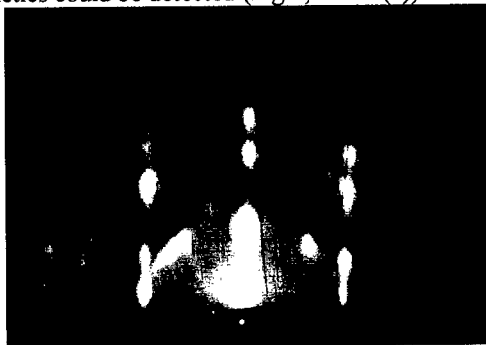
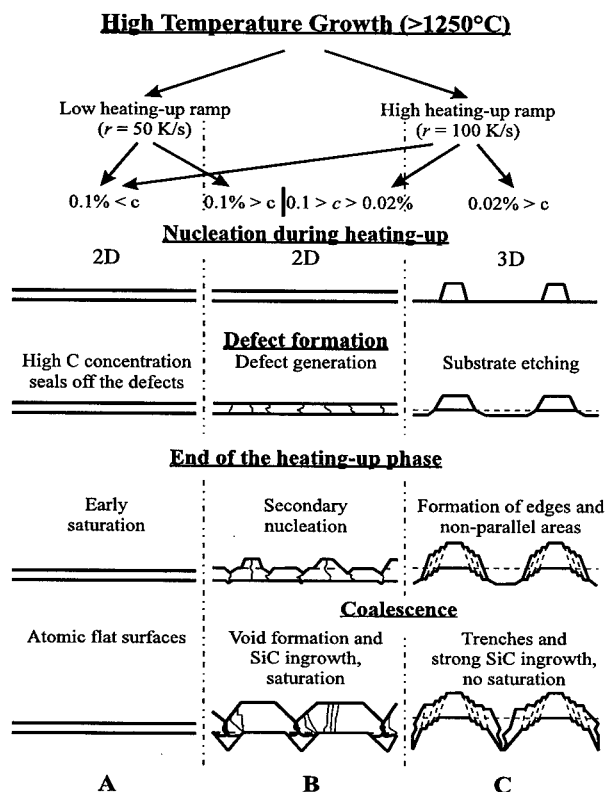


**Fig.6** RHEED pattern obtained from the sample carbonized at  $1280^\circ\text{C}/0.015\%/75 \text{ K s}^{-1}/1 \text{ s}$ .

The critical  $\text{C}_3\text{H}_8$  concentration leading to the different growth modes depends on the heating-up velocity as shown in detail in [12]. The different growth mechanisms are summarized in Fig.7.





### Conclusion

In dependence on the growth conditions ( $\text{C}_3\text{H}_8$  concentration and heating rates) three different growth modes were determined: (1) quasi-two dimensional growth with early saturation, (2) Stranski-Krastanov like growth with saturation and (3) three dimensional growth without saturation. These growth modes affect the structure and morphology of the grown SiC layer as well as the surface and interface roughness. For the formation of a pseudosubstrate only process conditions leading to quasi-two dimensional growth are suitable.

For  $\text{C}_3\text{H}_8$  concentrations above 0.02% the formation of an initial layer was found, which was not observed in previous study on (100)Si [6]. This initial layer acts like a template for the further layer growth and seems to be the precondition for the formation of a SiC layer with improved crystallinity.

### Acknowledgement

This work was supported by DFG under contracts Pe 624/2-1,2 and Li 449/8-1,2.

**Fig.7** Phenomenological growth model for the conversion process of Si into SiC under atmospheric pressure CVD conditions versus process conditions.

### References

- [1] W.G. Spitzer, D.A. Kleinmann, C.J. Frosch, Phys.Rev. 113 (1959), p.133.
- [2] H. Nakashima, T. Sugano, H. Yanai, Jap.J.Appl.Phys. 5 (1966), p.874.
- [3] C.J. Mogab, H.J. Leamy, J.Appl.Phys. 45 (1974), p.1075.
- [4] F. Boszo, J.T. Yates, Jr., W.J. Choyke, L. Muehlhoff, J.Appl.Phys. 57 (1985), p.2771.
- [5] L. Rimai, R. Ager, W.H.Weber, J. Hangan, A. Samman, W. Zhu, J.Appl.Phys. 77 (1995), p.6601.
- [6] J.P. Li, A.J. Steckl, J.Electrochem.Soc. 142 (1995), p.634.
- [7] V. Cimalla, J. Pezoldt, G. Eichhorn, Mater.Sci.Eng. B46 (1997), p.199.
- [8] G. Leitz, J. Pezoldt, I. Patzschke, J.-P. Zöllner, G. Eichhorn, MRS Symp. Proc. 303 (1993), p.171.
- [9] M. Bendler, F. Moldenhauer, V. Cimalla, J. Pezoldt, 42. Int. Wiss. Kolloq.; Ilmenau (in German); Bd. 3 (1997), p. 697.
- [10] V. Cimalla, Doctoral Thesis, TU Ilmenau, Shaker Verlag, 1998.
- [11] B. Schröter, unpublished results.
- [11] W. Attenberger, J.K.N. Lindner, V. Cimalla, J. Pezoldt, Mater.Sci.Eng. B61/62 (1999), p.544.
- [12] V. Cimalla, Th. Stauden, G. Eichhorn, J. Pezoldt, Mater.Sci.Eng. B61/62 (1999), p.553.

## The Influence of Foreign Atoms on the early Stages of SiC Growth on (111)Si

J. Pezoldt<sup>1</sup>, P. Masri<sup>2</sup>, M. Rouhani Laridjani<sup>2</sup>, M. Averous<sup>2</sup>, T. Wöhner<sup>1,3</sup>,  
J.A. Schaefer<sup>3</sup>, Th. Stauden<sup>1</sup>, G. Ecke<sup>1</sup>, R. Pieterwas<sup>1</sup> and L. Spieß<sup>4</sup>

<sup>1</sup> Institut für Festkörperelektronik, TU Ilmenau, Postfach 100 565, DE-98684 Ilmenau, Germany

<sup>2</sup> Groupe d'Etude des Semiconducteurs, CNRS, cc074, UMR 5650, Université Montpellier 2,  
Place E. Bataillon, FR-34095 Montpellier Cedex 5, France

<sup>3</sup> Institut für Physik, TU Ilmenau, Postfach 100 565, DE-98684 Ilmenau, Germany

<sup>4</sup> Institut für Werkstofftechnik, TU Ilmenau, Postfach 100 565, DE-98684 Ilmenau, Germany

**Keywords:** Germanium, Heteroepitaxy, Heterointerface Control, Molecular Beam Epitaxy

**Abstract** 3C-SiC was grown on (111)Si by solid source molecular beam epitaxy. The use of Ge during the carbonization leads to an improvement of the crystal quality of the grown layers. Electron spectroscopy revealed that Ge is incorporated mainly into the heterointerface. The observed effects are discussed in relation to different theories.

### Introduction

The lack of commercially available bulk crystals of 3C-SiC has retained over years the interest in thin film heteroepitaxy on Si substrates. Furthermore this heteroepitaxial system is a suitable alternative for heterojunction devices and new generations of sensors and the growth of III-nitrides. The most successful method is the chemical vapour deposition by a two step technique where first an initial layer is grown by carbonization [1]. In this technique the role of the initial layer is to act as a pseudosubstrate for the subsequent epitaxial growth and as a diffusion barrier against silicon transport into the growing film. Actually these layers are not able to compensate the large lattice mismatch and the differences in the thermal expansion coefficient. The residual stress can not be fully relaxed by misfit dislocations. This results in a bending of the Si wafer making further processing difficult. This and the high defect density in the grown films are the main drawbacks for this technology. To improve the quality of the SiC/Si heterosystem different approaches are possible. The first is a reduction of the processing temperature by using high reactive species and/or atomic layer epitaxial techniques [2-7], a second is the use of silicon on insulator substrates [8]. A further possible method is the SMART-CUT process or related technologies [9,10]. An alternative approach to improve the quality of the heteroepitaxial system is the incorporation of group IV atoms into the growth process [11-14]. The role of these elements during the growth of SiC on Si is currently under discussion. The aim of the work is to demonstrate that the use of Ge during the carbonization of Si by solid source molecular beam epitaxy (SSMBE) improves the crystallinity of the grown SiC layer on (111)Si. It will be shown that Ge is mainly incorporated near the heterointerface and changes the nucleation behaviour.

### Experimental

The SiC layers were deposited on 3" on-axis (111)Si substrates applying SSMBE. For the growth of the SiC layers on Si, we used an UMS 500 Balzers MBE system equipped with electron beam evaporators for Si, C and Ge. The wafers were cleaned without any wet chemical step. Prior to the deposition process the Si wafers were cleaned in a low energy H<sub>2</sub> plasma. After transferring the wafer into the reaction chamber an annealing step at 780°C for 1 h was employed. Subsequently the wafer was cooled down to 325°C and held at this temperature for 1 h. The deposition procedure was similar to the method reported in [7] and consists of the following process steps: (1) 0 ... 2 Monolayer (ML: with respect to the Si surface) Ge deposition on the (7x7) reconstructed Si surface at 325°C by electron beam evaporation, (2) 6 ML C deposition on the Si substrate, (3) heating up the Si wafer to

660°C for 3 minutes, (4) gradual increase of the substrate temperature in periods of 2 minutes by 50°C up to 1000°C or 1050°C, (5) the SiC deposition started at 950°C with a growth rate of 1 nm/min. The final epitaxial temperature was 1000°C and 1050°C. The SiC layers were grown at Si rich conditions and continuously operating Si and C sources. The growth process was controlled by using the (3×3)-Si (111)SiC surface reconstruction.

The growth process was monitored by *in situ* reflection high energy electron diffraction (RHEED) and *in situ* spectroscopic ellipsometry in real time. The films were investigated *ex situ* by atomic force microscopy (AFM), X-ray diffraction (XRD), X-ray photoelectron spectroscopy (XPS) and Auger electron spectroscopy depth profiling applying target factor analysis (AES-TFA).

### Results and Discussion

After the deposition of Ge onto the (111)Si surface we observed the following surface reconstructions at 325°C: (1) up to 1 ML Ge the (7×7)-Ge surface reconstruction, (2) between 1 ML and 2 ML Ge a mixture of (7×7)-Ge and (5×5)-Ge surface reconstructions (3) above 2 ML Ge the (5×5)-Ge surface reconstruction was observed. These observations are in agreement with the phase diagram reported in [15]. During the deposition of C on the Ge modified Si surface the diffraction pattern changes from the streaky one into a diffuse diffraction pattern with only a very weak evidence of a (1×1) surface reconstruction. To relax the formed compound system it was annealed at the deposition temperature for several minutes. The following step wise heating-up phase had the goal to transform the near surface layers of the Si substrate into Si and to stimulate the Ge incorporation. In dependence on the deposited amount of Ge we observed a decrease of the temperature where the 3D SiC spots could be detected with RHEED from 900°C (0 ML Ge) to 750°C (2ML Ge). The formed carbonized layer shows only a weak evidence of rotational. They vanished during growth after a thickness of 10 and 50 nm and a single domain SiC layer appeared. Within this thickness range the 3D-spotty diffraction pattern changed into a 2D-streaky one with (3×3)-Si reconstruction streaks. This is indicative for flat terraces and 2D growth. In Fig. 1 the RHEED pattern of three samples, having different amounts of predeposited Ge, are shown. No significant differences can be observed. They all show 2D diffraction with a strong (3×3)-Si reconstruction with a weak evidence of transmission features.

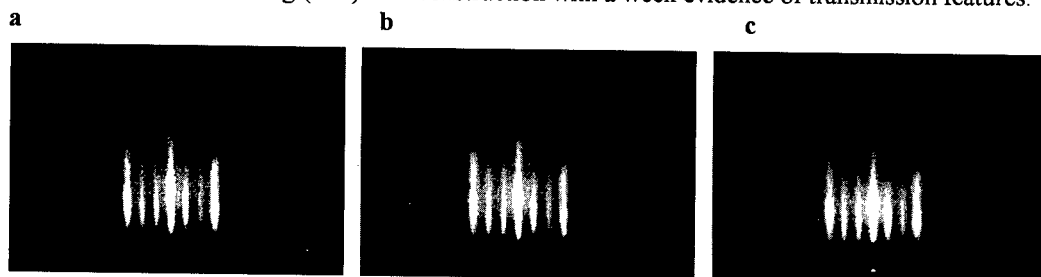


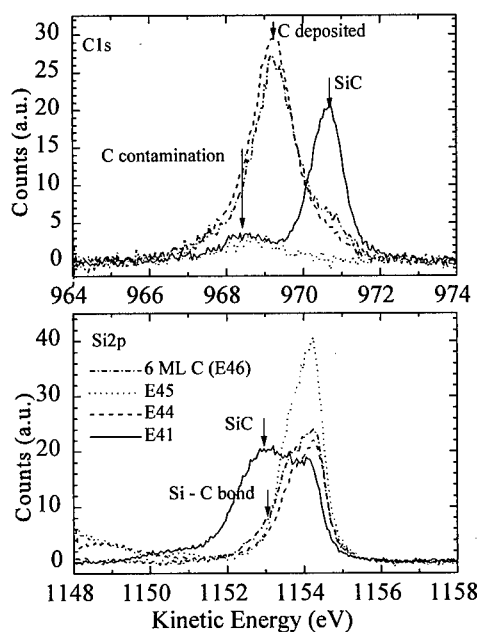
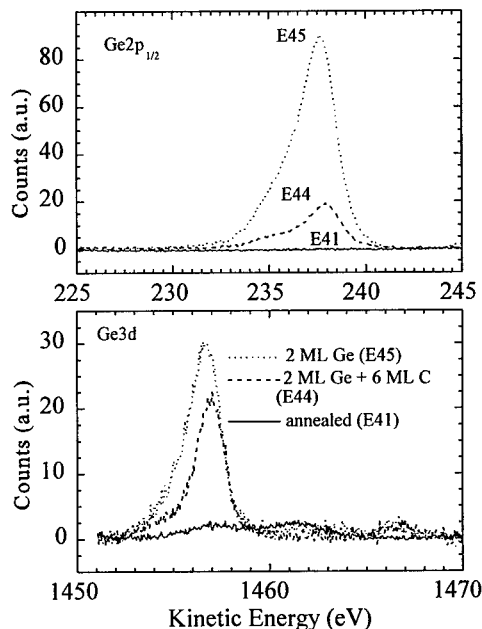
Fig.1 RHEED pattern recorded after the growth of 130 nm thick SiC layers grown at 1000°C: (a) 0 ML Ge, (b) 0.5 ML Ge, (c) 2 ML Ge. Azimuth [011].

To get a deeper insight into the influence of the Ge coverages on the SiC nucleation *in situ* spectroscopic ellipsometry was used to obtain information on the interface [16], *ex situ* AFM investigations were used to characterize the surface morphology and XRD in the  $\theta$ -2 $\theta$ -scan to characterize the overall crystallinity with the full width of the half maximum (FWHM) of the (111) 3C-SiC peak. The results are summarized in Table 1. The interface width given in Table 1 was determined after the growth of 100 nm SiC during the deposition. It was chosen to have an information about the near starting conditions. These results indicate on a positive effect of Ge introduction into the carbonization process of Si. An increase of the grain size and improvement of the flatness is evident if Ge is used. This can be explained by the reduction of the accumulated strain energy and an improved lattice match as can be predicted by the S-correlated theory of interface optimization developed in [17].

**Table 1** Variation of the surface, interface and crystallographic characteristics as a function of Ge coverages for 300 nm thick SiC layers grown at 1050°C

Sample	Ge coverage, ML	Terrace width/grain diameter, nm	Surface roughness rms, nm	Interface width, nm	FWHM, °
E17/19	0	133	1.8	1.2	0.241
E24	0.25	145	1.7	0.5	0.236
E25	0.5	192	1.5	1.1	0.232
E20/23	1	169	2.2	6.1	0.226
E23a	2	105	6.0	8.2	0.228

To get a deeper insight in the structure formed during the conversion process we carried out *ex situ* XPS and AES-TFA investigations. For this reason the conversion process was interrupted: (1) after the deposition of 2 ML Ge, (2) after the deposition of 6 ML C, and (3) after the step wise annealing procedure and compared to the case without Ge deposition. The XPS spectra obtained are shown in Fig. 2 and 3.

**Fig.2** XPS spectra of the C1s and the Si2p peak measured from the sample as build in.**Fig.3** XPS spectra of the low energy Ge2p<sub>1/2</sub> and high energy Ge3d peak measured from the sample as build in.

As can be seen on Fig.2 the XPS spectra of the deposited C is different from the XPS spectra of the C contamination (Fig.2, C1s). Furthermore the C forms SiC like bonds with Si even at this low temperatures. The amount of the SiC bonds is 0.9 ... 1 ML and 0.3 ML for the case without and with Ge respectively. Therefore the deposited Ge lowers the probability of the SiC formation at the interface and consequently may be another reason for decreased nucleation density, i.e. for increase of the grain size. After the step wise annealing the deposited C is completely transformed into SiC (Fig.2, C1s and Si2p). Furthermore no Ge could be detected at the surface. This is evident from the

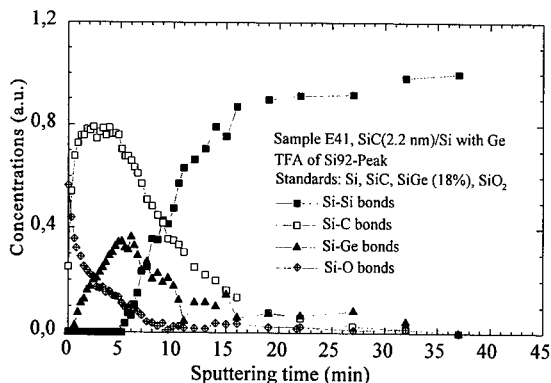


**Fig.4** AES depth profile of the Si, SiC, SiGe and SiO<sub>2</sub> bonds determined by AES-TFA.

vanishing low energy Ge2p<sub>1/2</sub> peak having an information depth of around 2 nm. In contrast the high energy Ge3d peak (information depth 8 nm) can be observed after the carbonization. This indicates on a segregation of Ge at the SiC-Si interface. This conclusion was confirmed by the carried out AES-TFA analysis (Fig.4). The Ge depth profile is located on both sides of the SiC-Si heterointerface. For the determination of the Ge distribution the Si-LVV peak of a Si<sub>0.82</sub>Ge<sub>0.18</sub> solid solution was used as the reference spectra. The Ge concentration in the maximum of the depth profile was determined to be around 2.5 ... 3%.

#### Conclusion

The use of group IV elements during the conversion of Si into SiC lead to an improved heteroepitaxy under SSMBE conditions even if the Ge coverage is below 1 ML. The observed effects can be explained by the common nucleation theory and within the framework of the S-correlated theory of interface optimization and its continuity conditions.

#### Acknowledgement

The work was supported in part by DFG under contracts Pe 624/2-1,2 and Ec 188/1-1,1-2.

#### References

- [1] S. Nishino, J.A. Powell, H.A. Will, Appl.Phys.Lett. 42 (1983), p.460.
- [2] I. Golecki, F. Reidinger, J. Marti, Appl.Phys.Lett. 60 (1992), p.1703.
- [3] S. Veprek, Th. Kunstmann, D. Volm, B.K. Meyer, J.Vac.Sci.Technol. A15 (1997), p.10.
- [4] T. Fuyuki, M. Nakayama, T. Yoshinobu, H. Shiomi, H. Matsunami, J.Cryst.Growth 95 (1989), p.461.
- [5] H. Nagasawa, K. Yagi, Phys.Stat.Sol. B202 (1997), p.335.
- [6] M. Kitabatake, J.E. Greene, Jap.J.Appl.Phys. 35 (1996), p.5261.
- [7] A. Fissel, K. Pfeninghaus, U. Kaiser, J. Kräußlich, H. Hobert, B. Schröter, W. Richter, Mater. Sci.Forum 264-268 (1998), p.255.
- [8] J. Camassel, J.Vac.Sci.Technol. B16 (1998), p.1648.
- [9] L. Di Ciocci, F. Letertre, Y. Le Tiec, A.M. Papon, C. Jassaud, M. Bruel, Mater.Sci.Eng. B46 (1997), p.349.
- [10] C. Serre, A. Romano-Rodriguez, A. Perez-Rodriguez, J.R. Morante, L. Fonseca, M.C. Acero, R. Kögler, W. Skorupa, Sensors and Actuators 74 (1999), p.169.
- [11] T. Hatayama, T. Fuyuki, H. Matsunami, Mater.Sci.Forum 264-268 (1998), p.235.
- [12] S. Mitchel, M.G. Spencer, K. Wongtchotigul, Mater.Sci.Forum 264-268 (1998), p.231.
- [13] K. Zekentes, T. Tsagaraki, Mater.Sci.Eng. B61-62 (1999) in press.
- [14] P. Masri, N. Moreaud, M. Averous, Th. Stauden, T. Wöhner, J. Pezoldt, MRS Symp.Proc. 572 (1999) p.213.
- [15] K. Kajiyama, Y. Tanishiro, K. Takayanagi, Surf.Sci. 222 (1989), p.38.
- [16] J. Scheiner, R. Goldhahn, V. Cimalla, G. Ecke, W. Attenberger, J.K.N Lindner, G. Gobsch, J. Pezoldt, Mater.Sci.Eng. B61-62 (1999), p.526.
- [17] P. Masri, Phys. Rev., B52 (1995), p.16627.

## Studies of the Initial Stages of Silicon Carbide Growth Using Molecular Hydrocarbon and Methyl Radical Gas Species

J.S. Gold<sup>1</sup>, J.S. Lannon, Jr.<sup>2</sup>, V.L. Tolani<sup>3</sup>, K.S. Ziemer<sup>3</sup> and C.D. Stinespring<sup>3</sup>

<sup>1</sup> Department of Physics, West Virginia University, Morgantown, WV 26506-6102, USA

<sup>2</sup> Electronic Technologies Division, MCNC, Research Triangle Park, NC 27709, USA

<sup>3</sup> Dept. of Chemical Engineering, West Virginia University, Morgantown, WV 26506-6102, USA

**Keywords:** Methyl Radicals, Molecular Growth Species, Surface Reactions, Thin Film Growth

**Abstract:** An ultrahigh vacuum compatible source of methyl radicals has been developed and used to investigate the initial stages of SiC growth on Si(100) 2x1 surfaces. This source produces a pure, high flux of methyl radicals ideally suited for film growth and surface kinetics studies. For comparable growth conditions, our studies reveal that radicals exhibit a propensity to maintain SiC stoichiometry, while molecular species (ethylene) tend to rapidly produce carbon-rich films. Films grown using radicals and molecular species also differ in microstructure. Methyl radicals produce films which have extremely smooth surfaces, while those films grown using molecular species exhibit hillocks or small grains.

### Introduction

Regardless of the deposition technology used, two factors complicate the growth of SiC. These are the large lattice mismatch between the substrate and thin film and the need to reduce the chemical activity of Si during initial layer growth. Both factors have generally been dealt with by the formation of a carbonized interface. Powell and coworkers[1] were among the first to use this approach in atmospheric pressure chemical vapor deposition (APCVD). They demonstrated significant improvements in SiC quality using a buffer layer formed by reacting a dilute mixture of C<sub>3</sub>H<sub>8</sub> in H<sub>2</sub> with the Si substrate as the substrate temperature was rapidly increased to 1400 °C. This approach, in various forms, is still widely practiced in APCVD, and similar methods are frequently used in gas source molecular beam epitaxy (GSMBE).[2-4]

Recently, Matsunami and coworkers[4] reported promising results which improve the potential for growing large diameter, single crystal 3C-SiC films on Si(100) substrates by GSMBE. They demonstrated significant improvements in epilayer quality using methyl (CH<sub>3</sub>) radicals (produced by pyrolysis of C<sub>3</sub>H<sub>8</sub>) to carbonize the Si substrate at low temperature (900 K-1000 K). Research in our laboratory has focused on development of an ultrahigh vacuum (UHV) compatible source of CH<sub>3</sub> radicals and the use of this source in GSMBE studies to characterize the initial stages of SiC growth on Si(100) surfaces. Our results corroborate the observations of Matsunami and coworkers and further define the conditions under which initial layer growth using a high purity radical source may provide an optimum substrate-film interface for subsequent SiC growth.

### Experimental Approach

The experimental studies were conducted in the UHV system shown in Figure 1. The analysis chamber is equipped with a hemispherical electron energy analyzer and x-ray source for x-ray photoelectron spectroscopy (XPS) as well as scanning Auger microprobe optics for Auger electron spectroscopy (AES). These *in-situ* techniques provide information on thin film surface composition, while *ex-situ* atomic force microprobe (AFM) analyses provide information on thin film microstructure. A quadrupole mass spectrometer in the growth chamber allows

characterization of the gas species sources and, in certain cases, species desorbed from the substrate during growth. The base pressure in the growth chamber is  $10^{-9}$  Torr.

As shown in Figure 1, the system may be fitted with a variety of growth species sources. In the present studies, we are concerned with the  $\text{CH}_3$  radical source which is illustrated more clearly in Figure 2. This UHV compatible source was designed and constructed to produce a pure, high flux of  $\text{CH}_3$  radicals for thin film growth and surface kinetics measurements. In operation, a

microwave discharge is established in a dilute, low pressure mixture of  $\text{CH}_4$  and Ar which is pumped through the source using an Alcatel 27 cfm roughing pump. The discharge products are "sampled" in the UHV chamber using a molecular beam skimmer having a  $400\text{ }\mu\text{m}$  aperture. The pressure in the source was measured at the outlet to the roughing pump by a capacitance manometer. Under growth conditions the substrate is located approximately one cm from the aperture. For source characterization studies the substrate is raised above the level of the source so the beam can be sampled directly by the mass spectrometer. The characteristics of the radical source are discussed in the next section.

The substrates ( $\sim 1.5\text{ cm} \times 1\text{ cm}$ ) were prepared from n-type electronic grade Si(100) substrates with a resistivity of 5 ohm-cm. These were cleaned *in-situ* by 2 keV  $\text{Ar}^+$  ion bombardment, and annealed for 15 minutes at 1100 K to produce the  $2\times 1$  surface reconstruction as verified independently by low energy electron diffraction (LEED). For the comparative studies, the Si(100)  $2\times 1$  surface was then heated to a growth temperature of 1000 K and exposed to a flux of either  $\text{CH}_3$  radicals or  $\text{C}_2\text{H}_4$  molecules. The  $\text{CH}_3$  radicals were produced using the source shown in Figure 2, while the flux of  $\text{C}_2\text{H}_4$  was produced using an effusive beam or simply back-filling the chamber to a pressure in the range of  $1\times 10^{-5}$  Torr.[5] The process could be stopped at any time to obtain *in-situ* AES analysis of the evolving film. Quantitative determinations of the  $\text{sp}^2\text{-C}$ ,  $\text{sp}^3\text{-C}$ , and SiC-C contribution to the C-KLL Auger line shape were obtained by factor analysis using methods described elsewhere.[5]

## Results and Discussion

Figure 3 shows a set of representative mass spectra which demonstrate the production of  $\text{CH}_3$  radicals. The upper spectrum shows the signal due to the  $\text{CH}_4$  present for a flow of 22.7 sccm Ar, 0.3 sccm Xe, and 2 sccm  $\text{CH}_4$  at a total pressure of 0.2 Torr. The energy of the ionizing electrons, 12.5 eV, is chosen to minimize the production  $\text{CH}_3$  in the mass spec ionizer by cracking of  $\text{CH}_4$ . When the microwave discharge is turned on, we observe the disappearance (or in some cases, simply the reduction) of the  $\text{CH}_4$  peak and the appearance of the  $\text{CH}_3$  and  $\text{C}_2\text{H}_x$  peaks.

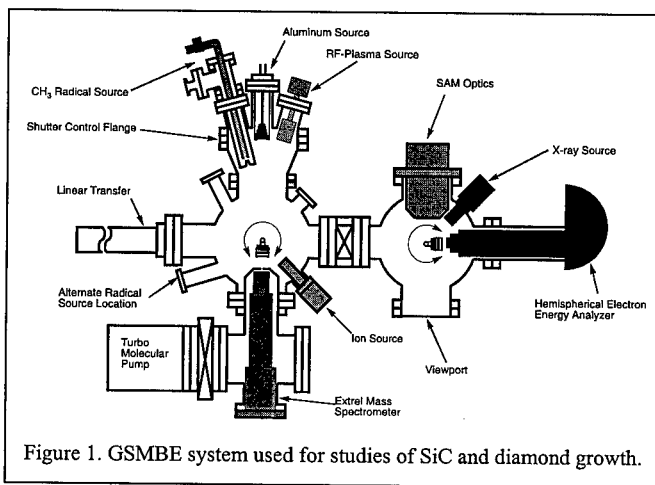


Figure 1. GSMBE system used for studies of SiC and diamond growth.

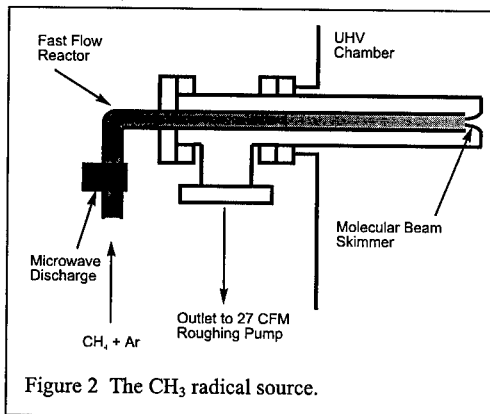


Figure 2 The  $\text{CH}_3$  radical source.

Taking into account species dependent ionization cross sections and mass spec transmission efficiencies, the relative concentrations of the  $\text{CH}_3$  and  $\text{C}_2\text{H}_x$  species produced for the indicated operating conditions are approximately 98%  $\text{CH}_3$  and 2%  $\text{C}_2\text{H}_x$ . The corresponding yield is  $\sim 23.6\%$   $\text{CH}_3$  and  $\sim 1.2\%$   $\text{C}_2\text{H}_x$ , while the  $\text{CH}_3$  flux is on the order of  $3 \times 10^{14} \text{ cm}^{-2} \text{ sec}^{-1}$ . This is equivalent to an effective beam pressure of  $6 \times 10^{-7}$  Torr. With the exception of very low levels of  $\text{C}_3\text{H}_x$  species, the remainder of the carbon appears to be deposited in the microwave discharge region, and no other hydrocarbons emerge from the source.

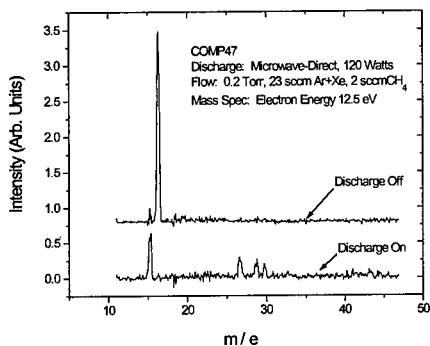


Figure 3. Mass spectra showing the production of  $\text{CH}_3$  radicals in a microwave-discharge of  $\text{CH}_4$  in Ar.

The performance characteristics of this  $\text{CH}_3$  radical source can be compared with that used by Matsunami and coworkers.[4] In their studies,  $\text{CH}_3$  radicals were produced by pyrolyzing  $\text{C}_3\text{H}_8$  in a high temperature cracker operating at 1473 K. They quote a  $\text{CH}_3$  density of  $3.3 \times 10^9 \text{ cm}^{-3}$  which corresponds to an effective beam pressure of  $1 \times 10^{-7}$  Torr. The  $\text{CH}_3$  flux or effective beam pressure in our source is a factor of approximately six times greater than that obtained by Matsunami and coworkers. Another major difference is the level of contaminant species. They quote a  $\text{CH}_3$  yield of 1.6%. Given the design of their source, virtually all of the input gas must emerge as pyrolysis products. Thus, the low  $\text{CH}_3$  yield suggests that their contaminant levels may be as much as two orders of magnitude higher than ours.

The initial stage of SiC growth on the Si(100) 2x1 surface was investigated under comparable conditions for  $\text{CH}_3$  radicals and  $\text{C}_2\text{H}_4$ . For a typical film grown using  $\text{CH}_3$  radicals, Figure 4 shows the evolution of the carbon species distribution, as determined by *in-situ* AES, with  $\text{CH}_3$  fluence. Figure 5 shows a corresponding plot for growth using  $\text{C}_2\text{H}_4$ . Here, an ML is defined as  $1 \times 10^{15} \text{ cm}^{-2} \text{ sec}^{-1}$ . It is evident that  $\text{CH}_3$  radicals tend to produce a more stoichiometric SiC film during the initial stages of growth, while  $\text{C}_2\text{H}_4$  produces a mixture of SiC and  $\text{sp}^3$  bound carbon. Although the latter bodes well for diamond nucleation, it indicates that  $\text{CH}_3$  radicals may be the best species for depositing the initial SiC layers.

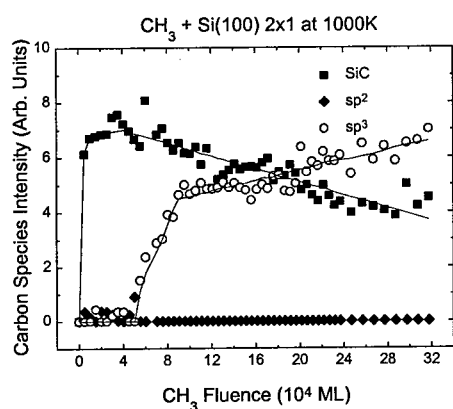


Figure 4. Carbon species distribution for growth using  $\text{CH}_3$  radical precursors.

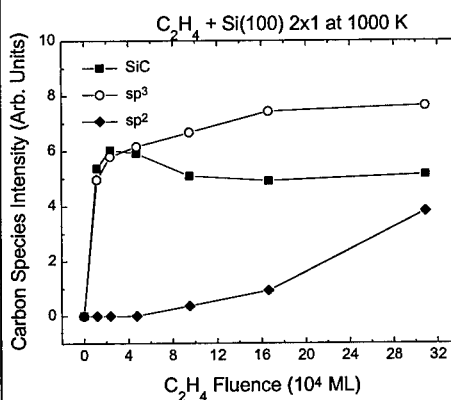


Figure 5. Carbon species distribution for growth using molecular precursors.



Representative AFM images for these films are shown in Figures 6 and 7. Surfaces of films grown with  $\text{CH}_3$  radicals are much smoother than those of films grown with molecular species. For films grown using  $\text{C}_2\text{H}_4$ , hillock diameters of  $\sim 0.2\ \mu\text{m}$  and an rms roughness of  $\sim 7\ \text{nm}$  are typical. Films grown using  $\text{CH}_3$  radicals, however, have much smaller hillocks and the rms roughness is less than  $1\ \text{nm}$ . In these films, the primary defect appears to be shallow pit-like features. Although not yet confirmed, the small hillocks on films grown using  $\text{CH}_3$  radicals may be associated with the appearance of the  $\text{sp}^3$ -carbon species. AFM measurements indicate that these films are much smoother if the growth sequence is stopped before  $\text{sp}^3$ -carbon species appear.

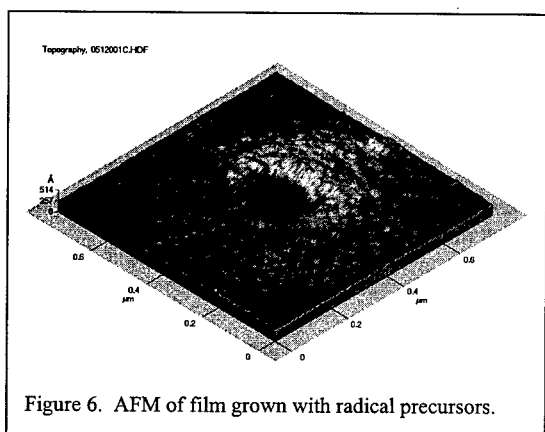


Figure 6. AFM of film grown with radical precursors.

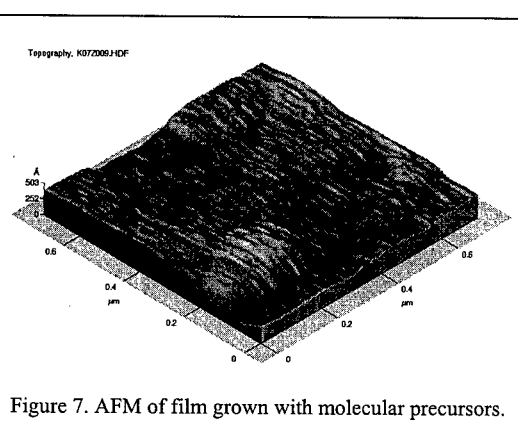


Figure 7. AFM of film grown with molecular precursors.

## Conclusions

The results presented here are consistent with those of Matsunami and coworkers.[4] They observed significant improvements in film quality when using  $\text{CH}_3$  radicals rather than molecular species ( $\text{C}_2\text{H}_2$  in their case) to carbonize the Si substrate. The remarkably high quality of their films may have been limited only by the high levels of molecular contaminants in their pyrolysis source. The results presented here suggest that their observed improvements may be due to a growth window characterized by very smooth, stoichiometric SiC layers. This window exists during initial layer growth just prior to the onset of an  $\text{sp}^3$ -carbon phase. The formation of both SiC and  $\text{sp}^3$ -carbon by molecular growth species has been previously described mechanistically using a surfactant mediated epitaxy model.[6] The use of  $\text{CH}_3$  radicals may lead to a suppression of the surfactant species (Si) and delay the onset of the  $\text{sp}^3$ -carbon phase. A major thrust of our present work is to establish the details of this mechanism and to determine the extent to which improvements in the initial layers formed using  $\text{CH}_3$  radicals can lead to improvements in SiC film quality. The growth "window" as well as subsequent SiC growth using organosilicon compounds are presently being investigated.

## References

- [1] S. Nishino, J.A. Powell, and H.A. Will, *Appl. Phys. Lett.* 42 (1983) 460.
  - [2] T. Yoshinobu, H. Mitsui, Y. Tarui, T. Fuyki, H. Matsunami, *Jpn. J. Appl. Phys.* 72 (1992) 2006.
  - [3] T. Hatayama, Y. Tarui, T. Yoshinobu, T. Fuyki, H. Matsunami, *J. Crystal Growth* 136 (1994) 333.
  - [4] T. Fuyuki, T. Hatayama, and H. Matsunami, *Phys. Stat. Sol. B* 202 (1997) 359.
  - [5] C.D. Stinespring, J.S. Gold, and J.M. Lannon, Jr., *J. Appl. Phys.* 77 (1995) 3823.
  - [6] J.M. Lannon, Jr., J.S. Gold, and C.D. Stinespring, *Appl. Phys. Lett.* 73 (1998) 226.
- Address all correspondence to: C.D. Stinespring at [cstinesp@wvu.edu](mailto:cstinesp@wvu.edu)

## Carbonization of SIMOX Substrates for Fabrication of Single-Crystal SiC-on-Insulator

S. Harada, M. Arita, Y. Ikoma and T. Motooka

Department of Materials Science and Engineering, Kyushu University,  
6-10-1 Hakozaki, Higashiku, Fukuoka, 812-8581, Japan

**Keywords:** Carbonization, Chemical Vapor Deposition, SiC-on-Insulator, SIMOX, Transmission Electron Microscopy

**Abstract.** We have developed a new method for fabrication of single-crystal SiC-on-insulator using SIMOX (Separation by IMplanted OXYgen) substrates. Carbonization of surface Si of SIMOX wafers induced cavities between the SiC and Si layers which resulted in low-quality SiC-on-insulator. On the other hand, crystalline SiC layers were formed on SIMOX substrates without cavities at SiC/Si interfaces by using CVD of SiC on as-implanted SIMOX substrates at 900 °C followed by N<sub>2</sub> annealing at 1350 °C.

### Introduction

Silicon-on-insulator (SOI) is a useful structure to enhance existing Si-CMOS technology. Separation by Implanted Oxygen (SIMOX) is one of the major methods to provide the SOI structure. It is interesting to form single-crystal SiC on SIMOX substrates, since it may give rise to a SiC-on-insulator structure which provides promising substrates for SiC-CMOS. Heteroepitaxial CVD growth of 3C-SiC on SIMOX substrates has been investigated by other researchers. Camassel *et al.* [1] and Reichert *et al.* [2] reported that large cavities were formed in the surface Si layer and these cavities extended into the buried oxide (BOX) layer. The optimal condition to form the SiC-on-insulator structure from SIMOX substrates has not yet been established. In this work, carbonization and CVD were carried out to both as-implanted and annealed SIMOX substrates, and the structures were examined based on cross-sectional transmission electron microscopy (XTEM).

### Experimental

SIMOX wafers were prepared by 180 keV O<sup>+</sup> implantation onto Si (100) substrates with a dose of  $4 \times 10^{17}$  cm<sup>-2</sup> at 550 °C. The implanted samples were annealed at 1350 °C for 1 hr in Ar + 0.5 % O<sub>2</sub> which resulted in formation of a continuous BOX layer with a thickness of 100 nm. Before the carbonization, the surface Si layer with a thickness of about 350 nm was chemically etched using KOH solution to obtain thinner surface Si layers. Carbonization was performed using 10 sccm of H<sub>2</sub>-diluted 10 % C<sub>3</sub>H<sub>8</sub> with additional 1000 sccm of H<sub>2</sub> for further dilution at 1300 °C and a total pressure of  $1 \times 10^5$  Pa. CVD of SiC was performed using pulsed supersonic free jets of CH<sub>3</sub>SiH<sub>3</sub> at a total pressure of  $\sim 10^{-3}$  Pa at a growth temperature of 900 °C [3] on as-implanted and annealed SIMOX wafers.

## Results and Discussion

### Carbonization of SIMOX substrates

Figure 1 shows XTEM images of the samples with various thicknesses of the surface Si layer carbonized at 1300 °C for 3 min. At a thickness of 140 nm, it can be seen that islands are formed on the surface with a thickness of about 50 nm and a width of about 400 nm in Fig. 1(a). The selected-area diffraction (SAD) pattern reveals that the island is SiC epitaxially grown on the Si surface. A large trapezoidal cavity is also seen below the SiC island. Reichert *et al.* also observed similar trapezoidal cavities in the surface Si layer of SIMOX wafer, and speculated that the inverse pyramidal cavities below SiC film extend to Si/SiO<sub>2</sub> interface and the shape of cavity is inverted [2]. At a thickness of 60 nm, both the SiC islands and the cavities become wider, as shown in Fig. 1(b), indicating that the width of the SiC island is nearly the same as that of the cavities below them. It is supposed that the cavities become wider since Si atoms are consumed extensively as the Si layer becomes thin. At a thickness of 40 nm, SiC islands grow much wider and result in a continuous thin film, as shown in Fig. 1(c). However, the each cavity is connected and becomes a cave, which results in the weak adhesion of the SiC film. It can be also seen a disorder at the lower SiO<sub>2</sub>/Si interface, suggesting that Si atoms below the SiO<sub>2</sub> layer are consumed to form the SiC film in this sample. It is confirmed from these results that the carbonization of SIMOX substrates does not result in SiC-on-insulator structure with good crystalline quality.

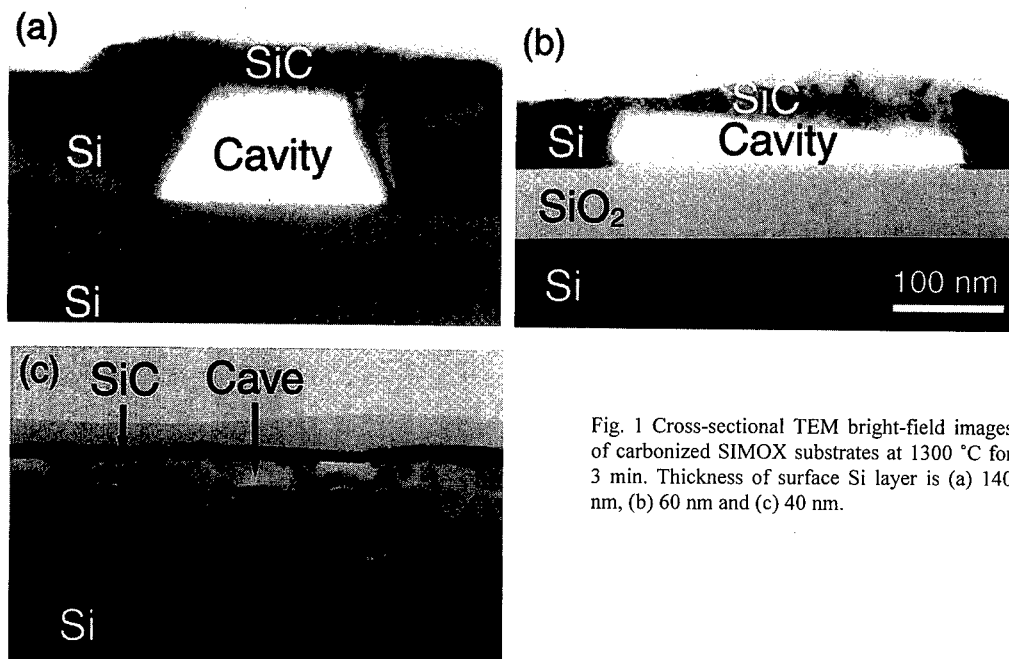


Fig. 1 Cross-sectional TEM bright-field images of carbonized SIMOX substrates at 1300 °C for 3 min. Thickness of surface Si layer is (a) 140 nm, (b) 60 nm and (c) 40 nm.

### CVD of SiC on SIMOX substrates

Figures 2(a) and (b) show XTEM images of 60 nm-thick SiC films formed on the as-implanted and annealed SIMOX wafers at 900 °C for 2 hrs, respectively. The SAD patterns reveal that all these films are epitaxially grown 3C-SiC. However, there is a difference in the morphology of their SiC/Si interface. There are cavities at the interface on the annealed SIMOX substrates, as shown in Fig. 2(b). These cavities are much smaller than those formed by the carbonization (see Fig. 1), since Si is included in the source gas and growth temperature is lower at the CVD growth. On the other hand, no appreciable cavities can be observed at the interface on the as-implanted wafer in Fig. 2(b). This may be due to ion-beam induced extended defects and strains in the surface region [4,5]. These defects and strains affect the diffusion processes of substrate Si atoms, which results in the cavity free interface.

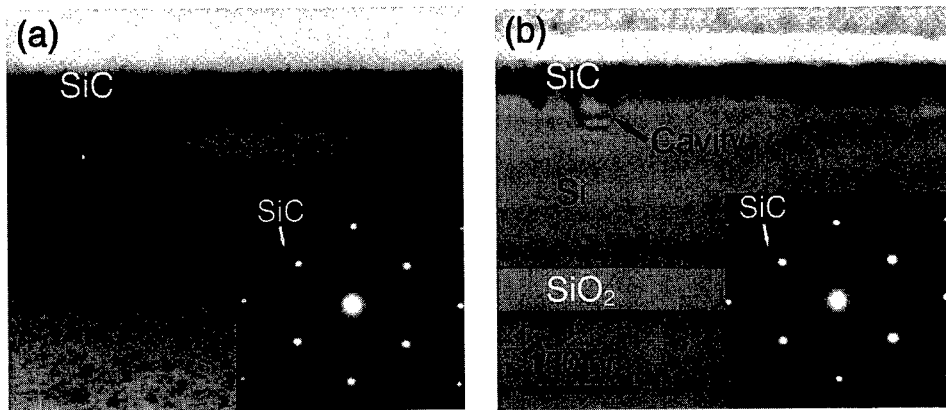


Fig. 2 Cross-sectional TEM bright-field images of SiC films formed by CVD on (a) as-implanted and (b) annealed SIMOX substrates. Inset shows the selected-area diffraction patterns from the images.

To obtain the buried SiO<sub>2</sub> layer in the sample shown in Fig. 2(a), the sample was annealed at 1350 °C for 1 hr. Figures 3 (a) and (b) show XTEM images of the samples annealed in N<sub>2</sub> and Ar+~5% O<sub>2</sub> ambient, respectively. It can be seen that buried SiO<sub>2</sub> layer is formed in both annealed samples. It is generally believed that O<sub>2</sub> gas is necessary in the ambient to form the continuous SiO<sub>2</sub> layer during the annealing. However, the continuous SiO<sub>2</sub> layer is obtained without O<sub>2</sub> gas in the ambient, suggesting that SiC film on the surface prevents the out-diffusion of the implanted O in the substrate. In Fig. 3(a), appreciable difference cannot be observed both in the SiC film and the SiC/Si interface before and after annealing in N<sub>2</sub> ambient. However, the thickness of SiC film is reduced to about 10 nm, and a film with bright contrast exists on SiC film after annealing in Ar+~5% O<sub>2</sub> ambient, as shown in Fig. 3(b). This bright film is supposed to be an oxide. In addition, cavities with {100} oriented facets exist below the SiC film, suggesting that Si element is provided from surface Si layer for the oxidation at the surface. It is confirmed from these results that SiC films can be formed on SIMOX substrates without cavities at the interface by using CVD of SiC on as-implanted wafers followed by annealing in N<sub>2</sub> ambient.

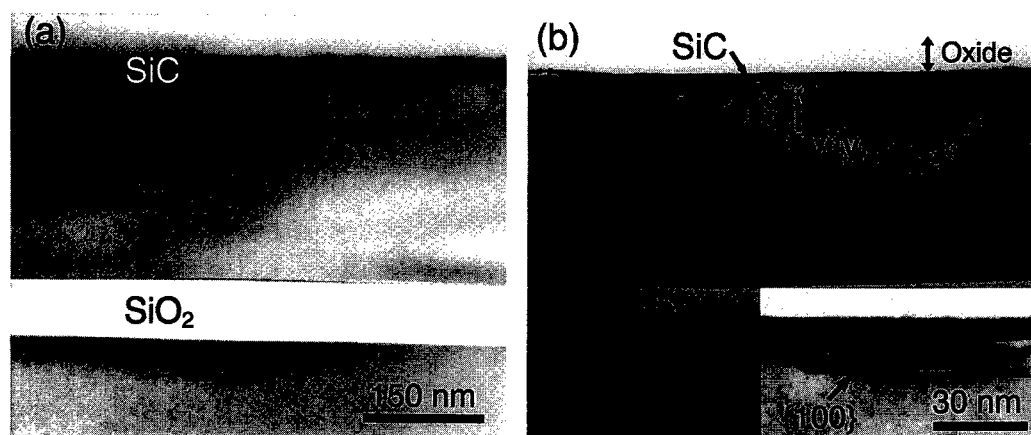


Fig. 3 Cross-sectional TEM bright-field images of SiC films on as-implanted SIMOX substrates after annealing at 1350 °C for 1 hr in (a) N<sub>2</sub> and (b) Ar+~5% O<sub>2</sub> ambient. Inset of Fig. 3(b) is the magnified image around the SiC/Si interface.

### Conclusion

SiC-on-insulator substrates have been fabricated by using SIMOX wafers. Carbonization of SIMOX wafers resulted in only low-quality SiC-on-insulator structures, since the surface region was composed of SiC islands and cavities. SiC films could be formed on SIMOX substrates without cavities at SiC/Si interface by using CVD on the as-implanted SIMOX wafers after N<sub>2</sub> annealing at 1350 °C.

### References

- [1] J. Camassel, J. V. Sci. Technol. B 16, (1998) 1648.
- [2] W. Reichert, E. Obermeier, J. Stoemenos, Diamond Relat. Mater. 6, (1997) 1448.
- [3] Y. Ikoma, T. Endo, F. Watanabe and T. Motooka, Jpn. J. Appl. Phys. 38, (1999) L301.
- [4] S. Nakashima and K. Izumi, J. Mater. Res. 8, (1993) 523.
- [5] D. Venables, K. S. Jones and F. Namavar, Appl. Phys. Lett. 60, (1992) 3147.

## SOL Thinning Effects on 3C-SiC on SOI\*

N. Planes<sup>1</sup>, H. Möller<sup>2,3</sup>, J. Camassel<sup>1</sup>, Y. Stoemenos<sup>4</sup>, L. Falkovski<sup>1,5</sup>,  
M. Eickhoff<sup>2</sup> and G. Krötz<sup>2</sup>

<sup>1</sup>Groupe d'Etude des Semiconducteurs (CNRS), cc074, Université Montpellier 2,  
FR-34095 Montpellier Cedex 5, France

<sup>2</sup>Department: FT2/M, Daimler Chrysler AG, Postfach 800465, DE-81663 München, Germany

<sup>3</sup>present address: Deutsche Bahn AG, Forschungs und Technologiezentrum,  
DE-München, Germany

<sup>4</sup>Physics Department, Aristotle University Thessaloniki, GR-54006 Thessaloniki, Greece

<sup>5</sup>permanent address: Landau Institute for Theoretical Physics, Russian Academy of Sciences,  
Kosygina 2, RU-117 334 Moscow, Russia

**Keywords:** 3C-SiC Deposition, SOI, Strain Relaxation, Thinning Process

### Abstract :

We have investigated the effect of reducing the SOL (Silicon OverLayer) thickness on the final structure of standard SOI (Silicon On Insulators) wafers. We show that the SOL morphology degrades when the SOL thickness decreases. This affects the growth of the 3C-SiC layers deposited on top.

### Introduction :

Silicon On Insulator (SOI) is a well-known material system to develop low power, low voltage and high speed electronic circuits [1, 2]. It has also promising applications as compliant substrate for 3C-SiC deposition [3]. Of course, in that particular case, the ideal situation would be to convert completely the thin Silicon OverLayer (or SOL) into cubic SiC during the carbonization step [4, 5]. In this way one would get directly a so-called SiCOI structure, with an active SiC layer directly grown on top of a thin SiO<sub>2</sub> insulating film [6]. This necessitates to grow on ultra-thin SOL thickness (~ 10 nm or less). Since these peculiar SOI structures are not directly available on the market, one must use a thinning process to modify the standard wafers.

In this work, we report on using a Sacrificial Oxidation (SO) or an Ion Beam Etching (IBE) process to thin the SOL of various SOI wafers. We have used SIMOX and Unibond<sup>®</sup> and, in both cases, started from ~ 200 nm (nominal) SOL thickness. Then we thinned progressively down to ~ 5 nm. In the first part, we show evidence of the dynamic response of the SOI structures to the thinning process and show that it comes mainly from internal strain relaxation. In the second part, we report on the morphology of the as-deposited SiC layers as a function of the SOL thickness.

### Effect of thinning the SOL on the final SOI morphology

Because of the difference in thermal expansion coefficients between silicon and silicon dioxide any direct bonding of two oxidized wafers, or any oxygen-ion implantation followed by a high temperature annealing step, must introduce a finite amount of stress at the various Si/SiO<sub>2</sub>

interfaces. This is a well-understood matter and the study of thermal strain [1, 7] as well as other process-induced (crystalline) defects (like for instance Oxygen Induced Stacking Faults [8] in nominal SOI materials) is well documented. However, to the best of our knowledge, no similar work as been done on the effect of thinning the SOL and not much is known on the resulting SOI morphology.

We started from standard 4" SOI wafers and, in both cases of SIMOX and Unibond® materials, used a thermal sacrificial oxidation process at 1050°C to thin the topmost Si overlayer. To determine the remaining SOL thickness, FTIR (Fourier Transform Infrared Reflectivity) measurements were done [9]. Apart from the change in SOL thickness (deduced from the change in interference pattern), the FTIR measurements provide evidence of a change in internal strain of the thin dielectric films. This is shown in Fig.1-a. Notice the drastic narrowing of the SiO<sub>2</sub>-related signal at about 1050 cm<sup>-1</sup>. Starting from a rather broad feature (~500 cm<sup>-1</sup>) for the as-delivered material, the strong Si-O bond signature [10] narrows rapidly as the SOL thickness decreases. This is true from the very beginning, when thinning from 200 to 100 nm, and does not depend on the type of material investigated.

To check that this was not due to any parasitic effect of the high temperature SO steps, we repeated the thinning process using oxygen-assisted IBE. Similar results were found, which is clear demonstration that we are dealing with real intrinsic properties. In other words the experimental improvement found in oxide properties relies only on an internal stress relaxation mechanism, where the stress originates from the difference in thermal expansion coefficients between Si and SiO<sub>2</sub> (~80% at room temperature). There is no artifact associated with the high temperature SO steps. To the best of our knowledge this provides the first, clear, evidence that all SOI materials are plastic systems, soft enough to relax when the SOL thickness decreases.

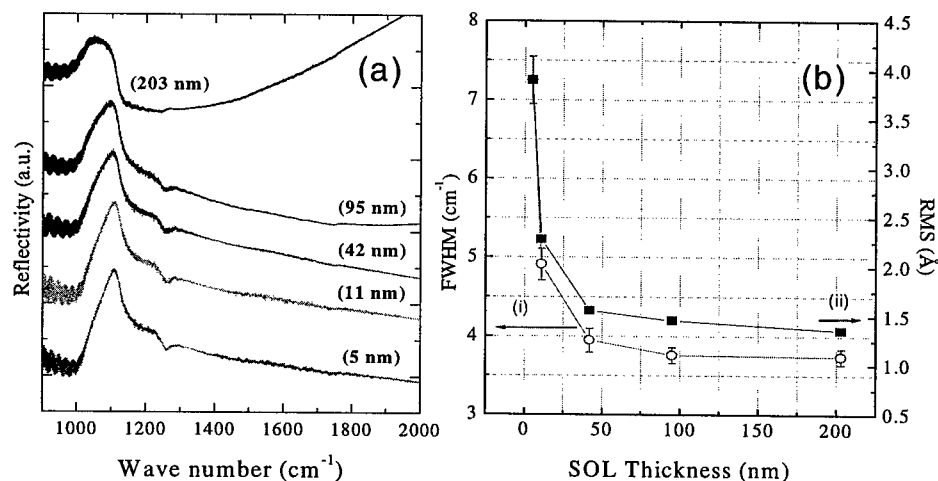


**Figure 1:** SOL thinning effects observed on : (a) infrared reflectivity spectra collected at room temperature; (i-b) the width of the ~ 521 cm<sup>-1</sup> Raman mode collected on top of the SOI wafer (transverse <X(Y,-)X> configuration); (ii-b) the AFM roughness (RMS value) measured on the SOL surface (see text).

Since, because of internal stress relaxation, the BOX properties improve when thinning the SOL in turn the SOL morphology must degrade. This is indeed what is found. First, using micro-Raman spectroscopy and a transverse configuration, we collected Raman spectra on the topmost part of the

SOI wafer. They evidenced an increased inhomogeneous shift and broadening when reducing the SOL thickness. Next, using Atomic Force Microscopy (AFM), we investigated the surface roughness. Again we found degradation when the SOL thickness decreases. Both series of results are shown in Fig.1-b. They show that decreasing the SOL thickness from 203, to 95, 42, 11 and finally 5 nm degrades the SOL morphology, and specially below 50 nm. The main difference from a thinning process to the next one is only the final roughness. With this respect, results obtained using SO appeared better than the one obtained using IBE [11].

To conclude this part, we have evidenced that the topmost part of any SOI wafer accommodates a complex admixture of stress, spatial inhomogeneity and local stress distribution [12]. This admixture extends a few  $\mu\text{m}$  inside the wafer and varies drastically when thinning the SOL. In this case, starting from a balanced strain system where both the SOL, BOX and topmost part of the SOI wafer are under equilibrium, the infrared spectra show that the strain localized in the BOX relaxes when the SOL thickness decreases. At the same time, the SOL morphology degrades.

#### Effect of thinning the SOL on the deposited SiC films

We have investigated the consequences of this phenomenon on the deposition of SiC layers. To minimize the negative effects of the temperature growth on the SOI material [3] monomethylsilane ( $\text{MeSi}_3$ ) was used as single precursor gas, with optimized carbonization and deposition conditions [12, 13]. The growth temperature was reduced to  $1200^\circ\text{C}$  and the thickness of the deposited layers was kept below  $\sim 2.5 \mu\text{m}$ . Finally, because in Fig.1-b two different regimes manifest, only SOI material with SOL thickness larger than 50 nm was used. After deposition, we analyzed the samples using TEM, DDX rocking curves and Raman spectroscopy. We have found the following:

Despite the (relatively) low deposition temperature, cavities still develop in the SOL during the SiC deposition. As usual [13], they start from the SiC/Si interface, penetrate the SOL and touch the BOX. This results in a partial decomposition of the BOX, with silicon redistribution. The total volume of the cavities increases when the SOL thickness decreases. This is shown in Table 1. If the SOL thickness reduces too much, the SiC layer usually delaminates.

SOL thickness (nm)	SiC thickness ( $\mu\text{m}$ )	Surface covered by cavities (%)	Mean size of cavities (nm)
200	2.3	4	400
100	2.4	20	1400
50	2.5	40	2125

**Table 1** : Evolution of cavities versus SOL thickness.

This reduced stability of the SOL does not help in improving the SiC layer properties. This is shown in Fig.2. We plot the change in Full Width at Half-Maximum (FWHM) of (a)  $\omega$ -scan rocking curves collected on the  $\langle 200 \rangle$  reflection of SiC and (b) Transverse Optical (TO) Raman mode. Taking into account the  $2.5 \mu\text{m}$  SiC thickness, and the low deposition temperature, the SiC layer deposited on the nominal SOL ( $\sim 200 \text{ nm}$  thickness) exhibits reasonable values. This is no longer true when decreasing the SOL thickness. In both cases, we notice that the width of experimental spectra increases. Similar results have been already found using SIMOX substrates [15] but, because of implantation related defects, the analysis was not straightforward. In this work only the SOL varies and, clearly, decreasing the SOL renders the SiC/Si/SiO<sub>2</sub> system unstable versus SiC deposition.



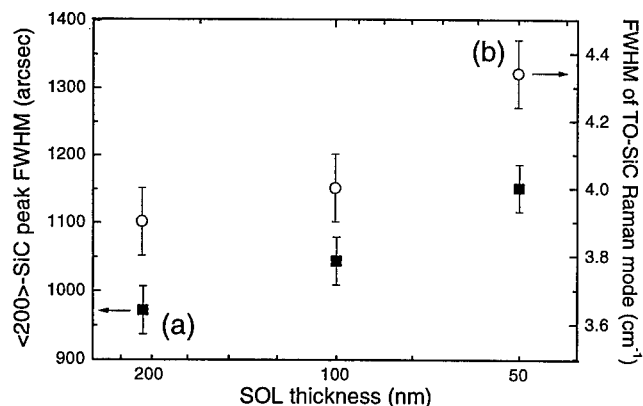


**Figure 2 :** FWHM experimental values of (a): the DDX rocking curves and (b) the micro-Raman spectra collected at the SiC/Si interface in the transverse configuration, in the case of 3C-SiC deposited on Unibond® with SOL thickness 200, 100 and 50 nm.

### Conclusion

Starting from nominal values ( $d_{\text{SOL}} \sim 200$  nm and  $d_{\text{BOX}} = 400$  nm) and thinning the SOL down to 5 nm, we have found a drastic effect of strain relaxation within the BOX. At the same time, the remaining SOL morphology degrades. This is independent of the thinning process used and of the type of SOI material investigated. This comes only from a close balance between internal strain, with internal dynamic equilibrium, which does exist in the starting material. In turn, the SiC layer becomes more and more defective when the SOL thickness decreases.

### Acknowledgements :

This work was supported in part by the EU commission under contract BRPR CT96 0261

### References :

- [1] Q.-Y. Tong and U. Gösele, *Semiconductor Wafer Bonding, Science and Technology*, Wiley Interscience, New York (1999)
- [2] P.K. Vasudev, *Solid-State Electron.* 39 (1996), p. 481
- [3] J. Camassel, *J. Vac. Sci. Technol. B* 16 (1998), p. 1648
- [4] S. Nishino, J.A. Powell and H.A. Will, *Appl. Phys. Lett.* 42 (1983), p. 460
- [5] S. Nishino, H. Suhara, H. Ono and H. Matsunami, *J. Appl. Phys.* 61 (1987), p. 4889
- [6] A.J. Steckl, C. Yuan, Q.Y. Tong, U. Gösele, and M.J. Loboda, *J. Electrochem. Soc.* 141 (1994), p. L66
- [7] T.J. Letavic, H. Baumgart, P. Pinker, S. Merchant and E. Arnold, *Proc. 1<sup>st</sup> Int. Symposium on Semiconductor Wafer Bonding: Science, Technology and Applications 92-7*, The Electrochemical society, Pennington, NJ, 1992, p. 397
- [8] D.-W. Shin, D.-O. Choi and G.-H. Kim, *Thin solid films* 346 (1999), p. 169
- [9] S. Charpenay, P.A. Rosenthal, P.R. Solomon, J. Xu, V.A. Yakovlev, L.P. Allen, M.W. Brandt and B. Cordts, *Proc. 1998 IEEE International SOI Conference*, 43 (1998)
- [10] J. Camassel, A. Goullet and J. Pascual, *Phys. Rev. B* 38 (1988), p. 8412
- [11] J. Camassel, N. Planes, L. Falkovsky, H. Möller, M. Eickhoff and G. Krötz, *Electron. Letters* 35 (1999), p. 1284
- [12] L. Falkovski, J.M. Bluet and J. Camassel, *Phys. Rev. B* 57 (1998), p. 11283
- [14] V. Papaioannou, E. Pavlidou, J. Stoemenos W. Reichert, E. Obermeier, *Materials Science Forum* 264-268 (1998), p. 445
- [14] H. Möller, M. Eickhoff, M. Rapp, H.W. Grueninger and G. Krötz, *Appl. Phys. A* 68 (1999), p. 461
- [15] G. Ferro, N. Planes, V. Papaioannou, D. Chaussende, Y. Monteil, Y. Stoemenos and J. Camassel, *J. Mat. Sci. Eng. B* 61-62 (1999), p. 586

## Low Temperature Growth of 3C-SiC on Silicon for Advanced Substrate Development

M.E. Okhuysen<sup>1</sup>, M.S. Mazzola<sup>1</sup> and Y.-H. Lo<sup>2</sup>

<sup>1</sup> Emerging Materials Research Laboratory, Department of Electrical & Computer Engineering,  
Mississippi State, MS 39762-9571, USA

<sup>2</sup> School of Electrical Engineering, Cornell University, Ithaca, NY 14853-5401, USA

**Keywords:** Antiphase Domain, Nano-structure, SOI, Twin, Universal Compliant

**Abstract** A lower temperature process for 3C-SiC (100) growth was investigated for use on compliant silicon substrates, including "universally compliant," SOI, and substrates patterned with nanostructures. The 3C-SiC (100) films improved as the film thickness increased due to the annihilation of defects in the [111] directions. This improvement due to thickness was greater than the effects due to the novel substrates.

### Introduction

Growth of 3C-SiC films on silicon was demonstrated by Powell *et al* [1] in 1987. However, because of a 20% mismatch in the lattice constants of silicon and 3C-SiC, the resulting 3C-SiC films were not of device grade quality. The major defects of 3C-SiC (100) films are twin boundaries (TBs) and antiphase boundaries (APBs) in the [111] direction. Novel substrates such as Silicon on Insulator (SOI), twist-bonded Universal Compliant (UC) substrates and nano-structures [2,7] have been considered for improving the quality of the 3C-SiC (100) films.

It is well known that very thin films should, in theory, be able to act as "compliant substrates" to seed heteroepitaxial deposition of materials with some lattice mismatch [2]. A UC substrate is made by bonding a thin layer of Si (100) at a 45° angle to a support substrate of Si (100). The weak bonding created by an array of screw dislocations between the thin layer of Si and the support substrate is anticipated to allow the thin layer to act as a compliant "free standing" film. A SOI substrate is made using the SIMOX process (implanted oxygen forms an SiO<sub>2</sub> layer under about a 100 nm Si film). The Si (100) film was mechanically polished and oxidized/wet etched until the film was reduced to a thickness of about 15 nm. The low viscosity of the SiO<sub>2</sub> at the 3C-SiC deposition temperatures is anticipated to provide isolation between the thin Si compliant film and the underlying silicon substrate. This allows weaker coupling between substrate and the overlying film possibly reducing stress at the Si/SiC interface [8]. A nano-structure substrate is made by etching 50 nm diameter post 80 nm center to center that are 250 nm tall on a Si(100) wafer. 3C-SiC should nucleate on each post and any defects form will glide to the edge of the post leaving a defect free region of 3C-SiC. Then these separate regions of 3C-SiC will grow together, however these regions may be separated by TBs of ATBs [7].

Typical temperatures used for single-crystal 3C-SiC growth are between 1310° C and 1360° C, which may be too high for the SOI and UC substrates to withstand. A lower temperature process to grow single-crystal 3C-SiC films is therefore required. Cimalla *et al* [4] demonstrated that the level of twinning depended on the Si/C ratio particularly at growth temperatures below 1300° C. This paper reports the temperature range which good quality 3C-SiC (100) films were grown on Si (100). This process was used to grow on twist-bonded (UC), (SOI), and nano-structure substrates.

## Experimental

An APCVD three step process of H<sub>2</sub> etch at 1000° C, carbonization at 890° C and growth at a temperature of 1335° C has already been established [3]. The temperature is measured by an optical pyrometer at the back end of a SiC coated graphite susceptor. For this work, the etch process and carbonization process remain the same and only the growth conditions have been modified. The growth temperature was lowered in 25° C increments. The growth temperature was first lowered without changing the precursor flow rates. Then the surface of the 3C-SiC films were characterized using an optical microscope. The surface morphology was then optimized by adjusting the precursor flow rates. First the SiH<sub>4</sub> flow rate was adjusted to eliminate super saturation of silicon while monitoring the growth rate. Then the C<sub>3</sub>H<sub>8</sub> flow rate was varied to achieve the smoothest surface morphology. Films were grown at temperatures from 1335° C to 1235° C.

3C SiC films were grown on UC ,SOI and nano-structure substrates. A 3C-SiC film of approximately 3.5  $\mu\text{m}$  was grown on a UC substrate at 1335°C. A 3C-SiC film approximately 0.5  $\mu\text{m}$  thick was grown on a SOI substrate at 1310°C. A film 3C-SiC of approximately 1.2 $\mu\text{m}$  was grown on a nano-structure substrate at 1310°C.

## Results

For temperatures between 1335° and 1260° the process parameters were optimized as shown in Table 1. At 1235° C the equipment did not allow a silane flow rate low enough to eliminate super saturation, also TEM and selected area electron diffraction showed a poor crystal quality. The grain size of a film grown at 1335° C shown in Figure 1(a) is similar to the film grown at 1285° C shown in Figure 1(b) both are 2  $\mu\text{m}$  thick, however the film in Figure 1(c) which is 13 $\mu\text{m}$  thick has a larger grain size. The TEM image of the baseline in Figure 2(a) shows a high density of defects at the Si/SiC interface. The TEM image of the film grown on the UC substrate in Figure 2(b) at the surface the grain size similar. The grain size of the film grown on the UC substrate shown in Figure 3(a) is comparable to the control Figure 3(b). The grain size of the film grown on the SOI substrate shown in Figure 3(c) is comparable to the control Figure 3(d). The grain size of the film grown on the nano-structure substrate Figure 3(e) is comparable to the control Figure 3(f).

Table 1 Optimized Growth Conditions

Temperature (°C)	SiH <sub>4</sub> (sccm)	C <sub>3</sub> H <sub>8</sub> (sccm)	Growth rate ( $\mu\text{m/hr.}$ )
1335	7	8.5	1.0
1310	7	7	1.0
1285	7	7	1.0
1260	7	7	1.0
1235	4	4.5	0.25

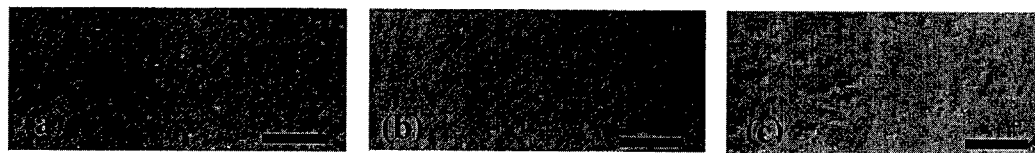


Figure 1 Optical micrographs of the surface of 3C-SiC films grown on Si at different temperatures and thickness (a) 1335° C (2 $\mu\text{m}$ ), (b) 1285° C (2 $\mu\text{m}$ ), (c) 1335° C (13 $\mu\text{m}$ ). Scale bar 25 $\mu\text{m}$ .

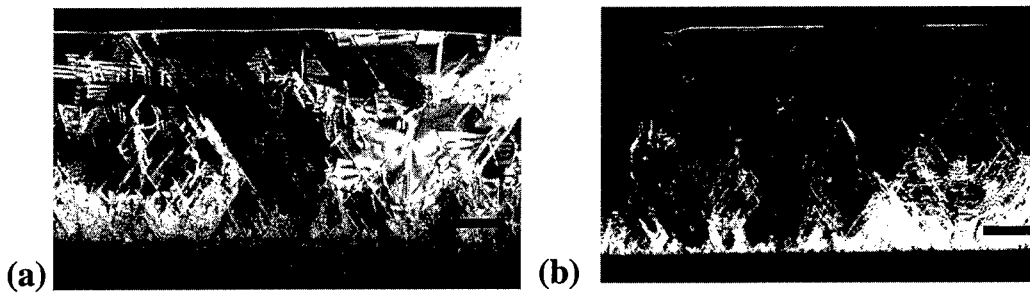


Figure 2 Cross-section TEM of the 3C-SiC .(a)film grown on Si and (b) film grown on UC substrate. Scale bar 1 $\mu$ m.

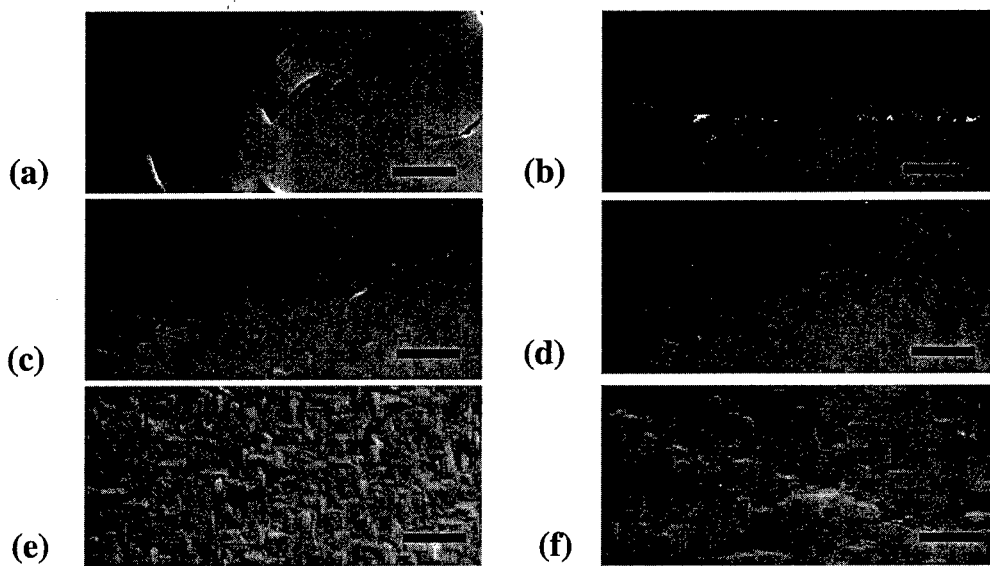


Figure 3.SEM micrographs of 3C-SiC films grown on novel substrates (a)UC (b)control(c)SIMOX(d)control(e)nano-structure(f)control. Scale bar 3 $\mu$ m.

## Discussion

We have found that once the proper process parameters have been optimized the grain size depends only on the film thickness. Many TBs and APBs are generated at the Si and 3C-SiC interface. It has been shown that these boundaries travel in the  $[111]$  directions. When these boundaries cross they are annihilated as shown in Figure 4 [5]. The process of annihilation creates larger and large low defect domains as the film grows thicker. This is evident in the TEM images of Figure 2. This is also demonstrated by the thicker film in Figure 1(c). If the growth conditions are not optimal these boundaries will nucleate away from the interface as the film grows [6].

The novel substrates may have a small improvement at the Si/SiC interface however, the surface of the films is not improved. This is because the annihilation of TBs and APBs improves the film as it grew thicker more than the improvement contributed by the novel substrates.

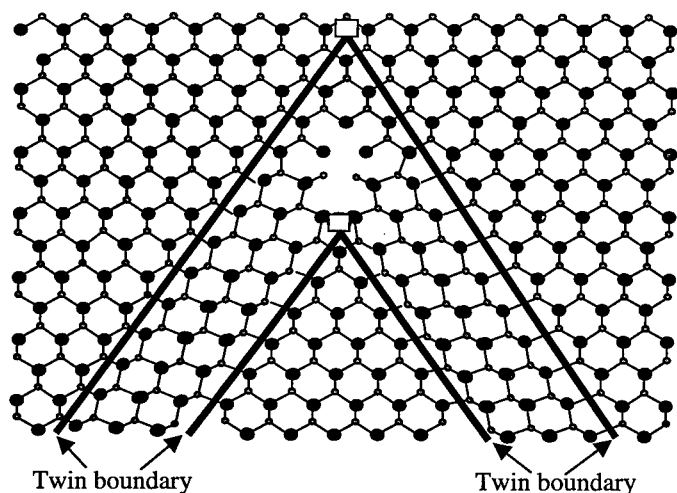
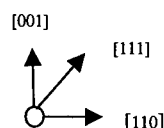


Figure 4. Schematic drawing showing the elimination of twin boundaries. Adapted from ref [5].



- C atom
- Si atom

## Conclusion

A process with a growth temperature as low as 1260° C was established. It was observed that as the 3C-SiC film grows thicker the quality improves. Several novel substrates were grown on, however the improvement due to the novel substrates did not surpass the improvement due to thicker growth.

## Acknowledgements

The authors acknowledge Eric Stach and Jason Wang of University of Virginia for the TEM characterization. This work was supported by the Office of Naval Research, Grant No. N0014-98-1-0824, Dr. C. Wood program manager.

## References

- [1] Powell, J.A., Matus L.G. and Kuczmariski, M.A., J. of the Electrochemical Soc., **134**, (1987) 1558.
- [2] Ejeckam, F.E., M.L. Seaford, Y.-H. Lo, H.Q. Hou, and B.E. Hammons, *Appl. Phys. Lett.* **71**, (1997) pp. 776-778
- [3] S. E. Sadow, M. E. Okhuysen, M. S. Mazzola, M. Dudley, X. R. Huang, W. Huang and M. Shamsuzzoha, Proceedings of the Materials Research Society, Boston, MA, Nov. 1998 pp107-112.
- [4] Cimalla, V., Pezoldt, J., Ecke, G. and Eichhorn, G, Inst. Phys. Conf. Ser. No 142: Chapter 1 pp 153-156.
- [5] K. Yagi and H. Nagasawa, *Materials Science Forum Vols. 264-268* (1998) pp.191-194.
- [6] T. Takahashi, Y. Ishida, H. Okumura, S. Yoshida and T. Sekigawa., *Materials Science Forum Vols. 264-268* (1998) pp.207-210.
- [7] D. Zubia and D. Hersee, *Journal of Applied Physics*, Vol **85**, No. 9, May 1999 pp.6492-6496.
- [8] A. R. Powell, S. S. Iyer and F. K. Legoues, *Appl. Phys. Lett.* **64** (14), (1994) pp. 1856-1858

Contact:

Mike Okhuysen

Tel. : 662-325-9476 Fax: 662-325-9478

e-mail: meo1@ece.msstate.edu

## Epitaxial Growth of $\beta$ -SiC on Ion-Beam Synthesized $\beta$ -SiC: Structural Characterization

A. Romano-Rodríguez<sup>1</sup>, A. Pérez-Rodríguez<sup>1</sup>, C. Serre<sup>1</sup>, J.R. Morante<sup>1</sup>,  
J. Esteve<sup>2</sup>, M.C. Acero<sup>2</sup>, R. Kögler<sup>3</sup>, W. Skorupa<sup>3</sup>, M. Östling<sup>4</sup>, N. Nordell<sup>5</sup>,  
S. Karlsson<sup>5</sup> and J. Van Landuyt<sup>6</sup>

<sup>1</sup> EME, Department of Electronics, University of Barcelona, Associated Unit to CNIM-CSIC,  
c/Martí i Franquès 1, ES-08028 Barcelona, Spain

<sup>2</sup> CNM-CSIC, Campus UAB, ES-08193 Bellaterra, Spain

<sup>3</sup> Forschungszentrum Rossendorf, PO Box 510119, DE-01314 Dresden, Germany

<sup>4</sup> KTH, Electrum 229, SE-16440 Kista, Sweden

<sup>5</sup> IMC Industrial Microelectronics Center, Electrum 233, PO Box 1084, SE-16440 Kista, Sweden

<sup>6</sup> EMAT-RUCA, University of Antwerpen, Groenenborgerlaan 171, BE-2020 Antwerpen, Belgium

**Keywords:** CVD Growth, FTIR, Ion Beam Synthesis, TEM, XRD

**Abstract.** In this work we present for the first time, to our knowledge, the CVD epitaxial growth of  $\beta$ -SiC using an ion beam synthesized (IBS)  $\beta$ -SiC layer as seed, which has been formed by multiple implantation into Si wafers at 500°C. The ion beam synthesized continuous layer is constituted by  $\beta$ -SiC nanocrystals that are well oriented relative to the silicon substrate. Comparison of the epitaxial growth on these samples with that on silicon test samples, both on and off-axis, is performed. The results show that the epitaxial growth can be achieved on the IBS samples without the need of the carbonization step and that the structural quality of the CVD layer is comparable to that obtained on a carbonized silicon sample. Improvement of the quality of the deposited layer is proposed.

### Introduction

The availability of large area high quality SiC substrates is an important topic for the development of SiC based technologies. Single crystal 6H-SiC wafers are nowadays commercially available in sizes up to 2" and attempts from Cree Research are ongoing to produce 4" 6H-SiC bulk wafers. However their crystalline quality is relatively poor and price is still too high. At the same time SiC epitaxy on large area Si wafers is also a route used by different laboratories [1-3] and this type of substrates are commercially available nowadays, although their crystalline quality is not yet as good as required.

Ion beam synthesis (IBS) is a highly versatile technique, which is commercially used for the production of SIMOX substrates [4] and which has been used for the synthesis of SiC in crystalline, polycrystalline and amorphous layers [5]. Such layers have been already employed for the fabrication of micromechanical test structures using a process directly derived from standard silicon bulk micromachining [6] and for the formation of SiCOI structures [7]. However the thickness which can be achieved using this method is rather limited to about a few hundred nanometers.

To circumvent this limitation in this work we present for the first time, to our knowledge, the CVD epitaxial growth of  $\beta$ -SiC using an IBS  $\beta$ -SiC layer as a seed. The resulting layer is compared with the CVD growth directly performed on Si wafers, either including or excluding a carbonization step.

## Experimental

The ion beam synthesized samples have been prepared by multiple carbon ion implantation into Si (001) substrates at a temperature of 500°C. This temperature is high enough in order to directly form  $\beta$ -SiC nanocrystals in the silicon substrates, which are well oriented to the silicon lattice according to the relation

$$([001]_{\text{Si}} \parallel [001]_{\beta\text{-SiC}}, (110)_{\text{Si}} \parallel (110)_{\beta\text{-SiC}})$$

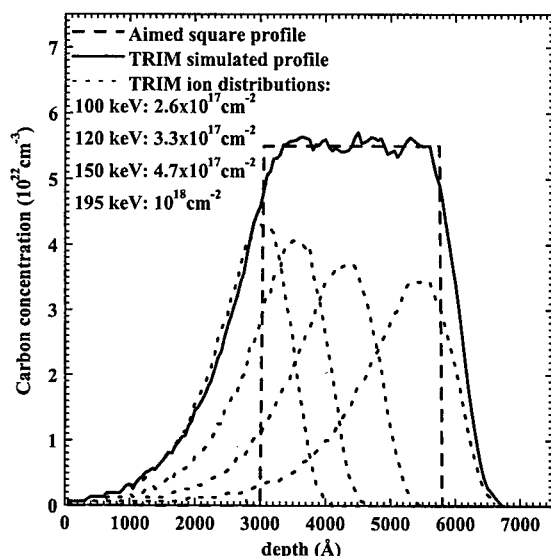


Fig. 1: Carbon profile obtained from TRIM simulations.

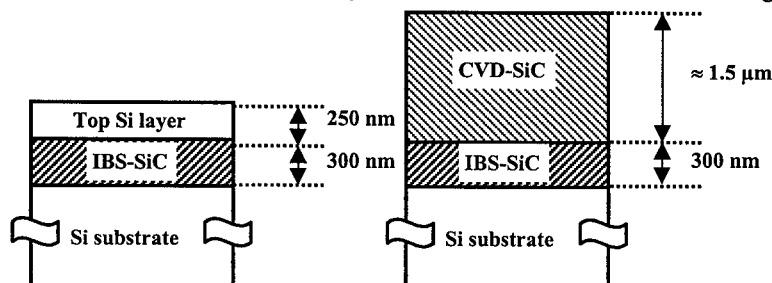


Fig. 2: Schematic representation of the technological process used for the CVD growth on the IBS sample.

while the second did not include this step. The CVD growth itself has been performed at 1350°C for 30 minutes, at a growth rate of about 3  $\mu\text{m/h}$ . The structure obtained on the IBS sample after CVD growth is schematically represented in Fig. 2.

Characterization of the obtained samples has been performed by cross-section Transmission Electron Microscopy (XTEM), X-Ray Diffraction (XRD), and Fourier Transform InfraRed (FTIR) spectroscopy.

## Results and discussion

The first result is obtained from optical inspection of the surface of the samples, which allows to divide them into 2 different groups. All 3 carbonized samples and the IBS that was not carbonized

without amorphizing the substrate. 4 implantations have been employed in order to obtain an almost flat carbon profile, as is shown in Fig. 1, followed by an annealing at 1150°C for 6 hours in order to improve the crystalline quality. The main process and properties of this material have been published extensively elsewhere [8]. Next the upper Si layer has been removed using TMAH (tetra-methyl ammonium hydroxide), the SiC layer acting as etch-stop for this process. These samples will be called hereafter IBS samples.

The CVD growth has been performed in a horizontal reactor [9], using silane and propane as growth precursors, and hydrogen as the carrier gas. Two different growth runs have been

performed, each run on one IBS sample and on two Si (001) non-implanted reference substrate, one on-axis and the other 2.5° off-axis. The first run included a carbonization step in a propane/hydrogen gas flow (hereafter referred to as carbonized samples),

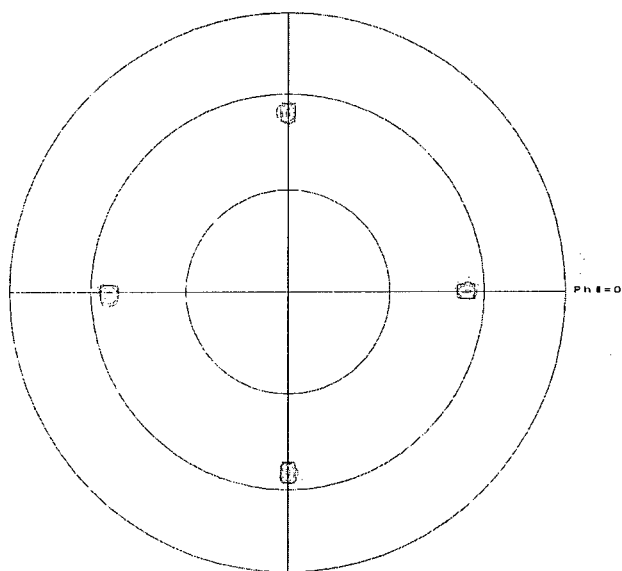


Fig. 3:  $(111)_{\beta-SiC}$  pole figure of the IBS sample not carbonized. The contour lines show the diffraction intensity divided into 8 segments.

improve the quality of the CVD layer, but it even gives rise to worst layers. On the other hand, the IBS sample carbonized shows slightly worse values than the best sample, probably because the measurements have been performed including the IBS SiC layer, which presents worst values prior to CVD deposition. Fig. 3 shows the  $(111)_{\beta-SiC}$  pole figure measured for the IBS not carbonized sample. It is clear that the poles are located at tilt angles of  $54.7^\circ$ , which are the values expected.

XTEM measurements on all these samples show that after CVD deposition a continuous layer is formed, with a high density of stacking faults. For the carbonized Si samples, the interface between the SiC and the Si substrate is very abrupt, which is not the case for the IBS samples, as shown in Fig. 4. For the latter, the IBS-SiC layer is clearly visible and a brighter area exists between this layer and the CVD layer. We believe that this interfacial layer is due to the etching in TMAH, which has been performed prior to CVD. An etching step for longer times or a RIE process might be necessary to eliminate this layer and an increase in the quality of the IBS-CVD SiC interface is expected. Furthermore, different deposition conditions might be required for the IBS samples, as the conditions employed in this work are the standard for heteroepitaxy on silicon wafers.

FTIR measurements performed in reflection mode also confirm the good quality of the IBS samples, as shown in Fig. 5. In this

exhibit a brilliant and smooth surface, indicating an epitaxial growth, while the other 2 Si test samples which were not carbonized present a dull surface. This initial result, thus, already shows that the IBS sample does not need to be carbonized in order to be used for the epitaxial growth of SiC. On the following we will center the discussion only on the 4 samples on which the CVD layer grows epitaxially.

These results are confirmed by XRD and XTEM measurements, which point out the high quality and monocrystallinity of the CVD SiC layer. Some differences are obtained when analyzing the XRD rocking curves for the 4 samples. The smallest values are obtained for the Si off-axis sample and the largest are for the IBS carbonized one. This result indicates that for the IBS sample, the carbonization not only does not

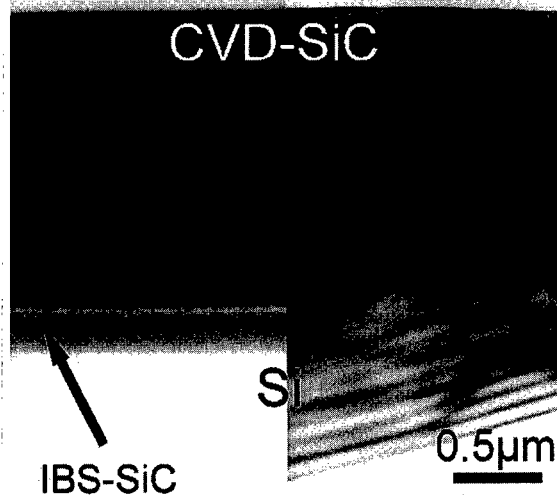


Fig. 4: XTEM images of the IBS not carbonized (left) and of the Si off-axis carbonized sample (right) after CVD growth.



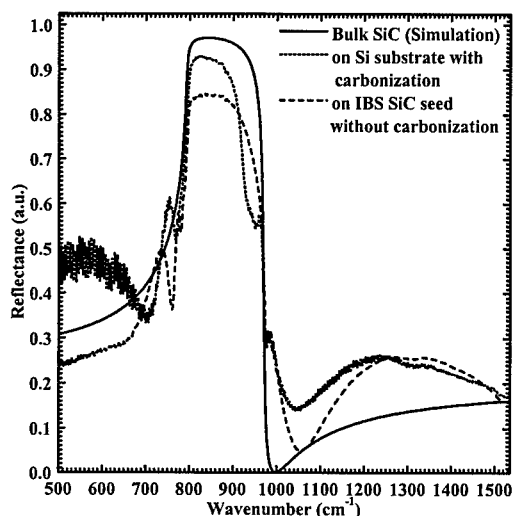


Fig. 5: FTIR spectra obtained for two different samples, compared to a simulated spectrum.

CVD growth on ion beam synthesized  $\beta$ -SiC. The results obtained show that this process is feasible without the need of a carbonization step and that the structural quality of the deposited SiC is comparable to that deposited on carbonized Si wafers. Optimization in the conditions employed for removal of the top silicon layer and a CVD growth process specially designed for this material might lead to improved SiC layers.

### Acknowledgements

This work has been partially financed by the Spanish-German "Acciones Integradas".

### References

- [1] S. Nishino, J.A. Powell and H.A. Will. *Appl. Phys. Lett.* 42 (1983), 460-462.
- [2] J.A. Powell, L.G. Matus and M.A. Kuczmarski. *J. Electrochem. Soc.* 134 (1987), 1558-1565.
- [3] I. Golecki, F. Reidinger and J. Marti. *Proc. Mater. Res. Soc. Symp.* 242 (1992) 519-524.
- [4] P.L.F. Hemment: *Perspectives, Science and Technologies for Novel Silicon on Insulator Devices* (Kluwer Academic Publishers, The Netherlands) 1999.
- [5] C. Serre, A. Pérez-Rodríguez, A. Romano-Rodríguez, J.R. Morante, J. Esteve, M.C. Acero, R. Kögler and W. Skorupa, presented at IBA-14 (Dresden, Germany), 1999.
- [6] C. Serre, A. Pérez-Rodríguez, J.R. Morante, J. Esteve, M.C. Acero, R. Kögler and W. Skorupa, presented at MME'99 (Gif-sur-Yvette, France) 1999.
- [7] C. Serre, A. Romano-Rodríguez, A. Pérez-Rodríguez, J.R. Morante, L. Fonseca, M.C. Acero, R. Kögler and W. Skorupa, *Sens. Act. A* 74 (1999) 169-173.
- [8] A. Romano-Rodríguez, C. Serre, L. Calvo-Barrio, A. Pérez-Rodríguez, J.R. Morante, R. Kögler and W. Skorupa. *Mater. Sci. Eng. B* 36 (1995) 282-285.
- [9] N. Nordell, A. Schöner and S.G. Andersson, *J. Electrochem. Soc.* 143 (1996) 2910-2969.

figure the results for both the IBS not carbonized and for the Si off-axis carbonized samples are presented, together with a simulation, for which the parameters of bulk SiC are used. The curves have been shifted vertically for clearer understanding. Beside reflectivity differences, which depend on the surface of the sample and on the measuring conditions, the curve corresponding to the IBS sample shows a shape which is closest to that of the ideal SiC sample. This result, again, confirms the good quality of the CVD growth on the IBS sample and even seems to indicate that this sample is better than the reference Si off-axis sample.

### Conclusions

In this work we have presented, for the first time to our knowledge, the SiC epitaxial

## Growth of Single Crystalline 3C-SiC and AlN on Si using Porous Si as a Compliant Seed Crystal

D. Purser<sup>1</sup>, M. Jenkins<sup>1</sup>, D. Lieu<sup>1</sup>, F. Vaccaro<sup>1</sup>, A. Faik<sup>1</sup>, M.-A. Hasan<sup>1</sup>,  
H.J. Leamy<sup>1</sup>, C. Carlin<sup>2</sup>, M.R. Sardela Jr.<sup>3</sup>, Qingxiang Zhao<sup>4</sup>,  
Magnus Willander<sup>4</sup> and M. Karlsteen<sup>4</sup>

<sup>1</sup> C.C. Cameron Applied Research Center & The Dept. of Electrical & Computer Engineering,  
University of North Carolina, Charlotte, NC 28223, USA

<sup>2</sup> Department of Chemistry, University of North Carolina, Charlotte, NC 28223, USA

<sup>3</sup> Materials Research Lab., University of Illinois, 104 S. Goodwin Avenue, Urbana, IL 61801, USA

<sup>4</sup> Physical Electronics and Photonics, Dept. of Microelectronics & Nanoscience,  
Chalmers University of Technology, SE-412 96 Göteborg, Sweden

**Keywords:** Aluminum Nitride, Compliant Substrate, Cubic Silicon Carbide, Gas- Source MBE, Heterojunction Diode, Low-Pressure CVD, MBE, Porous Si, RF Atomic Source, Trimethylsilane

**Abstract:** Single crystalline 3C-SiC layers were grown on a porous Si seed using a single gas source, trimethylsilane. The method is environmentally friendly, utilizes a non-toxic gas, and is economical. The porous Si layers were made by anodizing p-type Si(100) wafers in a mixture of hydrofluoric acid and ethanol. The SiC was grown in a high vacuum system that was converted into a low-pressure CVD reactor and was fitted with a resistive heating stage capable of heating the samples up to 1250 °C. The formation of stoichiometric SiC was confirmed by secondary ion mass-spectrometry (SIMS) while the crystal structure was examined by transmission electron microscopy (TEM) and X-ray diffraction. Fourier transform infrared spectroscopy (FTIR) showed a strong peak at 800 cm<sup>-1</sup> which corresponds to the Si-C vibrational mode. Atomic force microscopy (AFM) showed the formation of rough surfaces for thin SiC layers and large flat terraces for thick SiC layers. TEM selected area diffraction indicates the formation of fully relaxed single crystalline 3C-SiC(100) on Si(100) wafers. However, large area X-ray diffraction suggests the presence of other crystal orientations within the dominating SiC(100) layer. Heterojunction Si/SiC diodes were fabricated, which displayed a soft breakdown voltage as high as 375V. Growth of single crystalline AlN on Si and SiC was also demonstrated.

### 1. Introduction

Impetus for development of SiC materials and devices has been provided primarily by the multitude of extreme electronic, thermal, optical, and mechanical properties of the various polytypes of SiC. These properties make SiC the material of choice for a wide range of novel high-temperature, high-power, high-frequency, and radiation-hard devices. While hexagonal SiC materials have been developing at an accelerating rate due to the establishment of a substrate fabrication method, the development of the cubic phase 3C-SiC (also referred to as  $\beta$ -SiC) has been slower due to the lack of suitable substrates.

Most of the efforts to grow 3C-SiC has been centered on integrating 3C-SiC on Si substrates [1] mainly due to the vast advantages associated with utilizing the well established Si device processing technology. Moreover, 3C-SiC is an excellent substrate for AlN (lattice mismatch ~ 0.6%) and consequently for other group-III nitrides, which may permit optoelectronic integration on Si.

In this work, a new approach has been utilized to grow 3C-SiC on porous Si. Epitaxial growth of AlN on Si(111) as well as on SiC(100) was also demonstrated. For growth of SiC, porous Si was used as a compliant elastic seed in order to accommodate the strain in the porous

structure rather than in the overlayer while at the same time providing a single crystalline template for the growth. The resulting 3C-SiC layer then used as a substrate for growth of AlN. For AlN growth on Si(111), a thin (0.3 ML) layer of Al is deposited first at 700 °C followed by AlN growth using Al thermal evaporation and atomic nitrogen RF source.

## II. Experimental procedure

For growth of SiC, a high-vacuum system pumped by a combination of turbo/mechanical pumps was used for these experiments. The chamber has a base pressure of  $< 10^{-7}$  mbar and is fitted with gas delivery and handling system capable of controllable mass flow rate between ~0.1 and 100 sccm. The samples were cut from p-type Si wafers into rectangles of 2.5x1.5 cm<sup>2</sup> and was heated resistively up to 1250 °C by passing a current through the sample. Prior to deposition, the samples were anodized in a mixture of hydrofluoric acid and ethanol in a Teflon anodization cell to form the porous layer. The samples were then introduced into the vacuum chamber and upon achieving a pressure below  $1 \times 10^{-7}$  mbar, were heated to 1000 °C for 5 minutes to desorb the residual oxide layer on the surface. The temperature was then set to the desired growth temperature and trimethylsilane was introduced to the chamber for the duration of growth. The purity of the gas was 99.7% and was limited by the supplier. The samples then were examined by FTIR to determine the presence of SiC and by SIMS to confirm stoichiometry. For the heterojunction diode fabrication, Ni pads with a diameter of either 1 mm or 0.2 mm were used for ohmic contact to the SiC layer and Al was used to ohmically contact the Si side (back of the wafer).

For growth of AlN on Si and SiC, an RF source was used to generate atomic N flux together with an effusion cell to supply the Al vapor. The experiments were carried in a VG80 MBE system. 3" Si wafers were used for growth on Si while rectangular SiC/Si samples, described above, were used for growth on 3C-SiC.

## III. Experimental results and discussion

### III.A. Growth of 3C-SiC:

Figure 1 shows a TEM diffraction pattern from 3C-SiC layer grown on porous Si substrate at 1050 °C. The diffraction pattern indicates a fully relaxed single crystalline 3C-SiC(100) layer on Si. However, large-area X-ray diffraction indicated the presence of a minute amount of other phases in most of the samples. The presence of other phases is most likely related to the purity (99.7%) of the gas used in these experiments. In the present study, we were limited by the available gas purity from the supplier.

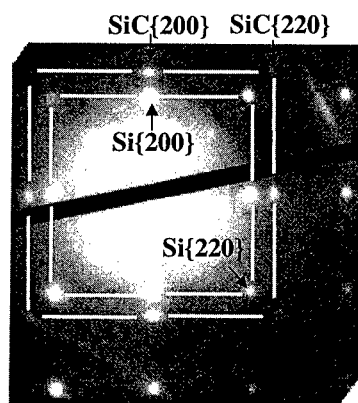


**Figure 1.** Selected area diffraction from single crystalline 3C-SiC grown on porous Si substrate. The diffraction pattern represents fully relaxed Si(100) and SiC(100).

Initial TEM investigation of planar view samples indicated the absence of misfit dislocations. This is mainly due to the gradual change in C concentration throughout the porous layer and the absence of continuous interface between Si and SiC. Porous Si contains 20% to 80% of interconnected pores in otherwise single-crystalline Si skeleton. Depending on anodization

parameters used (anodization current, HF content in the solution, time, exposure to light) the dimensions of the Si skeleton can be tuned between a few nanometers to a few microns. Even when misfit dislocations are generated, they may become terminated at the pores, which minimizes their effect on the overlayer. AFM measurements indicated the formation of rough surfaces mainly due to the surface roughness of the porous layer. SIMS measurement confirmed the stoichiometry of the SiC layers and indicated a low level of oxygen, fluorine, and hydrogen in the layers.

### III.B. Fabrication of heterojunction diodes

Heterojunction diodes were fabricated using 0.2 mm and 1 mm Ni contacts to the SiC layer and Al to the Si substrates. Annealing of the structure up to 450 °C did not change the I-V characteristics significantly. A breakdown voltage as high as 375 V was obtained with a rather high leakage current. The leakage current is most likely related to conduction along the pores' surfaces since the interface is not continuous. A typical I-V curve is shown in Fig. 2. Using the forward I-V curve, an ideality factor of 1.25 was obtained. The breakdown voltage of the current device is more than twice the values reported in the literature [2-5]

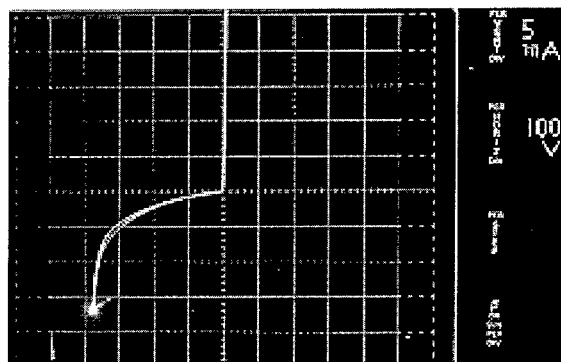


**Figure 2.** A typical I-V curve for 3C-SiC/Si heterojunction diodes fabricated with 1 mm Ni pads.

### III.C. Deposition of AlN on Si(111)

Deposition on Si(111) was carried out in a VG80 MBE chamber fitted with an Al source and a RF atomic source. Deposition was conducted by first changing the surface reconstruction from Si(111)7x7 to Si(111)- $\sqrt{3}\times\sqrt{3}$  followed by simultaneous exposure to atomic N and Al evaporated from an effusion cell. Figure 3 shows X-ray diffraction from a sample grown at 650 °C. The hexagonal AlN(200) peak is sharp indicating good crystal quality. No other phases could be identified from the X-ray measurement. The layers have a specular and smooth surface as judged from optical microscopy. We believe that the passivating, Al-induced  $\sqrt{3}\times\sqrt{3}$  reconstruction plays a major role in providing a template for epitaxial growth of AlN.

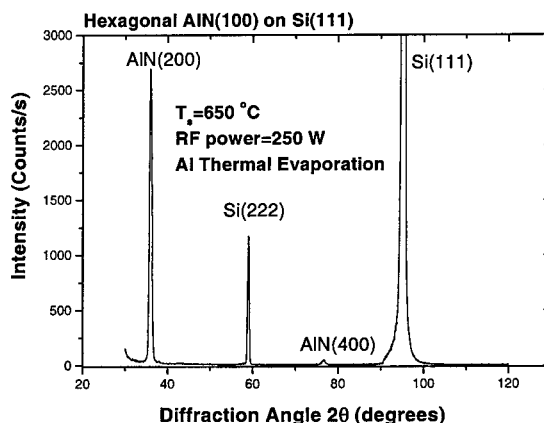


**Figure 3.** X-ray diffraction results from AlN grown on Si(111).

### III. D. AlN on 3C-SiC overlayers

Single crystalline hexagonal AlN(100) layers were also obtained on 3C-SiC(100) layers grown by the method described above.

Figure 4 shows X-ray diffraction demonstrating single crystalline hexagonal Al(100) on 3C-SiC(100). A small signal that can be attributed to Al(102) can be also seen within the background at  $2\theta \cong 50^\circ$ . The formation of Al(102) is most likely due to the large surface roughness of the 3C-SiC layer, which may promote nucleation of other phases at the macroterraces on the surface. No interfacial Al layer was deposited at the interface. Similar results were reported using CVD from ammonia and trimethylaluminum [6] at much higher growth temperatures.

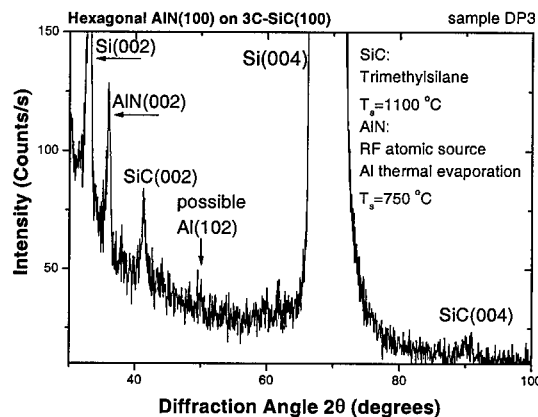


**Figure 4.** X-ray diffraction from AlN(100)/SiC(100)/Si(100) structure. Single crystalline hexagonal AlN(100) is formed on cubic 3C-SiC(100) grown on porous Si(100) substrate

**Acknowledgment:** The authors gratefully acknowledge the financial support of the Office of Naval Research (ONR) administered by Dr. Colin Wood and the Defense Advanced Research Project Agency (DARPA) administered by Dr. Daniel Radack. Special thanks to Mr. John Hudak for an outstanding technical support and to South Bay Technology, Inc. for donating a tripod polisher for TEM sample preparation.

### References

1. For example, see: R.C. Marshall, C. E. Ryan, J. Litter, and I. Berman: Silicon Carbide 1973 (University of South Carolina, Columbia, 1974), p. 123; R. F. Davis, G. Kelner, M. Shur, J. W. Palmour, and J. A. edmond, Proc. IEEE 79 (1991), p.677; T. Fuyuki, T. Yoshinobu, and H. Matsunami, Thin Solid Films, 225 (1993), p.225 and references therein.
2. Q. Wahab, M. Karlsteen, O. Nur, L. Hultman, M. Willander, and J.-E. Sundgren, J. of Electronic Materials, 25 (1996), p.1495
3. J. D. Hwang, Y. K Fang, K.H. Chen, and D. N. Yaung, IEEE Elect. Device Let., 16 (1995), p.193
4. J. D. Hwang, Y. K Fang, K.H. Wu, and S. M. Chou, IEEE Trans. Electron Devices, 44 (1997), p.2029
5. P. H. Yih, J. P. Li, and J. Steckl, IEEE Trans. Electron Devices, 41 (1994), p.281
6. R. F. Davis et. al, ICSCRM-99, (1999), p. 1471

Correspondence should be made to: M.-A. Hasan, [mhasan@uncc.edu](mailto:mhasan@uncc.edu), Fax. (704)547-2352, Tel. (704)510-6414. <http://www.coe.uncc.edu/~mhasan>

## The Growth and Characterization of 3C-SiC/SiN<sub>x</sub>/Si Structure

Kwang Chul Kim<sup>1</sup>, Chan Il Park<sup>1</sup>, Kee Suk Nahm<sup>1,2</sup> and Eun-Kyung Suh<sup>1,3</sup>

<sup>1</sup> Semiconductor Physics Research Center, Dept. of Semiconductor Science & Technology,  
Chonbuk National University, Chonju, 561-756, Korea

<sup>2</sup> School of Chemical Engineering and Technology, Chonbuk National University,  
Chonju 561-756, Rep. Of Korea

<sup>3</sup> School of Science and Technology, Chonbuk National University, Chonju, 561-756, Rep of Korea

**Keywords:** Crystal Quality, Electrical Properties, Nitridation, SiN<sub>x</sub>/Si Structure

**Abstract :** Single crystal 3C-SiC (111) films were grown on SiN<sub>x</sub>/Si (111) structures fabricated by both ammonia nitridation of the Si surface with SiN<sub>x</sub> and RF-magnetron sputtered SiN<sub>x</sub> deposition. The nitrided Si substrates accommodated the growth of better quality SiC films with a flat and smooth film/substrate interface than a pure Si substrate. The crystallinity of SiC layers improved as the nitridation time increased. It seemed that the growth of better quality of SiC films was ascribed to the prevention of Si out-diffusion from the substrate by the coverage of Si with the thermally stable silicon nitride film and to the decrease of Si surface roughness. Crystalline 3C-SiC films was also grown on 3000 Å thick SiN<sub>x</sub>/Si structure.

### 1. Introduction

Among the more than 200 polytypes of Silicon Carbide (SiC), cubic SiC ( $\beta$ -SiC) has higher electron mobility, and can be grown on Si substrates to provide large area substrates. But the growth of cubic SiC using a conventional chemical vapor deposition (CVD) system requires high temperatures (above 1300°C), which leads to the formation of various microstructural defects in the SiC films because of large mismatch in lattice constants ( $\approx 20\%$ ) and thermal expansion coefficients ( $\approx 8\%$ ) between SiC and Si [1].

A two-step growth process is mostly accepted as a successful method to grow high quality of SiC films on Si. In the two-step growth process, an initial SiC buffer layer is grown by a carbonization of Si surface at low temperature, followed by very fast heating up to 1300~1350°C, and then a Si source is added for subsequent SiC growth. In spite of the successful growth of these SiC films, the crystal quality of  $\beta$ -SiC is not comparable to  $\alpha$ -SiC grown by the sublimation method, which is dominantly employed in the fabrication of SiC devices [2].

In this work, we have grown SiC films on Si substrates whose surfaces were modified with SiN<sub>x</sub> by NH<sub>3</sub> nitridation, or SiN<sub>x</sub> deposition, and the crystal quality and interfacial properties of the SiC films examined. The use of a SiN<sub>x</sub>/Si substrate is preferred for the application of SiC in electronics since the SiC epitaxial film is isolated from the Si substrate.

### 2. Experiment

Tetramethylsilane (TMS), which decomposes easily at temperatures as low as 800°C, was employed to deposit SiC films on Si substrates. A p-type Si (111) wafer with a resistivity of 20  $\Omega \cdot \text{cm}$  was used as the

substrate. SiC films were grown in a RF-induction heated CVD reactor system as described in our previous report [3]. The reactor was a quartz tube with the internal diameter of 39 mm and a length of 300 mm, respectively. The base pressure in the reactor was maintained at  $10^{-4}$  Torr using a rotary vacuum pump. The temperature of the Si substrate was monitored and controlled with a pyrometer calibrated with a Pt/Ru thermocouple.

Nitridation of the Si surface was carried out in a rapid thermal chemical vapor deposition (RTCVD) reactor. Chemically treated Si wafers were nitrided at  $1050^{\circ}\text{C}$  in a mixed gas of 1000 sccm  $\text{NH}_3$  and 500 sccm  $\text{H}_2$  for various reaction times from 3 to 60 min.  $\text{SiN}_x$  was also deposited on the Si surface with the thickness of 3000 Å in an RF-magnetron sputtering system using a silicon nitride target.

The surface-modified Si substrate was moved to a graphite substrate holder with a tilt angle of  $4.5^{\circ}$  toward the gas flow in an RF-induction heated CVD reactor to grow the SiC film. SiC films were then grown on the  $\text{SiN}_x/\text{Si}$  structure at  $1250^{\circ}\text{C}$  with TMS and  $\text{H}_2$  flow rates of 0.5 and 1500 sccm, respectively.

The thickness and surface morphology of the SiC epilayers were examined with a cross sectional transmission electron microscope (XTEM) and an atomic force microscope (AFM). Raman spectra and transmission electron diffraction (TED) were used to investigate the crystal quality of the SiC films.

### 3. Results and discussion

Cross sectional transmission electron microscopy (XTEM) and transmission electron diffraction (TED) were used to investigate the SiC/Si interfaces and the crystallinity of the SiC films, respectively. Figure 1 shows XTEM photographs and TED patterns of SiC film grown on Si substrates. The growth was carried out for 30 min at a substrate temperature of  $1250^{\circ}\text{C}$  and a gas pressure of 10.1 Torr. XTEM photographs show that voids were formed in the silicon side of the SiC/Si interfaces from the SiC films grown on pure Si substrate, while the nitrided Si substrate accommodates the growth of SiC films with a flat and smooth film/substrate interface without the formation of voids. The formation of voids in the silicon side of the SiC/Si interface was attributed to the out-diffusion of Si atoms from the Si substrate during the growth process, as discussed in literature[4].

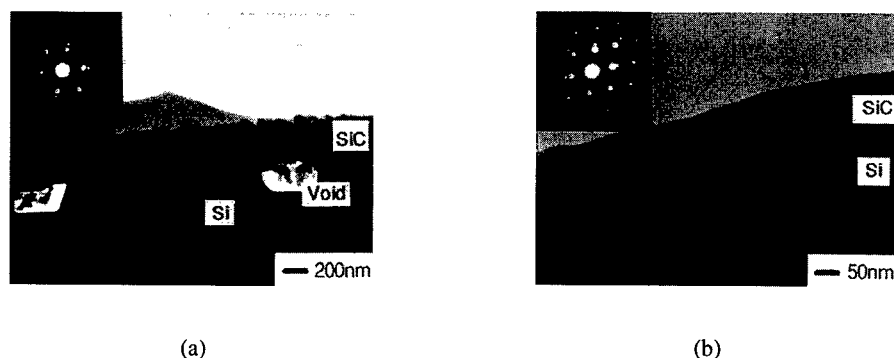


Figure 1. Cross-section TEM micrographs and TED patterns of 3C-SiC films grown at  $1250^{\circ}\text{C}$  and 10.1 Torr for 30 min nitridation times of (a) 0 and (b) 60 min, respectively.

TED patterns in Fig.1 show that SiC diffraction patterns are well aligned with Si diffraction patterns, indicating the epitaxial growth of crystalline 3C-SiC(111) films on the Si substrate. The crystallinity of SiC layers improves as the nitridation time increases. Raman measurements for 3C-SiC films grown at the same conditions of Fig. 1 also confirmed the improvement of SiC crystal quality when Si surface were nitrided with  $\text{NH}_3$ . From the Raman spectra of Fig. 2, transverse optical (TO) and longitudinal optical (LO) phonons for 3C-SiC(111) were observed at 795 and 971.5  $\text{cm}^{-1}$ , respectively, indicating that the films have the preferred orientation of [111]. When a SiC film was grown for 360 min on a 60 min nitrided Si substrate, the thickness of the film reaches almost 7  $\mu\text{m}$  and a flat and smooth SiC/Si interface also appears without the formation of voids as shown in Fig. 3.

In order to investigate the variation of the crystallinity of SiC epilayers as a function of nitridation time, the surface average roughness of the substrate was measured using an AFM as shown in Fig. 4. The rough substrate surfaces produced the growth of poor-quality SiC epilayers, while better-quality SiC epilayers were grown on the relatively smooth substrate surfaces. This indicates that the crystal quality of SiC was strongly influenced by the surface morphology of the Si substrate. The thickness of the 3C-SiC films decreased with the nitridation time, indicating that the thermally stable silicon nitride layer prevents the out-diffusion of Si atoms from the substrate.

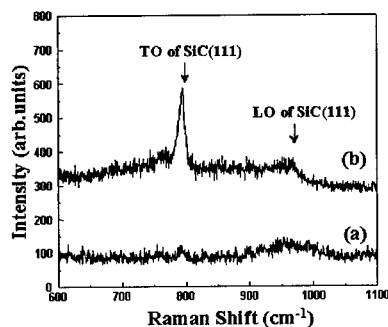


Figure 2. Raman spectra of 3C-SiC films on Si nitrided for (a) 0 and (b) 60 min, respectively.

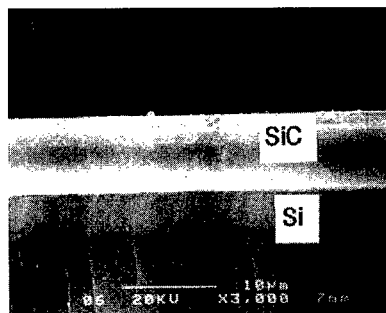


Figure 3. SEM photographs of cross-sectional SiC/Si grown after 60 min nitridation

SiC films grown on nitrided Si substrates appear to be n-type with the carrier concentration of  $1.5 \times 10^{17} \text{ cm}^{-3}$  with an electron mobility of  $358 \text{ cm}^2/\text{V} \cdot \text{s}$ , which are much better than those for SiC films grown on pure Si substrates[5]. We observed that the electrical properties were greatly improved in the void-free SiC films[6].

$\text{SiN}_x$  films were deposited on Si with the thickness of 3000 Å by an RF-magnetron sputtering and  $\beta$ -SiC was grown on these  $\text{SiN}_x/\text{Si}$  structures. Figure 5 shows an XTEM micrograph together with a TED pattern. In this case SiC was grown for 360 min at 1250°C and 10.1 Torr with the TMS and  $\text{H}_2$  flow rates of 1.0 and 1000 sccm, respectively. TED pattern shows the growth of crystalline 3C-SiC films with (111) orientation. XTEM shows that the films mainly consists of columnar grains and the growth rate is very slow (27 nm/hr) compared to the growth on nitrided Si surface.



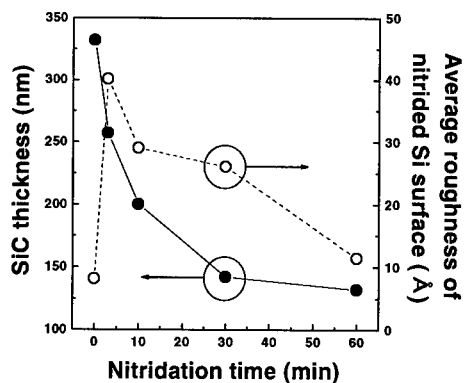


Figure 5. The thickness of SiC epilayer grown on Si substrate and average surface roughness of Si substrates as a function of the nitridation time

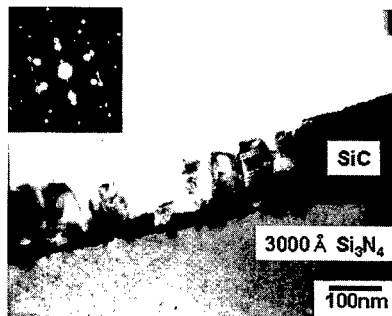


Figure 6. Cross-section TEM micrographs and TED patterns of 3C-SiC/3000 Å-SiNx/Si

#### 4. Conclusions

Crystalline 3C-SiC(111) films with a flat and smooth surface interface without voids were grown on nitrified Si substrates. An increase in the nitridation time reduces the thickness of the SiC film as well as the size and density of the voids at the SiC/Si interface. It was concluded that the surface of the Si substrate covered with the thermally stable silicon nitride film formed by  $\text{NH}_3$  nitridation, prevents the out-diffusion of Si atoms from the Si substrate, resulting in the growth of better quality SiC films without the formation of voids. Crystalline 3C-SiC films was also grown on 3000 Å thick SiNx/Si structure.

#### Acknowledgement

The authors wish to acknowledge the financial support of the Korean Research Foundation made in the program year of 1998 (1998-016-D00004).

#### References

- [1] P. Liaw and R. F. Davis, J. Electrochem. Soc., 132 (1985), p. 642.
- [2] S.Nishino, Y.Hazuki, H.Matunami, T. Tanaka, J. Electrochem. Soc., 127 (1980), p. 2674.
- [3] K. C. Kim, H. W. Shim, Y. H. Seo, E.-K. Suh, K. S. Nahm, and H. J. Lee, J. Korean Physical Soc., 32(4) (1998), p. 588.
- [4] J. P. Li and A. J. Steckl, J. Electrochem. Soc., 142(2) (1995), p. 634.
- [5] J. D. Hwang, Y. K. Fang, Y. J. Song and D. N. Yaung, Jpn. J. Appl. Phys., 34, Pt. 1(3), (1995), p. 1447.
- [6] H.W.Shim, K.C.Kim, Y.H.Seo, K.S.Nahm, E.-K.Suh, H.J.Lee and Y.G.Hwang, Appl. Phys. Lett., 70(13) (1997), p. 1757.

## The Diffusion Coefficient of Silicon in Thin SiC Layers as a Criterion for the Quality of the Grown Layers

V. Cimalla<sup>1</sup>, Th. Wöhner<sup>2</sup> and J. Pezoldt<sup>2</sup>

<sup>1</sup> Foundation for Research and Technology Hellas, Microelectronics Research Group, PO Box 1527, GR-71110 Heraklion/Crete, Greece

<sup>2</sup> Institut für Festkörperelektronik, TU Ilmenau, Postfach 100 565, DE-98684 Ilmenau, Germany

**Keywords:** Carbonization, Diffusion Coefficients, Growth Model, Layer Growth Kinetics

**Abstract.** The diffusion coefficient for silicon in thin SiC was estimated analyzing the layer growth kinetics during the carbonization with different growth techniques. The silicon diffusion was described by the classical parabolic law as well as by models, taking the peculiarities of the carbonization process into account. Generally, low diffusion coefficients correspond to layer with good morphological and structural properties. The best results were obtained by CVD, followed by GSMBE and finally by the techniques using elemental carbon as source for the carbonization.

### Introduction

The cubic polytype of SiC currently receives a renewed interest due to the highest electron mobility, the isotropy of the properties and the possibility to grow it heteroepitaxially on silicon. Conceivable applications include sensors using the feasibility of silicon for micromachining as well as the direct utilization of the heterojunction in hetero-pn-diodes or heterobipolar transistors. Furthermore, in the case of sensoric applications the deposition on SOI (silicon on insulator) becomes more and more attractive. With those substrates the leak currents through the silicon at temperatures above 150°C and the defect formation due the mismatch in the thermal expansion coefficients can be reduced. However, a serious problem limiting the application of SOI substrates is the formation of large cavities in the silicon layer up to the buried oxide layer due to silicon-oxide reactions and diffusion processes through the growing layer. In all the mentioned cases a stable interface is an inevitable precondition for the application of the system SiC on Si. In addition thin SiC layers on (111)Si layers are promising pseudo substrates for the heteroepitaxy of group III nitrides where the presence of silicon on the growing surface can strongly disturb the growth. For all that reasons the diffusion processes through the growing layers have to be minimized. Seeing that the diffusion coefficient of silicon in single crystalline SiC is negligible small the possibility for silicon diffusion through the growing SiC layer is directly correlated to structural or morphological imperfections.

In this work we want to describe the estimation of the diffusion coefficient for silicon in SiC at growth temperatures from the layer growth kinetics during the carbonization by different growth techniques: Chemical Vapor Deposition (CVD), Solid State Molecular Beam Epitaxy (SMBE), Gas Source Molecular Beam Epitaxy (GSMBE), Laser Ablation and Evaporation of Fullerenes. The obtained data are compared to the structural and morphological quality of the grown layers.

### Description of the layer growth kinetics

Generally the carbonization process represents the initial stage of the heteroepitaxial growth of SiC on Si, i.e. the reaction between carbon containing molecules from the gaseous phase and the silicon substrate. This reaction regularly occur on the growing surface and therefore Si has to diffuses out to the surface leaving morphological defects behind [1]. The growth rate can be determined by the

reaction rate to SiC, the carbon supply of carbon containing molecules to the growing surface or by the silicon diffusion through the growing layer. If the reaction rate or the carbon flux is the limiting factor the thickness is increasing linearly at progressing time and an estimation of the diffusion coefficient is hardly possible. However, if the availability of Si on the surface is the limiting factor for the growth, the growth rate will be decreasing. Due to the extremely small diffusion coefficient in single crystalline SiC silicon can diffuse either very locally (for example at the boundaries between large crystallites) or rather homogeneous in the case of highly defective layers. In the first case geometrical effects of the growth play a role resulting in complicated growth models while in the second case the classic model of parabolic diffusion controlled growth can be applied.

**(I) Parabolic growth kinetics** Assuming an infinitive source of silicon atoms at the interface and a negligible concentration of free atoms at the surface the layer thickness  $d_{Si}$  can be estimated by:

$$d_{Si} = \sqrt{2 * N_0 a^3 D_{Si} [t - t_0]} \quad (1)$$

with  $N_0$ : Si interface concentration,  $a^3$ : a quarter of the SiC unit cell volume and  $t_0$ : the time of the initial linear growth which is not diffusion limited. The diffusion coefficient  $D_{Si}$  is the only parameter to fit the experimental data. An example for the growth of polycrystalline SiC in methane – hydrogen mixture is shown in fig.1. This behavior was mainly found for the growth of “thicker” layers (up to some micrometer) under CVD conditions. However, only a few kinetics for the carbonization in high vacuum or ultra high vacuum (UHV) can be fitted by this law [2-6].

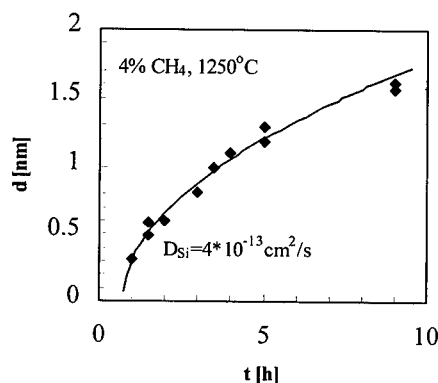


Fig.1 Parabolic growth law [1]

**(II) Saturation in growth** In this case the growth stops after reaching a distinct layer thickness, the saturation thickness  $d_{sat}$ . There are two possible reasons for this behavior: (i) a closed SiC layer seals off the surface and prevents any silicon diffusion to the surface [7] or (ii) an equilibrium between silicon diffusion and sublimation (or etching in hydrogen) averts the further growth. For the latter case the constant thickness and the constant silicon flux  $F_{Si}$  reduce Fick's 1st law to a linear dependence:

$$F_{Si} = D_{Si} \frac{N_0}{d_{sat}} \quad (2)$$

This behavior was mainly found for the carbonization under CVD conditions introducing the hydrocarbons at room temperature and heating up the substrates with a moderate rate or by GSMBE at high hydrocarbon pressure and very low heating-up rate [6,8]. In both cases the resulting layers had a thickness of only a few nanometer and the best structural and morphological properties. In contrary, in SSMBE the high reaction probability of elemental carbon suppresses the sublimation of silicon from the growing surface.

Most problematic is the distinction between the two cases sealing off and silicon sublimation. Consequently, if no additional data is available the estimated diffusion coefficient represents only the upper limit. A variant of the procedure is the heating in vacuum and the observation of the growth of the etch pits below the thin SiC layer [9].

**(III) Homogeneous diffusion and sublimation** Another way to analyze the saturation behavior is the combination of the homogeneous diffusion of silicon through the growing layer and the

sublimation from the surface, i.e. models (I) and (II). The result is an indirect time–thickness dependence:

$$t = -\frac{n_{Si}}{F_{Si}} \left\{ D_{Si} \frac{N_0}{F_{Si}} \ln \frac{D_{Si} \frac{N_0}{F_{Si}} - d}{D_{Si} \frac{N_0}{F_{Si}}} + d \right\} \quad (3)$$

with  $n_{Si}$ : density of silicon in SiC. The limiting case in the growth, the saturation, results in a thickness which is identical to the condition in eq. (2). This type of growth kinetics was mainly observed under CVD conditions [10,11]. It should be noted here, that the present authors derived a description for this type of growth kinetics taking geometrical effects into account. In that model the diffusion is assumed to occur preferred at grain boundaries which explained the dependence of the saturation thickness on the nucleation density [11]. Therefore the diffusion coefficient estimated by eq. (3) represents actually only an average value for the layer (Fig.2).

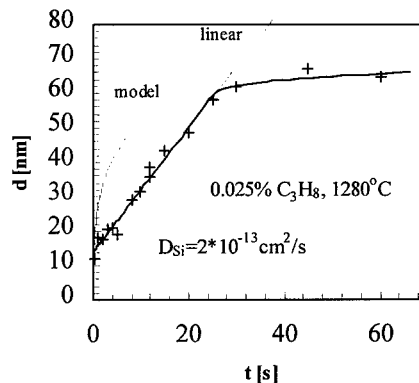


Fig.2 Model for diffusion and sublimation, data from [2]

**(IV) Rimai model for laser ablation** The Rimai model was developed for the carbonization by laser ablation of a C target [12] (Fig.3). As mentioned above the outdiffusion of silicon leaves voids at the SiC-silicon interface behind. The Rimai model assumes a homogeneous diffusion of silicon through the layer but a decreasing SiC-silicon contact area due to the void growth. Therefore the amount of available silicon is decreasing during the layer growth. As a result again an indirect time–thickness dependence characterizes the growth kinetics:

$$t = -\frac{1}{u_0} \left( \frac{1}{b} + \frac{1}{ab^2} \right) \ln(1 - bz) - \frac{z}{ab} \quad (4)$$

with  $u_0$ : initial growth rate,  $a$ : diffusion length and  $b$ : interface factor describing the influence of the void growth. According to the derivation in [12]  $D_{Si}$  is given by:

$$D_{Si} = \frac{N_0}{n_{Si}} u_0 a \approx u_0 a \quad (5)$$

This model allows no saturation. Instead the growth stops when the contact area between SiC and silicon is becoming zero, i.e. the layer peels off. This model could be applied only in the case of carbonization using elemental carbon, i.e. the laser ablation and the SSMBE.

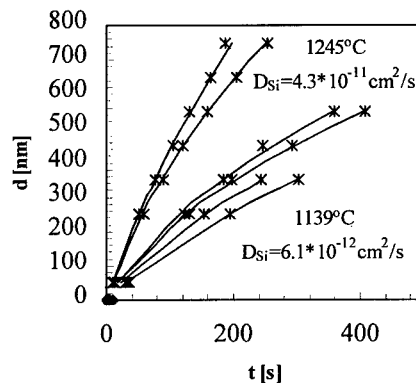


Fig.3 Rimai model [12]

## Conclusion

A summary of the estimated diffusion coefficients is given in fig.4. All these values are several orders of magnitude higher than for single crystalline bulk SiC. Best results were obtained by CVD. The difference between the thin single crystalline layers, where the growth saturates after a few nanometer [16], and the thicker, rough, twinned or polycrystalline SiC layers is connected to a change in  $D_{Si}$  by more than two orders of magnitude. A similar behavior was found for the best layer grown by GSMBE [3,5]. The highest diffusion coefficients appear using elemental carbon in SSMBE, laser ablation or fullerene evaporation, where in most of the cases only a linear growth was

observed. In conclusion, assuming the diffusion coefficient as a criterion for the quality of the grown layers, as more hydrogen is contributing in the growth as better the structure and quality of the SiC layer grown by carbonization.

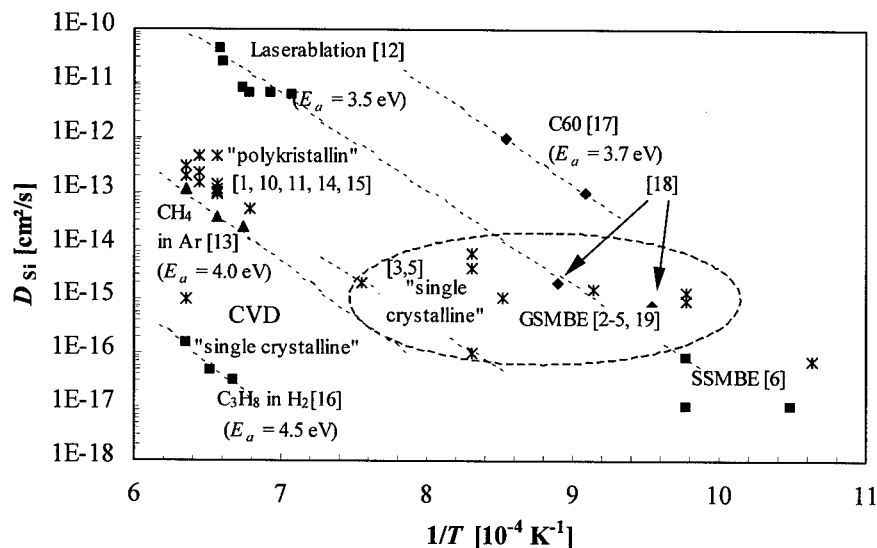


Fig.4 Diffusion coefficient for silicon at growth temperatures for different carbonization methods

#### References

- [1] J. Graul, E. Wagner, Appl. Phys. Lett. 21 (1972), p. 67.
- [2] F. Boszo, J.T. Yates jr., W.J. Choyke, L. Muelhoff, J. Appl. Phys. 57 (1985), p. 2771.
- [3] S. Motoyama, N. Morikawa, M. Nasu, S. Kaneda, J. Appl. Phys. 68 (1990), p. 101.
- [4] T. Hatayama, T. Fuyuki, H. Matsunami, Inst. Phys. Conf. Ser. 142 (1996), p.117.
- [5] V. Cimalla, J. Pezoldt, K. Linthicum, R.F. Davis, unpublished results.
- [6] T. Wöhner, V. Cimalla, Th. Stauden, G. Eichhorn, J. Pezoldt, Thin Solid Films (1999) to be published.
- [7] C.J. Mogab, H.J. Leamy, J. Appl. Phys. 45 (1974), p. 1075.
- [8] T. Yoshinobu, H. Mitsui, Y. Tarui, T. Fuyuki, J. Appl. Phys. 72 (1992), p. 2007.
- [9] J. Hofmann, S. Veprek, J. Appl. Phys. 85 (1999), p. 2652.
- [10] A.P. Steckl, J.P. Li, IEEE Trans Electr. Dev. ED39 (1992), p. 64.
- [11] V. Cimalla, K.V. Karagodina, J. Pezoldt, G. Eichhorn, Mater. Sci. Eng. B29 (1995), p. 170.
- [12] L. Rimai, R. Ager, W.H. Weber, J. Hangas, A. Samman, W. Zhu, J. Appl. Phys. 77 (1995), p. 6601.
- [13] H. Nakashima, T. Sugano, H. Yanai, Jap. J. Appl. Phys. 5 (1966), p. 874.
- [14] P. Rai-Chaudhury, P. Formigoni, J. Electrochem. Soc. 116 (1969), p. 1440.
- [15] M. Balog, A. Reisman, M. Berkenblit, J. Electronic Mater. 9 (1980), p. 669.
- [16] G. Ferro, Y. Monteil, H. Vincent, F. Cauwet, J. Bouix, P. Durupt, J. Olivier, R. Bisaro, Thin Solid Films 278 (1996), p. 22.
- [17] A.V. Hamza, M. Balooch, M. Moalem, Surf. Sci. 317 (1994), p. L1129.
- [18] S. Henke, B. Stritzker, B. Rauschenbach, J. Appl. Phys. 78 (1995), p. 2070; S. Henke, M. Philipp, B. Rauschenbach, B. Stritzker, Mater. Sci. Eng. B36 (1996), p. 291.
- [19] F.C. Stedile, F. Rochet, C. Poncey, G. Dufour, R. Gunnella, M. De Crescenzi, M. Foment, Nucl. Instr. Meth. Phys. Res. B136-138 (1998), pp. 301.

## Plasma Enhanced Chemical Vapor Deposition and Characterization of Hydrogenated Amorphous SiC Films on Si

Yihua Wang<sup>1</sup>, Jianyi Lin<sup>1\*</sup>, Zhe Chuan Feng<sup>2</sup>, Soo Jin Chua<sup>2</sup>  
and Cheng Hon Huan Alfred<sup>1</sup>

<sup>1</sup> Department of Physics, National University of Singapore, Singapore 119260, Singapore

<sup>2</sup> Institute of Materials Research & Engineering, 3 Research Link, Singapore 117602, Singapore

**Keywords:** Amorphous Silicon Carbide, PECVD, Photoluminescence, Raman Spectroscopy

**Abstract.** In this study, hydrogenated amorphous silicon carbon ( $a\text{-Si}_{1-x}\text{C}_x\text{:H}$ ) thin films were synthesized on Si substrates by plasma enhanced chemical vapor deposition (PECVD) technique. The source gases used were  $\text{C}_2\text{H}_4$ ,  $\text{SiH}_4$ , and  $\text{H}_2$  (for dilution). The compositional parameter  $x$  is found to be closely relevant to practical vibrational and optical properties of this material. XPS and FTIR spectra strongly support the existence of C-Si covalent bonds in the grown thin films. Raman spectra do not show a strong Si-C Raman peak. The Photoluminescence result is quite different from the previous reports.

### 1. Introduction

Hydrogenated amorphous silicon carbon ( $a\text{-Si}_{1-x}\text{C}_x\text{:H}$ ) alloys have attracted much attention in recent years for optoelectronic and electronic applications of solar cells [1], light emitting diodes [2], microelectronic dielectric layers [3], color sensors [4] and flat-screen full-color displays etc [5,6].  $a\text{-Si}_{1-x}\text{C}_x\text{:H}$  films were usually prepared by the glow discharge or plasma enhanced chemical vapor deposition (PECVD), or the rf sputtering techniques. The compositions of the silicon and carbon in the films were found to be strongly dependent on the preparation condition [7]. In this work, we report the growth and characterization of  $a\text{-Si}_{1-x}\text{C}_x\text{:H}$  thin films on Si substrates by PECVD technique. Hydrogen diluted mixtures of silane and ethylene served as the reaction sources. Variable flow rates and other growth conditions were applied. A variety of techniques, including X-ray photoelectron spectroscopy (XPS), Fourier transform infrared (FTIR) spectroscopy, Raman scattering (RS) and Photoluminescence (PL) were used to characterize the grown materials.

### 2. Experimental

The  $a\text{-Si}_{1-x}\text{C}_x\text{:H}$  films were grown in a capacitively coupled rf PECVD system PlasmaQuest PQM-9157-A series III, with a gaseous mixture of silane ( $\text{SiH}_4$ ), ethylene ( $\text{C}_2\text{H}_4$ ) and hydrogen ( $\text{H}_2$ ) as the source gases. The substrate, Si (100) was placed on the sample stage, which was maintained at 220 °C. The working pressure was 200 mTorr. Deposition was performed using a rf plasma power of 50 W for one hour, which resulted in the film thickness of several hundred nanometers. The composition of the film was controlled by varying the flow ratio of  $\text{C}_2\text{H}_4$  to  $\text{SiH}_4$ .

The XPS analysis was carried out in a VG Escalab MKII system using 120 W Mg  $K\alpha$  x-ray source. The FTIR measurements were made in transmission mode by using Perkin-Elmer 2000 with a resolution of 4  $\text{cm}^{-1}$ . The Raman scattering and PL spectra were obtained under excitation with an Ar-ion laser ( $\lambda = 514.5 \text{ nm}$ ) at room temperature.

### 3. Results and discussion

### 3.1 XPS

The XPS scans (Fig. 1) show the Si 2p, C 1s and O 1s peaks at photoelectron take-off angle of  $75^\circ$  for all the samples. The O 1s spectra (not shown here) are composed mainly of a single peak with a binding energy which corresponds to  $\text{SiO}_2$  (532.4 eV). At photoelectron take-off angle of  $20^\circ$  the intensity ratio of O 1s over Si 2p is higher than that of  $75^\circ$ , indicating that oxygen is mainly present on the surface. The compositions of the  $\text{a-Si}_{1-x}\text{C}_x\text{:H}$  films were obtained by peak-fitting of the C 1s and Si 2p peaks. Essentially the same peak components are present at all samples but with different relative intensities. The C 1s spectra exhibited three main peaks assigned to Si-C (283.3 eV), C-C/C-H (284.6 eV) and C-O-H (286.0 eV). The Si 2p spectra could be fitted with four peaks due to Si-Si/Si-H (99.5 eV), Si-C (100.4 eV), O-Si-C (101.7 eV) and Si-O (103.0 eV). Wide range of the carbon content  $x$  (0.40-0.90, including adventitious C) was obtained from the samples with varying flow rate ratio between silane and ethylene. It should be pointed out that due to the ex-situ nature of the study, the adventitious carbon component would also contribute to C-C/C-H peak.

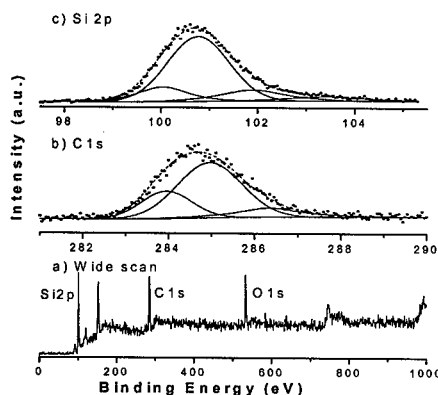


Fig. 1 Typical XPS spectra of  $\text{a-Si}_{1-x}\text{C}_x\text{:H}$  film prepared by PECVD. a) Wide scan, b) C 1s energy range, c) Si 2p energy range.

### 3.2 FTIR

FTIR transmission spectra (Fig. 2) reveal the prominent Si-C stretching mode at  $\sim 780\text{ cm}^{-1}$ , Si-H wagging or rocking mode at  $\sim 660\text{ cm}^{-1}$ , C-H<sub>n</sub> wagging mode in  $\text{Si-CH}_3$  at  $\sim 1000\text{ cm}^{-1}$ , Si-H<sub>n</sub> stretching mode at  $\sim 2100\text{ cm}^{-1}$ , and C-H<sub>n</sub> stretching mode at  $\sim 2900\text{ cm}^{-1}$ . Three modes at  $\sim 1250\text{ cm}^{-1}$ ,  $\sim 1340\text{ cm}^{-1}$  and  $\sim 1400\text{ cm}^{-1}$  are due to the  $\text{Si-CH}_3$  bending vibration. The bands of Si-H stretching between 2000 and  $2300\text{ cm}^{-1}$  decrease greatly with increasing  $x$ . Fig. 2 also shows that the Si-C absorption of the samples with  $x = 0.40$  and  $0.50$  is significantly stronger than that of the samples with higher  $x$  values. This is in good agreement with the XPS results that the samples of  $x = 0.40$  and  $0.50$  actually have higher concentration of the SiC species. Therefore, the two samples are the expected  $\text{a-Si}_{1-x}\text{C}_x\text{:H}$  samples. For the higher  $\text{C}_2\text{H}_4$  concentrations, the lower availability of silicon justifies the decrease of the Si-C band but, as the other detectable carbon incorporation forms remain essentially constant, the extra carbon atoms must be incorporated through C-C bonds, which are not detectable with FTIR spectrometry. The interference fringes in the region between 3000 and  $6000\text{ cm}^{-1}$  can be used to estimate the film thicknesses, which are about 0.4-1.0 microns.

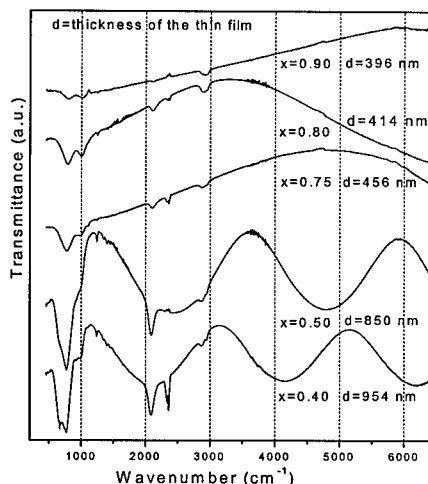


Fig. 2 Infrared spectra of  $\text{a-Si}_{1-x}\text{C}_x\text{:H}$  samples prepared under PECVD.

### 3.3 Raman spectroscopy

Combined room temperature (RT) Raman and Photoluminescence (PL) measurements were performed under 514.5 nm excitation for these samples. Figs. 3 and 4 show crystalline Si Raman mode and the second order Raman band (silicon substrate) at 521 and 970  $\text{cm}^{-1}$  respectively. Amorphous Si-Si Raman modes at 480  $\text{cm}^{-1}$  (first order scattering), and Si-H<sub>n</sub> Raman modes at 2000-2100  $\text{cm}^{-1}$  [8] are also observed. It is worth to point out that the later band is observed only in the sample of  $x = 0.40$  and  $0.50$ , indicating the presence of amorphous silicon. Nevertheless the band which was expected to observe in the region of 600-1000  $\text{cm}^{-1}$  [9] and associated with Si-C bonds is very weak due to low Raman efficiencies of the Si-C band. Note that the Raman band for C-C bonds in the region of 1300-1600  $\text{cm}^{-1}$  [10] is not detected in our spectra, indicating the low C-C bond concentration in the sample of  $x = 0.40$  and  $0.50$ . But for  $x > 0.50$ , the Raman band for C-C bonds is not evident either. One reason for this could be the very intense fluorescence, the other could be that the Raman cross-section of C-C bonds depends strongly on hybridization, and is much larger for  $\text{sp}^2$  sites than that for  $\text{sp}^3$  sites. Therefore a peak corresponding to  $\text{sp}^3$  sites could easily be lost in the background. Theoretical work [11] on the electronic and atomic structure of a-C and a-C:H has shown that a-C:H films will tend to form clusters of  $\text{sp}^2$  sites, such as graphite clusters containing four or more rings in order to relieve the overall strain in the film. In other words, the properties of a-C and a-C:H will depend on the degree of medium-range order, rather than just on the short-range order as is generally believed to be the case for amorphous semiconductors. Robertson [12] has also shown that this clustering of  $\text{sp}^2$  sites in a-C:H is found on a-Si<sub>1-x</sub>C<sub>x</sub>:H. As carbon-carbon bonds are present in these films then it is likely that some  $\text{sp}^2$  clusters will be present. Unfortunately the Raman spectra were not sensitive enough to this form of bonding.

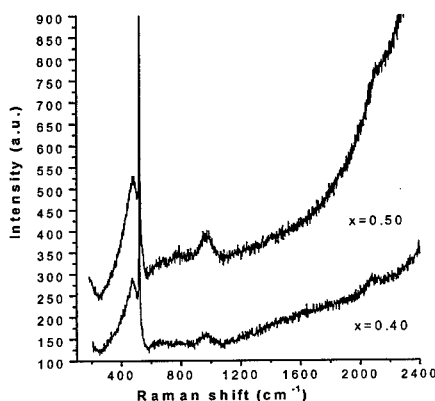


Fig. 3 Room temperature (RT) Raman spectra of a-Si<sub>1-x</sub>C<sub>x</sub>:H samples under excitation of 514.5 nm laser.

### 3.4 Photoluminescence

Broad RT PL features are detected spreading between 1.4 and 2.4 eV in Fig. 4. The shape and energy positions of the PL band vary, depending on the sample compositions and growth conditions. No peak is observed in the range of 1.2-1.4 eV, which is in contrast to an early report [13], but is in agreement with the recent results reported by Sussmann et al [14] and Ghosh et al [15]. For the samples of  $x = 0.40$  and  $0.50$  the RT PL bands are strong, with two maxima at 1.63 eV and 1.81 eV. For  $x = 0.75, 0.80$  and  $0.90$ , the 1.63 eV band disappears, but the 1.81 eV band shifts to the maximum value 1.99 eV ( $x = 0.80$ ), then decreases to 1.94 eV ( $x = 0.90$ ). This band was previously assigned to the radiative tunneling between tail states. The blue shift of the luminescence peak centered at 1.81 eV and maximum at  $x = 0.80$ , indicate that the optical

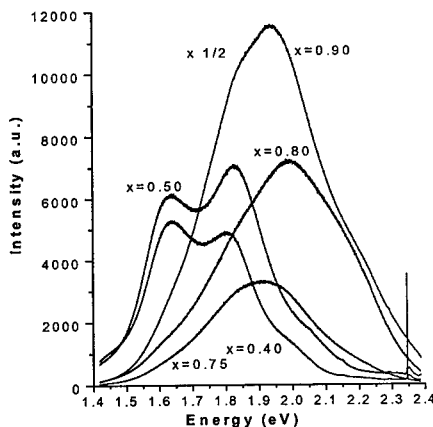


Fig. 4 Room temperature PL spectra of PECVD a-Si<sub>1-x</sub>C<sub>x</sub>:H films under the excitation of 514.5 nm. Note that the intensity of  $x = 0.90$  was timed by 1/2.



band gap increases with carbon content. But the increase of optical band gap is accompanied by an increase in film disorder, which makes the band tails become wide. For  $x = 0.90$ , the photoluminescence spectrum can be regarded as the PL spectrum of a-C: H. Engemann et al [13] studied the PL spectra of silane-ethylene mixtures in the whole composition range at 77 K. Their PL spectra consist of two bands for  $0 < x < 0.57$ . Band 1 at 1.35 eV dominates the spectra in the Si-rich region, whereas band 2 is similar to the 1.81 eV band in our results. The room temperature PL band at 1.63 eV has not been reported. It may be due to an inter-band transition related to a mid-gap level. However, no definitive model of the structure of the optical center has yet been proposed. A detail work is needed to understand the origin and the emission mechanism of the new PL band, and the nature of 1.34 eV emission, which is still in debate, either due to a-SiC or due to a-Si clusters and inhomogeneities.

#### 4. Summary

A wide range of a-Si<sub>1-x</sub>C<sub>x</sub>: H films have been produced using the PECVD technique with SiH<sub>4</sub>, C<sub>2</sub>H<sub>4</sub> and H<sub>2</sub> as the precursor gases. The chemical and structural nature of these films has been characterized using XPS, FTIR, Raman spectroscopy and Photoluminescence. The source gases system play an important role regarding the film composition and the film structure as well as properties. The RT Raman spectra indicate the low concentration of C cluster in the C-rich a-Si<sub>1-x</sub>C<sub>x</sub>: H films. The RT Photoluminescence shows a different result from the previous reports. A new room temperature PL band centered at 1.63 eV was observed in the grown a-Si<sub>1-x</sub>C<sub>x</sub>: H films.

#### References

- [1] M. K. Han, Y. Mastsumoto, G. Hirata, H. Okamoto, and Y. Hamakawa, *J. Non-Cryst. Solids*, **115** (1989), p. 195.
- [2] D. Kruangam, T. Endo, and G. P. Wei, S. Nonomura, H. Okamoto, and Y. Hamakawa, *J. Non-Cryst. Solids* **77 & 78** (1985), p. 1429.
- [3] A. M. Mearns, *Thin Solid Films* **3** (1969), p. 201.
- [4] H. K. Tsai and S. C. Lee, *Appl. Phys. Lett.* **52** (1988), p. 275.
- [5] Y. Tawada, K. Tsuge, M. Kondo, H. Okamoto and Y. Hamakawa, *J. Appl. Phys.* **53** (1982), p. 5272.
- [6] J. Bullo and M. P. Schmidt, *Phys. Status Solidi B* **143** (1987), p. 345.
- [7] J. Robertson, *Phil. Mag. B* **66** (1992), p. 615.
- [8] S. E. Hicks, A.G. Fitzzyerd and H. Baker, *Phil. Mag. B* **62** (1990), p. 193.
- [9] S. P. Gerault, R. Morancho, G. Constant, et al, *Thin Solid Films* **101** (1983), p. 83.
- [10] R. J. Nemanich, J. T. Glass, G. Lucovski, et al, *J. Vac. Sci. Technol. A* **6** (1988), p. 1783.
- [11] E. P. O'Reilly, J. Robertson, D. Beeman, *J. Non-Cryst. Solids* **78 & 79** (1985), p. 83.
- [12] J. Robertson and E. P. O'Reilly, *Phys. Rev. B* **35** (1987), p. 35.
- [13] D. Engemann, R. Fischer, and J. Knecht, *Appl. Phys. Lett.* **32** (1978), p. 567.
- [14] R. S. Sussmana and R. Ogden, *Phil. Mag. B* **44** (1981), p. 137.
- [15] S. Ghosh, P. Bhattacharya, and D. N. Bose, *Appl. Phys. Lett.* **68** (1996), p. 2979.
- [16] R. A. Street, D. K. Biegelsen, and R. L. Weisfield, *Phys. Rev. B* **30** (1984), p. 5861

\* Corresponding author. Fax: 65-7776126; Tel: 65-8742616; E-mail: phylinjy@nus.edu.sg.

## Thin Films of $\alpha$ -Si<sub>1-x</sub>C<sub>x</sub>:H Deposited by PECVD: The r.f. Power and H<sub>2</sub> Dilution Role

R.J. Prado<sup>1</sup>, M.C.A. Fantini<sup>1</sup>, M.H. Tabacniks<sup>1</sup>, I. Pereyra<sup>2</sup> and A.M. Flank<sup>3</sup>

<sup>1</sup> Instituto de Física, Universidade de São Paulo, CP 66318, 05315-970 São Paulo SP, Brazil

<sup>2</sup> Escola Politécnica, Universidade de São Paulo, DEE, CP 8174, São Paulo, 05508-970, Brazil

<sup>3</sup> LURE, Bat. 209 D, B.P. 34, FR-91898 Orsay Cedex, France

**Keywords:** Amorphous Silicon Carbide, Silane Starving Plasma Regime

**Abstract** The growth of amorphous hydrogenated silicon carbide thin films with short-range order structure similar to crystalline silicon carbide is reported. The films were grown by plasma enhanced chemical vapor deposition at "silane starving plasma" regime. The radio frequency (rf) power and the hydrogen dilution of the gaseous mixture were controlled in order to improve the chemical and structural order in the solid phase. The composition was determined by Rutherford back scattering and forward recoil spectrometry. The chemical bonds were analyzed by Fourier transform infrared spectrometry. The structural properties were investigated by X-ray absorption near edge structure and extended X-ray absorption fine structure spectroscopies at the Si K edge. The results showed that the material with the desirable properties is obtained at higher rf power, provided the "silane starving plasma" regime is maintained, at higher hydrogen dilution and, with a carbon content,  $x$ , close to 0.5.

### Introduction

The deposition of amorphous hydrogenated silicon carbide ( $\alpha$ -Si<sub>1-x</sub>C<sub>x</sub>:H) thin films by plasma enhanced chemical vapor deposition (PECVD) has been extensively explored due to the ability of this technique to control the carbon content in the solid phase and, therefore, the optical gap ( $E_g$ ). The increase in the optical gap, following the increase in the carbon concentration, is desirable for many device strategies [1-3]. The advantageous electrical, optical and chemical properties of these films are achieved at the so-called "silane starving plasma" [4] regime. The experimental parameters that have to be controlled, at this particular deposition condition, are already established [5,6].

The experimental strategy in the present work was to explore not only the ratio between the silane and methane flows, but also other deposition parameters, as the rf power and hydrogen dilution. The aim of the work was to improve the chemical and structural order in hydrogenated silicon carbide films deposited by PECVD, since H<sub>2</sub> dilution is extensively used for obtaining microcrystalline hydrogenated silicon ( $\mu$ c-Si:H) by PECVD [7,8].

### Experiment

The  $\alpha$ -Si<sub>1-x</sub>C<sub>x</sub>:H films were deposited by PECVD, from appropriated gaseous mixtures of silane, methane and hydrogen, in a capacitively coupled reactor. The substrate temperature was kept at 300/350 °C. The rf power density and the hydrogen flow were varied. All the samples were grown with the same methane and silane flows, 3.6 and 32.4 standard cubic centimeters per minute (sccm) respectively, but with different rf power or H<sub>2</sub> flow, from 5 to 200 W and 100 to 300 sccm, respectively. The silane and methane flows were chosen taking into account previous results [9-11]. Tables 1, 2 and 3 present the deposition conditions used to deposit the analyzed films.

The atomic concentrations of Si, C and O (contamination) were determined in films deposited on ultra dense amorphous carbon [12] slides, by Rutherford back scattering (RBS). Forward recoil spectrometry (FRS) [13] was used for H analysis of some samples. The analyses were done at the IBM-Almaden Research Center, San Jose, California, and at the LAMFI/IFUSP, São Paulo, Brazil.

Table 1 – Power variation series (H<sub>2</sub> flow of 100 sccm).

Sample		Power (W)	Deposition Time (h)	Thickness (Å)
1	36902h5w	5	3.0	762
2	36902h20w	20	2.0	2697
3	36902h30w	30	3.0	4382
4	36902h50w	50	3.0	5350
5	36902h100w	100	-	6595
6	36902h200w	200	-	9552

Table 2 – Hydrogen flow variation series with low rf power (rf power of 5 W).

Sample		H <sub>2</sub> flow (sccm)	Deposition Time (h)	Thickness (Å)
1	36902h5w	100	3.0	762
9	36904h5w	200	10	2200
10	36906h5w	300	10	1300

Table 3 – Hydrogen flow variation series with high rf power (rf power of 200 W).

Sample		H <sub>2</sub> flow (sccm)	Deposition Time (h)	Thickness (Å)
6	36902h200w	100	-	9552
7	36904h200w	200	3.9	8000
8	36906h200w	300	3.9	7200

The chemical bonding was analyzed by Fourier transform infrared spectrometry (FTIR), using polycrystalline or monocrystalline (100) silicon substrate. The infrared spectra were normalized by the film's thickness. The FTIR peaks were analyzed assuming a gaussian profile of the experimental data. The extended X-ray absorption fine structure (EXAFS) and the X-ray absorption near edge structure (XANES) measurements were performed in films deposited on ultra dense amorphous carbon [12] slides at the Si K absorption edge (1839 eV), using the line SA32 of the SUPERACO ring at the LURE synchrotron radiation facility, Orsay, France. Polycrystalline silicon carbide, crystalline silicon and crystalline silicon oxide were used as reference compounds. The software EXAFS *pour le Mac* [14] was used for data treatment and simulations. The EXAFS simulations were performed using the Fourier transform filter of the first coordination shell, supposing a mixing of Si-O, Si-C and Si-Si bonds.

## Results and Discussion

The RBS/FRS data for both series are listed in Table 4. From these results one can notice that the composition of samples 1 and 2 are very similar. The carbon content,  $x$ , is defined as the ratio between the number of C atoms and the total number of C plus Si atoms.

The oxygen content increases with the decrease of the deposition rate, for lower rf power or higher H<sub>2</sub> flow, indicating that the oxygen atoms are incorporated during the growth process either by degassing from the walls or due to small leakage in the vacuum system. The H/C ratio in the

films (0.7 up to 1.2) decreases with the increase of the rf power and H<sub>2</sub> dilution. The Si-C peak position, from FTIR data, depends on both rf power and H<sub>2</sub> dilution, increasing from 767 to 790 cm<sup>-1</sup> with the increase of the rf power, approaching the value of 800 cm<sup>-1</sup>, reported for recrystallized a-SiC [3].

Table 4 – Atomic Content obtained from RBS and FRS data.

Sample	Power (W)	H <sub>2</sub> flow (sccm)	H (at. %)	C	Si	O
1	5	100	0.33	0.39	0.51	0.10
2	20	100	0.33	0.39	0.54	0.07
3	30	100	0.27	0.49	0.47	0.04
4	50	100	0.26	0.51	0.45	0.04
5	100	100	-	0.56	0.41	0.03
6	200	100	-	0.62	0.36	0.02
7	200	200	-	0.57	0.40	0.03
8	200	300	-	0.55	0.42	0.03
9	5	200	0.20	0.35	0.55	0.10
10	5	300	0.20	0.35	0.52	0.13

The Si-C peak position as a function of the H<sub>2</sub> dilution shows an increase from 767 to 785 cm<sup>-1</sup>, for a rf power of 5 W, but is invariant for a rf power of 200 W. For a constant rf power of 5 W, varying the H<sub>2</sub> dilution, the carbon content is almost constant, but both Si-C peak position and area increase with the increase of the hydrogen dilution flow, which is associated to a better short range order structure of the material. For a constant rf power of 200 W, the carbon content decreases with the increase of the H<sub>2</sub> dilution flow. It happens together with the increase of the FTIR Si-C peak area, confirming the decrease of the carbon content, that leads to a more stoichiometric material. The ratio of Si atoms bonded to one atom of hydrogen did not change (10% to 20%). It indicates that the Si atoms have a partial coordination number with Si, C and O of about 3.8 or 3.9. The calculations were done with the Si-H stretching peak around 2090 cm<sup>-1</sup>, supposing a a-SiC:H matrix [9].

The XANES spectra show shift and sharpening towards the value of the  $\beta$ -SiC edge with the increase in the rf power. The Fourier transform of the EXAFS spectra demonstrate that the higher rf power the larger the peak associated to the Si-C coordination. The data also reveal that the sample deposited at the highest H<sub>2</sub> dilution presents a medium range order structure, with distances greater than 3 Å, related to the second coordination shell. Tables 5 and 6 report the EXAFS results, where N is the coordination number ( $\pm 10\%$ ),  $\sigma$  is the Debye-Waller ( $\pm 15\%$ ) and R is the atomic distance ( $\pm 2\%$ ).

Table 5 – EXAFS simulation data for the rf power series.

	1	2	3	4	5	6	
Si-C	2.2	2.4	3.4	3.8	3.8	3.7	N <sub>Si-C</sub>
	0.07	0.07	0.07	0.07	0.05	0.05	$\sigma_{\text{Si-C}}$ (Å)
	1.91	1.91	1.89	1.90	1.88	1.88	R <sub>Si-C</sub> (Å)
Si-Si	1.2	1.2	0.4	0.2	-	-	N <sub>Si-Si</sub>
	0.03	0.03	0.00	0.00	-	-	$\sigma_{\text{Si-Si}}$ (Å)
	2.35	2.35	2.36	2.37	-	-	R <sub>Si-Si</sub> (Å)
Si-O	0.5	0.5	-	-	-	-	N <sub>Si-O</sub>
	0.00	0.00	-	-	-	-	$\sigma_{\text{Si-O}}$ (Å)
	1.64	1.64	-	-	-	-	R <sub>Si-O</sub> (Å)
N <sub>Si-Si</sub> +N <sub>Si-C</sub>	3.4	3.6	3.8	4.0	3.8	3.7	-
N <sub>Total</sub>	3.9	4.1	3.8	4.0	3.8	3.7	-

Table 6 – EXAFS simulation data for the H<sub>2</sub> dilution series.

	1	9	10 <sup>(a)</sup>	6	7	8	
Si-C	2.2	2.5	2.4	3.7	3.8	3.7	N <sub>Si-C</sub>
	0.07	0.07	-	0.05	0.04	0.03	$\sigma_{\text{Si-C}}$ (Å)
	1.91	1.91	-	1.88	1.88	1.88	R <sub>Si-C</sub> (Å)
Si-Si	1.2	1.2	1.0	-	-	-	N <sub>Si-Si</sub>
	0.03	0.04	-	-	-	-	$\sigma_{\text{Si-Si}}$ (Å)
	2.35	2.35	-	-	-	-	R <sub>Si-Si</sub> (Å)
Si-O	0.5	0.5	0.5	-	-	-	N <sub>Si-O</sub>
	0.00	0.00	-	-	-	-	$\sigma_{\text{Si-O}}$ (Å)
	1.64	1.63	-	-	-	-	R <sub>Si-O</sub> (Å)
N <sub>Si-Si</sub> +N <sub>Si-C</sub>	3.4	3.7	3.4	3.7	3.8	3.7	-
N <sub>Total</sub>	3.9	4.2	3.9	3.7	3.8	3.7	-

<sup>(a)</sup> Extrapolated from atomic concentration due to noise in EXAFS data.

### Conclusions

The increase of the rf power of the PECVD deposition method, but keeping its value low enough to remain under "starving plasma" conditions, contributes to the growth of silicon carbide films with improved chemical and structural properties. It was observed a systematic behavior of the first coordination shell with the increase of the rf power. Combining both, the rf power and H<sub>2</sub> dilution effects on the film's properties, the results confirmed the growth of films chemically and structurally more ordered, similar to the crystalline phase.

### References

- [1] A. Madan and M.P. Shaw, (1988). In "Physics and Applications of Amorphous Semiconductors", ed. Academic Press Inc., p. 149.
- [2] P.G. LeComber, J. Non-Cryst. Solids **115** (1989), p. 1.
- [3] J. Bulot and M.P. Schmidt, Phys. Status Solidi B **143** (1987), p. 345.
- [4] I. Solomon, M.P. Schmidt and H. Tran-Quoc, Phys. Rev. B **38** (1988), p. 9895.
- [5] M.N.P. Carreño and I. Pereyra, J. Non-Cryst. Solids **201** (1996), p. 110.
- [6] V. Mastelaro, A.M. Flank, M.C.A. Fantini, D.R.S. Bittencourt, M.N.P. Carreño and I. Pereyra, J. Appl. Phys. **79** (1996), p. 1324.
- [7] C.C. Tsai, G.B. Anderson and R. Thompson, Mat. Res. Soc. Symp. Proc., Vol.192, 475.
- [8] Zhenrui et al, Brazilian J. of Phys **27A**(4) (1997), p. 105.
- [9] I. Pereyra, M.N.P. Carreño, M.H. Tabacniks, R.J. Prado and M.C.A. Fantini, J. Appl. Phys **84** (5), 1 (1998).
- [10] R.J. Prado *et al.*, J. Appl. Cryst. **30** (1997), p. 659.
- [11] I. Pereyra, M.N.P. Carreño, R.J. Prado, M.H. Tabacniks and M.C.A. Fantini, Braz. J. Phys. **27A**(4) (1997), p. 150.
- [12] UDAC (Ultra Dense Amorphous Carbon), supplied by Kao Co. Akabane 2606, Ichikaimachi, Haga, Tochigi, Japan 321-34.
- [13] J.E.E. Baglin, A.K. Kellock, M.A. Crockett and A.H. Shih, Nucl. Instrum. Meth. Phys. Res. **B64** (1992), p. 469.
- [14] A. Michalowicz, EXAFS *pour le Mac*, Logiciels por la Chimie, Societé Française de Chimie, Paris (1991), p. 102.

Correspondent author: mfantini@if.usp.br, fax number (55) 11 818 6749.

# Chapter 3

## Physical Properties of SiC

## Surface Composition of 4H-SiC as a Function of Temperature

K.W. Bryant and M.J. Bozack

Surface Science Laboratory, Department of Physics, Auburn University, Auburn, AL 36849, USA

**Keywords:** AES, Auger Electron Spectroscopy, ELS, Energy Loss Spectroscopy, Polar Faces, Sublimation, Volatility

**Abstract:** We report surface compositions of the 4H-SiC(000 $\bar{1}$ ) C-face and 4H-SiC (0001) Si-face over the temperature range 300 to 1400 K, studied by Auger electron spectroscopy (AES), energy loss spectroscopy (ELS) and quadrupole mass spectroscopy (QMS). Below 800 K, no significant changes in surface composition are observed. Between 800 K and 1200 K, silicon preferentially volatilizes, leaving a slightly graphitized surface. Above 1200 K, preferential volatility of silicon results in a heavily graphitized surface. The thickness of the graphitized layer is greatest on the 4H-SiC(000 $\bar{1}$ ) C-face surface ( $\sim 8 \text{ \AA}$  @ 1400 K). Results are compared with earlier work involving the polar faces of 6H-SiC.

**Introduction:** Hexagonal SiC is a polar semiconductor whose ideal (0001) and (000 $\bar{1}$ ) surfaces are terminated with a layer of Si and C atoms respectively. Comprehensive studies of the two polar faces of 6H-SiC have shown differences in etch rate [1,2], oxidation [3,4], gross reactivity [5], and graphitization [6] at high temperature. Unfortunately, there have been few such studies for 4H-SiC, the current SiC polytype of choice for device applications. In this paper we report compositional changes in the 4H-SiC(000 $\bar{1}$ ) C-face and 4H-SiC (0001) Si-face surfaces over the temperature range 300 to 1400 K and compare the results with earlier work involving the polar faces of 6H-SiC. Our work examines the kinetics of carbon enrichment for the two polar surfaces of 4H-SiC and extends earlier work on 6H-SiC to corresponding 4H-SiC surfaces.

**Experimental:** The on-axis Epitronics n-type 4H-SiC crystals used in this work were 0.012" thick with orientations of (0001)  $\pm 5^\circ$  and (000 $\bar{1}$ )  $\pm 5^\circ$  for the Si- and C-face surfaces respectively. To independently check the surface polarity, we oxidized the polar faces at 1373 K (500 sccm of O<sub>2</sub> passed through a bubbler). Götz et al. [7] has shown that the 4H-SiC(0001) Si-face oxidizes slower than the C-face. Rutherford backscattering spectroscopy (RBS) verified that there was a thicker oxide layer on the C-face surface. Surface temperatures were measured by an ice-junction referenced W-5%Re vs W-26%Re thermocouple clip attached to the crystal. For temperatures above 970 K, the thermocouple measurement was compared to a single wavelength (0.65  $\mu\text{m}$ ) optical pyrometer and showed excellent agreement [8].

Preparing an atomically clean SiC surface is not a trivial task. In our cleaning procedure, the crystals were first ultrasonically cleaned in electronics grade 1,1,1-trichloroethane followed by acetone and 12 M $\Omega$ /cm deionized water, then mounted and placed in the UHV chamber. After evacuation to  $3 \times 10^{-10}$  torr, the surfaces were in-situ cleaned by a combination of annealing and ion bombardment. We first ramp the crystal temperature to 1400 K to volatilize the native oxide and graphitize the surface. Next, the crystal is maintained at 700 K while it is sputtered using Ar<sup>+</sup> ions at 75° from the surface normal with stepwise decreases in ion energy from 6 keV to 3 keV to 1 keV. The crystal is then annealed at 700 K for 10 minutes. The procedure has been shown to maintain near perfect surface stoichiometry and minimize the amount of implanted argon.

The surfaces were heated resistively in vacuum by using a temperature programmer that controlled a Hewlett Packard 6012B auto ranging 1000 W DC power supply. The programmer had a 1 kHz sampling rate and fast feedback to prevent thermal runaway while passing through the temperature range where exponential promotion of charge carriers into the conduction band occurs. In the experiments reported below, after achieving an atomically clean surface, the crystals were heated with stepwise increasing temperatures at five-minute intervals and AES and ELS spectra were recorded. In the mass spectrometer studies, the crystal was ramped at a rate of 1 K/s while the mass range from 1-100 amu was continuously recorded.

**Auger Surface Concentration vs Temperature:** In Figures 1-2 the Auger intensities as a function of annealing temperature for the two polar faces of 4H-SiC are plotted. By intensity we mean the peak-to-peak amplitude of the derivative Auger peak. The results show that the 4H-SiC surface composition with temperature is controlled more by the behavior of Si than C at the surface, since the C(KLL) increases only slightly between 300-1400 K. On the C-face, there is a monotonic decrease in Si(LVV) below 1100 K followed by a rapid decrease in amplitude above 1100 K. On the Si-face, the behavior of Si(LVV) and C(KLL) is similar, but there is an additional notable increase in Si(LVV) in the temperature range 900-1100 K before the rapid decrease in Si(LVV). It is shown from mass spectrometer studies below that the increasing C/Si Auger ratios above 1200 K are attributable to a decrease in silicon at the surface due to preferential volatility at high temperature. The results are similar to 6H-SiC polar surfaces, reported earlier [9].

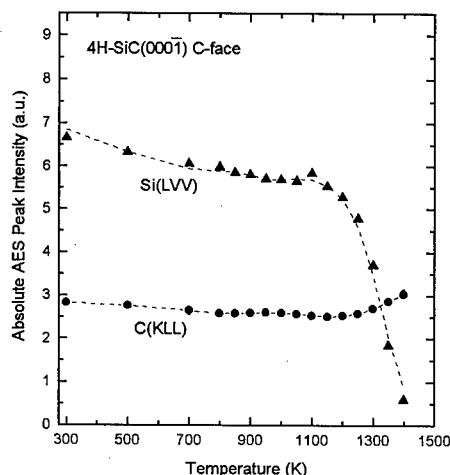


Fig. 1. Auger C(KLL) and Si(LVV) peak intensities vs temperature for the 4H-SiC (C-face) surface.

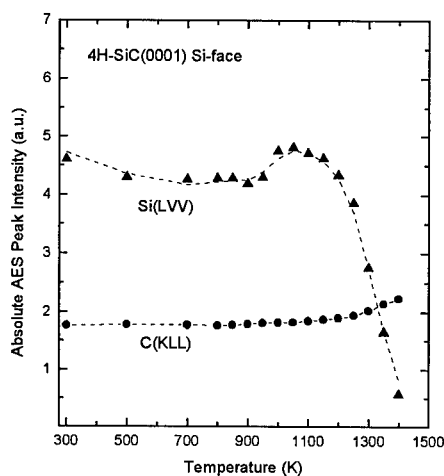


Fig. 2. Auger C(KLL) and Si(LVV) peak intensities vs temperature for the 4H-SiC (Si-face) surface.



**Auger C(KLL) Lineshape Analysis vs Temperature.** Lineshape analysis of the AES C(KLL) signal and observation of a SiC plasmon loss feature at -22.4 eV below the elastic peak show that the surface at high temperature is largely graphite. Figures 3-4 show a series of C(KLL) AES spectra for both SiC faces in the derivative mode  $E \cdot dN/dE$  as a function of annealing temperature. Heavily disordered C- and Si-faces (not shown) at 300 K exhibit a broadened SiC-type [10]

lineshape compared to spectra measured on annealed SiC single crystals. Annealing in the temperature range 800-1400 K resulted in sharper Auger features with a continuous downward shift in kinetic energy (from 272 eV). The C-face C(KLL) shifted to 264 eV during annealing while the Si-face C(KLL) shifted to 268 eV. A slight increase in the C(KLL) peak-to-peak amplitude throughout the annealing range is observed for both faces, in agreement with the C/Si ratio studies above. Above 1350 K, C(KLL) line shape changes occur on both faces of 4H-SiC, and significant new features are observed on the low kinetic energy side of the principal peak. At 1400 K, the C-face shows a complete line shape change to one characteristic of graphite [11], whereas the Si-face shows an AES line shape that is a superposition of the line shape for graphite and SiC. Consistent with our other data, a higher graphite surface concentration is observed on the 4H-SiC(000 $\bar{1}$ ) C-face surface than on the 4H-SiC(0001) Si-face surface.

On the assumption that the surface carbon enrichment is due to a graphite layer on the surface, the layer thickness can be estimated by the attenuation of the Si (LVV) Auger electron as it passes through this layer. The silicon signal can be expressed as  $I_{Si} = I_0 e^{[-x/\lambda \cos \theta]}$  where  $I_{Si}$  is the Si (LVV) Auger intensity from the carbonized surface,  $I_0$  is the Si

**Table I**  
Thickness of Surface Graphite Layer  
vs Temperature for 4H-SiC

Annealing Temperature (K)	Graphite Thickness (Å)	
	Si-face	C-face
800	0.3	0.5
850	0.3	0.7
900	0.4	0.8
950	0.4	0.8
1000	0.5	0.9
1050	0.7	0.9
1100	0.7	1.0
1150	0.8	1.0
1200	0.9	1.1
1250	1.0	1.3
1300	1.9	2.1
1350	3.7	4.2
1400	7.2	8.2

Auger system is  $42^\circ \pm 6^\circ$ . The IMFP is given by Seah [12] as  $\lambda = 0.41 a^{1.5} E^{0.5}$  where  $a$  is the atom size in Å and  $E$  is the energy of the electron in eV. This yields an IMFP for the Si

(LVV) Auger intensity from a clean SiC surface,  $x$  is the thickness of the graphite layer,  $\lambda$  is the inelastic mean free path (IMFP), and  $\theta$  the angle of emission from the surface normal, which for our cylindrical mirror analyzer (CMA)

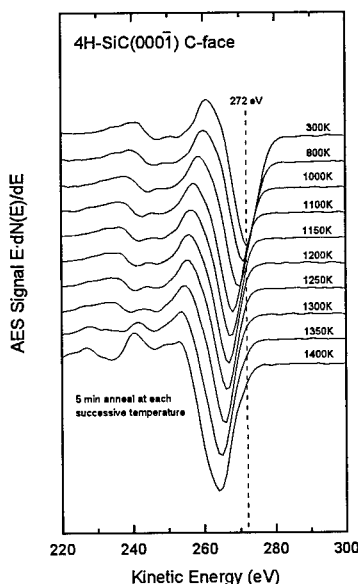


Fig. 3. C(KLL) Auger lineshape vs temperature for the 4H-SiC (C-face) surface.

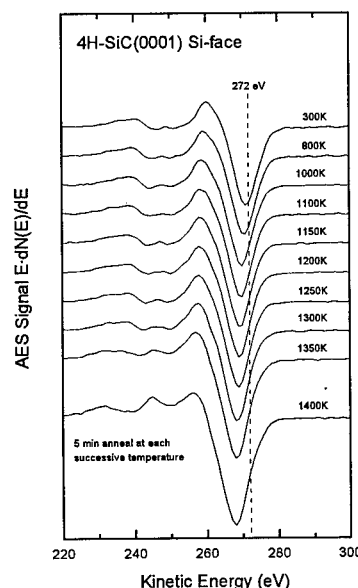


Fig. 4. C(KLL) Auger lineshape vs temperature for the 4H-SiC (Si-face) surface.

(LVV) Auger electron with energy of 89.9 eV of 6 Å, which was used for our calculation. By comparison, Biberian and Somorjai [13] observed the graphite surface concentration on platinum crystals and determined the IMFP of 64, 237, and 272 eV electrons in graphite to be 5, 9 and 8.7 Å respectively. Table I shows a tabulation of graphite thickness at various temperatures for the two polar surfaces of 4H-SiC.

**Energy Loss Spectroscopy vs Temperature.** Electron energy loss (ELS) spectra provide confirmatory evidence of the development of graphite on 4H-SiC surfaces at temperatures above ~ 1300 K. In the ELS experiment, the energy lost to plasmon excitation from a monoenergetic incident beam of electrons is measured. Characteristic energy losses for both SiC and graphite have been previously measured by Bozso et al [14]; a SiC bulk plasmon occurs at 27 eV below the elastic loss peak while graphite has a bulk plasmon at 6.5 eV below the elastic loss peak. Figures 5-6 report representative ELS spectra for the 4H-SiC(0001) C-face surface for two incident beam energies (70 and 370 eV). The higher primary electron energies probe deeper surface layers. Kanaya and Okayama [15] (K-O) have considered the effects of elastic and inelastic scattering in the form of an energy-loss law to derive an expression for the maximum electron range in a material. For incident beam energies 70 eV and 370 eV in SiC, the O-K electron range is calculated to be 2.9 Å and 46.3 Å respectively. By comparing the intensities of the 6.5- and 27-eV graphite loss features with the 22.5 eV SiC loss feature as a function of temperature, we conclude that graphite forms on the 4H-SiC(0001) C-face at temperatures ~ 1350 K. With increasing primary electron energy, the graphite-loss features diminish and the 22.5 eV SiC bulk plasmon dominates the spectrum; at a primary electron energy of 370 eV, the dominant feature is the 22.5 eV SiC plasmon but graphite is observed to grow to this depth at a temperature ~ 1350 K. Results for the Si-face (not shown) are qualitatively similar, but the 6.5 eV graphite ELS feature at 370 eV primary energy does not appear until 1400 K, indicating a thinner graphite layer on this face. The C-face shows a thicker graphite layer than the Si-face, based on the observation that graphite-loss features are observed by ELS at 1350 K with 370 eV primary electrons on the C-face but not on the Si-face. Similar behavior has been observed on the polar faces of 6H-SiC.

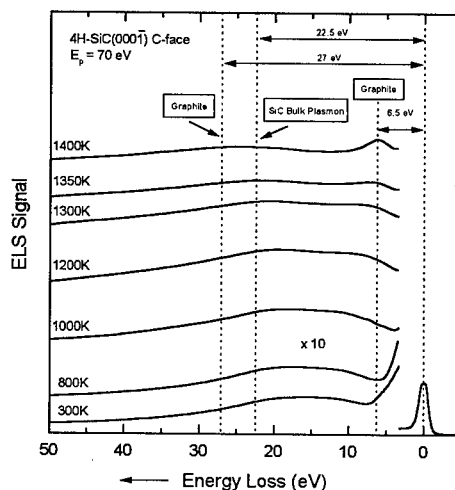


Fig. 5. Electron energy loss spectrum vs temperature for the 4H-SiC (C-face) surface ( $E_p = 70$  eV).

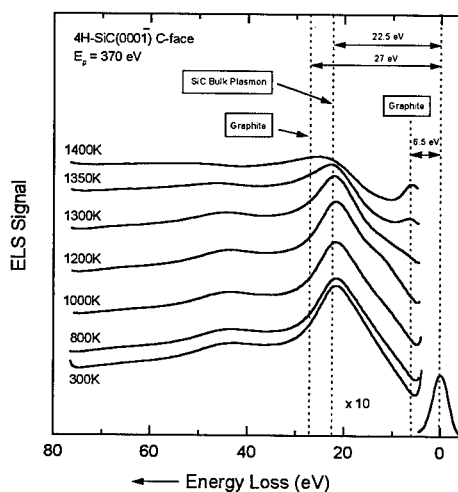


Fig. 6. Electron energy loss spectrum vs temperature for the 4H-SiC (C-face) surface ( $E_p = 370$  eV).

**4H-SiC Volatility vs Temperature.** It is known from mass spectrometer investigations [16,17] that SiC dissociates in many different Si-C compound molecules. At thermodynamic equilibrium, the predominant vapor species are Si(g) and the carbon transporting gases Si<sub>2</sub>C(g) and SiC<sub>2</sub>(g). Other molecules (e.g., Si<sub>2</sub>, SiC, and Si<sub>2</sub>C<sub>2</sub>) are insignificant. Behrens [18] has studied the Langmuir vaporization of freely sublimating hexagonal SiC crystals in near-ultrahigh vacuum conditions over the temperature range 1835-2264 K and found similar results. We have used quadrupole mass spectroscopy (QMS) to monitor sublimating chemical species from the polar faces of 4H-SiC during annealing in the temperature range 300-1400 K.

The lower temperature range allows for investigation of the graphitization onset for 4H-SiC. Figure 7 reveals that 4H-SiC undergoes dissociation and incongruent vaporization beginning at temperatures of ~ 800 K. Si(g) is the only vaporizing species observed < 1400 K; no other evaporating species were observed over the mass range 1-100 amu. The sublimation is complex and occurs in a multistep process that is face-dependent. For the 4H-SiC(0001) Si-face surface, two initial small increases in Si(g) volatility occur at ~ 800 and 1000 K before the onset of massive Si(g) sublimation at ~ 1300 K. For the 4H-SiC(0001) C-face surface, only one initial increase in Si(g) volatility is observed at ~ 900 K. The onset temperature of Si(g) evaporation is connected to the surface C enrichment observed in the AES and ELS experiments.

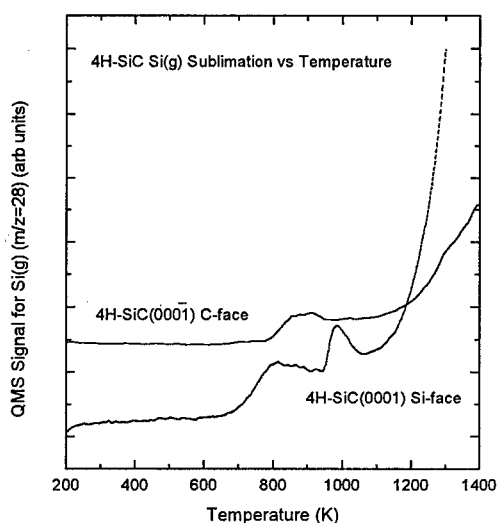


Fig. 7. 4H-SiC Si(g) sublimation vs temperature.

From the vapor pressure data of Drowart, et al. [19] it is possible to estimate the rate of sublimation of Si(g) at the approximate onset temperature of 900 K for the initial evaporation and 1300 K for massive volatility. We use the vapor pressures of Drowart but note that the vapor pressures reported by Behrens and Rinehart are somewhat higher. Further, the values reported by both authors were measured at much higher temperatures (1800-2200 K) and are probably not representative of the vaporization enthalpies and equilibrium partial pressures at lower temperature. Given the limitations, the calculations indicate that at 900 K, the rate of evaporation of Si(g) is  $4 \times 10^7$  Si(g) atoms/cm<sup>2</sup>-s, corresponding to  $4 \times 10^{-5}$  monolayers of Si(g) during 5 minutes. On the other hand, at 1300 K, the evaporation rate of Si(g) is  $2.7 \times 10^{12}$  Si(g) atoms/cm<sup>2</sup>-s, corresponding to the loss of 2.7 monolayers of Si(g) during 5-min of annealing. Thus, it is likely that incongruent vaporization of Si(g) leads to rapid C enrichment and surface graphitization at temperatures  $\geq 1300$  K. The effects of Si(g) sublimation on the surface in the range 700-1100 K is more difficult to explain. It is possible that the QMS signal at  $m/z = 28$  in this temperature range is due to N<sub>2</sub> or CO desorption rather than Si(g) volatility, but no N or O was observed on the surface and the volatility curves are continuous. Further, the complex nature of the initial sublimation appears to be connected to the complications observed in the C/Si AES studies vs temperature. It may be that 4H-SiC undergoes surface reconstruction that favors the sublimation of silicon off the surface but leaves carbon on the surface. However the temperatures appear to be too low. In a photoemission study of an off-axis Si-face of 4H-SiC, Johansson et al. [20] observed a  $1 \times 1$  LEED pattern directly after introduction into vacuum. Upon heating to ~ 1223 K, a  $(\sqrt{3} \times \sqrt{3})$ -R30° LEED pattern developed. Further heating at temperatures above 1273 K produced a gradual transition to a  $(6\sqrt{3} \times 6\sqrt{3})$ -R30°

pattern, which was found to be completed at a temperature of  $\sim 1523$  K. Incidentally, Johansson et al. report that C enrichment in the surface region is observed on the  $6\sqrt{3}$  reconstructed surface but the surface carbon is not graphite. Graphitization, revealed by the presence of a graphitic C1s peak, is only observed after heating to  $\sim 1600$  K, which is higher than that required to obtain a fully developed  $6\sqrt{3}$  LEED pattern. The results reported here show that the onset of surface graphite occurs at much lower temperatures, in agreement with previous studies on 6H-SiC. More work is needed to resolve these questions, which may arise due to the different SiC crystals used here (on-axis, Epitronics) and by Johansson (off-axis, CREE) or the surface cleaning technique. In any case, details concerning the decomposition mechanism of SiC cannot be presented at the present time. However, on the basis of the model developed by Searcy [21,22] for endothermic decomposition reactions which form porous solid reaction products, the preliminary vaporization data indicate that either a chemically activated mechanism of surface diffusion or a step involving the gaseous reaction products (for equilibrium conditions) is rate-limiting.

**Acknowledgements:** This work was supported in part by NASA Grant No. NAGW-1192 through the Center for Commercial Development of the Auburn University Space Power Institute. Special thanks are due to Tony Gichuhi for his help in acquiring the AFM images.

#### References:

- [1] F. Bozso, L. Muehlhoff, M. Trenary, W. J. Choyke, and J. T. Yates, Jr., *J. Vac. Sci. Technol. A* 2 (1986) 1271.
- [2] K. Brack, *J. Appl. Phys.* 36 (1965) 3560.
- [3] A. Suzuki, H. Matsunami, and T. Tanaka, *J. Electrochem. Soc.* 125 (1978) 1897.
- [4] L. Muehlhoff, W. J. Choyke, M. J. Bozack, and J. T. Yates, Jr., *J. Appl. Phys.* 60 (1986) 2558.
- [5] A. Suzuki, H. Ashida, N. Furui, K. Mameno, and H. Matsunami, *Jpn. J. Appl. Phys.* 21 (1982) 579.
- [6] L. Muehlhoff, W. J. Choyke, M. J. Bozack, and J. T. Yates, Jr., *J. Appl. Phys.* 60 (1986) 2842.
- [7] A. Golz, G. Horstmann, E. Stein von Kamienski, and H. Kurz, *Inst. Phys. Conf. Ser.* 142 (1996) 633.
- [8] M. J. Bozack, W. J. Choyke, J. N. Russell, Jr., L. Muehlhoff, and J. T. Yates, Jr., *J. Vac. Sci. Technol. A* 5 (1987) 1.
- [9] Ibid, L. Muehlhoff, *J. Appl. Phys.* 60 (1986) 2842.
- [10] M. J. Bozack, *Surf. Sci. Spect.* 3 (1995) 86; see also reference 1 and J. T. Grant and T. W. Haas, *Phys. Lett.* 33A (1970) 386.
- [11] Ibid, Bozso.
- [12] M. P. Seah in *Practical Surface Analysis by Auger and X-ray Photoelectron Spectroscopy*, ed. D. Briggs and M. P. Seah (Wiley and Sons, New York, 1983), pp. 181-216.
- [13] J. P. Biberian and G. A. Somorjai, *Appl. Surf. Sci.* 2 (1979) 352.
- [14] Ibid, Bozso. Also see F. Bozso, J. T. Yates, Jr., W. J. Choyke, and L. Muehlhoff, *J. Appl. Phys.* 57 (1985) 2771.
- [15] K. Kanaya and S. Okayama, *J. Phys. D. Appl. Phys.* 5 (1972) 43.
- [16] J. Drowart, G. DeMaria, and M. G. Inghram, *J. Chem. Phys.* 29 (1958) 1015.
- [17] H. Sadoski and R. Helbig, *J. Electrochem. Soc.* 145 (1998) 3556.
- [18] R. G. Behrens and G. H. Rinehart, *Nat. Bur. Stand. U.S. Spec. Publ.* 561 (1979) 125.
- [19] Ibid, Drowart.
- [20] L. I. Johansson, F. Owman, P. Martensson, *Surf. Sci.* 360 (1996) L483.
- [21] A. W. Searcy and D. Beruto, *J. Phys. Chem.* 80 (1976) 425.
- [22] A. W. Searcy and D. Beruto, *J. Phys. Chem.* 82 (1978) 163.

## Stacking Rearrangement on SiC Surfaces: A Possible Seed for Polytype Heterostructure Growth

U. Starke, J. Bernhardt, J. Schardt, A. Seubert and K. Heinz

Lehrstuhl für Festkörperphysik, Friedrich-Alexander Universität Erlangen-Nürnberg,  
Staudtstr. 7, DE-91058 Erlangen, Germany

**Keywords:** 4H-SiC, 6H-SiC, Heterostructures, Hexagonal Surfaces, Low-Energy Electron Diffraction, Polytype, Reconstruction, Scanning Tunneling Microscopy, Stacking Sequence, Surface Structure

**Abstract:** The bilayer stacking sequence at the surface of SiC samples can be influenced by the preparation of superstructure phases as retrieved by quantitative low-energy electron diffraction (LEED). On 4H-SiC(0001) the preparation of a  $(\sqrt{3} \times \sqrt{3})R30^\circ$  reconstruction under Si rich conditions increases the number of identically oriented bilayers in the topmost slab from two to three, thus breaking the 4H periodicity in favor of a more cubic type of stacking. In contrast, in a  $(2 \times 2)$  phase on SiC(000 $\bar{1}$ ) the topmost bilayers are found to be rotated by  $60^\circ$  with respect to each other. This reconstruction obviously favors hexagonal stacking at the very surface. These surface bilayer arrangements may be viewed as potential seed for a polytype heterojunction.

### Introduction

The physical properties of SiC have opened up a wide field of electronic applications in areas such as high temperature, high power and high frequencies. A particular difficulty for a large scale fabrication of SiC based devices is caused by material related problems. Growth of high quality SiC still imposes technological difficulties resulting in high defect densities in the wafer material. Some of these difficulties may be due to the fact that SiC exists in different crystal structures [1] with practically degenerate total energies. These so-called polytypes differ by the stacking sequence of hexagonal SiC bilayers which represent the basic building block of the material [2]. Adjacent bilayers can be stacked either in identical orientation or rotated by  $60^\circ$  with respect to each other. Different periodic sequences of this stacking result in the different polytypes, cubic 3C-SiC (Zinkblende) in the extreme of alignment of all bilayers and hexagonal 2H-SiC (Wurtzite) when every other bilayer is rotated. 4H, 6H and other hexagonal and rhomboedric polytypes are characterized by combinations of the cubic (identical bilayer orientation) and hexagonal (mutual bilayer rotation) type of stacking. The 6H polytype for example consists of slabs of three identically oriented bilayers which in turn are stacked on top of each other rotated by  $60^\circ$ .

Noteworthy, the stability of SiC in different polytypes is accompanied by a considerable spread of their electronic energy gap [3]. As the lattice parameters of these structures parallel to the hexagonal bilayers are practically equal, the development of strain free heterostructures composed from different polytypes appears feasible. However, for such an application it is necessary to develop the means to switch between different polytypes during growth and generate sharp and well defined interfaces. In contrast to the off-normal oriented substrates commonly used for homoepitaxy of SiC films by chemical vapor deposition (CVD), for the formation of such a heterojunction one would need a flat surface to suppress the influence of the underlying substrate. Yet, in such cases up to now island nucleation has been observed leading to a large number of grain boundaries [4]. In the present paper we demonstrate that by application of a careful control of the formation procedure of superstructures on SiC samples a particular stacking sequence can be induced in the surface region which can even be different from that of the substrate.

At the surface we have to expect different terminating stacking sequences for a given polytype depending on the actual truncation of the bulk unit cell [2, 5]. On a 6H-SiC sample the corresponding stacking termination could be (ABCACB)A.., (BCACBA)B.. and (CACBAB)C.. which we denote shortly S3, S2 and S1 according to the number of bilayers in identical orientation in the topmost slab (see Fig. 1). They also represent three other possible termination structures which are identical to S1...3 except for a 60° rotation of the whole semi-infinite crystal [2]. Correspondingly, a 4H sample can display (ABCB)A.. and (BCBA)B.. stacking at the bulk truncated surface, i.e. S2 and S1 termination.

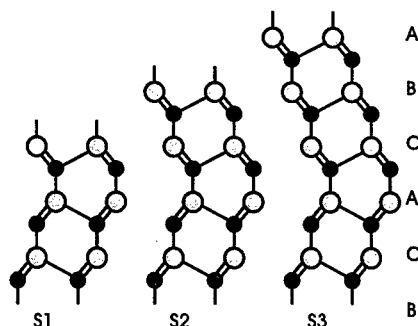


**Figure 1:** Possible bulk terminated surface layer stacking sequences on 6H-SiC(0001) with double lines indicating two Si-C bonds not lying in the (11 $\bar{2}$ 0) projection plane. The stacking sequence is depicted by the letters on the right.

### Surface preparation and analysis

Bulk samples from Lely type growth processes as well as samples with epitaxial layers grown by CVD were used. A thermal hydrogen treatment was used to smoothen and clean the samples. Regardless of the sample type this results in a reconstructed silicon oxide adlayer on top of an otherwise bulk like SiC surface as observed in ultra-high vacuum (UHV) [6, 7]. Annealing of these samples in UHV is used to prepare different surface reconstruction phases. By varying the temperature and simultaneously depositing Si from an electron beam heated evaporator, silicon enriched as well as depleted structures can be generated [5, 8].

For the crystallographic analysis of the surface structures quantitative low-energy electron diffraction (LEED) was used. The diffraction spot intensities were recorded as a function of primary beam energy using a computer controlled video-LEED system [9]. The corresponding intensity curves were calculated for different surface models applying full dynamical scattering theory [10, 11]. Tensor LEED [12, 13] was applied for the fine variation of model parameters. For the structural search an automated algorithm [14] was used guided by the Pendry R-factor [15]  $R_p$  for the model optimization.

### Results

On SiC(0001) three stable reconstruction phases can be prepared: a  $(3 \times 3)$ , a  $(\sqrt{3} \times \sqrt{3})R30^\circ$  and a  $(6\sqrt{3} \times 6\sqrt{3})R30^\circ$  phase [5, 16]. We focus on the  $(\sqrt{3} \times \sqrt{3})R30^\circ$  phase [17] which develops upon annealing the *ex situ* prepared surface ( $\sim 950^\circ\text{C}$ ,  $\sim 30$  min). Alternatively and most reliably, the structure can be obtained by heating ( $\sim 1000^\circ\text{C}$ ,  $\sim 30$  min) the Si rich  $(3 \times 3)$  phase [18]. A third and the most delicate method is heating under simultaneous Si deposition ( $\sim 1000$ - $1100^\circ\text{C}$ ). Then the initial surface phase is not of importance, but it is difficult to maintain the proper balance between Si depletion and redeposition and the  $(\sqrt{3} \times \sqrt{3})R30^\circ$  phase often fails to develop in full order. We performed LEED structure analyses in order to determine the atomic geometry of these phases. Regardless of the preparation technique the  $(\sqrt{3} \times \sqrt{3})R30^\circ$  phase contains one Si adatom per unit cell in a three-fold hollow site on top of a carbon atom of the topmost SiC bilayer, the so-called  $T_4$  site [17]. This model and its detailed geometry parameters are in good agreement with theoretical calculations [19-22] as well as very recent work using X-ray diffraction (XRD) [23]. A very surprising result of the LEED analyses concerns the surface terminating stacking sequence on our 4H-SiC sample for the three preparation methods. We recall that the chemical preparation of  $(1 \times 1)$  phases was found earlier to lead to a dominance of the cubic type of stacking termination, i.e. S3 on 6H- and S2 on

**Table 1:** Weights of domains with different surface terminating stacking sequences for the three differently prepared  $(\sqrt{3}\times\sqrt{3})R30^\circ$  structures on 4H-SiC(0001), the  $(2\times 2)_C$  reconstruction on SiC(000 $\bar{1}$ ) and the silicon oxide phase on each sample.

Sample	Phase description	Surface stacking		
		S1	S2	S3
4H-SiC(0001)	Silicon oxide phase	15%	85%	—
	Annealing <i>ex situ</i> sample	15%	75%	10%
	Direct prep. in Si-flux	15%	50%	35%
	Annealing $(3\times 3)$ phase	15%	20%	65%
6H-SiC(000 $\bar{1}$ )	Silicon oxide phase	45%	40%	15%
	$(2\times 2)_C$	60%	15%	25%

4H-SiC(0001), respectively [2, 5, 24]. The same holds for our initial silicon oxide phase on 4H-SiC which is covered mainly by S2 [6]. Preparation of the  $(\sqrt{3}\times\sqrt{3})R30^\circ$  phase by annealing basically leaves the stacking unchanged (The domain weights are listed in Table 1). However, modelling the data of the two other preparation methods failed until S3 domains which should not occur on a bulk truncated 4H sample were included in the LEED calculations. The amount of S3 stacking at the surface depends on the amount of Si used for the preparation (see Table 1). In the Si rich extreme case when prepared from the  $(3\times 3)$  phase the surface contains as much as 65% of this unusual stacking sequence. This could be viewed as beginning of 3C stacking or part of a 6H unit cell. It should be noted that the development and increase of S3 domains on the surface can again be reversed by using a less Si rich preparation for the  $(\sqrt{3}\times\sqrt{3})R30^\circ$  phase.

Comparison of the stacking domain weights of the oxide phase and the  $(\sqrt{3}\times\sqrt{3})R30^\circ$  structure (see Table 1) indicates that the S3 domains form by the addition of a third bilayer on top of S2 domains (same orientation) rather than a rotation of bilayers in the crystal [17]. The necessary material transport obviously occurs during a severe disordering in the intermediate state between the  $(3\times 3)$  and  $(\sqrt{3}\times\sqrt{3})R30^\circ$  phases. The LEED pattern contains spots corresponding to several different phases of e.g.  $(3\times 3)$ ,  $(2\times 2)$ ,  $(\sqrt{7}\times\sqrt{7})R19.1^\circ$  and other periodicities as shown in Fig. 2. In scanning tunneling microscopy (STM) the development of mesa like structures on a length scale of 150-300 Å (typical height of  $\sim 20$  Å) is observed (bottom left of Fig. 2). In contrast the  $(3\times 3)$  and the  $(\sqrt{3}\times\sqrt{3})R30^\circ$  phase are flat and ordered on a scale of 1000 Å. On top of these mesas we find small patches of different periodicities simultaneously: in the enlargement (right panel of Fig. 2) a  $(4\times 4)$  and a  $(4\sqrt{7}\times 4\sqrt{7})R19.1^\circ$  area are shown.

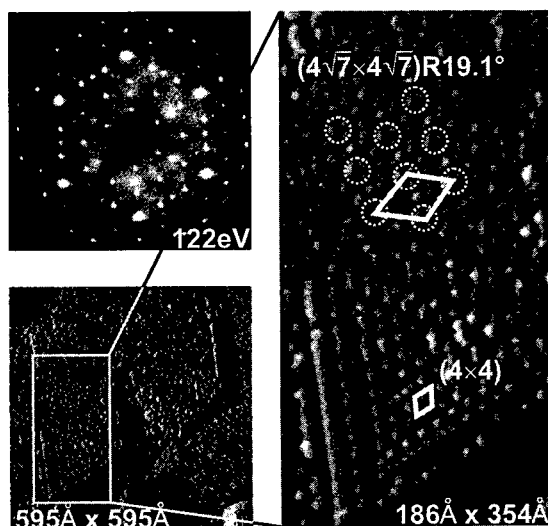


**Figure 2:** LEED and STM images of the transformation regime between  $(3\times 3)$  and  $(\sqrt{3}\times\sqrt{3})R30^\circ$  phase. The right STM image shows a zoomed area from within the image on the left. See text for details.

On SiC(000 $\bar{1}$ ) a completely different set of stable surface phases can be prepared in UHV, again by annealing with or without additional Si deposition as reported in detail elsewhere [8]. Different from the case of SiC(0001), on the initial silicon oxide covered surface the cubic type of stacking (S3 termination) is barely present (15%, cf. Table 1) [6, 7]. S2 and S1 appear to be equally distributed covering the majority of the surface. Nevertheless, the stacking sequence can again be influenced by the development of a surface reconstruction. The  $(2\times 2)_C$  phase (the index C is used to distinguish it from a second, strongly Si enriched  $(2\times 2)_{Si}$  phase) contains a single Si adatom per unit cell in a

true threefold hollow site ( $H_3$ ) as determined by quantitative LEED [25]. The distribution of stacking domains in this phase is shifted towards the S1 type (60%). In other words, the rotation between two adjacent bilayers inherent to hexagonal SiC polytypes is preferably located directly at the surface. Apparently, the  $(2 \times 2)_C$  reconstruction on SiC(000 $\bar{1}$ ) stabilizes hexagonal stacking at the surface.

## Conclusions

We have shown that the surface stacking on hexagonal SiC {0001} surfaces can be influenced by the preparation of surface reconstruction phases. Very different effects have been observed on the two possible orientations. By preparing the  $(\sqrt{3} \times \sqrt{3})R30^\circ$  phase on SiC(0001) under silicon rich conditions the addition of bilayers continuing the orientation already present can be initiated leading to a shift to cubic stacking at the surface (S3 termination). This trend can be reversed by an alternative, less Si rich preparation method. On SiC(000 $\bar{1}$ ) a  $(2 \times 2)_C$  adatom phase distinctively stabilizes the hexagonal stacking (S1) termination. Other reconstruction phases on this surface orientation have still to be examined. One might speculate that the stacking rearrangement induced by surface reconstructions can be used as seed for the formation of polytype heterostructures in actual growth processes of thicker films, a perspective for new types of devices to be produced on SiC.

This work was supported by Deutsche Forschungsgemeinschaft (DFG) through SFB 292.

## References

- [1] R. Verma and P. Krishna, *Polymorphism and Polytypism in Crystals* (Wiley, New York, 1966).
- [2] U. Starke, *phys. stat. sol. (b)* **202** (1997) p. 475.
- [3] G. L. Harris (ed.), *Properties of Silicon Carbide*, in: EMIS Datareviews Series, No. 13 (Inspec, London, 1995).
- [4] S. Tanaka, R.S. Kern and R.F. Davis, *Appl. Phys. Lett.* **65** (1994) p. 2851.
- [5] U. Starke, J. Schardt and M. Franke, *Appl. Phys. A* **65** (1997) p. 578.
- [6] J. Bernhardt, J. Schardt, U. Starke and K. Heinz, *Appl. Phys. Lett.* **74** (1999) p. 1084.
- [7] J. Bernhardt, J. Schardt, U. Starke and K. Heinz, *Mat. Sci. Forum*, *this volume*, p. 383.
- [8] J. Bernhardt, M. Nerdling, U. Starke and K. Heinz, *Mat. Sci. Eng. B* **61-62** (1999) p. 206.
- [9] K. Heinz, *Rep. Prog. Phys.* **58** (1995) p. 637.
- [10] J. B. Pendry, *Low Energy Electron Diffraction*, Academic Press, London, (1974).
- [11] M. A. Van Hove, W. H. Weinberg and C.-M. Chan, *Low Energy Electron Diffraction*, Springer-Verlag, Berlin (1986).
- [12] P.J. Rous, *Prog. Surf. Sci.* **39** (1992) p. 3.
- [13] K. Heinz, R. Döll and M. Kottcke, *Surf. Rev. Lett.* **3** (1996) p. 1651.
- [14] M. Kottcke and K. Heinz, *Surf. Sci.* **376** (1997) p. 758.
- [15] J.B. Pendry, *J. Phys. C* **13** (1980) p. 937.
- [16] U. Starke, M. Franke, J. Bernhardt, J. Schardt and K. Heinz, *Mat. Sci. Forum* **264** (1998) p. 321.
- [17] U. Starke, J. Schardt, J. Bernhardt, M. Franke and K. Heinz, *Phys. Rev. Lett.* **82** (1999) p. 2107.
- [18] U. Starke, J. Schardt, J. Bernhardt, M. Franke, K. Reuter, H. Wedler, K. Heinz, J. Furthmüller, P. Käckell and F. Bechstedt, *Phys. Rev. Lett.* **80** (1998) p. 758.
- [19] F. Bechstedt, P. Käckell, A. Zywiets, K. Karch, B. Adolph, D. Tenelsen and J. Furthmüller, *Phys. stat. sol. (b)* **202** (1997) p. 35.
- [20] J.E. Northrup and J. Neugebauer, *Phys. Rev. B* **52** (1995) R17001.
- [21] J. Pollmann, P. Krüger and M. Sabisch, *Phys. stat. sol. (b)* **202** (1997) p. 421.
- [22] J.E. Northrup and J. Neugebauer, *Phys. Rev. B* **57** (1998) R4230.
- [23] A. Coati, M. Sauvage-Simkin, Y. Garreau, R. Pinchaux, T. Argunova and K. Aïd, *Phys. Rev. B* **59** (1999) p. 12224.
- [24] J. Schardt, J. Bernhardt, M. Franke, U. Starke and K. Heinz, *Mat. Sci. Forum* **264** (1998) p. 343.
- [25] J. Bernhardt, A. Seubert, M. Nerdling, U. Starke and K. Heinz, *Mat. Sci. Forum*, *this volume*, p. 345.

\* corresponding author. phone: +49-9131-8528405, fax: +49-9131-8528400 email: ustarke@fkp.physik.uni-erlangen.de



## Atomic Structure of 6H-SiC(000 $\bar{1}$ )-(2x2)<sub>c</sub>

J. Bernhardt<sup>1</sup>, A. Seubert<sup>1</sup>, M. Nerding<sup>1</sup>, U. Starke<sup>1</sup> and K. Heinz<sup>1</sup>

<sup>1</sup> Lehrstuhl für Festkörperphysik, Friedrich-Alexander Universität Erlangen-Nürnberg,  
Staudtstr. 7, DE-91058 Erlangen, Germany

**Keywords:** Adatom Structure, Hexagonal Surfaces, Low-Energy Electron Diffraction, Reconstruction, Scanning Tunneling Microscopy, Stacking Sequence, Surface Structure

**Abstract.** The atomic structure of a (2×2) reconstruction prepared on the 6H-SiC(000 $\bar{1}$ ) surface by annealing of an as-introduced or silicon-capped sample was determined. The structure is denoted (2×2)<sub>c</sub> to distinguish it from another (2×2)-periodic structure on the same surface. The reconstruction is characterized by a single silicon adatom per unit cell occupying a threefold-coordinated hollow site (H3). This result of the low-energy electron diffraction (LEED) analysis is consistent with scanning tunneling microscopy (STM) images showing one single protrusion per unit cell and a slightly silicon enriched stoichiometry with respect to bulk SiC as identified by Auger electron spectroscopy (AES). Furthermore, we found that this surface is preferably terminated by hexagonal stacking, i.e. on 60% of the surface the stacking switch characteristic for 6H-SiC is located below the first bilayer.

### Introduction

Industrial scale use of siliconcarbide for device production is still inhibited by the lack of sufficient amounts of this material in controlled high quality. Though the polytypism of SiC offers new possibilities in device design, it currently makes controlled growth rather problematic. To improve this situation, in either case an understanding of the decisive mechanisms during growth or interface formation at the atomic level is needed. This raises the question for the geometric and - intimately related - the electronic structure of the involved surfaces.

The stable phases which can be prepared on the nominally Si-terminated (0001) oriented surfaces of SiC have been extensively studied in the past (see reviews [1] and references therein). Recently, the atomic geometries of the ( $\sqrt{3}\times\sqrt{3}$ )R30° and the (3×3) phase have been determined in detail and their relevance for growth has been elucidated [2, 3]. In contrast, little is known about the (000 $\bar{1}$ ) oriented surfaces. For a better understanding of the different growth behaviour of this crystal orientation we investigated the atomic structure of stable surface phases on 4H- and 6H-SiC(000 $\bar{1}$ ) using quantitative low-energy electron diffraction (LEED), Auger electron spectroscopy (AES) and scanning tunneling microscopy (STM).

### Experimental

The results presented here were obtained using several samples cut from the same 6H-SiC(000 $\bar{1}$ ) wafer. 4H-SiC(000 $\bar{1}$ ) samples yielded similar spectra, so no separate LEED analysis needed to be carried out. In a first step, the samples (n-type doped, obtained from CREE research) were chemically cleaned and dry oxidized using standard procedures. After removal of the sacrificial oxide, the samples were either etched in atmospheric pressure H<sub>2</sub>-gas flow at 1500°C or treated with hydrogen plasma at 800°C and finally loaded into the ultra high vacuum analysis system. Both preparation

procedures improve the general surface morphology and cause a passivating epitaxial oxide layer to develop on an otherwise bulk truncated SiC crystal [4]. *In situ* different phases were prepared by heating and/or providing additional silicon through an evaporation source. In this way, the surface stoichiometry could be varied in a wide range corresponding to a graphitic or silicon covered surface. Details of the preparation and an overview of the structural development are given in ref. [5].

## Results and Discussion

We focus on a  $(2\times 2)$  reconstruction denoted  $(2\times 2)_C$  to distinguish it clearly from a separate, silicon enriched  $(2\times 2)$  phase [5]. The preparation of the particular  $(2\times 2)_C$ -phase proceeds via heating an as-introduced sample at  $1050^\circ\text{C}$  for at least 15 min. This produces a  $(3\times 3)$  superstructure. With subsequent heating at slightly higher temperatures, i.e.  $1075^\circ\text{C}$ , the  $(2\times 2)_C$  phase evolves in coexistence with the  $(3\times 3)$  structure (Fig. 1a). Prolonged heating at this temperature makes the  $(3\times 3)$  spots disappear and a pure  $(2\times 2)_C$  phase remains (Fig. 1b).

Applying higher temperatures, however, inhibits the formation of well ordered  $(2\times 2)_C$ -reconstructed areas. Moreover, the best  $(2\times 2)_C$  structure in terms of LEED spot brightness, sharpness and low background was achieved only in coexistence with the  $(3\times 3)$  phase (Fig. 1a). The preparation of the  $(2\times 2)_C$  structure without residual contributions from the  $(3\times 3)$  phase is a rather delicate task as found also in previous investigations [6, 7]. Therefore, it is rather difficult to evaluate the phase-specific stoichiometry from AES, as the method integrates over both phases. However, the Auger peak-to-peak height ratio determined for the  $(2\times 2)_C$  structure ( $\text{Si}/\text{C} = 1.4$ ) is practically identical to that obtained for the oxidic  $(\sqrt{3}\times\sqrt{3})\text{R}30^\circ$  (the only phase of the  $\text{SiC}(000\bar{1})$  surface whose atomic geometry is known so far [4]). The latter contains  $2/3$  of a silicon-layer in addition to an otherwise bulk truncated surface. So, bearing in mind the above mentioned uncertainty, roughly the same stoichiometry should hold for both phases.

STM images show a single protrusion per  $(2\times 2)$  unit cell in both empty (Fig. 2) and filled state images (corrugations in constant current mode are  $0.4\text{ \AA}$  and  $0.2\text{ \AA}$ , respectively). As can be seen in Fig. 2a, this protrusion appears practically undistorted even in the very surrounding of vacancy-type defects and antiphase domain boundaries (labeled A and B respectively in Fig. 2a). These findings strongly favour a simple adatom model. Assuming the protrusion to be an adatom, one can furthermore conclude from the appearance of the antiphase domain boundaries that the adatoms in both domains occupy the same adsorption site.

Under certain tunneling conditions and only for almost defect free  $(2\times 2)_C$  recon-

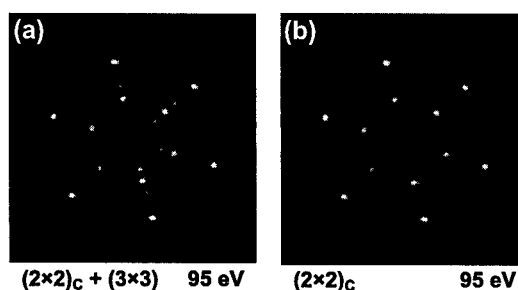


**Figure 1:** LEED-images of  $6\text{H-SiC}(000\bar{1})$  surfaces taken at 95 eV. (a) mixture of  $(3\times 3)$  and  $(2\times 2)_C$  reconstructed areas obtained after heating to  $1075^\circ\text{C}$ . (b)  $(2\times 2)_C$  structure obtained after prolonged heating at  $1075^\circ\text{C}$ .

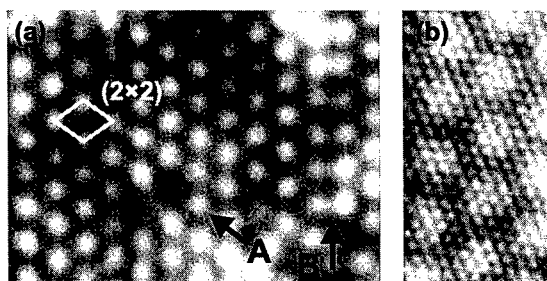


**Figure 2:** STM-images of empty states ( $V_{\text{tip}} = -2.75\text{ V}$ ) of  $6\text{H-SiC}(000\bar{1})-(2\times 2)_C$ . (a)  $67\text{ \AA} \times 49\text{ \AA}$  wide area. Missing adatom defects and antiphase domain boundaries are labeled A and B, respectively. (b)  $70\text{ \AA} \times 125\text{ \AA}$  wide section of an almost perfectly  $(2\times 2)_C$  reconstructed surface area, which displays an incommensurate, large-periodic corrugation.

structured areas the STM images show an incommensurate, large-periodic corrugation in addition to the well resolved  $(2 \times 2)_C$  structure (Fig. 2b). From Fourier analysis we derived an estimated periodicity of  $(9.1 \times 9.1)R27.5^\circ$ . An apparent corrugation of  $0.8 \text{ \AA}$  is measured, however, it is not clear whether this is a pure electron density effect or accompanied by real atomic displacements. Further STM and spectroscopic measurements are needed to reveal the origin of this phenomenon.

So far only fragments of the complete atomic structure could be revealed. The complete information can be retrieved by quantitative LEED structure analysis. Here, electron diffraction intensity versus energy spectra are computed for an assumed model of the surface and compared to their experimental counterparts. If they agree, the model represents the actual surface structure. The experimental pre-information available is crucial for making educated guesses for the structural models. The calculation of LEED intensities was performed using standard full dynamical LEED programs [8, 9]. For the fine tuning of structural parameters Tensor-LEED was applied [10, 11]. The Pendry R-factor [12] was used to quantify the agreement between experimental and theoretical spectra and to guide an automated structural search algorithm [13].

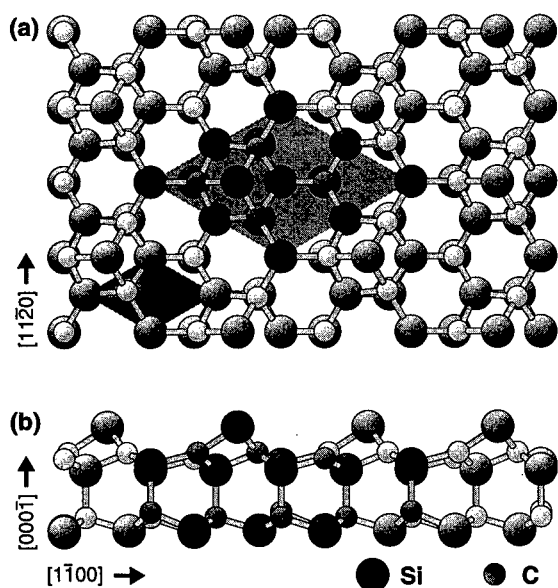


**Figure 3:** Topview (a) and sideview (b) of the  $(2 \times 2)_C$  model; large atoms represent Si, small atoms C, darker atoms belong to one  $(2 \times 2)_C$  unit cell.

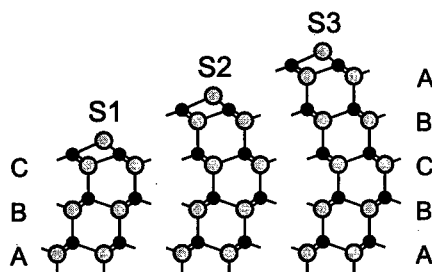


**Figure 4:** Possible stacking sequences below the  $6H\text{-SiC}(000\bar{1})$  surfaces resulting from the different possible truncations of the (six bilayers high)  $6H\text{-SiC}$  unit cell. S1..3 denote number of linearly stacked bilayers as counted from the surface to the first stacking switch.

As found by the LEED analysis, the  $(2 \times 2)_C$  reconstruction consists of a single Si adatom in a  $H_3$ -site, i.e. located above the center of the Si-C hexagons of the topmost SiC bilayer and thus threefold coordinated to the outermost carbon atoms of the substrate (Fig. 3). The presence of the adatom causes remarkable displacements of the atoms in the first two bilayers. The three first-bilayer carbon atoms supporting the silicon adatom move laterally  $0.16 \text{ \AA}$  towards the adatom (Fig. 3a). Together with the vertical distance of  $1.06 \text{ \AA}$  between the adatom and those carbon atoms, the  $\text{Si}_{\text{adatom}}\text{—C}$  bond length of  $1.94 \text{ \AA}$  is only slightly enlarged compared with the bulk value ( $1.89 \text{ \AA}$ ). The unsaturated carbon atom relaxes into the surface by  $0.22 \text{ \AA}$  (Fig. 3b). Similar displacements apply for the silicon atoms of the topmost bilayer and even deeper layers are affected. The Pendry R-factor of 0.20 is low enough to safely exclude other plausible models, which have been tested in great variety, i.e. different adatom-adsorption sites and adatom species. (Details of the analysis will be published elsewhere [14]).

The H3-adatom position determined is remarkable in view of the T4-position found to be characteristic for SiC(0001) adstructures theoretically as well as experimentally, i.e. for the  $(\sqrt{3} \times \sqrt{3})R30^\circ$  and  $(3 \times 3)$  reconstructions. Yet, even more remarkable is the bilayer stacking found below the surface. As low-energy electrons penetrate some atomic layers into the crystal, also the stacking sequence below the surface is probed by LEED. The unit cell of 6H-SiC contains six bilayers with slabs of three equally oriented, i.e. linearly stacked bilayers rotated against each other by  $180^\circ$ . So, three possible stacking sequences below the surface are possible: Three, two or one bilayer of one orientation on top of the next three bilayers of the other orientation (we denote these possible surface truncations S3..1, see Fig. 4). The 6H-SiC(0001) surfaces are usually dominated by S3-type domains [15], which can be even enforced by preparation methods using Si-rich ambient [2]. This is in contrast to the results obtained for the  $(2 \times 2)_C$ -structure on 6H-SiC(0001). While the as-introduced sample exhibits an equal distribution of S1, S2 and S3 domains, the  $(2 \times 2)_C$  structure is dominated by about 60% S1 stacking and S2+S3 together make up only 40% of the surface. In other words, this structure is characterized by hexagonal - or hcp-type - stacking at the very surface (cf. Fig. 3), while on SiC(0001) linear stacking seems to be favoured. Together with the different adatom position, these findings may be a first clue to explain the significantly different growth modes observed on the two orientations.

This work was supported by Deutsche Forschungsgemeinschaft (DFG) through SFB 292.

## References

- [1] J. Pollmann, P. Krüger, and M. Sabisch, Phys. Stat. Sol. (b) **202** (1997), p. 421;  
U. Starke, Phys. Stat. Sol. (b) **202** (1997), p. 475; P. Mårtensson, F. Owman, and L. I. Johansson, Phys. Stat. Sol. (b) **202** (1997), p. 501.
- [2] U. Starke, J. Schardt, J. Bernhardt, M. Franke, and K. Heinz, Phys. Rev. Lett. **82** (1999), p. 2107.
- [3] U. Starke, J. Schardt, J. Bernhardt, M. Franke, K. Reuter, H. Wedler, K. Heinz, J. Furthmüller, P. Käckell and F. Bechstedt, Phys. Rev. Lett. **80** (1998), p. 758.
- [4] J. Bernhardt, J. Schardt, U. Starke, and K. Heinz, Appl. Phys. Lett. **74** (1999), p. 1084.
- [5] J. Bernhardt, M. Nerding, U. Starke, and K. Heinz, Mat. Sci. Eng. **B61-62** (1999), p. 206.
- [6] A. J. van Bommel, J. E. Crombeen and A. van Tooren, Surf. Sci. **48** (1975), p. 463.
- [7] S. Nakanishi, H. Tokutaka, K. Nashimori, S. Kishida and N. Ishihara, Appl. Surf. Sci. **41/42** (1989), p. 44.
- [8] M. A. van Hove, S. Y. Tong, Surface Crystallography by LEED, Springer, Berlin, Heidelberg, 1986.
- [9] J. B. Pendry, Low-Energy Electron Diffraction, Academic Press, London, 1974.
- [10] P. J. Rous, J. B. Pendry, D. K. Saldin, K. Heinz, K. Müller and N. Bickel, Phys. Rev. Lett. **57** (1986), p. 2951.
- [11] K. Heinz, M. Kottcke, U. Löffler and R. Döll, Surf. Sci. **357-358** (1996), p. 1.
- [12] J. B. Pendry, J. Phys. C **13** (1980), p. 937.
- [13] M. Kottcke and K. Heinz, Surf. Sci. **376** (1997), p. 352.
- [14] A. Seubert, J. Bernhardt, M. Nerding, U. Starke, and K. Heinz, *to be published*.
- [15] J. Schardt, J. Bernhardt, M. Franke, U. Starke, and K. Heinz, Mat. Sci. Forum **264** (1998), p. 343.

\* corresponding author. phone: +49 91 31 - 852 84 05, fax: +49 91 31 - 852 84 00  
email: jbernhardt@fkp.physik.uni-erlangen.de

## Ab Initio Calculation on Clean and Oxygen Covered 6H-SiC(0001) Surfaces: ( $\sqrt{3} \times \sqrt{3}$ )R30° Reconstruction

Wenchang Lu, Peter Krüger and Johannes Pollmann

Institut für Theoretische Physik II-Festkörperphysik, Universität Münster,  
Wilhelm-Klemm-Strasse 10, DE-48149 Münster, Germany

**Keywords:** (0001) Surface, Local Spin Density Approximation, Oxygen

**Abstract** Clean and oxygen covered 6H-SiC(0001) surfaces with a ( $\sqrt{3} \times \sqrt{3}$ )R30° reconstruction are investigated using the local spin-density approximation (LSDA) of density-functional theory. For the Si(T<sub>4</sub>) model of the clean surface, the ground state is found to be anti-ferromagnetic whereby a dangling bond derived band splits into a fully occupied and an empty band separated by a gap of 0.7 eV. The widths of the occupied and empty surface-state bands are in good agreement with photoemission and inverse photoemission experiments. For the oxygen covered (0001) surface, our calculations confirm a structural model suggested on the basis of a recent LEED analysis. Within the LSDA a semiconducting surface with a band gap of 1.0 eV is obtained for this system.

**Introduction:** The 6H-SiC(0001) surface shows a number of reconstructions depending sensitively on sample-preparation techniques. Here we concentrate on clean and oxygen covered Si-terminated surfaces with a ( $\sqrt{3} \times \sqrt{3}$ )R30° reconstruction. For the clean SiC(0001) surface, Owman and Martensson[1] observed a well-ordered ( $\sqrt{3} \times \sqrt{3}$ ) array of protrusions in their scanning tunneling microscopy (STM) experiments. A structural model composed of 1/3 monolayer of Si or C adatoms in threefold-symmetric sites was suggested. Angle-resolved photoemission spectroscopy (ARPES)[2] and *k*-resolved inverse photoemission spectroscopy (KRIPES)[3] found that the surface is semiconducting with a band gap of 2.0 eV. The widths of the occupied and of the empty surface-state bands are 0.2 and 0.35 eV, respectively. *Ab initio* calculations[4, 5] showed that a structure with Si adatoms in T<sub>4</sub> positions is the most stable. Within the framework of the local density approximation (LDA) these calculations predict the existence of a half-filled dangling-bond derived band in the fundamental bulk gap. The metallic character of the surface, as resulting from these calculations, is in marked contrast to the experimental observations. In order to resolve this conflict, Northrup and Neugebauer[6] have employed a Hubbard model [7] describing a metal-insulator transition resulting in a splitting of the dangling-bond band into an occupied lower and an empty upper Hubbard band. The surface band gap is determined by the intra-atomic Coulomb interaction *U* which is obtained from LDA calculations for various charged states of the dangling bonds. The resulting values for *U* of 1.6 eV [6] and of 2.1 eV [8] are in reasonable agreement with experimental results. The lower and upper Hubbard bands have the same dispersion with their band width being half of the one obtained in the one-particle picture. The measured widths of the occupied and the empty dangling-bond band, on the contrary, differ by 0.15 eV which is beyond the experimental uncertainty. For the oxygen covered (0001) surface, Starke et al.[9] have suggested on the basis of their LEED data a structural model with Si-O-Si honeycomb rings on the surface. Similar to the adatom induced Si(T<sub>4</sub>) model for the clean surface, this surface also has one dangling bond per unit cell. Therefore, similar electronic properties can be expected. In this contribution we will show that the semiconducting behavior of the clean and oxygen covered SiC(0001) surface can also be rationalized within the LSDA framework without invoking a Hubbard model.

**Calculational method:** Our calculations are carried out within LSDA of density functional theory [10]. Nonlocal, norm-conserving pseudopotentials in separable form, and the exchange and correlation functional of Ceperley and Alder, as parametrized by Perdew and Zunger[11], are employed. The wave function is expanded as a linear combination of Gaussian orbitals (see Ref.[12] for details). A supercell including eight layers of SiC and eight vacuum layers is used to describe the surface system. The dangling bonds on the bottom-layer of the slab are saturated by hydrogen atoms in order to avoid artificial surface states in the gap. Six  $k_{||}$  points in the irreducible part of the surface Brillouin zone turn out to be sufficient for the  $(\sqrt{3} \times \sqrt{3})$  unit cell in order to get converged results. To get the optimal geometric structure, the atoms in the first three surface layers and those in the adlayer are relaxed by eliminating the forces up to  $10^{-3}$  Ry/au.

**Clean (0001) surface:** Here we only consider the Si( $T_4$ ) model, since it was confirmed to be the most stable one[4, 5]. We have carried out a non-spin-polarized (NSP) LDA calculation and LSDA calculations initialized by ferromagnetic (FM) or anti-ferromagnetic (AFM) configurations of the spins at the surface. A section of the resulting band structures is given in Fig. 1. In the LDA-NSP calculation, the dangling-bond band  $D$  is half-filled and has a dispersion of 0.4 eV. In the FM case, the dangling-bond band splits into two bands with roughly the same dispersion as that of the LDA  $D$  band. The total energy of this configuration is 0.03 eV lower than that of the non-spin-polarized one. The spin-up state  $D\uparrow$  is fully occupied and the spin-down state  $D\downarrow$  is empty. The splitting of 0.5 eV between these two bands results in a semimetallic surface with a zero band gap. Comparing with experimental results, the band width of  $D\downarrow$  is in agreement with the KIRPES data but the band width of  $D\uparrow$  is larger than the one resulting from ARPES measurements. The calculated band splitting of 0.5 eV is also much smaller than the experimental value of about 2 eV.

Now we address the AFM case. For the two dimensional triangular lattice there are a lot of conceivable AFM arrangements. Here we consider one simple example. All the electrons in a line along the  $[2\bar{1}10]$  direction occupy the same spin orbit and those in a line along the  $[\bar{1}2\bar{1}0]$  or  $[\bar{1}\bar{1}20]$  direction occupy the spin-up or spin-down orbits alternatively. Each site has two neighboring sites with the same spin and four neighboring sites with the opposite spin. The total energy of this configuration is lower than in the case of the NSP configuration by 0.04 eV per  $(\sqrt{3} \times \sqrt{3})$  unit cell and is also lower than in the case of the FM configuration by 0.01 eV. Although the total energy difference is very small, the band structure changes significantly. The band width of the occupied state  $D1$  is 0.2 eV and that of the empty state  $D2$  is 0.3 eV. These

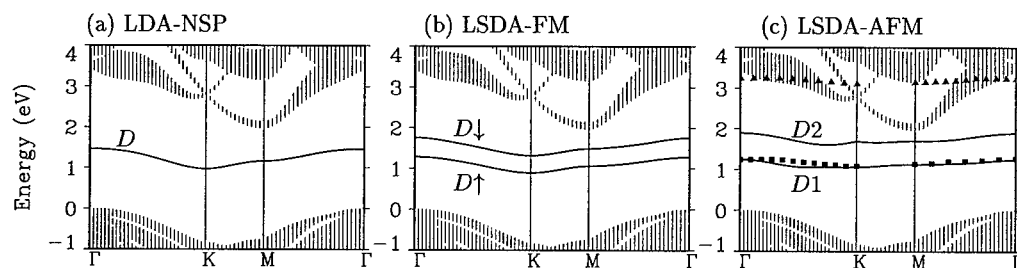


Figure 1: Band structures of the  $(\sqrt{3} \times \sqrt{3})R30^\circ$  reconstruction for Si( $T_4$ ) models with different spin polarization. The solid squares and triangles are from photoemission [2] and inverse photoemission [3] spectroscopy, respectively. For the AFM case, the calculation has been carried out using a doubled unit cell. For comparison, the resulting band structure has been plotted along the same  $k$ -vector as in the NSP and FM cases.

two values are in good agreement with experimental results from ARPES[2] and KIRPES[3]. The band splitting of 0.7 eV is larger than that in the FM configuration but it is still much smaller than the experimental one. Due to the very small total energy difference between the FM and AFM configurations, the spin may arrange in a disordered way and the real surface will show a paramagnetic phase.

Furthermore, we have also calculated the Coulomb interaction  $U$  by using the same method as Northrup and Neugebauer[6]. Our value of 1.8 eV is comparable with the other theoretical estimates [6, 8]. As a result, the Mott-Hubbard model gives the value for the band-splitting in better agreement with experiment than the LSDA calculation which suffers from the band-gap problem. However, when emphasizing this point one has to keep in mind that the uncertainty of the calculated Hubbard  $U$  is very large [6]. Furthermore, the anti-ferromagnetic ground state for this surface as resulting from the LSDA calculation gives the band widths for both occupied and empty surface states in very good agreement with experiment.

**Oxygen covered surface:** Adsorption of oxygen on Si-terminated SiC(0001) leads to a  $(\sqrt{3} \times \sqrt{3})$  reconstructed surface. By fitting their LEED data, Starke et al. [9] have suggested a structural model where Si-O-Si honeycomb rings in the top layer are bound by linear Si-O-Si bridges to the substrate. A top view and a side view of this structure are given in Fig. 2. Our optimized structure parameters are in excellent agreement with the experimental values[9]. In the top bilayer, i.e., the Si-O-Si honeycomb ring, the interlayer distance  $d_1$  is 0.52 Å. The resulting Si-O bond length of 1.62 Å is approximately equal to the sum of the Si and C covalent radii. The Si-O-Si angle of  $142^\circ$  is very close to that in  $\alpha$ -quartz. In the linear Si-O-Si bridge, the Si-O distances  $d_2$  and  $d_3$  are 1.60 Å and 1.62 Å, respectively. The interlayer distance (0.59 Å) is compressed by 6% in the substrate-surface bilayer. In the center of the honeycomb ring, there is one substrate-surface Si atom with an unsaturated dangling bond.

Furthermore, we have considered another model in which the Si-O-Si ring is bound to the substrate-surface atoms directly. However, the calculation of the formation energy shows that this model is less stable than the previous one. These findings are consistent with the LEED results[9].

The band structures calculated within LDA, LSDA, and the Mott-Hubbard model are shown in Fig. 3 together with the projected band structure of bulk-6H-SiC(0001). In the LDA calculation, a very flat band derived from the dangling bonds of the substrate-surface Si atoms at the center of the Si-O-Si honeycomb ring is located at 1.2 eV above the valence band maximum. Similar to the clean surface, this band is half-filled. Its band width of 0.16 eV is smaller than the one of 0.4 eV at the clean surface. Although the distance between neighboring dangling bonds is the same for both systems, the interaction between them is weaker at the oxygen covered surface. This may be related to a screening effect of the adlayer. In the case of the FM configuration the total energy is 0.15 eV per unit cell lower than in the case of the NSP configuration. Because of the

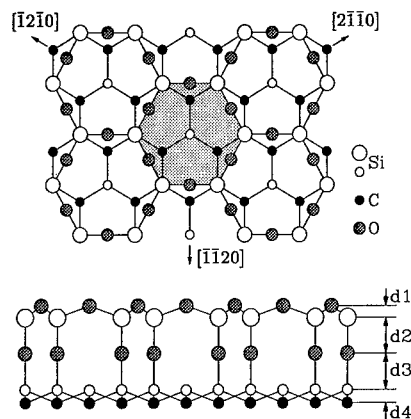


Figure 2: Schematic views of oxygen adsorption on Si-terminated 6H-SiC(0001) surface. The top panel shows the top view and the bottom panel the side view. The normal distances between atomic layers are labelled  $d_1$ ,  $d_2$ ,  $d_3$  and  $d_4$ . The shaded area in the top view is a  $(\sqrt{3} \times \sqrt{3})$  Wigner-Seitz cell.

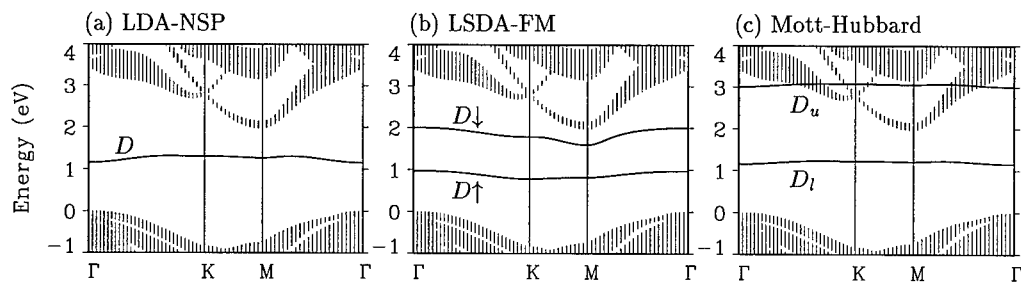


Figure 3: Band structures of oxygen covered (0001)  $(\sqrt{3} \times \sqrt{3})R30^\circ$  surface. See Fig. 2 for the atomic structure. The hatched area is the LDA calculated projected band structure of bulk 6H-SiC crystal.

very weak interaction and the respective small dispersion, there is no overlap between spin-up  $D\uparrow$  and spin-down  $D\downarrow$  bands. The spin-up band  $D\uparrow$  is fully occupied and the spin-down band  $D\downarrow$  is empty. The splitting at the  $\Gamma$  point is 1.1 eV and the surface shows a semiconducting character. A calculation for the AFM configuration (as discussed for the clean surface) shows that the total energy difference between both configurations is less than 2 meV per  $(\sqrt{3} \times \sqrt{3})$  unit cell. Moreover, the corresponding band structures are very similar with the same values of band splitting. This indicates that the spin may arrange in a disordered way and the surface will show a paramagnetic phase. The calculated Coulomb interaction  $U$  for this surface is 1.8 eV which happens to coincide with the respective value at the clean surface. Our results for the Hubbard model show that both systems have the same surface band gap. However, on the basis of our LSDA results the oxygen covered surface is expected to have a larger surface band gap than the clean surface.

**Summary:** Clean and oxygen covered 6H-SiC(0001) surfaces are studied by LSDA calculations and by employing a Mott-Hubbard model. Both methods show that the surfaces are semiconducting in agreement with experiment. For the clean surface, the width of the unoccupied surface-state band resulting from LSDA is in better agreement with experiment than that resulting from the Mott-Hubbard model.

It is our great pleasure to thank U. Starke for fruitful discussions. We acknowledge financial support of this work by the Deutsche Forschungsgemeinschaft (Bonn, Germany) under contract No. Po 215/13-1 and a grant of Cray computer time at the John von Neumann-Institute for Computing (NIC) of the Forschungszentrum Jülich (Germany) under contract No. K2710000.

- [1] F. Owman and P. Martensson, *Surf. Sci.* **330** (1995), p. L639.
- [2] L. I. Johanson, F. Owman, and P. Martensson, *Surf. Sci.* **360**(1996), p. L478.
- [3] J.-M. Themlin, *et al.*, *Europhys. Lett.* **39** (1997), p. 61.
- [4] J. E. Northrup and J. Neugebauer, *Phys. Rev. B* **52** (1995), p. R17001.
- [5] M. Sabisch, P. Krüger, and J. Pollmann, *Phys. Rev. B* **55** (1997), p. 10561.
- [6] J. E. Northrup and J. Neugebauer, *Phys. Rev. B* **57** (1998), p. R4230.
- [7] J. Hubbard, *Proc. R. Soc. London, Ser. A* **281** (1964), p. 401.
- [8] J. Furthmüller, *et al.*, *Phys. Rev. B* **58** (1998), p. 13712.
- [9] J. Bernhard, J. Schardt, U. Starke and K. Heinz, *Appl. Phys. Lett.*, **74** (1999), p. 1084.
- [10] W. Kohn and L. J. Sham, *Phys. Rev.* **140** (1965), p. A1133.
- [11] J. P. Perdew and A. Zunger, *Phys. Rev. B* **23** (1981), p. 5048.
- [12] W. Lu, P. Krüger, and J. Pollmann, *Phys. Rev. B* **60**(1999), p. 2495.



## Photo-Emission Electron Microscopy (PEEM) of Cleaned and Etched 6H-SiC(0001)

J.D. Hartman<sup>1</sup>, K. Naniwae<sup>2</sup>, C. Petrich<sup>2</sup>, V. Ramachandran<sup>3</sup>, R.M. Feenstra<sup>3</sup>,  
R.J. Nemanich<sup>2</sup> and R.F. Davis<sup>1</sup>

<sup>1</sup> Department of Materials Science and Engineering, North Carolina State University,  
Raleigh, NC 27695, USA

<sup>2</sup> Department of Physics, North Carolina State University, Raleigh, NC 27695, USA

<sup>3</sup> Department of Physics, Carnegie Mellon University, Pittsburgh, PA 15213, USA

**Keywords:** Free Electron Laser, Hydrogen Etching, PEEM, Photo Emission Electron Microscopy, Silicon Carbide, Surface Preparation, Surface Reconstruction

### Abstract

The surface structures of both cleaned and etched 6H-SiC(0001)<sub>Si</sub> wafers have been investigated using the photo emission electron microscope (PEEM). In the first study, the SiC wafers were exposed to two different cleaning processes to obtain a  $(\sqrt{3} \times \sqrt{3})R30^\circ$  and a  $3 \times 3$  reconstructed surface. The PEEM images were obtained with a mercury arc lamp as the photon source and revealed that the clean reconstructed surfaces were non-uniform. In the second study, characterization of a hydrogen etched surface using the PEEM with the Duke University free electron laser (DFEL) as the photon source revealed a high density of dislocations and a stepped surface structure.

### Introduction

The surface preparation of SiC plays an important role in terms of the density of defects generated in epitaxially grown films[1] and the electrical characteristics of subsequently fabricated devices[2]. Recent reflective high energy[3] and low energy electron diffraction[4-8], scanning tunneling [7-11] and atomic force[11-13] microscopies, low energy electron microscopy [14], electron energy loss spectroscopy[6,8], and Auger electron[5-8] and x-ray photoelectron[5] spectroscopy studies have provided critical microstructural, structural, and chemical information regarding the efficacy of different chemical process routes for the preparation of these surfaces. Two generic preparations that have generated considerable interest are surface cleaning and hydrogen etching. The reconstructed surfaces of 6H-SiC(0001)<sub>Si</sub> using a Si flux and annealing may have an atomic structure of either  $3 \times 3$ ,  $(\sqrt{3} \times \sqrt{3})R30^\circ$ ,  $(6\sqrt{3} \times 6\sqrt{3})R30^\circ$  or  $1 \times 1$  [5-7]. Hydrogen etching of 6H-SiC(0001)<sub>Si</sub> surfaces removes the polishing scratches and replaces them with atomic steps that have a unit cell height[11-13]. These single unit cell steps apparently eliminate stacking mismatch boundaries[13,15] associated with the growth of 2H-AlN and 2H-GaN. A complimentary method to characterize these surfaces is through photo emission electron microscopy using an intense and/or tunable UV source.

In the research associated with this paper, the PEEM was used to examine the silicon face, (0001)<sub>Si</sub> surfaces, of cleaned or etched 6H-SiC. In general, different surface preparations produce different atomic arrangements and structures on the surface, which affect both the photo-threshold energy and the topography, and, therefore, provide two different contrast mechanisms for imaging the surface with the PEEM. The first set of experiments exploited these differences in photo-threshold energies to achieve observations of the surfaces of 6H-SiC(0001)<sub>Si</sub> before and after cleaning. In the second set of experiments the stepped surface structures produced by hydrogen

etching on 6H-SiC(0001)<sub>Si</sub> wafers were imaged in the PEEM using the topographic differences of the steps to achieve contrast imaging. The following sections provide the experimental details as well as the results and a summary of these investigations.

### Experimental Procedure

**Ex Situ Preparation.** The samples used in the cleaning experiments consisted of 9 mm x 9 mm pieces diced from n-type 6H-SiC(0001)<sub>Si</sub> wafers obtained from Cree Research, Incorporated. Prior to processing in vacuum, the as-received samples were dipped into a 10:1 HF acid solution to remove the silicon oxide from the polished surface.

Tungsten was then deposited on the unpolished (000-1) back of each substrate to assist in radiative and electron bombardment heating (see below). After deposition, the pieces were cleaned by boiling in trichloroethylene, acetone, and methanol for 10 minutes in each solvent. The samples were then placed over a 10:1 HF buffered oxide etch to remove the remaining oxide[16]. The hydrogen etched samples were prepared at Carnegie Mellon University. A detailed description of the etching process and AFM results is given elsewhere[12]. The etched samples were boiled in trichloroethylene, acetone, and methanol for 5 minutes in each solvent. Both sets of samples were then transferred through a load lock to the Nitride Growth and Characterization System (NGCS).

**In Situ Surface Preparation and Characterization.** The NGCS consists of a gas source molecular beam epitaxy system (GSMBE), an Auger electron spectroscopy (AES) system, and a PEEM, as shown schematically in Figure 1. Detailed descriptions of the PEEM system and its operation with the Free Electron Laser Facility are given elsewhere[17]. The SiC pieces to be cleaned were transferred from the load lock chamber into the Physical Electronics #10-155 AES system for initial surface analysis, and subsequently transferred to the GSMBE for cleaning and RHEED studies. Each sample was cleaned in situ via exposure to a Si flux provided by a Thermionics 4-pocket Linear Evaporation System. The surface was monitored during this exposure using a Staib Instruments NEK-1025-R reflection high energy electron diffraction (RHEED) system. Sample heating consisted of radiative heating from a tungsten filament to approximately 400°C and electron bombardment for higher temperatures. The temperature measurements were obtained using an optical pyrometer with an emissivity setting of 0.5. The samples were then returned to the AES system for analysis of the reconstructed surface, and transferred to the PEEM for observation using a mercury arc lamp with a high energy cut-off at ≈5.1 eV. The hydrogen etched samples were transferred directly to the PEEM without in situ surface preparation. The images were obtained using the free electron laser at Duke University in spontaneous mode with a 5.95 eV photon energy.

### Results and Discussion

**Surface Cleaning of SiC.** Figure 2a, shows the PEEM image of an ex-situ prepared 6H-SiC(0001) sample in the as-loaded condition. The image shows uniform emission across the sample. To obtain a 3x3 reconstruction, the SiC substrate was annealed without a Si flux at 900 °C in the GSMBE until a (√3 x √3)R30° RHEED pattern became evident. The Si flux was then initiated, and the process was monitored using RHEED. Deposition was discontinued when a 3x3

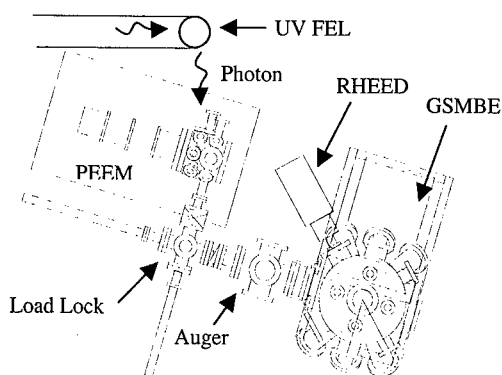


Figure 1: Schematic arrangement of the Nitride Growth and Characterization System located at the Free Electron Laser Laboratory at Duke University.

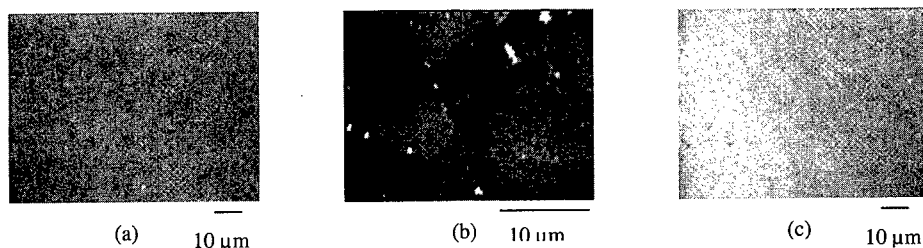


Figure 2: PEEM images of the surface of a 6H-SiC (0001) samples obtained using a mercury arc lamp. a) A 266x of an as-loaded SiC sample with a 1x1 reconstruction. b) A 800x of the same sample after a 3x3 RHEED pattern had been obtained with a superimposed spotty pattern produced by the presence of Si islands. c) A 266x of a different sample after a  $(\sqrt{3} \times \sqrt{3})R30^\circ$  RHEED pattern had been obtained.

pattern was obtained. A spotty pattern also appeared concurrently superimposed on the 3x3 pattern and was attributed to excess Si islands on the surface [10]. The 3x3 pattern remained upon cooling. A calculated Si/C peak-to-peak ratio of 4.33 was obtained from the Auger spectrum, which is close to the value of 5.16 reported by Starke et al.[7] for the 3x3 reconstruction on 4H-SiC(0001). The difference in values is likely due to the incomplete coverage by the Si, as observed in the PEEM image in Figure 2b. The bright areas indicate either a 1x1 or  $(\sqrt{3} \times \sqrt{3})R30^\circ$  reconstruction both of which have an estimated threshold values of 5.06 eV [18]. The dark areas, which were not excited by the photons, indicate a 3 x 3 reconstruction, which has an estimated threshold energy of 6.1 eV [18]. The Auger spectrum did not indicate the presence of oxygen on the surface above the concentration limit of this system.

A strong  $(\sqrt{3} \times \sqrt{3})R30^\circ$  RHEED pattern was obtained by depositing Si on the surface of the 6H-SiC(0001) at room temperature followed by annealing at 950 °C for 5 minutes. This procedure did not produce the Si islands as seen in the 3 x 3 sample. The Auger spectrum showed a Si/C ratio of 1.0 and the presence of a small concentration of oxygen. This ratio is in disagreement with the 2.21 value reported by Starke et al.[7] for the  $(\sqrt{3} \times \sqrt{3})R30^\circ$  4H-SiC(0001). The cause for the discrepancy may be attributed to the different processing techniques. Figure 2c shows the PEEM image of a  $(\sqrt{3} \times \sqrt{3})R30^\circ$  reconstructed area indicating a uniform emission. The  $(\sqrt{3} \times \sqrt{3}) R30^\circ$  reconstruction has an estimated threshold energy of 5.06 eV [18], which appears bright in the PEEM images.

**Hydrogen Etching.** The PEEM images from a hydrogen etched sample are shown in Figure 3. In Figure 3a, the surface shows a stepped structure, with several dislocations intersecting the

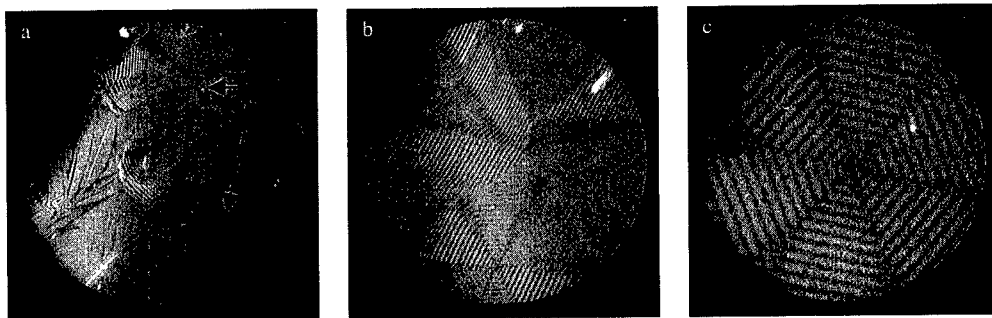


Figure 3: PEEM images of an etched, on-axis 6H-SiC (0001) wafer using spontaneous emission of the FEL at 5.95 eV as the excitation source. a) 150 μm F.O.V. b) 50 μm F.O.V. c) 20 μm F.O.V. of a screw dislocation intersecting the surface.

surface in the region, labeled A. Figure 3b shows a magnified view of the stepped structure at a 50  $\mu\text{m}$  field of view. Finally, Figure 3c, shows a 20  $\mu\text{m}$  field of view image of a screw dislocation intersecting the surface. The step height, determined by AFM, is 15 Å, which is the length of the 6H-SiC unit cell along the [0001] axis [12].

### Summary

In situ RHEED monitoring of 6H-SiC(0001) surfaces during in-situ cleaning via the exposure to evaporated Si does not give a complete picture of the surface structure. A complementary and unique technique to RHEED is the use of a PEEM with an intense UV light source to study the efficacy of different surface preparations of 6H-SiC(0001)<sub>Si</sub> substrates through the different threshold energies. The RHEED patterns obtained in this study showed a spotty 3x3, which was attributed to excess Si, and a clear ( $\sqrt{3} \times \sqrt{3}$ )R30° patterns. The PEEM images with the mercury arc lamp in this study revealed a non-uniform surface structure that was attributed to different or incomplete reconstructed regions. The PEEM images of the hydrogen etched 6H-SiC(0001) surface showed a stepped structure with each step having the height of one unit cell (15Å). The intersections of dislocations with the surface were observed by the etched patterns around them.

### Acknowledgments

This research was supported by the Office of Naval Research. Robert Davis was supported in part through the Kobe Steel, Ltd. Professorship. We gratefully acknowledge the Duke Free Electron Laser Laboratory.

### Reference:

- [1] P. Ruterana, Philippe Vermaut, G. Nouet, A. Salvador, and H. Morkoç, MRS Internet Journal of Nitride Semiconductor Research, 2 (1997), Article 42.
- [2] D. Alok, R. Egloff, and E. Arnold, Materials Science Forum, Vols. 264-268(1998), p.929-32
- [3] M. Kitabatake, Materials Science Forum, Vols. 264-268 (1998), p. 327-330.
- [4] J. Schardt, Ch. Bram, S. Müller, U. Starke, K. Heinz, and K. Müller, Surface Science, 337 (1995), p. 232.
- [5] V. van Elsbergen, T.U. Kampen, and W. Mönch, Surface Science, 365 (1996), p. 443-452.
- [6] R. Kaplan, Amorphous and Crystalline Silicon Carbide, Springer Proceedings In Physics, 34(1989), p. 100-106.
- [7] U. Starke, J. Schardt, M. Franke, Appl. Phys. A., 65 (1997), p. 587-596.
- [8] T. Tsukamoto, M.Hirai, M.Kusaka, M. Iwami, T.Ozawa, T. Nagamura, and T.Nakata. Surface Science, 371 (1997), p. 316-320.
- [9] L. Li and I.S.T. Tsong, Surface Science, 351(1996), p. 141-148.
- [10] M.A. Kulakov, G.Henn, and B. Bullemer, Surface Science, 346 (1996), p. 49-54.
- [11] Fredrik Owman, C. Hallin, Per Mårtensson, E. Janzén, Journal of Crystal Growth, 167(1996), p. 391-395.
- [12] V. Ramachandran, M.F. Brady, A.R. Smith, R.M. Feenstra, and D.W. Greve, Journal of Electronic Materials, 27 (1998), p. 308-312.
- [13] V.M. Torres, J.L. Edwards, B.J. Wilkens, David J. Smith, T.B. Doak, and I.S.T. Tsong, Appl. Phys. Lett, 74 (1999), p. 985-7.
- [14] A. Pavlovska, E. Bauer, V. M. Torres, J. L. Edwards, R. B. Doak, I. S.T. Tsong, V. Ramachandran, and R. M. Feenstra, J. Cryst. Growth, 189/190(1998), p. 310.
- [15] B.N. Sverdlov, G.A. Martin, H. Morkoç, and David J. Smith, Appl. Phys. Lett., 67 (1995), p. 2063-2065.
- [16] S. W. King, R. J. Nemanich, and R. F. Davis, Journal of Electrochemical Soc., 146 (1999), p. 2648-2651
- [17] H. Ade, W. Yang, S.L. English, J.Hartman, R.F. Davis, R.J. Nemanich, V.N. Litvinenko, I.V. Pinayev, Y.Wu, and J.M.J. Madey, Surface Review and Letters, 5 (1998), p 1257.
- [18] M.C. Benjamin, Ph.D. Dissertation, NCSU, 1996, p 31.

## High Resolution Electron Energy Loss Spectroscopy of $\sqrt{3} \times \sqrt{3}$ 6H-SiC(0001)

Kunimasa Takahashi, Masao Uchida and Makoto Kitabatake

Advanced Technology Research Laboratories, Matsushita Electric Industrial Co. Ltd.,  
Hikaridai 3-4, Seika-cho, Kyoto, 619-0237, Japan

**Keywords:** ( $\sqrt{3} \times \sqrt{3}$ )R30° Reconstructed 6H-SiC(0001) Si-Face, High Resolution Electron Energy-Loss Spectroscopy, Surface Reconstruction

**Abstract:** The surface structure of the reconstructed 6H-SiC(0001) Si-faces were investigated by using high resolution electron energy loss spectroscopy (HREELS). The 6H-SiC(0001) Si-faces exhibited the stable ( $\sqrt{3} \times \sqrt{3}$ )R30° reconstruction when it was annealed in a Si flux at temperatures greater than 900°C. The HREELS results verified that the adatom of the most stable  $\sqrt{3} \times \sqrt{3}$  6H-SiC(0001) surface is the Si atom with only one dangling bond. Therefore, the  $\sqrt{3} \times \sqrt{3}$  reconstruction stabilizes the 6H-SiC(0001)Si surface by compensating the dangling bonds of top-surface Si atoms with additional 1/3 monolayer Si atoms.

### 1. Introduction

Analysis of the atomic structures of the surface reconstruction on SiC appears to be the key to understand the kinetics of homoepitaxial growth of SiC. It has been reported that the 6H-SiC(0001) Si-face surface exhibited ( $\sqrt{3} \times \sqrt{3}$ )R30° reconstruction when it was annealed in a Si flux at temperatures greater than 900°C.[1] The reconstructed surfaces have been investigated extensively by scanning tunneling microscopy (STM).[2] It was reported that the  $\sqrt{3} \times \sqrt{3}$  reconstruction was formed by 1/3 monolayer (ML) adatoms on the Si-face of 6H-SiC(0001). From STM data alone, however, it was not possible to identify which element, Si or C, constitutes the adatoms. As a result of these studies, considerable knowledge about reconstruction patterns on 6H-SiC(0001) was accrued;[2,3] nevertheless the atomic structure of the reconstruction could not yet be resolved. In this study, we have investigated the most stable  $\sqrt{3} \times \sqrt{3}$  reconstructed 6H-SiC(0001) Si-faces, annealed in hydrogen atmosphere, by using high resolution electron energy loss spectroscopy (HREELS).

### 2. Experimental

A commercially available n-type (nitrogen doping,  $n=1.3 \times 10^{18} \text{ cm}^{-3}$ ) 6H-SiC(0001) on-axis Si-face wafer was used in this experiment. The wafer was degreased and cleaned ultrasonically in ethanol and acetone, both for about 15 min. Wet oxidation of SiC surface was done in a quartz tube at 1100°C for 3 hours to form an SiO<sub>2</sub> layer with

a thickness of about 400 Å. Samples sized 7 mm × 7 mm were cut from the wafer. Following the ultrasonic cleaning in ethanol and acetone, the oxidized layer on the sample was etched by the buffered hydrofluoric acid solution (HF:NH<sub>4</sub>F=1:7 (volume ratio); pH~5) for approximately 15 min. at room temperature. The defective layer near the surface was oxidized and removed by this preparation. The cleaned sample surface was introduced into a separately-pumped load-locked chamber and transported into a molecular beam epitaxy (MBE) chamber with a background pressure in the 10<sup>-10</sup> Torr range. The MBE chamber was equipped with an effusion cell for Si source and a reflective high energy electron diffraction (RHEED) system. The surface of the sample was monitored *in situ* by the RHEED system in the MBE chamber. The temperature of sample was measured and controlled using an optical pyrometer.

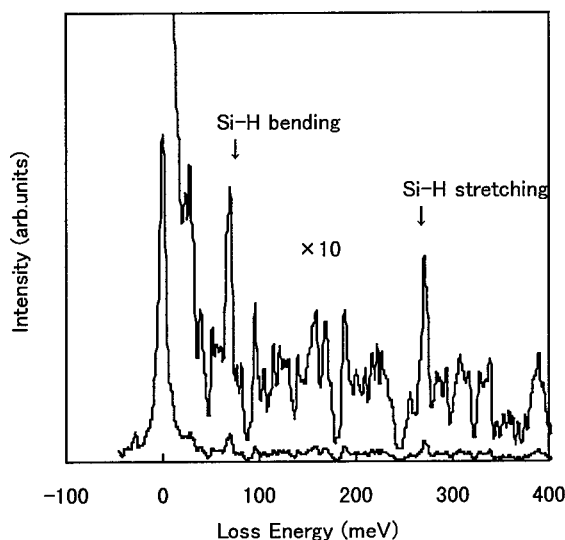
The HREELS spectrometer used in this experiment was contained in an analysis chamber isolated by means of a gate valve from the MBE chamber. The analysis chamber was evacuated using both a diffusion pump and a liquid-nitrogen-cooled titanium sublimator to provide a base pressure of 10<sup>-10</sup> Torr. In the HREELS experiments, we measured the electron energy losses of the specularly reflected electron beam at room temperature. The angle of incidence of primary electrons was 85° with respect to the surface normal. The incident energy of the primary electrons was about 5 eV. The instrumental energy resolution, as characterized by the full width at half maximum (FWHM) of the elastic peak, was about 10 meV.

### 3. Results and Discussion

We observed a 1 × 1 reflective high energy electron diffraction (RHEED) pattern on the cleaned sample surface at room temperature directly after introduction into the MBE chamber. The sample was resistively heated to 600°C for 5 min. in the MBE chamber to evaporate water and organic impurities from the surface of the sample. The bright  $\sqrt{3} \times \sqrt{3}$  RHEED pattern was observed after heating up to >800°C in vacuum. Then the Si flux from the effusion cell was directed to the substrate at 1000°C to supply Si adatoms below 1 ML. The  $\sqrt{3} \times \sqrt{3}$  RHEED pattern became clearer and sharper, and the most stable  $\sqrt{3} \times \sqrt{3}$  reconstruction was formed. Small amount of Si flux helped to stabilize the  $\sqrt{3} \times \sqrt{3}$  reconstructed surface.

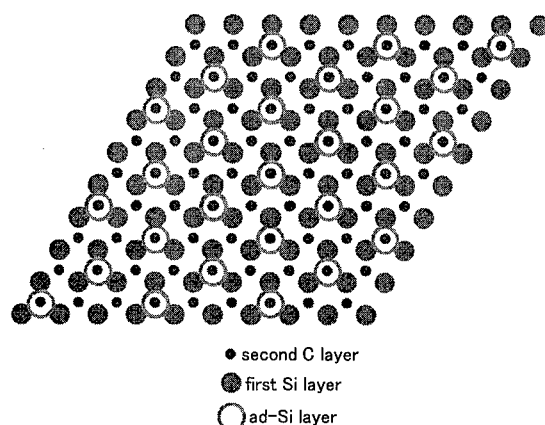
The temperature of the sample was immediately decreased to 600°C to prevent the surface degradation by the reevaporation of Si atoms. Then hydrogen gas was introduced into the MBE chamber through a variable-leak valve, up to a pressure of 1 × 10<sup>-6</sup> Torr. The sample was annealed in a hydrogen atmosphere at 600°C for 45 min. The total hydrogen exposure was 2700 Langmuir (10<sup>-6</sup> Torr sec.) during this period. After hydrogen annealing, the sample was transferred immediately from the MBE chamber to the analysis chamber without exposing to the air to characterize the surface structure using HREELS.

Figure 1 shows HREELS spectrum of the 6H-SiC(0001)Si  $\sqrt{3} \times \sqrt{3}$  reconstructed surface after hydrogen annealing. It exhibits two pronounced energy loss peaks at around 260 and 80 meV. The two modes are considered to be due to the Si-H stretching and bending modes at 260 and 80 meV, respectively. They were assigned in a straightforward way by comparison with HREELS results on the Si(001)  $2 \times 1$  monohydride surface.[4] The FWHM of the two peaks are the same as that of the elastically reflected electrons. There are no signals that indicate that the surface exhibits a dihydride structure. Furthermore, there is no indication of any C-H vibrational mode in the HREELS spectra of this reconstructed surface. Consequently, we concluded that there is only one kind of adsorption site for a hydrogen atom to compensate one dangling bond of the Si atom on  $\sqrt{3} \times \sqrt{3}$  reconstructed 6H-SiC(0001) surfaces in the monohydride phase.



**Fig. 1.** HREELS spectrum of hydrogen adsorption on the 6H-SiC(0001)Si  $\sqrt{3} \times \sqrt{3}$  reconstructed surface after hydrogen annealing

The HREELS results offer convincing proof that the adatom of the most stable  $\sqrt{3} \times \sqrt{3}$  6H-SiC(0001) surface reconstructed under Si flux is the Si atom with only one dangling bond. Therefore it elucidated that the additional  $1/3$  ML Si atoms stabilize the  $\sqrt{3} \times \sqrt{3}$  reconstructed 6H-SiC(0001) Si-face surface by compensating three dangling bonds of top-surface Si atoms. A possible model of the atomic configuration of the  $\sqrt{3} \times \sqrt{3}$  reconstructed 6H-SiC(0001) Si-face surface with Si adatoms in  $T_4$  site is illustrated in Fig. 2.



**Fig. 2.** Possible model of the atomic configuration of the  $\sqrt{3} \times \sqrt{3}$  reconstructed 6H-SiC(0001) surface with Si adatoms in  $T_4$  sites

#### 4. Conclusion

The adsorption of atomic hydrogen at  $(\sqrt{3} \times \sqrt{3})R30^\circ$  reconstructed 6H-SiC(0001) Si-face surface after annealing in hydrogen atmosphere was investigated by HREELS. The experimental data of HREELS give direct evidence for monohydride adsorption on the  $\sqrt{3} \times \sqrt{3}$  reconstructed 6H-SiC(0001) Si-face surface after annealing in hydrogen atmosphere. It is concluded that the  $\sqrt{3} \times \sqrt{3}$  reconstruction stabilizes the 6H-SiC(0001)Si surface by compensating the dangling bonds of top-surface Si atoms with additional 1/3 ML Si atoms.

#### Acknowledgements

Part of this work was supported by NEDO (New Energy and Industrial Technology Development Organization) Japan.

#### References

- [1] M. Kitabatake, Mater. Sci. Forum, Vols.264-268 (1998), p.327.
- [2] F. Owman and P. Martensson, Surf. Sci. 330 (1995), L639.
- [3] M. Sabisch, P. Kruger, and J. Pollmann, Phys. Rev. B55 (1997), 10561.
- [4] F. Stucki, J. A. Schaefer, J. R. Anderson, G. J. Lapeyre, and W. Gopel, Solid State Commun. 47 (1983), 795.

*E-mail:* hoho@crl.mei.co.jp, *Tel:* +81-774-98-2511, *Fax:* +81-774-98-2586



## In-Situ RHEED Analysis During $\alpha$ -SiC Homoepitaxy on (0001)Si- and (000 $\bar{1}$ )C-Faces by Gas Source Molecular Beam Epitaxy

T. Hatayama<sup>1</sup>, T. Fuyuki<sup>1</sup>, S. Nakamura<sup>2</sup>, K. Kurobe<sup>2</sup>, T. Kimoto<sup>2</sup>  
and H. Matsunami<sup>2</sup>

<sup>1</sup> Graduate School of Materials Science, Nara Institute of Science and Technology, Takayama  
8916-5, Ikoma, Nara 630-0101, Japan

<sup>2</sup> Department of Electronic Science and Engineering, Kyoto University, Yoshidahonmachi,  
Sakyo, Kyoto 606-8501, Japan

**Keywords:** Gas Source Molecular Beam Epitaxy, RHEED, Surface Structure

**Abstract** Surface structure transitions during  $\alpha$ -SiC{0001} homoepitaxy in a high vacuum were studied based on an *in-situ* RHEED analysis. The reversible surface structure transitions ((1 $\times$ 1) $\rightleftharpoons$ (3 $\times$ 3) and (1 $\times$ 1) $\rightleftharpoons$ (2 $\times$ 2)) around 1150°C were observed only with Si adsorption on (0001)Si- and (000 $\bar{1}$ )C-faces.  $\alpha$ -SiC growth was carried out by gas source molecular beam epitaxy, and homoepitaxial layers could be grown on the Si- and C-faces above 1150°C with an alternate supply of source gases. An activation energy of about 32.5 kcal/mol was obtained in the SiC growth.

### 1. Introduction

Silicon carbide (SiC) has received considerable attention for application to high-temperature and high-power electronic devices. Homoepitaxy of  $\alpha$ -(4H- and 6H-) SiC has been demonstrated in chemical vapor deposition (CVD)[1] and molecular beam epitaxy (MBE)[2-5]. With an optimum growth procedure, the crystallinity of  $\alpha$ -SiC homoepitaxial layer has become high quality. However, fundamental investigations on  $\alpha$ -SiC homoepitaxy such as growth mechanism and surface structures are still not enough. The analysis of a growing surface is very useful to control SiC growth, and thus gas source MBE is a powerful technique for such a purpose.

The surface structures of  $\alpha$ -SiC have been reported by a combination of annealing experiments in an ultrahigh vacuum and room-temperature analysis using low-energy electron diffraction (LEED) and/or a scanning tunneling microscope (STM) [6-10]. In the case of (0001) Si-face, the surface structures of (6 $\sqrt{3}\times$ 6 $\sqrt{3}$ ) and (1 $\times$ 1) were revealed with the increase of annealing temperature [6-9]. In the case of (000 $\bar{1}$ ) C-face, the surface structures of (3 $\times$ 3) and (1 $\times$ 1) appeared with the increase of annealing temperature [6,10].

Our group has reported a surface structure transition during  $\alpha$ -SiC growth on a (0001) Si-face [5]. An  $\alpha$ -SiC (3 $\times$ 3) structure formed by adsorbed Si atoms changed to a (1 $\times$ 1) structure above 1150°C and the reversible transition from the (1 $\times$ 1) to (3 $\times$ 3) at the temperature was observed [5]. However, few reports are available on surface structures during the growth on the (0001) Si and (000 $\bar{1}$ ) C-faces.

In this paper, surface structures during  $\alpha$ -SiC homoepitaxy on (0001)Si- and (000 $\bar{1}$ )C-faces are revealed systematically for the first time using time-resolved reflection high-energy electron diffraction (RHEED).

## 2. Experiments

CVD-grown  $\alpha$ -SiC {0001} with  $3.5 \sim 5^\circ$  off-orientation toward the  $[11\bar{2}0]$  direction were used as substrates. After a substrate was loaded in a gas source MBE system, a clean surface showing a clear  $(1 \times 1)$  structure was obtained at  $1150^\circ\text{C}$  in a low flux of disilane ( $\text{Si}_2\text{H}_6$ ) by removal of an oxide layer. Subsequently, the substrate temperature was settled at a given value to grow a SiC layer. Substrate temperature was measured with an optical pyrometer. Pure  $\text{Si}_2\text{H}_6$  ( $1 \times 10^{17} \text{cm}^{-2} \text{s}^{-1}$ ) and acetylene ( $\text{C}_2\text{H}_2$ ,  $5 \times 10^{15} \text{cm}^{-2} \text{s}^{-1}$ ) were used as source gases, and they were supplied alternately. Crystallographic features of growing surfaces were analyzed using an *in-situ* RHEED system. During SiC growth, diffraction patterns on a RHEED screen were monitored with a charge-couple device (CCD) camera, and the change of diffraction intensity was processed by a microcomputer.

## 3. Results and discussion

Figure 1 shows the diagram of change in surface structures of  $\alpha$ -SiC{0001}. In the case of (0001)Si-face, Si-adsorbed  $(1 \times 1)$  changed to  $(3 \times 3)$  below  $1150^\circ\text{C}$ . This phenomenon reversed above  $1150^\circ\text{C}$  [5]. On the other hand, in the case of  $(000\bar{1})$ C-face, Si- and C-adsorbed surfaces showed  $(1 \times 1)$  and  $(3 \times 3)$  structures above  $1150^\circ\text{C}$ , respectively. The Si-adsorbed  $(1 \times 1)$  changed to  $(2 \times 2)$  below  $1150^\circ\text{C}$ . This phenomenon reversed above  $1150^\circ\text{C}$ . The reversible surface structure transitions ( $(1 \times 1) \rightleftharpoons (3 \times 3)$  and  $(1 \times 1) \rightleftharpoons (2 \times 2)$ ) at  $1150^\circ\text{C}$  are newly observed only with Si adsorption on both (0001)Si- and  $(000\bar{1})$ C-faces. It can be considered that the migration of Si atoms on the surface is enhanced above  $1150^\circ\text{C}$ , and Si atoms forming the  $(3 \times 3)$  and  $(2 \times 2)$  structures may migrate to form the  $(1 \times 1)$  structures. Among many models for the  $\alpha$ -SiC  $(3 \times 3)$  structure on the (0001) Si-face, an adsorbed Si layer model was proposed based on STM images and LEED analysis [8,9]. The  $(2 \times 2)$  structure on the  $(000\bar{1})$  C-face has been observed by a LEED/AES system with an annealing experiment at around  $800 \sim 1000^\circ\text{C}$  in a high vacuum [6]. Though the surface structure of  $(2 \times 2)$  is still not clear, it is expected to relate with Si adlayers.

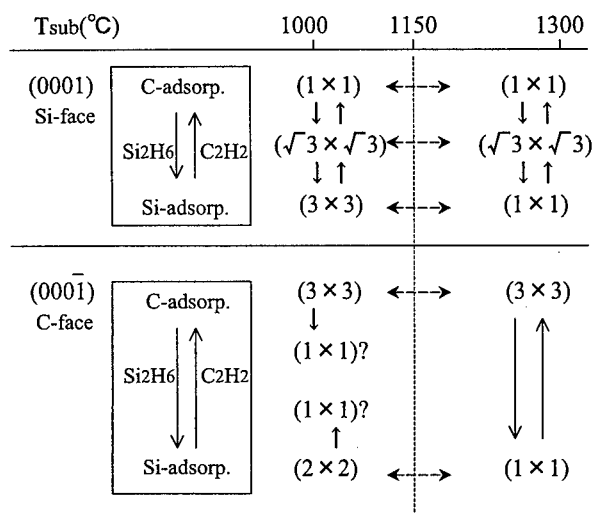


Fig.1 Diagram of change in surface structures of  $\alpha$ -SiC{0001}.

SiC growth was carried out at different growth temperatures. Above 1150°C, homoepitaxial layers of  $\alpha$ -SiC were obtained : on the (0001)Si-face, the Si-adsorbed (1×1) changed to a C-adsorbed (1×1) through  $(\sqrt{3}\times\sqrt{3})$  with  $C_2H_2$  supply, and, on the (000 $\bar{1}$ )C-face, the Si-adsorbed (1×1) changed to a C-adsorbed (3×3). Below 1150°C, homoepitaxial layers of  $\alpha$ -SiC could be obtained on the Si-face : the Si-adsorbed (3×3) changed to a C-adsorbed (1×1) through  $(\sqrt{3}\times\sqrt{3})$ . However, on the C-face, the Si-adsorbed (2×2) became (1×1), and the (1×1) did not return to the (2×2) during growth. With subsequent growth, the (1×1) structure changed to a spotty pattern. The spotty RHEED pattern corresponds to  $\beta$ -SiC (3C-SiC) ( $\bar{1}\bar{1}\bar{1}$ ) double-domain twin structure [2,5] : islands on the surface consist of  $\beta$ -SiC. Since the migration of Si atoms on the (000 $\bar{1}$ )C-face is insufficient below 1150°C, two-dimensional growth occurs and low-temperature stable  $\beta$ -SiC islands are formed.

Figures 2 (a) and (b) show the RHEED patterns from the  $\langle 1\bar{1}00 \rangle$  azimuth during  $\alpha$ -SiC growth on the (0001) Si-face at 1120°C. Fine 1/3-order streaks (marked with "↓" in Fig.2(a)) between the fundamental streaks of  $\alpha$ -SiC indicate the Si adsorption showing the  $(\sqrt{3}\times\sqrt{3})$  structure. At the disappearance of 1/3-order streaks, Si atoms on the surface are completely carbonized, and the growing surface is terminated fully with C-species, showing the (1×1) structure (Fig.2(b)). The diffraction intensity of 1/3-order streaks changed with  $C_2H_2$  supply (Fig.2(c)). The change of RHEED intensity is believed to relate to the SiC growth.

To discuss the SiC growth on the (0001)Si-face, we assumed that the reciprocal number of time ( $t_{SiC}$  in Fig.2(c)) from the intensity decrease of  $(\sqrt{3}\times\sqrt{3})$  structure formed by the  $\frac{4}{3}$  adlayer of Si [11] to the disappearance corresponds to a growth speed for the  $\frac{4}{3}$  layer of SiC.

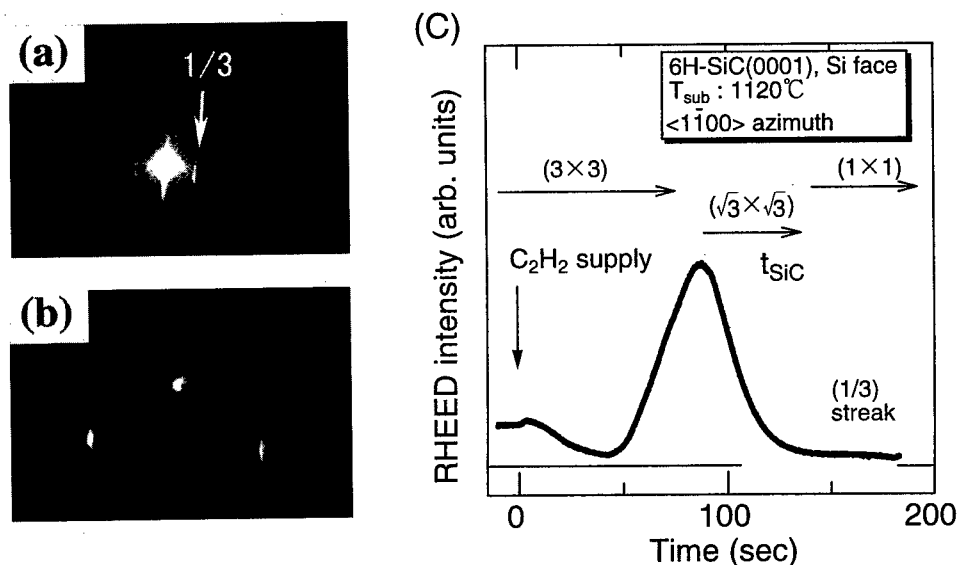


Fig.2 Change of RHEED patterns and intensity from  $\langle 1\bar{1}00 \rangle$  azimuth during SiC growth. (a)  $(\sqrt{3}\times\sqrt{3})$  and (b) (1×1) structures. (c) The profile of 1/3-order streaks indicate the Si-adsorbed structure.

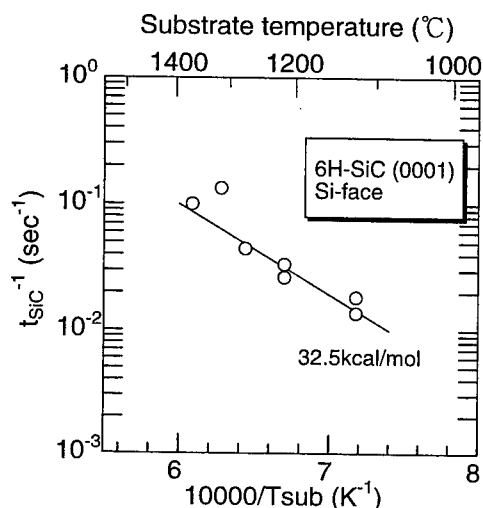


Figure 3 shows the reciprocal time ( $t_{\text{SiC}}^{-1}$ ) as a function of the reciprocal substrate temperature. The growth speed is limited by the substrate temperature, indicating surface-reaction limited growth. The activation energy calculated from the slope is about 32.5 kcal/mol. This energy is close to an initial stage in a carbonization of Si(111) [12]. The activation energy of 32.5 kcal/mol is considered to relate with the  $\alpha$ -SiC growth on the (0001)Si-face.

**Fig.3** Arrhenius plot of growth speed of SiC layers.

#### 4. Conclusions

Surface polarity and growth temperature dependence of surface structure transitions during  $\alpha$ -SiC{0001} homoepitaxy were studied systematically using *in-situ* RHEED analysis. The reversible surface structure transitions ( $(1 \times 1) \rightleftharpoons (3 \times 3)$  and  $(1 \times 1) \rightleftharpoons (2 \times 2)$ ) at 1150°C were observed with Si adsorption on (0001)Si- and (000 $\bar{1}$ )C-faces. In the case of (0001) Si-face, a homoepitaxial layer of  $\alpha$ -SiC was obtained at 1120°C. However, in the case of (000 $\bar{1}$ ) C-face,  $\beta$ -SiC islands were formed below 1150°C. The activation energy in homoepitaxy on the (0001) Si-face during the surface structure transition from  $(\sqrt{3} \times \sqrt{3})$  to  $(1 \times 1)$  is revealed, which is about 32.5 kcal/mol.

#### References

- [1] T. Kimoto, A. Ito, and H. Matsunami, *Phys.Stat.Sol.*, (b) 202 (1997), p.247.
- [2] T. Yoshinobu, H. Mitsui, I. Izumikawa, T. Fuyuki, and H. Matsunami, *Appl.Phys.Lett.*, 60 (1992), p.824.
- [3] A. Fissel, U. Kaiser, E. Ducke, B. Schroter, and W. Richter, *J.Cryst.Growth*, 154 (1995), p.72.
- [4] R. S. Kern, K. Jarrendahl, S. Tanaka, and R. F. Davis, *Phys.State.Sol.(b)* 202 (1997), p.379.
- [5] T. Hatayama, S. Nakamura, K. Kurobe, T. Kimoto, T. Fuyuki, and H. Matsunami, *Mat.Sci.Eng.*, B61-62 (1999), p.135.
- [6] A. J. van Bommel, J. E. Crombeen, and A. van Tooren, *Surf.Sci.*, 48 (1975), p.463.
- [7] R. Kaplan, *Surf.Sci.*, 215 (1989), p.111.
- [8] F. Owman and P. Mårtensson, *J.Vac.Sci.Tech.*, B14 (1996), p.933.
- [9] U. Starke, J. Schardt, J. Bernhardt, M. Franke, K. Reuter, H. Wedler, and K. Heinz, *Phys.Rev.Lett.*, 80 (1998), p.758.
- [10] K. Nishimori, H. Tokutaka, S. Nakanishi, S. Kishida, and N. Ishihara, *Jpn.J.Appl.Phys.*, 8 (1989), p.L1345.
- [11] A. Fuse, private communication.
- [12] T. Hatayama, S. Nakamura, K. Kurobe, T. Kimoto, T. Fuyuki, and H. Matsunami, in preparation.

## (10 $\bar{1}0$ )– and (11 $\bar{2}0$ )–Surfaces in 2H–, 4H– and 6H–SiC

E. Rauls<sup>1</sup>, Z. Hajnal<sup>1,2</sup>, P. Deák<sup>3</sup> and Th. Frauenheim<sup>1</sup>

<sup>1</sup> Fachbereich Physik, Theoretische Physik, Universität-GH Paderborn,  
Warburgstr. 100, DE-33095 Paderborn, Germany

<sup>2</sup> MTA Research Institute for Technical Physics and Materials Science,  
PO Box 49, HU-1525 Budapest, Hungary

<sup>3</sup> Dept. of Atomic Physics, Technical University of Budapest,  
Budafoki út 8, HU-1111 Budapest, Hungary

**Keywords:** (10 $\bar{1}0$ ), (11 $\bar{2}0$ ), 4H-SiC, 6H-SiC, Adstructures, Nonpolar Surfaces

### Abstract

We investigated the nonpolar surfaces in hexagonal 2H–, 4H– and 6H–SiC using a density–functional–theory based tight–binding method (*DFTB*). In contrast to the surfaces in 2H–SiC, the clean ideal (10 $\bar{1}0$ )–surfaces in 4H– and 6H–SiC, which probably occur e.g. at the walls of micropipes, turn out to be non-planar in 4H and 6H. The (11 $\bar{2}0$ )–surfaces, however, turn out to be similarly smooth in 4H– and 6H–SiC as it is in 2H. The surfaces can be stabilised by simple adstructures.

Although the experimentally relevant polytypes are 4H and 6H, most theoretical investigations of nonpolar surfaces in SiC focus on the 2H–polytype, – mainly because of the computational cost, that is growing with the longer periodicity along the [0001]–axis in 4H– and 6H–SiC. The similarities of the hexagonal polytypes often allow to transfer the results from 2H to 4H and 6H. Nevertheless, problems evolve looking at the (10 $\bar{1}0$ )–surfaces which turn out to be much more complicated in 4H and 6H than in 2H.

Therefore, we started detailed investigations of these polytypes using a density–functional–theory based tight–binding method (*DFTB*). For a detailed description of our method, see Refs. [1–3]. The formula we used for the calculation of the surface energies according to Refs. [1,4] is given by

$$E = E_{\text{structure}} - E_{\text{SiC(bulk)}} n_{\text{C}} - \mu_{\text{Si}} (n_{\text{Si}} - n_{\text{C}}) ,$$

where  $E_{\text{structure}}$  is the total energy of the supercell we used.  $E_{\text{SiC(bulk)}}$  is the energy of a SiC–pair in the perfect SiC–bulk,  $n_{\text{Si}}$  and  $n_{\text{C}}$  the number of Si– and C–atoms in the structure and  $\mu_{\text{Si}}$  the chemical potential of Silicon. The value of  $\mu_{\text{Si}}$  varies with the environmental conditions during growth:

$$\mu_{\text{Si(bulk)}} - \Delta H_f \leq \mu_{\text{Si}} \leq \mu_{\text{Si(bulk)}} ,$$

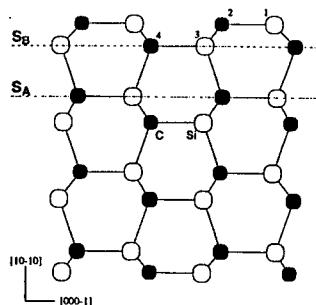


Fig. 1. Two possible cleaved  $[10\bar{1}0]$ -surfaces in 2H-SiC.  $S_A$  is the ideal surface with only threefold coordinated surface-atoms.

with the heat of formation  $\Delta H_f$  for SiC. In this paper we present our results concerning the clean  $(10\bar{1}0)$ - and  $(11\bar{2}0)$ -surfaces in 4H-SiC and compare them to our recently published results for the 2H-polytype [5].

In 2H-SiC two inequivalent  $(10\bar{1}0)$ -surfaces can be obtained by cleaving the crystal. A schematic view is given in Fig. 1. In surfaces of type  $S_A$  each surface atom is threefold coordinated, thus having one dangling bond. Each atom on a type  $S_B$ -surface exhibits two dangling bonds. Therefore,  $S_B$ -surfaces are found to be unstable, since their surface energy is much higher than that of  $S_A$ -surfaces. Within the *DFTB*-method we calculated the absolute surface energy to be  $188 \text{ meV}/\text{\AA}^2$  ( $3.03 \text{ J/m}^2$ ) for the  $S_A$ -surface. Relaxation results in a slight contraction and buckling of the surface dimers.

The 4H- and 6H-polytypes are more complicated. Because of the restricted space in the paper we will only present the results for the 4H-polytype here, but a more detailed report of our investigations (including results on 6H-SiC) is to be published soon.

In 4H-SiC, there are three possibilities to cleave the crystal in  $[10\bar{1}0]$ -planes, see Fig. 2 (*left*). Among the three inequivalent surface types the surfaces  $S_B$  and  $S_C$

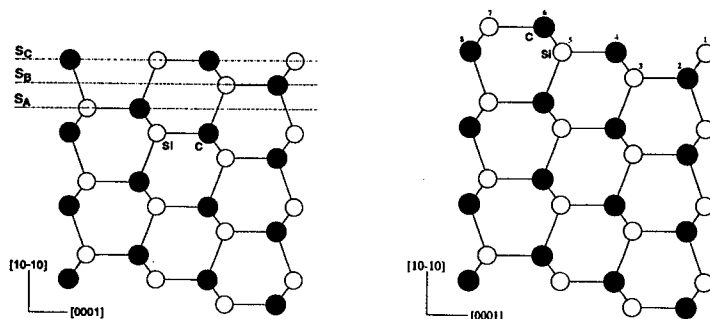


Fig. 2. Three possible cleaved  $[10\bar{1}0]$ -surfaces in 4H-SiC (*left*).  $S_A$  is the ideal surface (*right*).

consist of two three- and two twofold coordinated surface atoms per unit cell, while surface  $S_A$  has only threefold coordinated atoms. Since the surfaces  $S_B$  and  $S_C$  have two dangling bonds more per unit cell, they have a higher surface energy which makes them very unlikely to occur. Thus, the ideal  $(10\bar{1}0)$ -surface in 4H-SiC should be nonplanar and terminated by only threefold coordinated atoms, as in  $S_A$ . We determined the absolute energy of the corresponding optimised surface structure to be  $224 \text{ meV}/\text{\AA}^2$  ( $3.61 \text{ J/m}^2$ ).

In the 2H-surface all surface dimers consisting of only threefold coordinated atoms can freely relax and rehybridise to lower their surface energy. However, in the stepped nonplanar 4H-surface some of the surface atoms do not find a threefold coordinated counterpart. Instead, they are constrained by fourfold coordinated surface neighbors, representing the edge atoms (5,8) in 4H-SiC, compare Fig. 2.

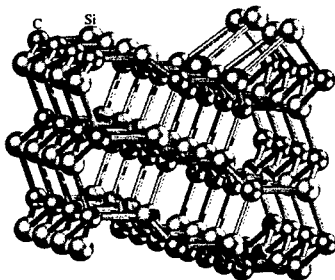


Fig. 3. A possible Si-adstructure on the  $(10\bar{1}0)$ -surface in 4H-SiC.

These characteristics and their higher surface energies made us think about possible adstructures for these surfaces to reduce the number of dangling bonds and as a result the surface energy. Adstructures consisting only of C-atoms have very high surface energies and are not stable. On the contrary, we found, that a stabilisation can e.g. be achieved by the Si-adstructure shown in Fig. 3. On the 4H- $(10\bar{1}0)$ -surface the most stable structure is obtained by inserting Si-dimers bridging the Si- and C-atoms labeled by 1 and 4 in Fig. 2, yielding a  $(2\times 1)$ -reconstruction in the  $[11\bar{2}0]$ -direction. The number of dangling bonds is reduced to 75 % compared to the lowest energy unreconstructed surface.

We calculated the surface energy of this structure to be  $156 \text{ meV}/\text{\AA}^2$  ( $2.51 \text{ J/m}^2$ ) under Si-rich conditions, which means a stabilisation by  $68 \text{ meV}/\text{\AA}^2$ .

The ideal  $(11\bar{2}0)$ -surface in 4H-SiC is much more similar to that of 2H-SiC than this is the case for the  $(10\bar{1}0)$ -surface, as shown above. One important point to mention is that  $(11\bar{2}0)$  is – unlike the  $(10\bar{1}0)$  – a smooth surface, see Fig.4. In contrast to the  $(10\bar{1}0)$ -surface the surface atoms are all threefold coordinated with one bond to the bulk and two bonds to the neighboring surface atoms, which enables them to relax and lower their energy by a much larger amount than this is possible in the  $(10\bar{1}0)$ -surface. Due to relaxation the surface C-atoms move slightly outwards and the Si-atoms move slightly towards the bulk, tending to a  $sp^2$ -like configuration. The surface bonds are thereby contracted by  $\approx 3\text{--}7\%$ . We determined the energy of

the 4H-(11 $\bar{2}$ 0)-surface to be 208.6 meV/Å<sup>2</sup> (3.4 J/m<sup>2</sup>). We found an adstructure of

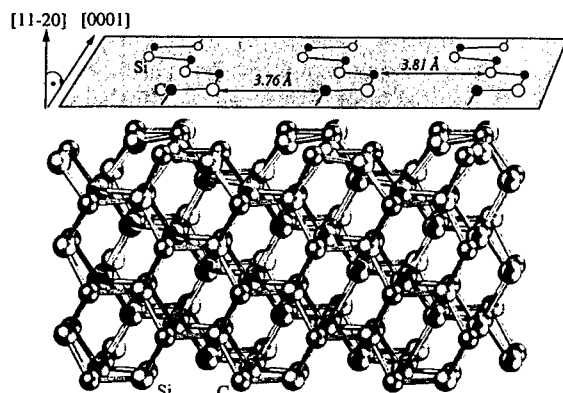


Fig. 4. Side view of the relaxed ideal (11 $\bar{2}$ 0)-surface in 4H-SiC (along [0001]).

Si-atoms that leads to a reduction of the number of dangling bonds by 50 %. The Si-atoms of the adstructure are twofold bonded to the clean surface, thus forming bridges between all the surface atoms in neighboring "chains". Furthermore, they tend to dimerize, such that they are threefold coordinated. The surface energy is thereby lowered to 91.4 meV/Å<sup>2</sup> (1.5 J/m<sup>2</sup>) under Si-rich conditions.

For certain environmental conditions a stabilisation and full passivation of both non-polar surfaces in 4H- and 6H-SiC can also occur via insertion of SiO-adstructures. These results will be presented in a forthcoming paper.

The authors gratefully acknowledge the DFG-grant FR 889/12-1 for its support. D. P. thanks OTKA T-22139, FKFP 0289/97 and AKP 97-92 2,2/27.

## References

[\*] -mail: rauls@phys.uni-paderborn.de

- [1] J. Elsner, R. Jones, M.I. Heggie, M. Haugk, R. Gutierrez, Th. Frauenheim, S. Öberg and P.R. Briddon, *Appl. Phys. Lett.* **73**, (1998) p. 3530.
- [2] M. Elstner, D. Porezag, G. Jungnickel, J. Elsner, M. Haugk, Th. Frauenheim, S. Suhai, G. Seifert, *Phys. Rev. B* **58**, (1998), p. 7260.
- [3] J. Elsner, R. Jones, P. K. Sitch, V. D. Porezag, M. Elstner, Th. Frauenheim, M. I. Heggie, S. Öberg and P.R. Briddon, *Phys. Rev. Lett.* **79**, (1997), p. 3672.
- [4] J.E. Northrup and J. Neugebauer, *Phys. Rev. B*, **52**, (1995), p. R17001.
- [5] E. Rauls, J. Elsner, R. Gutierrez and Th. Frauenheim, *Sol. Stat. Comm.*, **111**, (1999), p. 459.
- [6] P. Mårtensson, F. Owman and L.I. Johansson, *Phys. Stat. Sol. (b)* **202**, (1997), p. 501.



## Theory of Structural and Electronic Properties of Cubic SiC Surfaces

Johannes Pollmann, Peter Krüger and Wenchang Lu

Institut für Theoretische Physik II-Festkörperphysik, Universität Münster,  
Wilhelm-Klemm-Strasse 10, DE-48149 Münster, Germany

**Keywords:** Atomic Structure, Electronic Structure, Local Density Theory, Surface

**Abstract:** The current understanding of the atomic and electronic structure of polar cubic 3C-SiC(001) surfaces, as it derives from *ab-initio* calculations, is briefly addressed in the light of recent experimental data. Very encouraging agreement between the theoretical results and the available data is observed. The origin and nature of the distinctively different reconstructions of 3C-SiC(001) surfaces, as compared to those of the C(001) and Si(001) surfaces, is discussed.

**Introduction:** Cubic and hexagonal polytypes of the wide-band-gap semiconductor SiC are very promising candidates for applications in micro- and optoelectronics. The very basis for such applications is the specific electronic structure of SiC polytypes and their surfaces [1]. A most quantitative description of their bulk and surface atomic as well as electronic structure is highly desirable, therefore [2]. From a fundamental point of view, SiC is unique in that it is a fairly ionic IV-IV compound semiconductor. It resides at the borderline between homopolar elemental or heteropolar covalent and heteropolar ionic or ionic compound semiconductors. While the former crystallize in either the diamond or the zincblende structure, the latter occur in the wurtzite or the sodium chloride structure. SiC, lying 'in between', occurs in an extremely large number of polytypes, the cubic 3C-SiC and the hexagonal 6H-SiC of which seem to be the most important for technological applications [3]. Cubic  $\beta$ - or 3C-SiC crystallizes in the zincblende structure. The bulk crystal has one Si and one C atom per unit cell. The nearest-neighbor configuration of Si and C atoms is tetrahedral and the SiC bond length is close to 1.89 Å. The bulk lattice constant  $a_0 = 4.36$  Å of SiC is some 20% smaller than that of bulk Si ( $a_0 = 5.43$  Å) and some 22% larger than that of bulk diamond ( $a_0 = 3.57$  Å). In addition, the pronounced ionicity of the SiC bond, amounting to  $g = 0.475$  on the Garcia-Cohen scale [4], is of particular importance for the reconstruction of SiC surfaces, as well. The ionicity stems from the different strengths of the C and Si potentials, respectively, giving rise to the very different covalent radii and electronegativities of C ( $r_C = 0.77$  Å,  $e_C = 2.5$ ) and Si ( $r_{Si} = 1.17$  Å,  $e_{Si} = 1.7$ ). The large difference in electronegativities leads to a charge transfer from the Si to the C atoms so that the electronic charge density distribution along the Si-C bond is strongly asymmetric [5]. Due to the charge transfer, Si atoms act as cations while C atoms act as anions in SiC. In consequence, there are nonpolar and polar SiC surfaces. For the polar (001) surfaces, addressed in this contribution, C and Si layers alternate along the [001]-direction so that there are two distinctly different SiC(001) surfaces which are usually referred to as C- or Si-terminated, respectively. They both show reconstructions that are distinctively different from those of respective diamond and Si surfaces. Critically depending on the actual growth and surface preparation conditions (1×1), (2×1), c(2×2), c(4×2), (3×2), (5×2) and (7×2) structures have been observed [1]. Among these both C-rich and Si-rich structures have been obtained and investigated in experiment, e.g., by low-energy electron diffraction [6, 7, 8, 9, 10], Auger electron spectroscopy [6, 7, 10, 11], scanning tunneling microscopy [12, 13, 14, 15],

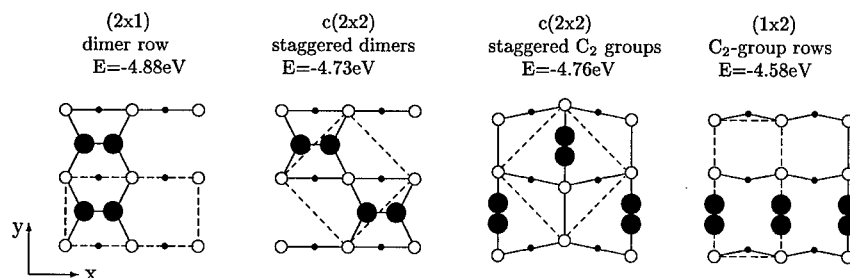


Figure 1: Structure models for the C-terminated SiC(001) surface.

electron-energy loss spectroscopy [16], x-ray photoelectron spectroscopy [10, 17], near-edge x-ray absorption fine structure [17], core-level, photoelectron and angle-resolved photoelectron spectroscopy [18, 19, 20]. Polar SiC(001) surfaces have recently been investigated theoretically, as well, by a number of 'state of the art' first-principles LDA calculations [2, 21, 22, 23, 24, 25, 26]. For detailed descriptions of the used theoretical approaches, see e.g., Refs. [21, 22, 23, 26].

**C-terminated 3C-SiC(001) surfaces:** A number of structural models for the reconstruction of the C-terminated 3C-SiC(001) surface has been suggested in the literature [1, 7, 8, 10, 17, 18] on the basis of experimental results. They all derive from the C-terminated bulk-truncated lattice with the C atoms of the top layer moving into new positions at the free surface. They comprise (2×1) or (1×2) row structures and staggered c(2×2) structures. These four structural models have been optimized by total energy minimization calculations [21, 22, 23]. Top views of the four structures, as resulting from our calculations, are shown in Fig. 1. It is quite obvious, that C dimers or more strongly bound C<sub>2</sub> groups bridging subsurface Si atoms are the building blocks for these reconstructions. Both of these basic structural units can be distributed at the surface in (2×1) or (1×2) rows or in c(2×2) staggered configurations. From a TLEED analysis, Powers *et al.* [8] found that the surface is terminated with C<sub>2</sub> groups in staggered Si bridge sites. Long *et al.* [17] have confirmed this conclusion by a polarization analysis of their NEXAFS data. They carried out a study 'to settle the long-standing controversy over the structure of this surface' and came as well to the conclusion that it is terminated with staggered rows of unusual nearly triply-bonded C dimers bridging underlayer Si dimers.

While the experimental results [8, 17, 18] indicate a staggered c(2×2) C<sub>2</sub>-group reconstruction the theoretical results [21, 22, 23] slightly favor the (2×1) dimer-row structure (see Fig. 1). In this context it is very important to note that the total energy gain for all four addressed structures is of the order of - 4.7 eV per unit cell (see Fig. 1). On the contrary, the total-energy difference between the (2×1) dimer-row structure ( $E_{tot} = - 4.88$  eV) and the staggered C<sub>2</sub>-group configuration ( $E_{tot} = - 4.76$  eV) is only 0.12 eV [23]. This small difference might explain why the calculations for T = 0 K favor the dimer-row structure while experiment observes at room temperature after high-temperature growth the staggered C<sub>2</sub> group reconstruction. Temperature effects might be quite different for the two surfaces since the electronic structure of the two models is basically different [23]. For the (2×1) dimer-row model, the LDA band structure is slightly metallic due to the existence of C surface states in the gap. The staggered C<sub>2</sub>-group reconstruction, on the contrary, has an LDA gap of about 1 eV. This surface is manifestly semiconducting and there are no C dangling bonds at this surface. This lack of surface states in the gap is in accord with the data [10, 18].

Most recently, Yeom *et al.* [18] have 'unambiguously' determined the c(2×2) reconstruction

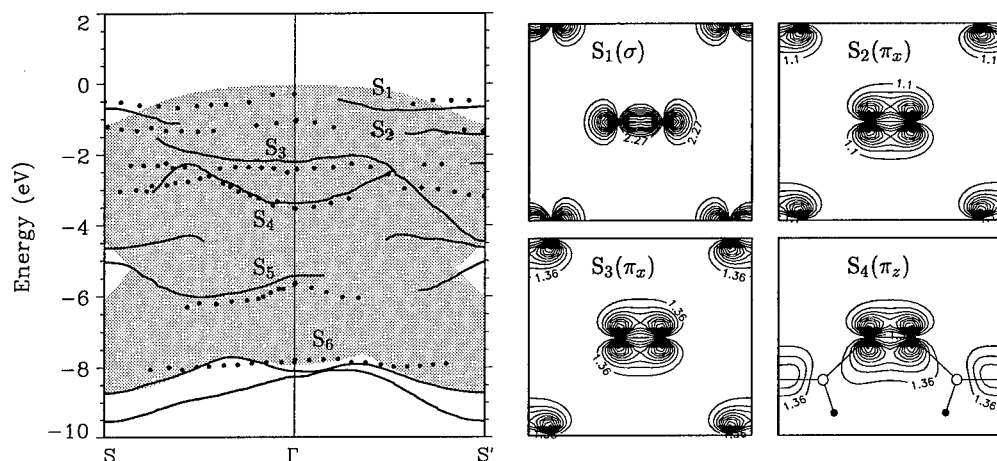


Figure 2: Surface band structure and charge-density contours of surface states for the C-terminated c(2x2) surface with staggered C<sub>2</sub> groups. Solid circles are ARPES data from Ref. [18]. The charge-density contours of states S<sub>1</sub> to S<sub>3</sub> are plotted in the x-y plane and that of state S<sub>4</sub> is plotted in the y-z plane.

of the C-terminated 3C-SiC(001) surface by scanning tunneling microscopy, surface-core-level-resolved photoelectron diffraction and an extensive angle-resolved photoelectron spectroscopy study. The authors found this surface 'to uniquely and uniformly consist of anomalous bridge-bonded C dimers with a C-C bond length of 1.22 Å'. The authors arrived at the conclusion, that the c(2x2) structure consists of staggered C<sub>2</sub>-groups which form bridges between the Si atoms of the second layer of the system. The measured bond length of the C<sub>2</sub> groups and the bond length between top layer C and sublayer Si atoms exactly agree with our results [23]. Yeom *et al.* [18] have also carried out a detailed ARPES study and have compared their data to the small section of the respective surface band structure, as given in Ref. [23]. A fairly good agreement was found as far as that was possible for the reduced theoretical data set. To improve the basis for this comparison, we have calculated the surface-band structure of the staggered C<sub>2</sub>-group model with 30 atomic layers in the supercell. Our results are shown in Fig. 2 in direct comparison with the data. In addition, we have plotted the charge-density distributions for the states S<sub>1</sub> and S<sub>2</sub> at the S'-point and for the states S<sub>3</sub> and S<sub>4</sub> at the Γ-point of the surface Brillouin zone. There are no surface states in the fundamental gap which means that there are no unsaturated C dangling bonds. This is corroborated by the charge densities which clearly exhibit one σ state (S<sub>1</sub>) and three π states (S<sub>2</sub> to S<sub>4</sub>). The measured and calculated bands for the c(2x2) surface are in good agreement.

**Si-terminated SiC(001) surface:** A whole variety of (1x1), (2x1), c(4x2) and (Nx2) structures with N being an odd integer has been studied both in experiment [1] and theory [2]. Yet, most of these structures are still under debate, their determination constituting a major challenge. Contrary to the case of the C-terminated (001) surface, for the Si-terminated (001) surface both *clean* and *adlayer-covered* surface models have been suggested and discussed in great detail in the literature.

Experimental data on the (2x1) and c(4x2) surfaces have been interpreted assuming that the observed reconstructions occur at the *clean* surface [1, 9, 14]. For the (2x1) surface, a reconstruction model with rows of buckled Si dimers with a dimer-bond length of 2.31 Å, very

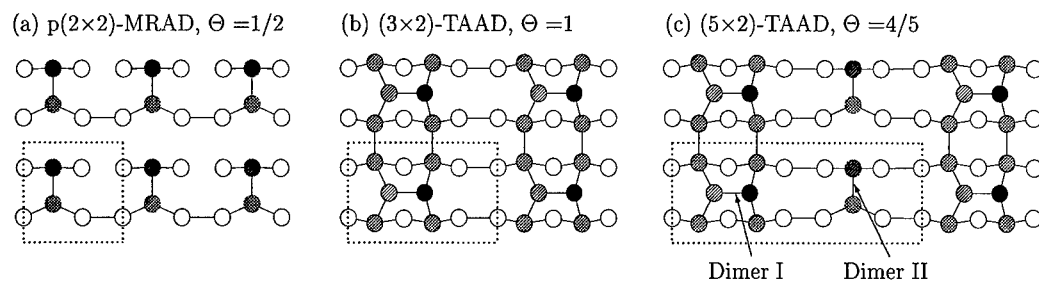


Figure 3: Structure models for the Si-terminated SiC(001) surface.

similar to the reconstruction of Si(001)-(2×1) [27], was suggested [9]. This interpretation, however, contradicts the results of *ab-initio* calculations [21, 22, 23, 24] which agreeingly find that no strongly bound Si dimers are formed at this surface.

For the  $c(4 \times 2)$  surface Soukiassian *et al.* [14] have suggested an alternatively up- and down-dimer (AUDD) model in which both the up and down dimers are symmetric. They explained many of their experimental results using this model [14, 15, 28, 29]. This configuration, however, is neither stable nor metastable with respect to Si adlayer structures [25]. In their studies Aristov *et al.* [15] found that the room-temperature  $c(4 \times 2)$  is semiconducting with a gap of about 1.7 eV while the high-temperature (2×1) surface was found to be metallic. On the contrary, theory indicates that the electronic structure of the *clean* (2×1) and  $c(4 \times 2)$  surfaces is very similar (cf. Ref. [24]).

To resolve this issue various structural models of the Si-terminated surface covered by partial adlayers of Si have been investigated by *ab-initio* total energy and grand canonical potential calculations [25, 26]. A missing-row asymmetric-dimer (MRAD) model with an adatom coverage of  $\Theta_{Si} = 1/2$  ML was suggested [25]. The MRAD model has the lowest grand-canonical potential among all the  $c(4 \times 2)$  structures which were considered. The calculations reveal that the energy of the surface can drastically be lowered by *dimerization* of neighboring Si atoms in the adatom rows forming  $c(4 \times 2)$  or  $p(2 \times 2)$  (see left panel of Fig. 3) reconstructions. The dimers in the partial Si adlayers turn out to be asymmetric with a bond length of 2.30 Å. This dimer-bond length is very close to that at the clean Si(001)-(2×1) surface [27] and also agrees with the surface dimer-bond length as obtained by Powers *et al.* [9].

In more recent studies, we have addressed the (3×2) and the (5×2) reconstructions of the Si-terminated surface and have proposed for both of these surfaces two-adlayer asymmetric-dimer models (TAADM) [26]. In the (3×2) model, two partial layers of Si adatoms are adsorbed on the clean surface. The coverage of the lower adlayer is 2/3 ML and that of the top adlayer is 1/3 ML. So the nominal coverage with adatoms is 1 ML for this (3×2) model. A top view of the structure is shown in the middle panel of Fig. 3. For the (5×2) reconstruction we also find a TAADM as the optimal structure. A top view of this model is shown in Fig. 3, as well (right panel). In this model, the lower adlayer contains 3/5 ML and the upper one contains 1/5 ML. The nominal coverage with adatoms is 4/5 ML in this case. All of these results are in good accord with experimentally determined surface Si coverages and their ratios (for details see, Refs. [13, 25, 26, 30]).

To explain the (N×2) reconstructions, several models have been proposed by different authors [1]. Our optimized models for the  $p(2 \times 2)$  MRAD, (3×2) TAADM and (5×2) TAADM are shown in Fig. 3. They originate from two basic building blocks. The  $p(2 \times 2)$  model is char-

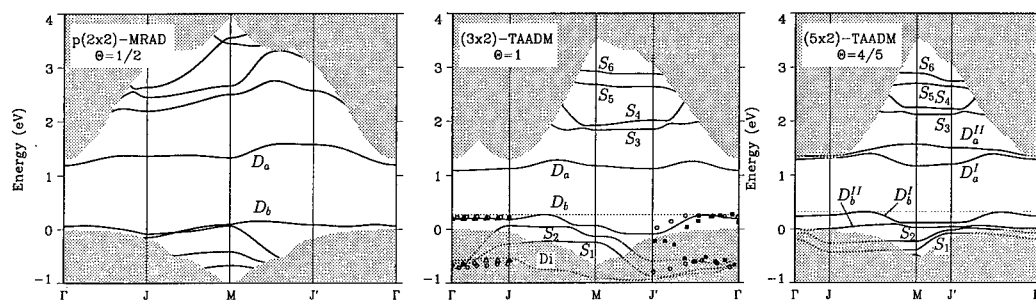


Figure 4: Sections of the surface band structure for different Si-terminated SiC(001) reconstructions. In the middle panel, circles, triangles and squares are from experiments of Refs. [19, 20].

acterized by one asymmetric Si dimer adsorbed per surface unit cell. The  $(3 \times 2)$  TAADM is characterized by one Si hexamer adsorbed per surface unit cell. Finally the  $(5 \times 2)$  TAADM is characterized by one asymmetric Si dimer and one Si hexamer adsorbed per surface unit cell. With these basic structural units all kinds of higher reconstructions can be formed which minimize the number of dangling bonds in each case. Obviously, the structure in the right panel of Fig. 3 is just a superposition of the two structures in the left and the middle panel.

Finally, we compare in Fig. 4 the surface band structures for these three surfaces. It is quite obvious that a 'superposition' of the band structures in the left and the middle panel yields all basic surface-state bands in the right panel. This is simply due to the fact, that the interactions between the various dimers at either the  $p(2 \times 2)$  or the  $(3 \times 2)$  surface are fairly weak for one reason. For another reason, the dimers in the  $(3 \times 2)$  TAADM and the  $p(2 \times 2)$  MRAD model which both occur in the  $(5 \times 2)$  TAADM (Dimer I and Dimer II) are orthogonal which reduces their interactions, as well.

**Synopsis:** From the reconstruction models discussed above it is easy to see that the C-terminated SiC(001) surface is characterized by C atoms in the top layer of the bulk-terminated structure which are free to move into new positions upon surface creation. They either form double-bonded C dimers or even triple-bonded  $C_2$  groups bridging the second layer Si atoms. Due to the topology of the surface, the small covalent radius of C, as compared to Si, and the very strong  $\sigma$  and/or  $\pi$  bonds between the C surface-layer atoms, these configurations form in a very stable way without additional adatoms. The respective mechanism does not occur at the clean C(001) surface since the lattice constant of diamond is too small to allow for  $C_2$  groups bridging second layer C atoms.

The Si-terminated structures, on the contrary, are more complex. They are *not* simply characterized by the bulk-terminated lattice. In this case the surface topology, the large Si orbitals in the small surface-layer unit cell and the lack of triple-bonded  $Si_2$  groups give rise to entirely new reconstructions which are formed by Si uptake from the gas phase. Employing two basic building blocks  $c(4 \times 2)$ ,  $p(2 \times 2)$ ,  $(3 \times 2)$ , and  $(5 \times 2)$  structures can easily be formed. One of these building blocks is a Si dimer, as in the  $c(4 \times 2)$  and  $p(2 \times 2)$  structure. The other is a Si hexamer as in the  $(3 \times 2)$  structure. Finally, the  $(5 \times 2)$  structure has both a Si dimer and a Si hexamer per unit cell. These mechanisms do not occur at the Si(001) surface, since the Si lattice constant is large enough to allow for the formation of strong Si dimers at the clean surface.

We acknowledge financial support of this work by the Deutsche Forschungsgemeinschaft (Bonn,

Germany) under contract No. Po 215/13-2 and a grant of Cray computer time at the John von Neumann-Institute for Computing (NIC) of the Forschungszentrum Jülich (Germany) under contract No. K2710000.

#### References:

- [1] For a review, see V. M. Bermudez, *Phys. Status Solidi (b)* **202** (1997), p. 447.
- [2] For a review, see J. Pollmann, P. Krüger and M. Sabisch, *Phys. Status Solidi (b)* **202** (1997), p. 421.
- [3] See, e.g., C. E. Weitzel *et al.*, *IEEE Trans. Electron Devices* **43** (1996), p. 1732.
- [4] A. Garcia and M. L. Cohen, *Phys. Rev. B* **47** (1993), p. 4215 and p. 4221.
- [5] M. Sabisch, P. Krüger, and J. Pollmann, *Phys. Rev. B* **51** (1995), p. 13367.
- [6] M. Dayan, *J. Vac. Sci. Technol. A* **4** (1986), p. 38.
- [7] S. Hara, W. F. J. Slijberman, J. F. van der Veen, I. Ohdomari, S. Misawa, E. Sakuma, and S. Yoshida, *Surf. Sci.* **231** (1990), p. L196.
- [8] J. M. Powers, A. Wander, P. J. Rous, M. A. Van Hove, and G. A. Somorjai, *Phys. Rev. B* **44** (1991), p. 11159.
- [9] J. M. Powers, A. Wander, M. A. Van Hove, and G. A. Somorjai, *Surf. Sci.* **260** (1992), p. L7.
- [10] V. M. Bermudez and J. P. Long, *Appl. Phys. Lett.* **66**, p. 475 (1995).
- [11] R. Kaplan, *Surf. Sci.* **215** (1989), p. 11.
- [12] V. Derycke, P. Soukiassian, A. Mayne, G. Dujardin, and J. Gautier, *Phys. Rev. Lett.* **81** (1998), p. 5868.
- [13] S. Hara, J. Kitamura, H. Okushi, S. Misawa, Y. Yoshida, and Y. Tokumaru, *Surf. Sci.* **357 – 358** (1996), p. 436.
- [14] P. Soukiassian, F. Semond, L. Douillard, A. Mayne, G. Dujardin, L. Pizzagalli, and C. Joachim, *Phys. Rev. Lett.* **78** (1997), p. 907.
- [15] V. Yu. Aristov, L. Douillard, O. Fauchoux, and P. Soukiassian, *Phys. Rev. Lett.* **79** (1997), p. 3700.
- [16] M. L. Shek, *Surf. Sci.* **349** (1996), p. 317.
- [17] J. P. Long, V. M. Bermudez, and D. E. Ramaker, *Phys. Rev. Lett.* **76** (1996), p. 991.
- [18] H. W. Yeom, M. Shimomura, J. Kitamura, S. Hara, K. Tono, I. Matsuda, B. S. Mun, W. A. R. Huff, S. Kono, T. Ohta, S. Yoshida, H. Okushi, K. Kajimura, and C. S. Fadley, *Phys. Rev. Lett.* **83** (1999), p. 1640.
- [19] H. W. Yeom, Y.-C. Chao, S. Terada, S. Hara, S. Yoshida, and R. I. G. Uhrberg, *Phys. Rev. B* **56** (1997), p. R15525.
- [20] M. Lübke, K. Lindner, S. Sloboshanin, S. Tautz, J. Schäfer and D.R.T. Zahn, *J. Vac. Sci. Technol. A* **16** (1998), p. 3471.
- [21] P. Käckell, J. Furthmüller, and F. Bechstedt, *Appl. Surf. Sci.* **104 – 105** (1996), p. 45.
- [22] A. Catellani, G. Galli, and F. Gygi, *Phys. Rev. Lett.* **77** (1996), p. 5090.
- [23] M. Sabisch, P. Krüger, and J. Pollmann, *Phys. Rev. B* **53** (1996), p. 13121.
- [24] A. Catellani, G. Galli, F. Gygi, and F. Pellacini, *Phys. Rev. B* **57** (1998), p. 12255.
- [25] W. Lu, P. Krüger, and J. Pollmann, *Phys. Rev. Lett.* **81** (1998), p. 2292.
- [26] W. Lu, P. Krüger, and J. Pollmann, *Phys. Rev. B* **60** (1999), p. 2495; and accepted for publication.
- [27] P. Krüger and J. Pollmann, *Phys. Rev. Lett.* **74** (1995), p. 1155.
- [28] P. Soukiassian, F. Semond, A. Mayne, and G. Dujardin, *Phys. Rev. Lett.* **79** (1997), p. 2498.
- [29] F. Semond, P. Soukiassian, A. Mayne, G. Dujardin, L. Douillard, and C. Jaussaud, *Phys. Rev. Lett.* **77** (1996), p. 2013.
- [30] T. Yoshinobu, I. Izumikawa, H. Mitsui, T. Fuyuki, and H. Matsunami, *Appl. Phys. Lett.* **59** (1991), p. 2844.

## Characterization of Anisotropic Step-bunching on as-grown SiC Surfaces

M. Syväjärvi<sup>1</sup>, R. Yakimova<sup>1,2</sup>, T. Iakimov<sup>2</sup> and E. Janzén<sup>1</sup>

<sup>1</sup> Department of Physics and Measurement Technology, Linköping University,  
SE-581 83 Linköping, Sweden

<sup>2</sup> Okmetic AB, Box 255, SE-17824 Ekerö, Sweden

**Keywords:** Anisotropy, Lateral Growth, Step Bunching

### Abstract

We report the presence of anisotropic step-bunching in SiC epitaxy on off-oriented substrates. This is an effect of step-flow growth. The anisotropic step-bunching is discussed in relation to the temperature dependence of lateral growth velocities and the interface roughness. The macrostep appearance is probably related to formation of morphologically stable faces with low surface free energy.

### Introduction

Growth of device quality 4H and 6H-SiC layers is generally performed on substrates with surfaces off-oriented from the (0001) plane in the [11 $\bar{2}$ 0] direction. This provides conditions for homoepitaxy, i.e. polytype reproduction from the substrate to the grown material. Growth on off-oriented substrates proceeds via step-flow growth. Most often step-bunching takes place during growth and this phenomenon is a coalescence of several small steps into larger steps with increased step heights. This effect influences the epilayer quality. The step-bunching is probably formed by a rearrangement of the surface to a hill and valley structure which lowers the total surface free energy even though this causes an increasing surface area [1,2].

For step-bunching in SiC epitaxy, one has to distinguish between (i) microsteps made up of several steps of unity height (one Si-C bilayer); (ii) macrosteps which consist of a large number of superimposed microsteps. Step-bunching in SiC has been studied earlier [1,3] where most attention was given to the microsteps. Those studies were performed on thin layers (10  $\mu\text{m}$ ) grown with CVD which is the most common technique for SiC epitaxy with growth rates <5  $\mu\text{m}/\text{h}$ . Further advancement of SiC for high-power and high-frequency applications may require thick layers (up to 100  $\mu\text{m}$ ). Increased growth rates (several tens of  $\mu\text{m}/\text{h}$ ) are thus preferred. Higher growth rates and thicker layers may have an effect on the step appearance. Even though SiC growth has been widely studied to date, there still remain basic issues which have not yet been understood.

We have studied as-grown surfaces related to macrosteps and we will provide an explanation for the anisotropic character of step-bunching which is a fundamental property in SiC growth. To our knowledge this is the first report on the different stages of anisotropic step-bunching. This was possible since we have studied as-grown crystal surfaces from different high growth rate and high-temperature growth techniques such as liquid phase epitaxy, sublimation epitaxy and sublimation bulk growth.

### Experimental

The growth rates for the epitaxial techniques are 50-120  $\mu\text{m}/\text{h}$  at growth temperatures 1800 to 1850°C at the substrate and usual layer thicknesses vary from 50 to 120  $\mu\text{m}$ . For details on liquid

phase and sublimation epitaxy, see [4,5]. Surfaces of crystals grown by seeded sublimation bulk growth [6] have been studied as well. The surfaces were studied using optical microscopy in Nomarski interference contrast (NDIC) mode, scanning electron microscopy (SEM) and atomic force microscopy (AFM).

## Results

Since the substrate surfaces are off-oriented a few degrees in the  $[1\bar{1}20]$  direction, the steps on the epilayers are expected to be straight and perpendicular to the step-flow direction. We observed that for thick ( $\geq 50 \mu\text{m}$ ) layers grown by sublimation epitaxy, the macrosteps are not completely straight. Typical features observed are some sort of splicing or cross-over of steps. An illustration for 6H-SiC is given in Fig. 1 but we had similar findings for 4H-SiC. This splicing suggests that some instability occurs in the course of step-flow growth giving rise to anisotropic step-bunching. This effect was only possible to observe using AFM. We could not observe any features on the epilayer surfaces using NDIC microscopy. Anisotropic step-bunching on atomic scale has been observed on spiral grown hillocks in layers grown by CVD [7]. A model was suggested based on anisotropic growth rates of doublet steps (0.5 nm high) and triplet steps (0.75 nm high) for 4H and 6H-SiC, respectively, between adjacent  $\langle 1\bar{1}00 \rangle$  directions due to difference in the number of dangling bonds. However, provided the model is also valid for large steps, this effect would cause different widths of the neighbouring  $\langle 1\bar{1}00 \rangle$  facets on a terrace of a macrostep in step-flow growth on off-oriented substrates. This is obviously not the case as observed in Fig. 2 where the length of the facets are similar. Consequently other explanations than given by the model presented in Ref. [7] have to be found. For sublimation grown epilayers, we have mostly observed anisotropic step-bunching on the Si-face of 6H and 4H-SiC but occasionally also on the C-face. The surface free energy is higher on the Si-face than on the C-face [8] and the total surface free energy is reduced by a formation of the hill and valley structure. On the C-face the surface free energy is lower and the hill and valley structure does not appear to the same extent which would explain why anisotropic step-bunching is more frequently found on the Si-face than on the C-face.

We have observed similar splicing as shown in Fig. 1 for thin LPE grown layers ( $\sim 0.1 \mu\text{m}$ ) using SEM. The anisotropic step-bunching effect becomes pronounced in LPE layers (Fig. 2) when the thickness reaches a few  $\mu\text{m}$ . For layers grown by LPE, step heights up to  $\sim 1 \mu\text{m}$  are commonly observed. The apex of the step caused by anisotropic step-bunching points in the  $[1\bar{1}20]$  direction. The phenomenon becomes even more pronounced in crystal growth at high temperatures as used in bulk growth and facets in the  $\langle 1\bar{1}00 \rangle$  directions become well developed, Fig. 3.

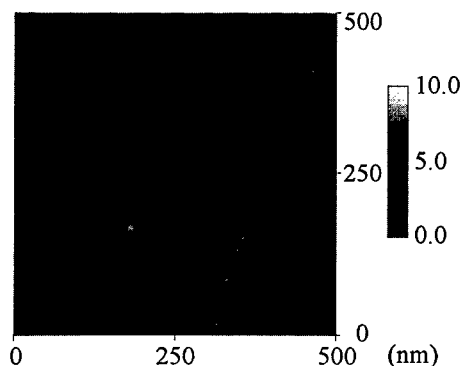


Fig. 1. AFM height image of a 6H-SiC layer grown on a  $3.5^\circ$  off-oriented 6H-SiC Si-face substrate for one hour by sublimation epitaxy; layer thickness  $50 \mu\text{m}$ .

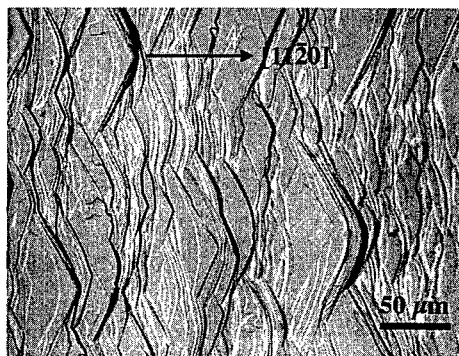


Fig. 2. Large steps in a 4H-SiC epilayer grown by LPE; NDIC micrograph.



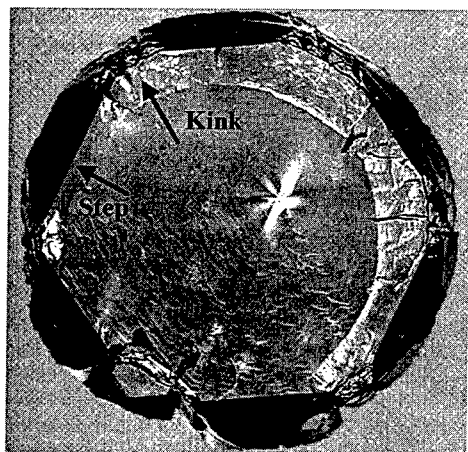


Fig. 3. A cut wafer from a 4H-SiC crystal top grown by seeded sublimation bulk growth.

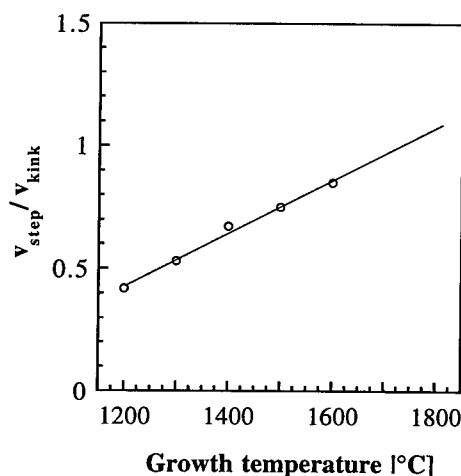


Fig. 4. Temperature dependence of  $v_{\text{step}}/v_{\text{kink}}$  ratio; data taken from [9].

#### Discussion.

In the following, denote growth in  $\langle 1\bar{1}00 \rangle$  and  $\langle 11\bar{2}0 \rangle$  directions as *step growth* and *kink growth* [9], respectively (Fig. 3). It was shown that the lateral velocity of steps ( $v_{\text{step}}$ ) and kinks ( $v_{\text{kink}}$ ) are different both in case of vapor growth [9] and LPE [10]. A step in a certain direction contains small straight steps and kinks. Kinks are locations where atoms preferably attach. The kink density increases with the deviation from a  $\langle 1\bar{1}00 \rangle$  direction and becomes maximum in a  $\langle 11\bar{2}0 \rangle$  direction. The ratio of incorporation probabilities at steps and kinks is directly given by the ratio of the lateral growth rates [9]. The temperature dependence of the  $v_{\text{step}}/v_{\text{kink}}$  ratio is shown in Fig. 4. At low temperatures the lateral growth rate is higher in a  $\langle 11\bar{2}0 \rangle$  direction than in a  $\langle 1\bar{1}00 \rangle$  direction. However, extrapolation of the data to higher temperatures (Fig. 4) gives that the lateral growth rate should be higher in a  $\langle 1\bar{1}00 \rangle$  direction than in a  $\langle 11\bar{2}0 \rangle$  direction (assuming a linear dependence) at temperatures above  $\sim 1750^\circ\text{C}$ . Sublimation epitaxy and liquid phase epitaxy are typically performed at temperatures around  $1800^\circ\text{C}$ . At this temperature conditions for anisotropic growth are present. This is in agreement with results shown in Fig. 1 and Fig. 2 for sublimation epitaxy and LPE, respectively. In both cases the growth temperature was above  $1750^\circ\text{C}$ . For bulk growth, which is applied at temperatures  $>2200^\circ\text{C}$ , anisotropic growth is most pronounced.

For characterization of epilayer surfaces, data such as step (consisting of a terrace and a riser) width, terrace width, riser width, step height, etc. have been collected. We found that the step widths vary (roughly) from 30 to 66 nm, terrace widths vary from 20 to 54 nm, riser width vary from 7 to 17 nm, and step height vary from 1 to 3 nm for 6H-SiC layers grown on the Si-face (Fig. 5a). For 4H-SiC step widths vary from 10 to 32 nm, terrace widths vary from 5 to 20 nm, riser width vary from 5 to 12 nm, and step height vary from 1 to 4 nm (Fig. 5b). Variations were also found for layers grown on C-face for both polytypes. The variations in the data occur for one given sample and are probably given by a growth instability as discussed below.

One question which arises is why the anisotropic step-bunching is more pronounced on layers grown by LPE than sublimation epitaxy at equal growth temperatures and similar growth rates. The surfaces are far more smoother on the sublimation grown layers. The interface roughness, its anisotropy and dependence on growth parameters is a very important issue in crystal growth. The general expectation for the same material is that the interface will be rougher in liquid phase growth and smoother in vapor phase growth [11]. This would explain why larger steps and pronounced anisotropic behaviour is allowed to occur in liquid phase growth compared with sublimation growth at equal growth temperatures. The surface of a growing crystal is bounded by interfaces with different roughnesses and the smoothest interface will eventually remain as the morphologically stable face [11]. For SiC, the morphologically stable surfaces on a macrostep will be  $\{0001\}$

and  $\{1\bar{1}0x\}$  where  $x$  differs for 6H and 4H-SiC due to different stacking sequences. It was reported that for 6H-SiC  $\{1\bar{1}04\}$  is a low-index surface [12] whereas a corresponding surface for 4H-SiC has not been reported to our knowledge. The interface roughness increases with increasing growth temperature [11] which explains why well developed facets occurs in sublimation bulk growth as compared with the splicing features which occur in sublimation epitaxy.

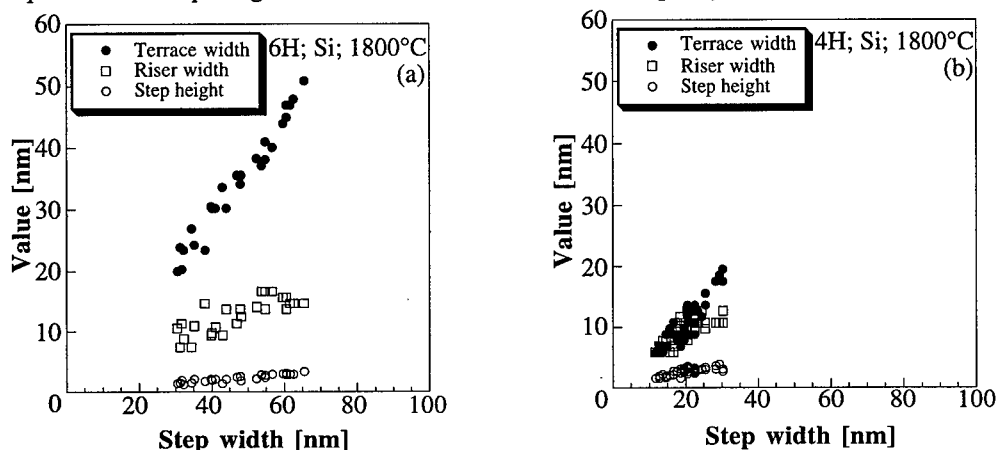


Fig. 5. Data taken from AFM images of (a) 6H-SiC layer (substrate off-orientation  $3.5^\circ$ ); (b) 4H-SiC layer (substrate off-orientation  $8^\circ$ ) grown by sublimation epitaxy; terrace width, riser width and step height vs step width; layer thicknesses  $50\ \mu\text{m}$ .

### Summary

The property of anisotropic step-bunching is an important issue in step-flow growth, especially in high-temperature, high growth rate epitaxy. From the results, step-flow growth should be applied at temperatures around  $1700\text{--}1800^\circ\text{C}$  for reducing anisotropic step-bunching due to different lateral velocities in the  $\langle 1\bar{1}00 \rangle$  and  $\langle 11\bar{2}0 \rangle$  directions. The growth parameters for individual growth techniques must be carefully selected for achieving a small interface roughness. The appearance of  $\{1\bar{1}00\}$  facets suggests an anisotropy in the interfacial energy which for surfaces perpendicular to  $\{0001\}$  is explained by a change in the bond configuration from  $\{1\bar{1}00\}$  to  $\{11\bar{2}0\}$  surfaces.

### Acknowledgement

This work was supported by the SSF program SICEP and Lennanders Foundation.

### References

- [1] T. Kimoto, A. Itoh, and H. Matsunami, *Appl. Phys. Lett.* **66** (1995) p. 3645.
- [2] "The science of crystallization: Microscopical interfacial phenomena", W.A. Tiller, Cambridge University Press, Cambridge (1990).
- [3] T. Kimoto, A. Itoh, H. Matsunami, and T. Okano, *J. Appl. Phys.* **81** (1997) p. 3494.
- [4] M. Syväjärvi, R. Yakimova, H.H. Radamson, N.T. Son, Q. Wahab, I.G. Ivanov, and E. Janzén, *J. Crystal Growth* **197** (1999) p. 147.
- [5] M. Syväjärvi, R. Yakimova, M. Tuominen, A. Kakanakova-Georgieva, M.F. MacMillan, A. Henry, Q. Wahab, and E. Janzén, *J. Crystal Growth* **197** (1999) p. 155.
- [6] M. Tuominen, R. Yakimova, A. Vehanen, and E. Janzén, *Mat. Sci. Eng.* **B57** (1999) p. 228.
- [7] J.A. Powell, D.J. Larkin, P.B. Abel, L. Zhou, and P. Pirouz, *Inst. Phys. Conf. Ser.* **142** (1996) p. 77.
- [8] M. Syväjärvi, R. Yakimova, and E. Janzén, *J. Electrochemical Soc.* **146** (1999) p. 1565.
- [9] T. Kimoto and H. Matsunami, *J. Appl. Phys.* **76** (1994) p. 7322.
- [10] A.E. Nikolaev, V.A. Ivantsov, S.V. Rendakova, M.N. Mlashenkov, and V.A. Dmitriev, *J. Crystal Growth* **166** (1996) p. 607.
- [11] "Morphology of crystals", I. Sunagawa (Ed), Terra Scientific, Tokyo (1987), p. 515.
- [12] J. Yang, S. Nishino, M. Mehargany, and P. Pirouz, *Inst. Phys. Conf. Ser.* **137** (1994) p. 17.

Correspondence; Phone: +46 13 285708; Fax: +46 13 142337; E-mail: msy@ifm.liu.se

## Observation of Macrostep Formation on the (0001) Facet of Bulk SiC Crystals

N. Ohtani\*, M. Katsuno, T. Aigo, H. Yashiro and M. Kanaya

Advanced Technology Research Laboratories, Nippon Steel Corporation,  
20-1 Shintomi, Futtsu, Chiba 293-8511, Japan

**Keywords:** Growth Surface Morphology, Step Bunching, Step Kinetics, Step Repulsive Interaction

### Abstract

Surface topography of the (0001) facet plane of as-grown 6H-SiC bulk crystals was observed *ex-situ* by Nomarski optical microscopy (NOM) and atomic force microscopy (AFM). NOM observations revealed giant steps of a few micrometers in height on the (0001) growth facet, and it was found that a morphological transition of the growth facet occurred when the growth conditions were changed. AFM imaging of the stepped structure of 6H-SiC(0001) detected steps of height equal to the unit *c*-lattice parameter. They are fairly straight and very regularly arranged, giving rise to equidistant step trains. Upon nitrogen doping, these regular step trains on the 6H-SiC(0001)C surfaces became unstable: the equidistant step trains were transformed into meandering macrosteps of height greater than 10nm.

### Introduction

The macrostep formation (step bunching) is one of the characteristic morphological features of growing crystal surfaces, where the spacing between succeeding surface steps changes in some slowly varying manner. These step systems frequently exhibit typical step heights which are considerably greater than that of a monolayer. The importance of the step bunching phenomenon has been well recognised in crystal growth of many material systems. It would have a crucial effect on various aspects in crystal growth: for example, the step bunching into macrosteps may result in a dopant striation in grown crystals [1], and the resulting macroscopic roughness of the crystal surface could also affect the crystal quality. For thin film growth of SiC, macrostep formation causes a growth mode transition, from the step flow to two-dimensional (2D) nucleation, which subsequently leads to undesirable foreign polytype inclusions in the crystals [2]. In this paper, we report on the observation of the growth surface morphology of bulk 6H-SiC crystals and discuss the mechanism of step bunching during sublimation bulk crystal growth of SiC.

### Experimental

6H- and 4H-SiC crystals are grown by the physical vapor transport (PVT) method, where SiC source powder sublimates in a heated graphite crucible and is recrystallized on a slightly cooled seed crystal.

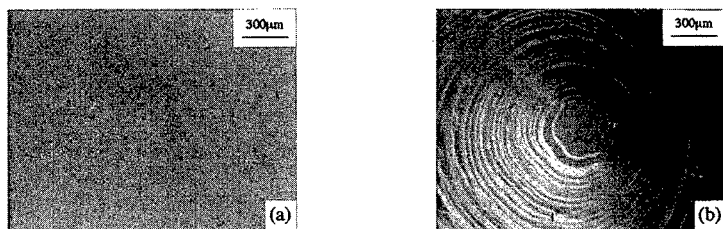


Fig. 1. Nomarski reflection optical micrographs from the 6H-SiC(0001)Si facet plane: (a) extremely smooth growth facet, and (b) concentric circular giant steps.

The growth system and conditions used in this study were previously described [3]. The crystals were nominally undoped or *n*-type doped with nitrogen in the range of mid  $10^{18}\text{cm}^{-3}$ . The nitrogen doping was carried out by adding gaseous nitrogen into the growth ambience. The top of the grown crystals was domed, where a flat (0001) facet appeared. The samples were examined by both Nomarski optical microscope (NOM) and atomic force microscope (AFM). NOM and AFM observations were conducted on the (0001)Si and the (000 $\bar{1}$ )C facets of 6H-SiC bulk crystals.

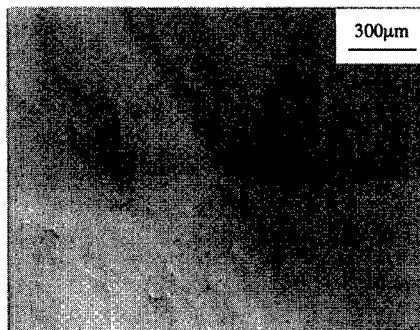


Fig. 2. NOM image of the 6H-SiC(000 $\bar{1}$ )C growth facet. A clear hexagonal symmetry around the *c*-axis with ridges in the six equivalent  $\langle 11\bar{2}0 \rangle$  directions was detected.

### Results and Discussion

Figure 1 shows NOM images of the growth surface morphology of the 6H-SiC(0001)Si facet, where either extremely smooth surface (Fig. 1(a)) or concentric circular giant steps whose height was in the order of a few micrometers (Fig. 1(b)) emerged on the surface. The occurrence of these two dissimilar surface morphologies appeared to be related to the fluctuation of growth conditions such as growth rate. Larger growth rates generally yielded the giant steps, and smaller growth rates resulted in a smooth surface morphology.

An optical microscope image of typical surface morphology observed on the 6H-SiC(000 $\bar{1}$ )C facet plane is shown in Fig. 2. As revealed in the figure, a clear hexagonal symmetry around the *c*-axis with ridges in the six equivalent  $\langle 11\bar{2}0 \rangle$  directions was observed. The hexagonal symmetry reflects the crystallographic symmetry of crystal, and the morphology on the 6H-SiC(000 $\bar{1}$ )C facet appeared stable even when the growth conditions, such as growth rate, fluctuated.

For 6H-SiC(0001)Si, AFM observations revealed a very regular stepped morphology for both the extremely smooth facet and the facet with the circular giant steps. Figure 3 shows a typical AFM image of the extremely smooth (0001)Si facet of nitrogen-doped 6H-SiC, where the observed area was  $5\mu\text{m} \times 5\mu\text{m}$ . A striking feature of the image is the highly regular character of the stepped structure. The steps do not meander and are very straight. For the undoped surface, we observed even more regular equidistant step trains.

The spacing between the steps was also fairly uniform and the average spacing was around  $1.4\mu\text{m}$ . In general, smooth vicinal SiC(0001) surfaces are assumed to provide steps of  $0.25\text{nm}$  height, which is the height of a single bilayer of Si and C atoms that are stacked in the *c*-direction to form various polytypes. The observed step height, however, was  $1.5\text{nm}$ , which is six times the bilayer height and corresponds to the unit *c*-lattice parameter of 6H-SiC ( $=1.512\text{nm}$ ). Steps of height less and more than the unit cell size, *e.g.*,  $1.25\text{nm}$ ,  $2.0\text{nm}$  and  $2.25\text{nm}$ , were also occasionally observed, however the surface was dominantly occupied by the unit cell size steps.

Figure 4(a) shows an AFM image of the undoped 6H-SiC(000 $\bar{1}$ )C surface, where the observed area was  $8.7\mu\text{m} \times 3\mu\text{m}$ . In the figure, a highly regular stepped structure similar to that on the 6H-SiC(0001)Si surface is observed; equidistant step trains appear on the

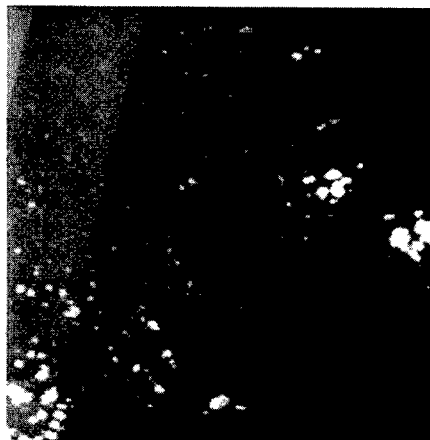


Fig. 3. AFM image of the stepped structure of the nitrogen-doped 6H-SiC(0001)Si surface grown by the PVT method. The step direction is from the upper left to the lower right.

surface and most of them have a step height of 1.5nm. The steps appear less stable compared to those on 6H-SiC(0001)Si and are often decomposed into two steps of identical height (0.75nm) equivalent to three Si-C bilayers. They are paired and placed close together (~50nm apart).

When the crystal was doped with nitrogen, the stepped morphology of the 6H-SiC(0001)C surface showed a drastic change. Figure 4(b) shows a

50 $\mu\text{m} \times 50\mu\text{m}$  AFM image of the (0001)C surface of nitrogen-doped 6H-SiC. The step behavior is largely different from that of the undoped crystal in several aspects. A major difference is the step bunching behavior: on nitrogen-doped 6H-SiC(0001)C, macrosteps, *i.e.*, steps much greater than the unit cell dimension, are observed. The height of macrosteps ranged from 7nm to greater than 15nm, ten times the unit height of the 6H polytype, and the average spacing between the macrosteps was 5–6 $\mu\text{m}$ . The macrosteps meandered, and often coalesced into larger steps or split into smaller steps. When a larger area observation was performed, the macrostep trains were found to be nominally directed in six equivalent  $\langle 1\bar{1}00 \rangle$  directions, reflecting the crystallographic symmetry of the crystal. The terraces between the macrosteps were occupied by steps of height from 0.5 to 3.0nm, among which the occurrence of 1.0nm height steps was relatively large.

In this study, we observed the unit cell size steps on the (0001) surfaces of PVT SiC crystals, which were highly regularly arranged, giving rise to an equidistant step train. In general, equidistant step trains can be achieved both energetically and kinetically. Asymmetric step kinetics (Schwoebel effect [4]) is one mechanism leading to a regularly arranged step structure, which has a larger sticking coefficient for adatoms reaching a step from the terrace under it compared to that for adatoms reaching the step from the terrace above it. Therefore the velocity of a step is high when the terrace under it is wide and small otherwise: there is a negative feedback, wide terraces shrink and narrow ones grow. Another possible mechanism is step repulsive interaction, which also gives rise to a fairly regular step distribution through the minimization process of the total surface energy. Both mechanisms provide similarly an equidistant step train, however we assume that the highly regular character of the step trains observed on 6H-SiC(0001) favors the step repulsion mechanism.

The unit cell size steps observed on SiC(0001) greatly repel each other due to the elastic step-step interaction [5]. Marchenko and Parshin [6] derived an analytical expression for the elastic potential between steps at the surface of an isotropic solid:

$$U(x) = \frac{2(1-\sigma^2)}{\pi E} (\beta a)^2 \frac{1}{x^2} \quad (1)$$

Here,  $E$  and  $\sigma$  are Young's modulus and Poisson's ratio, respectively,  $\beta$  is the surface tension at the step (step stiffness) and  $a$  the step height. For SiC(0001), the height of steps is as large as the  $c$ -lattice parameter, so that the step repulsive interaction is enhanced by one to two orders of magnitude compared to those on Si(111) and Si(001). The extremely uniform distribution of surface steps on SiC(0001) is a clear manifestation of the strong repulsive step interaction on the surface.

As revealed in Fig. 4(b), the equidistant step trains of unit cell dimension were unstable against nitrogen doping of crystal and bunched into meandering macrosteps of height greater than 10nm. Chien *et al.* demonstrated that a particular terrace with the lowest energy dominates the surface and the possible step bunching in 6H-SiC is the formation of three-bilayer height steps (ABC or ACB layer steps) [7]. Kimoto *et al.* [8] suggested that further step bunching up to the unit cell size steps results

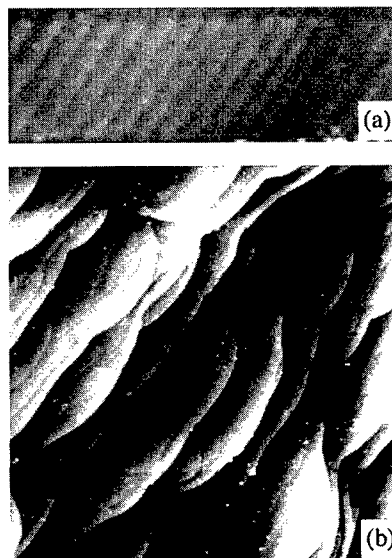


Fig. 4. AFM images of the stepped structure on (a) the undoped and (b) the nitrogen-doped 6H-SiC(0001)C surfaces. Upon nitrogen doping, meandering macrosteps evolved on the surface.

from the different incorporation probabilities of adatoms at the *ABC* and *ACB* type steps due to the different number of dangling bonds at the steps. However, the mechanism of further coalescence of the unit cell size steps (macrostep formation) has yet to be clarified.

Foreign particles and impurities deposited on the surface are a possible cause of step bunching, and the particles or impurity agglomeration could be too small to be visible for the scanning size used. However, we rarely observed sharp cusps along the steps, which are usually formed when steps are trying to squeeze through the fences of impurities, and thus the possibility of the impurity pinning being the cause of the step bunching is precluded.

Asymmetric step kinetics is another possible cause, leading to step bunching, which is the opposite case to that described for equidistant step trains: a smaller sticking coefficient for adatoms reaching a step from the terrace under it and a larger sticking coefficient for adatoms reaching the step from the terrace above it. However, such simple asymmetric kinetics for incorporation rates of adatoms from the upper and lower terraces only gives rise to local pairing of steps and does not bring about a large-scale modulation of step density like those observed on the nitrogen-doped 6H-SiC(0001)C surface.

Recently Sato and Uwaha demonstrated that such an equidistant step train with a repulsive step interaction becomes unstable by the asymmetric step kinetics and is transformed into a density-modulated step train at a long wavelength [9]. We assume that the nitrogen adsorption influences the stepped structure of 6H-SiC(0001)C through the modification of the asymmetric step kinetics. The adsorbed nitrogen enhances the incorporation rate of adatoms from the upper terraces or reduces that from the lower terraces; the detailed mechanism for this impurity-induced asymmetric step kinetics is not clear at present. The increased asymmetry in step kinetics by the nitrogen adsorption causes a morphological transition through the competition against the repulsive step interaction (stabilizing force): for the undoped 6H-SiC(0001)C, the repulsive step interaction dictates the equidistant step trains, while, for the doped 6H-SiC(0001)C, the increased asymmetry in step kinetics prevails over the repulsive step interaction, resulting in the step bunching.

It is clear from Eq. 1 that a larger step energy (step stiffness)  $\beta$  yields a larger step repulsion force. Since 6H-SiC(0001)Si has proved to be an extremely stable surface [10], a large step energy and consequent step interaction are expected during crystal growth on 6H-SiC(0001)Si. As revealed in Fig. 3, equidistant step trains remained stable even under nitrogen doping. For the nitrogen-doped 6H-SiC(0001)Si, the strong step repulsion force due to the large step stiffness overcomes the increased asymmetry in step kinetics by the nitrogen adsorption and preserves a highly uniform equidistant step train. The extremely smooth step edges observed on the doped 6H-SiC(0001)Si surface lend support to this conclusion.

Finally, we note that the existence of an energetic step-step repulsion also provides a natural mechanism for the formation of giant steps observed on the 6H-SiC(0001)Si facet. For the 6H-SiC(0001)Si facet, we observed concentric circular giant steps of height in the order of a few micrometers when the growth rate was large. Assuming that the steps emanate from a spiral growth center, a larger growth rate, *i.e.* larger supersaturation results in a smaller step separation. In general, an isolated giant step costs more energy than equivalent height of distributed unit cell size steps. However, with increasing growth rate (supersaturation) and consequently with increasing step density, this energy is outweighed by the decrease in step repulsive energy since the formation of giant steps increases the average separation between the unit cell size steps.

## References

- [1] E. Bauser, H.P. Strunk, *J. Cryst. Growth* 69 (1984) p. 561.
- [2] T. Kimoto, Matsunami, *J. Appl. Phys.* 75 (1994) 850.
- [3] J. Takahashi, M. Kanaya, Y. Fujiwara, *J. Cryst. Growth* 135 (1994) p. 61.
- [4] R.L. Schwoebel, E.J. Shipsey, *J. Appl. Phys.* 37 (1966) p. 3682.
- [5] N. Ohtani, M. Katsuno, J. Takahashi, H. Yashiro, M. Kanaya, *Phys. Rev. B* 59 (1999) p. 4592.
- [6] V.I. Marchenko, A.Ya. Parshin, *Sov. Phys. JETP* 52 (1980) p. 129.
- [7] F.R. Chien, S.R. Nutt, W.S. Yoo, T. Kimoto, H. Matsunami, *J. Mater. Res.* 8 (1994) p. 940.
- [8] T. Kimoto, A. Itoh, H. Matsunami, *Appl. Phys. Lett.* 66 (1995) p. 3645.
- [9] M. Sato, M. Uwaha, *Phys. Rev. B* 51 (1995) p. 11172.
- [10] L. Muehlhoff, W.J. Choyke, M.J. Bozack, J.T. Yates, Jr., *J. Appl. Phys.* 60 (1986) p. 2842.

\*Corresponding author: Fax +81-439-80-2746; e-mail: ohtani@re.nsc.co.jp

## Silicate Monolayers on the Hexagonal Surfaces of 4H- and 6H-SiC

J. Bernhardt, J. Schardt, U. Starke and K. Heinz

Lehrstuhl für Festkörperphysik, Friedrich-Alexander Universität Erlangen-Nürnberg,  
Staudtstr. 7, DE-91058 Erlangen, Germany

**Keywords:** Hexagonal Surfaces, Low-Energy Electron Diffraction, Oxide, Reconstruction, SiO<sub>2</sub>/SiC Interface, Surface Structure

**Abstract.** Using thermal hydrogen etching or a microwave powered hydrogen plasma for *ex-situ* preparation, a  $(\sqrt{3} \times \sqrt{3})R30^\circ$  reconstruction can be prepared on both {0001} oriented hexagonal surfaces of 4H and 6H silicon carbide. Their structures are determined using Auger electron spectroscopy (AES) and quantitative low-energy electron diffraction (LEED). The surfaces of both orientations are found to be terminated by a monolayer of silicon oxide, whose bond angles and bond lengths agree with those of bulk SiO<sub>2</sub>. This adlayer strongly passivates the semiconductor surfaces. Thus, the reconstruction is stable in air and against annealing up to 1000°C in ultra high vacuum. Due to the epitaxial relationship the adlayer may serve as a seed for growing crystalline SiO<sub>2</sub> and therefore enable the formation of high quality SiO<sub>2</sub>/SiC interfaces.

### Introduction

One of the shortcomings in SiC device technology is the poor electronic quality of the oxide-semiconductor interface compared to Si based devices. According to a variety of investigations this is, in short, due to chemical disorder - which is inevitably related to structural disorder - of the interface region [1]. In this paper we introduce a preparation method which induces the formation of an ideal oxide-semiconductor interface, i.e. an epitaxial oxide monolayer on both hexagonal surfaces of 6H- and 4H-SiC [2]. The atomic geometry of this adlayer and the underlying SiC was determined using Auger electron spectroscopy (AES) and quantitative low-energy electron diffraction (LEED). We discuss the structure of the reconstructed surfaces and envisage potential applications of this particular configuration.

### Experimental

Both orientations of hexagonal {0001} SiC surfaces were investigated. We used commercially available (000 $\bar{1}$ ) oriented 6H- and 4H-SiC wafers (CREE, research-grade) and homoepitaxial, chemical vapor deposition (CVD) grown 4H- and 6H-SiC(0001) film samples (all material n-type doped). In order to remove possible structural damages a sacrificial oxidation was performed which, after removal of the oxide with hydrofluoric acid (HF), yields atomically flat and bulk truncated surfaces [3, 4]. Then the samples were either etched in a CVD system with H<sub>2</sub> gas flow under atmospheric pressure (sample temperature 1500°C for 5 min, H<sub>2</sub> flow 3000 sccm, H<sub>2</sub> supply switched on/off at ~1000°C sample temperature) or, performed only with the 6H-SiC(000 $\bar{1}$ ) samples, treated with hydrogen plasma (H<sub>2</sub> pressure  $5 \times 10^3$  Pa, H<sub>2</sub> mass flow 100 sccm, sample temperature ~800°C, microwave power 500 W for 30 min, sample unbiased). Without further treatment the samples were then introduced into the ultra high vacuum (UHV) analysis system. For the quantitative LEED structure analyses intensity versus energy spectra, I(E), were recorded using a video LEED data acquisition system [5]. The spectra were also used as a fingerprint in order to identify similar or different structures

resulting e.g. after different preparation procedures [3, 4]. Complementary information regarding the elemental composition of the surface was obtained from AES measurements.

## Results

Without further treatment in the analysis chamber, the samples showed a well developed  $(\sqrt{3} \times \sqrt{3})R30^\circ$  periodic LEED pattern with bright and sharp diffraction spots and low background (Fig. 1). Based on comparison of the corresponding  $I(E)$  spectra we can conclude that for a given orientation the resulting structure does neither depend on the substrate polytype nor on the hydrogen preparation used. The average intensity of the fractional order beams was more than half of that of the integer order beams indicative for a rather strong reconstruction. The

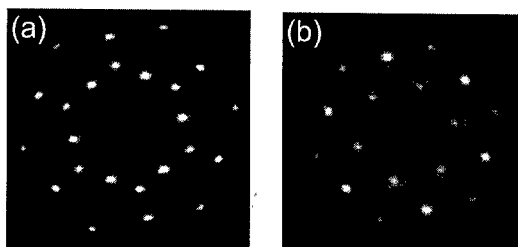


**Figure 1:** LEED patterns of the *ex-situ* prepared, as-introduced  $(\sqrt{3} \times \sqrt{3})R30^\circ$  reconstructed SiC surfaces. (a) 6H-SiC(0001) at 164 eV, (b) 4H-SiC(0001) at 115 eV.

reconstruction is stable, even when exposed to air and reloaded again, or against degassing at temperatures below  $1000^\circ\text{C}$  in UHV. Even more remarkable, on the (0001) samples the  $(\sqrt{3} \times \sqrt{3})R30^\circ$  reconstruction withstands HF etching. Upon reintroduction after treatment in 5% HF and again in 50% HF (both for 10 min), the samples showed basically the same  $I(E)$  spectra (Fig. 2). Therefore, despite a somewhat higher background the atomic order of the surface seems to be preserved even after such harsh treatment. However, the (0001) oriented samples exhibited a  $(1 \times 1)$  pattern after such treatments and  $I(E)$  spectra indicated bulk truncated SiC surfaces similar to those reported in [3, 4].

Typical AES spectra, obtained after degassing, are shown in Fig. 3. On both surface orientations, besides the peaks of the two bulk components silicon and carbon, an oxygen signal and an additional feature around 65 eV originating from oxygen-bonded silicon is detected. Based on peak-to-peak height comparison of the differentiated signals the amount of oxygen can be roughly estimated to be about one monolayer. Both oxygen-related signals vanish when the samples are heated to temperatures above  $1000^\circ\text{C}$ . This is accompanied by an orientation specific change in the atomic geometry as

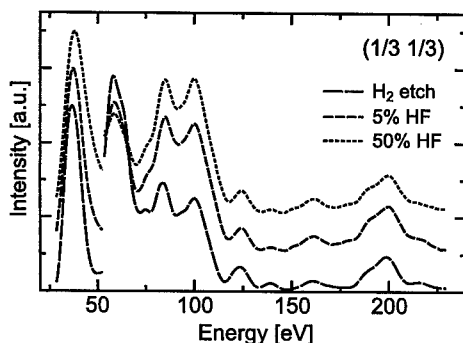


**Figure 2:** LEED  $I(E)$  spectra of the  $(\frac{1}{3} \frac{1}{3})$  spot taken from one  $(\sqrt{3} \times \sqrt{3})R30^\circ$  reconstructed 6H-SiC(0001) sample after  $\text{H}_2$  plasma preparation, after additional treatment with 5% and finally again with 50% hydrofluoric acid, both for 10 min (zero line shifted for each curve; intensity scale enlarged above 53 eV).

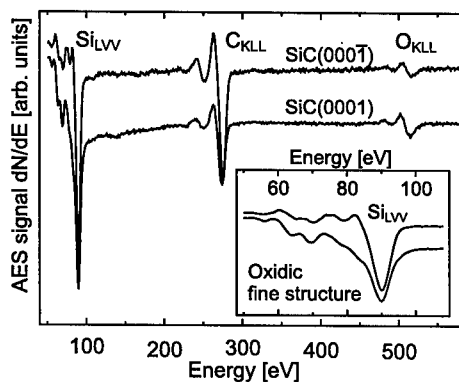
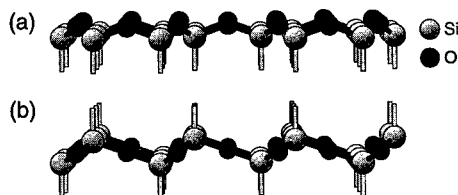
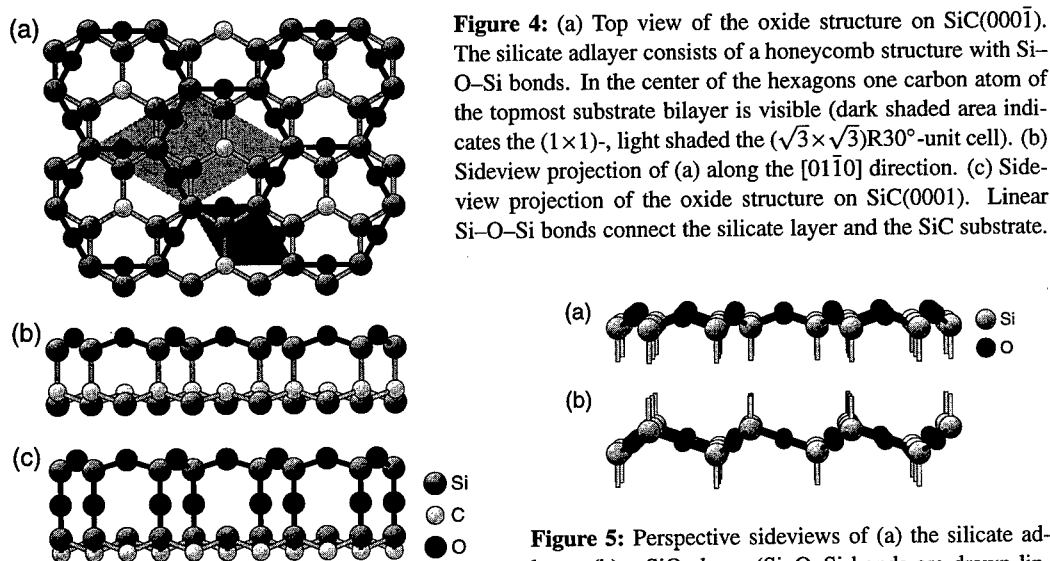


**Figure 3:** AES spectra obtained for the  $(\sqrt{3} \times \sqrt{3})R30^\circ$  reconstructed hexagonal SiC surfaces. Besides the bulk components Si and C, an oxygen as well as an oxygen-related silicon signal is detected. The inset displays the  $\text{Si}_{\text{LVV}}$  peak on a spread energy scale.



observed in the LEED pattern: on  $(000\bar{1})$  oriented surfaces a  $(3 \times 3)$  develops above  $1050^\circ\text{C}$  [6]; the LEED pattern of the  $(0001)$  surfaces remains  $(\sqrt{3} \times \sqrt{3})R30^\circ$  periodic when annealing above  $1000^\circ\text{C}$ . However, the I(E) spectra change drastically indicating a completely different surface structure described earlier [7]. Conclusively, these findings strongly support the assumption that oxygen is rather involved in the reconstruction than a contaminant in disordered areas.



To derive a complete picture of these oxygen containing reconstructions we performed quantitative LEED structure analyses. The electron scattering was calculated full dynamically; Tensor LEED and an automated search procedure were used for the structural refinement [5]. The agreement between computed and measured spectra was quantified by the Pendry R-factor.

We first focus on the  $(000\bar{1})$  surfaces. A silicon oxide layer is found to reside on an otherwise bulk-truncated crystal (Fig. 4a+b). The two silicon atoms in the adlayer form a honeycomb arrangement. Three oxygen atoms each connecting two of the silicon atoms complete the layer to a ring type structure as shown in the top view (Fig. 4a). In the side view (b) it can be seen that these oxygen atoms reside above the silicon atoms; the vertical distance was determined to be  $0.47 \text{ \AA}$ . Given the lateral lattice parameter for SiC of  $3.08 \text{ \AA}$ , a bond length of  $1.61 \text{ \AA}$  and a bond angle  $\varphi(\text{Si-O-Si})$  of  $146^\circ$  can be derived for the adlayer. As this structure resembles the layers found in sheet silicates we denote the adlayer *silicate adlayer*. The silicon atoms of the adlayer are bonded to carbon atoms of the topmost bulk bilayer (Fig. 4b). Note, that those carbon atoms maintain a fourth bulk-type Si-C bond ( $d_{\text{Si(adlayer)-C}} = 1.90 \text{ \AA}$ ) in this arrangement. For one carbon atom of the surface unit cell no saturating adspecies could be found in the LEED analysis. However, due to the nature of the preparation process, hydrogen is likely to passivate this dangling bond, though this cannot be confirmed by the LEED analysis due to the low scattering power of hydrogen. The excellent quality of the fit, which is possible to be achieved by the high degree of surface ordering resulting from our preparation, is reflected by a rather low Pendry R-factor of 0.14. On the oxidic  $\text{SiC}(0001)-(\sqrt{3} \times \sqrt{3})R30^\circ$  surfaces, a similar adlayer is found, however, here it is connected to the silicon atoms of the underlying SiC bilayer via linearly bridged oxygen (Fig. 4c). A somewhat higher but still satisfying Pendry R-factor of 0.20 is achieved for the  $\text{SiC}(0001)$  surfaces. This may be due to the enhanced complexity of the

adstructure which in turn makes it more difficult to achieve an equally high level of order as on the (000 $\bar{1}$ ) oriented samples.

### Discussion

With the results described above, one can easily explain the inertness of the hydrogen treated surfaces. All atoms in the adlayer are saturated, the only remaining broken bond (one per  $(\sqrt{3} \times \sqrt{3})R30^\circ$  unit cell) is located at carbon atoms of the topmost substrate bilayer and therefore shielded by the rigid oxide adlayer. Furthermore, the structures determined provide a possible explanation for the resistance against HF different for the two orientations. Assuming HF to attack Si-O but not Si-C bonds, on the SiC(000 $\bar{1}$ ) surfaces the adlayer may be only partially dissolved, i.e. the silicon atoms of the adlayer should remain on the surface due to their Si-C backbond. When taken out of the HF solution, the exposed Si atoms would immediately oxidize again restoring the initial adlayer. On the (0001) oriented surfaces, however, with HF destroying all Si-O bonds the complete adstructure is removed. The subsequent reoxidation proceeds statistically with no long range order resulting in the known (1 $\times$ 1) periodic, bulk-truncated surfaces with statistical oxygen coverage [3, 4].

We can only speculate how the ordered oxide layers develop. Up to now, for *ex-situ* prepared samples only (1 $\times$ 1) periodic diffraction patterns were observed. Those reflect the symmetry of the bulk below some disordered oxide having resulted from statistical oxidation of the bulk truncated surface. Siliconoxide is not stable during the hydrogen-using preparations. Therefore, we conclude that a  $(\sqrt{3} \times \sqrt{3})R30^\circ$  ordering is triggered by the preparation which then leads to the formation of the ordered oxide layer when the surface is exposed to air.

The surface structures described here may find applications in two areas. First, the inertness of the sample can be utilized as an effective passivation for this semiconductor material. Second, the general layout and the geometrical parameters of the adlayers, i.e. Si-O bond lengths of 1.61Å-1.63Å and Si-O-Si bond angles of 141°-146° compare very well to those of typical SiO<sub>2</sub> bulk phases. By only a slight modification - every second Si atom of the adlayer has to move upwards - adding further SiO<sub>2</sub> layers can be facilitated (see Fig. 5). So, there might be a chance that by using the structures as seed for depositing siliconoxide a perfect epitaxy between semiconductor and oxide can be obtained. This would considerably reduce the electronic interface defect density, a serious problem for SiC based oxide-semiconductor structures.

This work was supported by Deutsche Forschungsgemeinschaft (DFG) through SFB 292. We thank M. Stammeler and K. Christiansen for performing the hydrogen preparations.

### References

- [1] V. V. Afanasev, M. Bassler, G. Pensl, and M. Schulz, Phys. Stat. Sol. (a) **162** (1997), p. 321, and references therein.
- [2] J. Bernhardt, J. Schardt, U. Starke, and K. Heinz, Appl. Phys. Lett. **74** (1999), p. 1084.
- [3] U. Starke, Phys. Stat. Sol. (b) **202** (1997), p. 475.
- [4] J. Schardt, J. Bernhardt, M. Franke, U. Starke, and K. Heinz, Mat. Sci. Forum **264** (1998), p. 343.
- [5] K. Heinz, and L. Hammer, Z. Kristallogr. **213** (1998), p. 615, and references therein.
- [6] J. Bernhardt, M. Nerdling, U. Starke, and K. Heinz, Mat. Sci. Eng. **B61-62** (1999), p. 206.
- [7] U. Starke, J. Schardt, J. Bernhardt, M. Franke, and K. Heinz, Phys. Rev. Lett. **82** (1999), p. 2107.

\* corresponding author. phone: +49 91 31 - 852 84 05, fax: +49 91 31 - 852 84 00  
email: jbernhardt@fkp.physik.uni-erlangen.de

## Electronic and Atomic Structure of an Ordered Silicate Adlayer on Hexagonal SiC

M. Hollering<sup>1</sup>, N. Sieber<sup>1</sup>, F. Maier<sup>1</sup>, J. Ristein<sup>1</sup>, L. Ley<sup>1</sup>, J.D. Riley<sup>2</sup>,  
R.C.G. Leckey<sup>2</sup>, F. Leisenberger<sup>3</sup> and F. Netzer<sup>3</sup>

<sup>1</sup> Institut für Technische Physik II, Universität Erlangen-Nürnberg,  
Erwin-Rommel-Str. 1, DE-91058 Erlangen, Germany

<sup>2</sup> Department of Physics, La Trobe University, Australia

<sup>3</sup> Karl-Franzens-Universität Graz, Austria

**Keywords:** Angle Resolved Photoelectron Spectroscopy, Silicon Oxide, Surface States, X-Ray Induced Photoelectron Spectroscopy

**Abstract.** We prepared an ordered oxide adlayer with  $(\sqrt{3} \times \sqrt{3})R30^\circ$  periodicity on carbon-terminated 6H-SiC(000 $\bar{1}$ ) by means of a hydrogen microwave plasma. This adlayer was investigated by X-ray induced photoelectron spectroscopy (XPS) and angle resolved ultra-violet photoelectron spectroscopy (ARUPS). The XPS results are in good agreement with the recently published atomic structure of the adlayer. The ARUP spectra reveal oxygen derived surface states at 6,  $\sim 10$ , and 24 eV binding energy and a dangling bond state 0.4 eV above the valence band maximum. The band bending of 1.1 eV is compatible with a description of the dangling bond state as the lower Hubbard band with a Hubbard  $U$  of  $> 1.4$  eV.

### 1 Introduction

The formation of an insulating oxide layer on SiC is a key requirement for any device based on this new semiconductor material. Most of the investigations performed by photoelectron spectroscopy deal with the interface between the SiC bulk material and amorphous oxide layers of different thicknesses [1, 2]. In our work we study the atomic configuration and the electronic properties of an ordered silicon oxide with a thickness of one monolayer. For this purpose we use high resolution X-ray photoelectron spectroscopy (XPS) and angle resolved ultra-violet photoelectron spectroscopy (ARUPS).

### 2 Experiment

The C-terminated 6H-SiC samples (substrate material by Cree Res., Inc.) were polished in a hydrogen microwave plasma (power 500 W,  $H_2$  pressure  $5 \times 10^3$  Pa,  $H_2$  mass flow 100 sccm, sample temperature  $\approx 800^\circ\text{C}$ ) which etches the surface and yields ordered surface phases. This surface spontaneously oxidizes at room temperature in atmosphere and shows a  $(\sqrt{3} \times \sqrt{3})R30^\circ$  LEED pattern immediately after introduction into the vacuum. Nevertheless, the samples were heated *in situ* up to  $650^\circ\text{C}$  in order to evaporate physisorbed hydrocarbons and water. For the highly resolved XPS and the ARUPS measurements we used synchrotron radiation of the Berlin electron storage ring BESSY. A Scienta analyser was used at the monochromator PM5 ( $\Delta E \approx 280$  meV for the Si 2p core line at  $h\nu = 150$  eV). In order to clarify the stoichiometry of the examined sample surfaces a curve fitting procedure was applied to the recorded spectra using a Voigt line shape. The ARUPS data were acquired with a toroidal energy analyser [3] at TGM4 of BESSY. The energy resolution there was 250 meV and the angular resolution about  $\pm 2^\circ$ .

### 3 Results and Discussion

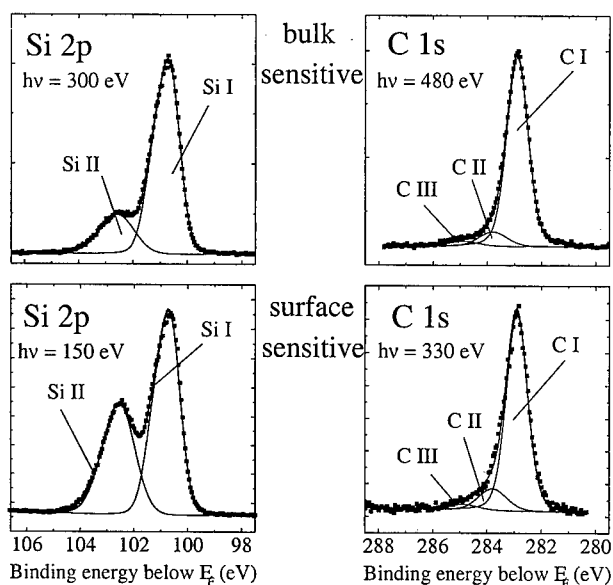


Figure 1: Core level spectra.

$h\nu = 150$  eV is more than twice as large as for  $h\nu = 300$  eV these silicon atoms must be located in a surface layer.

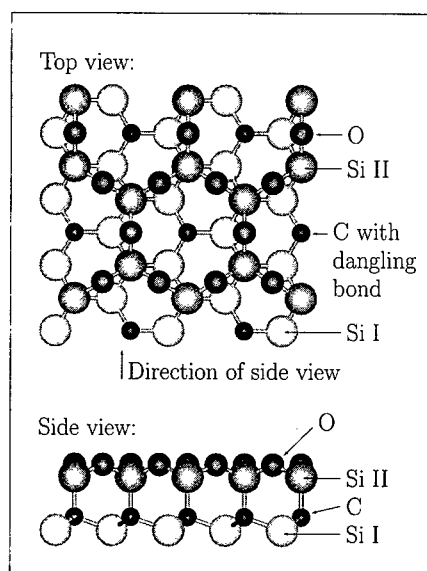


Figure 2: Atomic configuration of the silicate adlayer on 6H-SiC(000 $\bar{1}$ ).

bonded to a Si atom of the oxide layer and thus has a *dangling bond* (Fig. 2).

Valence band spectra of this surface were recorded at 50 and 60 eV photon energy along the azimuths  $\bar{\Gamma}M'$  and  $\bar{\Gamma}K'$ . Figs. 3a and 3b show the dispersion of a surface state *S* between 9.1 and 11.0 eV binding energy below the valence band maximum (VBM) within the ionic gap of

Fig. 1 shows high resolution core level spectra of Si 2p and C 1s. They were recorded with photon energies which constitute "bulk" sensitive (upper spectra in Fig. 1) and "surface" sensitive (lower spectra) measurements, respectively. The Si 2p lines (left spectra) were fitted with a bulk component (Si I) at a binding energy of 100.6 eV below the Fermi edge and a second component Si II shifted by 1.8 eV to higher binding energies. On account of the chemical shift, Si II is attributed to silicon atoms bonded to three oxygen atoms and one carbon atom. The estimated energy shift of around 1.6 eV for this configuration on the basis of known group shifts is slightly lower.

As the intensity ratio Si II/Si I for

For the C 1s spectrum a main component (C I) at 282.9 eV is observed. Two further components are shifted by 0.8 eV (C II) and 2.1 eV (C III) to higher binding energies, respectively. The origin of C II can be explained with a surface core level shift. As C is more electronegative than Si a missing Si bonding partner at C atoms of the topmost SiC bilayer causes a decrease of valence charge density at C, and therefore, the C 1s binding energy is expected to increase. C III is the contribution of small graphitized areas which arise in the course of the preparation. However, these surface areas are negligible as judged by the integrated intensity of C III that amounts to no more than 5% of the entire C 1s intensity for the surface sensitive spectrum at 330 eV photon energy. All these findings are in agreement with a structural model for this reconstruction as derived from a LEED I(E) analysis [4]: Si atoms which are located *on top* of C atoms in the bulk-terminating substrate bilayer are connected by oxygen atoms in bridge sites. One third of the C atoms in the bulk-terminating substrate layer is not

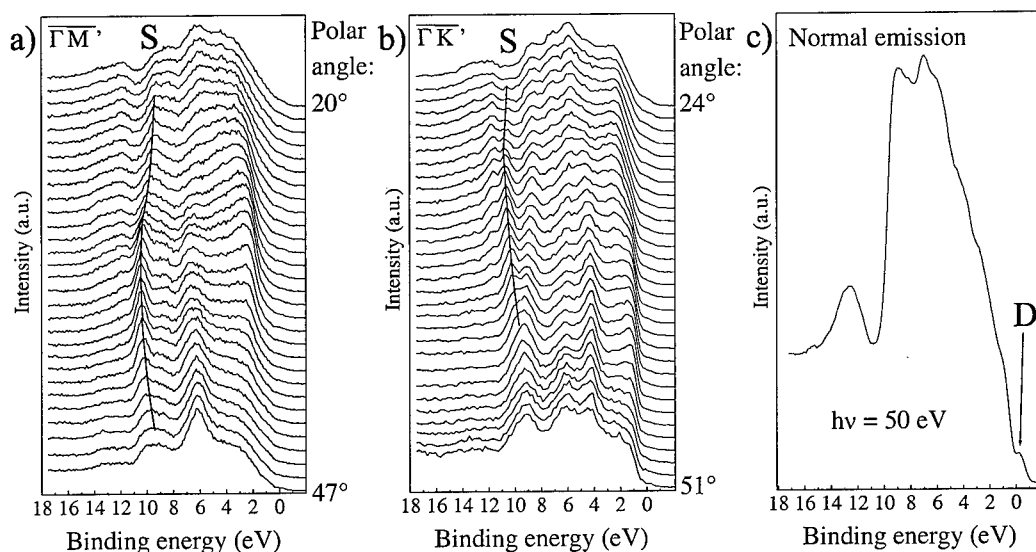


Figure 3: Valence band spectra for the azimuths (a)  $\bar{\Gamma}\bar{M}'$  ( $h\nu = 60$  eV) and (b)  $\bar{\Gamma}\bar{K}'$  ( $h\nu = 50$  eV). (c) Normal emission spectrum.

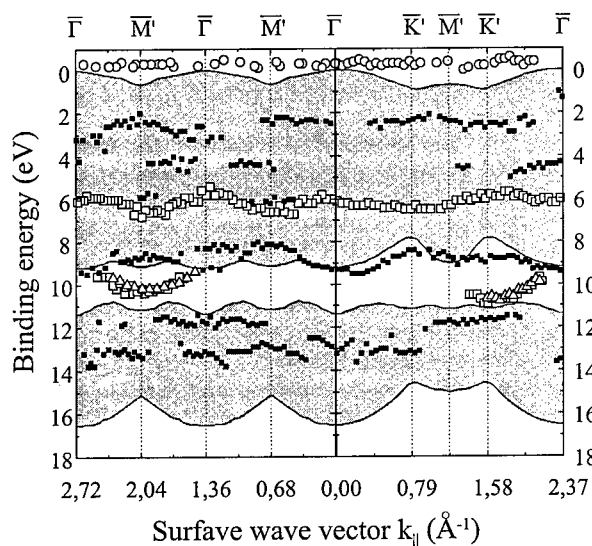


Figure 4: Energy dispersion  $E(k_{\parallel})$  for the azimuths  $\bar{\Gamma}\bar{M}'$  and  $\bar{\Gamma}\bar{K}'$ . The zero of energy is the valence band maximum.

0.4 eV above the VBM (Figs. 3c and 4) which has considerably weaker intensity than *S* and does not show a distinct dispersion. The energy of *D* is typical for a dangling bond state and indeed in the structural model one third of the C atoms of the topmost SiC bilayer has a dangling bond. These dangling bonds are saturated by adsorbates when the sample is exposed to air after the plasma treatment because the energy of any bonding state is considerably lower than the dangling bond state. Therefore, the state *D* is not visible in the spectra before annealing.

the projected bulk band structure. The dispersion is the same for both photon energies and it fulfills the symmetry requirements for the azimuth  $\bar{\Gamma}\bar{M}'$  (Fig. 4). On the basis of previous investigations of the electronic structure of stoichiometric  $\alpha$ -quartz [5] and amorphous nonstoichiometric silicon oxide [6] we conclude that the state *S* corresponds to oxygen(2p)-silicon(3s,3p) bonding states of the well ordered silicon oxide monolayer. Another feature at around 6 eV binding energy (cf. Fig. 4) can be attributed to emission from the non-bonding oxygen(2p) state. Not shown in the figures is the core like oxygen(2s) state at 24 eV binding energy which we observed in our spectra as well.

There is also a surface state *D* around

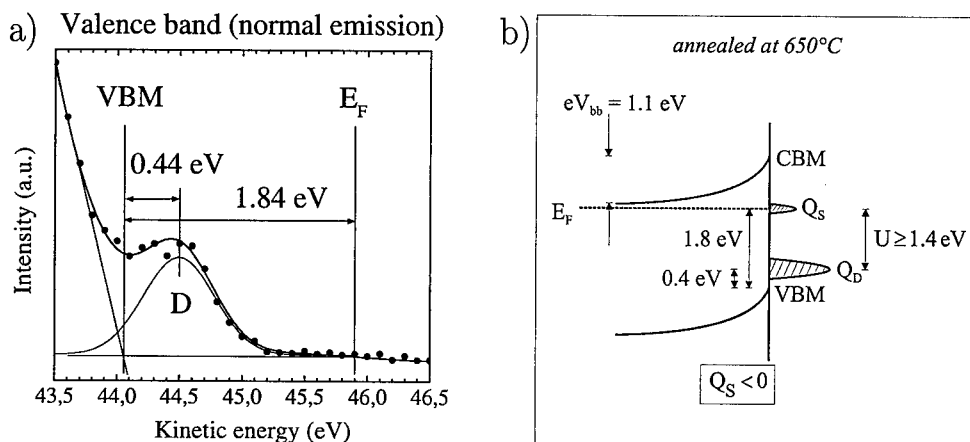


Figure 5: a) Surface state  $D$  above VBM. b) Band bending after annealing.

$D$  is located around 1.4 eV below the Fermi energy  $E_F$  (Fig. 5a) which is in contradiction to the expectation that for one dangling bond per surface unit mesh a half filled surface band crosses the Fermi edge. One possible explanation could be that  $D$  is more likely due to a disordered array of dangling bond defect states rather than a surface state band. On the other hand the question arises if  $D$  should be identified with the lower Hubbard band of a highly correlated surface band. This possibility was discussed for the  $(\sqrt{3} \times \sqrt{3})R30^\circ$  reconstruction on Si-terminated 4H- and 6H-SiC(0001) [7]. In this context we consider the experimentally observed band bending  $eV_{bb}$  of 1.1 eV after annealing (Fig. 5b). This indicates that the energy position of  $E_F$  is pinned by a negative surface charge  $Q_s$  at 1.8 eV above the VBM. If we assume that Hubbard bands are established and  $Q_s$  resides in the upper Hubbard band then we deduce from the pinned position of  $E_F$  1.4 eV above  $D$  that 1.4 eV is a lower limit for the Hubbard correlation energy  $U$ . From the measured value of  $eV_{bb}$  we can estimate that  $Q_s$  is only about 1% of the charge density  $Q_D$  which resides in the dangling bond state  $D$ . Therefore,  $Q_s$  is not sufficient to be detected in the spectra.

In summary, we prepared a well ordered silicon oxide adlayer with  $(\sqrt{3} \times \sqrt{3})R30^\circ$  periodicity on 6H-SiC(0001). The electronic structure of this adlayer is characterized by oxygen derived states, in particular a dispersing O(2p)-Si(3s,3p) bonding state, and a dangling bond state above the VBM.

This work was supported by BMBF under contract No. 05 SE8 WEA0, and by the Deutsche Forschungsgemeinschaft, SFB 292.

## References

- [1] B.Hornetz, H.-J.Michel and J.Halbritter, J.Mater.Res. **9** (1994) 3088.
- [2] B.Mattern, M.Bassler, G.Pensl and L.Ley, Mater.Sci.Forum **264-268** (1998) p. 375.
- [3] R.C.G.Leckey and J.D.Riley, Appl.Surf.Sci. **22/23** (1985) 196.
- [4] J.Bernhardt, J.Schardt, U.Starke and K.Heinz, Appl.Phys.Lett. **74** (1999) 1084.
- [5] J.R.Chelikowsky and M.Schlüter, Phys.Rev.B **15** (1977) 4020.
- [6] F.G.Bell and L.Ley, Phys.Rev.B **37** (1988) 8383.
- [7] J.E.Northrup, J.Neugebauer, Phys.Rev.B **57** (1998) R4230.

## Photoemission Study of the Silicate Adlayer Reconstruction on Si-terminated 6H-SiC (0001)

N. Sieber, M. Hollering, J. Ristein and L. Ley

Institut für Technische Physik II, Universität Erlangen-Nürnberg,  
Erwin-Rommel-Str. 1, DE-91058 Erlangen, Germany

**Keywords:** Photoelectron Spectroscopy, Silicate Adlayer, Silicon Dioxide, Surface States

**Abstract** We present a photoemission study of a highly ordered silicate adlayer structure on Si-terminated 6H-SiC showing a  $(\sqrt{3}\times\sqrt{3})R30^\circ$  LEED pattern. The adlayer has a nominal stoichiometry of  $\text{SiO}_2$  and forms during the preparation of 6H-SiC (0001) at 1000 °C in  $5\cdot 10^4$  Pa of hydrogen. The binding energy signature of the Si 2p (three components), C 1s (one component) and O 1s (one component) core level spectra is compatible with a structural model of the adlayer as derived from a previously published LEED analysis. Angle resolved valence band spectra show a surface state in the ionic gap of SiC assigned to Si-O bonding states. A silicon dangling bond state that is expected on the basis of the structural model for the adlayer is not observed. An analysis of the relative intensities of the three Si 2p components indicates that the dangling bond is initially hydrogen terminated and transforms into a Si-O bond above 500 °C.

### Introduction

The production of high quality MOSFET devices on SiC requires a thin insulating layer with a low density of defect states. As on silicon the most convenient insulating material for SiC is  $\text{SiO}_2$  since it is readily formed by thermal oxidation at temperatures of about 1100°C. However, up to now it is not possible to produce  $\text{SiO}_2$  layers on SiC with low interface defect densities. All studies report defect densities about two magnitudes higher than those attained at the Si/SiO<sub>2</sub> interface. The problem appears to be the efficient removal of excess carbon; a carbon cluster model was proposed which could explain the poor interface properties by invoking  $\text{sp}^2$ - and  $\text{sp}^3$ - bonded carbon clusters which remain at the SiC/SiO<sub>2</sub> interface after oxidation [1,2].

Here we consider a highly ordered, oxygen rich  $(\sqrt{3}\times\sqrt{3})R30^\circ$  reconstruction that develops during a hydrogen treatment of 6H-SiC (0001) at elevated temperatures. According to a LEED study a model for this surface was developed that involves a silicate adlayer structure on top of SiC with a two dimensional network of Si atoms connected by oxygen bridges to form hexagonal rings. Each Si atom is furthermore connected to the topmost bulk silicon atom of SiC by a linear oxygen bridge [3]. This surface might be an excellent starting point for the growth of  $\text{SiO}_2$  on SiC to improve the interface qualities since it is stable in ambient air and the bond lengths and angles of the adlayer fit those of bulk  $\text{SiO}_2$  quite well.

We present here a study of this surface using high resolution core level and angle resolved photoelectron spectroscopy. The nature of the Si 2p, C 1s and O 1s core level spectra and of valence band features are discussed in terms of the atomic structure given by the LEED model.

## Experiment

In order to produce the  $(\sqrt{3}\times\sqrt{3})R30^\circ$  surface phase the SiC samples (epitaxially overgrown 6H-SiC (0001), CREE Research) were first treated chemically and subsequently introduced into the preparation chamber with a base pressure of  $2\times 10^{-6}$  Pa. Using infrared radiation the sample mounted on a graphite susceptor inside a quartz tube was heated to 1000 °C in a hydrogen (6.0) atmosphere. The  $H_2$  pressure was  $5\cdot 10^{-4}$  Pa and a gas flow of 4 slm was maintained 30 min. To avoid atmospheric contamination the samples were transferred under ultra high vacuum (UHV) conditions between preparation and analysis chambers. Here they were examined by photoelectron spectroscopy and the surface reconstruction was verified by LEED. The core level spectra were taken using the Mg  $K_\alpha$  line as exciting source and at higher resolution the PM5 beamline at the BESSY storage ring. The angle resolved photoemission measurements were also carried out at the BESSY storage ring (beamline TGM4) using a toroidal energy analyzer [4] with an energy resolution of 0.25 eV and an angle resolution of  $\pm 2^\circ$ . All core level spectra were fitted using Voigt functions.

Additionally, the sample was heated up to 1300 °C in UHV to study the temperature stability of the silicate adlayer structure. The annealing temperatures were measured with an optical infrared pyrometer which measures the temperature of the sample holder and the real sample temperatures are about 150°C lower with an error of  $\pm 50$  °C [5].

## Results and Discussion

The LEED pattern of the as prepared sample is depicted in Fig 1a) and shows a clear  $(\sqrt{3}\times\sqrt{3})R30^\circ$  structure. Annealing the sample at 1200° leads to a (1x1) LEED pattern (Fig. 1c) via an intermediate state in the range of 1000°C to 1100°C with increased background intensity and streaks between the reconstruction reflexes (Fig. 1b). This points towards a structural change of the surface which is also observable in the Si 2p core level and in the valence band spectra. A set of core level spectra for the as prepared surface is shown in Fig. 2.

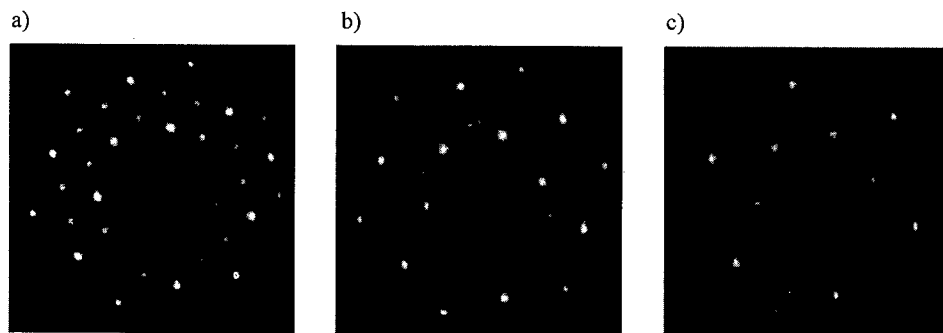


Fig. 1. LEED pictures from the as prepared surface (a), after annealing at 1000°C (b) and 1200°C (c).

The C 1s spectrum shows one component which must be ascribed to bulk SiC. Also, the O 1s spectrum shows essentially one component in agreement with the adlayer model where oxygen is bonded in one configuration only, namely in the Si-O-Si bridge bond. The Si 2p core level spectra exhibit three components. Si I can be attributed to bulk SiC and Si II to Si atoms in a  $C_3$ -Si-O environment which form the anchoring atoms for the adlayer. Si III, finally represents the Si atoms in an  $O_4$ -Si environment which constitute the adlayer. The chemical shifts of 0.6 eV (Si II - Si I) and 1.8 eV (Si III - Si I) are in agreement with this assignment on the basis of known group shifts for Si-C and Si-O bonds.

According to the structural model a fourth, chemically different Si atom at the SiC (0001) surface is present [3]. This atom is situated below the center of the ring-like structure of the adlayer and is not



connected to the adlayer. Therefore it should ideally carry one dangling bond. The corresponding Si 2p core level component which corresponds to a Si-C<sub>3</sub> unit is expected at a binding energy 0.3 eV lower than that of Si I where it is not observed. We argue that the dangling bond is initially saturated by hydrogen. The resulting C<sub>3</sub>-Si-H is expected to have a binding energy close to the bulk component Si I because the electronegativities of C and H are similar and is thus not resolved.

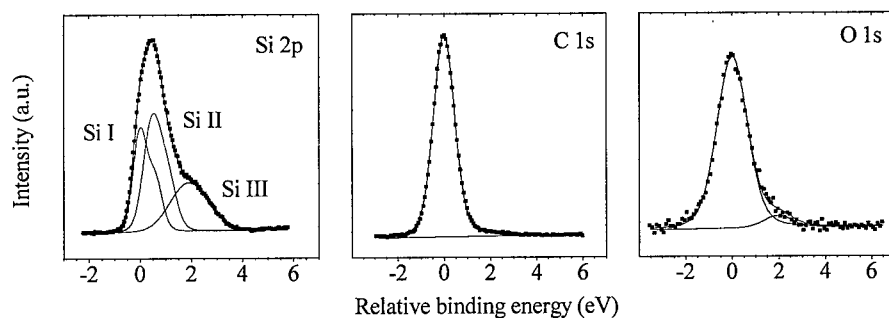


Fig. 2. Photoemission spectra from the Si 2p, C 1s and O 1s core levels after the hydrogen treatment. The Si 2p spectrum was measured with a resolution of 0.28 eV and the C 1s and O 1s core levels with a resolution of 0.7 eV.

This expectation is born out by the annealing series. Between 450 °C and 800 °C a transfer of intensity from the Si I to the Si II component takes place while Si III and the LEED pattern remain unchanged (see Fig. 3). We interpret this as a replacement of the H by O as a means to saturate the dangling bond (C<sub>3</sub>-Si-H is replaced by C<sub>3</sub>-Si-O). Above 900 °C the destruction of the ordered SiO<sub>2</sub> adlayer sets in. It is accompanied by an oxidation that encompasses previously unoxidized Si atoms of the substrate. This process is evident by the increase of the Si III signal (SiO<sub>2</sub>) in the Si 2p spectra at the expense of all other components and by the blurring of the LEED pictures.

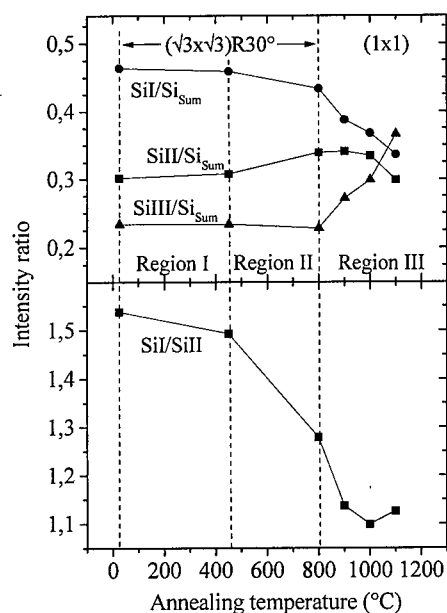


Fig. 3. The intensity ratio of the components SiI, SiII and SiIII to the total Si 2p signal as a function of the annealing temperature is depicted in the upper picture. The lower picture shows the intensity ratio of the components SiII/SiI.

In Fig. 4 we compare angle resolved valence band spectra taken at four different polar angles along the  $\Gamma K'$  azimuth for the C- and the Si-terminated 6H-SiC surfaces. Both surfaces have undergone a hydrogen treatment and exhibit a very similar silicate adlayer structure with a  $(\sqrt{3} \times \sqrt{3})R30^\circ$  unit mesh [6]. They differ essentially in the anchoring of the silicate adlayer: through Si-O-Si bonds on 6H-SiC (0001) and C-Si bonds on SiC (000 $\bar{1}$ ). Not surprisingly, both sets of spectra contain in addition to bulk related states common features related to the silicate adlayer. These are the O 2p<sub>y</sub> lone pair state at 6 eV below the valence band maximum (VBM) and a surface state S that falls into the ionic gap of the bulk bands. This state has Si-O bonding character [6]. The two sets of spectra differ,

however, in one important aspect. The spectra of the C-terminated surface show emission from a surface state D, 0.4 eV above VBM, i. e. in the fundamental gap of SiC. This state which appears

after annealing at 650°C was assigned to the dangling bonds of C atoms that are the analog of the Si dangling bonds discussed above. The absence of this dangling bond derived surface state on the Si side is in agreement with our analysis of the Si 2p spectra in connection with Fig. 3. It is obviously the higher reactivity of the Si radical compared to the C radical that prevents the stability of silicon dangling bonds after H has been desorbed. This brings us to our last point, the formation of the

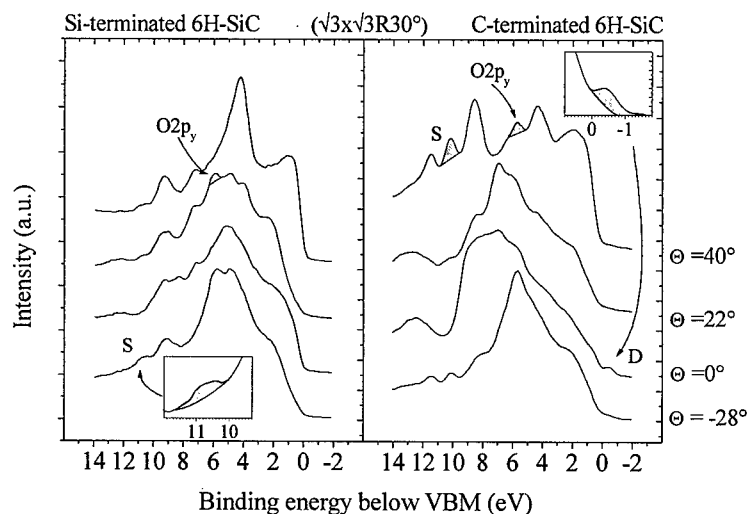


Fig. 4. Comparison of angle resolved valence band spectra at four different polar angles along the  $\overline{\Gamma K'}$  azimuth for the C- and the Si-terminated 6H-SiC surfaces.

silicate adlayer. The hydrogenation and all further treatments of the sample are performed in nominally oxygen-free atmospheres. Therefore, only residual oxygen contamination of the H<sub>2</sub> or oxygen desorbing from the quartz reactor wall can be made responsible for the formation of the silicate adlayer. It should be stressed, however, that the hydrogen treatment is necessary. The ordered oxide layer cannot be produced by heating the as prepared sample with a nominally unreconstructed (1x1) surface up to 1100°C in ultra high vacuum nor by doing the same thing with an additional exposure to 300L of O<sub>2</sub>.

### Summary

We have prepared an ordered silicate adlayer with a  $(\sqrt{3} \times \sqrt{3})R30^\circ$  unit mesh on Si-terminated 6H-SiC by a thermal treatment in H<sub>2</sub>. The Si 2p, O 1s, C 1s core level and the valence band spectra are in agreement with a structural model for this adlayer derived from a LEED analysis. The exception is a dangling bond state that is expected for every third bulk-terminating Si atom on the basis of this model and that is not observed. We present evidence that this dangling bond is hydrogen terminated for temperatures below about 450°C and oxygen terminated above. The ordered adlayer is stable in vacuo up to 1000°C; beyond that temperature a redistribution of the oxygen occurs that destroys the ordered adlayer.

### References

- [1] V.V. Afanas'ev, A. Stesmans, M. Baßler, G. Pensl, M.J. Schulz, C.I. Harris, *Appl. Phys. Lett.* **68**, 2141 (1996).
- [2] V.V. Afanas'ev, M. Baßler, G. Pensl, M. Schulz, *phys. stat. sol. (a)* **162**, 321 (1997).
- [3] J. Bernhardt, J. Schardt, U. Starke, K. Heinz, *Appl. Phys. Lett.* **74**, 1084 (1998).
- [4] R.C.G. Leckey and J.D. Riley, *Appl. Surf. Sci.* **22/23** (1985) 196.
- [5] R. Graupner, F. Maier, J. Ristein, and L. Ley, *Ch. Jung, Phys. Rev. B* **57** (1998) 12397.
- [6] M. Hollering, N. Sieber, F. Maier, J. Ristein, L. Ley, J.D. Riley, R.C.G. Leckey, this conference, p. 387

## Initial Oxidation of the Si-terminated 6H-SiC(0001) 3x3 Surface

F. Amy<sup>1,2</sup>, Y.-K. Hwu<sup>3</sup>, C. Brylinski<sup>4</sup> and P. Soukiassian<sup>1,2</sup>

<sup>1</sup> Commissariat à l'Energie Atomique, DSM - DRECAM - SRSIM, Centre d'Etudes de Saclay,  
Bâtiment 462, FR-91191 Gif sur Yvette Cedex, France

<sup>2</sup> Département de Physique, Université de Paris-Sud, FR-91405 Orsay Cedex, France

<sup>3</sup> Institute of Physics, Academia Sinica, Nankang, Taipei 115, Taiwan ROC

<sup>4</sup> Laboratoire Central de Recherches, Thomson-CSF, Domaine de Corbeville, B.P. 10,  
FR-91401 Orsay Cedex, France

**Keywords:** Core Level Photoemission, Interface, Oxidation, Surface, Synchrotron Radiation

### Abstract

The initial oxidation of the Si-terminated 6H-SiC(0001)3x3 reconstructed surface is studied by core level photoemission spectroscopy using synchrotron radiation. Even at low temperatures (500°C), the direct oxidation of the 6H-SiC(0001)3x3 surface leads to SiO<sub>2</sub> formation with a non abrupt interface including significant amounts of intermediate (Si<sup>3+</sup>, Si<sup>2+</sup>, Si<sup>+</sup>) and mixed (Si-O-C) oxidation products. In contrast, thermal oxidation using same conditions of a pre-deposited Si overlayer leads to C-free and abrupt SiO<sub>2</sub>/6H-SiC(0001) interface formation.

### 1. Introduction

Silicon carbide surface passivation remains one of the key issues in successful SiC device technology [1-3]. However, it is only recently that very important progress has been achieved into the knowledge of SiC surfaces and interfaces [1,4,5]. Silicon has been the semiconductor of choice for microelectronics in part because of the excellent properties of its native oxide (SiO<sub>2</sub>) and the low defect density of SiO<sub>2</sub>/Si interface. In this view, SiC appears to be also promising since its native oxide is also SiO<sub>2</sub> [1,2]. Nevertheless, the SiO<sub>2</sub>/SiC interface has generally poor electrical properties: due to the presence of C, conventional oxidation results in mixed oxides products including carbon and rough interfaces with high density of interface states [1,2,6,7]. SiC oxidation has been investigated by various experimental electrical and spectroscopic techniques using different approaches such as oxygen chemisorption, plasma assisted oxidation, thermal oxidation or catalytic oxidation [1-3,6-14]. However, most of hexagonal α-SiC oxidation studies have been performed on non-reconstruction specific surfaces. Interestingly, surface reconstruction and composition have been shown to play a crucial role in cubic β-SiC(100) initial surface oxidation [2,11]. In order to achieve rather abrupt interfaces, especially for thin passivation layers, it is indeed important to initiate surface oxidation on well controlled and defined surfaces.

In this work, we study SiO<sub>2</sub>/6H-SiC(0001) interfaces by core level photoemission spectroscopy using synchrotron radiation, which provides much higher energy resolutions than conventional x-ray sources allowing easier identification of oxide products. We use the 6H-SiC(0001)3x3 surface reconstruction terminated by 4 layers of Si atoms [5]. The initial SiO<sub>2</sub>/6H-SiC(0001)3x3 interface formation is studied in two manners: i) direct surface oxidation and ii) oxidation of a pre-deposited Si layer onto the 6H-SiC(0001)3x3 surface. For a low O<sub>2</sub> exposure (1000 L) at a low temperature (500°C) the Si-oxide/6H-SiC interface is not abrupt, including significant amounts of intermediate (Si<sup>3+</sup>, Si<sup>2+</sup>, Si<sup>+</sup>) and mixed (Si-O-C) oxides when directly grown on the 6H-SiC(0001)3x3 surface. In contrast, using same conditions, the Si-covered 6H-SiC(0001)3x3 surface oxidation results in dominant SiO<sub>2</sub> product and leads to an interface formation containing smaller amount of low oxidation states resulting with a more abrupt SiO<sub>2</sub>/SiC interface having a carbon-free oxide layer.

### 2. Experimental Details

The photoemission experiments were performed at the Synchrotron Radiation Research Center in Hsinchu (Taiwan) using the 6m-HSGM monochromator beam line. The photoelectron energy was measured by a VSW spherical electrostatic analyzer having a 150 mm radius. The

overall (monochromator and analyzer) energy resolution was 180 meV at Si 2p and 360 meV at C 1s core levels. The pressure in the vacuum chamber was in the  $10^{-11}$  Torr range. We used a nitrogen doped n-type 6H-SiC(0001) sample having a low step density Si face. Native oxides removal was achieved by UHV annealing at 1150°C resulting in C-rich surface. Subsequent Si deposition at 650°C for 10 minutes followed by a 2 minutes annealing at 750°C produce a clean 6H-SiC(0001)3x3 surface as checked by sharp low energy electron diffraction (LEED) 3x3 patterns. O<sub>2</sub> exposures were performed with research grade oxygen. We have decomposed the Si<sub>2p</sub> spectra using conventional peak fitting procedure with Voigt functions using branching ratio of 0.52, a spin-orbit splitting of 0.608 eV and a 0.15 eV Lorentzian width.

### 3. Results and Discussion

We use the Si<sub>2p</sub> core level to follow the 500°C oxidation process for an oxygen exposure of 1000L (1 Langmuir = 1 L =  $10^{-6}$  Torr.sec) on the 6H-SiC(0001)3x3 surface. Fig. 1a displays the Si<sub>2p</sub> spectrum recorded at grazing photoelectron emission and using a 150 eV photon energy to optimize surface sensitivity. The spectrum exhibits large core level chemical shifts at higher binding energy related to different oxidation states. The clean 6H-SiC(0001)3x3 surface shows Si<sub>2p</sub> core level surfaces shifted components [15]. We have performed peak curve decomposition and fitting including the Si 2p core level for the non-oxidized clean SiC surface. The origin of the relative binding energy scale is set at 99.2 eV, i.e. the binding energy of Si 2p for clean silicon. The Si 2p core level for the clean 6H-SiC(0001)3x3 surface reconstruction exhibits three components labeled A (0.2 eV), B (0.6 eV) and C (1.2 eV) that are assigned to Si-adatoms (A) and to trimers + Si ad-layer plane located underneath (B) and to bulk-like Si atoms (C) [15], following the 6H-SiC(0001)3x3 surface reconstruction model [5].

The Si<sub>2p</sub> peak decomposition shown in Figure 1a allows us to identify the oxidation products. Note that using conventional peak decomposition for Si surfaces with oxidation states (Si<sup>+</sup>, Si<sup>2+</sup>, Si<sup>3+</sup> and Si<sup>4+</sup>) shifted by 0.9 eV, 1.8 eV, 2.6 eV and 3.9 eV from Si<sub>2p</sub> core level [16] does not give any satisfactory fitting in the present case. The dominant oxide peak, labeled Si<sup>4+</sup>, is shifted by 4.5 eV to higher binding energies which would correspond to SiO<sub>2</sub> formation [17]. This large chemical shift, compared to what is observed for thin SiO<sub>2</sub> films on clean Si surfaces (3.9 eV) is similar to what is observed for thicker SiO<sub>2</sub> films (> 50 Å) and is principally due to different Si-O bond angles [17]. Since the oxide layer here is very thin ( $\approx 10$  Å), this large core level shift indicates that the Si-O bond angles for the SiO<sub>2</sub>/6H-SiC(0001)3x3 interface are close from that of bulk-like silicon dioxide. In the same way, the other oxidation products peak components rise at significantly higher binding energies compared to what is observed for Si. These chemical components shifted by 3.2 eV, 2.5 eV and 1.9 eV denotes a rather complex interface formation and can be assigned to Si<sup>3+</sup>, Si<sup>2+</sup> and Si<sup>+</sup> respectively. However, the 2.5 eV component (Fig. 1a) is of special interest since it is unlikely to result only from the Si<sup>2+</sup> oxidation state but probably includes other contributions, possibly from C atoms.

Additional information about the SiO<sub>2</sub>/6H-SiC(0001)3x3 interface formation could be found when looking at the C<sub>1s</sub> core level evolution upon a 1000 L O<sub>2</sub> exposure at 500°C. Fig. 1b displays the C<sub>1s</sub> core level for clean and oxidized 6H-SiC(0001)3x3 surfaces. The behavior of the C<sub>1s</sub> peak is of special interest since it is only slightly affected with a 26% broadening and no major chemical shift. This broadening suggest that the C atoms are somehow involved in the oxidation process, bonded to both O and Si atoms as Si-O-C species which can be correlated to the 2.5 eV core level shift that is observed at the Si<sub>2p</sub> core level. At this point, both C<sub>1s</sub> and Si<sub>2p</sub> core levels suggest that the interface between SiC and SiO<sub>2</sub> is not really abrupt and involves "mixed" oxide.

We now use a different approach to passivate the 6H-SiC(0001) surface. To achieve SiO<sub>2</sub> growth on the surface, we first deposit at room temperature a Si thin film (few atomic layers) onto a 3x3 reconstructed surface and then expose it to 1000L O<sub>2</sub> at 500°C, as for the 3x3 surface reconstruction. The Si<sub>2p</sub> core level (Fig. 2a) shows that the dominant spectral feature is the component shifted by 4.5 eV to higher binding energies, indicating that SiO<sub>2</sub> is the major oxidation product. When compared to the case of the 6H-SiC(0001) 3x3 surface oxidation (Fig. 1a), one can clearly see that the interface is more abrupt with less intermediate oxides. In addition, the intensity of the 2.5 eV shifted Si<sub>2p</sub> component (Fig. 2a) is considerably smaller when compared to the 6H-SiC(0001) 3x3 surface (Fig. 1a) indicating that the relative importance of the mixed Si-O-C oxide is significantly decreased.

The evidence of a more abrupt interface can be also suggested by looking at Fig. 2b which displays the C<sub>1s</sub> core level for the clean and oxidized Si/6H-SiC(0001) surfaces. In opposition to

### $O_2/6H-SiC(0001) 3 \times 3$

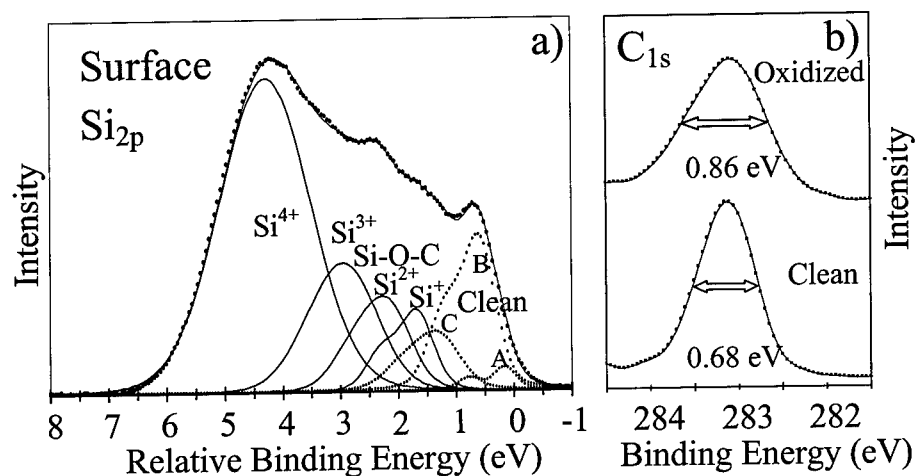


FIG 1: 1000 L of  $O_2/6H-SiC(0001) 3 \times 3$  at  $500^\circ C$ :

a)  $Si_{2p}$  core level recorded at a photon energy of  $h\nu = 150$  eV and grazing emission angle (surface sensitive mode). The binding energy scale is relative to  $Si_{2p}$  binding energy (99.2 eV) for a silicon surface. The surface and bulk shifted components A, B, and C (.....) and the chemically shifted components (—) are also displayed.

b)  $C_{1s}$  core level shift for clean and oxidized (as above) surfaces recorded at a photon energy of  $h\nu = 330$  eV and grazing emission angle (surface sensitive mode).

### $O_2/Si/6H-SiC(0001)$

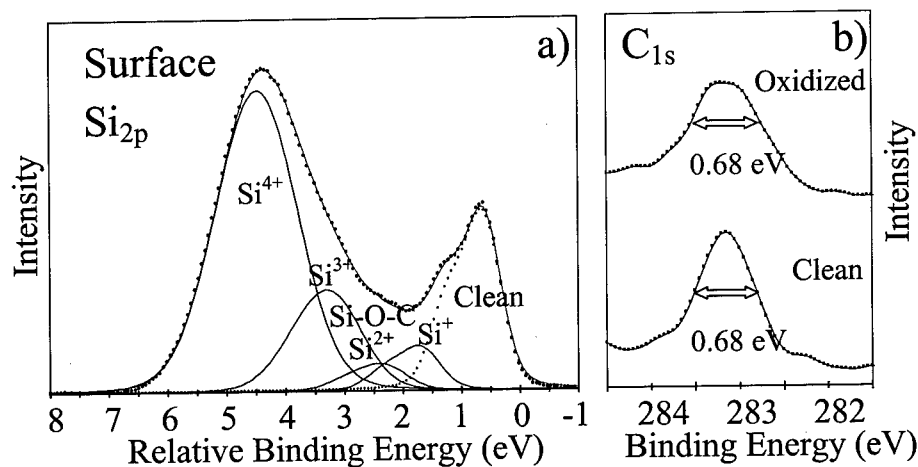


FIG 2. 1000 L of  $O_2/Si/6H-SiC(0001)$  at  $500^\circ C$ :

a)  $Si_{2p}$  core level recorded at a photon energy of  $h\nu = 150$  eV and grazing emission angle (surface sensitive mode). The binding energy scale is relative to  $Si_{2p}$  binding energy (99.2 eV) for a silicon surface. The  $Si_{2p}$  for SiC (.....) and the chemically shifted components (—) are also displayed.

b)  $C_{1s}$  core level shift for clean and oxidized (as above) surfaces recorded at a photon energy of  $h\nu = 330$  eV and grazing emission angle (surface sensitive mode).

behavior of the 6H-SiC(0001) 3x3 surface upon exposure to 1000L of O<sub>2</sub> at 500°C, the C<sub>1s</sub> core level peak intensity is decreased, but keeps the same line width at 0.68 eV. This result indicate clearly that the C atoms are not significantly involved in the interface formation, and are probably oxidized as CO or CO<sub>2</sub> molecules that are most likely desorbed from the surface/interface region [12,13]. Taking into account the Si<sub>2p</sub> spectrum (Fig. 2b) that shows a much more abrupt interface, this result support an interface model in which the oxidation layer is lying on a carbon plane.

#### 4. Conclusions

In conclusion, using core level photoemission spectroscopy with synchrotron radiation, we have shown that the oxidation of a pre-deposited Si thin film on the 6H-SiC surface leads to a more abrupt SiO<sub>2</sub>/6H-SiC(0001) interface than by direct oxidation of the 6H-SiC(0001)3x3 surface. With low temperature (500°C) and low oxygen exposure (1000 L O<sub>2</sub>), we identify various Si oxidation states (Si<sup>+</sup>, Si<sup>2+</sup>, Si<sup>3+</sup> and Si<sup>4+</sup>) and mixed oxide (Si-O-C) species, but the dominant oxidation product is SiO<sub>2</sub>. However, if direct oxidation of the 6H-SiC(0001)3x3 surface leads to a non abrupt SiO<sub>2</sub>/6H-SiC(0001) interface involving intermediate oxidation Si species and C atoms, oxidation of the 6H-SiC(0001)3x3 surface covered by an excess of few atomic layers of Si result in C-free oxides with reduced amount of intermediate Si oxides [18].

This work has been supported by the Institut Français de Taipei and by the National Science Council (NSC, Taipei). It is based upon research conducted at the Synchrotron Radiation Research Center (SRRC), Hsinchu, Taiwan. The authors are especially grateful to the SRRC staff for expert and outstanding assistance and to Dr. Tseng for the use of his experimental system.

#### References

- 1 Silicon Carbide, A Review of Fundamental Questions and Applications to Current Device Technology, edited by W.J. Choyke, H.M. Matsunami and G. Pensl, Akademie Verlag, Berlin, Vol. I & II (1998); and references therein.
- 2 P. Soukiassian, in Fundamental Aspects of Ultrathin Dielectrics on Si-based Devices, edited by E. Grafunkel, E. Gusev and A. Vul', NATO Science Series 3, High Technology, Kluwer Academic Press (Dordrecht) (1998) 257.
- 3 G. Lucovsky and H. Niimi, in Ref. 2 (1998) 447.
- 4 F. Semon, P. Soukiassian, A. Mayne, G. Dujardin, L. Douillard and C. Jaussaud, Phys. Rev. Lett. **77** (1996) 2013; P. Soukiassian, F. Semon, L. Douillard, A. Mayne, G. Dujardin, L. Pizzagalli and C. Joachim, Phys. Rev. Lett. **78** (1997) 907.
- 5 K. Reuter, J. Bernhardt, H. Wedler, J. Schardt, U. Starke and K. Heinz, Phys. Rev. Lett. **79** (1997) 4818; U. Starke, J. Schardt, J. Bernhardt, M. Franke, K. Reuter, H. Wedler, K. Heinz, J. Furthmüller, P. Käckell and F. Bechstedt, Phys. Rev. Lett. **80** (1998) 758.
- 6 V.R. Vathulya, D. Wang, M.H. White, Appl. Phys. Lett. **73** (1998) 2161; V.V. Afanas'ev, A. Stesmans, M. Bassler, G. Pensl, M.J. Schulz, C.I. Harris, *ibid* **68** (1996) 2141.
- 7 J.N. Shenoy, J.A. Cooper Jr. and M.R. Melloch, Appl. Phys. Lett. **68** (1996) 803; W. Xie, J.N. Shenoy, S.T. Sheppard, M.R. Melloch and J.A. Cooper Jr., *ibid* **68** (1996) 2231.
- 8 J.M. Powers and G.A. Somorjai, Surf. Sci. **244** (1991) 39.
- 9 A. Mayne, F. Semon, G. Dujardin and P. Soukiassian, Phys. Rev. B **57**, Rapid Communication (1998) R 15108
- 10 V.M. Bermudez, Appl. Surf. Sci. **84** (1995) 45.
- 11 C. Öneby and C.G. Pantano, J. Vac. Sci. Technol. A **15** (1997) 1597.
- 12 F. Semon, L. Douillard, P. Soukiassian, D. Dunham, F. Amy and S. Rivillon, Appl. Phys. Lett. **68** (1996) 2144.
- 13 M. Riehl-Chudoba, P. Soukiassian, C. Jaussaud and S. Dupont, Phys. Rev. B **51** (1995) 14300.
- 14 J. Bernhardt, J. Schardt, U. Starke and K. Heinz, Appl. Phys. Lett. **74** (1999) 1084.
- 15 F. Amy, Y.K. Hwu and P. Soukiassian, recent core level photoemission results
- 16 F.J. Himpsel, F.R. McFeely, A. Taleb-Ibrahimi, J.A. Yarnoff and G. Hollinger, Phys. Rev. B **38** (1988) 6084; and references therein.
- 17 F.J. Grunthaner, P.J. Grunthaner, R.P. Vasquez, B.F. Lewis, J. Maserjian and A. Madhukar, Phys. Rev. Lett. **22** (1979) 1683.
- 18 F. Amy, P. Soukiassian, Y.K. Hwu, C. Brylinski, Appl. Phys. Lett. **75** (1999), in press.

## XPS Analysis of SiO<sub>2</sub>/SiC Interface Annealed in Nitric Oxide Ambient

H.-F. Li, S. Dimitrijević, D. Sweatman and H.B. Harrison

School of Microelectronic Engineering, Griffith University, Nathan, Brisbane, QLD 4111, Australia

**Keywords:** Interface, Nitridation, Oxide, XPS

**Abstract:** XPS analysis of the SiO<sub>2</sub>/SiC interface annealed in NO has been presented in the paper. Nitrogen accumulation of 1.6 at.% close to the SiO<sub>2</sub>/SiC interface was observed in the NO annealed sample. The N 1s XPS spectrum indicates the formation of Si ≡ N bonds at a binding energy of 397.8eV at the SiO<sub>2</sub>/SiC interface. The XPS spectrum of the NO annealed sample was compared with that of the Ar annealed sample. The Si 2p spectra demonstrate a clear difference between NO and Ar annealed SiO<sub>2</sub>/SiC MOS capacitors at the interface. The spectrum of the Ar annealed sample is much broader than that of the NO annealed sample, showing quite different chemical structures between Ar annealed and NO annealed SiO<sub>2</sub>/SiC interface. It is obvious that the NO annealed SiO<sub>2</sub>/SiC interface is less complex than the Ar annealed SiO<sub>2</sub>/SiC interface, indicating less interface defects in NO annealed SiO<sub>2</sub>/SiC interface.

### Introduction

The SiO<sub>2</sub>/SiC interface plays a crucial role in fabricating SiC-based MOSFET electron devices. It has been shown that the oxide charge and interface trap densities of the SiO<sub>2</sub>/SiC structure are much higher than those of the SiO<sub>2</sub>/Si structure [1, 2]. However, the breakdown electric field of the SiO<sub>2</sub>/SiC structure is comparable to that of the SiO<sub>2</sub>/Si structure [3,4]. These facts indicate that the main difference lies in the interface between SiO<sub>2</sub>/SiC and SiO<sub>2</sub>/Si structures. Compared with the SiO<sub>2</sub>/Si interface, the SiO<sub>2</sub>/SiC interface is complicated by the presence of carbon at the interface. Hornetz *et al* [5] revealed that an interface oxide Si<sub>4</sub>C<sub>4-x</sub>O<sub>2</sub> (x ≤ 2) exists between SiC and SiO<sub>2</sub> using ARXPS and claimed that the existence of this complex interface compound is responsible for the higher interface trap density at the SiO<sub>2</sub>/SiC interface. Onneby *et al* [6] exposed SiC to various oxygen sources at room temperature and found the formation of silicon oxycarbide species on top of the SiC surface. They argued that the native oxide on the single crystal SiC consists mainly of silicon oxycarbide species.

We have applied NO nitridation to SiC technology to improve the SiO<sub>2</sub>/SiC interface [7~9]. It has been shown that NO nitridation reduces the interface trap density greatly in both n- and p-type SiC and improves the reliability of SiO<sub>2</sub>/SiC MOS structures [10]. This paper presents the physical analysis of the NO nitrided SiO<sub>2</sub>/SiC interface using XPS. We show evidence of a less complex SiO<sub>2</sub>/SiC interface after NO nitridation compared to Ar annealed samples.

### Experimental details

A Si-faced n-type 4H-SiC wafer, purchased from CREE Research, was used in this experiment. The wafer is n-type SiC with a resistivity of 0.044 ohm-cm, on top of which is a 4.5μm-thick n-type

epilayer with nitrogen doping concentration of  $9.5 \times 10^{15} \text{ cm}^{-3}$ . The wafer was first cleaned in a mixture of  $\text{H}_2\text{SO}_4$  and  $\text{H}_2\text{O}_2$  followed by an RCA clean. Immediately prior to oxidation the wafer was dipped in 1%HF for 1 minute and then oxidized in a quartz furnace in ultrahigh purity oxygen at  $1150^\circ\text{C}$  for 3 hours, followed by an *in situ* anneal in Ar for 30 minutes. After oxidation, the wafer was cut into pieces. One set of samples was then annealed in pure NO (99%) in a quartz tube furnace at  $1130^\circ\text{C}$  for 1.5h. The other set of samples was annealed in Ar in the same furnace under exactly the same conditions for comparison. The oxide thicknesses were estimated from high frequency Capacitance-Voltage (C-V) measurements to be about 21nm for both NO and Ar annealed samples. Conductance measurements performed at  $330^\circ\text{C}$  showed minimum interfacial trap densities of  $4.7 \times 10^{10} \text{ eV}^{-1} \cdot \text{cm}^{-2}$  for the NO nitrated sample and  $1.3 \times 10^{11} \text{ eV}^{-1} \cdot \text{cm}^{-2}$  for the Ar annealed sample.

XPS analyses were performed using a non-monochromatic Mg  $\text{K}\alpha_{1,2}$  x-ray source (1253.6eV) with a Perkin Elmer PHI model 560 XPS/SAM/SIMS I multitechnique surface analysis system incorporating a PHI model 25-270 AR cylindrical mirror analyzer (CMA). Ar sputtering was used to slowly remove the  $\text{SiO}_2$  layer. It has been shown that preferential sputtering does not occur on SiC surfaces under Ar bombardment. After each Ar sputtering step, the XPS spectra were recorded by performing multiple scans in each binding energy range of interest with a pass energy of 25eV. Since the Model 560 double pass CMA has no entrance lens, the area analyzed cannot be controlled. Specified analyzed area is about 4mm in diameter. Each time the sample was aligned in the x, y, and z directions using the Scanning Electron Microscopy (SEM) and elastic peak so that the sputtered area would be concentric with the analyzed area. The Si 2p, O 1s, C 1s, and N 1s core level spectra were recorded. At the interface, all spectra were charge compensated to a Si-C bond at 100.1eV to compensate for surface charging.

## Results and discussions

The relative atomic concentration of the elements can be obtained from the area under each elemental spectrum by taking its sensitivity factor into account as shown in Fig.1 for the NO

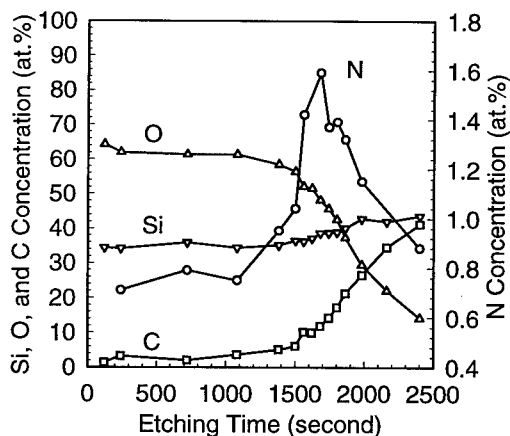


Fig.1 XPS depth profile of the NO annealed  $\text{SiO}_2/\text{SiC}$  MOS capacitor

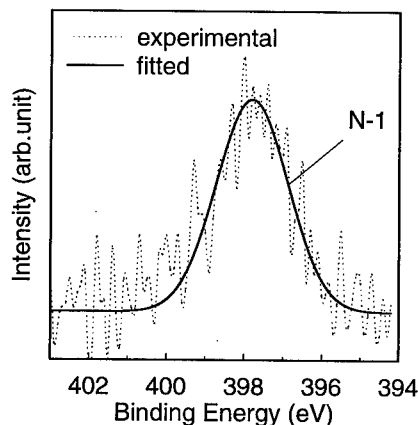


Fig.2 N 1s XPS spectrum at NO annealed  $\text{SiO}_2/\text{SiC}$  interface



annealed sample. We define the point where the oxygen and silicon distribution lines cross each other as the dielectric/silicon carbide interface. It can be seen that there is a nitrogen peak close to the interface. The value of nitrogen peak is 1.6 at.%. The characteristic of nitrogen pile-up close to the interface is similar to the case of NO nitrided Si samples [11]. It is also observed that there is also a uniform concentration of nitrogen of around 0.7 at.% throughout the dielectric. The nitrogen depth profile is asymmetrical. The nitrogen atomic concentration rises sharply on the dielectric-side but drops slowly on the SiC-side, showing a long tail into the SiC bulk. This is an artificial broadening of the concentration depth profiles at the interface due to the 'knock-on' effect and the atomic mixing. The long tails in the oxygen depth profiles for both NO and Ar annealed samples could also be caused by the 'knock-on' effect and the atomic mixing.

Fig. 2 shows the N 1s XPS spectrum at the NO annealed SiO<sub>2</sub>/SiC interface. It is symmetrical and can be fitted with one peak N1 with binding energy of 397.8eV (FWHM=2.16eV). This value is very close to the binding energy for N 1s in silicon nitride which is 397.7eV, indicating the formation of Si≡N bonds at the interface of SiO<sub>2</sub>/SiC. This is the same as for the NO annealed SiO<sub>2</sub>/Si interface where it has been demonstrated that NO nitridation creates Si≡N bonds [12].

The Si 2p XPS spectrum At the NO and Ar annealed SiO<sub>2</sub>/SiC interfaces is shown in Fig.3 and Fig.4, respectively. The Si 2p spectra show a clear difference between NO and Ar annealed SiO<sub>2</sub>/SiC interfaces. The Si 2p spectrum at the Ar annealed SiO<sub>2</sub>/SiC interface is much wider than

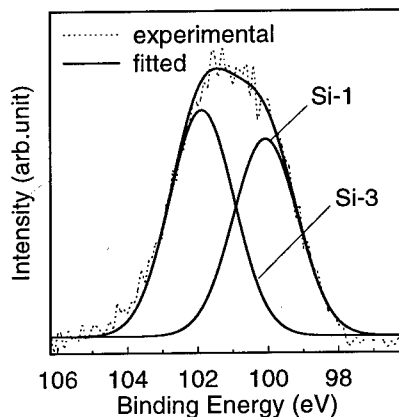


Fig.3 Si 2p XPS spectrum at the NO annealed SiO<sub>2</sub>/SiC MOS capacitor

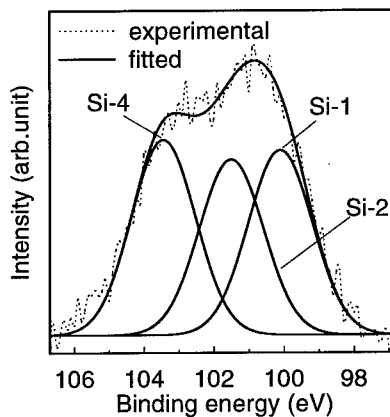


Fig.4 Si 2p XPS spectrum at the Ar annealed SiO<sub>2</sub>/SiC interface

that at NO annealed SiO<sub>2</sub>/SiC interface, indicating a complex interface for the Ar annealed sample. The Si 2p spectrum of the NO annealed sample can be fitted with two peaks, i.e. Si-1 (100.1eV, FWHM=2.16eV) and Si-3 (101.9eV, FWHM=2.16eV). However, the Si 2p spectrum of the Ar annealed sample can be fitted with three peaks, named Si-1, Si-2 (101.4eV, FWHM=2.16eV), and Si-4 (103.5eV, FWHM=2.16eV). The common peak, Si-1, appears in each spectrum and represents SiC from the substrate. The peak Si-4 indicates that SiO<sub>2</sub> is found at the Ar annealed interface. It is well known that some intermediate silicon oxide states exist at the SiO<sub>2</sub>/Si interface region. These intermediate silicon oxide states have the same tetrahedral structure as SiO<sub>2</sub> (Si-O4) but with oxygen partly replaced by Si to form the tetrahedra: Si-Si<sub>2</sub>O<sub>2</sub> (Si<sup>2+</sup> oxidation state) and Si-SiO<sub>3</sub> (Si<sup>3+</sup>

oxidation state) with binding energies of 101.5eV and 102.5eV, respectively [13]. In the case of the SiO<sub>2</sub>/SiC structure, it appears that carbon is also included in the silicon tetrahedron, because of the appearance of carbon at the interface. Onneby *et al* [6] investigated the SiO<sub>2</sub>/SiC system and claimed the formation of silicon oxycarbide at the interface. They identified the silicon oxycarbide as SiO<sub>3</sub>C (binding energy 102.1-102.2eV) and SiO<sub>2</sub>C<sub>2</sub> (binding energy 101.2-101.6eV). Hornetz *et al* [5] studied the SiO<sub>2</sub>/SiC interface with ARXPS and revealed interface oxide as Si<sub>4</sub>C<sub>4-x</sub>O<sub>2</sub> (x≤2) with binding energy of 101.25eV. Therefore we regard Si-2 as a complex intermediate oxide/carbon compound. The determination of Si-3 in the NO annealed sample needs more detailed consideration since its binding energy of 101.9eV falls in the energy range where a few possible compounds would occur including SiO<sub>3</sub>C as discussed above. It has also been reported that binding energies of 101.9eV for Si 2p in Si<sub>3</sub>N<sub>4</sub> [14] and 101.8eV for Si 2p in surface silicon oxide contaminated Si<sub>3</sub>N<sub>4</sub> [15] were observed. Because of the pileup of nitrogen at the interface in the NO annealed sample, we assume that the observed Si-3 peaks indicate the formation of Si≡N bonds.

### Conclusions

The effects of NO annealing on the SiO<sub>2</sub>/SiC interface have been investigated using XPS analysis. The results show that NO annealing has benefit effects on the SiO<sub>2</sub>/SiC interface. The NO annealed SiO<sub>2</sub>/SiC interface is less complex than the Ar annealed SiO<sub>2</sub>/SiC interface, showing an improved interface. The accumulation of nitrogen at the interface, forming Si≡N bonds, is responsible for the difference between NO and Ar annealed SiO<sub>2</sub>/SiC interface. The results indicate that NO nitridation is a promising technique in future SiC MOSFET technology.

### References

1. J. N. Shenoy, G. L. Chindalore, M. R. Meloch, J. A. Cooper, Jr., J. W. Palmour, K. G. Irvine, J. Electronic Materials, **24** (1995), p. 303.
2. L. A. Lipkin and J. Palmour, J. Electron. Mater., **25** (1996), p. 909.
3. D. Alok, P. K. McLarty, and B. J. Baliga, Appl. Phys. Lett., **64** (1994), p. 2845.
4. R. Friderichs, E. P. Burte, and Schorner, J. Appl. Phys., **79** (1996), p. 7814.
5. B. Hornetz, H-J. Michel, and J. Halbritter, J. Mater. Res., **9** (1994), p. 3088.
6. C. Onneby and C. G. Pantano, J. Vac. Sci. Technol. A, **15** (1997), p. 1597.
7. S. Dimitrijević, H.-F. Li, H. B. Harrison, and D. Sweatman, IEEE Electron Device Lett., **18** (1997), p. 175.
8. H.-F. Li, S. Dimitrijević, H. B. Harrison, and D. Sweatman, Appl. Phys. Letters, **70** (1997), p. 2028.
9. H.-F. Li, S. Dimitrijević, H. B. Harrison, D. Sweatman, and P. Tanner, MRS Spring Meeting, April 13-17, San Francisco, CA, USA, 1998.
10. H.-F. Li, S. Dimitrijević, H. B. Harrison, IEEE Electron Device Lett., **19** (1998), p. 279.
11. Z.-Q. Yao, J. Appl. Phys., **78**, 2906 (1995)
12. R. I. Hegde, P. J. Tobin, K. G. Reid, B. Maiti, and S. A. Ajuria, Appl. Phys. Lett., **66** (1995), p. 2882.
13. T. P. Nguyen and S. Lefrant, J. Phys.: Condens. Matter., **1** (1989), p. 5197.
14. J. A. Taylor, Appl. Surf. Sci., **7** (1981), p. 168.
15. PHI Application Note No. 8504, Surface Oxidation of Silicon Nitride, Physical Electronics Laboratories, 6509 Flying Cloud Drive, Eden Prairie, MN, USA.

## Surface Studies on Thermal Oxidation on 4H-SiC Epilayer

A. Koh<sup>1</sup>, A. Kestle<sup>1</sup>, S.P. Wilks<sup>1</sup>, P.R. Dunstan<sup>1</sup>, C.J. Wright<sup>2</sup>, M. Pritchard<sup>1</sup>,  
G. Pope<sup>1</sup>, P.A. Mawby<sup>1</sup> and W.R. Bowen<sup>2</sup>

<sup>1</sup> Department of Electrical and Electronic Engineering, University of Wales Swansea,  
Singleton Park, Swansea, SA2 8PP, UK

<sup>2</sup> Department of Chemical & Biological Process Engineering, University of Wales Swansea,  
Singleton Park, Swansea, SA2 8PP, UK

**Keywords:** Interface, Oxidation, Surface Topography

### Abstract

Surface studies of the wet and dry thermally oxidized SiO<sub>2</sub>/SiC interface using Atomic Force Microscopy (AFM) shows the formation of nano-islands at the interface. These nano-islands are resistant to HF acid etch and have been previously linked to residual carbon [1]. From X-ray Photoelectron Spectroscopy (XPS) results, a slight shift in binding energy was observed between the wet and dry process. The high frequency capacitance-voltage measurements display the presence of deep interface traps on both wet and dry thermal oxides and a net effective oxide charge,  $Q_{eff}$  of approximately  $7 \times 10^{11} \text{ cm}^{-2}$  on the wet thermal oxide and approximately  $1.3 \times 10^{12} \text{ cm}^{-2}$  for the dry thermal oxide.

### Introduction

Silicon Carbide (SiC) possesses excellent properties as a semiconductor material due to its wide band gap, high thermal conductivity and high breakdown electric field [2]. In particular, the ability to grow thermal oxide (SiO<sub>2</sub>) on SiC makes it possible to fabricate Metal-Oxide-Semiconductor (MOS) Devices. The interest in the development of Silicon Carbide MOS devices originated from the ability to grow high quality dielectrics able to withstand the tough operating condition set for the SiC MOS technology. Recent improvements in processing techniques [3,4] and the use of new gate dielectric materials [2] have demonstrated oxide quality comparable to that of Silicon based MOS technology. However a report on the observation of nano-islands, believed to be of carbonaceous species, on the SiC surface after the removal of the thermal oxide layer [1,5] has sparked a new interest. Particularly in investigating the correlation between the formation of nano-islands, the surface preparation techniques, the thermal oxidation process and the resulting electrical characteristic. Within this work, we combine the surface science technique of X-ray Photoelectron Spectroscopy (XPS), Atomic Force Microscopy (AFM) and Capacitance-Voltage measurement to investigate this phenomenon and identify its nature for both wet and dry thermal oxidation.

### Experimental Procedure

MOS capacitors were fabricated on n-type 4H-SiC wafer with 10  $\mu\text{m}$  thick n-type epitaxial layer with a doping concentration of  $1.1 \times 10^{16} \text{ cm}^{-3}$  obtained from CREE Research Inc.. The samples were solvent cleaned followed by a standard RCA clean as a method of surface preparation. Sample A was subjected to a wet oxidation at 1050°C in a 2" wide quartz tube Pyrotherm Furnace in O<sub>2</sub> bubbling DI water at 95°C for 4hrs to produce an oxide thickness of 200 Å thick. This was followed by a Re-Oxidation Anneal (ROA) at 950°C for 3hrs. Sample B was subjected to a dry oxidation in pure O<sub>2</sub> at 1050°C for 14hrs to produce an oxide thickness of approximately 200 Å. This was immediately followed by an Ar anneal for 1hr. Both samples were loaded into the furnace at 850°C under pure O<sub>2</sub> (at 1 l/min flow rate) and unloaded at 850°C under Ar ambient immediately after post oxidation anneal. To form the back ohmic contact, Ni was e-beam evaporated and annealed for 5 mins at 975°C under high vacuum conditions. Finally, to form the gate contacts, Al was evaporated through a shadow mask under HV conditions to form a range of circular contacts of diameter 250-750  $\mu\text{m}$ .

### Characterisation

Owing to the wide band gap of SiC, the interface traps behave like slow traps at room temperature and can be regarded as fixed charge. These traps together with the mobile ion charge and fixed oxide charge form the effective net oxide charge, ( $Q_{eff}$ ). The  $Q_{eff}$  can be determined using the high frequency capacitance-voltage measurement technique [6,7].

The electrical characteristics of the thermal oxides were extracted from high frequency C-V measurements. These were performed at room temperature using the HP 4274 impedance analyzer with the sample placed in a shielded probe station. The analysis of the surface morphology was performed under contact mode using a CP 100 Auto-probe Thermo-microscope. This provided the AFM topography of the SiC surface on as-received and after the removal of the thermal oxide using HF acid. To identify the remaining surface content after the oxide strip, XPS was utilized to characterise the chemical species present on the 4H-SiC epilayer surface. A detailed study was performed in order to observe any changes to the Si and C peaks of the SiC surface that may have influence on to the electrical characteristic of the SiO<sub>2</sub>/SiC interface.

### Results and Discussion

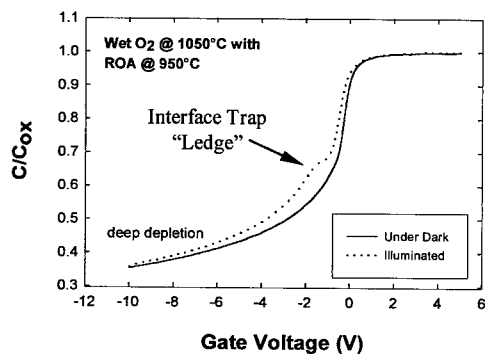


Figure 1. High frequency C-V curve of Sample A - wet oxidized at 1050°C with ROA at 950°C, n-MOS capacitor measured under dark & illuminated conditions.

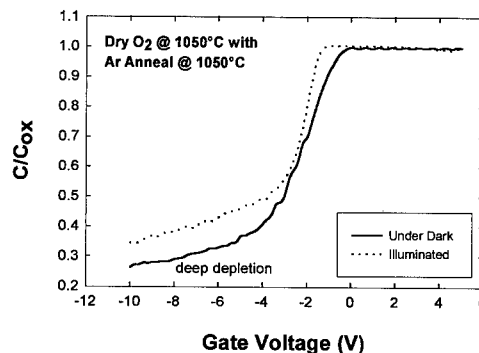


Figure 2. High frequency C-V curve of Sample B - dry oxidized with an Ar anneal at 1050°C, n-MOS capacitor measured under dark & illuminated conditions.

#### (1) High Frequency-C-V Characterisation.

The high frequency C-V curves in Fig. 1 were measured for sample A at 40kHz. Initially a bias was swept from accumulation to deep depletion in the dark condition. This was followed by a reverse sweep from deep depletion back to accumulation under constant illumination of the MOS capacitor with a 100W power tungsten lamp. From the high frequency C-V curve, the oxide thickness calculated from the accumulation region of the C-V data was determined to be 237Å. By calculating the flat band capacitance,  $C_{fb}$  [8], the flat band voltage shift,  $\Delta V_{fb}$  can be obtained from the high frequency C-V curve corresponding to the  $C_{fb}$ , which in this case was approximately -0.8V. The effective net oxide charge,  $Q_{eff}$  was calculated to be  $\sim 7 \times 10^{11} \text{ cm}^{-2}$ . Fig. 2 shows the high frequency C-V curves taken from Sample B. Again the same bias sweep condition were identical to those used for sample A. For sample B, the oxide thickness was calculated to be 300Å with a  $V_{fb}$  shift of approximately -2V. The effective net oxide charge,  $Q_{eff}$  was determined to be  $1.3 \times 10^{12} \text{ cm}^{-2}$ .

Consider the high frequency C-V curve taken during illumination, as shown in Fig.1. A bump in the characteristic was observed caused by charge carrier dynamics [9,10]. This indicated the presence of deep states at the SiO<sub>2</sub>/SiC interface. However, it was difficult to quantify these deep states explicitly. No such effect was observed in Fig. 2, implying fewer deep states within the

SiO<sub>2</sub>/SiC interface. The low negative  $\Delta V_{fb}$  measured for sample A indicated lower positive fixed charge for the wet oxidation. In contrast, the higher negative  $\Delta V_{fb}$  in Sample B is predominantly caused by positive fixed charges occurring during dry oxidation. These results imply that while wet oxidation produces a better bulk oxide quality the dry oxidation yielded a better SiO<sub>2</sub>/SiC interface.

## (2) AFM Scan.

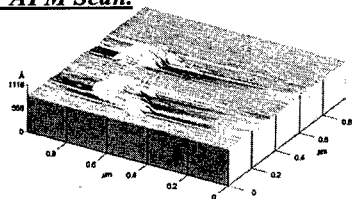


Figure 3a. AFM topography of 4H-SiC epilayer surface on sample A after removal of thermal oxide.

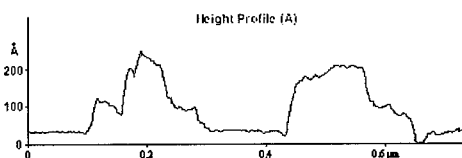


Figure 3b. Line profile of sample A nano-islands. Height range ~ 17-20nm and ~ 152nm across.

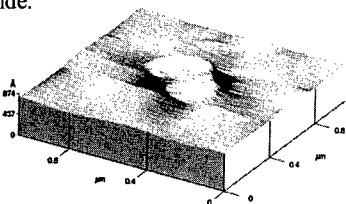


Figure 4a. AFM topography of 4H-SiC epilayer surface on sample B after removal of thermal oxide.

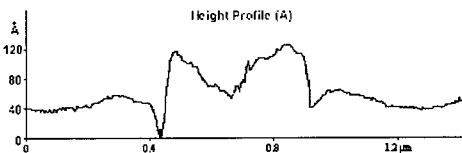


Figure 4b. Line profile of sample B nano-islands. Height range ~ 7-8nm and ~200nm across.

From the 50×50μm AFM image taken on the as-received 4H-SiC epilayer surface (not shown), a "pit hole" of ~1.39μm wide and a planar defect of 1.81μm wide were revealed as typical features across the whole surface. Although the planar defects were effectively removed after the standard RCA clean, the presence of the screw defect remained. AFM scans were also performed on both samples on a 50×50μm scan area on three different locations after the removal of thermal oxide (not shown). Nano islands with a typical height of 8-20nm were observed widely spread across all three scanned areas on sample A. However, only one scanned area on sample B revealed the presences of nano-island formation with a typical height of 7-8nm. Figs. 3 and 4 show the AFM topography and line profile of sample A and B respectively under a 1×1μm scale after the removal of thermal oxide. The line profile of sample A in fig. 3b shows the nano-islands height of 17-20nm and 150nm across. In Fig. 4 the size of the nano-islands were between 7-8nm in height and 200nm across on sample B. We are unable to identify the chemical species of these nano-island at the present but their presence may explain the cause of the poor interface observed in the high frequency C-V curve for sample A.

## (3) XPS Analysis.

The XPS scans were performed on the surface of the 4H-SiC epilayer after the removal of the thermal oxides by HF acid etches. Fig. 5a and 5b shows the spectra of the Si 2p and C 1s core level of both samples A and B. A slight shift in the binding energy, ~0.12eV of both the Si 2p and C 1s core level was observed. This is indicative of bandbending i.e. the surface barrier on sample A was larger than that on sample B after oxide removal. The 0.12eV difference in surface barrier could be related to the different density of nano-islands on these samples. For example, if the larger density of nano-islands on sample A resulted in additional interface states located within the band

gap, a different surface barrier could occur. This is in agreement with the 'ledge' observed in the C-V characteristic of sample A where a higher interface states density would occur.

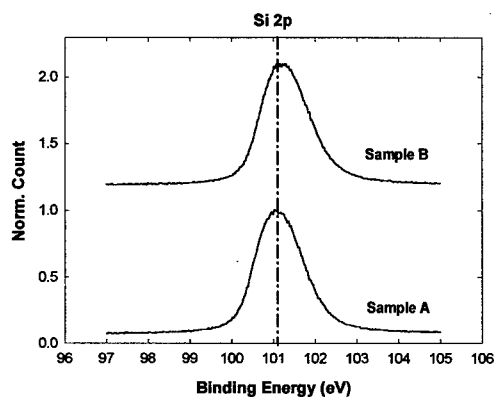


Figure 5a. XPS spectra of Si 2p core level for sample A (binding energy of 101.16eV) & B (binding energy of 101.28eV) surface after removal of thermal oxide.

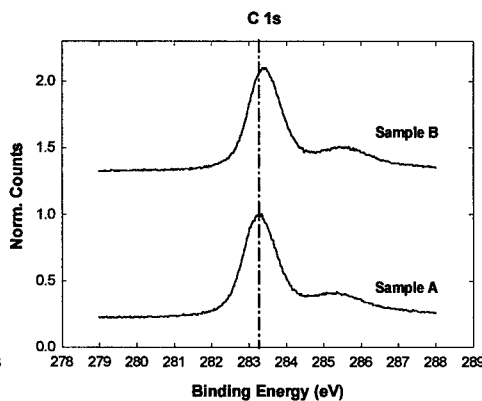


Figure 5b. XPS spectra of C 1s core level of sample A (binding energy of 283.32eV) & B (binding energy of 283.45eV) surface after removal of thermal oxide.

The stoichiometry of both surfaces was similar, as estimated by the ratio of the C 1s to Si 2p peak intensity. Furthermore, due to the limited energy resolution of the XPS system ( $\sim 0.8$  eV), it was unclear whether there were any elemental C deposits (binding energy of 284.9 eV [11]) on the SiC surface. More detailed studies are in progress and will be reported at a later date.

### Conclusion

In summary, from the high frequency C-V, AFM and the XPS results, we can relate that the presence of nano-islands at the interface contributes to the SiO<sub>2</sub>/SiC interfacial quality. These results also show the effect the oxidation process has on the interface and surface physics of the 4H-SiC epilayer. Although nano-islands were found on both wet and dry oxidised samples at different densities, it is not clear that these nano-islands are of a graphite nature. XPS results show core level shift in binding energy between the two samples. We believe the shift can be attributed to a varying degree of bandbending for the different sample surfaces. However, more detailed studies are necessary and will be reported at a later date.

### References

- [1] V.V. Afanas'ev, A Stesmans, and C.I. Harris, *Mat. Sci Forum* 264-268 (1998), p.857.
- [2] J.B. Casady and R.W. Johnson, *Sol. Stat. Elect.* Vol.39, No. 10 (1996), p. 1409.
- [3] L.A. Lipkin, D.B. Slater, Jr. and J.W. Palmour, *Mat. Sci. Forum* 264-268 (1998), p.853.
- [4] X.W. Wang, Y. Takahashi, T.P. Ma, G.J. Cui, T. Tamagawa, B. Halpern and J.J. Schmitt, *Mat. Sci. Forum* 264-268 (1998) p.865.
- [5] V.V. Afanas'ev, M. Bassler, G. Pensl and M.J. Schulz, *Phys. Stat. Sol. (a)*, (1997), p.162.
- [6] H. Yano, F. Katafuchi, T. Kimoto and H. Matsunami, *IEEE Trans. Elec Dev.* Vol.46, No. 3, p.504.
- [7] J. Campi, Y. Shi, Y. Luo, F. Yan, Y.K. Lee and J.H. Zhao, *Mat. Sci Forum* 264-268 (1998), p.849.
- [8] E.H. Nicollian and J.R. Brews, *MOS Physics and Technology* (Wiley Interscience, NY 1982)
- [9] M. Sadeghi and O. Engstrom, *Microelec. Eng.*, 1997, 36, p.183.
- [10] S. Berberich, P. Godignon, M.L. Locatelli, J. Millan and H.L. Hartnagel, *Sol. Stat. Elect.*, Vol. 42, No. 6, p. 915.
- [11] F. Owman, L.I. Johansson and P. Martensson, *Inst. Phys. Conf. Ser. No. 142, Chpt 2.* (1996), p. 477.

## Quantified Conditions for Reduction of ESO Contamination During SiC Metalization

G.Y. McDaniel<sup>1</sup>, S.T. Fenstermaker<sup>1</sup>, D.E. Walker Jr.<sup>1</sup>, W.V. Lampert<sup>1</sup>,  
S.M. Mukhopadhyay<sup>2</sup> and P.H. Holloway<sup>3</sup>

<sup>1</sup> Air Force Research Laboratory, Wright-Patterson AFB, OH 45433, USA

<sup>2</sup> Wright State University, Dayton, OH 45435-0001, USA

<sup>3</sup> University of Florida, Gainesville, FL 32611-6400, USA

**Keywords:** Adsorption Kinetics, Auger Electron Spectroscopy, Surface Kinetics

**Abstract:** In metalization work, controlled semiconductor surfaces and interfaces are necessary. Trace impurities such as carbon and oxygen at the metal/semiconductor interface may improve or degrade the electrical characteristics of a desired contact. In this study, Auger Electron Spectroscopy (AES) was used to investigate electron stimulated oxidation (ESO) of SiC. The research focused on chamber conditions necessary to prevent oxide formation on SiC surfaces during thin film metal deposition. Oxidation rate was studied as a function of beam exposure (on and off), primary electron beam energy,  $E_p$ , (3-6 keV), electron beam current,  $I_p$ , (25-500 nA), and total chamber pressure. Oxidation rate had a stronger correlation to overall chamber pressure rather than the partial pressure of  $H_2O$ ,  $CO$ , or  $CO_2$  alone. Oxidation rate decreased slightly as  $E_p$  was increased. Rate of oxidation increased at higher pressures ( $2.2 \times 10^{-7}$  Torr) with respect to  $I_p$  but was nearly independent of  $I_p$  at lower pressures ( $7.1 \times 10^{-9}$  Torr). No oxide growth was detectable to AES in the absence of exposure to the electron beam.

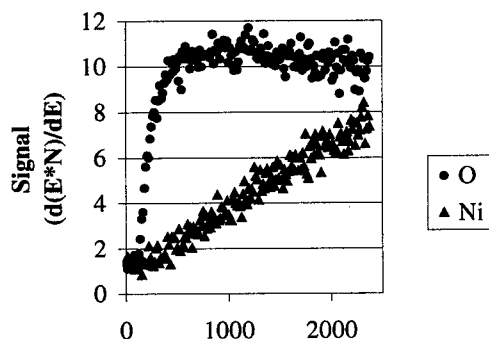


Figure 1. Typical Auger signal intensity for Ni (LMM) and O (KLL) transitions as a function of beam irradiation (sec) during a Ni

**Introduction:** The properties of SiC are attractive relative to other semiconductors for microelectronics devices operating in high temperature and harsh environments.[1,2,3,4,5,6,7] A production restriction is limited knowledge of contact properties and design. In-situ monitoring of contact formation provides growth control and yields valuable information on final performance properties. One technique commonly used is Auger Electron Spectroscopy (AES). In conventional chamber environments,  $10^{-6}$  Torr, the very technique used for control may introduce contaminants which degrade the final contact. Electron stimulated adsorption (ESA) and oxidation (ESO) are well-documented phenomena on Si that result in very thin (10-20Å)  $SiO_2$  layers.[8,9,10,11,12,13]

Figure 1 shows how substantial O levels can be achieved during metalization under normal deposition conditions. While the mechanism for oxygen absorption and oxide formation are well studied for Si, there is little or no characterization of the similar phenomenon on SiC. It is believed that the Si in the SiC matrix is predominantly responsible for ESO. As a result, the models used to describe ESO on Si will be applied to SiC. This study will characterize ESO of SiC as a function of chamber pressure, primary beam energy,  $E_p$ , and primary beam current,  $I_p$ . This data will help reduce contamination due to in-situ analysis with AES during metalization work.

**Experimental:** Sample preparation and equipment are described elsewhere.[14] Clean surfaces were irradiated by a continuous primary electron beam. Si, C, and O KLL transitions were

monitored in 60 eV windows for the duration of each experiment. Primary beam energies and currents ranged from 3 to 6 keV and from 25 to 500 nA. The beam size was approximately 0.008 mm<sup>2</sup>. Secondary electron yield curves for these experimental conditions were previously determined for SiC, slightly oxidized SiC, and molybdenum.[14]

**Results:** Data showed that SiC surfaces remained oxygen free, as detectable to AES, for as long as 17 hours in a UHV chamber with a background pressure of  $2.6 \times 10^{-8}$  Torr. Exposure to an electron beam under the same conditions stimulated growth of a surface layer of oxide in less than 25 minutes. McDaniel et.al., document signal trends for Si (KLL), C (KLL), and O (KLL) transitions during electron beam irradiation.[14]

To study oxidation as a function of background gas pressure, samples were exposed to an electron beam with  $E_p = 5$  keV and 300 nA resulting in an estimated current density of 0.375 mA/cm<sup>2</sup>. Total chamber pressure ranged from  $3.8 \times 10^{-10} \leq P_{\text{residual}} \leq 1.6 \times 10^{-8}$  Torr. Oxidation rate ( $dI_o/dt$ ) was determined for each experiment as described by McDaniel et. al. and is shown in Figure 2 vs. total system pressure.

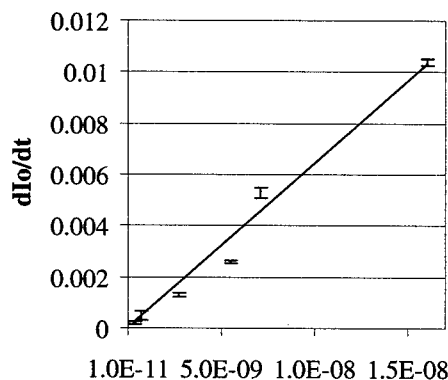


Figure 2. Instantaneous oxidation rate ( $dI_o/dt$ ) at time = 0 as a function of total residual chamber pressure (Torr).

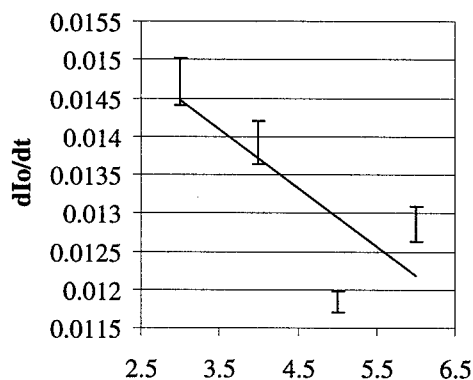


Figure 3. Instantaneous oxidation rate ( $dI_o/dt$ ) at time = 0 as a function of  $E_p$  (keV).  $I_p$  was 300 nA for each experiment.

Primary voltage and current were varied to determine their effects on oxidation rate. At a chamber pressure of  $1.6 \times 10^{-8}$  Torr and current of 300 nA (0.375 mA/cm<sup>2</sup>),  $dI_o/dt$  approximated a linear decrease as  $E_p$  was increased from 3 to 6 keV (see Figure 3). At a pressure of  $2.2 \times 10^{-7}$  Torr and  $E_p$  of 5 keV, the initial oxidation rate increased linearly as the current was increased from 25 to 300 nA (0.031-0.375 mA/cm<sup>2</sup>) (see Figure 4, curve B). At a pressure of  $7.1 \times 10^{-9}$  Torr, there was less dependence of the rate on current from 200 to 500 nA (0.25-0.625 mA/cm<sup>2</sup>) as shown in curve A.

**Discussion:** Irradiating solid surfaces with moderate to high-energy electron beams (characteristic of AES) results in many processes. Some of these include electronic excitation of surface species; adsorption, dissociation and/or desorption of gas species; bond breaking; diffusion; and charge build-up.[10,15] The electron beam may excite gaseous or adsorbed gases causing them to interact more strongly or rapidly with the surface. Adsorbed or gas-phase molecules can be dissociated directly by the primary beam and/or by secondary electrons.[10] Atomic oxygen from dissociation can then rapidly and easily oxidize the substrate.

Electron-beam stimulated oxidation depends on several factors. These include: concentration of oxygen-containing species, probability of dissociation into a reactive species, diffusion over the surface or to the oxide/substrate interface, and the reaction rate constant. Oxidation can be enhanced by any mechanism that aids dissociation of adsorbed species on the substrate surface.[10,13] In previous experiments on Si substrates, the electron-stimulated oxidation rate was controlled by maintaining a known pressure of oxygen-containing gas in the analysis chamber.[9,10,11,13] RGA analysis confirmed the majority fraction of the gas phase in



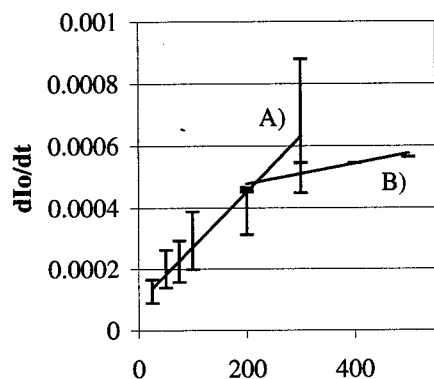


Figure 4. Instantaneous oxidation rate ( $dI_0/dt$ ) at time = 0 as a function of  $I_p$  (nA) at A)  $7.1 \times 10^{-9}$  Torr and B)  $2.2 \times 10^{-7}$  Torr.  $E_p$  was 5 keV for each experiment.

our experimental vacuum system was  $H_2O$ ,  $CO$ , and  $CO_2$ . No reagent gases were leaked into the system. This setup mimics actual deposition conditions. After dissociation, atomic oxygen can cause oxidation by diffusion to the oxide/SiC interface.[16] Si is kinetically favored for oxidation versus C and the Gibbs Free Energy of amorphous  $SiO_2$  (-215.91 kcal/mol) is considerably lower than that of SiC (-14.4 kcal/mol).[17] As a result, oxygen is expected to easily break the SiC bond to oxidize Si at the oxide/substrate interface. McDaniel et. al. suggest formation of a mixture of Si oxides or oxide precursors rather than pure  $SiO_2$  at this interface and removal of C from the surface presumably in the form of  $CO$  and  $CO_2$ . [14] The growing oxide layer, however, limits diffusion of oxygen, and is presumably the reason for the decline in reaction rate (saturation of the oxygen signal) for longer electron beam exposure times.

Oxidation rate ( $\alpha\beta$  or  $dI_0/dt$ ) vs. time was modeled using the equations described by Tougaard et. al., McDaniel et. al., and Darici et. al.[9,14,18] The linear dependence of oxidation rate versus pressure, shown in Figure 2 is consistent with the proposed mechanism. While the linear trend is present for total chamber pressure, it does not follow for any one constituent. This suggests more than one species is contributing to the oxidation of the surface. Tougaard, Kirby, and Coad report that both  $CO$  and  $H_2O$  physisorbed on the surface are dissociated by interaction with primary and/or secondary electrons forming reactive atomic oxygen for oxidation.[9,10,11,12] Regardless of the parent species, the rate of oxidation is expected to depend on (i) the concentration of atomic oxygen on the surface and (ii) the diffusion probability for oxygen to the oxide/SiC interface for reaction with Si to form  $SiO_x$ . It is commonly assumed that reaction of atomic oxygen with Si is very rapid. Coverage of the substrate surface by oxygen containing compounds would affect step (i). The linear correlation between overall gas pressure and oxidation rate supports the conclusion that the coverage of oxygen containing species was the limiting factor in these experiments.

A negative correlation between  $E_p$  and oxidation rate is shown in Figure 3. McDaniel et. al. characterized the secondary electron yield for SiC, slightly oxidized SiC, and Mo. Results indicate secondary electron yield should be constant or decrease with increasing  $E_p$  in the range of 3-6 keV. A reduction in yield provides fewer electrons for dissociation, therefore, a reduction in oxidation rate is expected. This is consistent with the data shown in Figure 3. The cross section for molecular dissociation by primary beam electrons may also be reduced with increasing  $E_p$ . Based on a reduced cross-section and reduced secondary electron generation, a decrease in oxidation rate above 3 keV is not surprising.

Darici et.al.[18] have modeled the data for electron-stimulated oxidation of ZnS in  $CO$  and  $CO_2$  atmospheres. In their model,  $\beta$  was directly proportional to current density and the rate of reaction was linearly related to pressure. Figure 4 curve A, shows  $dI_0/dt$  for various primary beam currents. There is very little dependence of oxide growth on  $I_p$  at this chamber pressure. Coad et.al.[12] report similar results on Si when no reagent gases were leaked into the chamber with a background pressure of  $5 \times 10^{-10}$  Torr,  $E_p = 2$  keV, and beam currents of 650 nA to 1600 nA. This observation is consistent with surface coverage rate limiting the oxidation reaction. With these current densities, the oxidation rate only depends on the availability of atomic oxygen. This would be expected if the flux of electrons was much greater than the flux of molecules. At a current density of  $0.375$  mA/cm<sup>2</sup>, the electron flux would be  $6.0 \times 10^{15}$  electrons/cm<sup>2</sup>-sec. The molecular flux at  $7.1 \times 10^{-9}$  Torr would be  $\approx 2.8 \times 10^{12}$  molecules/cm<sup>2</sup>-sec. Thus, the apparent lack of dependence upon  $I_p$  is consistent.

On the other hand, the data in Figure 4, curve B, shows a strong positive linear correlation with  $I_p$ . At this pressure,  $2.2 \times 10^{-7}$  Torr, surface coverage is sufficiently high and the rate of dissociation is a product of the molecular surface coverage and the current density, rather than the

surface coverage alone. This observation is consistent with both the model of Tougaard, et al[9] and Darici, et al.[18]

**Summary and Conclusions:** Conditions to reduce ESO due to AES analysis have been quantified for 6-H SiC. A linear increase in the rate of electron-stimulated oxidation has been determined for increasing residual gas pressure. The oxidation rate decreased linearly with respect to primary beam energy above 3 keV. At a pressure of  $2.2 \times 10^{-7}$  Torr, the oxidation rate increased linearly with increasing current. However, little dependence of oxidation rate on beam current was measured at  $7.1 \times 10^{-9}$  Torr. These data for higher pressure support a dependence of oxidation rate on availability of oxygen as well as the number of electrons at the surface for dissociation. A dependence on surface coverage only is noted at very low pressures. At pressures less than  $2.0 \times 10^{-9}$  Torr and very low currents,  $\sim 10$  nA, successful metal depositions have been achieved with little contamination (see Figure 5).

**Acknowledgments:** Special thanks are given to LeAnne Petry for her help in characterizing the oxidation films. Jim Solomon and John Grant provided valuable guidance with respect to electron effects for oxygen on Si and SiC.

#### References:

- [1] Morkoc, S. Strite, G. B. Gao, M. E. Lin, B. Sverdlov, and M. Burns, *J. Appl. Phys.* 76 (1994), p. 1363-1371.
- [2] Robert A. Metzger, *Compound Semiconductors 1* (1995), p. 26-28.
- [3] Simon Lande, *III-V's Review 9* (1996), p. 58-62.
- [4] Cree Research, *Properties and Specifications for 6H-Silicon Carbide*. Cree Research, Durham, NC. (1995).
- [5] Papanicolaou, A. Christou, and M. L. Gipe, *J. Appl. Phys.* 65 (1989), p.3526-3530.
- [6] Moki, A. P. Shenoy, D. Alok, and B. J. Baliga, *J. Elect. Mat.* 24 (1995), p. 315-317.
- [7] J. W. Lee, S. J. Pearton, C. J. Santana, J. R. Mileham, E. S. Lambers, and C. R. Abernathy, *J. Electrochem. Soc* 143 (1996), p. 1093-1098.
- [8] T. Miyake, S. Soeki, H. Kato, T. Nakamura, and A. Namiki, *Phys. Rev. B* 42 (1990), p. 11801-11807.
- [9] S. Tougaard, P. Morgen, and J. Onsgaard, *Surf. Sci.* 111 (1981), p. 545-554.
- [10] R. E. Kirby, and D. Lichtman, *Surf. Sci.* 41 (1974), p. 447-466.
- [11] R. E. Kirby, and J. W. Dieball, *Surf. Sci.* 41 (1974), p. 467-474.
- [12] J.C. Coad, H.E. Bishop, and J.C. Riviere, *Jap. J. Appl. Phys.* 31 (1992), p. L1707-L1709.
- [13] Jiazhan Xu, W.J. Choyke, and John T. Yates Jr. *J. Appl. Phys.* 82 (1997), p. 6289-6292.
- [14] G. Y. McDaniel, S. T. Fenstermaker, D. E. Walker Jr., W. V. Lampert, S. M. Mukhopadhyay, and P. H. Holloway, *Surf. Sci.* Not yet published (1999), p. X.
- [15] C. G. Pantano, T. E. Madey, *Appl. Surf. Sci.* 7 (1981), p. 115-141.
- [16] Takayuki Narushima, Takashi Goto, Yasutaka Iguchi, and Toshio Hirai, *J. Am. Ceram. Soc.* 73 (1990), p. 3580-3584.
- [17] Lide, David R, *CRC Handbook of Chemistry and Physics*. CRC Press, Boca Raton, (1991-1992), p. 5-16-59.
- [18] Darici, Y. P. H. Holloway, J. Sebastian, T. Trottier. S. Jones, and J. Rodriguez, *J. Vac. Sci. Tech. A* 17 (1999), p. X.

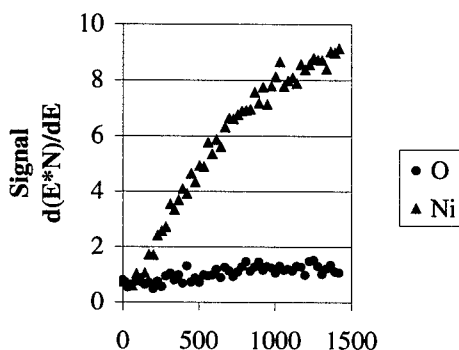


Figure 5. Typical Auger signal intensity for Ni (LMM) and O (KLL) transitions as a function of beam irradiation (sec) during a Ni deposition at pressure less than  $2.0 \times 10^{-9}$  Torr and low current  $\sim 10$  nA.

## Thermal Annealing Effect on TiN/Ti Layers on 4H-SiC: Metal-Semiconductor Interface Characterization

D. Defives, O. Durand, F. Wyczisk, J. Olivier, O. Noblanc and C. Brylinski

Laboratoire Central de Recherches, Thomson-CSF, Domaine de Corbeville,  
B.P. 10, FR-91404 Orsay Cedex, France

**Keywords:** AES, Annealing, Interfacial Layer, Metal/SiC, Reflectivity, TEM, XRD

**Abstract :** A microstructural study of a TiN/Ti/4H-SiC stack is reported. The evolution of the stack with annealing has been studied by X ray-diffraction, X ray-reflectivity, Auger Electron Spectroscopy and Transmission Electron Microscopy for as-deposited, 300°C, 500°C and 800°C annealed samples. Up to 500°C, the crystalline structure of the Ti and TiN layers are unchanged and well-textured. An interfacial layer between Ti and SiC is evidenced by X-ray reflectivity and TEM. AES analysis reveals Ti-C bonds at the interface for all the annealing temperatures investigated. Oxygen diffusion at the interface after a 500°C anneal is also shown. Annealing of the stack at 800°C induces the formation of new crystalline phases consisting of  $Ti_5Si_3$ ,  $C_{0.7}N_{0.3}Ti$  and titanium oxide as revealed by the XRD pattern.

### Introduction

Due to its large bandgap, SiC is a suitable material for devices operating at high temperatures and high power. On one hand, Schottky barrier diodes have been identified as near ideal fast rectifiers for medium and high voltages. On the other hand, the immaturity of MOS structures led to the development of the metal-semiconductor gated transistor devices such as power MESFETs and SITs. Refractory metals are preferably chosen for Schottky contacts because of their high temperature stability. In particular, first results on titanium makes it a promising metal barrier on SiC showing good forward current and low reverse leakage current [1,2]. Several microstructural analyses described the behavior of Ti/SiC contacts on 6H- [3,4], 3C- [5] and, more, recently on 4H-SiC [6]. In the present study, we report on the effect of annealing on the microstructure of the TiN/Ti/SiC stack deposited onto n-type 4H-SiC, where TiN is used to prevent the Ti layer from oxidation. For different annealing temperatures, we focus our attention on the characterization of the interface between titanium and silicon carbide.

### Experimental

Ti (1000Å) and TiN (1000Å) are deposited by sputtering and reactive sputtering respectively, on the Si face of n-doped 4H-SiC substrate purchased from Cree. Prior to metal deposition, SiC substrate is prepared using the RCA cleaning in order to obtain reproducible surfaces. With this surface preparation, we expect to obtain an oxygen rich SiC surface. After metal deposition, the substrate is divided into  $1 \times 1 \text{ cm}^2$  squares. Then, some of the square samples are annealed under  $N_2$  atmosphere with the following conditions : 300°C for 2 minutes, 500°C for 2 and 4 minutes, and 800°C for 2 minutes. Both X-ray diffraction(XRD) and small angle X-ray reflectivity are performed using a

Seifert-MZ-IV  $\theta/2\theta$  goniometer, equipped with a graphite monochromator which selects the  $\lambda_{K\alpha Cu}$  wavelength.

Reflectivity gives both individual thickness and interfacial roughness in the stack. The modulation of the reflected intensity (Kiessig fringes), depending on the incidence angle, are directly related to thickness. Surface roughness is related to the loss of the high order fringes contrast. The reflectivity data are fitted using the GIXA software, provided by Philips Analytical. Auger Electron Spectroscopy (AES) profiles were carried out using a Phi 680 Field Emission Scanning nanoprobe. Sputter depth profiling is performed using a

2 keV, 500 nA  $Ar^+$  ion beam used to etch the samples over a  $2\text{ mm}^2$  area. Transmission Electron Microscopy (TEM) experiments were performed on a 200kV microscope with a point to point resolution of  $1.8\text{\AA}$ . Cross-sections were performed by mechanical grinding and polishing with final surface milling. Samples were observed along the  $[100]$  axis of SiC.

## Results and discussion

On the as-deposited sample,  $\theta/2\theta$  spectrum provides diffraction peaks characteristic of Ti (002) and TiN (111) oriented crystalline phases. No other diffraction peaks appear, meaning that the phases are well-textured. This is confirmed by the Full-Width at Half-Maximum of the rocking curves, close to  $1^\circ$  ( $0.78^\circ$  for the Ti layer and  $1.12^\circ$  for the TiN layer). The numerous substrate diffraction peaks allow the determination of the value of the 4H-SiC lattice parameter  $c$  ( $1.088 \pm 0.007\text{\AA}$ ) which is found to be in good agreement with results published previously [7]. Annealing of the samples up to  $500^\circ\text{C}$  does not change the main figures of the XRD pattern. For the samples annealed below this limit, X-ray reflectivity spectrum is fitted using the stacking composition given in Fig. 1 (sample annealed at  $300^\circ\text{C}$  for 2 minutes). The plot shows Kiessig fringes from  $2\theta_c = 0.4^\circ$ , with  $\theta_c$  the critical angle, up to  $2\theta = 3^\circ$ . For the fit, we only fix the theoretical refractive index value  $n$  ( $n = 1 - \delta$ ) for SiC with  $\delta_{SiC} = 10.4 \times 10^{-6}$  and its roughness around  $3\text{\AA}$  in accordance with AFM measurements. As shown in the inserted table (Fig.1), the calculated thickness of the Ti layer agrees with the expected value ( $1000\text{\AA}$ ) and the fitted refractive index is very close to the theory ( $\delta_{Ti} = 13.0 \times 10^{-6}$ ). On the other hand, the TiN layer thickness is smaller than expected because of the surface contamination. Moreover, the refractive index of this layer is smaller than the theoretical value, which is  $\delta_{TiN} = 16.6 \times 10^{-6}$ . As a matter of fact, the TiN

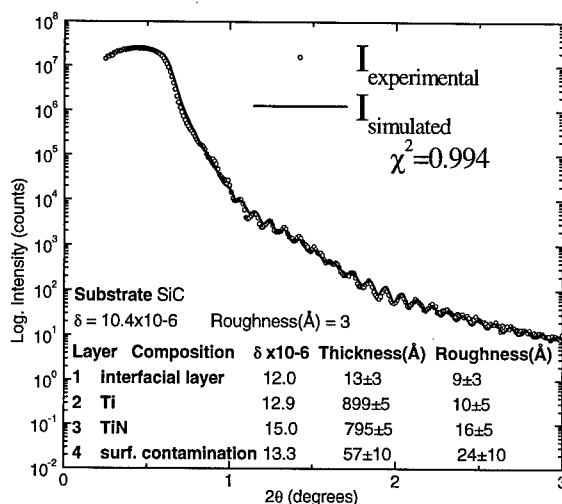


Fig. 1 : Reflectivity analysis of TiN/Ti/4H-SiC of a sample annealed  $300^\circ\text{C}$  for 2 minutes. Both experimental and simulated plots are shown together.

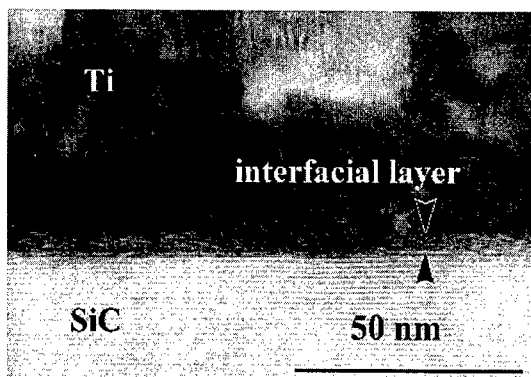


Fig. 2 : high resolution TEM image of as-deposited Ti on 4H-SiC showing the Ti layer, interfacial layer and SiC.

layer obtained by reactive sputtering is not expected to be stoichiometric. X-ray reflectivity also reveals the presence of an interfacial layer between titanium layer and silicon carbide for as-deposited samples and samples annealed up to 500°C. For all the samples, the mean thickness value is  $13 \pm 5 \text{ \AA}$ . The corresponding roughness value between this interfacial layer and the Ti layer is  $11 \pm 4 \text{ \AA}$ . No significant evolution of thickness and roughness are evidenced with annealing up to 500°C. High resolution TEM technique confirms the interfacial reflectivity results. Figure 2 shows an image of the Ti//SiC interface for the as-deposited sample. It evidences the interfacial layer between metal and semiconductor around 40 Å thick. This last thickness value can be compared to the sum of the thickness and the roughness obtained in reflectivity. As expected, 'interfacial layer/Ti layer' roughness appear in TEM to be larger than the 'SiC/interfacial layer' one. The microstructural composition of the interface is still under investigation by this technique.

Figure 3 shows AES depth profiles for different annealing temperatures. The investigated Auger peaks and their respective positions were C(KLL, 272eV), O(KLL, 510eV), N(KLL, 387eV), Ti<sub>1</sub>(LMM, 390eV), Ti<sub>2</sub>(LMM, 421eV) and Si(KLL, 1621eV). Due to their close Auger energies, nitrogen and titanium contributions cannot be dissociated in TiN. Depth profiles in Fig.3 show the well-known TiN surface contamination (essentially carbon and oxygen). For as-deposited and samples annealed up to 500°C (Fig. 3a and 3b) where there is no or only a slight interdiffusion as shown by the reflectivity measurements, the sputtering times of both TiN and Ti layers are proportional to the expected thickness of the layers. For the as-deposited and 300°C annealed samples (Fig. 3a), we note at the Ti//SiC interface the presence of oxygen traces due to the surface preparation that becomes undetectable after annealing at 500°C (Fig.3b), probably by diffusion into the whole structure. For this last temperature, the annealing time does not bring any difference between 2 and 4 minutes, meaning that the diffusion occurs between 300 and 500°C. In addition, for as-deposited and annealed samples up to 500°C, the shape of the C and Ti profiles suggest a Ti-C reaction at the Ti//SiC interface (on some nanometers). However, no bulk TiC crystalline phase appears in XRD patterns. The small thickness and the probably poor crystallinity of the interfacial layer could explain that. Moreover, during the Auger profile, ion mixing due to surface bombardment at the Ti//SiC interface can contribute to the formation of Ti-C bonds[8]. No Ti-Si bonds could be evidenced by this technique whatever the

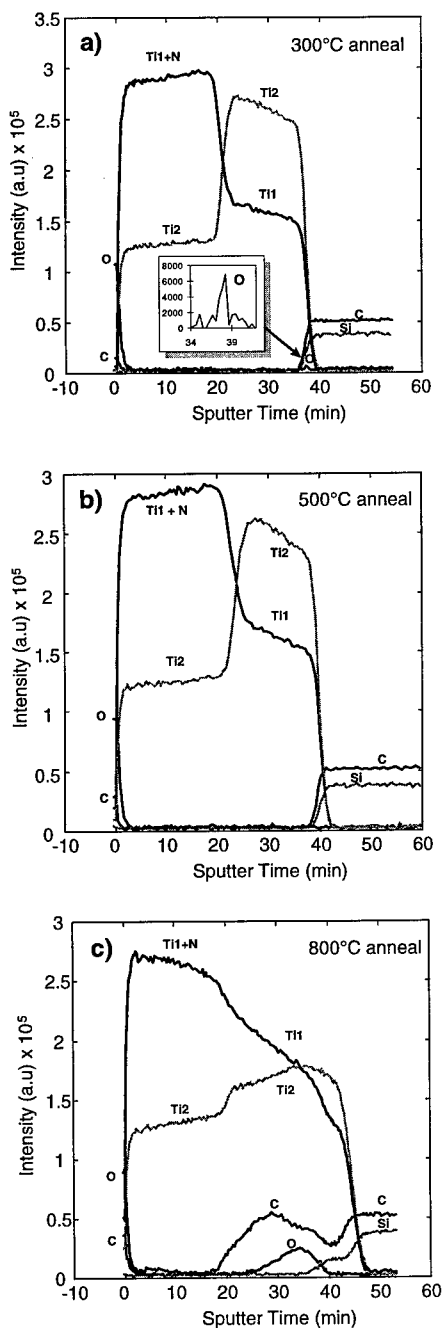


Fig. 3 : intensity vs depth profiles of Ti, N, Si, C and O atoms determined by Auger electron Spectroscopy (AES) for a sample annealed at : a) 300°C 2 minutes, b) 500°C 4 minutes, c) 800°C 2 minutes.

annealing temperature up to 500°C. Therefore, it seems that the oxygen leaving allows the formation of Ti-C bonds at the interface preferentially to Ti-Si bonds up to 500°C annealing. Similar result have been reported on 3C-SiC[5] which indicates that no titanium silicides are formed below 600°C.

Above 500°C annealing, some changes occur in the microstructure of the TiN/Ti//SiC stack. For a sample annealed at 800°C for 2 minutes, Ti and TiN diffraction peaks have disappeared in XRD pattern and oriented  $\text{Ti}_5\text{Si}_3$  (420), oriented  $\text{C}_{0.7}\text{N}_{0.3}\text{Ti}$  (111) and a titanium oxide crystalline phases are evidenced. There is no more constructive interferences that can be observed on reflectivity curve, showing that all the interfaces are poor-defined due to layer intermixing. Figure 3c shows the corresponding AES depth profile. It shows that the metal multilayer is considerably affected. Silicon of SiC reacts with titanium to give the  $\text{Ti}_5\text{Si}_3$  crystalline phase. Ti-C bonds are clearly observed at the interface. For 700°C anneal, similar results on the Ti//6H-SiC interface had been previously observed with Ti-C bonds and involving a  $\text{TiC}_{1-x}$  phase[3]. It was shown that the faster diffusivity of the carbon than the silicon in the titanium layer could explain the early formation of TiC crystallites at the interface. As for lower annealing temperatures, this phase is either too thin or too disordered to appear in the XRD pattern. Far from the interface, carbon and nitrogen atoms diffuse and react with titanium of the Ti layer to give the  $\text{C}_{0.7}\text{N}_{0.3}\text{Ti}$  crystalline phase. Probably due to a loss of nitrogen, the  $\text{TiN}_{1-x}$  layer is no more a diffusion barrier and allows oxygen to penetrate from atmosphere into the titanium layer to react with it. Thus, the titanium oxide phase found in the XRD pattern is located between  $\text{C}_{0.7}\text{N}_{0.3}\text{Ti}$  and  $\text{Ti}_5\text{Si}_3$ . Conversely, the  $\text{TiN}_{1-x}$  phase seems to prevent carbon from diffusing.

## Conclusion

Annealing of the TiN/Ti//SiC structure up to 500°C leave the stacking microstructure well-textured. It shows the presence of an interfacial layer between titanium and SiC, chemically characterized by Ti-C bonds. It also evidences the presence of oxygen in the as-deposited interfacial layer that diffuses and completely disappears for the sample annealed at 500°C. Above 500°C, annealing induce chemical reaction of the titanium layer with SiC producing  $\text{Ti}_5\text{Si}_3$  and  $\text{C}_{0.7}\text{N}_{0.3}\text{Ti}$  crystalline phases. Moreover, the nitrogen diffusion in TiN layer allows the oxygen to diffuse from atmosphere into the Ti layer.

**Acknowledgments** : This work was supported by French Ministry of Research (Saut Technologique) and ST Microelectronics.

## References

- [1] D.Alok, B.J.Baliga, P.K.McLarty, IEEE Electron Device Lett., Vol. 15, n°10 (1994), p. 394.
- [2] A.Itoh, T.Kimoto, H.Matsunami, 1995 Int. Symp. on Power Semiconductor Dev. Proc., (1995), p. 101.
- [3] L.M.Porter, R.F.Davis, J.S.Bow, M.J.Kim, R.W.Carpenter, J. Mat. Res., Vol.10, n°3 (1995), p. 668.
- [4] R.S.Okojie, A.A.Ned, D.Kurtz, W.N.Carr, IEEE Trans. on El. Devices, Vol. 46, n°2 (1999), p. 269.
- [5] F.Touati, K.Takemasa, M.Saji : IEEE Trans. on Electron Devices, Vol. 46, n° 3 (1999), p. 444.
- [6] L.Kassamakova, A.Kakanakova-Georgieva, R.Kakanakov, Ts.Marinova, I.Kassamakov, Tz.Djambova, O.Noblanc, C.Arnode, Semicond. Sci. technol., Vol. 13 (1998), p. 1025.
- [7] H.Romanus, G.Teichert, L.Spiess, Material Science Forum, Vol. 264-268 (1998), p. 437.
- [8] S.Ingre, M.B.Johnson, R.W.Streater, G.I.Sproule, J. Vac. Sci. Technol., 20 (4), 1982, p. 968.

## A Surface/Interfacial Structural Model of Pd Ultra-thin Film on SiC at Elevated Temperatures

W.J. Lu, D.T. Shi, T.R. Crenshaw, A. Burger and W.E. Collins

Department of Physics, Center for Photonic Materials and Devices, Fisk University,  
Nashville, TN 37208, USA

**Keywords:** Atomic Force Microscopy, Interfacial Structures, Pd, Surface Structure, X-Ray Photoelectron Spectroscopy

### ABSTRACT

In the work, the surface/interface structures of Pd/SiC were investigated by angle resolved X-ray photoelectron spectroscopy (ARXPS) and atomic force microscopy (AFM) after consecutive annealing from 100°C to 600°C with 100°C increments in air for 30 minutes. The thickness of the Pd ultra-thin film on SiC was about 30 Å. The relative intensities of the Si(2p), C(1s), Pd(3d), and O(1s) core level XPS peaks from the Pd/SiC samples changed quite strongly with various electron emission angles since the effective probing depth decreases with increasing emission angle. SiC became more chemical active due to the presence of Pd on the SiC surface. The Pd silicides were formed above 300°C. SiC<sub>x</sub>O<sub>y</sub>, Si, and Pd were found on the top of graphite and Pd silicides from 300°C to 400°C. With increasing temperatures, the concentration of the SiC<sub>x</sub>O<sub>y</sub> decreased and SiO<sub>2</sub> was formed. At 500°C and 600°C, graphite was on the top of the film, and the Pd silicides and SiO<sub>2</sub> were between the SiC substrate and the graphite. Oxygen is absorbed strongly on Pd surface at room and elevated temperatures. A surface/interfacial structural model for Pd/SiC at various elevated temperatures was suggested.

### INTRODUCTION

SiC-based device developments require that the metal contacts and interconnects are physically, chemically, and electrically stable under severe conditions, such as at high temperatures. In recent years, the SiC-based devices have become commercially available [1]. However, the diffusions and reactions between metal thin films and the SiC substrate result in the formation of various interfacial compounds, and alter the electrical properties.

Pd/SiC Schottky diodes have been successfully demonstrated as hydrogen and hydrocarbon sensors [2,3] operated at high temperatures. The heat treatment significantly promotes interfacial diffusion and chemical reactions, and broadens the interface region. The two-dimensional surface diffusion and surface segregation of Si from dissociated SiC result in a thin silicon oxide layer on the top of the Pd film [2]. After annealing at 425°C, the Pd chemical states are various co-existing palladium silicides (Pd<sub>x</sub>Si, x = 1,2,3,4) for the Pd thickness of about 400 Å [3]. Our previous results [4,5] show that Pd exists as PdSi and Pd<sub>2</sub>Si for the ultra-thin Pd film (~30 Å thickness) on SiC, and various silicon and carbon related compounds in Pd/SiC are formed at elevated temperatures.

In this study, the surface and interfacial composition and the morphological features of Pd ultra-thin films on 6H-SiC after thermal annealing were investigated using angle resolved X-ray photoelectron

spectroscopy (ARXPS) and atomic force microscopy (AFM). The surface morphology and the variations in ARXPS intensity were used to determine the surface/interface structures of Pd ultra-thin film on 6H-SiC after consecutive annealing from 100 to 600°C in air.

## EXPERIMENTAL

### 1. Samples and Pd ultra-thin film fabrication:

n-type, Si-face 6H-SiC wafers with  $3.5^\circ$  off-axis on Si (0001) substrates were purchased from Cree Research Inc. The doping concentration was  $2.6 \times 10^{18} \text{ cm}^{-3}$ . An RF sputtering system (Kurt J. Lesker Company) was used for the Pd ultra-thin film preparation. The SiC wafer was cleaned by a modified RCA procedure [4]. The thickness of Pd thin film on SiC was about 30 Å, so that XPS can effectively detect the Pd/SiC interfacial compositions.

The Pd/6H-SiC samples were analyzed and annealed consecutively from 100°C to 600°C in 100°C increments in air for 30 minutes each time.

### 2. Characterization

The XPS experiments were performed on a Kratos X-SAM 800 spectrometer with an energy resolution of 0.1 eV. The base pressure was at  $10^{-9}$  Torr. The Mg K $\alpha$  ( $h\nu=1253.6$  eV) radiation was used. The energy scale of the analyzer was calibrated by the Cu (2p $_{3/2}$ ) XPS peak at 932.67 eV, and the Au (4f $_{7/2}$ ) XPS peak at 84.00 eV.

The exit angles of the photoelectron were varied by rotating the sample. The data were smoothed and satellite peaks were subtracted before background subtraction and deconvolution were performed. The background of the XPS was subtracted using the Shirley algorithm. The Gaussian-Lorentzian method was applied to deconvolute the XPS.

A NanoScope E (Digital Instruments, Inc.) was used for AFM measurements. The standard silicon nitride cantilever supplied by Digital Instruments, Inc. was employed. The force constant of the silicon nitride cantilever is 0.12 N/m. At least three different regions on the surface were measured by AFM for each sample.

## RESULTS AND DISCUSSION

### 1. Chemical compounds in Pd/SiC at elevated temperatures.

XPS was used to examine the surface/interface composition on Pd/6H-SiC from the as deposited and after each annealing step. The surface/interface species formed on the Pd/SiC surface are quite complex, and our previous reports show [4,5] that the surface/interface compounds on Pd/SiC samples after annealing include Pd silicides, Pd element, and the silicon and carbon related compounds.

The reaction products between Pd and SiC are different at different temperatures. At 300°C, the Pd reacts to SiC to form Pd $_2$ Si on 6H-SiC substrate, and the Pd $_2$ Si reacts with SiC to form PdSi at 600°C for Pd/6H-SiC [4]. Various carbon and silicon compounds [5] are formed with the presence of Pd ultra-thin film on SiC surface after different annealing temperatures. Silicon oxycarbides (SiC $_x$ O $_y$ ) are found and the atomic ratio of C to O decreases with increasing annealing temperatures. SiO $_2$  is formed after annealing at 500°C and above. The amorphous Si is formed after annealing in the temperature region of 200-400°C, and Pd seems to act as a catalyst to break the Si-C bonds in SiC into Si and C phases. A low concentration of the C=O group exists on Pd/SiC through the annealing temperature up to 600°C. Table I lists the XPS peaks of the C(1s), Si(2p $_{3/2}$ ), and Pd (3d $_{5/2}$ ) after deconvolution for Pd/6H-SiC as deposited and after each annealing step.



TABLE I. Carbon, silicon, and palladium compounds on Pd/SiC as deposited and after consecutive annealing in air for 30 minutes.

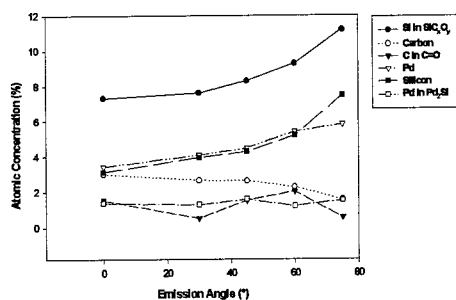
Annealing Temperatures (°C)	Compounds
as deposited	C, SiC <sub>x</sub> O <sub>y</sub> , C=O, Pd
100°C	C, SiC <sub>x</sub> O <sub>y</sub> , C=O, Pd
200°C	Si, C, SiC <sub>x</sub> O <sub>y</sub> , C=O, Pd
300°C	Si, C, SiC <sub>x</sub> O <sub>y</sub> *, Pd, Pd <sub>2</sub> Si, C=O, C-O
400°C	Si, C, SiC <sub>x</sub> O <sub>y</sub> *, Pd <sub>2</sub> Si, C=O
500°C	C, SiC <sub>x</sub> O <sub>y</sub> *, Pd <sub>2</sub> Si, C=O, SiO <sub>2</sub>
600°C	C, SiO <sub>2</sub> , PdSi, C=O

\* atomic ratio of C to O decreases with increasing annealing temperatures.

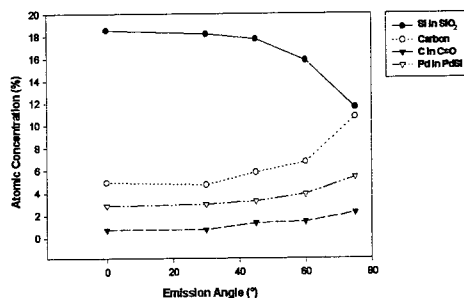
## 2. Surface/interface structures on Pd/SiC.

The relative intensities of the Si(2p), C(1s), Pd (3d), and O(1s) core level XPS peaks from Pd/SiC were measured at the electron emission angles from 0 to 75° after each step annealing. For the Pd/SiC samples as deposited, and after annealing at 100 and 200°C, Pd is at the elemental state. A strong O(1s) peak indicates that oxygen can be absorbed on Pd surface at room and elevated temperatures. The atomic concentration of oxygen on Pd/SiC is 40-50% from the XPS data.

At 300°C, Pd reacts with SiC to form Pd<sub>2</sub>Si [4], and the presence of Si shows that the Si-C bonds in SiC break into Si and C phases. Figure 1(a) shows the atomic concentrations of various compounds on Pd/SiC at different electron emission angles after thermal annealing at 300°C in air. As shown, the concentrations of SiC<sub>x</sub>O<sub>y</sub>, Si, and Pd increase rapidly with increasing emission angles. The intensities of graphite and Pd<sub>2</sub>Si decrease slightly with increasing emission angles. Therefore, SiC<sub>x</sub>O<sub>y</sub>, Si, and Pd are on the top of graphite and Pd<sub>2</sub>Si. The surface/interface structure on Pd/SiC has no significant change after annealing at 400°C.



(a) 300°C



(b) 600°C.

Figure 1: Atomic concentrations of various compounds on Pd/SiC with different electron emission angles after thermal annealing in air.

Figure 1(b) shows the atomic concentrations of various compounds on Pd/SiC at different

electron emission angles after thermal annealing at 600°C in air. As shown, graphite is on the top of the film, and SiO<sub>2</sub> and PdSi are between the graphite and the SiC substrate. The AFM images show that the Pd film becomes a nanostructured layer with the average size of 20-30nm. At 600°C, the nanosize rounded clusters on SiC are formed. A surface/interface structural model of Pd/SiC at elevated temperatures is suggested in Figure 2.

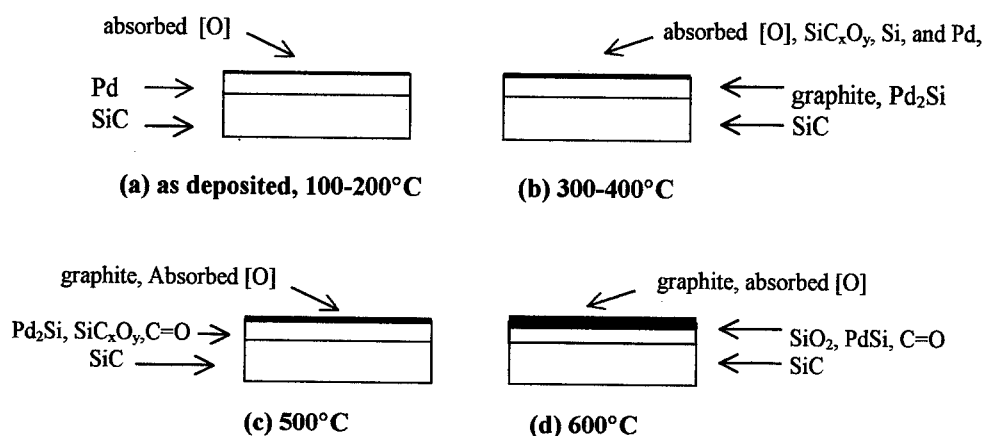


Figure 2. A surface/interface structures of Pd/SiC at elevated temperatures

## CONCLUSIONS

A surface/interface structural model for Pd/SiC at elevated temperatures is suggested. Oxygen is absorbed strongly on Pd surface at room and elevated temperatures. The Pd silicides are formed above 300°C. SiC<sub>x</sub>O<sub>y</sub>, Si, and Pd are found on the top of graphite and Pd silicides on SiC from 300°C to 400°C. At 500°C and 600°C, graphite is on the top of the film, and the Pd silicides and SiO<sub>2</sub> are between the graphite and the SiC substrate.

## ACKNOWLEDGMENTS

The work was supported by NASA grant Nos NAG3-2126 and NCC8-133. The authors are thankful for the discussion with Dr. Gary W. Hunter at NASA Glenn Research Center.

## REFERENCES

- [1] V. Saxena, and A.J. Steckl, "SiC Materials and Devices", Semiconductors and Semimetals, Vol. 52, edited by Y.S. Park, Academic Press, San Diego, CA, USA, 1998, p.77.
- [2] L.-Y. Chen, G.W. Hunter, P.G. Neudeck, G. Bansal, J. B. Petit, and D. Knight, *J. Vac. Sci. Technol. A* **15**(3), (1997), p.1228.
- [3] L.-Y. Chen, G.W. Hunter, P.G. Neudeck, and D. Knight, *J. Vac. Sci. Technol. A* **16**(5), (1998), p.2890.
- [4] W.J. Lu, D.T. Shi, A. Burger, and W.E. Collins, *J. Vac. Sci. Technol. A*, **17**(4), (1999), p.1182.
- [5] W.J. Lu, D.T. Shi, T. Crenshaw, A. Burger, and W.E. Collins, *the Materials Research Society Symposium Proceedings*, Vol. 572, Eds., S. C. Binari, et al., 1999, p.87.

## Study of a Clean Surface of $\alpha$ -SiC and its Metallization Process by Cu, Au and Ni using STM and Electron/Photon Spectroscopies

M. Iwami<sup>1</sup>, M. Hirai<sup>1</sup>, M. Kusaka<sup>1</sup>, I. Mihara<sup>1</sup>, T. Saito<sup>1</sup>, M. Yamaguchi<sup>1</sup>,  
T. Morii<sup>2</sup> and M. Watanabe<sup>3</sup>

<sup>1</sup> Research Laboratory for Surface Science, Faculty of Science, Okayama University,  
Okayama 700-8530, Japan

<sup>2</sup> Matsushita Research Inst. Tokyo Inc., 3-10-1 Higashimita, Tama-ku, Kawasaki 214-8501, Japan

<sup>3</sup> Ion Engineering Co., Hirakata, Osaka 573-0128, Japan

**Keywords:** Heat Treatment, Initial Stage, Interface Silicides, Metallization, Surface Structure, X-Ray Emission Analysis

**Abstract** We have studied clean surfaces of 6H(4H)SiC(0001)Si and C and metal(film)-SiC(substrate) contact systems, where noble and transition metals are adopted. Heat treated SiC surfaces in ultra high vacuum(UHV) has shown surface super structures depending on temperature. In the case of metal deposition on SiC substrates, it has been clarified that deposited metal atoms form islands in the initial stage. Soft X-ray emission spectroscopy (SXES) study has elucidated the fact that there is a Ni<sub>2</sub>Si buried interface layer for a Ni(film)-SiC(substrate) contact heat treated at 600-800°C.

**1. Introduction** Metal contacts formation process on semiconductor SiC substrates has been intended to study in order to fabricate a reliable contacts in a controlled manner. SiC surfaces heat treated in UHV has also been studied considering possible important roles to have reliable overlayer.

Auger electron spectroscopy(AES), low energy electron diffraction(LEED) and scanning tunneling microscopy(STM) were used for the characterization of SiC surfaces with and without metal atoms on top. We have also adopted soft X-ray emission spectroscopy(SXES) method for either structural or electronic property analysis[1].

**2. Experimental** Metal atoms deposition process on SiC has been characterized in an ultra high vacuum(UHV; less than 10<sup>-7</sup>Pa) chamber. Metal atoms deposition was carried out by vacuum evaporation of metal atoms from a tungsten basket. Nominal metal film thickness was monitored by a quartz micro balance. In UHV- STM studies, we adopted those commercially available from UNISOKU, Japan, and OMICRON. SXES experiment was carried out by using SHIMADZU NEB 0789[1].

### 3. Results and discussion

3.1 6H(4H)- SiC(0001) surfaces heat treated in UHV: Before loading in a UHV chamber, SiC specimens were rinsed in an organic solvent by giving ultrasonic vibration to be followed by an etching in KOH or HNO<sub>3</sub>/HF. In a UHV camber, they were heated at ~600°C for more than several hours to desorb volatile contaminants. Samples were then heated at 900~1300°C for several minutes. Above 900°C, oxygen atoms were ascertained to be eliminated from SiC

surfaces by AES. AES analysis also showed Si(LVV)/C(KLL) signal intensity ratio increased up to  $\sim 1000^\circ\text{C}$  to decrease at higher temperatures. LEED studies showed  $1\times 1$  SiC to change into  $\sqrt{3}\times\sqrt{3}$  and  $6\sqrt{3}\times 6\sqrt{3}$  structures with raising heating temperature. STM showed similar structures except for  $6\times 6$  instead of  $6\sqrt{3}\times 6\sqrt{3}$  which could be explained by considering the existence of a graphite layer on top of SiC(0001) surface. Sometimes  $3\times 3$  structure was also observed[2,3].

3.2 Initial stage of metal atoms deposition: Auger spectra for Cu atoms deposition on  $6\text{H-SiC}(0001)\sqrt{3}\times\sqrt{3}$  surfaces are shown in Fig.1, where the Cu coverage is shown in mono layer (ML) unit. 1ML is defined by the atomic number of the SiC(0001) surface in the bulk like structure. Structure patterns observed by LEED are also shown for discussion. Auger signals at around 63, 93 and 274eV correspond to Cu(MVV), Si(LVV) and C(KLL) peaks, respectively. Cu(MVV) signal intensity is increasing with Cu deposition, whereas Si(LVV) and C(KLL) peak intensities are decreasing with Cu coverage. The  $6\text{H-SiC}(0001)\sqrt{3}\times\sqrt{3}$  LEED pattern for the zero coverage changes into  $1\times 1$  at the Cu coverage of  $\sim 1$  ML. The  $1\times 1$  LEED pattern continues up to 5ML of Cu deposition. Above 5ML, no LEED pattern could be observed. This LEED observation shows the fact that Cu islands are formed on top of a SiC surface.

Auger Peak to peak (P-P) intensity of Si(LVV) is shown in Fig.2 as a function of the nominal

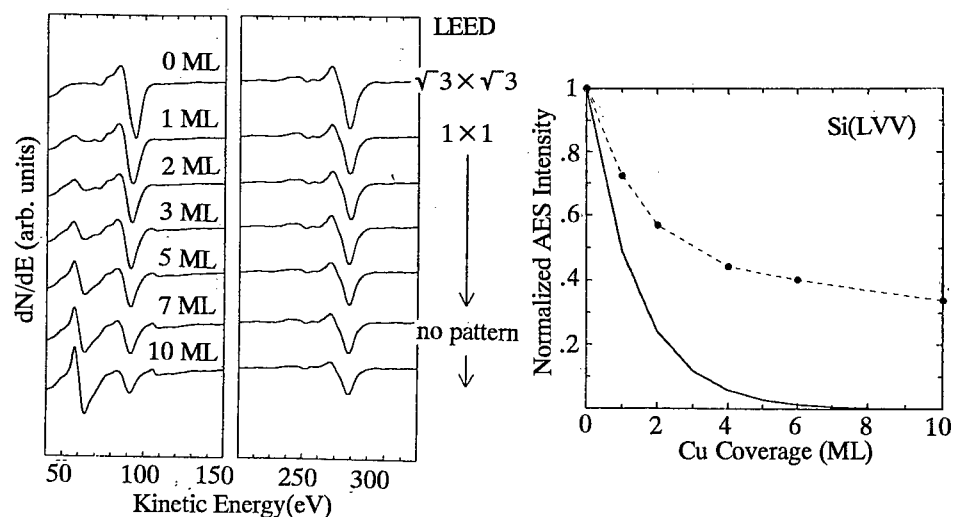


Fig.1 Auger spectra for Cu deposition on top of  $6\text{H-SiC}(0001)\sqrt{3}\times\sqrt{3}$ . Structural information obtained by LEED observation are also shown for discussion.

Fig.2 Si(LVV) signal intensities vs. nominal Cu layer thickness. Filled circles connected by dotted lines are experimental data, where the dotted lines are simple connection of the experimental data points. Solid line indicates an expected change in signal intensity for the layer by layer growth.

Cu film thickness for an experiment of Cu atoms deposition on the 6H-SiC(0001) $\sqrt{3}\times\sqrt{3}$  substrate. The filled circles connected with dotted lines are experimental data, where dotted lines are simple connection of experimental data points. The solid line indicates the expected decrease of the Si(LVV) signal for the case of layer by layer growth of Cu overlayer, i.e., the Franck van der Merwe growth. The calculated solid line is deduced by considering the decrease of the Si(LVV) Auger electron intensity as  $\exp(-nd/\lambda_e \cos \theta)$ , where  $n$  is the number of the Cu layer thickness,  $d$  is the thickness of the one monolayer (ML) of Cu,  $\lambda_e$  is the mean free path of the Si(LVV) Auger electron and  $\theta$  is the angle of detection of the Auger electron with respect to the sample surface normal. It is clear that experimental data points, filled circles, deviate clearly from the calculated solid line. This fact, i.e., the experimental signal intensities are larger than the solid line, claims that Cu atoms deposited form islands. This conclusion is consistent with the above explanation for the Cu overlayer formation deduced by the LEED results. Therefore, it can be said that small Cu metal islands form at the initial stage of Cu atoms deposition on the 6H-SiC(0001) $\sqrt{3}\times\sqrt{3}$  surface. Similar was the case for different surfaces with various surface structures. Almost the same results were obtained for Au deposition on SiC, although the growth mode is more layer like than Cu.

**3.3 SXES study of heated Ni(film)/SiC(substrate) specimen:** SXES study has been carried out in the case of a Ni(film)/SiC(substrate) system. In the electron excited SXES study, we can perform nondestructive in depth analysis of a film-substrate contact system by using the fact that a soft X-ray emission band spectrum is characteristic for a material[1]. For example, the Si-L<sub>2,3</sub> emission band spectrum shows quite different features for Si crystal and Si compounds, even in the case that the spectral shapes of Si(LVV) Auger signals for Si crystal and Si compounds are almost the same. An interesting point of the electron excited SXES analysis is that one can perform a study of a buried interface layer without using a destructive tool like ion sputtering. That is because both the X-ray production depth( $d_x$ ) of an energetic electron and the mean free path of a soft X-ray( $\lambda_x$ ) are larger than the mean free path of an electron( $\lambda_e$ ) with energies less than a few keV which is used generally in electron spectroscopies, i.e.,  $d_x$  and  $\lambda_x \gg \lambda_e$ .

Fig.3 shows SXE spectra for a Ni(20nm)-SiC(substrate) system heat treated at 800°C measured by varying the incident electron energy( $E_p$ ), where the spectral region at the photon energies of  $h\nu = 85-105\text{eV}$  corresponds to the Si-L<sub>2,3</sub> emission band. At large  $E_p$ , the spectra are almost the one of crystalline SiC. By decreasing  $E_p$ , i.e., by decreasing the X-ray production depth( $d_x$ ), the shape of the spectra changes from that of the SiC single crystal. The change in the spectral shape of the Si-L<sub>2,3</sub> emission band means the fact that Si atoms have a different chemical bonding state at the Ni(film)-SiC(substrate) interface region. Ni does not give any meaningful signal at this photon energy region except structureless Bremsstrahlung. A possibility to induce such a spectral change in the Si-L<sub>2,3</sub> emission band spectrum is a formation of a different Si compound at the Ni-SiC interface. Considering the contact system is composed by Ni and SiC, possible compounds including Si atoms are Ni-silicides. We have tried to reproduce the experimental Si-L<sub>2,3</sub> emission band spectra. The spectrum of Fig.3(c) can be reproduced by adding the spectrum of SiC single crystal[Fig.3(a)] and that of Ni<sub>2</sub>Si[4] at the ratio of around 0.5: 0.6. At  $E_p = 1.5\text{keV}$ , the spectra[Fig.3(d)] is more Ni<sub>2</sub>Si like. This result can be explained by considering Ni<sub>2</sub>Si layer formation at the Ni(film)-SiC(substrate) interface. Similar result was obtained in the case of 600°C heating of a

Ni(film)/SiC(substrate) specimen.

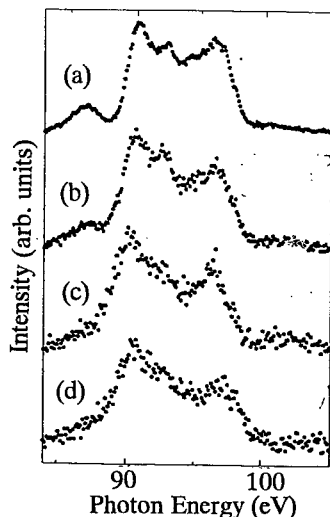


Fig.3

Si L<sub>2,3</sub> soft X-ray emission spectra for Ni(20nm)/SiC(substrate) specimen heat treated at 800°C for 15min:  
 (a) SiC bulk,  
 (b)  $E_p=3\text{keV}$ ,  
 (c)  $E_p=2\text{keV}$ ,  
 (d)  $E_p=1.5\text{keV}$ .

**4. Summary** The present study can be summarized as follows:

- (1) Several different surface structures have been clarified by LEED and STM for UHV heated 6H(4H)-SiC(0001) surfaces.
- (2) Metal islands formation has successfully been shown for the initial stage of metal atoms deposition on 6H(4H)-SiC(0001) surfaces.
- (3) Ni<sub>2</sub>Si layer formation has been indicated at the buried Ni(film)-SiC(substrate) interface heat treated at 600-800°C by SXES non-destructively.

**Acknowledgments** The authors would like to thank the grant in aid from the Ministry of Education, Science, Sports and Culture(Monbusho), in the special project. This work is also partly supported by NEDO(New Energy and Industrial Technology Development Organization).

#### References

- [1] M.Iwami, M.Hirai, M.Kusaka, M.Kubota, S.Yamamoto, H.Nakamura, H.Watabe, M.Kawai and H.Soezima: Jpn. J. Appl. Phys. **29** (1990) 1353.
- [2] Y.Marumoto, T.Tsukamoto, M.Hirai, M.Kusaka, M.Iwami, T.Ozawa, T.Nagamura and T.Nakata: Jpn. J. Appl. Phys. **34** (1995) 3351.
- [3] T.Tsukamoto, M.Hirai, M.Kusaka, M.Iwami, T.Ozawa, T.Nagamura and T.Nakata: Surf. Sci. **371** (1997) 316.
- [4] S.Yamauchi, M.Iwami, H.Ohshima and T.Hattori, Tech. Rept. Inst. Elec. Inform. Commun. Engr. Jpn., **ED94-28**, **CPM94-29** (1994) 83 (in Japanese).

## Monolayer Growth Modes of Re and Nb on the Polar Faces of 4H-SiC

K.W. Bryant and M.J. Bozack

Surface Science Laboratory, Department of Physics, Auburn University, Auburn, AL 36849, USA

**Keywords:** AES, Auger Electron Spectroscopy, Epitaxy, Metal Growth Modes

**Abstract:** Auger electron spectroscopy (AES) and secondary electron emission has been used to determine how thin monolayer films of Re and Nb grow on the 4H-SiC(000 $\bar{1}$ ) C-face and 4H-SiC(0001) Si-face surfaces at room temperature. The secondary electron emission was monitored by the crystal current (SEEC) method and compared to the change in Auger electron peak-to-peak intensities for both substrate and adsorbate. On the 4H-SiC(0001) Si-face, both metals first form a single monolayer followed by growth of simultaneous monolayers (MSM mode). On the 4H-SiC(000 $\bar{1}$ ) C-face, both metals grow layer-by-layer (Frank-van der Merwe, FM mode).

**Introduction:** The existence of surface polarity in SiC has implications for process technology and practical device structures. In the case of metal growth, layered growth is preferred in semiconductor films and superlattices because interfaces with specified geometry can be engineered [1]. Of particular theoretical interest is the transition between uniform layer-by-layer growth, which wets the surface, and 3D-island formation, which does not wet the surface [2]. The production of thin metal films on solid surfaces is accomplished by many techniques like molecular beam epitaxy (MBE) [3], evaporation from a refractory wire [4], electron beam evaporation [5], and others [6].

Studies of the two polar faces of 6H-SiC have shown differences in etch rate [7,8], oxidation [9,10], gross reactivity [11], and graphitization [12] at high temperature. Unfortunately, there have been few studies for 4H-SiC, the current SiC polytype of choice for device applications. In this paper we report monolayer metal growth kinetics of Re and Nb on 4H-SiC(000 $\bar{1}$ ) C-face and 4H-SiC(0001) Si-face surfaces at room temperature. This is accomplished by observing the attenuation of substrate Si Auger electrons as they traverse the growing metal layer. The Auger signals are corroborated by measurements of total crystal current as the incident electron beam interacts with the surface during metal growth. To our knowledge, there have been no prior reports of monolayer metal adsorption on 4H-SiC and only one study on 6H-SiC [13]. In that work, van Elsbergen et al. found that Cs grows layer-by-layer on the 6H-SiC(0001) Si-face surface at 130°C, with the films becoming metallic after the first Cs layer. Formation of the metal-semiconductor contact is of particular importance in the device fabrication of large scale integrated electronics [14]. Our recent work [15] with Nb contacts to n-type 4H-SiC shows that Nb results in a high-performance ohmic contact with good stability over hundreds of hours at 500°C.

Thermodynamic considerations predict three basic growth modes for epitaxial growth processes [16]. Frank-van der Merwe (FM) [17] growth is two-dimensional layer-by-layer growth. The impinging atoms adsorb onto the surface with a sufficiently high rate of diffusion, find a vacant site

and complete a layer prior to the start of the next layer. Stranski-Krastanov (SK) [18] growth involves the formation of a monolayer followed by 3D-island or crystallite growth. Films that have a strong film-substrate interaction usually exhibit SK growth [19]. Volmer-Weber (VW) [20] growth involves the formation of 3D-islands or crystallites. Rhead et al. [21] report two additional modes. The first is simultaneous monolayer (SM) growth (also called Poisson growth), which occurs when the adsorbed atoms have no lateral diffusion and remain where they are adsorbed. Given a uniform flux over the surface and no coalescence of the adatoms, there is no formation of crystallites. The other mode is monolayer formation followed by simultaneous monolayer (MSM) growth. Here, the diffusion of the adsorbate on the substrate is adequately high to allow the uniform growth of the first monolayer, which is then followed by very slow or no lateral diffusion of the adsorbate on the initial monolayer. A first monolayer is formed, followed by growth of simultaneous monolayers. The (MSM) mode is difficult to distinguish from SK growth unless exponential variation of the Auger intensities is observed after the first monolayer or careful LEED studies are undertaken. In a comprehensive review of 440 investigations performed between 1968-88, Argile and Rhead [22] report that many systems originally reported as exhibiting SK growth more correctly exhibit MSM growth.

**Experimental:** The on-axis Epitronics n-type 4H-SiC crystals used in this work were 0.012" thick with orientations of  $(0001) \pm 5^\circ$  and  $(000\bar{1}) \pm 5^\circ$  for the Si- and C-face surfaces respectively. The dopant concentrations were  $1 \times 10^{19}/\text{cm}^3$  for the Si-face surface and  $1.5 \times 10^{18}/\text{cm}^3$  for the C-face surface. To independently check the surface polarity, we oxidized the polar faces at 1373 K (500 sccm of  $\text{O}_2$  passed through a bubbler). Gölz et al. [23] has shown that the 4H-SiC(0001) Si-face oxidizes slower than the C-face. Rutherford backscattering spectroscopy (RBS) verified that there was a thicker oxide layer on the C-face surface.

The 4H-SiC crystals were first ultrasonically cleaned in electronics grade 1,1,1-trichloroethane followed by acetone and 12 M $\Omega$ /cm deionized water, then mounted and placed in the UHV chamber. After evacuation to  $3 \times 10^{-10}$  torr, the surfaces were in-situ cleaned by a combination of annealing and ion bombardment. We first ramp the crystal temperature to 1400 K to volatilize the native oxide and graphitize the surface. Next, the crystal is maintained at 700 K while it is sputtered using  $\text{Ar}^+$  ions at  $75^\circ$  from the surface normal with stepwise decreases in ion energy from 6 keV to 3 keV to 1 keV. The crystal is then annealed at 700 K for 10 minutes. The procedure has been shown to maintain near perfect surface stoichiometry and minimize the amount of implanted argon.

**Growth of Re on 4H-SiC:** Adsorption of rhenium on the 4H-SiC(0001) Si-face surface is shown in Fig. 1, where the peak-to-peak intensities for the Si (LVV) 90 eV Auger peak and the Re (NVV) 176 eV Auger peak is plotted as a function of deposition time. Also shown is the crystal current as a function of deposition time. A clear break in the crystal current is evident at a time of 9.7 min. The Si (LVV) Auger peak intensity breaks from a straight line at 13.2 min and the Re (NVV) Auger peak intensity breaks at 12.8 min. The breaks in the Auger peak intensities are within experimental error of each other but the break in the crystal current at a slightly earlier time may be indicative of a surface process that may not be detectable by AES. The secondary electron emission is sensitive to the

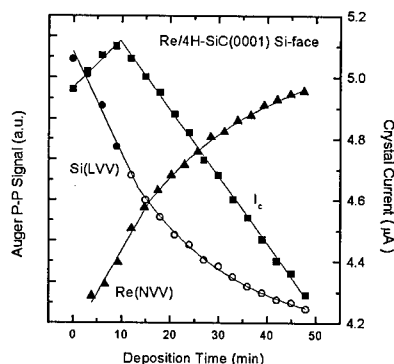


Fig. 1. Auger signal and crystal current vs deposition time for adsorption of Re on the 4H-SiC (Si-face) surface.



surface composition as well as the surface structure and the early break could be indicative of a change in surface structure as Re is adsorbed. Beyond the first break there is a linear decrease in crystal current throughout the remainder of the Re deposition. Argile et al. [22] notes that increases in the crystal current during adsorption corresponds to an increase in the secondary emission of electrons from the surface. This can usually be explained by a decrease in the work function of the surface. After 10 minutes, the work function increases, which may be an indication that the surface has become metallic after the first monolayer of Re, as Re has a relatively high work function (5.0 eV) [24,25] compared to SiC (4.5 eV)[26]. The Auger data after the first break have been best-fit to a first order exponential. The chi-squared goodness of fit is in excellent agreement with the exponential decrease expected for growth by simultaneous monolayers (MSM).

The adsorption of rhenium on the 4H-SiC(000 $\bar{1}$ ) C-face surface is shown in Fig. 2. The Si (LVV) Auger peak intensity shows three lines with two clear breaks at deposition times of 11.6 min and 34.5 min while the two breaks for the Re (NVV) Auger peak intensity occur at times of 10.4 min and 32.2 min. The Re (NVV) Auger peak intensity shows atypical behavior by showing the slope of the third line increasing rather than decreasing. The crystal current also shows two distinct breaks from straight-line plots occurring at 11.9 min and 31.2 min which is within experimental error of the Auger data. Such sequence of straight-line segments is expected for layer-by-layer or Frank-van der Merve growth (FM). The irregular behavior of the adsorbate Auger intensity indicates complex, second-order effects in the growth, such as an increased sticking coefficient or the coalescence of small crystallites upon completion of the second layer which acts to complete the third layer more rapidly and increase the measured adsorbate intensity.

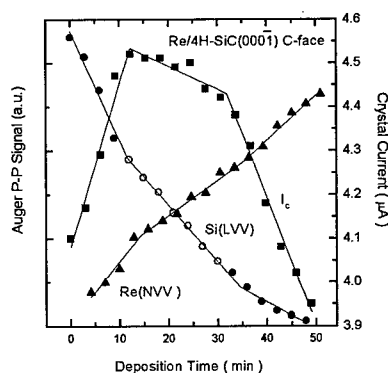


Fig. 2. Auger signal and crystal current vs deposition time for adsorption of Re on the 4H-SiC (C-face) surface.

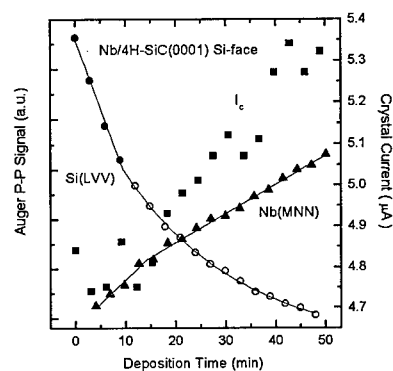


Fig. 3. Auger signal and crystal current vs deposition time for adsorption of Nb on the 4H-SiC (Si-face) surface.

**Growth of Nb on 4H-SiC:** Niobium adsorption on the 4H-SiC(0001) surface is shown in Fig. 3. The Auger intensity plots show a single break from the initial straight lines with the Si (LVV) plot occurring at a time of 8.0 min and the Nb (MNN) plot occurring at 10.6 min. After the time of 8 min the Si (LVV) Auger peak intensity signal was also fit to an exponential decay with excellent agreement. The Nb (MNN) was also fit to the associated exponential function after 10.6 min and was better fit by the exponential function but the variation is quite slow and a linear function produced more error with a deviation from linearity at 36 min. The crystal current exhibited too much scatter to be curve fitted but a general increasing trend is noticed after the formation of the first monolayer. The Auger data are an indication for monolayer growth followed by simultaneous monolayer (MSM) growth.

Fig. 4 shows the growth of niobium on 4H-SiC(000 $\bar{1}$ ) C-face surface. The Si (LVV) Auger peak intensity plot shows two distinct breaks at times of 9.5 min and 26.4 min. The Nb (MNN) Auger

peak intensity plot also shows two breaks at times of 10.7 min and 26.4 min. The crystal current plot shows a monotonic increase with deposition time and two breaks occurring at 9.3 min and 25.2 min. All breaks are within experimental error of each other and show layer-by-layer growth (FM). The breaks are assigned to the completion of continuous adsorbate layers. The reduction of the slope after the deposition of the first layer is explained by a lowered sticking probability of the Nb atoms on the first Nb adlayer. Again the increase in crystal current has been associated with the lowering of the work function of the surface and if this is the case then for Nb on 4H-SiC(000 $\bar{1}$ ) the work function is continuously lowered with deposition time. The work function of Nb is 4.30 eV as compared to the work function of SiC of 4.5 eV.

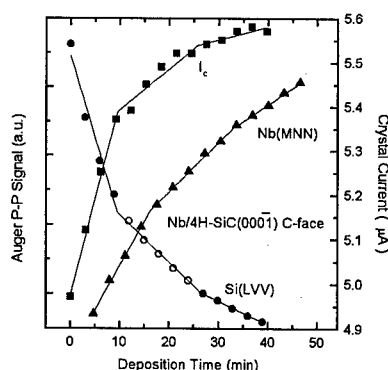


Fig. 4. Auger signal and crystal current vs deposition time for adsorption of Nb on the 4H-SiC (C-face) surface.

**Acknowledgements:** This work was supported in part by NASA Grant No. NAGW-1192 through the Center for Commercial Development of the Auburn University Space Power Institute.

## References

- [1] S. Stoyanov, *Surf. Sci.* 199 (1988) 226.
- [2] S. Stoyanov and I. Markov, *Surf. Sci.* 116 (1982) 313.
- [3] J. R. Arthur, *Surf. Sci.* 299/300 (1994) 818.
- [4] Y. Wu, E. Garfunkel, and T. E. Madey, *Surf. Sci.* 365 (1996) 337.
- [5] V. A. Dmitriev, K. Irvine, and M. Spencer, *Appl. Phys. Lett.* 64 (1994) 318.
- [6] J. Crofton, L. M. Porter, and J. R. Williams, *Phys. Stat. Sol. B* 202 (1997) 581.
- [7] F. Bozso, L. Muehlhoff, M. Trenary, W. J. Choyke, and J. T. Yates, Jr., *J. Vac. Sci. Technol. A* 2 (1986) 1271.
- [8] K. Brack, *J. Appl. Phys.* 36 (1965) 3560.
- [9] A. Suzuki, H. Matsunami, and T. Tanaka, *J. Electrochem. Soc.* 125 (1978) 1897.
- [10] L. Muehlhoff, W. J. Choyke, M. J. Bozack, and J. T. Yates, Jr., *J. Appl. Phys.* 60 (1986) 2558.
- [11] A. Suzuki, H. Ashida, K. Mameno, and H. Matsunami, *Jpn. J. Appl. Phys.* 21 (1982) 579.
- [12] L. Muehlhoff, W. J. Choyke, M. J. Bozack, and J. T. Yates, Jr., *J. Appl. Phys.* 60 (1986) 2842.
- [13] V. van Elsbergen, T. U. Kampen, and W. Monch, *J. Appl. Phys.* 79 (1996) 316.
- [14] H. Balaska, R. C. Cinti, T. T. A. Nguyen, and J. Derrien, *Surf. Sci.* 168, 225 (1986).
- [15] T. N. Oder, et al., this conference, p. 997.
- [16] S. Stoyanov, *Surf. Sci.* 172 (1986) 198.
- [17] F. C. Frank and J. H. van der Merwe, *Proc. Roy. Soc. (London)* A200 (1949) 125.
- [18] J. N. Stranski and L. Krastanov, *Ber. Akad. Wiss. (Wien)* 146 (1938) 797.
- [19] M. H. Grabow and G. H. Gilmer, *Surf. Sci.* 194 (1988) 333.
- [20] M. Volmer and A. Weber, *Z. Phys. Chem.* 119 (1926) 277.
- [21] G. E. Rhead, M.-G. Barthès, and C. Argile, *Thin Solid Films* 82 (1981) 201.
- [22] C. Argile and G. E. Rhead, *Surf. Sci. Rept.* 10 (6/7) (1989) 277.
- [23] A. Golz, G. Horstmann, E. Stein von Kamienski, and H. Kurz, *Inst. Phys. Conf. Ser.* 142 (1996) 633.
- [24] V. S. Fomenko, *Handbook of Thermionic Properties* (New York, Plenum, 1966).
- [25] H. B. Michaelson, *J. Appl. Phys.* 48 (1977) 4729.
- [26] van Elsbergen, p. 318.

## Group-III Adsorption and Bond Stacking on SiC(111) Surfaces

Ulrike Grossner, J. Furthmüller and F. Bechstedt

Friedrich-Schiller-Universität Jena, Max-Wien-Platz 1, DE-07743 Jena, Germany

**Keywords:** Adsorption, Polytypism, Stacking, Surface

**Abstract:** Results of *ab initio* calculations are reported for the adsorption of boron and aluminum on  $\beta$ -SiC(111)  $\sqrt{3} \times \sqrt{3}$  R30° surfaces. We discuss structural and energetical properties of the most favourable adsorbate models and their influence on the stacking sequences.

Si(111) surfaces chemisorbed by group-III elements have been widely studied as prototype metal-semiconductor systems. At a coverage of one third of a monolayer, chemisorption of the group-III elements on a Si(111) surface leads to the formation of  $\sqrt{3} \times \sqrt{3}$  R30° structures [1]. As the preferred bonding site of larger group-III atoms as aluminum the T<sub>4</sub> site has been well established [1] whereas for boron a S<sub>5</sub> site is widely accepted and recently confirmed by photoelectron diffraction [2]. In the recent years more and more interest focused on SiC because of its outstanding properties for various devices. Heterocrystalline structures based on two polytypes allow the engineering of novel properties. The growth of the polytypes may be influenced by surfactants. For the  $\beta$ -SiC(111) and  $\alpha$ -SiC(0001) surfaces a  $\sqrt{3} \times \sqrt{3}$  R30° structure with one silicon adatom in T<sub>4</sub> position has been found to be energetically favourable over a wide range of growth conditions and to stabilize the growth of the hexagonal polytypes [3]. The question arises whether the well-known effects of the metal-Si(111) interface can be transferred to the group-III-SiC(111) system and similar kinds of surfactants for SiC can be found. These adsorbates may also induce changes of the surface energies and surface dipoles and thus influence the epitaxial process leading to a possibility to control polytype growth.

Our calculations are based on the density-functional theory within local-density approximation (DFT-LDA). We employ fully separable, non-normconserving ultrasoft pseudopotentials. The **k**-space integration is replaced by a sum over 6 special points in the irreducible part of the surface Brillouin zone. The many-body electron-electron interaction is described by the Ceperley-Alder exchange-correlation functional. Our calculations employ the conjugate-gradient method to minimize the total energy. Explicitly we use the Vienna Ab-initio Simulation Package [4]. For our calculations of silicon-terminated (111) surfaces slabs containing 12 atomic Si-C layers, and a vacuum region of about the same thickness are used. The bottom layers of these polar slabs are saturated with hydrogen atoms. The coordinates of the atoms in the lower C-terminated half of the slab are kept fixed in their ideal bulk positions, whereas the uppermost 6 surface layers are fully relaxed.

We consider different adsorbate-covered surfaces with 1/3 monolayer of the considered group-III atom and one silicon adatom in the boron case. The  $\sqrt{3} \times \sqrt{3}$  R30° translational symmetry is fixed. For aluminum we also consider geometries, where Al is fully substituting the Si adatom. These models of the B/SiC and Al/SiC adsorbate systems are combined out of the standard adsorption sites known for group-III metal adsorption on Si. The relevant sites are the threefold-coordinated T<sub>4</sub>, lying above a second-layer carbon atom, and the H<sub>3</sub>, lying above a fourth-layer carbon atom. For

boron we also consider the  $S_5$  site, where the boron atom substitutes a second-layer carbon atom directly under a  $T_4$  site. We classify these structures with the particular adatom sites for the considered atoms. To obtain the most favourable adsorption site we choose the cubic stacking of the Si-C bilayers. The results are in principle also valid for hexagonal substrates. The actual stacking only slightly influences the surface geometry and total energy changes [5]. However, to evaluate the role of the adsorbate atoms for the stacking sequence under the surface we also calculate structures with built-in stacking faults below the surface atomic layers. The considered *intrinsic* and the *extrinsic stacking faults* (ISF and ESF) have been found energetically favourable for the bulk cubic silicon carbide [6]. Because of the varying numbers of Si atoms per surface unit cell the total energies cannot directly compared for the different adsorption configurations considered. Instead the grand-canonical thermodynamical potential (for zero temperature and per surface unit cell, the surface energy) is used. It allows the description of the surface preparation conditions by varying the chemical potentials of the respective species. Upper limits on the chemical potentials  $\mu$  are set by the bulk elements indicating corresponding element-rich preparation conditions. The minimum value  $\mu_{\text{Si}} = \mu_{\text{Si-bulk}} - \Delta H_f$  follows after reduction by the heat of formation  $\Delta H_f$  of the corresponding solid SiC compound. To estimate the stability of one structure compared to the others, we show the phase diagram obtained as a function of the Si chemical potential in Fig. 1. Because of the mass action law the C chemical potential depends linearly on the Si one and, hence, has not to be considered. The thermodynamically relevant regions are indicated.

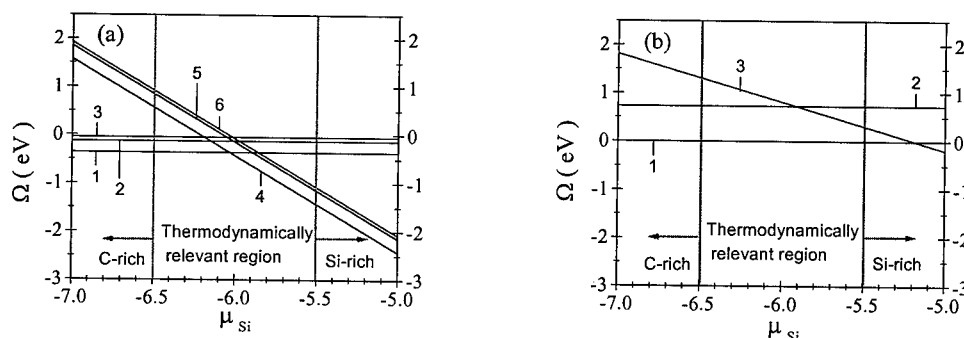


Fig. 1: Surface energy of (a) B:SiC(111) and (b) Al:SiC(111) structures in dependence of chemical potential of Si. The B and Al chemical potentials are fixed at their bulk values. The zero level of the surface energy is set to the values of the  $H_{3(\text{Si})} + S_{5(\text{B})}^{\text{sub}}$  and  $T_{4(\text{Al})}$  structures, respectively. (a) 1:  $T_{4(\text{Si})} + S_{5(\text{B})}^{\text{sub}}$  with cubic stacking; 2:  $T_{4(\text{Si})} + S_{5(\text{B})}^{\text{sub}}$  with ESF; 3:  $T_{4(\text{Si})} + S_{5(\text{B})}^{\text{sub}}$  with ISF; 4:  $T_{4(\text{Si})} + S_{5(\text{B})}$  with cubic stacking; 5:  $T_{4(\text{Si})} + S_{5(\text{B})}$  with ESF; 6:  $T_{4(\text{Si})} + S_{5(\text{B})}$  with ISF; (b) 1:  $T_{4(\text{Al})}$ ; 2:  $H_{3(\text{Al})}$ ; 3: Bridge $_{(\text{Si})} + T_{4(\text{Al})}$  structure.

The comparison of the surface energies for Al:SiC(111) leads to similar results as already established for silicon substrates: the energetically favourable adsorption site for aluminum is the  $T_4$  site directly above a second-layer carbon atom. Its surface energy is about 0.7 eV more favourable than the  $H_3$  site lying above a fourth-layer carbon atom. Under Si-rich conditions the Bridge $_{(\text{Si})} + T_{4(\text{Al})}$  structure is also more favourable than the  $H_{3(\text{Al})}$ . However, even under very Si-rich conditions this structure is energetically less favourable by about 0.4 eV in comparison to the  $T_{4(\text{Al})}$ , so that the same adsorption behaviour of aluminum as on Si(111) surfaces is confirmed also for the SiC(111)- $\sqrt{3} \times \sqrt{3}$  R30° surface.

For the adsorption behaviour of boron on SiC(111)- $\sqrt{3} \times \sqrt{3}$  R30° surfaces we find an interesting difference compared to the Si(111) case: whereas under Si-rich conditions boron replaces the carbon atom directly under the Si- $T_4$  adatom ( $T_{4(\text{Si})} + S_{5(\text{B})}$ ), under C-rich conditions one of the three basis atoms of the Si- $T_4$  adatom is replaced resulting in a ( $T_{4(\text{Si})} + S_{5(\text{B})}^{\text{sub}}$ ) structure. This observation

seems to be in agreement with the findings made after co-implantation of C and B [7]. It suppresses the formation of *D* centers (probably  $B_C-V_{Si}$  complexes). The co-implantation corresponds in the surface case to a B adsorption under C-rich conditions. In both cases, implantation and adsorption under C-rich conditions, the tendency of a substitution of C by B is weakened.

The two favourable structures are up to 1 eV lower in energy than the energetically next structures represented by the  $H_{3(Si)}+S_{5(B)}$  and  $H_{3(Si)}+S_{5(B)}^{sub}$ , respectively. A more closer look to the  $T_{4(Si)}+S_{5(B)}^{sub}$  structure (Fig. 2) shows that the boron atoms are laterally situated nearly in the middle of the first and the second surface layer and that the bonds to the three nearest-neighbour C atoms and to the Si adsorbate atom are shortened. Moreover, the bonding tetrahedron of the  $T_4$ -Si adatom is deformed from its ideal structure. The tetrahedron is flipped into the direction of the B atom, the Si adatom position changes a little from the  $T_4$  site. The tetrahedron-flipping mechanism is found to be relevant for polytypic transformations in the presence of applied shear stress and/or higher temperatures [8,9]. This mechanism may hence enforce the tendency for a change of the stacking in the growing surface on a 3C substrate but in the presence of B atoms. In other words, the B atoms may act as subsurfactant atoms and push a twisting of tetrahedron bonds resulting in a stacking fault in the uppermost Si-C bilayer on a 3C structure.

Whereas the tetrahedron-flipping process happens more or less during growth, it can be therefore more related to the kinetic effects influencing polytype growth. However, there is also an influence of the particular surface on the stacking in the atomic layers below the surface in the limit of the thermodynamic equilibrium [3,10]. In order to test this surface influence we have studied an *intrinsic* and an *extrinsic* stacking fault introduced into the cubic stacking of the slab used. The systems containing one of the two stacking faults give rise to a slightly higher energy (0.31 and 0.23 eV, respectively) in the case of a stable ( $T_{4(Si)}+S_{5(B)}^{sub}$ ) surface geometry. So the adsorption of boron under carbon-rich conditions seem to stabilize the cubic polytype under the surface. In contrast to the bulk case [6], the formation of a stacking fault needs energy. The question arises whether this is a result of the special surface considered or a more general result. For that reason we also study the adsorption under silicon-rich conditions and repeat the calculation for the  $T_{4(Si)}+S_{5(B)}$  structure. Here the *intrinsic* and an *extrinsic* stacking fault introduced to the slabs are also energetically more unfavourable by about 0.28 and 0.21 eV, respectively. Compared to the two B-covered surfaces the intrinsic and extrinsic stacking faults underneath a clean  $SiC(111)-\sqrt{3} \times \sqrt{3}R30^\circ$  surface with  $T_4$ -silicon adatom give rise to formation energies of 0.14 and 0.09 eV, respectively. This means that the influence of the surface to stabilize the cubic stacking increases due to the adsorption of boron.

Based on *first-principles* total energy calculations we present energetical and structural properties of B:SiC(111) and Al:SiC(111) interfaces. As for the metal-Si(111) systems the adsorption of B and Al leads to different results due to the smaller covalent radius of B. For Al:SiC(111) we find the adsorption of Al on  $T_4$  site energetically favourable. Aluminum acts also in the Al:SiC(111) system as a surfactant. For B:SiC(111) we find two different possibilities in dependence on the growth conditions. Under Si-rich conditions the carbon-substituting  $S_5$  site is energetically favourable, whereas under C-rich conditions a silicon-substituting sub- $S_5$  site is found. There is a certain tendency that the bond-tetrahedron of the uppermost Si atom is flipped. Investigations of different stacking faults within the cubic slab, however, show that a boron-covered surface stabilizes the cubic stacking in the near-surface region, at least in the thermodynamical equilibrium. Thus, it may lead to the possibility to support the growth of cubic SiC with the adsorption of boron.

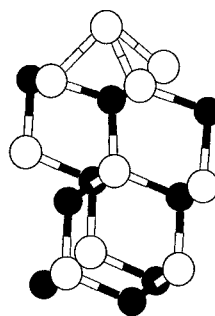


Fig. 2: Structural model of the  $T_{4(Si)}+S_{5(B)}^{sub}$  geometry. White (black, shaded) circles indicate Si, C, B atoms.

This work was supported by the Deutsche Forschungsgemeinschaft (Sonderforschungsbereich 196).

### References

- [1] see i.e. W. Mönch, *Semiconductor Surfaces and Interfaces* (Springer-Verlag, Berlin 1995); S. Wang, M. W. Radny, and P. V. Smith, Phys. Rev. B, **59** (1999), 1594; S. Kono, Surf. Rev. and Lett., **1** (1994), 359; H. Nagayoshi, Surf. Rev. and Lett., **1** (1994), 369; and references cited therein.
- [2] P. Baumgärtel et al., Phys. Rev. B, **59** (1999), 13014.
- [3] J. Furthmüller, P. Käckell, F. Bechstedt, A. Fissel, K. Pfennighaus, B. Schröter, and W. Richter, J. Electronic Mater., **27** (1998), 848-852.
- [4] G. Kresse and J. Hafner, Phys. Rev. B, **47** (1993), R558; G. Kresse and J. Furthmüller, Comput. Mat. Sci., **6** (1996), 15; Phys. Rev. B, **54** (1996), 11169.
- [5] F. Bechstedt, P. Käckell, A. Zywietz, K. Karch, B. Adolph, K. Tenelsen, and J. Furthmüller, phys.stat.sol. (b), **202** (1997), 35.
- [6] P. Käckell, J. Furthmüller, and F. Bechstedt, Phys. Rev. B, **58** (1998), 1326.
- [7] T. Frank, T. Troffer, G. Pensl, N. Nordell, S. Karlsson, and A. Schöner, Mat. Sci. For., **264-268** (1998), 681.
- [8] P. Pirouz and J. W. Yang, Ultramicroscopy, **51** (1993), 189.
- [9] P. Pirouz and P. M. Hazzledine, Sol. State Phen., **35-36** (1994), 183.
- [10] U. Starke, J. Schardt, J. Bernhardt, M. Franke, and K. Heinz, Phys. Rev. Lett., **82** (1999), 2107.

Corresponding author: [ulrike@ifo.physik.uni-jena.de](mailto:ulrike@ifo.physik.uni-jena.de), Fax: +49 - 3641 - 947152

## **Characterization of SiC using Synchrotron White Beam X-ray Topography**

**Michael Dudley and Xianrong Huang**

Department of Materials Science and Engineering, State University of New York at Stony Brook,  
Stony Brook, NY 11794-2275, USA

**Keywords:** Defects, Micropipe, Screw Dislocation, Synchrotron Topography

**Abstract.** A short review of recent synchrotron white beam X-ray topography (SWBXT) studies of defects in 4H and 6H SiC is presented. Defects observed include closed-core and hollow-core screw dislocations (micropipes) in 6H and 4H, deformation induced basal plane dislocations in 6H and 4H, and small angle boundaries in 4H. These studies include the analysis of the relationship between hollow-core diameter and the Burgers vector for micropipes using SWBXT and scanning electron microscopy (SEM), the principles of a set of SWBXT techniques and associated simulations for characterizing micropipes and closed-core screw dislocations, and the nucleation mechanism of micropipes obtained using SWBXT in combination with other techniques.

**Introduction.** Although SiC technology has reached the market place as an important semiconductor material for high-temperature, high-field and high-frequency devices, crystals currently grown by physical vapor transport can contain crystallographic defects such as screw dislocations with closed cores and hollow cores (micropipes), deformation-induced basal plane dislocations, heteropolytypic inclusions, planar defects, etc. While the densities of hollow-core screw dislocations have been drastically reduced and the incidence of heteropolytypic inclusions is rare, the densities of the closed-core screw dislocations (although decreasing) and basal plane dislocations are such that their characterization is very important both to help crystal growers develop strategies for their minimization or elimination and to aid in the understanding of the influence of these defects on device performance. The invited paper of Neudeck [1] at this conference, as well as previously published work [2,3], highlights the significant effect closed-core screw dislocations can have on device performance.

Compared with other characterization methods, SWBXT is a very powerful technique for observing almost all the aforementioned defects in SiC. The main advantage of SWBXT, as will be described in the following, is that this technique is a fast and nondestructive imaging method capable of revealing the distribution of defects over large areas (several tens of square inches). In particular, this technique can be used to clearly image micropipes and screw dislocations at both a microscopic and macroscopic level. The images of these dislocations not only provide much quantitative information concerning the detailed dislocation structures, such as the magnitudes and senses of the Burgers vectors and the interaction between adjacent dislocation groups, but also help us understand the formation mechanisms of these dislocations.

In this paper, we describe a set of SWBXT methods along with the corresponding image simulations, to show the principles and broad applicability of SWBXT in characterizing SiC single crystals. From various results obtained using SWBXT in combination with other techniques, we will also discuss a possible mechanism for micropipe nucleation in SiC.

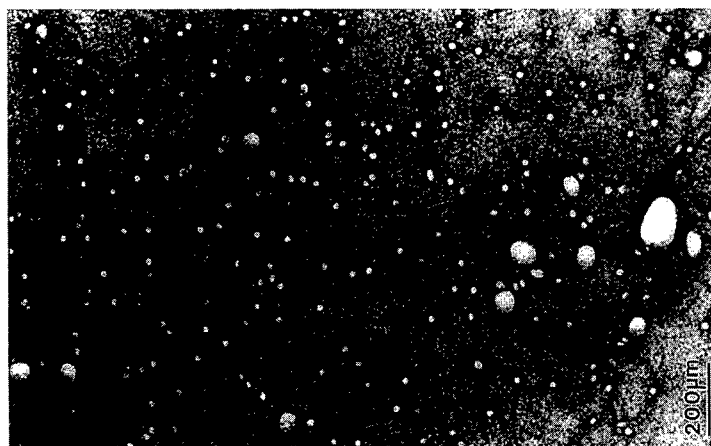


Fig. 1. SWBXT back-reflection images of closed-core (smaller white spots) and hollow-core (large white spots) screw dislocation in a (0001) 6H SiC wafer. The faint lines connecting these screw dislocation images are basal plane

**Micropipe-related screw dislocations in SiC.** Among the various defects that exist in SiC crystals, screw dislocations lying along the [0001] axis are the most significant and are generally accepted to be one of the major factors limiting the extent of the successful application of SiC. These screw dislocations have been shown to have Burgers vector equal to  $nc$  (where  $c$  is the lattice parameter and  $n$  is an integer), with hollow cores becoming evident with  $n \geq 2$  for 6H SiC and  $n \geq 3$  for 4H SiC. These latter hollow-core dislocations are generally referred to as *micropipes*, and their hollow cores can be understood from Frank's theory [4]. This theory predicted that a screw dislocation whose Burgers vector exceeds a critical value in crystals with large shear modulus should have a hollow core with the equilibrium diameter  $D$  related to the magnitude of the Burgers vector  $b$  by  $D = \mu b^2 / 4\pi^2\gamma$ , where  $\mu$  is the shear modulus and  $\gamma$  is the specific surface energy. Experimentally the diameter  $D$  can be directly measured by SEM or atomic force microscopy (AFM), while the Burgers vector magnitude  $b$  can be obtained using techniques such as measuring the height of the growth spiral on the as-grown surface using optical interferometry or AFM, or directly using X-ray topography. Detailed experimental results indicate the direct proportional relationship between  $D$  and  $b^2$  for micropipes in both 6H- and 4H-SiC [5-7]. In these studies the magnitudes of the Burgers vectors were obtained using a set of SWBXT methods including back-reflection topography, transmission topography, and section topography, as described in the following. The results obtained both explicitly verify Frank's theory and simultaneously reveal that micropipes in SiC are screw dislocations with large Burgers vectors (superscrew dislocations).

**Synchrotron back-reflection observation of micropipes and screw dislocations.** Both AFM and SEM are capable of revealing the hollow cores as well as the growth spirals associated with the large Burgers vector screw-dislocations on the as-grown surface, but the limitation of these techniques is that they cannot usefully reveal the density of screw dislocations with closed cores (which is typically in the range  $10^3$ - $10^4$  cm $^{-2}$ ), even on as-grown surfaces. For transmission electron microscopy (TEM), the large scale of the micropipes (with diameters being of the order of microns) makes it difficult to image a whole micropipe at the atomic level. On the other hand, the narrow visualization area of all the high-resolution imaging techniques also makes it impractical for these techniques to characterize large-size SiC wafers. Compared with these methods, SWBXT is a more effective technique for observing micropipes nondestructively due to its high strain sensitivity and suitable spatial resolution.

For imaging micropipes and screw dislocations in SiC, the most efficient geometry is the back-reflection geometry [8]. Fig. 1 shows a typical back-reflection topograph taken from a (0001) SiC wafer grown by Cree Research Inc. In this figure, the screw dislocations, whether hollow-core or



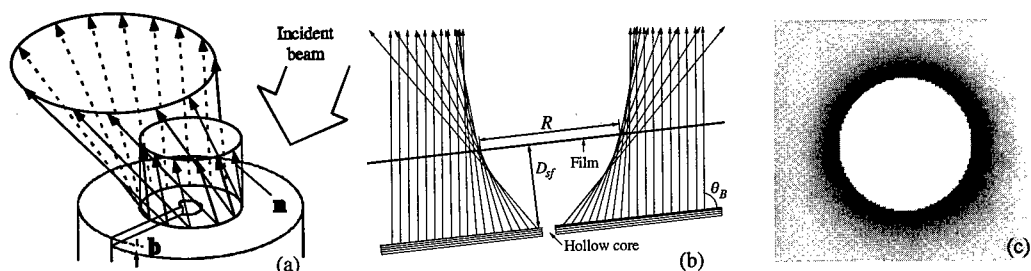


Fig. 2. The contrast formation mechanism of micropipes on SWBXT back-reflection topographs. (c) is a simulation of a 6c micropipe.

closed-core, are clearly revealed as white circular spots surrounded by black rings. From such images, the distribution of the micropipes and screw dislocations as well as their detailed structures can be obtained. Wafers up to several inches in diameter can be imaged in a single exposure by employing a scanning device. Moreover, the imaging can even be performed on wafers with devices fabricated on them, further emphasizing the advantages of this technique.

The formation mechanism of the circular images in Fig. 1 can be described using a simple geometric X-ray diffraction model [9-12]. As indicated in Fig. 2(a), due to the strain field of the screw dislocation, the normal  $\mathbf{n}$  to the (0001) lattice plane varies from point to point near the dislocation core. When a nearly parallel white synchrotron beam is incident on the surface, the X-rays diffracted from successive circular regions surrounding the core form numerous twisted cones [one of these cones is schematically shown in Fig. 2(a)]. The overlap of these cones in space results in the formation of the circular images [see Fig. 2(b)]. Based on this principle, the images of micropipes and screw dislocations can be rigorously simulated, as shown in Fig. 2(c).

Back-reflection SWBXT images of micropipes or screw dislocations contain abundant information concerning the dislocation structures. The most important information is that the diameter of a screw dislocation image quantitatively indicates the magnitude of the Burgers vector. From Fig. 1 one can see that two factors determine the image diameter: one is the Burgers vector magnitude of the dislocation and the other is the film-to-sample distance ( $D_{sf}$ ). The relationship between these three quantities is shown Fig. 3. From the curves in this figure it is easy to estimate the Burgers vector magnitude of any micropipe or screw dislocation revealed in the back-reflection topograph taken at a particular specific film-to-sample distance. For example, the smallest white

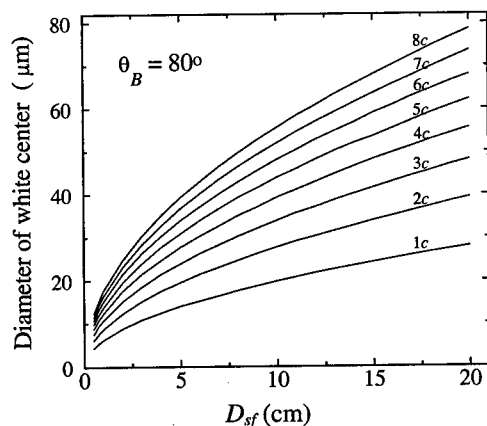


Fig. 3. Dependency of contrast diameter on Burger vector

spots, which have the highest density in Fig. 1, can be determined to be images of 1c screw dislocations, while the larger spots are images of micropipes with Burgers vectors ranging from 2c to 8c (micropipes with Burgers vector as large as several tens of the  $c$  lattice parameter can also occasionally be found in low-quality SiC crystals).

The other kind of structural information that can be obtained by back-reflection SWBXT is that the twist direction of the diffraction cones unambiguously indicates the dislocation sense, i.e. the sense of the Burgers vector. The clockwise twist of the diffracted X-rays (viewed toward the surface) in Fig. 2(b) actually results from a right-handed screw dislocation. For a left-handed screw dislocation, the twist direction is opposite. Such

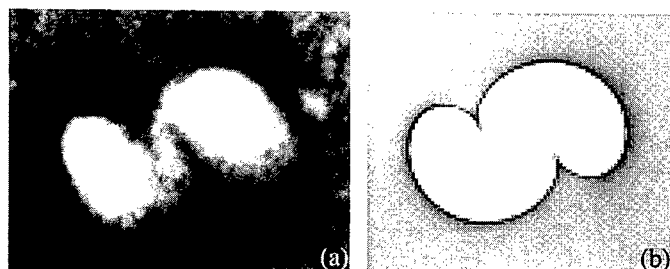


Fig. 4. Recorded (a) and simulated (b) images of a pair of micropipes with the same dislocation Burgers vector magnitude and sense.

phenomena can be explicitly demonstrated using synchrotron back-reflection section topography (using a slit collimated incident beam) [9,10].

We have shown that an isolated micropipe appears as a circular black ring surrounding a white center under the symmetric back reflection, but noncircular white spots are also frequently observed (see Fig. 1). Observations of etched crystal surfaces using SEM show that the noncircular white regions generally contain several micropipe etch pits close to each other, indicating that these images correspond to groups of micropipes. Again, the complicated images of grouped micropipes can be precisely simulated with the same geometric diffraction model [11].

Fig. 4(a) shows a SWBXT image of two identical micropipes ( $b_1 = b_2 = 4c$ , 6H-SiC) separated by a distance  $L = 25 \mu\text{m}$ , and Fig. 4(b) is the image simulated on the basis of the superimposition of the two independent strain fields. It is apparent that the two images exactly coincide with each other. The corresponding image and simulation of two opposite-sense screw dislocations ( $b_1 = -b_2$ ) will be presented below. From this principle, we can actually simulate images of arbitrarily distributed micropipe groups so as to extract the configurations of the individual dislocations.

**Characterization of SiC by transmission topography.** Back-reflection SWBXT is the most efficient method for characterization of closed-core and hollow core screw dislocations in (0001)-cut SiC wafers because the image of each dislocation is "magnified" to tens to hundreds of micrometers in dimension. For longitudinally cut wafers, however, the most suitable diffraction geometry is the commonly used transmission geometry.

For example, Fig. 5(a) shows a SWBXT image recorded from a (11-20) 6H-SiC wafer, grown by Cree Research Inc., taken with the symmetric 0006 reflection, in which the image of each screw dislocation along the [0001] axis exhibits double contrast with a bimodal intensity profile. It is clearly evident from this image that these dislocations are growth dislocations in that they are long and mostly straight. Micropipes tend to run exactly parallel to [0001]; while closed-core screw

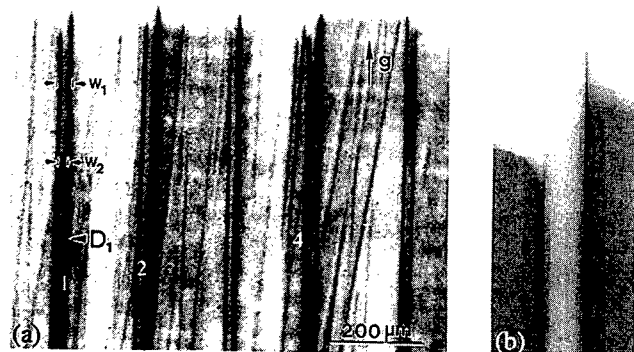


Fig. 5. (a) Synchrotron transmission topograph showing the double contrast images of micropipes in a longitudinally cut SiC wafer. (b) Simulated image of a right-handed micropipe in the transmission geometry.

dislocations are only approximately parallel to [0001] (deviating by up to  $15^\circ$ ). This is due to the fact that deviation from [0001] for the micropipes would cost too much energetically due to the

much higher line energy. Such transmission images make it possible to observe the nucleation (and potentially, annihilation) and propagation of the screw dislocation during the growth process.

Again, the transmission image can be rigorously simulated using the geometrical diffraction method, as plotted in Fig. 5(b). This enables us to obtain both the dislocation distributions and the Burgers vector magnitudes of individual dislocations. Moreover, the vertical shift of the double contrast of each dislocation image unambiguously indicates the dislocation sense. For example, micropipes 1, 2, 3, and 4 in Fig. 5(a) are right-handed screw dislocations while micropipe 5 is a left-handed one. The vertical shift of the screw dislocation image can be revealed in further detail (see [6,11]).

Transmission topography is also capable of revealing basal plane dislocations in basal-cut SiC [8]. Detailed Burgers vector analysis of these dislocations can be easily performed. Observation of the morphologies of the basal plane dislocation loops clearly indicates that they are deformation induced and that they appear to have been nucleated both at the crystal edges and at the sites of micropipes. This is an interesting phenomenon and is the subject of ongoing study in our group.

In addition to the above SWBXT methods, another useful diffraction geometry is grazing-reflection. This is an especially useful geometry for characterizing micropipes and screw dislocations in SiC films. The detailed characteristics of these images have been presented in [10].

Another defect, which is receiving increasing attention in 4H SiC, is the small angle boundary. Preliminary characterization using transmission topography (as well as reflection) indicates that the tilt angles associated with these boundaries are only a few seconds of arc although detailed analysis of the nature of these defects has not yet been completed.

**Model for the origin of micropipes.** In our numerous investigations of micropipes using SWBXT and other techniques, an important phenomenon we have observed is that micropipes can nucleate at what appear to be either inclusions or voids. This can sometimes be observed optically, but is always visible using SWBXT. This phenomenon of screw dislocation nucleation at inclusions or voids has been modeled [13] using an approach first developed by Chernov [14] and later extended by Neuroth [15]. According to this model, pairs of oppositely signed screw dislocations are nucleated at the inclusion or void, as shown schematically in Fig. 6(a).

Evidence in support of this model can be found by the occasional observation of isolated pairs of micropipes nucleated at a single inclusion or void, as shown in Fig. 6(b) (crystal grown by ATMI). Further evidence can be found in the routine observation of the formation of mesa structures, associated with pairs of oppositely signed screw dislocations, in the early stages of PVT growth

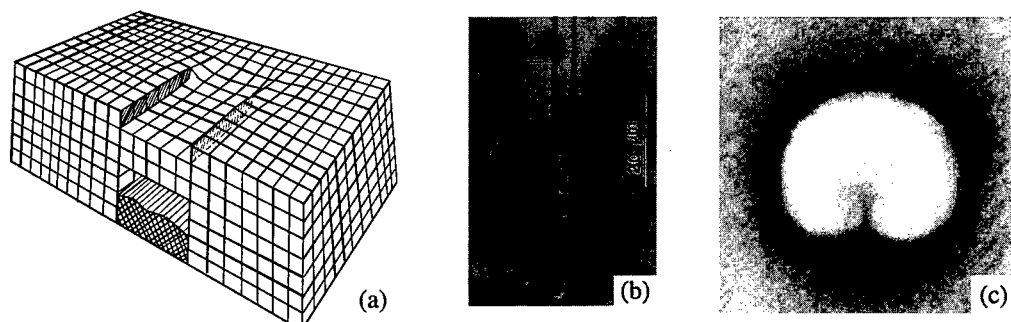


Fig. 6. (a) Schematic diagram illustrating the creation of a pair of opposite-sign screw dislocation during the process of inclusion overgrowth. (b) Optical observation of the nucleation of a micropipe pair in 4H-SiC. (c) SWBXT image of a pair of opposite-sign micropipes with the same Burgers vector magnitudes in a Lely platelet..

In addition, by carefully imaging self-nucleated Lely SiC platelets where the density of micropipes and screw dislocations is very low, we found that many of the dislocations appear in the form of pairs. One of the dislocation pairs is shown in Fig. 6(c). In Fig. 4, we have shown the recorded image and simulation of a dislocation pair with the same sense. Here we strictly simulated the back-reflection SWBXT image of an opposite-sign dislocation pair which has been shown in Ref. 13. The significant difference between the images in Fig. 4(a) and Fig. 6(c) shows that SWBXT can conveniently distinguish the two cases of dislocation pairs with the same and opposite senses. Therefore, the verification of the equal Burgers vector magnitudes and the opposite signs of the two dislocation in Fig. 6(c) is unambiguous. It should be noted that large inclusions or groups of inclusions may result in the creation of distributed groups of opposite-sign screw dislocations. However, these groups may not necessarily be distributed symmetrically, but in all cases, the sum of all the Burgers vectors of the dislocations created must equal zero. In this sense, the diagram in Fig. 6(a) is the basic mechanism of the nucleation of micropipes and screw dislocation in SiC.

**Conclusions.** SWBXT is an extremely useful technique for the characterization of defects in SiC crystals. To date, it has provided complete quantitative characterization of both closed-core and hollow-core screw dislocations and basal plane dislocations, and has also provided insight into the formation mechanisms of these defects. Being capable of imaging defects in wafers with devices fabricated on them, it has also enabled much light to be shed on the influence of the various defects on device performance. The complete characterization of defects such as small angle boundaries and their influence on device performance is the subject of ongoing study.

**Acknowledgments.** Support is acknowledged from the U.S. Army Research Office under contract number DAAG559810392 (contract monitor Dr. John Prater), partially funded by the DARPA Microsystems Technology Office (Order#E111/3 monitored by Dr. Dan Radack) and NASA Glenn Research Center. Topography carried out at the NSLS, at BNL, which is supported by the U.S. Department of Energy, under contract number DE-AC02-98CH10886.

## References

- [1] P. Neudeck, this conference, p. 1161
- [2] P.G. Neudeck, W. Huang, and M. Dudley: *Mat. Res. Soc. Symp. Proc.* **483** (1990), p. 285.
- [3] P. Neudeck, W. Huang, and M. Dudley: *IEEE Trans. Electron. Devices* **46** (1999), p. 478.
- [4] F.C. Frank, *Acta Cryst.* **4** (1951), p. 497.
- [5] W. Si, M. Dudley, R. Glass, V. Tsvetkov, and C. H. Carter, Jr.: *J. Electronic Materials* **26** (1997), p. 128.
- [6] M. Dudley, W. Si, S. Wang, C.H. Carter, Jr., R. Glass, and V.F. Tsvetkov: *Il Nuovo Cimento* **19D** (1997), p. 153.
- [7] W. Si and M. Dudley, R. Glass, V. Tsvetkov, and C.H. Carter, Jr.: *Materials Science Forum* **264-268** (1998), pp. 429.
- [8] M. Dudley, S. Wang, W. Huang, C.H. Carter, Jr., and V. Tsvetkov: *J. Phys. D* **28** (1995), p. A63.
- [9] X.R. Huang, M. Dudley, W.M. Vetter, W. Huang and C.H. Carter, Jr.: *Mat. Res. Soc. Symp. Proc.* **524** (1998), p. 71.
- [10] X.R. Huang, M. Dudley, W. M. Vetter, W. Huang, S. Wang, and C. H. Carter, Jr.: *Appl. Phys. Lett.* **74** (1999), p. 353.
- [11] X. R. Huang, M. Dudley, W. M. Vetter, W. Huang, and W. Si, and C. H. Carter, Jr.: *J. Appl. Cryst.* **32** (1999), p. 516.
- [12] M. Dudley, X.R. Huang, and W. Huang: *J. Phys. D: Appl. Phys.* **32** (1999), p. A139.
- [13] M. Dudley: *Appl. Phys. Lett.* **75** (1999), p. 784.
- [14] A.A. Chernov, *Contemp. Phys.* **30** (1989), p. 251.
- [15] G. Neuroth, Ph.D. Thesis, University of Bonn, Germany (1996).

## **Growth of Low Micropipe Density SiC Wafers**

Adrian Powell, Shaoping Wang and George Brandes

ATMI, Inc, 7 Commerce Dr., Danbury, CT 06810, USA

**Keywords:** Hexagonal Voids, Micropipe, Super Screw Dislocations

### **Abstract:**

Mechanisms for the creation of the micropipe defect are discussed. In particular, the generation and propagation of hexagonal voids is shown to be one source of the micropipe defect within SiC material. The micropipes can be directly traced to hexagonal voids and we find the micropipes terminating at the hexagonal void within the crystal.

### **1. Introduction**

The development of the SiC-based, high power device market is dependent upon the availability of high quality, large area, micropipe free SiC material. In the previous few years the micropipe density in commercially available wafers has decreased dramatically to the point where prototype large area devices can be produced. In this work we will discuss some of the mechanisms for micropipe formation and annihilation that occur in the modified Lely approach to SiC boule growth.

It is well understood that the micropipe defect in SiC is a super-screw dislocation [1,2,3] with a Burgers vector generally in excess of 2 nm. For such large dislocations the strain energy required to maintain atoms in the dislocation core sites is sufficiently high so as to drive preferential evaporation. Thus the core regions of these large dislocations are found to be hollow leading to the term "micropipe". The challenge in producing low micropipe SiC material is in eliminating the nucleation sources for super screw formation and in providing routes for either the annihilation or dissociation of already present super screw dislocations. In this paper we focus on the reduction of nucleation sources.

### **2 Experimental**

The material characterized in this study was grown by the modified Lely sublimation growth process [4,5,6,7,8]. In the modified Lely process, a seed crystal of SiC is attached to the lid of a graphite crucible and the lower region of the crucible is packed with a charge of SiC material. The SiC source and seed crystal is heated in a closed crucible under conditions of reduced pressure to temperatures in the range of 2100 - 2400°C. The SiC source is held at a temperature 20 - 100°C higher than the seed crystal. The SiC powder sublimates incongruently to produce Si, Si<sub>2</sub>C and SiC<sub>2</sub>. This growth nutrient is transported to the crystal surface and SiC forms on the growing crystal. The crystals are then either sliced perpendicular to the c-axis to create SiC substrates or along the c-axis for characterization purposes, that is to provide insight into defect nucleation mechanisms.

### 3 Results and Discussion

Super screw dislocations may be produced in the growing boules by many mechanisms, including:

- 1 Super screw dislocations present in the seed wafer will directly transfer into the grown boule. This source of pipes is eliminated through the use of higher quality seed wafers.
- 2 Micropipes are introduced as a by-product of polytype switching as shown in Figure 1. Here new pipes are generated at both the 4H to 6H, and 6H to 4H transitions. For this reason it is critical to control the growth process to maintain a single polytype.
- 3 Graphite and silicon inclusions disrupt the SiC growth surface and can lead to the production of new micropipe defects [9].
- 4 Similarly, if there are metallic clusters present during growth these can also act as micropipe nucleation sites. A demonstration of this has been presented previously by Northrop [10].
- 5 Micropipes may also be generated from hexagonal voids, as will be discussed in the following section.

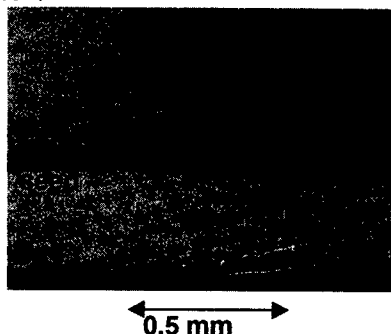


**Figure 1. 6H polytype inclusion observed in a 4H growth. Micropipes are introduced when the polytype changes.**

#### Pipe formation from the hexagonal void

Unlike most other bulk crystal growth systems, PVT of SiC requires that the growing crystal be held at a temperature at which it possesses a significant vapor pressure - approximately 1 torr. For comparison, Si boules are grown at a temperature where the vapor pressure is  $2 \times 10^{-4}$  torr. The consequence of this is that the SiC crystal can lose material through evaporation from the back surface of the crystal. Because there may be areas with grain boundary and/or dislocation clusters that will allow preferential evaporation, one might expect to see increased material loss from this region and the creation of a void space. Figure 2 shows schematically how this process progresses to produce a hexagonal void in the growing SiC material. Note that the void space created in this manner will have an effective Burgers vector equal to the sum of the dislocations that intersect the top surface of the void. At the lower surface of the void, where the SiC material re-deposits the net burgers vector remaining must also be incorporated into the crystal. If the net burgers vector is  $> 2$  nm then it is reasonable to assume that a hollow core micropipe will be formed at this stage.

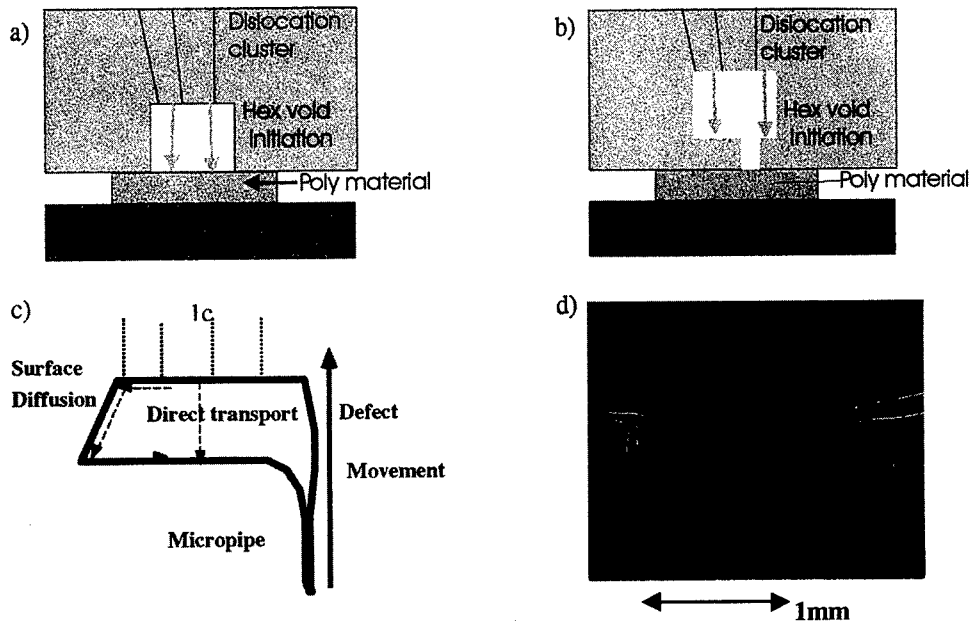


**Figure 2. Hexagonal void formation:** a) Initial evaporation of material from back surface of SiC crystal to the crucible lid. b) Once the gap between the SiC and the lid is full, growth occurs on the void sidewalls. c) Process continues to produce a void space within the crystal. d) Sectional view of a hexagonal void trailing a micropipe.

Observation of the side of a growing crystal (Figure 2d) and plan views of hexagonal voids (Figure 3) confirms that micropipe defects trail behind voids in a manner consistent with the hypothesis.

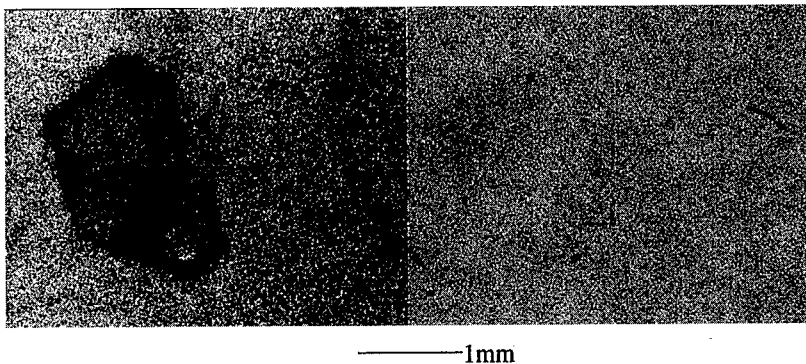


**Figure 3.** (a) shows a hexagonal void in a SiC wafer, (b) the defect etch of the wafer directly below reveals 12 micropipes, generated at the edges of the hex defect.

By minimizing the formation of hexagonal voids and other defect nucleation mechanisms we have achieved significant reductions in the micropipes present in our material. Figure 4 shows a wafer, produced from a boule grown with the improved process, following a defect characterization etch.

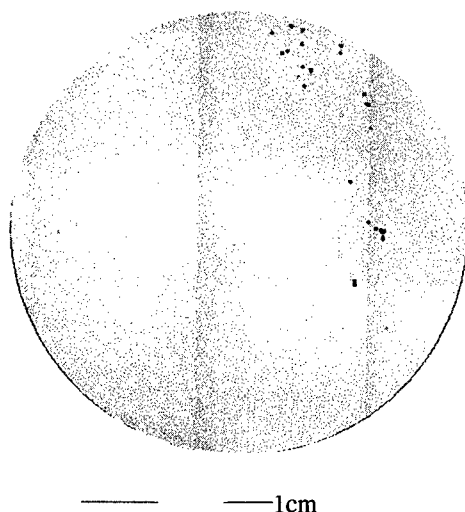


Figure 4. Low micropipe SiC wafer produced with 22 pipes in a 30mm diameter area and 4cm<sup>2</sup> free of micropipes.

In the 7cm<sup>2</sup> region shown in Figure 4 there were 22 micropipes counted, corresponding to a pipe density of 3.1 cm<sup>-2</sup>. Furthermore, the pipes were clustered in one region leaving the remainder free of micropipes. The pipe free area is approximately 4cm<sup>2</sup>, providing further proof that micropipe free wafers are possible, and should be expected in the next few years.

### Conclusion

By removing the sources of hexagonal void formation and through a reduction of other pipe formation sources we have been able to produce significant improvements in the SiC quality produced. Recent modified Lely growths have yielded wafers with <5 pipes cm<sup>-2</sup> and large (>1cm<sup>2</sup>) areas entirely devoid of micropipes.

### Acknowledgments

This work was supported by DARPA contract #F336115-95-c-5425

### References

- 1 F.C.Frank, Acta Cryst., 4 (1951), p497
- 2 W.Si, M.Dudley, R.Glass, V.Tsvetkov and C.Carter Mat. Sci. Forum Vol 264-268 (1998) p429
- 3 J.Giocondi et al, Mat. Sci. Forum Vol 264-268 (1998) p371
- 4 Y. M. Tairov, and V. F. Tsvetkov, J. Crystal Growth, 52, 146 (1981).
- 5 G. Ziegler, P. Lanig, D. Theis and C. Weyrich, IEEE Trans. Electron Dev. ED-30, 277 (1983).
- 6 R. F. Davis, C. H. Carter and C. F. Hunter, U. S. Patent 4,866,005, (1989) and references cited therein.
- 7 D. L. Barrett, R. G. Seidensticker, W. Gaida, R. H. Hopkins and W. J. Choyke, J. Crystal Growth 109, 17 (1991).
- 8 M. Kanaya, J. Takahashashi, Y. Fujiwara and A. Moritani, J. Appl. Phys. 58, 56 (1991).
- 9 V.Tsvetkov et al. Mat. Sci. Forum Vol 264-268 (1998) p3
- 10 R.N.Thomas, Presented at DARPA SiC High Power Electronic Materials Program Review 13 Nov 1997.



## Investigation of the Origin of Micropipe Defect

A. Okamoto, N. Sugiyama, T. Tani and N. Kamiya

Toyota Central R & D Labs, Inc., Nagakute, Aichi, 480-1192, Japan

**Keywords:** Cleavage Surface, Dislocation, Micropipe, Vickers Indenter

**Abstract** We have investigated the origin of micropipe defects (MPs). 6H-SiC single crystals including MPs were grown at both conditions of normal and Si-added atmosphere. The MP densities (MPDs) were  $0 \text{ cm}^{-2}$  and  $22.5 \text{ cm}^{-2}$  for representative area of the crystals grown in normal and Si-added atmosphere, respectively. A new technique with the Vickers indenter was used to expose an inner surface of a MP for Auger electron spectroscopy analysis. The analysis revealed that no specific evidence for Si-droplet was found at the starting point of the MP in 6H-SiC single crystal that was grown in the Si-added atmosphere. Although a large number of small angle boundaries and screw dislocations were observed in the region around MPs even in a low MPD ( $\sim 1 \text{ cm}^{-2}$ ) crystal, screw dislocation density were  $\sim 6 \times 10^2 \text{ cm}^{-2}$  in other region.

### Introduction

The commercial availability of relatively large-sized SiC wafers has activated the research and development of SiC-based devices for high-power, high-frequency and/or high-temperature electronics. A 100mm wafer of 6H-SiC single crystal with micropipe defects (MPs) and no peripheral striations was also demonstrated most recently [1]. For the production of SiC devices, however, high quality wafers without MP and screw dislocation which affect device performance [2] must be supplied at a reasonable cost. Recent reports presented the fabrication of SiC wafers with low MP density (MPD) of  $\sim 1 \text{ cm}^{-2}$  [1, 3, 4, 5]. It was reported that the MPD depended on the initial stage of the growth [6]. It has also been discussed that there were several possible reasons for the occurrence of the hollow cores (MPs): high transport rate, constitutional supercooling, dislocation centers, and defect formation after growth [7]. Several authors have investigated the origin of MPs. One has reported that MPs present in the seed crystal penetrate into the growing crystal [8]. The others have reported that MPs can be generated in SiC during the process of incorporation of inclusions such as graphite particles and Si droplets into the growing crystal [3, 4, 6, 7, 8, 9]. However, the studies on the chemical identification of the inclusions are presently underway in the previous reports. The objective of this work is, thus, to identify an inclusion by Auger electron spectroscopy (AES) analysis, at the starting point of an MP.

In this work, a new technique with the Vickers indenter was used to expose an inner surface of an MP for AES analysis. Various types of the other defects in a SiC crystal were also examined on the etched surface by optical microscopy (OM). Possible causes for the MP formation are discussed on the basis of the experimental results.

### Experimental

Bulk 6H-SiC single crystals were grown on MP-free 6H-SiC Acheson seeds by the modified Lely method. The seed and source temperatures and inert gas pressure were 2200-2250 and 2250-2350°C and 1Torr, respectively. Control of Si/C ratio in the initial stage of growth was carried out by changing the amount of Si added in a crucible. MPDs in the grown crystals were measured by OM for wafers sliced parallel to the c axis. The Dislocation density of a grown crystal with a low MPD of  $\sim 1 \text{ cm}^{-2}$  was also determined by OM after etching in molten KOH (500°C, 10 min).

The exposure of the inner surface at the starting point of an MP was made by the following technique:

- (1) preparing the polished wafer ( $\sim 400 \mu\text{m}$  thickness) sliced parallel to the  $c$  axis,
- (2) making crack traces by Vickers indenter (100 gf) at every  $\sim 100 \mu\text{m}$  on the both surfaces of the wafer,
- (3) accurately cleaving the wafer by utilizing the crack traces.

Characterization of the MP origin was conducted by OM, scanning electron microscopy (SEM) and auger electron spectroscopy (AES).

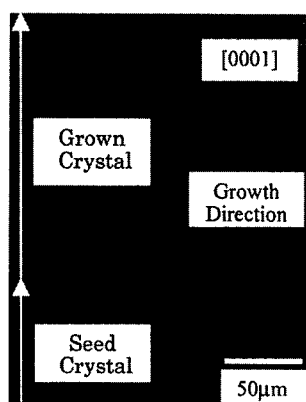


Fig. 1 Optical micrograph of a vertical slice of the grown 6H-SiC crystal in transmission light.

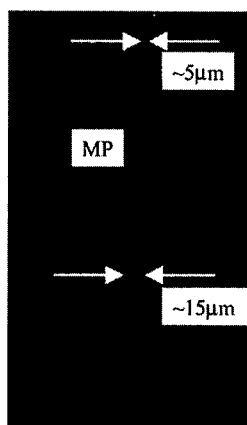


Fig. 2 optical micrograph at a starting point of an MP in transmission light.

## Results and discussion

MPDs in the sliced wafers were  $0 \text{ cm}^{-2}$  (no MP /  $0.4 \text{ cm}^2$ ) and  $22.5 \text{ cm}^{-2}$  (9MPs /  $0.4 \text{ cm}^2$ ) for the bulk SiC crystals grown in normal and Si-added atmosphere, respectively. Figure 1 shows an optical micrograph of a vertical slice of the 6H-SiC crystal grown in the normal atmosphere at the optimal growth condition. Neither MPs nor inclusions were observed close to the interface between the seed and grown crystals. On the other hand, a large number of oval shaped macro defects were observed in the crystal grown in the Si-added atmosphere.

Figure 2 shows an optical micrograph of an MP in a wafer that was grown in the Si-added atmosphere. The MP has originated from the "oval defects" with  $\sim 15 \mu\text{m}$  in diameter. Figure 3 shows the cleavage surface including an MP. The starting point of the MP was a

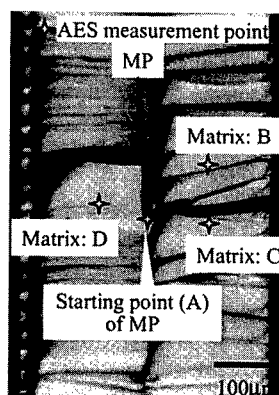


Fig. 3 Optical micrograph of a cleavage surface including the MP. No condensed matter was observed at the starting point of the MP.

Table 1 Si/C intensity ratio of AES spectrum from MP inner surface after sputtering with  $\text{Xe}^+$

Measurement Point	Intensity			Intensity Ratio	
	Si (LVV)	Si (KLL)	C	Si (LVV)/C	Si (KLL)/C
A(Starting Point)	5.4	2.1	3.9	1.4	0.5
B	5.0	1.9	2.8	1.8	0.7
C	6.8	2.1	3.2	2.1	0.7
D	5.0	1.9	2.9	1.7	0.7

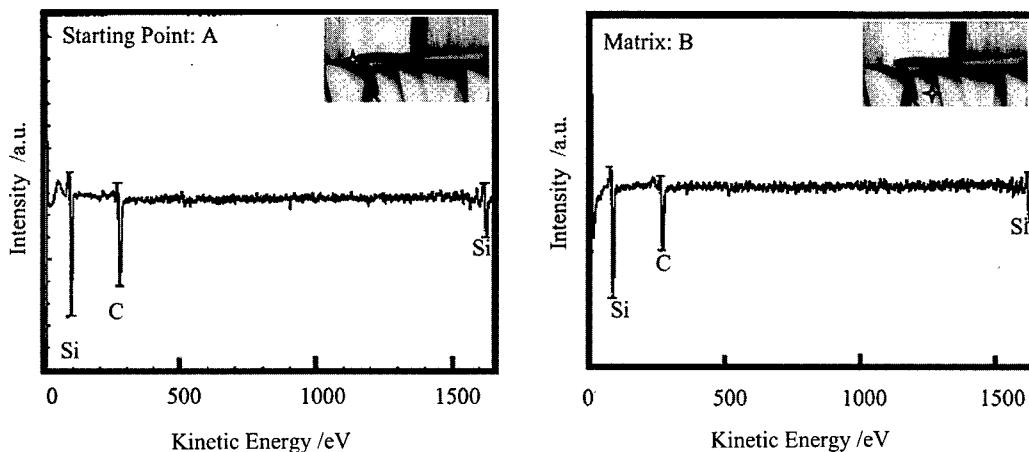


Fig. 4 AES spectra of the cleavage surface after sputtering with  $\text{Xe}^+$ ; A: Starting point of the MP, B: Matrix

void without condensed matter in it, according to the observation by OM. AES spectra from the inner surface of the MP origin gave a similar pattern to those from a matrix, without concentrated metal impurities detected (Fig.4). Quantitative analysis in terms of the spectrum intensity revealed that neither Si-rich nor C-rich compositions were found at the starting point of the MP (Table 1). It should be noted that no specific evidence for Si-droplet and graphite inclusions (including local carbonization on the growing surface) was found at the MP origin.

The higher MPD value in the crystal grown in the Si-added atmosphere suggests that transitively formed Si droplets on the growing surface could be responsible for the generation of MPs. However, remnant Si droplets were not observed in the starting point of the MP by the analysis mentioned above. We also investigated a large number of oval defects that had not generated MPs in the crystal grown at the Si-added condition. They are closed voids and some of them contain a condensed matter, as shown in Fig. 5. We suppose that the condensed matter was a Si droplet transitively formed on the growing surface and then confined in the closed void. For the Si droplet which triggered the generation of an MP (for example, the model of Dudley [9]), Si could have vaporized during the growth through the MP. The existence of other MP formation mechanisms cannot be ruled out. Detailed studies on the chemical identification of the condensed matter using AES analysis are underway in our group and hence will be reported in a subsequent publication.

KOH etching of the crystal with a low MPD ( $\sim 1\text{cm}^{-2}$ ) revealed the relationship between the

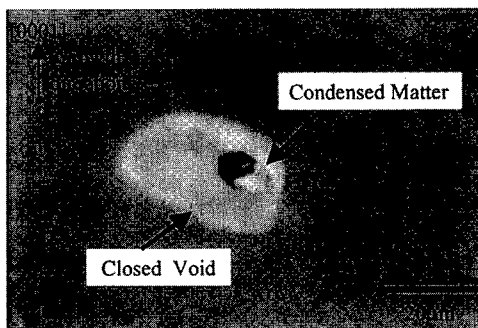


Fig. 5 A closed void contained a condensed matter, which was found in a crystal grown in a Si-added ambience. The closed void generates no MP.

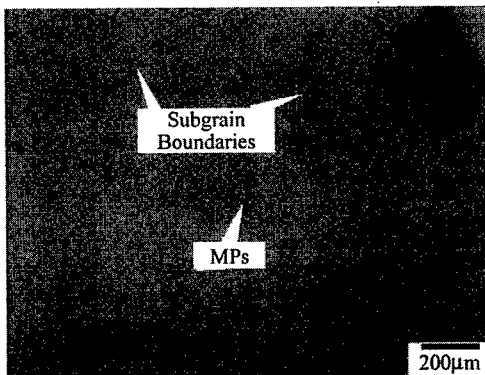


Fig. 6 An etched surface in the mosaic structure region of a high quality 6H-SiC wafer (density of MP:  $\sim 1\text{cm}^{-2}$ ). Rows of etch pits (subgrain boundaries) and medium-size etch pits (screw dislocations) were observed in the region.

MP and the other defects. A region with a high etch pit density was observed close to MPs, which turned out to be a mosaic structure region. Rows of etch pits which correspond to small angle boundaries were also observed in the mosaic structure region (Fig. 6). The density of medium-sized etch pits, i.e. screw dislocations, in the mosaic structure region was  $\sim 3 \times 10^4 \text{ cm}^{-2}$  which was two order higher than that in the other region ( $\sim 6 \times 10^2 \text{ cm}^{-2}$ ). The origins of screw dislocations are either dislocations in the seed or defects which are generated by local instabilities in temperature or pressure during growth. As the spiral steps created by screw dislocations contact each others at tilt angles, edge dislocations are easily created. It is likely that the formation of small angle boundaries is attributed to polygonized edge dislocations formed by plastic deformation during growth.

### Conclusions

The MPD of the crystal grown in the Si-added atmosphere was higher than that of the crystal grown in the normal atmosphere. However, AES analysis revealed that no specific evidence for Si droplet was found at the starting point of the MP in 6H-SiC single crystal that was grown in the Si added atmosphere. Further investigation suggests that transitively formed Si droplets on the growing surface could be responsible for the generation of MPs. The existence of other MP formation mechanisms cannot be ruled out. KOH etching of the crystal with a low MPD ( $\sim 1 \text{ cm}^{-2}$ ) also revealed that a large number of small angle boundaries and screw dislocations were observed in the region around MPs. The result of low screw dislocation density in the representative area shows that it will be possible to produce SiC wafer with very low density of screw dislocation in the future.

### References

- [1] D. Hobgood, V. Tsvetkov, R. Glass, D. Henshall, M. Henshall, J. Jenny, G. Fechko, R. Leonard, D. Malta, S. Mueller and C. H. Carter, Jr., Abstracts of *International Conference on Silicon Carbide and Related Materials 1999*, (1999), p. (138).
- [2] P. G. Neudeck, W. Huang and J. M. Dudley, *IEEE Trans. Electron Devices* **46** (1999) p.478.
- [3] R. C. Glass, D. Henshall, V. F. Tsvetkov and C. H. Carter, Jr., *Phys. Stat. Sol. (b)* **202** (1997), p.149.
- [4] V. Tsvetkov, R. Glass, D. Henshall, D. Asbury and C. H. Carter, Jr., *Silicon Carbide, III-Nitrides and Related Materials*, Materials Science Forum **264-268** (Trans Tech Publications, Switzerland, 1998), p.3.
- [5] A. Okamoto, N. Sugiyama, T. Tani and N. Kamiya, *ibid.* **264-268** (Trans Tech Publications, Switzerland, 1998), p.21.
- [6] M. M. Anikin, R. Madar, A. Rouault, I. Garcon, L. Di. Cioccio, J. L. Robert, J. Camassel and J. M. Bluet, *Silicon Carbide and Related Materials 1995*, Inst. Phys. Conf. Ser. No.142: Chapter 2 (IOP Publishing Ltd, Bristol and Philadelphia, 1996), p.33.
- [7] R. A. Stein, *Physica B* **185** (1993) p.211.
- [8] D. Hofmann, M. Bickermann, R. Eckstein, M. Kölbl, St.G. Müller, E. Schmitt, A. Weber and A. Winnacker, *J. Crystal Growth* **198/199** (1999), p.1005.
- [9] M. Dudley, X. R. Huang, W. Huang, A. Powell, S. Wang, P. Neudeck and M. Skowronski, *Appl. Phys. Lett.* **75** (1999), p.784.

## Analysis on the Formation and Elimination of Filamentary and Planar Voids in Silicon Carbide Bulk Crystals

Dieter Hofmann, Matthias Bickermann, Wolfgang Hartung and  
Albrecht Winnacker

Department of Materials Science 6, University of Erlangen-Nürnberg,  
Martensstr. 7, DE-91058 Erlangen, Germany

**Keywords:** Macrodefects, Micropipe, Planar Defects

**Abstract** The closing of micropipes during SiC solution growth is frequently observed. This closing is investigated theoretically showing that both mechanical and surface energy are similar for the open and closed defect geometry. Thus capillary action should be the dominating mechanism for the elimination of micropipes during SiC liquid phase growth. A model for planar/macrodefect formation is presented giving indications that these defects are a result of negative crystal growth.

**Introduction** Silicon carbide (SiC) represents the only technologically relevant semiconductor in which voids having dimensions from mesoscopic to nanoscopic scale are generated during the bulk growth process from the vapor phase. They can play a detrimental role in the performance of electronic devices, especially for high power application due to the need of large defect-free crystal regions. These voids can be classified according to their physical nature and size (diameter d):

i) Micro-/nanopipes ( $5 \text{ nm} \leq d \leq 15 \text{ }\mu\text{m}$ ); ii) Macrodefects ( $d \geq 20 \text{ }\mu\text{m}$ ); iii) Planar defects ( $d \geq 50 \text{ }\mu\text{m}$ ). Besides geometry the striking difference between micropipes and the other defects is the fact that micropipes are associated with a dislocation structure [1].

**Micropipe formation** The exact formation mechanism of micropipes is not totally clear up to now. Several aspects are considered as source for micropipe generation: excessive stress, second phases [2,3], stacking fault clusters on tilted closed packed planes [4], low angle grain boundary dislocations that exist in order to accomodate the small twist between neighboring grains [5] etc.. In any case micropipes are hollow core dislocations which should be described by Franks formula [1] for the radius of the pipe  $R_F = b^2 \mu / K 8 \pi^2 \gamma_{sv}$  with b: Burgers vector,  $\mu$ : shear modulus,  $\gamma_{sv}$ : solid-vapor surface energy. The factor K takes into account details of the dislocation character (screw/edge dislocation component) [6]. It is frequently observed during our SiC solution growth experiments from the liquid phase that micropipes present in the vapor grown seed crystal are closed [7]. But according to the formulation for  $R_F$  even a larger diameter of the hollow core dislocation should be present when liquid phase crystallization is conducted due to the lower solid-liquid interface energy. Any model approach which should explain this phenomenon has to address details of both crystallization around a micropipe and aspects of mechanical and surface energies.

**Model for the closing/elimination of micropipes** Fig. 1a shows schematically the seed/solution geometry with the boundary condition that the seed is fixed at the seed holder in a way which does not allow a gas exchange between the micropipe and the process environment. Under these conditions a liquid meniscus is build at the periphery. This three phase region has now defined angles, the interface angle  $\Theta_I$  and liquid angle  $\Theta_L$  (Fig 1b). The constraints of this arrangement forces the vertical walls to become progressively inclined (Fig. 1c). Further crystallisation results in the closing of the pipe by these capillary forces. This consideration is so far only valid if additional forces can be neglected. Therefore, we consider quantitatively the existing surface and mechanical energies. In contrast to Franks formula we will take now the fact into account that the diameter  $2R$  of the hollow core dislocation is variable with pipe lenght  $L$ . For the energy due to mechanical forces at a micropipe holds in general:

$$dE_{dis} = - b^2 \mu / 4 \pi \ln (R/R^*) dL \quad (1)$$

For the surface energy between solid and vapor holds in general:

$$dE_{\text{sur}} = 2 R \pi \gamma_{\text{sv}} dL \quad (2)$$

Now it has to be considered that the radius  $R$  can vary with the pipe length  $L$ . Assuming a spherical surface area which should result under capillary action, then the following relation is valid:

$$R = (R_F^2 - L^2)^{1/2} \quad (3)$$

The integration of equation (1) along the spherical surface gives the energy of the closed hole:

$$E_{\text{dis}} = -b^2 \mu / 4\pi \{ -(R_F^2 - R^{*2})^{1/2} + R_F / 2 \ln \{ [R_F + (R_F^2 - R^{*2})^{1/2}] / [R_F - (R_F^2 - R^{*2})^{1/2}] \} \} \quad (4)$$

Equation (4) has now to be compared to the mechanical energy  $E_{\text{dis}}^*$  of a cylinder of a hollow core dislocation with a constant radius  $R_F$  and height  $R_F$ :

$$E_{\text{dis}}^* = -b^2 \mu / 4\pi \ln (R_F / R^*) R_F \quad (5)$$

As both surface energies for the spherical hole and the cylindrical part are equal the further discussion is focused only on the comparison of equations 4 and 5. A detailed numerical analysis reveals that the energetic contributions of a cylindrical tube and a spherical half shell differ less than 6% for  $R_F = 10 \mu\text{m}$  and  $R^* = 0.05 \mu\text{m}$ . This holds over a large range of  $R$ - and  $R^*$ -values.

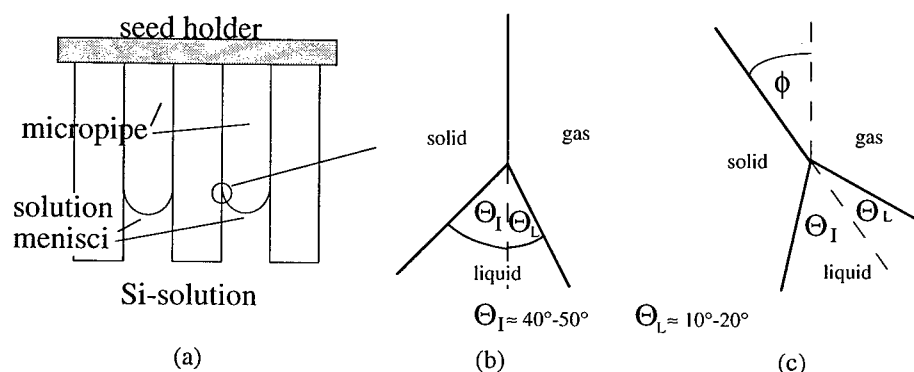


**Fig.1** Scheme of the seed/seed holder geometry (a), three phase boundary with the contacting angles  $\Theta_L$  and  $\Theta_I$  (b) and resulting crystallization front which causes the closing of the micropipe (c).

From this result it is probable that a dislocation void with a tube-like geometry will practically close completely under the capillary action as the energetic terms of the mechanical and surface energy for the closed and unclosed micropipe are rather similar. This might be the explanation for the observed closing of micropipes during liquid phase growth. In the case of gas exchange between micropipe and seed holder capillary forces will push the liquid into the whole pipe. The three phase equilibrium will not be established near to the main solid-liquid interface. Here a different argumentation has to be made to explain micropipe closing including e.g. the higher supersaturation for growth from liquids at highly concave shaped crystalline bodies like the walls of micropipes.

In general there exists a deficiency in understanding of the nature of the hollow dislocation after closing as it should not be energetically stable due to the high Burgers vectors. Experimentally a dissociation of dislocations has not been observed up to now. This phenomenon is still under investigation. SiC wafers with closed micropipes are taken as seed crystals for vapor growth experiments. This should elucidate the stability of closed micropipes.

#### Generation of planar/macros defects

Although being a defect type with negative influences on device properties the formation of macro-defects/planar defects in SiC has been addressed only little in the past. E.g. Stein [8] concluded that the reasons for channels might not lie in instabilities of the growing interface but in secondary evaporation. Fig. 2a shows a typical geometry of a planar defect/macros defect association. A planar defect is a void mainly with crystallographic orientation of the walls (parallelepiped) having an aspect ratio  $X/L \geq 5$  ( $X$ : length perpendicular to  $[0001]$  axis,  $L$ : thickness parallel to  $[0001]$  axis) as measured in several SiC crystals. The planar void is followed by a pipe having diameters exceeding

the size of micropipes ( $d \geq 15 \mu\text{m}$ ). These macropipes are not oriented crystallographically like micropipes. They have a serpentine-like geometry. Both for the planar defect and the connected macrodefect (pipe) an explanation is given as follows. Fig. 2b shows a model sequence of the generation of a planar defect. At first there is the probability that voids exist at the transition between the seed holder and the SiC seed due to an inadequate fixation technique. In this void mass transfer will occur when the typical temperature field for PVT (physical vapor transport) growth of SiC is established. A sort of micro-PVT process will cause the migration of the void towards the higher temperature. Both the radial temperature gradients due to the twodimensionality of heat transfer around the void and the difference of kinetics at the crystallization part and sublimation part might result in the parallelepiped geometry of the planar defect. The residual pipe (macrodefect) can be thought as a trace resulting from the changing minimum of the critical supersaturation.

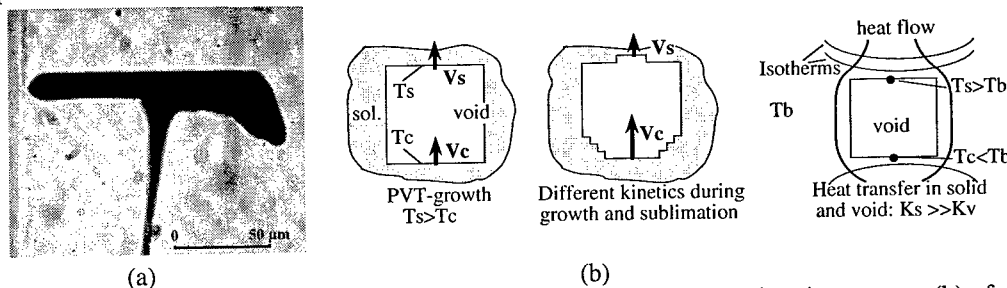


Fig. 2: Typical planar defect in SiC (a) and sequence of the micro-PVT migration process (b) of a void taking into account kinetics and heat transfer.

This hypothesis of "negative crystal growth" is now discussed by comparing experimental results and theoretical descriptions of the ongoing processes. At first the geometric data of thickness  $L$  and lateral dimension  $X$  have been measured in various crystals. In addition it could be clearly proven that these defects migrated during growth by correlating solid-vapor interface demarcation lines with the defect geometry. With these interface demarcation lines produced by doping striations from nitrogen pulses the growth rate is evaluated routinely in our SiC crystals. The absolute values of migration velocities have been determined and will be discussed later.

Now we present the theoretical description for the formation/migration of planar defects. The thermomigration velocity  $V$  of a void through a solid can be considered in an analogous way to Cline and Antony [9] who treated the movement of liquid droplets in silicon by the product of the driving force on the void  $F$  and the void mobility  $M$

$$V = M F \quad \text{with } M = C_v/C_s D/RT \quad V_s/V_v \quad (6)$$

$C_v$ : concentration of SiC gas species in the void,  $C_s$ : concentration in the solid phase,  $D$ : diffusion coefficient in the gas phase,  $V_s$ : molar volume of the solid,  $V_v$ : volume of the void.

In a thermal field the relation (7) holds:

$$V = M (F_T - F_K) \quad \text{where} \quad (7)$$

$$F_T = V_v/V_s RT [1/C_e dC_e/dT] \quad G_v \text{ is the thermal force and } F_K = Q/L V_s/V_v \text{ the kinetic force,} \quad (8)$$

$C_e$  = equilibrium concentration of gas species in the void,  $G_v$  = thermal gradient at the void,  $Q$  = kinetic potential,  $L$  = dimension of the void parallel to the thermal gradient.

As already explained a compositional gradient in a void is generated because of the change in vapor pressure of the solid with temperature. This concentration gradient causes a transport of the solid atoms through the void from the front to the rear end and causes the void to migrate. From interest it is now the question how fast voids can migrate and which kind of geometry they will adopt.

In steady state the SiC species move from the hot subliming face to the cold depositing face. It can be shown that for the steady state velocity of the void holds [9]:

$$V = D C_v/C_s \{ [1/C_e dC_e/dT] G_v - \Delta Q/RTL \} \quad (9)$$

From this equation it is clear that the effects of kinetics will rise with decreasing void size  $L$  and below a critical size there will exist no void migration. Also it is clear that the void velocity depends on the thermal field (temperature gradient). At this point we compare the experimentally found migration rates with the theoretical estimates according to equation 9. Under typical growth

conditions we measure migration rates of planar defects of 40...225  $\mu\text{m}/\text{h}$ . The same numbers 50...300  $\mu\text{m}/\text{h}$  are evaluated by the theoretical model.

The changes in shape of voids from a cube to a parallelepiped demand a vapor transport from the lateral facets to the rear facets of the voids while vapor species are simultaneously travelling from the front to the rear facet of the void to cause migration. This physical phenomenon has been also described by Cline and Antony [9] for liquid inclusions. For vapor transport in voids the following relation holds for the aspect ratio  $X/L$  versus  $X$  ( $X$ : length of void,  $L$ : thickness of void,  $Q^*$ =kinetic potential,  $\gamma_{sv}$ = solid-vapor interface energy):

$$X/L = 1 + Q^* X / 4V_s \gamma_{sv} \quad (10)$$

$X$  and  $L$  have been measured in 4 crystals and correlated according to equation 10. The result is shown in fig.3. It is evident that the physical dependence could be verified experimentally. But every crystal exhibits a different slope being  $Q^*/4V_s \gamma_{sv}$ . We argue that this reflects the variation in the kinetic potential  $Q^*$  due to the interaction with dislocations. During the migration process there is a finite probability that the void meets a dislocation changing the kinetics of growth and sublimation and so for the  $Q^*$  value. The serpentine-like morphology of the following macropipes is a further hint of this dislocation interaction.

Additional experimental results are:

- (i) Within one crystal there exist a lateral variation of the migration rate up to a factor of 2.
- (ii) A change of the growth temperature from 2200 °C to 2300 °C showed no significant variation in the migration rate.
- (iii) It has to be emphasized that each planar defect is followed by a non micropipe hollow tube which is not oriented crystallographically (macrodefect).

For the reduction of the planar/macrodefect density in SiC crystals the main issue seems only a proper fixation technique preventing the formation of voids at the seed/seed holder interface. According to equation 9 also a reduction of the void size would be helpful as it decreases the migration rate through the crystal. But the technical realization of defined sizes of planar defects at the beginning of the growth process seems not to be feasible.

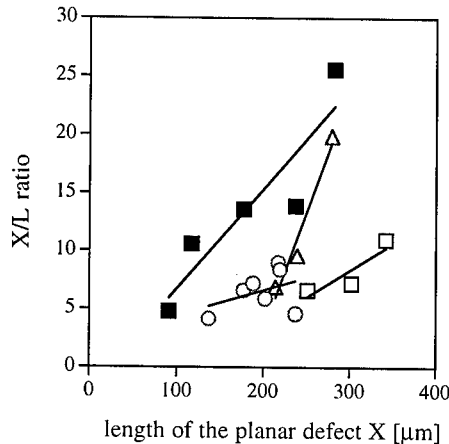


**Fig. 3:** Aspect ratio  $X/L$  versus length of planar defect  $X$  for 4 different SiC growth experiments

**Acknowledgement** This work has been supported by the Bavarian Research Foundation and SiCrystal AG under contract 176/96.

#### References

- [1] F.C. Frank, Phil. Mag. 42 (1951) p.1014
- [2] M. Dudley, X.R. Huang, W. Huang, A. Powell, S. Wang, P. Neudeck, M. Skowronski, Applied Phys. Lett. 75 (1999) p.784
- [3] D. Hofmann, M. Bickermann, R. Eckstein, M. Kölbl, St.G. Müller, E. Schmitt, A. Weber, A. Winnacker, J. Crystal Growth 198/199 (1999) p.1005
- [4] J. Heindl, V.D. Heydemann, G. Pensl, H.P. Strunk, Inst. Phys. Conf. Ser. 160 (1997) p.331
- [5] P. Pirouz, Mat. Res. Soc. Symp. Proc. 512 (1998) p.113
- [6] J. Heindl, W. Dorsch, H.P. Strunk, St. G. Müller, R. Eckstein, D. Hofmann, A. Winnacker, Phys. Rev. Lett. 80 (1998) p.740
- [7] D. Hofmann, M. Müller, Mat. Sci. Eng. B 61/62 (1999) p.29
- [8] R. Stein, Physica B 185 (1993) p.211
- [9] T.R. Antony, H.E. Cline, J. Appl. Phys. 42 (1971) p.3380



## Origin of the Internal Stress Around the Micropipe of 6H-SiC Single Crystal

Tomohisa Kato\*, Hitoshi Ohsato and Takashi Okuda

Department of Materials Science and Engineering, Nagoya Institute of Technology,  
Gokiso-cho, Showa-ku, Nagoya, 466-8555, Japan

**Keywords:** Defects, Interference, Internal Stresses, Micropipe, Photoelasticity

**Abstract.** The origin of the internal stress around micropipes existed in the hexagonal silicon carbide single crystals has been investigated by strain model. The model designed from acrylate resin perfectly demonstrates the strain distribution around micropipes. The strain distribution was confirmed by interference patterns observed by photoelastic measurements under the crossed polars condition. Generally it is argued that micropipes are formed by stress relaxation in the center of the screw dislocation, however, the strain model adopted demonstrates that the stress origin around micropipes occurred by the edge dislocation. Therefore, we argue that micropipes contain the mixed dislocation.

### Introduction

Silicon carbide (SiC) bulk single crystal is expected as a new substrate material for high power, high temperature and high frequency semiconductor devices. In addition, SiC single crystals are appropriate as substrate material for thin films growth of III-V nitrides because it has a small lattice mismatch (3.5%) compared with the sapphire substrates [1,2]. However, the SiC bulk

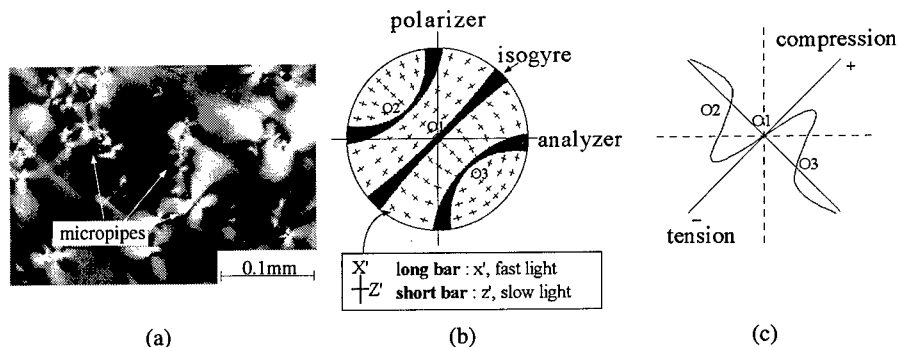


Fig.1 (a) A photograph of the interference pattern around micropipes of (00·1)6H-SiC by means of a polarizing optical microscope. (b) and (c) are illustrations of vibration directions and stress distribution around a micropipe, respectively. O1 is micropipe, O2 and O3 are no double refractions points.

\* To whom correspondence should be addressed. Present address: Electrotechnical Laboratory, 1-1-4 Umezono, Tsukuba, Ibaraki 305-8568, Japan; Tel +81-298-54-5397; Fax. +81-298-54-3397; e-mail ktomo@etl.go.jp

crystals grown by the modified Lely method include many large hollow defects called as micropipes [3-5]. The existence of micropipes is considered as one of the most serious problems for semiconductor devices, because its presence gives rise to current leakage [6,7]. The micropipes penetrate along the [001] growth direction with diameters from sub  $\mu\text{m}$  to about  $10\ \mu\text{m}$ . The formation of these micropipes has been discussed by several research groups in order to clarify their nature [8-11]. According to Frank's theory, the formation is generally interpreted as depending on the stress relaxation of the screw dislocation with large Burgers vector [8]. However, the interference pattern of the screw dislocation reported by Ming *et al.* [12] could not be observed around the micropipes by polarizing optical microscope. In a previous paper, we reported the unique interference pattern and large internal stress around the micropipes in (00•1) 6H-SiC single crystals substrate grown by the modified Lely method [4]. Stress distribution and its magnitude by photoelastic measurements was presented in [13]. We showed that the internal stress gives aggravation for crystallinity of the SiC single crystal. In this study, we report the origin of the internal stress around the micropipes. The origin was investigated using the designed strain model which imitates the micropipes.

### General description

The internal strain around the micropipes can be observed as birefringence (double refraction) image with unique interference pattern as shown in Fig.1a. The image was often observed in a (00•1) 6H-SiC substrate developed by modified Lely method by means of a polarizing optical microscope under the crossed polars condition. The interference pattern is generated by photoelastic effect from the strain, which is acting perpendicular to a micropipe, because the (00•1) 6H-SiC usually has no double refraction along [001] direction. Vibration directions of polarized lights on optional points distributed around micropipe (O1) are presented as the crossed marks composed by faster and slower light directions as shown in Fig.1b. Dark zones indicate the extinct lines so called isogyre. We reported previously that the maximum internal stress located on both sides of a micropipe between O2 and O3 where there were no birefringence points [4], and the stress distribution on a O2-O3 line was due to alternate compression and tension as shown in Fig.1c. These results were confirmed around all of the micropipes. The magnitude of the maximum internal stress was around 113~166MPa as observed by photoelastic measurements [13].

### Experimental

The internal strain around the micropipes in the (00•1) 6H-SiC substrates was investigated as interference pattern by polarizing optical microscope under the crossed polars

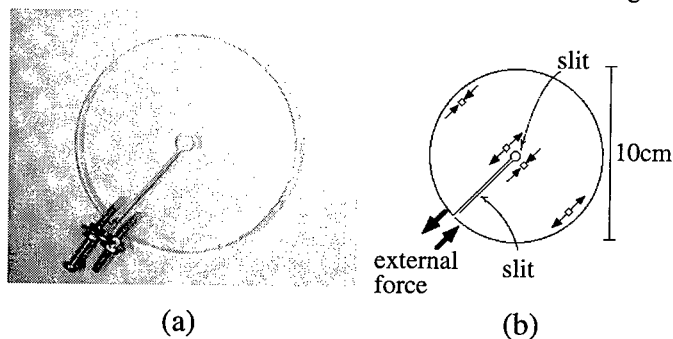


Fig.2 A strain model for analysis of the internal strain around micropipe. (a) is a photo of the model. In order to model the stress distribution, the model was cut leading from the center hole to the edge, and the external force was added along the cut line like as shown in Fig2(b).

condition. The SiC modified Lely crystals containing high density of micropipes were used.

A strain model designed from an acrylate resin board for analysis of the internal strain around the micropipes is shown in Fig.2. It was cut into a circular shape with 10cm in diameter, and having a opened hole at the center. The center hole represents the micropipe. In order to add stress distribution, the model was cut from the center hole towards the edge, and compressive and tensile stress was added along the cut line by means of metal screws and plates. The model was investigated by photoelastic measurements under the crossed polars condition.

### Results and Discussion

The distribution and origin of the internal stress around micropipes were investigated using the above strain model. When the model was observed under the crossed polars condition, the identical interference pattern was observed around the center hole compared with the micropipe. The typical example is shown in Fig.3. Specimens in the model and a micropipe were rotated in each basal plane with same degrees, their interference patterns also changed in a similar way. It was clarified that the model completely demonstrates the internal strain around the micropipe of SiC single crystal. The external force, which was added along the cut line in the model, concentrates around the center hole. Hence, with each compressive and tensile stress, strain occurred on both sides of the hole, and reasonably generated the identical stress distribution like in Fig.1c.

The origin of strain generation using this model could be interpreted in terms of an edge dislocation in the crystal structures, because stress distributions around an edge dislocation are usually formed due to compression and tension on both sides of the dislocation line. Therefore the cut end direction in the model represents the Burgers vector.

As already mentioned, the micropipes are formed by relaxation of stress which occurred by screw dislocation with large Burgers vector [8]. However, the birefringence image of the screw dislocation, which was reported by Ming *et al.* [12] were not observed around micropipes in this

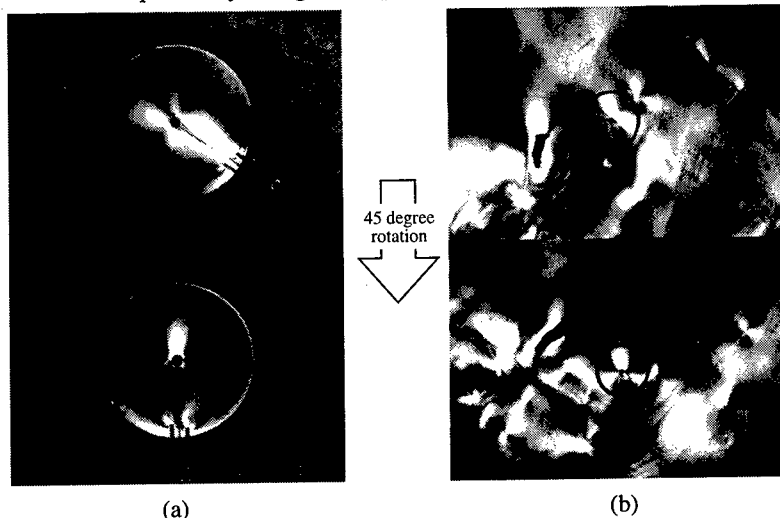


Fig.3 Interference pattern of (a) the strain model and (b) a micropipe under crossed polars condition. As both interference images indicate identical patterns, the model reappears the stress distribution of the micropipe perfectly.

study. Hence we conclude that the stress caused by screw dislocation may scarcely remain. By these analysis of the strain model we argue that the micropipe contains not only the element of screw dislocation but also of the edge dislocations, i.e. the mixed dislocation. The internal stress around micropipe mainly originates from the element of edge dislocation. Our results agree well with theoretical analysis of the micropipe formation reported by J.Heindl *et al.* [9].

### Conclusions

We succeeded in designing the strain model of the micropipe for investigating the origins of the internal stress around it by means of photoelastic measurements under the crossed polars condition. The model demonstrates that the internal stress around the micropipe occurs by the edge dislocation located at the center of the micropipe in the (00•1) basal plane. The micropipe formation was thought to be occurring due to mixed dislocation composed of screw and edge dislocations.

### Acknowledgements

The authors wish to thank Prof. M. Razeghi in Northwestern University, Mr. A. Okamoto in Toyota Central R&D Laboratories, Inc. and Prof. H. Awaji and Dr. W. Wunderlich in Nagoya Institute of Technology for many appropriate advices.

### Reference

- [1] S. Strite and H. Morkoç, J. Vac. Sci. Technol. **B10** (1992) p. 1237.
- [2] H. Morkoç, S. Strite, G.B.Gao, M. E.Lin, B. Sverdlov and M. Burnes, J. Appl. Phys. **76** (1994) p. 1363.
- [3] Y. M. Tairov and V. F.Tsvetkov, J. Cryst. Growth **43(2)** (1978) p. 209.
- [4] T.Kato, H.Ohsato, M.Razeghi and T.Okuda, Proceedings of ICSCRM-95, InstPhys.Conf.Ser. **142** (1996) p. 417.
- [5] D.L.Barrett, J.P.McHugh, H.M.Hobgood, R.H.Hopkins, P.G.McMullin, R.C.Clarke and W.J.Choyke, J. Cryst. Growth **128**, (1993) p. 358.
- [6] P.G.Neudeck and J.A.Powell, IEEE Electron Device Lett. **15** (1995) p. 63.
- [7] K.Koga, Y.Fujikawa, Y.Ueda and T.Yamaguchi, Springer Proc. in Phys., 71 Amorphous and Crystalline Silicon Carbide IV, Springer-Verlag, Berlin, 1992, p. 96.
- [8] F.C.Frank, Acta Cryst. **4** (1951) p. 497.
- [9] J.Heindl, W.Dorsch and H.P.Strunk, Phys. Rev. Lett. **80(4)**, 1998 p.740.
- [10] M.Dudley, S.Wang, W.Huang, C.H.Carter Jr., V.F.Tsvetkov and C.Fazi, J. Phys. D: Appl. Phys., **28** (1995) p.A63.
- [11] H.Yamaguchi, S.Nishizawa, W.Bahng, K.Fukuda, S.Yoshida, K.Arai and Y.Takano, Mat. Sci. and Eng. **B61-62** (1999) p. 221.
- [12] N.Ming and C.Z.Ge, J. Cryst. Growth **99** (1990) p. 1309.
- [13] T.Kato, H.Ohsato, A.Okamoto, N.Sugiyama and T.Okuda, Mat. Sci. and Eng. **B57** (1998) p. 147.

## Structural Investigation on the Nature of Surface Defects Present in Silicon Carbide Wafers Containing Varying Amount of Micropipes

M. Shamsuzzoha<sup>1</sup>, S.E. Sadow<sup>2</sup>, T.E. Schattner<sup>2</sup>, Li. Jin<sup>3</sup>, M. Dudley<sup>3</sup>,  
S.V. Rendakova<sup>4</sup> and V.A. Dmitriev<sup>4</sup>

<sup>1</sup> Department of Metallurgical Eng. and School of Mines Energy Development,  
University of Alabama, Tuscaloosa, AL 35487, USA

<sup>2</sup> Department of Electrical & Computer Engineering, Mississippi State University,  
Box 9571, Mississippi State, MS 39762, USA

<sup>3</sup> Dept. of Materials Science and Engineering, State University of New York at Stony Brook,  
Stony Brook, NY 11794, USA

<sup>4</sup> TDI, Inc., 8660 Dakota Drive, Gaithersburg, MD 20877, USA

**Keywords:** Micropipe, Screw Dislocation, SWBXT, TEM

**Abstract** The surface of 4H-SiC and 6H-SiC substrates, both processed with and without LPE to fill micropipe defects, has been investigated by transmission electron microscopy and x-ray topography techniques to determine the status of existing unfilled and filled micropipes. Unfilled micropipes are hollow-core pure screw dislocations extending along the [0001] direction of the hexagonal crystal. Substrates processed with the micropipe filling process appear to possess a lower density of micropipes than those fabricated without the micropipe filling process. Initial homoepitaxial growth of SiC inside the micropipe channels by LPE techniques appears to fill or partially fill the micropipe core but likely retain screw dislocations in closed core form. Subsequent LPE layer growth on these modified substrates keeps the continuity of close packed atomic stacking of the original substrate with closed-core screw dislocations from the filled micropipes transforming into either a nano-pore extending mostly along the [0001] direction of the substrate, or a grain boundary dislocation. Homoepitaxial growth into micropipe channels is suggested to produce an incoherent interface between the substrate and filled material and produces misfit dislocations in the subsequent LPE layer. CVD SiC epitaxially grown on these materials exhibited a smooth interface with the LPE SiC layer and greatly reduced the step-bunching present in the LPE layer.

### Introduction

Commercially available 4H and 6H-SiC wafers manufactured by the modified Lely method [1] are known to possess a high density of defects, such as micropipes, stacking faults and other crystallographic defects [2]. A high density of micropipes can lead to catastrophic failure in devices fabricated on these SiC substrates. Hence a reduction of micropipe density in substrates is needed. One technique for reducing the micropipe density has been developed and demonstrated by TDI Inc. [3,4,5]. This technique involves filling the micropipe channels with SiC by the liquid phase epitaxy (LPE) method. However, LPE layers grown on SiC substrates are known to produce poor surface morphology [6]. They exhibit a high degree of step bunching which is detrimental for subsequent SiC device manufacturing. In this respect, CVD growth of SiC on LPE layer has been shown to greatly improve the surface morphology [6]. Preliminary characterization results of devices using commercially available SiC substrates with consecutive LPE and CVD epitaxial layers have shown encouraging results. Therefore, it is of interest to perform a structural study of filled micropipes in the initial SiC substrate, so the impact of subsequent LPE and CVD growth of SiC can be ascertained. The present study was undertaken to determine the filled, or unfilled, status

of micropipes in 4H and 6H-SiC wafers fabricated by LPE and CVD techniques, and to understand the mechanisms by which micropipes are eliminated from the surface of these substrates.

### Experimental Procedure

Silicon carbide wafers with reduced micropipe density were fabricated using micropipe-filling technology developed at TDI, Inc. [3-5]. Research grade 35 mm and 40 mm diameter 3.5° off-axis 6H-SiC and 8° off-axis 4H-SiC wafers manufactured by Cree Research, Inc. were used as the substrates. All experiments were performed on the (0001) face of the SiC wafers. The average micropipe density in the initial SiC wafers was on the order of  $100 \text{ cm}^{-2}$  or greater. After the micropipe filling process, the micropipe density was found to be less than  $20 \text{ cm}^{-2}$ . CVD growth experiments were then performed using a cold-wall chemical vapor deposition (CVD) reactor at the Emerging Materials Research Laboratory (EMRL) [6]. Epitaxial layers on the order of 6-8  $\mu\text{m}$  thick were deposited using a silicon-to-carbon (Si/C) ratio of 0.3.

Transmission electron microscopy (TEM) and synchrotron white beam x-ray topography (SWBXT) were used for the structural investigation of SiC wafers to obtain information on the nature of material defects. For the preparation of cross-sectional thin foil specimens, 0.2-mm thick plates with the 2.3x5 mm specimen on the surface were sectioned from the sample. The plates were soaked with epoxy and squeezed into a slotted opening of an Al rod of 2.3 mm diameter. The rod, loaded with the specimen, was then cut into 0.2-mm discs, and then thinned to electron transparency following standard procedures of polishing, dimpling and ion milling. Thin foils thus prepared were examined with a 200 keV Hitachi transmission electron microscope.

### Results and Discussion

TEM investigation on cross-sectional specimens of commercially available 4H and 6H-SiC wafers revealed many micropipes in the form of line defects normal to the basal plane of the hexagonal crystal. Figure 1a shows a bright field TEM micrograph of a typical micropipe extending from top to bottom of the crystal. The application of the two beam invisibility criterion of characterization of a dislocation established the micropipe to be a pure screw dislocation and identified the direction of Burgers vector to be [0001]. X-ray topography (SWBXT) performed on these substrates also identified the direction of the pure screw dislocation associated with these micropipes as [0001]. The topography investigation also established that the size of the hollow core associated with these micropipes is dependent upon the magnitude of the Burgers vector, which assumes a value that is an integral multiple of unit-cell height  $c$  of the hexagonal SiC unit cell. Figure 1b shows a SWBXT image taken in back-reflection geometry from a basal plane of hexagonal SiC. The image exhibits hollow core screw dislocations (M) with Burgers vectors in the range of 4-5 $c$ .

Samples in which micropipe channels were filled by the LPE technique appear to exhibit a low density of micropipes on their surface. TEM observations on cross-sectional specimens of these samples revealed that the hollow core at the surface of the micropipe in the initial substrate is filled or partially filled either by homo-epitaxial growth or random deposition of LPE SiC. Figure 2a is a TEM bright field micrograph showing the surface core of a micropipe (indicated by an arrow) in a 4H-SiC substrate filled by homo-epitaxial growth of LPE SiC. Present studies also found that the LPE layer deposited on the initial SiC substrate appears to possess either a nano-pore extending from top to bottom of the layer or a small angle tilt plus twist (mixed character) grain boundary at the location where the micropipe is filled or partially filled by homo-epitaxial growth.

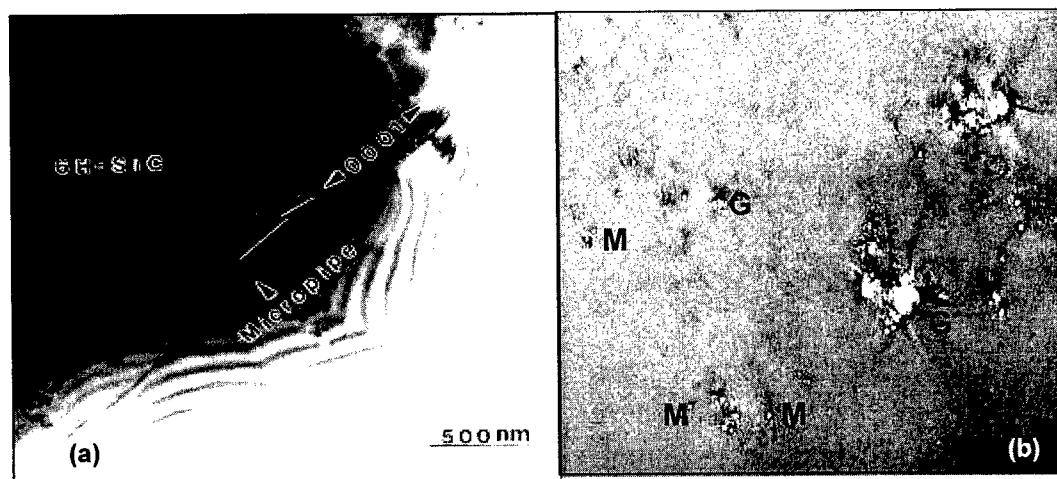


Figure 1. Structural characterization of commercial (unprocessed) substrates. (a) TEM micrograph showing micropipe segment in the matrix of a 6H-SiC wafer. The micropipe originates in the SiC wafer (only segment present near tip of wafer shown). (b) SWBXT topograph from a 4H-SiC wafer in back reflection geometry showing individual micropipes (M), and group of micropipes (G) with range of Burgers vectors. Faint images of closed core 1c dislocations barely visible in background.

The interface between neighboring LPE layers at the tip of a filled micropipe (Fig. 2a) exhibits a mixed character grain boundary, partially formed by edge and screw dislocations. The presence of a mixed-character small angle grain boundary at the tip of a filled micropipe suggests that if the screw dislocation associated with the original hollow core micropipe survived the LPE filling process by transforming into a closed core screw dislocation, it can maintain its continuity by transforming into a mixed-character small angle grain boundary dislocation. This means that the LPE filling process may not have created an obstruction to the continuity of the dislocation. The nano-pore shown in the TEM micrograph of Figure 2b runs from top to bottom of the LPE layer deposited on a 6H-SiC substrate and appears to originate from a partially filled micropipe present in the substrate. The existence of nano-pores in the LPE layer can be attributed to the partial filling characteristics of homo-epitaxial growth of LPE SiC inside the micropipe channels. These deposits inhibit the atomic deposition during subsequent LPE layer growth.

Filling of micropipes by the homo-epitaxial growth of LPE SiC can result in a coherent interface between the filled micropipe and the substrate. Such a coherent interface is likely to facilitate the continuity of the close packed atomic stacking order of the substrate in the LPE layer that is deposited on the substrate. The present study supports the idea of possible occurrence of analogous close packing arrangement of atoms in neighboring layers between substrate and LPE deposit due to homo-epitaxial growth inside the micropipe. The LPE layer on the 4H-SiC substrate surface containing a filled micropipe (Fig. 2a), has its close packed (111) planes parallel to (0001) planes of the substrate, even though the LPE layer assumes the stacking order of face centered SiC. In the present TEM study, it was also found that micropipes filled by random deposition of LPE SiC appear to assume an incoherent interface between the substrate and the deposited LPE layer. The LPE deposit is therefore believed to participate in the development of an incoherent interface

between the substrate and LPE layer grown in the vicinity of a filled or partially filled micropipe, and thereby introduces space misfit dislocations in the matrix of the LPE layer. The TEM study also revealed that the epitaxially grown CVD SiC deposited on the LPE layer yields a smooth surface free of any step bunching which is favorable for subsequent device processing.

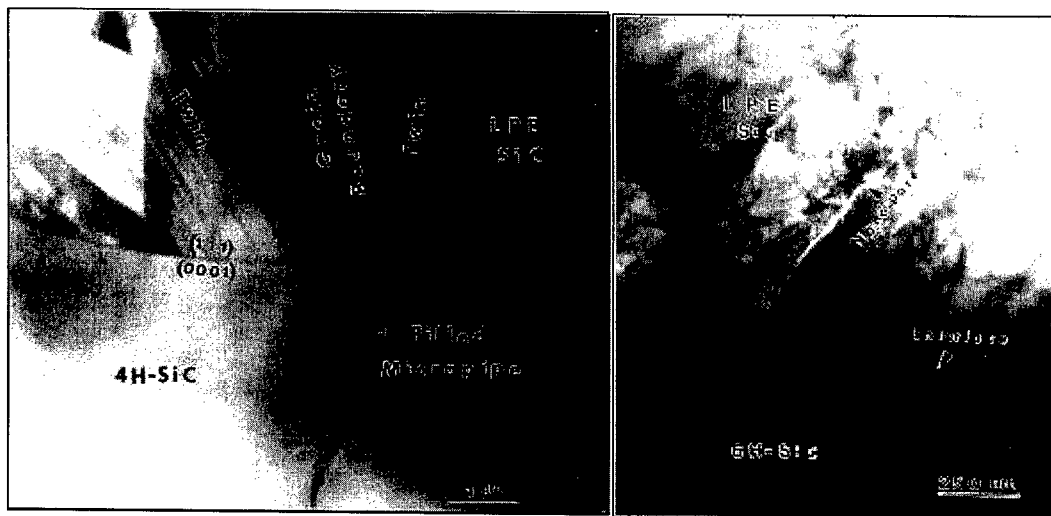


Figure 2. Structural characterization of processed (LPE, CVD) substrates. (a) Bright field TEM micrograph showing status of filled micropipe at interface between 4H-SiC and LPE SiC. Dark arrow identifies the interface between 4H-SiC and LPE SiC; (b) Bright field TEM micrograph showing origination of nano-pore from tip of partially filled micropipe in 6H-SiC wafer.

### Conclusion

Based upon the present TEM and x-ray topography studies of micropipes in commercially available 4H and 6H-SiC wafers before and after LPE and CVD epitaxial layers, it can be concluded that the homo-epitaxial growth of SiC inside a micropipe channel can be used to fill the hollow core of the micropipe and thereby improve the substrate quality for subsequent epitaxial or device processing. However, the resulting crystal structure in the vicinity of filled, or partially filled, micropipes was observed to contain both closed-core dislocations as well as mixed character grain boundary, partially formed by edge and screw dislocations.

### References

- [1] J. A. Lely, *Berichte der Deutschen Keramischen Gesellschaft*, **32**, 229-31.
- [2] M. Dudley, W. Si, S. Wang, C.H. Carter, Jr., R. Glass, V.F. Tsvetkov, *Il Nuovo Cimento*, **19D** (1997).
- [3] S. Rendakova and V. Dimitriev, Abstracts Fall 1997 MRS meeting, Dec. 1-5, 1997, Boston, pp.149-150.
- [4] S.V. Rendakova, I. P. Nikitina, A. S. Tregubova, and V. A. Dmitriev, *J. Electr. Materials*, **27** (1998), 292.
- [5] S. Rendakova, V. Ivantsov, and V. Dimitriev, *Materials Science Forum*, 264-268(1998), pp. 163-165.

This work was at EMRL supported by the Office of Naval Research, Grant No. N0014-98-1-0824, Dr. C. Wood program manager. Research at TDI was partly supported by Ballistic Missiles Defense/Innovative Science and Technology and managed by the Office of Naval Research (Dr. Colin Wood).



## In-situ Observation of SiC Bulk Single Crystal Growth by X-Ray Topography

Tomohisa Kato<sup>1</sup>, Naoki Oyanagi<sup>2</sup>, Hirotaka Yamaguchi<sup>1</sup>, Yukio Takano<sup>3</sup>,  
Shin-ichi Nishizawa<sup>1</sup> and Kazuo Arai<sup>1</sup>

<sup>1</sup>Electrotechnical Laboratory, UPR Ultra-Low-Loss Power Device Technology Research Body,  
1-1-4 Umezono, Tsukuba, Ibaraki, 305-8568, Japan

<sup>2</sup>R&D Association for Future Electron Devices, UPR Ultra-Low-Loss Power Device Technology  
Research Body, 1-1-4 Umezono, Tsukuba, Ibaraki, 305-8568, Japan

<sup>3</sup>Faculty of Industrial Science and Technology, Science University of Tokyo,  
2641, Yamazaki, Noda, Chiba, 278-8510, Japan

**Keywords:** Defects, In Situ Observation, Modified Lely Method, X-Ray Topography

**Abstract** We report here for the first time on the *in-situ* observations for SiC bulk single crystal growth by x-ray topographic technique. Occurrence and dynamic observation of the defects such as micropipes and domain boundaries during SiC crystal growth by the modified Lely method was investigated in a real time display. The *in-situ* observation was considered to contribute for optimizing the growth conditions and to interpret the mechanism of defects and dislocations formation.

### Introduction

Silicon carbide (SiC) is one of the well-known wide bandgap materials for high power, high temperature and high frequency semiconductor devices. Currently, SiC wafers are produced from a bulk single crystal grown by the modified Lely method [1]. Although the size of SiC single crystals increased large, many defects and dislocations are still contained in the crystals and have limited the quality of SiC-based devices [2-3]. The possible reason is that research for crystal growth until now is carried out by the usual conventional ways. So it was difficult to find the optimum conditions for growth. *In-situ* observation technique has been used for long times for the investigation of crystal growth mechanism and origin of defects [4]. However, the *in-situ* observation for SiC bulk single crystal growth has not been realized until now, because the crystal growth is performed in a carbon crucible (like a black box) and at high temperature, over 2000°C. In a previous paper, we reported on *in-situ* observation of the SiC crystal growth process using x-ray topographic technique for direct analysis inside the growth crucible [5]. The technique was considered to contribute for optimizing the growth conditions and to interpret the mechanism of defects

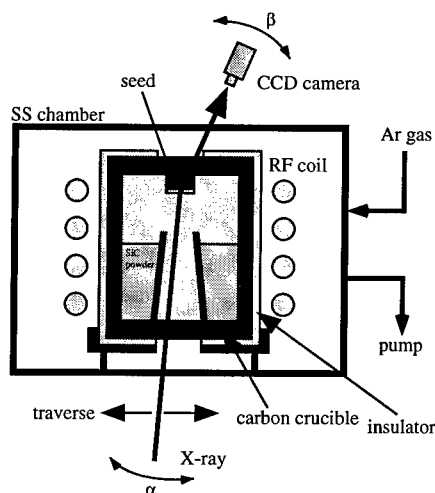


Fig.1 X-ray topographic system for *in-situ* observation of SiC bulk single crystal growth by the modified Lely method

and dislocations formation. In this study, we report on the growth of SiC crystals and the occurrence and dynamical behavior of the defects investigated in a real time display by the x-ray topography system.

### Experimental

The experiments for the growth of SiC crystals by the modified Lely method [1] were performed in an rf induction furnace combined with an x-ray topography system as shown in Fig.1. The seeds were chosen from (0001)6H-SiC crystals developed by Acheson and Lely methods [6]. The thickness of the seeds are about 0.5mm, and their surface was polished in order to make them mirror likes before growth. The crystals were grown at 2200°C and 10~400 Torr chamber pressure of the high purity Ar gas. A molybdenum rotating-anode was used as a source to generate the x-rays with maximum output of 18kW. The diffraction selected from (10 $\bar{1}1$ ) plane of the grown crystal was directly scanned as topographic images using a CCD camera. The system has been explained in the previous paper in detail [5]. A polarizing optical microscope and x-ray topography at room temperature were utilized for the post process observation of the SiC specimens. The grown thickness was calculated from the growth rate which was measured by the transmission x-ray technique [7].

### Results and Discussion

Fig.2(a) is an x-ray topograph of a (0001) 6H-SiC seed crystal made by Acheson method at room temperature and atmospheric pressure. The topograph was taken from the area including the crystal edge of the seed. Some defects and damage in the seed was confirmed clearly by the topograph. The negative crystals and voids contained in the crystal edge were observed as spot like images. Moreover, scratch damages remained on the top surface of the seed by the polishing process were also captured as line contrast images. As the temperature rose to 2200°C and the pressure in the chamber is decreased from atmospheric pressure, the growth started gradually and the appearance of the topograph changes as shown in Fig.2(b). The topograph was taken by the *in-situ* observation at 2200°C and 200 Torr, 10 minutes after the pressure began decreasing. The line images are gradually washed out soon after the start of the growth. We interpret that the scratch damages caused by the polishing have almost recovered their crystallinity during the initial growth. Simultaneously, a hill of the grown crystal was formed with the height of about 1~2  $\mu\text{m}$ . The hill was confirmed

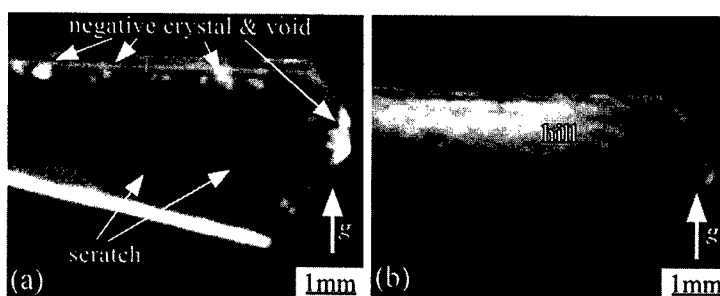


Fig.2 The *in-situ* observation of the SiC growth on Acheson seed crystal. (a) is the seed image before growth. The negative crystals, voids and scratch damages were captured as contrast images. (b) is the image captured 10 minutes after the start of growth. The scratch damages are gradually washed out, and a hill of the grown crystal was confirmed as an island like image.

as light contrast image of an island like shape by the topography.

*In-situ* observations were also made for SiC crystal growth using Lely crystals as seeds. Fig.3(a) is the x-ray topograph captured before start of the growth. From this topograph, it is visible that the Lely seed crystal contains defects and dislocations with relatively low density. However, right after the growth started and the pressure in the chamber was gradually decreased, many light and dark contrasts appeared in the topograph as shown in Fig.3(b). We interpret these as many dislocations appeared in the grown crystal just above the surface of the seed. Besides this we notice, the crystal edge starts becoming rounded, because the edge was more exposed to higher temperature than the center. This phenomenon was observed almost in all of the growth experiments. As the growth reaches about 150 $\mu$ m thickness, the typical defects like micropipes [1,8-9] and domain boundaries also occurred. These large defects were distinguished as clear images as shown in Fig.3(c) marked by "MPs" and "DBs". Existence of these defects was also checked from the post process observation. As the SiC crystal grows and enlarges over 300 $\mu$ m thickness, the MPs and the DBs images showed a dynamic elongation from its original position towards the edge of the growing crystal, as shown in Fig.3(d). Lateral enlargement of SiC single crystal and the change of MPs and DBs position during the growth by the modified Lely method has been described effectively by the thermal conductive flux around the crystal in [10].

The *in-situ* observation of the SiC single crystal growth was realized by the x-ray topographic technique using this system. The system is a reliable one and offers effective methods for future investigation of optimizing the growth conditions and for analyzing the origin of defects and dislocations.

## Conclusion

The *in-situ*

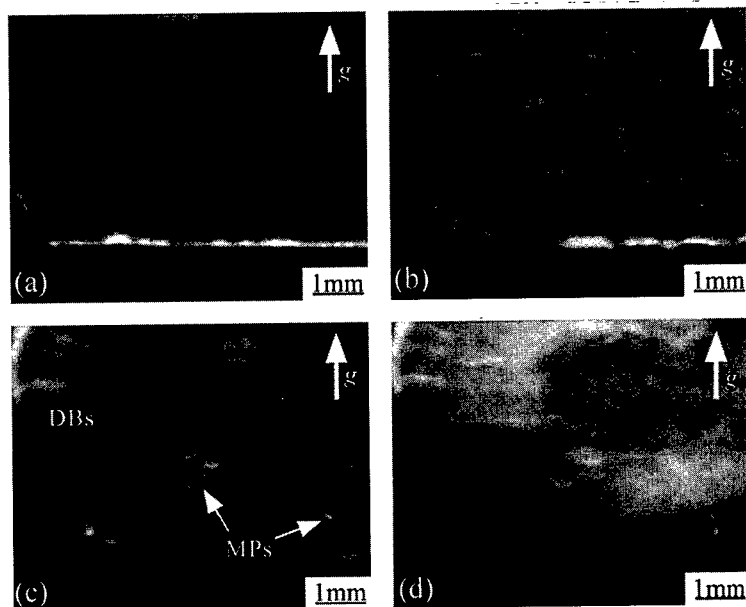


Fig.3 The in-situ observation of the SiC growth on Lely seed crystal. (a) is the seed image before growth. (b), (c) and (d) are images; 1.5, 3.5, 4 hrs after the start of growth. Right after the growth started and the pressure in the chamber was gradually decreased, many light and dark contrasts appeared in the topograph. We interpret these as dislocations appeared in the grown crystal just above the surface of the seed. The typical defects like micropipes and domain boundaries also occurred. These large defects were distinguished as clear images marked by "MPs" and "DBs". These defects images showed a dynamic elongation from its original position towards the edge of the growing crystal.

observations for SiC bulk single crystal growth was successful by the x-ray topography system. The growth behavior in the modified Lely method was clarified in a real time display. Especially, occurrence and dynamic observation of defect features in SiC grown crystals were captured for the first time. The *in-situ* observation was considered to contribute for optimizing the SiC crystal growth in future.

#### Acknowledgements

This study was performed under the management of FED as a part of the MITI NSS (R&D Ultra-Low-Loss Power Device Technologies) supported by NEDO of Japan.

#### References

- [1] Y. M. Tairov and V. F. Tsvetkov, J. Cryst. Growth 43(2) (1978) p. 209.
- [2] P.G. Neudeck and J.A. Powell, IEEE Electron Device Lett. 15 (1995) p. 63.
- [3] K. Koga, Y. Fujikawa, Y. Ueda and T. Yamaguchi, Springer Proc. in Phys., 71 Amorphous and Crystalline Silicon Carbide IV, Springer-Verlag, Berlin, 1992, p. 96.
- [4] J. Chikawa, J. Cryst. Growth 24/25 (1974) p. 61.
- [5] H. Yamaguchi, S. Nishizawa, W. Bahng, N. Oyanagi, T. Kato, S. Yoshida, K. Arai, Y. Machitani and T. Kikuchi, in preparation.
- [6] J.A. Lely, Ber. Deut. Keram. Ges., 32 (1955) p229.
- [7] N. Oyanagi, T. Kato, H. Yamaguchi, S. Nishizawa and K. Arai, in preparation.
- [8] D.L. Barrett, J.P. McHugh, H.M. Hobgood, R.H. Hopkins, P.G. McMullin, R.C. Clarke and W.J. Choyke, J. Cryst. Growth 128, (1993) p. 358.
- [9] T. Kato, H. Ohsato, M. Razeghi and T. Okuda, Proceedings of ICSCRM-95, Inst. Phys. Conf. Ser. 142 (1996) p. 417.
- [10] S. Nishizawa, Y. Kitou, N. Oyanagi, W. Bahng, M.N. Khan and K. Arai, in preparation.

Tomohisa Kato

E-MAIL : ktomo@etl.go.jp

FAX : +81-298-54-3397

## X-ray Topographic Study of SiC Crystal at High Temperature

H. Yamaguchi<sup>1\*</sup>, N. Oyanagi<sup>2</sup>, T. Kato<sup>1</sup>, Y. Takano<sup>3</sup>, S. Nishizawa<sup>1</sup>,  
W. Bahng<sup>1</sup>, S. Yoshida<sup>1,4</sup> and K. Arai<sup>1</sup>

<sup>1</sup> Electrotechnical Laboratory, UPR Ultra-Low-Loss Power Device Technology Research Body,  
1-1-4 Umezono, Tsukuba, Ibaraki, 305-8568, Japan

<sup>2</sup> R&D Association for Future Electron Devices, UPR Ultra-Low-Loss Power Device Technology  
Research Body, 1-1-4 Umezono, Tsukuba, Ibaraki, 305-8568, Japan

<sup>3</sup> Faculty of Industrial Science and Technology, Science University of Tokyo,  
2641, Yamazaki, Noda, Chiba, 278-8510, Japan

<sup>4</sup> Faculty of Engineering, Saitama University, 255 Shimo-Okubo, Urawa, Saitama 338-8570,  
Japan

**Keywords:** Crystal Growth, High-Temperature Topography, In Situ Observation, X-Ray  
Topography

### Abstract

We have developed an instrument for *in-situ* X-ray topography during crystal growth of silicon carbide (SiC). A vertical X-ray goniometer is combined with a furnace for sublimation growth. A high-power X-ray source and a TV imaging system using a CCD camera make possible to display the behaviors of defects in SiC crystal inside crucible. For a demonstration of the developed instrument, we show the topographs of a SiC crystal at high temperature. The topographs show distinct deformations developing with increasing temperature.

### Introduction

Bulk crystal growth of silicon carbide (SiC) is an indispensable technique to realize the low-loss-power electronics based on SiC in the coming century. At present, sublimation method is most successful in growing large and pure SiC crystals. The grown crystals, however, includes many imperfections such as undesirable modifications and micropipes. These imperfections should be eliminated from boules, and the boules are required to increase their diameters. To clear these problems, further information about the crystal growth is necessary. The events taking place in crucible are, however, rarely known because it is difficult to observe the growing crystals directly. As a mean of finding a way out of the present difficulty, we propose an *in-situ* observation of the crystal growth process by X-ray topography.

X-ray topography projects imperfections in a crystal on a two-dimensional picture. In addition, X-ray beam has good transmissivity in materials, particularly large in graphite crucible. The *in-situ* observation of a growing crystal inside a crucible using x-ray topography, therefore, would be possible. This technique would reveal the behaviors of the growing crystals and the accompanying undesirable events during the growth, and the obtained knowledge will be helpful to optimize the growth conditions. In this paper, we explain the design of the instrument and show the first topograph of a SiC crystal at 2100 °C.

### Design of instrument

The instrument for the *in-situ* observation consists of X-ray goniometer and crystal growth chamber (Fig. 1). In order to reproduce an ordinary growth condition during the *in-situ* observation and to retain reasonable spatial resolution of the topograph, a vertical type

goniometer is designed for the Laue-case topograph. A cylindrical crystal-growth chamber is installed at the center of the vertical goniometer.

A rotating-anode 18-kW X-ray generator with a molybdenum target is employed as X-ray source. The X-ray generator and the incident optics are mounted on a circle to determine the incident angle ( $\alpha$ -circle). The sample is positioned at the 1400-mm point from the X-ray source, and the X-ray beam is introduced into the crystal-growth chamber through a beryllium window mounted on the bottom flange of the chamber. The scattered beams are extracted through the other beryllium window on the top flange of the chamber. The scattered beams are extracted through the other beryllium window on the top flange of the chamber. The scattered beams are detected by a CCD camera on the  $\beta$ -circle. Inside the crystal-growth chamber, a crucible is mounted on an azimuthal-rotation stage ( $\phi$ -circle). The distance between the sample and the detector is as long as 280 mm because the detector is required to place outside the crystal-growth chamber. This long distance between the sample and detector is disadvantageous to the spatial resolution of the topograph. In this case, the resolution is estimated at 14.9  $\mu\text{m}$  and 100.0  $\mu\text{m}$  respectively for parallel and perpendicular to the scattering plane, whereas the CCD camera gives the spatial resolution of about 50  $\mu\text{m}$ .

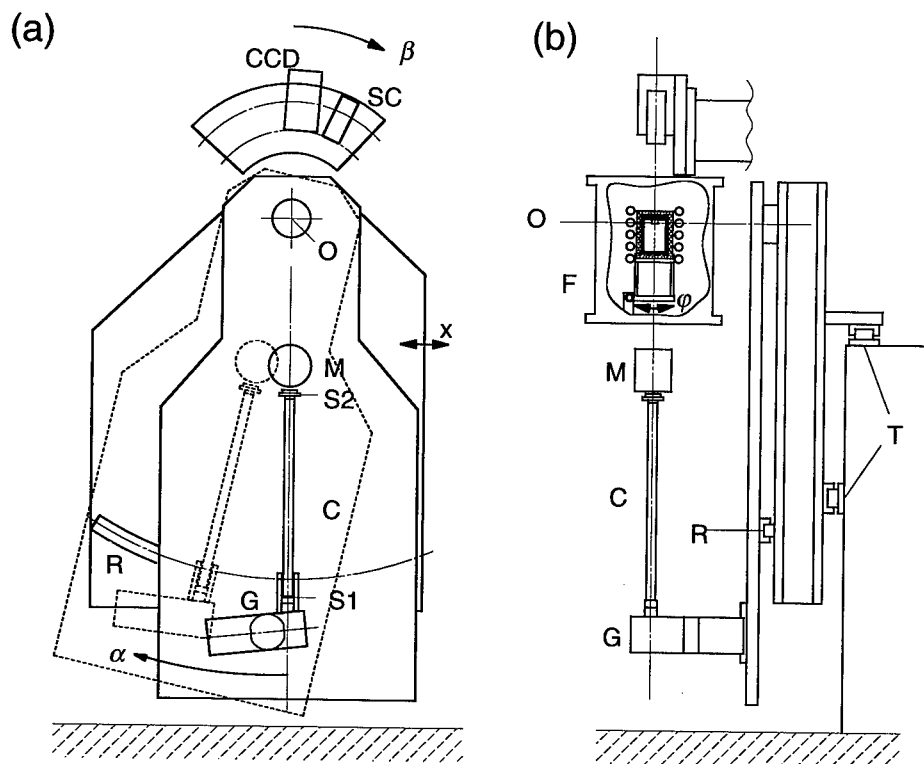


Fig. 1 Schematic displays of the *in-situ* topography instrument. (a) Front view and (b) side view.

G: X-ray generator, S1 and S2: slits, C: beam collimator, M: double-crystal monochromator, O: Center of the goniometer, CCD: CCD camera, SC: scintillation counter, F: Crystal-growth chamber (omitted in the front view), R: guide rail for the  $\alpha$ -circle, T: guide rail for the  $x$ -axis.

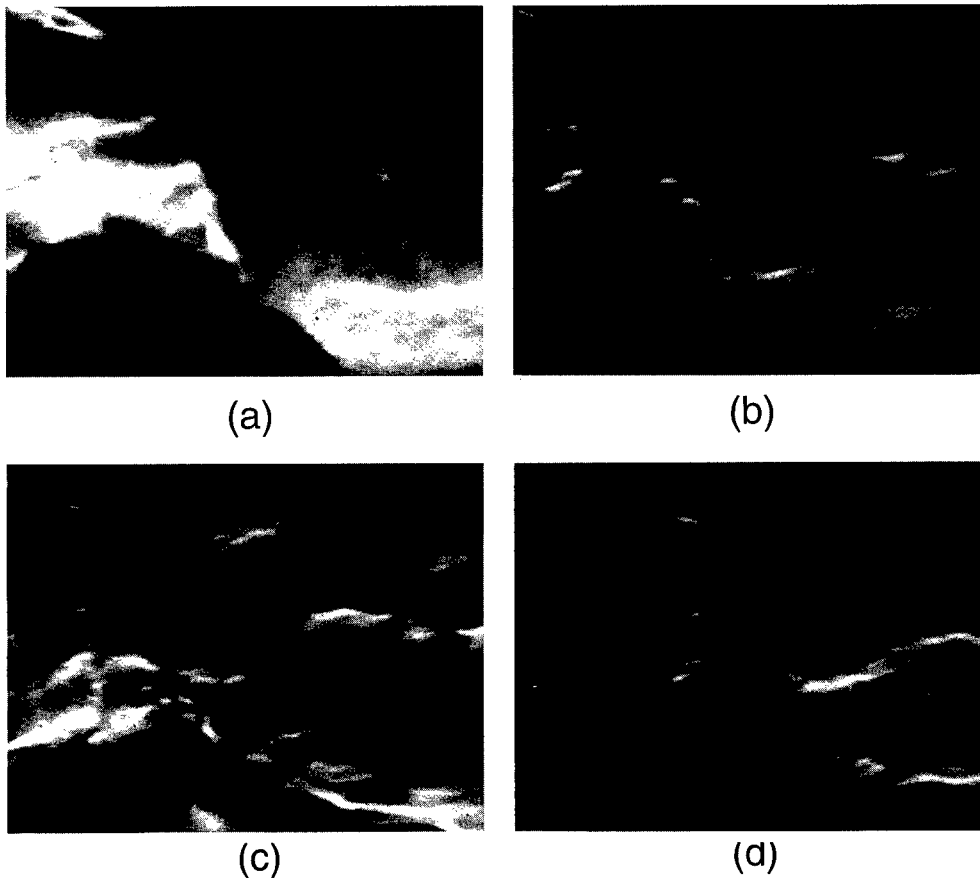


Fig. 2 X-ray topographs of 6H-SiC using the asymmetric  $(1\ 0\ \bar{1}\ 1)$  reflection at (a) room temperature before heating, (b) 1400 °C, (c) 2100 °C, and (d) room temperature after the process.

The diffraction images detected by the CCD camera are displayed on a video monitor on the spot. In order to facilitate the selection of the probing position in the sample and take traverse topograph, the  $\alpha$ -circle is mounted on a stage with a linear axis ( $x$ -axis). In the traverse topograph, approximately  $7 \times 7\text{-mm}^2$  area of the sample is projected, and a standard measurement time is 1-5 min depending on the intensity of the diffraction beam.

#### High Temperature Topography

We show topographs of a crystal at high temperature inside a crucible. The sample was a 6H-SiC  $(0\ 0\ 0\ 1)$  plate with the thickness of 0.1 mm, which was cut from a crystal boule grown by the sublimation method in our laboratory. The crystal plate was glued on a crucible lid with carbon paste, and no material was charged in the crucible. The crucible was heated with the heating rate of 10 °C/min in the 700-torr Ar atmosphere. The maximum temperature was 2100 °C. Traverse topographs were taken in an asymmetric  $(1\ 0\ \bar{1}\ 1)$  reflection at several temperatures.

At room temperature before the process, as shown in Fig. 2(a), strongly illuminated regions due to heavy distortion were observed in the left and lower right part of the photograph. In this experiment, we focused on the fairly good quality region, upper right part where some spots coming from micropipes and lines from edge dislocations were seen. Some additional lines are found to appear and increase in intensity as temperature increases, indicating that some defects are induced during heating. Figure 2(d) is a topograph taken at room temperature after this process. The defects induced at high temperature are found to remain at room temperature after the process, indicating that they were plastic deformations.

Our preliminary topographic observations of a SiC wafer at 1300 °C using a conventional Lang camera in vacuum atmosphere showed no indication of additional defects introduced. In the observation, the wafer was placed on a heating stage so that any external stress was not applied to the sample. In the present observation, the deformation began to emerge at temperatures as low as ~500 °C. The deformation is likely to be induced by the stress on the lid side of the plate as a result of the difference in thermal expansion between graphite and SiC.

After another several trials with different sample settings, this type of deformation was not observed in thick samples with the thickness more than 0.5 mm. Thus the *in-situ* topography of the SiC crystals is possible without undesirable effects incidental to fixing to the crucible lid.

### Summary

We explained the design of the instrument for *in-situ* topography, and demonstrated the possibility of the observation of the sample inside crucible. For the practical experiments during the crystal growth, we have developed a special crucible that separates the charged materials from the X-ray path. Using this type of crucible, *in-situ* observations are now in progress [1].

As shown in Fig. 1, a channel-cut double-crystal Si(111) monochromator is mounted on the  $\alpha$ -circle, and optionally available to make the parallel Mo K $\alpha$  beam. In addition, a scintillation counter is mounted on the  $\beta$ -circle. Using the combination of these components, this instrument is also utilized as a diffractometer, which is useful to measure a rocking curve of a diffraction line and distinguish the modifications intergrown. Another useful application is a growth-rate monitor by measuring the intensity of the Mo K $\alpha$  beam transmitted through the grown crystal. The growth rate is determined precisely because the absorption coefficient for SiC is well defined [2].

### Acknowledgment

The authors are grateful to Y. Machitani and T. Kikuchi of RIGAKU Corporation for the useful suggestions and the designing the instrument. The *in-situ* topography instrument was constructed with the support of the Proposal-Based New Industry Creative Type Technology R&D Promotion Program from NEDO of Japan. This work was performed under the management of FED as a part of the MITI R&D Program (Ultra-Low Loss Power Device Technology Project) supported by NEDO.

### References

- [1] T. Kato, N. Oyanagi, H. Yamaguchi, Y. Takano, S. Nishizawa and K. Arai, in these Proceedings, p. 457
- [2] N. Oyanagi, S. Nishizawa, T. Kato, H. Yamaguchi and K. Arai, in these Proceedings, p. 75

\* TEL: +81-298-54-5398 FAX: +81-298-54-5085 E-MAIL: hirotaka@etl.go.jp



## Synchrotron White Beam Topography Studies of 2H SiC Crystals

M. Dudley<sup>1</sup>, W. Huang<sup>1</sup>, W.M. Vetter<sup>1</sup>, P. Neudeck<sup>2</sup> and J.A. Powell<sup>2</sup>

<sup>1</sup> Department of Materials Science and Engineering, State University of New York at Stony Brook,  
Stony Brook, NY 11794-2275, USA

<sup>2</sup> NASA Glenn Research Center, Lewis Field, M.S. 77-1,  
21000 Brookpark Road, Cleveland, OH 44135, USA

**Keywords:** 2H Polytype, Eshelby Twist, Pendellosung

**Abstract.** Synchrotron White Beam X-ray Topography (SWBXT) has been used to characterize 2H silicon carbide crystals grown at NASA Glenn Research Center by the chemical reduction of methyltrichlorosilane at 1400°C. The crystals studied have the form of tapered needles around 0.5 millimeters long and had hexagonal cross-sections 0.2 millimeters in diameter. Transmission Laue patterns confirmed the wurtzite structure of the 2H crystal. SWBXT images recorded in transmission geometry from two different crystals revealed excellent crystal quality, as evidenced by the presence of Pendellosung fringes, a result of the dynamical diffraction processes occurring inside the crystal. Close examination of these topographs and others recorded with different diffraction vectors revealed no evidence for the presence of the axial screw dislocations reported by Setaka and Ejiri, based on their observations of spiral growth steps, and also observed, for example, in  $\alpha$ -Al<sub>2</sub>O<sub>3</sub> and AlN whiskers. Nor was any evidence found for the presence of the "Eshelby Twist" associated with the presence of such dislocations. The absence of axial screw dislocations evidently indicates that the growth was not screw dislocation-assisted, and suggests that the stacking sequence was determined by the thermodynamic growth conditions. Isolated inclusions, with characteristic contrast, were also observed in both crystals.

**Introduction.** Among the many known polytypes of SiC, the 2H polytype, which crystallizes in the pure hexagonal Wurtzite structure, has the largest bandgap, possibly the highest electron mobility, and a much lower growth temperature (<1500°C) than the commonly grown polytypes. As a result, some effort was expended in determining the crystal growth mechanism and optimum growth conditions for this polytype [1]. Analysis of the growth morphology of these crystals provided evidence that they grew via a vapor-solid mechanism rather than the vapor-liquid-solid mechanism suggested previously for both 2H SiC and Si growth [2]. Despite the fact that subsequent study showed the stability of this structure to be questionable, with solid state transformation to the cubic structure being reported at temperatures as low as 400°C [3], small single crystals of the 2H polytype were successfully grown. In this paper we report the results of Synchrotron White Beam X-ray Topographic (SWBXT) analysis of two of the crystals grown in this original effort.

**Experimental.** The 2H crystals used in this study were grown at NASA Glenn Research Center by the chemical reduction of methyltrichlorosilane at 1400°C [1]. The crystals grew in the form of tapered needles up to 3 millimeters long and had hexagonal cross-sections up to 0.5 millimeters in diameter. The c-axis was aligned along the axis of the needles. Spherical deposits of polycrystalline 3C SiC were frequently found attached to the pointed end of the needles (see figure 1). Near the base of the needle (and occasionally close to the tapered end of the needle), thin regions (normal to the needle axis) consisting of a highly disordered mixture of 3C and 2H SiC were found. The

specific crystals studied here were around 0.5 millimeters long and had hexagonal cross-sections of around 0.2 millimeters in diameter. The SWBXT imaging was carried out at the Stony Brook Synchrotron Topography Station, beamline X-19C, at the National Synchrotron Light Source at Brookhaven National Laboratory. Images were recorded on large area, high-resolution SR5 X-ray film. Internegatives were then made of individual images of interest, and positive prints made so that, according to the normal convention, enhanced intensity on the print corresponds to enhanced X-ray intensity on the film.

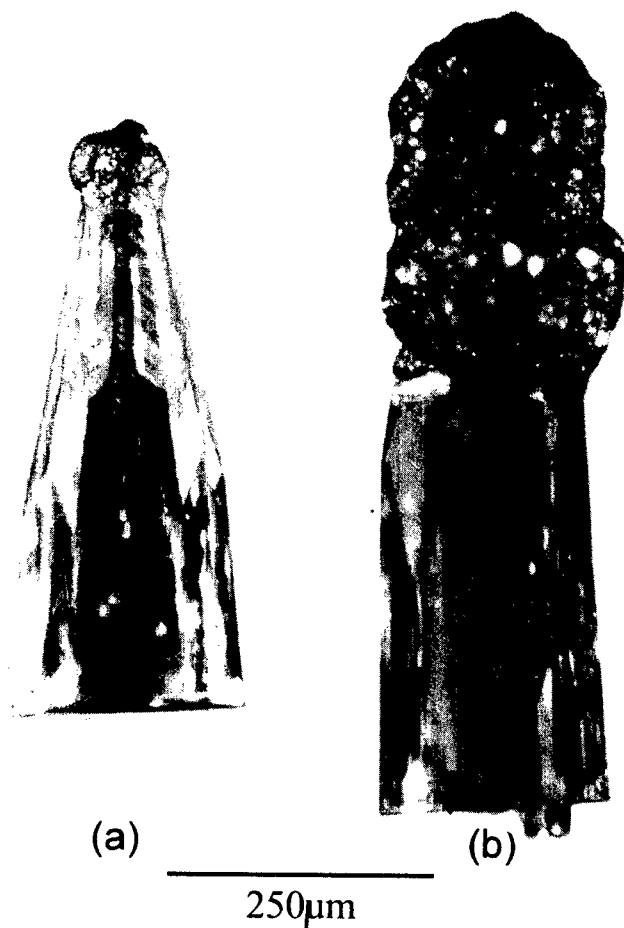


Figure 1. Optical images of the two crystals examined. Note the roughly spherical deposits of polycrystalline 3C SiC

**Results and Discussion.** Transmission Laue patterns recorded from the crystals using synchrotron radiation, confirmed the 2H crystal structure. Figures 2(a) and (b) show SWBXT images, recorded in transmission geometry, from the two crystals shown in Figure 1. Pendellösung fringes are visible on both images [4]. These fringes have their origins in dynamical diffraction processes that occur in nearly perfect single crystals. These processes comprise interference interactions between X-ray wavefields (Bloch waves) which propagate along the same path inside the crystal. These interference effects result in beating between wavefields associated with the two branches of the dispersion surface, where the planes of constant phase (for projection images such as the SWBXT images presented here) are oriented parallel to the crystal surface and are separated by the extinction

length for the particular Bragg reflection. For parallel-sided crystals, Pendellösung fringes are not visible on projection topographs since the crystal surfaces are parallel to the planes of constant phase (the fringes are, however, visible on section topographs recorded from such crystals). However, in crystals which have wedge shaped regions, or regions where the crystal surfaces are not parallel, these fringes can become visible on projection topographs, with each fringe observed corresponding to an intersection between the X-ray exit surface and a plane of constant phase for the beating process. The crystals observed here have hexagonal cross-sections and thus when images are recorded with the X-ray beam perpendicular to the needle axis, wedge shaped regions are presented to the incident X-ray beam. The extinction length for these images is around 80 micrometers, so that one would expect to see approximately 4 fringes. This is consistent with observation.

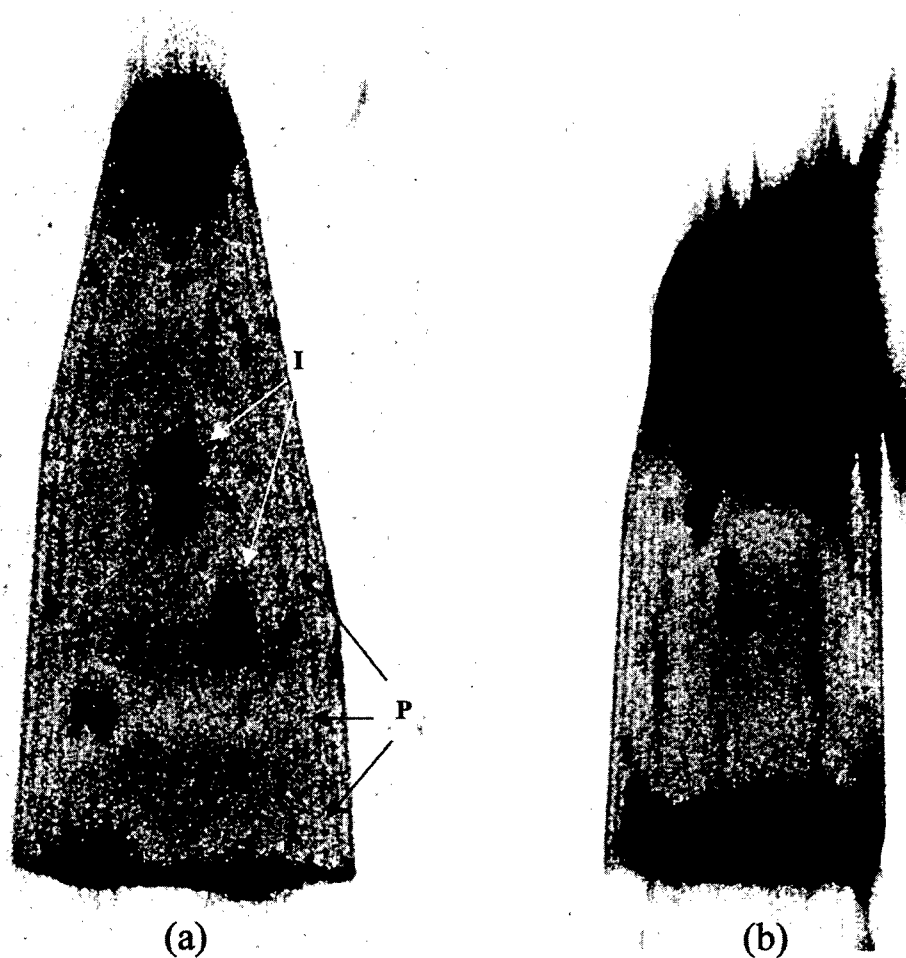


Figure 2. Transmission X-ray Topographs ( $g=0002$ ,  $\lambda=0.44\text{\AA}$ ), recorded from the 2H crystals in figure 1. Note the Pendellösung fringes, P, and the inclusions, I.

The Pendellösung process is highly sensitive to the local distortion in the crystal, with minute distortions completely eliminating the effect. The clear visibility of these fringes on figures

2(a) and (b) is therefore indicative of a very high degree of perfection. Also visible on these topographs are images of a few isolated inclusions. These inclusions are visible via the images of their strain fields, which are likely to be much larger in extent than the inclusions themselves. These images indicated that the strain centers are spherically symmetric as indicated by the fact that they comprise two lobes of contrast separated by a line of no-contrast perpendicular to the projection of the active reciprocal lattice vector on the image. This line of no-contrast has its origins in the fact that along this direction, the distortion associated with the inclusion is parallel to the diffracting planes. The strain along this direction is therefore sensed to be zero thus explaining the absence of contrast. The chemical nature of these inclusions has not yet been determined.

It is important to note that it is clear from these topographs that these crystals have no visible dislocation content. In particular, there are no screw dislocations parallel to the growth axis. It has been postulated that the nearly one-dimensional growth of whiskers, such as those studied here, may be facilitated by the presence of a screw dislocation along the growth axis. Such dislocations have been observed using various techniques. For example, measurement of the so-called "Eshelby Twist" [5], which results from the torque exerted by the dislocation stress field on the free surfaces at the tips of whisker-like crystals, was used for the cases of  $\alpha$ -Al<sub>2</sub>O<sub>3</sub> [6] and AlN [7]. These measurements were carried out using X-ray Laue diffraction ( $\alpha$ -Al<sub>2</sub>O<sub>3</sub>) and electron microscopy and electron diffraction (AlN). Such axial screw dislocations were also reported in 2H SiC [8], where they were revealed by the presence of spiral growth steps near the tip of the whisker (it should be noted that the data presented in favor of this conclusion was, in the opinion of the authors, somewhat unconvincing). The topographs presented here show unequivocally that there were no such axial screw dislocations in these crystals.

Assuming that axial screw dislocations were not forced to either glide (under stress) or climb (via interaction with vacancies) out of the crystal following growth, it would appear that dislocation-assisted growth did not occur in these crystals. In the absence of the growth template provided by the spiral steps associated with such screw dislocations, it seems likely that the ability to isolate the 2H polytype was simply a function of the thermodynamic growth conditions.

**Conclusions.** SWBXT imaging of 2H SiC needles has revealed a high degree of crystal perfection, indicated by the absence of dislocations, and the presence of Pendellösung fringes. A few isolated inclusions were also observed. The absence of axial screw dislocations most likely indicates that growth was not dislocation-assisted, but rather that the control of the polytype was achieved solely by adjustment of the thermodynamic growth conditions.

**Acknowledgments.** Support is acknowledged from the U.S. Army Research Office under contract number DAAG55-98-1-0392 (contract monitor Dr. John Prater), partially funded by the DARPA Microsystems Technology Office (Order#E111/3 monitored by Dr. Dan Radack) and NASA Glenn Research Center. Topography carried out at the NSLS, at BNL, which is supported by the U.S. Department of Energy, under contract number DE-AC02-98CH10886.

## References

1. J.A. Powell, J. Appl. Phys. 40 (1969), p. 4660.
2. R.S. Wagner and W.C. Ellis, Appl. Phys. Lett. 4 (1964), p. 89.
3. J.A. Powell and H.A. Will, J. Appl. Phys. 43 (1965), p. 1400.
4. B.K. Tanner, "X-ray Diffraction Topography", Oxford: Pergamon (1976).
5. J.D. Eshelby, J. Appl. Phys. 24 (1953), 176.
6. R.D. Dragsdorf and W.W. Webb, J. Appl. Phys. 29 (1958), p. 817.
7. C.M. Drum, J. Appl. Phys. 36 (1965), p. 824.
8. N. Setaka and K. Ejiri, J. Amer. Ceram. Soc. 52 (1969), p. 400.

## **Synchrotron White Beam X-ray Topography and Atomic Force Microscopy Studies of a 540R-SiC Lely Platelet**

W.M. Vetter<sup>1</sup>, M. Dudley<sup>1</sup>, W. Huang<sup>1</sup>, P. Neudeck<sup>2</sup> and J.A. Powell<sup>2</sup>

<sup>1</sup>Department of Materials Science and Engineering, State University of New York at Stony Brook,  
Stony Brook, NY 11794-2275, USA

<sup>2</sup>NASA Glenn Research Center, Lewis Field, M.S. 77-1,  
21000 Brookpark Road, Cleveland, OH 44135, USA

**Keywords:** Gaseous Etching, Long-Repeat Polytype, Silicon Carbide, X-Ray Topography

**Abstract.** Optical Microscopy and Atomic Force Microscopy (AFM) of a SiC Lely platelet revealed a macrostep pattern the periodicity of which led to speculation that it possessed a structure with a repeat distance roughly 350 times the SiC bilayer thickness. Transmission Laue patterns recorded from the crystal revealed a 3-fold symmetric pattern, qualitatively similar to that obtained from the 6H structure, but displaying an immense number of closely-spaced reflections. The diffraction spots were resolved with a specimen-film distance of 1.4m. The spacing of the spots in the  $10\bar{1}$  row indicated that the specimen's polytype was 540R. Synchrotron White Beam X-ray Topography (SWBXT) revealed the presence of growth dislocations emanating towards the platelet's growth facets, deformation-induced basal plane dislocations, and a group of superscrew dislocations close to the crystal's nucleation point. Optical microscopy revealed micropipes, which correlated with the superscrew dislocation images revealed by SWBXT. Preliminary calculations indicate that the total of the Burgers vectors of the observed micropipes was between 100 and 200nm. Trails of basal plane dislocation etch pits were shown by Nomarski microscopy to intersect the etched crystal surface in a roughly periodic fashion. The trails were attributed to enhanced etching of the intersection across a  $1^\circ$  surface tilt of a series of basal plane dislocations distributed along the crystallographic c-axis with a periodicity related to that of the crystal surface's stepped ledges. This was confirmed using AFM, which revealed a faster etch rate at the intersections of basal plane dislocations at the ledges.

### **Introduction**

One of our authors recently reported on results of high temperature,  $H_2/C_3H_8$  gaseous etching of SiC crystals [1]. During that study an unusual pattern of macrosteps on a Lely-grown platelet was observed after etching the deep grooves cut by a dicing saw. These macrosteps covered most of the platelet and matched exactly on opposite sides of a groove. A  $5\mu m$  long periodicity in the pattern of steps and a surface tilt of about  $1^\circ$  was observed with AFM. From these values a vertical repeat distance for the terraces of 88 nm, or approximately 350 times the 0.25 nm bilayer thickness for SiC, was calculated. It was concluded that the crystal contained a long-period polytypic stacking. In this paper we present results of further studies on this crystal using synchrotron white-beam X-ray topography (SWBXT), optical microscopy, and AFM.

### **Experimental**

SWBXT imaging was carried out at the Stony Brook Synchrotron Topography Station, Beamline X-19C, at the National Synchrotron Light Source at Brookhaven National Laboratory. Diffraction patterns and topographic images were recorded on Kodak Industrex SR-5 X-ray film.

## Results

Figure 1(a) shows a transmission Laue pattern recorded from the Lely platelet using a pinhole collimated synchrotron radiation beam. Figure 1(b) is a similar pattern recorded from a 6H-SiC crystal. Note the highly dense zones of diffraction spots emanating from the central beam stop shadow. The reflections distributed along these zones were very closely spaced and were resolved by recording the diffraction pattern at specimen-to-film distances larger than 1 meter.

The unit cell's class was identified as trigonal by considering the transmission Laue photograph in figure 1(a) (the intensities of its individual diffraction spots show a three-fold symmetry) and its length was found by analyzing the spacing of diffraction spots in figure 1(c) using a method detailed in the literature [2,3]. These closely-spaced pinhole Laue spots could be well-separated by recording them on a sheet of film mounted on the back wall of Beamline X19-C's radiation hutch 1.4m from the specimen. The  $10\bar{1}1$  and  $10\bar{1}2$  spots of a similar 6H-SiC Laue photograph were superimposed over this Laue photograph (for analysis both lattices are regarded as hexagonal). In the gap between these two 6H spots were counted thirty gaps between spots of the sample's  $10\bar{1}l$  row. This number was regarded as one sixth of the row's total gaps. Since  $l \neq 3m + 1$ , where m is an

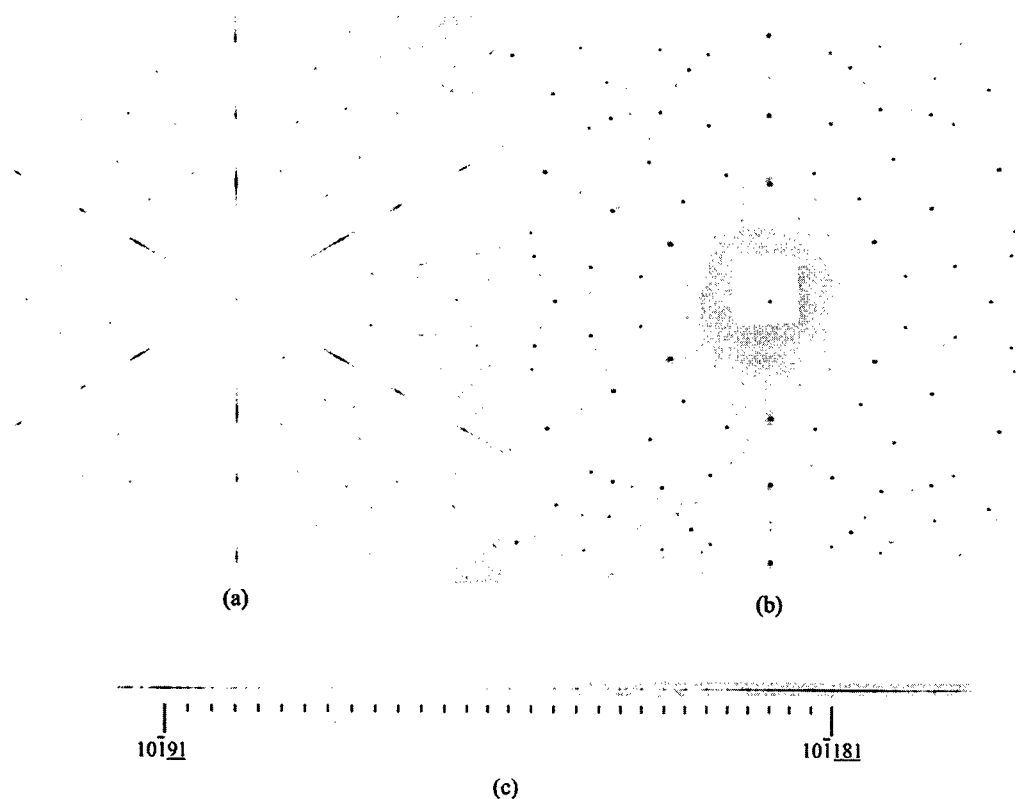


Figure 1. (a) Transmission Laue pattern recorded from the full crystal. Note the three-fold symmetry, and the high density of spots in the zones radiating from the central beam stop shadow, (b) Laue pattern from a 6H crystal, shown for comparison, (c) Detail from the  $10\bar{1}l$  row.



Figure 2. Back reflection topograph recorded from the 540R-SiC crystal ( $g=00012960$ ,  $\lambda=1.24\text{\AA}$ ).

integer, are structurally extinct for a rhombohedral polytype; each gap represented three values of  $l$  and a total of 540 atomic layers were indicated in the unit cell. The polytype is therefore 540R. Polytypes of comparable repeat length have been occasionally observed elsewhere in the literature [4].

Syntactic coalescence between large repeat distance polytypes and shorter ones are commonly observed, yet figures 1(a) and (c) show only a single polytype present in this Lely platelet. Streaking between the diffraction spots does, however, indicate a positional disorder in the crystal.

Figure 2 shows a synchrotron white-beam X-ray topographic (SWBXT) image recorded from the crystal in back-reflection geometry. Groups of large Burgers vector screw dislocations (superscrews) can be observed close to the crystal growth nucleation point, which appear to be at the center of the crystal's lower edge. Preliminary calculations indicate that the sum total of the Burgers vectors of all the observed micropipes is between 100 and 200nm. Nearly straight growth dislocations emanating towards the various growth facets and the deformation-induced basal plane dislocation loops are also visible. These which appear to be linked to the crystal nucleation point and/or the groups of micropipes. Transmission and Nomarski reflection optical microscopy revealed hollow-cores or micropipes which correlated one-to-one with the superscrew dislocation images revealed by SWBXT.

"Etch trails" of dislocations were observed intersecting the etched crystal surface in a roughly periodic fashion by Nomarski microscopy. One of these trails is shown in figure 3(a). Because there is a  $1^\circ$  tilt angle to the crystal's surface, these etch trails were identified with dislocations lying in the crystal's basal planes which intersect the surface at a very slight angle. Basal plane dislocations of this sort are visible in the SWBXT image in figure 2. The trails are attributed to the enhanced etching of intersection of series of these basal plane dislocations, distributed nearly periodically down the depth of the crystallographic c-axis, with the ledges in the stepped pattern of the crystal surface. This association of the etch pits with the ledges was confirmed using AFM, which revealed a faster etch rate where the basal plane dislocations intersected with the ledges (figure 3(b)).

## Conclusions

The Lely platelet was composed purely of the 540R polytype, but exhibited some positional disorder in its structure. X-ray topography revealed groups of superscrew dislocations near the presumed nucleation point of the crystal's growth, as well as basal plane dislocations, some straight and probably grown-in; and others that were curved, probably a result of deformation. Trails of etch pits marked the crystal's surface at regular intervals, likely arising from the same basal plane

dislocations observed by X-ray topography. Under AFM examination, these etch pits were observed at the ledges.

A literature study of polytypism in Lely platelets involving 200 samples [5] observed no long-period polytypes in isolation, but invariably found them as lamellae sandwiched between syntactically-coalesced shorter-period polytypes; and that none of the crystals examined contained superscrew dislocations (micropipes) that might have influenced their polytypism. It was concluded that a crystal composed purely of a single long-repeat polytype was a statistical unlikelihood and that polytype content was thermodynamically-determined. The specimen reported here is an exception that suggests that screw dislocation-assisted growth may, in some cases, exert an influence over the purity of long-repeat distance polytypes.

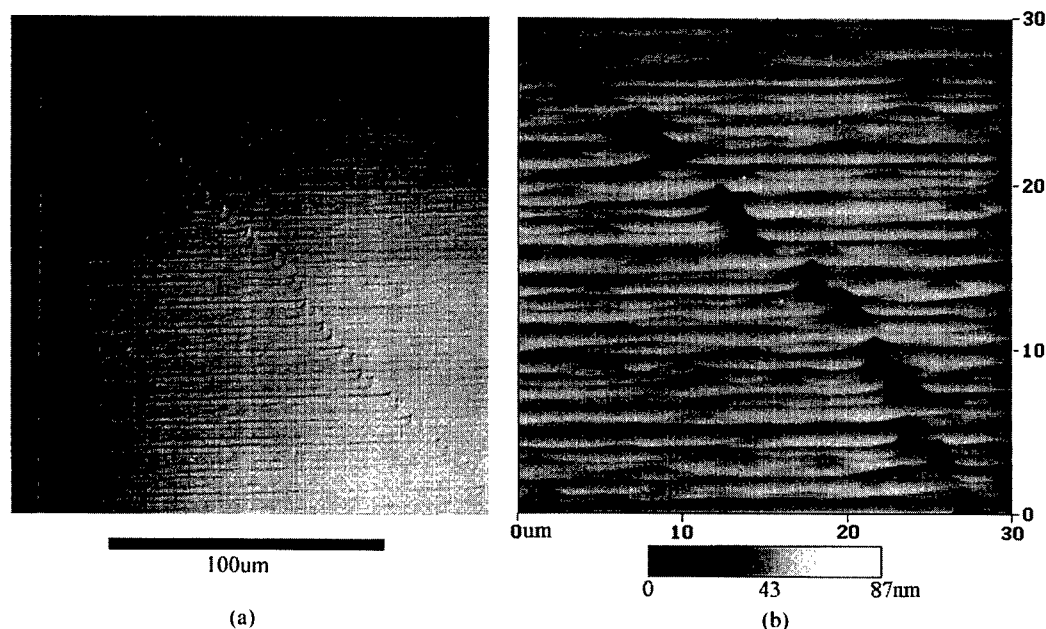


Figure 3. (a) Nomarski optical micrograph of a small area of the platelet's etched surface. The vertical groove was cut by a dicing saw and the horizontal striations are the macrosteps. The "etch trails" run diagonally across the picture. (b) AFM image of an "etch trail."

#### Acknowledgments

Support is acknowledged from the U.S. Army Research Office under contract number DAAG55-98-1-0392 (contract monitor Dr. John Prater), partially funded by the DARPA Microsystems Technology Office (Order#E111/3 monitored by Dr. Dan Radack) and NASA Glenn Research Center. We gratefully acknowledge the assistance of L. Keys, J. Heisler and A. Trunek at NASA Glenn. Topography carried out at the NSLS, at BNL, which is supported by the U.S. Department of Energy, under contract number DE-AC02-98CH10886.

#### References

1. J.A. Powell, D.J. Larkin, and A.J. Trunek, *Mater. Sci. Forum* 264-268 (1998), p. 421.
2. R.S. Mitchell, *Amer. Mineralogist* 38 (1953), p. 60.
3. C.-L. Kuo, *Sci. Sin.* 13 (1964), p. 1605.
4. G. Honjo, S. Miyake and T. Tomita, *Acta Cryst.* 3 (1950), p. 396.
5. G.R. Fisher and P. Barnes, *Phil. Mag.* B 61 (1990), p. 217.



## **X-ray Characterization of 3 inch Diameter 4H and 6H-SiC Experimental Wafers**

T.A. Kuhr<sup>1</sup>, W.M. Vetter<sup>2</sup>, M. Dudley<sup>2</sup> and M. Skowronski<sup>1</sup>

<sup>1</sup>Department of Materials Science and Engineering, Carnegie Mellon University,  
5000 Forbes Ave, Pittsburgh, PA 15213, USA

<sup>2</sup>Department of Materials Science and Engineering, State University of New York at Stony Brook,  
Stony Brook, NY 11794, USA

**Keywords:** Dislocation Arrays, High-Resolution X-Ray Mapping, X-Ray Topography

**Abstract:** Experimental 3 inch diameter 4H and 6H SiC wafers have been examined using synchrotron white beam x-ray topography, x-ray peak position mapping, and KOH etching. Topographic images of the wafer show dark lines of orientation contrast associated with the presence of small angle boundaries that have a radial distribution around the wafers' highly contrasted central regions. Misorientations associated with the boundaries were measured by high-resolution diffraction mapping to be on the order of 500 arcsec, and to be either a pure tilt type with rotation axis in the basal plane or mixed tilt and twist. KOH etching provided further evidence for the types of dislocations associated with these boundaries.

### **Introduction**

In order to make silicon carbide-based electronic devices more economical, it is essential to increase the currently available 2 inch substrate size to 3 and 4 inch diameters. Scaling up the wafer size is a difficult process and usually, larger diameters result in lower crystalline quality in the boules. Several characterization techniques have been previously employed to examine crystalline quality of SiC substrates, with the primary figures of merit being micropipe and dislocation densities. Synchrotron white-beam x-ray topography (SWBXT) is currently the best way to image defects over large wafer areas. For example, it has revealed the detailed natures of the various kinds of dislocations present in SiC, including basal plane dislocations and screw dislocations with closed and hollow-cores (micropipes) [1]. It is also capable of revealing local orientation changes, such as those associated with small angle boundaries, and their spatial distributions. While it is possible to quantitatively reveal the tilt angles associated with such boundaries with SWBXT, the subtle distinctions between tilt and twist components are best quantified by the high-resolution x-ray diffraction (HRXRD) mapping of peak positions. The complementary application of SWBXT and HRXRD, along with more traditional methods such as etching (to observe the high defect densities typically encountered inside small angle boundaries) can reveal detailed information that would otherwise be unobtainable. For example, by determining the defect orientations and concentrations in the arrays comprising the small angle boundaries, defect formation mechanisms can be postulated, giving necessary information about the processing conditions during and after growth.

### **Experimental**

Two experimental 3 inch diameter undoped SiC wafers (one 4H, one 6H) grown by Cree Research, Inc. were examined using SWBXT, HRXRD mapping, and optical microscopy. The wafers were cut on axis and double-side polished. Back-reflection topographs were taken at the Stony Brook Synchrotron Topography Facility, Beamline X-19C, at the National Synchrotron Light Source, at Brookhaven National Laboratory. X-ray diffraction mapping was performed on a Philips MRD

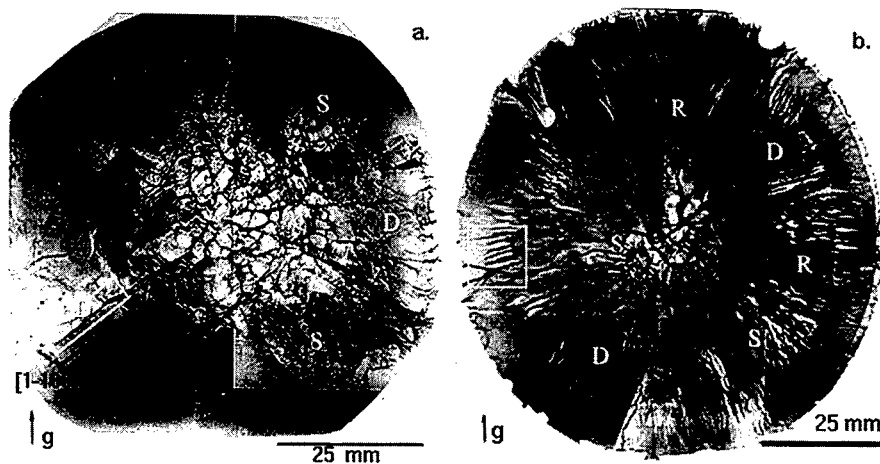


Fig. 1 Back-reflection topographs of experimental 3 inch SiC wafers. (a) 4H(00016),  $\lambda=1.26 \text{ \AA}$  and (b) 6H(00024),  $\lambda=1.26 \text{ \AA}$ .

diffractometer in triple axis mode using  $\text{CuK}\alpha$  radiation, Ge(220) 4-bounce monochromator, 1.5 mm x 1.5 mm beam footprint, and a Ge(220) analyzer crystal. The wafers were etched in molten KOH at 500°C at various times to produce the best contrast.

### Results and Discussion

Back-reflection SWBXT images of the two wafers are shown in Figs. 1(a) and 1(b). Prominent features in both images include dark lines (D) having a radial distribution around a more highly contrasted center region, and clusters of white spots that have been previously determined to correspond to micropipes and elementary screw dislocations [1]. In Fig. 1(a), the dark lines extend from the center of the wafer along the  $\langle 11\bar{2}0 \rangle$  and  $\langle 1\bar{1}00 \rangle$  crystallographic directions, whereas in Fig. 1(b) the lines have a more even radial distribution and do not necessarily originate at the center of the wafer. In Fig. 1(b) there are also two partial rings (R) that bisect the shorter dark line segments, indicating an additional type of deformation not apparent in Fig. 1(a). HRXRD was utilized to determine the type of misorientation associated with the defects, and followed by KOH etching to confirm the types of dislocations producing

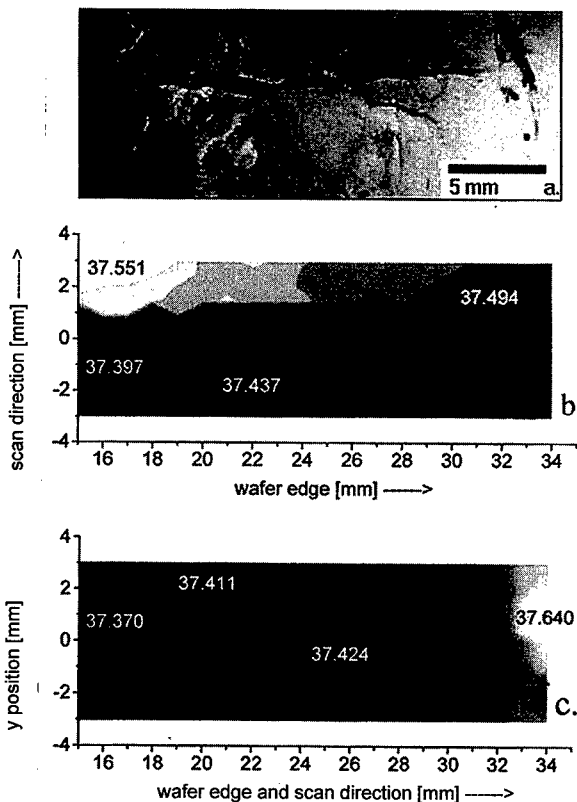


Fig. 2 (a) The boundary lined up along  $[1\bar{1}00]$  in the box in Figure 1(a). (b) HRXRD rocking curve map of corresponding area with rocking axis parallel to the boundary line, and (c) perpendicular to the boundary line. The maps are of the 4H(0008) omega peak positions.

contrast in the images.

Fig. 2 shows the corresponding HRXRD maps for a segment of the wafer topograph shown inside the box in Fig. 1(a). The HRXRD maps are taken from a series of rocking curves where the omega angle is recorded at the maximum intensity for an individual rocking curve. The resulting map shows the change in orientation of the basal planes along the directions perpendicular to the rocking axis. In Fig. 1(b), the rocking axis is parallel to the defect line, thus being sensitive to the tilt component across the boundary. In Fig. 2(c), the rocking axis is perpendicular to the boundary, thus being sensitive to twist along the boundary. The boundary is clearly visible in Fig. 2(b) but not in Fig. 2(c), indicating that the boundary has only a tilt component with rotation axis in the basal plane. Fig. 2(c) shows a uniform bending of the basal planes toward the outer edge of the wafer that was not associated with this specific defect, but present over much of the wafer. The misorientation across the boundary is greatest near the center of the wafer at a value of 540 arcsec and decreases to near zero at the outer edge of the wafer. A similar defect lying along the  $[11\bar{2}0]$  (on the right side of Fig. 1a) was also shown to be a tilt boundary by HRXRD. No measurable strains were associated with these boundaries. The wafer was cleaved across the boundary, and the  $(1\bar{1}00)$  planes of the wafer cross-section were examined to determine the second component of tilt that might be associated with the boundary, but misorientations associated with other defects close by masked any misorientation that may be associated with the boundary under examination. Two common types of dislocation arrays can produce misorientations that affect basal plane reflections; basal plane dislocations stacked above one another, or threading screw dislocations. Only basal plane dislocations can produce the pure tilt boundary shown in Fig. 2. Etching of the Si-face revealed micropipes and threading dislocations in several arrays on various areas of the wafer, but not above the known locations of the grain boundaries, indicating that the boundaries are likely to be composed of basal plane dislocations.

Fig. 3 shows the same sequence of images for the second wafer. As can be seen in Fig. 3(a), a region not containing the black ring on the left side

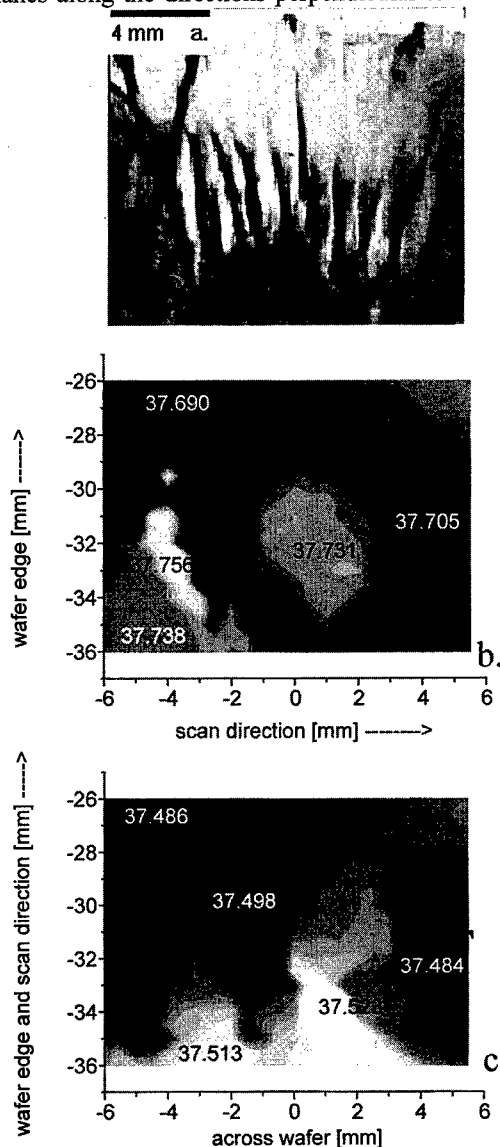


Fig. 3 (a) The boundaries in the box in Figure 1(a). (b) HRXRD rocking curve map of corresponding area with rocking axis parallel to the lines, and (c) perpendicular to the lines. Maps are of the 6H(00012) rocking curve positions.

of Fig. 1(b) was used to simplify the interpretation of the contrast associated with the dark lines. Figs. 3(b) and 3(c) show that there is more than one component of misorientation associated with each defect line even without the presence of the dark ring. One reason that the HRXRD maps do not show the same scale of detail as in the topograph could be that the beam footprint is larger than the distance between the boundaries. KOH etching of the second wafer revealed etch pits that closely matched the contrast in the topograph. These etch pits could be associated with threading dislocations adding a twist component to the misorientation. It is important to note that the orientation change across each radial boundary line in a circular trace around the wafer alternates between a positive and negative change in position, giving a zigzag shape to the basal planes in the line of the trace. The range of misorientations in the 6H wafer is approximately 500 arcsec, as shown in Figs. 3(b) and 3(c). The third component of misorientation (second tilt) was not measured.

The resulting defect arrays for the topographs shown above could have been produced by radial buckling. This is possible considering that buckling has been observed in SiC at moderate temperatures [3]. It is also possible that the dark lines could represent the effect of polygonization of basal plane dislocations [4]. Further work is required to distinguish between these two plausible mechanisms.

### Conclusions

The 3 inch experimental 4H and 6H wafers examined have large scale dark line contrasts in the SWBXT images. HRXRD mapping has shown that these lines are low angle grain boundaries with a misorientation of approximately 500 arcsec, having a either a pure tilt component or a combination of a tilt and twist components. Etching of the wafers has confirmed that basal plane dislocations make up the tilt boundaries and threading dislocations add a twist component. Based on the orientations and distributions of the defect arrays, the authors postulate that radial buckling or basal plane dislocation polygonization could produce these boundaries.

### Acknowledgments

This work was supported by AFOSR grant F49620-97.1.0452 and by the ARO under contract number DAAG559810392. SWBXT was carried out at the NSLS, at BNL, which is supported by the DOE, under contract number DE-AC02-98CH10886. Wafers were supplied by Dr. W.C. Mitchel at Wright-Patterson Airforce Base (Dayton, OH) and Dr. C. Carter at Cree Research, Inc.(Durham, NC).

### References

- [1] W.Si, M. Dudley, C. Carter, R. Glass, and V. Tsvetkov, *Mat. Res. Soc. Symp. Proc.* 437(1996), p.129.
- [2] K. Wessel and H. Alexander, *Phil. Mag.* 35 (1977), p.1523.
- [3] S. Fugita, K. Maeda, and S.Hyodo, *Phil. Mag. A* 55, No.2 (1987), p.203.
- [4] S. Ha, N.T. Nuhfer, G.S. Rohrer, M. De Graef, and M. Skowronski, *this proceedings*, p. 477

## Origin of Threading Dislocation Arrays in SiC Boules Grown by PVT

S. Ha, N.T. Nuhfer, M. De Graef, G.S. Rohrer and M. Skowronski

Department of Materials Science and Engineering, Carnegie Mellon University,  
5000 Forbes Ave, Pittsburgh, PA 15213, USA

**Keywords:** Bulk Crystal Growth, Physical Vapor Transport, Polygonization, Slip Bands, Threading Dislocation Array

### Abstract

Transmission electron microscopy (TEM), high resolution x-ray diffraction (HRXRD), and KOH etching have been used to study the dislocation structure of 4H SiC crystals grown by physical vapor transport (PVT). Many of the observed etch pits form arrays extending along the  $\langle 11\bar{2}0 \rangle$  and  $\langle \bar{1}100 \rangle$  directions on (0001) wafers. Plan view conventional and high resolution TEM show that both types of arrays consist of pure edge dislocations threading along the c-axis with identical Burgers vectors of the  $a/3\langle 11\bar{2}0 \rangle$  type. The former arrays are interpreted as slip bands formed by dislocation glide in the slip system  $\langle 11\bar{2}0 \rangle \{ \bar{1}100 \}$  of hexagonal SiC during post-growth cooling. The latter arrays constitute low angle tilt boundaries with tilt axis parallel to the [0001] direction. Evidence is presented that such boundaries can form by polygonization of the threading edge dislocations introduced by plastic deformation.

### Introduction

Two critical issues in the development of substrates for SiC-based electronics are increasing the size of boules and reducing the structural defect density. Of particular interest are extended defects propagating along the [0001] growth direction. Such threading defects are known to penetrate active device layers deposited by epitaxy and to degrade device performance [1, 2].

In previous studies, three characteristic etch pit types were observed on the surfaces of [0001] grown crystals and assigned to three different threading defects, i.e. micropipes, screw dislocations, and threading edge dislocations [3, 4]. In addition, a domain structure was postulated to be related to the distribution of these threading defects [4-6].

Glass *et al.* [5] first postulated the domain structure on the basis of HRXRD data. They showed that  $\omega$  rocking curves of either symmetric or asymmetric reflections on (0001) SiC wafers exhibit multiple peaks, implying that parts of the crystal are misoriented with respect to others. They suggested that because a SiC crystal grows by the spiral mechanism with numerous independent nuclei, the initial misorientations between nuclei are accommodated in the form of domain walls when the nuclei grow and coalesce. This interpretation was supported by Tuominen *et al.* [6], who showed a well defined domain structure on a KOH etched wafer. Centers of domains exhibit relatively few dislocation etch pits, while the domain walls have high etch pit densities. Further data were provided by Takahashi *et al.* [4]. They concluded, in agreement with the above authors, that domains are grown-in type with most of the defects inherited from the seed or originating at the seed-boule interface. The misorientation between domains was determined to have both twist and tilt components.

In this work, we identified one type of characteristic threading dislocation array and determined its relation with the domain structure. Based on these observations, we propose a new formation mechanism for the dislocations and the domain structure.

### Experimental Procedures

The crystals were grown by Cree Research, Inc. (Durham, NC) as a part of the development program on High Temperature Electronics, supported by the Defense Advanced Research Project Agency. Two inch diameter wafers were undoped or n-doped ( $\sim 10^{18} \text{ cm}^{-3}$ ) and oriented along (0001) to within  $0.5^\circ$ . KOH etching was applied at  $500^\circ\text{C}$  or  $510^\circ\text{C}$  for 10 minutes on Si(0001) faces of the wafers. The etch pits were observed using Nomarski-contrast optical microscopy. Laue x-ray diffraction was employed to determine the orientation of etch pit arrays. The TEM observations were carried out on a Philips EM420-TEM and on a JEOL 4000 EX-TEM, operated at 120 and 400 kV, respectively. HRXRD was conducted using  $\text{Cu K}\alpha_1$  radiation on a Philips MRD diffractometer, equipped with a four bounce monochromator and a two bounce analyzer crystal employing Ge (220) reflection. The angular resolution was better than  $0.004^\circ$  ( $\sim 14''$ ).

### Results and Discussion

Two kinds of linear arrays of small dislocation etch pits were observed. One type was oriented along the  $\langle 11\bar{2}0 \rangle$  directions and the other was along the  $\langle \bar{1}100 \rangle$  directions. The  $\langle 11\bar{2}0 \rangle$  oriented etch pit arrays usually formed bands approximately  $30\sim 200 \mu\text{m}$  wide, and appeared along the periphery of the boules. An example of such structure is shown in Fig. 1. The wafer edge is visible in the lower right corner and a part of a polytypic inclusion or a misoriented grain is shown in the lower center. Two parallel bands of small etch pits extend vertically. The wider of the two is marked with an arrow. Their extended lengths were about 4 and 10 mm. It is also noticeable that there are several additional poorly defined bands rotated  $60^\circ$  away from the two prominent bands. The etch pit densities of the bands were in the range of  $0.5\sim 2.2 \times 10^6 \text{ cm}^{-2}$ .

The second type, the  $\langle \bar{1}100 \rangle$  oriented etch pit arrays form definite single lines (Fig. 2), and spread over the center region almost uniformly up to  $3/4$  of the radius of a typical two inch wafer. A few large etch pits due to micropipes could also be seen and are marked M. The lines marked S are due to scratches. All three equivalent  $\langle \bar{1}100 \rangle$  array directions were observed. The linear etch pit densities along the arrays were on the order of  $10^4 \text{ cm}^{-1}$ , while the areal etch pit densities away from these arrays were on the order of  $10^4 \text{ cm}^{-2}$ . The corresponding average distances between neighboring dislocations are on the order of  $1 \mu\text{m}$  and  $100 \mu\text{m}$ , respectively.

Closer inspection of the small etch pits in Fig. 1 and 2 at high magnification revealed that they appear conical in shape with a pointed bottom and circular outline on the wafer surface. Such shape implies that the etch pits are due to threading dislocations extending approximately normal to the (0001) wafer surface. Subsequently, we applied conventional and high resolution TEM to determine the character of the dislocations in both types of arrays [7, 8]. Fig. 3 is a plan view high

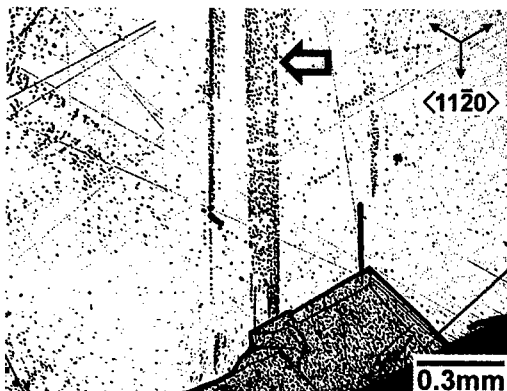


Fig. 1 Optical micrograph of the  $\langle 11\bar{2}0 \rangle$  etch pit bands on Si(0001) face of a 4H SiC wafer

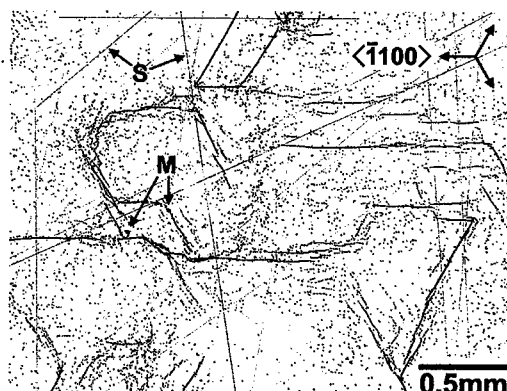


Fig. 2 Optical micrograph of the  $\langle \bar{1}100 \rangle$  etch pit arrays on Si(0001) face of a 4H SiC wafer

resolution lattice image around one of the threading dislocations. The image was taken by choosing the c-axis as the zone axis. The dislocation is of the pure edge type and threading along the c-axis without tilt. Its core is at the intersection of the two extra half planes marked with two rows of dots. The corresponding Burgers vector is of the  $a/3\langle 11\bar{2}0 \rangle$  type with a direction marked by an arrow. The Burgers vectors were identical for all dislocations in an array, and determined to be parallel to the array direction for the  $\langle 11\bar{2}0 \rangle$  arrays and perpendicular for the  $\langle \bar{1}100 \rangle$  arrays.

The fact that the pure edge dislocations are aligned in an array parallel to the Burgers vectors suggests that the  $\langle 11\bar{2}0 \rangle$  arrays were formed by dislocation glide in the corresponding slip system  $\langle 11\bar{2}0 \rangle \{ \bar{1}100 \}$ . The same slip system in 6H SiC crystals has been observed by Maeda *et al.* [9] to be activated at room temperature by an indentation hardness test. Hence, the slip is expected to occur in the high temperature conditions of PVT growth, at lower stresses than are encountered in the indentation test. As illustrated in Fig. 1, the apparent origin of most slip bands is a misoriented grain or a polytypic inclusion at the periphery of the wafers. Such grains are frequently observed to nucleate on the growth crucible walls. It is plausible to assume that the crystal growing around the misoriented grains is stress free at the growth temperature. During post-growth cooling, the thermal expansion anisotropy between the matrix boule and the misoriented grains leads to stress build-up at the interface as well as inside the grains and the boule. Similarly, any polytypic inclusions would result in stresses due to differences in thermal expansion. As the temperature decreases, the stress will increase until it exceeds the critical resolved shear stress and causes the dislocation glide in the corresponding slip system.

The  $\langle \bar{1}100 \rangle$  arrays of dislocations which have identical Burgers vectors perpendicular to the array direction can be viewed as low angle grain boundaries. The average distances between neighboring dislocations estimated by TEM were 0.3~1  $\mu\text{m}$ . These correspond to misorientation values of 60~200 arcsec across the arrays, assuming all the dislocations are of same type. The expected type of misorientation is pure tilt with a rotation axis parallel to the c-axis contained in the boundary plane. The type and magnitude of misorientation have been verified by HRXRD experiments [8]. The rotation component around the c-axis across an array was about 140 arcsec, while the other two components corresponding to the misorientation of the basal plane were below 10 arcsec. The arrays frequently formed hexagonal or triangular patterns on the wafer surface as shown in Fig. 2, which is reminiscent of the domain wall pattern reported by Tuominen *et al.* [6]. In this case, the domain walls are made of pure edge threading dislocations with Burgers vectors of the  $a/3\langle 11\bar{2}0 \rangle$  type. It is worth noting that this kind of domain structure cannot result in misorientations that can be detected in (000n) rocking curves. On the other hand, many authors

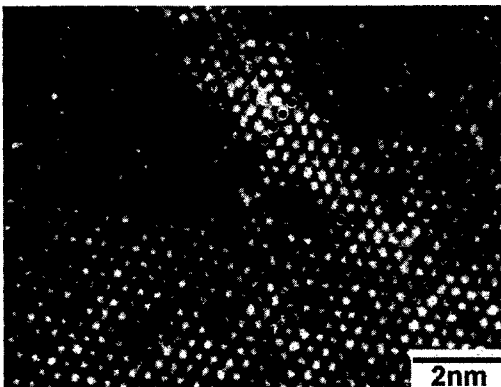


Fig. 3 C-axis plan view lattice image around a threading dislocation in the array of Fig. 1

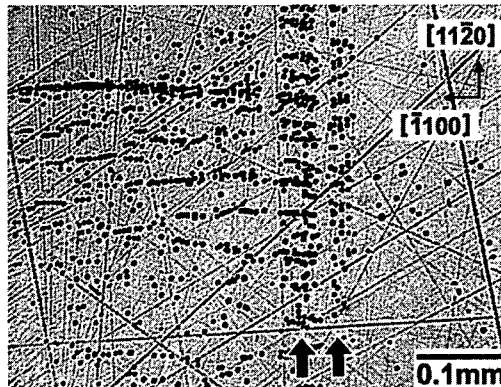


Fig. 4 Optical micrograph of the detail of two slip bands showing partial polygonization

reported multiple peaks present in such reflections. This implies that, in addition to the domain structure described above, there is a different type of boundary with different structure and probably different origin.

The remaining question is the formation mechanism of the domain structure. Presented above is evidence of the activation of the secondary slip system in the PVT growth of SiC crystals. In some cases, slip bands almost reached the center of crystals. Hence, these are major sources of the threading dislocations. In Fig. 4, two slip bands marked with arrows extend vertically. It is clear that etch pits in the bands form fine structure consisting of many small fragments aligned in the direction perpendicular to that of the bands. Since the Burgers vectors of the dislocations within a slip band are identical and parallel to the slip direction, they must be perpendicular to the fragment direction. It is plausible to suggest that the fine structure formation occurred in order to lower the energy of the system. It is well known that the low energy configuration for an array of edge dislocations corresponds to that in which Burgers vectors are perpendicular to the array direction. The alignment process is referred to as polygonization. Fig. 4 shows an initial stage of polygonization of the threading edge dislocations in the slip bands. It is surmised to occur either during post-growth cooling or during post-growth high temperature annealing. It is easy to visualize that if this wafer was subsequently used as a seed in the PVT growth process, the high growth temperature and long time would allow the polygonization to complete. Through glide and/or climb, dislocations introduced by slip could align themselves into the pattern shown in Fig. 2. Thus, we propose that the domain structure of tilt boundaries could be the consequence of plastic deformation of the already solidified crystal followed by dislocation polygonization.

### Summary

Threading dislocations forming etch pit arrays along the  $\langle 1100 \rangle$  and  $\langle 11\bar{2}0 \rangle$  directions on Si(0001) faces of [0001] grown crystals were studied. Conventional and high resolution TEM have identified pure edge dislocations lying along the c-axis with Burgers vectors of the  $a/3\langle 11\bar{2}0 \rangle$  type. Based on relation between the Burgers vectors and the array direction, the  $\langle 11\bar{2}0 \rangle$  arrays are interpreted as resulting from dislocation glide in the slip system  $\langle 11\bar{2}0 \rangle \{1100\}$  during post-growth cooling. The  $\langle 1100 \rangle$  arrays were interpreted as being formed by polygonization of the threading edge dislocations introduced by the slip.

### Acknowledgements

This work was supported in part by the Commonwealth of Pennsylvania through the Ben Franklin Technology Center (Grant No. 98W.CM00562R-1) and by National Science Foundation (Grant No. DMR.9903702).

### References

- [1] P. G. Neudeck, J. A. Powell, IEEE Electron Device Letters **15** (1994), p. 63
- [2] P. G. Neudeck, W. Huang, M. Dudley, IEEE Trans. Electron Devices **46** (1999), p. 478
- [3] J. Takahashi, M. Kanaya, Y. Fujiwara, J. Crystal Growth **135** (1994), p. 61
- [4] J. Takahashi, N. Ohtani, M. Kanaya, J. Crystal Growth **167** (1996), p. 596
- [5] R. C. Glass, L. O. Kjellberg, V. F. Tsvetkov, J. E. Sundgren, E. Janzen, J. Crystal Growth **132** (1993), p. 504
- [6] M. Tuominen, R. Yakimova, R. C. Glass, T. Tuomi, E. Janzen, J. Crystal Growth **144** (1994), p. 267
- [7] S. Ha, N. T. Nuhfer, G. S. Rohrer, M. De Graef, M. Skowronski, submitted to Journal of Electronic Materials (1999)
- [8] S. Ha, N. T. Nuhfer, G. S. Rohrer, M. De Graef, M. Skowronski, submitted to Journal of Crystal Growth (1999)
- [9] K. Maeda, K. Suzuki, S. Fujita, M. Ichihara, S. Hyodo, Phil. Mag. A **57** (1988), p. 573



## Structural Characterization of Silicon Carbide Etched by Using a Combination of Ion Implantation and Wet Chemical Etching

T. Henkel\*, G. Ferro, S. Nishizawa, H. Pressler, Y. Tanaka, H. Tanoue  
and N. Kobayashi

Electrotechnical Laboratory, Quantum Radiation Division,  
1-1-4 Umezono, Tsukuba, Ibaraki, 305-8568, Japan

**Keywords:** 6H-SiC, Damage, Etching, Ion Implantation, Surface Morphology

### Abstract

Silicon carbide has been etched using a combination of high-dose ion implantation and wet chemical etching. Structural properties with respect to the remaining damage after etching have been studied using atomic force microscopy, Rutherford backscattering / channeling, and Raman spectroscopy. No significant deterioration of the crystal quality has been found after the etching process. Moreover, the as-etched surface is characterized by a lower roughness compared to virgin material. The results demonstrate that this etching method can be used for the fabrication of contacts on silicon carbide surfaces.

### Introduction

Silicon carbide (SiC) is a superior semiconductor for high frequency, high temperature, and high power device applications. The fabrication of devices requires patterning of the material. Patterning of SiC by wet chemical etching however, is difficult because most of the common laboratory etchants do not attack the crystal. Therefore, plasma etching techniques including reactive ion etching are commonly used to pattern SiC. On the other hand, the etched surface has been reported to be carbon rich and too rough for device fabrication [1,2]. Further, these dry etching processes leave behind a damaged surface due to the bombardment of energetic ions [3,4]. Alternatively, SiC can be easily patterned using a combination of ion implantation and wet chemical etching [1,5,6]. The implantation process is necessary to amorphize the material to be etched because only amorphous SiC is attacked by HF:HNO<sub>3</sub> solutions. Etching rates in the order of 100 nm/min were obtained [5]. Although the SiC crystal etched in this way was found to be suitable for the fabrication of Schottky contacts and passivation layers [2], comprehensive studies with respect to the remaining damage after the etching process have not yet been reported. Therefore, structural properties of the SiC surface etched by using this method are investigated in this work.

### Experiment

6H-SiC ([0001] orientation, *n*-type, off-axis, Si face) from Cree Research [7] was used as starting material. A thin amorphous surface layer was produced by 200 keV Xe<sup>+</sup> implantation using an ion dose of  $1 \times 10^{16}$  cm<sup>-2</sup>. Samples were maintained at room temperature (RT), and were tilted 7° with respect to the ion beam to minimize channeling effects during implantation. The amorphous layer was then etched for 10 min using a boiling 1:1 mixture of HF:HNO<sub>3</sub> followed by an ultrasonic cleaning step in de-ionized water. For a comparative study, some samples were annealed in flowing argon (Ar) or nitrogen (N<sub>2</sub>) gas at 1100 °C for 5 min using a rapid thermal annealing (RTA) system. Finally, contacts were prepared on all samples by titanium (Ti) deposition (300 nm) followed by a RTA cycle at 1100 °C for 5 min in flowing Ar gas. Structural analysis was performed applying

atomic force microscopy (AFM), Rutherford backscattering spectrometry / channeling (RBS/C), Raman spectroscopy, and step height measurements.

## Results

For the nuclear energy deposition of 200 keV  $\text{Xe}^+$  ions at the surface, about 600 eV/ion/nm was calculated using the TRIM code (SRIM-98, full cascade, displacement energy: 25 eV) [8]. Further, 40 nm was obtained for the depth which is correlated with the maximum of the damage distribution. Considering the critical energy density for amorphization of the near SiC surface region at RT ( $6 \times 10^{24}$  eV/cm<sup>3</sup>) [9] an ion dose of  $1 \times 10^{15}$  cm<sup>-2</sup> would be sufficient to amorphize the crystal up to the surface. However, due to the tail of the nuclear damage distribution a highly defective crystalline layer would remain after etching the amorphous surface layer. In particular, a displacement rate of about 1 dpa near the amorphous/crystalline (a/c) interface can be estimated using the ion dose and energy deposition as stated above. Hence, a much higher dose ( $1 \times 10^{16}$  cm<sup>-2</sup>) was used to reduce defect density and thickness of the underlying damaged layer. The height of the step separating the as-etched region from the virgin unimplanted one was found to be 150 nm using a surface profilometer. Though TRIM is not very precise in predicting the number of the produced vacancies in the far tail region, the energy deposition at 150 nm below the surface can be estimated to be less than 0.5 % compared to the surface energy deposition.

An AFM image of the as-etched surface is shown in Fig. 1. Using a scan over a  $5 \mu\text{m} \times 5 \mu\text{m}$  area, a root-mean-square (rms) surface roughness of 0.9 nm was determined which is lower in comparison to virgin material (1.7 nm). An analysis of the AFM data has shown that reduced heights of needle-like asperities and reduced depths of scratches arising from the polishing process mostly contribute to the lower roughness. However, both asperities and scratches did not disappear after etching. This means that the ion-beam-induced amorphization process follows the surface morphology.

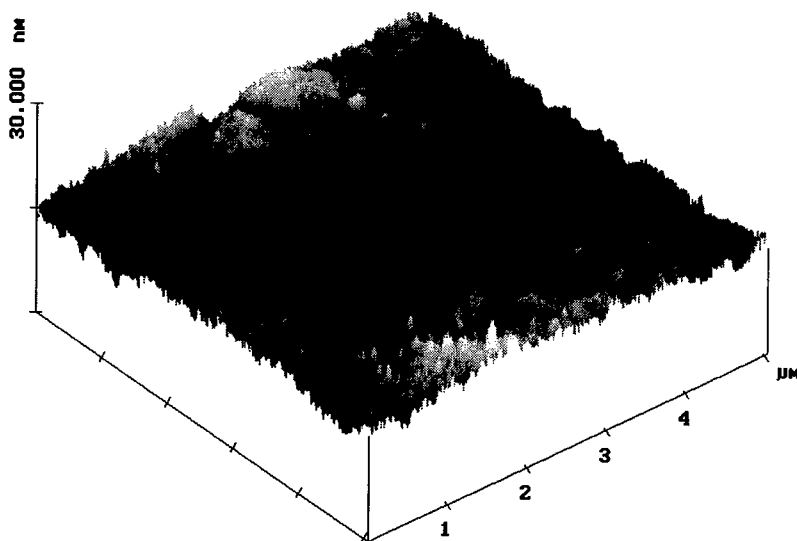


Fig. 1. AFM image of the as-etched SiC surface.

It can be speculated that preferential sputtering of surface inhomogeneities reduces the scattering of the nuclear energy deposition at the a/c interface resulting in a lower roughness as observed.

Annealing of as-etched samples in Ar and N<sub>2</sub> atmosphere, respectively, caused an increase in surface roughness. For example, a rms roughness of 1.3 nm has been found after annealing in Ar atmosphere at 1100 °C. An AFM image of this sample is shown in Fig. 2. In addition, the morphology has been changed. Oxygen volatilization and carbon segregation are suggested to be responsible for this behaviour. It is well known that the SiC surface deteriorates at 1100 °C due to silicon sublimation leading to carbon enrichment and surface graphitization [10].

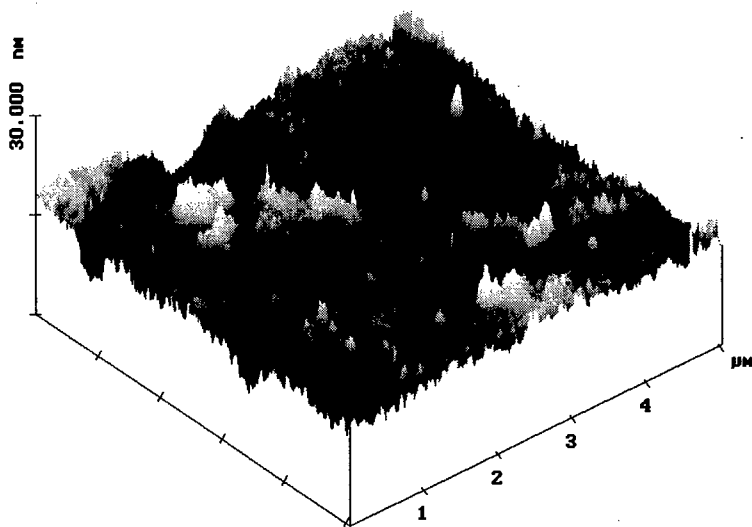


Fig. 2. AFM image of the as-etched SiC surface after annealing at 1100 °C in Ar atmosphere.

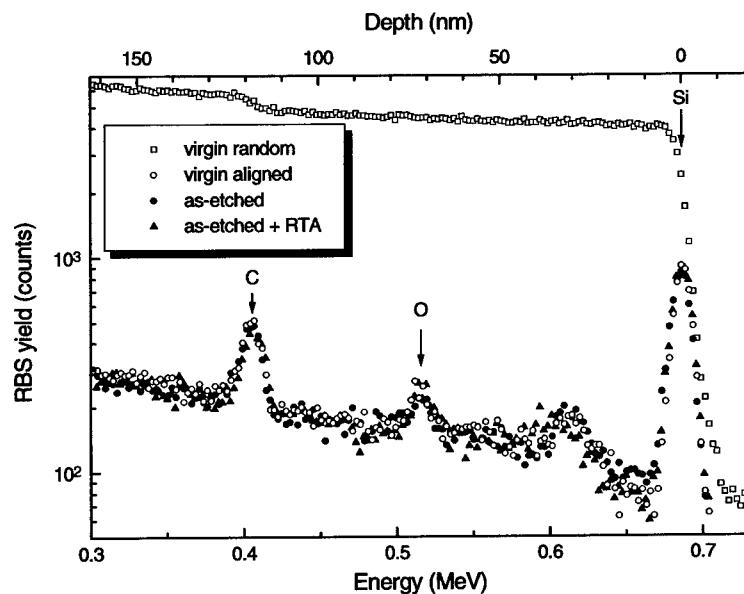


Fig. 3. RBS/C spectra of 1 MeV <sup>4</sup>He<sup>+</sup> backscattered from as-etched SiC before and after RTA.

To evaluate the crystal quality after etching and annealing, respectively, 1 MeV  $^4\text{He}^+$  RBS/C measurements along the [0001] axis were performed. A scattering angle of  $105^\circ$  was used in order to improve the depth resolution. Careful alignment of the sample with respect to the ion beam as well as measurements on several samples revealed no significant differences in the scattering yield in the aligned spectra obtained from as-etched, as-etched + annealed, and virgin samples, respectively, within the limits of this technique (see Fig. 3). It should be mentioned however, that in case of the as-etched sample the minimum yield just behind the surface peak is slightly increased indicating a thin weakly disordered surface layer.

These findings were corroborated by Raman spectroscopy results obtained using a confocal microscope system. In particular, neither a broadening nor a shift of the first-order vibrational modes in comparison to virgin material was detected. Additionally, no significant changes in the scattering intensity of these modes were found within the accuracy of these measurements ( $\pm 10\%$ ). Finally, all Ti contacts displayed ohmic behaviour. In addition, the resistance of the as-etched sample (no RTA step before metal deposition) was found to be lower by a factor of 2 compared to samples that were annealed before metal deposition. Crystalline disorder in the near surface region can reduce the contact resistance [11]. Thus, the weakly disordered surface layer as detected by RBS/C is believed to be responsible for the lower resistance measured.

### Conclusions

Structural properties of 6H-SiC etched by using a combination of high-dose ion implantation and wet chemical etching were investigated by AFM, RBS/C, and Raman spectroscopy. No significant deterioration of the crystal quality was found after etching. Moreover, it was shown that surfaces with a lower roughness compared to virgin material can be obtained. The results demonstrate that this etching method can be used for the fabrication of contacts on SiC surfaces.

### Acknowledgments

One of the authors (T.H.) gratefully acknowledges the support of this work by Science and Technology Agency of Japan.

### References

- [1] D. Alok and B.J. Baliga, J. Electron. Mater. 24 (1995), p. 311.
- [2] D. Alok, K. Makeswar, and B.J. Baliga, J. Electron. Mater. 26 (1997), p. 108.
- [3] V. Khemka, T.P. Chow, and R.J. Gutmann, J. Electron. Mater. 27 (1998), p. 1128.
- [4] D. Alok, R. Egloff and E. Arnold, Mater. Sci. Forum 264-268 (1998), p. 929.
- [5] J.A. Edmond, J.W. Palmour, and R.F. Davis, J. Electrochem. Soc. 133 (1986), p. 650.
- [6] R. Menzel, T. Bachmann, W. Wesch, H. Hobert, J. Vac. Sci. Technol. B16 (1998), p. 540.
- [7] Cree Research, Inc., 4600 Silicon Drive, Durham, NC 27703.
- [8] J.F. Ziegler, J.P. Biersack, and U. Littmark: *The Stopping and Range of Ions in Solids* (Pergamon, New York 1985), pp. 1.
- [9] T. Henkel, V. Heera, R. Kögler, and W. Skorupa, J. Appl. Phys. 84 (1998), p. 3090.
- [10] L. Muehlhoff, W.J. Choyke, M.J. Bozack, and J.T. Yates, J. Appl. Phys. 60 (1986), p. 2842.
- [11] A.A. Iliadis, S.N. Andronesco, K. Edinger, J.H. Orloff, R.D. Vispute, V. Talyansky, R.P. Sharma, T. Venkatesan, M.C. Wood and K.A. Jones, Appl. Phys. Lett. 73 (1998), p. 3545.

\* Email: henkel@etl.go.jp / Fax: +81-298-54-5673

## Polytype and Defect Control of Two Inch Diameter Bulk SiC

M. Sasaki<sup>1</sup>, H. Shiomi<sup>1</sup>, H. Harima<sup>2</sup> and S. Nishino<sup>1</sup>

<sup>1</sup> Faculty of Engineering & Design, Kyoto Institute of Technology,  
Matsugasaki Gosyokaido-tyou, Kyoto 606-8585, Japan

<sup>2</sup> Dept. of Applied Physics, Osaka University, Yamadagaoka 2-1, Suita, Osaka 565-0871, Japan

**Keywords:** Dislocation, Micropipe, Planar Defects, Polytype, Sublimation

**Abstract.** By cross sectional observation of 6H-SiC basal plain, we found two kinds of planar defects. One looks like a triangular, another looks like thin rectangular with long edge parallel to interface. These defects are related to edge dislocations. Micropipes induce the planar defects and the screw dislocations change into edge dislocation. Consequently, micropipe disappears or becomes small. In the high N-doped layer, a mixed polytype layer (6H, 4H and 15R) was observed.

### 1. Introduction

SiC-based device technology has made remarkable progress in recent years. But still the wafer quality is one of the most important problems, especially the existence of some defects. Sublimation is the general method of making SiC bulk crystals. But it is difficult to remove defects and to control the polytype by this method. The most important problem is the micropipe formation mechanism which influence device operation[1]. There have been some reports about the formation of micropipes. For example, high axial and radial temperature gradients[2] and the silicon/carbon ratio of chemical species in the crucible[3] were reported as the reason for the formation of micropipe. But these do not fully explain the formation of micropipe. So it is important to trace the defect formation and, at the same time, try to eliminate these defects.

### 2. Experimental procedure

Sample A is a 6H-SiC crystal grown by sublimation method on c-face substrate. Abrasive SiC powder was used as the source material. The growth conditions were  $P = 5-10$  Torr,  $T_b = 2250-2350^\circ\text{C}$ , where  $P$  was the growth pressure and  $T_b$  was the growth temperature of the bottom of graphite crucible which was measured by an optical two-color pyrometer. An RF-generator was used for induction heating. The diameter of sample was about 2 inches.

### 3. Result and Discussion

Figure.1 is the optical microscope image of the cross section of sample A. Sample A was grown in two stages by recharging the source material. A high N-doped layer was observed at the interface of 1st and 2nd growth layer. Some places marked show X where the micropipe density decreased around the interface. But at other places(Y), the micropipe density did not decrease very much. Images of these two places are compared in fig.1. Two kinds of planar defects were observed in sample A. One looks like a flat defect. Another looks like a triangle defect. We called them "flat defect" and "arrow defect", respectively. At position X of fig.1, the "flat defects"(fig.1 A) were observed in large numbers. However at position Y, the "flat defect" was not observed as often, though there were a lot of "arrow defect"(fig.1 B). Takanaka et. al reported that micropipes were annihilated by planar defects[4]. In this case, it was observed that the micropipes annihilated upon

meeting "flat defects". A number of micropipes meeting the "flat defect" have angles between c-axis and its perpendicular, around the "flat defect". But it did not always annihilate upon meeting "arrow defect". A number of micropipes which met an "arrow defect" decreased in size, but were not annihilated.

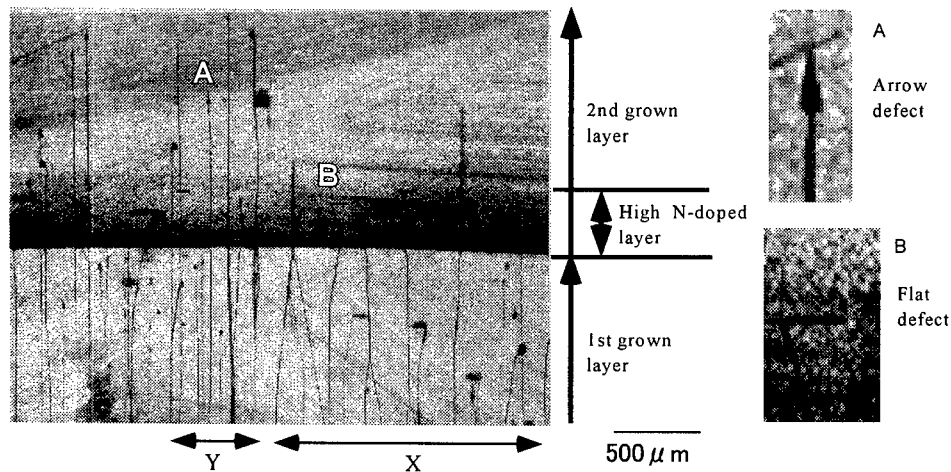


Fig.1 The optical microscope image of the cross section of grown layer (sample A)

Details of these planar defects were further studied. Figure 2 shows the relationship between the size of micropipes and planar defects. The sizes of micropipes meeting planar defects were between 10 and 40  $\mu\text{m}$ . When the micropipe was under 10  $\mu\text{m}$  in diameter, it was not affected by the planar defect. When the width of planar defect was over 200  $\mu\text{m}$ , it became a "flat defect" and when it was under 200  $\mu\text{m}$ , it became an "arrow defect". Additionally, there is no direct relationship between the micropipe diameter and the size of the planar defects.

Figure 3 shows the schematic of a possible defect formation mechanism. Micropipes are defects related to screw dislocations whose line directions are parallel to the c-axis. Planar defects are mainly of two types. One is a "stacking fault". The other is an anti-site defect (Si-site and C-site). On basal plain, the simplest planar defects are "stacking fault"[5]. Pirouz [5] and Heindl et al.[6] reported that planar defects and micropipes contain a mixed Burgers vector with a c-screw component and a basal plane vector edge component. And Takahashi et al. suggested that the strains parallel to the seed surface bring about edge dislocations, while the ones perpendicular to the surface are relaxed by screw dislocations and micropipes for  $\langle 0001 \rangle$  growth[7]. Therefore, we suppose that the screw dislocation line becomes perpendicular to the c-line and that the planar defect is related to edge dislocations. And on the c-face, there are a number of subgrain boundaries. These subgrain boundaries are made of many plural edge dislocations and a number of etch pits lie on these boundaries [8]. Moreover, the screw dislocation energy,  $E_s$ , and edge dislocation energy,  $E_e$ , are given by

$$E_s \cong lGb^2 \quad (1)$$

$$E_e \cong \frac{lGb^2}{1-\nu} \quad (2)$$

where  $G$  is ratio of stiffness,  $b$  is the magnitude of Burgers vector,  $l$  is the length of dislocation and  $\nu$  is the Poisson's ratio. From these two equations, it can be seen that  $E_e$  is larger than  $E_s$ .

Micropipes have screw dislocations with Burgers vector  $\mathbf{b}$  ranging from  $2c$  to  $7c$  at 6H-SiC ( $c=1.512\text{nm}$ ) [9]. Therefore, planar defects have very large distortion energy. So these become large enough to be visible without chemical etching of edge dislocations.

In fig.1, "flat defects" exist in the high N-doped layer. Okamoto et.al reported that doping amounts of nitrogen did not directly affect the micropipe density, but nitrogen incorporation might cause the generation of subgrain boundaries. Moreover, due to nitrogen incorporation, the screw dislocation cross-slips and becomes parallel to the  $c$ -face i.e. edge dislocation. We think that nitrogen incorporation cause "flat defects" and it suggests the possibility of decreasing micropipes.

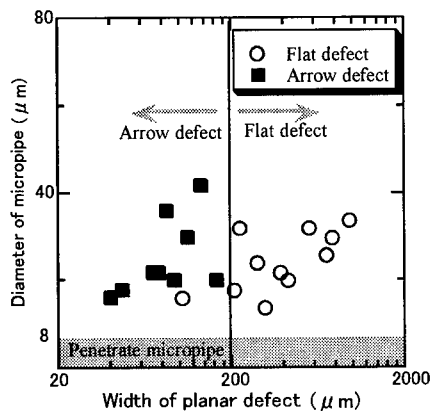


Fig.2 Relation of size of micropipe and planar defect

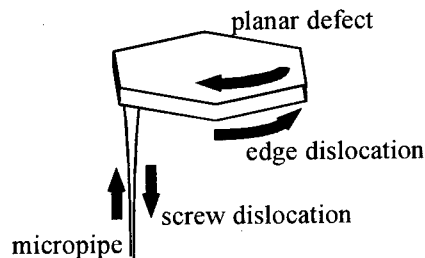


Fig.3 Schematic of defect formation

Figure 4 shows the cross section of an area around the interface of sample A. In the low N-doped layer, only one polytype was grown (6H-SiC). But, in the high N-doped layer, other polytypes, like 4H- and 15R-SiC, were observed by Raman spectroscopy and fluorescence optical microscopy. There is a possibility of changing the polytype by doping with nitrogen.

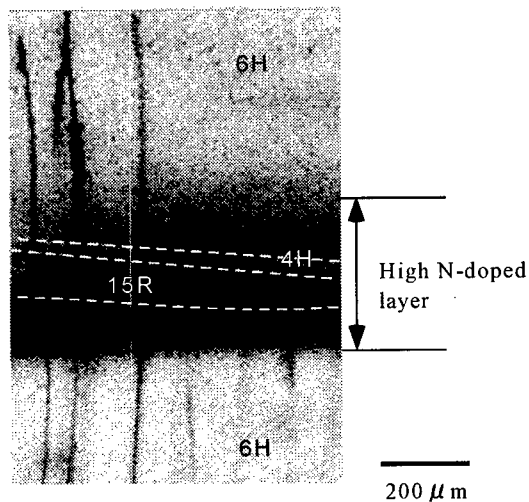


Fig.4 Some polytypes in high N-doped layer of sample A

#### 4. Conclusion

SiC crystals grown in c-axis direction have two kinds of planar defects. Large size planar defects with an over width of  $200\text{ }\mu\text{m}$  are called "flat defects" and small size defects are called "arrow defects". These defects are related to edge dislocations. When the micropipe induces a "flat defect", screw dislocation changes to edge dislocation and the micropipe is annihilated. "Flat defects" are observed in high N-doped layer. So it is possible to decrease micropipe density by nitrogen incorporation.

Other polytypes (4H and 15R) were also observed in the high N-doped layer of 6H-SiC crystal. This suggests that polytype might change easily by doping with nitrogen.

## 5. Acknowledgments

This work was partially supported by a Grant-in-Aid for Science Research No.0945001 from the Ministry of Education, Science and Culture, Japan and FED,NEDO Japan, and Ion Engineering Institute (Osaka, Japan).

## References

- [1] K.Koga, Y.Fujikawa, Y.Ueda and T.Yamaguchi : Springer Proc. Phys. 71 (1992) p.96
- [2] St.Müller, R.Eckstein, W.Hartung, D.Hofmann, M.Kölbl, G.Pensl, E.Schmitt, E.J.Schmitt, A.-D.Weber and A.Winnacker :Materials Science Forum 264-268 (1998) p.33
- [3] M.Sasaki, Y.Nishio, S.Nishino, S.Nakashima and H.Harima :Materials Science Forum 264-268 (1998) p.41
- [4] N.Takanaka, S.Nishino and J.Saraie :Inst.Phys.Conf.Ser. 142(1996) p.49
- [5] P.Pirouz : Materials Science Forum 264-268 (1998) p.399
- [6] J.Heindl, H.P.Strunk, V.D.Heydemann and G.Pensl :Phys. stat. sol.(a)162 (1997) p.251
- [7] J.Takahashi and N.Ohtani:Phys. stat. sol.(b)202 (1997) p.163
- [8] A.Okamoto, N.Sugiyama, T.Tani and N.Kamiya :Materials Science Forum 264-268 (1998) p.21
- [9] W.Si, M.Dudley, R.Glass, V.Tsvetkov and C.H.Carter,Jr. :Materials Science Forum 264-268 (1998) p.429

E-mail address : nishino@ipc.kit.ac.jp



## Correlation of EBIC and SWBXT Imaged Defects and Epilayer Growth Pits in 6H-SiC Schottky Diodes

C.M. Schnabel<sup>1</sup>, M. Tabib-Azar<sup>1</sup>, P.G. Neudeck<sup>2</sup>, S.G. Bailey<sup>2</sup>, H.B. Su<sup>3</sup>,  
M. Dudley<sup>3</sup> and R.P. Raffaele<sup>4</sup>

<sup>1</sup> Case Western Reserve University, Glennan 517, 10900 Euclid Ave., Cleveland, OH 44106, USA

<sup>2</sup> NASA Glenn Research Center, M.S. 77-1, 21000 Brookpark Road, Cleveland, OH 44135, USA

<sup>3</sup> State University of New York at Stony Brook, Stony Brook, NY 11794, USA

<sup>4</sup> Rochester Institute of Technology, Rochester, NY 14623, USA

**Keywords:** Defects, Diffusion Length, Electron Beam Induced Current (EBIC), Epilayer Growth Pits, Recombination Centers, Screw Dislocation, Synchrotron White-Beam X-Ray Topography (SWBXT)

**Abstract:** We show the first direct experimental correlation between the presence of closed core screw dislocations in 6H-SiC epilayers with recombination centers, as well as with some of the small growth pits on the epilayer surface in lightly-doped 6H-SiC Schottky diodes. At every SWBXT-identified closed core screw dislocation, an EBIC image showed a dark spot indicating a recombination center, and Nomarski optical microscope and Atomic Force Microscope (AFM) images showed a corresponding small growth pit with a sharp apex on the surface of the epilayer.

**Introduction:** The ability to readily identify the electrical properties of an extended crystal defect in a semiconductor is paramount in determining whether the defect influences the performance of various devices. Electron-beam-induced current (EBIC) measurement using the planar mapping technique enables quantitative analysis and spatial visualization of recombination centers that reduce the diffusion length of minority carriers in 6H-SiC Schottky diodes [1,2,3]. Such a procedure coupled with synchrotron white-beam x-ray topography (SWBXT), through which closed core screw dislocations may be identified by their stress signature in the crystal lattice [4], gives insight into the effects of these defects on the minority carrier diffusion length. The SWBXT image may also be correlated to the as-grown homoepilayer surface by comparison with Nomarski optical microscopy and atomic force microscopy (AFM) images.

**Experimental Procedure:** Following the growth of a 3.5  $\mu\text{m}$  thick  $1.2 \times 10^{16} \text{ cm}^{-3}$  n-type homoepilayer on a 3.5 ° off-axis commercial 6H-SiC substrate [5] by CVD [6], we generated a map of closed core screw dislocations using SWBXT [4]. The wafer backside was polished prior to SWBXT to ensure sufficient X-ray image quality that individual closed core screw dislocations were clearly resolvable throughout the entire sample. Following deposition and annealing of a backside Ni ohmic contact (~925 °C, 5 minutes in argon ambient), thin gold Schottky contacts (approx. 400 Å thick) of up to 0.86 mm x 0.86 mm in area were then patterned on the epilayer surface using E-beam evaporation and lift-off photolithography. High magnification (400X) Nomarski optical images of the surface features of individual dies were made. With the assistance of AFM analysis, the observed features evident on the Au Schottky contacts were categorized as either particulates on the top surface of the Schottky metal due to sample handling, or growth pits in the as-grown epilayer observable through the thin metallization.

EBIC images were generated by raster-scanning the 25 keV electron-beam across the entirety of the die while measuring the collected current as a function of position. Lighter shades correspond

to higher collected currents indicating longer minority carrier lifetime, while areas of enhanced minority carrier recombination (i.e., lower carrier lifetime and lower collected currents) are imaged as dark spots [1]. Because raw images collected by SWBXT and EBIC were somewhat distorted, computer image processing was needed to restore raw images to the proper aspect ratio corresponding to the proper aspect ratio of the original sample. All images were digitally scanned into a computer so that the images could be undistorted, scaled, and digitally overlaid as separate image layers using the four corners of the 7.5 mm x 6 mm rectangular sample as common reference coordinates. The computer contrast enhancement of images and creation of partially transparent derived layers expedited correlation of data from all three measurements.

**Results:** The figures below illustrate the same device region showing part of a 0.86 mm x 0.86 mm Schottky diode recorded by SWBXT (Figure 1), EBIC (Figure 2), and optical microscope (Figure 3, with AFM inset of a small growth pit). All the closed core screw dislocations revealed in Figure 1 are clearly reflected by correspondingly located dark spots in the EBIC image of Figure 2. It is readily apparent, however, that there are additional dark spots in the EBIC image for which no screw dislocation is present. While less obvious in Figure 3 due to their very small size, small growth pits typical of the AFM inset were also identified at every screw dislocation. However, not all EBIC-revealed recombination centers and not all small growth pits are associated with screw dislocations. The small growth pits correlated with screw dislocations appear similar in size and shape, while those that are not associated with screw dislocation sometimes have different shapes. Some EBIC dark spots and some epilayer small growth pits appear completely independent in that they show up in none of the other images (such as RC-1 in Figure 2 and GP-1 in Figure 3). Most, but not all, growth pits unassociated with screw dislocations did not yield strong EBIC signatures. Table 1 shows the defect statistics recorded at six locations consisting of four different 860  $\mu\text{m}$  x 860  $\mu\text{m}$  diodes plus two similar-sized areas consisting of many smaller patterned Schottky contacts.

Screw dislocations significantly reduce the effective diffusion length of carriers in the sample. Figure 4 shows the diffusion length as a function of position across screw dislocation SD-1 shown in Figure 2. The diffusion length is calculated on the order of 3.4  $\mu\text{m}$  far from the defect, but drops around 30% to as low as 2.4  $\mu\text{m}$  near the center of the defect. This behavior is typical of the screw dislocations measured in this 6H-SiC sample.

Figure 5 shows the AFM sectional data plot taken through the middle of the small growth pit associated with SD-1, as illustrated by the white line in the middle of the AFM inset of Figure 3. One end of the metal-covered small growth pit consists of a sharp apex of at least 18 nm in depth. This data is typical of all the small growth pits associated with screw dislocations measured by AFM on this sample. Such sharp interface features could conceivably enhance carrier emission/leakage from the semiconductor impacting SiC Schottky diode I-V properties as well as MOS insulator reliability. Once very small area devices have been fabricated (i.e., small enough that some are free of certain defects), a comprehensive study of Schottky I-V properties as a function of imaged defects is planned. If successful, such a study might be able to conclusively link specific kinds of crystal defects to important electrical anomalies observed in the SiC Schottky diode literature (particularly Refs. [2], [7], and [8]).

## Conclusion

All screw dislocations result in EBIC-identified minority carrier recombination centers in the SiC epilayer, and in small growth pits at the sample surface. However, not all growth pits are due to screw dislocations. Not all minority carrier recombination centers are due to screw dislocations.

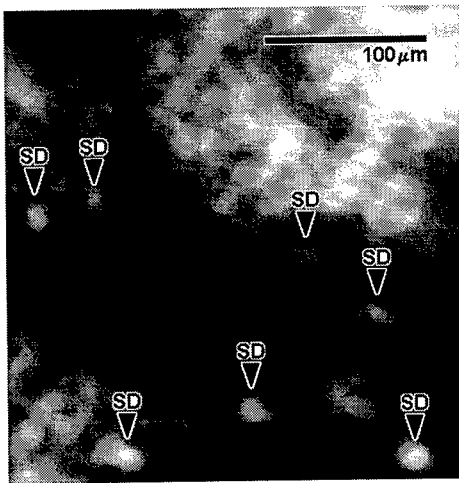


**Fig. 1.** SWBXT map of a selected diode section. The lighter spots in the image are elementary screw dislocations causing high stress regions in the crystal lattice.

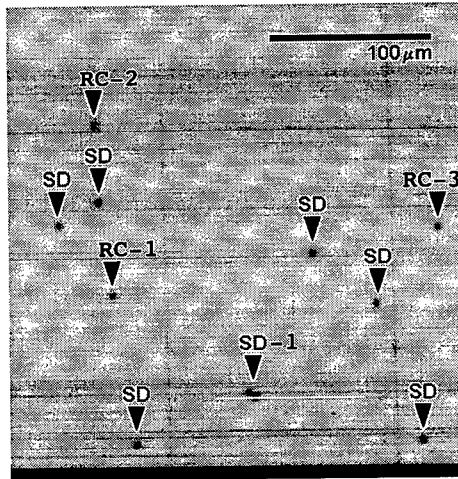


**Fig. 2.** EBIC image of a selected diode section. Darker regions indicate lower collected current, which corresponds to a reduction in the effective diffusion length.

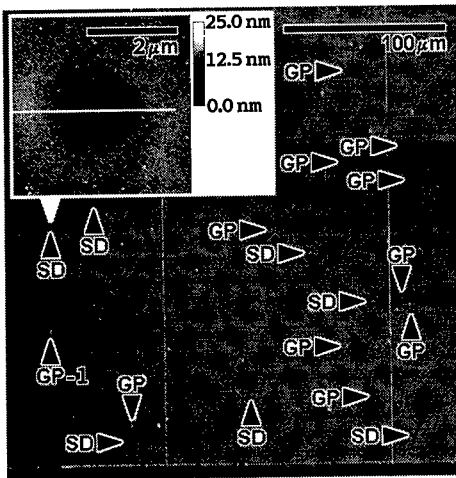


**Fig. 3.** Nomarski image of a selected diode section. Both growth pits and other particulates are evident on the sample surface. The inset shows an AFM image of a growth pit typical of a screw dislocation.

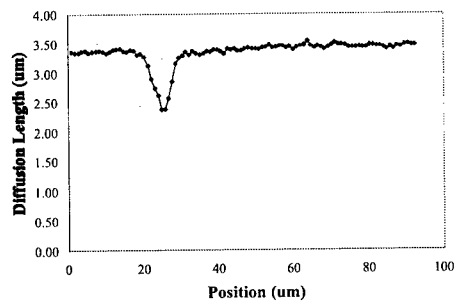


**Fig. 4.** Diffusion length as a function of position extracted from the EBIC linescan, as shown by the white line across SD-1 of Figure 2.

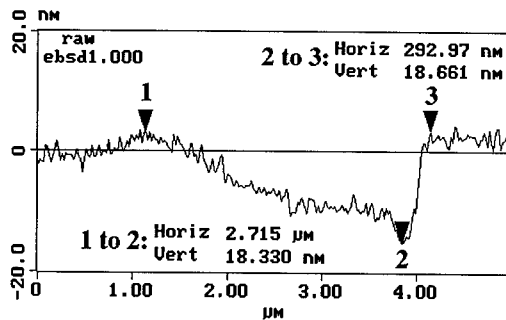


**Fig. 5.** AFM sectional data plot taken through the middle of the small growth pit associated with SD-1, as illustrated by the white line in the middle of the AFM inset of Figure 3. One end of the metal-covered small growth pit consists of a sharp apex of at least 18 nm in depth. This data is typical of all the small growth pits associated with screw dislocations measured by AFM on this sample.

**Table 1** Number of defects on different 1 mm x 1 mm dies by observation category.

Die I.D. Label on Chip ->	Bd	Dc	Db <sup>5</sup>	Df <sup>5</sup>	Ab <sup>3,5</sup>	Bc <sup>3,5</sup>
EBIC recombination centers	126	105	98	161	31	32
SWBXT identified screw dislocations over die(s) <sup>1</sup>	40	27	41	43	7	10
Nomarski identified small growth pits <sup>5</sup>	176	159	-	-	-	-
Recombination centers matching screw dislocations <sup>2</sup>	36 <sup>4</sup>	27	41	43	7	10
Growth pits matching screw dislocations <sup>2,5</sup>	40	27	-	-	-	-

1. Large areas of high stress are counted as a screw dislocation, although it may be due to many screw dislocations or another defect such as a micropipe.

2. If one growth pit or recombination center is within approx. 20 μm of the screw dislocation it is considered correlated with that screw dislocation.

3. Ab and Bc represent many smaller dies that lie close together, and therefore have much smaller measured areas than dies Bd, Dc, Db, and Df.

4. Probe tip and contact damage obscured EBIC observation of some screw dislocations.

5. Growth pit data not collected on die Db, Df, Ab, and Bc.

**Acknowledgements:** NASA Glenn: J. A. Powell, D. Larkin, C. Salupo, G. Beheim, J. Heisler, A. Trunek, L. Keys. CWRU work supported by NASA Glenn Grant NCC3-593. SUNY support from the U.S. Army Research Office under contract number DAAG559810392 (contract monitor Dr. John Prater), partially funded by the DARPA Microsystems Technology Office (Order#E111/3 monitored by Dr. Dan Radack) and NASA Glenn. Topography carried out at the NSLS, at BNL, which is supported by the U.S. Department of Energy, contract number DE-AC02-98CH10886.

## References

- [1] H. J. Leamy, J. Appl. Phys. 53 (1982), p. R51.
- [2] M. Bhatnagar, et. al., IEEE Trans. Electron Devices 43 (1996), p. 150.
- [3] M. Tabib-Azar, et. al., J. Appl. Phys. 84 (1998), p. 3986.
- [4] M. Dudley and X. Huang, this conference, p. 431
- [5] Cree Research, Inc., 4600 Silicon Drive, Durham, NC 27703.
- [6] D. J. Larkin, MRS Bulletin 22 (1997), p. 36.
- [7] R. Raghunathan and B. J. Baliga, Appl. Phys. Lett. 72 (1998), p. 3196.
- [8] D. Defives et. al., IEEE Trans. Electron Devices 46 (1999), p. 449.

## Investigation of Low Angle Grain Boundaries in Modified-Lely SiC Crystals by High Resolution X-ray Diffractometry

M. Katsuno\*, N. Ohtani, T. Aigo, H. Yashiro and M. Kanaya

Advanced Technology Research Laboratories, Nippon Steel Corporation,  
20-1 Shintomi, Futtsu, Chiba, 293-8511, Japan

**Keywords:** Defect Selective Etching, HRXRD, Low Angle Grain Boundaries

### Abstract

The structural properties of low angle grain boundaries in modified-Lely SiC crystals have been studied using high resolution x-ray diffraction (HRXRD) and molten KOH defect selective etching. The defect selective etching revealed that the low angle grain boundaries were polygonized into  $\langle 1\bar{1}00 \rangle$  directions and more often occurred at the peripheral parts of crystal. The relative misorientation between adjacent subgrains was examined by HRXRD, and it was found that the tilting of the (0001) lattice plane occurred at the low angle grain boundaries and had a rotation axis parallel to the boundary plane. Based on these results, we have discussed the cause and mechanism of the formation of low angle grain boundaries in modified-Lely SiC crystals.

### Introduction

Modified-Lely SiC single crystals typically contain slightly misoriented subgrains bordered by regions of high dislocation density. These subgrains are fully replicated into the device epitaxial layers by a thin film growth process, and consequently the subgrain structure of the substrate has a major impact on the performance of SiC devices made on it. To understand the subgrain formation process during modified-Lely growth of SiC, it is crucial to obtain information on the subgrains existing in SiC crystals, particularly on their distribution and misoriented structure. The objective of this paper is to conduct a detailed study of misorientation of subgrains in modified-Lely SiC crystals using high-resolution x-ray diffractometry (HRXRD) and discuss the possible causes of subgrain formation during modified-Lely growth of SiC.

### Experimental

6H-SiC crystals were grown by the modified-Lely method, and the grown crystals were sliced into {0001} wafers. The wafers were examined by HRXRD and molten KOH defect selective etching. HRXRD measurements were performed using a double-axis diffractometer, where a four-crystal monochromator with Ge 220 reflections was used for  $\text{CuK}\alpha_1$  radiation. The resolution of the diffractometer was as good as 12arcsec. Analysis of x-ray rocking curves was used to quantitatively assess the lattice misorientation around subgrain boundaries. In these experiments, the symmetric reflection of 0006 and the asymmetric reflections of  $1\bar{1}010$  and  $11\bar{2}12$  in the rocking curves for 6H-SiC crystals were acquired.

Defect selective etching was performed by molten KOH. For reproducible etching, the stirring of the melt and the atmosphere control are of great importance [1]. To resolve each etch pit, shallow etching is required, and thus the etching conditions of 3–5min at 520°C were employed. Prior to the etching, careful surface polishing using a fine diamond slurry was conducted, otherwise scratches caused by the polishing process significantly hamper the observations of the detailed structure of etch features.

### Results and Discussion

Defect selective etching revealed several size etch pits on the 6H-SiC(0001)Si surface. They are categorized into three sizes: large, medium and small. The large and medium size etch pits correspond to micropipes and (unit *c*) screw dislocations, respectively, while the small size etch pits are caused by edge dislocations and often aligned in rows forming low angle grain boundaries

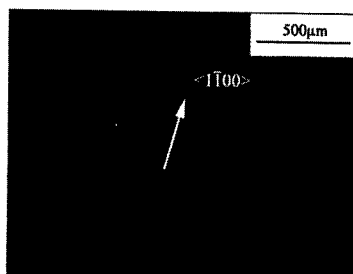


Fig. 1. Etch pit features on the 6H-SiC(0001)Si surface revealed by KOH defect selective etching. The low angle grain boundaries are polygonized into  $\langle 1\bar{1}00 \rangle$  directions.

(subgrain boundaries) [2]. They separate two adjacent misoriented subgrains and, as shown in Fig. 1, are polygonized into  $\langle 1\bar{1}00 \rangle$  directions due to the stresses introduced by the growth process or its environment. The low angle grain boundaries more often occurred at the peripheral parts of crystal, and they tended to be radially distributed.

In the past HRXRD studies, various diffraction curves were reported for modified-Lely SiC crystals. The reported rocking curves varied from a sharp single peak to multiple peaks distributed over several hundred arcseconds depending on the quality of crystals examined. However, in most of the studies, the crystal areas, from which the diffraction curves were obtained, contained several different types of defects and were often not well-defined. Thus it was difficult to study the influence of a particular type of defect (pits) on the shape of rocking curve. To solve these problems, we used a Pb mask which had a thickness of 0.1mm and a 1.6mm $\times$ 1.6mm window. The Pb mask sufficiently attenuates the incident x-ray beam, so that the diffraction only occurs in the window area. This Pb mask technique enables a detailed study of influence of a particular type of defect on the diffraction curve by carefully choosing the diffraction area so that it contains only a particular type of defect (pits).

With the Pb mask technique, we first examined the effects of micropipes and unit  $c$  screw dislocations on the x-ray rocking curve. The rocking curve diffracted from an area that almost exclusively contained medium size etch pits (unit  $c$  screw dislocations) showed a sharp single peak with a full width at half maximum (FWHM) of 12arcsec which is as narrow as the resolution of the diffractometer. The rocking curve diffracted from an area that accommodated several large hexagonal etch pits (micropipes) and hundreds of medium size etch pits also showed a narrow single diffraction (FWHM: typically 18-25arcsec). Glass *et al.* [3] reported that the variation of domain (subgrain) density is well correlated with the density of spiral growth centers. In particular, they found that the micropipe density was approximately consistent with the number of multiple peaks or the magnitude of broadening of x-ray rocking curves, and thus suggested that micropipes are a main cause of the mosaicity in modified-Lely SiC crystals. However, our results preclude this possibility and proved

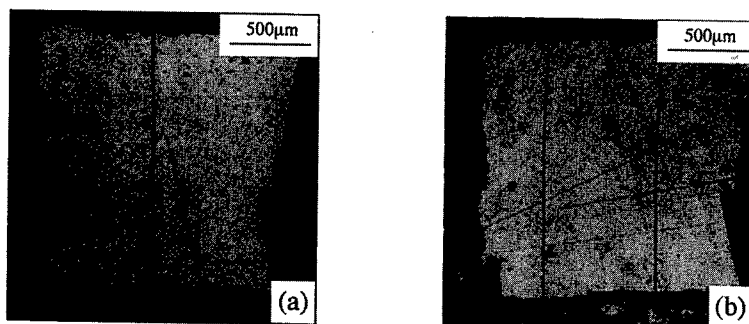


Fig. 2. Etch pit row due to (a) an isolated low angle grain boundary and (b) two parallel low angle grain boundaries. The square shape window is a Pb mask for the selected area x-ray diffraction.

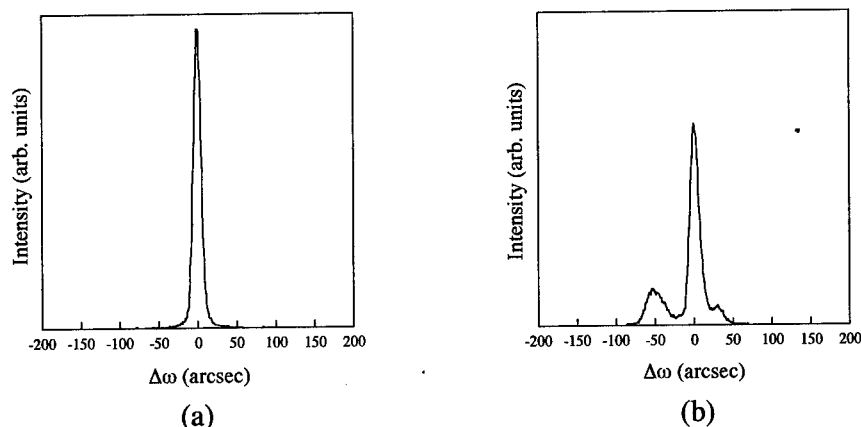


Fig. 3. 0006 x-ray rocking curves obtained from the two parallel low angle grain boundaries (Fig. 2(b)) with the incident plane (a) parallel and perpendicular to the etch pit rows.

that micropipes and unit  $c$  screw dislocations hardly affect the shape of the x-ray rocking curves.

The misorientation of the (0001) lattice plane around small etch pit rows (low angle grain boundaries) was also examined by the selective area x-ray diffraction. The incident plane was chosen either parallel or perpendicular to the etch pit row. For an isolated low angle grain boundary (Fig. 2(a)), the 0006 rocking curve with the incident plane parallel to the boundary showed a narrow single diffraction peak (FWHM: typically 13–20 arcsec), while the one with the incident plane perpendicular to the boundary exhibited a slightly broader peak (15–30 arcsec). This tendency became prominent when a couple of low angle grain boundaries were bunched together (Fig. 2(b)). Figure 3 shows typical x-ray rocking curves obtained from the crystal area shown in Fig. 2(b) with the incident plane (a) parallel and (b) perpendicular to the boundaries. For these coupled low angle grain boundaries, the 0006 rocking curve with the incident plane parallel to the boundaries still remained narrow; however, the one with the incident plane perpendicular to the boundaries became much broader (40–50 arcsec) and often split into multiple peaks.

The rocking curves with the asymmetric reflections showed the same tendency as those for the symmetric 0006 reflection, where the rocking curves with the incident plane parallel to the coupled etch pit rows, *i.e.*  $1\bar{1}010$  reflection, showed a narrow single diffraction peak, while the one with the incident plane perpendicular to the etch pit rows ( $11\bar{2}12$  reflection) exhibited split peaks separated by about 50 arcsec. We also compared the two rocking curves with the incident beam direction from the center to the outer of the crystal and vice versa; however, little or no difference was detected between the two rocking curves.

The results of our rocking curve measurements revealed that modified-Lely SiC crystals has a strong [0001] texture around low angle grain boundaries and the tilting of the (0001) plane has an axis of rotation parallel to the boundary plane (Fig. 4(a)). Several causes and mechanisms of the misoriented subgrain formation in modified-Lely SiC crystals have been proposed and discussed.

Pirouz [4] discussed the dislocation systems lying on a prism plane, *e.g.*,  $\{11\bar{2}0\}$  or  $\{1\bar{1}00\}$  plane.

$\{1\bar{1}00\}$  and  $\{11\bar{2}0\}$  have never been reported as a slip plane in hexagonal SiC polytypes, even though the low angle grain boundaries commonly observed in modified-Lely SiC crystals lie in the  $\{11\bar{2}0\}$  plane, which implies that the dislocations comprising the low angle grain boundaries are not introduced by thermal stress after growth, and they are grown-in type dislocations and rather introduced during growth by the growth process itself. Pirouz [4] and Glass *et al.* [5] claimed that the strong [0001] texture in modified-Lely SiC crystals originates in spiral growth mechanism. The interaction between two growth spirals can be assumed to result in low angle grain boundaries due to twist misorientation between the two growth spirals. However it should be recalled that a low angle twist grain boundary consists of arrays of screw dislocations on the grain boundary plane and has a rotation axis perpendicular to the boundary plane (Fig. 4(b)), which is quite contradictory to the results of our rocking curve measurements.

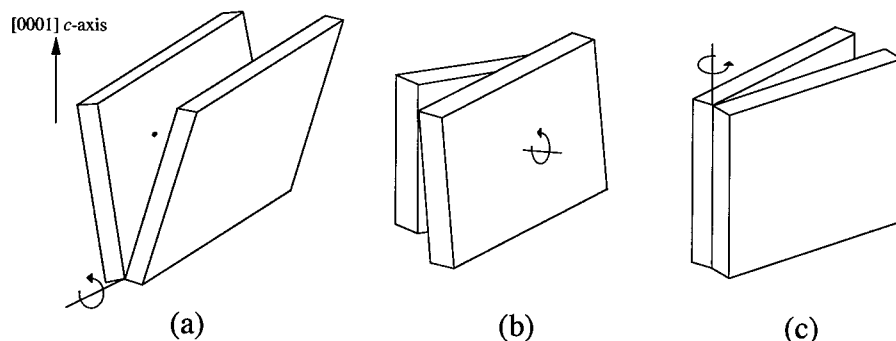


Fig. 4. Schematic diagrams of relative misorientation of adjacent subgrains; (a) tilting with a rotation axis parallel to both the boundary plane and the (0001) basal plane, (b) tilting with a rotation axis perpendicular to the boundary plane, (c) tilting with a rotation axis parallel to the boundary plane and perpendicular to the (0001) basal plane.

We found that one of the major causes of the subgrain formation in modified-Lely SiC crystals is the inclusion of foreign polytypes during growth. The non-basal plane interfaces between the different polytypes accommodate crystallographic imperfections which relax into polygonized low angle grain boundaries during growth. Takahashi *et al.* examined by x-ray topography the low angle grain boundaries in modified-Lely SiC crystals and found that the boundaries are edge dislocation walls having a  $\langle 1\bar{1}20 \rangle$  Burgers vector [6]. In general, edge dislocations having the same Burgers vector minimize their total strain energy by aligning themselves along the direction perpendicular to the Burgers vector. In that case, however, the low angle grain boundaries yields only a tilting of planes perpendicular to the (0001) basal plane (Fig. 4(c)). One of the possibilities being the cause of the tilting of the (0001) basal plane is that the edge dislocations have an inclination from the  $c$ -axis.

The polygonization of edge dislocations along  $\langle 1\bar{1}00 \rangle$  directions requires glide and climb motions of the dislocations. The glide and climb of dislocations are temperature activated processes, and thus they most probably occur during growth [7]. In the course of these motions, the edge dislocations predominantly lie along the  $c$ -axis but often kink toward  $\langle 1\bar{1}00 \rangle$  directions due to climb motion. We assume that these kinks virtually bend the edge dislocations at the grain boundary from the  $c$ -axis and bring about a slight tilting of the (0001) basal plane around it.

### Conclusion

The structure of low angle grain boundaries in modified-Lely SiC crystals has been studied, and it was found that the tilting of the (0001) lattice plane occurred at the low angle grain boundaries and had a rotation axis parallel to the boundary plane. We found that a main cause of the low angle grain boundary formation in modified-Lely SiC crystals is the polytype mixing during growth. The observed [0001] texture of modified-Lely SiC crystals is assumed to be caused by edge dislocation walls comprising inclined dislocations from the  $c$ -axis toward  $\langle 1\bar{1}00 \rangle$ .

### References

- [1] M. Katsuno, N. Ohtani, J. Takahashi, H. Yashiro, M. Kanaya, Jpn. J. Appl. Phys. 38 (1999) p. 4661.
- [2] J. Takahashi, M. Kanaya, Y. Fujiwara, J. Cryst. Growth 135 (1994) p. 61.
- [3] R.C. Glass, L.O. Kjellberg, V.F. Tsvetkov, J.E. Sundgren, E. Janzén, J. Cryst. Growth 132 (1993) p. 504.
- [4] P. Pirouz, Phil. Mag. 78 (1998) p. 727.
- [5] R.C. Glass, D. Henshall, V.F. Tsvetkov, C.H. Carter, Jr., Phys. Stat. Sol. (b) 202 (1997) p. 149.
- [6] J. Takahashi, N. Ohtani, M. Kanaya, J. Cryst. Growth 167 (1996) p. 596.
- [7] K. Maeda, K. Suzuki, S. Fujita, M. Ichihara, S. Hyodo, Phil. Mag. A 57 (1988) p. 573.

\*)Corresponding author: Fax +81-439-80-2746; e-mail: katsuno@re.nsc.co.jp



## Structural, Electrical and Optical Properties of Bulk 4H and 6H p-Type SiC

E.V. Kalinina<sup>1</sup>, A.S. Zubrilov<sup>1</sup>, N.I. Kuznetsov<sup>1</sup>, I.P. Nikitina<sup>1</sup>, A.S. Tregubova<sup>1</sup>,  
M.P. Shcheglov<sup>1</sup> and V.Ya. Bratus'<sup>2</sup>

<sup>1</sup> Ioffe Institute, 26 Polytekhnicheskaya Str., RU-194021 St. Petersburg, Russia

<sup>2</sup> Institute Semiconductor of Physics, National Academy of Science of Ukraine,  
45 Pr. Nauki, Kiev, 252028, Ukraine

**Keywords:** 4H Polytype, 6H Polytype, Al, Defects, p-Type, SiC Bulk Crystal

**Abstract.** Structural, electrical and optical characteristics of commercial 4H and 6H p-SiC substrate crystals doped with Al were studied. Radial non-uniformity in extended defect distribution over the substrates was found to be a typical feature of the p-SiC substrates grown by modified Lely method. In the central region of the wafers a relatively uniform distribution of dislocations with a density less than  $10^5 \text{ cm}^{-2}$  was observed. While in the peripheral regions of the crystals the dislocation density was found to exceed  $10^6 \text{ cm}^{-2}$  and was highly non-uniform. Domain structure of the investigated crystals was confirmed. Ionization energy of the Al acceptors were measured to be 0.18 eV. Some electrical transport and luminescence characteristics of the crystals are also presented.

### 1. Introduction

SiC devices are attractive for high-temperature, high-power and high-frequency applications. The quality of single-crystal SiC wafers both n- and p-types is an important aspect of the device fabrication. Properties of n-type bulk SiC crystals have been studied in details, while information about p-type bulk SiC crystals (especially commercially available high-size crystals grown by modified Lely method) is limited. There is a practical interest to p-SiC substrates doped with Al. Ionization energy of the Al acceptor has been measured [1-3] for Lely crystals and epitaxial layers. For 6H and 4H SiC with the Al concentration below  $10^{20} \text{ cm}^{-3}$ , this energy was found to be 0.24–0.27 eV and 0.19–0.24 eV, respectively [1-3]. Electrical transport properties of p-type SiC Lely crystals and epitaxial layers doped with Al were studied [1,4,10]. Doping processes of 6H and 4H-SiC boules with Al in the case of sublimation growth were also investigated [5]. We report on characteristics of commercially available bulk 4H and 6H p-type SiC:Al crystals.

### 2. Experimental

Investigated materials were commercially available 6H and 4H SiC crystals fabricated by modified Lely method [6]. The crystals were doped with Al. Concentration of the uncompensated acceptors  $N_a - N_d$  was in the range from  $10^{16}$  to  $3 \times 10^{18} \text{ cm}^{-3}$  for different crystals. Substrates with thickness of 0.35–0.40 mm were oriented  $3.5^\circ$  off-axis and polished. Before the study, these substrates were subjected to a short-time etching in a molten KOH to remove the surface layer damaged by mechanical polishing.

Structural quality of SiC samples was characterized by x-ray diffraction (XRD) and x-ray topography using Lang method. Besides, structural defects were analyzed by photoluminescence (PL) under the nitrogen laser excitation at temperature ranging from 77 to 500K as well as cathodoluminescence (CL). In combination with spectroscopic methods, the full-color PL surface mapping was used. The electron paramagnetic resonance (EPR) technique was used to identify impurities and defects in the crystals. EPR experiments have been carried out at X-band ( $\nu=9.5$

GHz) spectrometer at 4.2K and 77K. Element distributions in the samples were studied using secondary ion mass-spectroscopy (SIMS). Concentration and distribution of electrically active impurity in the samples were determined by C-V characteristics of Schottky barriers at a frequency of 10 kHz. I-V characteristics for Schottky barriers were measured at temperatures 77-500K. The concentration of free carriers, their mobility and the ionization energies of impurity levels were determined using the Van der Pauw technique at temperatures from 77 to 300K.

### 3. Results

According to x-ray data, the crystal structure of both 4H and 6H p-SiC crystals was usually domain, especially on the peripheral areas of wafers. Two or more broadened peaks on double-crystal x-ray rocking curves (RC) measured at  $\omega$ -scan were usually observed. The similar features of n-type SiC wafers have been discussed by Glass and co-authors [7]. The structural perfection of 4H-SiC wafers was worse than that of 6H-SiC wafers. The domain structure was often observed near the center of 4H- wafer. The number of peaks on RC( $\omega$ ) and their broadening varied for different areas of the wafer. The FWHM of separate peaks ranged from 17 to 60 arc.sec (Fig.1a). However, the only single peak (FWHM=10-14 arc.sec) was usually observed for RC taken at  $\omega, 2\theta$ -scan on the symmetric (0006), (0008) and (00012) reflections (Fig.1b).

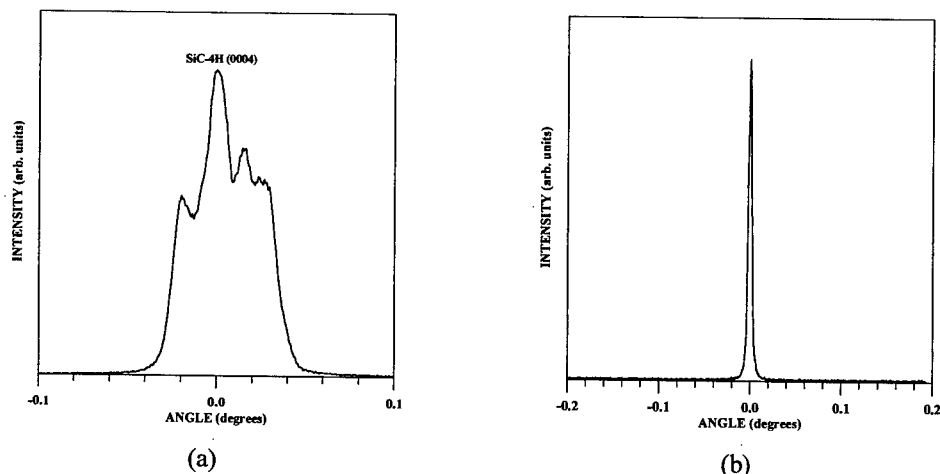


Figure 1. Typical rocking curves from p-type SiC-4H wafer grown by modified Lely method, measured at:

(a)  $\omega$ -scan, (b)  $\omega, 2\theta$ -scan.

The existence of two or more peaks on RC( $\omega$ ) was explained by scattering from large strongly misoriented domains having the angle of mutual disorientation higher than the FWHM of the separate peak. Domain structure of investigated crystals was confirmed by x-ray topography (Fig.2a). Radial non-uniformity of defect distribution over the wafers was detected. Two areas with different defect structure can be seen in Fig.2a: a more perfect region in the center of the wafer, and a strongly strained peripheral region. A relatively uniform distribution of dislocations with a density less than  $10^5 \text{ cm}^{-2}$  without large micropipes was observed in the central region of the wafer. The only one peak with the FWHM of about 17-22 arcsec was usually observed on RC( $\omega$ ) taken from the center of the wafer. While for the sample presented in Fig. 2a, the FWHM of RC( $\omega$ ) is 10-12 arcsec in the center of the wafer. Misoriented domains were clearly seen in the periphery of the wafer. A lot of broadened well-resolved peaks were observed on RC( $\omega$ ), taken from peripheral regions.

A big number of dislocations and sizable strain-induced kinks were detected at the boundaries of these domains together with single and clustered pores. The dislocation density at the boundaries was found to be above  $10^6 \text{ cm}^{-2}$  and was highly non-uniform. Optical observations of the strain distribution over the substrates were in good agreement with x-ray data (Fig.2b).

The typical EPR spectra for the substrates observed at 4.2K consists of two distinct lines (Fig.3). The first one presents a broad ( $\Delta B_{pp} \approx 5 \text{ mT}$ ) structureless line with g-value  $g_{||} = 2.457$  for orientation of the magnetic field along [0001] crystal axis. Its position is given by expression  $g(\theta) = g_{||} \cos(\theta)$ , where  $\theta$  is the angle between the applied magnetic field and crystal c axis.

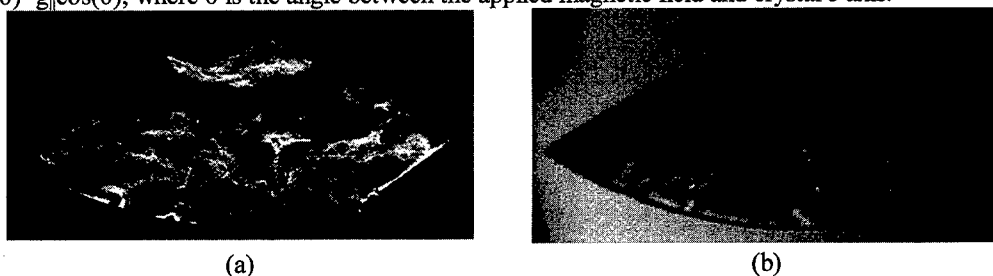


Figure 2. X-ray topograph (a) and optical image in the cross-polarized light (b) of a piece of 4H p-SiC:Al substrate.

Such EPR line was tentatively assigned to aluminum acceptor with an effective-mass character [8] and recent ENDOR study [9] confirmed the validity of this suggestion. The second EPR line is slightly anisotropic in a range of free-spin  $g = 2.0023$  value. Observation of hyperfine structure allows to attribute it unambiguously to boron acceptor contamination. Boron concentration in the samples determined with EPR relative to a standard sample at 77K has been found in the range  $1.7 \times 10^{17} - 2.0 \times 10^{18} \text{ cm}^{-3}$ . A great linewidth and distorted lineshape of the spectrum make difficult the determination of Al acceptor absolute or relative to B concentration.

At a low temperature (about 80K) the PL and CL spectra for the p-SiC substrates were usually dominated by the well-known band [9] of the donor-acceptor (DA) recombination through N-Al pairs (Fig.4). Exciton-related luminescence has not been detected in the crystals. Besides the N-Al associated luminescence, some SiC bulk crystals exhibited boron-attributed luminescence [3] indicating boron acceptor contamination in accordance with EPR data. For some 4H-SiC crystals, the 6H-heteropolytype inclusions were detected. For all the wafers, deep levels-attributed PL and CL bands in the orange-red spectral region were observed. At room temperature the N-Al donor-acceptor luminescence band is strongly quenched. At higher temperature up to 500K the deep level luminescence bands are also quenched with the corresponding activation energy in the range of 0.18-0.47 eV. High lateral uniformity of Al doping of the crystals was supported by PL mapping method.

According to Hall measurements, the hole mobility in the crystals with the Al concentration as high as  $3 \times 10^{18} \text{ cm}^{-3}$  was found to be about 2-3  $\text{cm}^2/\text{V.s.}$  The activation energy for the Al acceptors in such crystals was estimated to be 180 meV. According to SIMS data, all 4H and 6H crystals were uniformly doped with Al. For 4H-SiC sample presented in Fig.2, the concentration of Al is as high as  $3 \times 10^{18} \text{ cm}^{-3}$ . Also, the boron concentration of  $8 \times 10^{16} \text{ cm}^{-3}$  was measured by SIMS in this sample. This SIMS results are in accordance with EPR and PL data. The SIMS data obtained are in accordance with C-V data, that the depth profile of impurity in the samples was uniform.

A dependence of the Schottky barrier height on the SiC polytype (4H or 6H) was observed for all employed metals (Ni, Cr, Pd). But no correlation between the barrier height and the metal work functions was observed. This fact is probably connected with the Fermi level fixed on the crystal surface due to an excess of the carbon vacancies  $V_C$  in the surface layer. According to I-V characteristics for such Schottky barriers, forward current depended exponentially on the voltage.

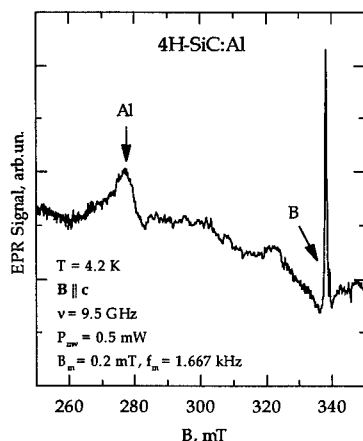


Figure 3. EPR spectrum of 4H-SiC:Al sample observed at 4.2K under conditions of adiabatic rapid passage.

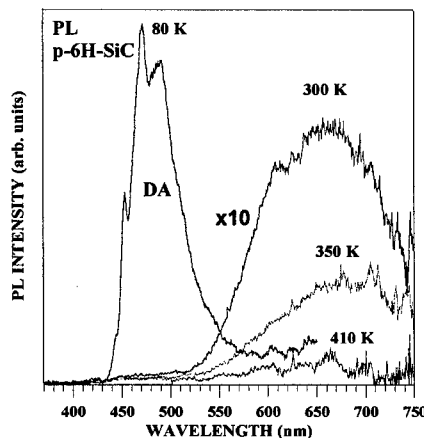


Figure 4. PL spectra of 6H p-SiC:Al substrate at different temperature. The quenching activation energy for the deep level defect band with a maximum at 663nm (1.87eV) is 0.47 eV

#### 4. Conclusion

Commercial p-type 4H and 6H-SiC wafers were characterized. Domain structure of the wafers was revealed by x-ray data. Radial non-uniformity in the defect distribution over the substrates usually observed for n-SiC substrates was found to be also a typical feature of the p-SiC substrates. In the central region of the wafers a relatively uniform distribution of dislocations with a density less than  $10^5 \text{ cm}^{-2}$  was observed. While in the peripheral regions, the dislocation density was found to be highly non-uniform and exceed  $10^6 \text{ cm}^{-2}$ . The hole mobility in the crystals with the Al concentration of  $3 \times 10^{18} \text{ cm}^{-3}$  was found to be about  $2\text{-}3 \text{ cm}^2/\text{V.s}$ . Ionization energy of the Al acceptors was 0.18 eV. Besides Al impurity, boron contamination was detected in some crystals by SIMS, EPR and PL. For 4H-SiC crystal, the 6H-SiC inclusions were found by EPR and PL.

#### 5. Acknowledgments

The authors thank A.P. Kovarski for SIMS and D.S. Poloskin for Hall measurements, and N.V. Seredova for PL mapping. This work has been supported by ISTC Projects No.197-98, by INTAS Project No. 96-0254, and INTAS Project No. 98-2141.

#### 6. References

- [1] H.J. Van Daal, W.F. Knippenberg and J.D. Wasscher, *J. Phys. Chem. Solids*, **24** (1963), p.109.
- [2] G.A. Lomakina, Yu.A. Vodakov, E.N. Mokhov, V.G. Oding and G.F. Kholuyanov, *Solid State Physics*, **12** (1970), p. 2918.
- [3] M. Ikeda, H. Matsunami and T. Tanaka, *Phys. Rev. B*, **22**, (1980), p. 2842.
- [4] W.J. Schaffer, G.H. Negley, K.G. Irvine and J.W. Palmour, *Inst. Phys. Conf. Ser.*, **177** (1994), p. 155.
- [5] V.F. Tsvetkov, S.T. Allen, H.S. Kong and C.H. Carter, Jr, *Inst. Phys. Conf. Ser.*, **142** (1996), p.17.
- [6] Yu.M. Tairov and V.F. Tsvetkov, *J. Cryst. Growth*, **43** (1978), p.209.
- [7] R.C. Glass, L.O. Kjellberg, V.F. Tsvetkov, J.E. Sundgren and E. Janzen, *J. Cryst. Growth*, **132** (1993), p.504.
- [8] J. Schneider, K.Maier. *Physica B*, **185** (1993), p. 199.
- [9] B.K.Meyer, A.Hofstaetter, P.G.Baranov. *Material Science Forum*, **264-268** (1998), p.591.
- [10] V.A. Dmitriev and A.E. Cherenkov, *J. Cryst. Growth*, **128** (1993), p. 343.

## High Order X-ray Diffraction and Internal Atomic Layer Roughness of Epitaxial and Bulk SiC Materials

G. Xu<sup>1</sup> and Z.C. Feng<sup>2</sup>

<sup>1</sup>Department of Materials Science, National University of Singapore,  
Lower Kent Ridge Road, Singapore, 119260, Singapore

<sup>2</sup>Institute of Materials Research & Engineering, 3 Research Link, Singapore, 117602, Singapore

**Keywords:** Electron Density, Molybdenum Target, Structure Factor, X-Ray Diffraction

### Abstract

The atomic distortion and internal layer roughness in epitaxial 3C- and 4H-SiC thin films and bulk 6H-SiC are studied by means of short wavelength X-ray diffraction using a 0.71 Å X-ray source from a molybdenum anode. Up to five order Bragg peaks along (100) were measured. Through the detailed theoretical calculation, the crystallographic structure factors were obtained. The electron density distributions along the surface normal were reconstructed via Fourier transform. Comparison with the ideal situation calculated from the atomic scattering factors was presented.

### 1. Introduction

Silicon carbide (SiC) is an attractive material system for modern electronic and optoelectronic devices working in high temperature, high power, high frequency and harsh environments [1-4]. It possesses many unique properties, such as wide band gap, high electric breakdown strength, high thermal conductivity and excellent thermal and chemical stability. For the device applications, heterogeneous epitaxial 3C-SiC thin film, grown on top of single crystal silicon and homoepitaxial SiC on SiC (6H on 6H and 4H on 4H) substrate by chemical vapour deposition (CVD) are the most popular [1,2,4,5].

X-ray diffraction (XRD) measurement technique has been widely used for SiC materials and devices. Traditionally, most of the XRD studies on SiC materials [1-4,6,7] were employing the copper source with 1.54 Å radiation. The analyses of the XRD patterns on the diffraction peak position, intensity and width can lead to the information on sample structure, crystallinity, perfection, defects, strain etc.

Usually no knowledge on information inside the unit cell, such as the internal atomic layer arrangement, can be extracted from the XRD measurement of SiC. Due to the lattice mismatch, for example for the case of 3C-SiC grown on Si, the internal Si and C atomic layers near the interface region might be distorted or have a complicated arrangement. Up to now, there were no detailed studies in these internal atomic layer arrangements. Here we present a new method to retrieve the atomic internal layer distortion or roughness by way of short wavelength X-ray diffraction.

### 2. Experiment

In the measurements, we employed a molybdenum anode to generate a wavelength of 0.71 Å, less than one half of that from a copper anode. This allows us to measure the Bragg reflections up to the 5<sup>th</sup> order, as shown in Figure 1 for an example of a 3C-SiC film grown on Si (100). This is in contrast to the availability of only 2 orders of Bragg peaks from a common copper anode with a radiation wavelength of ~1.54 Å.

Care must be taken when trying to obtain the peak intensity. In a usual diffractometer, due to simple collimation and a broad spectrum ( $K\alpha_1 + K\alpha_2$ ) in the incident beam, any intensity maximum will contain simultaneous diffraction contributions from a large volume surrounding a reciprocal lattice point. Therefore, this intensity maximum is not equivalent to the Bragg peak intensity, which should only be contributed by the center of this volume surrounding a reciprocal lattice point [8]. To obtain the structural factors, which are proportional to the square root of the peak intensity, a sample is usually scanned continuously, to first measure the "integrated intensity" over a range of  $2\theta$  (e.g.,  $0.5^\circ$ ). Assuming that the Bragg peak has a standard peak profile, one can then calculate the peak intensity from the integrated intensity. The Lorentz Factor must be used in the calculation, to compensate for the changing sweeping time of various reciprocal lattice points through the Ewald sphere [8].

However, such a scheme is not applicable here, because our samples contain lattice distortions, thus may not follow the standard peak profile, which is only computable for an ideal lattice. Therefore, in this case we have to use a highly collimated and monochromatic beam ( $K\alpha_1$  only), to insure that only a tiny volume surrounding a reciprocal lattice point is covered at any time moment. (In fact, with a 4-bounce crystal monochromator, the  $2\theta$  resolution is  $<0.003^\circ$ , which is much less than the Bragg peak width.) With the step mode, we are able to measure the intensity variation near the reciprocal lattice point. The peak intensity can then be directly obtained by the intensity maximum without involving the Lorentz Factor.

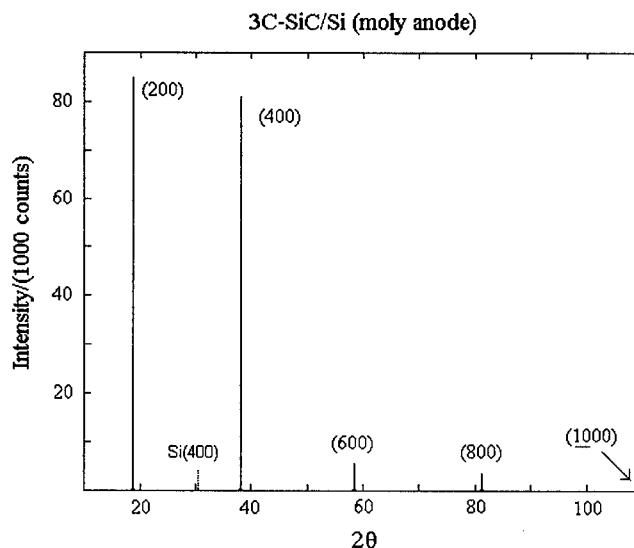


Figure 1. The first 5 integrated Bragg peak intensities of 3C-SiC.

### 3. Theory

From the peak intensities, the absolute values of the crystallographic structure factors,  $|F(hkl)|$ , can then be deduced, after which the electron density of thin film crystal can be recovered using Fourier transform, via [8],

$$\rho(x,y,z) = \sum_{hkl} |F(hkl)| \cos(2\pi[hx/a + ky/b + lz/c] - \phi_{hkl}) \quad (1)$$

where  $a$ ,  $b$ ,  $c$  are the lattice constants along  $x$ ,  $y$ ,  $z$ , and  $\phi_{hkl}$  is the phase. They are compared with the calculated electron distribution using documented atomic scattering factors. The atomic layer roughness can therefore be quantified from the broadening (flattening) of the electron distribution maxima for silicon and carbon atoms.

The Bragg peak intensities are proportional to the square of the structure factors  $|F(hkl)|^2$ :

$$I(hkl) \propto (1 + \cos^2 2\theta) / 2 \exp(-2M) |F(hkl)|^2 \quad (2)$$

where  $M = B(\sin\theta/\lambda)^2$ , and  $B$  is the thermal Debye parameter measuring the thermal motion.

Figure 2 shows the calculated electron density maps of 3C-SiC and its comparisons with two measured data along the surface normal.  $|F(200-1000)|$  from these two samples can be obtained. To use these  $F(hkl)$  to reconstruct the atomic arrangement via Fourier Transform using Eq. (1), we compare the measured structure factors with the calculated ones for the ideal situation, i.e., when the silicon atoms are sitting on 0, 1/2 and 1, and the carbon atoms are in 1/4 and 3/4 of the relative co-ordinates of the unit cell. In this case, the internal atomic layer arrangement is not distorted and no internal atomic layer roughness is involved. We have

$$F(h00) = \sum_j f_j(\sin\theta/\lambda) \exp(2\pi i h x_j/a) = f_{Si}(\sin\theta/\lambda) + f_C(\sin\theta/\lambda) \exp(2\pi i h/4) \quad (3)$$

where  $f_{Si}(\sin\theta/\lambda)$  and  $f_C(\sin\theta/\lambda)$  are the atomic scattering factors for silicon and carbon atoms, respectively. Following Eq. (1), the 1D electron densities along the film normal can now be constructed using Fourier transform. The resulting experimental and theoretical values of the structure factors are listed as:

	F(200)	F(400)	F(600)	F(800)	F(1000)
Experimental 3C-SiC film (6 $\mu\text{m}$ )	9.54	8.53	2.32	2.01	0.59
Experimental 3C-SiC film (12 $\mu\text{m}$ )	8.38	8.85	2.67	2.41	0.69
Theoretical values of 3C-SiC	5.83	8.49	3.05	4.40	1.19

From the resulting plot (Fig. 2), it is clear that the Si peak is wider for both hetero-epitaxial SiC thin films. This indicates that there is indeed a roughening of the Si-plane within the silicon-carbide layers, although there is an amorphous region in between the thin film and the substrate silicon. The amount of distortion or roughness of the Si planes inside the epitaxial SiC film can be estimated by the increase of the full widths at half maximum (FWHM) of the Si maxima from that of the ideal case. The FWHM of sample 1 is 41% and that of sample 2 is 29%, both of which are larger than that of the theoretical value. This indicates that the distortion of atomic layers or the internal roughness of the individual atomic plane must be less serious for the layers far away from the substrate. Therefore, the averaged internal roughness, which is shown by the X-ray diffraction, becomes smaller when the films are thicker.

These results can be confirmed by the bulk silicon carbide crystals, as well as by the homo-epitaxial silicon carbide thin films, which are provided in Fig.3, and Fig.4. For the bulk 6H-SiC sample, the theoretical prediction is almost identical to the measure the electronic density function

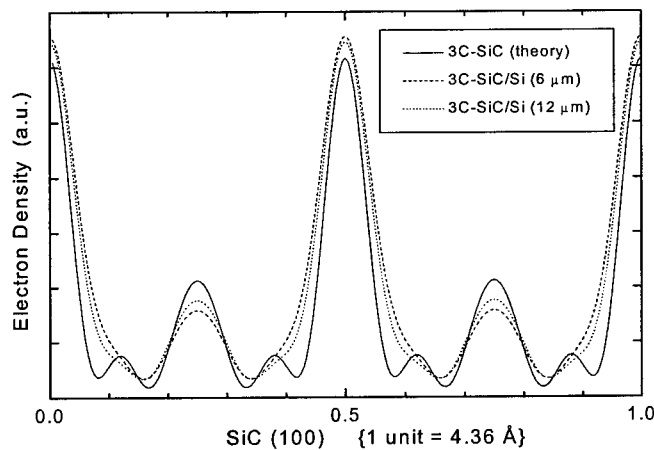


Figure 2. Calculated and measured electron density maps of 3C-SiC along the surface normal.

(Fig. 3), whereas little deviation can be found for the homo-epitaxial 4H-SiC/4H-SiC sample (Fig.4), which has a film of about 6 microns was grown on a single crystal 4H-SiC substrate. It should be noted, however, that in this case there are non-vanishing phases, and they were taken from the calculated values for both curves.

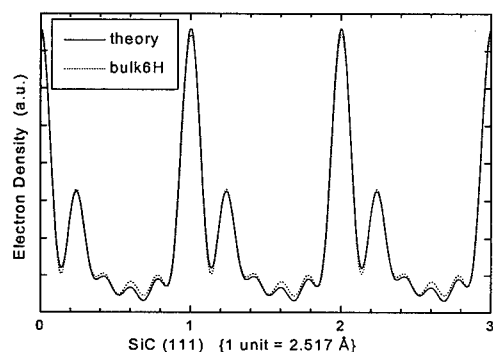


Figure 3. Measured and calculated electron density maps of bulk 6H-SiC.

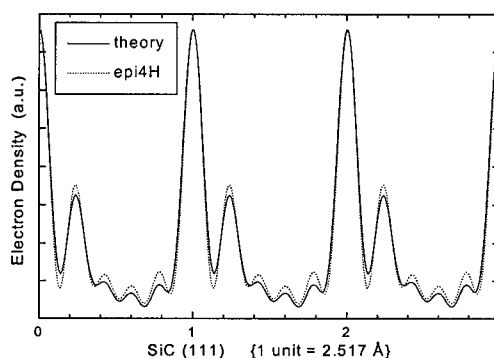


Figure 4. Measured and calculated Electron density of homo-epitaxial 4H-SiC on single crystal 4H-SiC.

#### 4. Conclusion

Through this new method, we have achieved a quantitative characterization of the internal atomic layer roughness and distortion of hetero-epitaxial 3C-SiC and homo-epitaxial 4H-SiC thin films, and bulk 6H-SiC. The electron density distribution has been reconstructed, using short wavelength X-ray to measure high order Bragg reflections. Comparing with the theoretically calculated values from atomic scattering factors, the deviation of the unit cell structure from the ideal case can be identified. It was found that, due to the lattice mis-match, the silicon atoms are no longer fixed on the same atomic plane, thus the corresponding electron distribution maxima were broadened. In the meantime the maxima for carbon atoms are flattened, which indicate that their locations are randomised. By way of the combination of theory and experiment, this study provides a practical and useful method to investigate the other materials and thin film systems.

#### References

- [1] R. F. Davis and J. T. Glass, *Advances in Solid-State Chemistry* **2** (1991), p. 1.
- [2] J. A. Powell, P. Pirouz and W. J. Choyke, in *Semiconductor Interfaces, Microstructures and Devices: Properties and Applications*, ed. Z. C. Feng, Institute of Physics Publishing, Bristol, (1993), p. 257.
- [3] Gary L. Harris ed., *Properties of silicon carbide*, in series of *Electronic Materials Information Service*, IEE (Institute of Electrical Engineers), UK, (1995).
- [4] W. J. Choyke, H. Matsunami and G. Pensel ed., *Fundamental questions and applications of SiC*, in *Phys. Stat. Sol. (a)* Vol. **162**, No.1, and (b) Vol. **202**, No. 1, (1997).
- [5] S. Nishino, J. A. Powell and H. A. Will, *Appl. Phys. Lett.* **42** (1983), p. 460.
- [6] Th. Kunstmann and S. Veprek, *Appl. Phys. Lett.* **67** (1995), p. 3126.
- [7] C. A. Zorman, A. J. Fleischman, A. S. Dewa, M. Mehregany, C. Jacob, S. Nishino and P. Pirouz, *J. Appl. Phys.* **78** (1995), p. 5136.
- [8] B.E. Warren, *X-ray Diffraction*, Addison-Wesley, New York (1969).



## 4H-SiC CVD Epitaxial Layers with Improved Structural Quality Grown on SiC Wafers with Reduced Micropipe Density

E.V. Kalinina<sup>1</sup>, A. Zubrilov<sup>1</sup>, V. Solov'ev<sup>1</sup>, N.I. Kuznetsov<sup>1</sup>, A. Hallen<sup>2</sup>,  
A. Konstantinov<sup>2</sup>, S. Karlsson<sup>2</sup>, S. Rendakova<sup>3</sup> and V. Dmitriev<sup>3</sup>

<sup>1</sup> Ioffe Institute, 26 Polytekhnicheskaya Str., RU-194021 St. Petersburg, Russia

<sup>2</sup> Department of Electronics, KTH Electrum, SE-16440 Kista, Sweden

<sup>3</sup> TDI, Inc., 8660 Dakota Drive, Gaithersburg, MD 20877, USA

**Keywords:** Epitaxy, Micropipe Filling Technique, Micropipes, Schottky Barrier

### Abstract

Reduction of defect densities in SiC epitaxial materials is the key issue for a development of SiC large area devices. We report on improvement of material characteristics and Schottky barrier breakdown voltages for 4H-SiC epitaxial layers grown by chemical vapor deposition (CVD) on 4H-SiC epitaxial wafers with reduced micropipe density (RMD).

Initial substrates were two 4H-SiC 8 degrees off-axis commercial wafers cut from the same boule. Micropipe filling process was performed on one wafer. CVD epitaxial layers 25  $\mu\text{m}$  thick with concentration  $N_{\text{A}}-N_{\text{A}} = (2-4) \times 10^{15} \text{ cm}^{-3}$  were grown on both wafers in the same epitaxial run.

Structural quality of the CVD epitaxial layers was characterized by x-ray diffraction methods, x-ray topography and optical methods. X-ray topography and electron beam induced current (EBIC) technique revealed defect density reduction in the CVD layer grown on RMD epitaxial wafer. Schottky barriers made without edge termination for CVD layer grown on the RMD wafer had a breakdown voltage up to 1500 V while the breakdown voltage for the another sample did not exceed 1000 V.

### Introduction

Recently significant progress has been achieved in the fabrication of silicon carbide power devices [1,2]. However, the area of SiC devices is still much less than 1  $\text{cm}^2$ . A typical area of SiC devices does not exceed a few square millimeters. In order to compete with Si power devices, the operating area of SiC devices has to be increased at least up to 10  $\text{cm}^2$ . Currently the area of SiC devices is limited by high defect density in SiC epitaxial structures. Reduction of defect densities in SiC epitaxial material is the key issue for a development of large area SiC devices.

Micropipe density reduction has been demonstrated by micropipe filling process [3]. Schottky barriers up to 8  $\text{mm}^2$  were fabricated on SiC epitaxial wafers with reduced micropipe density [4]. It has also been demonstrated that SiC epitaxial layers grown on SiC wafers with reduced micropipe density have a much smoother surface than initial SiC wafers after the micropipe filling process [5].

In this paper, we report on material characteristics and Schottky barrier breakdown voltages for 4H-SiC epitaxial layers grown by CVD on 4H-SiC epitaxial wafer with reduced micropipe density.

### Sample preparation and characterization techniques

For these experiments, two wafers cut from the same SiC bulk crystal were used as initial substrates. These substrates were 4H-SiC 8 degrees off-axis commercial wafers (research grade, micropipe density ranged from 30 to 100  $\text{cm}^{-2}$ ) with (0001)Si face polished. X-ray topography performed on these wafers revealed micropipe density of about 30  $\text{cm}^{-2}$  and dislocation density  $> 10^4 \text{ cm}^{-2}$ . In some areas the dislocation density exceeded  $10^5 \text{ cm}^{-2}$ .

One wafer was subject of the micropipe filling process, which resulted in a 4H-SiC epitaxial wafer with reduced micropipe density [1]. This process results in SiC growth inside the micropipe

channels in the initial 4H-SiC wafer. The micropipe density after micropipe filling process was reduced by a few times and did not exceed  $5 \text{ cm}^{-2}$ . Then both 4H-SiC wafers were used as substrates for CVD growth process in the same epitaxial run. The CVD epitaxial layers were  $25 \text{ }\mu\text{m}$  thick.

The structural quality of the CVD layers was characterized by x-ray diffraction methods, x-ray topography and optical methods. The surface of CVD grown layers was studied by optical microscopy and atomic force microscopy (AFM). Photoluminescence measurements were done at 80 K. Concentrations and distributions of electrically active impurities in the samples were determined from capacity-voltage (C-V) characteristics of Cr Schottky barriers at frequencies ranging from 200 Hz to 1 MHz. The scanning electron microscopy technique was used to study surface morphology of grown material and to determine carrier diffusion lengths in the CVD epitaxial layers by EBIC technique.

## Results

Both samples after CVD growth had mirror-like surfaces. Atomic force microscopy showed that surface peak to valley amplitudes for both samples are in the same range despite the fact that after micropipe filling processes severe step bunching was observed [3]. This result is in agreement with the observation [5] stating that surfaces of SiC wafers after the micropipe-filling process may be significantly improved by subsequent CVD growth. However, smooth waves were observed on the surface of the CVD layer grown on the RMD wafer (Fig. 1). Reflectance high-energy electron diffraction measurements showed that for both wafers the surface material is a single crystal with a high degree of perfection. On both samples, sharp clearly seen Kikuchi lines were observed.

X-ray rocking curves for the (0004) reflection measured in  $\omega$ - $2\Theta$ -scanning geometry for both samples were almost of the same width of about 14 arc sec. X-ray topography and EBIC technique revealed defect density reduction in the CVD layer grown on the epitaxial wafer with a reduced micropipe density. The EBIC measurements were performed on 3 mm diameter transparent Schottky barriers. X-ray topography was done for (1128) and (1016) reflections corresponding to the x-ray penetration depth of  $30 \text{ }\mu\text{m}$  and  $10 \text{ }\mu\text{m}$ , respectively. These measurements allowed us to study defects in the substrate and in the CVD layer. It was found that for 4H-SiC CVD layer grown on the RMD substrate, both micropipe and dislocation densities were reduced in comparison with that in the initial wafer (Fig. 2). The EBIC measurements showed that not only the density but also the defect type is different for these samples (Fig. 3). Mechanism of defect reduction is not clear yet and requires further investigation. A detailed study of the defect structure for these samples is under way.

Results of photoluminescence measurements did not show any significant difference for the studied samples. For both CVD grown samples, an intense exciton-related luminescence at photon energy of  $\sim 3.18 \text{ eV}$  was detected. This line was absent in the PL spectra measured for the initial wafers.

Deep level transient spectroscopy (DLTS) performed on Schottky barriers detected a presence of centers with an ionization energy of  $0.65 \text{ eV}$ , which is probably the Z center, with a concentration of  $2 \times 10^{13} \text{ cm}^{-3}$  for the layer grown on the standard substrate and of  $9 \times 10^{12} \text{ cm}^{-3}$  for the sample grown on the RMD wafer.

Schottky barriers  $300 \text{ }\mu\text{m}$  in diameter made without edge termination for the CVD layer grown on RMD wafer had a breakdown voltage up to 1500 V while the breakdown voltage for the CVD layer grown on commercial wafer did not exceed 1000 V. Background donor concentration,  $N_d - N_a$ , measured using C-V characteristics of the Schottky barriers was the same for both samples ( $N_d - N_a \sim 3 \times 10^{15} \text{ cm}^{-3}$ ).

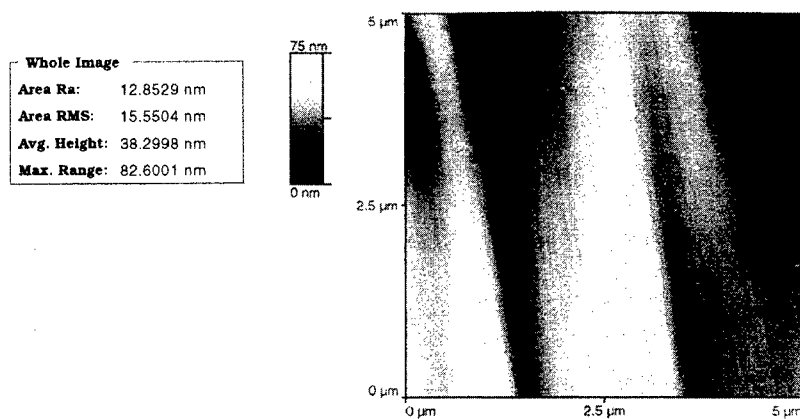
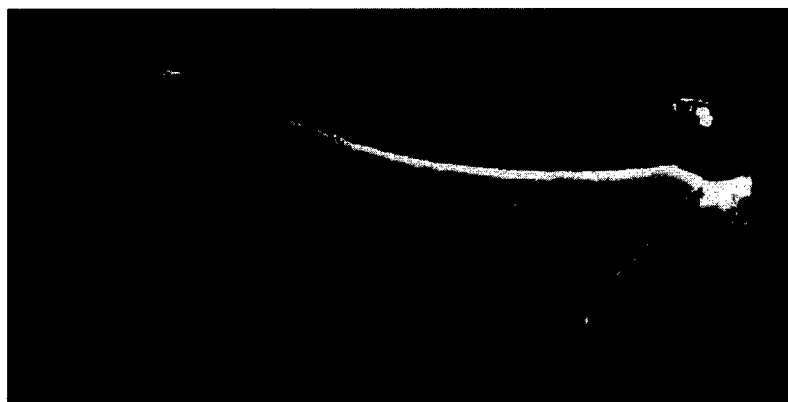


Figure 1. AFM image of 4H-SiC CVD layers grown on RMD wafer.

a



b

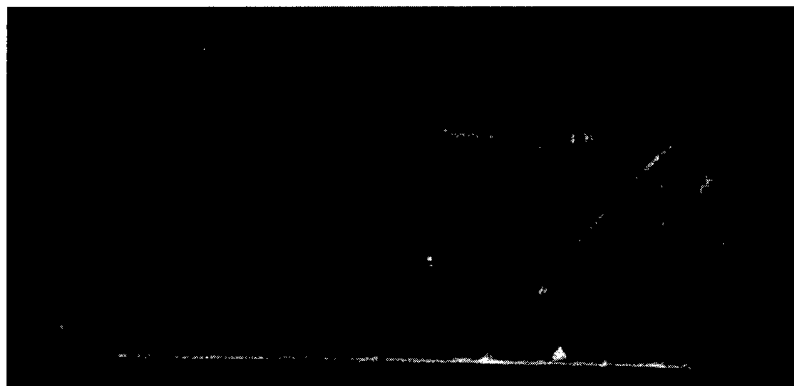


Figure 2. X-ray topographic images of 4H-SiC sample with CVD layer grown on RMD wafer for (1128) reflection (a) and (1016) reflection (b). For the (1128) reflection, x-ray penetration depth is less than CVD layer thickness.

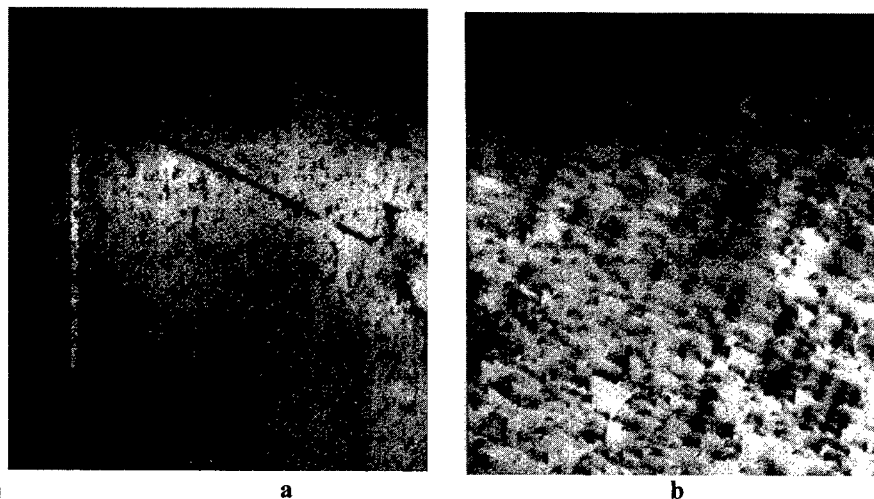


Figure 3. EBIC surface images (x100) measured using transparent Schottky barriers: (a) – layer grown on RMD wafer and (b) – layer grown on standard wafer.

### Conclusion

Defect density reduction was clearly demonstrated for a 4H-SiC epitaxial layer grown by the CVD technique on a 4H-SiC epitaxial wafer with reduced micropipe density.

### Acknowledgments

We would like to thank Gerhard Pensl for valuable discussions, Irina Nikitina for x-ray diffraction measurements, Irina Kotousova for RHEED measurements, James Griffin for AFM measurements, A. Tregubova for x-ray topography study, and Vladimir Ivantsov for his help in this work. This work at Ioffe Institute was supported by ISTC Project No.197-98, and INTAS projects 96-0254 and 98-2141. Research at TDI was supported by Ballistic Missiles Defense/Innovative Science and Technology and managed by the Office of Naval Research (contract manager Colin Wood).

### References

- [1] J.A. Cooper, S-H. Ryu, Y. Li, M. Matin, J. Spitz, D.T. Morisette, H.M. McGlothlin, M.K. Das, M.R. Melloch, M.A. Capano, and J.M. Woodal, *Mat. Res. Soc. Symp. Proc.*, **572** (1999), p. 3.
- [2] S. Seshadri, A.K. Agarwal, W.B. Hall, S.S. Mani, M.F. MacMillan, R. Rodrigues, T. Hanson, S. Khatri, and P.A. Sengen, *Mat. Res. Soc. Symp. Proc.*, **572** (1999), p. 23.
- [3] S. Rendakova, N. Kuznetsov, N. Savkina, M. Rastegaeva, A. Andreev, M. Minbaeva, A. Morozov, and V. Dmitriev, *Mat. Res. Soc. Symp. Proc.*, **512** (1999), p. 131.
- [4] V. Dmitriev, S. Rendakova, N. Kuznetsov, N. Savkina, A. Andreev, M. Rastegaeva, M. Mynbaeva, A. Morozov, *Materials Science and Engineering*, **B61-62** (1999), p. 446.
- [5] S. Sadow, M.S. Mazzola, S.V. Rendakova, V.A. Dmitriev, *Materials Science and Engineering*, **B61-62** (1999), p. 158.

## Structural and Optical Studies of Low-Doped n-6H SiC Layers Grown by Vacuum Sublimation

N.S. Savkina, A.A. Lebedev, A.S. Tregubova and M.P. Scheglov

Ioffe Physico-Technical Institute, Russian Academy of Sciences,  
Polytekhnicheskaya st. 26, RU-194021 St.-Petersburg, Russia

**Keywords:** Dislocation, Optical Microscopy, Pipes, Scanning Electron Microscopy, Vacuum Sublimation Epitaxy, X-Ray Topography

**Abstract.** 6H-SiC epitaxial layers on a substrate with irregular distribution of dislocations with density  $10^4$ - $10^5$  cm<sup>-2</sup> have been grown by vacuum sublimation. X-ray and optical methods have been used to study structural defects in 6H-SiC substrates and epitaxial layers. It is shown that during layer growth the structural perfection is improved as compared with the initial state of the substrate, namely, the dislocation density decreases and fine pores are overgrown. With increasing layer thickness, this process becomes more pronounced.

**Introduction.** The development of modern silicon carbide technologies is due to the promise of this material for semiconductor power electronics. Only large area devices are of practical interest. However, fabricating such devices still encounters difficulties. It is well known that in this case the main limiting factor is the high defect density (micropipes, dislocation) of commercial SiC substrates. Despite substantial recent achievements in this field, the problem of improving the structural perfection of such substrates by growing on them high-quality epitaxial layers remains currently pressing. The possibilities for filling micropipes in commercial SiC substrates with use of liquid phase epitaxy (LPE) were reported in [1,2]. But smooth mirror-like surface of this wafer received only after subsequent sublimation growth of additional epilayer [3]. This communication presents the results obtained in determining the potential of vacuum sublimation epitaxy for improving the structural perfection of the initial substrates.

**Experimental.** A one inch CREE Co. (USA) substrate with dislocation density in the range of  $10^4$ - $10^5$  cm<sup>-2</sup> was chosen for experiments. The substrate was n-type 6H-SiC oriented 3.5° off the (0001) plane. Epitaxial layers were grown on the Si-face of the substrate by vacuum sublimation [4,5] in a vertical water-cooled quartz reactor at a growth temperature of 2000°C. Previously the substrate was divided into several pieces of area ~ 1 cm<sup>2</sup>. 6H-SiC epitaxial layers of n-type conductivity Nd-Na =  $[(2-5) \times 10^{15}]$  cm<sup>-3</sup> of thickness in the range from 2 to 15 μm were grown at the rate of 15 μm/h.

The epilayers were studied by X-ray topography and diffraction analysis and also by optical and scanning electron microscopy (SEM). X-ray topography taken under different geometrical conditions (Lang's method, method of Berg-Barret and method of double-crystal topography) makes it possible to visualize structural defects - dislocations, twins, inclusions, and pores - present in the sample bulk and to determine their type and distribution in relatively large samples. X-ray diffraction analysis allows reliably separating the contribution from near-surface and deeper lying layers owing to different penetration depths for symmetric (000.6), (000.12) and asymmetric (10  $\bar{1}$ .10) Bragg's reflection peaks. In addition, X-ray diffraction analysis enables qualitative analysis of the structural perfection of the samples by measuring the full width at half maximum (FWHM) of reflection curves ( $\omega_0$ ). Optical microscopy was used to visually inspect and register patterns of dislocation etching pits and channels in transmitted and reflected light.

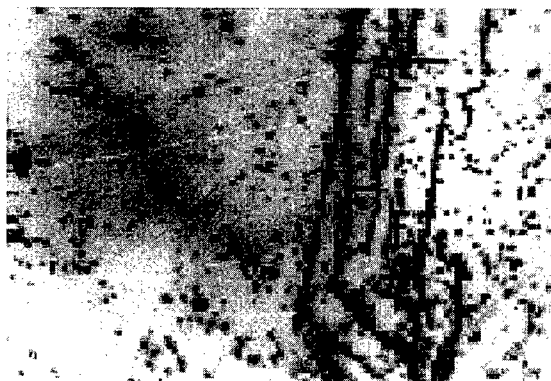


Fig.1. Optical image a Si face fragment of the sample etched in KOH melt with hexagonal pores and shadows corresponding to projections of hollow channels, magnification 80 $\times$ .

semiconductor structures. Among other essential disadvantages, mention should be made of the presence in the substrates of strongly deformed regions causing misorientation of separate parts, accompanied by an increase in dislocation density and irregular distribution of dislocations over substrate area.

Commonly, substrates are etched in a molten alkali for several minutes to reveal structural defects in the sample bulk and obtain high-quality X-ray topographs [6]. In the process, the outcrops of screw dislocations are revealed as hexagonal dislocation etching pits, well visible under an optical microscope. Using sample tilt with respect to the horizontal plane, traces of channels (shadows) were revealed, running away from pit images and visible even at low microscope magnification [Fig. 1]. A more detailed inspection of the sample surface after etching the substrate in molten KOH at 500 $^{\circ}$ C for 1 min was done using a scanning electron microscope [Fig. 2]. Optical patterns corresponded to pore images in topographs, appearing as defects with black core and light halo of asymmetric shape (rosette), which points to their dislocation nature (no adduction here).

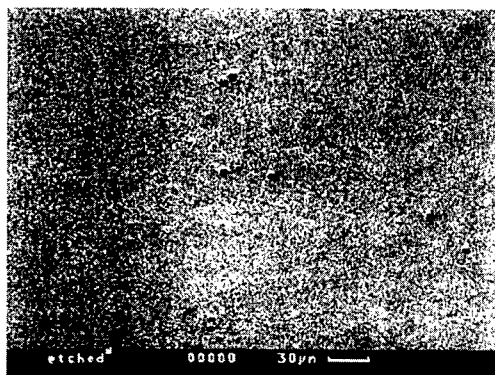


Fig.2. SEM view of the substrate surface after etching in molten KOH at 500 $^{\circ}$ C for 1 min.

Using these mutually complementary methods secures receipt of the most full information about the individual distribution of dislocations and other defects (micro- and macropipes, inclusions, etc.) in substrates and layers without mechanically damaging them. Also this allows one to determine conditions for overgrowing defects during epitaxial growth and to correlate the structural perfection with electrical parameters of the layers.

**Results and discussion.** An important disadvantage of commercial substrates is the presence of a great number of micropipes of various dimensions, having a detrimental effect on characteristics of

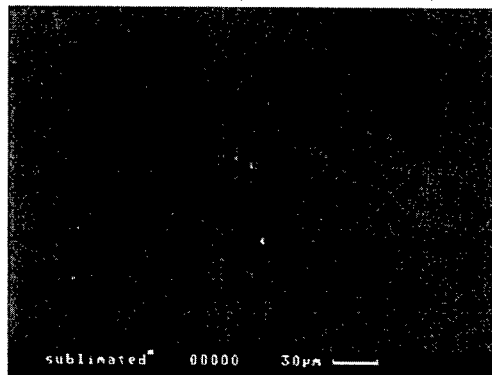


Fig.3. SEM view of the substrate surface after sublimation etching in vacuum for 10 min.

The advantage of the method of sublimation epitaxy over other techniques (CVD, liquid-phase epitaxy) is the possibility of *in situ* polishing. That is why a SEM view of the substrate surface was taken after sublimation etching in a vacuum at 2000 $^{\circ}$ C for 10 min [Fig.3]. The obtained image strongly differs from that in Fig. 2. Dislocation pores with clear-cut faceting are much smaller

(1  $\mu\text{m}$  in diameter at most) and, moreover, their number in the field of vision of the microscope is much smaller at the same magnification. The dislocation nature of these pores was established by comparing the SEM view and an X-ray topograph of the corresponding part of the substrate.

In our technology, sublimation etching is done immediately before layer growth by changing the gradient sign in the growth cell. Consequently, the number of pores that can grow into a layer is substantially reduced already in the first stage of the epitaxial process.

Of much interest was to observe changes in pore size, depending on the layer thickness, on growing epitaxial layers on all parts of the substrate. On Fig.4a presents a SEM view of a deep pore in a layer of thickness  $7\mu\text{m}$ , grown on a substrate preliminarily etched in KOH. The pore has the form of a hexagonal funnel with a deep channel with minimum visible diameter of about  $6\mu\text{m}$ . Minimum diameter of the pore decreased to  $3\mu\text{m}$  [Fig.4b] with the channel partly filled when the layer thickness was increased to  $15\mu\text{m}$ . At present we have no answer to the question as to what substance fills the channel. This will be the subject of further investigations.

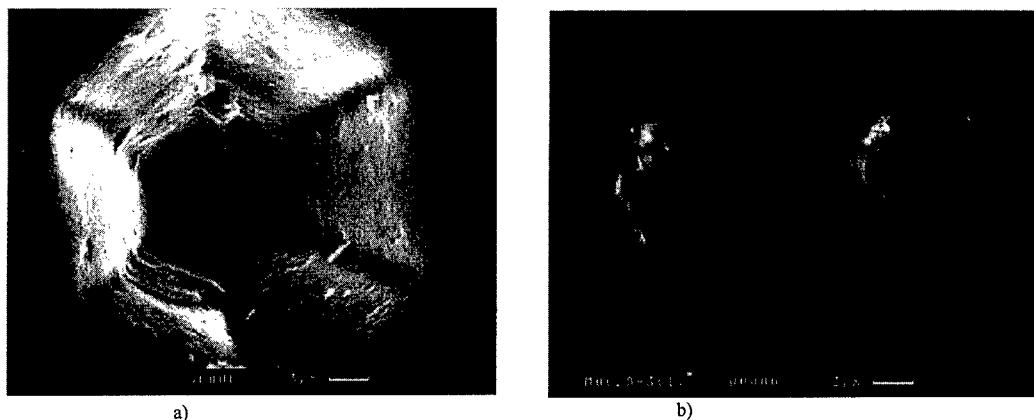


Fig.4. SEM view of hexagonal deep pore after sublimation epilayer growth on the substrate with preliminary etching in KOH melt: a) – epilayer thickness  $7\mu\text{m}$ ; b) – epilayer thickness  $15\mu\text{m}$ .

SEM view of deep pore in a layer grown on 6H-SiC substrate not subjected the preliminary etching in KOH is presented in Fig.5. The channel diameter does not exceed  $0.5\mu\text{m}$ . Consequently, if substrate etching in KOH melt is not necessary (the Si face is already identified and polished and there is no need to reveal defects) then sublimation growth combined with sublimation etching allows substantially reduced size and number of pores growing from the substrate into the epilayer.

X-ray topographs taken on substrates with epilayers demonstrated high quality of the process of layer growth by the vacuum sublimation method. The layers obtained are area-uniform. No new structural defects (dislocations, polytype particles, etc.) are formed during growth. Improved structural perfection was observed for epitaxial layers grown on all parts of the substrate under study. However, irregular distribution of growth defects over the substrate area and the presence of strongly



Fig.5. SEM view deep pore after sublimation growth of epilayer on the substrate without preliminary etching in KOH melt.

distorted regions affect the structural perfection of the epitaxial layers. In regions [A] with uniform distribution of basal dislocations and only isolated fine pores observed [Fig.6a], epitaxial layers have higher structural perfection as compared with the substrates. In these regions the dislocation density is lower and fine pores ( $>1-3\ \mu\text{m}$ ) are overgrown. However, strongly distorted regions [B] affect the quality of epitaxial layers [Fig.6b]. In these regions, large pores ( $>10\ \mu\text{m}$ ) and small-angle boundaries composed of sloping dislocations grow into epitaxial layers, and strong misorientation of one parts with respect to others can be revealed.

Quantitative analysis of the structural perfection of the samples by X-ray diffractometry [7] has shown that for regions with uniform distribution of dislocations the FWHM of rocking curves at  $\omega$ -scan on (0006) reflection decrease from  $18''$ - $21''$  to  $14''$ - $16''$ . In those regions where the initial substrates showed high FWHM ( $40''$ - $60''$ ), these same values were observed after growing a layer. Analysis of the substrate peaks from these regions by triple-crystal diffractometry has shown that large FWHM values are characteristic of bending deformations and weak misorientation of substrate structure fragments.

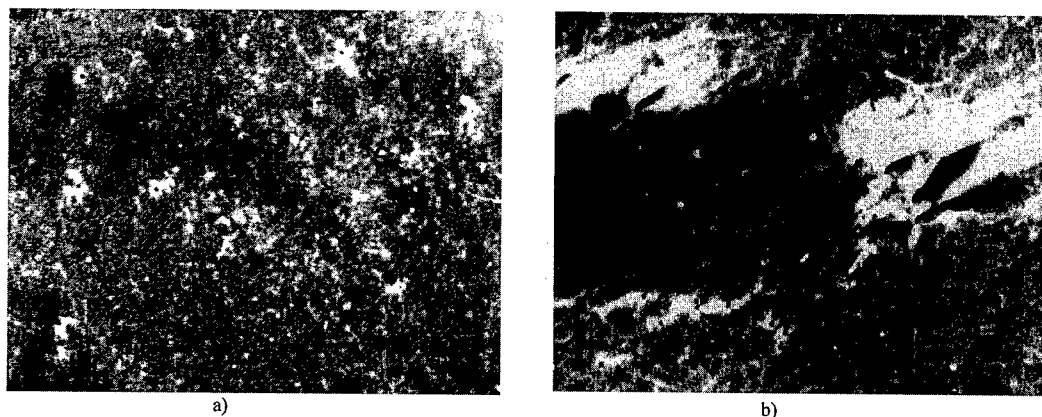


Fig.6. X-ray topographs of the substrate with epitaxial layer, Bragg's reflection 101.10,  $\text{CuK}\alpha$  radiation, magnification  $50\times$ ; a) – region [A] with uniform distribution of basal dislocation and individual pores; b) – strongly distorted region [B] with ensembles of large pores.

**Summary.** Structural defects have been studied in commercial 6H-SiC substrates and epitaxial layers grown by vacuum sublimation. It was established that this technology gives possibility to produce layers of high structural perfection. The potential of the technique was demonstrated in reducing the dislocation density in layers as compared with that in the initial substrate and making smaller the size and number of pores that have grown from the substrate into the layer. Combination of special technological procedures used in growth of epitaxial layers and a detailed analysis of defect distribution in the substrates creates prerequisites for successful use of commercial SiC substrates in semiconductor technology.

#### References.

- [1] R.Yakimova et al, Inst.Phys. Conf. Ser. 142 (1996) 101.
- [2] S.Rendakova et al, Mater.Sci.For, 264-268 (1998) 163-166.
- [3] V.Dmitriev et al, Mater. Sci. Eng. B61-62 (1999) 446-449.
- [4] M.M.Anikin et al, Mater. Sci. Eng. B11 (1992) 113.
- [5] N.S.Savkina et al, Mater. Sci. Eng. B61-62 (1999) 165-167.
- [6] R.Yakimova et al, Diamond and Related Materials 6 (1997) 1456-1458.
- [7] R.N.Kyutt et al, J.Appl.Cryst, 28 (1995) 700-706.



## Stacking Fault Energy of 6H-SiC and 4H-SiC Single Crystals

M.H. Hong, A.V. Samant and P. Pirouz

Department of Materials Science and Engineering, Case Western Reserve University,  
10900 Euclid Ave., Cleveland, OH 44106-7204, USA

**Keywords:** 4H-SiC, 6H-SiC, ANNNI Spin Model, Deformation, Dissociation Width, Stacking Fault Energy

### Abstract

Single crystal 4H and 6H polytypes of SiC have been deformed in compression at 1300 °C. Using two-beam bright-field and weak-beam dark-field techniques of TEM, the stacking fault energy of these two SiC polytypes has been determined to be  $14.7 \pm 2.5 \text{ mJ/m}^2$  (4H-SiC) and  $2.9 \pm 0.6 \text{ mJ/m}^2$  (6H-SiC). The experimental values of stacking fault energy for 4H- and 6H-SiC have been compared with estimates obtained from a generalized axial next-nearest-neighbor Ising (ANNNI) spin model. It is found that the theoretical models predict the lower stacking fault energy of 6H-SiC compared to that of 4H-SiC, and the predicted energies are, respectively, within 5% and 40% of the experimental values.

### Introduction

SiC occurs in many different phases (polytypes) mostly with hexagonal or rhombohedral structure, generally known as  $\alpha$ -SiC, and also a unique cubic phase, with the zincblende structure, known as  $\beta$ -SiC. A number of investigators have studied the mechanical deformation of 6H-SiC single crystals. The results of these studies show that, above ~1100°C, plastic deformation of this material occurs by the activation of the (0001)<11 $\bar{2}$ 0> slip system with the uncorrelated motion of partial dislocations. From the width of partial separations, Maeda *et al.* [1] evaluated the stacking fault (SF) energy of 6H-SiC to be  $2.5 \pm 0.9 \text{ mJ/m}^2$ . In the present paper, we report the results of a transmission electron microscopy (TEM) study of dissociated dislocations in 6H- and 4H-SiC single crystals produced by plastic deformation at 1300°C. To the author's knowledge, there are no reports of the dislocation configuration in deformed 4H-SiC, and on the experimental determination of the SF energy of this polytype. We also use the ANNNI model, as developed by Heine and coworkers [2] to estimate the SF energy of 6H- and 4H-SiC and compare these with the experimentally-determined values.

### Experimental procedures

The 6H and 4H-SiC bulk single crystals used in this study were grown by the modified sublimation technique. Specimens with nominal dimensions  $2 \times 2 \times 4 \text{ mm}^3$  were compressed at 1300°C to a strain of ~4-6%. From the deformed specimens, 0.3 mm thick slices parallel to (0001) were sectioned with a diamond wheel cutter. Subsequently, the slices were ground with emery paper to a thickness of ~100  $\mu\text{m}$ , dimpled to a thickness of ~20  $\mu\text{m}$ , and ion-thinned to electron transparency at a voltage of 5 kV at an angle of ~15°. The thin TEM foils were examined in a Philips CM20 electron microscope operating at an accelerating voltage of 200 kV.

### Results and discussion

Figure 1 is a typical example of the dislocations produced in a 6H-SiC single crystal specimen deformed to a normal strain of 2.4% at 1300°C at a strain rate of  $6.3 \times 10^{-5} \text{ s}^{-1}$ . The Burgers vector of dislocation segments denoted by A and B were determined using the standard  $\mathbf{g} \cdot \mathbf{b} = 0$  invisibility criterion. Dislocation A is out of contrast with reflection  $\mathbf{g} = 2\bar{1}10$  [Fig. 1(b)]. This indicates that A is a partial dislocation with a Burgers vector  $\mathbf{b}_A = 1/3 [01\bar{1}0]$ . On the other hand, dislocation B is out of contrast with  $\mathbf{g} = \bar{1}210$  [Fig. 1(c)]. This indicates that the Burgers vector of dislocation B is  $\mathbf{b}_B = 1/3 [10\bar{1}0]$ . Figure 1(d) shows a dark-field micrograph of the dislocation configuration in the same region taken with  $\mathbf{g} = [\bar{1}01\bar{1}]$  near the  $[\bar{1}012]$  zone axis. It clearly shows the stacking fault contrast between the two partials that lie on the same basal plane confirming that A and B are the two partials of the same dissociated  $\mathbf{b} = 1/3 [11\bar{2}0]$  dislocation. Similar micrographs from other dislocation segments in this specimen confirmed that all the dislocations observed in the deformed 6H-SiC sample are indeed partial dislocation pairs of dissociated  $\mathbf{b} = 1/3 \langle 11\bar{2}0 \rangle$  dislocations.

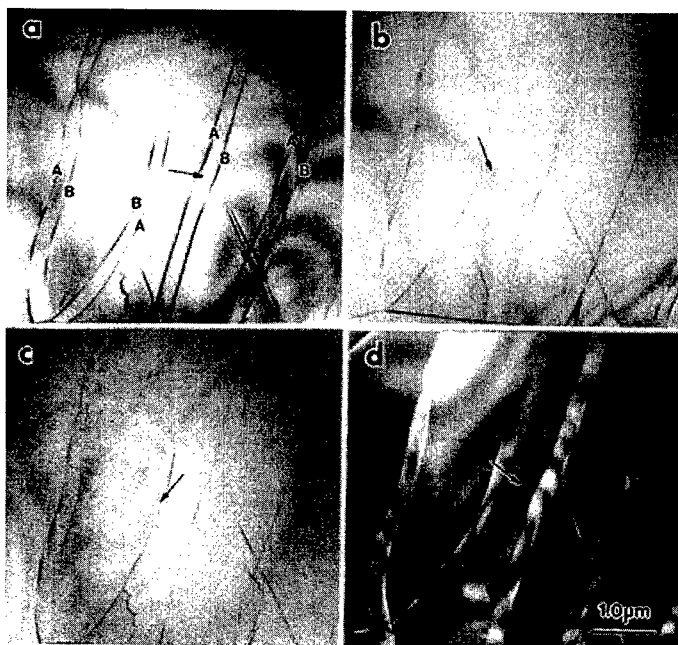


Fig. 1 Dissociated dislocations in 6H-SiC introduced by compression at 1300 °C.

The stacking fault energy,  $\gamma$ , of a dissociated dislocation segment can be obtained by balancing it to the sum of the self energies of the two partials plus their interaction energy. For an anisotropic hexagonal structure,  $\gamma$  is related to the separation distance,  $d$ , of the two partials of a dissociated dislocation by the following equation [3]:

$$\gamma = \frac{b^2}{24\pi\delta} \left\{ (3\sin^2 \phi - \cos^2 \phi) K_1 + (3\cos^2 \phi - \sin^2 \phi) K_3 \right\} \quad (1)$$

where  $b=|\mathbf{b}|$  is the magnitude of the Burgers vector of the perfect dislocation,  $\phi$  is the angle between the Burgers vector and dislocation line, and  $K_1$  and  $K_3$  are the energy factors calculated from elastic constants.

As expected, the separation distance,  $\delta$ , of the dissociated dislocations in 6H-SiC is much larger than in other tetrahedrally coordinated semiconductors. Using Eq. 1, the stacking fault energy of 6H-SiC was calculated to be  $2.9 \pm 0.6 \text{ mJ/m}^2$ .

The stacking fault energy of 4H-SiC was estimated from the minimum radius of extended nodes produced by the deformation process ( $\epsilon=4.2\%$ ,  $T=1300^\circ\text{C}$ ,  $\dot{\epsilon}=3.0 \times 10^{-5} \text{ s}^{-1}$ ). Such an extended node, consisting of dislocation arms A, B and C, is shown in the weak-beam image of Fig. 2. The Burgers vectors of the three arms were determined by the standard  $\mathbf{g} \cdot \mathbf{b} = 0$  invisibility criterion. Dislocation A is out of contrast with  $\mathbf{g} = \bar{1}\bar{1}20$  [Fig. 2(c)]. This indicates that segment A is a partial dislocation with a Burgers vector  $\mathbf{b}_A = 1/3[\bar{1}\bar{1}00]$ . On the other hand, dislocations B and C are out of contrast with  $\mathbf{g} = 2\bar{1}\bar{1}0$  [Fig. 2(b)] and  $\mathbf{g} = \bar{1}2\bar{1}0$  [Fig. 2(a)], respectively. Thus, the Burgers vector of dislocations B and C is  $\mathbf{b}_B = 1/3[0\bar{1}\bar{1}0]$  and  $\mathbf{b}_C = 1/3[10\bar{1}0]$ , respectively. Figure 2(d) shows the node imaged with the reflection  $\mathbf{g} = \bar{1}0\bar{1}\bar{1}$  near the  $[\bar{1}012]$  zone axis. Similar to the case of 6H-SiC in Fig. 1(d), the stacking fault contrast within the extended dislocation node ABC is in contrast, confirming that all the three partials lie on the same (0001) basal plane.

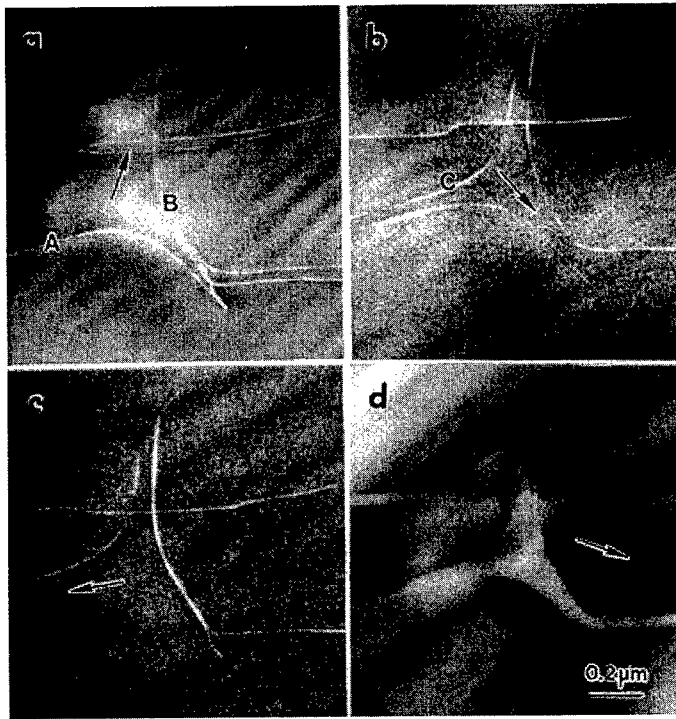


Fig. 2 Micrographs of an extended node in 4H-SiC introduced by compression at  $1300^\circ\text{C}$ .

According to Brown and Tholen [4], the minimum radius of an extended dislocation node is given by:

$$\frac{\gamma w}{\mu b_p^2} = 0.055 \left( \frac{2-\nu}{1-\nu} \right) - 0.06 \left[ \frac{\nu}{(1-\nu)^2} \right] \cos 2\alpha + \left[ 0.018 \left( \frac{2-\nu}{1-\nu} \right) + 0.036 \left( \frac{\nu}{1-\nu} \right) \cos 2\alpha \right] \log_{10}(\rho / \epsilon) \quad (2)$$

where  $\mu$  is the shear modulus,  $b_p$  is the length of the partial dislocation Burgers vector,  $w$  is the radius of the inscribed circle in the node,  $\nu$  is Poisson's ratio,  $\alpha$  is the character of the partial at the midpoint of the node,  $\rho$  is the loop radius and  $\epsilon$  is the cut-off radius taken to be equal to  $b_p$ . Using this equation, and the elastic coefficients of Lambrecht *et al.* [5], the node radius gives a value of  $\gamma=12.2\pm1.1$  mJ/m<sup>2</sup>. Additional measurements from partial separations showed that the stacking fault energy of 4H-SiC is  $\gamma_{4H}=14.7\pm2.5$  mJ/m<sup>2</sup>. Note that the SF energy of 4H-SiC is nearly 4-5 times larger than that of 6H-SiC ( $=2.9\pm0.6$  mJ/m<sup>2</sup>).

The SF energy per SiC layer can be written as [6]:

$$\gamma = \frac{\Delta E}{A} = \frac{E(\text{faulted}) - E(\text{perfect})}{A} \quad (3)$$

where  $A$  is the area per atom in the (0001) plane.

The energy of a crystal of  $n$  layers is calculated from the following equation (see Ref. [2]):

$$nE = nE_0 - \sum_{i=1}^n \sum_{j=1}^{\infty} J_j \sigma_i \sigma_{i+j} \quad (4)$$

Calculation results show that  $\gamma_{4H}$  is proportional to  $J_2$ , the interaction between fourth-nearest neighbor bonds, while  $\gamma_{6H}$  is proportional to  $J_3$ , the interaction between sixth-nearest neighbor bonds. Using the interaction parameters of Limpijumnong and Lambrecht [7], we obtain  $\gamma_{4H}=20.035$  mJ/m<sup>2</sup> (4H) and  $\gamma_{6H}=2.759$  mJ/m<sup>2</sup> (6H), respectively. The reason that  $\gamma_{4H}$  is larger than  $\gamma_{6H}$  is that  $J_2$  is a shorter range interaction than  $J_3$ . This is consistent with the experimental results ( $\gamma_{4H}=14.7\pm2.5$  mJ/m<sup>2</sup> vs.  $\gamma_{6H}=2.9\pm0.6$  mJ/m<sup>2</sup>); the theoretically estimated values differ from the experimental values by ~5% (6H) and ~40% (4H).

### Acknowledgements

Support of this work by grant number FG02-93ER45496 from the Department of Energy, and subcontract number 95-SPI-420757-CWRU from the Silicon Carbide consortium is gratefully acknowledged.

### References

- [1] K. Maeda, K. Suzuki, S. Fujita, M. Ichihara and S. Hyodo, *Phil. Mag. A*, **57** (1988), p. 573.
- [2] V. Heine, C. Cheng, G. E. Engel and R. J. Needs, *The Origin of Polytypes in SiC and ZnS*, In *Wide Band Gap Semiconductors*, edited by T. D. Moustakas, J. I. Pankove and Y. Hamakawa, **242** (1992), p. 507, (Pittsburgh, PA: Materials Research Society).
- [3] J. W. Steeds, *Introduction to Anisotropic Elasticity Theory of Dislocations* (Oxford: Clarendon Press), 1973.
- [4] L. M. Brown and A. R. Thölen, *Disc. Faraday Soc.*, **38** (1964), p. 35.
- [5] W. R. L. Lambrecht, B. Segall, M. Methfessel and M. van Schilfgaarde, *Phys. Rev. B*, **44** (1991), p. 3685.
- [6] P. Käckell, J. Furthmüller and F. Bechstedt, *Phys. Rev. B*, **58** (1998), p. 1326.
- [7] S. Limpijumnong and W. R. L. Lambrecht, *Phys. Rev. B*, **57** (1998), p. 12017.

## Deformation Tests on 4H-SiC Single Crystals between 900°C and 1360°C and the Microstructure of the Deformed Samples

J.L. Demenet<sup>1,2</sup>, M.H. Hong<sup>1</sup> and P. Pirouz<sup>1</sup>

<sup>1</sup>Department of Materials Science and Engineering, Case Western Reserve University,  
10900 Euclid Ave., Cleveland, OH 44106-7204, USA

<sup>2</sup>permanent address: UMR 6630 CNRS, SP2MI, Bd 3, Laboratoire de Métallurgie Physique,  
Teleport 2, BP 179, FR-86960 Futuroscope Cedex, France

**Keywords:** 4H-SiC, Partial Dislocation, Perfect Dislocation, Plasticity, Yield Stress

**Abstract** Bulk single crystals of 4H-SiC have been deformed in compression at low strain rates in the temperature range 900°C-1360°C and their microstructures have been observed by TEM. Results of mechanical tests show that the variation of the yield stress as a function of temperature is not monotonous but decreases strongly for  $T > 1100^\circ\text{C}$ . It is observed that deformation proceeds by leading Si(g) partials at  $T < 1000^\circ\text{C}$ , total dislocations at  $T > 1200^\circ\text{C}$  and mixture of leading Si(g) partials and total dislocations between 1050°C and 1150°C.

### Introduction

The availability of almost defect-free single crystals of SiC with relatively large dimensions has made it possible to study the bulk plasticity of this material. This coincides with a renewal of interest in the field of plasticity of semiconducting materials, something that is primarily promoted by new measurements of the yield stress ( $\tau_y$ ) as a function of temperature in several III-V compounds (InP, GaAs, InSe) [1,2]. In fact, a plot of  $\ln(\tau_y)$  versus  $1/T$  shows two straight lines with different slopes. The intersection of these lines occurs at a critical temperature  $T_c$  which is assumed to correspond to a change of deformation mechanism. Similar results were found in the wide bandgap semiconductors 4H-SiC and 6H-SiC, deformed at a constant (slow) strain rate ( $3.1 \times 10^{-5} \text{ s}^{-1}$ ) [3]. The critical temperature  $T_c$  seems to be close to  $1100^\circ\text{C}$  for both materials, but the number of experiments at  $T > 1100^\circ\text{C}$  was not enough to determine the critical temperature accurately. The aim of the present study is to deform the 4H-SiC single crystals between  $900^\circ\text{C}$  and  $1360^\circ\text{C}$  in order to obtain accurate data for  $\tau_y$  in this temperature range. The microstructure of deformed samples was investigated by transmission electron microscopy (TEM).

### Experimental procedure

The 4H-SiC bulk single crystal was provided by Cree Research Inc. (Durham, North Carolina, USA) and was grown by a modified sublimation technique. The nitrogen content was  $\approx 2 \times 10^{18} \text{ cm}^{-3}$ . Samples with nominal dimensions  $\approx 2.2 \times 2.2 \times 4.7 \text{ mm}^3$  were prepared from this crystal and oriented by the X-ray Laue back-reflection technique such that their basal plane was at  $45^\circ$  to the compression axis. Each specimen thus had the optimal orientation for maximum resolved shear stress (i.e. Schmid factor,  $S=0.5$ ) for one of the three independent  $\langle 2\bar{1}\bar{1}0 \rangle (0001)$  primary slip systems. After cutting, all the faces of each specimen were ground using a  $20 \mu\text{m}$  diamond-impregnated disc followed by a  $9 \mu\text{m}$  and  $3 \mu\text{m}$  diamond polish. The samples were tested using a MTS machine equipped with an electromechanical actuator, in a specially machined polycrystalline SiC jig. Tests were conducted at temperatures between  $900^\circ\text{C}$  and  $1360^\circ\text{C}$ , in an inert atmosphere

of ultra-high purity argon gas, at the initial strain rate of  $3.6 \times 10^{-5} \text{ s}^{-1}$ . From the deformed samples (plastic strain  $\epsilon \approx 1.5\%$ ), 0.3 mm thick slices parallel to (0001) plane were cut with a diamond saw. Subsequently, the slices were ground with emery paper followed by a  $3 \mu\text{m}$  and  $1 \mu\text{m}$  diamond polish to a thickness of  $\approx 100 \mu\text{m}$ , dimpled to a thickness of  $\approx 20 \mu\text{m}$ , and ion-milled to electron transparency. The thin TEM foils were examined in a Philips CM20 electron microscope at an accelerating voltage of 200 kV.

### Results and Discussion

Fig. 1 shows the variation of the critical resolved shear stress or yield stress ( $\tau_y$ ) as a function of deformation temperature. The value of  $\tau_y$  was assumed to be the stress value at the onset of non-linearity after the elastic region of the engineering stress-strain curve, multiplied by the Schmid factor ( $S=0.5$ ), assuming that slip occurred on the  $\langle 2\bar{1}\bar{1}0 \rangle(0001)$  primary slip system. Error bars indicate the accuracy in determination of the onset of non-linearity. It must be noted that, in the lower stress regions of deformation curves, irregularities have been sometimes observed, in spite of the precautions taken in the experimental procedure. Stress-strain curves are not straight and show zig-zags. The more surprising is that this occurs at high temperature, in the temperature range where the samples are assumed to be ductile. The same events have been already pointed out in Ref. [3]. Currently, no explanation can be given to this behaviour.

As shown in Fig. 1, the lower the temperature, the higher the  $\tau_y$  value, indicating that, as in other semiconducting materials, deformation of 4H-SiC is a thermally activated process. At the strain rate used in this study, it was difficult to obtain plastic deformation below  $\approx 1000^\circ\text{C}$  without some fracture occurring in the samples. This means that the actual values of  $\tau_y$  below this temperature are probably a little higher than those indicated in Fig. 1. However, at  $T \geq 1100^\circ\text{C}$ , significant plastic deformation, more than 1%, could be achieved.

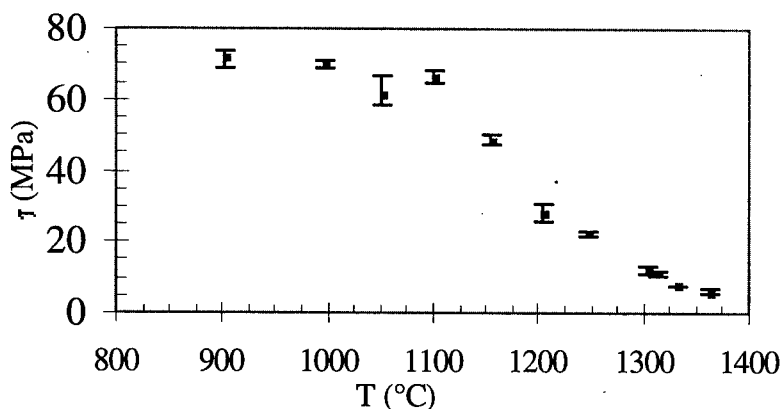


Fig. 1. Variation of the yield stress ( $\tau_y$ ) versus temperature (T).

One way to represent the variation of the yield stress of semiconductors with respect to temperature is to plot  $\ln(\tau_y)$  versus  $1/T$ , as suggested by the kink-diffusion model. The activation energy for the glide of dislocations responsible for crystal deformation ( $Q$ ) is assumed to be independent of stress ( $\tau_y$ ), and the stress-dependence of the plastic strain rate ( $\dot{\gamma}$ ) is introduced in a pre-exponential term as,

$$\dot{\gamma} = A\tau_y^n \exp(-Q/kT), \quad \text{Eq. 1}$$

where A is a constant and n is the stress exponent.

Fig. 2 is the plot obtained from present experiments. The variation of  $\ln(\tau_y)$  can be described by two straight lines, with a break around 1100°C. In a previous study on 4H-SiC from Northrop-Grumman deformed at  $3.1 \times 10^{-5} \text{ s}^{-1}$  [3,4], this break was suspected, but the number of experiments (five experiments at 600-700-900-1100 and 1300°C), especially those at  $T > 1100^\circ\text{C}$ , was not enough to assert it unambiguously. From Fig. 2, variations of  $\ln(\tau_y)$  versus  $1/T$  between 1100 and 1360°C can be described by a line with a slope  $Q/n = 1.8 \text{ eV}$ , with an estimated accuracy of 0.2 eV. Below 1100°C, the slope of  $\ln(\tau_y)$  versus  $1/T$  is difficult to determine with good accuracy due to the occurrence of microcracks in the deformed samples, and also the restricted temperature range explored. In contrast, in the previous study, reported in Refs. [3, 4], the slope was estimated to be  $Q/n = 0.7 \pm 0.3 \text{ eV}$  between 600 and 1100°C.

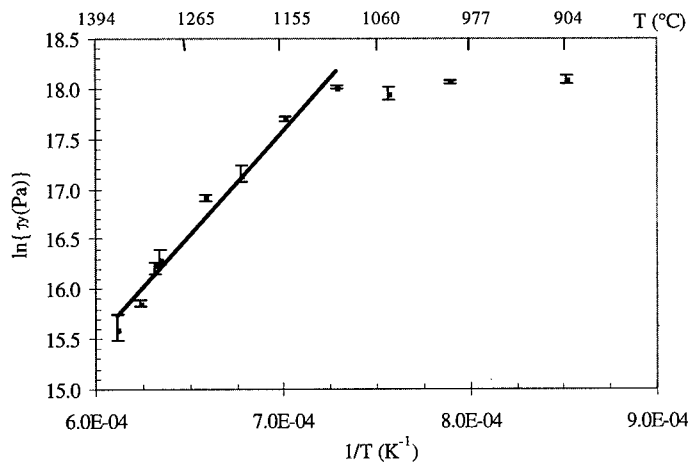
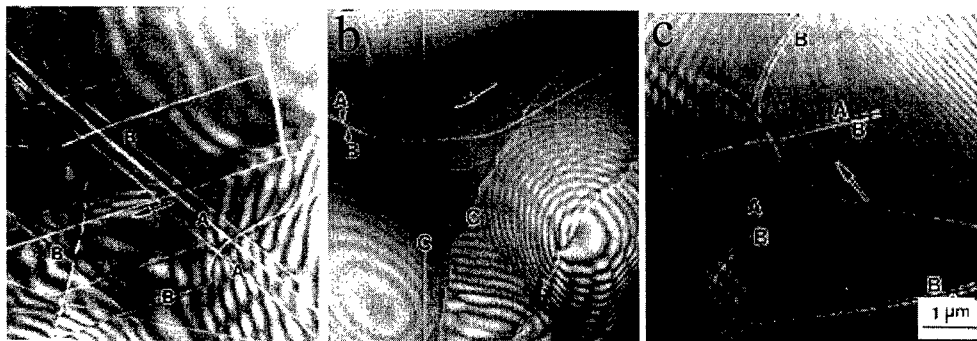


Fig. 2.  $\ln(\tau_y)$  versus  $1/T$ .

Fig. 3 shows the weak-beam TEM micrograph of 4H-SiC deformed at (a) 1000°C, (b) 1100°C and (c) 1360°C. All micrographs are observed with the electron beam close to the [0001] direction. Below 1000°C, dislocations are relatively linear compared with those at the higher temperature. Combining the  $\mathbf{g} \cdot \mathbf{b}$  contrast experiments with large angle convergent beam electron diffraction (LACBED) shows all the dislocations to be leading single partial with a silicon core, without the associated trailing partials. The Burgers vector of dislocations is parallel to the  $\langle 1100 \rangle$  directions. Between 1050-1150°C, as shown in Fig. 3(b), the microstructure consists of perfect dislocation (denoted by A and B) and single leading partials (denoted by C). This indicates that deformation of the 4H-SiC at this temperature range proceeds by nucleation and glide of two different types of dislocations: single leading Si(g) partials as well as total dislocations. Above 1200°C however, as shown in Fig. 3(c), the microstructure consists of dissociated dislocation comprised of leading/trailing partial pairs, as denoted by the two partials A and B. Tilting experiments near the  $[1012]$  zone axis clearly show a ribbon of intrinsic stacking fault between the leading and trailing partial dislocations. It has already been argued in Ref. [4] that there are two competing mechanisms for generating the dislocations in deformed semiconductor materials. Thus,

at higher temperatures, thermal activation is sufficient to form the trailing partials with the higher activation energy and plastic deformation proceeds by the glide of total dislocations. In contrast, in the samples deformed below 1000 °C, where the only leading partial dislocations can be nucleated without corresponding trailing partials, the crystal will be not ductile and small strains are obtained in compression. From the above results, it is interesting to note that in the temperature between 1050-1150 °C deformation proceeds by the nucleation of single leading Si(g) partials as well as total dislocations. The transition occurs in the deformation microstructure from the leading partial to total dislocations is well correlated to the variation of  $\ln(\tau_y)$  (Fig.1) around 1100 °C. In order to determine the stress exponent  $n$  and the activation energy  $Q$  below and above 1100 °C accurately, deformation experiment, as strain rate jumps, are in progress. In addition, other experiments at lower strain rate are planned to investigate the influence of these parameters on the transition temperature.



**Fig.3.** Weak-beam TEM microstructure of 4H-SiC deformed at (a)1000 °C, (b)1100 °C and (c) 1360 °C.

#### Acknowledgements

The authors wish to thank Dr. Calvin Carter of Cree Research Inc. for providing the bulk 4H-SiC used in this study. One of the authors (JLD) would like to thank the staff of the Department of Materials Science and Engineering at Case Western Reserve University who made his two months stay fruitful and pleasant.

#### References

- [1] T. Suzuki, T. Nishisako, T. Taru, and T. Yasutomi, *Phil. Mag. Lett.* **77** (1998), p.173.
- [2] T. Suzuki, T. Yasutomi, T. Tosukuoka, and I. Yonenaga, *phys. stat. sol. (a)* **171** (1999), p. 47.
- [3] A. V. Samant, Ph. D. thesis, Case Western Reserve University (1999).
- [4] P. Pirouz, A. V. Samant, M.H. Hong, A. Moulin, and L. P. Kubin, *J. Mater. Res.* **14** (1999), p. 2783.



## Void Shapes in the Si (111) Substrate at the Heteroepitaxial Thin Film / Si Interface

J. Jinschek, U. Kaiser and W. Richter

Institut für Festkörperphysik, Friedrich Schiller Universität Jena,  
Max-Wien-Platz 1, DE-07743 Jena, Germany

**Keywords:** Interface, MBE Growth, Si Outdiffusion, TEM, Void

**Abstract:** Transmission electron microscopy (TEM) images of 3C-SiC thin films on Si (111) grown by solid-source molecular beam epitaxy (MBE) often reveal interfacial voids just underneath the film because of the Si outdiffusion from the substrate into the layer. The same phenomenon can be seen in the 2H-AlN thin film / Si (111) heterosystem grown by plasma-assisted MBE. We demonstrate in both cases the influence of growth parameters on the created voids. In the SiC/Si system we show an important influence of the growth temperature. At 850°C a well-known triangular void is formed, whereas at 1050°C we found an unusual hexagonal void shape. In this case not only low surface energy {111} facets form the void shape, but also facets with higher surface energy. We discuss this new appearance as a void shape which is near the equilibrium void shape in a cubic crystal. In the AlN/Si heterosystem the initial covering of the substrate has an influence on the amount of the Si outdiffusion and therefore on the size of the voids. In samples with an initial nitrogen cover the Si content in the AlN layer is higher ( $\sim 10^{21} \text{ cm}^{-3}$ ) and the voids are more larger compared to samples with an initial Al cover (Si content  $\sim 10^{18} \text{ cm}^{-3}$ ).

### 1. Introduction

Silicon carbide (SiC) is a leading wide-band-gap semiconducting material with unique thermal, electronical and physical properties which make it suitably for high power, high temperature and high frequency devices [1]. Aluminium nitride (AlN) is a wide-band-gap III-V compound with desirable thermal conductivity, chemical and thermal stability, electrical resistivity, and acoustical properties. Therefore it can be a promising material for applications in microelectronic and optoelectronic devices such as passivation and dielectric layers in integrated circuits, short wavelength emitters, high frequency surface acoustic wave (SAW) devices [2], and also as a template substrate for epitaxial group III nitride layers [3]. The heteroepitaxial growth of cubic (3C) SiC thin films on Si and the growth of hexagonal (2H) AlN thin films on Si is a challenging task due to the large mismatches in lattice constants ( $\sim 20\%$ ) and thermal expansion coefficients but the deposition allows to integrate the SiC and the nitride technology into the mature Si technology.

In the heteroepitaxy of these two materials on Si one of the problems is the Si outdiffusion from the substrate into the layer during the film growth process. That can lead to a formation of voids at the film/substrate interface just beneath the film [4,5,6]. This poses a great problem in device applications requiring an excellent interface such as the wide-band-gap emitter SiC/Si heterobipolar transistor (HBT) [7]. First the void creation has to be understood before it can be avoided.

In SiC/Si(111) it is known [8] that the interfacial voids are formed by coalescence of Si vacancies which result from the Si outdiffusion into the growing SiC film. The void shape in a Si(111) substrate is always described as reverse truncated trigonal pyramid [9], mainly faceted by {111}. We found an unusual hexagonal shape of the voids [10] which have not been reported so far.

In the AlN/Si(111) heterosystem an outdiffusion of the Si also takes place from the film/substrate interface into the layer and leads under special conditions to a void creation [5,6]. There should be the same void creation process as described in the SiC/Si case because the Si outdiffusion as the reason is similar. To the best of our knowledge we found no description about the interfacial voids in the AlN/Si(111) case in the literature.

In this work we show by transmission electron microscopy (TEM) studies that the appearance of the interfacial voids is influenced in both cases by special film growth parameters. In the 3C-SiC/Si heterosystem, deposited by solid-source MBE, we compare the influence of the substrate temperature (850°C (for more details see [11]) and 1050°C (for more details see [12]) on the resulting void shape. We discuss the appearance of void facets with higher surface energy than Si{111}. In the 2H-AlN/Si heterosystem, deposited by plasma-assisted MBE [13], we compare the influence of the initial process (Al cover or nitridation) on the Si substrate during the film growth. We discuss how the initial process has an influence on the Si content in the grown AlN film and therefore on the size of the created interfacial voids.

## 2. Results

### 2.1. SiC/Si(111) heteroepitaxial system

#### 2.1.1 Triangular void shape at 850°C substrate temperature

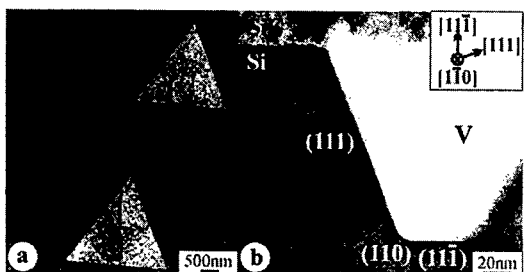


**Figure 1** (a) Plan-view bright-field TEM image, obtained in the [111] zone of Si, and (b) high-resolution cross-sectional bright-field TEM image, viewing along the [1-10] zone axis of Si, showing the shape of an interfacial triangular void

Figure 1 shows TEM images of an interfacial void in a SiC thin film specimen grown at 850°C substrate temperature on Si (111). In the plan-view TEM image (Fig. 1a) the exact void shape as a triangular is seen. This is formed by the energetically favourable {111} planes in the Si substrate showing the typical angle of 70.53° between them. The cross-sectional HRTEM image in the [1-10] zone (Fig. 1b) shows a {110} facet between the {111} planes. Although they have a higher surface energy [14], their occurrence reduces the surface area and the entire surface energy of the void [10].

#### 2.1.2 Hexagonal void shape at 1050°C substrate temperature

**Figure 2** (a) Plan-view bright-field TEM image, obtained in the [111] zone of Si, and (b) high-resolution cross-sectional bright-field TEM image (zone axis close to the [1-10] of Si) showing the shape of an interfacial hexagonal void

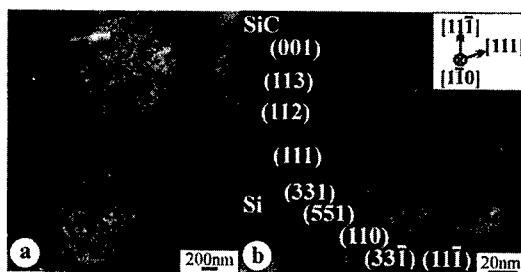
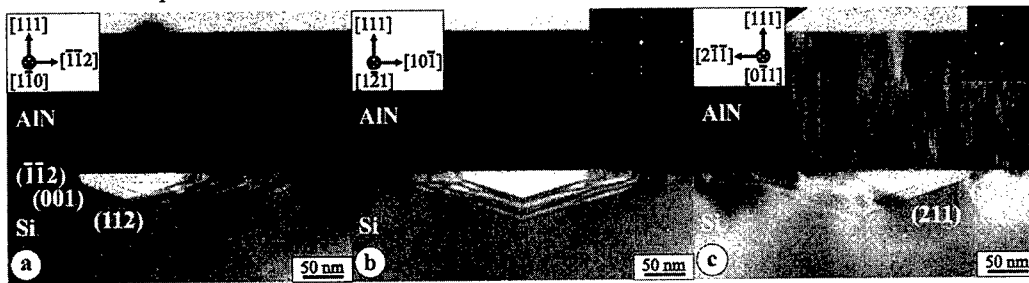


Figure 2 shows an unusual void shape in a SiC specimen grown at 1050°C substrate temperature on Si (111). The modification to the hexagonal void is possible to see in the plan-view TEM image (Fig. 2a). There are truncations of the corners compared to the regular shape of a hexagon. All facets of the hexagonal void are indexed in the cross-sectional HRTEM image (Fig. 2b). In addition to

facets of a triangular void ( $\{111\}$ ,  $\{110\}$ ), other facets (see indexes in Fig. 2b) with higher surface energies [14] are formed. Their appearance can be explained due to the higher substrate temperature during the growth [10].

## 2.2 AlN/Si(111) heteroepitaxial system

### 2.2.1 Voids in specimens with initial nitridation



**Figure 3** Cross-sectional bright-field TEM images of the same void in different zone axes of Si (tilted perpendicular to the  $[111]$  Si axis), (a) and (c) show two  $\langle 110 \rangle$  zones ( $[1-10]$  and  $[0-11]$ , tilt of  $60^\circ$ ) and (b) shows the  $[1-21]$  zone which is exactly between them ( $30^\circ$ )

The cross-sectional TEM images in Figure 3 show the same void in  $[1-10]$  (a), in  $[1-21]$  (b), and in  $[0-11]$  respectively zone axis orientation at the interface in a AlN/Si(111) system. The layer was grown under initial nitridation of the Si substrate. The void is relatively elongated along the interface underneath the layer. The main facets are the Si  $\{112\}$  planes which could be indexed in the different Si  $\langle 110 \rangle$  zone axes (see Fig. 3a,c). A small truncation at  $\{100\}$  planes is seen.

### 2.2.2 Voids in specimens with an initial aluminium cover

**Figure 4** Cross-sectional TEM images of the same void in different zone axes of Si (tilted perpendicular to the  $[111]$  Si axis), (a) at  $[1-10]$  zone and (b) at  $[1-21]$  zone axis orientation (tilt of  $30^\circ$  between them), (c) showing the void edge (arrowed in (a)). Note the bright contrast along the AlN/Si interface starting at a defect (arrowed) and ending at the void edge (right-hand side)

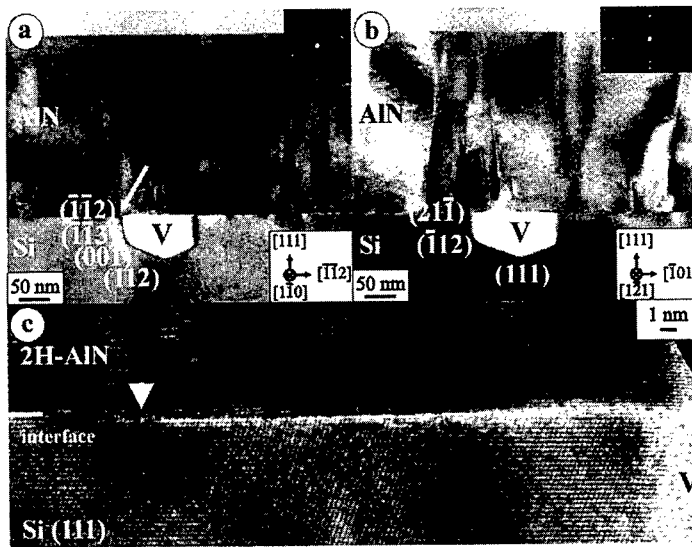


Figure 4a,b shows in cross-sectional view the void shape in a specimen with an initial Al cover on the Si(111) substrate. These micrographs are taken at the same magnification and at the same zone axes orientation as shown in Fig. 3a,b. Here also the Si  $\{112\}$  facets are important but this void is dominantly truncated by facets ( $\{111\}$ ,  $\{100\}$ , and  $\{113\}$ ) (compared with Fig. 3). The result is a smaller expansion of the voids along the interface underneath the AlN film. As the depth of the voids in both cases is very similar, the voids volume is smaller in case of an initial Al cover. SIMS

measurements have proved that the Si content in the sample with the initial Al cover is much lower ( $\sim 10^{18} \text{ cm}^{-3}$ ) than in the specimen with initial nitridation ( $\sim 10^{21} \text{ cm}^{-3}$ ). Figure 4c shows a arrowed part of Fig. 4a at higher magnification. A stripe of bright contrast along the AlN/Si interface is obviously seen starting at a surface defect of the Si substrate (arrowed) and ending at the void (right-hand side). Because of the lighter contrast, there should be less amount of material, which can be explained by Si diffusion from the defect as an energetically favourable place along the interface to the already created void.

### 3. Conclusions

Interfacial voids formed in the Si (111) substrate underneath the film were investigated by TEM in the 3C-SiC/Si(111) and in the 2H-AlN/Si(111) heteroepitaxial systems. We demonstrated the influence of special growth parameters on the shape of the created voids.

In the SiC/Si case we found an influence of the growth temperature on the void shape. At 850°C a well-known triangular void with its primary {111} facets was founded and indexed. At 1050°C an unusual hexagonal void shape was created. In the latter case not only low surface energy facets ({111}Si) were observed, but also facets with higher surface energy [14]. Their appearance can be understood due to the higher mobility of the Si adatoms on these facets. Therefore a void shape approaching the equilibrium shape in Si (tetrakaidecahedron [14]) could be reached.

In the AlN/Si heterosystem we found an influence of the initial covering of the Si. The volume of the interfacial voids and the Si content in specimens with an initial nitridation are larger than in samples with an initial Al cover. For these reasons we assume that an initial nitridation process not absolutely leads to a thin silicon nitride layer which prevents the Si outdiffusion. This seems to be in agreement with [15] where is reported based that a considerable amount of N species migrates into the subsurface layers of the substrate.

*The authors would like to thank Dr. Andreas Fissel and Vadim Lebev for providing the specimen. This work was supported by the Deutsche Forschungsgemeinschaft.*

- [1] R.F. Davis, J. Vac. Sci. Technol., **A11** (1993), p. 829.
- [2] T. Suetsugu, T. Yamazaki, S. Tomabechi, K. Wada, K. Mazu, K. Tsobuchi, Appl. Surf. Sci., **117** (1997), p. 540.
- [3] S. Guha, N.A. Bojarczuk, Appl. Phys. Lett., **72** (1998), p. 415.
- [4] C.J. Mogab and H.J. Leamy, J. Appl. Phys., **45** (1974), p. 1075.
- [5] D.M. Follstaedt, J. Han, P. Provencio, J.G. Fleming, MRS Internet J. Nitride Semicond. Res., **4S1** (1999) G3.72.
- [6] U. Kaiser, P.D. Brown, I. Khodos, C.J. Humphreys, H.P.D. Schenk, W. Richter, J. Mater. Res., **14** (1999), p. 2036.
- [7] J.P. Li and A.J. Steckl, J. Electrochem. Soc., **142** (1995), p. 634.
- [8] J. Graul and E. Wagner, Appl. Phys. Lett., **21** (1972), p. 67.
- [9] C.H. Wu, C. Jakob, X.J. Ning, S. Nishino, P. Pirouz, J. Crystal Growth, **158** (1996), p. 480.
- [10] J. Jinschek, U. Kaiser, W. Richter, J. Crystal Growth, (1999), submitted.
- [11] U. Kaiser, S.B. Newcomb, W.M. Stobbs, M. Adamik, A. Fissel, W. Richter, J. Mater. Res., **13** (1998), p. 3571.
- [12] A. Fissel, K. Pfennighaus, U. Kaiser, J. Kräußlich, H. Hobert, B. Schröter, W. Richter, Mater. Sci. Forum, **264-268** (1998), p. 255.
- [13] S. Karmann, H.P.D. Schenk, U. Kaiser, A. Fissel, W. Richter, Mater. Sci. & Eng., **B50** (1997), p. 228.
- [14] D.J. Eaglesham, A.E. White, L.C. Feldman, N. Moriya, D.C. Jacobson, Phys. Rev. Lett., **70** (1993), p. 1643.
- [15] J.S. Ha, K.-H. Park, W.S. Yun, Y.-J. Ko, S.K. Kim, Surface Science, **426** (1999), p. 373.

Phone: +49-3641-947443, Fax: +49-3641-947442, e-mail: joerg.jinschek@uni-jena.de

## Defect Characterization in 3C-SiC Films Grown on Thin and Thick Silicon Top Layers of SIMOX

M.H. Hong<sup>1</sup>, J. Chung<sup>1</sup>, F. Namavar<sup>2</sup> and P. Pirouz<sup>1</sup>

<sup>1</sup>Department of Materials Science and Engineering, Case Western Reserve University,  
10900 Euclid Ave., Cleveland, OH 44106-7204, USA

<sup>2</sup>Optoelectronic Division, Spire Corporation, One Patriots Park, Bedford, MA 01730, USA

**Keywords:** 3C-SiC, Compliant Substrate, CVD, Low Defect Density, Thin SIMOX

### Abstracts

Cubic 3C-SiC has been heteroepitaxially grown on the top Si layer of SIMOX (separation by implantation of oxygen) by chemical vapor deposition. One of the films is grown on a SIMOX that has a thick (~200 nm) topmost Si layer while the other is deposited on a SIMOX with a thin (~35 nm) topmost Si layer. The microstructure of two such films has been compared by cross-sectional and plan-view transmission electron microscopy. The defects in both films are predominantly planar in nature. The defect density of 3C-SiC epilayer deposited on the thin Si substrate is much lower than that on the thick Si substrate. The difference in the defect content of the two systems is tentatively attributed to the difference in compliance of the two substrates.

### Introduction

The electronic properties of an epitaxial film are related to its crystalline quality and, thus, the microstructure of SiC epitaxial layers grown on various substrates have been extensively studied by many researchers [1,2]. One of the interesting SOI structures is SIMOX (separation by implantation of oxygen) that is fabricated by implanting a high dose of oxygen into a standard silicon substrate. The multilayer structure of SIMOX consists of two silicon layers separated by an SiO<sub>2</sub> layer: Si(II)/SiO<sub>2</sub>/Si(I). Standard SIMOX is fabricated by a single high-dose oxygen implantation ( $1.5$  to  $1.8 \times 10^{18}$  O<sup>+</sup> cm<sup>-2</sup> at 150 to 200 kV) followed by annealing at or above ~1300 °C to regrow the silicon and redistribute the oxygen. This process results in a SIMOX structure that has a silicon top layer, Si(II), of about 140 to 240 nm thick and a buried SiO<sub>2</sub> layer of about 350 to 400 nm thick. On the other hand, an ultrathin SIMOX structure with a 35 nm silicon top layer is produced by ion implantation at 30 kV followed by high-temperature annealing using a multiple implantation process [3]. Because of the higher compliancy of thin Si layers, it is expected that when an ultrathin SIMOX wafer is used as a substrate for 3C-SiC epitaxy, the density of lattice defects in the SiC film would be lower as compared to that in SiC films deposited on standard SIMOX and/or bulky Si substrates. In the present study, we examine the microstructure of 3C-SiC films grown on both thin (newly-developed [3]) and thick (standard) Si(II) layer of SIMOX substrates by transmission electron microscopy (TEM). As expected, we find a pronounced difference in the defect density between the two different substrates.

### Experimental procedures

5  $\mu\text{m}$ , 20  $\mu\text{m}$  and 40  $\mu\text{m}$ -thick epilayers of 3C-SiC were respectively deposited on thick and thin (0001) SIMOX at 1350 °C. The thick SIMOX consisted of  $\sim 200\text{ nm}$  top layer of Si(II) on a  $\sim 400\text{ nm}$ -thick layer of  $\text{SiO}_2$ . On the other hand, the thin SIMOX had a  $\sim 35\text{ nm}$  layer of Si(II) on a  $\sim 40\text{ nm}$ -thick  $\text{SiO}_2$  layer. For TEM thin foil preparations, the conventional sandwich technique was used for cross-sectional foils with the foil surface normal to the  $[110]_{\text{Si}}$  direction. The multi-layer samples were ground with emery papers to a thickness of approximately 100  $\mu\text{m}$ , dimpled to a thickness of 15  $\mu\text{m}$ , and subsequently ion-thinned to electron transparency. Due to the very different thinning rates between Si and SiC, a low angle ( $\sim 6\text{--}7^\circ$ ) was adopted for ion-beam thinning. In order to analyze the defect density more accurately, plan-view TEM specimens were also prepared using one-side thinning from the back Si(I) layer. TEM observations were carried out in a Philips CM20 electron microscope operated at 200 kV.

### Results and discussion

Cross-sectional bright-field TEM micrographs of the 3C-SiC film on (a) thick SIMOX and (b) thin SIMOX are shown in Fig. 1. They are obtained from a region close to the SiC/Si(II) interface. Thin and thick Si(II) top layer of both SIMOX samples are clearly observed. As expected, the defect density decreases in going away from the SiC/Si(II) interface towards the SiC surface [4,5]. This is consistent with previous results in 3C-SiC epitaxial films and, indeed, films of other compound semiconductors [6] grown on Si substrates. The defect density seems to be lower in Fig. 1(b) (deposition on the thin SIMOX) than in Fig. 1(a) (deposition on the thick SIMOX sample). In Fig. 1(a), there is a highly strained region, extending by about 2  $\mu\text{m}$  from the SiC/Si(II) into the SiC epilayer; it is impossible to resolve the defects in this region within the resolution of the present TEM experiments. On the other hand, in the case of the thin SIMOX (Fig. 1 (b)), the highly strained region at the SiC/Si(II) interface is somewhat less extended. Also, as reported for the SiC/Si system, the majority of the lattice defects are planar faults with most of them being stacking faults (SFs) or microtwins. As judged from the  $\langle 110 \rangle$  trace directions of the SFs, they lie on inclined  $\{111\}$  planes as shown in the upper-right hand side of Fig. 1 (b).

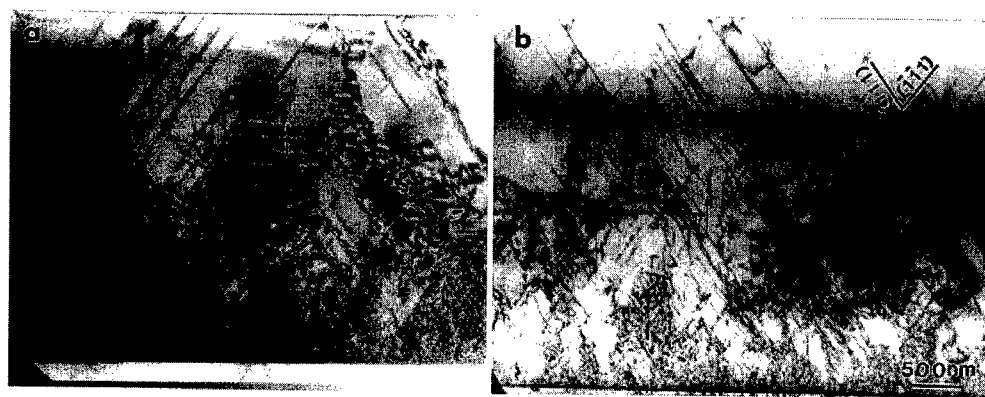


Fig. 1. Cross-sectional TEM micrograph of the 3C-SiC film close to the SiC/Si(II) interface in (a) thick SIMOX and (b) thin SIMOX.

A further comparison was made by preparing plan-view TEM foils from the two systems with observations made along the  $B=[001]$  electron beam direction (Fig. 2). The micrographs are obtained from a region close to the top 3C-SiC surface. The majority of the defects in Fig. 2 are SFs, similar to the defects observed in the cross-sectional micrographs of Fig. 1. The difference in the SF arrangement between cross-sectional (Fig. 1) and plan-view (Fig. 2) observations lies in the different projection of the equivalent  $\{111\}$  planes along  $\langle 110 \rangle$  and  $\langle 001 \rangle$  directions. In one case (cross-sectional direction), the projection of stacking fault intersections makes an angle of  $70.32^\circ$ , while in the other case (plan-view), the projected intersections are at  $90^\circ$ . The lengths of SFs in the thin SIMOX is rather shorter than those in the thick SIMOX. Furthermore, the SF density in the thick SIMOX is approximately twice as large as that in the thin SIMOX.

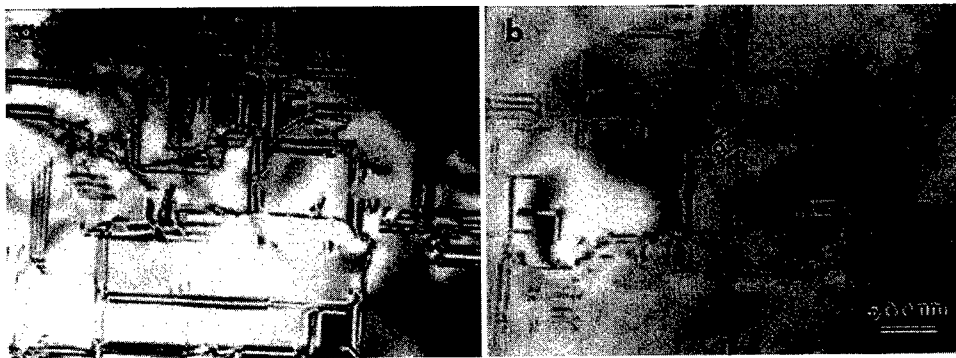


Fig. 2. Plan-view TEM micrograph of the 3C-SiC film close to the film surface in (a) thick SIMOX and (b) thin SIMOX.

A reasonable explanation for the difference in the density of planar faults in the two films is the higher compliance of the thin Si(II) substrate in the thin SIMOX as compared to that in the thick SIMOX. In a low stacking fault energy material such as SiC ( $\gamma \approx 2.9 \text{ mJ/m}^2$ ), the film/substrate lattice and/or thermal mismatches are predominantly relaxed by nucleation of partial dislocations at the interface, and their subsequent glide on  $\{111\}$  planes that give rise to stacking faults. If the substrate is more compliant, then it will accommodate part of these interfacial stresses by itself and result in a lesser residual stress in the film [7]. In order to compare the stress of the Si(II) layer in the thick and the thin SIMOX, detailed cross-sectional TEM of this region were performed (see Fig. 3). Clearly, a much higher density of defects can be observed in the thin Si(II) layer (Fig. 3(b)) than in the thick Si(II) layer (Fig. 3(a)). This indicates that the Si(II) layer in the thin SIMOX is more compliant than that in the thick SIMOX, and is plastically deformed by the epitaxial stresses. Thus, there is a lesser fraction of epitaxial stresses that is accommodated by the defects in the 3C-SiC epilayer. Hence, the relaxation of the film occurs by nucleation and glide of a lower density of partial dislocations. For this increased compliancy of the Si substrate, it is of course essential that the underlying amorphous  $\text{SiO}_2$  layer be able to relax. In fact, the glass transition temperature,  $T_g$ , of  $\text{SiO}_2$  is (depending on the cooling rate) about  $1100^\circ\text{C}$  [8]. Since, the growth temperature used for depositing SiC on the thin Si top layer of SIMOX is  $\sim 1350^\circ\text{C}$ , stress release by structural relaxation in  $\text{SiO}_2$  should be

appreciable because this is above  $T_g$  and is able to partially relax the elastic stresses transmitted to it by the overlaying Si(II) wafer.

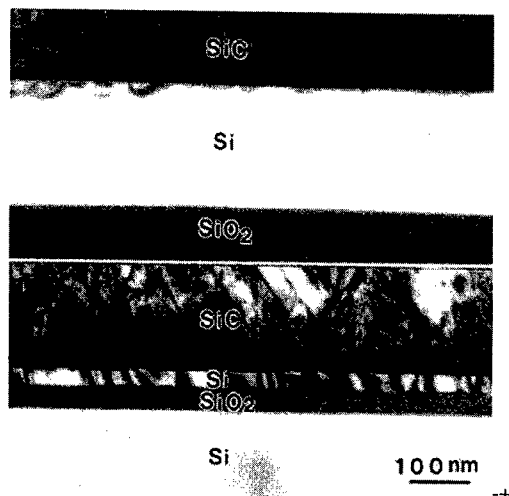


Fig. 3. Cross-sectional TEM micrograph of the Si(II) substrate in (a) thick SIMOX and (b) thin SIMOX.

#### Acknowledgements

The work at SPIRE was supported in part by NASA SBIR Phase II Contract Number NAS3-27747 and monitored by Dr. David Larkin. MHH and PP would also like to acknowledge partial support from the Department of Energy (grant #FG02-93ER45496).

#### References

- [1] S. Nishino, J. A. Powell and H. A. Will, *Appl. Phys. Lett.* **44**(5) (1983), p. 460-462.
- [2] Y. Nakajima, "Epitaxial Growth of SiC Single Crystal Films" in *Silicon Carbide Ceramics-1: Fundamental and Solid Reaction*, ed. S. Somiya and Y. Inomata (Elsevier Applied Science: London and New York, 1991), P. 45-75.
- [3] F. Namavar, P. Colter, A. Cremins-Costa, C.-H. Wu, E. Gagnon, D. Perry and P. Pirouz, in *III-Nitride, SiC and Diamond Materials for Electronic Devices*, ed. D. K. Gaskill, C. D. Brandt and R. J. Nemanich, (Materials Research Society: Pittsburgh, PA), *Mat. Res. Soc. Symp. Proc.* **423** (1996), p. 409-414.
- [4] C. M. Chorey, P. Pirouz, J. A. Powell and T. E. Mitchell, in *Semiconductor-Based Heterostructures: Interfacial Structure and Stability*, ed. M. L. Green, J. E. E. Baglin, G. Y. Chin, H. W. Deckman, W. Mayo and D. Narasinhham, (The Metallurgical Society Publications) (1986), p. 115-125.
- [5] S. R. Nutt, D. J. Smith, H. J. Kim and R. F. Davis, *Appl. Phys. Lett.* **50**(4) (1987), p. 203-205.
- [6] P. Pirouz, F. Ernst and T. T. Cheng, in *Heteroepitaxy on Silicon: Fundamentals, Structures, and Devices*, ed. H. K. Choi, H. Ishiwara, R. Hull and R. J. Nemanich, (Materials Research Society: Pittsburgh, PA). *Mat. Res. Soc. Symp. Proc.*, **116** (1988), p. 57-70.
- [7] Y. H. Lo, *Appl. Phys. Lett.* **59**(18) (1991), p. 2311-2313.
- [8] W. D. Kingery, H. K. Bowen and D. R. Uhlmann, *Introduction to Ceramics*, (John Wiley & Sons: New York, 1976).



## Structural Characteristics of 3C-SiC Films Epitaxially Grown on the Si/Si<sub>3</sub>N<sub>4</sub>/SiO<sub>2</sub> System

S. Zappe<sup>1</sup>, H. Möller<sup>2</sup>, G. Krötz<sup>2</sup>, M. Eickhoff<sup>2</sup>, W. Skorupa<sup>3</sup>, E. Obermeier<sup>1</sup>  
and J. Stoemenos<sup>4</sup>

<sup>1</sup> Microsensor and Actuator Technology Center, Technical University of Berlin, Sekr. TIB 3.1,  
Gustav-Meyer-Allee 25, DE-13355 Berlin, Germany

<sup>2</sup> Department: FT2M, Daimler Benz AG, Postfach 800465, DE-81663 München, Germany

<sup>3</sup> Institut für Ionenstrahlphysik und Materialforschung, Forschungszentrum Rossendorf,  
PO Box 510119, DE-01314 Dresden, Germany

<sup>4</sup> Physics Department, Aristotle University Thessaloniki, GR-54006 Thessaloniki, Greece

**Keywords:** 3C-SiC, 3C-SiC / Silicon-On-Insulator, Cavities, SiC/Si/Si<sub>3</sub>N<sub>4</sub>/Si System

**Abstract:** The improvement of the stability in the SiC/ Silicon-On-Insulator system by partial or complete replacement of the SiO<sub>2</sub> by Si<sub>3</sub>N<sub>4</sub> was studied by Transmission Electron Microscopy (TEM). The beneficial effects of the nitrogen implantation for the reduction of cavities, which are formed in the Si side at the SiC/Si interface during the epitaxial growth of 3C-SiC, are shown. The high dislocation density developed in the Si-overlayer during nitrogen implantation does not affect the quality of the 3C-SiC overgrown.

### Introduction

Cubic SiC thin films deposited on Si On Insulator (SOI) are very promising as sensing elements for the control of processes occurring at high temperatures and in harsh environment. SiC films, deposited on silicon substrates have the potential for such extreme range applications. However, the intrinsic conductivity of silicon at high temperatures, short-circuits the SiC sensing element. This can be avoided by using SiC on SOI wafer, which ensures the insulation of the SiC overgrown from the Si-substrate [1]. However cavities which are formed in the Si-overlayer at the SiC/Si interface during the early stage of the SiC deposition may cause serious implications during the micro-machining process.

There are three main reasons for the formation of the cavities[2].

- i- consumption of Si for the formation of the SiC buffer layer during the carbonization process [3]
- ii-out-diffusion of Si through the SiC during the early stage of growth [4].
- iii-ball-up of the Si at the edges of the cavities. This occurs in the SiC/SOI wafer due to instability of the Si/SiO<sub>2</sub> system at high temperatures [5].

In this paper the improvement of the stability in the SiC/SOI system by partial or complete replacement of the SiO<sub>2</sub> by Si<sub>3</sub>N<sub>4</sub> was studied by Transmission Electron Microscopy (TEM).

### Experimental procedure

The 3C-SiC was deposited on commercially available high quality SOI wafers (UNIBOND®) from SOITEC. The deposition was carried out in a low pressure CVD reactor at 1200°C using methylsilane [6].

The buried SiO<sub>2</sub> was partially replaced by Si<sub>3</sub>N<sub>4</sub> in SOI wafers by low dose nitrogen implantation  $1 \times 10^{17} \text{N}^+/\text{cm}^2$ , with an energy of 80 keV at 500 °C, which results in a maximum N-concentration directly at the Si-overlayer/BOX interface of the SOI sample. After a subsequent annealing for two hours at 1100°C in nitrogen atmosphere, an intermediate thin Si<sub>3</sub>N<sub>4</sub> layer, about 5nm thick, was formed between the Si-overlayer (SOL) and the Buried Oxide (BOX). SOI specimens were also implanted with the same dose and higher energy, 180keV, so that the

implanted nitrogen was well inside the BOX. After the subsequent annealing an intermediate thin  $\text{Si}_3\text{N}_4$  layer was formed between the SOL and the BOX. This is expected because nitrogen under a high temperature annealing preferentially migrates to the  $\text{Si}/\text{SiO}_2$  interfaces [7]. No defects due to the low dose nitrogen implantation were observed in the implanted and subsequently annealed specimens.

High dose nitrogen implantations were performed in order to replace the BOX by a buried nitride layer. Two Si wafers were implanted with high nitrogen doses to form  $\text{Si}_3\text{N}_4$  buried layers. In the first was implanted with nitrogen dose  $1 \times 10^{18} \text{N}^+ \text{cm}^{-2}$  and energy 130keV, at implantation temperature  $650^\circ\text{C}$ . The specimen was subsequently annealed at  $1150^\circ\text{C}$  for two hours, so that a silicon nitride buried layer about 200nm thick was formed. A  $2.8\mu\text{m}$  thick 3C-SiC film was deposited under standard deposition conditions (specimen L1713). The second specimen was implanted with a dose  $0.8 \times 10^{18} \text{N}^+ \text{cm}^{-2}$  and energy 130keV, at implantation temperature  $500^\circ\text{C}$ , subsequently annealed at  $1000^\circ\text{C}$  for two hours. A  $2.8\mu\text{m}$  thick 3C-SiC film was deposited on this specimen (L1707).

### Results and discussion

The density and the size of the cavities, which are formed in the Si-overlayer during SiC deposition on SOI wafers is higher than in the bulk silicon wafers, because in bulk Si the substrate is the reservoir for the Si supply. When bulk Si is replaced by SOI wafers only the thin SOL is the Si supplier. However due to the limited thickness of the SOL the density and the size of the cavities were directly measured by Atomic Force Microscopy. In this way quantitative measurements of the silicon migration from the SOL during SiC deposition were performed [6].

#### a) Low dose nitrogen implantation

The stability of the SOI structure was substantially improved by the formation of an intermediate 5nm thick  $\text{Si}_3\text{N}_4$  layer between the SOL and the BOX after the low dose nitrogen implantation and subsequent annealing [7]. The cross-section TEM micrograph (XTEM) of this structure after SiC deposition is shown in Fig.1a. The letter N in Fig.1a denotes the thin  $\text{Si}_3\text{N}_4$  layer, which was formed at the SOL/BOX interface. Small cavities were formed close to the SiC/Si interface. In general the cavities are not extended to the  $\text{Si}/\text{SiO}_2$  interface where the thin  $\text{Si}_3\text{N}_4$  layer was formed. A reference specimen not implanted with nitrogen, is shown in Fig1b. In this sample the cavities were extended deeper into the BOX, denoted by the letter C in Fig.1b.

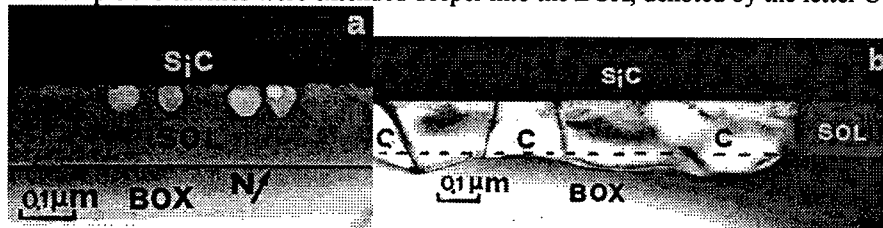


Fig.1 XTEM micrographs a) SiC deposited on a UNIBOND wafer implanted with low dose nitrogen. Small cavities were formed at the SiC/Si interface. The rich in nitrogen zone at the  $\text{Si}/\text{SiO}_2$  interface is denoted by the letter N. b) SiC deposited on a non implanted part of the specimen. Large cavities, denoted by the letter C, are extended to the BOX. The dash line marks the initial  $\text{Si}/\text{SiO}_2$  interface. Significant redistribution of Si occurred.

#### b) High dose nitrogen implantation

In the specimen L1713 the silicon nitride buried layer was amorphous about 200nm thick [8]. Threading dislocations were formed in the SOL with a density of  $10^{11} \text{cm}^{-2}$  as shown in Fig.2a. During the SiC deposition at  $1200^\circ\text{C}$  annihilation of the defects in the SOL occurs and the dislocation density was reduced to  $5 \times 10^9 \text{cm}^{-2}$ , as shown in Fig.2b, also the  $\text{Si}_3\text{N}_4$  buried layer was partially crystallized. In spite of the high density of the defects in the SOL, the quality of the

deposited SiC is comparable with those of the standard 3C-SiC epitaxially grown on Si, i.e. Stacking Fault (SF) density  $5 \times 10^9 \text{cm}^{-2}$  and Antiphase Boundaries (APBs)  $5 \times 10^8 \text{cm}^{-2}$  [9]. The good quality of the uppermost SiC film is shown in the XTEM micrograph in Fig.2c and the plane view TEM micrograph in Fig.2d. Small spherical cavities with density of the order  $5 \times 10^8 \text{cm}^{-2}$ , were formed in the SOL at the SiC/Si interface. This density is comparable with the density of the threading dislocations in the SOL, it is evident that the cavities are preferentially generated at the dislocations. Due to their small size none of the cavities was extended up to the SOL/Si<sub>3</sub>N<sub>4</sub> interface.

In the specimen L1707 the nitrogen dose was lower and the dislocation density before SiC deposition was  $10^{10} \text{cm}^{-2}$ . After deposition the dislocation density was reduced to  $5 \times 10^7 \text{cm}^{-2}$ .

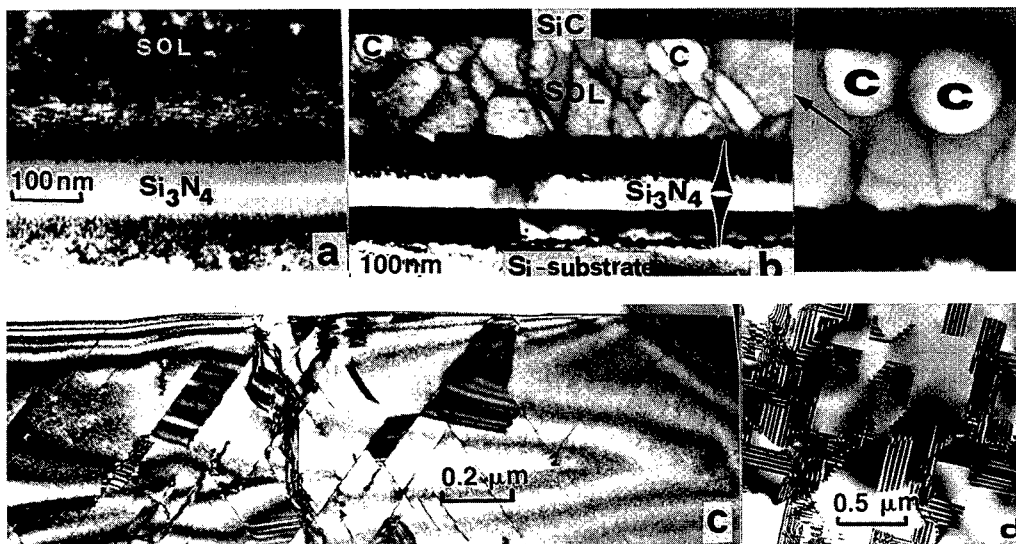


Fig.2 Formation of Si<sub>3</sub>N<sub>4</sub> buried layer after high dose nitrogen implantation ( $1 \times 10^{18} \text{N}^+ \text{cm}^{-2}$ ) into Si (specimen L1713) a) As implanted, a high density of dislocation is evident in the SOL b) After 3C-SiC deposition. Small cavities in the SOL are denoted by the letter C. The Si<sub>3</sub>N<sub>4</sub> buried layer was partially crystallized, only the central part remains amorphous. The relation of the cavities with the dislocations in the SOL is shown in the inset c) The 3C-SiC at the uppermost part of the film, the quality is comparable to the standard 3C-SiC/Si. d) PVTEM micrograph.

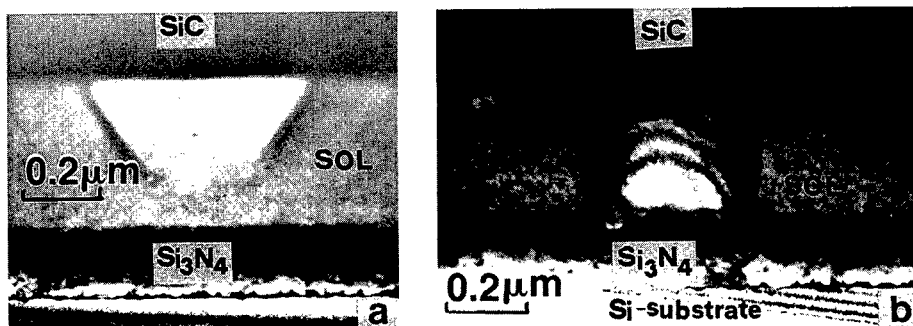


Fig.3 Cavities formed in the SOL of the specimen L1707 implanted with a nitrogen dose  $0.8 \times 10^{18} \text{N}^+ \text{cm}^{-2}$ , exhibiting a low dislocation density. a) A typical cavity in the SOL before touching the Si/Si<sub>3</sub>N<sub>4</sub> interface, having the form of a reverse tetragonal pyramid b) After touching the Si<sub>3</sub>N<sub>4</sub> buried layer the cavity takes cylindrical shape. The cavity is not extended into the Si<sub>3</sub>N<sub>4</sub> buried layer.

In this case the density of the cavities was  $5 \times 10^6 \text{ cm}^{-2}$  having the typical shape of the reverse tetragonal pyramids, as shown in Fig.3a. When these pyramids touch the SOL/Si<sub>3</sub>N<sub>4</sub> interface take a cylindrical form with vertical walls as shown in Fig.3b. No decomposition of the Si<sub>3</sub>N<sub>4</sub> buried layer was observed when the cavities touch the SOL/Si<sub>3</sub>N<sub>4</sub> interface as frequently occurs in the SiO<sub>2</sub> buried layer [6]. This is because silicon nitride has the strongest covalent-bond property next to silicon carbide. No balling-up of the Si in the SOL, at the edges of the cavities, was observed revealing the enhanced stability of the Si<sub>3</sub>N<sub>4</sub>/Si system at high temperatures [5].

In spite of the high density of the defects in the SOL the quality of the deposited SiC is comparable to the standard 3C-SiC epitaxially grown on the Si wafers, as shown in the XTEM micrograph taken from the uppermost part of the film, in Fig.2c.

The dislocation density in the SOL was substantially reduced when the nitrogen dose was reduced, specimen L1707. The lower dislocation density does not improve the quality of the SiC overgrown. This can be explained by taking into account that the defect density of the SiC near the SiC/Si interface is about two orders of magnitude higher than the dislocation of the Si-overlayer. Therefore the dislocations in the SOL do not affect the growth. Moreover the existing dislocations in the SOL facilitates the relaxation of the SiC/Si system. This is in agreement with 3C-SiC films grown on thin Si-overlayers of SIMOX [10].

## Conclusions

The formation of cavities can not be fully avoided because these are related with the formation of the first layer of SiC after carbonization, also with the out-diffusion of Si from the SOL during the early stage of SiC deposition. The Si<sub>3</sub>N<sub>4</sub> buried layer remains stable not affected by the cavities. No balling-up of the SOL at the edges of the cavities was observed revealing the very good wetting of the Si/Si<sub>3</sub>N<sub>4</sub> interface.

The cavities are preferentially formed at the dislocations. When the number of dislocations is high, the density of the cavities is also high and the size of the cavities is small. This means that by controlling the density of the dislocations we can control the size and the density of the cavities in the SOL.

**Acknowledgements:** This work was supported by the EU, BRITE-EURAM project CT96-0261

## References

- [1] V. Papaioannou, E. Pavlidou, J. Stoemenos W. Reichert, E. Obermeier, Materials Science Forum, vol. 264-268, (1998), p 445.
- [2] H. Möller, S. Zappe, V. Papaioannou G. Krötz, W. Skorupa, E. Obermeier, J. Stoemenos, Proceedings of 195<sup>th</sup> Meeting of the Electrochemical Society, Ninth International Symposium on Silicon-on Insulator, Technology and Devices, Seattle, May 2-7, 1999. Vol.99-3 Ed. P.L.F. Hemment, p131.
- [3] S.Nishimo, J.A.Powell and H.A.Will App. Phys. Lett. 45 (1983), p 460.
- [4] G. Ferro, Y. Monteil, H. Vincent, F. Cauwet, J. Bouix, P. Durupt, J. Olivier and R. Bisaro, Thin Solid Films 278, (1996), p. 22.
- [5] E. Yablonoich and T. Gmitter, J. Electrochem. Soc. 131, (1984), p 2625.
- [6] H. Moller, M. Rapp, L. Vogelmeier, M. Eickhoff, G. Krötz, V. Papaioannou, J. Stoemenos, 2<sup>nd</sup> Eur. Con.on Silicon Carbide and Related Materials, Montpelier, Sept. 1998, P2-48.
- [7] W.J.M.J. Josquin, Nucl. Instr. Methods 209/210 (1983), p 581.
- [8] N. Hatzopoulos, U. Bussmann, A.K. Robinson and P.L.F Hemment, Nuclear Instr. Phys. Res. B55, (1991) p 134.
- [9] J. Stoemenos, C. Dezausier, G. Arnaud, J. Camassel, J. Pascual, J.L. Robert Mat. Scien. Eng. B29, (1995), p 160.
- [10] M.H. Hong, J. Chung, P. Pirouz, F. Namavar, This Conference, paper MP64 , p. 525

## Illusion of New Polytypes

U. Kaiser<sup>1</sup>, A. Chuvilin<sup>2</sup> and W. Richter<sup>1</sup>

<sup>1</sup> Institut für Festkörperphysik, Friedrich Schiller Universität Jena,  
Max-Wien-Platz 1, DE-07743 Jena, Germany

<sup>2</sup> Borekov Institute of Catalysis, SB RAS, av. Lavrentieva 5, RU-630090 Novosibirsk 90, Russia

**Keywords:** Image Simulation, MBE Growth, Polytypes, TEM

**Abstract:** High-resolution transmission electron microscopy (HRTEM) images of the [1-10] and [11-20] zones of cubic and hexagonal SiC layers grown by molecular beam epitaxy (MBE) often reveal regions of material exhibiting an unusual periodicity. We describe the identification of 3 and 4-fold periodicities. The 3-fold contrast was found in earlier works of Jepps and Page to appear in HRTEM images of polycrystalline SiC when it was attributed to the 9R-SiC polytype. In this paper we demonstrate by HRTEM image simulations that the models of the 9R and the 12H polytypes can fit qualitatively the experimental HRTEM images. However, by comparison of the FFT patterns of the experiments and the simulations, we demonstrate that the periodical structures disagree with the 9R and 12H polytypes. We show unambiguously that the model of overlapping crystals does fully match the experiments.

### 1. Introduction

SiC polytype band-gap differences can be used to form novel electronic device structures grown on SiC substrates in case the growth condition for different SiC polytypes can be controlled exactly. This in turn requires fine scale structural analysis of the SiC stacking sequences in order to understand and thereby gain insight into how to control the different modes of growth. In principle the stacking sequence in SiC may range from 2 to  $\infty$ , however, only a few polytypes, i.e. 6H, 3C, 4H, 15R and 2H are usually observed within polycrystalline SiC [1].

High resolution transmission electron microscopy (HRTEM) of the [1-10] zone axis of cubic SiC (or the corresponding [11-20] zone axis for hexagonal SiC), coupled with a careful investigation of the diffraction intensities, is capable of providing a direct representation of the stacking sequence of the SiC polytypes [2] and allows the spatial occurrence of various structures to be investigated. Examples of rare polytypes such as 21R, 129R and 9R have been identified within small parts of specimen volumes of polycrystalline SiC [3]. In particular, the 9R polytype was described on the basis of HRTEM observations [2], as an important structural intermediary between SiC twinning. The stacking of layers within the 9R polytype can be described using the Hägg notation as [++-++-++-++-...] with a spacing of 0.252 nm between the layers. The repetition occurs each three layers, making a 0.756 nm repeat unit, as observed experimentally [3]. The electrical properties of the 9R polytype have been calculated [4] and its comparatively wide band-gap would make its controlled growth a very interesting task for future device development.

When growing SiC layers, conditions for the controlled overgrowth of 3C-SiC, 6H-SiC and 4H-SiC by molecular beam epitaxy (MBE) on 6H or 4H-SiC substrates have been found based on their different nucleation stages [5]. In addition, we obtained layers comprising only a 3-fold superstructure when growing at low temperatures (<1200K) under conditions for cubic growth [6]. Comparison of our 3-fold structure and the reported 9R polytype [3] show that these images were visually identical. However, as shown by HRTEM image simulation, the experimentally observed

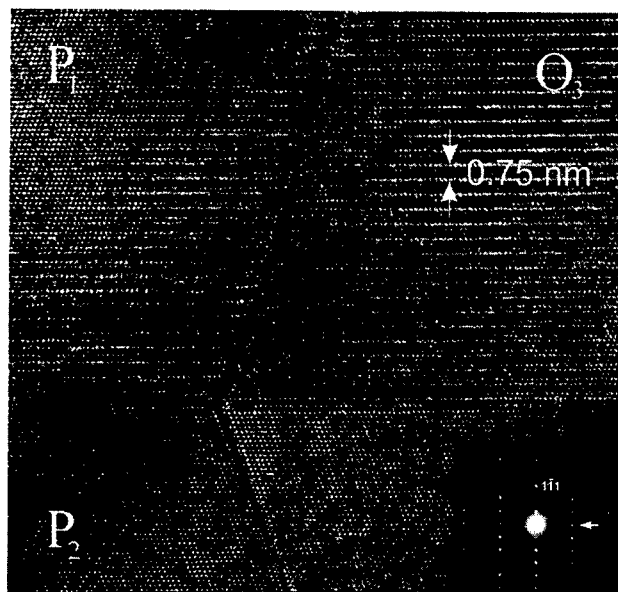


**Fig. 1** 110 HRTEM image of a SiC layer showing cubic crystals  $P_1$  and  $P_2$  in twinned orientation and an unusual 3-fold periodicity in region  $O_3$  of 0.75nm spacing together with the SAED pattern of region  $O_3$ . Note the reflection perpendicular to the 1-11 growth direction.

contrast can be fitted either by the 9R polytype model or by a model of overlaying twins [7]. When growing at high substrate temperatures (>1500K) alternatively at conditions for cubic and hexagonal growth, 3C and 4H layers could be grown on top of each other [8]. Within

these layers we found material exhibiting a 4 to 12 fold superstructure.

The purpose of this paper is to consider the origin of these structural phases and to demonstrate that the periodical structures can be easily misinterpreted as new polytypes such as 9R or 12H.

## 2. Results

### 2.1. TEM images

Fig. 1 shows a HRTEM image of a SiC thin film grown on a 4H-SiC substrate at a substrate temperature of 1500K. Along with regions of perfect 3C-SiC polytype denoted  $P_1$  and  $P_2$  ( $P_1$  and  $P_2$  are in twin orientation), a region (denoted  $O_3$ ) showing the 3-fold periodicity with a spacing of 0.75 nm (arrowed) is observed in the layer. In the corresponding selected area electron diffraction (SAED) pattern of region  $O_3$  (insert) the 3-fold periodicity can be seen by the appearance of extra reflections in 1/3 and 2/3 of the 1-11 reflection. It is noted that there exists a reflection (arrowed) that is perpendicular to the growth direction ([1-11] direction). Detailed HRTEM and selected area diffraction investigation of many different cubic SiC layers grown under different conditions always associated this 3-fold periodicity with twinning, either spread through the whole layer or visible in small parts of the specimen volume only.

The layered specimen in Fig. 2 was grown at 1500K (in the case of 3C growth) and 1600K (in the case of 4H growth) substrate temperature. (For more detail see [8]). In Fig. 2a an image is shown where regions of 4H-SiC and 3C-SiC can be distinguished. In-between exists a region marked  $O_4$  showing an unusual 4-fold periodicity which differs significantly from the 4-fold contrast in the 4H-SiC structure making a 3nm repeat as marked. The SAED pattern in the insert corresponds to the region  $O_4$ . It shows 12 reflections within the  $g_{1-11}$  vector of  $4\text{nm}^{-1}$ . As can be seen in the high resolution image of the right lower part of region  $O_4$ , the contrast varies strongly in dependence on the imaging conditions used, as tilt, defocus and specimen thickness.

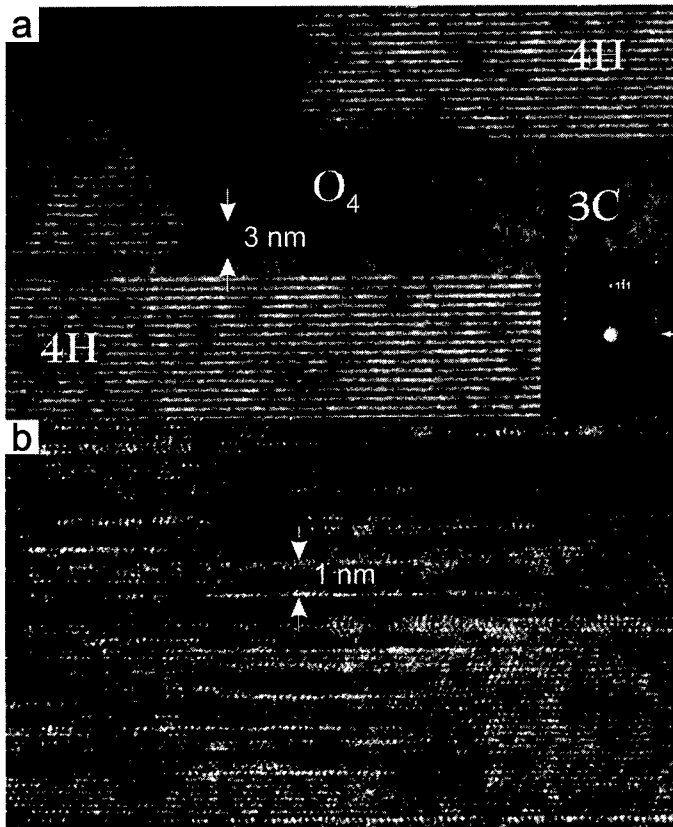


**Fig.2 a)** 110 Bright field image of 3C and 4H-SiC on 4H-SiC substrate. A region marked  $O_4$  shows an unusual 4-fold periodicity together with the SAED patterns. Note the reflection perpendicular to the growth direction.

In **b)** a part of region  $O_4$  is seen in higher resolution which shows that the contrast is strongly dependent on the imaging conditions.

## 2.2 9R and 12H image simulation

Image simulations for the 9R-SiC polytype and 12H-SiC were performed for conditions of different thickness, defocus and crystal tilt. It was possible to choose some which reflect main details of the

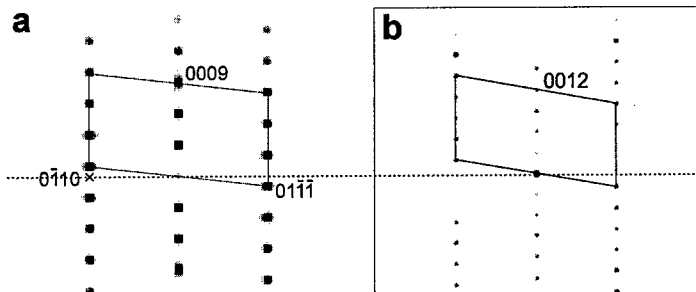


**Fig.3** Simulated diffraction patterns of a) 9RSiC and b) 12HSiC. Note that no reflection perpendicular to the growth direction is present.

experimental patterns show a reflection perpendicular to the growth direction. For example, the 9R-SiC structure exhibits no 3-fold translation repeat in the  $[1-11]$  direction, because the stacking sequence is  $[ABCBCACAB...]$  or similarly, the 12H-SiC structure exhibit no exact 4-fold

3-fold respectively 4-fold contrast. However, more detailed inspection of the simulations highlights the principle discrepancies between the experimental and simulated images which are also clearly seen when comparing the FFT patterns from the simulations (Fig. 3a, b) with the SAED patterns from the experimental images (see back Fig. 1, and 2a). As can be noted, only the

translation repeat as the stacking is [ABCACABCBCAB...]. In summary, we now can conclude that the 3- and 4-fold periodicities observed are not due to the 9R and 12H-SiC polytypes.

### 2.3 Image simulations of the overlay model

Fig. 4 shows calculated images for the case of overlapping 4H-SiC and 3C-SiC crystals (Fig. 4a) and overlapping cubic crystals in twinned orientation (Fig. 4c) together with their calculated diffraction patterns (Fig. 4b, d). The calculations were performed for equal thicknesses of

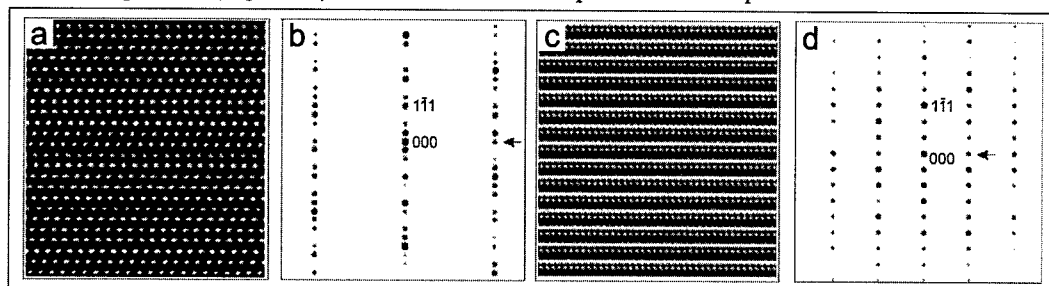


**Fig. 4** Calculated images of overlaying a) 4H-SiC and 3C-SiC and b) 3C crystal in twinned orientation crystals of the same thickness. Note the reflection perpendicular to the growth direction.

the overlaying crystals. The reflections perpendicular to the growth direction is marked. In order to perform a calculation as close to the proposed experimental image as possible, a simulation was also performed assuming different thicknesses of the overlaid crystals. The result give a good principal agreement.

Thus, we can unambiguously conclude that the periodicities within the HRTEM images of thin SiC films arises because of the overlap of crystal domains.

### 3. Conclusions

Comparison of FFT patterns from experimental and simulated images of MBE grown thin SiC films confirmed that the unusual 3-fold and 4-fold contrast observed within some regions of HRTEM images was due to the overlap of crystals in these foil regions rather than being due to the presence of the rare 9R or 12H-polytype.

Our result may be more generally valid for crystals forming twins or forming different polytypes. When these crystals overlap, a superperiodicity arises in the [110] structural projection and hence within the associated [110] HRTEM image which can be easily misinterpreted as a new polytype..

*The author thank Dr. Andreas Fissel for providing the SiC material, Jörg Jinschek for sample preparation and the Sonderforschungsbereich 196 (No.A03) and the Transform Program 01 BM 804/5 for financial support.*

### References

- [1] Pandey, D. and Krishna, P. The Origin of Polytype Structures (1983), p. 213.
- [2] Jepps, N. W., Page, T. F. J. Americ. Ceram. Soc., **63**, (1980), p. 102.
- [3] Jepps, N., W., Page, T. F. Prog. Cryst. Growth and Charact; **7** (1983 ), p. 259.
- [4] Lambrecht, W. R. L., Limpijumnong, S., Rashkeev, S., Segall, B., Phys. Stat. Sol. (b) **202**, (1997), p. 5.
- [5] Fissel, A., Schröter, B., Richter, W., Festkörperprobleme (Adv. Solid State Phys), **38**, (1998), p. 351.
- [6] Kaiser, U., Khodos, I., Brown, P. D., Chuvilin, A., Albrecht, M., Humphreys, C. J., Fissel, A., Richter, W. (1999) J. Mater. Res., **8** (1999), p. 3226.
- [7] Kaiser, U., Chuvilin, A., Brown, P.D., Richter, W. Microscopy and Microanalysis accepted
- [8] Fissel, A: at this conference , p. 209



## Microstructural, Optical and Electronic Investigation of Anodized 4H-SiC

S. Zangooie<sup>1</sup>, P.O.A. Persson<sup>1</sup>, J.N. Hilfiker<sup>2</sup>, L. Hultman<sup>1</sup>, H. Arwin<sup>1</sup>  
and Q. Wahab<sup>1</sup>

<sup>1</sup> Department of Physics and Measurement Technology, Linköping University,  
SE-581 83 Linköping, Sweden

<sup>2</sup> J.A. Woollam Co., Inc., 645 M Street, Suite 102, Lincoln, NE 68508, USA

**Keywords:** Amorphous Phase, Anisotropic Etching, Electric Resistivity, Porous SiC

**Abstract** Pores in 4H porous SiC were found to propagate first nearly parallel with the basal plane and then gradually change plane of propagation from, e.g., (1104) to (1103) and (1102) etc. A disordered phase is formed at the interface between the pores and the crystalline SiC. Optical analysis of this phase reveals a more dielectric like nature of the material compared to crystalline SiC. The measured electrical resistivity at 296 K and 347 K were  $2.9 \times 10^8 \cdot \text{cm}$  and  $9.2 \times 10^7 \cdot \text{cm}$ , respectively.

### 1. Introduction

Since the first report on electrochemical etching of crystalline SiC in hydrofluoric acid (HF) [1], a considerable attention has been paid to better understanding the physical properties of the material which is known as porous SiC (PSC). The anodization results in formation of a high surface area material with room-temperature light-emitting properties much stronger than those obtained from bulk SiC [2]. Of special importance here is the simplicity and the high etching rate of the electrochemical process. The promising luminescence properties of PSC open up application possibilities within SiC-based integrated electronics. Further applications of PSC in areas such as optics, gas- and biosensor technologies may also be realized. Applications of PSC demand a detailed understanding of the microstructure and its correlation with fabrication parameters such as HF-concentration, applied current density, illumination, doping type and levels. In this report, we focus our investigation on the microstructure, optical and electronic properties of 4H-PSC. It has to be noted that 4H-SiC is the most promising polytype for high temperature and high power devices due to its wide bandgap and high electron mobility [3]. Anisotropic etching is encountered with in porous silicon [4] and porous GaAs [5]. A similar phenomenon is observed in 4H-SiC as will be discussed here.

### 2. Preparation and characterization

PSC samples were prepared using n-type 4H-SiC wafers of doping around  $1 \times 10^{19} \text{ cm}^{-3}$ . Photo-assisted electrochemical anodization was performed on the polished silicon face of the samples using a 24 W UV-light source and in a mixture of HF, water and ethanol (volume ratio 1.5 : 2.5 : 6). The applied current density was  $25 \text{ mA/cm}^2$ .

The cross-sectional transmission electron microscopy (XTEM) sample preparation consisted of clamping two sample pieces with their PSC side face to face in a titanium grid and glued together using a mixture of araldite and graphite powder. The sample was then ground mechanically down to about  $50 \mu\text{m}$  using a  $30 \mu\text{m}$  diamond paper. Final thinning to make the sample electron transparent was done in a Baltec RES 010 precision ion mill operated at 8.0 kV and 4.5 mA with Ar as sputter gas. The TEM images were recorded using Philips CM20 UT microscope, operated at 200 kV using a LaB<sub>6</sub> filament. SEM studies were done using a 1550 FEG instrument from Leo Co., USA. The image contrast was obtained using secondary electron mode with an accelerating voltage of 5 kV. A variable angle infrared ellipsometer (J. A. Woollam Co., USA) operated in the photon energy range

0.03-0.98 eV was used for optical investigation of the material. Optical modeling is realized using multiple sample analysis [6] of two samples with etching times of 5 s and 1 min. The optical characteristics of crystalline SiC and an amorphous phase (AP) are modeled using a parametric equation which is a sum of so called ionic and Drude expressions [7]. Electrical characterization has been performed in order to determine the electrical resistivity of PSC layers. For this measurements a back side substrate contact was employed by depositing Ni and subsequent annealing at 950°C to form the silicide for obtaining a good ohmic behaviour. For the front side on PSC, circular dots of diameter 1.2, 0.8, 0.6, 0.3 and 0.1 mm were deposited in vacuum. Current voltage (I-V) measurements were performed using a Keithley 237 source-measure unit. These measurements were performed at room temperature and 347 K.

### 3. Results and discussions

Figure 1 shows an XTEM image of a 1.7  $\mu\text{m}$  thick PSC sample along  $(1\bar{1}20)$  plane. Close to the PSC/ambient interface, the cross-sections of channels which propagate in a direction out from the plane are visible. In general, these channels are well separated with little interconnection. This is the indication of etching in directions other than along c-axis. In a number of cases two or more adjacent channels are connected by an elongated pore in the plane of the image. These pores have a relatively low angle with the PSC/ambient interface. Further down, most of the pores take on roughly triangular or v-shaped forms. The change in the shape of the pores is due to an increase of branching and channel interconnections with depth. These pores and the fact that they pose a limited extent in the plane of the image is an evidence for existence of a zigzag shaped morphology where channels suddenly change direction and proceed along other planes with similar preferential etch properties.



Fig. 1 XTEM image of a 1.7  $\mu\text{m}$  PSC sample with an etching time of 1 min along  $(1\bar{1}20)$  plane.

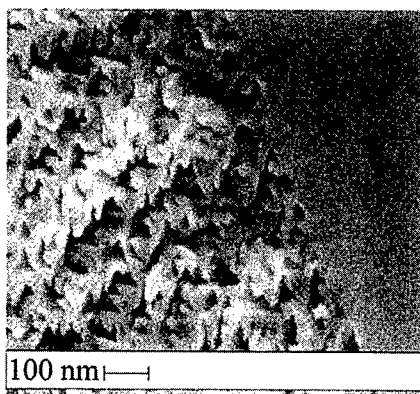


Fig. 2 XSEM image of a 13.5  $\mu\text{m}$  PSC sample with an etching time of 10 min close to the PSC/SiC interface.

The shape of the pores and their cross-sections are primarily decided by the crystallographic planes along which SiC dissolution is taking place. The triangular channel cross-sections were used to identify the crystallographic orientation of the preferential etch planes. Near the PSC surface, the angle between two sides of the triangles is 140°. It is thus likely that the pores, along the plane of the image, are channels which propagate along  $(1\bar{1}04)$  and  $(\bar{1}104)$  planes. By symmetry, it is

expected that pores also propagate along  $(10\bar{1}4)$ ,  $(\bar{1}014)$ ,  $(01\bar{1}4)$  and  $(0\bar{1}14)$  planes. The four latter planes intercept the  $(11\bar{2}0)$  plane by a relatively low angle of about  $30^\circ$ . The symmetry of these planes relative to the  $(11\bar{2}0)$  causes the predominant triangular appearance of the pore cross-sections. It has to be noted that the pore morphology appears slightly different when it is viewed from directions such as  $[1\bar{1}00]$ . In such cases channels which propagate along the  $(1\bar{1}04)$  and  $(\bar{1}104)$  planes intercept the  $(1\bar{1}00)$  plane with low angles, whereas channels which belong to the other four planes are symmetrically situated around the c-axis with a higher angle of about  $60^\circ$  from the plane of view. Hence, the characteristics of symmetric triangular pores are less dominating. However, electron microscopy observations from different crystallographic orientations evidence existence of a six fold symmetry concerning pore propagation in SiC. These angles can be estimated to be about  $120^\circ$  close to the well defined PSC/SiC interface. In Fig. 2 the pore morphology of a  $13.5 \mu\text{m}$  thick PSC sample at the vicinity of the PSC/SiC interface is shown. The angle is even smaller here and can be estimated to be about  $90^\circ$ . Thus, we are not able to identify a unique set of planes which would pose preferential etch properties along the entire sample thickness. It is therefore likely that channels are formed first nearly parallel with the basal plane (see above) and then gradually change plane of propagation from  $(1\bar{1}04)$  to  $(1\bar{1}03)$  and  $(1\bar{1}02)$  etc. So far we have no direct evidence for alignment of the pores with the c-axis. It is because the porous layers formed at longer etching times than about 20 min spontaneously came loose from the substrate. The reason could be an increase of the porosity and pore sizes with depth resulting in an instability of the porous layers at the PSC/SiC interface. This phenomenon was mainly due to a decrease of the HF-concentration with depth and an increase of the absorption of the UV-light with sample thickness.

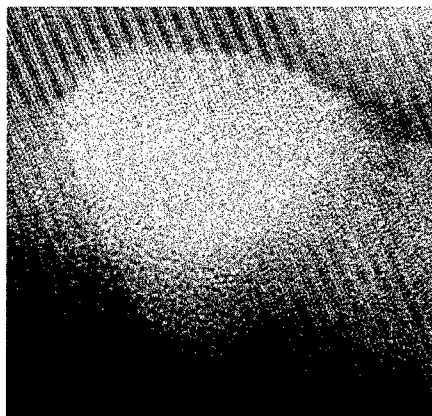


Fig. 3 High resolution TEM image of a channel cross-section revealing existence of a disordered region at the interface between crystalline SiC and void.

Danishevskii et al. [8] reported on formation of an AP in 6H-PSC. It was however not clarified whether the AP was created during the anodization process or by the employed sample preparation procedure used prior to the TEM analysis. To reveal that the formation of an AP is due to the anodization conditions, the samples are prepared by crushing the etched layers and some of the substrate (the ion milling step is avoided). A high resolution TEM image of a channel cross-section is presented in Fig. 3. The AP, at the interface between crystalline SiC and void, is clearly visible as a disordered strip.

Existence of an AP was also predicted by our optical models (to be discussed in detail in a future communication). Analysis of the samples revealed that mixtures of crystalline SiC and void, using different effective medium approximations [9], does not result in satisfactory fits. In order to

obtain good fits the AP had to be taken into consideration. In addition, the Drude expression (see above) representing the free carrier contribution vanished during the optical analysis of the AP. It was an evidence for a more dielectric like behaviour of this phase compared with crystalline SiC. A large network of pores surrounded by the electric isolating AP influences the electronic properties of the material extensively as will be discussed below. The true nature of the AP can be very complex since it may represent amorphization of the pore walls during the etching process and/or remaining etch products which are not efficiently transported from the sample and are deposited on its pore walls. Such a deposition may in turn be a complex temperature, time and pH-dependent phenomenon.

Since the substrate used was n-type and highly doped, the resistivity of the substrate and contact was assumed to be very low and neglected in this measurement. Figures 4a and 4b show the I-V characteristics measured on the 1.7  $\mu\text{m}$  PSC layer. It can clearly be seen that the PSC layer is highly resistive. The resistivity measured at room temperature (296 K) was in the order of  $2.9 \times 10^8$  whereas at 347 K it was  $9.2 \times 10^7 \cdot \text{cm}$ . The activation energy ( $E_a$ ) calculated by the temperature measurements was 1.45 eV, which is believed to be responsible for such a high resistance in PSC. This value is comparable to the activation energy of V-doped semi-insulating 4H-SiC substrates, which is in the range of 1.4-1.6 eV. Since it is possible to make masking and patterning, this highly resistive PSC also can find applications for isolation of electronic devices from each other on a chip.

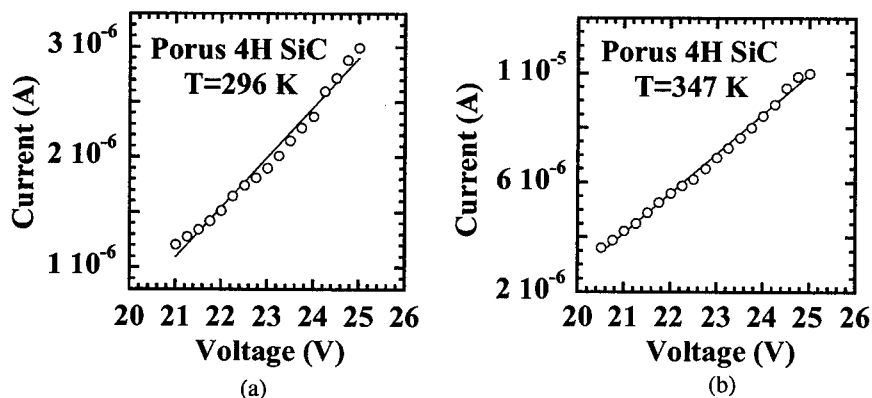


Fig. 4 a) I-V characteristics of a 1.7  $\mu\text{m}$  PSC sample at 296 K. b) I-V characteristics of the sample at 347 K.

## References

- [1] J.S. Shore, I. Grimberg, B.Z. Weiss and A.D. Kurtz, *Appl. Phys. Lett.* **62** (1993), p. 2836.
- [2] A.O. Konstantinov, A. Henry, C. Harris and E. Janzén, *Appl. Phys. Lett.* **66** (1995), p. 2250.
- [3] W.J. Schaffer, G.H. Negley, K.G. Irvin and J.W. Palmour, in *Diamond, Silicon Carbide and Nitride Wide bandgap Semiconductors*, edited by C. H. Carter, Jr., G. Gildenbalt, S. Nakamura and R. Nemanich, MRS Symposium Proceedings Vol. 339 (MRS, Pittsburgh, 1994), p. 595.
- [4] R.L. Smith, and S.D. Collins, *J. Appl. Phys.* **71** (1992), p. R1.
- [5] G. Oskam, A. Natarajan, P.C. Searson and F.M. Ross, *Appl. Surf. Sci.* **119** (1997), p. 160.
- [6] W.A. McGahan, B.D. Johs and J.A. Woollam, *Thin Solid Films* **234** (1993), p. 443.
- [7] P.Y. Yu, and M. Cardona, *Fundamentals of Semiconductors: Physics and Materials Properties*, Springer-Verlag, Berlin 1996, Chap 6.
- [8] A.M. Danishevskii, M.V. Zamoryanskaya, A.A. Sitnikova, V.B. Shuman and A.A. Suvorova, *Semicond. Sci. Technol.* **13** (1998), p. 1111.
- [9] D.E. Aspnes, *Thin Solid Films* **89** (1982), p. 249.

## Characterization of Polycrystalline SiC Grown on SiO<sub>2</sub> and Si<sub>3</sub>N<sub>4</sub> by APCVD for MEMS Applications

Chien-Hung Wu<sup>1</sup>, Christian A. Zorman<sup>2</sup> and Mehran Mehregany<sup>2</sup>

<sup>1</sup> Department of Materials Science and Engineering, Case Western Reserve University,  
10900 Euclid Ave., Cleveland, OH 44106, USA

<sup>2</sup> Department of Electrical Engineering and Computer Science, Case Western Reserve University,  
Cleveland, OH 44106, USA

**Keywords:** Polycrystalline SiC, Si<sub>3</sub>N<sub>4</sub>, SiO<sub>2</sub>

### Abstract

Polycrystalline silicon carbide (poly-SiC) films were deposited on SiO<sub>2</sub> and Si<sub>3</sub>N<sub>4</sub> substrates at temperatures between 1050°C and 1280°C by APCVD and characterized using SEM and TEM. In general, the average grain size of the as-deposited films on both substrate types increases with increasing deposition temperature. Poly-SiC films deposited on Si<sub>3</sub>N<sub>4</sub> have a dense microstructure and small grain size, whereas poly-SiC deposited on SiO<sub>2</sub> have a large grain size, and a low density interface region which contain voids. The observed differences in the deposited films may be due to a high energy barrier for poly-SiC deposited on SiO<sub>2</sub>.

### Introduction

Historically, research in SiC growth has mainly focussed on heteroepitaxy of single crystalline 3C-SiC on Si substrates and homoepitaxy of hexagonal polytypes for electronic device applications. SiC has, however, shown great promise as a micromechanical material for harsh environments because of its excellent electrical, chemical and mechanical properties [1]. For SiC surface micromachining, polycrystalline SiC (poly-SiC) structural layers are often deposited on amorphous layers such as SiO<sub>2</sub>, and Si<sub>3</sub>N<sub>4</sub>. Although poly-SiC surface micromachining has been demonstrated for several device applications [2,3], little has been reported on the properties of poly-SiC on SiO<sub>2</sub> [4-6], and even less about such deposition on Si<sub>3</sub>N<sub>4</sub>. This paper presents an investigation of poly-SiC films deposited on SiO<sub>2</sub> and Si<sub>3</sub>N<sub>4</sub> substrate layers at growth temperatures between 1050°C and 1280°C by APCVD, in order to develop suitable structural layers and substrate materials for SiC MEMS.

### Experimental

A rf-induction heated APCVD system was used to deposit poly-SiC films using silane (5% in H<sub>2</sub>) and propane (15% in H<sub>2</sub>) as source gases, and hydrogen as a carrier gas. Phosphine (100 ppm in H<sub>2</sub>) was used as a doping gas. 1.5 µm-thick thermally-grown SiO<sub>2</sub>, and 200 nm-thick LPCVD-deposited Si<sub>3</sub>N<sub>4</sub> on 100 mm-diameter Si wafers were used as substrates. Susceptor temperatures ranged between 1050°C and 1280°C and deposition periods of 30 sec and 30 min were used. In all cases, the deposition process was initiated with a 5 min *in-situ* cleaning of the substrate in a hydrogen ambient at 1000°C, after which the susceptor temperature was raised to the deposition temperature, and silane, and propane were introduced into the hydrogen carrier gas. The silane flow rate was fixed at 102 sccm for all depositions. To obtain stoichiometric poly-SiC films, the propane flow rate was varied from 26 sccm to 46 sccm, with the higher

propane flow rates needed for the lower deposition temperatures. A hydrogen flow rate of 25 slm was maintained throughout the process, and a phosphine flow rate of 180 sccm was used to deposit doped poly-SiC films. A deposition time of 30 sec was chosen to investigate the nucleation of poly-SiC on both substrate types, while a deposition time of 30 min was used to study the microstructure of continuous films.

SEM was used to determine the nucleation density for the 30 sec depositions and to investigate the surface morphology of the continuous films. Crystal orientation and grain size were characterized by XRD and TEM. The interface between the poly-SiC film and the substrate was examined by conventional cross-sectional TEM.

### Results and Discussion

Poly-SiC deposited for 30 sec at 1050°C and 1160°C have a higher nucleation density on  $\text{Si}_3\text{N}_4$  than on  $\text{SiO}_2$ , as shown in the SEM micrographs of Fig. 1. In addition, the nucleation density at 1160°C is higher than that at 1050°C for both substrates. The estimated nucleation density of SiC on  $\text{Si}_3\text{N}_4$  is about  $1.7 \times 10^{10}/\text{cm}^2$  at 1050°C and  $1.6 \times 10^{11}/\text{cm}^2$  at 1160°C. On  $\text{SiO}_2$ , the nucleation density is about  $7 \times 10^8/\text{cm}^2$  at 1050°C and  $8.8 \times 10^9/\text{cm}^2$  at 1160°C. However, at 1280°C (not shown), the nucleation density of SiC on  $\text{SiO}_2$  is only about  $1.7 \times 10^6/\text{cm}^2$ , whereas no nuclei are found on  $\text{Si}_3\text{N}_4$ , but the  $\text{Si}_3\text{N}_4$  surface was significantly roughened.

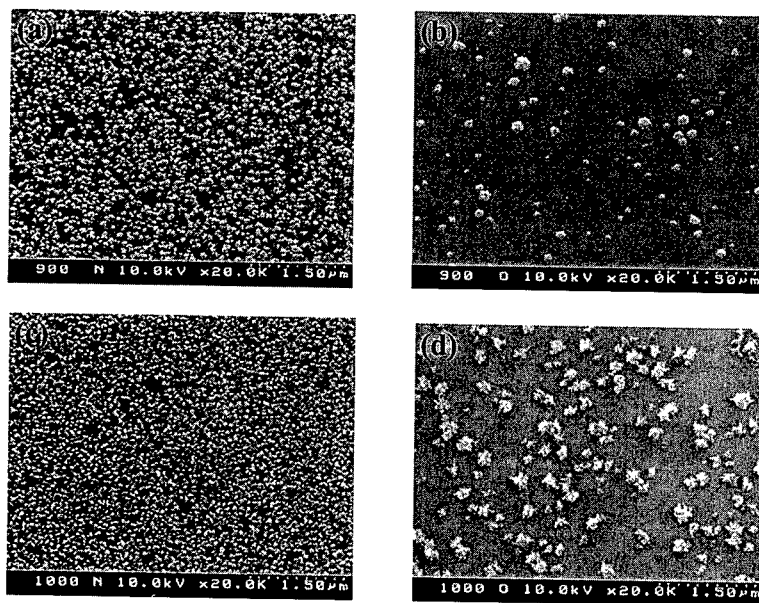


Figure 1. Plan-view SEM micrographs of poly-SiC deposited for 30 sec: (a) on  $\text{Si}_3\text{N}_4$  at 1050°C; (b) on  $\text{SiO}_2$  at 1050°C; (c) on  $\text{Si}_3\text{N}_4$  at 1160°C; and (d) on  $\text{SiO}_2$  at 1160°C.

For the 30 min depositions, the poly SiC films on  $\text{Si}_3\text{N}_4$  had a specular optical appearance, whereas the films on  $\text{SiO}_2$  were matted. SEM micrographs show that the poly-SiC films grown at 1050°C on  $\text{Si}_3\text{N}_4$  exhibit a smooth and relatively featureless surface, whereas the poly-SiC film deposited on  $\text{SiO}_2$  had a much rougher surface with numerous depressions [6]. The

surface morphology of the poly-SiC films grown at 1160°C appear similar to those at 1050°C, with numerous small grains decorating the surface. The poly-SiC films deposited at 1280°C on  $\text{Si}_3\text{N}_4$  substrates are continuous, faceted, and exhibit good adhesion (Fig. 2a), but poly-SiC films deposited on  $\text{SiO}_2$  substrates are discontinuous, particle-like, and exhibit poor adhesion, as shown in Figs. 2b and 2c. Although continuous poly-SiC films form on  $\text{SiO}_2$  in some small areas, delamination is always observed. Etch pits are found on the  $\text{SiO}_2$  surfaces, with the density of etch pits being highest beneath the delaminated sections.

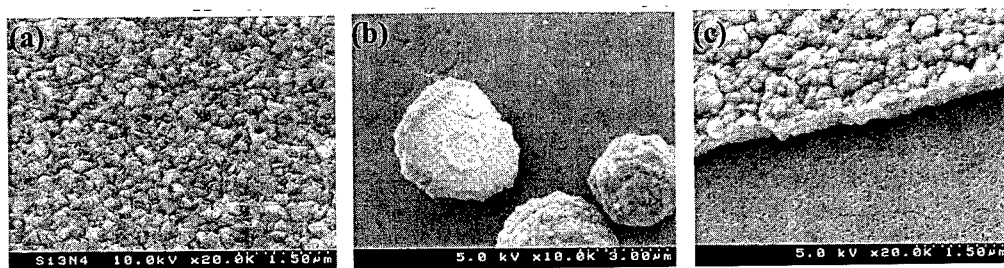


Figure 2 SEM micrographs of poly-SiC deposited for 30 min at 1280°C: (a) a continuous film on  $\text{Si}_3\text{N}_4$ ; (b) SiC particles on  $\text{SiO}_2$ ; and (c) a delaminated SiC film on  $\text{SiO}_2$ .

The average grain size of the continuous SiC films was estimated from the measured full width half maximum of the 3C-SiC (111) XRD peak. The average grain size of poly-SiC films on both substrate types increased with increasing deposition temperature. In general, poly SiC films on  $\text{SiO}_2$  had larger grains than on  $\text{Si}_3\text{N}_4$ . The average grain size of poly-SiC on  $\text{SiO}_2$  ranged from  $\sim 5.4$  nm at 1050°C to  $\sim 0.16$   $\mu\text{m}$  at 1280°C, whereas the average grain size of poly-SiC films on  $\text{Si}_3\text{N}_4$  ranged from  $\sim 3.7$  nm at 1050°C to  $\sim 0.12$   $\mu\text{m}$  at 1280°C.

Cross-sectional TEM samples were prepared to characterize the microstructure of the poly-SiC films as well as the SiC/ $\text{SiO}_2$  and SiC/ $\text{Si}_3\text{N}_4$  interfaces. TEM micrographs confirm that the grain size increased with increasing deposition temperature. For the films deposited at 1050°C on both substrates, the films exhibit a fine grain structure and a sharp, featureless interface between the poly-SiC film and the substrate. However, TEM micrographs from poly-SiC films on  $\text{SiO}_2$  substrates show evidence that a lower density region exists near the film/substrate interface [6], an effect not seen for poly-SiC on  $\text{Si}_3\text{N}_4$ . This less dense region may be related to the surface depressions observed by SEM. In contrast to the films deposited 1050°C, the interface between poly-SiC and  $\text{Si}_3\text{N}_4$  is rough for a deposition temperature of 1280°C (Fig. 3a), which is consistent with the SEM observation for 30 sec growth. However, no localized etch pits were found for the 30 min growth. For poly-SiC films grown on  $\text{SiO}_2$  at 1280°C, columnar-like grain structures are observed. In addition, etch pits are formed on the  $\text{SiO}_2$  substrate and sealed voids are formed in the film, as shown in Fig. 3b. The etch pit in Fig. 3b is only about 90 nm in depth and does not completely penetrate the  $\text{SiO}_2$  underlayer. TEM analysis suggests that etch pits are related to the original nucleation sites of poly-SiC particles on  $\text{SiO}_2$ . The poly-SiC films on both substrates have a columnar-like structure, with SiC grains on  $\text{SiO}_2$  substrates showing a radial distribution from etch pits.

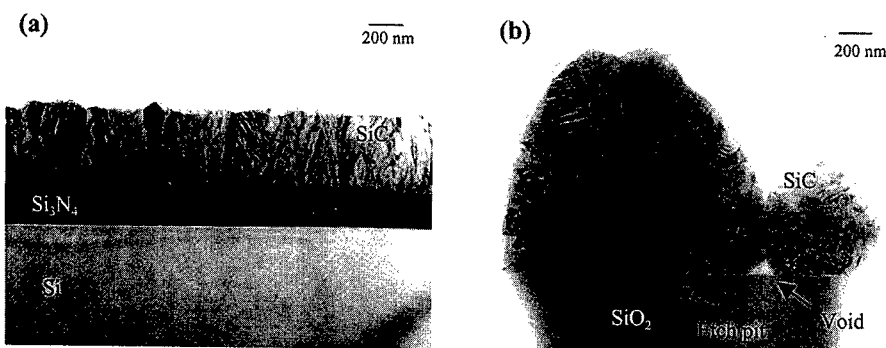


Figure 3. XTEM micrographs of poly-SiC deposited at 1280°C: (a) on  $\text{Si}_3\text{N}_4$ ; and (b) on  $\text{SiO}_2$ .

The observed differences for poly-SiC films on the two substrate types may be due to differences in the surface free energy, which leads to a higher energy barrier and larger critical nucleus size for poly-SiC deposited on  $\text{SiO}_2$ . In general, a higher deposition temperature will lead to a higher energy barrier, which leads to a lower nucleation density. This generalization is not consistent with the observations for SiC nucleation at 1050°C and 1160°C. Because two precursor gases are used in the CVD process, the temperature dependence of the decomposition kinetics of  $\text{C}_3\text{H}_8$  and  $\text{SiH}_4$  govern the process, which may result in a higher concentration of active species at 1160°C than at 1050°C. However, at 1280°C, a much higher energy barrier may cause problems with the SiC nucleation process on smooth  $\text{Si}_3\text{N}_4$  and  $\text{SiO}_2$  surfaces. Roughing and etch pit formation at 1280°C may create alternative SiC nucleation mechanisms on  $\text{Si}_3\text{N}_4$  and  $\text{SiO}_2$ . The delamination of SiC on  $\text{SiO}_2$  is most likely related to the nucleation mechanism (etch pits).

### Summary

A comparison of poly-SiC films deposited on  $\text{SiO}_2$  and  $\text{Si}_3\text{N}_4$  substrates by APCVD is presented in this paper. Poly-SiC films deposited on  $\text{Si}_3\text{N}_4$  have dense microstructures and small grain sizes for deposition temperatures between 1050°C and 1280°C, whereas the poly-SiC films deposited on  $\text{SiO}_2$  have a lower density region near the interface and etch pits in the substrate. The observed differences may be due to a higher energy barrier for poly-SiC deposited on  $\text{SiO}_2$ .

### Acknowledgments

The authors gratefully thank John Sears of CWRU for his help with SEM. This work was supported by ARO MURI (Contract # DAAH04-95-1-0097).

### References

- [1] M. Mehregany, C. A. Zorman, N. Rajan, and C. H. Wu, *Proceeding of the IEEE*, **86**, (1998), p.1594.
- [2] A.J. Fleischman, X. Wei, C.A. Zorman, and M. Mehregany, *Proc. 7<sup>th</sup> Inter. Conf. On SiC, III-Nitrides and Rel. Mat.*, Stockholm, Sweden, Aug.31-Sep.5, 1997, Trans Tech Publications Ltd, Switzerland, (1998), p.885.
- [3] A.A.Yasseen, C. H. Wu, C.A. Zorman, M. Mehregany, *12<sup>th</sup> IEEE Inter. Micro Electro Mechanical Systems Conf.*, Orlando, U.S.A., Jan.17-21, (1999), p.644.
- [4] J. Rodríguez-Viejo, N. Clavaguera, Z. El Felk, M. T. Clavaguera-Mora, G. Arnaud, J. Camassel, J. Pascual, S. Berberich, and J. Millán, *Mater. Sci. Technol.* **12**, (1996), p.98.
- [5] Y. Sun, T. Miyasato, *J. Appl. Phys.* **84**, (1998), p.2602.
- [6] C. H. Wu, C. A. Zorman, and M. Mehregany, *Thin Solid Films*, in press, (1999).



## Theory of Below Gap Absorption Bands in n-Type SiC Polytypes; Or, How SiC Got Its Colors

Walter R.L. Lambrecht, Sukit Limpijumnong, Sergey Rashkeev  
and Benjamin Segall

Department of Physics, Case Western Reserve University, Cleveland, OH 44106-7079, USA

**Keywords:** Band Structure, n-Type, Optical Absorption

**Abstract:** Optical absorption bands below the band gap in n-type SiC are discussed in the framework of first-principles band structure calculations. While the peak positions and their polarization are well reproduced in a pure band-to-band model, the widths of the spectra obtained for samples with high impurity concentrations indicate a significant role of the band tailing due to the N-impurities. This leads to a partial breakdown of the vertical selection rule, which we take into account by means of a density of states calculation over a limited region of k-space, and a weaker breakdown of symmetry selection rules. Differences for samples with low concentration of dopants and the possibility of impurity resonances in the continuum are discussed.

### 1. INTRODUCTION

In this paper, we discuss the optical absorption bands in n-type SiC. These absorption bands among others are responsible for the color of platelet crystals of SiC, which accounts for the subtitle of this paper. In reality the color is mostly determined by the absorption for  $\mathbf{E} \perp \mathbf{c}$  in platelets, whereas the stronger absorption bands occur for  $\mathbf{E} \parallel \mathbf{c}$ . While pure 6H-SiC crystals only absorb in the far violet and UV and are therefore transparent, the extra absorption bands at  $\sim 2$  eV (red-orange) and at 2.8-3 eV (blue) in n-type material eliminates essentially red and blue primary colors and leaves green leading to a greenish color in this polytype. In 4H and 15R the  $\mathbf{E} \perp \mathbf{c}$  absorption band at 2 eV is not present and only the blue is absorbed, which would explain a more yellowish appearance. Of course, these effects on the colors depend on the doping concentration. It is not our intention to investigate the details of how the color of the crystals comes about but rather what the nature is of these absorption bands.

These absorption bands are known to some as the "Biedermann bands" because Biedermann in a paper in 1965 [1] presented results on these optical absorption bands for a number of polytypes (4H, 6H, 8H and 15R) and showed distinct spectra for different polarizations. There is however a more extensive literature on these absorption bands, see [2], and some aspects of them are still not entirely clear. We viewed them originally as providing a good test for the details of the conduction band structures in various polytypes. While our previous work on the Biedermann spectra [2] has addressed all polytypes for which we are aware of experimental data 3C, 4H, 6H, 8H and 15R, we here focus mainly on 6H for lack of space. It turns out that in view of the high concentration of dopants in the original samples, (of estimated order of  $10^{19}/\text{cm}^3$ ) the transitions have a mixed character of defect-level-to-band and band-to-band nature [2]. Different behavior of these spectra was found in samples with low dopant concentrations by Dubrovskii and Radovanova [3], Stiasny and Helbig [4] and most recently Sridhara et al.[5]. We discuss how these various results fit into a unified picture.

### 2. COMPUTATIONAL APPROACH

The general computational method taken as the starting point for our analysis is the density functional theory (DFT) [6] combined with the full-potential [8] linear muffin-tin orbital (LMTO) band structure method [7]. Optical absorption matrix elements were calculated using the atomic sphere approximation (ASA).

The main possible source of error remaining on the energy bands lies in the fact that Kohn-Sham eigenvalues in the local density approximation differ from the true quasiparticle energies. The Kohn-Sham equation contains a local exchange correlation potential instead of the non-local and energy dependent exchange-correlation self-energy operator. The corrections due to this difference have been investigated for SiC using the GW approximation—in which the self-energy operator is given schematically by  $\Sigma_{xc}(1, 2) = iG(1, 2)W(1, 2)$  with  $G$  the one electron Green's function and  $W$  is the screened Coulomb interaction  $W(1, 2) = \int d^3v(1, 3)\epsilon^{-1}(3, 2)$ , and the numbers indicate  $(\mathbf{r}, t)$ —by a number of authors [9, 10, 11]. While the difference with LDA is mainly to shift up the entire conduction band by a constant gap correction, small variations from  $\mathbf{k}$ -point to  $\mathbf{k}$ -point and band to band occur in the calculations. These are of order 0.1 eV which is the accepted errorbar of the GW calculations.

### 3. HIGH CONCENTRATION LIMIT

Fig. 1 shows the Biedermann absorption bands [1] in 6H-SiC for the two polarizations and compares them to two different model calculations together with the relevant portion of the band structure. First, as a general overview of the spectrum, the region below 1 eV corresponds to an intra band or Drude-like absorption. It indicates that the carrier concentration in these samples was above that for the metal insulator transition. In fact, the estimated concentration mentioned in the paper is  $10^{19} \text{ cm}^{-3}$ . This is important because under these circumstances, one expects a significant band tail effect. The N donor levels broaden into a band which merges with the conduction band edge and forms an exponential band tail in the density of states due to the random fluctuations in potential associated with the distribution of impurities. The upper end of the spectrum near 3 eV is where the intrinsic indirect valence band to conduction band edge absorption sets in. The window in between is what we are concerned with here. Several specific absorptions occur in this region with a definite polarization dependence and variation from polytype to polytype. These arise from transitions of the doping carriers from their lowest initial states (impurity level or bottom of the conduction band) to the higher bands.

The first model we consider is a pure band-to-band model. The lowest conduction band is simply filled according to Fermi statistics and an estimated carrier concentration, assuming complete ionization of the donor levels into the lowest band. The optical absorption is then calculated from the imaginary part of the dielectric constant assuming strict adherence to the vertical  $\mathbf{k}$ -selection rule.

$$\epsilon_2^j(\omega, T) = \frac{e^2}{m^2\omega^2\pi} \sum_{if} \int \frac{d^3k}{(2\pi)^3} (f_{ik}(T) - f_{fk}(T)) |\langle i\mathbf{k} | p^j | f\mathbf{k} \rangle|^2 \delta(E_{fk} - E_{ik} - \hbar\omega), \quad (1)$$

with  $f_{i(f)}$  the Fermi factors for the initial and final states,  $p^j$  the  $j$ -Cartesian component of the momentum matrix element,  $E_n(\mathbf{k})$ , the energy bands and  $\hbar\omega$  the photon energy.

From the comparison of this model to the experiment it is clear that this model explains the energy differences and polarization dependence rather well, but it completely fails to predict the width of these bands. One observes transitions from the lowest band of  $U_1$  symmetry to the next two higher bands of the same symmetry for  $\mathbf{E} \parallel \mathbf{c}$  and to the bands of  $U_3$  symmetry for the  $\mathbf{E} \perp \mathbf{c}$  polarization.  $U_1$  and  $U_3$  are respectively even and odd with respect to the mirror plane passing through the  $\Gamma A H K$  plane of the Brillouin zone [12]. In the figure, we label the bands as  $c_n$  in increasing order of energy at the  $\mathbf{k}$ -point where the minimum occurs in  $c_1$ , which is at  $k_z = 0.4 \times \pi/c$  along  $U \equiv ML$ . Note that bands  $c_5$  and  $c_6$  cross near  $M$ . This circumstance could potentially be used to experimentally confirm the  $\mathbf{k}$ -location of the conduction band minimum (CBM) because it means that the  $(\mathbf{E} \parallel \mathbf{c})$   $c_1 \rightarrow c_5$  transition should have lower energy than the  $(\mathbf{E} \perp \mathbf{c})$   $c_1 \rightarrow c_6$  transition, whereas if the minimum occurred at  $M$ , the ordering of the  $\mathbf{E} \parallel \mathbf{c}$  and  $\mathbf{E} \perp \mathbf{c}$  transitions would be inverted. Unfortunately, this is not possible with the original Biedermann spectrum because of the  $\mathbf{k}$ -space broadening of the bands and because of the overlap of these bands to the onset of the intrinsic absorption.

In the next improvement of our model, we take into account that for high donor concentration, band tailing takes place and gives rise to initial states for the transitions which are essentially of a mixed impurity level and band character. They become progressively more band-like as we go to higher energies (closer to the nominal band edge or above it.) Within this model, one expects that the initial state wave function becomes somewhat localized, and, as a consequence, the vertical

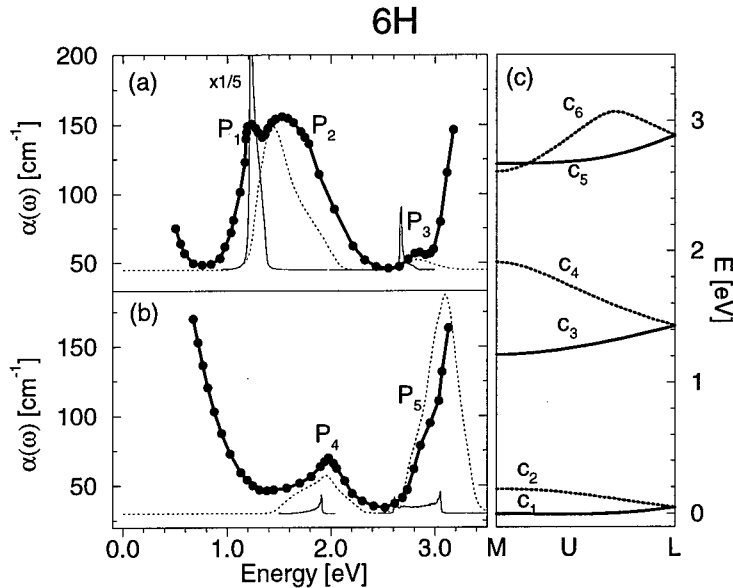


**Figure 1.** Biedermann [1] absorption bands, (thick line joining dots), in 6H, SiC, for (a)  $E \parallel c$ , and (b)  $E \perp c$ , compared to pure band-to-band model (thin solid line) and  $k$ -selection rule relaxed model (dashed line), in which the absorption is modeled as a superposition of matrix element weighted DOS to specific bands within a  $\delta k$  sphere around the  $k$ -point of the band minimum. The peak heights  $P_2$  and  $P_4$  are adjusted because the precise carrier concentration is unknown for the samples. Panel (c) gives the corresponding band structure, with solid lines corresponding to  $U_1$  and dashed lines to  $U_3$  symmetry.

$k$ -selection rule should be relaxed. In fact, one expects to reach final states within a  $k$ -space region around that of the initial state determined by the  $k$ -uncertainty corresponding to the extent of the initial state in real space. The latter is determined by a combination of the effective Bohr radius of the individual donor states and the random inter donor spacings at high concentration. In practice, we use a plausible  $\delta k$  of  $0.1 \times 2\pi/a$  (see [2] for estimates) and calculate the density of states within a sphere around the  $k$ -point location of the conduction band minimum. Instead of a single  $k$ -point joint density of states factor (the delta function part of Eq. 1), one now obtains a convolution of the initial and final densities of states weighted by the same average momentum matrix elements as before. This model now accounts semiquantitatively for the widths of the absorption bands, the relative magnitudes of the peaks and the shift of the experimental features towards slightly higher energy than the pure band-to-band model predicted. In particular, we note that the  $k$ -space broadening combined with the relatively strong dispersion of the upper bands leads to a significant shift of the peak maxima towards higher energy. The peak is strongly influenced by where we cut off in  $k$ -space. The shift arises in part also from the fact that the initial states lie in the band tail extending below the nominal band edge. In this picture, the initial states being derived from the shallow impurity level of a particular band edge still largely retain the symmetry character of the conduction band minimum and hence, one expects the symmetry selection rules to be largely but not perfectly maintained. The spectra of 4H-SiC indicate some smaller signatures of the "forbidden" bands and in 6H the "forbidden"  $c_1 \rightarrow c_4$  transition contributes to the very large width of the peak labeled  $P_2$ . However, this new model fails to account for the peak  $P_1$ .

We believe that the origin of the  $P_1$  peak is due to the special nature of the lowest conduction band of 6H. In fact, such a feature does not occur for 4H SiC, 15R, or 8H SiC. As already mentioned

the lowest band in 6H is very flat and in fact in the band structure calculations is found to have a camelback structure with a saddle point at  $M$  at about 5 meV above the minimum. With the estimated carrier concentration of Biedermann's samples, this saddle point is below the Fermi level and contributes as initial state. Since this state is expected to be extended, the vertical  $k$ -selection rule should be obeyed for transitions originating from it. It turns out that the band masses of the third band and the first band in the directions perpendicular to ML (given in Table 1) are nearly the same. This means that in the JDOS of Eq. 1 a quasi one-dimensional  $1/\sqrt{E}$  van-Hove singularity will occur. Thus, we view the peak  $P_1$  as a signature of the camelback structure.

#### 4. LOW CONCENTRATION LIMIT

Elsewhere in this conference, Sridhara et al. [5] report on an investigation of the Biedermann spectra as function of temperature in low concentration samples. Our present model predicts that at low concentrations the peak  $P_1$  which we ascribe to the saddle-point feature should be strongly suppressed and at low temperatures should disappear because we do no longer expect carriers with energy above the saddle point. In addition, one expects the relevant electrons to be frozen in the defect level at low temperatures and to be ionized to the band at high temperatures. This is precisely what these authors observe and is also in agreement with the observations of Dubrovskii and Radovanova [3]. At room temperature Sridhara et al. [5] obtain a fairly narrow peak at 1.3 eV, slightly higher than peak  $P_1$  in Biedermann's spectrum and indicating that the saddle point contribution is indeed lost. In fact, our band-to-band model predicts a peak at 1.25 eV for transitions from the minimum on the  $U$  axis, which shifts somewhat to higher energies with increasing temperature. This peak corresponds essentially to pure band-to-band transitions and has a FWHM of about 0.1 eV, consistent with our band model. In other words, this width arises from a band structure effect, namely that the very flat lowest band spreads the carriers out over some width in  $k$ -space as far as initial states are concerned and the corresponding final band's dispersion over this  $k$ -range then leads to the width of the peak even if perfect vertical  $k$ -conservation is assumed. On the other hand, at low temperatures, one expects essentially all carriers to be frozen in the isolated impurity level (81 meV below the band for the h-site N donor). Thus, at low temperatures one expects a impurity level to band absorption shifted up from the band-to-band one by 81 meV. This is indeed what is observed. Surprisingly, however, Sridhara et al. [5] observe the lower energy peak to come back at the lowest temperatures. It is interpreted by them as a new transition and tentatively described as a transition from a localized impurity level to a resonance. Such transitions have been previously reported in GaP [13, 14].

To see whether such resonances are plausible, we performed a calculation for a 6H-SiC cell with one of the C atoms (the h-site one) replaced by N. This is of course far from the dilute limit and the N in this model in fact occurs in a layer containing only N. Thus, it strongly exaggerates the N-N impurity interaction in the basal plane. Nevertheless, inspection of the density of states of this model system, shown in Fig. 2, reveals that a new peak is pulled out of the density of states peak (of pure 6H-SiC) at 1.5 eV above the CBM, i.e. precisely where the bands  $c_3, c_4$  contribute to the DOS. This lower peak, labeled  $R$  in the figure furthermore has a stronger N than C component, indicating it is in some sense localized on the N. Being an antibonding state in the conduction band, its main atomic orbital character is Si-like and the  $R$ -peak is dominated by Si atoms which are nearest neighbors to the N.

Resonances induced by impurities have been discussed in terms of the effective mass approach by Bassani et al. [15] and in the context of excitons also by Kane [17] and by Velický and Sak [16]. For an attractive potential, as is the case here, they can be associated either with minima or with saddlepoints. The general idea of the effective mass approach is that the perturbation is relatively weak and the impurity state is associated with a specific portion of  $k$ -space (near some band extremum) and only weakly coupled to other regions in  $k$ -space. So, we have to look for such features at the relevant energy in our band structures. The general condition for the resonance to survive broadening by the interaction with the continuum is that the coupling to states at the same energy but other  $k$  is weak. The conditions that make this favorable are either a real minimum well separated in  $k$ -space from other bands or an  $M_1$  saddlepoint for which the negative mass is much larger in absolute value than the positive masses. In both 4H and 6H-SiC there are minima in the  $c_3$  band nearby in  $k$ -space to the absolute minimum of the conduction band which leads to the defect

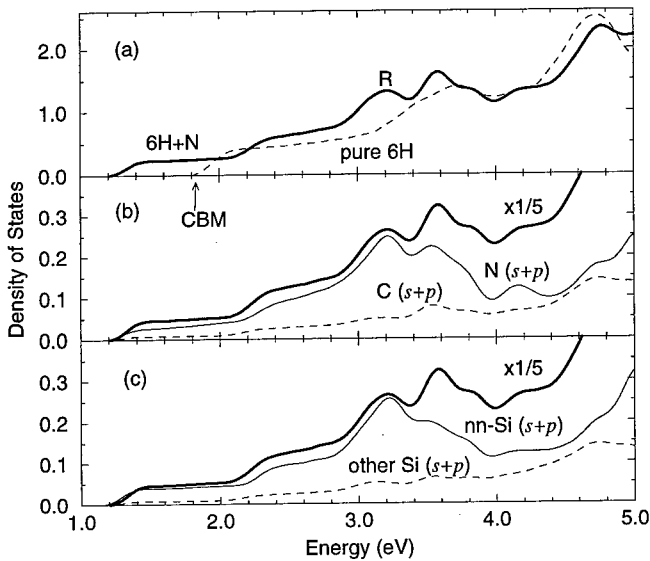


**Figure 2.** (a) Density of states of 6H-SiC with a N in every hexagonal C position (solid line) compared to that of pure 6H-SiC (dashed line) in the conduction band range. CBM indicates the conduction band minimum. In (b) and (c) relevant partial densities of states (PDOS) are compared to the total to help identify the peak R as a Nitrogen induced resonance. Each PDOS corresponds to one atom.

**Table 1.** Effective mass tensors of lowest bands involved in Biedermann transitions and resonances

polytype	band extremum	$m_z^a$	$m_y$	$m_x$
6H	minimum in $c_1$ at $U^b$	2.08	0.72	0.25
	saddle in $c_1$ at $M$	-4.17	0.76	0.27
	minimum in $c_3$ at $M$	0.62	1.05	0.16
4H	minimum in $c_1$ at $M$	0.33	0.57	0.29
	saddle in $c_3$ at $M$	-0.28	25.8	0.17
	minimum in $c_3$ at $U^c$	0.23	0.84	0.21

<sup>a</sup>  $x$ ,  $y$  and  $z$  are along  $M-K$ ,  $M-\Gamma$  and  $M-L$  directions of BZ

<sup>b</sup> The minimum occurs at  $k_z = 0.4 \times \pi/c$

<sup>c</sup> The minimum occurs at  $k_z = 0.65 \times \pi/c$

state. They are therefore the primary candidates to associate the resonances with. However, there are also some saddlepoints to consider. One of the saddle points occurs near the  $K$ -point along the  $KT$  line. It is a  $M_1$  type saddle but none of its masses are particularly large. Also, even if a discernable resonance would be associated with this extremum, it should be kept in mind that it lies several  $\delta k$  away from the position of the conduction band minimum, where  $\delta k$  is an estimate of the  $k$ -space broadening associated with the donor wave function extent. So, it can fairly safely be ruled out as playing a significant role. In 4H, the minimum in the  $c_3$  band occurs along  $U$  rather than at  $M$  and  $M$  has a  $M_1$ -type saddle point. This saddle point has one very large positive mass but the negative mass is comparable to the other small positive mass. This situation is less favorable for a sharp resonance to form. The mass tensors are given in Table 1. An effective spherical mass approximation  $(m_x m_y m_z)^{1/3}$  for the minimum in  $c_1$  ( $c_3$ ) in 4H gives 0.38 (0.34). Thus similar binding energies are expected for the impurity state below the band and for the resonance below the upper band. In 6H, we obtain similarly 0.72 and 0.56 for the masses of the lower and higher band minima. Thus perhaps, a slightly shallower resonance than bound defect level is expected.

Stiasny and Helbig[4] obtained a rather different spectrum in low carrier concentration samples. The main differences are that the spectrum is shifted to 1.9 eV, is significantly broader and shows less polarization dependence and little temperature effect over the range 10–300 K. They interpreted

it as arising from a deep center, possibly due to N on Si site, based on similarity in shape to the photoluminescence spectrum from which it is, according to them, Stokes shifted. In Ref. [2] we argued that this is not conclusive and that the spectrum could alternatively be explained within our general picture as due to transitions to the bands from a level that is only slightly deeper than the one considered above. In fact, a shift as high as 0.3 eV can be accounted for by the dispersion of the upper band if the  $\delta k$  in our model is increased in accordance with expectations for a more localized state. This explains at the same time the further loss of polarization and the temperature dependence. A plausible candidate for this slightly deeper level is N at the k-site.

## 5. CONCLUSIONS

A unified model for the description of the behavior of optical absorption bands in n-type SiC was presented. It is shown to account both for the high and low concentration behaviors. The possibility of resonance effects in the conduction band recently proposed by Sridhara et al. was discussed.

We wish to thank R. P. Devaty and W. J. Choyke for communicating their experimental results to us prior to publication and for stimulating discussions on the topic of resonances. This work was supported by NSF under grant No. DMR95-29376.

## References

- [1] E. Biedermann, *Solid State Communn.* **3** (1965), p. 343.
- [2] S. Limpijumnong, W. R. L. Lambrecht, S. N. Rashkeev, and B. Segall, *Phys. Rev. B* **59** (1999), p.12890.
- [3] G. B. Dubrovskii and E. I Radovanova, *Fiz. Tverdogo Tela* **11** (1969), p. 680 [*Sov. Phys. Solid State* **11** (1969), p. 545].
- [4] Th. Stiasny and R. Helbig, *Phys. Stat Solidi (a)* **162** (1997), p. 239.
- [5] S. G. Sridhara, S. Bai, O. Schigiltchoff, R. P. Devaty, and W. J. Choyke, this conference, p. 551
- [6] P. Hohenberg and W. Kohn, *Phys. Rev.* **136** (1964), p. B864; W. Kohn and L. J. Sham, *ibid.* **140** (1965), p. A1133.
- [7] O. K. Andersen, O. Jepsen, and M. Šob, in *Electronic Band Structure and its Applications*, edited by M. Yussouff (Springer, Heidelberg 1987) p. 1
- [8] M. Methfessel, *Phys. Rev. B* **38** (1988), p. 1537.
- [9] M. Rohlfing, P. Krüger, J. Pollmann, *Phys. Rev. B* **48** (1993), p. 1791.
- [10] W. H. Backes, P. A. Bobbert, and W. van Haeringen *Phys. Rev. B* **51** (1994), p. 4950.
- [11] B. Wenzien, P. Käckell, F. Bechstedt, and G. Cappellini, *Phys. Rev. B* **52** (1995), p. 10897.
- [12] Symmetry labeled energy bands for 3C, 2H, 6H and 4H SiC are available in Sukit Limpijumnong, Ph. D. thesis, Case Western Reserve University, 1999.
- [13] A. Onton, *Phys. Rev. B* **4** (1971), p. 4449.
- [14] E. Goldys, P. Galtier, G. Martinez and I. Gorczyca, *Phys. Rev. B* **36** (1987), p. 9662.
- [15] F. Bassani, G. Iadonisi, and G. Preziosi, *Rep. Prog. Phys.* **37** (1974), p. 1099.
- [16] B. Velický and J. Sak, *Phys. Status Solidi* **16** (1966), p. 157.
- [17] E. O. Kane, *Phys. Rev.* **180** (1969), p. 852.

email to W. R. L. Lambrecht: wxl2@po.cwru.edu

## Absorption Bands Associated with Conduction Bands and Impurity States in 4H and 6H SiC

S.G. Sridhara, S. Bai, O. Shigiltchoff, R.P. Devaty and W.J. Choyke

Department of Physics and Astronomy, University of Pittsburgh, Pittsburgh, PA 15260, USA

**Keywords:** Absorption, Band Structure, Conduction Bands, Donors, Nitrogen

**Abstract** Absorption spectra of n-type 4H and 6H SiC are presented and tentatively interpreted. The absorption bands are assigned to transitions involving the lowest conduction band, higher conduction bands, nitrogen donor levels, and/or possible donor induced resonances.

### Introduction

Several groups have studied absorption bands below the fundamental absorption edge in n-type 3C [1], 4H [2-5], 6H [2,3,6-12], 8H [2,3] and 15R [2,3] SiC crystals. The spectra measured with polarizations  $E||\hat{c}$  and  $E\perp\hat{c}$ , where  $\hat{c}$  is parallel to the crystal c-axis, are quite distinct. The absorption bands measured using  $E||\hat{c}$  are generally stronger. The observed peaks have been assigned to electronic transitions from nitrogen donor levels to higher conduction bands or to direct transitions from the lowest conduction band near its minima to higher conduction bands. Lambrecht et al. [13,14] recently found good agreement between absorption coefficients and selection rules calculated from the band structures and published data for both polarizations for several SiC polytypes. However, the experimental data upon which their comparison is based was obtained using heavily doped ( $\sim 10^{19} \text{ cm}^{-3}$ ) samples. Thus, the observed peaks are quite broad and effects such as band tailing may be present. Here we present polarized absorption spectra obtained using relatively moderately doped samples of 6H and 4H SiC and discuss the interpretation. The spectra presented here are selected from a comprehensive data set that will be published elsewhere.

### Experiment

The absorption measurements are performed using two setups: (1) a specially designed two-beam apparatus for measurements from 4000Å-8500Å and (2) a single-beam near infrared monochromator for measurements from 0.8μm-1.8μm. Spectra are measured in both  $E||\hat{c}$  and  $E\perp\hat{c}$  polarizations. A custom designed cold finger cryostat is used to obtain spectra in the temperature range 77 K-300 K. An immersion type liquid He cryostat is used to obtain spectra at 2 K.

### 6H SiC

Fig. 1 shows near infrared absorption spectra, polarized  $E||\hat{c}$ , of an n-type (estimated to be  $n \sim 1.0 \times 10^{17} \text{ cm}^{-3}$ , with very low compensation) boule sample of 6H SiC taken at four temperatures ranging from 2 K to room temperature. The spectra in the range 77 K – 300 K show some resemblance to published spectra [3,9-11]. However, the 2 K spectrum, not shown in the referenced literature, leads us to reinterpret the observed temperature dependence. As the temperature decreases from room temperature, peak B (1.31 eV) decreases and peak A (1.39 eV) grows. At 2 K a new feature C replaces peak B. Following the notation of Limpijumngong et al. [14], the absorption transitions are related to the lowest conduction band  $c_1$  and the third conduction band  $c_3$ .

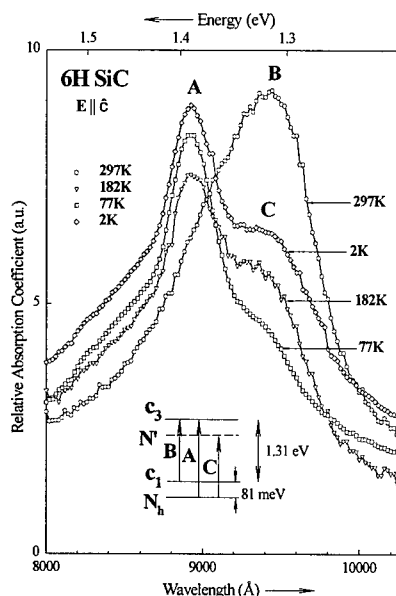


Fig.1  $E||\hat{c}$  absorption spectrum of n-type ( $n \sim 1 \times 10^{17} \text{ cm}^{-3}$ ) 6H SiC measured at four temperatures. The inset schematically represents the interpretation discussed in the text.

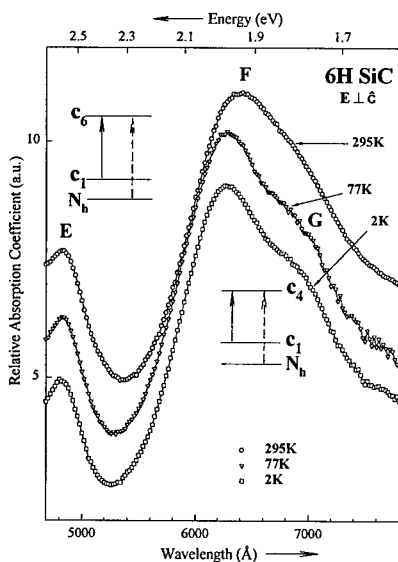


Fig. 2  $E \perp \hat{c}$  absorption spectra of n-type ( $n \sim 1 \times 10^{18} \text{ cm}^{-3}$ ) 6H SiC measured at three temperatures. The insets schematically represent the interpretation discussed in the text.

Both bands have  $U_1$  symmetry along the M-L line on the Brillouin zone boundary, so that  $c_1 \rightarrow c_3$  transitions are allowed for  $E||\hat{c}$ . The ionization energies of nitrogen donors in 6H SiC are 81 meV, 137 meV and 143 meV for the hexagonal (h) and two quasicubic ( $k_1$  and  $k_2$ ) sites, respectively, as determined by analysis of infrared absorption data [15]. The schematic diagram shown as an insert on Fig. 1 shows the shallowest nitrogen donor level, marked  $N_h$  and the two relevant conduction bands. Also shown is a resonant donor level, marked  $N'$ , associated with the  $c_3$  conduction band. Bassani et al. [16] review the theory of donor induced resonances in the conduction band. Such resonances have been proposed to explain infrared absorption spectra associated with Te, Se, and Si doped n-type GaP [17,18]. At 2 K all transitions must originate in the shallow nitrogen level  $N_h$ . In this interpretation, the deeper k-site nitrogen donor levels are not observed because the absorption cross sections are smaller due to tighter binding. The features marked A and C on Fig. 1 are assigned to transitions from  $N_h$  to conduction band  $c_3$  and its associated h-site nitrogen resonance level  $N'$ , respectively. To obey the selection rules, we assume that both  $N_h$  and  $N'$  have the same symmetry. We have in mind that they are both 1s-like, analogous to the interpretation of Goldys et al. [18]. With increasing temperature, electrons are thermally excited from  $N_h$  into conduction band  $c_1$ . Thus, peaks A and C decrease while peak B, which we assign to inter-conduction band transitions  $c_1 \rightarrow c_3$ , grows.

Fig. 2 shows  $E \perp \hat{c}$  absorption spectra of an n-type ( $n \sim 1 \times 10^{18} \text{ cm}^{-3}$ ) 6H SiC Lely sample, taken at 2 K, 77 K and 295 K. This sample is relatively free of internal stress. Because the three spectra were measured using different setups, it is not possible to directly compare the magnitudes of the absorption. The peak at 4800 Å (labeled E), observed as a shoulder by Biedermann [2], exhibits essentially no temperature dependence from 2 K to 295 K. There is no evidence for changes in occupation of a conduction band versus nitrogen donor levels, and no shift of the wavelength position. The fundamental indirect energy gap of 6H SiC shifts about 30 meV over this temperature range. Following the notation of Limpijumnong et al. [14], peak E is assigned to  $c_1(U_1) \rightarrow c_6(U_3)$  inter-conduction band transitions (The initial states might also be the donor states associated with the  $c_1$  band.), which are allowed for polarization  $E \perp \hat{c}$ . The data imply that the energy separation of these bands is independent of temperature between 2 K and 295 K. A stronger peak F is observed near 6260 Å at 2 K with a long wavelength shoulder G near 6900 Å. At 77 K



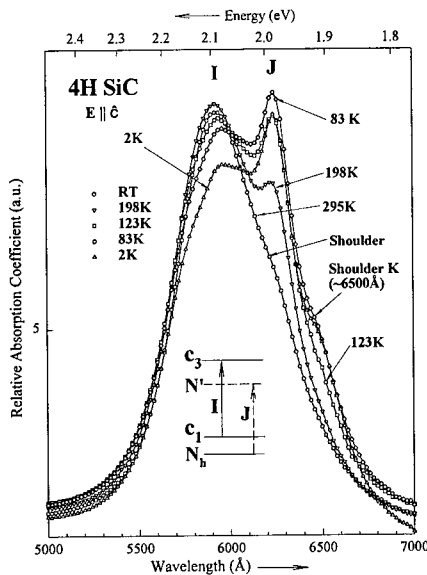


Fig. 3  $E||\hat{c}$  absorption spectrum of an n-type ( $n \sim \text{mid-}10^{17} \text{ cm}^{-3}$ ) 4H SiC boule sample measured at five temperatures. The inset schematically represents the interpretation discussed in the text.

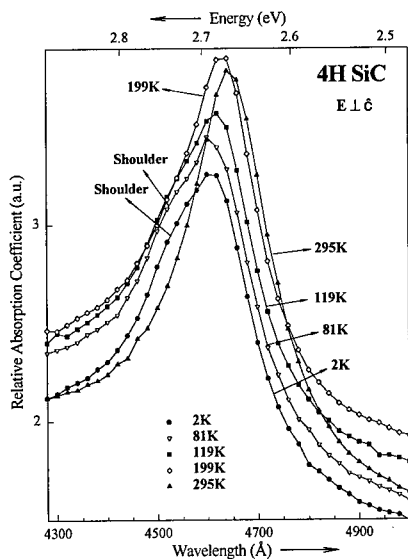


Fig. 4  $E\perp\hat{c}$  absorption spectrum of an n-type ( $n \sim \text{mid-}10^{17} \text{ cm}^{-3}$ ) 4H SiC boule sample measured at five temperatures.

peak F shows a slight redshift, while shoulder G is little changed. At 295 K peak F is shifted to 6400 Å (a shift of about 59 meV from its position at 2 K) and the shoulder G is weaker. This temperature dependence is consistent with the relative shift of the two conduction bands with temperature, which tends to be weak at low temperatures. In the notation of Limpijumnong et al. [14], peak F is associated with  $c_1(U_1) \rightarrow c_4(U_3)$  inter-conduction band transitions (The initial states might also be nitrogen donor levels.), which are allowed for polarization  $E\perp\hat{c}$ . To the best of our knowledge, the shoulder G is new, although we do not observe the sharper features reported by Kolesnikov et al. [8]. The origin of shoulder G is uncertain, but it is possible that the shape of the F-G band can be explained by application of the arguments for broadening discussed by Limpijumnong et al. [14].

#### 4H SiC

Fig. 3 shows measured  $E||\hat{c}$  absorption spectra of an n-type (estimated  $n \sim \text{mid-}10^{17} \text{ cm}^{-3}$ ) 4H SiC boule sample measured at five temperatures from 2 K to 295 K. To the best of our knowledge, detailed data on the temperature dependence of this absorption band have not been previously published. The 295 K spectrum shows a peak I near 5900 Å and a shoulder on the long wavelength side. With decreasing temperature, the peak I decreases and shifts to longer wavelengths and a sharper peak J near 6200 Å grows. The 2 K spectrum also shows a long wavelength shoulder near 6500 Å marked K. The description of this spectrum in terms of only three features may be oversimplified. It is not possible to explain the observed temperature dependence in terms of nitrogen donor levels vs conduction band initial states because the low energy features J and K are strongest at the lowest temperature. Based on the calculations of Limpijumnong et al. [14], this absorption band is associated with  $c_1(M_1) \rightarrow c_3(M_1)$  transitions, which are allowed for polarization  $E||\hat{c}$ . The energy shifts of features J and K with respect to peak I imply the existence of final states below the  $c_3$  conduction band. To explain the temperature dependence, we once again propose the existence of nitrogen donor resonances associated with higher conduction bands. The absolute minimum of the conduction band  $c_3$  is calculated to be about 0.6 of the way along M-L line and about 0.24 eV below the energy of  $c_3$  at the M point [19]. We suggest that the line J might be a shallow donor level to shallow donor resonance transition. In this case, the donor induced

resonance final state is associated with a minimum along the M-L line, not the M point. Peak I might be due to nitrogen donor to  $c_3(M_1)$  and/or  $c_1(M_1) \rightarrow c_3(M_1)$  inter-conduction band transitions. Further study is required to achieve a detailed, convincing explanation of the temperature dependence of this absorption band.

Fig. 4 shows measured  $E \perp \hat{c}$  absorption spectra of the same n-type 4H SiC boule material as presented in Fig. 3. At 2 K there is an absorption peak with a shoulder on the high energy side. The shoulder disappears and the peak undergoes a redshift with increasing temperature. The energy difference between the shoulder and the peak is roughly equal to the binding energy of the shallow h site nitrogen donor. Gorban' et al. [4] observed similar behavior and discussed as an explanation the changing population of the nitrogen donor  $1s(A_1)$  and  $1s(E)$  levels for nitrogen donors at the h and k sites with temperature. For a sufficiently lightly doped sample that impurity banding and band tailing are absent, it is clear that the initial states at low temperature must be the nitrogen donor levels rather than states near the bottom of the lowest conduction band. At room temperature, n is a significant fraction of  $N_D - N_A$ . In the notation of Limpijumnong et al. [14] the transitions are associated with  $c_1(M_1) \rightarrow c_4(M_3)$ , which are allowed for  $E \perp \hat{c}$ .

### Conclusion

Absorption spectra of nitrogen doped SiC polytypes provide a wealth of information about the conduction bands as well as the nitrogen donors themselves. Continuing progress in both the growth of both high quality boule material and very thick, unstrained, low doped epitaxial films will aid in elucidating what is at present a puzzling set of questions.

### Acknowledgements

We thank the Office of Naval Research and NASA for partial support of this work. We also wish to thank Dr. G. Augustine of Northrop-Grumman and the Cree Research Inc. crystal growth group for generously making boule samples of 4H and 6H SiC available to us.

### References

- [1] Lyle Patrick and W.J. Choyke, Phys. Rev. 186 (1969), p. 775.
- [2] E. Biedermann, Solid State Commun. 3 (1965), p. 343.
- [3] G.B. Dubrovskii, A.A. Lepneva and E.I. Radovanova, Phys. Stat. Sol. (b) 57 (1973), p. 423.
- [4] I.S. Gorban, A.P. Krokhmal, V.I. Levin, A.S. Skirda, Yu.M. Tairov and V.F. Tsvetkov, Sov. Phys. Semicond. 21 (1987), p. 119.
- [5] B.I. Seleznev and Yu.M. Tairov, Sov. Phys. Semicond. 7 (1973), p. 680.
- [6] G.B. Dubrovsky and E.I. Radovanova, Phys. Lett. 28A (1968), p. 283.
- [7] G.B. Dubrovskii and E.I. Radovanova, Sov. Phys.-Solid State 11 (1969), p. 545.
- [8] A.A. Kolesnikov, E.A. Makarov and G.N. Guk, Sov. Phys.-Solid State 15 (1973), p. 1105.
- [9] I.S. Gorban', Yu.A. Marazuev and A.S. Skirda, Sov. Phys.-Solid State 14 (1972), p. 664.
- [10] O.V. Vakulenko and O.A. Govorova, Sov. Phys.-Solid State 12 (1970), p. 1478.
- [11] O.V. Vakulenko, O.A. Govorova and B.M. Shutov, Sov. Phys.-Solid State 14 (1972), p. 242.
- [12] O.V. Vakulenko and B.M. Shutov, Sov. Phys. Semicond. 13 (1979), p. 1166.
- [13] W.R.L. Lambrecht, S. Limpijumnong, S.N. Rashkeev and B. Segall, Mater. Sci. Forum 264-268 (1998), p. 271.
- [14] S. Limpijumnong, W.R.L. Lambrecht, S.N. Rashkeev and B. Segall, Phys. Rev. B 59 (1999), p. 12890.
- [15] W. Suttrop, G. Pensl, W.J. Choyke, R. Stein and S. Leibenzeder, J. Appl. Phys. 72 (1992), p. 3708.
- [16] F. Bassani, G. Iadonisi and B. Preziosi, Rep. Prog. Phys. 37 (1974), p. 1099.
- [17] A. Onton, Phys. Rev. B 4 (1971), p. 4449.
- [18] E. Goldys, P. Galtier, G. Martinez and I. Gorczyca, Phys. Rev. B 36 (1987), p. 9662.
- [19] Walter Lambrecht, private communication.

## Determination of the Polarization Dependence of the Free-Carrier-Absorption in 4H-SiC at High-Level Photoinjection

Vytautas Grivickas<sup>1</sup>, Augustinas Galeckas<sup>1,2</sup>, Paulius Grivickas<sup>1</sup>  
and Jan Linnros<sup>2</sup>

<sup>1</sup>Institute of Materials Research and Applied Sciences, Vilnius University,  
Saulėtekio 10, LT-2054 Vilnius, Lithuania GUS

<sup>2</sup>Department of Solid State Electronics, Royal Institute of Technology,  
Electrum 229, SE-16440 Stockholm, Sweden

**Keywords:** Free Carrier Absorption, Interband Optical Transitions, Optical Anisotropy

**Abstract.** Strong polarization anisotropy of the free-carrier-absorption (FCA), induced by a pulsed pump beam, has been observed in low-doped 4H-SiC. The FCA cross-sections are determined at four energies for the electrical vector **E** being perpendicular and parallel to the **c**-axis. The connection to Biedermann's inter-conduction-band transitions is found by comparing the FCA cross-sections with those measured in the n-type heavily doped substrate. The energy dependencies of the FCA cross-section value also provide evidence for the existence of an additional FCA intraband optical transition for **E**⊥**c**. An astonishing effect of the fractional absorption damping is identified in the FCA-transient at lower detected energies for the **E**||**c** cases.

**Introduction.** Silicon carbide of hexagonal structures is characterized by anisotropy in many optical and electric properties. In the sixties, absorption with polarized light was extensively used to help identify optical properties. In this way, Biedermann [1], Patrick and Choyke [2], and Ellis and Moss [3] observed anisotropy of the FCA spectra for heavily doped SiC polytypes. The spectra have shown that n-type samples below the fundamental absorption edge exhibit polarization-dependent absorption. Biedermann's bands can be clearly resolved and were interpreted as inter-conduction-band optical transitions. Theoretical treatment of these vertical transitions has been performed recently by Lembrecht et al. [4]. While the theory can explain the positions of the main peaks and the polarization dependence, the widths are however strongly underestimated by the theory. It was suggested that impurity effects introduced by heavily doping, including the shift of states and a partial breakdown of the vertical selection rule ( $\Delta k = 0$ ), can explain the differences in broadening and the small differences in peak positions.

Epitaxial growth of high-quality low-doped films with impurity level of  $10^{14} \text{ cm}^{-3}$  has enabled new optical investigations of FCA. In 4H-SiC, spatially- and time-resolved FCA has been our diagnostic workhorse, enabling us to learn a great deal about the excess carrier recombination and transport [5-7]. In this work, the capability to perform photoinduced measurements of FCA transients in 4H-SiC epilayers is applied further to investigations of the free carrier absorption mechanism itself. The results presented below can be of particular importance for band structure theoretical study.

**Experimental.** The samples investigated here are from 34  $\mu\text{m}$ -thick 4H-SiC n-type epilayer grown by chemical vapor deposition on N doped substrate with  $8^\circ$  off orientation with respect to the **c**-axis of the material. The extrinsic electron concentration  $n_0$  is  $7 \times 10^{14} \text{ cm}^{-3}$  in the epilayer and  $6.1 \times 10^{18} \text{ cm}^{-3}$  in the substrate, respectively. The 0.43-1 mm wide strips were sawed and polished to optical quality. FCA measurements at 296 K were performed in the orthogonal geometry between the pump and the probe beam (Fig. 1 a). We have used continuous wave lasers as a polarized probe-beam at four wavelengths: 0.6328  $\mu\text{m}$  ( $\hbar\omega \approx 1.96 \text{ eV}$ ), 0.861  $\mu\text{m}$  ( $\hbar\omega \approx 1.44 \text{ eV}$ ), 1.3  $\mu\text{m}$  ( $\hbar\omega \approx 0.953 \text{ eV}$ ) and 1.54  $\mu\text{m}$  ( $\hbar\omega \approx 0.8 \text{ eV}$ ). In-depth scanning was provided by motorized sample translation. In this way, the diameter of the focused probe beam determines the resolution, which is

about 3-8  $\mu\text{m}$ , depending slightly on the wavelength. The polarization of the probe-beam is rotated using the Berel compensator, maintaining a polarization ratio of about 1:200. In Fig. 1 b, we show the depth dependence of the transmitted intensity at the detected energy of 1.96 eV. Transmission in the epilayer is determined barely by reflection losses and has no polarization dependence. While, in the substrate, absorption by extrinsic electrons is evident. This absorption,  $\alpha_0$ , has a strong polarization dependence.

For uniform  $e$ - $h$  pair excitation in the epilayer we have used 2.5 ns duration pulses of a Nd:YAG laser at 355 nm wavelength. Photoinduced transients of absorption  $\Delta\alpha(t)$  were detected in the center of the epilayer (Fig. 1 a) with a 10 ns time resolution [5,6]. The FCA cross-section was calculated at variable photoinjection level as  $\sigma_{eh} = \Delta\alpha/\Delta n$ , where  $\Delta\alpha$  is the absorption peak value and  $\Delta n = \Delta p$  are the injected electron and hole concentrations. The  $\Delta n$  values are calculated providing calibration to the overall photon pulse density absorbed in the material and the reflection losses at 355 nm [7]. Simultaneously, in a heavily doped  $n$ -substrate, the FCA cross-section was determined as  $\sigma_e = \alpha_0/n_0$  after transmission measurements such as shown in Fig. 1 b.

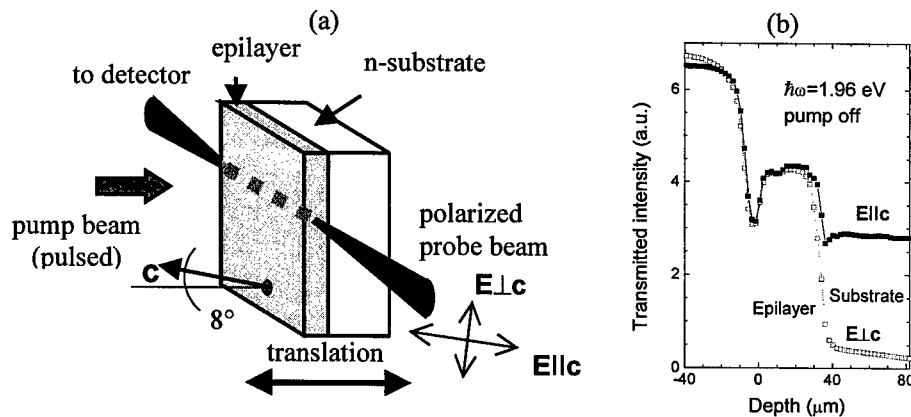


Fig. 1. (a) Schematic of the depth-resolved absorption measurements in 4H-SiC. The specimen can be translated to produce FCA measurements in the low-doped thin epilayer (with pump beam on) or in the heavily doped  $n$ -substrate (with pump beam off). The orientation of the  $c$ -axis is indicated. (b) Two depth-scans at detected energy 1.96 eV with indicated polarization. The pump beam is off.

**Results and Discussion.** In Fig. 2 we show the angular dependencies of the peak FCA cross-sections at three detection energies. A strong anisotropy for  $\sigma_{eh}$  is found in the photoexcited epilayer, which is equivalent to the  $\sigma_e$  dependency in  $n$ -substrate. The orientation of anisotropy is opposite with respect to the  $c$ -axis at 0.953 eV and 1.96 eV energies. Much weaker FCA anisotropy with opposite orientation for  $\sigma_{eh}$  and  $\sigma_e$ , is detected at 1.44 eV. We have examined the injection dependence of  $\sigma_{eh}$  at eight principal cases when  $E||c$  and  $E\perp c$ . With the exception of two case (at lower energies,  $E||c$ ), which is described below, we have found a linear relationship with the excess carrier concentrations ranging between  $10^{15}$ - $10^{19} \text{ cm}^{-3}$ . This shows that in these cases FCA polarization is independent of the level of occupation of states in the valence and the conduction bands, and that the  $\sigma_{eh}$  is an invariable experimental parameter which describes FCA optical transitions.

In Fig. 3 we provide a comparison of the spectral distributions for  $\sigma_{eh}$  and  $\sigma_e$ . Measured values in  $n$ -substrate ( $\sigma_e$ , small squares) are in a good agreement with spectra obtained by Biedermann [1]. Large circles in Fig.3 represent the determined FCA cross-section  $\sigma_{eh}$  in the low-doped epilayer when the pump is on. The similarity of the polarization dependencies demonstrates that the same

inter-conduction-band mechanism appears in the excited and in the heavily doped 4H-SiC. The pronounced polarization peaks and polarization anisotropy can be assigned to optical transitions, which are allowed between conduction bands of the same symmetry for  $E||c$  and different symmetry for  $E\perp c$  [4].

A closer inspection of the results in Fig 3 reveals, however, a few important differences. For  $E\perp c$ , a gradual enhancement of  $\sigma_{ch}$  respect to  $\sigma_e$  with decreasing energy is evident. Such enhancement, however, is small for the  $E||c$  case. Assuming that the overall FCA cross section can be written as  $\sigma_{ch} = \sigma_e + \sigma_h$ , where  $\sigma_h$  is the cross-section in the valence band, the enhancement of  $\sigma_{ch}$  can be understood if  $\sigma_h$  has the usual quadratic increase with decreasing wavelength. Note that such dependence is expected for intraband phonon-assisted transitions in the valence band. In fact, it was confirmed in Biedermann's work for p-type doped 6H-SiC [1]. Biedermann also has demonstrated that absorption in p-type 6H-SiC is lower for  $E||c$  than for  $E\perp c$  case by a factor of 1.5-2. We speculate that the small enhancement of  $\sigma_{ch}$  for  $E||c$  also may be explained by lower  $\sigma_h$  values at  $E||c$  for the valence band of 4H-SiC.

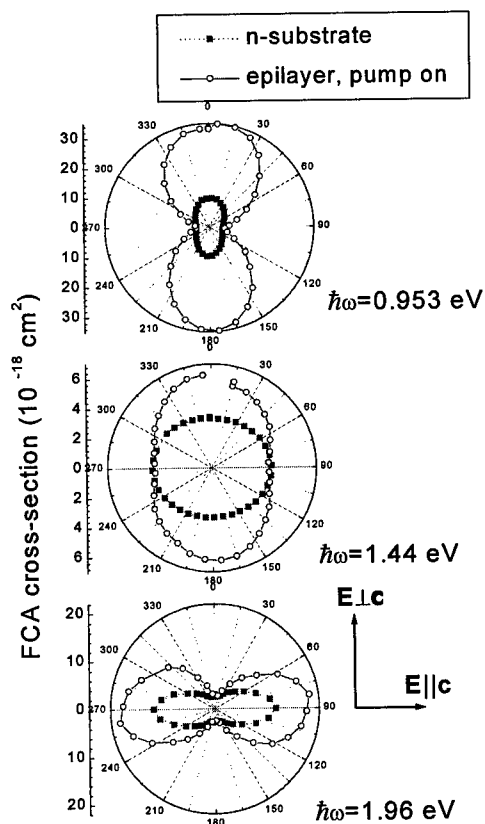


Fig. 2 Polar plots of the angular dependence of the FCA cross-sections in the n-substrate with pump off (filled symbols) and in the epilayer with pump on (open symbols). Results for three detection energies are shown. The polarization direction is indicated;  $E\perp c$  at zero degree and  $E||c$  at 90°.

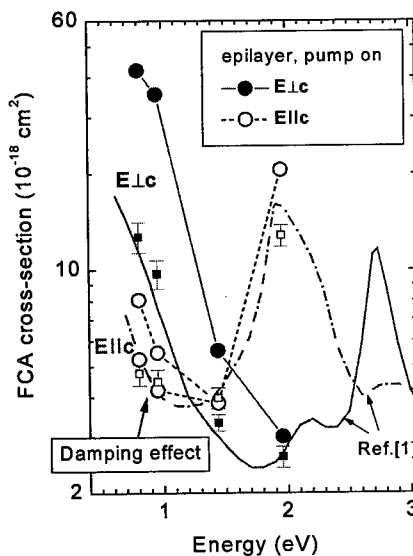


Fig. 3. Comparison of the spectral distributions of the FCA cross-sections. Solid lines and filled symbols are for  $E\perp c$ , and dashed lines and open symbols are for  $E||c$ . Measured values in n-substrate ( $\sigma_e$ , small squares) are in a good agreement with published spectral dependencies from Ref. [1]. Large circles represent the FCA cross-section  $\sigma_{ch}$  in low-doped epilayer when the pump is on.

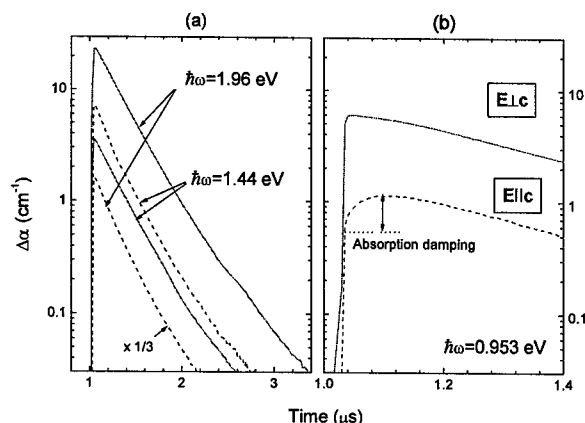


Fig. 4. The decays of the FCA at three detected energies and two polarization directions:  $E_{\perp c}$  (solid lines) and  $E_{\parallel c}$  (dotted lines). The differences at the detection energy 0.953 eV in the initial portion of two transients are shown (b) on an expanded time-scale.

eV. After the end of laser pulse, the absorption slowly rises and almost doubles within 0.1  $\mu s$ . The rest of the decay has the same shape as for all other cases. In addition, at very high injection levels of  $\Delta n > 10^{18} \text{ cm}^{-3}$ , we have observed a dramatic rise in FCA signals, which is followed by a fast FCA decay within 0.1  $\mu s$  (not shown here). Therefore, we tentatively suggest that this effect may result from supporting photoinduced phenomenon. More work should be performed to study this effect.

**Conclusions.** We have shown that similar inter-conduction band absorption mechanism appears in the excited and in the heavily n-type doped 4H-SiC. The phonon-assisted FCA in valence band can be responsible for absorption enhancement at lower energy for  $E_{\perp c}$ . Several details of absorption should be investigated more carefully for better understanding.

**Acknowledgments.** The authors would like to acknowledge financial support from the SiCEP program of the Swedish Council for Strategic Research and by the Swedish Institute (Visby program).

## References

- [1] E. Biedermann, Sol. State Commun. **3** (1965), p. 343. We have converted absorption values for n-type 4H-SiC to the  $\sigma_c$  values (see our Fig.3) by using slightly higher electron density  $n_0 = 10^{19} \text{ cm}^{-3}$  which doubles that reported in the paper.
- [2] L. Patrick and W. J. Choyke, Phys. Rev. **186** (1969), p. 775.
- [3] B. Ellis and T. S. Moss, Proc. Royal Soc. A, **299** (1967), p. 393.
- [4] W. R. L. Lambrecht, S. Limpijumnong, S. N. Rashkeev and B. Segall, Materials Science Forum **264-268** (1998), p. 271.
- [5] A. Galeckas, V. Grivickas, J. Linnros, H. Bleichner and C. Hallin, J. Appl. Phys. **81** (1997), p. 3522.
- [6] V. Grivickas, J. Linnros, P. Grivickas and A. Galeckas, Materials Science Forum, **264-268** (1998), p. 529.
- [7] V. Grivickas, Solid State Commun. **108** (1998), p. 561.

For correspondence: [vytautas.grivickas@ff.vu.lt](mailto:vytautas.grivickas@ff.vu.lt)

Next we examined FCA transients at different energy and polarization. We obtained that FCA transients are equivalent in six principal cases, which indicates identical recombination mechanism for the carriers. The characteristic recombination lifetime at moderate injection level is about 0.42  $\mu s$  as shown in Fig. 4 a. For the lower energies and  $E_{\parallel c}$ , in contrast, we have observed an astonishing effect of fractional absorption damping in the beginning of the transient. This is blown up on an expanded time scale in Fig. 4 b for a detected energy 0.953

## Bandstructure and Transport Properties of 4H- and 6H-SiC: Optically Detected Cyclotron Resonance Investigations

B.K. Meyer<sup>1</sup>, D.M. Hofmann<sup>1</sup>, D. Volm<sup>1</sup>, W.M. Chen<sup>2</sup>, N.T. Son<sup>2</sup> and E. Janzén<sup>2</sup>

<sup>1</sup> I. Physikalisches Institut, Universität Giessen, DE-35392 Giessen, Germany

<sup>2</sup> Department of Physics and Measurement Technology, Linköping University, SE-581 83 Linköping, Sweden

**Keywords:** Band Structure, Carrier Scattering, Cyclotron Resonance, Effective Mass, SiC

### Abstract

We present experimental data on the bandstructure and high mobility transport properties of 6H and 4H-SiC epitaxial films based on optically detected cyclotron resonance investigations. From the orientational dependence of the electron effective mass in 6H-SiC we obtain direct evidence for the camel's back nature of the conduction band between the M- and L-points. The broadening of the resonance signal in 4H-SiC as a function of temperature is used to extract information on electron mobilities and to conclude on the role of the different scattering mechanisms.

### Introduction

We have recently reviewed the cyclotron resonance (CR) determination of the electron effective masses in the three polytypes of SiC, 3C, 4H and 6H [1]. The experimental findings are in general agreement with theoretical calculations [2,3,4], although fine details in the conduction band of 6H SiC such as a camel's back structure have escaped experiments. Since then we have extended the CR experiments and it is now possible to present experimental evidence for the camel's back nature. From temperature dependent measurements we are also able to conclude on the nature of the scattering mechanisms at low temperatures.

### Experimental Details

The 4H- and 6H - SiC epitaxial films were grown by the hotwall-chemical vapour deposition technique on off-axis substrates. The films were nominally undoped and n-type with free carrier-densities between  $2$  and  $5 \times 10^{14} \text{ cm}^{-3}$  and Hall mobilities around  $1000 \text{ cm}^2/\text{Vs}$  at room temperature. The sample thickness was  $93 \text{ }\mu\text{m}$  for the 4H-SiC film and varied from  $15 - 35 \text{ }\mu\text{m}$  for the 6H-SiC films. For the determination of the electron effective mass and the transport properties optically detected cyclotron resonance (ODCR) experiments were conducted at  $36 \text{ GHz}$ . Excitation of the photoluminescence was performed using a HeCd laser at a wavelength of  $325 \text{ nm}$  (above band gap).

### Results and Discussion

For the ODCR measurements the D-A pair band was used as a monitor. The ODCR spectrum for the magnetic field parallel to the c-axis is shown in Fig. 1. The resonance is centered at  $0.62 \text{ T}$  and from the line position one calculates an effective mass in the basal plane of  $m_{M-K}^* = 0.48 \pm 0.03 m_0$ . As in the case of 4H-SiC one expects an anisotropic mass (tensorial mass) and therefore angular dependent measurements were performed with rotations of the magnetic field in the  $(11\bar{2}0)$  and  $(1\bar{1}00)$  planes. In both cases the resonance was only observable up to angles of  $60^\circ$  and its field position at this angle was within experimental error identical. This corresponds to spheroidal energy surfaces which are oriented parallel to the c-axis. A complete angular dependence for a rotation in the  $(1\bar{1}00)$  plane is shown Fig. 2. For comparison the effective masses determined at  $9 \text{ GHz}$  for parallel and perpendicular orientations are shown using full circles.

In order to determine the mass parallel to c-axis,  $m_{||}^*$ , a fit to the data points was performed. Under the assumption of an isotropic mass within the basal plane the mass is given by:

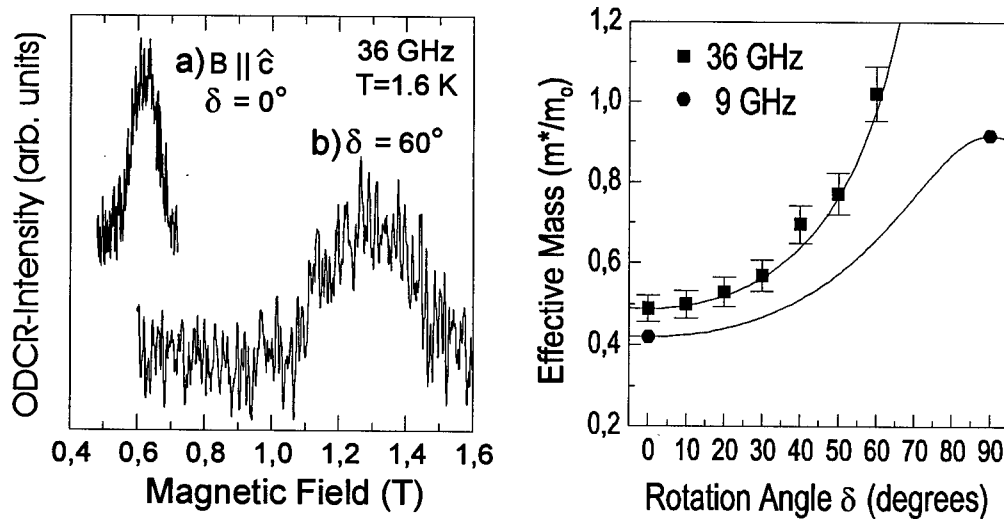


**Fig.1:** Optically detected cyclotron resonance of 6H-SiC at 36 GHz and  $T = 1.6$  K for an orientation of the magnetic field parallel to the c-axis a), and  $60^\circ$  off.

**Fig.2:** Orientation dependence of the electron effective mass in 6H-SiC obtained by rotating the sample in the  $(1\bar{1}00)$  plane. ( $\delta = 0^\circ$  corresponds to  $B \parallel c$ ). Experimental data are given by full squares and circles, the drawn line is a fit (see text).

$$m^* = \left[ \left( \frac{\cos^2 \Theta}{m_{\perp}^*} \right) + \left( \frac{\sin^2 \Theta}{m_{\parallel}^*} \right) \right]^{-1/2} \quad \text{where } \Theta \text{ is the angle between the magnetic field } B \text{ and the } c\text{-axis.}$$

The resulting values are given in Table 1.

One notes that the perpendicular mass is about 15 % higher for the 36 GHz measurements. Even more astonishing is that the parallel mass has an infinite value, but was 2 in the 9 GHz experiments [5]. In order to understand this surprising behaviour we take a closer look at the bandstructure in the light of recent theoretical calculations. Lambrecht et al. [3] derived for the masses in the hexagonal plane two values  $m_{\text{M}\Gamma}^* = 0.77 m_0$  and  $m_{\text{MK}}^* = 0.24 m_0$ . In the c-direction the value  $m_{\text{ML}}^*$  is  $1.42 m_0$ . The minimum of the conduction band is in the direction M to L, approximately in the middle between the symmetry points. This results in six equivalent energy ellipsoids. Through the three equivalent M-points two valleys are connected with a barrier of 9.5 meV in between, a "camel's back" structure. For the cyclotron mass in the basal plane one hence obtains  $m^* = \sqrt{m_{\text{M}\Gamma}^* \cdot m_{\text{MK}}^*} = 0.429 m_0$  in good agreement with the experimental result of Son et al. [5]. For the mass parallel to the c-axis the nonparabolicity of the conduction band plays a key role. Lambrecht et al. [8] predicted that the mass will increase from 1.1 to 2.0 (maximum energy at the barrier height) depending on the electron energy. Similar results were obtained by Persson et al. [4]. The barrier height is 5.3 meV. For the masses see Table 1. With this information we are able to explain the results of Fig. 3. According to Son et al. [5] the ODCR measurements at 9 GHz were conducted with a microwave power of 100 mW. Depending on the quality factor of the resonator the microwave electric field can reach values up to  $10^2$  V/cm. With a scattering time of  $\tau = 10^{-11}$  s the carriers can gain 10 meV in energy which is close to the barrier height and the mass of  $2.0 m_0$  is in agreement with the theoretical values. The ODCR measurement at 36 GHz used 200 mW ( $2 \times 10^2$  V/cm). The electron energy is approximately 40 meV using the  $\tau$  of  $5 \times 10^{-11}$  s and a mass of  $2 m_0$ . The energy would hence be four times higher than the barrier and thus an highly increased mass might be plausible.



**Table 1:** Comparison of the effective electron masses in 6H-SiC

Effective Masses (in units of $m_0$ )	Experimental Values		Theoretical Values		
	ref. 7 9 GHz	this work 36 GHz	ref. 2	ref. 3	ref. 4
$m_{M\Gamma}^* = m_{\perp 1}^*$	0.42	0.48	0.77	0.51	0.81
$m_{MK}^* = m_{\perp 2}^*$	0.42	0.48	0.24	0.3	0.25
$m_{ML}^* = m_{  }^*$	2.0	" $\infty$ "	1.42	0.71	2.07

For the determination of the carrier mobility we performed temperature dependent ODCR measurements at 36 GHz at a microwave power of 10 mW. The scattering time deduced from the resonance halfwidth and the mobility calculated according to  $\mu = e\tau/m^*$ . We assume that Mathiesen's rule is valid and the total scattering time is the sum of the individual scattering processes [6]. The data are shown in Fig. 3 as full squares. In addition the value from Hall effect measurements [7] at room temperature is shown (full triangle). The mobility increases slightly up to a temperature of 9 K and then steadily decreases up to 22 K. Above 22 K the ODCR signal has vanished in the noise. This behaviour can be described by three main scattering processes [see e.g. refs. 6 and 8] – scattering by impurities, for which one has to distinguish between neutral and ionized impurities and scattering by acoustical phonons dominating at higher temperatures (see Fig. 3, dashed lines). In most semiconductors scattering by impurities dominates at low temperature. For the scattering by neutral impurities with a concentration  $N$  we have the following relation [6]:

$$\mu = \frac{e}{20a_B\hbar} \frac{m^*/m_0}{\epsilon N} \quad (1)$$

with the Bohr radius  $a_B$  and the dielectric constant  $\epsilon$ .

For scattering by ionised impurities we used the relation from Brooks and Herring [6], which gives good results for low carrier densities and not too high carrier velocities. If one assumes that the concentration of ionized impurities  $N_I$  is constant, we obtain for the mobility:

$$\mu = \frac{2^{7/2} (4\pi\epsilon\epsilon_0)^2 (k_B T)^{3/2}}{\pi^{3/2} Z^2 e^3 (m^*/m_0)^{1/2} N_I [\ln(1+\beta^2) - 0.434\beta^2/(1+\beta^2)]} \quad (2)$$

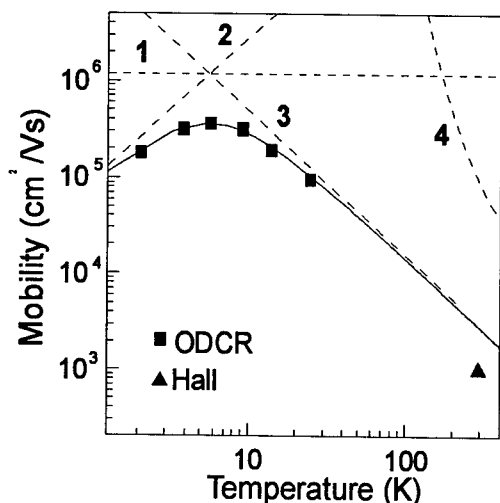
with

$$\beta = 2 \frac{(m^*/m_0)}{\hbar} \left( \frac{2}{m^*/m_0} - 3k_B T \right)^{1/2} L_D \quad \text{and} \quad L_D = \sqrt{\frac{k_B T \epsilon \epsilon_0}{e^2 n}}.$$

$N_I$  is the total concentration of ionized impurities in the crystal,  $L_D$  is the Debye screening length with the parameter  $n$ , which gives the concentration of free carriers. All other symbols have their usual meanings. The scattering by acoustic phonons is given by:

$$\mu = \frac{2\sqrt{2}\pi}{3} \frac{e\hbar^4 c_l}{(m^*/m_0)^{5/2} (k_B)^{3/2} \epsilon_{ac}^2} T^{-3/2} \quad (3)$$

$c_l$  is the longitudinal elastic modulus,  $6 \times 10^{12}$  dyn/cm<sup>2</sup> and  $\epsilon_{ac} = 20$  eV the deformation potential [9]. Polar optical scattering is not of importance at low temperatures (see Fig.3). Due to the high Debye temperature of 1200 K it contributes only at temperatures above room temperature. Although Eqs.1 to 3 include may simplifications which may be questionable for SiC the calculated total mobility explains the experimental data very well. The necessary parameters which enter into the equations are only partly known for 4H-SiC. For the neutral impurity scattering the concentration of impurities enters. From the Hall effect measurements the donor concentration was determined to be  $2 \times 10^{14}$  cm<sup>-3</sup>, a possible compensation by acceptors was not considered. In order to reach the high mobility, the impurity concentration must be less than  $5 \times 10^{14}$  cm<sup>-3</sup>. It is difficult to estimate the contribution of ionised impurities, since the total number as well as the free carrier concentration

**Fig. 3:**

Mobility in 4H-SiC as a function of temperature. Full squares are the data from ODCR, the triangle is from Hall effect measurements at room temperature. The dashed lines are calculated mobilities for scattering by neutral (1) and ionised (2) impurities, as well as the acoustic deformation potential (3) and polar optical (4) scattering. The drawn line takes into account all four processes.

has to be known. Free carriers are mainly generated by optical excitation. With a laser power of 10 mW and an average lifetime of  $10^{-6}$  s one calculates about  $n = 1 \times 10^{15} \text{ cm}^{-3}$ .

Taking the number of ionised impurities as a free parameter one obtains a value of  $1 \times 10^{13} \text{ cm}^{-3}$  from a fit to the data. This corresponds to an average distance between the scattering centres of about 300 nm. With a cyclotron radius  $\sqrt{\hbar/eB} = 35 \text{ nm}$  only a fraction of the electrons would be scattered by ionised impurities. Nevertheless it is the dominating scattering process for  $T < 10 \text{ K}$ . For temperatures  $T > 15 \text{ K}$  the mobility is determined by acoustic deformation potential scattering. Also the mobility at room temperature fits to this behaviour. Due to the contacts and averaging over a whole sample the Hall mobilities are always lower than mobilities from cyclotron resonance.

#### Summary

Photoluminescence and optically detected cyclotron resonance experiments have been performed on 4H- and 6H-SiC epitaxial films grown by the hotwall-chemical vapour deposition technique. From the ODCR experiments on 6H-SiC at 36 GHz we obtain direct evidence for the camels back nature of the conduction band. The minimum is located between the M- and the L-point. From temperature dependent ODCR experiments in 4H-SiC we extract information on electron mobility and on the contributions of different individual scattering processes to it. For temperatures  $T > 15 \text{ K}$  the mobility is determined by acoustic deformation potential scattering, which also explains the mobility at room temperature.

#### References

- [1] W.M. Chen, N.T. Son, E. Janzén, D.M. Hofmann, and B.K. Meyer, *phys. stat. sol. (a)*, **162** (1997), 79.
- [2] P. Käckell, B. Wenzien and F. Bechstedt, *Phys. Rev.*, **B 50** (1994), 10761.
- [3] W. R. L. Lambrecht and B. Segall, *Phys. Rev.*, **B 52** (1995), R2249.
- [4] C. Persson and U. Lindefelt, *Phys. Rev.*, **B 54** (1996), 10257.
- [5] N. T. Son, O. Kordina, A.O. Kostantinov, W.M. Chen, E. Sörmann, B. Monemar, and E. Janzén, *Appl. Phys. Lett.*, **65** (1994), 3209.
- [6] K. Seeger, *Semiconductor Physics*, (Vieweg Verlagsgesellschaft, Braunschweig 1993)
- [7] N.T. Son, E. Sörmann, W.M. Chen, O. Kordina, B. Monemar, and E. Janzén, *Appl. Phys. Lett.*, **65** (1994), 2687.
- [8] B.K. Ridley, *Quantum Processes in Semiconductors*, (Clarendon Press, Oxford, 1993).
- [9] Landolt-Börnstein, New Series, Vol. 17, Ed. O. Madelung (Springer Verlag, Berlin, 1982).

## Hole Effective Masses in 4H SiC Determined by Optically Detected Cyclotron Resonance

N.T. Son<sup>1</sup>, P.N. Hai<sup>1,2</sup>, W.M. Chen<sup>1</sup>, C. Hallin<sup>3</sup>, B. Monemar<sup>1</sup> and E. Janzén<sup>1</sup>

<sup>1</sup>Department of Physics and Measurement Technology, Linköping University,  
SE-581 83 Linköping, Sweden

<sup>2</sup>permanent address: Department of Physics, Hanoi University, 90 Nguyen Trai, Hanoi, Vietnam

<sup>3</sup>ABB Corporate Research, SE-721 78 Västerås, Sweden

**Keywords:** Hole Effective Masses, Optically Detected Cyclotron Resonance

**Abstract:** Optically detected cyclotron resonance (ODCR) at X-band frequency (~9.23 GHz) was used to study electron and hole effective masses in 4H SiC. In addition to the known ODCR signal related to the cyclotron resonance (CR) of electrons we have observed in 4H SiC epitaxial layers grown by chemical vapor deposition (CVD) a new ODCR peak at higher magnetic field, which is attributed to the CR of the holes. The angular dependence of the hole CR peak can be described by the usual cyclotron mass relation for the case of an elliptical energy surface, with the values of the transverse mass  $m_{\perp} = (0.66 \pm 0.02) m_0$  and the longitudinal mass  $m_{\parallel} = (1.75 \pm 0.02) m_0$ . The principal axis of the ellipsoid is parallel to the *c* axis.

### 1. Introduction

The effective masses of electrons and holes in semiconductors are fundamental parameters, which are required for many analyses. The characterization of the energy band structure and effective masses are therefore of vital importance. The most direct method for determination of effective masses is cyclotron resonance (CR). The observation of a well-defined CR requires  $\omega\tau > 1$ , here  $\omega$  is the frequency (usually the microwave frequency) used in the experiments and  $\tau$  the carrier scattering time. In SiC crystals available nowadays, the carrier mobility is usually low due to short carrier scattering time caused by high concentrations of defects and residual impurities. It is therefore very difficult to satisfy the requirement of  $\omega\tau > 1$  for conventional CR experiments in SiC, especially for holes, which often have a much lower mobility than that of electrons. In the past, CR experiments have been performed at far-infrared wavelengths and high magnetic fields to determine electron effective masses in 3C SiC [1]. However, even at such high frequencies and magnetic fields, a detailed study of the hole effective masses was still not possible [1]. Recently, using optically detected cyclotron resonance (ODCR) technique [2] with its advantages of improving the mobility due to photoneutralization of impurities [3], we were able to determine the electron effective masses in 6H and 4H SiC at X- and Q-band frequencies [4-6]. In the 4H polytype, the electron effective masses have been studied by both experiment [5,6] and theory [7-13]. The hole effective masses, however, have so far been predicted only by theory [7,11-13] but not experimentally determined. In this work, using low-doped 4H SiC epitaxial layers grown by chemical vapor deposition (CVD) we could detect ODCR signals of both electrons and holes.

### 2. Experiment

The samples used in this work are low-doped 4H SiC grown by CVD. The concentration of residual nitrogen donors in the layers is below  $10^{14} \text{ cm}^{-3}$  as determined from the photoluminescence (PL) of the N-bound excitons and free excitons. The samples are slightly compensated, but the concentration of Al acceptors is in the mid  $10^{13} \text{ cm}^{-3}$  range. The substrates have been removed by

polishing and the thickness of these free-standing layers is about 80  $\mu\text{m}$ . The ODCR measurements were performed on a modified Bruker ER-200D X-band ( $\sim 9.23$  GHz) ESR spectrometer using a cylindrical  $\text{TE}_{001}$  cavity with optical access in all directions. The cavity is fitted with an Oxford helium-continuous-flow cryostat, which allows a regulation of the sample temperature from 4 K to room temperature. The 334 nm line of an argon ion laser was used as the excitation source. In order to reduce the power density of the excitation, the laser beam was defocused on a large spot and the laser power was kept below 6 mW. The change of PL intensity in the visible region (400-600 nm) due to the amplitude-modulated microwave (MW) field was detected using a photomultiplier and recorded by a lock-in amplifier. The angular dependence studies of the ODCR signals were made with the magnetic field rotating in the  $(11\bar{2}0)$  and  $(\bar{1}100)$  planes. For most of the measurements the MW power was in the range 2-10 mW.

### 3. Results and discussion

At low temperatures, all samples show strong PL emissions from the free excitons and N-bound excitons. The PL from Al-bound excitons was also weakly detected. Fig. 1 shows ODCR signals observed in 4H SiC layers for different directions of the magnetic field. In these experiments, the band-edge PL emissions (in the range 400-600 nm) were monitored using different optical filters and the MW power was kept at low levels (2-10 mW) to avoid line-broadening effect. For  $\vec{B}$  parallel to the  $c$  axis [Fig. 1(a)], two broad and partly overlapping ODCR peaks were detected in the region 140-250 mT. The very sharp line at around 73 mT is an ODMR signal of an unidentified defect. The samples were specially mounted to avoid strain in the film and to ensure that no strain-induced splitting occurred. When rotating the magnetic field away from the  $c$  axis the low-field peak moved to the lower magnetic field while the other moved to the opposite direction. The separation between them is largest in the direction of  $\vec{B}$  perpendicular to the  $c$  axis [Fig. 1(b)]. The angular dependence studies of these two ODCR peaks were performed with the magnetic field rotating in the  $(11\bar{2}0)$  and  $(\bar{1}100)$  planes. At the X-band frequency, the angular dependencies of these peaks measured in the  $(11\bar{2}0)$  and  $(\bar{1}100)$  planes are the same within experimental errors. At the direction where these peaks are well separated [Fig. 1(b)], each peak appears to be symmetric in line shape, even measuring with the lowest possible MW power. Therefore each peak was considered as corresponding to only one cyclotron mass value  $m^* = (eB)/\omega$ . Here  $\omega$  is the MW frequency and  $B$  the magnetic field. Fig. 2 shows the angular dependencies of the cyclotron masses corresponding to these two ODCR peaks with the magnetic field rotating in the  $(11\bar{2}0)$  planes.

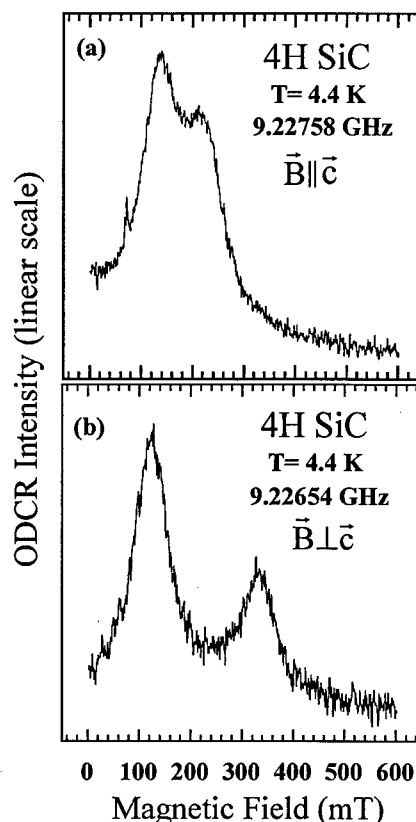


Fig.1. ODCR signals observed in 4H SiC with monitoring the near band-edge PL for the magnetic field  $\vec{B}$  (a) parallel and (b) perpendicular to the  $c$ -axis. In both figures, the peak at lower magnetic field corresponds to the CR of the electrons, while the higher field peak is due to the CR of the holes. The very sharp peak at  $\sim 73$  mT in (a) is an ODMR signal of an unidentified defect. The sample was excited by the 334 nm line of an Ar ion laser with an output power of 4 mW.

Comparing the obtained angular dependence with that of the electron cyclotron masses in 4H SiC measured also at X-band frequency [5], it can be concluded that the low-field peak corresponds to the ODCR of the electrons. From the experimental [5,6] and theoretical [7-13] studies of effective masses and energy band structure of 4H SiC, it can be excluded that the high-field peak is related to another component of the electron effective mass tensor. The peaks are already separately observed for  $\vec{B}$  parallel to the  $c$  axis and at all directions their separation is too large to compare with the splitting due to the anisotropy of the electron mass tensor. It is also not possible that the second peak is related to the ODCR of the electrons occupying the second lowest conduction band minimum, since the MW power used in this case is too low to be able to excite electrons to that band, which is about 122 meV above the conduction band minimum [12]. The intensity ratio between these two peaks did not change with increasing the MW power. This result also indicates that the peak is not related to the higher band. The high-field peak is therefore attributed to the ODCR of the holes. The angular dependence of the hole cyclotron mass can be described by the usual relation for the case of an elliptical energy surface

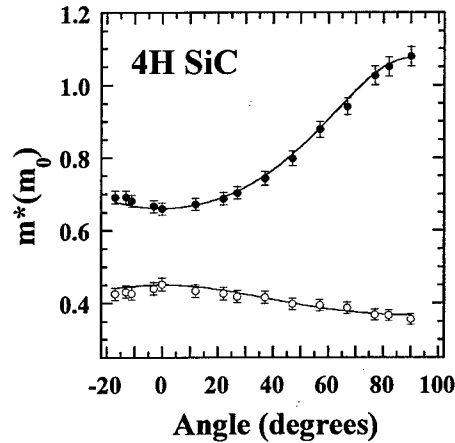


Fig.2. Angular dependencies of the electron (open circle) and hole (filled circle) cyclotron masses in 4H SiC measured in units of the free electron mass ( $m_0$ ) with the magnetic field rotating in the  $(11\bar{2}0)$  plane. The curves represent the fits using Eq. (1) and the effective mass values:  $m_{\perp}=0.45 m_0$  and  $m_{\parallel}=0.30 m_0$  for the electrons, and  $m_{\perp}=0.66 m_0$  and  $m_{\parallel}=1.75 m_0$  for the holes. The zero angle corresponds to  $\vec{B} \parallel \vec{c}$  while  $90^\circ$  corresponds to  $\vec{B} \perp \vec{c}$  and  $\vec{B} \parallel [\bar{1}100]$ .

$$\frac{1}{m^*} = \left( \frac{\cos^2 \theta}{m_{\perp}^2} + \frac{\sin^2 \theta}{m_{\perp} m_{\parallel}} \right)^{1/2}, \quad (1)$$

where  $\theta$  denotes the angle between  $\vec{B}$  and the  $c$  axis. The transverse mass,  $m_{\perp}$ , is the mass on the basal plane and the longitudinal mass,  $m_{\parallel}$ , is the mass parallel to the  $c$  axis. From the best fit, the values  $m_{\perp}=(0.66 \pm 0.02) m_0$  and  $m_{\parallel}=(1.75 \pm 0.02) m_0$  were obtained.

The hole effective masses in 4H SiC have been calculated by several groups. The *ab initio* calculations by Käckell et al [7] predicted very large values for the hole effective masses, which are anisotropic in the basal plane (the longitudinal mass:  $m_{\Gamma A}=1.73 m_0$ ; on the basal plane:  $m_{\Gamma K}=0.77 m_0$  and  $m_{\Gamma M}=0.45 m_0$  or their average values  $m_{\perp}=0.59 m_0$ ). In recent calculations, Lambrecht et al [11] and Persson et al [12,13] have both predicted parabolic energy surfaces for the highest valence band around  $\Gamma$  point of the Brillouin zone of 4H SiC and very similar hole effective masses. With taking into account the dependence on atomic positions in the hexagonal lattice, the hole effective masses in 4H SiC were determined as  $m_{\perp}=0.61 m_0$  and  $m_{\parallel}=1.62 m_0$  [13]. It should be noticed that these are the "bare" effective mass values since the effect on the carrier mobility caused by the coupling of the holes to optical phonons [14] (known as the polaron effect) was not considered in those cases. Including this effect, the polaron hole masses can be calculated from the "bare" values using the relation [15] obtained by assuming parabolic bands:

$$m_j^p = m_j / (1 - \alpha/6), \quad (m_j = m_{\perp}, m_{\parallel}). \quad (2)$$

Here  $\alpha = (e^2/8\pi\epsilon_0 \hbar \omega_{LO})(2m_d\omega_{LO}/\hbar)^{1/2}[(1/\epsilon_\infty) - (1/\epsilon_0)]$  with  $m_d = (m_\perp^2 m_\parallel)^{1/3}$  the density state of the effective masses. Using the values given for 6H SiC [16]:  $\epsilon_{0\perp} = 9.66$ ,  $\epsilon_{0\parallel} = 10.03$ ,  $\epsilon_{\infty\perp} = 6.52$ ,  $\epsilon_{\infty\parallel} = 6.7$  and optical phonon energy for 4H SiC,  $\hbar \omega_{LO} = 0.12$  eV, the polaron masses can be derived from the values given in Ref. 13 as  $m_\perp^p = 0.66 m_0$  and  $m_\parallel^p = 1.76 m_0$ . These values are almost the same as those determined in our experiments. This remarkably good agreement between theoretical calculations and our experimental determination is a strong support for our identification of the hole ODCR signal. The MW power-dependence studies of the hole ODCR signal with  $B$  in different planes and parallel to the  $c$  axis were performed, and no noticeable changes in the position of the peaks have been detected in the MW power range 1-15 mW. This indicates that the energy surface is parabolic in the vicinity of the valence band maximum, which is also in agreement with the theoretical predictions [11-13]. The MW power dependence of the ODCR signal at higher MW powers is currently investigated.

In summary, we have observed the ODCR of holes in 4H SiC epitaxial layers grown by CVD at X-band frequency. For the first time the hole effective masses have been directly determined for this polytype. The constant energy surface of the valence band near its maximum can be considered as ellipsoids with the principal axis along the  $c$  axis and the hole effective masses are determined as:  $m_\perp = (0.66 \pm 0.02) m_0$  and  $m_\parallel = (1.75 \pm 0.02) m_0$ .

**Acknowledgements:** The authors thank Dr C. Persson for fruitful discussions. Support for this work was provided by the Swedish Research Council for Engineering Sciences (TFR), the Swedish Natural Science Research Council (NFR), the SSF program SiCEP and ABB Corporate Research.

## References

- [1] J. Kono, S. Takeyama, H. Yokoi, N. Miura, M. Yamanaka, M. Shinohara, and K. Ikoma, *Phys. Rev. B* **48**, (1993) 10909.
- [2] P.G. Baranov, Yu.P. Veshchunov, R.A. Zhitnikov, N.G. Romanov, and Yu.G. Shreter, *JETP Lett.*, **26**, (1977) 249.
- [3] M. Godlewski, W.M. Chen, and B. Monemar, *CRC Crit. Rev. Solid State Mat. Sci.* **19**, (1994) 241.
- [4] N.T. Son, O. Kordina, A.O. Konstantinov, W.M. Chen, E. Sörman, B. Monemar, and E. Janzén, *Appl. Phys. Lett.* **65**, (1994) 3209.
- [5] N.T. Son, W.M. Chen, O. Kordina, A.O. Konstantinov, B. Monemar, E. Janzén, D.M. Hoffmann, D. Volm, M. Drechsler, and B.K. Meyer, *Appl. Phys. Lett.* **66**, (1995) 1074.
- [6] D. Volm, B.K. Meyer, D.M. Hoffmann, W.M. Chen, N.T. Son, C. Persson, U. Lindefelt, O. Kordina, E. Sörman, A.O. Konstantinov, B. Monemar, and E. Janzén, *Phys. Rev. B* **53**, (1996) 15409.
- [7] P. Käckell, B. Wenzien, and F. Bechstedt, *Phys. Rev. B* **50**, (1994) 10761.
- [8] W.R. Lambrecht and B. Segall, *Phys. Rev. B* **52**, (1995) R2249.
- [9] K. Karch, G. Wellenhofer, P. Pavone, U. Rössler, and D. Strauch, *The Physics of Semiconductors*, edited by D.J. Lockwood (World Scientific, Singapore, 1995), p. 401.
- [10] B. Wenzien, P. Käckell, F. Bechstedt, and G. Cappellini, *Phys. Rev. B* **52**, 10897 (1995).
- [11] W.R. Lambrecht, S. Limpijumnong, S.N. Rashkeev, and B. Segall, *Phys. Stat. Sol. (b)* **202**, (1997) 5.
- [12] C. Persson and U. Lindefelt, *J. Appl. Phys.* **82**, (1997) 5496.
- [13] C. Persson and U. Lindefelt, to appear in *J. Appl. Phys.* **86**, No 9, (1999).
- [14] In *Polarons in Ionic Crystals and Polar Semiconductors*, edited by J.T. Devreese (North-Holland, Amsterdam, 1972), p. 497.
- [15] G.D. Mahan, *Many-Particle Physics*, 2<sup>nd</sup> edition (Plenum, New York, 1990), p. 507.
- [16] In *Landolt-Börnstein*, Vol 17, *Semiconductors*, edited by O. Madelung (Springer-Verlag, Berlin, 1982), p. 139.

Author for correspondence: N.T. Son, fax: 46-13-142337, e-mail: son@ifm.liu.se

## Differential Absorption Measurement of Valence Band Splittings in 4H SiC

S.G. Sridhara, S. Bai, O. Shigiltchoff, R.P. Devaty and W.J. Choyke

Department of Physics and Astronomy, University of Pittsburgh, Pittsburgh, PA 15260, USA

**Keywords:** Absorption, Band Structure, Crystal Field Splitting, Spin-Orbit Splitting, Valence Bands

**Abstract** New differential absorption spectra showing the spin-orbit (SO) and crystal field (CF) splittings of the valence band in 4H SiC are presented here. The values of the two splittings are measured to be  $6.8 \pm 0.6 \text{ meV}$  for SO and about  $60 \text{ meV}$  for CF splitting.

### Introduction

For the hexagonal SiC polytypes, the crystal field (CF) interaction causes a splitting of the topmost valence bands at the  $\Gamma$  point into a two-fold degenerate and a single non-degenerate band (neglecting electron spin). Several calculations of the valence band structure in the different SiC polytypes have been reported in the recent literature [1-3]. Based on their calculations, Lambrecht et al. [1] predict a linear increase of the CF splitting of the valence band with the hexagonality of the polytypes. Reliable experimental support for this linear dependence is however lacking. Recently we reported the experimental measurement of the SO and CF splittings of the valence bands in 6H SiC [4]. In this paper we present the results of our differential absorption measurements of the valence band splittings in 4H SiC and compare them with the recent calculations.

### Experimental

High quality 4H SiC boule material with very low micropipe density was grown at Cree Research Inc. Slices of the boule were cut parallel to the  $\langle a \rangle$  face into thicknesses of 2.3cm, 0.9cm, 0.43cm, 0.145cm and 0.055cm and polished. This allowed us to make measurements in both  $E \perp \hat{c}$  and  $E \parallel \hat{c}$  polarizations where  $\hat{c}$  indicates the axis of uniaxial symmetry.

Measurements were made using a specially designed wavelength modulated spectroscopy apparatus. As shown in Fig. 1, a collimated beam of light from a Xe-arc lamp is torsionally modulated at 50Hz with an oscillating quartz plate after being focused at the entrance slit of the monochromator. The refraction of the incident light by the oscillating quartz plate results in a modulation of the grating dispersion across the exit slit. The photomultiplier tube (PMT) then measures  $dI/d\lambda$ , where  $I$  is the transmitted intensity. By taking a ratio of the derivative signal and the chopped 217Hz incident

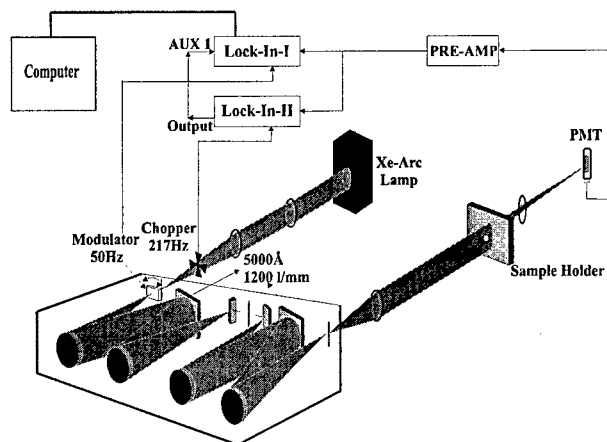


**Fig. 1:** Schematic drawing of the differential absorption setup.

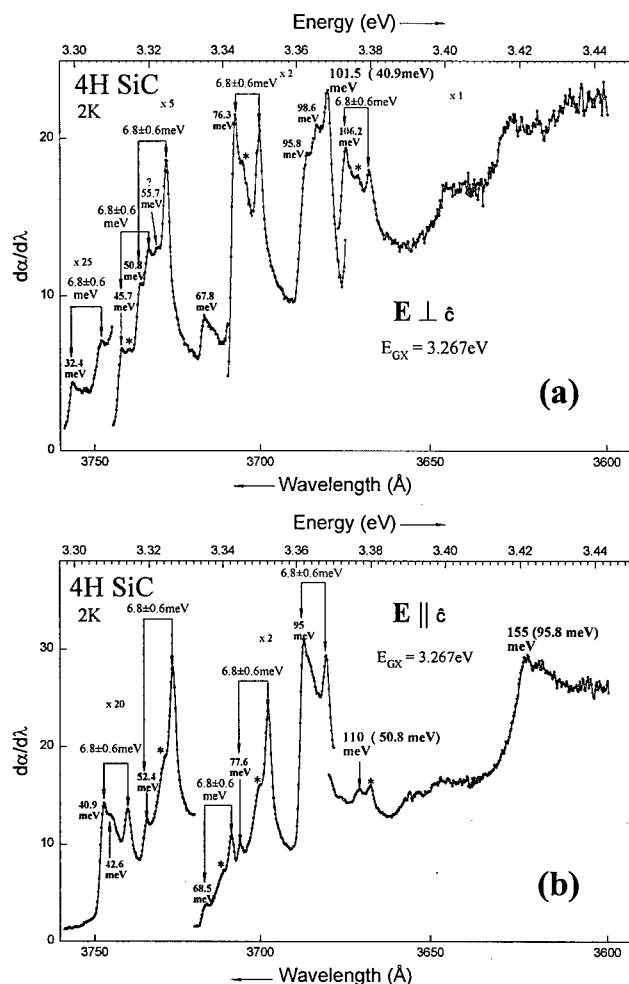


**Fig. 2:** Plots of  $d\alpha/d\lambda$  vs.  $\lambda$ , **Fig. 2(a)** for  $E \perp c$  polarization and **Fig. 2(b)** for  $E \parallel c$  polarization. The peak labels correspond to known phonon energies. The observed spin-orbit splitting is also indicated in the figures. The peaks labeled in larger font are tentatively associated with the crystal field splitting.

observed in our differential spectra with those reported in Ref. [6], we are able to assign some of the peaks to known phonon energies. These are labeled in Fig. 2(a) and 2(b). For each phonon the corresponding peak related to the spin-orbit split valence band has also been indicated on the two plots. From these assignments we obtain an average value of spin-orbit splitting as  $6.8 \pm 0.6$  meV. The features marked with an asterisk (\*) are remnants of peaks in the other polarization.

As mentioned above, in the hexagonal polytypes, under crystal field interaction, the three fold degenerate valence band splits into a two fold degenerate band with  $\Gamma_5$  symmetry in  $C_{6v}$  [7] and a single  $\Gamma_1$  symmetry non-degenerate band. Group theoretical analysis to determine polarization selection rules governing the PL spectra in 4H SiC was discussed in Ref. 5. We conducted a similar analysis of the absorption process to determine the allowed phonon assisted transitions from the  $\Gamma_5$

intensity signal we obtain  $1/I \, dI/d\lambda$ . According to the Beer-Lambert's law [5], if  $\alpha$  is the absorption coefficient of a sample and  $I_i$  is the incident radiation just inside the front surface of the sample, then the transmitted intensity is given by

$$I = I_i \exp(-\alpha t),$$

where  $t$  is the thickness of the sample. If we take the derivative with respect to wavelength on both sides of this equation we get

$$1/I \, dI/d\lambda = -t \, d\alpha/d\lambda + 1/I_i \, dI_i/d\lambda.$$

Based on experimental measurements, we are able to neglect  $1/I_i \, dI_i/d\lambda$ , where  $I_i$  is the incident intensity so that  $1/I \, dI/d\lambda$  is proportional to  $d\alpha/d\lambda$ . Measurements were made at 2K using an immersion type liquid He cryostat.

## Results and Discussion

Fig. 2(a) and 2(b) show the plots of  $d\alpha/d\lambda$  vs.  $\lambda$  in  $E \perp c$  and  $E \parallel c$  polarizations, respectively. The energy positions of the various peaks observed in our differential spectra were compared with those of the intrinsic lines, observed in the photoluminescence (PL) spectra of low doped 4H SiC epilayers [6]. In Fig. 2a, the peak at 3.343 eV was thus identified with the 76 meV LA phonon. From this assignment we obtain the value of the exciton bandgap  $E_{GX} = 3.267$  eV, which is in good agreement with the value of 3.266 eV obtained from PL measurements [6]. By comparing the peak energies in the two polarizations



**Table 1:** Possible transitions from the initial states ( $|i\rangle$ ) which are the  $\Gamma_5$  valence band and the  $\Gamma_1$  crystal field split off band, to the final state ( $|f\rangle$ ), which is the bottom of the conduction band, are listed. The symmetries of the different phonons are listed in the column " $\Omega$ ". The checks ( $\checkmark$ ) mark the allowed phonons and the (x) mark the phonons which are not allowed.

	$ i\rangle$	$\Omega$	$ f\rangle$			
			$M_1$	$M_2$	$M_3$	$M_4$
$E \parallel \hat{c}$	$\Gamma_5$	$M_1$	x	$\checkmark$	x	$\checkmark$
		$M_2$	$\checkmark$	x	$\checkmark$	x
		$M_3$	x	$\checkmark$	x	$\checkmark$
		$M_4$	$\checkmark$	x	$\checkmark$	x
	$\Gamma_1$	$M_1$	$\checkmark$	x	x	x
		$M_2$	x	$\checkmark$	x	x
		$M_3$	x	x	$\checkmark$	x
		$M_4$	x	x	x	$\checkmark$
$E \perp \hat{c}$	$\Gamma_5$	$M_1$	$\checkmark$	x	$\checkmark$	x
		$M_2$	x	$\checkmark$	x	$\checkmark$
		$M_3$	$\checkmark$	x	$\checkmark$	x
		$M_4$	x	$\checkmark$	x	$\checkmark$
	$\Gamma_1$	$M_1$	x	$\checkmark$	x	$\checkmark$
		$M_2$	$\checkmark$	x	$\checkmark$	x
		$M_3$	x	$\checkmark$	x	$\checkmark$
		$M_4$	$\checkmark$	x	$\checkmark$	x

and the  $\Gamma_1$  valence bands to the conduction band minimum at the M point [3]. Table 1 lists the selection rules for transitions involving phonons of different symmetry in the two polarizations. The transitions have been determined for all possible symmetries of the conduction band minimum. In all cases the following observations are made. First, not all phonons are allowed in transitions originating from the  $\Gamma_1$  crystal field split off band (CFB). E.g., if we take the symmetry of the conduction band minimum to be  $M_4$ , then  $M_2$  phonons are not allowed in transitions from the CFB. Second, in all cases, for a particular phonon, the transitions from the  $\Gamma_5$  valence band and the  $\Gamma_1$  CFB occur in opposite polarizations. We use this second observation to assign peaks in our differential spectrum as transitions involving the CFB.

The peaks, 101.5meV, 110meV and 155meV, labeled in a larger font in Fig. 2(a) and 2(b), could not be assigned to any known phonon energies or to the corresponding spin-orbit split counterpart of any known phonon. Using the criteria mentioned above, it is interesting to see that the peaks at 110meV and 155meV in  $E \parallel \hat{c}$  are about 60meV from the peaks at 50.8meV and 95.8meV, in  $E \perp \hat{c}$ . Also the peak at 101.5meV in  $E \perp \hat{c}$  is about 60meV from the 40.9meV peak in  $E \parallel \hat{c}$ . We therefore tentatively assign these three peaks to the CFB and obtain a value of about 60 meV for the CF splitting.

Table 2 lists the recent calculated values of the CF splitting by three different groups along with our experimentally measured values. As can be seen, our measurements are in good agreement with the values calculated by Lambrecht et al. [1] and are in fair agreement with the calculations of the other two groups. To our knowledge the only other measurement of the CF splitting in 4H SiC was

done by electroabsorption, by Dubrovskii and Sankin [8]. They reported a value of 83meV for CF splitting in 4H SiC. However their results are questionable as they did not see any polarization dependence of the lines in their spectra, which is contrary to our results and the PL results in Ref. [6].

It is unclear why only three peaks related to the CFB are seen in our differential spectra even though many more transitions are allowed by group theory. One possibility is that while group theory predicts the possible transitions, it does not predict their relative intensities. Therefore, peaks related to the CFB could be masked by strong peaks related to the top of the valence band.

It should be mentioned that the group theory analysis presented here was not done in the case of 6H SiC [4]. According to the authors of Ref. [3] the symmetry of the conduction band minimum in 6H SiC is the same as in 4H SiC. Therefore the selection rules determining the phonon assisted

**Table 2:** Comparison of the experimentally determined values of the CF splitting in the different polytypes with the calculated values by different theoretical groups.

Polytypes (% hexagonality)	Lambrech et al.	Wellenhofer and Rössler	Persson and Lindelfelt	Experimental
6H SiC (33)	46meV	44meV	53meV	42-44meV *
15R SiC (40)	54meV	-	-	-
4H SiC (50)	66meV	74meV	72meV	~60meV **
2H SiC (100)	132meV	144meV	160meV	-

\* Ref. [4]. \*\* This work.

transitions from the  $\Gamma_5$  and  $\Gamma_1$  valence bands in 6H SiC are the same as presented in this paper. If we use the above selection rules specified by group theory, we obtain a crystal field splitting of about 41meV, which is close to our previous assignment.

### Conclusion

We have determined the spin-orbit and crystal field splittings of the valence band in 4H SiC to be  $6.8 \pm 0.6$ meV and about 60meV, respectively, using wavelength modulated spectroscopy. The value of CF splitting obtained from our measurements shows good agreement with the splitting calculated by Lambrecht et al. [1]. When compared with our recently reported value of the CF splitting in 6H SiC, we see an almost linear increase of this splitting with hexagonality, as predicted by theory[1]. We are currently investigating the possibility of conducting these measurements in 15R SiC.

### Acknowledgement

We thank the Crystal Growth group at Cree Research Inc. for providing the high quality boule material essential for this project.

### References

- [1] W.R.L. Lambrecht, S. Limpijumnong, S.N. Rashkeev and B. Segall, *phys. stat. sol. (b)* 202 (1997), p. 5.
- [2] G. Wellenhofer and U. Rössler, *phys. stat. sol. (b)* 202 (1997), p. 107.
- [3] C. Persson and U. Lindelfelt, *J. Appl. Phys.* 82 (1997), p. 5496.
- [4] W.J. Choyke, R.P. Devaty and S.G. Sridhara, *Physica Scripta* T79 (1999), p. 9.
- [5] Nasser Peyghambarian, Stephan W. Koch and Andre Mysyrowicz, *Introduction to Semiconductor Optics*, Prentice Hall (1993), p. 56.
- [6] I.G. Ivanov, U. Lindelfelt, A. Henry, O. Kordina, C. Hallin, M. Aroyo, T. Egilsson and E. Janzén, *Phys. Rev. B* 58 (1998), p. 13634.
- [7] G.F. Koster, J.O. Dimmock, R.G. Wheeler and Hermann Statz, "Properties of thirty two point groups" MIT Press, Cambridge, MA, 1963.
- [8] G.B. Dubrovskii and V.I. Sankin, *Sov. Phys. Solid State* 17 (1975), p. 1847.

## Anisotropic Dielectric Function Properties of Semi-insulating 4H-SiC Determined from Spectroscopic Ellipsometry

M. Kildemo, M.B. Mooney, P.V. Kelly, C. Sudre and G.M. Crean

National Microelectronics Research Centre (NMRC), University College Cork,  
Lee Maltings, Prospect Row, Cork, Ireland

**Keywords:** 4H-SiC, Anisotropy, Birefringence, Dielectric Function, Ellipsometry

### ABSTRACT

The ordinary and extra-ordinary dielectric functions of semi-insulating 4H-SiC in the energy range 1.5-4.5 eV are determined by spectroscopic ellipsometry using a recently developed anisotropic incoherent reflection model. This model is further developed to perform rapid birefringence measurements. Below the minimum band gap the dielectric function is extracted using the Sellmeier dispersion relation. The complex dielectric function response above the band gap was extracted and extrapolated using both the Fourouhi and Bloomer and Tauc Lorentz dispersion models.

### INTRODUCTION

Silicon carbide exists in many different crystal polytypes, with each structure having unique electrical and optical properties [1]. In fact, the dielectric tensor of silicon carbide, depends strongly on anisotropy factors influenced by the crystal polytype. Few detailed dielectric function studies have been performed thus far for 4H-SiC, with the result that experimentally extracted values are not well established [2-5]. A precise knowledge of the anisotropy properties of the material is thus required for the further development of optoelectronic and process monitoring applications [2-5]. The anisotropic dielectric function of the most common polytypes has been estimated previously using *ab initio* methods [6]. The imaginary part of the dielectric function is found to exhibit uniaxial anisotropy, largely due to the difference in the optical transition element [6]. Spectroscopic ellipsometry (SE) was employed for the birefringence characterisation of semi-insulating 4H-SiC [7]. This work is based on experimental observations, that ellipsometric measurements of thick transparent anisotropic double side polished wafers, exhibit oscillations after reflection. These oscillations arise from the product of the thickness and the difference between the ordinary and extra-ordinary refractive indices [7]. In this paper, the dielectric function of 4H-SiC is extracted through the use of various approximate dispersion models used in conjunction with an anisotropic incoherent reflection model. The dielectric response below the minimum band gap energy can be adequately described using the Sellmeier dispersion equation. Other popular dispersion models such as the Fourouhi and Bloomer (FB) [8] or the Tauc Lorentz (TL) [9] were used to predict the complex anisotropic dielectric function above the minimum band gap.

### EXPERIMENTAL

The *UVISEL* Phase Modulated Spectroscopic Ellipsometer (PMSE) (of *Instruments SA Jobin-Yvon*) [10] was used to perform the UV-Visible spectroscopic ellipsometric measurements. Measurements were carried out with a resolution of 0.01 eV at angles of incidence of 65 and 70 °. A commercially available semi-insulating (resistivity > 10<sup>5</sup> Ωcm) {0001} on axis double side polished 4H-SiC wafer was used in this study. Ellipsometry is capable of partially determining the Mueller matrix of a sample used to describe the interaction of polarised light with generally depolarising

linear optical media [11]. In PMSE, measured quantities depend on the configuration used. In what is known as configuration II one measures the so-called "intensities" defined as  $I_s = \sin 2\psi \sin \Delta$  and  $I_{c2} = \sin 2\psi \cos \Delta$ , while configuration III measures  $I_s$  and  $I_{c3} = \cos(2\psi)$ , where  $\psi$  and  $\Delta$  are the standard ellipsometric parameters. The measured quantities  $I_s$ ,  $I_{c2}$  and  $I_{c3}$  correspond to elements of the Mueller matrix, and can be expressed in terms of the averaged products of the reflection coefficients:

$$I_s = 2 \operatorname{Im} \left( \frac{\langle r_s r_p^* \rangle}{\langle r_s r_s^* \rangle + \langle r_p r_p^* \rangle} \right), \quad I_{c2} = 2 \operatorname{Re} \left( \frac{\langle r_s r_p^* \rangle}{\langle r_s r_s^* \rangle + \langle r_p r_p^* \rangle} \right), \quad I_{c3} = \frac{\langle r_s r_s^* \rangle - \langle r_p r_p^* \rangle}{\langle r_s r_s^* \rangle + \langle r_p r_p^* \rangle}$$

where  $r_p$  and  $r_s$  are the sample reflection coefficients for  $p$  and  $s$  polarisations respectively, the asterisk stands for complex conjugate and the brackets (" $\langle \rangle$ ") denote the ensemble average over the varying quantities. Under normal coherent conditions (no depolarisation present) the degree of polarisation defined as  $P = \sqrt{I_s^2 + I_{c2}^2 + I_{c3}^2} = 1$ . In the current investigations the coherence length of the light is shorter than the thickness of the wafer, and hence  $P < 1$  [7].

## THEORY

A full description of the anisotropic incoherent reflection model goes beyond the scope of this work and has been omitted, however a full treatment is given elsewhere [7]. The averaged products required to fully calculate the PMSE measurements in case of a thick uniaxial layer with an anisotropy axis along its surface normal, was given as [7]:

$$\langle r_s r_p^* \rangle = r_{01s} r_{01p}^* + \frac{(t_{01s} t_{01p}^*)(t_{10s} t_{10p}^*)(r_{12s} r_{12p}^*) e^{2i(\beta_s - \beta_p)}}{1 - (r_{10s} r_{10p}^*)(r_{12s} r_{12p}^*) e^{2i(\beta_s - \beta_p)}} \quad (1)$$

The  $r_{01s,p}$  and  $r_{12s,p}$  are the ambient/anisotropic layer and anisotropic layer/semi-infinite-medium reflection coefficients for  $s$  and  $p$  polarisation respectively, given by the modified Fresnel relations [11]. Similarly  $t_{01s}$ ,  $t_{01p}$ ,  $t_{10s}$ ,  $t_{10p}$  are the ambient/anisotropic-substrate transmission coefficients [11]. In this work we are particularly interested in exploiting the oscillating contribution of Eq. 1. The oscillating "optical thicknesses"  $\beta_s$  and  $\beta_p$  are defined by:

$$\beta_s = 2\pi \frac{d}{\lambda} \sqrt{n_o^2 - n^2 \sin^2 \varphi_o} \quad \text{and} \quad \beta_p = 2\pi \frac{d}{\lambda} \frac{n_o}{n_e} \sqrt{n_e^2 - n^2 \sin^2 \varphi_o} \quad (2)$$

where  $d$  is the thickness of the layer,  $n_o$  and  $n_e$  are the ordinary and extraordinary refractive indices of the layer,  $n$  is the ambient refractive index,  $\lambda$  is wavelength of light and  $\varphi_o$ , the angle of incidence. Given the experimentally acquired data, the anisotropic behaviour of the dielectric function may then be extracted using this model in conjunction with an appropriate dispersion model.

The real part of the dielectric function, which is related through the Kramers-Kronig (KK) relationship to the imaginary part, produces thus a small birefringence, or refractive index difference that may be observed below the band gap. The real part of the anisotropic dielectric function is determined below the minimum band gap by fitting our ellipsometric data with a modified Sellmeier dispersion model:

$$\epsilon_q(E) = n_q^2(E) = \epsilon_\infty + \frac{f_q E_q^2}{E_q^2 - E^2}, \quad q = \begin{cases} \text{ordinary, direction perpendicular to } c\text{-axis} \\ \text{extra-ordinary, direction parallel to } c\text{-axis} \end{cases} \quad (3)$$

In previous work [3],  $\epsilon_\infty$  is set to 1, but it was proposed that background contributions could arise from higher electronic transitions [5]. The oscillator strength  $f_q$  is assumed to be the key parameter responsible for the birefringence; mainly due to the optical transition element for direct band gap transitions around 5.8 eV [6]. A direct "half-wave" method presented in detail in ref. 12, was also applied to estimate the birefringence by using two successive maxima in the  $I_c$  curve in Fig. 1.

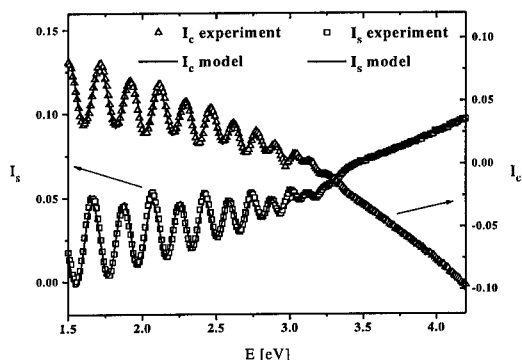


**Figure 1.** PMSE measured and model fitted intensities  $I_s$  and  $I_c$  using band gap dispersion models.

It is observed from Fig. 2, that the birefringence estimated from the "half-wave" method follows the fitted birefringence for low wavenumber values, while values closer to the minimum band gap are overestimated. This is attributed to the change in birefringence nominally neglected in the "half-wave" method [12]. The correction for the latter is also given in Fig. 2.

Further information may be extracted via approximate dispersion models incorporating parameters related to the minimum band gap and allowed higher transitions, such as the FB model [8] or the TL model [9]. Both models are based on the Tauc Gap approximation of the minimum gap, and a Lorentzian type model for the main direct transition. Both models were chosen given the relatively few parameters required for fitting compared to the Adachi type  $E_0$ ,  $E_{1A,B,C}$  dispersion models for zincblende and wurtzite hexagonal semiconductors [13,14]. For both TL and FB models, parameters relating to the ordinary dielectric function were fitted to coherent measurements, assuming in this case isotropic behaviour [2,4,5]. The resulting dielectric function was found to be in good agreement with previously measured values of 4H SiC [2-4]. The probability of transition of the dominating  $E_1$  like transition for the extra-ordinary component was then increased relative to the ordinary one, until the interference fringes were reproduced. All parameters were then fitted

simultaneously. The corresponding fit using the TL model, and the resulting dielectric function is shown in Figs. 1 and 3 respectively. The results obtained using the TL model displayed better fits above and below the minimum band gap compared to the FB model, and were furthermore in good agreement with the values extracted using the Sellmeier dispersion relation. Data from the TL dispersion model was further extrapolated to reveal band structure details, for comparison with ab-initio calculations [6]. Fig. 3 thus shows the simultaneously fitted anisotropic dielectric function of 4H SiC, using the TL model in conjunction with the anisotropic incoherent reflection model. Fig. 3 also shows the

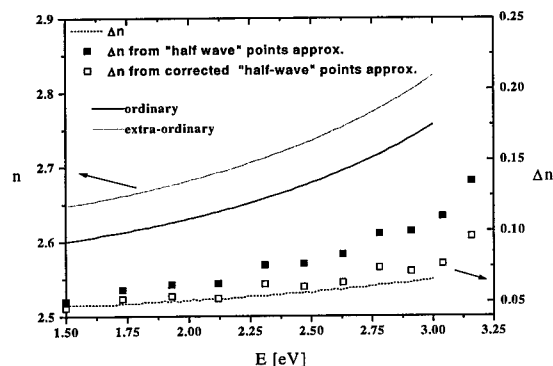


**Figure 2.** Fitted  $n_o$  and  $n_e$ , and resulting  $\Delta n$  (bottom dashed line), together with  $\Delta n$  obtained from the "half-wave-points" approximation, with and without correction.

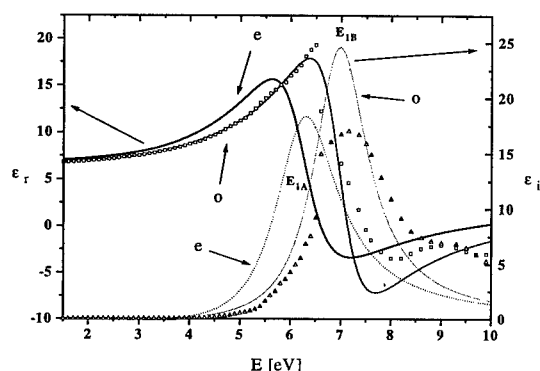


**Figure 3.** TL fitted Re(solid) and Im(dashed) part of ordinary (o) and extra-ordinary (e) dielectric functions of 4H-SiC, together with tabulated Re( $\Delta$ ) and Im( $\Delta$ ) part of ordinary component of 4H [2] up to 6.5 eV, and 6H [3] above 6.5 eV.

tabulated dielectric function of 4H SiC. [2,3]. In this work, we adopt the terminology of the hexagonal wurzite structures, and denote multiple  $E_1$  transitions, as  $E_{1A}$  (5.2-5.8 eV),  $E_{1B}$  (7 eV) [6,12]. It is observed that the broadened oscillator position of the ordinary component may represent an  $E_{1B}$  type direct transition [13,14]. The extra-ordinary component shows a downshift of the central energy position of the dominating optical transition. The latter may be attributed to the " $E_{1A}$ " transition being much stronger for parallel polarisations. The optical absorption in Fig. 3, is believed to be overestimated, but the extrapolated dielectric functions supplies the general trend of the anisotropic dielectric function.

## SUMMARY AND CONCLUSION

A newly formulated anisotropic incoherent reflection model has been applied for the first time to extract the dielectric function of semi-insulating 4H-SiC, using standard ellipsometric measurements. The anisotropic dielectric function can be accurately described by a modified Sellmeier dispersion relation below the minimum gap. The "half-wave" method reveals a dispersion dependence requiring a correction factor to accurately predict results of the birefringence for higher wavenumbers. In addition, the FB and TL dispersion models were evaluated. The TL model was found to best describe the ordinary and extra-ordinary optical properties above and below the minimum band gap. In conclusion we have demonstrated that conventional SE can accurately characterise birefringence, provided the material under study is in the form of an optically thick slab, allowing for the study of anisotropy related band structure characteristics.

## REFERENCES

- [1] W. R. L. Lambrecht and B. Segall, *Phys. Rev. B*, **52** (1995), p. R2249.
- [2] S. Zollner, J. G. Chen, E. Duda, T. Wetteroth, S.R. Wilson and J. N. Hilfiker, *J. Appl. Phys.* (1999), p. 8353.
- [3] W. J. Choyke and E. D. Palik, in *HOC I* (E. D. Palik ed., Academic Press, Orlando, 1985) p. 587.
- [4] O. P. A. Lindquist, U. Forsberg, J. P. Bergman, H. Arwin and K. Jarrendahl, this conference, p. 575
- [5] S. Logothetis and J. Petalas, *J. Appl. Phys.*, **80** (1996) p. 1768.
- [6] B. Adolph, K. Tenelsen, V. I. Gavrilenko, and F. Bechstedt, *Phys. Rev. B*, **55** (1997), p. 1422.
- [7] R. Ossikovsky, M. Kildemo, M. Stchakovsky and M. Mooney, *Appl. Opt.* (Accepted for publ.).
- [8] A. R. Forouhi and I. Bloomer, *Phys. Rev. B*, **34** (1986) p. 7018.
- [9] G. E. Jellison and F. A. Modine, *Appl. Phys. Lett.*, **69** (1996) p. 371.
- [10] B. Drévilion, *Prog. in Cryst. Growth and Charact.* **27** (1993) 1.
- [11] R. M. A. Azzam and N. M. Bashara, *Ellipsometry and Polarised Light* (North-Holland, Amsterdam, 1977), pp. 491, 358.
- [12] M. Kildemo, M. Mooney, C. Sudre, P.V. Kelly, *Appl. Opt.* (Submitted).
- [13] A. B. Djuricic, E. Herbert Li, *Opt. Comms.*, **157** (1998) p. 67.
- [14] S. Adachi, *Phys. Rev. B*, **35** (1987) p. 7454.

## Optical Characterization of 4H-SiC by Variable Angle of Incidence Spectroscopic Ellipsometry

O.P.A. Lindquist\*, H. Arwin, U. Forsberg, J.P. Bergman and K. Järrendahl

Department of Physics and Measurement Technology, Linköping University,  
SE-581 83 Linköping, Sweden

**Keywords:** Doping Concentration, Ellipsometry, SiC Dielectric Function

### Abstract

A variable angle of incidence spectroscopic ellipsometer equipped with a compensator has been used to determine the dielectric functions in the 0.74 – 6 eV photon energy range of n-type bulk 4H-SiC with doping concentrations between  $10^{17}$  and  $10^{19}$  cm<sup>-3</sup>. The resulting dielectric function for different SiC wafers depends on the doping concentration, especially around the absorption onset and higher photon energies. Measurements on different wafers with the same doping show good reproducibility. Simulations and preliminary measurements show that ellipsometry might be useful for thickness determination of thin (<1 µm) homoepitaxial films.

### Introduction

Due to its favorable electronic properties, SiC is recognized as one of the most promising materials for high-power, high-frequency and high temperature devices [1]. SiC also possesses excellent mechanical properties making it even more attractive. However, in order to fully understand the possibilities and limitations, a thorough characterization of the optical and electrical properties has to be done. Up to this date, there are few publications on the optical properties (e.g. the dielectric function,  $\epsilon$ ) of SiC [2-5]. This is mainly due to the earlier lack of high quality SiC, especially of the 4H polytype.

Presently, the published dielectric data are confined to one doping and also often in a rather narrow photon energy range. The aim of this paper is to present dielectric functions of 4H-SiC for a larger range of doping concentrations. The optical properties are determined by spectroscopic ellipsometry, a powerful, non-destructive technique for high accuracy measurements. The technique is surface sensitive and allows measurements in air. One advantage with ellipsometry compared to some other techniques is that no Kramers-Kronig transformation is needed.

### Experimental details

In this study a variable angle spectroscopic ellipsometer (VASE) with rotating analyzer from J.A.Woollam Co. Inc. has been used. Measurements were made at several angles of incidence ranging between 55° and 75° and at photon energies between 0.74 – 6 eV (200-1700 nm). The ellipsometer was equipped with a compensator, making it possible to measure the low-absorbing bulk samples with high accuracy [6]. Measurements were made at nine different input polarization states with both positive and negative signs in order to reduce systematic errors. The measurements were made at the center of the wafers. All samples were measured both before and after sample cleaning. The cleaning procedure used is a five-step process consisting of three baths: pyrralidone, acetone, and ethanol in ultra sonic environment. Thereafter follows two steps with cleaning at 80°C in hydrogen peroxide solutions with a high and a low pH value, respectively. These two steps are specially designed to remove organic and metallic contaminants [7]. The Si-faced 4H-SiC substrates used in this study were from Cree Research Inc. The wafers had n-type doping

concentrations specified to be  $7.7 \cdot 10^{17}$ ,  $1.0 \cdot 10^{18}$ ,  $7.4 \cdot 10^{18}$ ,  $7.5 \cdot 10^{18}$ ,  $1 \cdot 10^{19}$  and  $3.3 \cdot 10^{19} \text{ cm}^{-3}$ . The angle between the surface normal and the hexagonal axis i.e. the miscut was about  $8^\circ$ . All measurements were made with air as an ambient and at room temperature. Anisotropy and depolarization effects were neglected since they are believed to have very little impact on the result in the measured energy region [4]. Analysis of the measurements was carried out using the WVASE software.

### Results and Discussion

The pseudo-dielectric function  $\langle \epsilon \rangle$  was obtained by inversion of the measured complex reflectance ratio in terms of the ellipsometric angles  $\Delta$  and  $\psi$ .  $\langle \epsilon \rangle$  does not represent the dielectric function of 4H-SiC since corrections have to be made for surface overlayers such as an oxide or surface roughness. Thus, in order to determine a correct representation of the dielectric function, the oxide and/or surface roughness has to be taken into account. The obtained  $\langle \epsilon \rangle$  data were compared to an air/oxide layer/bulk model, where the oxide layer was represented by  $\text{SiO}_2$  reference data [2]. The  $\text{SiO}_2$  thickness was then determined by assuming that the resulting imaginary part of the dielectric functions of SiC should be zero below the band gaps. The obtained  $\text{SiO}_2$  thicknesses were around 2 nm. The dielectric functions determined on an energy-by-energy basis after numerically removing the oxide overlayer for three of the investigated wafers are shown in Fig. 1.

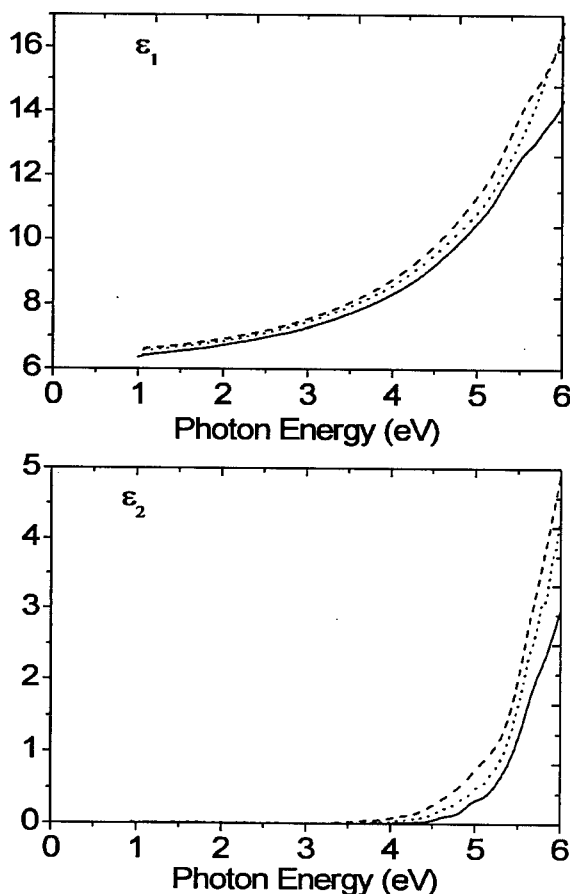


Fig. 1. The real and imaginary part of the dielectric function,  $\epsilon_1$  and  $\epsilon_2$ , of three different 4H-SiC wafers with doping concentrations of  $7.7 \cdot 10^{17}$  (dashed curve),  $7.5 \cdot 10^{18}$  (dotted curve) and  $3.3 \cdot 10^{19} \text{ cm}^{-3}$  (solid curve). The separation between the curves is larger for higher photon energies but there is also more noise in the spectra. This is mainly due to the lower intensity of the light source used for high energies. All curves show a feature around 5.54 eV, which is believed to be a critical point.



The data agree well with previously published data [4, 5] for wafers in the mid  $10^{18} \text{ cm}^{-3}$  range. In an alternative approach, the surface overlayer was modeled with a roughness layer using a Bruggeman effective medium approximation layer [8] consisting of equal parts of SiC and voids. However, within the accuracy of our measurements, the obtained dielectric functions are the same using this approach. This is an indication that it is difficult to distinguish between effects from an oxide and surface roughness. Using a parametric approach by employing e.g. Lorentz or Sellmeier models subsequently followed by an energy-by-energy fit resulted in the same optical properties. The sample cleaning gave slightly reduced overlayer thicknesses and improved signal-to-noise ratios, especially in the high-energy region of the spectra, but did not show new features in the  $\epsilon$  curves. The dielectric functions presented in this paper are all from measurements on cleaned samples.

The dielectric functions for the different SiC wafers depend on the doping concentration, especially around the absorption onset and at higher photon energies. The difference in absorption onsets with different doping agrees well with band structure calculations [9]. Very small differences in doping concentration are difficult to detect, due to noise limitations in experimental data. However, with our experimental setup, less than one order of magnitude in doping difference was easily resolved in the  $10^{17}$ - $10^{19} \text{ cm}^{-3}$  range. The reproducibility of the measurements is very good as shown in Fig. 2 for three different wafers with doping concentrations near  $7.5 \cdot 10^{18} \text{ cm}^{-3}$ . The same reproducibility was achieved for other doping concentrations.

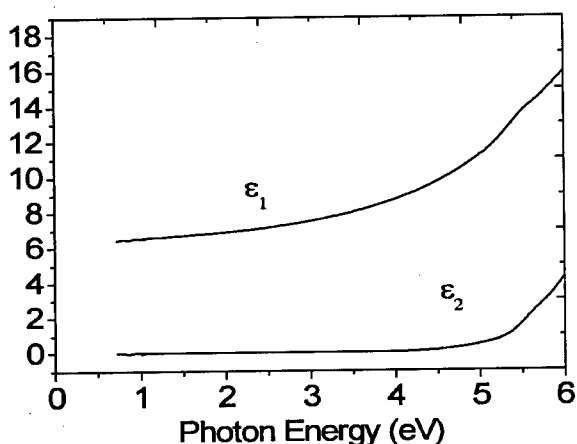


Fig. 2. The dielectric functions of three different 4H-SiC wafers with doping concentrations near  $7.5 \cdot 10^{18} \text{ cm}^{-3}$  showing an excellent reproducibility in the measurements. The different curves are indistinguishable.

All measurements show a shoulder feature around 5.54 eV, which is expected to be a  $M_1$  critical point, [9, 10]. A line-shape analysis shows good agreement with previously published results by Zollner *et al* [4]. No other critical point is found in the spectra.

Simulations and some preparatory measurements of 4H-SiC wafers with thin (typically  $<1 \mu\text{m}$ ) homoepitaxially grown layers were also done. In the simulations the obtained dielectric functions were used in epilayer/bulk models. According to these results a layer with a thickness between 100 nm – 1000 nm is detectable when the doping concentration between the substrate and the epilayer differ by one order of magnitude or more. This is comparable to FTIR (Fourier Transform Infrared Reflectance) thickness measurements where the thickness of the epilayer is required to be at least a couple of micrometers in order to produce interference oscillations [11]. Preliminary ellipsometry measurements in combination with cross-sectional scanning electron

microscopy studies show that it is possible to obtain values of thin epilayer thicknesses if the thickness is known within  $\pm 50$  nm. With further developments of the measurements and analysis it remains to be determined which accuracy that can be achieved in the thickness determination. It also remains to be investigated if non-uniform doping profiles seriously prevent accurate measurements.

### Conclusions

We have determined the dielectric function of n-type SiC in the 0.74 - 6 eV photon energy range for several doping concentrations in the range of  $10^{17}$ -  $10^{19}$  cm<sup>-3</sup> using a high accuracy spectroscopic ellipsometer equipped with a compensator. The results correspond well with previously published results on wafers with a doping concentration in the mid  $10^{18}$  cm<sup>-3</sup> range. Measurements before and after cleaning have been examined. A critical point at 5.54 eV was found in agreement with both theory and previously published optical data [4]. Simulations of the epilayer structures show a possibility to use ellipsometry for thickness determination of thin (<1  $\mu$ m) epilayers. The advantage of using ellipsometry compared to FTIR thickness measurements is that a smaller thickness can be accurately determined since the photon energy used is higher. It should be pointed out that the dielectric function is obtained using an isotropic approach since it has been pointed out that the anisotropy in the energy region concerned is small. A more thorough investigation of the anisotropy is necessary, especially for high energies (> 5 eV). The effect of the 8° off-axis needs to be included in such an investigation. It could also be discussed if the native oxide present is composed entirely of SiO<sub>2</sub> or if there are other materials present. However, the effect of any other material present is believed to be small which is motivated by the fact that the obtained dielectric functions are the same if modeled with a Bruggeman effective media approximation layer of almost the same thickness as the oxide overlayer.

### Acknowledgements

The authors would like to thank the Swedish Research Council for Engineering Sciences (TFR) for financial support.

### References

- [1] E. Janzén and O. Kordina, *Mat. Sci. Eng. B*, **46** (1997), p. 203.
- [2] E.D. Palik (editor) *Handbook of Optical Constants* (1985), New York: Academic.
- [3] S. Logothetidis and J. Petalas, *J. Appl. Phys.*, **80** (1996), p. 1768.
- [4] S. Zollner, J.G. Chen, E. Duda, T. Wetteroth, S.R. Wilson and J.N. Hilfiker *J. Appl. Phys.*, **85** (1999), p. 8353.
- [5] S. Zollner and J.N. Hilfiker, *Phys. Stat. Sol.*, **166** (1998), p. R9
- [6] D.E. Aspnes and A.A. Studna, *Phys. Rev. B*, **27** (1983), p. 985.
- [7] W. Kern and D.A. Puotinen, *RCA Review*, **187** (1970), p.187.
- [8] D.E. Aspnes, J.B. Theeten, and F. Hottier, *Phys. Rev. B*, **20** (1979), p. 3292.
- [9] C. Persson, *Dissertation No. 589*. (1999), Linköping Studies in Science and Technology, Linköping
- [10] G. Wellenhofer and U. Rössler, *Phys. Stat. Sol. B*, **202** (1997), p. 107.
- [11] M.F. Macmillan, A. Henry and E. Janzén, *J. Elec. Mat.* **27** (1998) p. 300.

\*Corresponding author: email: aleli@ifm.liu.se, fax: +46 13 137568, phone +46 13

## Isotope Effects on the Raman Spectrum of SiC

S. Rohmfeld<sup>1</sup>, M. Hundhausen<sup>1</sup>, L. Ley<sup>1</sup>, Norbert Schulze<sup>2</sup> and G. Pensl<sup>2</sup>

<sup>1</sup> Institut für Technische Physik II, Universität Erlangen-Nürnberg,  
Erwin-Rommel-Str. 1, DE-91058 Erlangen, Germany

<sup>2</sup> Institut für Angewandte Physik, Universität Erlangen-Nürnberg,  
Staudtstr. 7/A3, DE-91058 Erlangen, Germany

**Keywords:** <sup>13</sup>C Isotope, Modified Lely, Phonon Dispersion, Raman Spectroscopy

**Abstract:** Substituting <sup>12</sup>C by the <sup>13</sup>C isotope in SiC changes the Raman frequencies. We have used isotopic substitution in several polytypes of SiC (4H, 6H, 15R) to study the change in the phonon dispersion relation of SiC and compare the results with calculations based on a linear-chain model. In a second set of experiments we use isotopic substitution to study the incorporation of carbon from the crucible during the growth of SiC by the modified Lely technique. To this end, a stoichiometric mixture of silicon and pure <sup>13</sup>C was used as the charge. The incorporation of <sup>13</sup>C in the grown crystal as monitored by spatially resolved Raman spectroscopy yields a gradient of <sup>13</sup>C that increases beginning at the seed crystal and reaches a maximum of ~ 40 % within 300  $\mu$ m; the equilibrium concentration of <sup>13</sup>C is a mere 27 % after 1.5 mm growth.

## 1 Introduction

The vibrational properties of semiconductors and their lattice parameter depend on the mass of the atoms and can thus be changed by isotopic substitution [1]. This effect has been studied by Raman scattering in diamond [2], Ge [3], and ZnSe [4]. A limitation of first-order Raman spectroscopy is that, in principle, only phonons with wave vector  $q = 0$  ( $\Gamma$  point of the Brillouin zone, BZ) are accessible due to momentum conservation. For silicon carbide (SiC) it was shown that the phonon dispersion curves of the polytypes of SiC in the  $c$ -axis direction can be successfully interpreted as folded dispersion curves of cubic SiC [5]. As a result, the polytypism of SiC gives access to modes with  $q$ -vectors different from zero when referred to the Brillouin zone of cubic SiC. Thus, the phonon dispersion curves of 3C-SiC along [111] can be constructed from the study of Raman spectra of different SiC polytypes. By replacing natural silicon with <sup>30</sup>Si Widulle *et al.* have shown that Raman spectroscopy can provide information about the phonon eigenvectors throughout the Brillouin zone of cubic SiC [6]. Here, we study the effect of replacing the natural carbon isotope <sup>12</sup>C by <sup>13</sup>C on the dispersion relation of SiC. In a second set of experiments, we use isotope substitution together with Raman spectroscopy to investigate the incorporation of C from the crucible during the growth of SiC.

## 2 Experimental details

SiC crystals (4H, 6H, 15R) were grown using a modified Lely technique (physical vapor transport method) [7] from a source material that was obtained by sintering a stoichiometric mixture of 99 % pure <sup>13</sup>C and silicon powder with natural isotopic composition ( $m_{\text{Si}} = 28.09$  u) in a graphite crucible. Lely platelets of 4H, 6H, and 15R with natural carbon isotopic composition ( $m_{\text{C}} = 12.01$  u) were used as seed crystals. Spatially resolved Raman spectra were recorded in a Raman microprobe setup in backscattering configuration using the 514.5 nm Ar-ion-laser line.

From the samples grown cross-sectional slices parallel to the growth direction were cut in order to investigate the isotopic composition as a function of the distance from the seed crystal.

### 3 Results and Discussion

Representative Raman spectra of a 6H-SiC isotopically substituted sample at different distances from the seed crystal are shown in Fig. 1 in the frequency range of the TO phonon modes. In the spectrum, recorded from the seed crystal (bottom), the three characteristic TO modes of 6H-SiC can be seen. The modes are labelled by their wave vector in the extended zone scheme:  $n/m$  corresponds to  $q = (n/m) \cdot (\pi/c)$ , where  $c$  is the distance between two Si-C double layers. The isotopic composition  $x$  can be calculated from the frequency of the TO(0) mode, since the square of its frequency is proportional to the inverse of the reduced mass  $\mu$  ( $\omega_{\text{TO}(0)}^2 \propto \mu^{-1}$ ) with

$$\mu = (1/\bar{m}_C + 1/m_{\text{Si}})^{-1}, \quad (1)$$

where  $\bar{m}_C$  is the average mass of carbon atoms in a mixture of  $^{12}\text{C}$  and  $^{13}\text{C}$  ( $^{13}\text{C}_x \text{ } ^{12}\text{C}_{1-x}$ ) defined by:

$$\bar{m}_C = (12 + x) \cdot \text{atomic units}. \quad (2)$$

The relative concentration  $x$  of  $^{13}\text{C}$  is calculated for each spectrum and shown in Fig. 1 next to the corresponding spectrum. As  $x$  increases all modes shift to lower frequencies and the peaks broaden considerably. At the same time a broad structure is observed below the Raman spectrum between  $730 \text{ cm}^{-1}$  and  $790 \text{ cm}^{-1}$  that increases in intensity with  $x$ . We ascribe the peak broadening to elastic scattering by the isotopic disorder that results from the random mixture of the two isotopes. The scattering is fastest for phonons with energies where the phonon density-of-states is large [8]. The TO(6/6) mode originates from vibrational states at the 3C-SiC Brillouin zone boundary. There, the density-of-states, and hence the scattering induced line broadening, is largest [9] and the TO(6/6) mode disappears for  $x > 0.33$ .

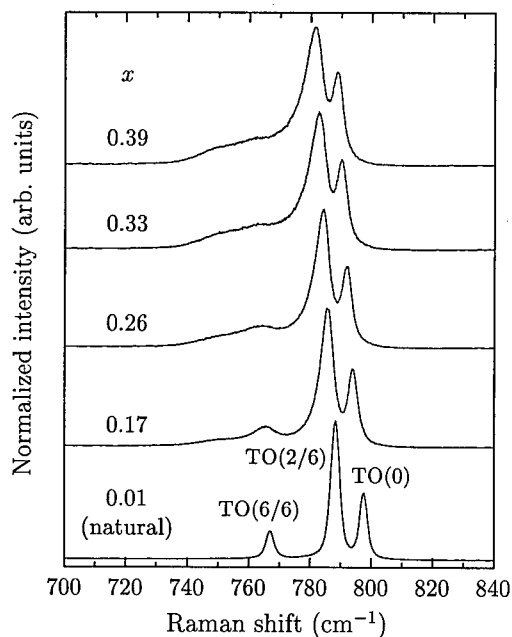


**Fig. 1.** Raman spectra of isotopically enriched 6H-SiC with different isotopic composition  $^{13}\text{C}_x \text{ } ^{12}\text{C}_{1-x}$  of carbon in the range of the TO mode. All spectra are normalized to the amplitude of the TO(2/6) mode.

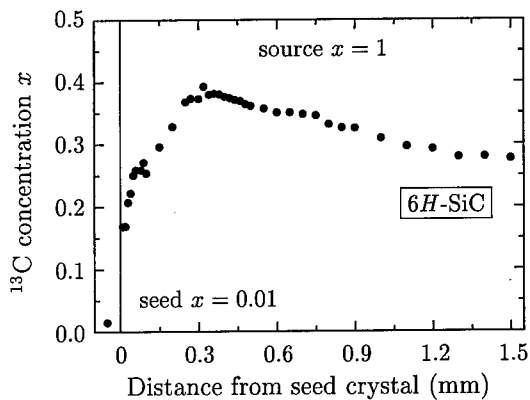


**Fig. 2.**  $^{13}\text{C}$  concentration  $x$  as function of the distance from the seed crystal. The vertical line marks the interface between seed crystal and grown SiC. The seed crystal was 6H-SiC with natural isotopic carbon composition ( $x = 0.01$ ).

The spectra of Fig. 1 were taken at different distances from the substrate. More spectra were taken and evaluated for  $x$  in order to study the  $^{13}\text{C}$  incorporation during sublimation growth. The result is shown in Fig. 2, where  $x$  is plotted as a function of the distance from the seed crystal. Within the first 300  $\mu\text{m}$  the concentration of  $^{13}\text{C}$  increases to a maximum of  $\sim 40\%$ , after which it drops gradually to  $\sim 27\%$  at 1.5 mm. We argue that at the beginning of growth the crucible and the seed crystal act as sources for  $^{12}\text{C}$ , resulting in the low  $^{13}\text{C}$  concentration within the first few hundred microns. A surprising result is, however, that during the whole growth less than 40% of the carbon in SiC is provided by the source charge.

We have systematically investigated the Raman spectra of TO and LO modes for 4H, 6H, and 15R SiC polytypes with a composition  $x = 0.25$ . Using these data we construct the phonon dispersion curves of SiC for that isotopic composition according to Ref. [5] and compare the result with the dispersion curve of SiC with natural carbon composition in Fig. 3. In addition

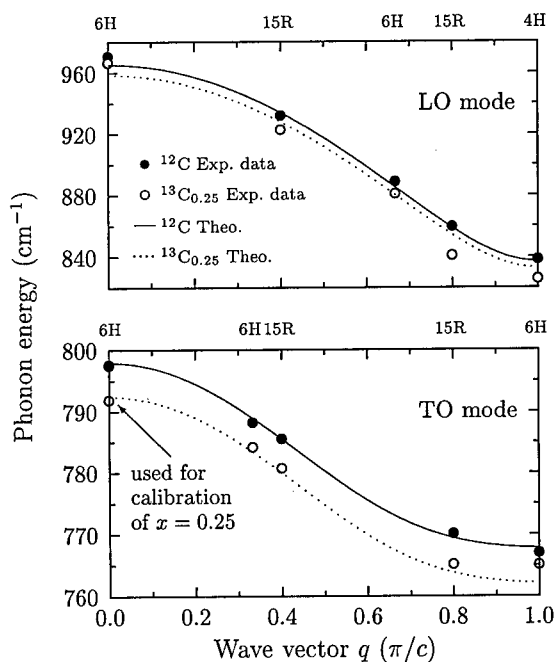


**Fig. 3.** Phonon dispersion curves of the optical branches determined from Raman scattering (symbols) and calculated with a linear-chain model [10] (lines). The polytype from which the data were obtained is indicated at the top of the figure. The ( $q = 0$ ) TO-mode was used to determine  $x$ .

to the experimental data, calculated dispersion curves using a linear-chain model [10] are shown. The calculations reproduce the dispersions and also the differences between the two isotopic compositions in general quite well. An exception are the modes at the BZ boundaries. Also the description of the acoustic modes (not shown here) is less than satisfactory. We, therefore, believe that the phonon eigenvectors are not well reproduced in the calculation with the set of force constants used in the linear chain model. A tuning of the parameters for this model appears to be required.

#### 4 Conclusion

We have grown 4H, 6H, and 15R polytypes of SiC using as source material sintered SiC enriched with 99%  $^{13}\text{C}$ . In the Raman spectra of these samples an isotope induced shift of the phonon lines is observed. We use the frequency shift of the highest lying TO mode to derive the isotopic composition as a function of sample thickness. We find that the  $^{13}\text{C}$  concentration is not constant, but increases within the first few hundred microns and levels off thereafter to a surprisingly low value of less than 30%.

The effect of isotopic substitution on the phonon frequencies of these polytypes is discussed in the large Brillouin zone of cubic SiC. In addition to the influence of the carbon mass on the phonon frequencies we find a line broadening that is largest for modes which lie in regions of high phonon density-of-states.

#### Acknowledgments

We thank Horst Sadowski and Reinhard Helbig for helpful discussions. This work was supported by the Deutsche Forschungsgemeinschaft under Sonderforschungsbereich 292 Mehrkomponentige Schichtsysteme (MEKOS).

#### References

- [1] M. Cardona, in *Festkörperprobleme/Advances in Solid State Physics*, edited by R. Helbig (Vieweg, Braunschweig/Wiesbaden, 1994), Vol. 34, p. 35.
- [2] K. C. Hass, M. A. Tamor, T. R. Anthony, and W. F. Banholzer, *Phys. Rev. B* **45** (1992), p. 7171.
- [3] H. D. Fuchs, P. Etchegoin, M. Cardona, K. Itoh, and E. E. Haller, *Phys. Rev. Lett.* **70** (1993), p. 1715.
- [4] A. Göbel, T. Ruf, J. M. Zhang, R. Lauck, and M. Cardona, *Phys. Rev. B* **59** (1999), p. 2749.
- [5] D. W. Feldman, J. H. Parker, Jr., W. J. Choyke, and L. Patrick, *Phys. Rev.* **173** (1968), p. 787.
- [6] F. Widulle, T. Ruf, O. Buresch, A. Debernardi, and M. Cardona, *Phys. Rev. Lett.* **82** (1999), p. 3089.
- [7] N. Schulze, D. L. Barrett, and G. Pensl, *Appl. Phys. Lett.* **72** (1998), p. 1632.
- [8] S. Tamura, *Phys. Rev. B* **27** (1983), p. 858.
- [9] M. Hofmann, A. Zywiets, K. Karch, and F. Bechstedt, *Phys. Rev. B* **50** (1994), p. 13401.
- [10] S. Nakashima and K. Tahara, *Phys. Rev. B* **40** (1989), p. 6339.

## Disappearance of the LO-Phonon Line in the UV-Raman Spectrum of 6H-SiC

R. Püsche, S. Rohmfeld, M. Hundhausen and L. Ley

Institut für Technische Physik, Universität Erlangen-Nürnberg,  
Erwin-Rommel-Str. 1, DE-91058 Erlangen, Germany

**Keywords:** Folded Phonon Modes, Raman Polarizability, Raman Spectroscopy

**Abstract:** We undertook a study of the intensities of optical vibrational modes in the Raman spectrum of 6H-SiC as a function of excitation energy between 2.4 eV and 4.9 eV. A disappearance of the  $LO_0$  mode which is the longitudinal optical mode with the highest frequency is observed at 4.38 eV. The result is explained in the framework of a bond-Raman-polarizability model for the Raman scattering cross section as due to the cancellation of the energy dependent bond-Raman polarizabilities of intra- and inter-bilayer bonds that connect the Si and C planes in SiC.

### 1 Introduction

Raman spectroscopy is commonly used as a tool for polytype determination of SiC. In the Brillouin zone folding concept the phonon dispersion curves of any polytype for a direction perpendicular to the Si-C double layers are regarded as folded replica of the dispersion curves of cubic SiC [1]. Modes are thus classified by their relative position in the 3C-SiC Brillouin zone along [111]. In the case of 6H-SiC the k-conservation for Raman scattering selects modes with k-vectors that are 0, 2/6, 4/6 and 6/6 of the dimension of the 3C-SiC Brillouin zone in [111] direction. These fractions are used as an index to distinguish different lines belonging to the same principle phonon branches. That simple selection rule, however, does not account for the intensities of the Raman modes. For the transversal modes (TA and TO) a quantitatively correct calculation of the intensities of folded phonon modes has been performed for back scattering along the c-axis in the framework of a bond-Raman-polarizability model [2, 3].

Recently, a selective resonance of folded modes in 6H, 4H, and 15R-SiC using UV-excitation was observed and traced back to excitation energy dependent bond-Raman polarizabilities of different bond groups in SiC [4]. In order to investigate these effects, we have undertaken a systematic study of optical phonon modes in 6H-SiC as a function of laser wavelength. We find in addition to the resonances a distinct antiresonance for the  $LO_0$  mode and show that the intensities are well accounted for by the bond polarizability model.

### 2 Experimental details

Raman spectra were recorded in back scattering configuration for 6H-SiC (0001) using a SPEX 1404 double monochromator. For excitation a tunable picosecond TiSa-laser was frequency doubled and tripled to provide photon energies between  $3.8 \text{ eV} < E_{exc} < 5 \text{ eV}$ . Excitation intensity and spectral band width were about 40 mW and  $25 \text{ cm}^{-1}$ , respectively. Highly resolved Raman spectra were recorded at 2.41 eV by the use of an Ar ion laser.

### 3 Results

Raman spectra of the TO and LO phonon branches normalized to the TO-intensity are shown in Fig. 1 arranged in order of increasing  $E_{exc}$  from top to bottom. For 2.41 eV, three transversal ( $TO_0$ ,  $TO_{2/6}$ , and  $TO_{6/6}$ ) and two longitudinal modes ( $LO_0$  and the  $LO_{4/6}$ -doublet) are observed. Note, that the folded  $LO_{4/6}^{\pm}$  peaks have less than 0.4% intensity relative to the strongest TO-mode. For the UV-spectra the transversal modes could not be resolved. Scattering from the  $LO_0$  and  $LO_{4/6}$  modes is observed with relative intensities that depend on  $E_{exc}$ . For UV-excitation the  $LO_{4/6}$ -peak is by more than one order of magnitude more intensive than for visible excitation, in agreement with Ref. [4]. In contrast, the  $LO_0$  intensity initially increases and then drops to nearly zero at 4.38 eV. Above that energy the mode appears again and reaches an intensity larger than that of the TO-modes at  $E_{exc}=4.93$  eV.

In Fig. 2 the intensities of  $LO_0$  and  $LO_{4/6}$  modes normalized to the TO-intensity are shown as a function of  $E_{exc}$ . The  $LO_{4/6}$  intensity is large compared to its value of 0.3% at visible excitation ( $E_{exc}=2.41$  eV) over the whole range of  $E_{exc}$  shown, with a distinct resonance at  $E_{exc}=4.25$  eV. The intensity of the unfolded  $LO_0$  mode, however, has a minimum at  $E_{exc}=4.38$  eV, as was anticipated from inspection of the corresponding Raman spectrum (see Fig. 1). In the following we will show, how the disappearance of the  $LO_0$  peak can be explained as the competing contributions of two kinds of bond groups to the Raman polarizabilities in SiC.

### 4 Theory

In classical theory the Raman intensity is described by:

$$I_{Raman,\lambda} \propto \left| \mathbf{e}_s \cdot \frac{\partial \underline{\chi}}{\partial \mathbf{Q}_\lambda} \cdot \mathbf{e}_i \right|^2, \quad (1)$$

where  $\lambda$  denotes the phonon mode,  $\mathbf{e}_i$  and  $\mathbf{e}_s$  are incident and scattered polarization vectors, respectively,  $\underline{\chi}$  the susceptibility tensor, and  $\mathbf{Q}_\lambda$  the phonon normal coordinates.

In the bond polarizability approach the modulation of the polarizability by a phonon (mode  $\lambda$ ) implied by  $\frac{\partial \underline{\chi}}{\partial \mathbf{Q}_\lambda}$  in Eq. 1 is expressed as a sum over the modulations of the polarizabilities of individual bonds due to the motion of their end atoms [2]:

$$I_{Raman,\lambda} \propto \left| \mathbf{e}_s \cdot \sum_{n=1}^{N_B} \left[ \frac{\partial \alpha_n}{\partial \mathbf{r}} \cdot \Delta \mathbf{u}_{n,\lambda} \right] \cdot \mathbf{e}_i \right|^2. \quad (2)$$

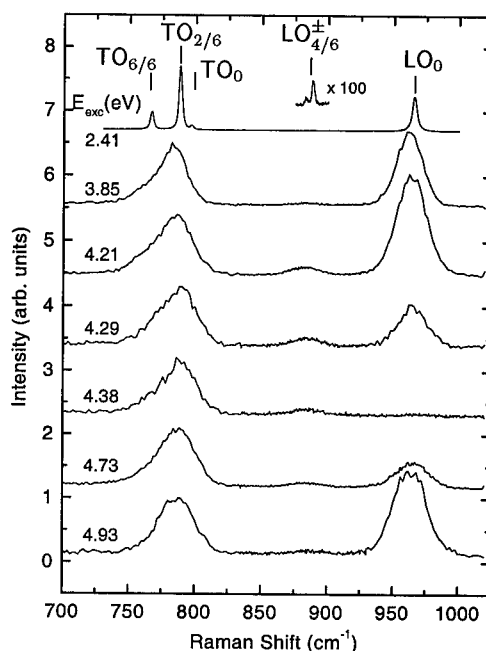


Fig. 1. Raman spectra of optical phonons in 6H-SiC for different excitation energies. Note, that except for the uppermost spectrum the TO-modes are not resolved due to the large spectral band width of the tunable laser used.



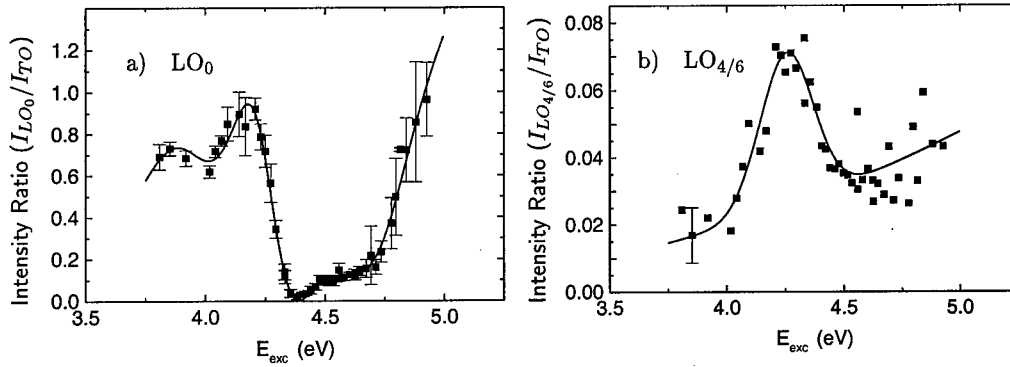


Fig. 2. Intensity of the  $LO_0$  phonon mode (a) and of the  $LO_{4/6}$  mode (b) as a function of excitation energy. The data are normalized to the total intensity of the TO-lines.

Here,  $N_B$  is the number of bonds, that are indexed by  $n$ .  $\underline{\alpha}_n$  is the bond polarizability tensor of the  $n$ 'th bond and  $\Delta \mathbf{u}_{n,\lambda}$  the bond stretching vector for that bond in the vibronic mode  $\lambda$ . For longitudinal modes propagating along the  $c$ -axis,  $\Delta \mathbf{u}_{n,\lambda}$  is the one dimensional variation of the distance between neighboring lattice planes ( $\Delta z$ ). Grouping together all bonds arranged in planes perpendicular to the  $c$ -axis for 6H-SiC we thus arrive at a sum over 12 bonds per unit cell after the appropriate polarization vectors have been inserted into Eq. 2:

$$I_{Raman,\lambda} \propto \left| \sum_{n=1}^{12} d_n \cdot \Delta z_{n,\lambda} \right|^2. \quad (3)$$

For  $d_n$  inter- and intra-bilayer bond groups have to be distinguished and the inter bilayer bond groups are further differentiated according to cubic and hexagonal stacking sequence:

$$d_n = \begin{cases} a : & \text{intra bilayer} \\ e_c : & \text{inter bilayer, cubic} \\ e_h : & \text{inter bilayer, hexagonal} \end{cases} \quad (4)$$

For the time being, we ignore the difference between cubic and hexagonal stacking by replacing  $e_c$  and  $e_h$  with an effective bond-Raman polarizability  $e_{\text{eff}}$ . For the  $LO_0$  vibronic mode close to the  $\Gamma$ -point the Si and C sublattices vibrate against each other, so that  $\Delta z_n \approx -\Delta z_{n+1}$  and we arrive at:

$$I_{Raman,\lambda} \propto |6(a - e_{\text{eff}})|^2. \quad (5)$$

The result implies that the scattering intensity does vanish if the bond-Raman polarizabilities of inter-bilayer and intra-bilayer bond groups are equal. This is apparently what occurs at the excitation energy  $E_{\text{exc}} = 4.38 \text{ eV}$ , where we observe the disappearance of  $LO_0$  scattering intensity. Under the assumption that no strong energy dependence for the TO-modes exists, we have calculated the energy dependence of the ratio  $e_{\text{eff}}/a$  from the data of Fig. 2a) and show the result in Fig. 3. The two solutions correspond to the two possible roots of Eq. 5 that reproduce the experimentally determined intensity.

A discussion of the intensity of the  $LO_{4/6}$  mode (see Fig. 2b) is only possible, if the bond-Raman polarizabilities for cubic and hexagonal stacking ( $e_c$  and  $e_h$ ) are distinguished [4, 5], and is beyond the scope of this paper.

## 5 Conclusion

We have measured the Raman spectra of the LO modes in 6H-SiC as a function of excitation energy. Whereas for the folded mode with a wave vector of  $4/6$  of the dimension of the 3C-SiC Brillouin zone a distinct resonance is observed at  $E_{exc} = 4.25$  eV, the intensity of the highest frequency  $LO_0$  mode vanishes at 4.38 eV. We explain that result in the framework of a bond polarizability model in which the contributions to the polarization of the intra-bilayer Si-C bonds and the inter-bilayer bonds interfere destructively. The destructive interference is a result of the different energy dependencies of the two bond-Raman polarizabilities.

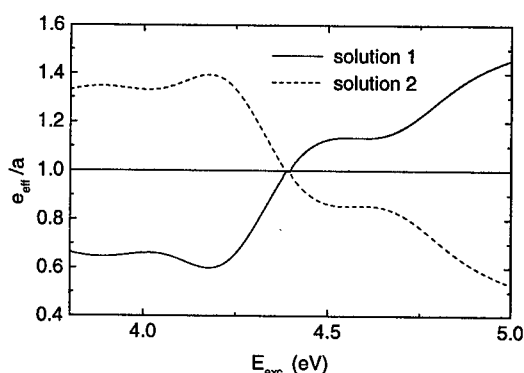


Fig. 3. Ratio of the bond-Raman polarizabilities of inter- and intra-bilayer bonds as a function of energy. A value of unity for  $e_{eff}/a$  at 4.38 eV implies a vanishing intensity of the  $LO_0$  mode (see Fig. 1).

## Acknowledgement

This work was supported by the Deutsche Forschungsgemeinschaft under SFB 292. We thank T. Suemoto and T. Tomita for helpful discussions.

## References

- [1] D. W. Feldman, J. H. Parker, Jr., W. Choyke, and L. Patrick, Phys. Rev. **173** (1968), 787.
- [2] S. Nakashima, H. Katahama, Y. Nakakura, and A. Mitsuishi, Phys. Rev. B **33** (1986), 5721.
- [3] S. Nakashima and K. Tahara, Phys. Rev. B **40** (1989), 6339.
- [4] T. Tomita, S. Saito, M. Baba, M. Hundhausen, T. Suemoto, and S. Nakashima, these proceedings.
- [5] R. Püsche, S. Rohmfeld, M. Hundhausen, and L. Ley, to be published.

## Selectively Resonant Raman Spectra of Folded Phonon Modes in SiC

T. Tomita<sup>1</sup>, S. Saito<sup>1</sup>, M. Baba<sup>1</sup>, M. Hundhausen<sup>2</sup>, T. Suemoto<sup>1</sup>  
and S. Nakashima<sup>3</sup>

<sup>1</sup> Institute for Solid State Physics, University of Tokyo,  
5-1-5 Kashiwanoha, Kashiwa, Chiba, 277-8581, Japan

<sup>2</sup> Institut für Technische Physik, Universität Erlangen-Nürnberg,  
Erwin-Rommel-Str. 1, DE-91058 Erlangen, Germany

<sup>4</sup> Department of Electrical and Electronic Engineering, Miyazaki University,  
1-1 Gakuenkibanadai-nishi, Miyazaki, 889-2192, Japan

**Keywords:** Bond-Raman-Polarizability Model, Folded Longitudinal Phonon Modes, Resonances, Selective

**Abstract:** The excitation energy dependence of the Raman intensities of folded longitudinal phonon modes in various SiC polytypes was measured in near resonant conditions. Selective enhancement of the folded longitudinal phonon modes relative to the non-folded longitudinal phonon mode was observed. We used a bond-Raman-polarizability model to analyze this selective enhancement effect. In this model, bond-Raman-polarizabilities of three bond arrangement are supposed to have different excitation energy dependence. By using this model, the excitation energy dependence of the relative intensities of the folded longitudinal phonon modes is successfully interpreted.

### Introduction

It is well known that silicon carbide (SiC) has many polytypes which can be regarded as natural superlattices (homo-superlattices). SiC-superlattices have the periodic structures consisting of a sequence of the Si-C bonds that have two different environment (hexagonal and cubic). These structures are of interest from a viewpoint of physics, because they provide various slightly different structures which are useful for investigating the electron-phonon interactions.

The resonant Raman effect has long been used to investigate the mechanism of electron-phonon interaction. In artificial superlattices such as the GaAs-AlAs system (hetero-superlattices), the resonant Raman spectroscopy has been used to show the coupling of specific phonons with the electronic states of the constituent materials [1]. This kind of effect is basically understood in terms of electron phonon coupling in each (bulk-like) material. In contrast to this rather simple case, the resonant Raman effect in the SiC-superlattices will provide a chance for studying microscopic mechanisms of the electron-phonon interaction.

However, there is no experimental nor theoretical report on the resonant Raman effect in SiC within the best knowledge of the authors. In this study, we measured the resonant Raman spectra of various SiC polytypes.

In  $\alpha$ -SiC, which has  $n$ -times larger unit cell than that of  $\beta$ -SiC (3C-SiC), the Brillouin zone is  $1/n$  of that of  $\beta$ -SiC. Then, the phonon dispersion curves of  $\beta$ -SiC are folded and give a new intersection at  $\Gamma$  point which is termed FLO( $m/n$ ), FLA( $m/n$ ) and so on.

### Experiment and results

The Raman spectra have been measured in back scattering geometry using a triple monochromator (SPEX 1877) equipped with a cooled CCD camera. We took the spectra at seven different

wavelengths using various lasers for excitation in the visible and ultraviolet regions. 514.5, 488.0 and 457.9nm (2.41, 2.54 and 2.71eV) lines were obtained from an Ar ion laser. For the 442 and 325nm (2.81 and 3.81eV) lines, we used an He-Cd laser. The second harmonic of a dye laser (Rh6G) synchronously pumped by a mode locked YAG laser was used at 302nm (4.11eV). The fourth harmonic of the Q-switched YAG laser was used as the 266nm (4.66eV) light source.

The SiC samples used in this study are flake like crystals having (0001) as-grown surfaces produced with Acheson process or modified Lely process. All samples are n-type and the impurity levels are below  $2 \times 10^{17} \text{ cm}^{-3}$ .

Excitation density dependence of the LO-phonon plasmon coupled mode (LOPC) were studied under resonant conditions with a pulsed laser at 266nm. Then, we used the low excitation density limit to avoid the effect of the LOPC, which reduces the intensities of the FLO(0) mode.

The relative intensity of the folded longitudinal phonon modes will not be affected by the geometrical configuration, because all the observable folded longitudinal phonon modes have  $A_1$  symmetry [2]. Therefore, we did not analyze the polarization of the scattered light in this measurement. The spectral response of the experimental system was checked by using a tungsten standard lamp, and the sensitivity was found to be practically flat within the wavenumber range of each Raman spectrum.

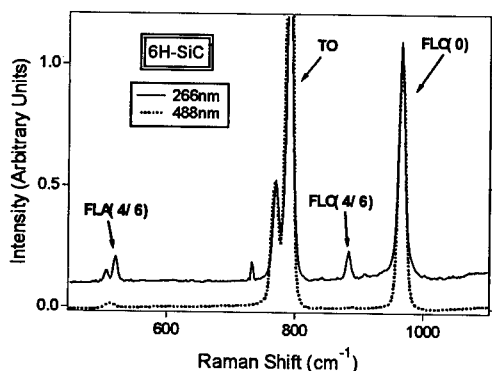


Fig. 1: Raman spectra of 6H-SiC. Solid and dotted lines correspond to 266nm and 488nm excitation, respectively. The solid curve is shifted by 0.1 along the ordinate.

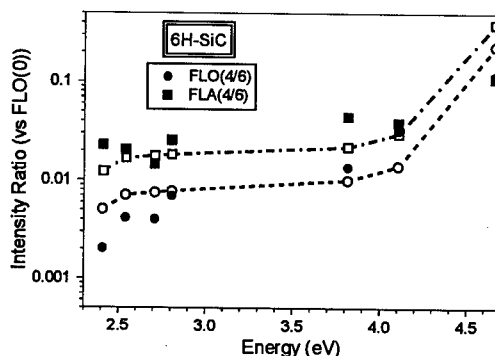


Fig. 2: Excitation energy dependence of the relative intensity of the folded longitudinal phonon modes for 6H-SiC. Filled symbols correspond to experimental data and open symbols with broken lines correspond to calculated results.

The Raman spectra of 6H-SiC are shown in Fig. 1. The solid line corresponds to 266nm excitation, and the broken line to 488nm. These spectra were normalized to the FLO(0) mode.

The spectra show enhancement of the intensity of the folded longitudinal phonon mode relative to the non-folded FLO(0) mode for ultraviolet excitation. In 6H-SiC, the FLO(4/6) and FLA(4/6) modes found for visible excitation are enhanced for ultraviolet excitation.

The excitation energy dependence of the intensity of folded longitudinal phonon modes relative to the FLO(0) mode in 6H-SiC, 4H-SiC and 15R-SiC is shown in Fig. 2, Fig. 3 and Fig. 4 by filled symbols, respectively. When the peaks were not discernible, the noise levels are plotted with error bars to indicate the upper limit of the peak intensities. In these figures, it can be seen that the normalized intensities of folded longitudinal phonon modes are strongly enhanced for ultraviolet excitation. It is also worth noting that the relative intensities of these folded phonon modes change. For example, the intensities of FLO(4/6) and FLA(4/6) are different by about ten times at 2.4eV, while they are almost the same at 4.6eV.

### Analysis

In order to understand the observed phenomena, we calculated the Raman intensity by using the bond-Raman-polarizability model. The eigenvector of each phonon mode was determined as a previous step in this calculation. The displacement of each atomic plane is calculated in a one-dimensional model, described by the equations of motion,

$$M_j \frac{d^2 u_j^n}{dt^2} = \sum_{r,s} D_{j,j+s}^r u_{j+s}^{n+r} \quad (1)$$

Here,  $D_{j,j+s}^r$  stands for the interplanar force,  $M$  the mass of each atom,  $u$  the displacement of each atomic plane,  $n$  the label of unit cells, and  $j$  the label of atomic plane in the unit cell.  $r$  equals 0,  $\pm 1$  corresponding to the neighboring unit cells and  $s$  equals 0,  $\pm 1$ ,  $\pm 2$ ,  $\pm 3$  corresponding to the interplanar force up to the third neighbor.

In this calculation, we considered the force constants up to third neighbor interactions by taking into account the stacking dependence of force-field. The nearest neighbor force constants were distinguished into hexagonal, cubic and inter-bilayer environments. The second neighbor interactions

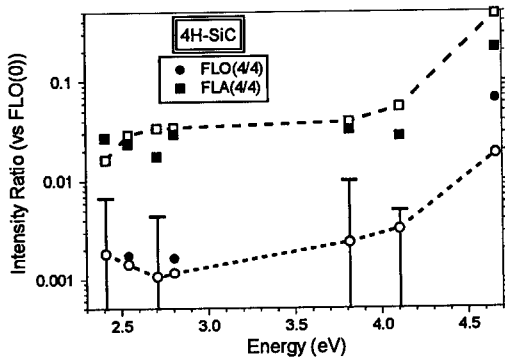


Fig. 3: Excitation energy dependence of the relative intensity of the folded longitudinal phonon modes for 4H-SiC. Filled symbols correspond to experimental data and open symbols with broken lines correspond to calculated results.

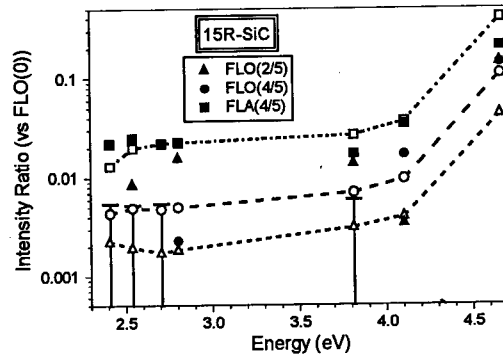


Fig. 4: Excitation energy dependence of the relative intensity of the folded longitudinal phonon modes for 15R-SiC. Filled symbols correspond to experimental data and open symbols with broken lines correspond to calculated results.

have only two variations, that is silicon-silicon and carbon-carbon interactions. As the third neighbor interactions, we assume three force constants depending on the stacking sequence. The same set of parameters was used to reproduce the energies of all the observed phonon modes in three polytypes, simultaneously. The calculated energies of folded longitudinal phonon modes reproduces the experimental ones within 1 percent.

The Raman polarizability of the  $\lambda$ -th folded longitudinal phonon mode can be expressed as,

$$\alpha^{(\lambda)} = \sum_j d_j \{ u^{(\lambda)}(j) - u^{(\lambda)}(j+1) \} \quad (2)$$

using the calculated displacement of each atom obtained from eq. (1). Here,  $d_j$  is the bond-Raman-polarizability. We supposed that the bond-Raman-polarizability has different values for different stacking orders as shown in eq. (3):

$$d_j = \begin{cases} e_h & \text{: (hexagonal stacking)} \\ e_c & \text{: (cubic stacking)} \\ a & \text{: (inter bilayers)} \end{cases} \quad (3)$$

It is obvious that these bond-Raman-polarizabilities are not constant, but depend on excitation energy. In addition, we assume different excitation energy dependence for the three bond-Raman-polarizabilities given in eq. (3).

The scattering intensity of the  $\lambda$ -th folded phonon mode ( $W^{(\lambda)}$ ) can be obtained from,

$$W^{(\lambda)} = S \frac{n(\omega^{(\lambda)}) + 1}{\omega^{(\lambda)}} |\alpha^{(\lambda)}|^2, \quad (4)$$

where,  $n(\omega^{(\lambda)})$  is Bose factor and  $S$  is a constant independent of  $\omega$  [3].

The values of bond-Raman-polarizability ( $e_c$ ,  $e_h$ ,  $a$ ) were adjusted to fit the experimental data for each excitation energy. It should be noted that the values of bond-Raman-polarizability and force constants can be commonly used for three polytypes.

The calculated intensities of the folded longitudinal phonon modes relative to the FLO(0) mode are shown in Fig. 2, Fig. 3, and Fig. 4 by open symbols with broken lines. As can be seen, the calculated intensities reproduces well the experimental data except the FLO(2/5) mode in 15R-SiC.

The ratios of bond-Raman-polarizabilities thus determined for various energies are shown in Fig. 5. From this figure, it is seen that the values of  $e_c$  and  $e_h$  are enhanced in ultraviolet region, relative to  $a$ . Going toward the direct band gap energy at the  $\Gamma$  point, which lies around 5eV in various SiC polytypes,  $e_c$  and  $e_h$  increase [4]. Furthermore, the difference between  $e_c$  and  $e_h$  also becomes larger in ultraviolet region. The intensities of folded longitudinal phonon mode relative to the FLO(0) mode are not sensitive to the magnitude of  $e_c$  and  $e_h$ , but to the difference between them.

The difference of resonance energies between  $e_c$  and  $e_h$  is supposed to be small, because only third neighbor arrangement differs between these two bonds. However, the difference of  $e_c$  and  $e_h$  is enhanced near the resonance conditions, because of the large excitation energy dependence of  $e_c$  and  $e_h$ .

## Conclusion

Selective enhancement in the relative Raman intensities of the folded longitudinal phonon modes was found under ultraviolet excitation. The excitation energy dependence of the intensities of folded longitudinal phonon modes relative to FLO(0) mode are successfully reproduced by using a bond-Raman-polarizability model by supposing different excitation energy dependence for three bond-Raman-polarizabilities. The calculation shows that the Raman intensities of the folded longitudinal phonon modes are dominated by the difference between  $e_c$  and  $e_h$ .

## References

- [1] A. K. Sood, J. Menéndez, M. Cardona, and K. Ploog, Phys. Rev. Lett. **54** (1985), p. 2111.
- [2] S. Nakashima and H. Harima, Phys. Status Solidi A **162** (1997), p. 39.
- [3] S. Nakashima and K. Tahara, Phys. Rev. B **40** (1989), p. 6345.
- [4] G. Wellenhofer and U. Rössler, Phys. Status Solidi. B **202** (1997), p. 107.

The corresponding author: T. Tomita

e-mail: tomita@wagner.issp.u-tokyo.ac.jp, Fax: +81-471-35-8105

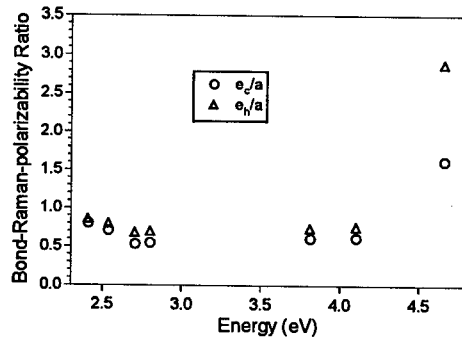


Fig. 5: Excitation energy dependence of the ratios of bond-Raman-polarizabilities,  $e_c/a$  and  $e_h/a$ .

## Raman Spectral Profiles of Folded Longitudinal Modes in SiC under Off-resonant Condition

S. Nakashima<sup>1,2</sup>, H. Harima<sup>2</sup>, T. Tomita<sup>3</sup> and T. Suemoto<sup>3</sup>

<sup>1</sup>Department of Electrical and Electronic Engineering, Miyazaki University,  
1-1 Gakuen-Kibanadai-nishi, Miyazaki, 889-2192, Japan

<sup>2</sup>Department of Applied Physics, Osaka University,  
Yamadagaoka 2-1, Suita, Osaka 565-0871, Japan

<sup>3</sup>Institute for Solid State Physics, University of Tokyo,  
5-1-5 Kashiwanoha, Kashiwa, Chiba, 277-8581, Japan

**Keywords:** Bond Polarizability Model, Folded Longitudinal Phonon Modes, Intensity Profiles, Raman Scattering

**Abstract :** Raman intensity profiles of folded longitudinal optic and acoustic modes in SiC polytypes have been examined under off resonant condition. The Raman bands for the folded longitudinal modes are weak except for the modes corresponding to phonon modes at the  $\Gamma$  point in the 3C polytype. The spectral features of these modes are interpreted based on the bond Raman polarizability model taking into account the stacking dependence of the bond Raman polarizability.

### Introduction

It is well known that long period SiC polytypes show a number of Raman lines which arise from the zone folding of the phonon dispersion in the basic polytype (3C polytype) [1]. Raman intensity profiles of  $\alpha$ -SiC have been well examined for folded transverse optic and acoustic modes which propagate along the  $c$  direction [1, 2]. However, only a few studies have so far been made on the spectra of the folded longitudinal modes [3], because their intensities are very weak except for a mode corresponding to the  $\Gamma$  point in the basic polytype,  $\text{LO}(\Gamma)$ , and quantitative analysis is difficult. Furthermore, the role of the long range polarization field associated with longitudinal vibrational modes in polar SiC crystals has not fully been understood.

In this work we have studied Raman intensity profiles of folded longitudinal optic and acoustic (FLO and FLA) modes in several polytypes under the off-resonant condition. One of the aims of this work is to provide the theoretical basis for the resonant Raman effect of the FLO modes which has recently been found [4]. The Raman spectra of the FLA and FLO modes are calculated based on a bond Raman polarizability model and a one-dimensional lattice dynamics model. The calculated Raman intensity profiles are compared with the experimental profiles.

### Raman intensity profiles of folded longitudinal modes

In the calculation of the Raman intensity profiles of the FLO and FLA modes, we take into account the stacking dependence of the bond Raman polarizability: The bond Raman polarizability is assumed to be different for the bonds in cubic and hexagonal environments as shown in Fig.1.

The Raman intensity of the  $\lambda$ -th mode is given by

$$W_{\lambda} = S [n(\omega) + 1] \omega^{-1} \sum [\mathbf{e}_i \cdot \alpha'(\lambda) \cdot \mathbf{e}_s]^2, \quad (1)$$

where  $S$  is a constant of proportionality,  $\omega$  is the frequency of the phonon mode,  $n(\omega)$  is the Bose factor and  $\mathbf{e}_i$  and  $\mathbf{e}_s$  are the polarization vector of the incident and scattered light, respectively. The Raman polarizability  $\alpha'(\lambda)$  consists of the bond Raman polarizabilities.

The bonds in  $\alpha$ -SiC are divided into three groups[2]: two groups of bonds inclined against the  $c$ -axis and a group of a bond parallel to the  $c$ -axis. The bond Raman polarizability tensors of the FLO and FLA modes are assumed to have the same sign and magnitude for the two inclined bond groups regardless of the environment. Furthermore, we assume that for the parallel bonds the bond Raman polarizability,  $e(j)$ , depends on the stacking as shown in Fig.(1)

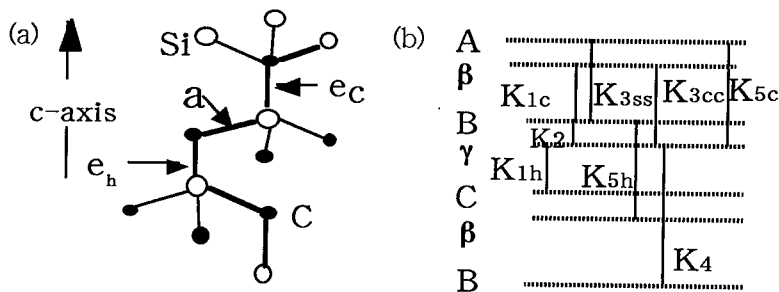


Fig.1(a) Bond Raman polarizabilities and (b) force constants for hexagonal and cubic stackings

For the Raman intensity of FTA and FTO modes, the contribution from the bonds inclined to the  $c$ -axis is dominant and a stacking independent bond polarizability model gives a good agreement between the experimental and calculated results [2]. On the other hand, the bond parallel to the  $c$ -axis plays a dominant role in the Raman intensity of the FLO and FLA phonons, because the bond stretching occurs dominantly for this bond. Under this assumption, the Raman polarizability of the  $\lambda$ -th FLO and FLA modes is reduced to the following form

$$\alpha_{pp}(\lambda) = a \sum [A_{\lambda}^a(z_i) - A_{\lambda}^a(z_{i+1})] + \sum e(j) [A_{\lambda}^c(z_j) - A_{\lambda}^c(z_{j+1})], \quad (2)$$

where we put  $e(j) = e_c$  for the cubic environment, and  $e(j) = e_h$  for the hexagonal environment. Here we assume that the bond Raman polarizability for the inclined bonds does not depend on the environment.  $A^c(z_i) - A^c(z_{i+1})$  is the relative displacement of the atomic planes connected by bonds parallel to the  $c$  axis (parallel bond). The summation is taken over a unit cell. When  $e(j)$  differs for cubic and hexagonal environments, the second term gives a nonzero value, although it is



small.

In the Raman intensity calculation, displacements of the atomic planes must be determined. They are obtained from a lattice dynamics model in which short range force-fields up to third neighbor forces, and a stacking dependence of the force field are taken into consideration for  $K_1$  and  $K_5$ . The displacement amplitudes of the atomic planes are obtained as solutions of the equation of motion,

$$M_j \omega^2 u(n, j) = \sum_{r,s} D_{j,j+s}^r u(n+r, j+s) \quad (3)$$

where  $u(n, j)$  and  $M_j$  are the displacement and mass of the  $j$ -th rigid plane in the  $n$ -th unit cell, respectively and  $D_{j,j+s}^r$  is the interplanar force constant.

The frequency of the folded phonon modes are determined from the secular equation,

$$|M_j \omega^2 \delta_{ij} - D_{ij}(q)| = 0, \quad (4)$$

where

$$D_{ij} = \sum_l D_{ij}^l \exp(-iqz_n). \quad (5)$$

The Si-C bond chain and the force parameters for cubic and hexagonal stackings are shown in Fig. 1. The 6H polytype contains two hexagonal and four cubic stackings in the unit cell. The interplanar forces are taken into account up to the third neighbor plane.

## Results and discussion

Raman spectra were measured at room temperature using the 488 nm line of an Ar laser. The phonon Raman spectra show no remarkable resonance enhancement for the laser light with wavelengths from 456.5 to 514.5 nm. A quasi-back scattering geometry was employed with the (0001) face. For this configuration the phonon modes propagating along the  $c$  direction are observed. The scattered light was dispersed by a monochromator and detected by a cooled CCD (charge coupled device) detector. We chose samples with the carrier concentrations less than  $5 \times 10^{16} \text{ cm}^{-3}$ , because the peak intensity of the LO phonons decreases with increasing carrier concentration.

Figure 2 shows the Raman profiles of FLA and FLO modes in 15R and 6H polytypes. The Raman intensity of these modes relative to that of the  $\text{LO}(\Gamma)$  mode is very weak, being  $10^{-2} \sim 10^{-3}$ . The dispersion curves of the longitudinal modes in the 3C polytype were deduced from the frequencies of FLO and FLA modes in various polytypes [1]. The force constants have been determined so that the calculated phonon dispersions for the 3C polytype, the splitting of the FLA modes and also Raman intensity profile fit the experimental results.

Table I Force constant parameters and bond Raman polarizabilities

$K_{1c}$	$K_{1h}$	$K_2$	$K_{3cc}$	$K_{3ss}$	$K_4$	$K_{5c}$	$K_{5h} (10^4 \text{ dyn/cm})$	$e_c/a$	$e_h/a$
14.8	14.2	32	-2.0	11	0.25	-0.9	0.35	0.6	0.75

The force constant parameters and bond Raman polarizabilities thus determined are listed in Table 1. The calculated Raman intensities are shown by horizontal arrows in Fig.2. The calculated Raman intensities normalized to the LO( $\Gamma$ ) mode intensity are comparable to the experimental values, though the relative intensity of the two components in the doublet is not well reproduced.

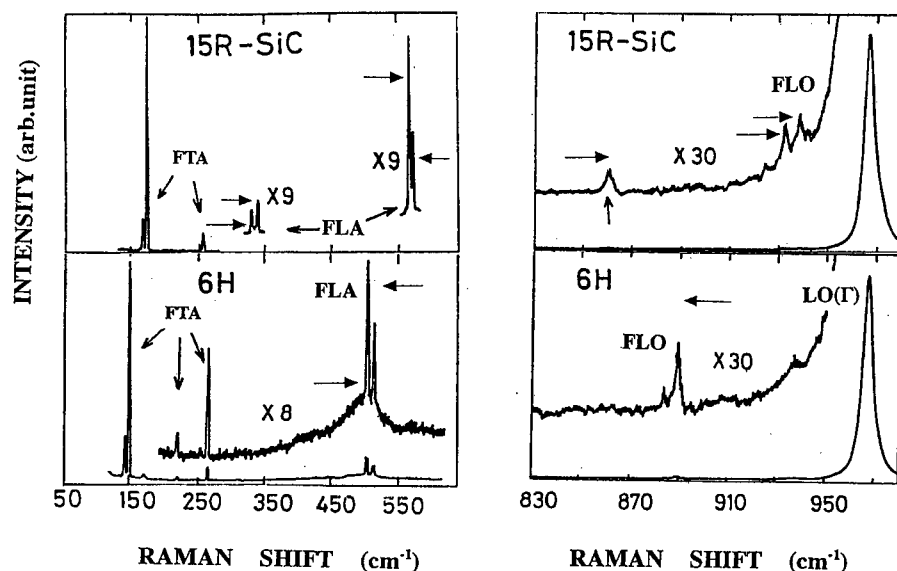


Fig.2 Raman spectra of the folded longitudinal acoustic and optic modes of 15R and 6H SiC. The horizontal arrows indicate the values of the calculated intensity.

This agreement indicates that our treatment of the Raman intensity based on the bond Raman polarizability model is valid for the longitudinal modes as well as the transverse modes in SiC polytypes.

The results of the calculation for the Raman intensity profiles reveal that the difference in the bond Raman polarizability as well as the force field should be taken into account to explain the observed Raman intensity profiles of the longitudinal folded modes in SiC polytypes.

## References

- [1] S.Nakashima and H.Harima, *phys.stat.sol.(a)* **162** (1997) 39
- [2] S.Nakashima and K.Tahara, *Phys.Rev.B* **40** (1989) 6339
- [3] S.Nakashima, *Elementally Excitations in Solids*, ed. by J.L.Birman, C.Seбенne and R.F.Wallis (North-Holland, Amsterdam, 1992) p169
- [4] T.Tomita, T.Suemoto and S.Nakashima, to be presented at ICSCRM'99, p. 587

The corresponding author : S.Nakashima,

email: nakashim@pem.miyazaki-u.ac.jp Fax: 81-985-58-2876

## Raman Spectroscopy on Biaxially Strained Epitaxial Layers of 3C-SiC on Si

S. Rohmfeld<sup>1</sup>, M. Hundhausen<sup>1</sup>, L. Ley<sup>1</sup>, C.A. Zorman<sup>2</sup> and M. Mehregany<sup>2</sup>

<sup>1</sup>Institut für Technische Physik, Universität Erlangen-Nürnberg,  
Erwin-Rommel-Str. 1, DE-91058 Erlangen, Germany

<sup>2</sup>Department of Electrical Engineering and Computer Science, Case Western Reserve University,  
Cleveland, OH 44106, USA

**Keywords:** APCVD, Biaxial Strain, Raman Spectroscopy, Residual Stress

**Abstract:** We measured Raman spectra of free-standing polycrystalline films of 3C-SiC as a function of the tunable biaxial strain in micromachined diaphragms. The results are used to determine the Raman stress coefficients  $\eta_S^{TO,LO}$  for uniaxial stress along the [100]-axis. From the stress induced shifts of TO- and LO-phonon frequencies the residual strain in 3C-SiC layers on Si(100) are determined as a function of the layer thicknesses. Largest tensile stress is found in thin films; it relaxes for thicker films to a value imposed by the different thermal expansion coefficients of SiC and Si. Accompanying the strain relaxation we observe a narrowing of the Raman lines that indicate an improved crystalline quality.

## 1 Introduction

One important application of SiC is the fabrication of pressure sensors that can operate at high temperature and/or in chemically aggressive environments. For that purpose the chemical vapor deposition (CVD) technique has been used to grow 3C-SiC epilayers on silicon wafers of large area [1]. Due to the lattice mismatch between 3C-SiC and Si (about 20%) and differences in thermal expansion coefficients these epilayers show in-plane tensile strain that might cause problems in further processing steps. It is important to have an convenient and fast method to measure the residual strain, preferably in a spatially resolved way.

Phonon Raman spectroscopy is useful for that purpose because the phonon frequencies depend among other things on stress. Raman spectroscopy has been successfully applied to measure stress in bulk semiconductors under hydrostatic pressure and uniaxial stress [2]. For 3C-SiC, however, only measurements under hydrostatic pressure have been reported [3, 4]. Due to the lack of uniaxial/biaxial stress measurements several groups tried to estimate stress in SiC quantitatively by using the known hydrostatic stress coefficients [5, 6]. That attempt is bound to yield erroneous results. This paper is intended to provide the Raman stress coefficient that is needed to allow a quantization of biaxial stress.

## 2 Theoretical treatment

In order to analyze biaxial stress with Raman spectroscopy the relationship between phonon frequencies and stress is required. It was shown by Feng *et al.* [6] that a general stress configuration can be regarded as a superposition of hydrostatic and uniaxial stress components  $X$  and  $P$ , respectively. For the biaxial stress configuration that we deal with here,  $P$  is along the direction perpendicular to the surface and opposite to the hydrostatic stress component

( $P = -X$ ), since the epitaxial layer can relax in that direction. The frequency shifts of TO and LO phonons ( $\Omega^{\text{TO}}$  and  $\Omega^{\text{LO}}$ ) under in-plane biaxial stress  $X$  in 3C-SiC are then described by

$$\Omega^{\text{TO}} - \Omega_0^{\text{TO}} = - \left( 2\eta_{\text{H}}^{\text{TO}} - \frac{1}{3}\eta_{\text{S}}^{\text{TO}} \right) \cdot X, \quad (1)$$

$$\Omega^{\text{LO}} - \Omega_0^{\text{LO}} = - \left( 2\eta_{\text{H}}^{\text{LO}} + \frac{2}{3}\eta_{\text{S}}^{\text{LO}} \right) \cdot X, \quad (2)$$

where  $\Omega_0^{\text{TO,LO}}$  are the corresponding phonon frequencies without stress given in  $\text{cm}^{-1}$ . The Raman stress coefficients  $\eta_{\text{H}}$  and  $\eta_{\text{S}}$  for hydrostatic and uniaxial strain components, respectively, can be written as functions of the phonon deformation potentials  $p$  and  $q$  [2] and the elastic compliance constants ( $S_{11}$  and  $S_{12}$ )

$$\eta_{\text{H}}^{\text{TO,LO}} = - \frac{(p^{\text{TO,LO}} + 2q^{\text{TO,LO}})(S_{11} + 2S_{12})}{6(\omega_0^{\text{TO,LO}})^2} \cdot \Omega_0^{\text{TO,LO}}, \quad (3)$$

$$\eta_{\text{S}}^{\text{TO,LO}} = \frac{(p^{\text{TO,LO}} - q^{\text{TO,LO}})(S_{11} - S_{12})}{2(\omega_0^{\text{TO,LO}})^2} \cdot \Omega_0^{\text{TO,LO}}. \quad (4)$$

Here,  $\omega_0^{\text{TO,LO}}$  is the phonon frequency in units of  $\text{s}^{-1}$ . It is important to distinguish the phonon deformation potentials for TO and LO modes [7] in order to account for the large stress dependence of the TO-LO splitting of 3C-SiC [3]. Note, that this distinction has not been considered in Ref. [6]. From Hooke's law the in-plane biaxial strain is obtained by  $\varepsilon_{\parallel} = \Delta a_{\parallel}/a_0 = (S_{11} + S_{12}) \cdot X$ . Only the hydrostatic stress coefficients  $\eta_{\text{H}}^{\text{TO,LO}}$  have been determined experimentally in the past [3, 4], but  $\eta_{\text{S}}^{\text{TO,LO}}$  needs also to be known, in order to obtain accurate information about biaxial in-plane stress from Raman measurements.

### 3 Experimental details

The 3C-SiC layers studied here were grown on Si(100) substrates by CVD at a temperature of 1280°C [1]. Silane (5 % in hydrogen) and propane (15 % in hydrogen) mixed with hydrogen as carrier gas with a flow rate of 25 slm (standard liter per minute) were used as source gases. The flow rate of the silane and propane precursor gas was 100 sccm and 25 sccm (standard cubic centimeter per minute), respectively. A square-shaped window of  $1 \times 1 \text{ mm}^2$  size was etched into the silicon substrate in order to manufacture a free-standing SiC film. The window was stressed by applying a differential nitrogen pressure across the membrane and thus stretching it in a controlled fashion. The deformation was measured interferometrically and from that the corresponding biaxial in-plane strain  $\Delta a_{\parallel}/a_0$  was calculated. Raman spectra were recorded in backscattering geometry with an argon-ion laser operating at 514.5 nm and a spot size of  $\approx 1 \mu\text{m}$ .

### 4 Results and Discussion

Two membranes with different thicknesses  $d$  (Membrane 1:  $1.5 \mu\text{m}$ , Membrane 2:  $1.8 \mu\text{m}$ ) were investigated. Raman spectra of the TO and LO modes were recorded as a function of differential nitrogen pressure and the peak positions obtained from these spectra are plotted as function of the biaxial in-plane strain  $\Delta a_{\parallel}/a_0$  in Fig. 1. A linear decrease of the phonon frequency with increasing strain is observed for both modes.

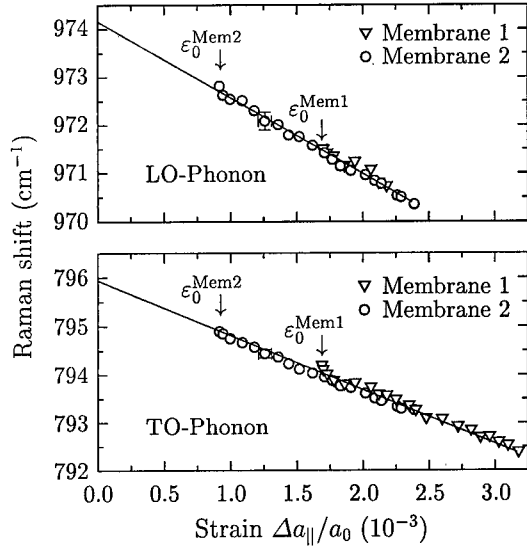


**Fig. 1.** Raman shift of the TO and LO mode as function of the biaxial strain ( $\Delta a_{||}/a_0$ ) for two membranes with different thickness. Note the existence of a residual strain even without applied pressure that is marked as  $\varepsilon_0^{\text{Mem1}}$  and  $\varepsilon_0^{\text{Mem2}}$ , respectively. The solid lines are least-square fits to the experimental data.

The linear regression shown as lines demonstrates that the strain dependence of TO and LO modes can be well described by

$$\frac{\Omega^{\text{TO}}}{\text{cm}^{-1}} = (795.9 \pm 0.1) - (1125 \pm 20) \cdot \frac{\Delta a_{||}}{a_0}, \quad (5)$$

$$\frac{\Omega^{\text{LO}}}{\text{cm}^{-1}} = (974.1 \pm 0.1) - (1585 \pm 32) \cdot \frac{\Delta a_{||}}{a_0}. \quad (6)$$

Note, that both membranes show the same strain dependence, although the residual strain ( $\varepsilon_0$ ) without deformation of the membrane as marked by arrows greatly differs for the two samples. We shall return to this point below.

With the elastic compliance constants from Ref. [8] ( $S_{11} = 3.67 \times 10^{-3}/\text{GPa}$ ,  $S_{12} = -1.05 \times 10^{-3}/\text{GPa}$ ) and the hydrostatic Raman stress coefficients calculated from Ref. [4] we obtain the uniaxial Raman stress coefficients  $\eta_s$  in (100)-direction from Eqs. (1) and (2). The results together with the values of the hydrostatic stress coefficients are given in the following table:

	TO	LO
$\eta_H (\text{cm}^{-1}/\text{GPa})$	1.38	1.64
$\eta_s (\text{cm}^{-1}/\text{GPa})$	$-0.56 \pm 0.16$	$1.31 \pm 0.13$

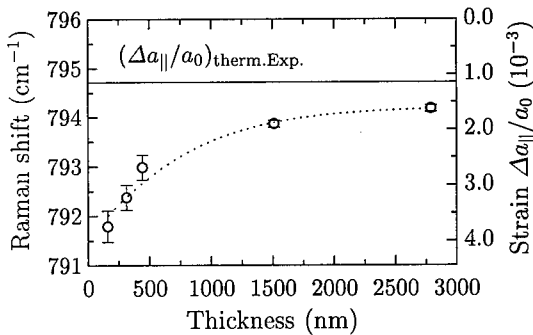


**Fig. 2.** Raman shift of the TO mode (left scale) and biaxial strain (right scale) vs film thickness. The strain was calculated with Eq. (1). The solid line marks the residual strain expected on account of the different thermal expansion coefficients of SiC and Si. The dotted line is a visual guide.

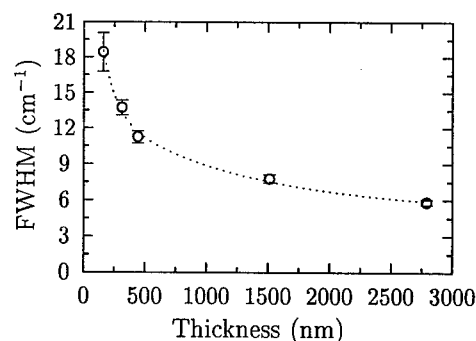


Fig. 3. Linewidth of the TO mode as a function of the film thickness. The dotted line through the experimental data is a visual guide.

to the effect of misfit dislocations parallel to the film-substrate interface [9]. Also, stacking faults and microcracks created at the SiC/Si interface have been reported to reduce the initial strain that exists after the nucleation of epitaxial SiC on Si [5]. If these arguments are correct, the crystalline quality is expected to improve with film thickness. Indeed, that expectation is supported by a linewidth analysis of the Raman spectra (see Fig. 3). The linewidth decreases from about  $18 \text{ cm}^{-1}$  for the thinnest films to about  $6 \text{ cm}^{-1}$  at  $3 \mu\text{m}$ .

## 5 Conclusion

We have measured Raman spectra of TO- and LO-phonon lines of 3C-SiC layers on Si. Using a pressure sensor made from these films we could tune the biaxial strain by applying a differential nitrogen pressure. We measure the influence of that strain on the phonon line positions and derive the Raman stress coefficients  $\eta_S^{\text{TO}}$  and  $\eta_S^{\text{LO}}$  for uniaxial strain in the (100)-direction. With these coefficients the strain in heteroepitaxial 3C-SiC layers was determined from the Raman spectra as a function of thickness. We observe large strain in thin films and a strong strain relaxation with increasing film thickness.

## Acknowledgments

This work was supported by the Deutsche Forschungsgemeinschaft under SFB 292.

## References

- [1] C. A. Zorman, A. J. Fleischman, A. S. Dewa, M. Mehregany, C. Jacob, S. Nishino, and P. Pirouz, *J. Appl. Phys.* **78** (1995), p. 5136.
- [2] F. Cerdeira, C. J. Buchenauer, F. H. Pollak, and M. Cardona, *Phys. Rev. B* **5** (1972), p. 580.
- [3] D. Olego, M. Cardona, and P. Vogl, *Phys. Rev. B* **25** (1982), p. 3878.
- [4] A. Debernardi, C. Ulrich, K. Syassen, and M. Cardona, *Phys. Rev. B* **59** (1999), p. 6774.
- [5] S. Vepřek, T. Kunstmann, D. Volm, and B. Meyer, *J. Vac. Sci. Technol. A* **15** (1997), p. 10.
- [6] Z. C. Feng, W. J. Choyke, and J. A. Powell, *J. Appl. Phys.* **64** (1988), p. 6827.
- [7] H. Harima, S. Nakashima, J. M. Carulli, C. P. Beetz, Jr., and W. S. Yoo, *Jpn. J. Appl. Phys.* **36** (1997), p. 5525.
- [8] K. B. Tolpygo, *Sov. Phys.-Solid State* **2** (1960), p. 2367.
- [9] J. Hofmann, S. Vepřek, and J. Heindl, *J. Appl. Phys.* **85** (1999), p. 2652.

## Characterization of 3C-SiC/SOI Deposited with HMDS

N. Planes<sup>1</sup>, P. Aboughé-Nzé<sup>2</sup>, M. Ravetz<sup>3</sup>, S. Contreras<sup>1</sup>, P. Vicente<sup>1</sup>,  
T. Chassagne<sup>2</sup>, B. Fraisse<sup>4</sup>, J. Camassel<sup>1</sup>, Y. Monteil<sup>2</sup> and S. Rushworth<sup>3</sup>

<sup>1</sup> Groupe d'Etude des Semiconducteurs, cc074, Université Montpellier 2,  
FR-34095 Montpellier Cedex 5, France

<sup>2</sup> Laboratoire des Multimatériaux et Interfaces, UCB-Lyon 1, 43, Boulevard du 11 Novembre 1918,  
FR-69622 Villeurbanne Cedex, France

<sup>3</sup> Epichem Ltd, Power Road, Bromborough, Wirral, Merseyside L62 3QF, UK

<sup>4</sup> Laboratoire des Agrégats Moléculaires et des Matériaux Inorganiques, Université Montpellier 2,  
cc0004, FR-34095 Montpellier Cedex 5, France

**Keywords:** Cubic SiC, HMDS, SOI Substrates

### Abstract :

We report on 3C-SiC deposited on <100> Si and SOI wafers using hexamethyldisilane (HMDS) as unique precursor gas. The growth temperature was 1350°C and the layer thicknesses ~ 4 µm. The layer properties were systematically checked using AFM, IR reflectivity, DDX, Low-Temperature Photoluminescence and micro-Raman spectroscopy. We compared with 3C-SiC films grown under the same conditions, using standard precursors.

### Introduction

Since the early work of Nishino et al. [1] at NASA in 1983, the hetero-epitaxial growth of cubic (3C or β) SiC on Si using a high temperature (1360°C) carbonization step and a two gas (silane and propane) precursor system has become a well documented subject [2]. However, despite impressive success, there are two main drawbacks which affect this popular material system. One is safety and, with this respect, silane which is a very flammable and toxic gas should be avoided. The other one is the constant need to grow at elevated temperature. In the case of micromachining applications where the intrinsic mechanical properties of the bulk Si substrate play a major role, this is not acceptable.

This is particularly true in the case of sensors designed to work at elevated temperature for automotive applications [3] and, in order to protect the bulk of the Si-wafer, the use of compliant substrates like SOI (Silicon On Insulator) has been proposed [4, 5]. The difficulty is that, during the high temperature (~1350°C) deposition step, either the Buried OXide (BOX) or the thin Silicon OverLayer (SOL) or both, may be severely damaged [6]. This degrades the sensors performance in an uncontrolled way and makes mass production hardly feasible. To reduce the temperature growth of 3C-SiC deposited by CVD, more and more organic compounds are being tested. Among them, HexaMethylDiSilane {(CH<sub>3</sub>)<sub>6</sub>Si<sub>2</sub> or HMDS} appears very appealing [7, 8].

The main goal of this work is to make a comparative investigation of the physical properties of 3C-SiC layers deposited on bulk Si and SOI substrates using HMDS at 1350°C and to compare with state of the art 3C-SiC grown using Standard Precursors (SPs) propane and silane.

### Growth procedure

The deposition experiments were carried out at atmospheric pressure in a vertical CVD reactor, using specially purified HMDS. The purification of the crude material was performed using a "freeze/pump/thaw" cycling procedure, followed by fractional distillation to obtain a product containing no permanent foreign gas by gas phase chromatography. The SiC layers were grown on exactly <100> oriented Si (55  $\Omega$ -cm) or Unibond® wafers. In the case of Unibond®, the SOL and BOX thicknesses were 200 nm.

The growth procedure is schematically drawn in Fig. 1 : step (1) results in a carbonization layer of (typically) 1 to 2 nm thickness; step (2) permits to lower the high temperature H<sub>2</sub> reduction effect and limits the in-situ attack of the SiC buffer layer [9]; step (3) is the growth step. It was done using HMDS diluted into H<sub>2</sub> (10 slm) with a flow rate of 0.6 sccm.

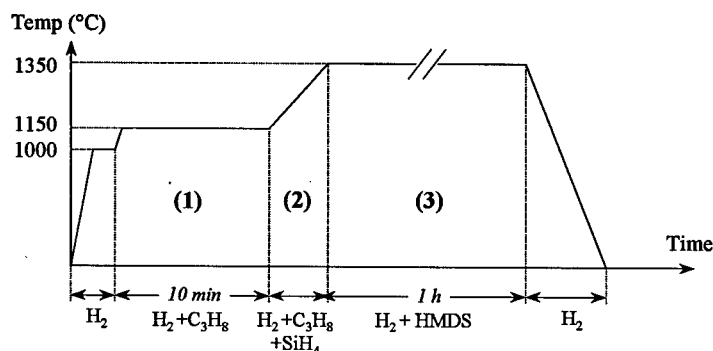


*Figure 1:* Schematic diagram of the SiC deposition process used in this work.

### Thin films characterization, results and discussion

All layers investigated had mirror-like surface and exhibited AFM roughness around 3 nm when measured on a 5x5  $\mu\text{m}^2$  template. This includes the large height difference frequently associated with antiphase domains. The Full Width at Half-Maximum (FWHM) of DDX rocking curves collected for the {200}-SiC reflection was  $\sim 650$  arcsec (0.18°). For comparison, we list in Table 1 a summary of literature data. Of course they depend on extrinsic factors like the growth rate or the layer thickness which vary from authors to authors but, given a temperature window, we believe that they are more or less representative of state of the art 3C-SiC/Si deposited using HMDS [8] and SP [11, 12].

To compute the growth rate, we have collected IR reflectivity spectra in the range 400-7500  $\text{cm}^{-1}$  and, from oscillator fits, we have deduced values of the film thickness and optical roughness at the SiC surface and SiC/Si interface [10]. Our typical growth rate using HMDS was 4.4  $\mu\text{m}/\text{h}$ , to be compared with 3.3  $\mu\text{m}/\text{h}$  using the SPs propane and silane. In good agreement with AFM data, the "optical" surface roughness was low. The interface roughness was 150-200 nm, slightly higher than the value ( $\sim 100$  nm) obtained when using SPs at the same temperature. This may come from the higher growth rate achieved with HMDS.

Growth temperature (°C)	Precursor gas	<200>-SiC FWHM (°)	Layer thickness ( $\mu\text{m}$ )	Growth rate ( $\mu\text{m}/\text{h}$ )	
1250-1300	SPs	0.18	5	1.5	Ref. [12]
1350	HMDS	0.6-0.9	1.2-9.1	4.3	Ref. [8]
1350	HMDS	0.18	4.4	4.4	this work
1360	SPs	$\sim 0.3$	2-3	2.4	Ref. [11]
1400	SPs	0.18	3.3	3.3	this work

*Table 1 :* DDX analysis of 3C-SiC layers grown on bulk Si substrates using two different precursors. All layers have been grown on <100>-oriented Si substrates.



To get information about the carrier concentration and mobility, we have performed Hall measurements at room temperature. Small (3000 Å thick) nickel dots were sputtered at the corners of  $5 \times 5 \mu\text{m}^2$  samples and annealing at  $500^\circ\text{C}$  during 10 mn. This gives for SiC/Si,  $\sim 5.5 \times 10^{17} \text{ cm}^{-3}$  and  $140 \text{ cm}^2/\text{V-s}$ , respectively. Obviously, this establishes the good purity of the starting material.

Because of improved strain relaxation, which is usually found in the bulk of the silicon substrate when using SOI rather than Si [13], we have also deposited on SOI. We have not found any (drastic) change in DDX rocking curves, but observed a lower density of residual carriers ( $3 \times 10^{17} \text{ cm}^{-3}$ ) and a 50% increase in mobility ( $210 \text{ cm}^2/\text{V-s}$ ). This suggests a reduction in growth defects. Because, usually, they originate from the interface and migrate into the bulk of the layer, this has been checked using micro-Raman spectroscopy. We focused on a cleaved edge of the sample in the transverse configuration  $\langle X(Y, -)\bar{X} \rangle$  where is sensitive to the TO frequencies [13] and moved from the SiC/Si interface towards the free SiC surface, on both the SiC/Si and SiC/SOI samples. In both cases a clear decrease in FWHM of the SiC-TO Raman mode is observed. This shows that the density of defects decreases rapidly from the interface and becomes very reasonable after  $\sim 1 \mu\text{m}$ . The interesting point is that, independent of the spot position with respect to the SiC/Si interface, we find a systematic narrowing when considering the sample deposited on SOI with respect to the one on bulk Si. This is shown in Fig. 2.

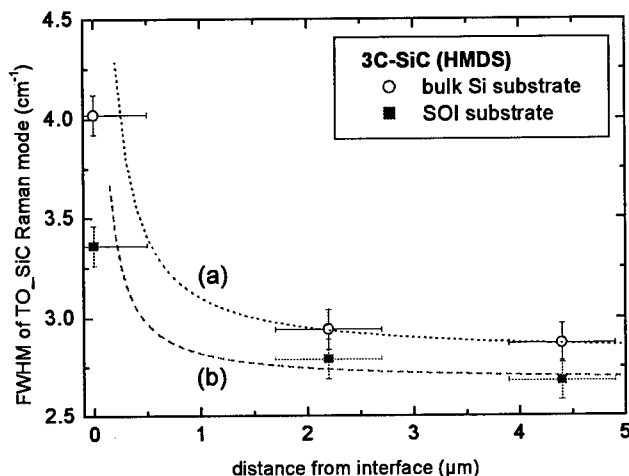


*Figure 2 : FWHM values extracted from Micro-Raman spectra collected on 3C-SiC films (transverse configuration) deposited on (a) Si bulk and (b) SOI substrates using HMDS as single precursor.*

Since they are very sensitive to all non-radiative centers, like defects in the SiC layer, we have investigated the LTPL (Low Temperature PhotoLuminescence) spectra of both materials. Results are shown in Fig. 3. The PL spectra are dominated by the N bound-exciton (N-BE) lines around 2.3 eV, and their second order phonons replicas around 2.15 eV. The no-phonon line (at 2.3779 eV for a stress-free film of 3C-SiC [14]) is not detected.

Comparing with the work of Ref. [8] (Fig. 3-a), the striking feature is less impurity related B0-line and corresponding phonon replicas. The G band, which is related to dislocations and interface defects, appears but with reasonably small intensity. The ratio of intensities of the weak G band and the strongest N-BE transverse-optical transition (TO) can be used as a figure of merit of crystalline perfection in 3C-SiC layers. Values of  $\sim 0.3$  are found. These values are lower than previously reported for similar thickness ( $5 \mu\text{m}$ ) SiC films [14]. This confirms a relatively good quality of our SiC layers grown with HMDS. We notice also a larger PL signal when deposited on SOI (Fig. 3-c) with respect to bulk (100)-Si (Fig. 3-b). This comes from the lower density of non-radiative (interface and/or bulk) recombination centers which have been formed in this case.

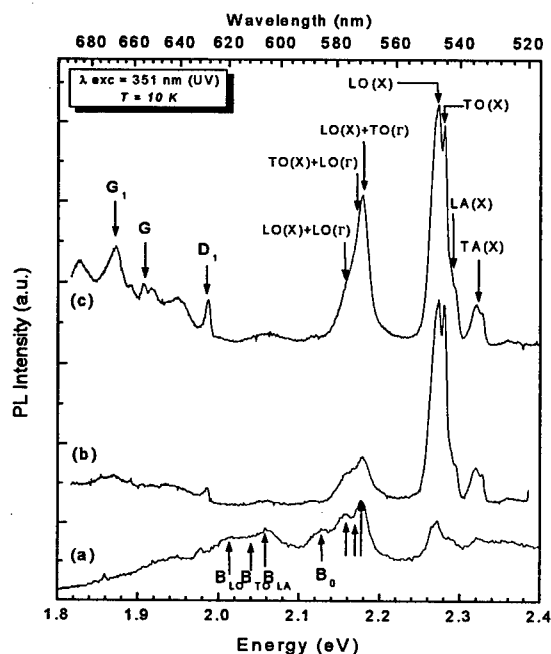


**Figure 3 :** LTPL spectra collected on 3C-SiC CVD films deposited on: (a): Si bulk (4.3  $\mu\text{m}$ , data extracted from ref. 8), (b): Si bulk (4.4  $\mu\text{m}$ , this work), (c): SOI (4.7  $\mu\text{m}$ , this work).

### Conclusion

We have used hexamethyldisilane as the single precursor gas for 3C-SiC deposition. We have shown that one can grow good quality material at 1350°C with a 4.4  $\mu\text{m}/\text{h}$  growth rate. We have obtained better results and less defects on SiC films deposited on SOI substrates than on Si bulk. A lower growth temperature is now expected to decrease the negative effect of high temperatures on SOI stability during the growth process.

### Acknowledgements

This work was supported in part by the EU commission under contract BRPR CT96 0261.

### References

- [1] S. Nishino, J.A. Powell and H.A. Will, Appl. Phys. Lett. 42 (1983), p. 460.
- [2] J. Stoemenos, C. Dezaudier, G. Arnaud, S. Contreras, J. Camassel, J. Pascual and J.L. Robert, Mat. Sci. Eng. B 29 (1995), p. 160
- [3] J.von Berg, R. Ziermann, W. Reichert, E. Obermeier, M. Eickhoff, G. Krötz, U. Thoma, Th. Boltshauser, C. Cavalloni and J.P. Nendza, Mater. Sci. Forum 264-268 (1998), p. 1101
- [4] A.J. Steckl, C. Yuan, Q.Y. Tong, U. Gösele, and M.J. Loboda, J. Electrochem. Soc. 141 (1994), p. L66
- [5] Q.-Y.Tong, U.Gösele, C.Yuan, A.J.Steckl et M.Reiche, J. Electrochem. Soc. 142 (1995), p. 232
- [6] J. Camassel, J. Vac. Sci. Technol. B 16 (1998), p. 1648
- [7] C.H. Wu, C. Jacob, X.J. Ning, S. Nishino and P. Pirouz, J. Crystal Growth 158 (1996), p. 480
- [8] Y. Chen, K. Matsumoto, Y. Nishio, T. Shirafuji and S. Nishino, J. Mat. Sci. Eng. B 61-62, p.579
- [9] G. Ferro, Y. Monteil, H. Vincent and V. Thevenot, J. Appl. Phys. 80 (1996), p. 4691
- [10] F.Namavar, P.C.Colter, N.Planes, B.Fraisse, J.Pernot, S.Juillaguet and J.Camassel, Mat. Sci. Eng. B 61-62 (1999), p. 571
- [11] S. Nishino, H. Suhara, H. Ono and H. Matsunami, J. Appl. Phys. 61 (1987), p. 4889
- [12] F.Wischmeyer, W.Wondrak, D.Leidich and E.Niemann, Mat. Sci. Eng. B 61-62 (1999), p.563
- [13] J.M.Bluet, L.A.Falkovsky, N.Planes and J.Camassel, Mater. Sci. Forum 264-268 (1998), p.395
- [14] W.J. Choyke, Z.C. Feng and J.A. Powell, J. Appl. Phys. 64 (1988), p. 3163

## Raman Imaging Characterization of Electric Properties of SiC Near a Micropipe

Hiroshi Harima<sup>1</sup>, Toru Hosoda<sup>1</sup> and Shin-ichi Nakashima<sup>2</sup>

<sup>1</sup>Department of Applied Physics, Osaka University,  
Yamadagaoka 2-1, Suita, Osaka 565-0871, Japan

<sup>2</sup>Department of Electrical and Electronic Engineering, Miyazaki University,  
1-1 Gakuenkibanadai-nishi, Miyazaki 889-2192, Japan

**Keywords:** Carrier Trapping, Coupled Mode, Defect, Micropipe, Raman Imaging

**Abstract.** Electrical and crystalline properties around micropipe defects have been studied in n-type 4H-SiC bulk crystals by using Raman imaging technique. We have observed clear decrease in carrier concentration and mobility in the vicinity of micropipe, indicating existence of carrier trapping centers. Experiments at high temperatures up to 1200°C showed that thermal excitation of carriers was negligibly small. This suggests that the trap levels are relatively deep.

### Introduction

It is generally considered that threading defect or micropipe will deteriorate electrical characteristics of SiC power devices such as the breakdown voltage. However, it is not well known how electrical and crystalline properties show anomalies in the vicinity of micropipe under high-voltage- or high-temperature operation. As a first step to answer this question, we have investigated here electrical and crystalline properties around micropipe defects in n-type 4H-SiC bulk crystals by using an imaging technique of Raman spectra. We have observed clear decrease in carrier concentration and mobility in the vicinity of micropipe, indicating existence of high density of carrier trapping centers. We have also discussed the depth of carrier trap levels from the high temperature characteristics up to 1200°C.

### Experimental Results and Discussion

In this study, we have tested some n-type 4H-SiC wafers with c-plane, grown by the modified-Lely method and both sides mechanically polished. The carrier concentration ranged in  $n=1-6 \times 10^{18} \text{ cm}^{-3}$  according to Hall measurements. Raman spectra were observed in backscattering geometry from the c-plane using the Ar<sup>+</sup> laser at 488 nm for excitation. The spectral slit width was about 0.6  $\text{cm}^{-1}$ . Local area around relatively thick micropipe was investigated by Raman microprobe imaging. Here we first describe a result for a sample with  $n=1.4 \times 10^{18} \text{ cm}^{-3}$ . **Figure 1** shows the probing method schematically: A micropipe has a cross section of an elongated elliptic hole of about  $20\mu\text{m} \times 7\mu\text{m}$  at the surface (dark spot in Fig.1). The laser beam was linearly expanded by a cylindrical lens to about  $400\mu\text{m} \times 10\mu\text{m}$  (dotted region), covering the cross section of the micropipe, and probed to a few tens of  $\mu\text{m}$  in depth. Scattered light from the illuminated region was collected to a double monochromator and the Raman signal was observed by a CCD detector. **Figure 2** shows the signal image for the E<sub>2</sub> (TO) phonon mode at  $\sim 776 \text{ cm}^{-1}$  (left side) and the axial LO phonon mode at  $\sim 964 \text{ cm}^{-1}$  (right side). Here, the vertical and horizontal axes correspond to the observed position and

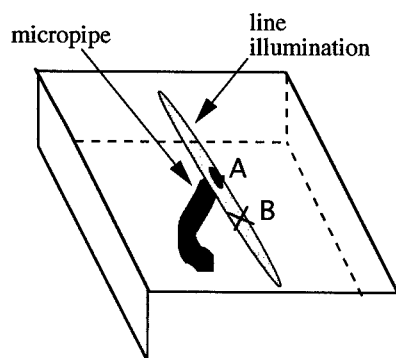
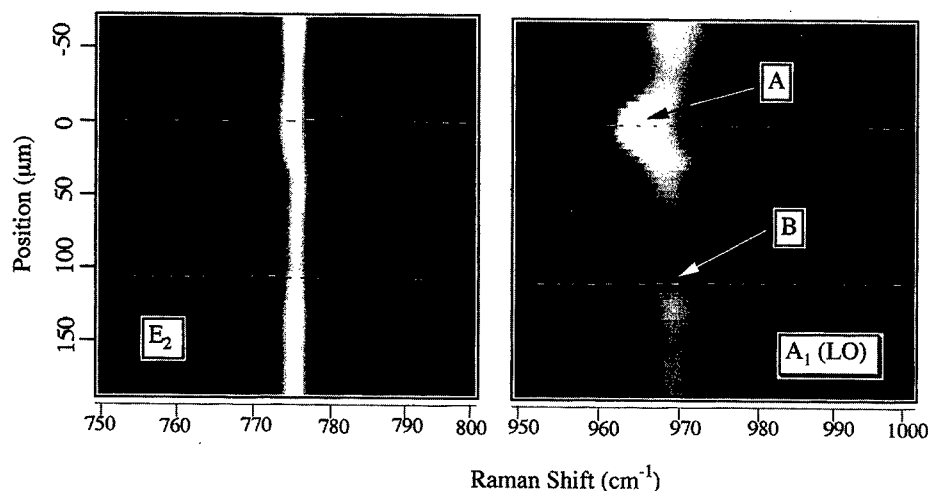


Fig.1 Probing scheme.

the Raman shift, respectively. The LO-phonon image (right) shows clearly that the Raman peak for point A (vicinity of micropipe) is located at lower frequency than for other positions such as the point B (marked by a cross in Fig.1, which is about  $100\text{ }\mu\text{m}$  away from the micropipe). This difference is more clearly recognized by comparing the spectra at each point as shown in Fig.3.

On the contrary, the  $E_2$ -phonon mode is sharp and uniformly peaked in the probed region as seen in Fig.2. This evidences that there is no observable anomaly in the crystallinity, such as mixture of different polytypes, inclination of crystal axes, and lattice distortion.[1] These observations imply that the carrier concentration is relatively low in the vicinity of the micropipe. This is because, as is well known,[2] the LO-

Fig.2 Raman image for the  $E_2$  phonon mode at  $\sim 776\text{ cm}^{-1}$  (left side) and axial LO phonon mode at  $\sim 964\text{ cm}^{-1}$  (right side)

phonon mode in n-type SiC strongly couples with the plasma oscillation of free carriers, and is broadened and shifted to higher frequency with the increase of carrier concentration as seen in Fig.4. We have evaluated the carrier concentration  $n$  as well as the carrier mobility  $\mu$  by a lineshape-fitting analysis [2] to the observed profiles as  $n=3.2 \times 10^{17}\text{ cm}^{-3}$  and  $\mu=20\text{ cm}^2/(\text{Vs})$  for point A, and  $n=1.3 \times 10^{18}\text{ cm}^{-3}$  and  $\mu=32\text{ cm}^2/(\text{Vs})$  for point B. The carrier concentration at B well agrees with that obtained from Hall measurement ( $1.4 \times 10^{18}\text{ cm}^{-3}$ ). It should be emphasized that the point A

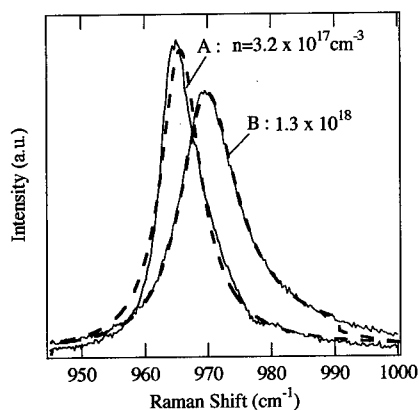


Fig. 3 LO-phonon spectra near the defect (A) and far from the defect (B). Solid and dashed lines give observed profiles and best-fit calculations, respectively.

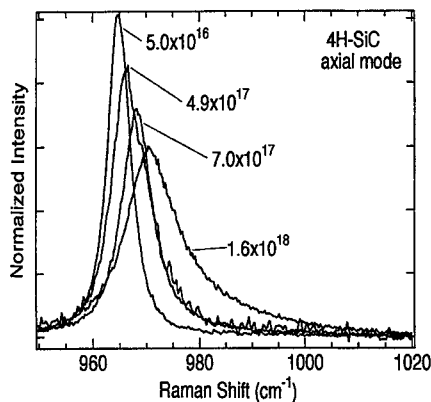


Fig.4 Variation of LO-phonon profile (axial mode) with the free-carrier concentration in 4H-SiC (from Ref.2).

gives slightly lower mobility than B, although the point A gives four times less carrier concentration than B. This fact suggests that there are high density of carrier trapping centers in the vicinity of the micropipe, which reduce the carrier concentration as well as the mobility. We observed similar results for most of the micropipe defects in the tested SiC samples. **Figure 5** shows a LO-phonon image (left) around a micropipe in a more heavily doped sample ( $n = 6 \times 10^{18} \text{ cm}^{-3}$  by Hall measurement) and its spectra (right) near the micropipe (A) and far from the micropipe (B). The local carrier density at A is estimated to be about 3 times smaller than that for B from the line-shape analysis.

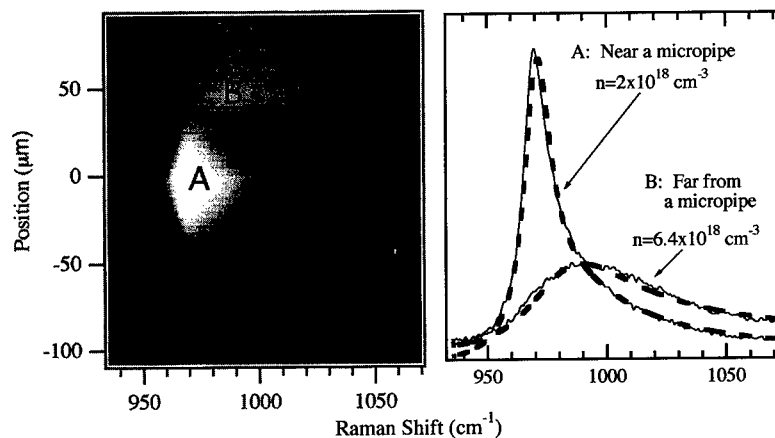


Fig. 5 Raman image (left) and spectra (right) for the LO phonon region in a heavily doped sample. The carrier densities were evaluated by the fitting analysis (thin solid lines are observed profiles).

If carriers trapped at micropipe defects are efficiently activated by thermal energy, the effect will appear clearly in high temperature region. From this viewpoint, we have heated the sample used in Fig.2 up to 1200°C and compared the LO-phonon-plasmon-coupled mode profile between the point A (near the micropipe) and B (far from micropipe). Figure 6 shows variation of

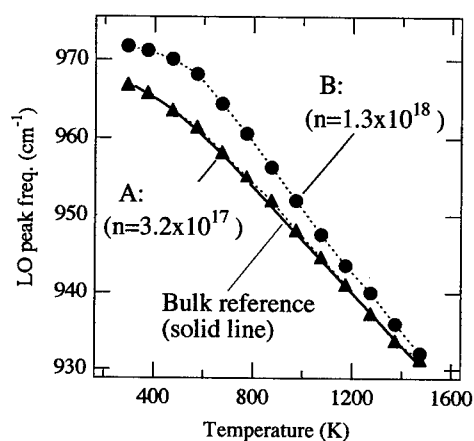


Fig. 6 Peak frequency of the LO-phonon-plasmon-coupled mode vs temperature. A and B (mark and dashed line) correspond to positions near and far from the micropipe defect, respectively. Results for a defect-free sample are shown for comparison (solid line).

the peak frequency with the temperature. Here, a result for a defect-free bulk sample with almost the same carrier concentration at room temperature as point A is also shown for comparison (solid line). All the results show frequency downshift at high temperatures because of lattice dilation as reported before.[3] This figure shows further that there is no difference between the point A and the defect-free sample, and that the point A always shows somewhat lower peak frequency than B. These results indicate that there is no efficient activation of carriers in the vicinity of micropipe or, in other words, the trapping level is relatively deep compared with the thermal energy.

### Summary

Characterization by Raman imaging in n-type SiC in the vicinity of micropipe clearly revealed the decrease in carrier concentration and mobility. This suggests existence of efficient carrier trapping centers around micropipe defects. Experiment up to 1200°C showed that thermal activation of carriers can be neglected, which means that the trapping levels are relatively deep.

**Acknowledgment** This work was partially supported by New Energy and Industrial Technology Development Organization (NEDO), Japan.

### References

- [1] S.Nakashima and H.Harima, *phys.stat.sol. (a)* **162** (1997) 39.
- [2] H.Harima, S.Nakashima and T.Uemura, *J.Appl.Phys.* **78** (1995) 1996.
- [3] H.Harima and S.Nakashima, *Materials Science Forum* **264-268** (1998) 449.

Corresponding author : Hiroshi HARIMA,

Tel: +81-6-6879-7855, Fax: +81-6-6879-7856, e-mail: harima@ap.eng.osaka-u.ac.jp

## Carrier Density Evaluation in p-type SiC by Raman Scattering

Hiroshi Harima<sup>1</sup>, Toru Hosoda<sup>1</sup> and Shin-ichi Nakashima<sup>2</sup>

<sup>1</sup>Department of Applied Physics, Osaka University,  
Yamadagaoka 2-1, Suita, Osaka 565-0871, Japan

<sup>2</sup>Department of Electrical and Electronic Engineering, Miyazaki University,  
1-1 Gakuenkibanadai-nishi, Miyazaki 889-2192, Japan

**Keywords:** Coupled Mode, Fano Interference, Hole Concentration, LO Phonon, Plasmon, p-type SiC, Raman Scattering

**Abstract.** Raman scattering spectra for p-type 6H-SiC bulk crystals have been measured in detail for various carrier concentrations. The spectra show very different features as compared with those for n-type materials: (i) The LO-phonon mode shows no frequency shift due to coupling with plasma oscillation of free carriers. (ii) A continuum band due to inter-valence-band transition clearly appears in the low frequency region, together with Fano interference features on sharp phonon lines. It is proposed that the continuum-band intensity and the Fano interference parameters can be conveniently used as a measure of free carrier concentration in p-type SiC.

### Introduction

Raman scattering is a powerful tool in characterizing electronic properties as well as crystalline properties in SiC.[1] In n-type materials, *e.g.*, the LO-phonon-plasmon coupled mode shows a drastic change in lineshape with the carrier doping condition, and we can easily evaluate electrical transport parameters such as free carrier density and mobility by analyzing the lineshape. [2] However, as we shall see below, coupled mode profiles in p-type materials are much less sensitive to the carrier doping condition, and such analysis is difficult. It is shown here that in p-type materials a continuum Raman band appears in the low frequency region and sensitively varies in intensity with the hole concentration. In heavily doped materials, furthermore, a Fano-type interference between the continuum and sharp phonon bands is clearly observed. These features could be used as a measure of free carrier concentration.

### Experimental Results and Discussion

We have tested several p-type 6H-SiC bulk crystals grown by the modified-Lely method. The hole concentration was evaluated mainly by Hall measurements, which ranged in  $10^{16}\sim 10^{20}$  cm<sup>-3</sup>. Raman microprobe spectra were observed at room temperature in the backscattering geometry from the c-face of plate samples using the 514.5 nm Ar<sup>+</sup> laser for excitation. The spectral slit width was about 0.6 cm<sup>-1</sup>. **Figure 1** shows typical Raman spectra, the intensity of which are normalized by the peak height of the strongest E<sub>2</sub> phonon mode at 789 cm<sup>-1</sup>. This figure shows that (i) A continuum band in the lower frequency region grows in intensity with the increase of hole concentration, extending up to ~800 cm<sup>-1</sup> or more. This intensity variation is shown more clearly in **Fig.2**, where the continuum band intensity at 200 cm<sup>-1</sup> is plotted against the hole density *p* after dividing by the peak height of the E<sub>2</sub> mode. **Figure 1** shows further that (ii) the low-frequency E<sub>2</sub> phonon modes at 145, 149 and

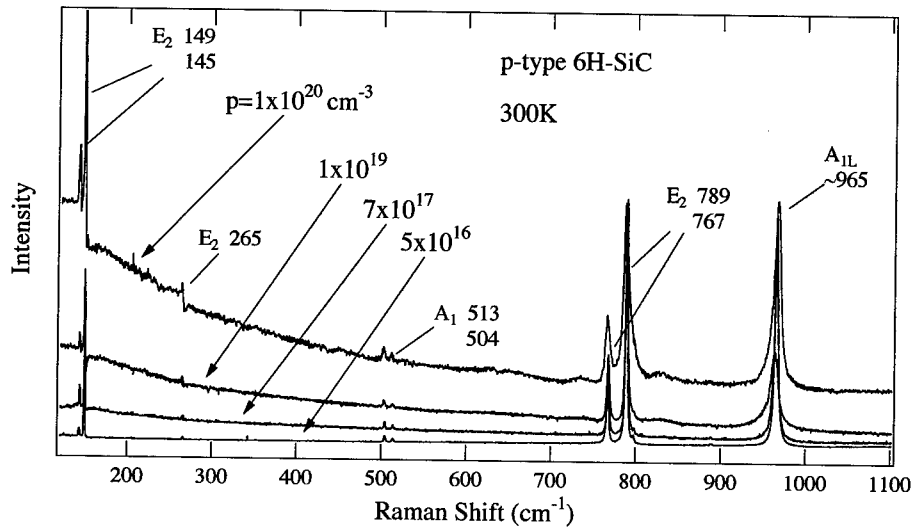


Fig.1 Raman spectra for p-type 6H-SiC with different carrier concentrations.

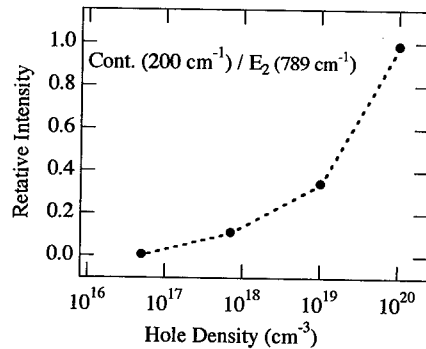


Fig.2 Continuum band intensity (at 200 cm⁻¹) divided by the peak height of the E₂-phonon band (at 789 cm⁻¹) in p-type 6H-SiC with different hole concentrations.

265 cm⁻¹ are distorted from Lorentzian lineshape due to a Fano-interference effect.[3] **Figure 3** shows a close-up of the 140-160 cm⁻¹ region of Fig.1. It is clearly observed that the E₂ mode peaked at 149 cm⁻¹ for small  $p$  values broadens and shifts to lower frequency and its asymmetric feature becomes more apparent with the increase of  $p$ . The weaker E₂-phonon mode at 145 cm⁻¹ shows similar behavior.

As previously observed in p-type silicon,[4] the continuum band is assigned to the inter-valence-band transition of hole. Since the band intensity varies drastically with  $p$  as shown in Fig.2, it can be conveniently used as a measure of hole concentration. The Fano interference on

the phonon bands arises because of coupling in the Raman transition matrix between the continuum (hole transition) and discrete (phonon) transition.[5] Its profile  $I(\omega)$  is theoretically described by a simple formula:

$$I(\omega) = (q + \varepsilon)^2 / (1 + \varepsilon^2). \quad (1)$$

Here  $q$  is the asymmetry parameter, and  $\varepsilon$  is a dimensionless frequency defined by  $\varepsilon = (\omega - \Omega_0 - \delta\Omega) / \Gamma$  with  $\omega$  being the Raman shift,  $\Omega_0$  being the phonon frequency without interference, and  $\delta\Omega$  and



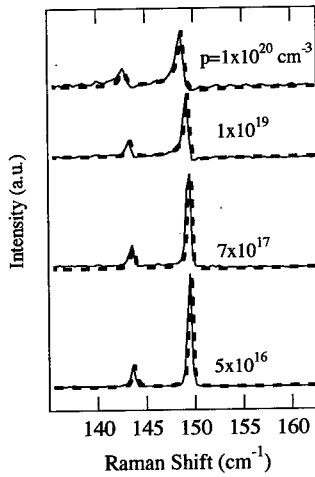


Fig.3 Variation of the low-frequency  $E_2$ -phonon modes with  $p$ . Solid and dashed lines correspond to observed and best-fit calculations, respectively.

$\Gamma$  being the peak shift and broadening due to the interference effect, respectively. These characteristic parameters are related to the Raman matrix elements and the hole concentration as follows; [5]

$$\delta\Omega = V^2 R(\omega) \quad (2)$$

$$\Gamma = \pi V^2 \rho(\omega) \quad (3)$$

$$q = [V T_p / T_e + V^2 R(\omega)] / [\pi V^2 \rho(\omega)] \\ = [V T_p / T_e + \delta\Omega] / \Gamma. \quad (4)$$

Here  $T_p$  and  $T_e$  are the Raman matrix elements for the phonon and hole transition, respectively,  $V$  is the matrix element for the coupling term,  $\rho(\omega)$  is the hole density of states, and  $R(\omega)$  is its Hilbert transform. These values,  $\delta\Omega$ ,  $\Gamma$  and  $q$  can be evaluated by fitting Eq.(1) to the observed profile. **Figure 4** shows the best-fit parameters obtained at various hole concentrations. There is a clear one-to-one correspondence between these parameters and the hole concentration, and we can estimate the hole concentration from the observed interference parameters by comparing with this figure.

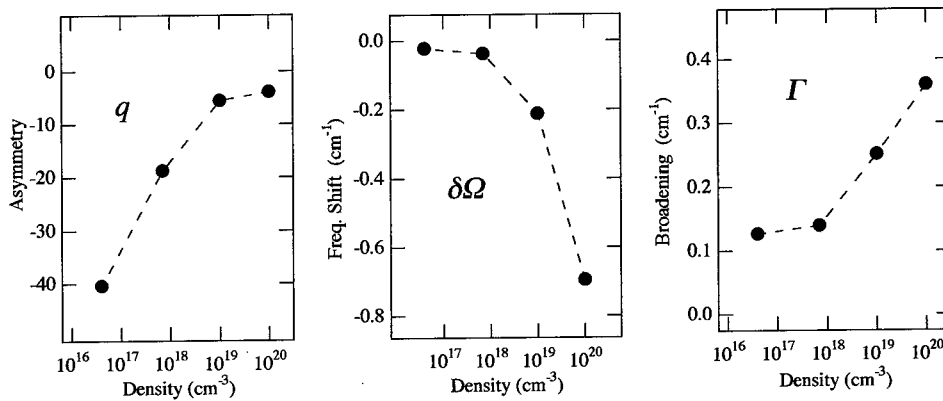


Fig.4 Fano interference parameters in p-type 6H-SiC.

Variation of the LO-phonon spectra ( $A_{1L}$  in Fig.1) with  $p$  is shown in detail in **Fig.5**. The result for n-type 6H-SiC is shown for comparison in **Fig.6**. [2] In n-type SiC, the peak clearly shifts to higher frequency and broadens asymmetrically with the increase of carrier concentration, because of a strong LO-phonon-plasmon coupling. This enabled us precise evaluation of electrical parameters such as carrier concentration and mobility from a lineshape analysis. [2] However, in

p-type materials, there is little frequency shift as seen here, and such analysis is difficult. A simulation on the LO-phonon-hole-plasmon-coupled mode [2] shows that such a weak coupling is attributed to fairly large carrier damping rates of hole, or, in other words, low carrier mobility in p-type SiC.

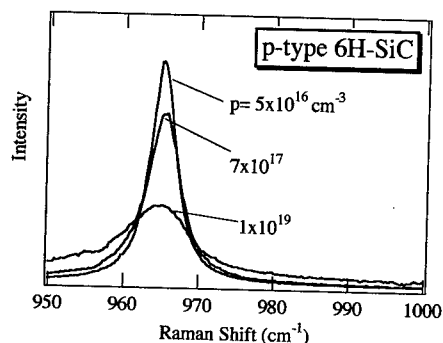


Fig.5 LO-phonon spectra for different carrier concentrations in p-type 6H-SiC.

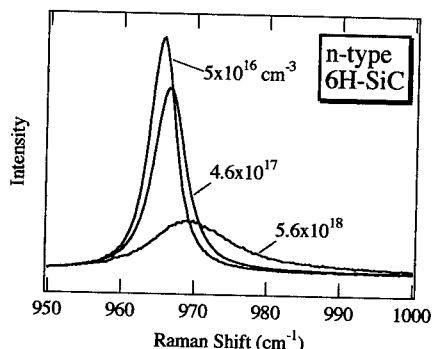


Fig.6 LO-phonon spectra for different carrier concentrations in n-type 6H-SiC (from Ref.2).

### Summary

Raman scattering spectra for p-type 6H-SiC bulk crystals were measured for various carrier concentrations. A continuum band due to inter-valence-band transition was observed in the low frequency region, together with clear Fano-interference features for sharp phonon lines superposed on this continuum. The continuum-band intensity and the Fano interference parameters could be conveniently used as a measure of free carrier concentration. In contrast to n-type materials, frequency shift of the LO-phonon mode is not observed probably because of heavy damping of hole-plasma oscillation.

**Acknowledgment** This work was partially supported by New Energy and Industrial Technology Development Organization (NEDO), Japan.

### References

- [1] S.Nakashima and H.Harima, *phys.stat.sol. (a)* **162** (1997) 39.
- [2] H.Harima, S.Nakashima and T.Uemura, *J.Appl.Phys.* **78** (1995) 1996.
- [3] U.Fano, *Phys.Rev.* **124** (1961) 1866.
- [4] F.Cerdeira, T. A.Fjeldly and M. Cardona, *Phys.Rev.B* **8** (1973) 4734.
- [5] M.V.Klein, in *Light Scattering in Solids I*, edited by M.Cardona, (Springer, Berlin, Heidelberg, New York, 1975) p.147.

Corresponding author : Hiroshi HARIMA,

Tel: +81-6-6879-7855, Fax: +81-6-6879-7856, e-mail: harima@ap.eng.osaka-u.ac.jp

## Shallow Nitrogen Donor States in 4H-SiC Investigated by Photothermal Ionization Spectroscopy

C.Q. Chen<sup>1</sup>, J. Zeman<sup>2</sup>, F. Engelbrecht<sup>1</sup>, Christian Peppermüller<sup>1</sup>, R. Helbig<sup>1</sup>  
and G. Martinez<sup>2</sup>

<sup>1</sup>Institute of Applied Physics, University of Erlangen-Nürnberg,  
Staudtstr. 7/A3, DE-91058 Erlangen, Germany

<sup>2</sup>CNRS/MPI-FKF, High Magnetic Field Laboratory, BP 166, FR-38042 Grenoble Cedex 9, France

**Keywords:** FTIR, Magnetospectroscopy, PTIS, Shallow Nitrogen Donor

**Abstract.** Photothermal ionization spectroscopy ( PTIS ) measurements were carried out on a high purity and high quality 4H-SiC epitaxial layer at various temperatures. The two step photothermal ionization process is clearly reflected in the temperature dependence of the photoconductivity. The spectrum at the temperature of 25.6 K reveals five well resolved electronic transition lines associated with the shallow nitrogen donor. The ionization energy of the shallow nitrogen donor is concluded to be  $60.2 \pm 0.5$  meV. Furthermore, PTI magnetospectroscopy measurements were performed to investigate the symmetry properties of these transitions. The results show no linear Zeeman splitting only diamagnetic shift, which is consistent with the fact that the effective mass tensor of 4H-SiC has three different diagonal components.

### Introduction

Nitrogen is the main donor in all SiC polytypes and dominates the electrical properties of n-type SiC. Nitrogen atoms substitute for carbon in the SiC lattice and may occupy two inequivalent lattice sites (one hexagonal site and one cubic site) in 4H-SiC. We investigated the infrared absorption spectra of nitrogen donors in 4H-SiC bulk material with a nitrogen concentration of  $8 \times 10^{17} \text{ cm}^{-3}$  at three different temperatures ( the polarization  $E \perp c$  ). Three broad electronic transition lines at 367, 397 and 450  $\text{cm}^{-1}$  are observed at 8K as shown in Fig. 1. Similar to Ref [1], we assign them to the shallow nitrogen donor. At 85 K, two additional absorption lines at 307, 337  $\text{cm}^{-1}$  can be observed, resulting from the thermal population due to valley-orbit splitting of 60  $\text{cm}^{-1}$  of the ground state. It is difficult to observe electronic transitions related to another deeper nitrogen donor at higher energies due to the oscillator strength of an electronic transition decreasing rapidly with increasing the ground state binding energy and the strong background absorption of the reststrahlen band.

Although the infrared absorption spectra of 4H-SiC bulk material reveal some important features of the shallow nitrogen donor states, it is obvious that transition lines are too broad to obtain the electronic transition fine structures. An accurate experimental determination of electronic transitions is essential to investigate the excitation spectrum of the shallow nitrogen donor. In order to minimize

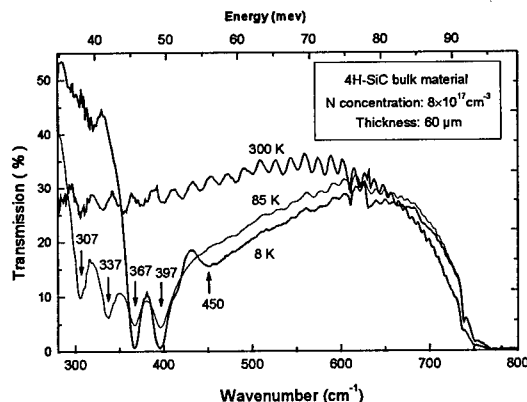


Fig. 1: Infrared transmission spectra of the 4H-SiC bulk material with the polarization  $E \perp c$  at 8, 85, 300 K.

line broadening which originates mainly from concentration broadening and internal strain effects, we used free-standing, highly pure epitaxial layers with the thickness of about 50  $\mu\text{m}$ . They are one of the purest and best quality 4H-SiC samples available at present. However, due to the low absorption coefficient resulting from the low nitrogen concentration and the low thickness of the epitaxial layers, conventional infrared absorption spectroscopy by transmission experiments is impossible. The technique of Fourier transform infrared photothermal ionization spectroscopy (PTIS) uses the sample itself as a detector and offers a very low concentration detection limit [2, 3]. It gives a photoconductivity spectrum which shows sharp discrete lines corresponding to electronic transitions from the ground state to the excited states of the impurity in a semiconductor. The photoresponse is based on a two-step ionization process of the impurity, which consists of an optical excitation of a bound electron from the ground state to an excited state and subsequent thermal ionization of the electron from the excited state to the conduction band. The technique of PTIS has been widely applied to Si, Ge, GaAs and has been proved to be an extremely sensitive method to study the shallow impurity states. In this work, we performed PTIS measurements on the 4H-SiC free-standing epitaxial layer at various temperatures. Sharp and well resolved electronic transition lines of the shallow nitrogen donor were observed and investigated.

### Experimental

n-type nitrogen doped 4H-SiC bulk material, grown by the modified Lely process, was used for infrared absorption measurements. A free-standing epitaxial layer was used in PTIS measurements, with the low nitrogen concentration in the  $10^{14} \text{ cm}^{-3}$  range and the thickness of about 50  $\mu\text{m}$ . It was grown on a highly nitrogen doped 4H-SiC substrate by the CVD method. The sample was obtained by removing the substrate by mechanical polishing. The high quality of the epitaxial layer was confirmed by low temperature photoluminescence spectra. The size of the sample is about 4 mm  $\times$  2 mm. Two ohmic contacts were fabricated on one surface of the sample by evaporating nickel with subsequent heat treatment. The PTIS experiments were performed with a Bruker IFS-113v Fourier transform spectrometer, in combination with a He contact gas cryostat and a 11 T superconducting magnet. The temperature was controlled by a heater and monitored by an adjacent Cernox resistor. The experimental error for the temperature is less than 0.5 K. The infrared radiation from the spectrometer was transferred onto the samples via a polished brass light pipe system with a black polyethylene film window. The photoconductivity signal of the sample was amplified by a preamplifier and then transferred to the external detector input of the spectrometer. All spectra were recorded with unpolarized light (the polarization of nearly  $E \perp c$ ) at a resolution of  $\pm 0.5 \text{ cm}^{-1}$ .

### Results and Discussion

Fig. 2 shows the photoconductivity spectra of the 4H-SiC epitaxial layer with the polarization of nearly  $E \perp c$  at four different temperatures from 4.2 K to 25.6 K. All these spectra are corrected by removing the influence of the window and

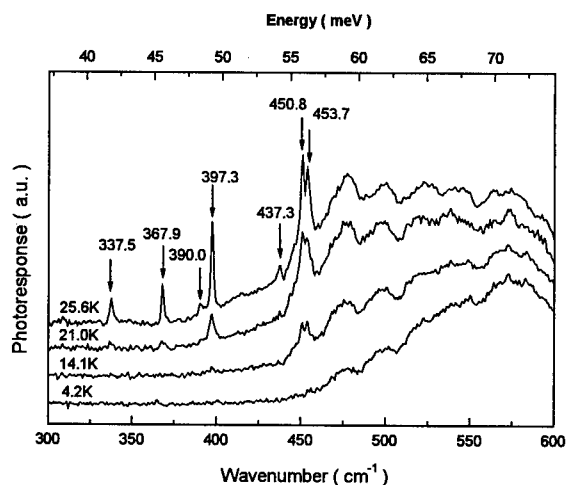


Fig. 2: Photoconductivity spectra of the 4H-SiC epitaxial layer at 4.2, 14.1, 21.0 and 25.6 K.

are normalized to the same continuum band height around  $570 \text{ cm}^{-1}$  for comparison. At  $4.2 \text{ K}$ , only the broad continuum band above the wavenumber of  $460 \text{ cm}^{-1}$  can be observed. It is mainly caused by direct optical transitions from the ground state into the conduction band. Several peak structures in the continuum band arise mainly from the Fabry-Perot interference since the interference spacing of about  $22 \text{ cm}^{-1}$  corresponds to the thickness of the sample [4]. At  $14.1 \text{ K}$ , two well resolved discrete lines at  $450.8$  and  $453.7 \text{ cm}^{-1}$  related to electronic transitions from the ground state to the higher excited states of the shallow nitrogen donor begin to appear. With increasing temperature  $T$ , more and higher energy phonons are provided for the thermal ionization process, the strengths of the electronic transition lines increase greatly, and the lower energies transitions from the ground states to the lower excited states can be observed. The best working temperature in our experiments is at  $25.6 \text{ K}$ . The PTIS spectrum at  $25.6 \text{ K}$  displays five strong, well resolved electronic transition lines at  $367.9$ ,  $397.3$ ,  $337.5$ ,  $450.8$  and  $453.7 \text{ cm}^{-1}$ . It can be seen that PTIS results are in agreement with the infrared absorption results. Moreover, the linewidths of the lines at  $367.9$ ,  $397.3$  and  $337.5 \text{ cm}^{-1}$  which are observed as broad lines ( $\Gamma_{\text{IR}} \sim 25 \text{ cm}^{-1}$ ) in the infrared transmission spectra, are only about  $2.6 \text{ cm}^{-1}$  ( $\Gamma_{\text{PTIS}}$ ) in PTIS spectra (the ratio of  $\Gamma_{\text{PTIS}}/\Gamma_{\text{IR}} \sim 0.1$ ). The closely spaced transition lines at  $450.8$  and  $453.7 \text{ cm}^{-1}$  are clearly resolved whereas they appear as a broad line around  $450 \text{ cm}^{-1}$  in infrared transmission spectra. Similar to the line at  $337.5 \text{ cm}^{-1}$ , the weak line at  $390.0 \text{ cm}^{-1}$  is related to the valley-orbit splitting corresponding to the transition at  $450.8 \text{ cm}^{-1}$ . The origin of the line at  $437.3 \text{ cm}^{-1}$  remains unknown.

An electronic transition line intensity in PTIS spectrum depends on the photoabsorption cross section and the thermal ionization probability. The thermal ionization probability  $P_{\text{th}}$  from an excited state to the conduction band is given by [5],

$$P_{\text{th}} \propto \left(1 + \frac{\Delta E}{k_B T}\right) \exp\left(-\frac{\Delta E}{k_B T}\right) \quad (1)$$

where  $\Delta E$  is the binding energy of an excited state. If there is no influence of the valley-orbit splitting and the photoabsorption cross section is assumed to be constant over the measured temperature interval, the strength of a line has the same temperature dependent relation as the thermal ionization probability when the spectra at various temperatures are normalized to the same continuum band height. As a result, the ionization energy of the shallow nitrogen donor can be evaluated from the temperature dependence of the strengths of the lines according to Eq. 1. In order to minimize the

influence of valley-orbit splitting, we choose the lines at  $450.8 \text{ cm}^{-1}$  and  $453.7 \text{ cm}^{-1}$  at  $14.1 \text{ K}$  and  $21.0 \text{ K}$  to evaluate the related excited states binding energies  $\Delta E$  by a fit procedure.  $\Delta E$  are taken as adjustable parameters.  $\Delta E$  of the excited states corresponding to the lines at  $450.8 \text{ cm}^{-1}$  ( $55.9 \text{ meV}$ ) and  $453.7 \text{ cm}^{-1}$  ( $56.3 \text{ meV}$ ) are deduced to be  $4.2 \pm 0.5 \text{ meV}$  and  $3.9 \pm 0.5 \text{ meV}$ , respectively. Therefore, the ionization energy of the shallow nitrogen donor is deduced to be  $60.2 \pm 0.5 \text{ meV}$ .

Magneto spectroscopy of shallow impurities can provide additional information on the involved impurities states by the investigation of the symmetry properties of electronic

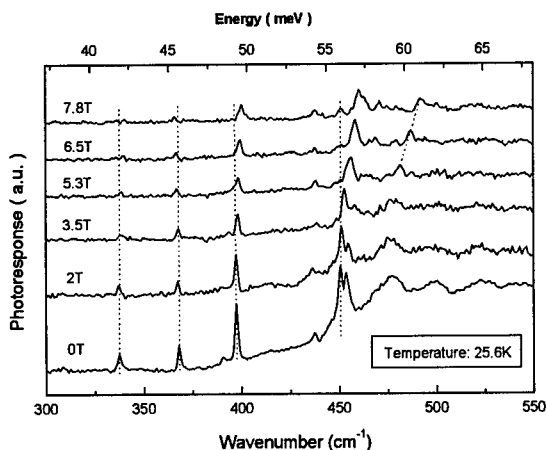


Fig.3: PTIS spectra at  $25.6 \text{ K}$  as a function of magnetic field in Faraday configuration ( $c \parallel B \parallel k$ ) from  $0 \text{ T}$  to  $7.8 \text{ T}$ .

transitions. Fig. 3 displays the PTIS spectra as a function of magnetic field in Faraday configuration ( $c||B||k$ ) from  $B = 0$  T up to  $B = 7.8$  T. No Zeeman splitting of the lines is observed. All five electronic transition lines show a diamagnetic shift in their energy positions. The line at  $367.9\text{ cm}^{-1}$  shifts to lower energies and the other four lines shift to higher energies. In Faraday configuration ( $c||B||k$ ), all three effective mass ellipsoids of the conduction band minima are equivalent with respect to the magnetic field (all have  $B||c||ML$ ). The fact that no linear Zeeman splitting and only a diamagnetic shift of the lines is observed, indicates that the excited states of the shallow nitrogen donor are nondegenerate at zero magnetic field. The excited states are only influenced by the quadratic Zeeman effect. This is consistent with an effective mass tensor of three different diagonal components. The excited states of the shallow nitrogen donor in 4H-SiC can be described by Hamiltonian  $H$  within the single valley effective mass approximation. Similar to our argument for 6H-SiC in Ref [6], for a Hamiltonian  $H$  including three different effective mass components, magnetic quantum numbers are no longer good quantum numbers. The excited states with magnetic quantum numbers  $\pm m$  which are degenerate in the case of two effective mass components will split into two nondegenerate states at zero magnetic field. In addition, the strengths of the diamagnetic shifts of electronic transitions provide information about the principle quantum numbers of the involved excited states. Let us have a look at the quadratic Zeeman effect on nondegenerate  $p_0$  donor states in Si. The energy shift of the  $p_0$  states increases with the increase of the principal quantum number  $n$  as  $n^2(n^2-1)B^2$  dependence on magnetic field [7]. For this reason in the case of 4H-SiC, there is strong evidence that the lines at  $367.9$ ,  $397.3$  and  $337.5\text{ cm}^{-1}$  are related to transitions from the ground states to lower excited states of the shallow nitrogen donor, while the transitions at  $450.8$  and  $453.7\text{ cm}^{-1}$  are associated with higher excited states of the shallow nitrogen donor.

### Summary

PTIS measurements of a free standing 4H-SiC epitaxial layer reveal five well resolved electronic transition lines associated with the shallow nitrogen donor. The ionization energy of the shallow nitrogen donor is concluded to be  $60.2 \pm 0.5\text{ meV}$ . PTI magnetospectroscopy measurements show no linear Zeeman splitting only diamagnetic shift of electronic transitions. It is consistent with the fact that the effective mass tensor of 4H-SiC has three different diagonal components.

**Acknowledgments:** We are indebted to R. Rupp and A. Wiedenhofer in the Siemens Research Laboratory in Erlangen for supplying samples. C. Q. Chen acknowledges financial support by the Volkswagen Stiftung. This work was supported by TMR Programme under contract n<sup>o</sup> ERBFMGECT950077 and DFG Sonderforschungsbereich 292.

### References

- [1] W. Götz, A. Schöner, G. Pensl, W. Suttrop, W. J. Choyke, R. Stein, and S. Leibenzeder, *J. Appl. Phys.* 73, ( 1993 ), p.3332.
- [2] S. M. Kogan and T. M. Lifshits, *Phys. Stat. Sol. (a)* 39, ( 1977 ), p.11.
- [3] G. E. Stillman, C. M. Wolfe, and J. O. Dimmock, in R. K. Willardson and A. C. Beer ( Eds. ), *Semiconductors and Semimetals*, Vol. 12, Academic Press, New York, ( 1977 ), p.169.
- [4] D. R. Bosomworth, R. S. Crandall and R. E. Enstrom, *Phys. Lett.* 28A, ( 1968 ), p.320.
- [5] G. Bambakidis and G. J. Brown, *Phys. Rev. B* 33, ( 1986 ), p.8180.
- [6] F. Engelbrecht, S. Huant, and R. Helbig, *Phys. Rev. B* 52, ( 1995 ), p.11008.
- [7] S. Zwerdling, K. J. Button, and B. Lax, *Phys. Rev.* 118, (1960), p.975.

## Characterization of Silicon Carbide using Raman Spectroscopy

J.C. Burton<sup>1</sup>, F.H. Long<sup>1</sup>, Y. Khlebnikov<sup>2</sup>, I. Khlebnikov<sup>2</sup>, M. Parker<sup>2</sup>  
and T.S. Sudarshan<sup>2</sup>

<sup>1</sup> Department of Chemistry, Rutgers University, 610 Taylor Road,  
Piscataway, NJ 08854-8087, USA

<sup>2</sup> Department of Electrical and Computer Engineering, University of South Carolina,  
Columbia, SC 29208, USA

**Keywords:** Electronic Raman Scattering, Lateral Epitaxial Overgrowth, Nitrogen Doping

### Abstract

Electronic Raman scattering from nitrogen defect levels in 4H-SiC and 6H-SiC has been seen to be significantly enhanced with excitation by red (633 nm, 1.98 eV) or near infrared (785 nm, 1.58 eV) laser light at room temperature. Peaks observed in the spectra of 4H-SiC are seen to shift to lower frequency with increasing nominal doping concentration. We have used confocal Raman microscopy to investigate Lateral Epitaxial Overgrowth (LEO) of SiC. Epitaxial overgrowth on a 4H-SiC substrate covered with a graphite mask with circular holes of 70  $\mu\text{m}$  has been observed to produce hexagonal and misshapen hexagonal mesa island structures with some mixed polytype structure, especially at the edges.

### Electronic Raman Scattering from Nitrogen Defect Levels

Electronic Raman scattering from nitrogen defect levels in SiC has been seen to be significantly enhanced with excitation by red (633 nm, 1.98 eV) or near IR (785 nm, 1.58 eV) laser light at room temperature. [1] Four additional peaks, which we attribute to nitrogen, are observed in 6H-SiC (at shifts of 380, 430, 510, and 638  $\text{cm}^{-1}$ ) and three peaks in 4H-SiC (at 400, 530, and 570  $\text{cm}^{-1}$ ). The origin of the resonant enhancement is the near IR absorption band associated with the green color characteristic of *n*-type SiC. Fig. 1, at right, shows three room temperature Raman spectra from a single 4H-SiC sample, using three different laser wavelengths. Additional peaks, labeled  $N_a$ ,  $N_b$  and  $N_c$  in the inset, appear as the excitation is moved to the red and IR. The data shown in Fig 1 has been normalized to the peak at 777  $\text{cm}^{-1}$ . This effect is also apparent at low temperature. Similar modes have long been observed in 6H-SiC using green laser light at 77 K. [2] These modes are also enhanced using red or infrared laser light.

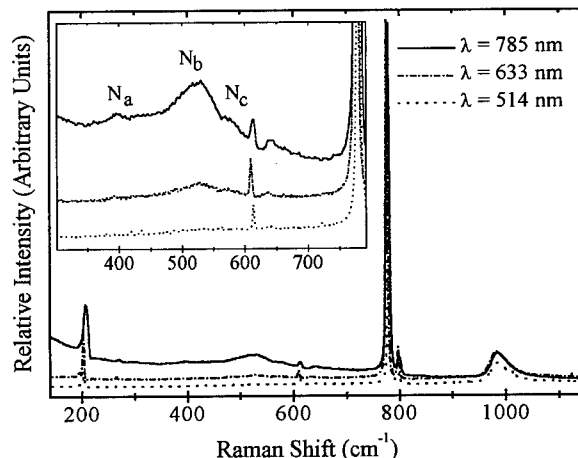


Fig. 1. Wavelength dependence of 4H-SiC Raman spectrum.

There is, however, an interesting effect observed in the spectrum of 4H-SiC, which also

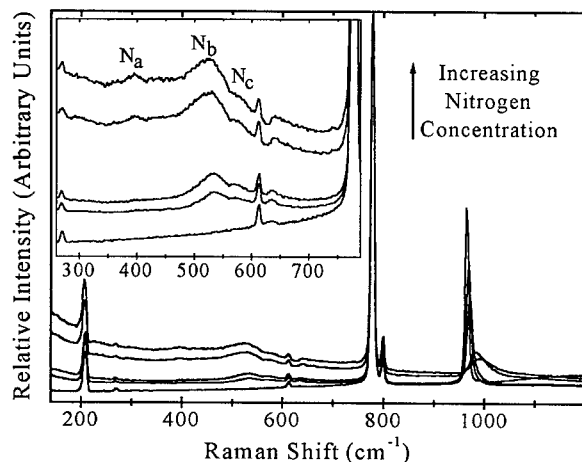


Fig. 2. Change in 4H-SiC Raman spectrum with nitrogen concentration.

exhibits a shift in these resonantly enhanced modes at room temperature. This shift is not seen in the 6H-SiC polytype. These modes in 4H-SiC are seen to increase in intensity and shift to lower frequency as the nominal doping concentration is increased, as can be seen in Fig. 2, at left. The mode labeled  $N_b$  shifts by about 10–11  $\text{cm}^{-1}$  at room temperature using 785 nm (1.58 eV) excitation. The spectra are organized in order of nominal doping concentration, from semi-insulating and  $2.1 \times 10^{18} \text{ cm}^{-3}$  at the bottom, to  $7.1 \times 10^{18} \text{ cm}^{-3}$  at the top. As with Fig. 1, the spectra are normalized to the peak at  $777 \text{ cm}^{-1}$ . A similar effect with enhanced peaks is also seen at 95 K.

This shift in the electronic Raman spectrum with increasing nitrogen concentration may be due to clustering effects.

We have also observed differences in the spectra of 6H-SiC samples grown by different methods. Using laser excitation at 647 nm (1.98 eV), and a cryostat cooled to 95 K with liquid nitrogen, spectra were taken of 6H-SiC wafers and a 6H-SiC platelet grown by the Lely process.

The resonant peaks in the spectrum of the platelet are more intense than those in the spectra of the 'state of the art' wafers. All the other peaks are of comparable intensities. On closer examination, it is also clear that there are additional peaks in the spectrum of the Lely grown platelet. Additional structure is visible in the spectrum of the platelet at frequencies both higher and lower than the main peaks, which are at about  $488 \text{ cm}^{-1}$  and  $506 \text{ cm}^{-1}$ . This is illustrated by Fig. 3, right. The extra peaks may be due to local modes of the nitrogen atom, but the differences may be due to a variety of factors. The mechanisms of growth and of the incorporation of dopants into the crystal lattice have a large influence in the properties of the sample. Work to further understand these effects is ongoing.

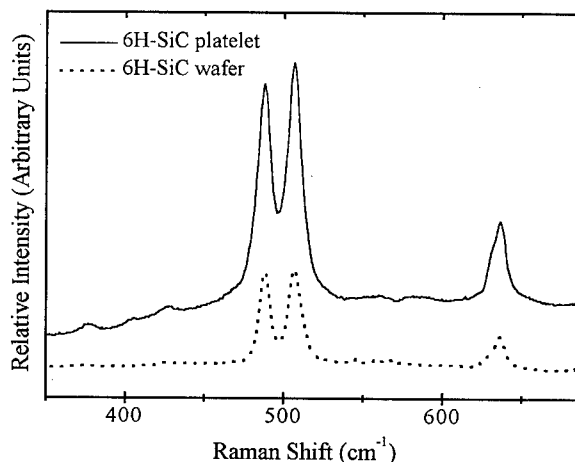


Fig. 3. Comparison of Raman spectra of Lely grown platelet and state of the art wafer.



### Investigation of Lateral Epitaxial Overgrowth of SiC by Raman Microscopy

We have very recently begun a study of Lateral Epitaxial Overgrowth (LEO) of SiC using confocal Raman microscopy. To the best of our knowledge, this is the first report of Raman

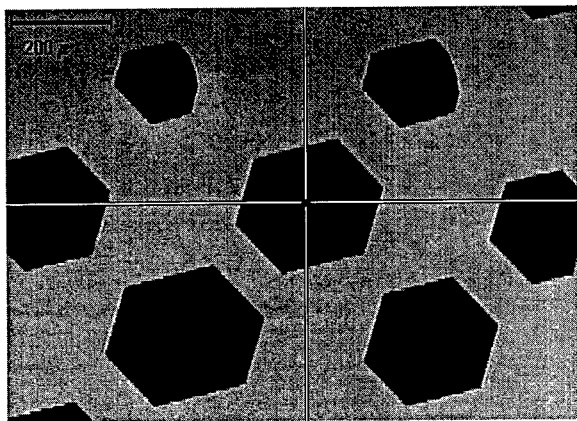


Fig. 4. LEO SiC hexagonal mesa structures.

spectra of LEO SiC. The sample under investigation consisted of a substrate of 4H-SiC, which was overlaid with a graphite mask. The mask was 2 microns thick and had an array of circular openings of diameter 70 microns. On this substrate, SiC was grown by physical vapor transport. We have observed that the circular openings allow growth of mesa island structures that are predominantly hexagonal, although some of them are misshapen. A picture of these structures taken through a 5x-microscope objective is shown in Fig. 4, left. At the stage of growth of this sample, it is found that there is no

evidence of SiC growth in the open areas of mask between the mesa structures, but there is a trace of SiC just off the edge of the structure.

The Raman spectrum at the surface of the center of most of the mesa structures is that of 4H-SiC. It has long been known that the Raman spectrum of SiC is polytype dependent, making Raman especially useful for polytype identification. [4] Using the confocal Raman microscope, a depth profile was measured down to 8 microns beneath the surface, in steps of 1 micron each. This showed that the polytype at this particular center was consistently 4H-, but that the doping level changed with depth. Fig. 5, right, shows the spectrum at the surface compared with the spectrum at 8 microns below the surface. The shape and position of the  $A_1(\text{LO})$  phonon is sensitive to the doping concentration, which we have previously used to spatially map the doping concentration in SiC wafers.[5] At the surface the peak is at a Raman shift of  $965 \text{ cm}^{-1}$  and at 8 microns below that the shift is  $970 \text{ cm}^{-1}$  (with a broader peak) which, while it does not indicate a high doping concentration, is a significantly higher doping level than at the surface. Investigation of a wide range of mesa structures reveals that some do not exhibit a similar change in the doping concentration, though most are consistently 4H-SiC at all depths.

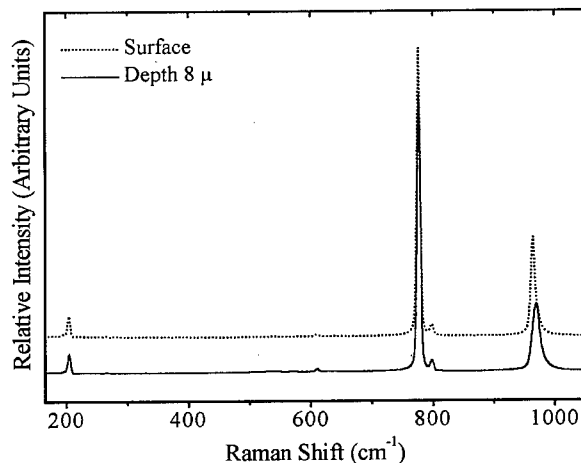


Fig. 5. Comparison of surface and 8 micron deep Raman spectra at center of mesa structure.

A series of surface micro-Raman spectra taken from the center toward the edge of the structure reveal that the polytype gradually changes from the single 4H- at the center to the mixture at the edge. At the edge of the mesa structure, a peak is observed in the Raman spectrum of 4H-SiC at  $788\text{ cm}^{-1}$ . There is no Raman allowed phonon peak at  $788\text{ cm}^{-1}$  for 4H-SiC.

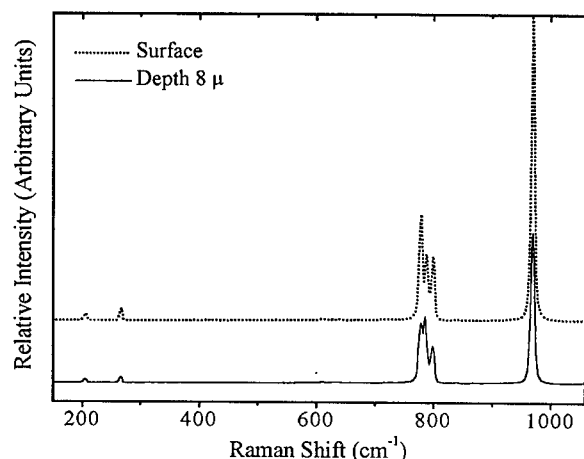


Fig. 6. Comparison of surface and 8 micron deep Raman spectra at edge of mesa structure.

However, this is the position of an  $E_2$  symmetry mode for 6H-SiC. Furthermore, the relative intensity of other 4H- Raman peaks is distorted from expected values. We have therefore concluded that the edges of the SiC mesa are of mixed polytype. Fig. 6, left, shows a comparison of two spectra taken at the edge of the mesa structure. These spectra both show a mixture of polytypes, with peaks due to 4H- and 6H-SiC both visible. There is a clear difference between the surface spectrum and the one at 8 microns below the surface. The mixture shows more 6H-polytype character as the depth increases. There does not appear to be any significant change in the doping concentration with depth at the edge of the structure. In other mesas, a clear progression can sometimes be seen from a pure 4H-SiC spectrum in the center, through the mixed spectrum, to a pure 6H-SiC spectrum at the edge, not just the change of polytype with depth at the edge. A few isolated mesa structures are found to consist of predominantly 6H-SiC at the edge and center. A systematic study will be undertaken in order to investigate the findings reported here, and explain the effects that have been observed. Further investigation of these materials is ongoing.

### Acknowledgements

The authors would like to thank Gary Lavigne at the University of Connecticut and Tim Prusnick of Renishaw Inc. for assistance with the Raman Microscopy. The authors would also like to thank EMCORE Corporation of Somerset, NJ for partial support of this work.

### References

- [1] J. C. Burton, F. H. Long, and I. T. Ferguson, *J. Appl. Phys.* **86** (1999), p. 2073.
- [2] P. J. Colwell and M. V. Klein, *Phys. Rev. B.* **6** (1972), p. 498.
- [3] J. C. Burton, L. Sun, F. H. Long, Z. C. Feng, and I. T. Ferguson, *Phys. Rev. B* **59**, (1999), p. 7282.
- [4] e. g. D. W. Feldman, J. H. Parker, Jr., W. J. Choyke, and L. Patrick, *Phys. Rev.* **173**, (1968), p. 787.
- [5] J. C. Burton, L. Sun, M. Pophristic, S. J. Lukacs, F. H. Long, Z. C. Feng, and I. T. Ferguson, *J. Appl. Phys.* **84**, (1998), p. 6268.

Correspondence should be addressed to F. H. Long. E-mail address: fhlong@rutchem.rutgers.edu

## Photoluminescence Study of CVD Layers Highly Doped with Nitrogen

U. Forsberg<sup>1</sup>, A. Henry<sup>1,2</sup>, M.K. Linnarsson<sup>3</sup> and E. Janzén<sup>1</sup>

<sup>1</sup> Department of Physics and Measurement Technology, Linköping University,  
SE-581 83 Linköping, Sweden

<sup>2</sup> also ABB Corporate Research, SE-721 78 Västerås, Sweden

<sup>3</sup> Solid State Electronics, Royal Institute of Technology, SE-164 40 Kista, Sweden

**Keywords:** Mott Transition, n-Type Doping, Photoluminescence

**Abstract.** From a systematic study of highly doped n-type 4H-SiC epilayers we observe a photoluminescence spectrum, which was previously associated with the recombination of a bound exciton at the neutral boron acceptor. Electrical measurements performed on these layers show clearly n-type conductivity. It was feasible to dope and measure reproducibly the layers from low  $10^{17}$  to mid  $10^{18}$  cm<sup>-3</sup>. It was not possible to determine the doping from Capacitance Voltage measurements for the samples grown with the highest doping ( $>6 \cdot 10^{18}$  cm<sup>-3</sup>). However Secondary Ion Mass spectrometry did not reveal any boron impurities in the layers and shows good agreement with electrical measurements regarding the nitrogen concentration.

### Introduction.

Whereas the electronic structure of intrinsic SiC is fairly well established theoretically, and to a certain extent also experimentally, there is very little known about the band structure in highly doped SiC. The change of the electronic properties of heavily doped SiC is of practical as well as basic interests. Contact layers for devices usually require highly doped layers. The effect of heavy doping on the electronic properties of a semiconductor can be described in terms of a reduction of the band gap and has been studied experimentally and theoretically in various semiconductors [1-3]. In SiC for our knowledge no experimental work has been done until now and only very recently theoretical calculations have been performed [4]. An estimation of the critical Mott concentration for the metal/non-metal transition has been achieved which shows a value of about  $5.6 \cdot 10^{18}$  cm<sup>-3</sup> for n-type 4H-SiC [5]

We present here results of a systematic study of highly doped n-type 4H-SiC epilayers and compare the data obtained from various experimental characterization techniques such as photoluminescence (PL), electrical measurements and secondary ion mass spectrometry (SIMS).

### Experimental.

The studied layers were grown in a hot-wall chemical vapor deposition (CVD) reactor [6] with a SiC coated susceptor on 4H-SiC n-type ( $1.2 \cdot 10^{18}$  cm<sup>-3</sup>) substrates with a 8° miscut from the c-axis. The thickness of these layers was typically 5-6 µm. The high n-type doping was achieved by additions of N<sub>2</sub>.

Schottky contacts (1.2 mm diameter) were fabricated by evaporating Ni on the epitaxial layer. A nickel-gold alloy was used on the opposite side of the sample (substrate) to produce an ohmic contact. The net carrier concentration of the layers was determined by capacitance-voltage (CV) using a HP4284 LCR meter operating at a frequency of 1 MHz.

The profile of the N doped layers was obtained by SIMS measurements with a Camera IMS 4f microanalyser. Possible contamination of the layers by Boron and Aluminum was also investigated.

Low temperature photoluminescence (LTPL) experiments were performed in a bath cryostat with liquid helium pumped below the lambda point ( $T=2K$ ). The 244 nm line of a FreD laser (double frequency of the 488 nm of an  $Ar^+$  ion laser) was used as the excitation source. The luminescence was dispersed by a single monochromator (JY HR460) fitted with one 1200 groves/mm grating blazed at 330 nm and detected by a UV sensitive CCD camera. The usual geometry used to record the PL spectra is very close to the so-called back-scattering geometry.

### Results.

By addition of  $N_2$  flow to the carrier and precursor gases during the growth high n-type doping has been achieved and all layers were showing n-type conductivity. It was feasible to dope and measure reproducibly the layers from low  $10^{17}$  to mid  $10^{18} \text{ cm}^{-3}$  range with CV measurements

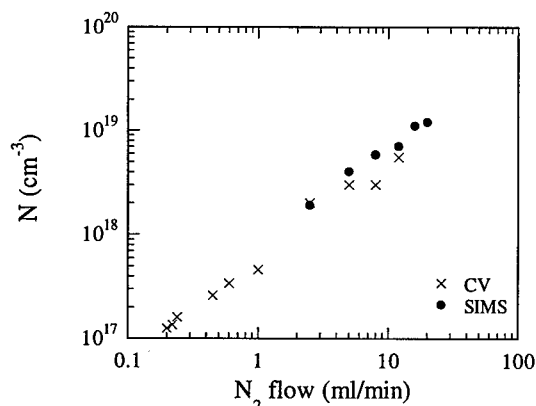


Fig.1: Nitrogen doping concentration as measured with CV (crosses) and SIMS (closed circles) as the function of the  $N_2$  flow used during growth.

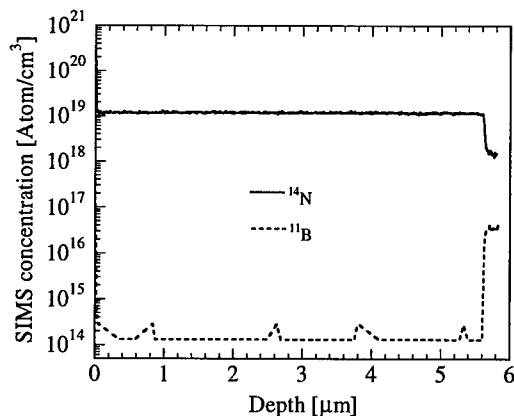


Fig.2 : SIMS profile of N and B impurities in a heavily doped ( $n=1.2 \cdot 10^{19} \text{ cm}^{-3}$ ) layer.

(crosses in Fig.1). However it was not possible to determine the doping from the CV measurements for the samples grown with the highest doping ( $> 6 \cdot 10^{18} \text{ cm}^{-3}$ ). No Schottky behavior was observed and only Ohmic contact was obtained.

SIMS analyses were performed on the highest doped layers. As can be seen in Fig.2 no impurities were detected in the layer whereas boron has a concentration around  $4 \cdot 10^{16} \text{ cm}^{-3}$  in the substrate. We would like to point out here that the background level to detect N and B impurities is about  $2 \cdot 10^{16}$  and  $2 \cdot 10^{14} \text{ cm}^{-3}$ , respectively. The profile for both the nitrogen and the boron allowed determining the thickness of the layer with a good agreement with estimation from the growth parameters. Fig.3 shows typical PL spectra recorded on various samples. The substrate used in this study was a relatively low-doped substrate ( $1.2 \cdot 10^{18} \text{ cm}^{-3}$ ) and its LTPL spectrum shows only nitrogen bound-exciton (N-BE) with very weak feature for the shallowest donor ( $P_0$  and its phonon replica).

As can be seen in Fig.3.a, a slight broadening of the  $Q_0$  N-BE no-phonon line was observed. Without addition of  $N_2$  flow only N-BE lines are observed together with the free-exciton (FE) phonon replica lines such as  $I_{76}$  (Fig.3.b).

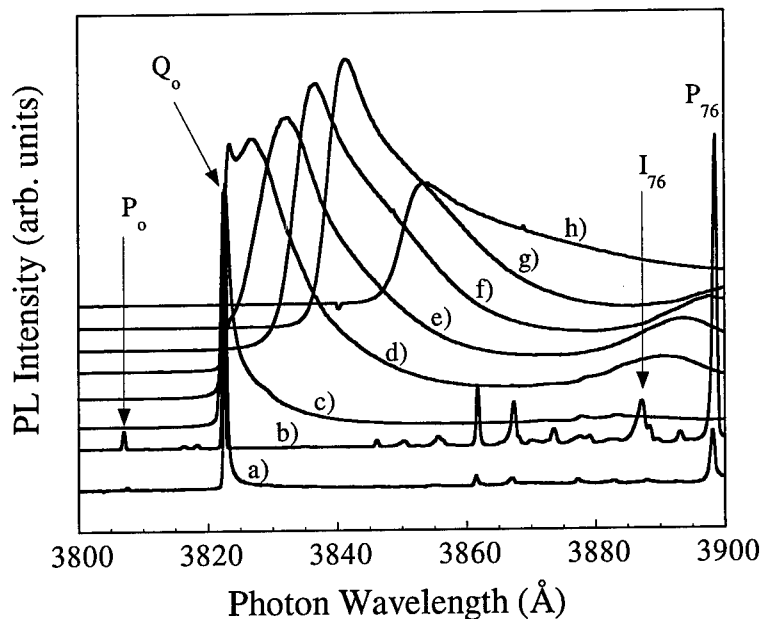


Fig.3: PL spectra recorded at 2K for a) the  $1.2 \cdot 10^{18} \text{ cm}^{-3}$  doped substrate, b) undoped layer (doping about  $1.1 \cdot 10^{15} \text{ cm}^{-3}$ ) and doped layers with increasing  $\text{N}_2$  flow of c) 2.5 ml/min, d) 5 ml/min, e) 8 ml/min, f) 12 ml/min, g) 20 ml/min and h) 200 ml/min. Note that the CVD growth parameters (such as persursors flows) were different for both the undoped sample b) and the highest doped sample h).

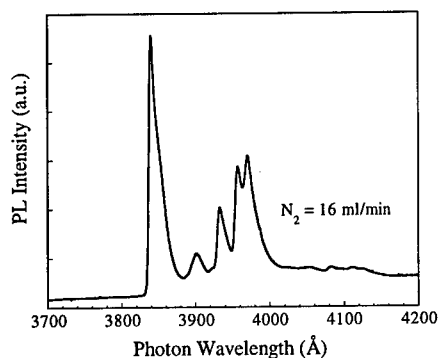


Fig.4: LTPL spectrum at 2K of a heavily doped ( $1.2 \cdot 10^{19} \text{ cm}^{-3}$ ) layer.

The relative intensity of the  $Q_0$  N-BE line and the FE  $I_{76}$  line allowed the estimation of the doping concentration [7] to about  $1.1 \cdot 10^{15} \text{ cm}^{-3}$  with good agreement with the CV result. With very small  $\text{N}_2$  flow the N-BE  $Q_0$  line is broadened (Fig.3.c). With further increase of the  $\text{N}_2$  flow a broad band (BB) is observed, first as a shoulder of the  $Q_0$  N-BE line (Fig.3.c and d) and after that as the only luminescence observed in the spectra (Fig.3.d-h). Its phonon replicas (Fig.4) accompany the BB band with momentum phonons energy of about 50, 76, 96 and 106 meV. The energy position of the BB band shifts towards lower energy when the  $\text{N}_2$  flow increases.

#### Discussion.

Recently a peak near 3838 Å appearing in the low temperature photoluminescence (LTPL) spectra of 4H-SiC has been associated with the recombination of a bound exciton at the neutral

shallow boron acceptor [8]. This bound exciton could appear as a sharp peak but also as a quite broad band. The intensity of the broad band was increased with added boron during growth and also with increasing C/Si. A large variation in the width suggested that this complex is very sensitive to environmental conditions as local strains and to growth conditions. No shift in energy position of this broad band was mentioned.

However, we did observe this broad band BB also on highly n-type doped substrates [9]. For n-type bulk material with doping concentration below  $2 \cdot 10^{18} \text{ cm}^{-3}$ , N-BE related lines were observed whereas highly doped substrates showed a broad band related spectrum for which the peak position could change from sample to sample and from spot to spot on the same wafer. The fact that this LTPL spectrum resembled the previously reported broad spectrum of the shallow boron acceptor influenced us to tentatively propose a hopping mechanism for the exciton bound to the N atoms in heavily doped samples, which will quench the recombination at the N-neutral centers and favors recombination of excitons at non-radiative center or boron related centers. Moreover, we also mentioned that this substrate luminescence could easily be observed when the epitaxial layer was of high quality and low doped even when using the 244 nm line as excitation for luminescence from relatively thick layers [9].

The work presented in this paper clearly shows that the broad band is due to the heavy nitrogen doping itself. The observed luminescence in the case of highly doped layer is expected to come only from the layer without contribution of substrate luminescence. The penetration depth of the excitation line (244 nm) is less than the microns [10] and due to the high doping of the layer exciton diffusion to the substrate is not expected to occur. The B concentration is below the SIMS detection limit in our layers and rules out the possibility to associate the BB with B-BE.

A shift of 20 meV is observed when the doping is increased from  $3 \cdot 10^{18} \text{ cm}^{-3}$  to a few  $10^{19} \text{ cm}^{-3}$ . These results should be compared with recently published calculation of band gap narrowing in SiC [4]. The energy position of the BB could be used for a calibration to obtain the N concentration in heavily doped n-type 4H-SiC.

#### Acknowledgments.

Support for this work was provided by the Swedish Council for Engineering Sciences (TFR), the SSF program SiCEP and ABB Corporate Research.

#### References

- [1] R.A. Abram, G.J. Rees and B.L.H. Wilson, *Adv. Phys.* 27 (1978) p. 799
- [2] J. Wagner, *Phys. Rev. B* 29, (1984) p. 2002
- [3] A.Souifi, G. Brémont, T. Benyattou, G. Guillot, D. Dutartre and P. Warren, *Appl. Phys. Lett.* 62 (1993) p. 2986
- [4] U. Lindefelt, *J. Appl. Phys.* 84 (1998) p. 2628.
- [5] C. Persson, U. Lindefelt, and B.E. Sernelius, submitted to *Phys. Rev. B* (1999)
- [6] O. Kordina, C. Hallin, A. Henry, J. P. Bergman, I. Ivanov, A. Ellison, N. T. Son, and E. Janzén; *Phys. Status Solidi B* 202, (1997) p. 321
- [7] I.G. Ivanov, C. Hallin, A. Henry, O. Kordina, and E. Janzén; *J. Appl. Phys.* 80, (1996) p. 3504
- [8] S.G. Sridhara, L.L. Clemen, R. P. Devaty, W. J. Choyke, D.J. Larkin, H.S. Kong, T. Troffer and G. Pensl, *J. Appl. Phys.* 83, (1998) p. 7909
- [9] A. Henry, I.G. Ivanov, A. Ellison and E. Janzén. *Mat. Science Eng. B* (1999) p. 234
- [10] S. G. Sridhara, R. P. Devaty, W. J. Choyke, *Journal Appl. Phys.* 84 (1998) p. 2963

Correspondence: A. Henry, Tel : 46 13 28 24 14, Fax: 46 13 14 23 37, e-mail : ahy@ifm.liu.se

## Low Temperature Photoluminescence of $^{13}\text{C}$ Enriched SiC-Crystals Grown by the Modified Lely Method

Horst Sadowski, Christian Peppermüller, Norbert Schulze, Michael Laube,  
Gerhard Pensl and Reinhard Helbig

Institute of Applied Physics, University of Erlangen-Nürnberg,  
Staudtstr. 7/A3, DE-91058 Erlangen, Germany

**Keywords:**  $^{13}\text{C}$ , Isotope, Low Temperature, Modified Lely Method, Photoluminescence, SIMS

**Abstract.** 6H-SiC was enriched with  $^{13}\text{C}$  during the sublimation growth in a modified Lely furnace. The samples were investigated by low temperature photoluminescence (LTPL). We report on an isotopic effect on the optical momentum-conserving phonon lines of the exciton recombination as well as on the zero phonon exciton recombination lines.

### Introduction

Atomic masses strongly influence the electronic and vibrational properties of semiconductors and, therefore, are a subject of current investigations for different semiconductor materials. Most papers are dealing with elemental semiconductors, like germanium (Ge) and diamond [1, 2]. The semiconductor with the largest mass spread is Ge [ $^{70}\text{Ge}$ ,  $^{73}\text{Ge}$ ,  $^{74}\text{Ge}$ ,  $^{76}\text{Ge}$ ]. Investigations of compound semiconductors especially of SiC were given by Widulle et al. [3]. In [3], the isotope composition in SiC was modified between natural Si (92.2%  $^{28}\text{Si}$ -atoms) and  $^{30}\text{Si}$ , in contrast we used substituted  $^{12}\text{C}$  by  $^{13}\text{C}$ . The isotope  $^{13}\text{C}$  in favor of  $^{30}\text{Si}$  was chosen because of the higher relative mass difference.

In this investigation, we have measured the photoluminescence emission spectrum of 6H-SiC at low temperature (1.9 K). SiC is an indirect semiconductor and the emission spectrum involves different electronic and vibronic processes and shows the influence of the isotopic composition on the different recombination processes.

### Experimental

The investigated 6H-SiC samples are nitrogen doped. They have been grown by the modified Lely method [4] using  $^{13}\text{C}$  powder and natural silicon powder ( $\approx^{28}\text{Si}$ ) in a graphite crucible. As a reference, a 6H-SiC boule has been grown under identical conditions, however, using  $^{12}\text{C}$  instead of  $^{13}\text{C}$ . The ratio of  $^{13}\text{C}$  to  $^{12}\text{C}$  in the samples was analyzed with secondary ion mass spectrometry (SIMS) in a ATOMIKA A-DIDA 3000-30 system (12 keV  $\text{O}_2^+$  beam).

For LTPL the SiC samples were immersed in superfluid helium in a bath cryostat at a temperature of 1.9 K. The excitation was done by a He-Cd laser at a wavelength of 325 nm and a power of 40 mW in back scattering geometry. To avoid the detection of plasma emission lines of the laser and to suppress the scattered UV light, two filters (Schott: UG11 and GG13) were used. A Czerny-Turner-monochromator (Spex 1700-III) with 1200/mm grating blazed at 5000 Å and slit widths of 50 µm and 25 µm gives a resolution of the photoluminescence light of 0.27 meV and 0.14 meV, respectively. A S20 photomultiplier tube operating in a photon-counting mode was used as detector.

### Results

SIMS measurements have shown that the ratio of  $^{13}\text{C}$  to  $^{12}\text{C}$  is about  $0.77 \pm 0.18$  in sample SN46. The ratio of  $^{12}\text{C}$  to  $^{13}\text{C}$  in sample SN52 ( $\sim 0.43$ ) is discussed elsewhere in this journal by S. Rohmfeld et al. by means of Raman measurements [5].

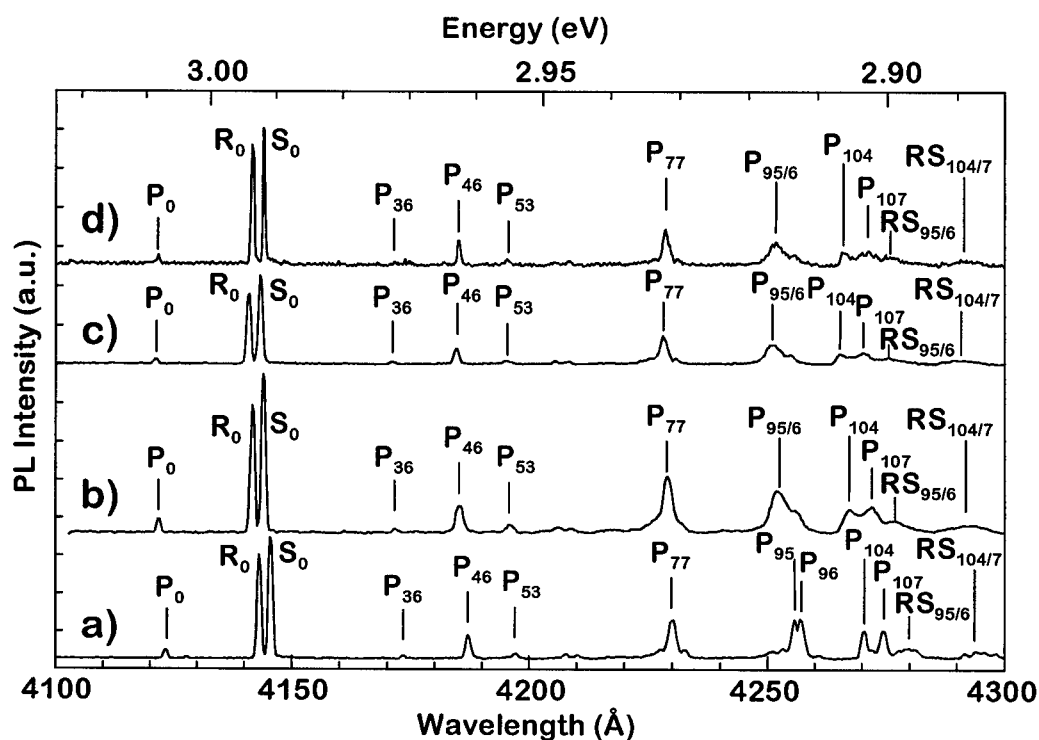


Fig. 1: Nitrogen-related LTPL spectra of 6H-SiC samples: (a) reference sample ( $^{12}\text{C}$ , monochromator slit width 50  $\mu\text{m}$ ), (b) sample SN52 ( $^{13}\text{C}$ , slit width 50  $\mu\text{m}$ ), (c) sample SN46 ( $^{13}\text{C}$ , slit width 50  $\mu\text{m}$ ), (d) sample SN46 ( $^{13}\text{C}$ , slit width 25  $\mu\text{m}$ ).

The LTPL spectra of nitrogen related zero phonon lines and their momentum conserving phonon lines as well as the titanium related zero phonon lines and their localized modes lines are shown in Fig. 1 and Fig. 2, respectively. To eliminate an absolute shift of the spectra due to the experimental setup, a reference spectrum of sample SN45 grown with  $^{12}\text{C}$  has always been recorded (see Figs. 1a) and 2a)). The LTPL spectra of sample SN52 are shown in Figs. 1b) and 2b) and of sample SN46 in Figs. 1c) and 2c) taken with a monochromator slit width of 50  $\mu\text{m}$ . To obtain a better resolution of the spectra (however with loss of intensity), we used a 25  $\mu\text{m}$  slit width to measure sample SN46 (see Figs. 1d) and 2d)).

The spectra show that the shift of the nitrogen related zero phonon LTPL lines relative to the reference sample in SN46 (~1.5 meV) is larger than in SN52 (~1.1 meV) (Tab. 1). The optical

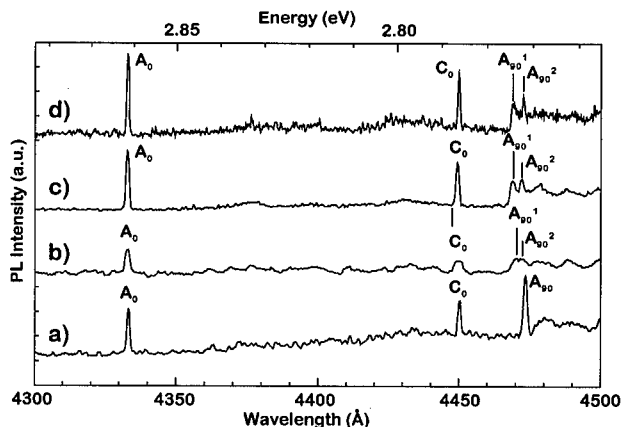


Fig. 2: Titanium-related LTPL spectra of 6H-SiC samples: (a) reference sample ( $^{12}\text{C}$ , monochromator slit width 50  $\mu\text{m}$ ), (b) sample SN52 ( $^{13}\text{C}$ , slit width 50  $\mu\text{m}$ ), (c) sample SN46 ( $^{13}\text{C}$ , slit width 50  $\mu\text{m}$ ), (d) sample SN46 ( $^{13}\text{C}$ , slit width 25  $\mu\text{m}$ ).



**Tab. 1:** Energies of zero-phonon lines and phonon-replica obtained from the LTPL data of Fig. 1 and Fig. 2.

	<sup>12</sup> C: SN45	<sup>13</sup> C: SN52	<sup>13</sup> C: SN46; 50 μm	<sup>13</sup> C: SN46; 25 μm
zero-phonon lines* : (meV)				
ΔE(P <sub>0</sub> )		1.2	1.6	1.5
ΔE(R <sub>0</sub> )		1.0	1.5	1.6
ΔE(S <sub>0</sub> )		1.0	1.4	1.5
ΔE(A <sub>0</sub> )		0.1	0.2	0.7
ΔE(C <sub>0</sub> )		0.7	0.7	0.3
momentum-conserving phonon energies				
-acoustic phonons (meV)				
P <sub>36</sub>	35.9	36.0	35.9	35.9
P <sub>46</sub>	45.7	45.6	45.7	45.6
P <sub>53</sub>	52.9	53.0	53.2	52.7
P <sub>77</sub>	76.0	76.4	76.1	76.0
-optical phonons (meV)				
The ratio of the phonon energies of the <sup>13</sup> C enriched to the <sup>12</sup> C reference sample are given in brackets (%)				
P <sub>95</sub>	93.5	92.2 (98.6)	92.0 (98.4)	92.0 (98.4)
P <sub>96</sub>	94.4			
P <sub>104</sub>	103.6	102.6 (99.0)	101.7 (98.1)	101.5 (98.0)
P <sub>107</sub>	106.3	105.9 (99.6)	105.2 (99.0)	105.3 (99.1)
RS <sub>95/96</sub>	95.0	94.0 (99.0)	93.5 (98.4)	92.6 (97.5)
RS <sub>104/107</sub>	104.4	105.1 (100.7)	102.6 (98.3)	103.3 (98.9)
A <sub>90</sub>	89.8	87.2 (97.1) 89.4 (99.6)	87.0 (96.9) 89.2 (99.3)	87.4 (97.3) 89.4 (99.6)

\* ΔE = zero-phonon line of <sup>13</sup>C enriched sample minus zero-phonon line of reference (e.g. SN45)

phonons also show a greater shift; whereas the acoustic phonons show no shift. The Ti-related shifts of the zero phonon lines are less than 0.7 meV.

### Discussion and Conclusion

As shown in Tab. 1, we have to discuss different radiative recombination processes and their observed isotopic shifts.

#### Recombination of bound excitons without phonon emission (P<sub>0</sub>-, R<sub>0</sub>-, S<sub>0</sub>-lines):

These emission lines were identified as radiative recombination of excitons bound to neutral nitrogen donors at different lattice sites [6]. If we neglect the dependence of the binding energy of excitons to a neutral impurity on the isotope masses, then the isotopic shift of the P<sub>0</sub>-, R<sub>0</sub>-, S<sub>0</sub>-lines is determined by the shift of the energy gap due to isotopic composition.

At a first glance, increasing masses vibrate with smaller amplitudes and the anharmonic contribution to the lattice free energy leads to a smaller lattice constant manifested in a larger band gap, as was observed by the shift of these recombination lines by hydrostatic pressure [7].

From first principles, the anharmonic terms are only one contribution to the isotopic shift of the band gap. The main part of the isotopic shift of the band gap is due to the renormalization of the electron phonon interaction [1, 2] and is not yet discussed in detail for a compound semiconductor. We like to point out that the shift of the P<sub>0</sub>-, R<sub>0</sub>-, S<sub>0</sub>-lines is proportional to a factor of 0.9996 as we go from <sup>12</sup>C to <sup>13</sup>C. This gives a hint to the expected dependence on the mass ratio  $\sqrt{Si^{12}C/Si^{13}C} \approx 0.988$  for a 100% <sup>13</sup>C substitution, if the motion of SiC-molecules in the different

sublattices is dominating the electron phonon interaction. If we take into account that our  $^{13}\text{C}/^{12}\text{C}$  substitution is about 77%, a satisfactory agreement with the experimental data is reached. Additionally we should mention that sample SN46 and sample SN52 have slightly different  $^{13}\text{C}/^{12}\text{C}$  ratios [5] because of their different shift of lines.

*Emission lines due to internal electronic transitions at an impurity (e.g.  $A_0$ -line):*

The  $A_0$  emission line was identified as an internal electronic transition at a Ti impurity [8]; the influence of the masses of the host crystal on the energy of this transition is expected to be very small, whereas a small isotope shift on the energy of the localized vibrational modes for this transition should exist (e.g. splitting of the  $A_{90}$  line). Both observations are firmed in Fig. 2 and Tab. 1.

*Emission lines due to phonon replica of radiative recombination of bound excitons ( $P_{36}$  to  $P_{107}$ ):*

The radiative recombination of bound excitons (e.g. at neutral nitrogen donors,  $P_0$ ,  $R_0$ ,  $S_0$ -lines) under emission of phonons ("little explosions") is a common recombination process in polar semiconductors. Since 6H-SiC is a indirect semiconductor, we can observe the contribution of different phonons to these recombination processes. The expectation that all these transitions show an isotopic shift is too simple.

For acoustic phonons with k-vectors near the L-point of the Brillouin zone, we observed no isotopic shift. In contrast samples enriched with  $^{30}\text{Si}$ , the isotopic shift for the LA- and the TA-phonons show a maximum [3], but in this case only the isotopes of the Si-sublattice are changed. We have observed a maximal isotopic shift for the mass ratio  $\sqrt{^{12}\text{Si}/^{13}\text{Si}} \approx 0.988$ . This experimental result has to be analyzed in detail by the corresponding phonon eigenvectors at the L-point of the Brillouin zone.

### Summary

We have shown that the influence of the isotopic composition of an indirect compound semiconductor on the LTPL-spectrum includes different contributions of the electron phonon interaction. Especially for SiC, it is promising to investigate the LTPL-spectra of samples with different Si-isotopes.

### Acknowledgment

We thank Stefan Rohmfeld and Martin Hundhausen for fruitful discussions. This project was supported by the Deutsche Forschungsgemeinschaft (Sonderforschungsbereich 292) and the Bayerische Forschungsförderung.

### References

- [1] C. Parks, A. K. Ramdas, S. Rodriguez, K. M. Itoh, and E. E. Haller, Phys. Rev. B **49** (1994), p. 14 244.
- [2] S. Zollner, M. Cardona, and S. Gopalan, Phys. Rev. B **45** (1992), p. 3376.
- [3] F. Widulle, T. Ruf, O. Buresch, A. Debernardi, and M. Cardona, Phys. Rev. Lett. **82** (1999), p. 3089
- [4] N. Schulze, D.L. Barrett, and G. Pensl, Appl. Phys. Lett. **72**, (1998), p. 1632.
- [5] S. Rohmfeld, M. Hundhausen, N. Schulze, G. Pensl and L. Ley, to be published in this Proceedings, p. 579
- [6] W.J. Choyke, L. Patrick, Phys. Rev. **127** (1962), p. 1868.
- [7] F. Engelbrecht, J. Zeman, G. Wellenhofer, C. Peppermueller, R. Helbig, G. Martinez, and U. Roessler, Phys. Rev. B **56**, 69 (1997), p. 7348.
- [8] L. Patrick and W.J. Choyke, Phys. Rev. B **10** (1974), p. 5091.

## Sub- $\mu\text{m}$ Scale Photoluminescence Image of SiC and GaN at a Low Temperature

Masahiro Yoshimoto<sup>1</sup>, Motoki Goto<sup>1</sup>, Junji Saraie<sup>1</sup>, Tsunenobu Kimoto<sup>2</sup>  
and Hiroyuki Matsunami<sup>2</sup>

<sup>1</sup>Department of Electronics and Information Science, Kyoto Institute of Technology,  
Matsugasaki, Sakyo-ku, Kyoto, 606-8585, Japan

<sup>2</sup>Department of Electronic Science and Engineering, Kyoto University,  
Yoshidahonmachi, Sakyo, Kyoto, 606-8501, Japan

**Keywords:** Defect, Donor-Acceptor Pairs, Excitonic Emission, Impurity, Non-Radiative Recombination, Photoluminescence Image, Polytypism, Sub-Micron Resolution

**Abstract:** We have developed a novel system to obtain a photoluminescence (PL) image with a resolution in a range of sub- $\mu\text{m}$  at 15 K. At a line-shaped surface defect in a 4H-SiC homoepitaxial layer, a PL image of an emission ascribed to excitons bound to neutral nitrogen atoms showed a dark line, indicating that a non-radiative recombination dominates the excitonic emission at the surface defect. The spatial distribution of cubic and hexagonal phases of GaN grown on sapphire by MBE was discriminated with a resolution of 0.4  $\mu\text{m}$ . The microscopic PL imaging is promising for characterization of distributions of polytypism, defects, and impurities in sub- $\mu\text{m}$  scale for SiC and GaN.

### Introduction

Many efforts have been made to obtain a photoluminescence (PL) image of a semiconductor with a resolution around 0.1  $\mu\text{m}$  by using a scanning near-field optical microscope (SNOM)[1,2]. Because of the nature of evanescent light, however, the PL signal exponentially decreases with improving spatial resolution in SNOM[2]. The low signal yield of SNOM limits its application to characterization of very luminescent materials such as InAs-related quantum dots. On the other hand, a microscopic PL equipment using ordinary optics has a potential to obtain a PL image with both a much higher signal yield than SNOM and a spatial resolution in an order of the wavelength of light. This leads to a high throughput and an improved signal-noise ratio. In addition, compared to cathode luminescence (CL), the PL system has the advantage of controllability of both the energy and the intensity of excitation light.

The spatial resolution  $\Delta$ , defined by the full width of the half maximum (FWHM) of the intensity of the focused light, is expressed as  $\Delta = 0.52\lambda/N_A$  based on the conventional optics. Here,  $N_A$  is the numerical aperture of an objective,  $\lambda$  the wavelength of light. The value of  $N_A$  is defined as  $N_A = n\sin(\varphi)$  where  $n$  is the refractive index of the medium between an objective and a sample, and  $\varphi = \arctan(D/2F)$  using the diameter of the objective,  $D$ , and the focal length,  $F$ . The larger value of  $N_A$  results in a more improved spatial resolution. Furthermore, the large  $N_A$  improves the optical outputs of PL signal in the form of  $N_A^2$ .

The large value of  $N_A$  coincides with a small focal length, resulting in a small working distance between a sample and the objective. An available objective with a high  $N_A$  for sub- $\mu\text{m}$  resolution has a small working distance less than 1 mm. While it is not difficult to realize a spatial resolution of sub- $\mu\text{m}$  in PL observation at room temperature, it has been difficult to carry out PL measurement with the high spatial resolution at a cryogenic temperature because of difficulty in thermal insulation at the small gap (< 1 mm) between a cooled sample and an objective[3,4]. In this study, a PL image with a resolution of sub- $\mu\text{m}$  was obtained at 20-30 K in the newly developed microscopic PL system.

### Cryogenic PL microscope with sub- $\mu\text{m}$ resolution

In the newly developed microscopic PL system, both an objective and a sample are equipped in a vacuum chamber. The sample holder was able to be cooled down to 15 K using a cryostat with circulated liquid-He flow. In vacuum, the small working distance is enough to make thermal insulation between the sample and the objective. The thermal conduction by radiation between the objective and the sample was estimated to be much less than the cooling capability of the cryostat equipped in the chamber. The excitation light emitted from He-Cd laser (wavelength: 325 nm) is focused on the sample via an objective consisting of quartz with  $N_A$  of 0.5 and a working distance of 1 mm. The spatial resolution defined as  $\Delta = 0.52\lambda/N_A$  is calculated to be 0.4  $\mu\text{m}$  at a wavelength of 400 nm. The PL emission from the sample was acquired by the same objective, and transmitted to a monochromator via lenses and an optical fiber. PL signal was detected by a photomultiplier with a photon counting system. The sample can be two-dimensionally scanned by a piezo actuator with a spatial resolution of 0.1  $\mu\text{m}$  and a travel of 25 mm for PL mapping.

### Influence of surface defect on PL in 4H-SiC epilayer

A homoepitaxial 4H-SiC layer with a thickness of 30  $\mu\text{m}$  was obtained using step-controlled epitaxial growth on off-oriented 4H-SiC{0001} faces at 1500 °C by atmospheric pressure CVD using a  $\text{SiH}_4\text{-C}_3\text{H}_8\text{-H}_2$  system[5]. The net donor concentration of the epilayer was determined to be  $1 \times 10^{16} \text{ cm}^{-3}$  based on the capacitance-voltage measurement. In the micro-PL system, PL spectra of a 4H-SiC homoepitaxial layer at 30 K showed a main peak  $Q_0$  at 3.25 eV ascribed to recombination of excitons bound to neutral nitrogen donors[6] as shown in Fig.1. In this measurement, the intensity of the laser beam with a diameter of  $\sim 1 \mu\text{m}$  was measured to be 5  $\mu\text{W}$  that corresponds to an order of 100  $\text{W}/\text{cm}^2$ . A broad peak ascribed to recombination of donor(N)-acceptor(B) pairs is observed in a range between 2.2-2.7 eV [7] as also shown in Fig.1. Emissions ascribed to free excitons and phonon replicas of the  $Q_0$  peak[8] were observed as a broad emission in a range from 3.0 to 3.2 eV in Fig.1 owing to a low wavelength resolution of the monochromator with a widely open slit to obtain an intense signal.

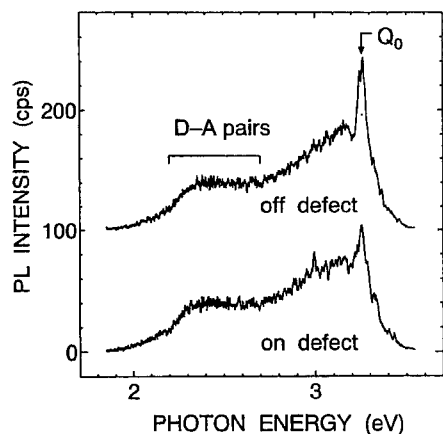


Fig. 1: PL spectra of 4H-SiC.

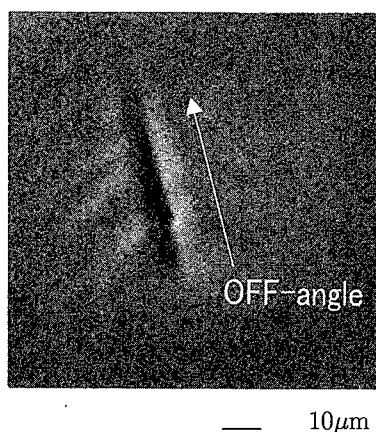


Fig. 2: Real image of line-shaped surface defect

PL images were obtained at 30 K for an area including a line-shaped surface defect. Figure 2 shows a real image of the defect observed by a Nomarski optical microscope. The line shape is formed along the direction to the off-angle of the substrate: a screw dislocation of the substrate probably disturbs the step-flow during the growth, which results in the defect. As shown in Fig.1, the excitonic PL peak is suppressed in the case that the excitation beam focused on the

defect. On the other hand, the PL intensity of the donor-acceptor pairs on the defect almost equals to that at a position outside the defect. An image of the excitonic peak intensity at 3.25 eV shows a dark line coincident with the line-shaped defect as shown in Fig.3(a). The intensity of dark line is evaluated to be 70 % of that outside the defect. In an image of the emission from the donor-acceptor pairs measured at 2.37 eV as shown in Fig.3(b), the area in which the dark line is observed in Fig.3(a) is surrounded by a slightly bright zone. The zone coincident with the edge of the defect is possibly caused by a reported gettering effect in which an emission from donor-acceptor pairs was enhanced at the defect[9]. The inside of the defect shows the almost same PL intensity as the outside of the bright zone. In other words, the PL image at 2.37 eV in Fig.3 (b) does not show a distinct fluctuation in the same dynamic range of the PL intensity in Fig. 3(a) except the tiny bright zone. Therefore, the nitrogen donors are uniformly incorporated into the epilayer independent of the existence of the defect. The dark line in the PL image at the excitonic peak indicates that a non-radiative recombination competitive to the excitonic recombination is enhanced at the defect including dislocations and point defects.

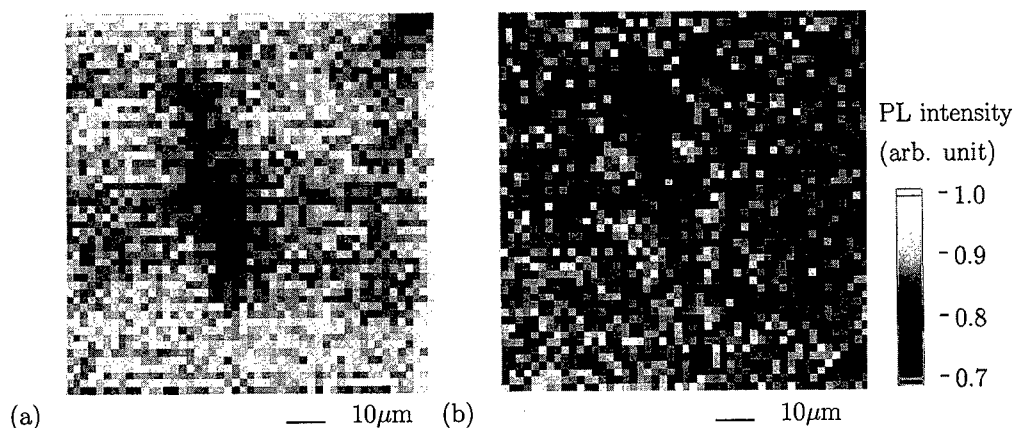


Fig. 3: PL image of 4H-SiC ascribed to (a) excitons bound to neutral N,  $Q_0$ , and (b) donor(N)-acceptor(B) pairs.

#### Discrimination of polytypism in GaN epilayer

GaN heteroepitaxial layers were grown on sapphire{0001} by MBE using Ga metal and nitrogen radicals generated in an rf plasma (13.6 MHz, 250 W). The sapphire substrate was nitrided with an irradiation of nitrogen radicals for 5 min prior to GaN growth. A buffer layer consisting of GaN or AlN was not grown before GaN growth. The Ga flux was changed from  $0.8 \times 10^{-7}$  to  $11 \times 10^{-7}$  Torr with a constant  $N_2$  supply of 1.0 sccm. In the case of small Ga flux less than  $3 \times 10^{-7}$  Torr, the growth rate increased with the Ga flux (Ga-supply controlled region), and the grown layer showed smooth surface. In the case of Ga flux more than  $3 \times 10^{-7}$  Torr, the growth rate was kept constant probably limited by the constant supply of nitrogen (N-supply controlled region), and the grown surface became rough including Ga droplets.

Figure 4 shows examples of PL spectra of GaN grown at N-supply controlled region. The spectra were obtained at 11K with a He-Cd laser (325 nm, 1 mm in diameter of the laser beam). The peak at around 3.45 eV is ascribed to an excitonic emission from hexagonal GaN. The spectra also include an excitonic peak of the cubic phase at 3.27 eV, indicating mixture of cubic and hexagonal phases[10]. Figure 5 shows an image of the ratio between the PL intensity at 3.27 eV,  $I_{\text{cub}}$ , and that at 3.45 eV,  $I_{\text{hex}}$ , at 20 K. The image indicates a mixture of cubic and hexagonal phases in a resolution of around  $0.4 \mu\text{m}$ . In the case of the sample with Ga flux of

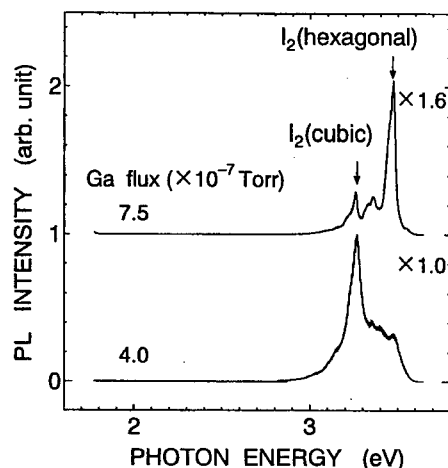
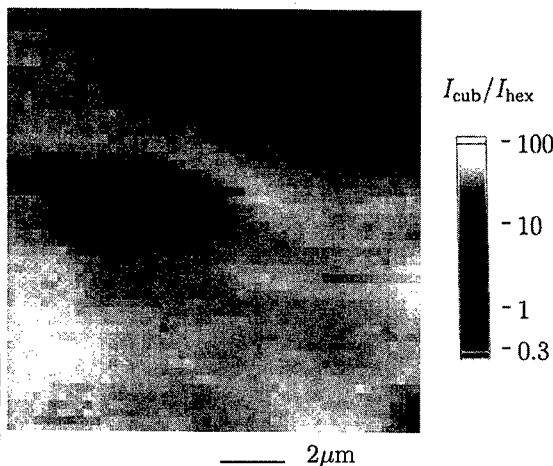


Fig. 4: PL spectra of GaN

Fig.5: PL image of peak intensity ratio  $I_{\text{cub}}/I_{\text{hex}}$ 

$4.0 \times 10^{-7}$  Torr in which the formation of Ga droplets was fairly suppressed compared to the case of Ga flux  $= 7.5 \times 10^{-7}$  Torr, the contribution of the hexagonal phase became much small in the PL image. The formation of Ga droplets in the N-supply controlled region probably enhances the formation of the hexagonal phase. The epilayer grown at the Ga-supply controlled region showed a fairly uniform PL image with a domination of the hexagonal phase.

### Summary

We have developed a novel system to obtain a PL image with a resolution of  $0.4 \mu\text{m}$  at a low temperature. At a line-shaped surface defect in a 4H-SiC homoepitaxial layer, a PL image ascribed to excitons bound to neutral nitrogen atoms showed a dark line coincident with the defect. The PL emission from donor(nitrogen)-acceptor(boron) pairs was spatially uniform independent of the presence of the defect. This indicates that the spatial distribution of nitrogen atoms in the 4H-SiC epilayer is fairly uniform, and a non-radiative recombination dominates the excitonic emission at the surface defect. The spatial distribution of cubic and hexagonal phases of GaN grown by MBE was discriminated with a resolution of  $0.4 \mu\text{m}$ . The microscopic PL imaging is promising for characterization of spatial distributions of polytypism, defects, and impurities in SiC and GaN.

### References

- [1] H. F. Hess, E. Betzig, T. D. Harris, L. N. Pfeiffer and K. West, *Science* 264 (1994) p.1740.
- [2] T. Sakai, Mononobe, M. Ohtsu, N. Saito, K. Kusano, *Appl. Phys. Lett.*, 68 (1996) p.2612.
- [3] J. Bellessa, V. Voliotis, R. Grousson, X. L. Wang, M. Ogura, and H. Matsushita, *Appl. Phys. Lett.*, 71 (1997) p.2481.
- [4] H. M. Cheong, A. Mascarenhas, S. P. Ahrenkiel, K. M. Jones, J. F. Geisz, and J. M. Olson, *J. Appl. Phys.*, 83 (1998) p.5418.
- [5] H. Matsunami and T. Kimoto, *Mat. Sci. & Eng. R20* (1997) p.125.
- [6] W. J. Choyke, L. Patrick and D. R. Hamilton, *Proc. 7th Conf. on Physics of Semiconductors, Paris*, (Dunod, Paris 1964), p.751.
- [7] M. Ikeda, H. Matsunami, and T. Tanaka, *Phys. Rev. B*, 22(1980) p.2842.
- [8] R. P. Devaty and W. J. Choyke, *Phys. Stat. Sol. (a)* 162 (1997) p.5.
- [9] M. Tajima, Y. Kumagaya, T. Nakata, M. Inoue, and A. Nakamura, *Jpn. J. Appl. Phys.*, 36 (1997) p.L1185.
- [10] A. Nakadaira and H. Tanaka, *J. Electron. Mater.* 26 (1997) p.320.

## Vanadium-related Center in 4H Silicon Carbide

B. Magnusson, Mt. Wagner, N.T. Son and E. Janzén

Department of Physics and Measurement Technology, Linköping University,  
 SE-581 83 Linköping, Sweden

**Keywords:** Electronic Structure, Photoluminescence, Vanadium

### Abstract

The  $V^{4+}$  ( $3d^1$ ) center in 4H SiC is investigated using photoluminescence (PL) and photoluminescence excitation (PLE). The energy position of the ground state of the defect is determined to be  $2.1 \pm 0.1$  eV **below** the conduction band for both the hexagonal and the quasi-cubic site. A broad peak in the PLE spectrum is tentatively ascribed to the excited  $A_1$  state, previously believed to be located in the conduction band.

### 1 Introduction

Vanadium in SiC has been identified in different polytypes [1], but the understanding of the internal transition within the open d-shell for both the hexagonal and quasi-cubic sites is not complete. The ordinary level scheme of the defect (Fig. 1) predicts an additional excited state ( $A_1$ ) which was not observed in previous investigations. This upper excited state was assumed to be located in the conduction band and therefore escaped detection.

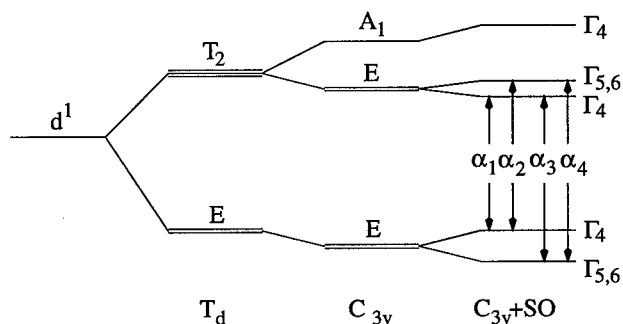


Fig. 1. Crystal field model of the  $V_{Si}^{4+}$  ( $3d^1$ ) applied to the hexagonal site. Successive level splittings due to the cubic field ( $T_d$ ), the trigonal field ( $C_{3v}$ ) and the spin-orbit interaction (SO) [2],[3].

In this investigation we have performed photoluminescence excitation (PLE) experiments to determine the energy position of the ground state of the V center. We have also tried to locate the excited state ( $A_1$ ), see Fig. 1.

## 2 Experiments

Most studies of V in SiC have concentrated on the 6H polytype. 4H SiC is somewhat less complicated than 6H SiC with one hexagonal site and only one quasi-cubic site instead of two. The larger bandgap of 4H SiC may allow the excited state ( $A_1$ ) to be in the bandgap instead of in the conduction band as assumed for the 6H polytype. The sample used in this study is a commercial semi-insulating 4H SiC wafer.

The PL measurements were done at low temperature (10 K) using a Fourier transform technique. The sample was excited with the ultraviolet lines (351.1-363.8 nm) of an Ar<sup>+</sup> laser, and the luminescence was detected with a Bomem DA8 Fourier transform spectrometer equipped with a quartz beamsplitter and a North Coast Ge detector.

Two different kinds of PLE techniques were used in this study; (1) a Fourier transform technique (FTPLE) performed at 10 K and (2) a conventional PLE technique using a lamp performed at 15 K. In the FTPLE technique the sample was excited with modulated light from a Bomem DA8 Fourier transform spectrometer equipped with a quartz halogen lamp and quartz beamsplitter. The detection were done with a Spex 0.22m double grating monochromator and a North Coast Ge detector. In the conventional PLE setup a 50W Xenon lamp together with a 0.25m ISA Jobin Yvon H25 monochromator were used as excitation source. The luminescence were dispersed by an ISA Jobin Yvon HRD1 monochromator and detected by a North Coast Ge detector.

## 3 Results and Discussion

In the FTPL spectrum in Fig. 2 we have completely resolved not only the no-phonon lines (NPLs) at the hexagonal and quasi-cubic sites but also the phonon-assisted spectrum. By comparing with published PL data from V doped SiC [1] it is concluded that the  $\alpha$  NPLs are related to the hexagonal site and  $\beta$  NPLs to the quasi-cubic site. The  $\alpha$  NPLs can be resolved into four sharp lines, while the  $\beta$  NPLs only into two lines.

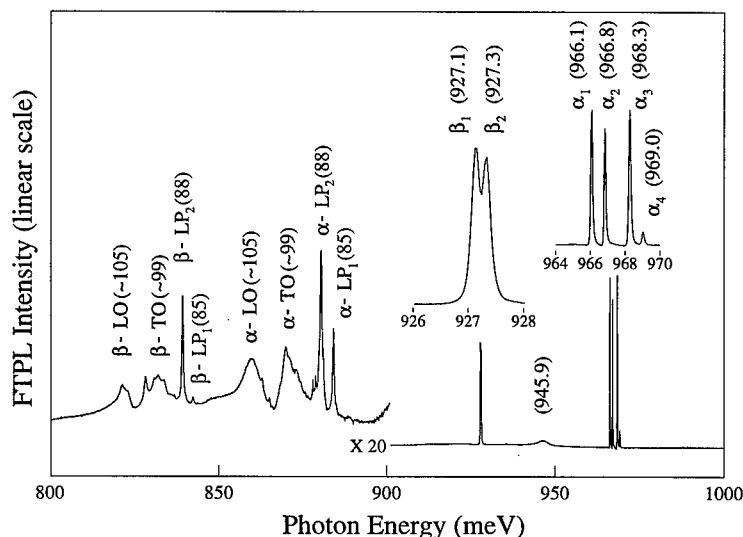


Fig. 2. FTPL measurement on V doped 4H SiC. Energy values are given in meV.



The phonon-assisted spectrum can be explained by two local phonons ( $LP_1$ : 85 meV,  $LP_2$ : 88 meV) and two optical lattice phonons (TO: 99 meV, LO: 105 meV). The same local phonons have earlier been observed for V doped 6H SiC [1] and they have similar energies to those reported for Cr doped SiC [4]. Note that for the  $\alpha$ - $LP_2$  all the four  $\alpha$  NPLs are replicated.

The energy position of the V defect at the two different sites is determined by PLE with a Xenon lamp. In Fig. 3a and 3b the PLE spectra are shown after filtering using standard Savitsky-Golay smoothing [5]. The  $\alpha$  NPLs and the  $\beta$  NPLs were used as monitor signals for the defect at the hexagonal and the cubic sites, respectively.

Two different processes may in principle give rise to the spectra in Fig. 3. Either the electron at the V defect is promoted to the conduction band and then later captured to the defect again or electrons and holes are generated via another deep defect not visible in PL, which after diffusion are captured to the V defect. In the latter case the two spectra should be identical. Since they deviate slightly from each other we can conclude that the PLE spectra in Fig. 3 are related to the V defect itself.

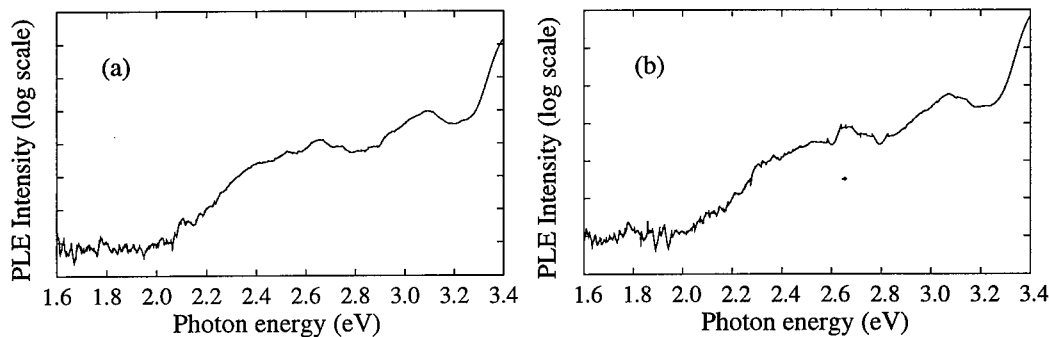


Fig. 3. PLE spectrum of V doped 4H SiC when a) the  $\alpha$  NPLs b) the  $\beta$  NPLs are used as monitor signals.

From Fig. 3a the energy position of V at the hexagonal site is determined to  $2.1 \pm 0.1$  eV from the conduction band, which is the same value as obtained for V at the quasi-cubic site, see Fig. 3b. The bandgap absorption edge at 3.3 eV is clearly observed. The two broad peaks at 2.65 eV and 3.1 eV are not related to the V defect but originate from the lamp.

To confirm the PLE measurement presented above selective photoluminescence measurements were performed. This was done with the FTPL setup described in section 2, but now with the Xenon lamp together with a monochromator as excitation source instead of an Argon laser. A weak PL spectrum like the one in Fig. 2 could be detected when the monochromator was set to 2.25 eV but no photoluminescence was observed when the excitation energy was decreased to 1.95 eV.

In the FTPL measurements, Fig. 4, we observed both the  $\alpha$  and the  $\beta$  NPLs. The  $\alpha$  NPLs are 25 times stronger than the  $\beta$  NPLs, since here PL from the  $\alpha$ -related phonon replicas was monitored. The lines between 1050 and 1100 meV originate from phonon-assisted absorption of the  $\alpha$  NPLs. These phonons are  $LP_1$ ,  $LP_2$ , TO and LO with energies given in Fig. 2.

In the crystal-field approach for the hexagonal site, the splitting between the two excited states was estimated to be 74 meV for the 6H polytype [6]. In 4H SiC it should be roughly the same, at least of the same order. In the FTPL measurement in Fig. 4, excitation up to 300 meV above the lowest excited state (E) was used. The only structure found besides the phonon assisted absorption of the  $\alpha$ -NPLs is a broad peak at 1000 meV (33 meV above the  $\alpha$ -NPLs), with the width of approximately 15 meV. Although we cannot explain the broadness we assume that this peak is related to the excited  $A_1$  state.

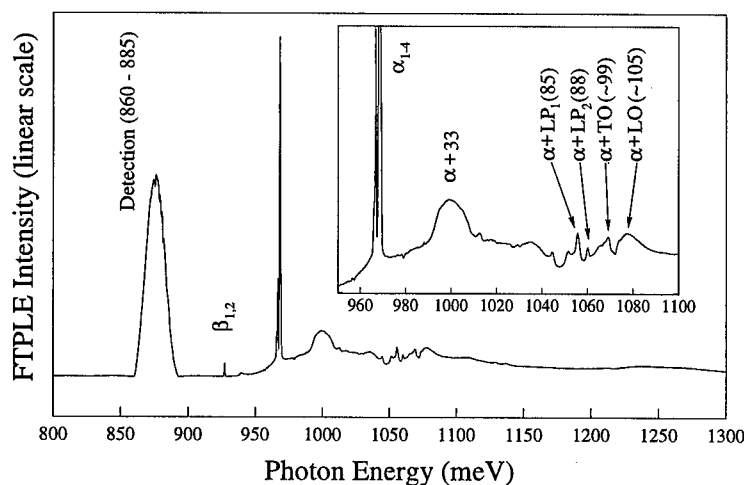


Fig. 4. FTPLE measurement on V doped 4H SiC. Energy values are given in meV.

## 4 Conclusion

In summary, the energy position of V in 4H SiC is about 2.1 eV below the conduction band for both the hexagonal and the quasi-cubic site as determined from PLE measurements. The FTPLE result show a new broad peak 33 meV above the hexagonal no-phonon line. We tentatively ascribe this peak to the excited  $A_1$  state.

## Acknowledgements

This work was supported by the SSF program SiCEP, Swedish Research Council for Engineering Sciences (TFR), Swedish Natural Science Research Council (NFR) and Ericsson Research Foundation.

## References

- [1] J. Schneider, H.D. Müller, K. Maier, W. Wilkening, F. Fuchs, A. Dörnen, S. Leibenzeder and R. Stein, *Appl. Phys. Lett.* **56** (1990), p. 1184.
- [2] K. Maier, H.D. Müller, and J. Schneider, *Mater. Sci. Forum.* **83-87** (1992), p. 1183.
- [3] J. Reinke, H. Weihrich, S. Greulich-Weber, and J-M. Spaeth, *Semicond. Sci. Technol.* **8** (1993), p. 1862.
- [4] N.T. Son, A. Ellison, M.F. MacMillan, O. Kordina, W.M. Chen, B. Monemar, and E. Janzén, *Mater. Sci. Forum* **264-268** (1998), p. 603.
- [5] A. Savitsky, and M. Golay, *Analy. Chem.* **36** (1964), p. 1627.
- [6] B. Kaufmann, A. Dörnen and F.S. Ham, *Phys. Rev. B* **55** (1997), p. 13009.

## Spectroscopic Investigation of Vanadium Acceptor Level in 4H and 6H-SiC

V. Lauer<sup>1</sup>, G. Brémond<sup>1</sup>, A. Souifi<sup>1</sup>, G. Guillot<sup>1</sup>, K. Chourou<sup>2</sup>, R. Madar<sup>2</sup>  
and B. Clerjaud<sup>3</sup>

<sup>1</sup>Laboratoire de Physique de la Matière (UMR CNRS 5511), INSA, 20 avenue A. Einstein,  
FR-69621 Villeurbanne Cedex, France

<sup>2</sup>Laboratoire des Matériaux et Génie Physique (UMR CNRS 5628), INPG-ENSPG, BP 46,  
FR-38042 Saint-Martin d'Heres, France

<sup>3</sup>Laboratoire d'Optique des Solides (UMR CNRS 7601) Case Courrier 80, Université Pierre et  
Marie Curie, 4 place Jussieu, FR-75252 Paris Cedex 05, France

**Keywords:** DLOS, Optical Absorption, Vanadium

### Abstract

We report a study on the  $V^{4+}/V^{3+}$  deep acceptor level in non intentionally vanadium doped 6H and 4H n-type SiC grown by the Lely modified method using Optical Absorption (OA) and Deep Level Optical Spectroscopy (DLOS). Comparison of DLOS and OA spectra measured on 6H and 4H substrate allows us to identify OA lines and DLOS resonance band as  $V^{3+}$  internal transition between the ground state  $^3A_2$  to excited states. We deduce the  $V^{3+}$  configuration in the 6H and the 4H-SiC band gap with energetic positions. Some of the DLOS spectra thresholds are interpreted as transition from the  $V^{3+}$  ground level to the successive conduction band minima.

### I - Introduction

The interest of Vanadium (V) in SiC is well documented in a series of papers showing that semi-insulating SiC had been obtained by vanadium doping [1-6]. It is known that vanadium acts as an amphoteric impurity causing both deep donor states ( $V^{4+}(3d^1)/V^{5+}(3d^0)$ ) and deep acceptor state ( $V^{4+}(3d^1)/V^{3+}(3d^2)$ ).  $V^{4+}$  charge state has been intensively studied by optical characterization techniques. The purpose of this investigation is to give more information about  $V^{3+}$  charge state in SiC using Optical Absorption (OA) and Deep Level Optical Spectroscopy (DLOS).

### II - Experiments

#### A- Samples

Bulk 6H and 4H-SiC crystals were grown by the modified Lely method. Samples were n-type and non-intentionally V doped. Schottky diodes were fabricated by evaporating Au dots 500  $\mu$ m diameter onto one side. Ohmic contacts were realized with Au large contact area on the back side after KOH etching. DLOS measurements require light transmission through the Schottky diode, achieving by a small thickness contact (< 250 Å).

#### B- Experimental set-ups

Absorption measurements have been performed with a Michelson Fourier-Transform interferometer, equipped with a tungsten quartz-halogen source, a quartz beam splitter, and a cooled InAs detector. The samples are cooled in a continuous flow helium cryostat. The polarization of the light beam is perpendicular to the c-axis of the crystals.

DLOS allowed us to measure at a fixed temperature the optical photoionization cross section  $\sigma_n^0$  of a deep level detected by DLTS. The basic point of DLOS is to control accurately via DLTS set up, the initial trap population before to measure the photocapitance transient. The details about the experimental methodology (filling pulse bias, light illumination conditions, data analysis) can be found in reference [7]. Photoionization spectrum of a transition metal can be interpreted as transitions towards conduction band minima or towards the excited states which can be near or resonant with the conduction band.

### III - Results and Discussion

#### A- DLTS Results

DLTS results have been presented in a previous paper [8]. DLTS measurements on 6H-SiC reveal two levels related to V acceptor state ( $V^{3+}/V^{4+}$ ) in 6H-SiC, at  $E_c - 0,68$  eV for the cubic sites and at  $E_c - 0,74$  eV for the hexagonal site [8-11]. For 4H-SiC, only one level associated to the V acceptor state is found at  $E_c - 0,8$  eV [8].

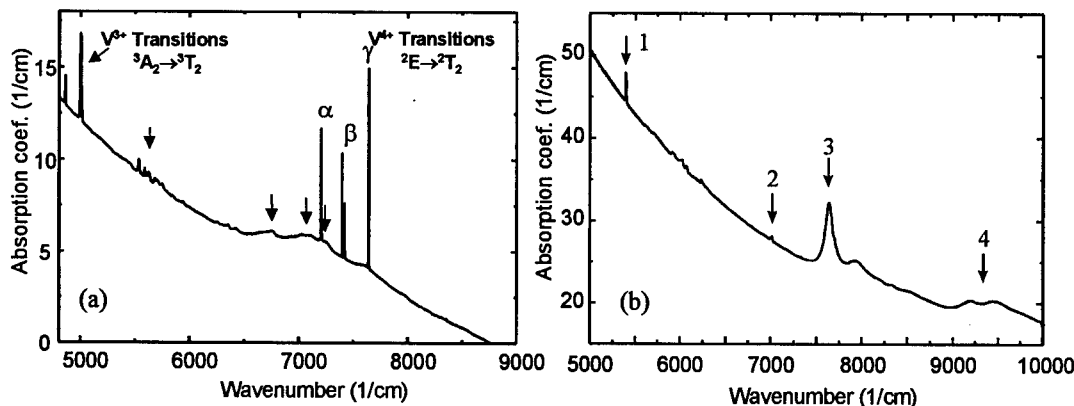
#### B- OA Results

OA measurements on 6H-SiC (fig. 1(a)) reveal classical absorption spectrum of  $V^{4+}$  ( $3d^1$ ) [8]. We can also distinguish connected additional lines between  $4800\text{ cm}^{-1}$  and  $5100\text{ cm}^{-1}$  and other structures between  $5400\text{ cm}^{-1}$  and  $5900\text{ cm}^{-1}$ . Based on DLTS results showing high vanadium contamination and according to works done on  $V^{3+}$  OA in III-V compound [12], we suppose that these lines are correlated to  $V^{3+}$  internal transitions. With this hypothesis, we confirm  $V^{3+}$  internal transition observation by MCD-ESR made by Kunzer et al. [13]. Lines at  $4860\text{ cm}^{-1}$  and  $5002\text{ cm}^{-1}$  are due to the  ${}^3A_2 \rightarrow {}^3T_2$  internal transition of the  $V^{3+}$  center. Lines between  $5400\text{ cm}^{-1}$  and  $5900\text{ cm}^{-1}$  are phonon replicas. Moreover we can distinguish absorption structures close to  $V^{4+}$  lines absorption. There could be related to  ${}^3A_2 \rightarrow {}^3T_1$   $V^{3+}$  transition.

Figure 1(b) shows OA spectrum for 4H-SiC sample with no evidence of classical  $V^{4+}$  absorption lines [8]. But the spectrum exhibits new lines and structures indicated by arrows. The spectrum interpretation has been done considering  $V^{3+}$  configuration in tetrahedral symmetry relevant for cubic site in 4H-SiC and showed on figure 2 [12]. The doublet (1) observed at  $5400\text{ cm}^{-1}$  is analog to the one observed for 6H substrate and related to  ${}^3A_2 \rightarrow {}^3T_2$   $V^{3+}$  transition. Structures between  $5600$  and  $6300\text{ cm}^{-1}$  are phonon replicas. Moreover, according to studies made on V doped GaAs or InP, we suppose that lines and structures on figure 2(b) are related to  $V^{3+}$  internal transition in 4H-SiC [12]. We confirm that the  ${}^3A_2 \rightarrow {}^3T_1$  transition (3) allowed by the crystal field is more important than the  ${}^3A_2 \rightarrow {}^3T_2$  transition (1) forbidden by the crystal field but allowed by the spin orbit coupling. Table 1 gives 4H OA spectrum interpretation.

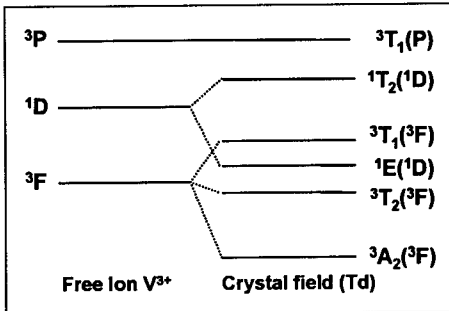
Besides, PL measurements on 4H-SiC revealed a line at  $5000\text{ cm}^{-1}$ . This result is presented in a previous paper [8]. This line is associated to the OA doublet 1 and attributed to  ${}^3T_2 \rightarrow {}^3A_2$  transition of  $V^{3+}$ . Up to now no PL line has been observed for 6H substrates in this energy range.

Fig 1: (a) 6H-SiC OA spectrum revealing classical  $V^{4+}$  absorption lines and additional lines or



structures (indicated by arrows) attributed to  $V^{3+}$  transition.

(b) 4H-SiC OA spectrum showing new structures attributed to  $V^{3+}$  intracenter transitions. Lines marked by arrows are respectively on  $5397$  and  $5403\text{ cm}^{-1}$  for doublet 1,  $7012\text{ cm}^{-1}$  for line 2,  $7641\text{ cm}^{-1}$  for structure 3 and  $9202\text{ cm}^{-1}$  for structure 4.



4H-SiC OA lines	Interpretation by $V^{3+}$ transition
1	${}^3A_2 \rightarrow {}^3T_2$
2	${}^3A_2 \rightarrow {}^1E$
3	${}^3A_2 \rightarrow {}^3T_1(F)$
4	${}^3A_2 \rightarrow {}^3T_1(P)$

Table 1: 4H-SiC OA lines and structures interpretation as  $V^{3+}$  intracenter transition.

Fig. 2: Crystal field level scheme of a  $3d^2$  ion in tetrahedral symmetry [12].

### C- DLOS Results

For DLOS measurements, temperatures were such that V acceptor level thermal emission rate was negligible. By using a filling pulse, we make sure that the level is in the  $V^{3+}$  charge state. Then DLOS spectra must be interpreted as  $V^{3+}$  photoionization spectra.

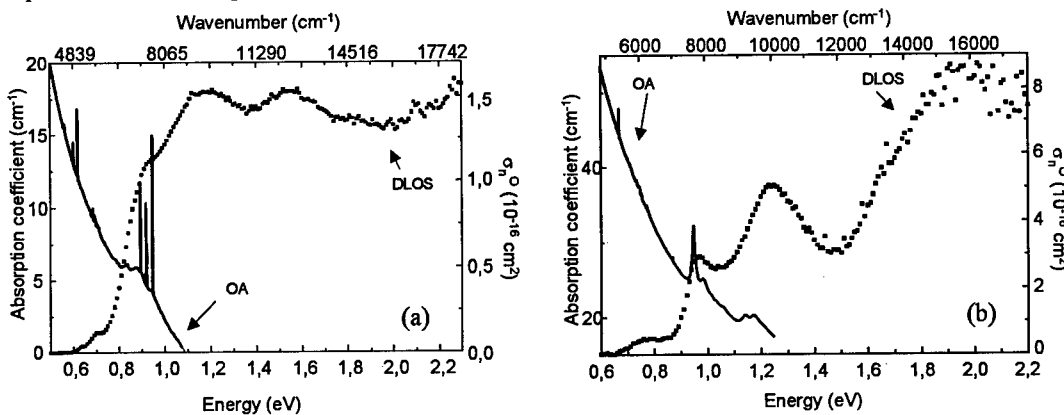


Fig. 3: (a) Comparison of 6H-SiC DLOS spectrum (200 K) and optical absorption spectrum (6K). (b) Comparison of 4H-SiC DLOS spectrum (300 K) and optical absorption spectrum (6K).

Figure 3 presents DLOS and OA spectra for 4H-SiC and 6H-SiC. Optical ionization cross section of  $V^{4+}/V^{3+}$  level is well correlated with the shape of OA spectra. First of all, 4H-SiC DLOS spectrum threshold at 0,65 eV is correlated to the first OA line and attributed to  $V^{3+}$  fundamental state photoionization towards the excited state  ${}^3T_2$  followed by a thermal emission towards the band conduction. This thermal effect is proved by a decrease in DLOS signal with decreased measurement temperature : at 200 K, the DLOS threshold appears at 0.8 eV and is interpreted as the transition of the  $V^{3+}$  fundamental state towards the first conduction band (CB) minimum. Then a large part of the DLOS spectrum is interpreted as  $V^{3+}$  transitions towards its excited states according to OA interpretation from table 1 (fig 4). However, two other thresholds at about 0.95 eV and 1.35 eV can be distinguished. We tentatively attribute them to  $V^{3+}$  photoionization towards the successive CB minima. According to Chen et al [14], 4H conduction band has four successive minima [14]. The first one is at the M point of the Brillouin zone, the others are on M, L and H points. We can then estimate the second M minimum at 0.15 eV from the first one in good agreement with theoretical calculations [15-17]. Threshold at 1.35 eV is attributed to  $V^{3+}$  photoionization towards the L minimum situated at 0.55 eV from the M minimum [14].

The same analysis has been done on 6H DLOS spectrum concerning the various  $V^{3+}$  transitions towards excited states (fig 4). Concerning transitions towards successive CB minima, it confirms the relative flatness between U, L and M minima. A threshold at about 1.05 eV is attributed to the  $V^{3+}$  ionization towards M minimum at about 0.3 eV from the U one in good agreement with Smith et al results obtained by optical admittance spectroscopy [18].

#### IV - Conclusions

According to our DLOS and OA measurements on 4H and 6H-SiC, we can give a complete  $V^{3+}$  configuration in both polytypes with respective positions of ground and excited states (fig 4). We can also distinguish CB minima with relative position determined by our interpretation.

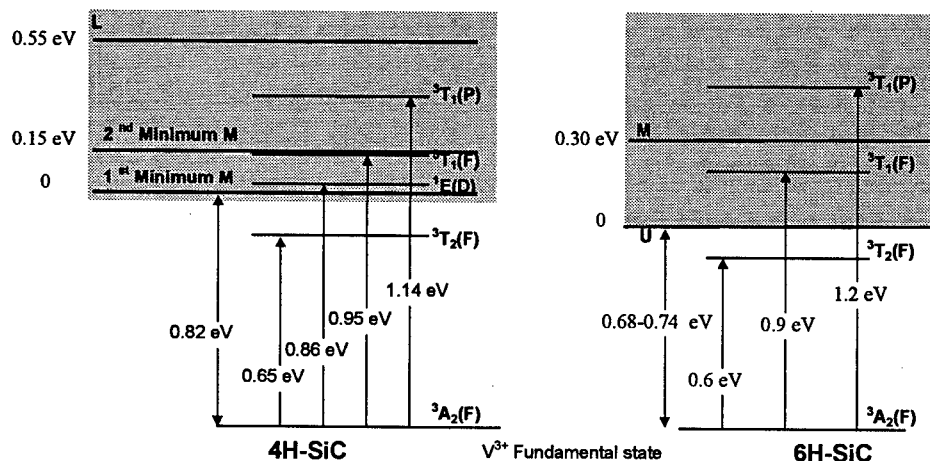


Fig. 4:  $V^{3+}$  configuration in 4H and 6H-SiC with relative positions for fundamental and excited states. Representation of conduction band minima for both polytypes.

#### References

- [1] McD. Hobgood H., Glass R.C., Augustine G., et al. - Appl. Phys. Lett., 66, (1995), p 1364.
  - [2] Glass R.C., Augustine G., Balakrishna V., et al. - Inst. Phys. Conf. Ser. 142, London : IOP Publishing Ltd, (1996), p 37.
  - [3] Augustine G., McD. Hobgood H., Balakrishna V., et al. - Mater. Sci. For., 264-268, (1998), p 9.
  - [4] Kimoto T., Nakajima T., Matsunami H., et al. - Appl. Phys. Lett., 69, (1996), p 1113.
  - [5] Mitchel W.C., Roth M.D., Evwaraye A.O., et al. - Inst. Phys. Conf. Ser. 142, London : IOP Publishing Ltd, (1996), p 313.
  - [6] Jenny J. R., Skowronski M., Mitchel W.C., et al. - J. Appl. Phys., 78, (1995), p 3839.
  - [7] Chantre A. et al. - Phys. Rev. B 23, (1981), p 5335.
  - [8] Lauer V. et al. - Mat. Sci. Eng., B61-62, (1999), p. 248
  - [9] Dalibor T., Pensl G., Matsunami H., et al. - Phys. Stat. Sol. (a), vol 162, (1997), p 29.
  - [10] Achtziger N., Grillenberger J., Witthuhn W. - Mater. Sci. For., 264-268 (1998), p 541.
  - [11] Jenny J. R., Skowronski M., Mitchel W.C., et al. - Appl. Phys. Lett., 68, (1996), p 1963.
  - [12] Clerjaud B., Naud C., Deveaud B., et al. - J. Appl. Phys., 58, (1985), p 4207.
  - [13] Kunzer M., Kaufmann U., Maier K., Schneider J. - Mater. Sci. and Eng. B, 29 (1995), p 118.
  - [14] Chen A-B., Srichaikul P. - Phys. Stat. Sol. (b), 202, (1997), p 81.
  - [15] Srichaikul P., Chen A-B. - Inst. Phys. Conf. Ser. 142, London : IOP Publishing Ltd, (1996), p 285.
  - [16] Wellenhofer G., Rössler U. - Phys. Stat. Sol. (b), 202, (1997), p 107.
  - [17] Bechstedt F. - Mater. Sci. For., 264-268 (1998), p 265.
  - [18] Smith S.R., Evwaraye A.O., Mitchel W.C. - Mater. Sci. For., 264-268, (1998), p 569.
- Corresponding author : Pr. Gérard Guillot ; E-mail : guillot@insa-lyon.fr. Tel : (+33) 4-72-43-81-61. Fax : (+33) 4-72-43-85-31.

## Photoluminescence and DLTS Measurements of 15MeV Erbium Implanted 6H and 4H SiC

Y. Shishkin<sup>1</sup>, W.J. Choyke<sup>1</sup>, R.P. Devaty<sup>1</sup>, N. Achtziger<sup>2</sup>, Th. Opfermann<sup>2</sup> and  
W. Witthuhn<sup>2</sup>

<sup>1</sup> Department of Physics and Astronomy, University of Pittsburgh, Pittsburgh, PA 15260, USA

<sup>2</sup> Institut für Festkörperphysik, Universität Jena, Max-Wien-Platz 1, DE-07743 Jena, Germany

**Keywords:** 1.54 $\mu$ m Luminescence, Deep Levels, DLTS, Erbium, Implantation

**Keywords:** Erbium, implantation, 1.54 $\mu$ m luminescence, deep level, DLTS

**Abstract.** Very sharp spectra are obtained with low temperature photoluminescence of 4H and 6H SiC implanted with low doses of Erbium ( $3 \times 10^{15} \text{ cm}^{-3}$  to  $1 \times 10^{17} \text{ cm}^{-3}$ ) at energies up to 15 MeV. A new temperature dependence of the luminescence is found at low temperature and attributed to an excitation barrier between nitrogen donors and defect centers associated with the Erbium. DLTS measurements on dilutely implanted samples of 4H SiC suggest a deep Erbium center in n-type material but results for p-type material are unclear at present.

### Introduction

The introduction of Erbium into semiconductors has been under intense study since 1983 [1, 2]. It has been motivated by the fact that the intra 4f-shell  $^4I_{13/2} \rightarrow ^4I_{15/2}$  transition of  $\text{Er}^{3+}$  occurs at 1.54  $\mu\text{m}$ , which is at the attenuation minimum of silica based optical fibers. At several hundred kilovolts the implants are very shallow and in order to see a reasonable signal, concentrations of  $10^{19} \text{ cm}^{-3}$  have frequently been used. Under these conditions, in many semiconductors, the intensity of the  $\text{Er}^{3+}$ , 1.54  $\mu\text{m}$ , light emission is a maximum at low temperatures and drops off drastically as one approaches room temperature. In SiC, implanted at concentrations of  $10^{19} \text{ cm}^{-3}$ , the integrated luminescence intensity over all 1.54  $\mu\text{m}$  transitions (from 1.49  $\mu\text{m}$  to 1.64  $\mu\text{m}$ ) is observed to decrease only above room temperature making this host very attractive from a practical point of view. We have previously reported spectra from heavily implanted SiC [3-6]. With the new ion accelerator of the University of Jena, Er implants up to 15 MeV are possible, yielding a projected range of about 2.2  $\mu\text{m}$ . This suggests experiments with far more dilute Er concentrations which might enable us to undertake new and detailed studies of the excitation mechanism of  $\text{Er}^{3+}$  in the SiC host. Since it has previously been suggested [6] that the excitation in 4H and 6H SiC requires both the nitrogen donor as well as a deep trap we are now revisiting this problem with a combination of low temperature photoluminescence (LTPL) and deep level transient spectroscopy (DLTS).

### Experimental

For our photoluminescence experiments we use n-type 4H and 6H CVD-grown SiC doped with nitrogen in the range from  $3 \times 10^{14} \text{ cm}^{-3}$  to  $1 \times 10^{16} \text{ cm}^{-3}$ . Doping with Erbium is done by multiple-energy implantation with energies of 2.5, 4.0, 6.0, 8.5, 11.5, and 15.0 MeV at room temperature. The individual fluences are adjusted to obtain a quasi-rectangular depth profile of Er in the depth interval 0.3 - 2.5  $\mu\text{m}$ . The samples are annealed at 1500°C for two hours in a SiC crucible in five-nines Argon at atmospheric pressure.  $\text{Er}^{3+}$  ions are excited by above bandgap optical pumping using a HeCd laser at 3250 Å. Optical measurements are made with a modified Nicolet 740 (FTIR) spectrometer. The integrated luminescence intensity is measured from 1.49  $\mu\text{m}$  to 1.64  $\mu\text{m}$ .

For DLTS studies, we use lightly doped (mid- $10^{15} \text{ cm}^{-3}$ ) epitaxial layers of n-type and p-type 4H-SiC. Implantation energies are restricted to the four lowest energies (2.5 to 8.5 MeV) leading to a quasi-rectangular concentration in a depth interval 0.3 - 1.3  $\mu\text{m}$ , which is sufficient for the depth region probed by DLTS. The average concentration of the implanted Er ions is  $10^{15} \text{ cm}^{-3}$ . We also use Rapid Thermal Annealing (RTA) at 1900 K in Ar for 5 minutes. After both annealings, the preparation of good Schottky contacts requires an additional oxidation (1600 K,  $\text{O}_2$ , 1-2 h, followed by oxide removal) prior to the contact deposition (evaporation of Ni on n-type, Ti on p-type). DLTS spectra are taken as described elsewhere [7]. Measuring voltages are adjusted to probe a depth interval of approximately 0.4 - 1.1  $\mu\text{m}$ , well embedded within the implanted region. For the spectra shown, the reference time constant (defining the peak position) is 12.4 ms.

### Results and Discussion

Despite the fact that our implants contain two to three orders of magnitude fewer erbium atoms than in typical shallow implant experiments we nevertheless obtained appreciable signals from our samples. Fig. 1 shows the spectra of 4H SiC implanted with Erbium to  $5 \times 10^{16} \text{ cm}^{-3}$  at 2 K, 77 K and 295 K. The line widths at 2 K and 77 K are instrumentally limited and in many ways superior to our previous results using Erbium concentrations of  $10^{19} \text{ cm}^{-3}$ . Fig. 2 shows the temperature behavior of the integrated intensity for 4H and 6H SiC samples implanted with Er at concentrations of  $1 \times 10^{19} \text{ cm}^{-3}$ ,  $5 \times 10^{16} \text{ cm}^{-3}$ , and  $6 \times 10^{15} \text{ cm}^{-3}$ . The  $1 \times 10^{19} \text{ cm}^{-3}$  curves in Fig. 2a show the form of the temperature variation that has been observed in almost all semiconductors to date [1]. We now find that the situation in dilutely implanted 4H and 6H SiC is quite different. For the  $5 \times 10^{16} \text{ cm}^{-3}$  and  $6 \times 10^{15} \text{ cm}^{-3}$  curves in Figs. 2b and c we have a new result in that the integrated intensity at 2 K is far below that at 77 K and 295 K. A detailed model cannot be presented here but if we assume that the energy transport of the  $\text{Er}^{3+}$  proceeds via the nitrogen donor to a defect associated with the Erbium, then it is also plausible that this process is governed by a barrier between the donor and the defect. At high doping,  $1 \times 10^{19} \text{ cm}^{-3}$ , the close proximity of the donor and Erbium atoms effectively wipes out this barrier even at 2 K. At Erbium concentrations below  $1 \times 10^{17} \text{ cm}^{-3}$  the donor-defect separation becomes such that at 2 K the energy transport is effectively controlled by a barrier which is a function of separation.

It is our hope that electrical measurements such as DLTS will elucidate on the nature of the Erbium related defect. We now report on preliminary DLTS spectra which were taken on

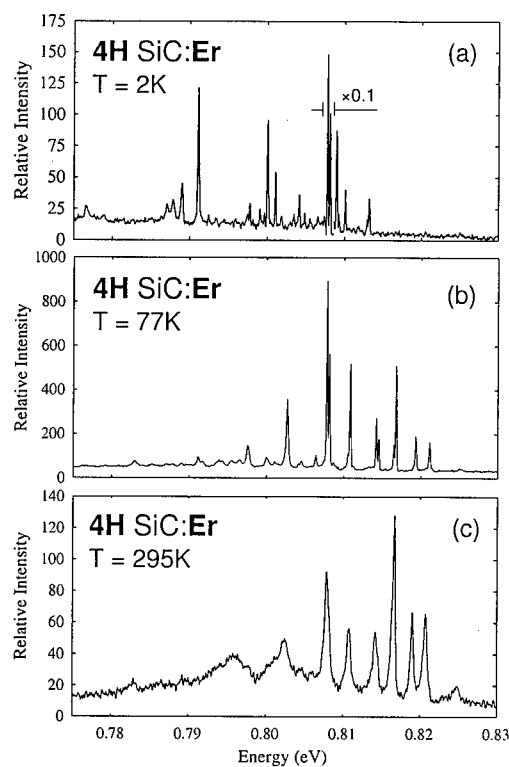


Figure 1: Photoluminescence spectra of 4H SiC:Er at (a) 2 K, (b) 77 K, and (c) 295 K at  $1 \text{ cm}^{-1}$  resolution. The sample is doped with Erbium at  $5 \times 10^{16} \text{ cm}^{-3}$ . The nitrogen concentration is  $n \sim 1 \times 10^{16} \text{ cm}^{-3}$ .



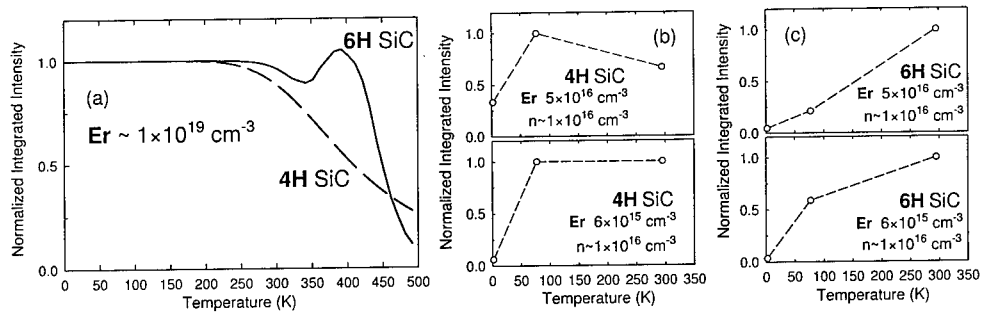


Figure 2: The temperature dependence of the integrated intensity for 4H and 6H SiC.

implanted and reference areas on a number of samples processed under similar conditions to the samples used for the optical experiments. The spectra, Figs. 3a and 3b, clearly demonstrate that several deep levels originate from the Er implantation in both n-type and p-type material. The level parameters are given in Table 1. The RTA process is obviously less efficient than the long-time anneal, resulting in higher trap concentrations in n-type material and completely failing to anneal p-type SiC sufficiently. The levels  $N_1$  to  $N_4$  are drastically reduced after long-time annealing compared to RTA. The levels  $N_6$  to  $N_8$  exist in the reference spectra as well. The height of the largest peaks in Fig. 3a correspond to deep level concentrations of  $7 \times 10^{13} \text{ cm}^{-3}$ . In p-type SiC, deep level concentrations are significantly higher ( $3 \times 10^{14} \text{ cm}^{-3}$ ) and the peaks in the reference spectrum are not observable on the scale of Fig. 3b.

The question arises whether any of the deep levels detected are due to an Er atom (or complex). Deep levels with parameters nearly identical to  $N_2$ ,  $N_3$ , and  $N_4$  have already been reported after ion implantation of other elements or electron irradiation [8,9]. Therefore, we interpret these levels as implantation-induced defects. Levels  $N_6$ ,  $N_7$ , and  $N_8$  are present in the reference as well and are, thus, not Er-related. Level  $N_5$  is hardly influenced by the type of annealing used. To our knowledge, no deep level with similar parameters has been reported. This is, however, a weak argument since MeV-implantation of heavy elements in SiC has not been studied up to now. Summarizing, level  $N_5$  remains a possible candidate for an Er-related level in the upper part of the band gap, but this is by no means a definite assignment. In the lower part of the band gap, studied by DLTS on p-type SiC, the interpretation is more vague since

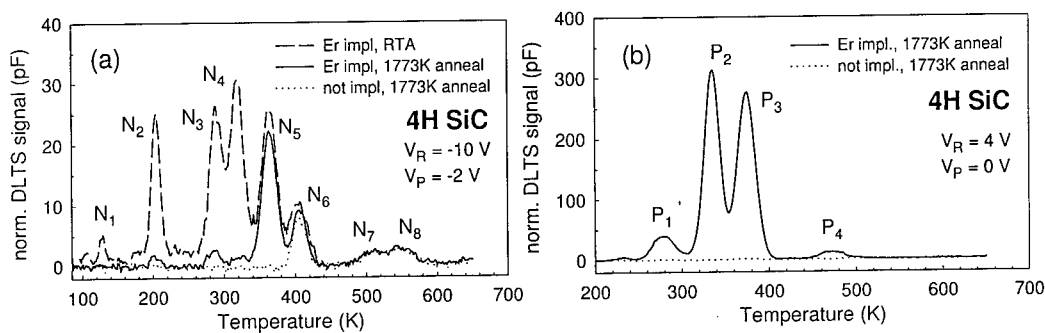


Figure 3: DLTS spectra of Er implanted 4H SiC: (a) n-type and (b) p-type. A reference spectrum from an unimplanted sample area is included. Voltages  $V_R$  and  $V_P$  are reverse and pulse bias, respectively.

Peak	N <sub>1</sub>	N <sub>2</sub>	N <sub>3</sub>	N <sub>4</sub>	N <sub>5</sub>	N <sub>6</sub>	P <sub>1</sub>	P <sub>2</sub>	P <sub>3</sub>	P <sub>4</sub>
Energy (eV)	-0.23(2)	-0.41(2)	-0.58(3)	-0.66(2)	-0.75(2)	-0.83(2)	0.60	0.74	0.80	1.05
$\sigma$ ( $10^{-14}$ cm <sup>2</sup> )	5	20	7	20	10	8	9	10	3	7

Table 1: Energy levels and capture cross section  $\sigma$  (assumed to be independent of temperature) of band gap states observed in Er-implanted SiC. Negative energies designate position relative to the conduction band, positive values refer to the valence band.

there is little literature with which to compare. The level parameters of  $P_1$  are similar to the boron-related D-center and  $P_3$  has also been detected previously after ion implantation [10]. In electron irradiated p-type SiC, we found five defect levels between 0.6 and 1 eV (unpublished) with parameters similar to the levels found here. At present, there is no strong evidence that any of the levels  $P_1$  to  $P_4$  is related to an Er center.

### Conclusions

High energy (15 MeV) dilute implantation of Erbium and annealing at 1500°C leads to extremely sharp LTPL lines enabling new studies of the structure of the  $\text{Er}^{3+}$  spectrum in polyp-types of SiC. A surprise discovery is the fact that below  $1 \times 10^{17}$  cm<sup>-3</sup> Erbium the integrated light intensity at temperatures below 77 K decreases rapidly with decreasing temperature. It is suggested that the excitation of the  $\text{Er}^{3+}$  is governed by a barrier between the donors and the defect centers associated with the Erbium. The lower the Erbium concentration for a given nitrogen concentration the lower the relative light output at low temperatures. The DLTS measurements give some indication of an Erbium specific deep center in n-type material. For p-type samples the situation is not clear at the moment. Further experiments are in progress and greater details will appear in future publications.

### Acknowledgments

We wish to thank the Office of Naval Research and NASA for partial support of this work.

### References

- [1] Mat. Res. Soc. Symp. Proc., Vol. 301 (1993).
- [2] Mat. Res. Soc. Symp. Proc., Vol. 422 (1996).
- [3] W.J. Choyke, R.P. Devaty, L.L. Clemen, M. Yoganathan, G. Pensl, and Ch. Hässler, Appl. Phys. Lett. 65 (1994), p. 1668.
- [4] W.J. Choyke, R.P. Devaty, L.L. Clemen, M.F. MacMillan, M. Yoganathan, Inst. Phys. Conf. Series, 142 (1996), p. 260.
- [5] M. Yoganathan, W.J. Choyke, R.P. Devaty, G. Pensl, and J.A. Edmond MRS Symp. Proc. Vol 422 (1996), p. 339.
- [6] A.J. Steckl, J. Devrajan, W.J. Choyke, R.P. Devaty, M. Yoganathan, S.W. Novak, J. Electr. Mat., Vol 25 (1996), p. 869.
- [7] N. Achtziger, W. Witthuhn, Phys. Rev. B57 (1998), p.12181.
- [8] T. Dalibor, G. Pensl, T. Kimoto, W.J. Choyke, A. Schöner, N. Nordell, phys. stat. sol. (a) 162 (1997), p. 199.
- [9] C. Hemmingsson, N.T. Son, O. Kordina, E. Janzen, J.L. Lindström, S. Savage, N. Nordell, Mat. Sci. Eng. B46 (1997), p. 336.
- [10] J. Grillenberger, N. Achtziger, F. Günter, W. Witthuhn, Appl. Phys. Lett. 73 (1998), p. 3698.

## Electronic States of Vacancies in 3C- and 4H-SiC

A. Zywietz, J. Furthmüller and F. Bechstedt

Friedrich-Schiller-Universität Jena, Max-Wien-Platz 1, DE-07743 Jena, Germany

**Keywords:** Defect, Electronic Structure, Luminescence, Spin Polarization, Vacancy

**Abstract:** Results of spin-polarized *ab initio* calculations are reported for the silicon and carbon vacancies in 3C- and 4H-SiC. The calculated electronic structures are compared with recent experimental findings.

In SiC a variety of vacancies exists due to (i) the two different Si and C sublattices, (ii) the inequivalence of the sublattice sites with cubic (k) or hexagonal (h) character, and (iii) the different charge states. In the presence of a monovacancy the system may gain energy at least by three mechanisms. The first mechanism is related to the lattice relaxation which frequently lowers the local symmetry around the vacancy. The basic mechanism for the symmetry breaking is the Jahn-Teller effect. For 3C-SiC crystallizing in zinc-blende structure with a local  $T_d$  symmetry, the four dangling bonds left at the neighbouring atoms of a vacancy give rise to a completely filled non-degenerate  $a_1$  and a partially filled threefold degenerate  $t_2$  defect state in the fundamental gap, i.e., the  $T_d$  symmetry gives rise to a degenerate ground state. According to the Jahn-Teller theorem, a degenerate ground state is usually expected to be unstable with respect to the formation of a non-degenerate ground state by means of a symmetry-breaking distortion. Consequently, vacancies in 3C-SiC should exhibit a lower local symmetry than  $T_d$ . Similar lattice relaxations should also happen in hexagonal SiC, e.g. in 4H, since the individual bonding tetrahedra are close to an ideal tetrahedron. The second driving force concerns the arrangement of the electron spins occupying the vacancy levels in high-spin configurations according to Hund's rule. The third mechanism is related to the so-called negative- $U$  property. A defect with such a property strengthens the binding energy of the carriers (electrons or holes) when capturing additional carriers. Consequently, recharging of vacancies happen. All mechanisms influence the electronic structure of the vacancies in the ground state as well as in the excited states.

In order to study the influence of the different relaxation mechanisms, the chemical nature of the vacancy, and the SiC polytype on the electronic structure of vacancies we perform first-principles calculations. The calculations are based on the density functional theory in the local density approximation (LDA) as well as local spin density approximation (LSDA). Explicitly a plane-wave-supercell approach is combined with ultrasoft Vanderbilt pseudopotentials to allow converged calculations. Extremely large supercells with 216 atoms (3C) or 128 atoms (4H) are used to avoid too strong vacancy-vacancy interactions and electrostatic effects. We study the atomic structure, the energetics, and the charge- and spin-dependent vacancy states by optimizing the corresponding total energies. All atomic coordinates are varied until the total energy reaches its minimum. The donor ionization levels (and acceptor levels, respectively) result from total energy differences. For instance, the donor ionization energies measured with respect to the conduction band minimum  $E_C$  are given as

$$\epsilon_D(q-1/q) = E_C + E_{\text{tot}}(V_X^q) - E_{\text{tot}}(V_X^{q-1}), \quad (1)$$

where  $(q-1)$  characterizes the charge state of the vacancy in the initial state on a  $X = \text{Si}, \text{C}$  site. The resulting energy level schemes are plotted in Figs. 1 and 2.

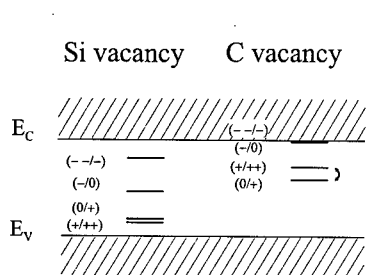


**Fig. 1** Energy level schemes for silicon and carbon vacancy centers in 3C-SiC.

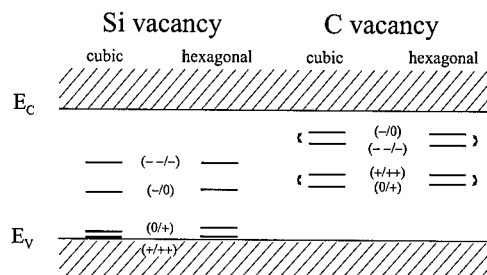


**Fig. 2** Energy level schemes for Si and C vacancies at cubic and hexagonal sites in 4H-SiC.

Independent of the polytype, 3C or 4H, the generation of the C-site vacancy is generally accompanied by a remarkable Jahn-Teller distortion apart from the double positively charged one. Disregarding the small deformations of the tetrahedra in 4H the local symmetry around a vacancy is changed from  $T_d$  to  $D_{2d}$  in both polytypes. The corresponding Jahn-Teller distortion is a combination of an inward-breathing mode and a pairing mechanism. For the positively charged vacancy the pairing effect is reduced and the breathing mode changes the sign. The huge geometrical changes in the  $V_C^0$  case in comparison to the  $V_C^+$  and  $V_C^{++}$  vacancies have remarkable consequences for the electronic structure of the vacancy. The normal sequence of the donor levels  $(+/++)$  and  $(0/+)$  is interchanged (cf. Figs. 1 and 2). The lowest vacancy level is  $(0/+)$ . The reason is a negative- $U$  behaviour of the C-site vacancy in SiC very similar to that found in silicon [2]. Due to the lattice relaxation the effective interaction of two holes is attractive. In the case of 4H (cf. Fig. 2) we predict such a negative- $U$  behaviour also for the negatively charged vacancy. Negative- $U$  centers have been recently observed in 4H- and 6H-SiC [3].

The situation is quite different for the Si-site vacancies. Because of the strong localization of the C dangling bonds, only an outward breathing relaxation occurs. For the systems with less electrons,  $V_{Si}^{++}$  and  $V_{Si}^+$ , the ground states are  $^1A_1$  and  $^2T_2$  according to the total spins  $S = 0$  and  $S = 1/2$ . The picture is completely changed for the neutral and negatively charged Si-site vacancies. The spin degeneracy of the single-particle  $t_2$ -level is lifted and high-spin states occur in agreement with Hund's rule. The ground states  $^3T_1$  ( $S = 1, V_{Si}^0$ ),  $^4A_2$  ( $S = 3/2, V_{Si}^-$ ), and  $^3T_1$  ( $S = 1, V_{Si}^{--}$ ) are stabilized by a spin-exchange coupling [1,4]. For  $V_{Si}^-$  this effect is also observed experimentally and theoretically by other authors [5-7].

The crystal-field splitting of the upper vacancy levels does not principally modify the properties of the vacancies in the hexagonal polytypes. The inequivalent sites give however rise to site-related shifts of the electronic states. The main influence of the polytypism is related to the widening of the energy gap from 3C to 4H by about 0.9 eV. As a consequence the double negatively charged C-site vacancy is stable in 4H-SiC but not in the cubic polytype (cf. Figs. 1 and 2). The energetical distances of the various vacancy levels with respect to the top of the valence bands vary only weakly with the polytype. In principle the vacancy levels can be used to align the band structures of 3C and 4H and to determine the valence-band discontinuity according to the Langer-Heinrich rule.

The electronic systems of the vacancies can be excited, e.g. by incident light. Excited electronic states are obtained by minimizing the system energy with the constraint of keeping a hole in an  $a_1$ -like single-particle vacancy orbital. However, multiplet effects [8] cannot be taken into account within LSDA. The transition energy from a ground state into an excited state is given as

$$\hbar\omega = E_{\text{tot}}(V_X^q, \text{excited}) - E_{\text{tot}}(V_X^q) \quad , \quad (2)$$

at least for intravacancy transitions without changing the charge state. In evaluating the excitation energies  $\hbar\omega$ , the positions of the cores were kept fixed at the equilibrium structure of the ground state in accordance with the Frank-Condon principle. On the other hand, we made the observation that the transition energies calculated according to Eq. (2) can be also obtained by taking the difference of the single-particle energy values  $\epsilon_{t_2} - \epsilon_{a_1}$  ( $\epsilon_{b_2} - \epsilon_{a_1}$ ), so far these eigenvalues are calculated for the considered charge state  $q$ . We make use of this observation by estimation of a dispersion correction. From a tight-binding fit to the single-particle vacancy bands [9] we derive the “true level energies”.

We focus our attention to single-particle transitions  $a_1 \rightarrow t_2$  ( $T_d$  symmetry) or  $a_1 \rightarrow b_2$ ,  $e$  ( $D_{2d}$  symmetry). The corresponding electronic transitions are observable in optical absorption, luminescence and photoluminescence excitation spectra. The results for several monovacancies with a certain electron configuration and transitions are given in Table 1. In addition the total spin  $S$  of the vacancy electronic system is given. The limitation of the used supercells gives rise to an artificial vacancy-vacancy interaction, so that the vacancy levels are broadened to bands. The accompanying band dispersion falsifies the transition energies. The 3C values for  $V_{\text{Si}}^q$  in Table 1 are reduced by the dispersion corrections. By careful analysis in the  $V_{\text{Si}}^+$  case we find an energy lowering of 0.35 eV (0.20 eV) for the excited electron in the same spin level (another level) as the other  $t_2$  electrons. For 4H-SiC we calculate similar values for the intravacancy transitions using the single-particle values. Apart from the fact that no reduction due to the dispersion corrections is used in the 4H case, the differences to 3C in Table 1 are of the order of magnitude of the variations in the donor levels between Figs. 1 and 2. However, there is an additional complication due to the crystal-field splitting of the higher vacancy levels, e.g.  $t_2$ .

**Table 1:** Lowest intravacancy excitations in 3C- and 4H-SiC. The site dependence in 4H is indicated by  $k$  and  $h$ .

vacancy	spin	transition	3C: $\hbar\omega$ (eV)	4H: $k, h$ : $\hbar\omega$ (eV)
$V_{\text{Si}}^+$	$\frac{1}{2}$	$a_1^2 t_2^{\uparrow} \rightarrow a_1^{\downarrow} t_2^{\uparrow\uparrow}$	1.06	1.42, 1.77
		$a_1^2 t_2^{\uparrow} \rightarrow a_1^{\uparrow} t_2^{\uparrow\downarrow}$	1.27	1.44, 1.74
$V_{\text{Si}}^0$	1	$a_1^2 t_2^{\uparrow\uparrow} \rightarrow a_1^{\downarrow} t_2^{\uparrow\uparrow\uparrow}$	1.07	1.44, 1.82
$V_{\text{Si}}^-$	$\frac{3}{2}$	$a_1^2 t_2^{\uparrow\uparrow\uparrow} \rightarrow a_1^{\uparrow} t_2^{\uparrow\uparrow\uparrow} t_2^{\downarrow}$	1.40	1.57, 1.40
$V_{\text{Si}}^{--}$	1	$a_1^2 t_2^{\uparrow\uparrow\uparrow} t_2^{\downarrow} \rightarrow a_1^{\uparrow} t_2^{\uparrow\uparrow\uparrow} t_2^{\downarrow\downarrow}$	1.23	1.73, 1.68
$V_{\text{C}}^{++}$	0	$a_1^2 \rightarrow a_1^{\uparrow} t_2^{\downarrow}$	2.87	3.38, 2.85
$V_{\text{C}}^+$	$\frac{1}{2}$	$a_1^2 b_2^{\uparrow} \rightarrow a_1^{\uparrow} b_2^{\uparrow\downarrow}$	2.53	—
$V_{\text{C}}^0$	0	$a_1^2 b_2^{\uparrow\downarrow} \rightarrow a_1^{\uparrow} b_2^{\uparrow\downarrow} e^{\downarrow}$	3.61	4.28, 4.27

In electron-irradiated 4H samples Sörman et al. [10,11] observed two sharp zero-phonon luminescence lines at photon energies of 1.35 and 1.44 eV (called  $v_2$  and  $v_1$ ). In 3C-SiC a photoluminescence at 1.12 eV occurs. Because of the results of the optically detected magnetic resonance (ODMR) measurements they argued that the lines in 4H originate from an internal transition of the neutral silicon vacancy, at least a silicon vacancy with an even number of electrons in order to explain the high-spin state  $S = 1$ . The occurrence of two different lines in 4H is related to the two different inequivalent lattice sites for the generation of a Si vacancy. Sörman et al. [10] relate the photoluminescence line at 1.12 eV in 3C to a  $S = 1/2$  centre, probably  $V_{Si}^+$ . In principle, we follow this interpretation. According to Table 1 transitions within the C-site vacancy can be clearly excluded because of too large excitation energies. For  $V_C^0$  in 3C intravacancy transitions cannot occur because of the small energy gap (cf. Table 1). Moreover, the optical transition  ${}^2E \rightarrow {}^2T_2$  in  $V_{Si}^+$  is electric-dipole allowed. We agree that in 4H the experimental findings could be related to a transition either  $a_1^{\downarrow}t_2^{\uparrow\uparrow\uparrow} \rightarrow a_1^2t_2^{\uparrow\uparrow}$  or  $a_1^{\uparrow}t_2^{\uparrow\uparrow\uparrow\downarrow} \rightarrow a_1^2t_2^{\uparrow\uparrow\downarrow}$  within the electron configurations of  $V_{Si}^0$  and  $V_{Si}^{--}$ , respectively. This is supported by the  $S = 1$  spin state and the calculated transition energy. Unfortunately, the calculated values are not accurate enough to give a final decision. Nevertheless, we favour the neutral silicon vacancy. However, we claim that the line splitting is a consequence of the crystal-field splitting of the  $t_2$  level into  $a_1$  and  $e$  ones. The calculated transition energies at cubic sites are much larger. Consequently, they should not occur in the photoluminescence spectra.

Another type of secondary radiation has been related to a strongly luminescent  $D_I$  center in neutron-irradiated samples [12]. The maximum photon energy of the characteristic emission band depends directly on the band gap energy. A sharp peak occurs at the position of about 1.97 eV (3C) and 2.91 eV (4H). These energies are in rather good agreement with the donor ionization energies  $\epsilon_D(+ / + +)$  of about 2.05 eV in 3C, 3.20 eV in 4H (cubic site), and 3.18 eV in 4H (hexagonal site). Therefore, we do not exclude an interpretation that the measured lines are accompanied by transitions of conduction electrons into levels of the  $V_{Si}^{++}$  vacancy. However, other interpretations, e.g. of the 2.9 eV transition in 4H as a  $V_C^{++}$  intravacancy one (cf. Table 1), are possible [13]. Moreover, defect complexes seem to be more likely [14].

## References

- [1] A. Zywietz, J. Furthmüller, F. Bechstedt, Phys. Rev. B **59** (1999), p. 15166.
- [2] F. Bechstedt, A. Zywietz, J. Furthmüller, Europhys. Lett. **44** (1998), p. 309.
- [3] C.G. Hemmingson, N.T. Son, A. Ellison, J. Zhang, E. Janzen, Phys. Rev. B **58** (1998), p. R10119; Appl. Phys. Lett. **74** (1999), p. 839.
- [4] J. Furthmüller, A. Zywietz, F. Bechstedt, Materials Science & Engineering B **61-62** (1999), p. 244.
- [5] H. Itoh, et al., phys. stat. sol. (a) **162** (1997), p. 173.
- [6] T. Wimbauer, B.K. Meyer, A. Hofstaetter, A. Scharmann, H. Overhof, Phys. Rev. B **56** (1997), p. 7384.
- [7] L. Torpo, R.M. Nieminen, K.E. Laasonen, S. Pöykkö, Appl. Phys. Lett. **74** (1999), p. 221.
- [8] G.T. Surratt, W.A. Goddard III, Solid State Commun. **22** (1977), p. 413.
- [9] A. Zywietz, J. Furthmüller, F. Bechstedt, phys. stat. sol. (b) **210** (1998), p. 13.
- [10] N.T. Son et al., J. Appl. Phys. **79**, (1996), p. 3784; Phys. Rev. B **55** (1997), p. 2863.
- [11] E. Sörman et al., Materials Science Forum **264-268** (1998), p. 473.
- [12] V.V. Makarov, Sov. Phys. Solid State **13** (1972), p. 1974.
- [13] H. Helbig, private communications.
- [14] W.J. Choyke, Inst. Phys. Conf. Ser. **31** (1977), p. 58.

## Pseudo-Donors in SiC

T. Egilsson<sup>1</sup>, I.G. Ivanov<sup>1</sup>, A. Henry<sup>1,2</sup> and E. Janzén<sup>1</sup>

<sup>1</sup>Department of Physics and Measurement Technology, Linköping University,  
SE-581 83 Linköping, Sweden

<sup>2</sup>ABB Corporate Research, SE-721 78 Västerås, Sweden

**Keywords:** Bound Excitons, Defects, Photoluminescence

**Abstract** We report on the properties of two well known bound excitons (BE) in silicon carbide, the D<sub>1</sub>-BE and a hydrogen related BE, here called the H-BE. We find that in both cases the BE may be regarded as a pseudo-donor, a strongly localised hole serving as the positive core. In order to study the donor-like states of the BE, we use photoluminescence excitation (PLE) spectroscopy. Where possible, we have compared our results with the predictions of effective-mass-theory.

**Introduction** Donors and acceptors have excess electrons/holes, and thus a defect region with a positively/negatively charged core. Isoelectronic defects on the other hand have no net charge in the local bonding region, but may be able to bind particles by a short range potential induced by either an electronegativity difference (e.g. when a crystal atom is replaced by another atom isovalent to the crystal atom) or by a local strain field at the defect. Once an isoelectronic defect has bound a particle it becomes charged. A second particle may then be bound in the resulting Coulomb potential, in a similar fashion as particles are bound to donors and acceptors. The electron-hole pair, that is in this way localised at an isoelectronic defect is usually called a bound exciton (BE). If the second particle is an electron the BE is called a pseudo-donor, if it is a hole the BE is called a pseudo-acceptor.

We have studied two excitons in SiC bound at isoelectronic defects, namely the D<sub>1</sub>-BE and a hydrogen related BE, here called H-BE. Emission due to annihilation of D<sub>1</sub>-BE's usually dominates the photoluminescence (PL) spectrum of SiC after any kind of bombardment (ions, neutrons or electrons) followed by high temperature annealing, whereas emission due to H-BE annihilation dominates the PL spectrum of SiC implanted with hydrogen. The defect responsible for the D<sub>1</sub>-BE has been suggested to be intrinsic [1], but its structure is not known. The defect responsible for the H-BE is known to include a C-H bond [2], and has been tentatively assigned to a H decorated Si-vacancy [3, 4]. Fig.1 shows the D<sub>1</sub>-BE PL spectrum in 4H-SiC, and the H-BE PL spectrum in 6H-SiC. In order to study the electronic structure of the D<sub>1</sub>-, and H-BE's, we have used PL excitation (PLE) spectroscopy.

**Results and discussion** PLE spectroscopy is a useful tool for investigating excited states of BE's [5-7]. In Fig. 2 we show the PLE spectrum of the D<sub>1</sub>-BE in 3C-, and 4H-SiC, whereas Fig. 3 shows the PLE spectrum of one of the H-BE's in 6H-SiC. In all cases, a series of states resembling a hydrogenic series of excited states is observed.

We have recently reported a detailed investigation of the magneto-optical properties of the D<sub>1</sub>-BE in 3C-, and 4H-SiC [8]. The Zeeman splitting is isotropic in 3C-SiC, whereas it is anisotropic in 4H-SiC. The anisotropy in the latter case is due to the uniaxial crystal field present in hexagonal polytypes. The detailed splitting pattern in both polytypes is consistent with a simple electron-hole pair, composed of an s-like electron and a strongly localised p-like hole. The strong localisation of the hole is deduced from the reduced orbital g-value and spin-orbit parameter compared to the values associated with free holes. Also, in the case of the H-BE, magneto-optical studies on 6H-SiC indicate a strong localisation of the hole [4].

Since the holes of the D<sub>1</sub>-, and H-BE are strongly localised, the electron must be the weakly localised particle giving rise to the excited states observed in the PLE spectra (Figs. 2 and 3). That is, the states are donor-like states. A good approximation to the states of shallow donors in cubic

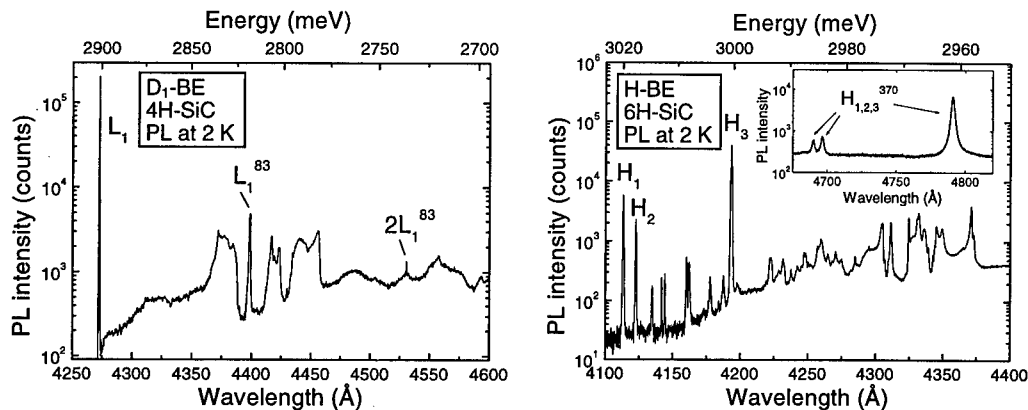


**Fig. 1.** PL spectra at 2 K due to the D<sub>1</sub>-BE in 4H-SiC (left) and the H-BE in 6H-SiC (right). Only transitions associated with the lowest energy states of the BE's are observed since thermal population of other states is insignificant at 2 K. There is only one D<sub>1</sub>-BE in 4H-SiC. On the other hand, there are three H-BE's in 6H-SiC, and thus three no-phonon lines H<sub>1,2,3</sub> (we are not concerned here with the so-called secondary H-PL spectrum also present in 6H-SiC [3, 4]). Phonon replicas characteristic for the D<sub>1</sub>- and H-BE spectra are indicated

semiconductors can be obtained by using effective-mass-theory (EMT). Usually, a one valley EMT is used, and thus splittings due to many valley effects in indirect bandgap semiconductors are not included. These so-called valley-orbit (VO) splittings are only important for low order S-like states however. The excitation spectrum of the carbon site nitrogen donor (N-donor) in 3C-SiC [9] is seen to be fit well by a one valley EMT if one allows for a VO-splitting of the 1S ground state. For other SiC-polytypes such as 4H-, and 6H-SiC the situation is less clear. The reason is twofold: Firstly, published donor excitation spectra for these polytypes [10, 11] are of much lower quality than in the case of 3C-SiC; Secondly, the electron effective mass in 4H-, and 6H-SiC has three independent components (instead of two in 3C-SiC), and the dielectric constant is anisotropic (instead of isotropic for 3C-SiC). This makes EMT calculations difficult, and to our knowledge such calculations have not been reported.

In Fig. 2 we compare the excited states of the D<sub>1</sub>-BE in 3C-SiC with a series of calculated effective-mass-like electron states (S-, P<sub>±</sub>-, and P<sub>0</sub>-like). For the comparison we use the calculations of Faulkner [12] using the transverse and longitudinal effective masses of the electron in 3C-SiC,  $m_t^* = 0.247m_0$  and  $m_l^* = 0.667m_0$ , as determined by cyclotron resonance [13]. Using these masses, linear interpolation of Faulkner's tables gives the series of effective-mass-like states as a function of the static dielectric constant  $\epsilon_s$  (approximately 9.7 for 3C-SiC [14, 15]). The absolute energy of the series limit for the calculated states is a free parameter, and has been chosen so as to optimize the fit of the calculated 2S, 2P<sub>±</sub>, 3S and 3D<sub>0</sub> states to peaks in the PLE spectrum. According to selection rules, excitons are created in even parity states. However, experiments show that this rule is not always strictly obeyed [16], and one can thus expect to observe also transitions to odd parity states in the PLE spectrum, albeit weakly. This may explain the apparent observation of the 2P<sub>±</sub> state in the PLE spectrum. The 1S ground state of the D<sub>1</sub>-BE in 3C-SiC is split due to a number of interactions [8], the strongest being the valley-orbit (VO) interaction. Estimating it from the separation between M and M2 PLE peaks gives:  $\sim 9.5$  meV. The VO-splitting depends on the amplitude of the electron wavefunction at the defect. In higher order states the electron wavefunction is more spread out and VO interaction is thus less important. The exchange interaction between the electron and the hole also decreases since it depends on the electron-hole overlap. In a crude approximation one can predict the VO-splitting to scale as the probability density of hydrogenic s-states at the origin. According to this, the expected VO-splitting in the 2S-state of the D<sub>1</sub>-BE is eight times less than the VO-splitting in the 1S state, or approximately



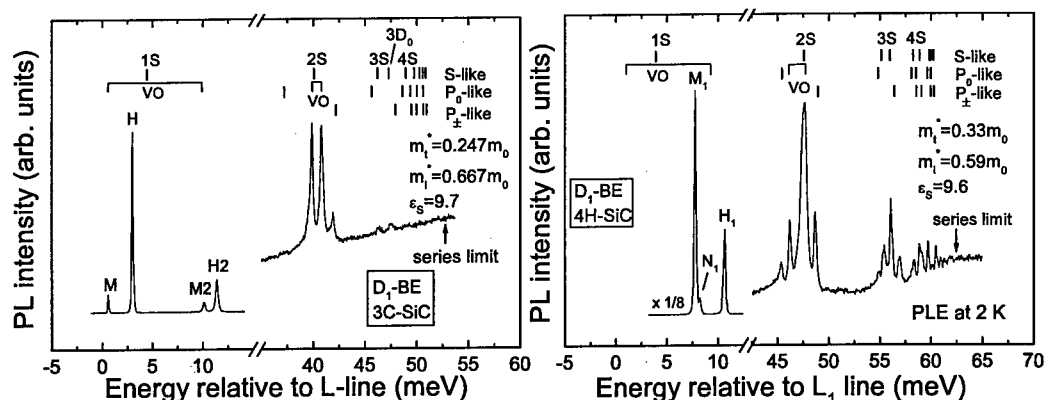


**Fig. 2.** PLE spectra of the D<sub>1</sub>-BE in 3C-, and 4H-SiC at 2 K. The high energy parts of the spectra were obtained by monitoring the L and L<sub>1</sub> no-phonon lines respectively, whereas the low energy parts were obtained by monitoring in the phonon assisted part of the PL spectra. Also shown in the figure, are the positions of calculated effective-mass-like electron states in 3C-, and 4H-SiC (S-like, P<sub>0</sub>-like and P<sub>±</sub>-like). Our assignments to VO-splitting of the 1S and 2S states are indicated. In the case of 4H-SiC the  $m_{MK}$  and  $m_{ML}$  electron masses are assumed to be equal and anisotropy in  $\epsilon_s$  is neglected.

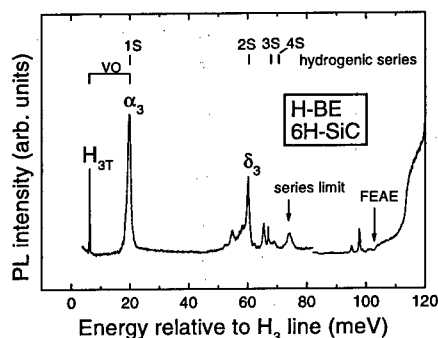


**Fig. 3.** PLE spectrum of the H<sub>3</sub>-BE in 6H-SiC. The PL was monitored at the H<sub>3</sub> no-phonon line. Our assignment to VO-splitting of the 1S state is indicated.

1.2 meV. The splitting between the two PLE peaks at the position of the calculated 2S state is ~0.9 meV. We attribute this splitting to VO interaction. As mentioned previously the effective mass of an electron in 4H-SiC is described by three independent components. Furthermore, the dielectric constant is anisotropic, characterized by two components:  $\epsilon_s(\text{Lc-axis})$  and  $\epsilon_s(\text{||c-axis})$ . Therefore, in principle, Faulkner's calculations cannot be used to describe the effective-mass-like states in 4H-SiC (the P<sub>±</sub> states are for instance expected to be split into two components). The values of the three masses are according to cyclotron resonance measurements [17],  $m_{MT} = (0.58 \pm 0.01)m_0$ ,  $m_{MK} = (0.31 \pm 0.01)m_0$ , and  $m_{ML} = (0.33 \pm 0.01)m_0$ , where  $\Gamma$ , M, L and K are high symmetry points in the Brillouin zone. The two masses,  $m_{MK}$  and  $m_{ML}$  perpendicular to  $m_{MT}$  are very similar and can to a good approximation be considered as identical. If we furthermore make the approximation that  $\epsilon_s$  is isotropic in 4H-SiC, we can estimate the effective-mass-like states of the electron by using Faulkner's calculations. To our knowledge, there are no reported values for  $\epsilon_s$  for 4H-SiC. Room temperature values for 6H-SiC have been reported however, and are:  $\epsilon_s(\text{Lc-axis}) = 9.66$  and  $\epsilon_s(\text{||c-axis}) = 10.03$  [14]. We obtain a rather good fit to the PLE spectrum of the D<sub>1</sub>-BE in 4H-SiC by using  $\epsilon_s = 9.6$ , and the upper bounds of the effective masses determined by cyclotron resonance measurements (the fitting aimed at achieving a good agreement between peaks in the spectrum and the series of calculated S-like states above 1S, as well as the calculated 2P<sub>0</sub> and 2P<sub>±</sub> states). The transverse and longitudinal masses used in the calculation are thus:  $m_t^* = \sqrt{m_{MK}m_{ML}} \approx 0.33m_0$  and  $m_l^* = m_{MT} = 0.59m_0$ . The series of states (S-, P<sub>±</sub>-, and P<sub>0</sub>-like) is shown in Fig. 2. As in the case of 3C-SiC we have assigned part of the splitting in the 1S and 2S states to VO splitting. Faulkner's calculations appear to provide a good fit to the D<sub>1</sub>-PLE spectrum in 4H- as well as 3C-SiC. This supports the pseudo-donor model for the D<sub>1</sub>-BE. Since good quality donor excitation spectra have been lacking for 4H-SiC, the D<sub>1</sub>-BE spectrum may prove to be of importance in the future for comparison with more elaborate EMT's for 4H-SiC.

Both experiment [18] and theory [19] indicate that all three components of the electron effective mass in 6H-SiC differ substantially from each other. Faulkner's calculations are thus probably a bad approximation in this case, and we are therefore not able to carry out an approximate analysis of the H-BE PLE spectrum as in the case of the D<sub>1</sub>-BE in 4H-SiC. There is nevertheless an indirect indication from the H-BE PLE spectra which supports a donor-like behaviour. Absorption and Raman [10, 20] studies indicate that the VO splitting associated with the three inequivalent sites of the nitrogen donor in 6H-SiC is very different. It is close to 13 meV for the hexagonal site but several times larger for the two cubic sites. The separation between the H<sub>3T</sub> peak and the  $\alpha_3$  peak in the H<sub>3</sub> PLE spectrum is 13.8 meV (see Fig. 3). On the other hand, we do not observe any  $\alpha$  peaks in the H<sub>1</sub> and H<sub>2</sub> PLE spectra (not shown here). Since the H<sub>1</sub> and H<sub>2</sub> lines are much closer to the FE absorption edge (FEAE) than the H<sub>3</sub> line, their PLE spectra span a narrower energy range than the H<sub>3</sub> PLE spectrum. But even so, the spectra show that the  $\alpha$  state of the H<sub>1</sub>-BE must be more than 35 meV above the H<sub>1T</sub> state, and the  $\alpha$  state of the H<sub>2</sub>-BE more than 45 meV above the H<sub>2T</sub> state. If we assume the H-BE behaves as a pseudo-donor, the above behaviour is easily explained by associating the separation between the H<sub>3</sub> and  $\alpha_3$  peaks with VO-splitting. In analogy with the N<sub>C</sub> donors, we can then explain the apparently large VO splitting in the case of the H<sub>1</sub> and H<sub>2</sub>-BE's by associating them with the two cubic sites, and consequently the H<sub>3</sub>-BE with the hexagonal site.

**Conclusions** We have shown that two D<sub>1</sub>-BE and the H-BE in SiC behave as pseudo-donors, a strongly localised hole serving as the positive core. In both cases previous magneto-optical studies have indicated strong localisation to the hole of the BE. The analysis of the PLE spectra of these BE's further supports that the secondary particle of the BE is donor-like.

**Acknowledgments** Support for this work was provided by the Swedish Council for Engineering Sciences (TFR), the SSF program SiCEP, and ABB Corporate Research.

## References

- [1] W. J. Choyke, in *Proceedings of the International Conference on Radiation Effects in Semiconductors*, IOP Conf. Proc. (Institute of Physics and Physical Society, London, 1977), p.58.
- [2] W.J. Choyke and L. Patrick, *Phys. Rev. Lett.*, **29** (1972), p. 355.
- [3] L. Patrick and W.J. Choyke, *Phys.Rev. B*, **8** (1973), p. 1660.
- [4] W.J. Choyke, L. Patrick, and P.J. Dean, *Phys.Rev.B*, **10** (1974), p. 2554.
- [5] T. Eglisson, I.G. Ivanov, A. Henry, and E. Janzén, *Physica Scripta T79* (1999), p. 50.
- [6] T. Eglisson, J.P. Bergman, I.G. Ivanov, A. Henry, and E. Janzén, *Phys. Rev. B*, **59** (1999), p. 1956.
- [7] T. Eglisson, A. Henry, I.G. Ivanov, J.L. Lindström, and E. Janzén, *Phys. Rev. B*, **59** (1999), p. 8008.
- [8] T. Eglisson, I.G. Ivanov, A. Henry, and E. Janzén, *Physica B*, to be published.
- [9] W.J. Moore, P.J. Lin-Chung, J.A. Freitas, Jr, Y.M. Altaiskii, V.L. Zuev, L.M. Ivanova, *Phys.Rev. B*, **48** (1993), p. 12289.
- [10] W. Suttrop, G. Pensl, W.J. Choyke, R. Stein and S. Leibenzeder, *J. Appl. Phys.* **72** (1992), p. 3708.
- [11] W. Götz, A. Schöner, G. Pensl, W. Suttrop, W.J. Choyke, R. Stein and S. Leibenzeder, *J. Appl. Phys.* **73** (1993), p. 3332.
- [12] R.A. Faulkner, *Phys. Rev.* **184** (1969), p. 713.
- [13] R. Kaplan, R.J. Wanger, H.J. Kim, and R.F. Davis, *Solid State Commun.* **55** (1985), p. 67.
- [14] L. Patrick, W.J. Choyke, *Phys. Rev. B* **2** (1970), p. 2255.
- [15] W.J. Choyke, D.W. Feldman, and L. Patrick, *Bull. Am. Phys. Soc.* **15** (1970), p. 279.
- [16] D. Labrie, T. Timusk and M.L.W. Thewalt, *Phys. Rev. Lett.* **58** (1984), p. 81.
- [17] D. Volm, B. K. Meyer, D. M. Hofmann, W. M. Chen, N. T. Son, C. Persson, U. Lindefelt, O. Kordina, E. Sörman, A. O. Konstantinov, B. Monemar, and E. Janzén, *Phys. Rev. B* **53** (1996), p. 15409.
- [18] M. Goiran, F. Engelbrecht, F. Yang, W. Knap, S. Huant, N. Negre, R. Barbaste, J. Leotin, R. Helbig, S. Askenazy, *Physica B* **246-247** (1998), p. 270.
- [19] C. Persson and U. Lindefelt, *J. Appl. Phys.* **82** (1997), p. 5496.
- [20] P.J. Colwell and M.V. Klein, *Phys.Rev. B* **6** (1972), p. 498.

## Metastability of a Hydrogen-related Defect in 6H-SiC

A. Henry<sup>1,2</sup>, T. Egilsson<sup>1</sup>, I.G. Ivanov<sup>1</sup> and E. Janzén<sup>1</sup>

<sup>1</sup> Department of Physics and Measurement Technology, Linköping University,  
SE-581 83 Linköping, Sweden

<sup>2</sup> also ABB Corporate Research, SE-721 78 Västerås, Sweden

**Keywords:** Hydrogen, Metastability, Photoluminescence

**Abstract.** We report on the metastability behavior of a hydrogen related defect in 6H-SiC. This defect gives rise to a low temperature photoluminescence spectrum and several excited states have been observed using photoluminescence excitation. A quenching of the luminescence intensity is observed when using prolonged optical excitation either with energy higher than the threshold for phonon assisted free-exciton formation or when the excitation energy is resonant with an excited state of the hydrogen related bound exciton. Depending on the initial conditions different types of behavior can be observed.

### Introduction

Metastability has been the subject of many studies in various semiconductors. This behavior has been observed using various experimental techniques. Low temperature photoluminescence (LTPL) is one of them, and often the decrease in intensity of a LTPL spectrum is observed together with the appearance followed by an increase until saturation of a second LTPL spectrum (see as example the chalcogen in Si [1]). In SiC the metastability of very few defects has been studied until now and electrical measurements were used in these cases [2].

Hydrogen has been studied in many semiconductors due to its interesting properties. As a small and light atom it can diffuse fast and it has also the property to passivate both deep and shallow donor or acceptor levels. Hydrogen is involved in many steps for the fabrication of SiC devices, starting with the material growth (bulk or epilayer) and continuing with various processes (cleaning, etching ...). After implantation with hydrogen atoms, the LTPL spectrum of SiC reveals strong bound exciton (BE) lines which were observed in 4H-, 6H- and 15R polytypes but not in the 3C material [3,4]. The PL spectra after H and D implantation are very similar and differ only for the energy position of some phonons assisted side-bands lines which were associated with C-H or C-D bond-stretching vibrational modes, respectively. The defect that gives rise to the LTPL spectrum was proposed to consist of an H (or D) atom bonded to one of the four C atoms neighboring a Si vacancy. This LTPL spectrum is also observed from SiC epilayers grown by chemical vapor deposition [5]. After intense excitation at low temperature the H-BE spectrum decreases in intensity. Annealing at room temperature can restore the original intensity of the spectrum.

We present here results for the so-called primary H<sub>3</sub>-BE and use results from photoluminescence excitation (PLE) study which reveals several excited states of the H<sub>3</sub>-BE.

### Experimental

The sample used in this study was a thick epilayer (180 µm) which was grown on Si face on-axis 6H-SiC substrate by high temperature chemical vapor deposition [6]. The substrate was removed after growth for the LTPL measurements. LTPL and PLE spectra were recorded at 2K. For the LTPL the 351 nm line of an Ar<sup>+</sup> ion laser was used as excitation (above band-gap), whereas for the PLE spectroscopy a tunable dye laser (in the range 4000 – 4300 Å) pumped with the UV multi lines

of the  $\text{Ar}^+$  ion laser was used with a power between 10 to 25 mW depending on the wavelength. The luminescence was spectrally resolved by a 0.85 m SPEX 1404 double monochromator fitted with 1800 grooves/mm gratings, and detected by a UV sensitive photomultiplier tube operating in photon counting mode.

## Results.

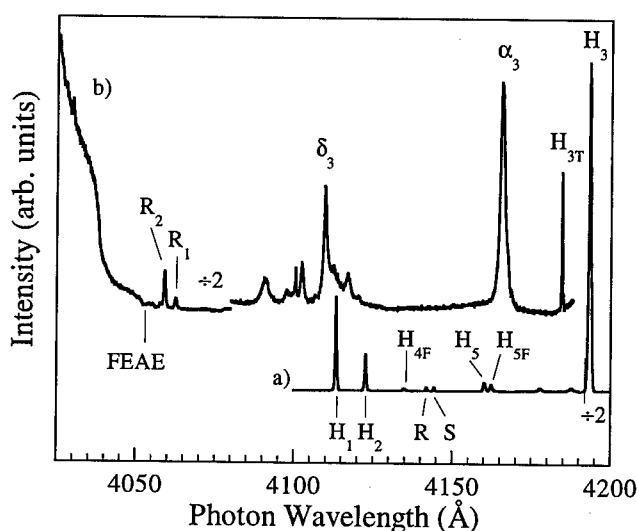


Fig1.a) LTPL spectrum of the H-BE in 6H-SiC and b) PLE spectrum of the  $\text{H}_3$ -BE line. FEAE denoted the free-exciton absorption edge.

When using above band gap excitation a typical H-BE LTPL spectrum is observed (Fig.1.a). The R and S lines are the no-phonon (NP) lines associated to the nitrogen bound exciton. The peaks at about 4178 and 4187 Å are to our knowledge of unknown origin. The  $\text{H}_{1-3}$  lines are the NP lines associated with the primary H-BE's and the  $\text{H}_{4,5}$  are the NP lines related to the secondary H-BE. They are attributed to exciton recombination at two different charge states of the same centers.

The PLE spectrum detected at the  $\text{H}_3$  NP line at 2K is shown in Fig.1.b. The high energy part of the spectrum shows clearly the step-like absorption edge due to the creation of the free-exciton (FE) with the assistance of momentum conserving lattice phonons. Some Raman peaks are also observed such as  $\text{R}_{1-2}$ , which are easily identified when shifting the detection wavelength from the  $\text{H}_3$  NP line. The other peaks ( $\text{H}_{3T}$ ,  $\alpha_3$  and  $\delta_3$ ) are related to various excited states of the  $\text{H}_3$ -BE.

It has been previously reported that with above band-gap excitation a slow decrease of the  $\text{H}_3$ -BE line is observed [5]. Room temperature annealing can restore the original intensity of the signal. Two explanations have been proposed: 1) a transition of the defects due to the illumination into a different charge state [7] could influence the LTPL spectrum intensity or 2) a dissociation due to a recombination-enhanced [8] defect reaction.

In Fig.2 the decrease of the  $\text{H}_3$ -BE line is shown as a function of time when exciting at the  $\alpha_3$  excited state energy position. Similar behavior was observed when exciting resonantly at the  $\text{H}_{3T}$  or  $\delta_3$  lines. After one minute of excitation the signal has decreased to about 70% of its original intensity and after one hour only 10% of the initial signal is detected.

The intensity of the  $\text{H}_3$ -BE line was studied while going through a sequence of different excitation energies. After a quenching during 1 minute (to obtain about 70% of its initial intensity), the

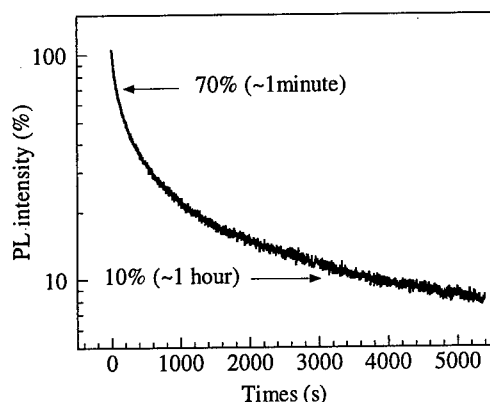


Fig.2 : Decay of the  $H_3$ -BE line at 2K during resonant excitation.

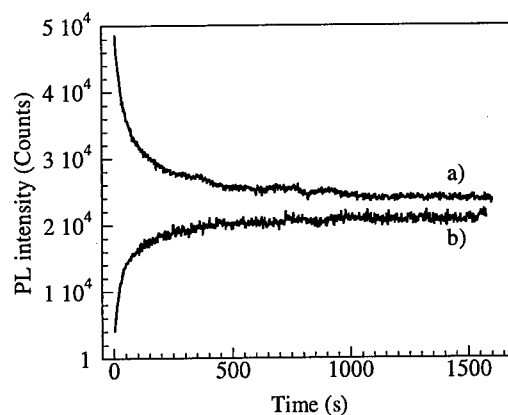


Fig. 3: Intensity of the  $H_3$ -BE line as a function of time at 2K during laser excitation above the FEAE, a) without previous excitation and b) after resonant excitation.

wavelength excitation was then changed to an off-resonant wavelength, which did not coincide with the position of any of the PLE peaks below the FE absorption energy (FEAE) and kept there for one hour. The excitation was then changed back to the  $\alpha_3$  position. The  $H_3$ -BE line intensity was the same as before the off-resonant excitation (70%). This experiment was repeated for various energies at off-resonant excitation. This shows that the quenching during off-resonant excitation is negligible.

The quenching observed here has a non-exponential behavior but that does not rule out the possibility to have a direct quenching of the H-BE. To be able to observe rapidly a quenching, the laser spot needs to be focused on the sample since the higher the excitation, the faster the quenching. However, the detected luminescence contains contribution from different regions: The intensity at the center of the laser spot is higher than that at the periphery. Weak luminescence coming from regions outside the laser spot due to exciton diffusion from the laser spot area can also influence the results.

In an other experiment the sample was cooled in complete darkness and the  $H_3$ -BE line intensity was recorded when excited with a photon energy above the FEAE (Fig.3.a). A decrease of the intensity was observed until a steady state was observed which corresponded to about 50% of its initial intensity. Thereafter the  $H_3$ -BE line was quenched with resonant excitation at the  $\alpha_3$  position during more than 90 minutes to reach only a few % of its initial value. The excitation was then changed to above the FEAE. An increase in intensity of the  $H_3$ -BE line was observed and the intensity was reaching about the same steady state value as previously (Fig.3.b).

#### Discussion.

We tentatively explain the results obtained in this study by proposing the existence of two forms of the H-defect, one stable A giving rise to the observed LTPL and a second metastable B which does not give rise to a LTPL (at least not within the energy region studied here). The transformation from stable to metastable ( $A \rightarrow B$ ) can be done by capture and recombination of a FE or a resonantly excited BE whereas transformation from metastable to stable ( $B \rightarrow A$ ) can be obtained by the capture and recombination of FE.

When the excitation is resonant with the H-BE only the transformation from stable to metastable ( $A \rightarrow B$ ) is possible, giving rise to an almost complete quenching the H-BE LTPL lines.

When the excitation is above the FEAE, both transformations operate. If all H-defects are in the stable state initially (cooling from room temperature to 2K in darkness), the H-BE PL line will decrease until there are enough H-defects in the metastable form to make the transformation  $B \rightarrow A$  as probable as the transformation  $A \rightarrow B$ . This fact explains the results illustrated in Fig.3.a, where the observed quenching is never complete.

These both forms A and B could be either two different charge states of the same H-defect, or two configurations of the same charge state of the H-defect. When using resonant excitation the transformation  $A \rightarrow B$  is observed to be very efficient, this means that the excitation of the H-defect depends of the BE formation. In this case an electron cannot be released or captured at the H-defect which could change the state charge of the defect. The second possibility is to change the charge state of the H-defect if an Auger process is involved in the H-BE recombination. However this type of process will be very fast (few nanoseconds) and does not agree with the experimental observed lifetime of the H-BE (in the hundred of microsecond range [3]). The change of charge state is thus not the plausible explanation for the quenching of the H-BE. We tentatively propose the existence of two configurations of the same charge state. The most probable mechanism by which the BE induces the change of the configuration is through vibrational excitation released by the recombination of the BE. The local vibrational energy could help the defect to overcome the barrier to the other configuration.

#### Acknowledgments.

Support for this work was provided by the Swedish Council for Engineering Sciences (TFR), the SSF program SiCEP and ABB Corporate Research. We are grateful to A. Ellison for providing the sample.

#### References

- [1] A. Henry, E. Sörman, S. Andersson, W.M. Chen, B. Monemar and E. Janzén, Phys. Rev. B 49 (1994) p. 1662
- [2] C.G. Hemmingsson, N.T. Son, O. Kordina, J.L. Lindström, and E. Janzén, submitted to Phys. Rev. B
- [3] W.J. Choyke and L. Patrick, Phys. Rev. Lett. 29 (1972) p. 355
- [4] L. Patrick and W.J. Choyke, Phys.Rev. B 8 (1973) p. 1660
- [5] L.L. Clemen, R.P. Devaty, W.J. Choyke, A.A. Burk, Jr., D.J. Larkin and J.A. Powell, in *Proceedings of the 5<sup>th</sup> International Conference on Silicon Carbide and Related Materials*, edited by M.G. Spencer, R.P. Devaty, J.A. Edmond, M. Asif. Khan, R. Kaplan and M.M. Rahman, IOP Conf. Proc. No. 137 (IOP Publishing, Bristol, 1994) p. 227
- [6] A. Ellison et al, this proceeding , p. 131
- [7] W.J. Choyke, L. Patrick, and D.J. Dean, Phys. Rev. B 10 (1974) p. 2554
- [8] P.J. Dean and W.J. Choyke, Adv. In Phys. 26 (1977) p. 1

Correspondence: A. Henry, Tel : 46 13 28 24 14, Fax: 46 13 14 23 37, e-mail : ahy@ifm.liu.se

## Optical Characterization of Lattice Damage and Recovery in Ion-Implanted and Pulsed Excimer Laser Irradiated 4H-SiC

D. Sands<sup>1</sup>, P.H. Key<sup>1</sup>, M. Schlaf<sup>1</sup>, C.D. Walton<sup>1</sup>, C.J. Anthony<sup>2</sup> and M.J. Uren<sup>2</sup>

<sup>1</sup> Department of Physics, University of Hull, Hull, HU6 7RX, UK

<sup>2</sup> DERA Defence Research and Evaluation Agency, Malvern, Worcs. WR14 3PS, UK

**Keywords:** Contact Preparation, Infrared, Laser Annealing, Lattice Recovery, Reflectivity, Reststrahlen Band

### Abstract

Infrared reflection measurements at near normal incidence between  $400\text{--}7800\text{ cm}^{-1}$  have been performed on ion-implanted and excimer laser irradiated bulk 4H-SiC wafers. A simulated annealing algorithm was used to fit a Lorenz-Drude model to the Reststrahlen region. The parameters of this model are directly related to the structure and electronic properties of the material. By examining the real and imaginary parts of the refractive index we are able to observe both damage induced by ion-bombardment and lattice recovery induced by excimer laser irradiation. The optimum laser fluence for lattice recovery is close to  $1\text{ J cm}^{-2}$ , after which the laser appears to damage the SiC surface. Ultraviolet/visible reflectivity and photoluminescence provide additional evidence of an optimal annealing fluence. A consequence of the modeling is the deduction of estimates for the plasma frequency and carrier densities in annealed material.

### Introduction

Silicon Carbide (SiC) receives strong attention for high power, high frequency, high temperature and radiation resistant devices [1, 2]. Essential for the realisation of Field Effect Transistors (FET's), are source/drain contacts with very low ohmic characteristics [3, 4]. In general contact regions are heavily doped in order to reduce the barrier height, but extrinsic doping of SiC presents a considerable challenge to device engineers. Thermal diffusion is not a feasible technology for self-aligned structures. The thermal diffusion coefficient of SiC is extremely low [5] and while diffusion can be enhanced at temperatures  $\sim 1800\text{K}$  dielectric masking layers begin to dissociate [6]. Similarly, thermal annealing of ion-implantation lattice damage presents difficulties and other methods of recovering the lattice while maintaining the polytype structure are essential in SiC. In this paper we present results of experiments on the use of excimer lasers to activate the dopants.

Excimer laser irradiation has the advantage that, with a typical pulse duration  $\sim 25\text{ns}$ , the high pulse power enables very high surface temperatures to be achieved with minimal lateral heat flow. We use Fourier Transform InfraRed (FTIR) reflection spectroscopy as a diagnostic technique to characterise the surface and subsurface modifications following ion implantation and excimer laser annealing. A simulated annealing algorithm has been developed to optimise a Lorenz-Drude description in order to quantify the electrical and physical properties of the modified SiC surface.

### Experimental

Experimental investigations were made on three different wafers of 4H-SiC bulk crystals from Cree Research, Inc. As-grown p-type, epitaxial p-type, and implanted p-type material. Samples #A, #B and #D were (0001) oriented and implanted with  $\text{N}^{14}$  ions at doses in the ratio 0.57:0.29:0.14 at energies of 140, 80, 30keV respectively to achieve a flat dopant profile. Sample #B was capped with

100-200nm of  $\text{Si}_3\text{N}_4$  as an attempt to prevent sublimation. An epitaxial sample, #E, was implanted at 20, 40, and 60keV to a total dose of  $1 \times 10^{15} \text{ cm}^{-2}$ . Prior to irradiation the samples were cleaned in a standard ethanol rinse in an ultrasonic bath and spun dry with de-ionized water.

The laser irradiation was carried out using a Lumonics TE-840-L XeCl excimer laser with a pulse duration  $\sim 25\text{ns}$ . The sample chamber was pressurised to 35 bar in order to sustain melting. A combination of a spherical and cylindrical lens was used to form a  $250 \mu\text{m} \times 5\text{mm}$  image of a square aperture. The sample was placed behind a proximity mask and translated horizontally across the beam to produce an irradiated area  $4.5\text{mm} \times 4.5\text{mm}$ . Neutral density filters were used to select the laser fluences in the range of  $0.7$  to  $1.5 \text{ Jcm}^{-2}$  at 2, 5, and 10 pulses.

PL and ultra violet/visible reflectivity measurements were carried out using an Ocean Optics S2000 CCD array spectrometer with a bifurcated fibre reflection probe situated normal to the sample surface. A broad band PL spectrum between 350 and 700nm at 77K was measured with a resolution  $\sim 2\text{nm}$ .

Room temperature infrared reflectance measurements were carried out on near normal incidence ( $16^\circ$ ) using a Perkin-Elmer Paragon 1000 FTIR spectrometer. Each sample received 64 scans at a resolution of  $1 \text{ cm}^{-1}$  between 400 and  $7800 \text{ cm}^{-1}$ .

The infrared reflectivity of the SiC wafer was modelled as an air/damaged-SiC/bulk-SiC system using the matrix algorithm introduced by Harbecke [7], in which the complex index of refraction and the thickness of the SiC layer determine the matrix elements. The substrate is modelled as half-infinite bulk material because the rough backside of the materials scatters the radiation and a negligible amount is reflected back.

The complex dielectric function  $\epsilon$  for silicon carbide in the infrared was calculated using the formalism given in [8, 9]

$$\epsilon = (n + ik)^2 = \epsilon_\infty - \frac{\epsilon_\infty \nu_p^2}{\nu(\nu + i\gamma)} + \frac{f \nu_{TO}^2}{\nu_{TO}^2 - \nu^2 + i\Gamma\nu} \quad (\text{Eq. 1})$$

where  $n$  is the refractive index,  $k$  is the extinction coefficient,  $i = \sqrt{-1}$ ,  $\nu$  is the infrared frequency,  $\epsilon_\infty$  is the high-frequency dielectric constant,  $\nu_p \equiv \sqrt{(Ne^2/(\pi m^* \epsilon_\infty))}$  is the plasma wavenumber due to free carrier of density  $N$ , effective mass  $m^*$  and electron charge  $e$ ,  $\gamma = e/(m^* \mu)$  is the free-carrier damping constant for carriers with mobility  $\mu$ ,  $f$  is the oscillator strength,  $\nu_{TO}$  is the resonant frequency (transverse optical mode) and  $\Gamma$  is the phonon damping coefficient.

The modelled and the measured infrared spectrum were compared and a least square sum was used to assess the quality of the fit. Global minimisation of this least square sum was achieved using a simulated annealing algorithm [10].

## Results and Discussion

Fig. 1 shows the infrared reflection measurements on the as-grown material and material implanted with doses of  $1 \times 10^{14} \text{ cm}^{-2}$  and  $3 \times 10^{15} \text{ cm}^{-2}$ . The reflectivity maximum of the Reststrahlen band decreases with implantation dose compared to the as-grown material. Shown in the same graph is the real part of the complex refractive index of the damaged layer which illustrates the difference in optical behaviour between the as-grown and modified material. The high reflectivity in the Reststrahlen region is due not to the real part of the refractive index, where  $n < 1$ , but to the extinction coefficient which is very high. Hence the absorption takes place very close to the surface. Figs. 2 and 3, show the optical behaviour of the sample implanted at a dose of  $1 \times 10^{14} \text{ cm}^{-2}$ . Recovery appears to have taken place at a laser fluence of  $1.0 \text{ J cm}^{-2}$ , where it can be seen that the



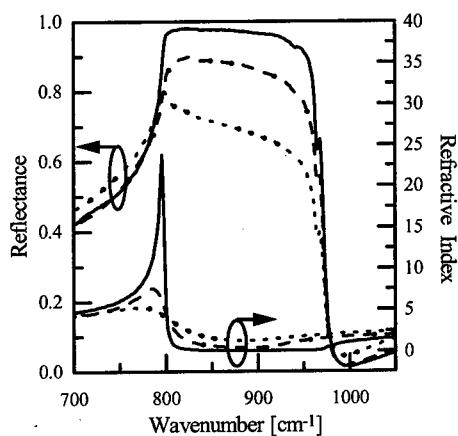


Fig. 1 IR reflection spectra and refractive index of nitrogen ion implanted and as-grown 4H-SiC (Dose: — as-grown, ---  $1 \cdot 10^{14} \text{ cm}^{-2}$ , ....  $3 \cdot 10^{15} \text{ cm}^{-2}$ )

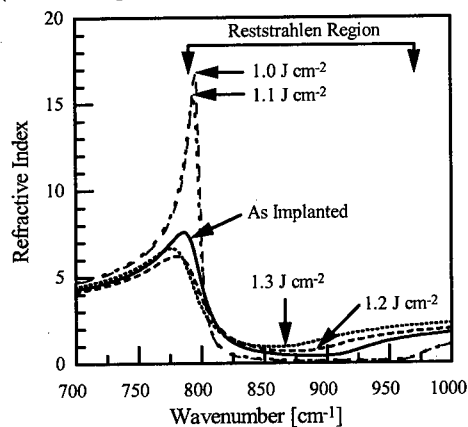


Fig. 2 Refractive index for laser annealed sample of 4H-SiC

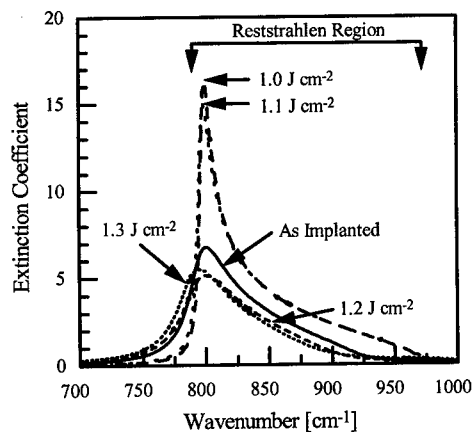


Fig. 3 Extinction coefficient for laser annealed sample of 4H-SiC

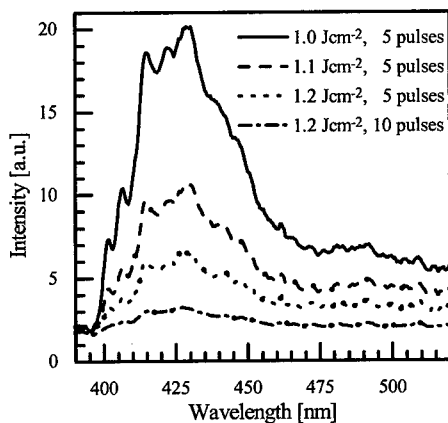


Fig. 4 Photoluminescence spectra for 4H-SiC at 77K

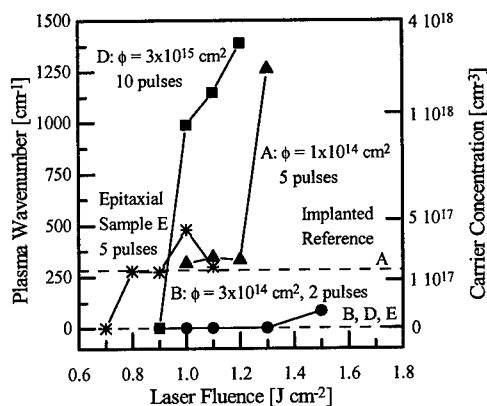


Fig. 5 Plasma wavenumbers for laser annealed 4H-SiC

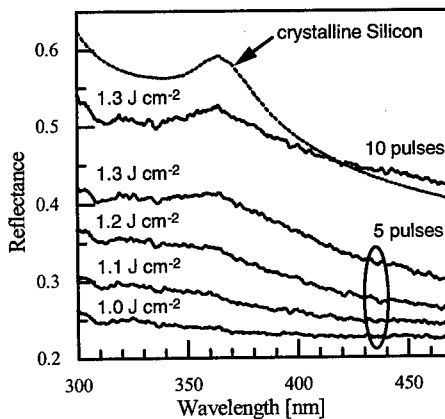


Fig. 6 Reflectivity of excimer laser annealed 4H-SiC

refractive index and extinction coefficient are vastly different from both the implanted and laser damaged material.

Fig. 4 shows the PL intensity as a function of incident laser fluence. The maximum PL intensity occurs at  $1.0 \text{ J cm}^{-2}$  and the reduction at higher fluences is consistent with  $n$  and  $k$  data in Figs. 2 and 3, which indicate some degree of lattice disorder. Fig. 5 shows the plasma frequencies of the laser irradiated material along with the values found for as-implanted material (horizontal lines). Ultraviolet/visible reflectivity data between 300 and 450nm of excimer laser irradiated material for the low dose implanted sample, ( $1 \times 10^{14} \text{ cm}^{-2}$ ) are shown in Fig. 6. Here it can be seen that the reflectivity increases with laser fluence. The top curve corresponds to the theoretical reflectivity of bare silicon [11] and the peak  $\sim 360 \text{ nm}$  matches the emerging peak in SiC. This indicates the existence of elemental polycrystalline silicon which is consistent with the thermodynamic argument [12] that SiC dissociates into molten Si with dissolved carbon at temperatures close to the melting point. This strongly suggests that lattice recovery, as indicated in figs. 2 and 3, occurs at fluences such that the surface is below the melting point and only at higher fluences does the surface melt.

Most interestingly, however, the shift in plasma frequency deduced from the modelling occur at the higher fluence and is still increasing with fluence. It is possible that lattice recovery using pulsed excimer laser annealing is not coincident with dopant activation and that the high carrier densities are a direct consequence of the laser induced damage to the surface. Comparisons can be made with the low contact resistivity data of Lliadis [13] *et al.* where surface modifications using Ga focused ion beams lower the surface barrier by increasing the amount of disorder.

### Conclusion

We are able to observe the recovery of the lattice and the onset of activation. From the modelling of the reflectivity spectra we conclude that material annealed at the optimal fluence resembles closely the as-grown material. We have also deduced estimates of the plasma frequencies and carrier concentrations, but it appears that the optimum fluence for carrier activation is not the same as the optimum fluence for lattice recovery.

### References

- [1] V. E. Chelnokov, *et al.*, Material Science and Engineering B46, (1997) p. 248.
- [2] E. Janzen, *et al.*, Material Science and Engineering B46, (1997) p. 203.
- [3] N. A. Papanicolaou, *et al.*, Appl. Phys. Lett 73, 14, (1998) p. 2009.
- [4] T. Teraji, *et al.*, Appl. Phys. Lett 71, 5, (1997) p. 689.
- [5] T. Kimoto, *et al.*, J. Elec. Mat. 24, (1995), p. 235.
- [6] R. F. Davis, *et al.*, Proc. IEEE 79, (1993), p. 677.
- [7] B. Harbecke, *et al.*, Appl. Phys B 39, (1986), p. 165.
- [8] S. S. Mitra, in: E. D. Palik (Ed.), Handbook of Optical Constants of Solids, Academic Press, New York, 1985, p. 213.
- [9] P. Grosse, *et al.*, M. Offenberg, Appl. Phys A 39, (1986), p. 257.
- [10] A. D. Rakic, *et al.*, Phys. Rev E 52, (1995), p. 6862
- [11] S. S. Mitra, in: E. D. Palik (Ed.), Handbook of Optical Constants of Solids, Academic Press, New York, 1985, p. 547.
- [12] S. V. Baranov, *et al.*, Inorganic Materials 18, 8, (1982) p. 1097.
- [13] A. A. Lliadis, *et al.*, Appl. Phys. Lett 173, 24, (1998) p. 3545.

Corresponding Author: Dr. D. Sands  
email: D.Sands@physics.hull.ac.uk  
Tel: +44-(0)1482-46-5826  
Fax: +44-(0)1482-46-5606

## Microscopic Probing of Raman Scattering and Photoluminescence on C-Al ion co-implanted 6H-SiC

Z.C. Feng<sup>1</sup>, S.J. Chua<sup>1</sup>, Z.X. Shen<sup>2</sup>, K. Tone<sup>3</sup> and J.H. Zhao<sup>3</sup>

<sup>1</sup> Institute of Materials Research & Engineering, 3 Research Link, Singapore, 117602, Singapore

<sup>2</sup> Department of Physics, National University of Singapore, Singapore, 119260, Singapore

<sup>3</sup> Department of Electrical and Computer Engineering, Rutgers University,  
 Piscataway, NJ 08855, USA

**Keywords:** 6H-SiC, Annealing, Ion Implantation, Photoluminescence, Raman

**Abstract** A series of hot (600°C) and room temperature (RT) C-Al ion co-implanted 6H-SiC epilayers were studied by micro-Raman scattering and photoluminescence. The damage and amorphization of SiC layer by co-implantation, and the elimination/suppression of the implantation induced amorphous layer via high temperature annealing are observed. The recovery of the crystallinity and the activation of the implant acceptors are confirmed. The results from hot or RT co-implantation are compared.

### 1. Introduction

Ion implantation is a promising technique for the SiC-based device development. It is, in particular, suitable for the selective doping in SiC device fabrication. The n-type doping with a high density of donor activation in SiC can be obtained by N ion implantation [1]. N<sup>+</sup> implantation into p-type 6H- and 4H-SiC epilayers at room and elevated temperatures has also been successful [2]. Efforts on the p-type Al and B ion-implantation into 6H-SiC have been explored [3,4]. To find a good way to improve the acceptor implant activation in SiC, we have explored the C-Al co-implantation [5-7]. Electrical characterization has shown a large reduction of both the sheet resistivity in the C-Al co-implanted 6H-SiC epilayer and the specific contact resistivity of Al contacts made on C-Al implanted layer, indicating enhanced acceptor activation efficiency [5,6]. Preliminary optical measurements have also provided the evidence on the activation of acceptors and the recrystallization of C-Al co-implanted 6H-SiC by high temperature annealing [7]. In this report, we further studied the effects of Al-C ion co-implantation on epitaxial n<sup>-</sup>/n<sup>+</sup> 6H-SiC and high temperature (1550°C) annealing by way of micro-Raman scattering ( $\mu$ -RS) and micro-photoluminescence ( $\mu$ -PL) spectroscopy. Focus is on the comparison of results from the hot (600°C) and room temperature implantation with different implanted dose levels.

### 2. Experiment

Table I Ion implantation concentration and temperature

type/concentration (cm <sup>-3</sup> )	temperature and sample No.			
C <sup>+</sup> : 6x10 <sup>20</sup> , Al <sup>+</sup> : 6x10 <sup>20</sup>	600°C	(E2)	RT	(E3)
C <sup>+</sup> : 8x10 <sup>20</sup> , Al <sup>+</sup> : 8x10 <sup>20</sup>	600°C	(E5)	RT	(E6)
C <sup>+</sup> : 1x10 <sup>21</sup> , Al <sup>+</sup> : 1x10 <sup>21</sup>	600°C	(F2)	RT	(F3)
C <sup>+</sup> : 2x10 <sup>21</sup> , Al <sup>+</sup> : 2x10 <sup>21</sup>	600°C	(F4)	RT	(F5)

Four pairs of C<sup>+</sup>-Al<sup>+</sup> co-implanted (with implant energies of 50-200 keV) 6H-SiC epitaxial films, ~10  $\mu$ m thick, n-type doped with nitrogen to ~1x10<sup>16</sup> cm<sup>-3</sup> and grown on n<sup>+</sup> (~1x10<sup>18</sup> cm<sup>-3</sup>)

6H-SiC substrates, were studied. The multiple-energy implantation was used to create box profiles of 0.2  $\mu\text{m}$  deep with uniform concentrations of both C and Al based on profile simulation as shown in Table I. Each pair consists of two samples with the same  $\text{C}^+-\text{Al}^+$  implanted concentrations but under hot ( $600^\circ\text{C}$ ) or room temperature (RT), listed in Table I. Two Renishaw Raman microscope systems with 514 nm and 325 nm excitations were used for Raman and photoluminescence (PL) measurements at RT.

### 3. Raman scattering under 514.5 nm visible excitation

Figure 1 shows micro-Raman spectra from several 6H-SiC samples. The spectrum for the non-implanted corner exhibits the main Raman modes for a perfect 6H-SiC crystal [7]. After  $\text{C}^+-\text{Al}^+$  co-implantation at RT with different concentrations, three broad Raman bands appeared, as shown in Figs. 1a-1c. They are caused by Si-Si, Si-C and C-C vibrations, respectively, which are typical for amorphous SiC [8]. Single crystalline 6H-SiC characteristic Raman bands [9] of two  $\text{E}_2(\text{TO})$  and one  $\text{A}_1(\text{LO})$  are weakly superposed on the top of the Si-C amorphous band. These indicate the damage of 6H-SiC crystallinity and the formation of amorphous phase due to the ion implantation. However, after annealing at  $1550^\circ\text{C}$  for 30 minutes, these broad features are almost eliminated, and a Raman spectrum similar to that

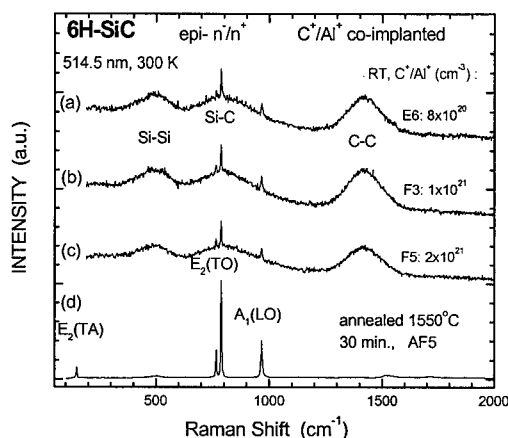


Figure 1. Raman spectra, under 514 nm excitation, from three  $\text{n}^+/\text{n}^+$  epitaxial 6H-SiC with C-Al ions co-implanted at RT with different concentrations, (a)-(c), and an annealed sample, (d).

from a single crystalline 6H-SiC appears as shown in Fig. 1d, implying the recovery of the SiC crystalline structure.

Samples under  $\text{C}^+-\text{Al}^+$  hot implantation at  $600^\circ\text{C}$  and before annealing showed quite different Raman spectral shapes. They did not show the three strong amorphous bands as shown in Figs. 1a-1c, instead, they showed only very weak amorphous features, as shown in Fig. 2a, with major features from crystalline 6H-SiC. This indicates that the hot implantation causes much less damage in 6H-SiC than that for RT ion co-implantation. After annealing at  $1550^\circ\text{C}$  for 30 minutes, they exhibited  $\mu\text{-RS}$  of Fig. 2b, which is close to Fig. 1d. Comparing two magnified (by a factor 10) spectra in Figs. 2a-2b, it can be found that after high temperature annealing, the weak a-SiC features have been further suppressed. The Raman spectrum from the hot-implanted/annealed sample is very close to that from a perfect crystalline 6H-SiC.

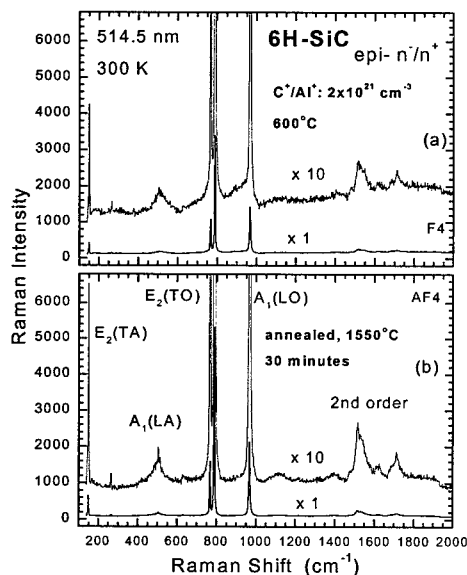


Figure 2. Raman spectra, excited under 514 nm, from a hot ( $600^\circ\text{C}$ )  $\text{C}^+-\text{Al}^+$  co-implanted 6H-SiC, F4, with a concentration of  $2 \times 10^{21} \text{ cm}^{-3}$  for  $\text{C}^+-\text{Al}^+$ , (a) before and (b) after annealing at  $1550^\circ\text{C}$  for 30 minutes.

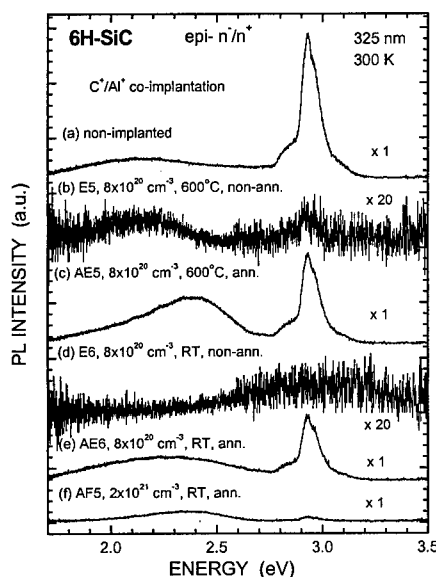


Figure 3. RT  $\mu$ -PL probing from  $n/n^+$  epitaxial 6H-SiC: (a) non-implanted, (b) non-annealed and (c) annealed (1,550°C)  $Al^+-C^+$  hot (600°C) co-implanted with C-Al concentration of  $8 \times 10^{20} \text{ cm}^{-3}$ , (d) non-annealed and (e) annealed RT  $Al^+-C^+$  co-implanted with C-Al doses of  $8 \times 10^{20} \text{ cm}^{-3}$ , and (f) annealed RT  $Al^+-C^+$  co-implanted with C-Al doses of  $2 \times 10^{21} \text{ cm}^{-3}$ .

implanted doses and after annealing under the same conditions, there exists a very broad band spreading over 1.7-2.7 eV. It is most likely due to a combination of the deep defect 2.1 eV band and the Al-activated 2.4 eV band. Furthermore, Fig. 3f exhibits a PL from a RT implanted/annealed sample with the implanted concentration much higher than the one in Fig. 3e. The  $FB_N$  band in Fig. 3f is much weaker than that in Fig. 3e, and its Al-acceptor activated 2.4 eV band component is weaker than one in Fig. 3e also. This indicates that too high an implantation dose will make it difficult to anneal out implantation damage completely.

#### 5. Raman scattering under 325 nm UV excitation

To better understand the spectral behavior from these co-implanted samples, further Raman measurements using other excitation wavelengths, such as 488 nm and 325 nm, were performed. When the 488 nm excitation was applied, the RT implanted samples showed Raman spectra with three Si-Si, Si-C and C-C amorphous bands similar to that of Figs. 1a-1c, but without the superposed sharp crystalline 6H-SiC features of  $E_2(TO)$  and  $A_1(LO)$  (not shown here). This indicates that the 488 nm laser line can probe the implantation induced a-SiC layer but can not penetrate through it to probe the underneath crystalline 6H-SiC.

#### 4. Micro-PL under 325 nm excitation

Figure 3 exhibits RT  $\mu$ -PL spectra of several hot and RT  $C^+-Al^+$  co-implanted 6H-SiC. The non-implanted corner shows a strong RT PL band at 2.93 eV, due to the free-to-bound transition involving nitrogen,  $FB_N$ , with a 100 meV phonon side band in its low energy side [10]. A deeper and very broad band with the peak energy at  $\sim 2.1$  eV might be due to the defects related emissions and its origin is unknown yet. After the  $C^+-Al^+$  co-implantation, these PL emissions, in particular the  $FB_N$  band, are weakened considerably, as shown in Figs. 3b and 3d, indicating the severe damage of the crystalline structure. However, the PL spectrum in Fig. 3b for a hot implanted sample E5 still showed the  $FB_N$  band and the 2.1 eV band weakly, while the spectrum in Fig. 3d for a RT implanted one showed no features at 2.1 eV and only a very broad bump between 2.5-3.4 eV. This comparison indicates that the hot implanted sample has less damage than the RT implanted one.

Through annealing at 1550°C for 30 minutes on implanted samples, the  $FB_N$  band was re-covered with its peak intensity close to the value before implantation in both cases (Figs. 3c and 3e). For the hot-implanted/annealed sample, a new broad PL band with a peak energy at  $\sim 2.4$  eV appeared (Fig. 3c), superimposed on the 2.1 eV defects related band. This is due to the Al acceptor [10] or C-Al complex. However, for the RT implanted/annealed sample with the same amount of

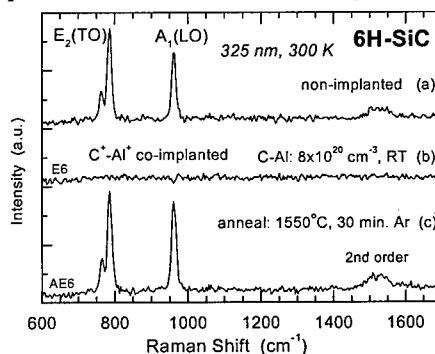


Figure 4. Raman spectra from a  $n/n^+$  epitaxial 6H-SiC, E-6, excited under 325 nm, for (a) non-implanted corner, and  $Al^+-C^+$  co-implanted region (b) before and (c) after annealing.

Figure 4 shows the UV (325 nm) excited  $\mu$ -RS probe on a  $n^+/n^+$  epitaxial 6H-SiC with RT implantation doses of  $2 \times 10^{21} \text{ cm}^{-3}$  for both  $\text{C}^+$  and  $\text{Al}^+$ . From the non-implanted corner, 6H-SiC characteristic  $\text{E}_2(\text{TO})$  and  $\text{A}_2(\text{LO})$  modes are exhibited. After  $\text{C}^+-\text{Al}^+$  RT co-implantation, neither these Raman features nor the broad amorphous bands can be detected under the same measurement conditions, unlike the case of 514 nm excitation as shown in Figs. 1a-1c. However, after high temperature annealing, the crystalline 6H-SiC characteristic Raman  $\text{E}_2(\text{TO})$  and  $\text{A}_2(\text{LO})$  features are re-covered as shown in Fig. 4c. Because the laser probe depth of the 325 nm excitation is much less than that of the 514 and 488 nm excitations, this shows that the near surface 6H-SiC layers were badly damaged under RT  $\text{C}^+-\text{Al}^+$  co-implantation, however, after high-T annealing, the implanted layers are recovered with good crystallinity.

The dramatic changes in above micro-probing RS-PL spectra for 6H-SiC can be explained from the behavior of the absorption coefficient of the implantation induced a-SiC layer [7]. The above results show that the 514 nm light can penetrate through the  $0.2 \mu\text{m}$  a-SiC layer slightly, the 488 nm light can not, and the 325 nm light can probe the very top thin layer of SiC only.

Further temperature-dependent studies of  $\mu$ -RS were also performed (data not shown here). The major  $\text{A}_1(\text{LO})$  and  $\text{E}_2(\text{TO})$  6H-SiC modes can be detected from all the  $\text{C}^+-\text{Al}^+$  co-implanted/annealed samples over a wide range of temperature, 80-870 K and they are very close to the spectra from non-implanted 6H-SiC. These provide a further evidence of the recrystallization of the C-Al co-implanted/annealed 6H-SiC and the activation of implant acceptors. Further analyses will provide more supports on our conclusions in details.

## 6. Conclusion

In summary, a series of hot ( $600^\circ\text{C}$ ) and RT  $\text{C}^+/\text{Al}^+$  co-implanted 6H-SiC epitaxial films were studied by means of micro-Raman and PL spectroscopy. Visible Raman probing on all the RT implanted samples before annealing showed broad amorphous bands corresponding to Si-Si, Si-C and C-C vibrations, while the hot implanted samples exhibited different spectra with weak a-SiC features and strong characteristic 6H-SiC modes. High temperature annealing recovered the crystalline 6H-SiC modes for both cases. Wavelength dependent Raman scattering has probed different depth of SiC layer, showing different features. UV PL micro-probing reveals the marvellous variations of RT PL spectra for samples without implantation,  $\text{C}^+-\text{Al}^+$  co-implanted but before annealing, and implanted/annealed. The annealing-recovered Al related 2.4-eV PL band is stronger in hot implanted sample than the RT implanted one. Too high a co-implantation dose beyond  $2 \times 10^{21} \text{ cm}^{-3}$  led to a poor activation of Al acceptors. This work provides a non-destructive and convenient way to investigate the effects of ion implantation/annealing on SiC materials.

## References

- [1] M. V. Rao, P. Griffiths, O. W. Holland, G. Kelner, J. A. Freitas, Jr., D. S. Simons, P. H. Chi and M. Ghezzi, *J. Appl. Phys.* **77** (1995), p. 2479.
- [2] T. Kimoto, N. Inoue and H. Matsunami, in W. J. Choyke, H. Matsunami and G. Pensl ed., *Fundamental Questions and Applications of SiC* (Part II), special issue, *Phys. Stat. Sol. (a)* **161** (1997), p. 263.
- [3] M. V. Rao, P. Griffiths, J. Gardner, O. W. Holland, M. Ghezzi, J. Hretchmer, G. Kelner and J. A. Freitas, *J. Electronic Mater.* **25** (1996) p. 75.
- [4] T. Troffer, M. Schadt, T. Frank, H. Itoh, G. Pensl, J. Heidl, H. P. Strunk and M. Maier, in [3], p.277.
- [5] J. H. Zhao K. Tone, S. R. Weiner, M. A. Caleca, H. Du and S. P. Withrow, *IEEE Electron Device Lett.* **18** (1997), p. 375.
- [6] K. Tone and J. H. Zhao, *IEEE Trans. Electron Dev.* **46** (1999), p. 612.
- [7] Z. C. Feng, S. J. Chua, K. Tone and J. H. Zhao, *Appl. Phys. Lett.* **75** (1999), p. 472.
- [8] V. N. Makarov, D. A. Plotkin and A. V. Suvorov, *Inst. Phys. Conf. Ser. No. 137* (1994), p. 545.
- [9] D. W. Feldman, J. H. Parker, Jr., W. J. Choyke and L. Patrick, *Phys. Rev.* **170** (1968), p. 698.
- [10] M. Yoganathan, W. J. Choyke, R. P. Devaty, P. G. Neudeck, *J. Appl. Phys.* **80** (1996), p. 1763.

## Confocal Raman Microprobe of Lattice Damage in $N^+$ Implanted 6H-SiC

N. Mestres<sup>1</sup>, F. Alsina<sup>2</sup>, F.J. Campos<sup>2</sup>, J. Pascual<sup>2</sup>, E. Morvan<sup>3</sup>, P. Godignon<sup>3</sup>  
and J. Millán<sup>3</sup>

<sup>1</sup> Institut de Ciència de Materials de Barcelona (CSIC), Campus UAB, ES-08193 Bellaterra, Spain

<sup>2</sup> Departament de Física, Universitat Autònoma de Barcelona, ES-08193 Bellaterra, Spain

<sup>3</sup> Centro Nacional de Microelectrónica (CSIC), Campus UAB, ES-08193 Bellaterra, Spain

**Keywords:** Ion Implantation, Radiation Damage, Raman Scattering

**Abstract:** We have investigated the defect accumulation and amorphisation in  $^{14}N^+$  implanted 6H-SiC as a function of ion fluence using confocal micro-Raman scattering. Raman spectra are very sensitive to changes in the chemical short-range order and to the formation of Si-Si- and C-C-bonds, which are not present in the unimplanted material. The technique also allowed the determination of the optical absorption coefficient. It increases proportional to the ion dose until the formation of the amorphous layer, and this increase is related to the formation of absorbing centers.

### 1.- Introduction

Silicon carbide (SiC) is an interesting material for the fabrication of electronic and optoelectronic devices operating under extreme conditions (high temperatures, reactive environments). In the device processing ion implantation is an important technological step, and seems to be the only feasible technique for local doping of SiC. However, the implantation process causes radiation damage, which has to be removed for most of the applications. Therefore, the study of ion-beam induced damage formation in SiC is of scientific as well as of technological interest. On the other hand, nitrogen has become the most common donor implant dopant in SiC. Nitrogen occupies C lattice sites, its low atomic mass offers low implant lattice damage and flexible ion range. In addition, the N donor has a low carrier ionization energy ( $\sim 80$  meV), which results in a high carrier concentration even at room temperature.

Raman spectroscopy has proved to be a powerful characterization technique for the analysis of damage effects. This technique is sensitive to the alterations of the chemical short-range order and bond types in semiconductors. One of the main drawbacks of the use of a conventional micro-Raman spectrometer is the poor depth resolution. In this way, at low absorption levels, most of the scattered light originates from the virgin portion of the sample, masking all traces coming from the damaged part of the crystal. In the last years, the development of the confocal micro-Raman setup has significantly improved the depth profile analysis. In a previous work [1] we have characterized the changes in the lattice damage of  $Al^+$  implanted 6H-SiC, changing the implantation energy at a constant ion dose below the amorphisation threshold. The aim of the present work is to correlate the changes in the Raman spectra to the lattice damage resulting from  $N^+$  implantation at a constant energy of 160 KeV varying the ion fluence.

### 2.- Experimental

The starting material was single crystalline  $3^\circ$  off-axis  $\langle 0001 \rangle$  oriented 6H-SiC wafers supplied by CREE Research. They were implanted at room temperature with  $^{14}N$  at a fixed energy of 160 keV

and ion fluences ranging from  $5 \times 10^{13} \text{ cm}^{-2}$  up to  $5 \times 10^{15} \text{ cm}^{-2}$ . The simulation [2] of the depth profiles of displaced silicon atoms and  $^{14}\text{N}$  ion concentration gives an estimate of  $\sim 0.3 \mu\text{m}$  for the damaged depth. The Raman scattering measurements were performed at room temperature in a backscattering geometry using a Jobin-Yvon T64000 spectrometer coupled with an Olympus metalographic microscope that contains an X-Y-Z stage. The microscope stage could be adjusted with an accuracy of  $0.2 \mu\text{m}$  along the optical axis. The spectra were excited with the 514.5 nm line of an Ar ion laser. The light was focused and collected through a  $\times 100$  short working length objective with a numerical aperture value of 0.90. In our confocal set-up the adjustable pinhole has been kept closed to  $100 \mu\text{m}$ .

### 3.- Results and discussion

Figure 1 shows typical Raman data for unimplanted and  $\text{N}^+$ -implanted 6H-SiC. The perfectly ordered crystal consists of  $\text{sp}^3$ -type Si-C<sub>4</sub>- and C-Si<sub>4</sub>-bonds, respectively. Every Si atom is thus surrounded by four C atoms and vice versa. This structural feature marks the chemical short-range order in the crystalline material, with no homonuclear C-C- and Si-Si-bonds being present. The ability of Raman spectroscopy to discriminate between different type of bonds gives information on the alterations of the chemical short-range order and bond types induced by ion implantation [3]. The Raman features present in the spectrum from the virgin sample are identifiable from previous studies [4]. The  $\text{E}_2$  planar acoustic doublet appears at 145 and  $149 \text{ cm}^{-1}$ . The  $\text{E}_1$  planar acoustic doublet is located at 235 and  $240 \text{ cm}^{-1}$ . The  $\text{E}_2$  planar acoustic mode at  $266 \text{ cm}^{-1}$  corresponds to the folding of the transversal acoustic (TA) mode of the zone edge of the basic Brillouin zone. The 505.0,  $513.5 \text{ cm}^{-1}$  doublet is an  $\text{A}_1$  axial or longitudinal acoustic (LA) mode. Two planar or transversal optic (TO) modes of  $\text{E}_2$  symmetry at  $767.5 \text{ cm}^{-1}$  and  $788.0 \text{ cm}^{-1}$ , and an  $\text{A}_1$  longitudinal optic (LO) phonon at  $966.5 \text{ cm}^{-1}$ . The mode at  $796.0 \text{ cm}^{-1}$  is a planar optical mode of  $\text{E}_1$  symmetry, forbidden in this scattering geometry, it may however become observable due to the large collection angle of the microscope objective. The mode at  $888.5 \text{ cm}^{-1}$  corresponds to an  $\text{A}_1$  axial optic mode. The optical branch of the second-order Raman spectrum expands the region between  $1350 \text{ cm}^{-1}$  and  $1800 \text{ cm}^{-1}$ , being the largest Raman intensity in the spectral range  $1510\text{-}1580 \text{ cm}^{-1}$ . The spectral features observed in the second order Raman spectra of 6H-SiC, have been recently discussed by Burton et al. [5].

At low ion dose implantation ( $\leq 5 \times 10^{14} \text{ cm}^{-2}$ ) the Raman spectra consist of a superposition of weakened sharp bands arising from the underlying undamaged crystal and four broad bands centered at 200-300, 550, 770 and  $900 \text{ cm}^{-1}$ . These bands, which reflect the 6H-SiC phonon density of states [6] are activated by the breaking of translation symmetry in the disordered implanted layer. The low energy modes ( $200\text{-}550 \text{ cm}^{-1}$ ) can be related to the formation of Si-Si homonuclear bonds. At the high energy side, a new phonon band emerges at  $1430 \text{ cm}^{-1}$ , even for ion implantation doses as low as  $5 \times 10^{13} \text{ cm}^{-2}$ , this band cannot be interpreted as a two phonon process because it does not correspond to the combination of high density phonon states. The band at  $1430 \text{ cm}^{-1}$  is characteristic of C-C homonuclear bonds.

As a consequence of the increasing disorder in the implanted layer increasing ion fluence, the absorption coefficient also increases. This fact leads to a decrease in the intensity of the sharp first- and second-order Raman lines arising from the underlying bulk material, and to a rising of the Raman signal originated in the implanted layer. For ion dose implantation above  $5 \times 10^{14} \text{ cm}^{-2}$  the Raman spectra in the full energy range show the evolution to an amorphous state with broad phonon bands at 250 and  $520 \text{ cm}^{-1}$ , associated to Si-Si bonds,  $800\text{-}900 \text{ cm}^{-1}$  assigned to Si-C bonds, and  $1430 \text{ cm}^{-1}$  corresponding to the C-C bonds.



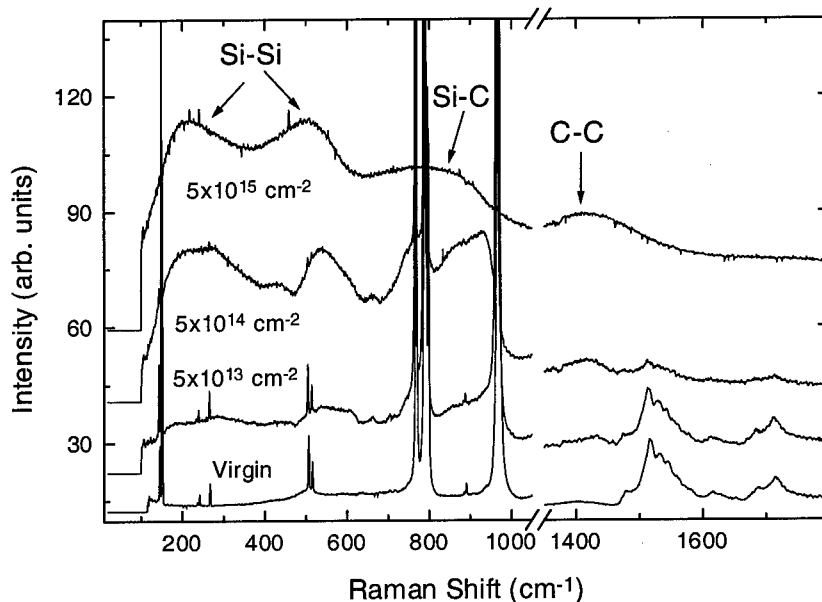


Figure 1: Raman spectra of 6H-SiC before and after implantation with 160 keV  $^{14}\text{N}^+$  ions at various fluences up to  $5 \times 10^{15} \text{ cm}^{-2}$ . The spectra are terminated by a horizontal line, which designates the zero of the intensity scale for each spectrum.

In a previous work [1], we have shown that the disorder induced changes in the optical absorption coefficient of the implanted layer can be extracted from the depth profiling of the  $966 \text{ cm}^{-1}$  LO-mode intensity of the undamaged portion of the sample, using confocal micro-Raman scattering. The Raman intensity of the LO mode is affected by the light absorption in the damaged portion of the epilayer. Raman scattering has to be regarded as an integration technique that evaluates the absorption all over the damaged portion of the sample ( $\alpha d$ ), regardless of the defect profile, it provides then information on the integrated damage. In our case, since the implantation energy is constant for all fluences, the spatial distribution of the damage profile should be very similar for all samples.

Following the method developed in reference [1] we have plotted in figure 2 the changes in the absorbance,  $\alpha d$ , as a function of the implanted ion dose. The evolution of the Raman spectra and the absorption with increasing implantation dose shows that bombardment with ion fluences below a critical value,  $\sim 5 \times 10^{14} \text{ cm}^{-2}$ , results in nucleation and accumulation of defect agglomerates or small amorphous zones, in a still crystalline surrounding. This nucleation regime is characterized by the appearance of Si-Si- and C-C-homonuclear bonds, and with the linear dependence of the integrated absorption with the ion fluence. This picture agrees with the work of Wolse et al. [3] who performed X-ray absorption fine structure spectroscopy (EXAFS) and Raman scattering to obtain information on the chemical short-range order and the type of bonds formed during ion bombardment of SiC. At higher fluences, in the so called growth regime, the absorption approaches a saturation value. The saturation of disorder is a consequence of the amorphisation of the whole implanted thickness when increasing the ion dose. A laterally coherent amorphous layer forms, which is buried at the depth of maximum energy deposition by elastic collisions. In SiC amorphisation occurs spontaneously after a critical defect density is accumulated in spatially overlapping collision cascade zones in the still crystalline matrix, independent of the ion nature and its energy. Further radiation at higher fluences results in the growth of this amorphous layer towards the surface and into larger depths at decreasing rate.

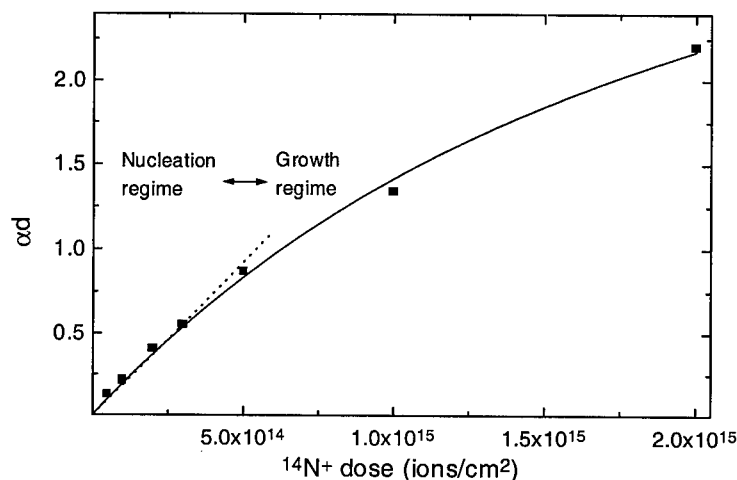


Figure 2: Evolution of the measured absorbance as a function of the ion fluence.

Similar behavior was found by Musumeci et al. in ref. [7], where the authors have performed in situ transmittance and reflectance measurements during SiC ion implantation, to extract the absorption coefficient.

#### 4. Conclusions

The damage produced in 6H-SiC single crystals by  $^{14}\text{N}^+$  ion implantation was investigated by confocal micro-Raman spectroscopy as a function of the implantation dose. The Raman spectra show the evolution to an amorphous structure with no chemical short range order at high fluences. The damage accumulation is approximately linear with fluence until amorphisation occurs when the elastic energy deposited by the ions overcomes a critical value.

#### Acknowledgements

This work has been partially supported by the Autonomous Government of Catalonia through a Projecte Interregional de Cooperació de la Comunitat de Treball dels Pirineus (ITT-CTP 98) and fellowships granted to F. Alsina and F.J. Campos, and the Comisión Interministerial de Ciencia y Tecnología (Grant TIC97-0694-C04-04).

#### References

- [1] F.J. Campos, N. Mestres, J. Pascual, E. Morvan, P. Godignon, and J. Millán, *J. Appl. Phys.* 85 (1999), p. 99.
- [2] E. Morvan, P. Godignon, J. Monserrat, J. Fernández, D. Flores, and J. Millán, *Mater. Sci. Eng., B* 46, (1997) p. 218.
- [3] W. Bolse, J. Conrad, F. Harbsmeier, M. Borowski, and T. Rödle, *Mater. Sci. Forum* 248-249 (1997) p. 319.
- [4] D.W. Feldman, J.H. Parker Jr., W.J. Choyke, and L. Patrick, *Phys. Rev.* 170, (1968) p. 698.
- [5] J.C. Burton, L. Sun, F.H. Long, Z.C. Feng, I.T. Ferguson, *Phys. Rev. B* 59, (1999) p. 7282.
- [6] M. Hofmann, A. Zywiets, K. Karch, and F. Bechstedt, *Phys. Rev. B* 50, (1994) p. 13401.
- [7] P. Musumeci, L. Calcagno, M.G. Grimaldi, G. Foti, *Nucl. Instr. Meth. B* 116 (1996), p. 327.

## Ion Beam Induced Change in the Linear Optical Properties of SiC

E.K. Williams<sup>1</sup>, D. Ila<sup>1</sup>, D.B. Poker<sup>2</sup>, D.K. Hensley<sup>2</sup> and David J. Larkin<sup>3</sup>

<sup>1</sup>Center for Irradiation of Materials, Alabama A&M University, Normal, AL 35762, USA

<sup>2</sup>Solid State Division, Oak Ridge National Laboratory, Oak Ridge, 37831, USA

<sup>3</sup>NASA Lewis Research Center, 21000 Brookpark Road, Cleveland, OH 44135, USA

**Keywords:** Colloids, Ion Implantation, Nanoclusters

### ABSTRACT

We present the results of our investigation of producing nanoclusters of gold and tin in 6H-SiC and changes in the linear optical properties induced by Au, Sn and Si implantation. This is accomplished by implanting 1.0 MeV Au, 160 keV Sn and 5.0 MeV Si into the Si face of SiC at room or elevated temperature followed by annealing at various temperatures. Using optical absorption spectrophotometry, we determined the location of the absorption band for each metal nanocluster in SiC. Elevated temperature implantation reduces optical absorption due to ion implantation induced defects. Using the Mie theory, we determined the index of refraction in the implanted volume and estimated the size of the Au nanoclusters.

### INTRODUCTION

Introducing metal colloids such as gold into an optical material, such as glass matrix, has been used to change the color of glasses for decoration and recently for fabricating optical devices. In recent years, more attention has been given to both linear and nonlinear properties of the material caused by optical absorption due to the surface plasmon resonance frequency, which depends on the index of refraction of the host substrate and the electronic properties of the colloids formed in the host material. The nonlinear properties allow the manufacturing of a wide range of optical devices. Ion implantation followed by thermal annealing has been used to introduce similar effects near the surface as well as to change the nonlinear optical properties [1-5].

It has long been known that small metallic particles or colloids embedded in dielectrics produce colors associated with optical absorption at the surface plasmon resonance frequency [6,7]. For clusters with diameters much smaller than the wavelength of light ( $\lambda$ ), the theories of Mie [8] can be used to calculate the absorption coefficient ( $\text{cm}^{-1}$ ) of the composite:

$$\alpha = \frac{18\pi Q n_0^2}{\lambda} \frac{\epsilon_2}{(\epsilon_1 + 2n_0^2)^2 + \epsilon_2^2} \quad (1)$$

where  $Q$  is the volume fraction occupied by the metallic particles,  $n_0$  is the refractive index of the host medium, and  $\epsilon_1$  and  $\epsilon_2$  are the real and imaginary parts of the frequency-dependent dielectric constant of the bulk metal. Equation 1 is a Lorentzian function with a maximum value at the surface plasmon resonance frequency ( $\omega_p$ ), where

$$\epsilon_1(\omega_p) + 2n_0^2 = 0 \quad (2).$$

Values of  $\epsilon_1$  for the metals as a function of wavelength are tabulated in [9] and the published index of refraction for SiC is 2.655. The index of refraction measured by prism coupling for the SiC used in this work was 2.26. From Equation (2) one can predict the photon wavelengths for the surface plasmon resonance frequencies for metallic colloids in the photorefractive host materials, as shown in Fig. 1. This figure shows that taking  $n_0 = 2.7$ , the theoretical value of  $n_0$  for SiC, the absorption bands should be near 688 nm and 446 nm for Au and Sn colloids, respectively.

## RESULTS

Figure 2 shows the optical absorption spectra for SiC bombarded by 1.5 MeV Si ions at various fluences, at room temperature and at 500°C. The room temperature bombardment caused severe darkening, even at fluences as low as  $4 \times 10^{16}/\text{cm}^2$ , red-shifting the absorption edge from 350 nm to 650 nm and causing an overall increase in the absorption baseline. Implantation at elevated temperature, 500°C, displayed markedly reduced damage.

Figure 3 shows typical optical absorption spectra for 6H Al-doped SiC implanted with 160 keV Sn at room temperature and annealed at 200°C in argon for one hour. This figure also shows that as implantation fluence increases the absorption baseline increases. Using the experimentally determined absorption peak, 406 nm, the permittivity from Fig. 1, and equation (2), the calculated index of refraction for SiC at the implanted volume is 2.4. That this value is lower than the accepted value of  $n = 2.7$  for SiC is almost certainly due to the implantation damage and disruption of the lattice [10]. Observation of the formation of Sn nanoclusters in SiC using visible optical photospectrometry was made possible because of the high index of refraction of the host material. Otherwise, the absorption band would have been located in the UV region. After heat treatment at 400°C and 600°C the peak at 406 nm disappeared.

Figure 4 shows optical absorption spectrum for a 6H, N doped SiC sample implanted with  $3 \times 10^{17} \text{ Au}/\text{cm}^2$  at 1.0 MeV and at a temperature of 500°C then and annealed at 1000°C in an argon ambient for one hour. Also shown is the absorption spectrum of the sample prior to implantation and the difference between the two. At Au fluences less than  $3 \times 10^{17}/\text{cm}^2$  no peaks due to plasmon resonance were discernible. It is clear from the difference spectrum that significant implantation damage remains after the heat treatment. Similar effects were observed in 6H, Al-doped SiC, as shown in Fig. 5. The peak was at 535 nm after heat treatment at 1100°C in air. The peak was expected to appear in the range of 630 to 680 nm, depending upon the value of the refractive index after implantation. Using Eq. 2 and Fig. 1 the index would need to change from 2.7 to 1.5 to account for the location of the plasmon resonance peak. One possible explanation is that  $\text{SiO}_2$  is formed during the annealing process. If this is so it indicates that the Ar atmosphere used in annealing the sample is Fig. 4 failed

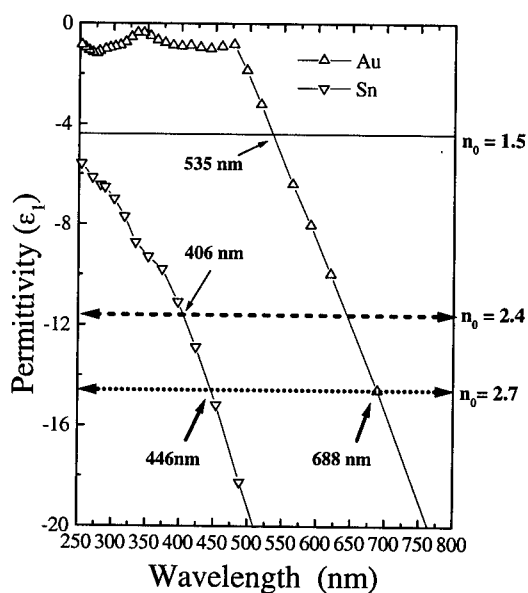


Figure 1. Permittivity vs Wavelength for Au and Sn. Expected resonances for given indices are indicated.

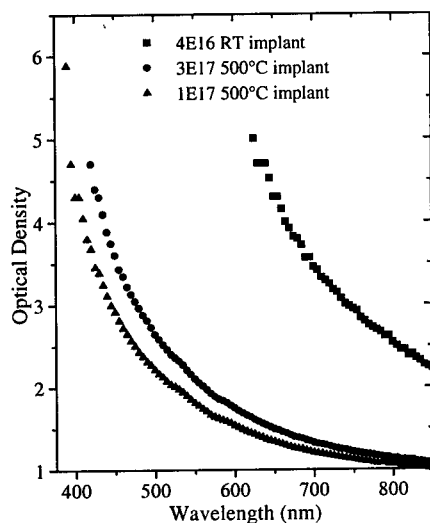


Figure 2. Optical Density vs Wavelength for 5 MeV Si implanted into SiC at 30 and 500°C to fluences of 0.4, 1, and  $3 \times 10^{17}$  ion/cm<sup>2</sup>.

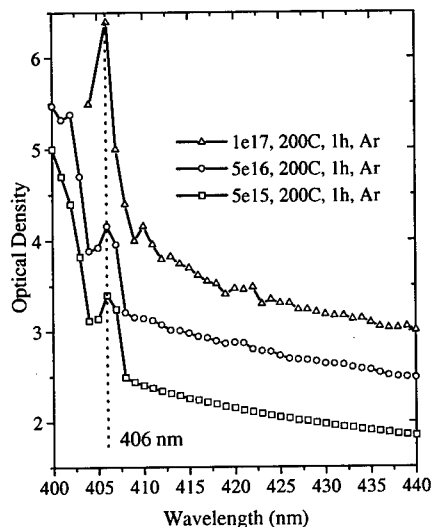


Figure 3. Optical Density vs Wavelength for 160 keV Sn implanted into SiC at 30°C to fluences of 0.5, 5, and  $10 \times 10^{16}$  ion/cm<sup>2</sup> then heated at 200°C.

to purge the O completely. Preliminary Rutherford backscattering analysis has indicated the presence of oxygen in the both implanted and unimplanted areas of the sample.

The size of the Au clusters can be estimated from the peak position and the width of the resonance through the relation  $r = A_m v_f / \Delta\omega_{1/2}$  [1] where  $A_m$  is a constant, taken to be 1.5 for Au,  $v_f$  is the Fermi velocity of gold and  $\Delta\omega_{1/2}$  is the full width at half maximum of the absorption peak. From Fig. 4 the Au cluster diameter is estimated at 5 nm. The cluster diameters in Fig. 5 are estimated to be at least 4 nm for the  $5 \times 10^{17}$  ion/cm<sup>2</sup> implant and 6 nm for the  $3 \times 10^{17}$  ion/cm<sup>2</sup> implant.

## CONCLUSIONS

Metallic nanocluster formation was observed in SiC implanted with Sn and Au ions. Implantation at room temperature results in a much larger increase in optical absorption than high temperature implantation. The optical signature of Sn clusters disappeared upon heat treatment above 200°C whereas Au cluster formation was not seen until annealing temperatures reached 1000°C. The approximately 5 nm diameter Au clusters appeared to be surrounded by SiO<sub>2</sub> rather than SiC. Further analysis is needed to determine the thickness of the SiO<sub>2</sub> around the Au clusters and to determine whether the implantation has enhanced the oxidation rate.

## ACKNOWLEDGMENTS

This project was supported by the Center for Irradiation of Materials at Alabama A&M University and NASA-LeRC Contract No. NAG3-2123. The work at ORNL was sponsored by the Division of Materials Science, U.S. Department of Energy, under Contract DE-AC05-96OR22464 with Lockheed Martin Energy Research Corp.

## REFERENCES

1. G. W. Arnold, J. Appl. Phys. **46** (1975), p. 4466.
2. C. W. White, D. S. Zhou, J. D. Budai, R. A. Zuhr, R. H. Magruder and D. H. Osborne, Mat. Res. Soc. Symp. Proc. **316** (1994), p. 499.
3. E. K. Williams, D. Ila, A. Darwish, D. B. Poker, S. S. Sarkisov, M. J. Curley, J-C. Wang, V. L. Svetchnikov, H. W. Zandbergen, Nucl. Instr. and Meth. in Phys. Res. **B148** (1998)1074 .
4. D. Ila, E. K. Williams, S. Sarkisov, C. C. Smith, D. B. Poker, and D. K. Hensley, Nucl. Instr. and Meth. in Phys. Res. **B141** (1998), p. 289.
5. R. L. Zimmerman, D. Ila, E. K. Williams, D. B. Poker, D. K. Hensley, C. Klatt, S. Kalbitzer, Nucl. Instr. and Meth. in Phys. Res. **B148** (1998), p. 1064.
6. G. Fuchs, G. Abouchacra, M. Treilleux, P. Thévenard, and J. Serughetti, Nucl. Instr. and Meth. in Phys. Res. **B32** (1988), p. 100.
7. G. Abouchacra, G. Chassagne, and J. Serughetti, Radiation Effects 64 (1982), p. 189.
8. G. Mie, Ann. Physik **25** (1908), p. 377.
9. D. R. Lide, Ed., *CRC Handbook of Chemistry and Physics, 76th Edition* (CRC Press, Boca Raton, 1987).
10. P. D. Townsend, P. J. Chandler, L. Zhang, *Optical Effects of Ion Implantation* (Cambridge University Press, Cambridge, 1994).

Contact Information: E.K. Williams, eric@cim.aamu.edu, Tel: 1 256 851 5866, Fax: 1 256 851 5868

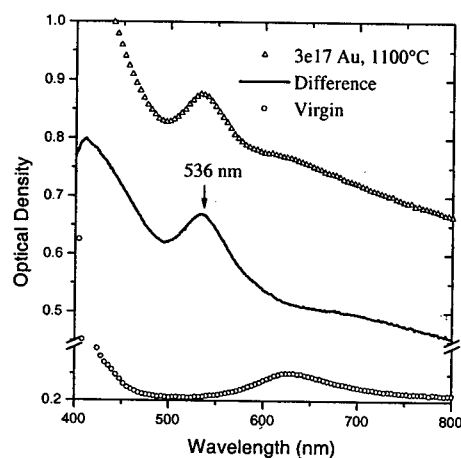


Figure 4. Optical Density vs. Wavelength for 1 MeV Au implanted at room temperature into 6H, N-doped SiC. Ion fluence was  $3 \times 10^{17}/\text{cm}^2$ . Sample was heated in Ar to 1100°C.

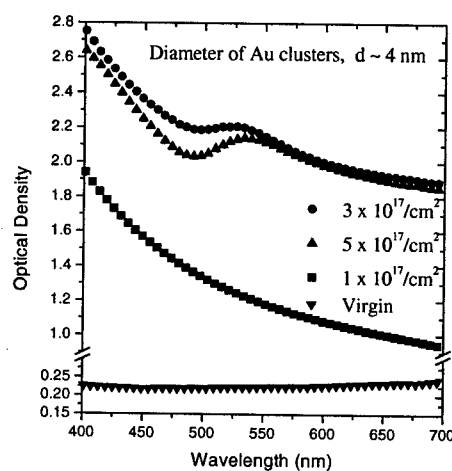


Figure 5. Optical Density vs. Wavelength for 1 MeV Au implanted at 500°C into 4H, Al-doped SiC then heated in air to 1100°C for 1 hr. Bottom trace is optical absorption of the unimplanted sample.

## Free Carrier Diffusion Measurements in Epitaxial 4H-SiC with a Fourier Transient Grating Technique: Injection Dependence

Paulius Grivickas<sup>1</sup>, Jan Linnros<sup>1</sup> and Vytautas Grivickas<sup>2</sup>

<sup>1</sup> Department of Solid State Electronics, Royal Institute of Technology,  
Electrum 229, SE-16440 Stockholm, Sweden

<sup>2</sup> Institute of Materials Research and Applied Sciences, Vilnius University,  
Sauletekio 10, LT-2054 Vilnius, Lithuania GUS

**Keywords:** Ambipolar Diffusivity, Epitaxial Layers, Free Carrier Absorption, Transient Grating

**Abstract.** A Fourier-transient-grating technique is applied for the measurement of carrier diffusivity in low-doped *n*-type 4H-SiC epitaxial layers. It is shown that the diffusion coefficient can be extracted in a wide excitation range,  $5 \times 10^{13} - 3 \times 10^{17} \text{ cm}^{-3}$ , which covers the transition region from the minority carrier diffusion to the ambipolar case. The minority hole and ambipolar diffusion coefficients have been determined:  $D_h = 2.35 \pm 0.4 \text{ cm}^2/\text{s}$  and  $D_a = 4.2 \pm 0.4 \text{ cm}^2/\text{s}$ , respectively. These values are 20% lower than the ones extracted from the Einstein relation using 4H-SiC Hall-mobility data presented in the literature.

**Introduction.** Silicon carbide (SiC) has been recognized as a superior semiconductor in high-temperature, high-frequency and high-power applications [1]. However, in spite of the successful achievements in practical device manufacturing, numerous fundamental physical parameters of the material are still unknown. Of particular interest are electrical ones, which are directly involved in theoretical device simulation as well as in functional engineering. Among them, the carrier diffusivity is a key parameter, which determines the minority carrier collection efficiency for a *p-n* junction (solar cell, photo diode, etc.), and affects several aspects of bipolar device operation (e.g. power devices). Diffusivity in SiC can be only approximately evaluated through the Einstein relation using mobility values presented in the literature. Furthermore, only the majority carrier mobility is available, which is measured with a Hall-effect technique in moderately doped samples [2]. Such mobility does not necessarily correspond to the diffusion mobility in intrinsic material or under high-injection conditions. Evidence for a definite difference between diffusion and drift mobility has been revealed in silicon and germanium and has been incorporated in several theoretical models based on transport calculations [3,4,5].

**Experiment.** In this work the Fourier-transient-grating (FTG) technique was adapted for diffusion coefficient measurements in the 4H-SiC epitaxial layers. The measurement is complicated in two ways: the perceivable carrier interdiffusion process has to be faster than the relatively low lifetime of the 4H-SiC material (0.53  $\mu\text{s}$  in our case). This requires the use of low modulated and shortly spaced transient gratings, which approach the dimension of the probe beam diameter. The second complication is related to the fact that until now intrinsic 4H-SiC is only available as epilayers which have tens of microns thick. Thus, compared to silicon, time- and spatial-resolution have to be increased by factors of  $\sim 100$  and  $\sim 10$ , respectively.

We have investigated *n*-type low doped ( $6 \times 10^{14} \text{ cm}^{-3}$ ) 4H-SiC films of 40  $\mu\text{m}$  thickness, grown by chemical vapor deposition on a heavily nitrogen-doped ( $6 \times 10^{18} \text{ cm}^{-3}$ ) 4H-SiC substrate. To fit the experimental conditions, narrow strip bars have been sawed from the 4H-SiC wafers, and cross-cut-walls of samples were polished to an optical quality. Measurements were performed at  $T = 296 \text{ K}$  using a pump and probe configuration shown in Fig. 1(a). Pump beam pulses of 2.5 ns duration and at 355 nm wavelength are generated by a Nd:YAG laser at a repetition rate of 20 – 100

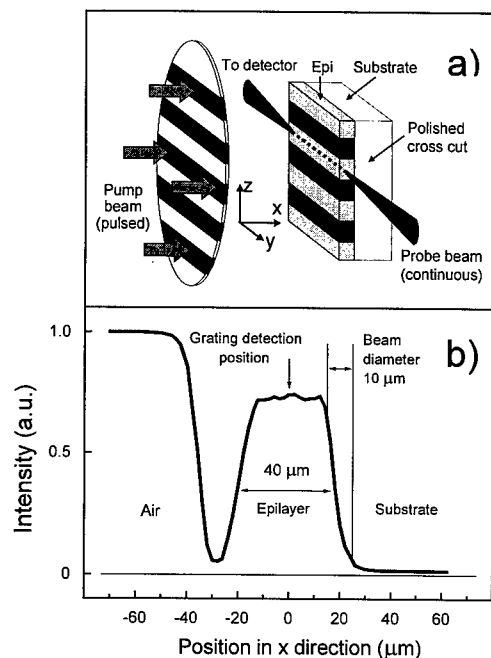


**Fig. 1.** (a) Schematic for FTG measurements in perpendicular probe-excitation geometry. (b) Scan profile of the epilayer in the x-direction.

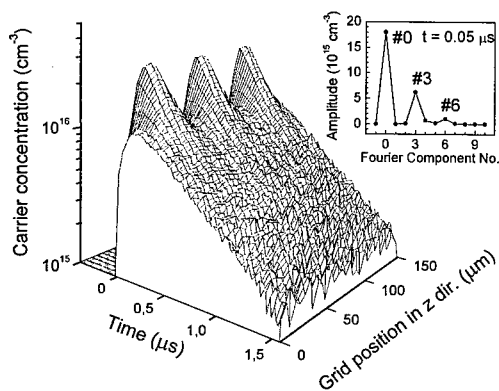


**Fig. 2.** Typical transient grating measurement data in 3D representation. The inset shows main components of the grating extracted after the Fourier analysis.

the probe beam in the sample being  $\sim 10 \mu\text{m}$ . The carrier grating detection position was located in the middle of the epilayer in order to minimise any influence of surface recombination on the diffusion data [6,8].

Measurement data was collected in a scanning manner: The modulating grid was stepwise shifted in the x-direction with a computer-guided micropositioner. A typical data set in a three-dimensional representation is shown in Fig. 2, where the three peaks correspond to a scan over three strips in the grid. This grating-induced modulation of the carrier plasma erases with  $\sim 0.5 \mu\text{s}$  by

Hz. The top-hat intensity profile of the 4 mm diameter pump beam and the low absorption coefficient ( $\alpha_{ex}$ ) in 4H-SiC [6] ensured a uniform concentration of the electron-hole plasma excitation within the epilayer (x- and y-directions in Fig. 1(a)). A spatial modulation of the pump intensity is obtained in the z-direction by placing on the optical pathway a grid with period in the range  $40 - 80 \mu\text{m}$ . Thus, the transient grating is perpendicular to the optical c-axis of the 4H-SiC.

A 1300 nm wavelength cw laser entering from the polished crosscut side of the sample (Fig. 1(a)) is used to detect absorption changes. The probe beam is perpendicularly polarized with respect to the c-axis of the material in order to optimize the absorption cross section [7]. The absorption decay is recorded by a digital oscilloscope at a sampling rate of  $10^5$  samples/s. The dynamics of the excess carrier density  $\Delta n$  of electron-hole pairs (e-h) is monitored by the probe beam absorption changes  $\Delta\alpha_{eh}(t)$ :  $\Delta n(t) = \Delta\alpha_{eh}(t) / \sigma_{eh} = \ln[I_0 / I(t)] / \sigma_{eh}d$  (1), where  $\sigma_{eh} = 4.5 \times 10^{-17} \text{ cm}^2$  stands for the free carrier absorption cross section in 4H-SiC [8],  $I_0$  and  $I(t)$  are incoming and transmitted probe beam intensities, respectively. According to Eq. (1), the probed path  $d$  has to be relatively large in order to achieve high sensitivity at low excitation regimes. Therefore, the width of one sample (in the y-direction) was chosen to be  $1000 \mu\text{m}$  (with respect to  $40 \mu\text{m}$  epilayer thickness in the x-direction). Such dimensions of the sample structure required a precise probe beam alignment within the epilayer plane. The success of this mechanical procedure is tested by probe beam scanning in the x-direction, as illustrated in Fig. 1(b). Two relatively sharp and uniform slopes of the probe beam intensity embracing the epilayer signify a good parallelism of the beam (the dip of the intensity at air-epilayer interface is due to the probe beam scattering in the surface plane). In addition, the intensity slopes identify the effective waist of



diffusion. The carrier plasma interdiffusion process and recombination processes (continuous decay of average carrier concentration) could be separated by an analytical solution of the characteristic lifetimes [5]:  $1/\tau_g = 1/\tau_r + 4\pi^2 D/\Lambda^2$  (2), where  $\tau_g$  represents the “erasure” time of the grating with period  $\Lambda$  (in our case  $\Lambda$  corresponds to modulation grid period),  $\tau_r$  stands for the recombination lifetime and  $D$  is the carrier diffusion coefficient. The given solution is valid for a sinusoidal type grating and for an injection-independent carrier recombination. The inset of Fig. 2 shows amplitudes of the sinusoidal Fourier components extracted at a time 0.05  $\mu\text{s}$  after the excitation. The Fourier component number is related to the spatial frequency of the grating: The most intensive component #0 represents the average carrier concentration while component #3 corresponds to the fundamental modulation (see three main peaks in Fig. 2). Component #6 with a low amplitude is the double frequency overtone which is omitted in the following analysis.

### Results. Individual decays of

component #3 for different grid periods have been measured at a constant excitation level as shown in Fig. 3(a). Since the average concentration (component #0) remained the same for all cases, it is represented by one curve (open symbols). The decay of this curve is determined by the recombination lifetime  $\tau_r = 0.53 \pm 0.01 \mu\text{s}$  in the epilayer. Characteristic lifetime for each of the curves is indicated at the bottom of the figure. Clearly, the grating erasure time decreases with gratings of smaller period. According to Eq. (2), the diffusion coefficient  $D$  can be extracted using the slope of the plot  $1/\tau_g$  vs.  $4\pi^2/\Lambda^2$  as given in Fig. 3(b). On the other hand, the diffusion coefficient can also be calculated at a single  $\Lambda$  from the difference  $1/\tau_g - 1/\tau_r$ . The relative error of such

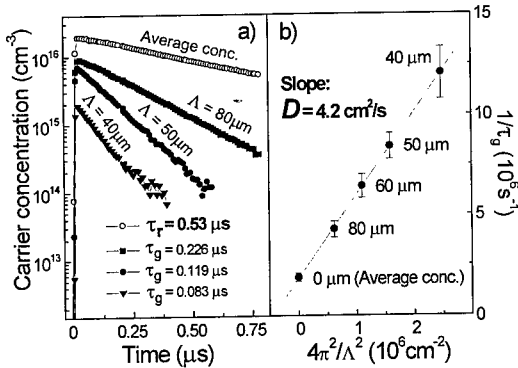


**Fig. 3. (a)** Fourier amplitude decays of the relative component #3 for different periods of the grating. **(b)** Transient grating inverse erasure lifetime  $1/\tau_g$  versus  $4\pi^2/\Lambda^2$ .

procedure is reduced for smaller periods (higher  $1/\tau_g$  values respect to  $1/\tau_r$ ), although the grating contrast is lost and the decay is influenced by noise as the period approaches the probe beam diameter (see Fig. 3(a) at  $\Lambda = 40 \mu\text{m}$ ). As a consequence, we have relied on the more simple measurement with the single  $\Lambda = 50 \mu\text{m}$  period, which exhibited almost the same accuracy as the slope measurement.

The diffusion coefficient measurements were performed within four orders of excitation range ( $5 \times 10^{13} - 3 \times 10^{17} \text{ cm}^{-3}$ ) and the result is shown in Fig. 4 by single dots with error bars. The expected dependence of the diffusion coefficient at this injection level is indicated by a dashed curve. This dependence originates from the analytical expression of the ambipolar diffusion coefficient:  $D_a = [n_0 + \Delta n + \Delta p] / [(n_0 + \Delta n)/D_h + \Delta p/D_e]$  (3), where  $\Delta n = \Delta p$  are the concentrations of the excited carriers.  $D_e$  and  $D_h$  are electron and hole diffusion coefficients, respectively, calculated from the Einstein relation ( $D_{e,h} = kT\mu_{e,h}/q$ ) using extrapolated low-doping electron and hole Hall-mobility values:  $\mu_e = 1000 \text{ cm}^2/\text{Vs}$  and  $\mu_h = 115 \text{ cm}^2/\text{Vs}$ , respectively [2]. The ambipolar diffusivity arises from the fact that an internal electric field develops due to the fast moving electrons with respect to the more slowly moving holes. This ties electrons and holes together in a coupled diffusive motion. Eq. (3) implies that the ambipolar diffusivity is applicable when the injected carrier concentration exceeds by a factor  $\sim 20$  the equilibrium electron concentration in the epilayer ( $n_0 = 6 \times 10^{14} \text{ cm}^{-3}$  in our case). As indicated in Fig. 4, the measured ambipolar diffusion coefficient peaks at a value  $D_a = 4.2 \text{ cm}^2/\text{s}$  at the injection level  $10^{16} \text{ cm}^{-3}$  and is slightly lower than the expected theoretical one of  $5.3 \text{ cm}^2/\text{s}$  (dashed curve saturation level at high

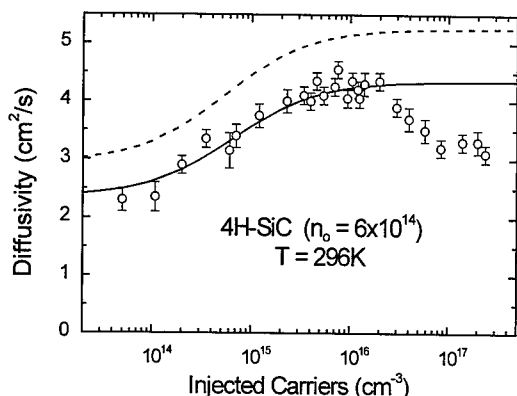


**Fig. 4.** Experimental results of carrier diffusivity (single dots with the error bars) versus the injected carrier density with comparison to the theory (dashed curve – expected and solid curve – adjusted dependencies, respectively).

Another important feature of the measured injection dependence is that an appreciable reduction of the ambipolar diffusivity is observed at high injections ( $\Delta n > 3 \times 10^{16} \text{ cm}^{-3}$ ). A similar reduction of diffusivity has been experimentally observed in crystalline silicon [5]. It has been interpreted as a combined effect from (i) dynamic band gap shrinkage, (ii) indirect influence from electron-hole scattering and (iii) excitonic effects [9]. While there may be similar models invoked for the explanation of this dependence in 4H-SiC, we note that more experimental results should be obtained at injection levels above  $10^{17} \text{ cm}^{-3}$  and at different temperatures, in order to clarify these results.

**Summary.** We have utilized a Fourier-transient-grating technique for the measurement of carrier diffusivity in low-doped *n*-type 4H-SiC epitaxial layers. We have determined 4H-SiC ambipolar and minority hole diffusion coefficients:  $D_a = 4.2 \pm 0.4 \text{ cm}^2/\text{s}$  and  $D_h = 2.35 \pm 0.4 \text{ cm}^2/\text{s}$ , respectively.

**Acknowledgement.** This research was performed within the Swedish SiCEP program, financed by the Strategic Research Council (SSF). Authors also acknowledge financial support from the Swedish Institute (Visby program) and Linköping University for samples.

## References

- [1] J. B. Casady and R. W. Johnson, *Solid-State Electron.* **39** (1996), p. 1409.
- [2] W. J. Schaffer, G. H. Negley, K. G. Irvine and J. W. Palmour, *MRS Symp. Proc.* **339** (1994), p. 595.
- [3] T. P. McLean and E. G. S. Paige, *J. Phys. Chem. Solids.* **18** (1961), p. 139.
- [4] T. T. Mnatsakanov, B. N. Gresserov and L. I. Pomortseva, *Sol. State Electron.* **38** (1995), p. 225.
- [5] J. Linnros and V. Grivickas, *Phys. Rev. B* **50** (1994), p. 16943.
- [6] A. Galeckas, J. Linnros and V. Grivickas, *Appl. Phys. Lett.* **71** (1997), p. 3269.
- [7] V. Grivickas, A. Galeckas, P. Grivickas and J. Linnros, unpublished.
- [8] V. Grivickas, J. Linnros, P. Grivickas and A. Galeckas, *Mater. Sci. and Eng.* **B56** (1999).
- [9] V. Grivickas, J. Linnros, A. Galeckas and V. Bikbajevs, *Proc. 23<sup>rd</sup> Int. Conf. Phys. Semicond.*, World Scientific, Singapore, **Vol. 1** (1996), p. 91.

injections). The measured dependence is also lower over all excitation range. The same result within the error range was obtained at different probe positions of several samples. This demonstrates that the measured diffusivity is an inherent characteristic of the 4H-SiC polytype. A better theoretical fit to the measured values can be obtained using a lower minority hole diffusion coefficient of  $D_h = 2.35 \pm 0.4 \text{ cm}^2/\text{s}$  (instead of predicted  $2.95 \text{ cm}^2/\text{s}$ ) as shown by the solid curve in Fig. 4. This discrepancy with respect to majority hole mobility data imply either that the minority hole mobility is reduced with respect to that of majority one or that the hole mobility value in general should be lower than previously reported [1] (indeed, very few data on  $\mu_h$  exist in the literature for 4H-SiC), i.e.  $\mu_h = 90 \text{ cm}^2/\text{Vs}$ .

## Time-Resolved Photoluminescence Study of Bound and Free Excitons in 4H SiC

G. Pozina, J.P. Bergman, C. Hemmingsson and E. Janzén

Department of Physics and Measurement Technology, Linköping University,  
SE-581 83 Linköping, Sweden

**Keywords:** Bound Excitons, Carrier Lifetime, Free Excitons, Time-Resolved Photoluminescence

**Abstract** We have measured the photoluminescence (PL) decay time of free exciton (FE) and bound excitons (BE) related to nitrogen in epitaxial 4H-SiC layers with different doping concentration. It is shown that the recombination mechanism for FE is not connected with capture of e-h pair to defects related to nitrogen. The PL decay times for the Q BE, as well as for excitons bound to Ga, Al or B, are determined by the FE recombination time with the PL decay time values about 8–15 ns at low temperature. That is different for P BE, for which the time decay is about 40 ns at  $T = 2$  K. In addition, detailed temperature studies of the PL decay were performed.

### Introduction

The low temperature photoluminescence spectrum of high quality 4H SiC is typically dominated by the emission from free excitons and excitons bound at the neutral nitrogen donor (BE:N). In 4H SiC there are two different BE related to N, known as P and Q, due to the two possible non-equivalent carbon lattice sites. In some samples the emission from bound exciton related to other impurities such as Al, B or Ga can also be seen in the near bandgap region. The intensity relation between the FE and the BE:N is often used to determine the nitrogen concentration, using an empirically determined relation [1].

Only a few previous investigations of exciton decay in SiC have been presented before. This includes studies in 3C:SiC [2, 3] and in 6H:SiC [4].

In this work we have made a detailed study of the decay kinetics of primarily the FE and the BE:N in a series of 4H:SiC samples with different nitrogen concentrations, in the temperature range from 2 K to 120 K. We have also studied the recombination process related to Al, B and Ga. The purpose of this investigation is to understand the recombination, formation and interaction mechanism between bound and free exciton states. This knowledge will eventually make it possible to use relative photoluminescence intensities for further and more detailed assignments of impurity content in the material.

### Experimental

The SiC samples used in this study were epitaxial SiC layers grown with the hot wall CVD technique, with a thickness of more than 30  $\mu\text{m}$ . The optical decays were studied using the third harmonics ( $\lambda_{\text{exc}} = 266$  nm) from a Ti:sapphire laser as a pulse excitation source. The photoluminescence was detected by a time-correlated photon counting system with a time resolution of better than 200 ps, or with a synchroscan streak-camera with 20 ps time resolution, for the fastest decays.

## Results and discussion

The low temperature PL spectra for three 4H SiC samples with different nitrogen concentrations are shown in Fig. 1. The spectra are dominated by the emission of the intrinsic free exciton (FE) and the two (BE:N<sub>P</sub> and BE:N<sub>Q</sub>) excitons bound at the neutral nitrogen donor, together with their respective phonon replicas [5]. Since all phonon replicas have the same temporal kinetics we have concentrated our study on the most dominant and most well resolved emission for each exciton. These are the no-phonon replica of BE:N<sub>Q</sub> and the 77 meV LA phonon replica of the FE and BE:N<sub>P</sub>.

Typical decay curves for FE and BEs are shown in Fig. 2. The measured values for the FE decay depend only weakly on nitrogen concentration and vary only from 13 to 8 ns, even though the nitrogen doping in the samples increases with more than 2 orders of magnitude, i. e. from  $<10^{14} \text{ cm}^{-3}$  to  $3 \cdot 10^{16} \text{ cm}^{-3}$ . This indicates that the main recombination mechanism for the FE is not connected to a capturing process of the electron-hole pair to the neutral nitrogen donor. The most probable recombination mechanism is instead the exciton Auger process [6], where the FE recombine in the vicinity of a deep impurity level. One particle from the FE is captured by the defect and the other particle takes the excess energy in an Auger process, and is excited into its respective band. The previously reported relationship between the ratio of the FE and BE:N emission intensity and the nitrogen concentration [4] could also be explained even if the population of FE's is not directly determined by the nitrogen concentration. With increasing nitrogen doping, or more generally with any additional doping which binds excitons, a competition arises for the photoexcited carriers, which eventually will increase the BE emission and reduce the FE emission.

The decay of the BE:N<sub>Q</sub> has in all samples a similar value as the decay of the FE. This is most probably due to a feeding of the BE population from the FE state, which then determines the measured decay time. The actual decay of the BE:N<sub>Q</sub> is probably faster, but bound excitons will be created as long as there exist FE's. The BE:N<sub>P</sub> on the other hand has a longer decay about 40 ns, which also is constant in all samples.

The interaction between the FE and BE's can also be seen on the initial rise time on the decay curve (see BE:N<sub>Q</sub> in Fig. 2). The evaluation of the rise time was done assuming a feeding to each BE state from a population with an exponential decay, determined by a

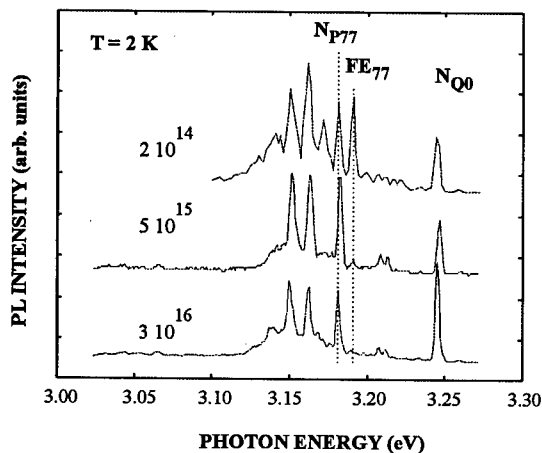


Fig.1. Low-temperature PL spectra for three 4H-SiC epilayers with different nitrogen concentration.

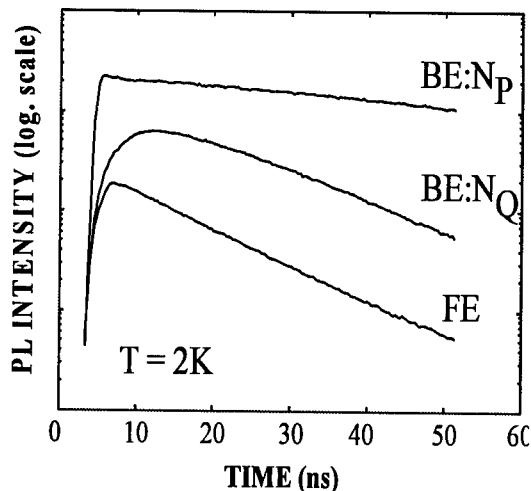


Fig.2. PL decay curves for the FE and BEs measured at 2 K, in a sample with  $N_D = 1 \cdot 10^{14} \text{ cm}^{-3}$ .

decay constant  $\tau_r$ . This decay constant will then be the rise time of the BE emission which will then have an exponential decay,  $\tau_d$ . The rate equations for this model can be expressed using the following equations:

$$I(t) = A \left( e^{-\frac{t}{\tau_d}} - e^{-\frac{t}{\tau_r}} \right),$$

which were used to fit the measured decay curves and to extract the rise time and the decay time of the BE emission, respectively. Good agreement was obtained between the model and the experimental results. From the fitting we observe that the rise time of the BE:N<sub>Q</sub> is substantially longer in low doped samples than the corresponding rise time of the FE and the BE:N<sub>P</sub>. The rise time increases with temperature to reach a maximum value at about 12 K, and is then drastically reduced. The observed rise time does not directly correspond to the measured decay of the FE, and the cause for the observed rise time on the BE:N<sub>Q</sub> is not fully understood. The difference between the rise time of the BE:N<sub>Q</sub> and BE:N<sub>P</sub>, is also surprising but could be related to different capture or formation processes of the BE to respectively defect state.

From a detailed study of the recombination lifetime as a function of the temperature, it was found that the temperature dependence of the PL decay for the FE and BE is rather complicated. At temperature about 15-20 K the PL decay time, as well as the intensity, for the P BE drops when the BE is thermally ionized from the neutral nitrogen donor. The decay of the FE decreases slightly with increasing temperatures up to 30-40 K, as seen in Fig. 3. With further increase of the temperature the recombination lifetime, which at all these temperatures is the same for all observed emissions and reflects the minority carrier lifetime, increases rapidly and then starts to level out at approximately 70 K. For samples with lower doping the lifetime values grow much faster with temperature and level out at slightly higher temperature. The increase in decay time, starting at 30-40K, is followed by an increase of the total PL intensity of the FE. A similar behavior of the carrier lifetime was also observed in Si, and could in this case be explained using the model for excitonic Auger process. The increase is then explained as due to the ionization of shallow defects acting as recombination centers. If the same explanation should be valid for SiC, the only possible defect, certainly present in the material, is the nitrogen donor. The most shallow of the two donor levels, the P-level, starts to ionize in this temperature range and could be the explanation of the increase of the lifetime. This is also consistent with doping dependence seen in Fig. 3. Also the decrease of the FE decay time, in the temperature range from 2 K to 20 K, is consistent with this suggestion since a BE on the nitrogen donor should lower the possibility for the defect to act as recombination center in the Auger process. When the BE on the neutral donor are thermally ionized the concentration of recombination centers increase, until the electron on the donor are ionized.

Finally, in low doped samples, below  $1 \times 10^{13} \text{ cm}^{-3}$ , an additional and relatively broad emission is observed at

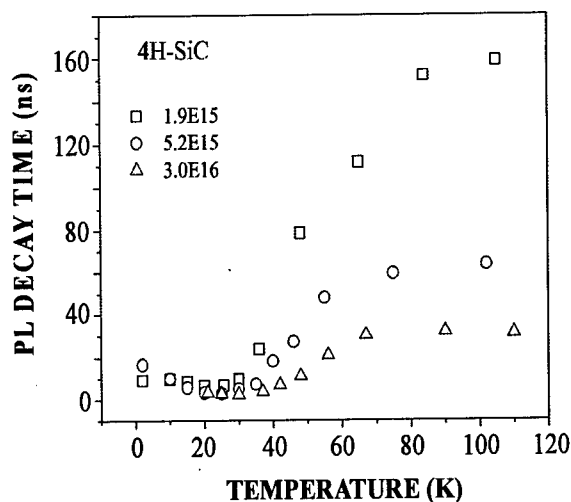


Fig.3. Temperature dependence of the decay time for FE measured in three samples with different concentration of N.

3.231 eV. This has previously been related to B in the epi-layer [7], or to B [8] or N [9] in the substrate. With time-resolved measurements we have observed that the onset of this emission has a time delay, as compared to the other exciton emissions, as can be seen in Fig. 4. This delay is different from the rise time observed for the BE's, and could in our opinion only be explained as due to an exciton diffusion from the surface, where excitons are created by the photoexcitation, towards the bulk where the emission occurs. The delay of this substrate emission is in the order of 3 ns for a 30  $\mu\text{m}$  thick epilayer. The dashed line in the lowest decay curve in figure 4 is the result of a fitting assuming a delay time together with a rise time for this emission. We conclude that the observed delay time in the onset of this emission is consistent with that it originates from the bulk, and that the delay is caused by exciton diffusion through the epi-layer.

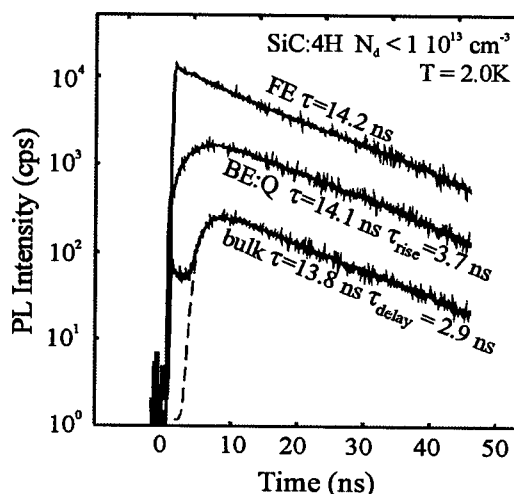


Fig. 4. Decay curves for the FE, the BE:N<sub>Q</sub>, and for an emission at 3.231 eV assumed to be related to emission from the substrate. The bulk related emission has a delayed onset proposed to be caused by exciton diffusion through the epi-layer.

#### Acknowledgment

Support for this work was provided by the SSF program SiCEP and ABB Corporate Research.

#### References

- [1]. A. Henry, O. Kordina, C. Hallin, C. Hemmingsson, and E. Janzén; Appl. Phys. Lett. **65**, (1994) p. 2457.
- [2]. J. A. Freitas, S. G. Bishop, P. B. Klein, P. E. R. Nordquist and M. L. Gipe, Springer Proceedings in Physics, Vol. **43**, Amorphous and Crystalline Silicon Carbide and Related Materials II (Editors: M. M. Rahman, C. Y.-W. Yang, G. L. Harris, Springer-Verlag berlin, Heidelberg 1989), p. 106.
- [3]. H. Okumura, K. Endo, S. Misawa, E. Sakuma, and S. Yoshida, Springer Proceedings in Physics, Vol. **43**, Amorphous and Crystalline Silicon Carbide and Related Materials II (Editors: M. M. Rahman, C. Y.-W. Yang, G. L. Harris, Springer-Verlag berlin, Heidelberg 1989), p. 94.
- [4]. O. Kordina, J. P. Bergman, A. Henry, and E. Janzén, Appl. Phys. Lett. **66**, (1995), p. 189.
- [5]. O. Kordina, A. Henry, J. P. Bergman, N. T. Son, W. M. Chen, C. Hallin, and E. Janzén, Appl. Phys. Lett. **66**, (1995), p. 1373.
- [6]. A. Hangleiter, Phys. Rev. B, **35**, (1992), p. 9149.
- [7]. S. G. Sridhara, L. L. Clemen, R. P. Devaty, W. J. Choyke, D. J. Larkin, H. S. Kong, J. App. Phys **83**, (1998), p. 7909.
- [8]. A. Henry, I.G. Ivanov, A. Ellison, E. Janzén, Mat. Sci. Eng. B. 61-62, 2 (1999), p. 34-238.
- [9]. U. Forsberg, A. Henry, E. Janzén, this conference, p. 619

## Optical Lifetime Measurements in 4H SiC

Y. Shishkin, R.P. Devaty and W.J. Choyke

Department of Physics and Astronomy, University of Pittsburgh, Pittsburgh, PA 15260, USA

**Keywords:** Free Excitons, Lifetime, Minority Carriers, Photoluminescence

**Abstract** Photoluminescence is used to investigate the radiative lifetime in n-type 4H silicon carbide homoepitaxial films under pulsed excitation for three laser wavelengths: 266 nm, 337 nm, and 355 nm. The differences between the responses to these excitation sources are discussed in terms of surface recombination and temperature dependence. Integrated pulse photoluminescence spectra are measured. The observed spectral lines are assigned to phonon assisted free exciton recombination.

### Introduction

It has been shown that 4H SiC can be successfully applied to high-voltage electronics: bipolar power devices, power Schottky rectifiers, etc. Low loss power devices require thick epilayers with minority carrier lifetimes on the order of several hundred nanoseconds to microseconds [1]. In practice, room temperature lifetime measurements at initial high injection level (when the nonequilibrium concentration of excess carriers exceeds the equilibrium concentration of majority carriers) will become important for many power device fabrication lines. Lifetimes as high as  $2.1 \mu\text{s}$  for a  $60 \mu\text{m}$  film of 4H SiC at room temperature have already been reported [2, 3]. However, there are still few reports on lifetimes at high-level injection [4, 5]. Here we report on direct optical measurements based on the photoluminescence decay of the excited carriers. The study is performed in an initial high injection mode achieved using pulse excitation on low doped n-type,  $n \sim 2 \times 10^{15} \text{ cm}^{-3}$ , 4H SiC homoepitaxial layers grown by chemical vapor deposition. We concentrate not so much on the values of the carrier lifetimes but rather on the origins and temperature and excitation wavelength dependence of the observed decays.

### Experimental

We use three excitation wavelengths  $\lambda_{\text{ex}}$  to produce an excess of electron-hole pairs: the 337 nm line of a pulsed nitrogen laser (excitation pulsewidth 10 ns) and the fourth (266 nm) and third (355 nm) harmonics of the fundamental frequency of a Q-switched Nd:YAG laser (excitation pulsewidth 3-5 ns). The energy of the pulse is sufficient to achieve high-injection, i.e., the nonequilibrium concentration of excess majority carriers immediately after the excitation exceeds the equilibrium concentration. A 9863 filter is used to eliminate residual second harmonic light of the YAG laser (532 nm), and a 5850 filter is put in front of the entrance slit of the monochromator to block any stray light. The photoluminescence is dispersed using a Spex 1700, 0.75 m Czerny-Turner monochromator equipped with an 1800 l/mm grating blazed at  $4000 \text{ \AA}$  and detected using a Hamamatsu R3788 uv-enhanced photomultiplier. The signal is averaged by a digital oscilloscope with a 500 MHz bandwidth. The luminescence intensity,

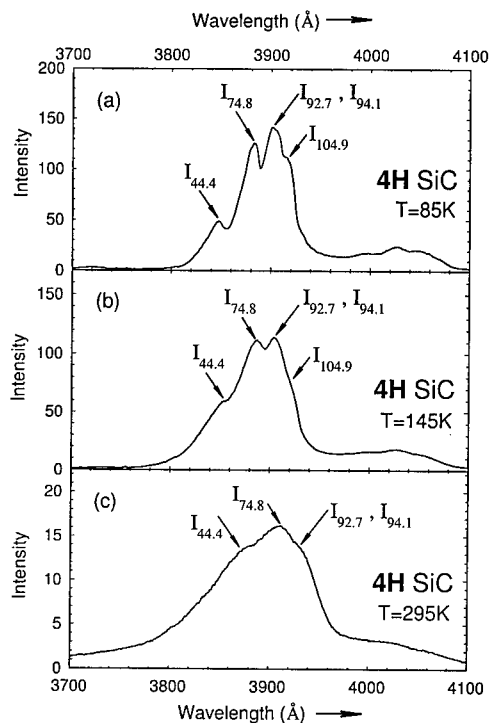


Figure 1: Integrated pulse photoluminescence spectra of a 4H SiC sample taken at (a) 85 K, (b) 145 K, (c) 295 K. Subscripts indicate the energies of momentum conserving phonons in meV.  $\lambda_{ex} = 337$  nm.

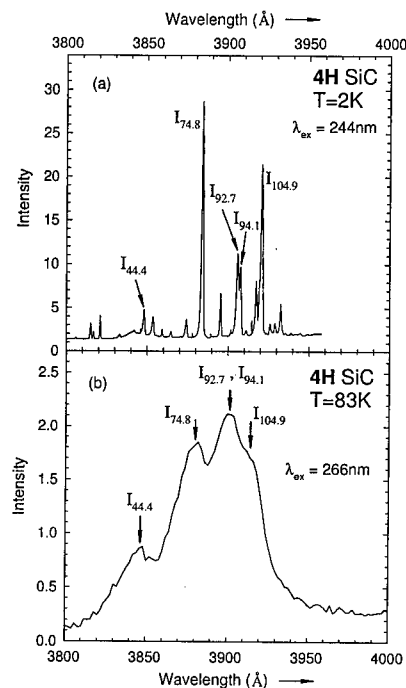


Figure 2: Photoluminescence spectra of an undoped 4H SiC sample taken at (a) 2 K, cw excitation, and (b) 83 K, pulsed light excitation. The 2 K spectrum is dominated by free exciton lines.

which is assumed to be proportional to the concentration of nonequilibrium minority carriers, is obtained by measuring the area under the average of a number of pulse decay curves. The lifetimes (or, decay constants) are determined by fitting an exponential to the data over the time interval for which the decay is linear on a semilogarithmic plot.

## Results and Discussion

Fig. 1 shows the integrated pulse photoluminescence spectra of a 50  $\mu\text{m}$  thick n-type 4H SiC layer taken at 85 K, 145 K, and 295 K. The nitrogen concentration of this sample is about  $2 \times 10^{15} \text{ cm}^{-3}$ . The 2 K spectrum of this sample (not shown), obtained using 244 nm cw excitation, is dominated by bound exciton lines. These lines are thermally quenched at 85 K. Fig. 2a and Fig. 2b show 2 K and 83 K spectra of an undoped epitaxial 4H SiC film excited by continuous 244 nm radiation. In Fig. 2a the 2 K spectrum is dominated by free excitons. In Fig. 2b the free exciton peaks are broadened but clearly identifiable and the bound exciton peaks are quenched. The comparison between Fig. 2b and Fig. 1a allows us to assign the observed lines to phonon assisted free exciton recombination. The assignment is facilitated by the fact that the free exciton line has a characteristic shape due to the combination of a parabolic free exciton band and a Boltzmann distribution of free exciton center-of-mass kinetic energies [6, 7]. We measured the radiative lifetime of the minority carriers, or free excitons in this particular case, at the wavelengths indicated on Fig. 1. Although the lifetime is measured optically using



the free exciton spectrum, it is likely strongly influenced by nonradiative processes including surface and film-substrate interfacial recombination. The second factor, of course, should take place only if the penetration depth for a given excitation wavelength (defined as  $\alpha^{-1}$ , where  $\alpha$  is the absorption coefficient) and/or diffusion allow minority carriers to reach the substrate. In this case, diffusion of carriers plays a significant role, and interfacial recombination due to different growth-related defects decreases the effective radiative lifetime [5]. It has already been shown [3] that the measured minority carrier lifetime increases as a function of epitaxial layer thickness. There were two principal explanations offered: either the quality of epitaxial layers increases with film thickness, or the concentration of deep levels responsible for non-radiative recombination (by the Auger process, for example) is higher closer to the interfaces of the film. Therefore, we studied the minority carrier lifetime as a function of the excitation wavelength. The penetration depth of the exciting radiation varies dramatically with its wavelength. The penetration depths in 4H SiC at room temperature for  $\lambda_{ex} = 266$  nm, 337 nm, and 355 nm are 0.3  $\mu\text{m}$  (estimate), 14  $\mu\text{m}$ , and 48  $\mu\text{m}$ , respectively [8].

At room temperature the decay measured using the excitation wavelength  $\lambda_{ex} = 266$  nm shows non-exponential behavior for the first 400 ns of the decay (Fig. 3a). Apparently, there is no well defined value for the lifetime in this region and one can only talk about an instantaneous lifetime given by  $\tau_{inst} = -\frac{I(t)}{dI(t)/dt}$ . The non-exponential character of the recombination process prevails in the first stage of the decay [9]. Therefore, to be specific we have chosen for analysis the linear portion of the decay on a semilog scale. Fig. 3b and especially Fig. 3c show nearly exponential decay over the entire interval. When fitted to a straight line, the last two cases give approximately equal values for the decay constant. The spot on the sample, both the position and the diameter, where we focused the laser beams was the same in all the cases. So, the difference in the luminescence response cannot be explained by inhomogeneity of the film (see Ref. [2]). It is reasonable to attribute the lower lifetime and non-exponential character of the decay curve in the case of 266 nm excitation to the fact that nonradiative surface recombination makes a more significant contribution in this case when measuring the radiative lifetime. Most of the generated excess carriers are confined in a 0.3  $\mu\text{m}$  layer. This creates an initial nonequilibrium density of electron hole pairs after excitation ( $\sim 10^{20} \text{ cm}^{-3}$ ) about a factor of one hundred greater than excitation using  $\lambda_{ex} = 355$  nm. Since the mobility at room temperature in 4H SiC doped to  $\sim 10^{15} \text{ cm}^{-3}$  is about  $800 \frac{\text{cm}^2}{\text{Vs}}$  [10], we use the Einstein relation to estimate the diffusion length as  $L = (D \cdot \tau)^{1/2} = 26 \mu\text{m}$  (nondegenerate conditions assumed). This implies that even at the excitation wavelength  $\lambda_{ex} = 266$  nm diffusion removes excess carriers from the front surface very quickly and we are able to give a more or less correct

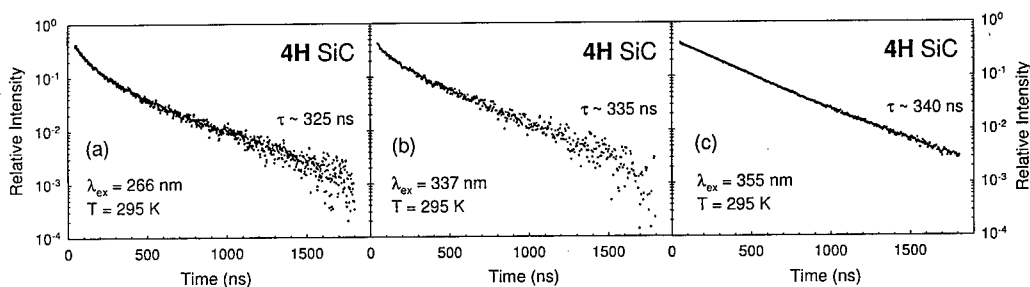


Figure 3: Photoluminescence decay curves of a 4H SiC epilayer (same sample as shown in Fig. 1) measured at 3910 Å, corresponding to the  $I_{74.8}$  free exciton phonon assisted transition. Measurements were taken using excitation wavelengths: (a)  $\lambda_{ex} = 266$  nm, (b)  $\lambda_{ex} = 337$  nm, and (c)  $\lambda_{ex} = 355$  nm.

estimate of the bulk radiative lifetime if we neglect the initial 300 - 400 ns transient behavior corresponding to one time constant  $\tau$ .

We have also measured the temperature dependence of the decay time. We find that the measured lifetime decreases as the temperature is increased for  $\lambda_{ex} = 266$  nm and 337 nm, but increases for  $\lambda_{ex} = 355$  nm. A possible explanation for the observed effect is that the front surface captures carriers more efficiently at  $\lambda_{ex} = 266$  nm and 337 nm, for which the optical penetration depth is smaller compared to  $\lambda_{ex} = 355$  nm. We are continuing work on the problem of the temperature behavior.

### Conclusions

By a comparison of integrated pulse photoluminescence and continuous excitation photoluminescence we have shown that under high injection optical excitation the spectral response may be attributed to free excitons. Conditions have been found for which the minority carrier lifetimes are comparable using excitation at  $\lambda_{ex} = 266$  nm, 337 nm, and 355 nm. The temperature dependence of the lifetime has been studied and found to decrease with temperature for shallow penetration of the excitation and increase with temperature for deep penetration of the light.

### Acknowledgments

We thank the Office of Naval Research and NASA for partial support of this work. We also wish to thank Dr. Olle Kordina and his colleagues at Cree Research for making available some of the samples used in these experiments.

### References

- [1] M. Bakowski, U. Gustafsson, and U. Lindefelt, Phys. Stat. Sol. (a) 162 (1997), p. 421.
- [2] O. Kordina, J.P. Bergman, C. Hallin, and E. Janzén, Appl. Phys. Lett. 69 (1996), p. 679.
- [3] J.P. Bergman, O. Kordina, and E. Janzén, Phys. Stat. Sol. (a) 162 (1997), p. 65.
- [4] N. Ramungul, V. Khemka, T.P. Chow, M. Ghezzi, and J. Kretchmer, Mat. Sci. Forum, Vols. 264-268 (1998), p. 1065.
- [5] A. Galeckas, J. Linnros, M. Frischholz, K. Rottner, N. Nordell, S. Karlsson, and V. Grivikas, Mat. Sci. and Eng. B61-62 (1999), p. 239.
- [6] J.R. Haynes, M. Lax, and W.F. Flood, Proc. Int. Conf. Semicond. Physics, Prague (1960), p. 423.
- [7] G.S. Mitchard and T.C. McGill, Phys. Rev. B 25 (1982), p. 5351.
- [8] S.G. Sridhara, T.J. Eperjesi, R.P. Devaty, and W.J. Choyke, Mat. Sci. and Eng. B61-62 (1999), p. 229-233.
- [9] Minority Carriers In III-V Semiconductors: Physics and Applications, editors R.K. Ahrenkiel, M.S. Lundstrom, Academic Press Inc. (1993), p. 47.
- [10] G. Rutsch, Ph.D. thesis (1998), unpublished.

## Optical Characterization of 4H-SiC $p^+n^-n^+$ Structures Applying Time- and Spectrally Resolved Emission Microscopy

Augustinas Galeckas<sup>1</sup>, Jan Linnros<sup>1</sup> and Bo Breitholtz<sup>1,2</sup>

<sup>1</sup>Department of Solid State Electronics, Royal Institute of Technology,  
Electrum 229, SE-16440 Stockholm, Sweden

<sup>2</sup>ABB Corporate Research, SE-721 78 Västerås, Sweden

**Keywords:** Carrier Diffusion Length, Defect, Electroluminescence, Optical Emission Microscopy, Recombination Lifetime

**Abstract.** Time- and spectrally resolved electron-hole ( $e-h$ ) recombination radiation from forward-biased kV-class 4H-SiC  $p^+n^-n^+$  structures is studied by combining an intensified gated charge couple device (ICCD) camera with backside and cross-sectional emission microscopy techniques. We demonstrate the capability of this method to visualize, spectrally analyze and map intrinsic and processing-induced structural defects in the active region of devices. Moreover, carrier diffusivity and lifetime parameters can be readily obtained by analyzing the spatial distribution and dynamics of injected carriers.

### Introduction

Reliability and reproducibility of applications in the area of SiC-based electronics depend essentially on the control efficiency of material and processing properties. Performance-limiting factors in SiC devices have scarcely been understood so far, though it is generally agreed that the presence of macro-defects severely diminishes the high-blocking capability. Thus, a diagnostic technique capable to provide a direct insight into both material properties and dynamic processes taking place in an operative SiC device is highly imperative in device engineering and optimization of test structures. In this work, we report on an optical characterization technique, which meets the main requirements for defect localization and analysis in a  $\mu\text{m}$ -scale and demonstrate its potential by imaging electroluminescence (EL) emission from forward biased  $p^+n^-n^+$  structures.

### Experimental Technique

The examined 4H-SiC diodes were different evaluation-type  $p^+n^-n^+$  structures with Al/B-implanted or epitaxially grown  $p^+$  layers. In all cases the low-doped  $n^-$  base comprises a 30  $\mu\text{m}$ -thick epilayer grown by CVD on a commercial  $n^+$  substrate. A strip-shaped specimen with centermost located diodes was cut out from the wafer for emission imaging in a cross-sectional geometry. One of the sidewalls was then polished straight to the edge of the diode. For imaging of EL emission in backside geometry, the cathode metallization was removed from the diodes and the rear surface was polished to optical quality. A sketch of experimental the technique is shown in Fig. 1. The optical emission microscopy setup included a Hamamatsu type C4880-10 LN-cooled digital CCD camera combined with a gated image intensifier, a 2 nm-resolution PC2000 fiber-optic spectrometer and a modified Nikon microscope, containing a zero-aperture diaphragm in the image plane and a retractable light-collecting module for an optical fiber. The optional variable-aperture component inside the microscope enables spatially resolved measurements of emission spectra from the selected emitting areas down to a few microns in size. Finally, optical interference filters positioned in front of the ICCD camera facilitate spectrally selective imaging of the emission from the whole area of test structures. The spectral response of the system is in the 200-950 nm wavelength range, whereas the spatial resolution is defined by the 1000×1000 pixels of the CCD sensor. The acquired

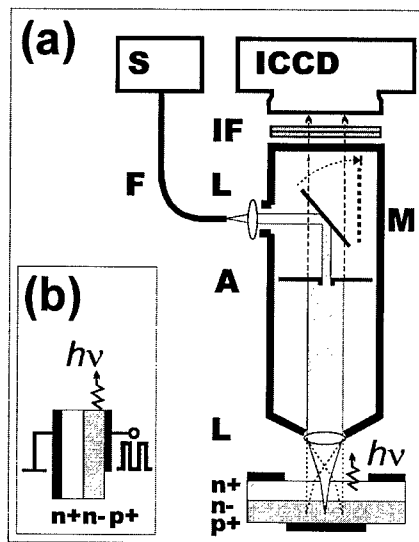


**Fig. 1.** Schematics of the optical emission microscopy setup in backside (a) and cross-sectional (b) imaging configurations: ICCD - intensified CCD camera, S - spectrometer, F - optical fiber, IF - interference filter, L - lens, M - mirror, A - adjustable aperture.

common types of imperfections - *micropipe*-type defects, *electrically inactive* areas and stress-current induced *bright line formations* are denoted by markers A, B and C in Fig. 2, respectively. Enhanced electrical field in the vicinity of structural imperfections may give rise to locally intensified EL emission. In addition, the strain field around the macro-defects attracts impurities and point defects, which may considerably add to the EL process. Note a circular pattern of enhanced emission, clearly decorating a micropipe in Fig. 2 (a). Extensive dark areas in the EL images complement an irreversible formation of bright line network, similar to that reported in Ref. [1]. The most likely cause is a displacement of adjacent crystal planes onwards each other, resulting from a non-uniform heating induced stress. The density of the line-defects is found in direct

images were stored and processed in 12-bit mode thus providing 4096 levels of gray. Timing of the imaging process could be implemented by activating a high-speed intensifier unit. The electronic shutter was synchronized with a pulsed forward bias generator and operated at 5 kHz. The adjustable gating delay permits a continuous scan of the ICCD exposure window throughout both on-state and off-state transients. The minimum exposure time of the system is 5 ns. The test specimen was clamped between contacts so that either a polished backside surface or a cross-section of the diode structure was exposed to the microscope objective, as shown in Figs. 1(a) and 1(b), respectively. A ring-shape top contact was utilized to minimize electric field inhomogeneity in backside imaging experiments. Injection of excess carriers was accomplished by pulsed forward biasing, yielding current densities in the range 1 - 1000 A/cm<sup>2</sup>.

## Results

**Backside emission.** Figure 2 outlines typical features of EL emission imaged in backside geometry, i.e. through the optically translucent  $n^+$  substrate, while keeping focus in the proximity of the  $p^+n^-$  junction plane. Most

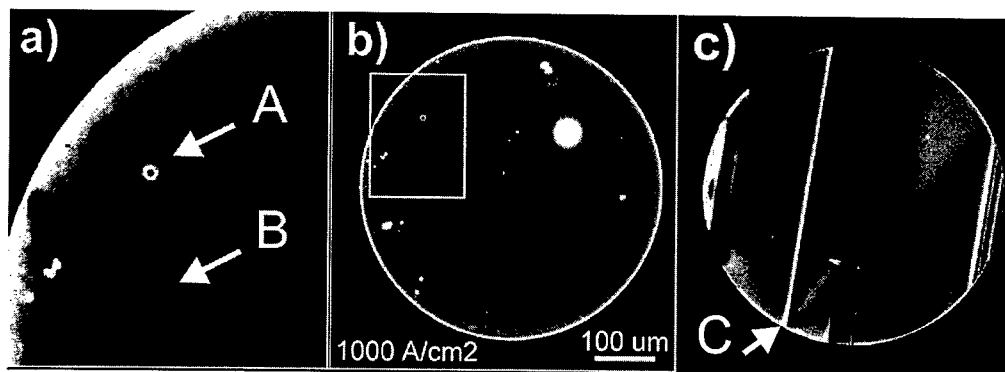


**Fig. 2.** Backside imaging of  $e-h$  recombination radiation from a forward biased 4H-SiC  $p^+/n^-/n^+$  structure. (a) Characteristic imperfections -  $\mu$ -pipe type defects (marker A), *electrically inactive* dark areas (marker B). (b) Overall EL emission pattern from a diode. (c) Spectrally selective EL image (555±20 nm) of electrical overstress induced *bright line formations* (marker C).

proportion with the electrical overstress time. Following displacement of crystal planes, the current flow across the split area is constrained, resulting in a darker, literally non-emitting area on the emission pattern.

**Time-resolved imaging.** Time-resolved imaging of light emission during voltage transients was accomplished in cross-sectional geometry by utilizing a gated intensifier unit (see Fig. 1 b). An overview of the temporal and spatial EL distributions after removal of the forward bias is displayed in Fig. 3. Note a nonlinear character of the EL transients, which can be approximated by limiting, i.e. fast and slow, time constants. The fast component is fairly similar in both  $n^-$  base and  $n^+$  substrate and is characterized by a  $\sim 35$  ns decay time. The subsequent slow decay asymptotically approaches a  $\tau_1 \sim 350$  ns time constant, which is in good agreement with typical lifetimes for 30  $\mu\text{m}$ -thick 4H-SiC epilayers [2]. The considerably faster decay ( $\tau_2 \leq 200$  ns) observed in the  $n^+$  substrate is an inherent feature of a highly doped material. Furthermore, the obtained EL intensity profiles stretching from the  $n^-n^+$  interface into the bulk of the substrate provide an insight into minority carrier transport properties. The recombination radiation profiles in the substrate suggest an average  $L_{\text{eff}} = 15$   $\mu\text{m}$  diffusion length for holes, which agrees well with diffusivity determined from mobility in 4H-SiC [3]. Given the actual effective lifetime  $\tau$  and diffusion length  $L_{\text{eff}}$  values, the diffusivity at a particular area of interest can then be quantified from the relationship  $D = L_{\text{eff}}^2/\tau$ . Finally, analysis of the time evolution of the EL profiles discloses the mutual role of  $p^+n^-$  and  $n^-n^+$  interfaces in the overall carrier relaxation process. A considerable carrier leakage through the  $p^+n^-$  junction can be observed after removing the forward bias. Conversely, an apparently negligible leakage at the  $n^-n^+$  interface suggests that the effect of minority carrier confinement due to the built-in high-low junction take over the effect of recombination at the epilayer-substrate boundary.

**Spectral analysis.** Figure 4 shows a typical EL spectrum, measured by integrating emission from the whole luminescent area of the diode. A deconvolution of experimental data applying Gaussian fits provides a basic multi-peak layout of the EL spectrum. The optical signatures of transitions with N-donor, Al-acceptor, shallow B-acceptor and deep boron related D-center can be distinguished in

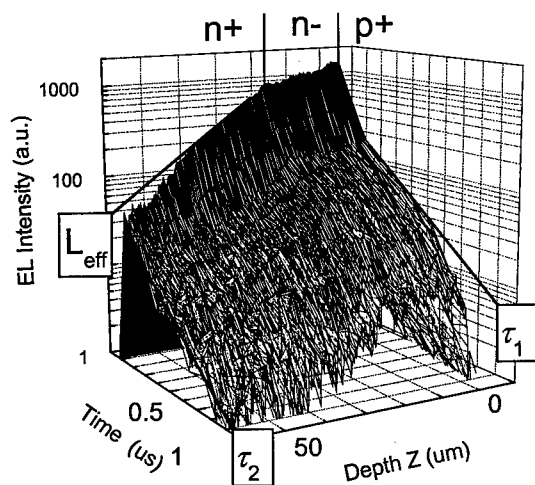


**Fig. 3.** Evolution of EL emission after removing of the forward biasing. Asymptotic straight lines indicate effective diffusion length  $L_{\text{eff}}$  for holes and lifetimes in the 4H-SiC epilayer  $\tau_1 = 350$  ns and substrate  $\tau_2 \leq 200$  ns, respectively.

the emission spectrum. The dominating blue peak in the region of 400 nm basically comprises free-to-bound transitions, involving N-donor and Al-acceptor levels. A broad green peak around 514 nm is attributed to optical transitions of conduction electrons to neutral deep B-acceptor. In addition, intrinsic and post-implantation defects give rise to energetically deep levels in the band gap [4, 5] with the corresponding peaks in the red region of the EL spectrum. We have observed a prominent variation of EL spectral yield versus injection. The EL spectra as a function of forward current in the range 5 - 58 A/cm<sup>2</sup> is summarized in the inset to Fig. 4. At low injection, only a broad emission peak in the green region of spectrum is detected. With the current increased, the blue peak rapidly emerges and completely dominates luminescence at high injections. A more detailed analysis, however, has implied self-heating effects to

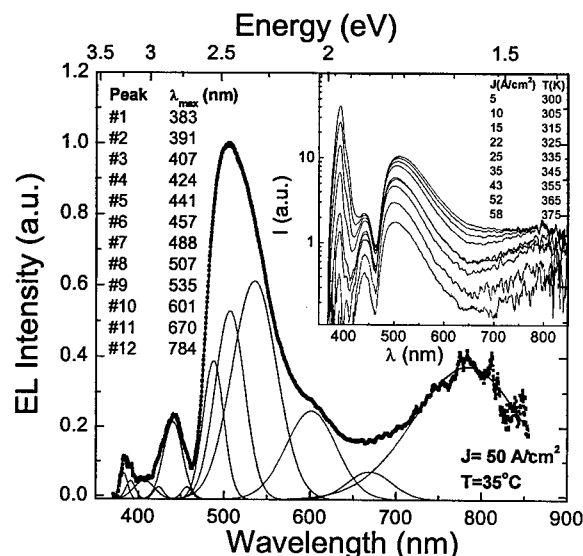


**Fig. 4.** EL spectrum (dots) and Gaussian fit (solid curve) along with corresponding deconvolution components. Inset shows EL spectra as a function of injection. The actual temperature of device is indicated next to current values.

### Summary

Our results suggest that imaging of light emission from the  $e$ - $h$  recombination, which is inherent to forward biased  $p$ - $n$  junction structures, is a direct, noninvasive and informative technique for defect localization and device performance control. We demonstrate the capability of this technique to visualize and analyze intrinsic and stress-induced defects. The basic characteristics like carrier lifetime, diffusivity and injection efficiency can be derived from experiments along with the spatial distributions of these parameters over the active device area.

### Acknowledgments

This work was financially supported by the SiCEP project of the Swedish Foundation for Strategic research. The ABB Corporate Research SiC Program is gratefully acknowledged for providing test structures used in this study.

### References

- [1] A.O. Konstantinov and H. Bleichner, Appl. Phys. Lett. 71 (1997), p. 3700.
- [2] A. Galeckas, J. Linnros, M. Frischholz, K. Rottner, N. Nordell, S. Karlsson and V. Grivickas, Mater. Sci. Engineering Vol. B61-62 (1999), p.239.
- [3] J. Casady and R.W. Johnson, Solid-State Electron. Vol. 39 (1996), p. 1409.
- [4] T. Dalibor, G. Pensl, H. Matsunami, T. Kimoto, W. J. Choyke, A. Schöner, and N. Nordel, Phys. Stat. Sol. (a) Vol. 162 (1997), p. 199.
- [5] T. Troffer, M. Schad, T. Frank, H. Itoh, G. Pensl, J. Heindl, H.P. Strunk, M. Maier, Phys. Stat. Sol. (a) Vol. 162 (1997), p. 277.

Corresponding author: Fax: +46 8 7527782, E-mail: galeckas@ele.kth.se

be responsible for the increase of blue emission, presumably due to thermal activation of  $N$ -donors. This assumption is supported by the fact that, in contrast to green spectral components, which are emitted mostly from the space charge region, the source of blue EL component is not localized in depth, and radiation comes from the whole  $n$  volume.

To clarify the origin of electrical stress-induced line formations, spatially resolved emission measurements were accomplished by utilizing adjustable aperture inside microscope, which enabled acquisition of emission from selected regions less than 10  $\mu\text{m}$  in size. The preliminary inspection has revealed an apparent build-up of near-infrared emission with peak position out of our spectral sensitivity range. A more detailed investigation of deep level impurities around stress-induced line-formations and their contribution to EL is underway.

## Electroluminescence From Implanted and Epitaxially Grown pn-Diodes

F.H.C. Carlsson, L. Storasta, C. Hemmingsson, J.P. Bergman and E. Janzén

<sup>1</sup> Department of Physics and Measurement Technology, Linköping University,  
SE-581 83 Linköping, Sweden

**Keywords:** Aluminium, Boron, Deep Levels, Defects, Electroluminescence, Implantation, pn-diodes

**Abstract** The electroluminescence from pn-diodes with (1) aluminum doped epitaxially grown, (2) aluminum implanted or (3) aluminum and boron implanted p-layer have been investigated. The temperature dependence for both the spectra and the decays of the major spectral components have been investigated at temperatures from 80 K to 550 K. The implanted diodes show implantation damage in the form of the D<sub>1</sub> center and lack of emission from the aluminum center. The epitaxial diodes show luminescence from the aluminum center. The band edge luminescence is visible above 150 K for the epitaxial diode and above 300 K for the implanted. The emission from deep boron can be seen in the aluminum and boron co-implanted diode and in the epitaxially grown diode that have an unintentional boron doping below  $10^{17} \text{ cm}^{-3}$ .

### Introduction

During the growth of the material and the processing of devices defects will be introduced. The performance of the device will be determined by these defects. The nature of these defects and the influence they have on the performance of the device need to be investigated and understood. Diodes are normally characterized with electrical methods such as IV, CV, admittance spectroscopy and deep level transient spectroscopy. Optical methods are usually not used because the difficulties in focusing on the small volume of the pn-junction. Electroluminescence (EL) bridges the electrical and optical methods making it possible to optically study the small volume of the pn-junction under operation like conditions. This gives further information on the pn-junction and makes it possible to retrieve information of the lifetimes. The luminescence spectra can be recorded as well as the decays after voltage pulses from specific emissions.

### Experiment

In this work we have investigated several different pn-diodes in 4H SiC. All samples had a low doped n-type base layer grown by hot wall CVD [1]. The p-layer were made either with ion implantation of Al or co-implantation of Al and B, followed by a high temperature anneal, or by an epitaxially grown Al-doped SiC layer.

The samples were mounted in an Oxford cryostat with a temperature range from 77 K to 550 K. EL measurements were made with forward voltage applied in pulsed mode, using a voltage pulse generator. The forward voltage pulses, of 3-6 V and 20-40 mA, had a duration of 10  $\mu\text{s}$  with a repetition frequency of 5 kHz. The variations of voltage and current depend on the different current voltage characteristics and its temperature dependence. The emission from the edge of the diode was collected and dispersed through a monochromator and detected by a photomultiplier tube using photon counting techniques. The emission from the diodes were detected either spectrally or as a function of time. During spectral measurements a gating technique was used to detect the signal

during two different conditions. One measurement was made during the last 5  $\mu\text{s}$  of the forward voltage pulse, corresponding to DC operation. The other measurement started 0.5  $\mu\text{s}$  after the forward pulse was turned off and was 5  $\mu\text{s}$  long. The delay was longer than the minority carrier lifetime at room temperature, and the measurement was made to enhance or separate emissions related to carriers trapped to defects. Time decay measurements during 70  $\mu\text{s}$  after the forward pulse was made for all emission energies to further determine the dynamics of each recombination. The response of the optical system was not calibrated.

Electrical measurements such as current voltage characteristics as a function of temperature and capacitance voltage characteristics were made to get general information about the diodes. The electrical characterization of defects was made by Deep Level Transient Spectroscopy (DLTS) for deep majority and minority traps and Admittance Spectroscopy for shallow majority carrier traps.

### Results and discussion

The normalized EL emission spectra at room temperature are shown in Fig. 1 for the three different studied diodes, where the spectra are shifted vertically for clarity. The spectra are dominated by four different emissions. Close to the bandgap at 3.18 eV there is an emission related to free carriers where the main recombination most probably is the free exciton recombination. At an energy of 2.92 eV there is a broader emission assigned to the donor-acceptor pair (DAP) recombination involving the nitrogen donor and the shallow Al acceptor. This is relatively stronger in the epitaxially grown diode while it is almost not observed in the implanted diodes. At lower energies, with an emission maximum at 2.48 eV, the DAP emission from the nitrogen donor and the deeper boron acceptor [2] are seen in the Al and B implanted diode as well as in the epitaxial diode. In the latter case the boron are introduced unintentionally ( $<10^{17} \text{ cm}^{-3}$ ) during the growth of the Al-doped p-layer. The DAP recombinations involving N and Al or B are at higher temperatures shifted towards higher

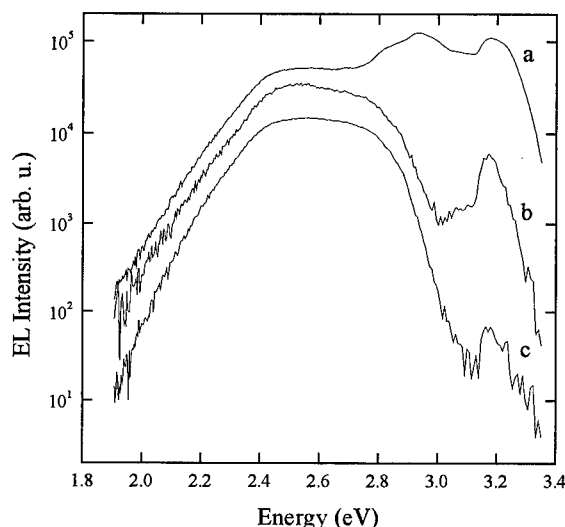


Figure 1. EL spectra at room temperature for the a) epitaxial diode, b) Al and B implanted diode and c) Al implanted diode.

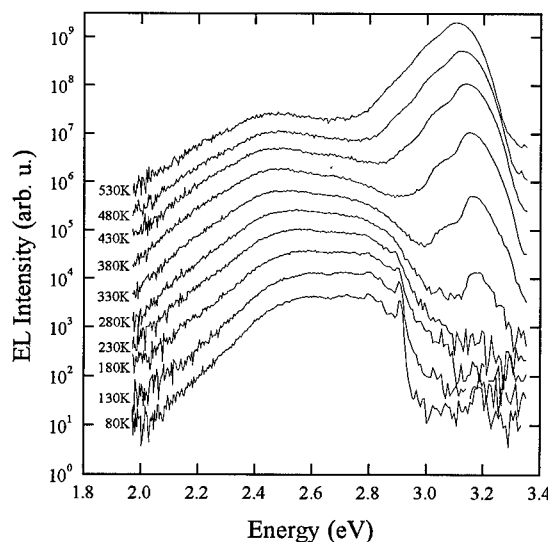


Figure 2. The temperature dependence from 80 K to 530 K in 50 K steps of the Al and B implanted diode. The curves are shifted vertically for clarity.



energies due to the contribution of free to bound recombinations. The Al implanted sample has a similar broad emission at lower energies. However this emission is slightly shifted towards higher energies, as compared to the other samples, with a peak at about 2.58 eV. It also lacks the slow decay at temperatures around 350 K that the Al and B implanted sample have as can be seen in Fig. 3b and Fig. 4b. Since we do not expect any boron in this sample an alternative explanation is needed. One possible explanation could be a DAP involving the deep Al acceptor as previously observed [3] in EPR. This has however not previously been observed optically or electrically, so a definite assignment of the observed emission can not be made.

At temperatures below 150 K a sharp emission line at 2.91 eV can be seen in the two implanted diodes but is absent in the epitaxially grown diode. This line, and another line at 2.902 eV at temperatures below 30 K, as well as the phonon structure at lower energies is known to originate from the center D<sub>1</sub> [4] which is well established from Photoluminescence (PL) of irradiated and annealed material. The D<sub>1</sub> center is believed to be an intrinsic defect here caused by the damage created by the ion-implantation of acceptors. The D<sub>1</sub> emission originates from an isoelectronic bound exciton which is thermally quenched at 150 K. The defect level does, however, remain at higher temperatures and could also be involved in a DAP recombination.

All the diodes have a broad luminescence around 2.58 eV from a DAP involving N and a deep acceptor level. The decays of these pair emissions become very fast at 250 K when the N is ionized. In the epitaxially grown diode the recombinations with Al are most probably originating from the p-layer. The n-layer has  $N_d=10^{15} \text{ cm}^{-3}$  and  $N_a=10^{11} \text{ cm}^{-3}$  while the p-layer has  $N_d=10^{16} \text{ cm}^{-3}$  and  $N_a=10^{19} \text{ cm}^{-3}$ . During the implantation high concentrations of vacancies are created and the implanted species can together with a vacancy create deep levels. The lack of luminescence from shallow Al in the Al implanted diode is probably due to a high degree of Al-V<sub>c</sub> pairs forming deep Al. The Al and B implanted diode also lacks luminescence from shallow acceptors for the same reason.

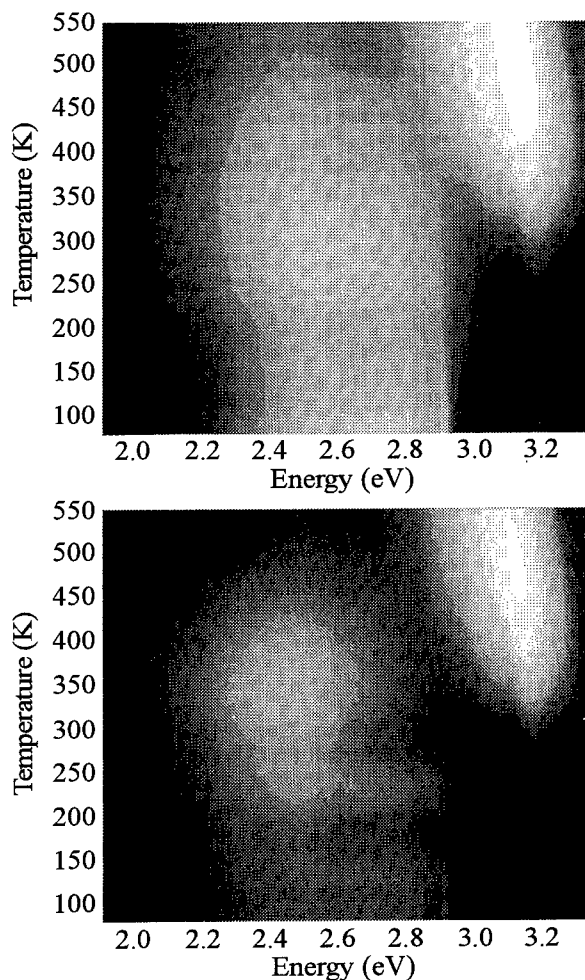


Figure 3. The temperature dependence of the EL during the pulse (upper) and directly after the pulse (lower). The logarithmic intensity is shown as a grayscale with black as 0 and white as 4.5 in arbitrary units.

The epitaxially grown diode and the Al and B co-implanted diode have both an emission around 2.48 eV with a slow decay, that can be seen in Fig. 4b, at temperatures from 300 K to 450 K. This is the emission from the free to bound recombination with deep boron. The intensity from this emission is weaker in the epitaxially grown diode.

The emission from free carrier recombination is observed at an energy of 3.18 eV. The epitaxially grown diode have free carrier recombination above 150 K whereas for the implanted diodes the emission is only visible above 300 K, as can be seen for the Al and B co-implanted diode in Fig. 2. This is due to the fewer deep levels and radiation induced recombination paths for the epitaxial diode compared to the implanted diodes. With DLTS the deep boron level is found in the diode implanted with both boron and aluminum.

### Conclusions

The comparison between implanted and epitaxially grown p-layers shows that the implantation process creates more deep acceptor levels on the expense of the shallow acceptor levels. The implanted diodes also have less band edge emission at lower temperatures and less emission from shallow acceptors as a result of higher concentration of defects. This implies that the epitaxial diode will have an advantage over the implanted diodes. The existence of the deep boron in the epitaxial diode will, however, reduce its performance and unless Al doped p-layers with less boron can be grown, implantation with Al may still be favorable.

### References

- [1] O. Kordina, C. Hallin, A. Henry, J.P. Bergman, I. Ivanov, A. Ellison, N.T. Son, E. Janzén, *Physica-Status-Solidi-B* **202**, (1997), p.321-34.
- [2] S.G. Sridhara, L.L. Clemen, R.P. Devaty, W.J. Choyke, D.J. Larkin, H.S. Kong, T. Troffer, G. Pensl, *J. of Appl. Phys.* **83**, (1998), p.7909-19
- [3] B.K. Meyer, A. Hofstaetter, P.G. Baranov, *Mater. Sci. Forum* **264-268**, (1998), p.591-4
- [4] L. Patrick, W.J. Choyke, *Phys. Rev. B* **5**, (1972), p.3253-9

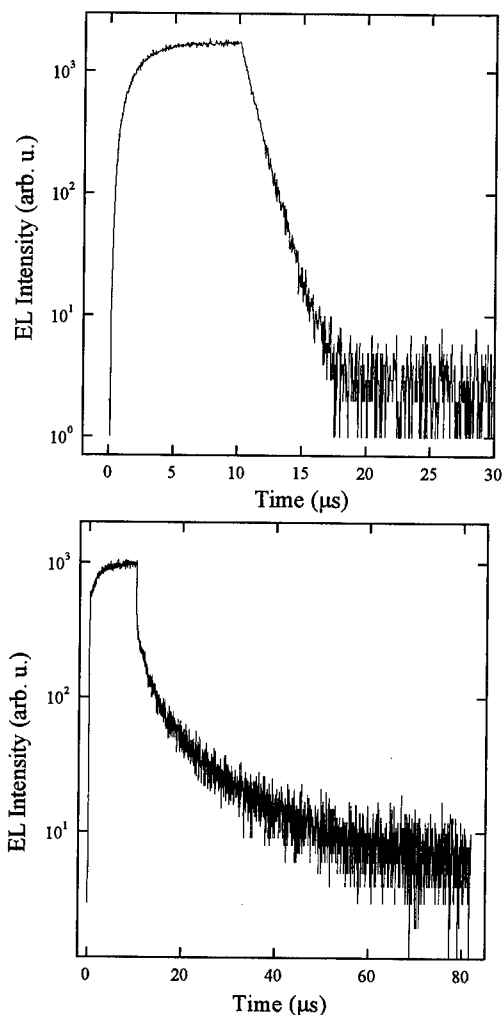


Figure 4. The decay at 350 K of the bandedge, 3.18 eV (upper) and the deep boron, 2.48 eV (lower) for the Al and B implanted diode.

## Avalanche Breakdown Electroluminescence in Silicon Carbide Light Emitting Diodes

S. Aboujja<sup>1</sup>, C. Carlone<sup>1</sup>, A. Houdayer<sup>2</sup>, P.F. Hinrichsen<sup>2</sup> and J.-P. Charles<sup>3</sup>

<sup>1</sup>Département de Physique, Université de Sherbrooke, Sherbrooke, Québec J1K 2R1, Canada

<sup>2</sup>Département de Physique, Université de Montréal, Montréal, Québec H3C 3J7, Canada

<sup>3</sup>LICM-CLOES, Supélec, 2 rue Edouard Belin, FR-57078 Metz Cedex, France

**Keywords:** Avalanche Breakdown Emission, Hot Carriers, Lifetime, Spectral Measurements

**Abstract.** Room temperature electroluminescence was obtained from silicon carbide diodes. The spectrum was recorded in the 1.1 to 3.2 eV energy range. In forward bias, the intensity maximum occurs at 2.64 eV and in avalanche breakdown at 2.2 eV. The lifetime of the latter is 179 ns. In forward bias, the lifetime was previously measured to be 2.3  $\mu$ s. It is concluded that, in SiC, forward and reverse bias emissions have different origins, and the reverse bias emission cannot be band to band. The SiC data supports the view that the mechanisms of avalanche breakdown electroluminescence are bremsstrahlung and intraband, involving hot carriers.

### Introduction

Light emission by hot carriers has been observed in reverse biased pn junctions based on silicon (Si) [1,2], germanium [3], gallium phosphide [4], gallium arsenide (GaAs) [5], and silicon carbide (SiC) [6]. The origin of this emission is still debated. The mechanisms proposed involve quantum interband and intraband transitions, and classical bremsstrahlung radiation. The quantum interband model depends on the gap of the material, whereas the classical model is less sensitive to it. Since the emission of the classical model falls in the infrared, electroluminescence (EL) from wide gap material can help to establish the mechanism of light emission in avalanche breakdown diodes. In this work, spectral and time dependent data from SiC diodes are presented, and compared with similar published data on Si [2] and GaAs [7] pn junctions. The SiC data presented here confirm the conclusion reached in Refs. 2 and 7 that reverse bias electroluminescence does not contain interband transitions, but is related to the hot carriers generated by the field.

### Experimental

SiC diodes, CREE Research Incorporation 900 series, were commercially bought. In forward bias, I-V curves were obtained using a standard parametric analyzer. In reverse bias, the breakdown voltage was above 60 V and the I-V curves could not be obtained. For spectral recording of the light emitted, a constant voltage source was applied. The light was dispersed with a Jarrell-Ash 1 m spectrometer and recorded with a Hamamatsu photomultiplier R636-10 operating in the photon counting mode. For the lifetime measurements, a Hewlett Packard HP 3325B square wave generator served to modulate the current and trigger a Tektronic TDS 360 oscilloscope. The detector was a Hamamatsu R406 photomultiplier. The detailed circuit used in the lifetime measurements has appeared [8].

Material	$E_g(\text{eV})$	Observed peaks in avalanche breakdown operation (eV)
Si	1.12	1.8
GaAs	1.43	1.44 and 1.9
SiC	2.89	$2.2 \pm 0.1$

Table I : Materials investigated, their gap, and observed transitions in avalanche breakdown operation of Si, GaAs and SiC junctions.

### Theory

The bandgap of the materials investigated is given in Table I. In forward bias operation, the light emitted corresponds to an electron-hole recombination across the band gap. In indirect gap materials, phonon assistance is required. In reverse bias operation, light is emitted in the avalanche region, but its origin has yet to be determined. The interband model attributes it to electron-hole recombinations across the bandgap. The intraband model attributes it to transitions between subbands in the conduction or valence bands. The bremsstrahlung model attributes it to electrons accelerated by ions.

### Results

Fig. 1 shows the I-V curve in forward bias operation. Fig. 2 shows the EL spectrum in forward and reverse bias. In reverse bias, it is rather broad, with a maximum, labeled a, between 2.1 and 2.3 eV. In forward bias, EL is shifted towards the blue. The energy of the weak peak labeled c, is 2.89 eV and corresponds to the optical gap of the SiC-8H polytype [9, 10]. The energy of the major signal labeled b, is 2.64 eV, and being smaller than that of the gap, corresponds to transitions involving defect states within the gap.

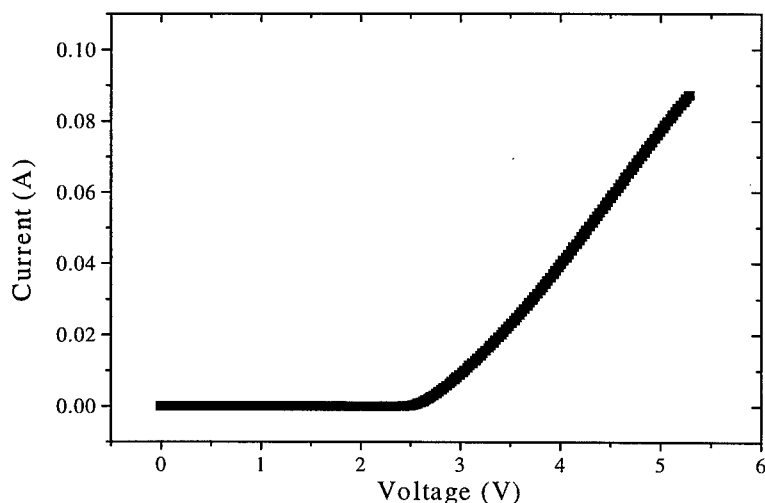


Fig. 1: SiC junction I-V curve in forward bias operation.

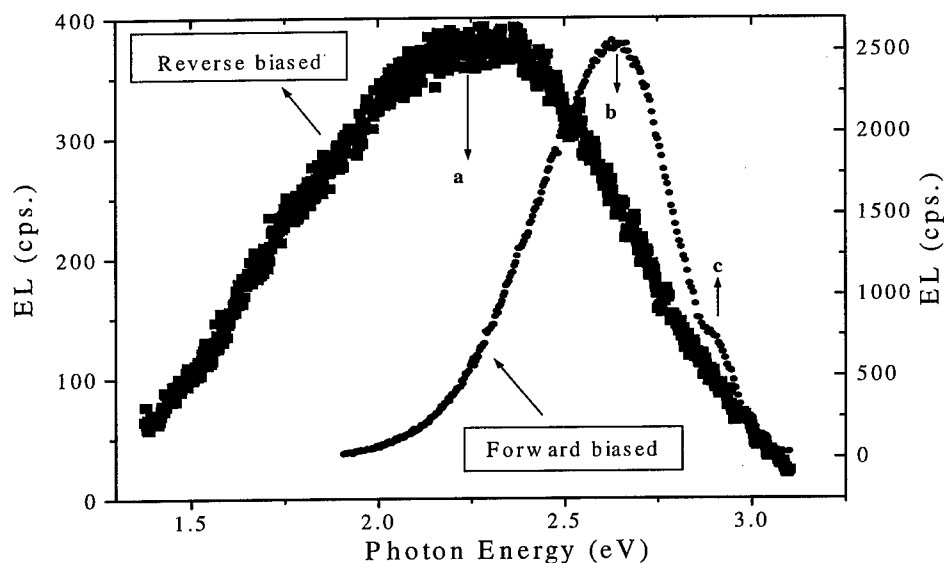


Fig. 2. Room temperature electroluminescence spectrum of SiC LED in forward (4 V) and reverse bias operation (100 V). The left scale applies to reverse bias, and the right to forward bias.

These observations in SiC can be compared to Si and GaAs avalanche breakdown emissions. For silicon junctions, the maximum occurs at 1.8 eV, corresponding to a yellow color, and for GaAs diodes, two peaks are observed, at 1.44 and 1.9 eV. See Table I.

Fig. 3 shows the time resolved spectrum of the EL in reverse bias operation. The measured response is 252 ns. The system response was measured to be 73 ns, and the lifetime of the SiC avalanche emission is estimated to be 179 ns. For the same diodes, the lifetime in forward has been published; it is 2.3  $\mu$ s [11].

### Discussion

In silicon junctions, the energy of the light emitted in reverse bias operation is larger than that of the optical gap. In GaAs diodes, the light emitted in reverse bias consists of two well resolved transitions. The one at 1.9 eV is close to that emitted in silicon junctions, but is larger than the GaAs bandgap. The other at 1.44 eV is band to band. The GaAs data clearly shows that the 1.9 eV transition cannot be band to band. In SiC diodes, the transitions in forward and reverse bias are also well resolved. Moreover, the reverse bias peak occurs at an energy smaller than that of the SiC bandgap. This observation that the reverse bias emission can be smaller or larger than the bandgap strongly suggests that it is not gap related. The SiC data confirm the view that the reverse bias emission is not interband in nature [2, 7].

Similarly the difference in lifetime confirms this conclusion. In Si, the lifetime in reverse bias has not been measured, although it is known to be less than 3 ns [12]. In GaAs, the reverse bias lifetime has not been measured. For SiC, the lifetime was measured in direct [11] and in reverse bias (present work) operations. They are quite different.

These observations suggest that the interband mechanism is not the origin of the yellow light emission occurring in reverse biased Si pn junctions. The Bremsstrahlung and the intraband models remain. In Bremsstrahlung, electrons placed in the ionization continuum, called "hot", are attracted by the ions and emit light. For SiC, modeling the data for energies between 2.3 and 3.2 eV requires temperatures of thousands of degrees. However, in the classical physics mechanism, the intensity of the light emitted decreases monotonically with energy, which is not observed for energies less

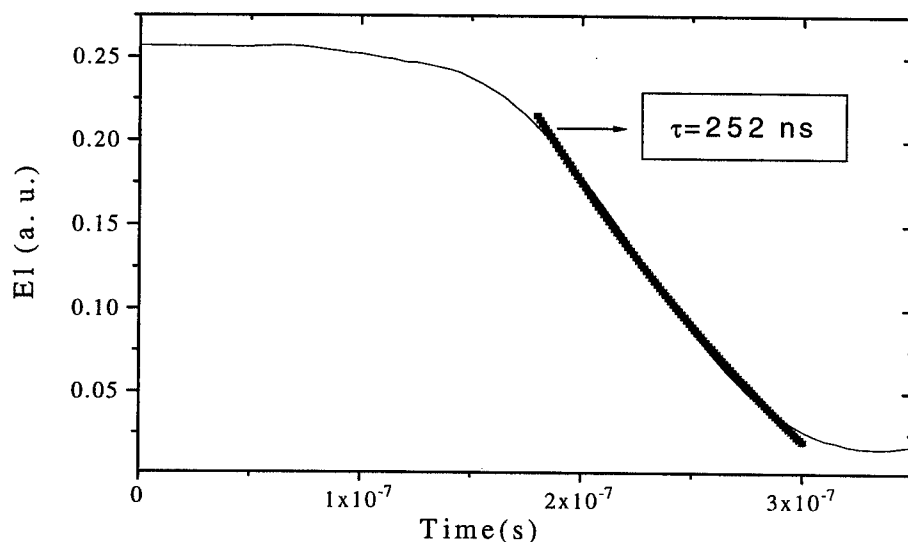


Fig. 3. Room temperature temporal decay of SiC reverse biased LED. The constant current was 10 mA.

than 2.3 eV. Carrier collisions with the lattice could further slow them down, with the result that the Bremsstrahlung mechanism ceases to operate at small energies. The slowed down electrons could emit photons and reach **discrete** levels. These are intraband transitions between sub-bands of the conduction band. Further theoretical work is needed to identify the **discrete** levels involved.

In Table I, the energy of the breakdown regime transition is dependent on material. The dependence could be due to ionization energy, which depends on material.

### Conclusion

Reverse bias EL from SiC diodes is different from that of Si and GaAs diodes because its energy is smaller than the bandgap. This observation and the different lifetime exclude the interband mechanism of the light emission process. It support the bremsstrahlung and intraband models.

### References

- [1] R. Newman, Phys. Rev. 100, (1955), p. 700.
- [2] S. Aboujja, C. Carlone, et al, IEEE Trans. Nucl. Scien. 45 (6), (1998), p. 2813.
- [3] S. Yamada, M. Kitao, Jpn. J. Appl. Phys. 32, (1993), p. 4555.
- [4] R. A. Logan, A. G. Chynoweth, J. Appl. Phys. 33, (1964), p. 1649.
- [5] R. A. Logan, A. G. Chynoweth, B. G. Cohen, Phys. Rev. 128, (1962), p. 2518.
- [6] G. F. Kholuyanov, Sov. Phys. Solide State 3, (1962), p. 2405.
- [7] S. Aboujja, C. Carlone, et al, Nucl. Sp. Rad. Conf., Norfolk, VA, paper I-2, (1999).
- [8] A. L. Barry, R. Maxseiner, R. Wojcik, M. A. Briere, D. Bräunig, IEEE Trans. Nucl. Scien. 37 (6), (1990), p. 1726.
- [9] L. Patrick, D. R. Hamilton, W. J. Choyke, Phys. Rev. 143, (1966), p. 526.
- [10] D. R. Hamilton, L. Patrick, W. J. Choyke, Phys. Rev. 138, (1965), p. A1472.
- [11] P. F. Hinirischsen, A. J. Houdayer, et al, IEEE Trans. Nucl. Scien. 45 (6), (1998).
- [12] J. Kramer, P. Seitz, E. F. Steigmeier, H. Auderset and B. Delley, Sensors and Actuators A. (1993), p. 527.

Author to whom readers should correspond: Sidi Aboujja, e-mail: [saboujja@physique.usherb.ca](mailto:saboujja@physique.usherb.ca)

## Photon Emission Mechanisms in 6H and 4H-SiC MOSFETs

C. Banc<sup>1</sup>, E. Bano<sup>1</sup>, T. Ouisse<sup>1</sup>, S. Scharnholz<sup>2</sup>, U. Schmid<sup>3</sup>, W. Wondrak<sup>3</sup>  
and E. Niemann<sup>3</sup>

<sup>1</sup> Laboratoire de Physique des Composants à Semiconducteurs (LPCS), UMR-CNRS 5531,  
ENSERG, 23 rue des Martyrs, BP 257, FR-38016 Grenoble Cedex 1, France

<sup>2</sup> Institut für Halbleitertechnik, Lehrstuhl II, RWTH Aachen, Sommerfeldstr. 24,  
DE-52074 Aachen, Germany

<sup>3</sup> Research and Technology 2, DaimlerChrysler AG, Goldsteinstrasse 235,  
DE-60528 Frankfurt, Germany

**Keywords:** 4H, 6H, Impact Ionization, Mechanism, MOSFETs, Photon Emission, Saturation

**Abstract:** We have considered 6H and 4H SiC n-MOSFETs from two different origins and studied the photon emission coming from the channel of the devices biased in the saturation regime. We have simultaneously measured the drain and the substrate currents, which enabled us to establish a specific relationship between the currents and the emission intensity. Additionally, we performed a spectral analysis which clearly indicates the contribution of one or more recombination center(s) inside the bandgap of silicon carbide.

### 1 Introduction

Photon emission measurements on SiC devices are of various interests. In addition to the localization of technologically induced defects characterized by local leakage currents and high electric fields, they can give detailed information about the mechanisms involved in hot carriers relaxation phenomena. Compared to silicon, for which most of the previous investigations considered energy ranges above the material's bandgap [1-5], our measurements lie below the silicon carbide bandgap. They unambiguously show that the emission mechanisms are different from those of silicon in the same conditions.

### 2 Devices and experimental set-up

We investigated two series of devices made on p-type epilayers:

- 6H & 4H-SiC inversion-mode n-channel MOSFETs from RWTH, Aachen (labeled "S"),
- 6H-SiC inversion-mode n-channel MOSFETs from DaimlerChrysler AG (labeled "N").

The channel doping levels are  $5.8 \cdot 10^{16} \text{ cm}^{-3}$  for the 4H devices and  $2.9 \cdot 10^{16} \text{ cm}^{-3}$  and  $1 \cdot 10^{16} \text{ cm}^{-3}$  for the 6H devices from RWTH and DaimlerChrysler, respectively. The channel length of all devices is  $3 \mu\text{m}$ . The channel width is  $500 \mu\text{m}$  for devices from RWTH and  $106 \mu\text{m}$  for device from DaimlerChrysler. The gate oxide thickness is  $36 \text{ nm}$  for devices from RWTH and  $50 \text{ nm}$  for device from DaimlerChrysler. The apparent surface mobility has been measured as  $6 \text{ cm}^2 \cdot \text{V}^{-1} \cdot \text{s}^{-1}$  for the 4H polytype,  $31 \text{ cm}^2 \cdot \text{V}^{-1} \cdot \text{s}^{-1}$  for the 6H device from RWTH, and  $44 \text{ cm}^2 \cdot \text{V}^{-1} \cdot \text{s}^{-1}$  for the 6H device from DaimlerChrysler (for more details, see [6,7]).

The emission behavior of the different devices was studied using the following procedure: the transistors were biased in the saturation regime and the photon emission coming from the channel was focused by a microscope on a CCD camera (Hamamatsu C4880). The camera output was transferred to a computer and the data were processed using an image control system. Emission profiles of the channel were calculated and then, each profile was averaged over the channel width on a distance related to the field of the camera (about  $100 \mu\text{m}$ ). For each biasing condition, the maximum light intensity ( $I_v$ ) was measured as well as the drain and the substrate currents ( $I_D$  and  $I_{SUB}$ , respectively). Note that the light intensity  $I_v$  corresponds to an integration over the spectral sensitivity range of the CCDs (1.2 to 3.2 eV). The spectra were measured using a set of discrete filters with wavelengths ranging from 400 to 1100 nm (bandwidth ranging from 6 to 16 nm). The whole system had previously been calibrated using a known light source.

### 3 Results and discussion

Figure 1a shows the light emission intensity normalized by the drain current density as a function of  $(V_D - V_{Dsat})$  for three 6H devices and one 4H device.  $V_{Dsat}$  is extracted from  $I_D(V_D)$  characteristics using the method proposed by Jang *et al.* [8] The difference between 4H and 6H reflects for one part the different impact ionization efficiencies of the two polytypes. However, we will see below that the light emission intensity is not directly correlated to the substrate current so that one must be careful when interpreting such a plot.

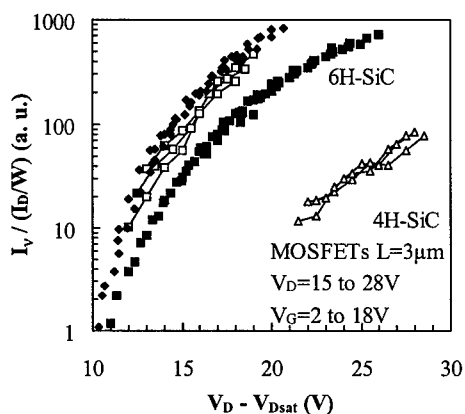


Figure 1a :

Normalized maximum light intensity versus  $(V_D - V_{Dsat})$  for one 4H and three 6H SiC devices.  $\Delta$  : 4H device,  $\square$  : 6H device S1,  $\blacksquare$  : 6H device S2,  $\bullet$  : 6H device N.

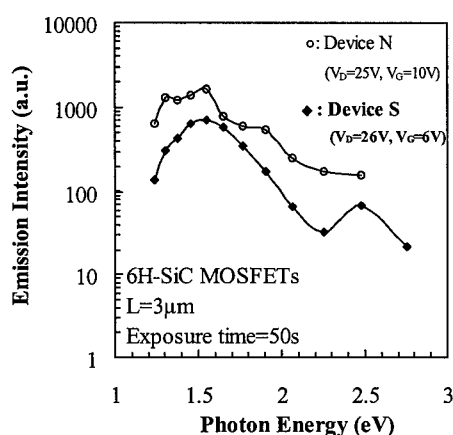


Figure 1b :

Emission spectra of device N and device S. The spectra are corrected taking into account the polysilicon gate absorption, using the data in [16].

Figures 2 and 3 show the relation between the light intensity and the drain and substrate currents. In Figure 2, we have plotted  $I_v$  as a function of  $I_{SUB}$  only. Had one done the same for a silicon device, one would have found a straight line [5,9]. It is clearly not the case for silicon carbide since we obtain a cloud of data points. Figure 3 reveals the appropriate relation between  $I_v$  and  $I_{SUB}$  in the case of SiC. Plotting  $I_v$  as a function of the product  $I_{SUB} \times I_D$  makes all the points converge to a single line: the light emission is proportional to  $(I_{SUB} \times I_D)^\alpha$  and we find the coefficient  $\alpha$  to be 0.50 for device N and 0.56 for device S.

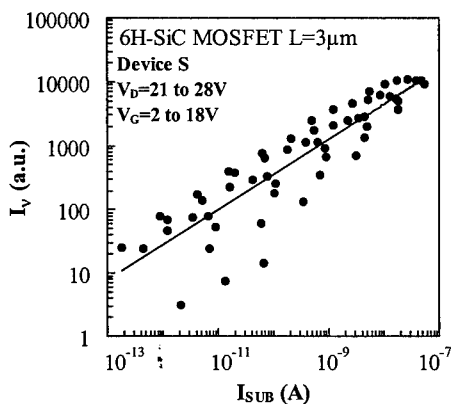


Figure 2 :

Maximum light intensity versus substrate current for device N.

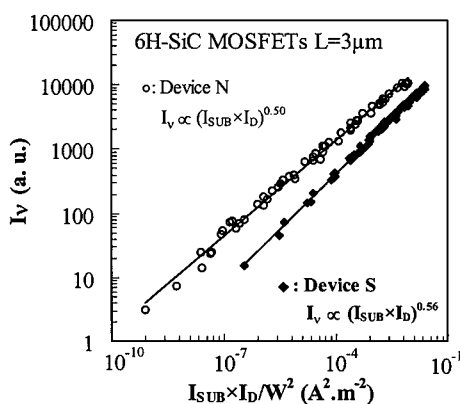


Figure 3 :

Maximum light emission versus the product  $I_{SUB} \times I_D$  for device N and device S.



Figure 1b shows the spectral distribution of the emitted light in a logarithmic scale. The spectra have been corrected by our experimental set-up spectral sensitivity as well as the polysilicon gate absorption. They are characterized by a strong emission peak whose maximum is located around 1.6 eV. This value (nearly the middle of the gap for 6H-SiC) can be compared to the position of the vanadium deep donor level ( $E_v + 1.55$  eV) found by optical admittance measurements by Evwaraye *et al.* [10] (they also determined the vanadium acceptor level to be located at  $E_c - 0.6$  eV). Device S shows a secondary emission peak around 2.5 eV. Device N does not exhibit this peak but, for energies greater than 2.5 eV, the emission was very faint due to the rapidly increasing absorption caused by the thick polysilicon gate (700 nm for device N to be compared with 150 nm for device S). This secondary peak could be due to donor-acceptor pair recombinations.

**Emission mechanisms :** The mechanisms involved in photon emission from SiC MOSFETs biased in saturation are different from those found in their silicon counterparts.

In silicon MOSFETs, experimental results [4,5,11] as well as theoretical calculations [12] attribute the photon emission to intraband transitions of electrons inside the conduction bands. The carriers excited in the silicon conduction bands by the high electric field relax towards the bottom of the band, partly by emitting photons and partly by impact ionizing valence band electrons. This leads to the nearly exponentially decreasing behavior of the spectra measured by several authors as well as by ourselves. Most authors [5,9] (including ourselves [13]) find a simple proportional relation between the emitted light and the substrate current. Although the reason for this is still not clear, it clearly indicates that the origin of both phenomena is common.

In the case of silicon carbide, we found a different behavior. First, the emitted light is not directly proportional to the substrate current (Figure 1a). One must take into account both the substrate current ( $I_{SUB}$ ) and the drain current ( $I_D$ ) for a proper correlation with the light intensity ( $I_v$ ). We found that the emission intensity is roughly proportional to the square root of the product  $I_{SUB} \times I_D$  ( $I_v \propto \sqrt{I_{SUB} \times I_D}$ ) (Figure 3). This means that the probability of emission depends on the free electron density (via  $I_D$ ) as well as the free hole density generated in the depletion region ( $I_{SUB}$ ). Second, the emission spectra do not exhibit the same exponential behavior as those measured on silicon [1-5,11]. In contrast, they reveal a main emission peak located near midgap. These two features lead us to conclude that the emission is associated to recombination mechanisms via a deep level in the bandgap of silicon carbide. Due to its position, this deep level could be due to vanadium impurities.

**Ionization coefficients:** Semi-empirical impact ionization models [14] show that in silicon MOSFETs, the substrate current can be approximated as :

$$I_{SUB} = I_D \cdot \frac{A_i}{B_i} \cdot (V_D - V_{Dsat}) \cdot \exp\left(-\frac{l_d \cdot B_i}{(V_D - V_{Dsat})}\right) \quad (1)$$

Where  $I_{SUB}$  is the substrate current,  $I_D$  the drain current,  $V_D$  the drain voltage,  $V_{Dsat}$  the drain voltage at which the channel electrons reach their saturation velocity,  $l_d$  is the effective ionization length, and  $A_i$  and  $B_i$  are the ionization constants. Following [14], we define  $l_d$  as  $((\epsilon_{SiC}/\epsilon_{ox}) \cdot t_{ox} \cdot X_j)^{0.5}$ , where  $X_j$  is the source/drain junction depth and  $t_{ox}$  the gate oxide thickness.

The formula was originally developed for silicon but a previous work [15] shows that it still holds for silicon carbide devices. Our measurements also confirm this result so that we can use (1) in our analysis. In SiC MOSFETs, since we found  $I_v$  to be related to  $I_{SUB}$  by the relation

$I_v = \beta \cdot (I_{SUB} \times I_D)^{\frac{1}{2}}$ , it is possible to extract  $B_i$  without measuring  $I_{SUB}$ . Indeed, using this relation and (1),  $B_i$  can be extracted from the slope of  $\ln\left(\frac{I_v}{I_D \cdot (V_D - V_{Dsat})^{\frac{1}{2}}}\right)$  as a function of  $\frac{1}{(V_D - V_{Dsat})}$ . Figure

5 shows such a plot for devices S and N and the extracted coefficients are compared with those obtained using  $I_{SUB}$  (Figure 6).

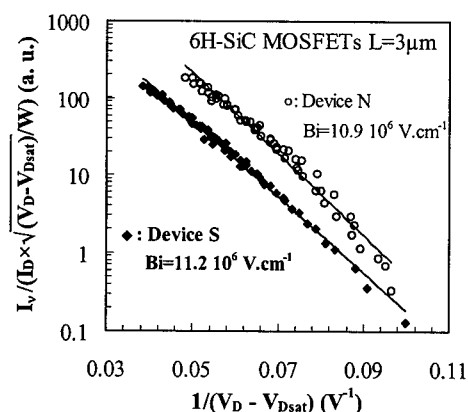


Figure 5 :

Extraction of the impact ionization coefficient  $B_i$  using the maximum light intensity. Extracted values of  $B_i$  are indicated on the graph.

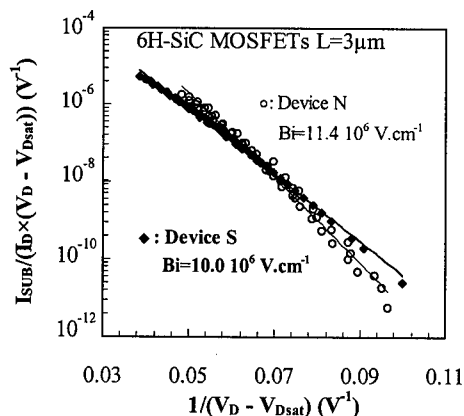


Figure 6 :

Extraction of the impact ionization coefficient  $B_i$  using the substrate current. Extracted values of  $B_i$  are indicated on the graph.

The coefficients extracted by both methods compare well, the difference being at most 10% for Device S. These two plots deserve a further comment: Figure 6 shows that the substrate current (hence the impact ionization efficiency) is very similar for both devices, since their curves almost superpose. It is different in the case of the light emission (Figure 5): "N" emits more than "S" for the same conditions. This can be due to a difference in the recombination center concentration.

#### 4 Conclusion

We investigated the photon emission characteristics of 6H and 4H-SiC MOSFETs biased under saturation conditions. The devices were from two different origins and showed the same behavior. First, the integrated light intensity is not a function of the substrate current alone as in silicon MOSFETs. In contrast, it is a function of the product of the substrate current by the drain current. This in turn allows us to extract the ionization coefficient  $B_i$  without measuring the substrate current. Second, the emission spectra exhibit a main peak located around midgap (1.6 eV). A secondary peak occurs at about 2.4 eV for one series of devices. We conclude that the measured emission is due to the recombination of channel hot electrons inside the depletion region near the drain via one or more deep level(s). The first peak could be associated to vanadium donor levels while the secondary peak is likely to be due to donor-acceptor pair recombinations.

#### 5 References

- [1] A. Toriumi *et al.*, IEEE Trans. Electron. Devices **ED-34** (7) (1987), pp. 1501-07.
- [2] M. Lanzoni *et al.*, IEEE Electron. Device Lett. **EDL-10** (5) (1989), pp. 173-76.
- [3] M. Lanzoni *et al.*, IEEE Electron. Device Lett. **EDL-12** (6) (1991), pp. 341-43.
- [4] A. L. Lacaita *et al.*, IEEE Trans. Electron. Devices **ED-40** (3) (1993), pp. 577-82.
- [5] J. M. Tao *et al.*, J. Phys. D: Appl. Phys. **29** (1996), pp. 1380-1385.
- [6] U. Schmid *et al.*, Proc. ECSCRM 1998, Montpellier, *in print*.
- [7] S. Scharnholtz *et al.*, Mat. Sci. For. **264-268** (1998), pp. 1001-04.
- [8] W.-Y. Jang *et al.*, Solid-State Electronics **31** (9) (1988), pp. 1421-31.
- [9] H.-S. Wong, IEEE Electron. Device Lett. **EDL-13** (8) (1992), pp. 389-91.
- [10] A. O. Evwaraye *et al.*, J. Appl. Phys. **79** (1) (1996), pp. 253-58.
- [11] M. Herzog *et al.*, Appl. Phys. Lett. **53** (26) (1988), pp. 2620-22.
- [12] J. Bude *et al.*, Physical Review B **45** (11) (1998), pp. 5848-56.
- [13] E. Bano *et al.*, submitted to Solid-State Electronics.
- [14] N. D. Arora *et al.*, IEEE Trans. Electron. Devices **ED-38** (6) (1991), pp. 1392-98.
- [15] E. Bano *et al.*, Mat. Sci. For. **264-268** (1998), pp. 1009-12.
- [16] G. Lubberts *et al.*, J. Appl. Phys. **52** (11) (1981), pp. 6870-78.

## Non-Contact Photovoltage Measurements in SiC

Y. Koshka and M.S. Mazzola

Emerging Materials Research Laboratory, Department of Electrical & Computer Engineering,  
Mississippi State University, Mississippi State, MS 39762-9571, USA

**Keywords:** Capacitive Contact, Junction Impedance, Non-Contact Characterization, Photovoltage

**Abstract** A non-contact ac photovoltage technique is reported for measuring capacitance and conductance of a buried junction in SiC. The photovoltage signal is generated by applying a chopped UV light source and is detected with a specially designed capacitive electrode. The values of junction capacitance and conductance are extracted from the real and the imaginary parts of the photovoltage. A new non-contact approach to perform C-V measurements of doping near the junction interface is suggested.

### Introduction

A growing interest in SiC as a promising material for power electronics has stimulated a need for non-contact methods to characterize the properties of SiC substrates and epi-layers. Photovoltage-based techniques that allow important semiconductor parameters to be determined without touching the surface of the wafer are actively used in the silicon industry. Non-contact photovoltage methods to characterize a buried junction in Si have been reported [1]. Another reason to use the ac photovoltage as a method to measure depletion region impedance is that the requirement to minimize series resistance in the bulk and contacts of a semiconductor, a potentially limiting factor for conventional C-V measurements, is significantly reduced [2].

### Method description

Photovoltage can be generated by UV light irradiating a SiC sample with a junction near the surface. The junction could be a buried p-n junction or depletion type surface barrier. If the excitation light is amplitude modulated, a capacitive electrode utilizing a dielectric spacer or even an air-gap can be used to detect the generated ac photovoltage.

A simple equivalent circuit for the process described is shown in Fig. 1. Here  $I_{ph}$  is the photocurrent;  $C_j$  and  $G_j$  are the total junction capacitance and conductance, respectively, that may in general include depletion capacitance and conductance, diffusion capacitance and conductance, as well as any other contribution from traps at the surface or in the bulk of the material;  $C_{electrode}$  is the capacitance of the spacer of the capacitive electrode. If the input resistance of the measuring device is sufficiently high to ensure negligible voltage drop on the  $C_{electrode}$ , the ac photovoltage  $V_{ph}$ , is given by

$$V_{ph} = I_{ph} * \frac{1}{G_j + j\omega C_j} \quad (1)$$

where  $I_{ph}$  is the photocurrent, which is frequency-independent at the low frequency range of interest. The real and imaginary parts of ac photovoltage are given by

$$\text{Re } V_{ph} = I_{ph} * \frac{G_j}{G_j^2 + \omega^2 C_j^2} \quad \text{Im } V_{ph} = I_{ph} * \frac{-\omega C_j}{G_j^2 + \omega^2 C_j^2} \quad (2)$$

By measuring the real and imaginary part of the photovoltage while properly calibrating the photocurrent the total capacitance and conductance can be determined from the following formulas [3]:

$$G_j = I_{ph} * \frac{\text{Re } V_{ph}}{(\text{Re } V_{ph})^2 + (\text{Im } V_{ph})^2} \quad \omega C_j = I_{ph} * \frac{-\text{Im } V_{ph}}{(\text{Re } V_{ph})^2 + (\text{Im } V_{ph})^2} \quad (3)$$

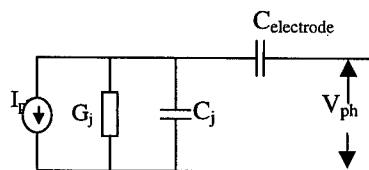


Fig. 1 Equivalent circuit for photovoltage measurements.

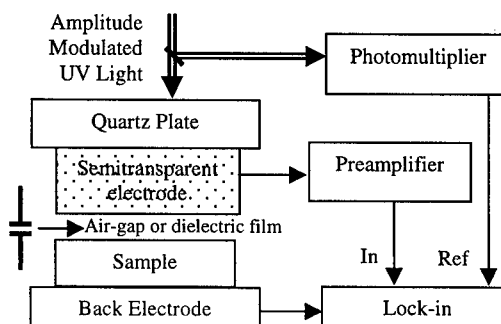


Fig. 2. Experimental set-up for phase-resolved photovoltage measurements.

### Experimental set-up

In our experiments, the measurements were performed on different 4H-SiC substrates with and without an epitaxial layer on the top. The substrates were obtained from Cree Research and the 4H epitaxial layers were grown in the Emerging Materials Research Laboratory at Mississippi State University by chemical vapor deposition.

The experimental set-up to measure phase-resolved ac photovoltage is shown in Fig. 2. A low intensity UV beam from an Ar laser with a wavelength varied between 275 nm and 528 nm and modulated with a mechanical chopper at different frequencies from 10 Hz to 3 kHz was used to generate a photovoltage. The beam irradiated the surface of the sample through a semitransparent capacitive electrode formed by a patterned metal film on a quartz plate. In these first experiments, a transparent mylar spacer was used instead of an air-gap in order to simplify the control of the spacing between the sample and the electrode. The generated ac photovoltage was detected by using a backside metal electrode under the sample in series with the capacitive semi-transparent electrode. The photovoltage was measured by a Stanford SR830 DSP lock-in amplifier. It was observed that the measured value of the photovoltage is reduced in comparison to the true value because a part of the voltage drops on the capacitive electrode at low frequencies. This problem was overcome by incorporating a unity gain preamplifier in the measurement circuit, which increased the input impedance of the lock-in amplifier. Since at low frequencies there is no phase shift between the ac modulated light and the photocurrent, the phase shift between the photovoltage and the photocurrent can in fact be measured as a phase shift between the photovoltage and the modulated light. To calibrate the phase of the modulated light, a part of the light was scattered on the input slit of a spectrometer and was measured by a Hamamatsu R928 photomultiplier tube (PMT). The final phase shift was determined as a phase difference between the photovoltage and the PMT current.

## Results and discussion

Measurements from a sample with a p-type epitaxial layer on a n-type substrate showed a strong photovoltage signal apparently generated at the p-n junction formed between the substrate and the epitaxial layer. The shape of the frequency dependence of the magnitude of the photovoltage from the same sample (Fig. 3) is similar to that measured from Si wafers with a p-n junction formed near the surface [1] and can be described by Eq. 1.

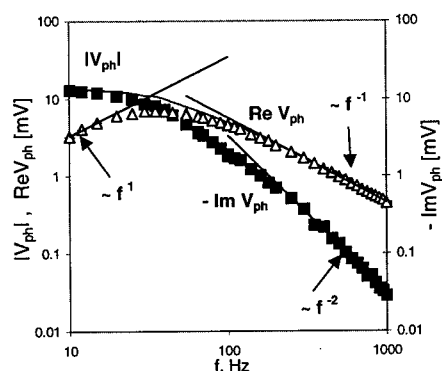


Fig. 3 Frequency dependence of the magnitude (solid line), the real (squares), and the imaginary (triangles) parts of the non-contact photovoltage.

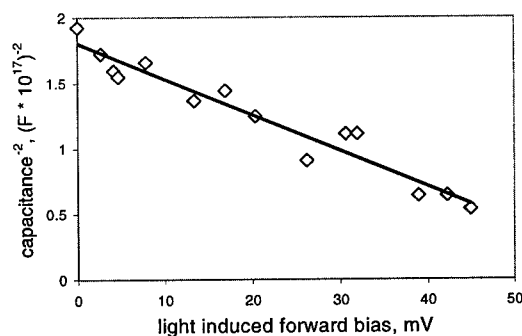


Fig. 4 Photovoltage measured capacitance plotted vs light induced forward bias. Near-the-junction doping determined from the slope of the dependence is of the order of  $1 \times 10^{15} \text{ cm}^{-3}$ .

The frequency dependence of the real and the imaginary parts of the photovoltage is proportional to  $f^{-1}$ , which is in accordance with a theoretical model for the case when the diffusion capacitance and conductance are either negligible or their frequency dependence can be neglected at the given frequency range. It is reasonable to suggest that at low excitation intensity the diffusion component of junction capacitance is small in SiC and thus we measure the depletion capacitance.

The measurements were done on different samples in order to qualitatively correlate the doping in the epi-layers on n-type substrates and the value of the depletion capacitance measured. For samples with epi layers doped n-type on n-type substrates the photovoltage could not be detected. The highest value of the depletion capacitance, measured in relative units, was observed for intentionally doped p-type epi-layers. In closely compensated p-type epi-layers, in which the series resistance was too high to permit measuring the doping profile with the traditional C-V technique, the value of capacitance was significantly smaller than for higher doped p-type layers.

The technique was applied to monitor the doping homogeneity across a sample. The values of  $C_j$  and  $G_j$  were measured at a few different points on a 4H SiC sample with a closely compensated p-type 4H SiC epitaxial film. Variations in the value of  $C_j$  were of the order of 5%, thus demonstrating a satisfactory doping homogeneity across the sample. Variations in the value of  $G_j$  were more significant, presumably reflecting a non-homogeneous distribution of defects at the epi-substrate interface.

A new approach was developed to permit traditional C-V doping profiling in non-contact capacitance measurements. With this approach we were able to apply a small forward bias to the junction and extract a value of doping near the junction interface from the slope of the C-V dependence. Because the major part of an externally applied voltage drops across the insulator of the non-contact electrode, it is extremely difficult in practice to apply a controlled dc bias to the junction in the non-contact experimental arrangement. We suggest an approach to provide a bias by illuminating the sample with a stronger dc light (biasing light) in addition to the small ac light used

for the photovoltage measurements. It is known that at high light intensity an accumulation of non-equilibrium carriers on different sides of a junction may induce an electric field strong enough to cause modification of the barrier height. This effect was verified for our SiC samples. The characteristic saturation of the photovoltage at high light intensity was observed. The process is equivalent to application of a forward bias. In order to determine the value of this Light-Induced Forward Bias (LIFB) the measurements were performed in two stages. In the first stage, the small-signal ac photovoltage were measured for a given intensity of the dc light. The value of  $C_j$  was extracted. In order to determine a corresponding value of the LIFB, the dc biasing light was also modulated and the corresponding photovoltage was measured in a similar manner. To insure that the amplitude of the ac photovoltage measured in this second stage is equal to the value of the LIFB under dc light conditions, the modulation frequency was selected low enough to keep the operating point at the horizontal part of the frequency curve in Fig. 3, but high enough to eliminate the influence of the impedance of the non-contact electrode. The expected increase of the capacitance with the forward bias was observed. The value of  $1/C_j^2$  is plotted versus the LIFB in Fig. 4. The doping near the junction interface in the low doped side of the junction can be determined from the slope of this dependence even though the epi series resistance is too high to measure with conventional CV techniques. However, because the value of  $C_j$  was extracted using an estimated value of the photocurrent, the value of the doping shown in Fig. 4 can only be considered an estimate.

### Conclusion

The non-contact ac surface photovoltage technique was shown to be effective for measurements of junction impedance in 4H SiC epi-layers on 4H SiC substrates at low frequencies. It was demonstrated that the measurements can be useful for monitoring homogeneity at the epi-substrate interface. The application of a light induced forward bias allowed a modified C-V approach to measure doping near the junction interface.

This work was supported by the Office of Naval Research, Grant No. N0014-98-1-0824, Dr. C. Wood program manager.

- [1] C. Munakata, N. Honma, Jpn. J. Appl. Phys. 20 (1981), p. L856.
- [2] E. Kamieniecki, J. Appl. Phys. 54 (1983), p. 6481.
- [3] R. S. Nakhmanson, Solid-State Electronics, 18 (1975), p. 617.

YKoshka@ece.MsState.edu

## **Ionization Energies and Electron Mobilities in Phosphorus- and Nitrogen-Implanted 4H-Silicon Carbide**

M.A. Capano<sup>1</sup>, J.A. Cooper, Jr.<sup>1</sup>, M.R. Melloch<sup>1</sup>, Adam Saxler<sup>2</sup>  
and W.C. Mitchel<sup>2</sup>

<sup>1</sup> School of Electrical and Computer Engineering, Purdue University,  
1285 EE Building,  
West Lafayette, IN 47907-1285, USA

<sup>2</sup> Materials and Manufacturing Directorate, Air Force Research Laboratory,  
3005 P Street, Suite 6, Wright-Patterson AFB, OH 45433-7707, USA

**Keywords:** Electron Mobility, Ionization Energies, Nitrogen Implantation, Phosphorus Implantation

### **Abstract**

Comparisons are made between the carrier concentrations, ionization energies, and electron mobilities in 4H-SiC samples implanted with similar doses of nitrogen or phosphorus, and annealed at 1300°C or 1700°C for 10 min in argon. Ionization energies of 53 meV and 93 meV are measured from phosphorus-implanted 4H-SiC, and are assigned to the hexagonal and cubic lattice positions in 4H-SiC, respectively. The corresponding ionization energies for nitrogen-implanted 4H-SiC are 42 meV and 84 meV, respectively. Phosphorus is not activated to the same extent that nitrogen is, and the carrier concentrations are about a factor of five lower for phosphorus-implanted 4H-SiC annealed at 1300°C than for nitrogen-implanted 4H-SiC annealed at the same temperature. A higher mobility measured from phosphorus-implanted 4H-SiC is observed, but is not sufficiently high to offset the lower carrier concentration of this material. For the doses considered in this study, the resistivity of nitrogen-implanted 4H-SiC is lower than the resistivity of phosphorus-implanted 4H-SiC following anneals at either 1300°C or 1700°C.

### **Introduction**

Ion implantation is a viable technology for both p-type and n-type doping of silicon carbide (SiC) electronic materials. Nitrogen is the most frequently used implanted dopant for n-type SiC.<sup>1,2</sup> Nitrogen simultaneously possesses two important characteristics: low atomic mass and low ionization energy. In 4H-SiC, the ionization energy for nitrogen is 45 meV.<sup>3</sup>

At first glance, there appears to be little motivation to develop other implant donor species for SiC, such as phosphorus, that are heavier than nitrogen and generate more lattice damage during implantation. If a significantly reduced ionization energy were associated with a heavier donor ion, such as phosphorus, interest in finding alternatives for nitrogen would increase. However, phosphorus has been implanted into 6H-SiC, and the measured ionization energies of 80 meV and 110 meV for the hexagonal and cubic lattice sites, respectively, are found to be nearly equivalent to those measured for nitrogen.<sup>4</sup> Recent sheet resistance data from 4H-SiC, though, suggests there is an advantage in replacing nitrogen with phosphorus for applications where low sheet resistances are required.<sup>5-7</sup> Sheet resistances in phosphorus-implanted 4H-SiC are as much as an order of magnitude lower than those measured in nitrogen-

implanted 4H-SiC with comparable doping and thermal processing.<sup>5</sup> Since the sheet resistance depends on the mobile carrier concentration and the electron mobility, comparing these parameters in nitrogen- and phosphorus-implanted 4H-SiC is needed to better understand donor implantation in this material. For these reasons, this article presents direct comparisons of the electron mobilities, carrier concentrations, and ionization energies measured from similarly-dosed 4H-SiC samples implanted with phosphorus or nitrogen.

### Experiment

Samples in this study consist of a 2  $\mu\text{m}$ -thick, Al-doped epitaxial layer ( $2 \times 10^{15} \text{ cm}^{-3}$ ) grown on a semi-insulating 4H-SiC substrate. One half of the epiwafer is implanted with phosphorus at 600°C to a total dose of  $2.0 \times 10^{13} \text{ cm}^{-2}$ , and the other half is implanted with nitrogen at 600°C to a total dose of  $2.0 \times 10^{13} \text{ cm}^{-2}$ . Energies of the specific implantation steps are adjusted to obtain box profiles, which extend to a depth of 350 nm for both implantations. Following implantation, 1 cm x 1 cm pieces are cut and annealed at either 1300°C or 1700°C for 20 min in argon. Measurements of the Hall effect are performed from 10 K to 1000 K using Ni/Au contacts arranged in a van der Pauw configuration. Contacts are annealed at 950°C for 5 min in forming gas.

### Results and Discussion

Temperature-dependent mobile carrier concentrations for all sample types are displayed in Fig. 1. Carrier concentrations ( $n$ ) are derived from the measured Hall constant ( $R_H$ ) according to the relationship,  $n = r_H/(qR_H)$ , where the Hall scattering factor ( $r_H$ ) is assumed to equal 1.0. The existence of inequivalent lattice sites requires that two donor levels be included in the fit of the carrier concentration profile to the charge neutrality equation.<sup>8</sup> These sites are referred to as hexagonal (h) and cubic (k) lattice sites,<sup>8</sup> and there are an equal number of each site in 4H-SiC. Ionization energies extracted from fitting the data are 42 meV (h) and 84 meV (k) for nitrogen, and 53 meV (h) and 93 meV (k) for phosphorus.

Ionization energies are presented only for the samples annealed at 1300°C for 10 min. Ionization energies derived from fits to the data obtained from the 1700°C annealed samples are affected by substantial hopping conduction in these samples, which is evident in the low-

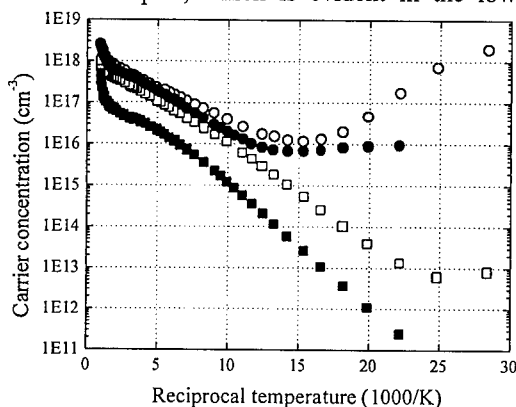


Figure 1. Carrier concentration as a function of reciprocal temperature for the element/anneal temperature combinations of (□) nitrogen/1300°C, (○) nitrogen/1700°C, (■) phosphorus/1300°C, and (●) phosphorus/1700°C.



temperature region of Fig. 1. The ionization energies measured from phosphorus-implanted 4H-SiC (4H-SiC:P) are, on average, 10 meV higher than those measured from nitrogen-implanted 4H-SiC (4H-SiC:N). The data in Fig. 1 suggests that nitrogen is more completely activated than phosphorus following 1300°C/10 min anneals. However, differences in activation are not responsible for the difference in ionization energies. Fully activated samples would have a carrier concentration of  $5.7 \times 10^{17} \text{ cm}^{-3}$ . Defining activation as  $n(\text{max})/5.7 \times 10^{17}$ , where  $n(\text{max})$  is the maximum carrier concentration observed in the epilayers, activation ratios following 1300°C annealing are 0.14 and 0.79, respectively, for 4H-SiC:P and 4H-SiC:N. Troffer, et al, observed activation ratios between 0.09 and 0.40 in phosphorus-implanted 6H-SiC (6H-SiC:P), corresponding to carrier concentrations of less than  $1.0 \times 10^{18}$ , and reported no effect of activation on ionization energies.<sup>4</sup> Moreover, the near equivalence of the room temperature carrier concentrations following 1700°C/10 min annealing of 4H-SiC:N and 4H-SiC:P indicates the nitrogen and phosphorus doses are similar in the present study. The conclusion about the difference in ionization levels seen here is that it is inherent to 4H-SiC and is not an artifact of the experimental conditions.

Electron mobility data as a function of temperature are plotted in Fig. 2. The peak mobility decreases with increasing annealing temperature for both 4H-SiC:N and 4H-SiC:P. For 4H-SiC:N annealed at 1300°C, the peak mobility is 800  $\text{cm}^2/\text{Vs}$  at 85 K, but drops to 680  $\text{cm}^2/\text{Vs}$  at 100 K after 1700°C annealing. Similarly for 4H-SiC:P, peak mobilities at 100 K of 1380  $\text{cm}^2/\text{Vs}$  and 1000  $\text{cm}^2/\text{Vs}$  are measured after 1300°C and 1700°C anneals, respectively. The mobility at room temperature is higher in 4H-SiC:P (414  $\text{cm}^2/\text{Vs}$  after 1300°C anneal) than in 4H-SiC:N (299  $\text{cm}^2/\text{Vs}$  after 1300°C anneal). This is attributed to there being fewer ionized charges in 4H-SiC:P that act as scattering centers. The decreasing electron mobility with increasing annealing temperature contradicts the observations of Troffer, et al, for 6H-SiC:P.<sup>4</sup> There are important differences between the two studies that account for the different

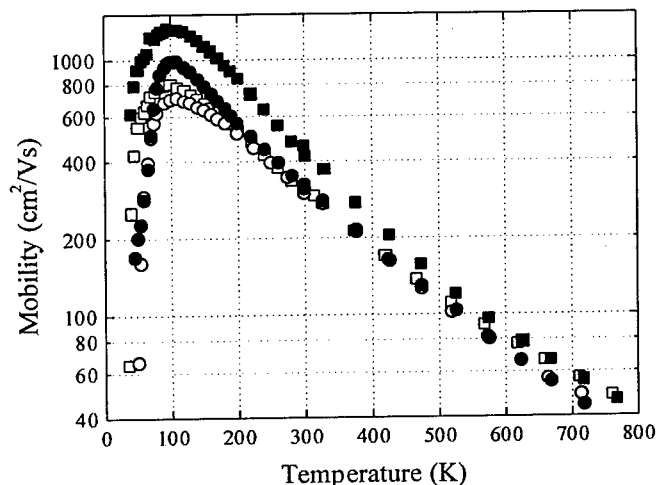


Figure 2. Mobility as a function of temperature for the element/anneal temperature combinations of (□) nitrogen/1300°C, (○) nitrogen/1700°C, (■) phosphorus/1300°C, and (●) phosphorus/1700°C.

observations. Troffer, et al, performed phosphorus implantations at room temperature and at higher doses than in the current study, leading to more residual lattice damage after implantation. The disappearance of defect lines in their photoluminescence data was attributed to the elimination of charged defects generated by implantation. Our 600°C implantation conditions are less severe, and less residual damage is expected. Consequently, the dependence of low-temperature mobility on annealing temperature observed here is believed to truly represent the behavior of bulk carrier transport with annealing temperature. The higher mobility of 4H-SiC:P does not offset the lower carrier concentration in this material, so resistivity values of 4H-SiC:P are greater than the resistivity of 4H-SiC:N following anneals at either 1300°C or 1700°C. For example, the room temperature resistivities of 4H-SiC:P and 4H-SiC:N following 1300°C annealing are 0.37  $\Omega\text{cm}$  and 0.09  $\Omega\text{cm}$ , respectively. Therefore, for the doses considered here, nitrogen appears to be the better choice for implantation into 4H-SiC.

#### Acknowledgements

The authors would like to acknowledge the assistance of R. Perrin, G. Landis, S. Davidson and R. Bertke, Air Force Research Laboratory. This work was supported by the Air Force Research Laboratory/Materials and Manufacturing Directorate and the Office of Naval Research under MURI grant N00014-95-1-1302.

#### References

1. T. Kimoto, A. Itoh, H. Matsunami, T. Nakata, and M. Watanabe, *J. Electronic Mater.*, **24** (1995), p. 235.
2. T. Kimoto, N. Inoue, and M. Watanabe, *phys. stat. sol.* **162**, (1997), p. 263.
3. W. Gotz, A. Schoner, G. Pensl, W. Suttrop, W.J. Choyke, R. Stein, and S. Leibenzeder, *J. Appl. Phys.* **73**, (1993), p. 3332.
4. T. Troffer, C. Peppermuller, G. Pensl, K. Rottner, and A. Schoner, *J. Appl. Phys.* **80**, (1996), p. 3739.
5. M.A. Capano, R. Santhakumar, R. Venugopal, M.R. Melloch, and J.A. Cooper, Jr., *J. Electronic Mater.*, (in press).
6. J. Gardner, A. Edwards, M.V. Rao, N. Papanicolaou, G. Kelner, O.W. Holland, M.A. Capano, M. Ghezzi, and J. Kretchmer, *J. Appl. Phys.* **83**, (1998), p. 5118.
7. V. Khemka, R. Patel, N. Ramungul, T.P. Chow, M. Ghezzi, and J. Kretchmer, *J. Electronic Mater.* **28**, (1999), p. 167.
8. W. Suttrop, G. Pensl, W.J. Choyke, R. Stein, and S. Leibenzeder, *J. Appl. Phys.* **72**, (1992), p. 3708.

## MicroRaman and Hall Effect Study of n-Type Bulk 4H-SiC

M. Chafai<sup>1,2</sup>, J. Jiménez<sup>1</sup>, E. Martín<sup>1</sup>, W.C. Mitchel<sup>3</sup>, A. Saxler<sup>3</sup> and R. Perrin<sup>3</sup>

<sup>1</sup>Física de la Materia Condensada, ETSII, ES-47011 Valladolid, Spain

<sup>2</sup>Departement de Physique, Faculté des Sciences, LETI, Mekness, 50003, Morocco

<sup>3</sup>Materials Directorate, Air Force Research Laboratory/MLPO, 3005 P Street, Suite 6,  
Wright-Patterson AFB, OH 45433-7707, USA

**Keywords:** 4H Polytype, Hall, Phonons, Plasmon, Raman, Temperature Phonon Shift

**Abstract.** N-type 4H-SiC crystals are studied by Hall effect and Raman spectroscopy. The transport parameters,  $n$  and  $\mu$ , obtained by both procedures are compared for a series of samples with different nitrogen concentrations. A good agreement between both is obtained. A Raman study in the temperature range between 300 and 650 K is also carried out, the temperature dependence of phonon parameters and plasmons is reported, and the results are compared with high temperature Hall effect measurements.

### Introduction

SiC has generated great interest for high temperature electronics. The excellent electric and thermal properties of SiC permit devices to operate at temperatures as high as 400°C. It is important to obtain information about the transport properties at high temperature. Transport measurements are usually done by means of the Hall effect [1], which requires electrical contacts and only provides average values of the transport properties over large areas. However, bulk SiC presents marked inhomogeneities that can affect the doping concentration and the thermal properties. In this context small size probes are very promising for a complete characterization of SiC in the temperature range at which these devices usually operate. MicroRaman spectroscopy is a promising technique for these purposes, since it is contactless, has a micrometer probe size and gives a variety of information, such as the transport parameters, thermal properties and stress with minimal sample preparation [2-4].

We present herein a Raman study of doping and mobility in bulk n-type 4H-SiC in the temperature range between RT (Room Temperature) and 625 K. The results are compared with those obtained in the same samples by Hall effect. A good agreement is obtained, showing the great expectations of microRaman spectroscopy for studying the local transport parameters in SiC and the characteristics of SiC-based devices under operation.

### Experimental and samples

Bulk n-type 4H-SiC crystals from different suppliers grown by the physical vapor transport (PVT) technique with different nitrogen concentrations were studied. The samples were cut with their  $c$  axis perpendicular to the surface.

Temperature dependent Hall effect measurements were done using the Van der Pauw method with Ni-Au contacts. Hall data were measured up to 750K (for more details see ref. 5).

Raman measurements were done with a DIOR XY Raman spectrometer attached to a metallographic microscope. The excitation was performed with an Ar<sup>+</sup> (514.5 nm line). Both the excitation and the scattered

light were collected through a long distance work microscope objective with a large numerical aperture, allowing a spatial resolution in the micrometer range. The Raman signal was detected with a liquid nitrogen cooled CCD that provided an excellent signal to noise ratio and short acquisition time. The samples were mounted on a miniature furnace adapted to the X-Y stage of the microscope. Temperatures up to 625 K were reached with an accuracy better than 0.1 K.

### Results and discussion

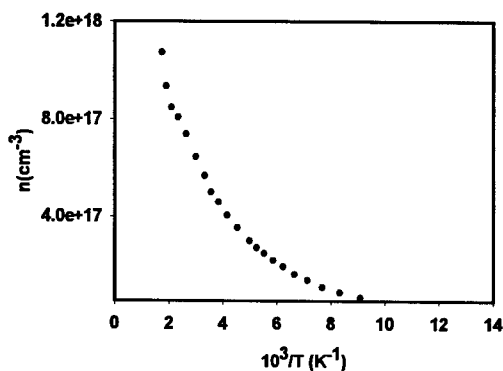


Fig.1.  $n_H$  vs.  $10^3/T$  (sample N0066-A)

Nitrogen is the main donor impurity in SiC. In the 4H-SiC polytype, it can replace C in the two inequivalent lattice sites (cubic like, k, and hexagonal like, h) giving shallow donor levels with activation energies of  $\sim 45$  meV for the hexagonal like site and  $\sim 100$  meV for the cubic like site [1]. Van der Pauw experiments were carried out in samples with different nitrogen concentrations. A typical  $n$  vs  $10^3/T$  plot is shown in Fig.1. These data were fitted to the neutrality equation to obtain the corresponding activation energies. The fit was optimal for two donor levels, and the activation energies were in good agreement with those reported for the two nitrogen related donor levels. The Hall data have a systematic error arising from the Hall scattering factor, for which the temperature dependence is unknown, then it was assumed to be temperature independent.

The Raman spectrum of 4H-SiC obtained in the spatial configuration of our measurements is characterized by three main peaks with symmetry  $A_1$ ,  $E_1$  and  $E_2$ . The planar  $E_2$  mode is observed at  $777\text{ cm}^{-1}$ , the  $E_1$  transverse optic (TO) mode at  $797\text{ cm}^{-1}$  and the  $A_1$  longitudinal optic mode (LO) at  $965\text{ cm}^{-1}$ . The Raman spectrum in doped materials is characterized by phonon-plasmon coupling, which in the case of phonon damping results in a deformation of the LO mode. The lineshape of this coupled mode was described by Irmer et al. [6], according to whom the Raman intensity is given by the following expression:

$$I(\omega) = SA(\omega) \text{Im} \left( -\frac{1}{\epsilon(\omega)} \right) \quad (1)$$

where  $\epsilon(\omega)$  is the dielectric function for the Brillouin zone center.

$$A(\omega) = 1 + 2C\omega_T^2 \frac{[\omega_p^2 \gamma(\omega_T^2 - \omega^2) - \omega^2 \Gamma(\omega^2 - \gamma^2 - \omega_p^2)]}{\Delta} + \left( \frac{C^2 \omega_T^4}{\Delta} \right) \frac{\omega_p^2 [\gamma(\omega_L^2 - \omega_T^2) + \Gamma(\omega_p^2 - 2\omega^2) + \omega^2 \Gamma(\omega^2 + \gamma^2)]}{(\omega_L^2 - \omega_T^2)} \quad (2)$$

with

$$\Delta = \omega_p^2 \gamma [(\omega_T^2 - \omega^2)^2 + \omega^2 \Gamma^2] + \omega^2 \Gamma (\omega_L^2 - \omega_T^2) (\omega^2 + \gamma^2) \quad (3)$$

( $\omega_L$  and  $\omega_T$  are the frequencies of the longitudinal and transverse optic phonons,  $\Gamma$  the linewidth of the LO phonon and  $C$  is the Faust-Henry coefficient). The plasma frequency,  $\omega_p$ , and the plasmon damping constant,

$\gamma$ , are fitting parameters and allow the calculation of the electron concentration and the mobility according to the following expressions:

$$\omega_p^2 = 4\pi n e^2 / \epsilon_\infty m^* \quad (4)$$

$$\gamma = e / \mu m^* \quad (5)$$

The transport parameters were obtained at room temperature by Hall and Raman (Table I). Note the good agreement between the two data sets, in agreement with previous reports [7].

Sample	$n_{\text{Hall}} (\text{cm}^{-3})$	$\mu_{\text{Hall}} (\text{cm}^2/\text{V.s})$	$\omega_p (\text{cm}^{-1})$	$\gamma_p (\text{cm}^{-1})$	$n_R (\text{cm}^{-3})$	$\mu_R (\text{cm}^2/\text{V.s})$
N0066-A	$5.43 \times 10^{17}$	219.45	159.31	155.94	$5.48 \times 10^{17}$	221.24
N0022-8	$5.44 \times 10^{17}$	254.18	161.61	188.95	$5.63 \times 10^{17}$	182.6
H0373	$4.27 \times 10^{18}$	73.3	356.34	529.7	$2.64 \times 10^{18}$	65
D6015-5	$2 \times 10^{19}$		-----	-----	-----	-----

Table I. Transport parameters at room temperature obtained from Hall and Raman data. The heavily doped sample (D6015-5) did not allow reliable Raman fitting. ( $C=0.35$ ,  $m^*=0.27 m_0$ ,  $\epsilon_\infty=6.8$ )

Also the transport parameters were obtained by Raman spectroscopy in the temperature range between 300 and 650 K. First, the temperature dependences of the frequencies and linewidths of the phonon modes,  $\omega_L$  and  $\Gamma_L$ , and  $\omega_T$  and  $\Gamma_T$ , were obtained in semiinsulating 4H-SiC in order to input those data into equation 1. The temperature dependence of both frequency and linewidth was fitted to a second order polynomial, indicating the contribution to the anharmonicity of three and four phonon processes ( $\omega_L = 966.9 - 1.8 \times 10^{-2} T - 1.48 \times 10^{-5} T^2$ ,  $\omega_T = 778.6 - 8.8 \times 10^{-3} T - 1.16 \times 10^{-5} T^2$ ,  $\Gamma_L = 4.25 - 1.6 \times 10^{-4} T + 7.9 \times 10^{-6} T^2$ ). These data were used for fitting the coupled phonon-plasmon modes of the doped samples to Eq.1. Fig 3 shows the Raman spectra of a doped sample at three different temperatures. The planar mode  $E_2$  shifts to lower frequency for increasing temperature. The temperature dependence of the peak frequency of the coupled phonon-plasmon mode is determined by a combination of two effects, a shift to lower frequency due to the temperature increase and a shift to higher frequency due to the increase of  $n$  with increasing temperature.

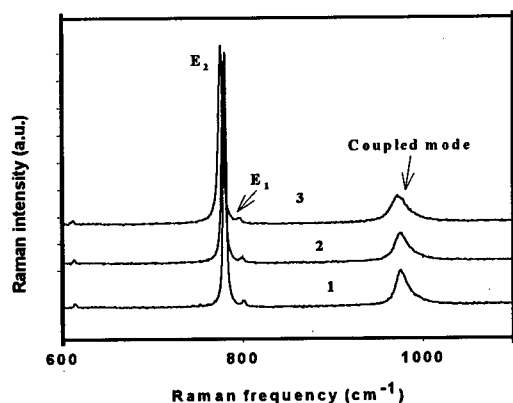


Fig.3. Raman spectra of n-type 4H-SiC for different temperatures (1)  $T=303\text{K}$ , 2)  $493\text{K}$  and 3)  $513\text{K}$ )

As was the case for the Hall scattering factor the temperature dependence of the static dielectric constant,  $\epsilon_\infty$ , and the effective mass,  $m^*$ , were unknown. An error is introduced into calculated values of  $n$  and  $\mu$  if one

assumes constant values for  $\epsilon_\infty$  and  $m^*$ . In order to reduce this error, empirical expressions for the temperature dependence of  $\epsilon_\infty$  and  $m^*$  were deduced using the Hall data of sample N0066-A as a reference. The Hall carrier concentration and mobilities were substituted into equations 4 and 5 together with the values  $\omega_p$  and  $\gamma$  deduced from the Raman fitting to obtain empirical results for  $\epsilon_\infty$  and  $m^*$  vs  $T$ . While the variation of  $\epsilon_\infty$  was small, a significant variation was observed for  $m^*$  at temperatures above 500K. These empirical values were used to calculate  $n$  and  $\mu$  in the other samples.

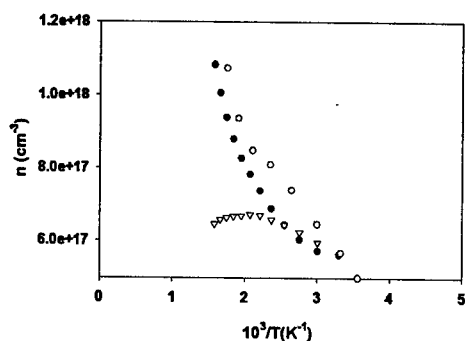


Fig.4. Electron concentration vs  $10^3/T$  calculated by Raman (dark circles) and Hall (empty circles). Triangles correspond to Raman data without taking into account the temperature dependence of  $m^*$  and  $\epsilon_\infty$  (sample N0022-8).

The results obtained were compared with Hall data, giving a good agreement. The electron concentrations calculated between 300 and 650 K by Hall and Raman, respectively, are shown in Fig. 4. The values obtained by Raman without the correction of the temperature dependence of  $\epsilon_\infty$  and  $m^*$  are also plotted, showing the important error introduced when neglecting such temperature dependence. This correction was not considered in a previous paper by Harima et al. (8), where no direct comparison between Hall and Raman data was reported.

Once the temperature dependence of  $\epsilon_\infty$  and  $m^*$  was considered the agreement between Hall and Raman transport parameters was fair, showing that Raman can be successfully used for studying transport properties in doped SiC.

## Conclusion

A reasonable agreement between Hall and Raman transport measurements was obtained. Raman spectroscopy appears to be a powerful technique for studying the transport properties of SiC at high temperature, though the knowledge of the temperature dependence of  $m^*$  and  $\epsilon_\infty$  is needed. The variety of information obtained by Raman spectroscopy and the high resolution of the microRaman probe warrant the possibility of a local study of SiC based devices under operation.

**Acknowledgements.** The Spanish group was funded by the Spanish Government (CICYT. MAT97-0686)

## References

- [1] W. Götz, A. Schöner, G. Pensl, W. Suttrop, W.J. Choyke, R. Stein, S. Leinbenzeder; J. Appl. Phys. 73 (1993) p. 3332
- [2] S. Nakashima, H. Harima; Phys. Stat. Sol. (a) 162 (1997) p. 39
- [3] E. Martín, J. Jiménez, M. Chafai; Sol. St. Electron. 42 (1998) p. 2309
- [4] J.C. Burton, L. Sun, M. Pophristic, S.J. Lukacs, Z.C. Feng, I.T. Ferguson; J. Appl. Phys. 84 (1998) p. 6268
- [5] W. C. Mitchel, R. Perrin, J. Goldstein, A. Saxler, M. Roth, S. R. Smith, J. S. Solomon, A. O. Evwaraye, aJ. Appl. Phys. 86 (1999) (in the press)
- [6] G. Irmer, V.V. Toporov, B.H. Bairamov, J. Monecke; Phys. Stat. Sol. (a) 119 (1983) p. 595
- [7] H. Harima, S. Nakashima, T. Uemura; J. Appl. Phys. 78 (1995) p. 1996
- [8] H. Harima, T. Hosoda, S. Nakashima; Mater. Sci. Forum 264-268 (1998) p. 449

## Electrical Properties of 3C-SiC Grown on Si by CVD Method using $\text{Si}_2(\text{CH}_3)_6$

Y. Masuda<sup>1</sup>, Y. Chen<sup>1</sup>, H. Matsuura<sup>2</sup>, H. Harima<sup>3</sup> and S. Nishino<sup>1</sup>

<sup>1</sup>Dept of Electronics & Information Science, Kyoto Institute of Technology,  
Matsugasaki, Sakyo-Ku, Kyoto 606-8585, Japan

<sup>2</sup>Dept. of Electronics, Osaka Electro-Communication University,  
Neyagawa, Osaka, 572-8530, Japan

<sup>3</sup>Dept. of Applied Physics, Osaka University, Yamadagaoka 2-1, Suita, Osaka 565-0871, Japan

**Keywords:** 3C-SiC, Carrier Concentration, Coupled Mode, Hall Effect, Hall Mobility, LO Phonon, Plasmon, Raman Scattering,  $\text{Si}_2(\text{CH}_3)_6$  (Hexamethyldisilane)

### Abstract

3C-SiC epitaxial layers were grown on Si substrates using  $\text{Si}_2(\text{CH}_3)_6$  as Si and C source material in place of  $\text{SiH}_4+\text{C}_3\text{H}_8$  system. Electrical properties of 3C-SiC layers were investigated by Hall-effect measurements at temperatures between 85K and 500K. Room temperature, carrier concentration decreased, and the mobility increased as the SiC film thickness increased. The ionization energies of several kinds of donors obtained from the temperature dependence of carrier concentration are 7-14meV, 46-54meV, 97-120meV. Electrical properties obtained from LO-phonon-plasmon-coupled modes of Raman spectra were compared with results obtained by Hall measurements. From Raman spectra, it was determined that tensile stress still exists in the SiC film to a thickness of at least 32  $\mu\text{m}$ .

### Introduction

Silicon carbide (SiC) is an excellent semiconductor for high power and high temperature electronic devices due to its superior material properties. 3C-SiC has been widely grown on Si substrates by chemical vapor deposition (CVD) using  $\text{SiH}_4+\text{C}_3\text{H}_8+\text{H}_2$  system. However, from the view point of safety, it is desirable to grow epilayers using other Si source materials, because  $\text{SiH}_4$  is very flammable. 3C-SiC films were grown using HMDS (hexamethyldisilane:  $\text{Si}_2(\text{CH}_3)_6$ ) as Si and C source material, and the electrical properties of the epilayers were investigated. In this work, temperature dependencies of carrier concentration and Hall mobility of the 3C-SiC epilayers are reported. Electrical properties obtained from LO-phonon-plasmon-coupled modes of Raman spectra were compared to those obtained by Hall measurements.

### Experimental

Non-doped single crystalline 3C-SiC films were heteroepitaxially grown on Si (100) substrates by atmospheric pressure CVD using HMDS+ $\text{H}_2$  gas system. HMDS was transferred to the reaction tube by bubbling  $\text{H}_2$  through the liquid HMDS in a cylinder. The Si substrate was put on a SiC-coated graphite susceptor in the reaction tube, and then heated by an rf generator at a frequency of 400kHz. The temperature of the substrate was measured by a pyrometer. Prior to the growth, the surface of the Si substrate was etched by HCl (10% in  $\text{H}_2$ ) at 1175°C, and was carbonized by  $\text{C}_3\text{H}_8$  (5% in  $\text{H}_2$ ) at 1350°C. Thereafter, HMDS was introduced into the reaction tube, and 3C-SiC was grown on the carbonized Si substrate at 1350°C. The growth rate was about 4.3  $\mu\text{m}/\text{h}$  and thicknesses of the epilayers were between 7 and 32  $\mu\text{m}$ . Carrier concentration and mobility of the epilayers were measured by the van der Pauw method at temperatures between 85 and 500K. The epilayers were cut into pieces of 5×5mm<sup>2</sup>. Before the measurements, Si substrates were removed by chemical etching. Ohmic contacts of about 0.5mm diameter were made on self-standing SiC films by depositing Al metal, on the four corners of the sample. A magnetic field of 5kG was used for all the measurement temperatures. Raman scattering spectra were measured at room temperature

using the Ar<sup>+</sup> laser line at 488nm. The TO-and LO-phonon bands were observed in the backscattering geometry. The scattered light was collected by a camera lens onto a slit of a double monochromator, which had a focal length of 0.85m. The spectra were observed with a cooled charge-coupled-device (CCD) detector.

### Results

The SiC epilayers grown with HMDS are single crystals of 3C-SiC, and the (100) plane of SiC is parallel to the substrate surface, which was confirmed by reflection high-energy electron diffraction (RHEED) analysis.

All the undoped epilayers showed n-type conduction, and were light yellow transparent films. Carrier concentration,  $n$ , was  $1.3\text{--}6 \times 10^{17} \text{ cm}^{-3}$ , and the mobility,  $\mu_H$ , was 200–450  $\text{cm}^2/\text{Vs}$  at room temperature. Carrier concentration decreased, and the mobility increased as the SiC film thickness increased. The surface morphology of grown layers with various thicknesses was observed by use of an atomic force microscope (AFM). Wedge shapes perpendicularly intersecting each other were observed in all the epilayers. However, these wedge shapes became broader as the SiC film thickness increased. This indicates that antiphase domains (APDs) became broader and concentration of antiphase boundaries (APBs) was reduced as the SiC film thickness increased. Therefore, we think that the improvement of electrical properties was caused by decrease of defects such as APDs and APBs. Figures 1 and 2 show temperature dependencies of carrier concentration and the mobility, respectively. The carrier concentration decreases monotonically with decreasing temperature, and the mobility varies as  $\mu_H \sim T^{-1.5}$  above room temperature. This is believed to be due to the fact that in 3C-SiC, acoustic phonon scattering dominates the scattering processes in this temperature range. To estimate the concentration and energy levels of the several kinds of donors from the temperature dependence of carrier concentration, the data was evaluated using the function  $H(T, E_{\text{ref}})$  of the product of  $n(T)$  and  $1/kT$ . In this analysis, the function  $H(T, E_{\text{ref}})$  is given by

$$H(T, E_{\text{ref}}) \equiv \frac{n(T)^2}{(kT)^{2.5}} \exp\left(\frac{E_{\text{ref}}}{kT}\right)$$

where  $T$  is temperature,  $k$  is the Boltzmann's constant and  $E_{\text{ref}}$  is a parameter.  $H(T, E_{\text{ref}})$  has peaks corresponding to each dopant level. From each peak value and peak temperature, the concentration and energy level of the corresponding dopant can be accurately determined[1]. Various energy

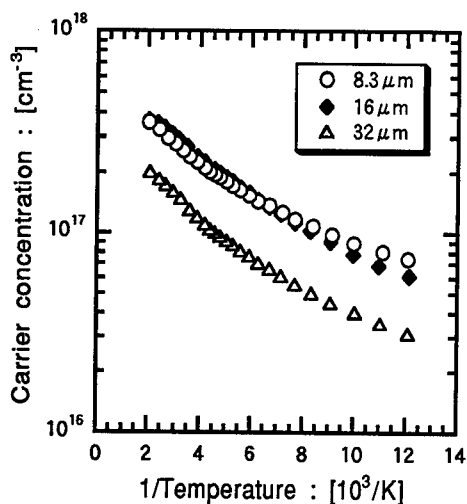


Fig.1 Temperature dependencies of the carrier concentrations of 3C-SiC epilayers

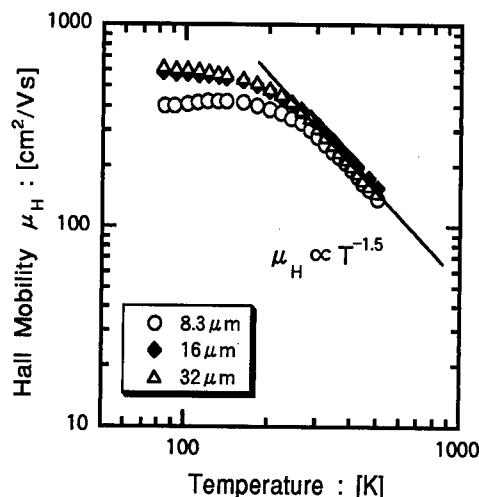


Fig.2 Temperature dependencies of the Hall mobilities of 3C-SiC epilayers

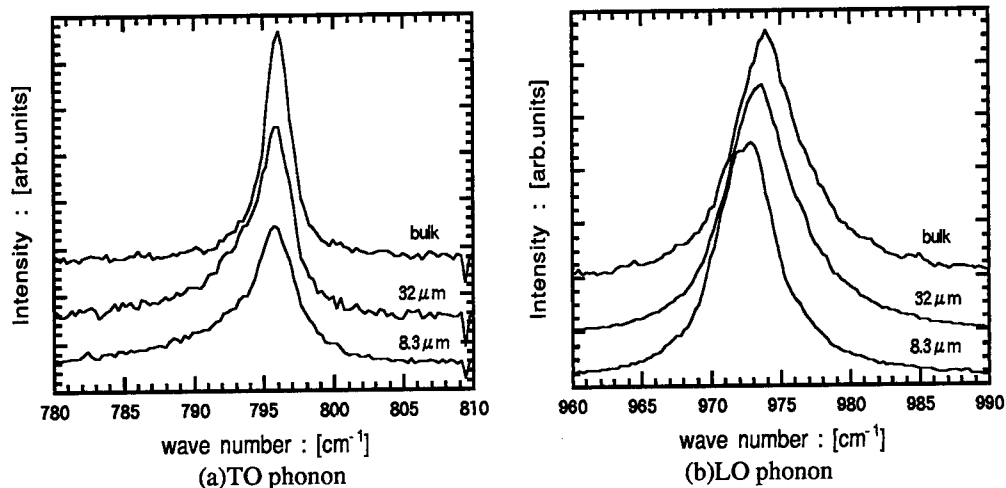


**Table 1:** Donor ionization energies  $E_{Di}$ , donor concentrations  $N_{Di}$ , and acceptor concentrations  $N_A$  obtained from the calculations fitted to the experimental data.

	8.3 $\mu$ m	16 $\mu$ m	32 $\mu$ m
ED1 (meV)	10	7	14
ND1 (cm <sup>-3</sup> )	$1.1 \times 10^{17}$	$8.1 \times 10^{16}$	$4.7 \times 10^{16}$
ED2 (meV)	46	46	54
ND2 (cm <sup>-3</sup> )	$1.7 \times 10^{17}$	$2.0 \times 10^{17}$	$8.1 \times 10^{16}$
ED3 (meV)	107	97	120
ND3 (cm <sup>-3</sup> )	$1.1 \times 10^{17}$	$1.3 \times 10^{17}$	$1.0 \times 10^{17}$
ED4 (meV)	157	-	-
ND4 (cm <sup>-3</sup> )	$4.6 \times 10^{16}$	-	-
$N_A$ (cm <sup>-3</sup> )	$1.3 \times 10^{16}$	$9.9 \times 10^{15}$	$5.7 \times 10^{15}$

levels of donors in undoped epilayers were obtained. Film thickness data and the corresponding energy levels obtained from this method, are given in table 1. The ionization energies of the donor level, ED1, (7-14meV) were close to the values reported for either ionization energy of N or defects (13-22meV)[2][3][4]. The ionization energy ED2 (46-54meV) agrees with the ionization energy (53-54meV) of N donor reported from photoluminescence measurements[5]. The ionization energies ED3 (97-120meV) were close to the values reported for ionization energy of either N or P (95-118meV)[6][7]. A value of 157meV for an unknown donor in 8.3  $\mu$ m epilayer was also obtained. However donor ionization energy levels of this range were also observed in other epilayers. But their concentration could not be calculated. The donor concentrations ND1, ND2 decrease as the SiC film thickness increases, while ND3 does not vary as much.

Raman scattering from LO-phonon-plasmon-coupled modes has been extensively studied in III-V semiconductors[8]. From the analysis of the frequency and band shapes of the coupled modes,

**Fig.3** The film thickness dependent Raman spectra of (a) TO and (b) LO phonons

carrier concentration and the drift mobility have been determined[9]. The carrier concentration and drift mobility obtained from LO-phonon-plasmon-coupled modes of Raman spectra were compared with results obtained by Hall measurements in 3C-SiC. Figure 3 shows the Raman spectra of the TO and LO phonon modes obtained from the samples used for Hall measurements and from a stress-free bulk 3C-SiC, respectively. From this data, carrier concentrations were estimated. However, the results from the LO mode of the Raman spectra did not agree with those obtained from Hall measurements. It is well known that stresses cause a shift in the Raman peaks, but the stress and strain are not considered in the fit to the theoretical curve to obtain carrier concentration[9]. From Fig. 3, the TO and LO phonon peaks are shifted to higher frequencies, and the difference between the two decreases as the SiC film thickness increases.

This indicates that the tensile stress in films decreases gradually. The stresses and strains still remain in the SiC film to at least  $32\mu\text{m}$ . The stresses were estimated from the shift in the TO and LO phonon peak of the epilayers as compared to a stress-free bulk 3C-SiC ( $n=3\times 10^{17}\text{cm}^{-3}$ )[10]. Figure 4 shows the stresses of 3C-SiC/Si epilayers and 3C-SiC free films. The stresses were tensile in all the samples, and decreased as the SiC film thickness increased. From Fig. 4, it could be deduced that the films would be free of tensile stress at  $45\mu\text{m}$ .

The C/Si ratio-dependence of the electrical property was studied by adding  $\text{C}_3\text{H}_8$  as C source for the growth of epilayer. However single crystals of 3C-SiC could not be obtained at the moment. Further investigations are under way.

### Conclusion

Single crystals of 3C-SiC on Si (100) plane were reproducibly obtained using HMDS+ $\text{H}_2$  reaction gas system at  $1350^\circ\text{C}$ . The electrical properties of the epilayers were as follows: the carrier concentration was  $1.3\text{--}6\times 10^{17}\text{cm}^{-3}$ , and the electron mobility  $\mu_{\text{H}}$  was  $200\text{--}450\text{cm}^2/\text{Vs}$  at room temperature. Calculated values of donor levels and concentrations were obtained from the temperature dependence of carrier concentration. At least 3 levels of donors, with ionization energies of  $7\text{--}14\text{meV}$ ,  $46\text{--}54\text{meV}$ ,  $97\text{--}120\text{meV}$  exist in all the epilayers. From Raman scattering, it was deduced that tensile stress existed to thicknesses of  $32\mu\text{m}$ .

### References

- [1] H.Matsuura, T.Kimoto, and H.Matsunami, *Jpn.J.Appl.Phys.* **38** (1999) p. 4013
- [2] B.Segall, S.A.Alterovitz, E.J.Haugland, and L.G.Matus, *Appl.Phys.Lett.* **49** (1986) p. 584
- [3] M.Yamanaka, H.Daimon, E.Sakuma, S.Misawa, and S.Yoshida, *J.Appl.Phys.* **61** (1987) p. 599
- [4] A.Suzuki, A.Uemoto, M.Shigeta, K.Furukawa, and S.Nakajima, *Appl.Phys.Lett.* **49** (1986) p. 450
- [5] P.J.Dean, W.J.Choyke, and L.Patrick J. Lumin. **15** (1977) p. 299
- [6] W.J.Choyke, L.Patrick, *Phys.Rev.B.* **2** (1970) p. 4959
- [7] S.A.Podlasov, V.G.Sidyakin, *Sov.Phys.-Semicond.* **20** (1986) p. 462
- [8] M.V.Klein, in *Light Scattering in Solids*, edited by M.Cardona, (Springer, Berlin, 1975) p. 147
- [9] H.Yugami, S.Nakashima, and A.Mitsuishi, *J.Appl.Phys.* **61** (1987) p. 354
- [10] Z.C.Feng, W.J.Choyke, J.A.Powell, *J.Appl.Phys.* **64** (1988) p. 6827

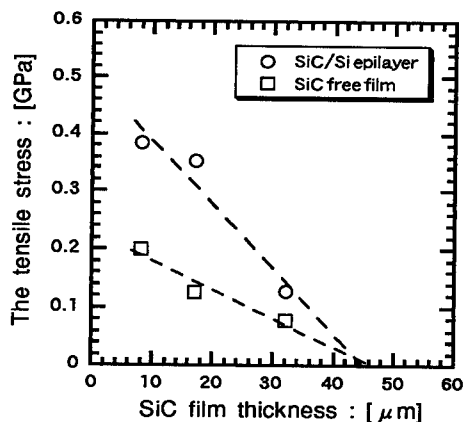


Fig.4 Film thickness dependence of the tensile stress using Raman peak positions

## Electrical and Physical Behavior of SiC Layers on Insulator (SiCOI)

E. Hugonnard-Bruyère<sup>1,5</sup>, F. Letertre<sup>2</sup>, L. Di Cioccio<sup>1</sup>, H.J. von Bardeleben<sup>3</sup>,  
J.L. Cantin<sup>3</sup>, T. Ouisse<sup>4</sup>, T. Billon<sup>1</sup> and G. Guillot<sup>5</sup>

<sup>1</sup> LETI-CEA Grenoble, 17 rue des Martyrs, FR-38054 Grenoble Cedex 9, France

<sup>2</sup> SOITEC SA, Parc Technologique des Fontaines, FR-38190 Bernin, France

<sup>3</sup> Groupe de Physique des Solides, Univ. Paris 6 & 7, UMR 75-88 au CNRS, FR-75251 Paris

<sup>4</sup> Laboratoire de Physique des Composants à Semiconducteurs (LPCS), UMR-CNRS 5531,  
ENSERG, 23 rue des Martyrs, BP 257, FR-38016 Grenoble Cedex 1, France

<sup>5</sup> Laboratoire de Physique de la Matière LPM, INSA de Lyon, Bât. 502, 20 avenue A. Einstein,  
FR-69621 Villeurbanne Cedex, France

**KW:** Deep Levels, EPR Spectroscopy, Hall Effect Measurement, SiC On Insulator, Smart-Cut

### Abstract :

4H- and 6H-SiC On Insulator structures (SiCOI) are successfully obtained using the Smart-Cut® process. As previously published [1,2], initial SiCOI samples exhibited an unacceptable high resistivity due to deep levels generated by implantation of large dose of protons required to induce thin film exfoliation. Hall effect measurements and EPR (Electron Paramagnetic Resonance) measurements were performed to determine the concentration and the microscopic structure of the compensating defects in layers obtained as the process conditions evolve. From the resistivity variation with temperature the activation energy of the compensating defect pinning the Fermi level is found to be 500 meV. The compensating defect content, as extracted by Hall effect measurement analysis, has been lowered down to a few  $10^{16} \text{ cm}^{-3}$  since the process reached maturity.

### Introduction :

The Smart-Cut process, developed by LETI and used by SOITEC to produce large volume high quality SOI wafers, is based on proton implantation and wafer bonding [3]. It has been also successfully applied to different materials such as SiC, GaAs and InP [4,5,6]. This technical approach, based on thin film separation from bulk wafer and transfer onto a low cost and large size substrate such as oxidized silicon, is of prime importance for the development of low cost structures for SiC devices processing.

Little is known about the nature of SiC defects induced by hydrogen implantation and their electrical activity. DLTS (Deep Level Transient Spectroscopy) measurements have shown that the  $Z_1/Z_2$  defect is the most common and most unavoidable defect introduced in bulk SiC samples, either by electron or heavier ions irradiation [1,7,8]. Moreover, only one EPR study of ion implantation induced defects has been published on this subject [9].

This study presents the results of electrical (C(V) and Hall effect) and EPR studies of the compensating defects in n-type SiCOI Smart-Cut processed layers.

### Experimental procedure :

N-type nitrogen doped 6H-SiC epitaxial layers (of initial doping in the  $1 \times 10^{17}$ -  $1 \times 10^{19} \text{ cm}^{-3}$  range) grown on 6H-SiC bulk substrates were transferred by the Smart-Cut process onto oxidized silicon wafer to produce SiCOI structures. In this study, the SiCOI structure has a thin SiC layer of typical thickness of 500-600 nm and a buried oxide layer of 1  $\mu\text{m}$ . This structure corresponds to process conditions detailed elsewhere [4].

EPR measurements were performed with an X-band spectrometer in the 4-77 K range. Absolute spin concentrations were determined with a calibrated Ruby standard sample. Hall effect measurements were carried out in the 40 K - 420 K range. The Van der Paw test patterns were realized with a mesa structure taking advantage of the SOI like structure.

### Experimental :

After splitting at the temperature of 900°C, C(V) measurements exhibit a compensation level higher than  $1 \times 10^{19} \text{ cm}^{-3}$  [1]. A higher annealing temperature is necessary for the partial recovery of the electrical activity by annealing the hydrogen implantation introduced defects. After a 1300°C annealing step, SiC films with a N doping concentration above  $1 \times 10^{18} \text{ cm}^{-3}$  exhibit an electrical activity measured by C(V).

These samples were analysed by Hall effect measurements. Good fits of the neutrality equation with the experimental Hall data are achieved for a compensation level  $N_A$  in the range of  $1 \times 10^{18} \text{ cm}^{-3}$ . Figure 1 shows the Hall effect results obtained for an SiC film with an initial doping level of  $3 \times 10^{18} \text{ cm}^{-3}$ . Experimental data are compared with theoretical curves simulated for different levels of compensation. The best fit is obtained for a compensation equal to 31.3% of the starting doping level i.e.  $9.4 \times 10^{17} \text{ cm}^{-3}$ .

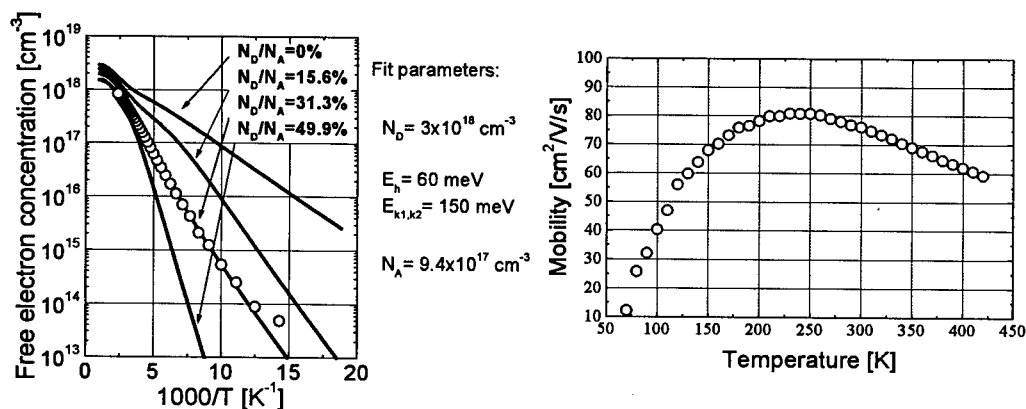


Fig. 1: Free electron concentration (left) and mobility (right) of SiCOI layer with initial doping level of  $3 \times 10^{18} \text{ cm}^{-3}$  after 1300°C annealing where  $E_h$  and  $E_{k1,k2}$  are respectively the hexagonal and cubic levels

The value of  $N_A$  includes compensating centres introduced by the Smart-Cut® process itself plus acceptors introduced during the epitaxial process. The last term can be neglected since a well controlled epitaxial process induces less than  $1 \times 10^{15} \text{ cm}^{-3}$  compensating centres. In this study, a good fit is obtained using hexagonal and cubic levels at respectively 60 meV and 150 meV below the conduction band. The hexagonal level value is slightly different from 92 meV, commonly accepted for low doped epitaxial layers in 6H-SiC [10]. Indeed, this level is known to decrease with dopant concentration [11] and compensation defects content due to the influence of a random field on the activation energy [12]. On the other hand, the cubic level is too deep in the band gap to be affected. Besides carrier concentration reduction, carrier mobility also suffers from interaction with compensating centres (fig. 1, right part). In this case, the initial 300 K mobility of  $130 \text{ cm}^2 \cdot \text{V}^{-1} \cdot \text{s}^{-1}$ , consistent with a  $3 \times 10^{18} \text{ cm}^{-3}$  doping level, in 6H SiC, is decreased to  $75 \text{ cm}^2 \cdot \text{V}^{-1} \cdot \text{s}^{-1}$  after SiCOI process.

These samples were also analysed by EPR spectroscopy. The EPR spectrum of the neutral N donor is observed at thermal equilibrium conditions at 4K (fig. 2) only for initial nitrogen doping levels higher than  $1 \times 10^{18} \text{ cm}^{-3}$ . The EPR spectra of the 6H-SiC sample with an initial doping level of  $3 \times 10^{18} \text{ cm}^{-3}$  after the Smart-Cut process® confirm the electrical results (fig. 2): after 1300°C annealing, only the EPR spectra of nitrogen donors at the quasi-cubic sites are observed. This demonstrates a remaining compensation equal or higher than the nitrogen concentration on the hexagonal sites, i.e. typically one third of the total donor concentration (approximately  $1 \times 10^{18} \text{ cm}^{-3}$ ).

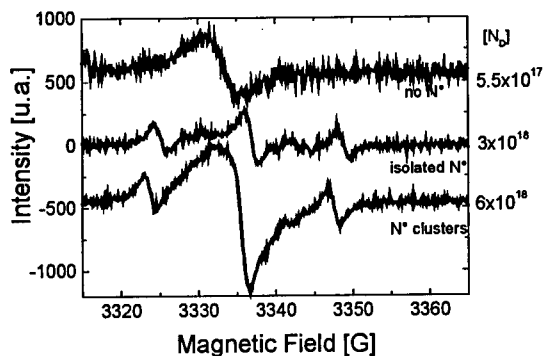


Fig. 2 : EPR spectra of the N donors in 1300°C annealed 6H-SiC SiCOI layers with  $[N_D]=5 \times 10^{17}$ ,  $3 \times 10^{18}$  and  $6 \times 10^{18} \text{ cm}^{-3}$ ;  $T=4\text{K}$ ,  $B//c$ .

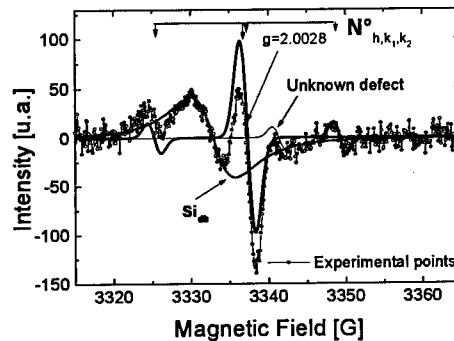


Fig. 3 : EPR spectrum of a 6H-SiC SiCOI layer with an initial doping concentration of  $5.5 \times 10^{17} \text{ cm}^{-3}$  after the Smart-Cut® process;  $T=4\text{K}$ ,  $B// [11 \bar{2} 0]$

The evolution of the implantation induced defects with the annealing temperature has already been reported in a previous study [2]: after splitting, the main paramagnetic defects are carbon dangling bonds centres in the  $10^{18} \text{ cm}^{-3}$  concentration range; as the annealing temperature is increased from 900°C to 1100°C these defects decrease in intensity and a di-vacancy centre is observed. Finally, after 1300°C, one defect is remaining, which may be responsible for the carrier compensation; it is not clearly identified but its EPR parameters suggest that it could be related to silicon clusters present in the SiC film.

Under these process conditions which leave  $1 \times 10^{18} \text{ cm}^{-3}$  compensating defects, SiCOI films with an initial doping level of  $1 \times 10^{17} \text{ cm}^{-3}$  are electrically insulating at 300 K with a resistivity of  $5 \cdot 10^6 \Omega \cdot \text{cm}$  (obtained by extrapolation of high temperature resistivity measurements). The Arrhenius plot gives a thermal activation energy of 500 meV (fig. 4). This result is in good agreement with previous DLTS measurements, which have shown, in 1300°C annealed hydrogen implanted SiC material, a main defect  $Z_1/Z_2$  located at  $E_c - 0.65 \text{ eV}$  [1].

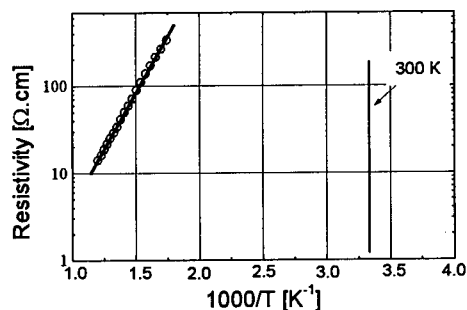


Fig. 4 : Resistivity of SiCOI layer after 1300°C annealing with initial doping level of  $1 \cdot 10^{17} \text{ cm}^{-3}$

The same characterization has been applied for SiCOI samples fabricated using improved process conditions. Hall effects results are shown in figure 5 for a 6H-SiC film with an initial doping level equal to  $5.5 \cdot 10^{17} \text{ cm}^{-3}$ .

A good fit of the neutrality equation with the experimental Hall data is, in this case, achieved for a compensation level approximately of  $4 \times 10^{16} \text{ cm}^{-3}$  (fig. 5). Fit parameters are respectively 92 meV and 150 meV for the nitrogen donor levels. Because of the low concentration of compensating defects

(~6,9%), the hexagonal level is not lowered in this case. The deviation from the fitting curve at low temperature (below 120 K) is explained by hopping conduction due to residual compensation [13]: free electron concentration increases and carrier mobility drops drastically. However, the carrier mobility above 300K is not affected by the Smart-Cut® process and is comparable with high quality epilayer. 4H-SiC films exhibit the same compensation concentration with an higher mobility.

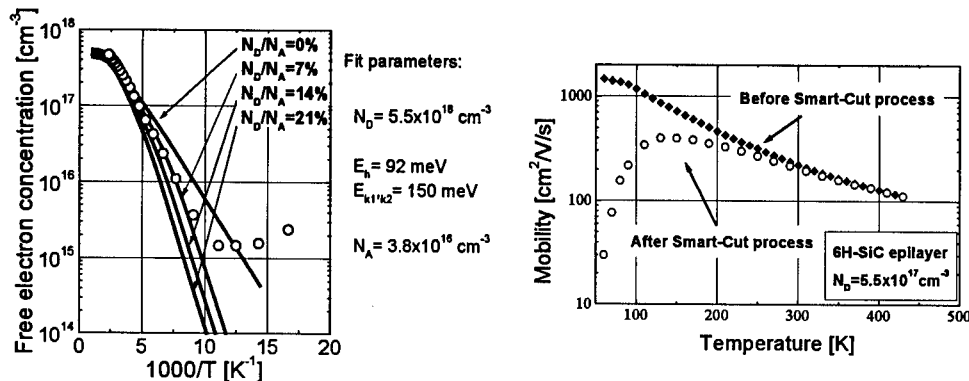


Fig. 5 : Free electron concentration (left) and carrier mobility (right) of SiCOI layer with initial doping level of  $5.5 \times 10^{17} \text{ cm}^{-3}$  after process evolution (carrier mobility before process is shown as reference)

This analysis is confirmed by the EPR results: in contrast with the first process, the EPR spectrum of the neutral N donor is now observed (fig.3) under thermal equilibrium conditions at 4K even for an initial doping level of  $5.5 \times 10^{17} \text{ cm}^{-3}$

### Conclusion:

Pseudo-substrates were already feasible using this process. It has been shown that the remaining defect level in thermally annealed transferred layers lies at  $E_C - 0.5 \text{ eV}$  in the band gap. Hall effect and EPR techniques give a consistent estimation of the compensation level introduced by the process. The concentration of the compensating defects has been reduced to  $4 \times 10^{16} \text{ cm}^{-3}$ . This result is very encouraging since SiCOI wafers are now compatible with device requirements. Device processing is under investigation to demonstrate both technical and economical interests of SiCOI structures.

- [1] E. Hugonnard-Bruyère, V. Lauer, G. Guillot and C. Jaussaud, *Materials Science & Engineering B, Solid State M*, Vol. 61-2 (1999), p. 382-388
- [2] E. Hugonnard-Bruyère, J.L. Cantin, H.J. von Bardeleben, F. Letertre, L. DiCioccio and T. Ouisse, *INFOS'99*, Erlangen, Germany (1999), to be published.
- [3] A.J. Auberton-Hervé, J.M. Lamure, T. Barge et al., *Semicond. Int.*, Vol. 11 (1995), p. 97-102.
- [4] L. Di Cioccio, Y. Le Tiec, F. Letertre et al., *Electronics letters*, Vol. 32 (1996), p. 1144-1445.
- [5] E. Jalaguier, B. Aspar, S. Pocas et al., *Electron. Lett.* Vol. 34 (1998), p. 408-409.
- [6] E. Jalaguier, N. Dessaud, B. Aspar et al., *JNMO'99*, Egat, France (1999), to be published.
- [7] T. Dalibor and G. Pensl., *Physica Status Solidi (a)*, Vol. 162 (1997), p. 199-225.
- [8] J.P. Doyle, M.K. Linnarson et al., *Mat. Res. Soc. Symp. Proc.* Vol. 423 (1996), p. 519-524.
- [9] R.C. Barklie, M. Collins et al., *Journal of Electronic Materials*, Vol. 26 (1997), p. 137-143.
- [10] W. Suttrop, G. Pensl, W.J. Choyke et al., *J. Appl. Phys.*, Vol. 72 (1992), p. 3708-3713.
- [11] B. Segall, S.A. Alterovitz, E.J. Haugland et al., *Appl. Phys. Lett.*, Vol. 49 (1986), p. 584-586.
- [12] M.V. Alekseenko, A.G. Zaroskii et al., *Sov. Phys. Semicond.*, Vol. 21 (1987), p. 494-499.
- [13] N.F. Mott. *Conduction in Non-Crystalline Materials.*, Oxford University Press (1987).

## Theoretical Treatments of Band Edges in SiC Polytypes at High Carrier Concentrations

U. Lindefelt<sup>1,3</sup> and C. Persson<sup>2</sup>

<sup>1</sup> ABB Corporate Research, SE-721 78 Västerås, Sweden

<sup>2</sup> Department of Physics and Measurement Technology, Linköping University,  
SE-581 83 Linköping, Sweden

<sup>3</sup> Department of Solid State Electronics, KTH, Royal Institute of Technology,  
Electrum 229, SE-16440 Stockholm, Sweden

**Keywords:** Band Edge Distortions, Band Gap Narrowing, Doping, Electron Gas, Electron-Hole-Plasma, Mott Transition

**Abstract.** We present a theoretical investigation of how n- and p-type doping affect the band structure around the band gap of 3C-, 2H-, 4H-, and 6H-SiC. For comparison we also consider Si. We have calculated for various values of the dopant concentration (i) the shift in energy of the bottom (top) of the conduction (valence) band, (ii) the band gap narrowing, (iii) the shift of the optical band gap, and (iv) the doping-induced changes in conduction band curvature, i.e., changes in effective electron masses in n-type materials. In addition we have also (v) estimated the critical concentration for Mott transitions and (vi) calculated the shifts in conduction- and valence bands caused, not by doping, but by injection of an electron-hole plasma of various concentrations. To study the effects of doping we have considered a system consisting of impurity ions immersed in a (high-density) gas of majority carriers and a low-density gas of minority carriers. The changes in the bands relative to the idealised crystal are then regarded as being due to interparticle Coulomb interactions and associated particle correlation in and between the gases, as well as to electron and hole interactions with the randomly distributed ions. We have considered two models. The simplest model for band edge displacements is analytical and based on relatively simple assumptions like parabolic energy bands and simple modelling of electron correlation effects. The second model is numerical and includes full band non-parabolicity, and the electron and hole gas interactions are treated in the random-phase approximation.

### Introduction.

Since semiconductor electronics devices contain regions of n- and p-type doping of various concentrations, it is clear that deviations from the ideal band structure due to doping (e.g., band gap narrowing and changes in charge carrier effective masses) can have important effects on device performance. Dopants generally shift the conduction band downwards in energy and the valence bands upwards, leading to a dopant concentration-dependent shrinkage of the band gap. Electrons and holes travelling across regions with different dopant concentrations will thus experience an energy barrier as a result of the doping-induced band edge shifts. This influences the transport of carriers across the junctions. For instance, the injection of carriers from emitters into the base of a diode or transistor is generally deteriorated by the band gap narrowing in the heavily doped emitters. Also from an academic point of view it is of course important to build up knowledge and an understanding of how doping may affect the basic material properties.

Doping also affects the shape of the conduction- and valence bands, thus leading to a change of the effective masses. Since the effective masses affect the scattering properties as well as the direct response of a charge carrier to an electric field, doping-induced changes of the effective masses

should be taken into account in detailed transport studies based on for instance the Monte Carlo method. Another effect of a change of the effective masses is that the Fermi level is also influenced. This can show up as an additional contribution to the shift of the optical band gap. Not only doping, but also an electron-hole plasma (injected either by electrical means as typically in power devices, or through optical excitation) will affect the band edges and give rise to band gap narrowing.

### The physical picture.

Consider an n-doped semiconductor at the finite absolute temperature  $T$ . The effect of the temperature is to ionise a certain (typically a major) fraction of the donors, leading to a concentration  $N_D^+$  of ionised donors having donated their electrons to the conduction band. We assume that the donor ions are randomly distributed in the lattice. The electrons in the conduction band form a (majority carrier) electron gas of density  $n \approx N_D^+$ . Compared to the undoped material, an electron in the conduction band thus feels the Coulomb interaction with the other electrons in the conduction band electron gas, as well as the Coulomb interaction with the donor ions. These interactions, not present in the undoped material, cause a shift in the position of the conduction band edge  $E_c$  and also a change in the band curvature around the conduction band minimum, i.e., a change in the conduction band effective mass, compared to the undoped material. But also the holes in the top of the valence band (minority carrier gas) interact with the electron gas and with the donor ions, causing a shift of the position of the valence band edge  $E_v$  compared to the undoped material. In our model for doping-induced effects on the band structure around the band edges, these are the interactions that are included. We thus neglect interactions involving bound donor electrons (or holes bound to acceptors).

Before we continue to describe the model in some more detail, let us introduce some useful concepts and notations. In this context the term "self-energy" (often denoted  $\hbar\Sigma_j$ , but here we will use the simpler notation  $\Sigma_j$ ) is used to denote the contribution to the conduction band electron ( $j = c$ ) or valence band hole ( $j = v$ ) energies stemming from interactions not present in the undoped material. Furthermore, we let "electron gas" (of density  $n$ ) mean the gas of (conduction band) electrons in a neutralising uniform positive background charge of density  $n$ , and "system of ionised donors" mean the positive ions in a neutralising uniform negative background charge of density  $n$ . Note that in the combined system, consisting of the "electron gas" and "system of ionised donors", the two background charge densities cancel, corresponding to the ions being immersed in a gas of electrons. This will be our model system.

Thus, in n-type materials, the conduction band shift  $\Delta E_c$  and the valence band shift  $\Delta E_v$  can, according to the description earlier, be expressed as

$$\Delta E_c = \Sigma_c^{ee} + \Sigma_c^{ed} \quad ; \quad \Delta E_v = \Sigma_v^{he} + \Sigma_v^{hd} \quad (1)$$

where  $\Sigma_c^{ee}$ ,  $\Sigma_c^{ed}$ ,  $\Sigma_v^{he}$  and  $\Sigma_v^{hd}$  are the self-energies for: a (conduction band) electron (e) interacting with the electron gas, the interaction of the conduction band electrons with the system of ionised donors (d), the interaction of the valence band holes (h) with the conduction band electron gas, and the interaction of the valence band holes with the system of ionised donors, respectively.

The situation for p-type doping is completely analogous. With the same notation we have

$$\Delta E_v = \Sigma_v^{ha} + \Sigma_v^{va} \quad ; \quad \Delta E_c = \Sigma_c^{eh} + \Sigma_c^{ea} \quad (2)$$

where the index 'a' refers to acceptor ions. The (positive) band gap narrowing is defined as

$$\Delta E_g = -\Delta E_c + \Delta E_v \quad (3)$$

Our task is to evaluate the magnitude of these band edge shifts, i.e., the self-energies, as functions of ionised donor and acceptor concentrations. This will be done using two methods to be described next, one relatively simple analytical theory and one more complex and more exact numerical method. To facilitate the presentation, we assume n-type material; p-type material is completely analogous.



### The analytical model.

To shed some light on the mechanisms involved causing the band edge displacements and on the relative importance of the various contributions, it is useful to start with a relatively simple theory[1]. One of the basic approximations in this model is to assume parabolic bands. We consider one conduction band and the two uppermost valence bands. The two valence bands are furthermore assumed to be spherically symmetric in wave vector ( $\mathbf{k}$ -) space.

In the Hartree-Fock (HF) approximation for the homogeneous electron gas, the average interaction between a given electron and the other electrons (the so-called direct Coulomb term) is exactly cancelled by the interaction between the electron and the uniform positive background charge, so that, apart from the kinetic energy, only the exchange energy survives. In the HF approximation, the exchange self-energy per electron at the band minimum is given by (in eV)

$$\Sigma_c^{ee, HF} = -13.6 \cdot \left( \frac{4a_0}{\kappa} \right) \cdot \left( \frac{3}{\pi} \cdot \frac{n}{N_b} \right)^{1/3} \quad (4)$$

where  $a_0$  is the Bohr radius,  $\kappa$  is the static relative dielectric constant of the host semiconductor (thus taking into account the fact that the host material is screening the electron-electron interaction) and  $N_b$  is the number of equivalent electron valleys. The reduction by  $N_b$  appears because the HF exchange energy is proportional to the Fermi wave vector, which depends on the number of electrons occupying states in each valley. To improve on the HF approximation and include some correlation energy, it was suggested by Jain and Roulston[2] to multiply the HF exchange energy by a factor 0.75. Thus, using this approximation we obtain  $\Sigma_c^{ee} = 0.75 \cdot \Sigma_c^{ee, HF} \propto -n^{1/3}$ . This self-energy is negative, corresponding to a downward shift of the conduction band. The physical reason for the negative sign of  $\Sigma_c^{ee}$  is that the electrons avoid each other for two different reasons. Electrons with the same spin avoid each other for statistical reasons (basically the Pauli exclusion principle), which is described by the HF exchange term (Eq. 4). Furthermore, all electrons independently of relative spin directions avoid each other because of the Coulomb repulsion. Therefore, the vicinity of each electron is depleted of electronic charge. Since there is a constant positive background charge, each electron is effectively surrounded by a positively charged exchange and correlation 'hole', which lowers the energy of the electron, i.e., the conduction band is shifted downwards.

Eq. 4 is valid for spherically symmetric conduction bands. The corresponding expression in the general case of three different effective mass components can be found in [1].

Assuming a random distribution of donor ions, the self-energy  $\Sigma_c^{ed}$  has been calculated to second order in perturbation theory, assuming that the donor ions are screened by the conduction band electrons using the Thomas-Fermi approximation[3]. The analytical result can be found in [1], where it is shown that  $\Sigma_c^{ed} \propto -n^{1/2}$ . This contribution is also negative, corresponding to an electron build-up around each (positive) ion. This further lowers the electron energies, causing the conduction band to shift downwards. With the same approximations it is found that [1,3]  $\Sigma_v^{hd} \propto n^{1/2}$ , giving an upward shift of the valence band edge, corresponding to the decrease in hole energy caused by the depletion of holes around the positive ions and the pile-up of holes in the negatively charged regions between the ions (in the system of ionised donors). To obtain the self-energy  $\Sigma_v^{he}$  for a hole interacting with the conduction band electron gas we have used the plasmon-pole approximation (which, contrary to the Thomas-Fermi approximation, takes into account dynamic screening effects) to describe the electron screening of the holes. This gives [1]  $\Sigma_v^{he} \propto n^{1/4}$ . The positive sign expresses the fact that the build-up of an electron screening charge around each hole lowers the energy of the hole, giving an upward shift of the valence band edge.

Adding the various contributions results in the following simple expressions:

$$\Delta E_c = A_{nc} \left( \frac{N_D^+}{10^{18}} \right)^{1/3} + B_{nc} \left( \frac{N_D^+}{10^{18}} \right)^{1/2}; \quad \Delta E_v = A_{nv} \left( \frac{N_D^+}{10^{18}} \right)^{1/4} + B_{nv} \left( \frac{N_D^+}{10^{18}} \right)^{1/2} \quad (5)$$

Similar expressions hold for p-type doping[1]. Using the theory sketched above to calculate the various coefficients A and B in Eq. 5 gives the results in Tables II and III in [1].

#### A more accurate numerical model.

The approximations in the analytical model that perhaps appear to be the crudest are the modelling of the sum of exchange and correlation energies (as 0.75 times of the HF exchange energy) and the assumptions of parabolic, and for the valence bands also spherically symmetric, energy bands. We have, however, developed a more accurate method in which these assumptions can be abandoned. The improved theory allows us not only to get rid of these assumptions, but also to investigate how doping affects the effective masses (influencing for instance the density-of-states and the Fermi level) and to investigate how an electron-hole plasma effects the positions of the band edges. Furthermore, by a slight extension of the theory, it also allows us to estimate the critical concentration for the Mott (metal-non metal) transition in n- and p-type materials.

The basic ingredients in this theory are the following[4]: The self-energies  $\Sigma_c^{ee}(\mathbf{k})$  and  $\Sigma_v^{he}(\mathbf{k})$  are calculated as functions of wave-vector  $\mathbf{k}$  around the respective band extrema using a well-established many-particle approximation theory for the electron gas known as the Random Phase Approximation (RPA). The ionic self-energies  $\Sigma_c^{ed}(\mathbf{k})$  and  $\Sigma_v^{hd}(\mathbf{k})$  are calculated in very much the same way as in the analytical model (second order perturbation theory and a random distribution of ions), except that the electronic screening of the ions is described in terms of a dielectric function obtained within the RPA (instead of using the less accurate Thomas-Fermi approximation as in the analytical model) and except that the full (non-parabolic) band structure has been used instead of a simple analytical band structure. Since the self-energies are  $\mathbf{k}$ -dependent and represent the change in energy of a given band at a wave vector  $\mathbf{k}$  due to doping, we can by simple differentiation evaluate the changes in effective masses caused by the doping.

We have also considered plasma-induced effects by performing the calculations for mutually interacting gases of electrons and holes when the concentrations of electrons ( $n$ ) and holes ( $p$ ) are equal. In this case no ions are present, and each electron, for instance, interacts with all other electrons and all holes. Similarly, each hole interacts with all other holes and with all electrons. First the total energy of the interacting electron- and hole gases is calculated, and then the self-energies for electrons (holes) are obtained by differentiating the total energy with respect to the electron (hole) occupation number. The resulting band edge shifts can very accurately be parameterised using an expression like

$$\Delta E_j = A_j \left( \frac{n}{10^{18}} \right)^{1/3} + B_j \left( \frac{n}{10^{18}} \right)^{1/4} \quad j = c, v \quad (6)$$

The values of the coefficients A and B can be found in [4].

The optical band gap for n-type material is the energy difference between the lowest unpopulated conduction band state and the top of the valence band. The doping-induced narrowing of the optical band gap is given by  $\Delta E_g^{opt} = \Delta E_g + E_F$ , where  $E_F$  is the Fermi energy of the electron gas. In this formulation, the conduction band curvature is allowed to change due to doping (affecting  $E_F$ ).

Another quantity of both practical and academic interest is the so-called critical Mott concentration  $N_{Mott}$  at which a doped semiconductor goes from a semiconducting phase to a metallic phase by a simultaneous ionisation (at  $T = 0K$ ) of all dopants if the dopant concentration becomes larger than  $N_{Mott}$ . To estimate  $N_{Mott}$  for donors we have followed a method expounded by Sernelius and Berggren [5,4]. In this method the total energy per electron of the system of bound but interacting donor electrons is modelled and compared with the total energy (per electron) of the electron gas in the metallic phase. The donor concentration at which these two energies are equal

marks the critical Mott concentration. The results are given in Table 1 for SiC doped with Nitrogen (SiC:N), and Si:P for comparison. A measured value for Si:P [6] is  $3.5 \times 10^{18} \text{ cm}^{-3}$ .

n-type	Si:P	3C-SiC:N	4H-SiC:N	6H-SiC:N
$N_{\text{Mott}} (\text{cm}^{-3})$	$4.9 \times 10^{18}$	$3.5 \times 10^{18}$	$2.8 \times 10^{18}$	$8.8 \times 10^{18}$

Table 1: Estimated critical (Mott) concentrations for metal-nonmetal transitions. For 4H- and 6H-SiC, which both have more than one ground-state donor level, the Mott transition has been calculated for the more shallow level.

#### A selection of results.

Because of the space limitation, only a few results can be shown. For more information, the reader is referred to [1,4].

In Fig.1 (Fig.2) the energy shifts  $\Delta E_c$  and  $\Delta E_v$  as functions of ionised donor (acceptor) concentration are shown using various approximations (full calculation, full calculation but assuming parabolic bands, and analytical model).

Fig.1

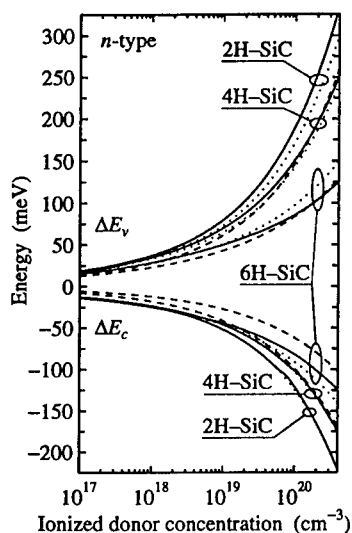


Fig.2

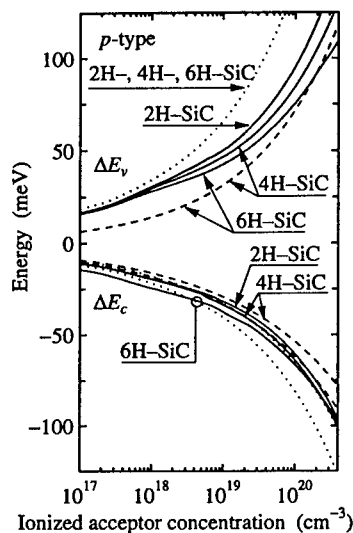


Fig.1: Energy shifts of the lowest conduction band and uppermost valence band as functions of ionised donor concentration for hexagonal polytypes of SiC. The solid lines represent the full calculation, the dotted lines represent the corresponding calculations assuming parabolic energy bands, and the dashed lines are from the analytical model in [1].

Fig.2: Same as in Fig.1 but for p-type doping.

ciently high concentrations the Fermi level increases faster than the reduction in the fundamental band gap, resulting in a minimum in the optical band gap narrowing at around  $3 \times 10^{20} \text{ cm}^{-3}$ . Fig.4 shows an example of how the doping can influence the band structure and effective masses for the lowest conduction band in 6H-SiC. It is clear that the effective mass near the conduction band minimum can change considerably in this material due to doping. Figs.5 and 6, finally, show the results for plasma-induced band edge displacements. The concentration axis extends only up to a few times  $10^{18} \text{ cm}^{-3}$ , since under normal circumstances in power devices, Auger recombination limits the electron-hole plasma concentration.

Fig.3

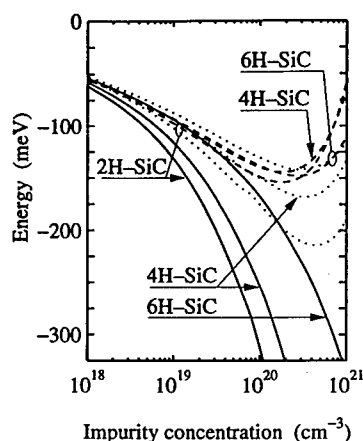


Fig.4

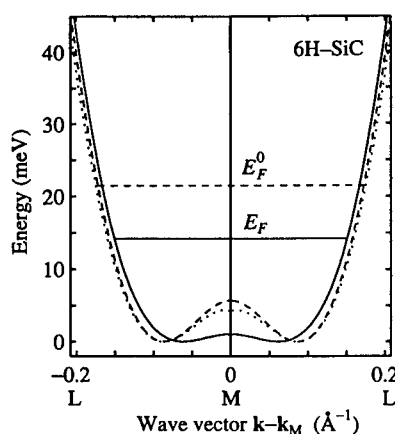


Fig.3: Energy shifts of the fundamental band gap (solid lines) and optical band gap (dashed lines) in hexagonal n-type polytypes of SiC. The dotted lines show the optical band gap shifts assuming the band curvatures to be unaffected by the doping.

Fig.4: Lowest conduction band in 6H-SiC

along the symmetry line LML for a donor concentration  $5 \times 10^{19} \text{ cm}^{-3}$  (solid line). Dashed lines are for the intrinsic material, and dotted line corresponds to a parabolic approximation in the self-energy calculations.

Fig.5

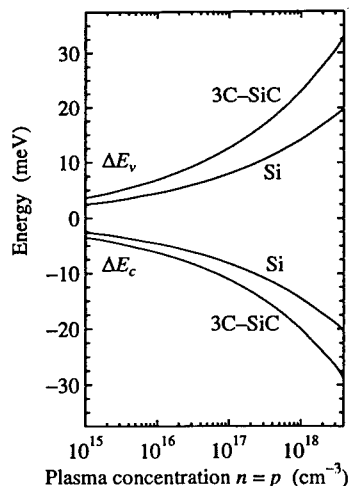


Fig.6

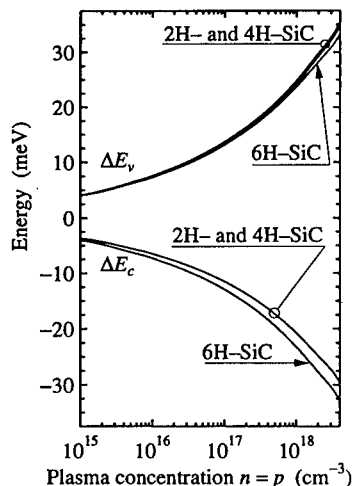


Fig.5: The plasma-induced energy shifts of the lowest conduction band and uppermost valence band in 3C-SiC and Si.

Fig.6: Same as Fig.5 but for 2H-, 4H- and 6H-SiC.

**Acknowledgment:** This work has been partially financed by the Swedish Research Council for Engineering Sciences (TFR) and by the Swedish Foundation for Strategic Research (SSF).

## References

- [1] U. Lindefelt, J. Appl. Phys. 84 (1998), p. 2628
- [2] S. Jain and D.J. Roulston, Solid-State Electron. 34 (1991), p. 453
- [3] K-F Berggren and B.E. Sernelius, Phys. Rev B24 (1981), p. 1971
- [4] C. Persson, U. Lindefelt and B.E. Sernelius, accepted for publication in Phys. Rev. B (basic formalism for n-type material), J. Appl Phys. (n- and p-type materials), and Solid State Electron. (plasma-induced band edge shifts)
- [5] B.E. Sernelius and K-F Berggren, Phil. Mag. B43 (1981), p. 115
- [6] T.G. Castner et al. Phys. Rev. Lett. 34 (1975), p. 1627

Electronic mail: Ulf.Lindefelt@seccr.abb.se

## A Theoretical Study of Electron Drift Mobility Anisotropy in n-type 4H- and 6H-SiC

Enn Velmre and Andres Udal

Department of Electronics, Tallinn Technical University, Ehitajate tee 5, EE-19086 Tallinn, Estland

**Keywords:** Anisotropic Scattering, Charge Carrier Concentration, Electron Mobility

**Abstract** The electron drift mobility ratios in 4H- and 6H-SiC have been calculated accounting for the acoustic phonon and the ionized impurity scattering. A comparison of our theoretical calculations and published experimental data suggest that the acoustic deformation potential tensor of 4H- and 6H-SiC is rather isotropic with a constant  $E_1 = 10 \pm 0.5$  eV for both 4H- and 6H-SiC. A factor, strongly influencing the electron mobility anisotropy is the electron effective mass tensor, which may be rather anisotropic as in case of 6H-SiC.

### Introduction

Experimental investigations [1-4] of various hexagonal and rhombohedral n-type silicon carbide (SiC) polytypes have been revealed a strong electrical conductivity anisotropy in direction parallel to  $c$  axis and perpendicular to  $c$  axis. An early paper [1] reported on anomalously large conductivity ratio  $\sigma_{\perp c} / \sigma_{\parallel c}$  up to  $10^4$  observed in many  $\alpha$ -SiC samples. More reliable anisotropy data measured in carefully selected and prepared SiC samples have been published in [2]. The strongest electron conductivity anisotropy and its temperature dependence was observed in 21R and 330R polytypes. Hexagonal polytypes 4H and 6H showed at  $T = 300\text{K}$   $\sigma_{\perp c} / \sigma_{\parallel c} \cong 0.76$  and 3.2, respectively. Recent Hall mobility anisotropy measurements [3, 4] confirm results of [2] in case of 4H-SiC, but deviate significantly in case of 6H-SiC.

In contrast to the number of experimental works only few theoretical papers on conductivity anisotropy have been published [5, 6]. In this paper we report some preliminary results on 4H- and 6H-SiC electron conductivity anisotropy calculations based on the carrier anisotropic scattering theory published by Samoilovich et al. in [7, 8] and later on in an extensive monograph [9].

### Theoretical models

In this study, the following assumptions and simplifications have been made:

1. Only the intravalley acoustic deformation potential and the ionized impurity scattering are considered in relaxation time approximation for electrons in the lowest conduction band (CB).
2. The real ellipsoidal constant energy surfaces in the vicinity of the CB minima are substituted for approximate ellipsoids of revolution (spheroids) in the same principal axis system. Thus, the electron effective mass tensor is assumed to be diagonal comprising components  $m_l$  and  $m_t$ .
3. The acoustic deformation potential tensor is assumed to be diagonal in the CB valley principal axis system with two components  $D_l \equiv C_1$  and  $D_t \equiv C_1 + C_2$ . In case of negligible deformation potential anisotropy  $D_l = D_t \equiv E_1$ , the conventional acoustic deformation potential constant for longitudinal acoustic modes.

4. 4H- and 6H-SiC, the crystals with hexagonal symmetry are treated as acoustically isotropic media characterized by two average sound velocities  $\bar{s}_l$  and  $\bar{s}_t$  for longitudinal and transverse modes, respectively.

Following the theory [9], the *relaxation time* tensor components may be expressed as:

$$\frac{1}{\tau_i} = \frac{1}{\tau_0} g_i(\mathcal{E}_e) \mathcal{E}_e^\nu$$

where  $i = t$  or  $l$  and  $\mathcal{E}_e$  is the electron kinetic energy.

In case of ionized impurity scattering  $\nu^{e-ion} = -3/2$  and

$$\tau_0^{e-ion} = \frac{\sqrt{2} m_t (4\pi\epsilon\epsilon_0)^2 (k_B T)^{3/2}}{\pi N_{ion} q^4 \sqrt{m_l}}, \quad (1)$$

$$g_l^{e-ion} \approx \frac{3}{\beta^2} \int_{\delta}^{\infty} \frac{(1+\alpha^2) \operatorname{arctg} \alpha^{-1} - \alpha}{(1+\alpha^2)(\alpha^2 \beta^2 - 1)} d\alpha \equiv \Phi_{0l}, \quad (2)$$

$$g_t^{e-ion} \approx \frac{3}{2\beta^2} \int_{\delta}^{\infty} \frac{(1-\alpha^2) \operatorname{arctg} \alpha^{-1} + \alpha}{\alpha^2 (\alpha^2 \beta^2 - 1)} d\alpha \equiv \Phi_{lt}, \quad (3)$$

where

$$\beta^2 = \frac{m_l}{m_t} - 1, \quad \delta = \frac{1}{\beta} \sqrt{1 + (1 + \beta^2) \gamma^2}, \quad \gamma^2 = \frac{q^2 \hbar^2 n_e}{8\epsilon\epsilon_0 m_l k_B T \mathcal{E}_e}.$$

In case of long-wave acoustic phonon scattering  $\nu^{e-ac} = 1/2$  and denoting  $a = \operatorname{arctg} \beta$ ,

$$\tau_0^{e-ac} = \frac{\pi \hbar^4 \rho \bar{s}_l^2}{\sqrt{2m_l m_t^2} C_1^2 (k_B T)^{3/2}}, \quad (4)$$

$$g_l^{e-ac} \approx 1 + \frac{2(1+\beta^2)}{\beta^2} \left( 1 - \frac{3}{\beta^2} + \frac{3a}{\beta^3} \right) \frac{C_2}{C_1} + \left\{ (1+\beta^2) \left[ 1 - \frac{6}{\beta^2} - \frac{3}{2\beta^2(1+\beta^2)} + \frac{15a}{2\beta^3} \right] \right. \\ \left. + \frac{\bar{s}_l^2}{\bar{s}_t^2} \left[ 2 + \frac{15}{2\beta^2} - \frac{3}{2\beta^3} (5+3\beta^2) a \right] \right\} \frac{1+\beta^2}{\beta^4} \frac{C_2^2}{C_1^2} \equiv \Phi_{0a}, \quad (5)$$

$$g_t^{e-ac} \approx 1 + \frac{1+\beta^2}{\beta^2} \left( 2 + \frac{3}{\beta^2} - \frac{3(1+\beta^2)}{\beta^3} a \right) \frac{C_2}{C_1} + \left\{ (1+\beta^2) \left[ 1 + \frac{15}{4\beta^2} - \frac{3}{4\beta^3} (5+3\beta^2) a \right] \right. \\ \left. + \frac{\bar{s}_l^2}{4\bar{s}_t^2} \left[ -13 - \frac{15}{\beta^2} + \frac{3(1+\beta^2)}{\beta^3} (5+\beta^2) a \right] \right\} \frac{1+\beta^2}{\beta^4} \frac{C_2^2}{C_1^2} \equiv \Phi_{1a}. \quad (6)$$

In the *sound velocity* calculations, due to the hexagonal symmetry of 4H- and 6H-SiC crystals a relatively simple exact solution of the Christoffel equation is available [10]. Thus, for any direction of the wave front propagation there exists one purely transverse mode polarized along the  $c$  axis. The phase velocity  $s_1$  of that may be expressed as

$$s_1^2 = c_0 + c_3. \quad (7)$$

Modes with phase velocities  $s_0$  and  $s_2$  are mixed longitudinal and mixed transverse ones, respectively:

$$s_{0,2}^2 = c_0 + \frac{1}{2} \left( c_1 + c_2 \pm \sqrt{(c_1 - c_2)^2 + 4c_1 c_2 \cos^2 \theta} \right). \quad (8)$$

In Eq. 1, and Eq. 2, the original notation of [10] has been retained. Thus

$$\rho c_0 = c_{44} \cos^2 \theta + (c_{11} - c_{13} - c_{44}) \sin^2 \theta, \quad \rho c_1 = c_{44} + c_{13},$$

$$\rho c_2 = (c_{33} - c_{13} - 2c_{44}) \cos^2 \theta - (c_{11} - c_{13} - 2c_{44}) \sin^2 \theta$$

where  $c_{ij}$  are the elastic constants,  $\rho$  is the mass density, and  $\theta$  is the angle between the wave front propagation direction and the  $c$  axis.

Recently, a set of elastic constants measured on 4H- and 6H-SiC has been published by Kamitani et al. [11]:  $c_{11}=501 \pm 4$ ,  $c_{33}=553 \pm 4$ ,  $c_{44}=163 \pm 4$ ,  $c_{12}=111 \pm 5$ ,  $c_{13}=52 \pm 9$ , all in units of GPa. As stated in [11], the data of 4H- and 6H-SiC were undistinguishable within experimental uncertainties. Using Eq. 7, Eq. 8 and  $c_{ij}$  from [11] the average sound velocities  $\bar{s}_l = 12.6 \times 10^5$  cm/s and  $\bar{s}_t = 7.9 \times 10^5$  cm/s were calculated. It is worth mentioning that the difference between the average sound velocities and the exact velocities of respective acoustic modes is less than 10%. Consequently, the hexagonal 4H- and 6H-SiC crystals may be considered in acoustic phonon scattering calculations as acoustically nearly isotropic media.

The electron *effective masses* of approximate spheroids were recalculated regarding ellipsoidal effective mass values reported in [12]. Thus, using experimental data from Table 1 in Ref. 12 we obtained  $m_t = (m_{MK} m_{ML})^{1/2} = 0.32 m_0$ ,  $m_l = m_{MT} = 0.58 m_0$  (the latter in perpendicular to the  $c$  axis) for 4H-SiC, and  $m_t = (m_{lMT} m_{lMK})^{1/2} = 0.42 m_0$ ,  $m_l = m_{ML} = 2.0 m_0$  (the latter in parallel to the  $c$  axis) for 6H-SiC.

To our knowledge, the *deformation potential* tensor components are so far unknown for 4H- and 6H-SiC. Therefore, relevant constants  $C_1$  and  $C_2$  are considered here as fitting parameters.

## Results and discussion

In the present mixed scattering mobility calculations the variational method [13] was employed. This enables us to extend easily the mobility model including of scattering mechanisms that cannot be treated in the relaxation time approximation. The overall, i.e. the multi-valley electron mobility was calculated regarding the positions and orientations of the ellipsoids reported in [12].

**Table 1.** Experimental and theoretical conductivity anisotropy ratios for 4H- and 6H-SiC.

Material, n-type	$\sigma_{\perp c} / \sigma_{\parallel c}$		Doping, cm <sup>-3</sup>	Sample type	Reference
	$T = 300K$	$T = 500K$			
4H-SiC	0.76 <sup>a</sup>	0.78 <sup>a</sup>	$N_D - N_A = (2 \div 3) \times 10^{18}$	bulk	[2]
	0.83 <sup>b</sup>	0.84 <sup>b</sup>	$N_D + N_A = 1 \times 10^{17}$	epilayer	[3]
	0.86 <sup>b</sup>	0.94 <sup>b</sup>	$N_D = 2.6 \times 10^{18}$	bulk	[4]
	0.8 <sup>c</sup>	0.8 <sup>c</sup>	$N_D = 6 \times 10^{16}$ , $N_A = 1 \times 10^{16}$	bulk	[5]
	0.79 <sup>d</sup>	0.77 <sup>d</sup>	$N_D = 1 \times 10^{17}$	bulk	this work
6H-SiC	3.2 <sup>a</sup>	3.3 <sup>a</sup>	$N_D - N_A = 6 \times 10^{17}$	bulk	[2]
	5 <sup>b</sup>	4.6 <sup>b</sup>	$N_D + N_A = 1 \times 10^{17}$	epilayer	[3]
	4.8 <sup>b</sup>	4.2 <sup>b</sup>	$N_D = 4.5 \times 10^{16}$	bulk	[4]
	4.5 <sup>c</sup>	4.0 <sup>c</sup>	$N_D + N_A = 1 \times 10^{17}$	bulk	[14]
	4.49 <sup>d</sup>	4.69 <sup>d</sup>	$N_D = 1 \times 10^{17}$	bulk	this work

<sup>a</sup> Schnabel's method measurements,

<sup>c</sup> Monte Carlo calculations,

<sup>b</sup> Hall measurements,

<sup>d</sup> Low-field BTE calculations.

As a result, for electron mobilities in the crystallographic axis system we obtain:

$$\mu_{\parallel c} = \mu_t, \quad \mu_{\perp c} = (\mu_t + \mu_l)/2 \quad \text{for 4H-SiC}, \quad \mu_{\parallel c} = \mu_l, \quad \mu_{\perp c} = \mu_t \quad \text{for 6H-SiC}.$$

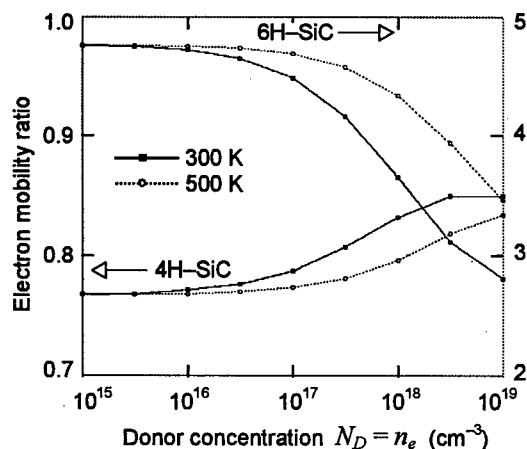


Fig. 1. The calculated electron drift mobility ratio  $\mu_{\perp c}/\mu_{\parallel c}$  versus ionized donor concentration in 4H- and 6H-SiC at temperatures  $T=300$  and  $500$  K.

Adjusting of deformation potential constants at different temperatures and doping concentrations yielded the best fit to the measured electron mobilities [3] and the mobility anisotropy ratios [2-4], if  $C_2=0$  and  $C_1=10 \pm 0.5$  eV for both 4H- and 6H-SiC. Thus, our calculations indicate that the acoustic deformation potential tensors of these hexagonal polytypes should be rather isotropic. Therefore, the final calculations presented in this work were performed taking  $C_2=0$  and  $C_1 \equiv E_1=10$  eV. As expected the anisotropy of the electron effective mass tensor is the main factor influencing the electron mobility anisotropy in 4H- and 6H-SiC.

#### Acknowledgements

The authors are grateful to Professor Ulf Lindefelt for helpful discussions. The Estonian Science Foundation (Project 2828), the Swedish Foundation for Strategic Research (SSF), and the Swedish Institute are acknowledged for financial support.

#### References

- [1] G. Bosch, J. Phys. Chem. Solids, **27** (1966), p. 795.
- [2] G.A. Lomakina, and Yu.A. Vodakov, Sov. Phys. Solid State, **15** (1973), p. 83.
- [3] W.J. Schaffer, G.H. Negley, K.G. Irvine, J.W. Palmour, Mater. Res. Soc. Symp. Proc., **337** (1994), p. 595.
- [4] M. Schadt, G. Pensl, R.P. Devaty, W.J. Choyke, R. Stein, D. Stephani, Appl. Phys. Lett., **65** (1994), p. 3120.
- [5] H.-E. Nilsson, U. Sannemo, C.S. Petersson, J. Appl. Phys., **80** (1996), p. 3365.
- [6] T. Kinoshita, M. Schadt, K.M. Itoh, J. Muto, G. Pensl, Mater. Res. Soc. Symp. Proc., **337** (1994), p. 631.
- [7] A.G. Samoilovich, I.Ya. Korenblit, I.V. Dakhovski, Dokl. Akad. Nauk, **139** (1961), p. 355.
- [8] A.G. Samoilovich, I.Ya. Korenblit, I.V. Dakhovski, V.D. Iskra, Fiz. Tverd. Tela, **3** (1961), p. 2939, 3285.
- [9] Electrical and Galvanomagnetic Effects in Anisotropic Semiconductors (ed. by P.I. Baranski), Kiev, 1977.
- [10] F.I. Fedorov, Theory of elastic waves in crystals, Moscow, 1965.
- [11] K. Kamitani, M. Grimsditch, J.C. Nipko, and C.-K. Loong, J. Appl. Phys., **82** (1997), p. 3152.
- [12] C. Persson, U. Lindefelt, Phys. Rev. B, **54** (1996), p. 10257.
- [13] E. Velme, A. Udál, T. Kocsis, F. Masszi, Physica Scripta, **T54** (1994), p. 263.
- [14] H.-E. Nilsson, M. Hjelm, C. Fröjdh, C. Persson, U. Sannemo, C.S. Petersson, J. Appl. Phys., **86**, (1999), p. 965.

For correspondence with readers:

Phone: (372) 6 202 152, (372) 6 202 150, Fax: (372) 6 202 151, E-mail: evelmre@va.ttu.ee



## Theoretical Calculation of the Electron Hall Mobility in n-type 4H- and 6H-SiC

Hisaomi Iwata and Kohei M. Itoh

Department of Applied Physics and Physico-Informatics, Keio University,  
 3-14-1 Hiyoshi, Kohoku-ku, Yokohama, 223-8522, Japan

**Keywords:** Electron Transport, Hall Effect, Mobility

**Abstract:** We report on the theoretical calculation of the electron Hall mobility in nitrogen doped n-type 4H- and 6H-SiC as a function of temperature, net-doping concentration ( $[N_D]-[N_A]$ ), and compensation ratio ( $[N_A]/[N_D]$ ). The electron Hall mobility is found for two temperatures,  $T=77K$  and  $300K$ , covering a wide range of the net-doping concentration ( $10^{14}$ - $10^{19}[cm^{-3}]$ ) and the compensation ratio (0-0.6).

### Introduction

The electron Hall mobility in 4H- and 6H-SiC depends strongly on the geometrical configurations of the Hall measurement due to the anisotropic structure of conduction bands. [1] Our previous works revealed that the large anisotropy of the electron transport was explained very well by the anisotropy in the effective mass tensors. [2,3] Unlike the results of Monte Carlo simulation which neglects the effect of the magnetic field, [4-7] our analytical Hall mobility calculation makes it possible for the first time to compare directly with the experimentally measured Hall mobility with the externally applied magnetic field. Based on this success, we calculate the electron Hall mobility as a function of temperature, net-doping concentration, and compensation ratios in this work. Fig.1 shows three distinct configurations for the Hall measurements; (a)  $[j \perp c, B \parallel c]$ , (b)  $[j \perp c, B \perp c]$ , and (c)  $[j \parallel c, B \perp c]$ , where  $j$  is the externally applied current vector,  $B$  is the magnetic field, and  $c$  is the direction of the  $c$ -axis of a hexagonal unit cell. This work focuses on the Hall measurement configuration  $[j \perp c, B \parallel c]$  since most of the Hall measurements on the device quality 4H- and 6H-SiC thin films are performed in this manner.

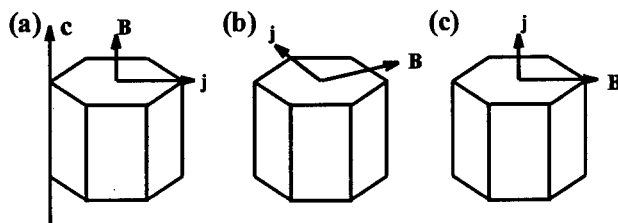


Fig.1. Schematic diagram of the three distinct Hall measurement configurations:  
 (a)  $[j \perp c, B \parallel c]$ , (b)  $[j \perp c, B \perp c]$ , and (c)  $[j \parallel c, B \perp c]$ .

### Method and Model

Our model is based on the conduction band structure determined recently by first-principle calculations. [8,9] We assume that there are six semiellipsoidal and parabolic constant energy surfaces centered exactly at M-points in the first Brillouin zone for both 4H- and 6H-SiC. Our strategy for obtaining the Hall mobility consists of the following steps. First, we derive an expression of the conductivity tensor including the magnetic field for one ellipsoid from the Boltzmann transport equation, using relaxation time approximation and Maxwellian

approximation. Then, we place three ellipsoids in proper positions in the reciprocal space. Finally, we obtain the total conductivity tensor by adding the contribution from each of the three ellipsoids. This procedure leads to analytical expressions for the drift and Hall mobility as a function of the average electron relaxation time and the effective masses. Table 1 lists the effective masses employed for 4H- and 6H-SiC.

In order to calculate the momentum relaxation time, we have considered five scattering mechanisms: ionized impurity scattering, acoustic phonon deformation potential scattering, polar optical phonon scattering, zero-order inter-valley phonon deformation potential scattering, and first-order inter-valley phonon deformation potential scattering. Brooks-Herrings theory is used for ionized impurity scattering. Table 2 lists parameters we employed in this work.

Table 1. Effective masses.

	4H-SiC [ $m_0$ ]	6H-SiC [ $m_0$ ]
$m_{M-\Gamma}$	0.57	0.75
$m_{M-K}$	0.28	0.24
$m_{M-L}$	0.31	1.83

Table 2. Parameters used to calculate relaxation time.

	4H-SiC	6H-SiC
Static relative permittivity	9.7	9.7
Optical relative permittivity	6.5	6.5
Density [ $\text{g/cm}^3$ ]	3.166	3.166
Sound velocity [ $10^4 \text{ m/s}$ ]	1.37	1.37
Acoustic deformation potential [eV]	10.9	10.8
Inter-valley coupling:		
Zero-order [ $10^9 \text{ eV/cm}$ ]	2.2	2.0
First-order [eV]	5	5
Inter-valley phonon energy		
Zero-order [meV]	85.4	85.4
First-order [meV]	33.2	33.2
Polar optical phonon energy [meV]	120	120

## Results and Discussion

Fig.2 (a) and (b) show the comparison of our Hall mobility calculations with the Hall effect measurements in the configuration  $[\mathbf{j} \perp \mathbf{c}, \mathbf{B} // \mathbf{c}]$  for 4H- and 6H-SiC, respectively. The 4H-SiC sample is an epitaxially grown thin film having  $N_D = 7.0 \times 10^{15} \text{ cm}^{-3}$  and  $N_A = 1.3 \times 10^{15} \text{ cm}^{-3}$  [10] and the 6H-SiC sample is an epitaxially grown thin film having  $N_D = 1.05 \times 10^{16} \text{ cm}^{-3}$  and  $N_A = 1.0 \times 10^{14} \text{ cm}^{-3}$ . [11]  $N_D$  and  $N_A$  are concentrations of donors and acceptors, respectively. The calculation for both 4H-SiC and 6H-SiC agrees very well with the experiment. [Fig.2 (a), (b)] In our calculation, the most dominant scattering mechanism for both 4H- and 6H-SiC changes from inter-valley scattering to acoustic phonon scattering at the temperature between 200K and 300K. The change of slope at this temperature can be seen in the experimental data.

Fig.3 shows the electron Hall mobility as a function of the net-doping concentration and the compensation ratio at 77K and 300K. As shown in Fig.3, the electron Hall mobility depends strongly on the compensation ratio. At  $T=77\text{K}$ , the difference between the curves, compensation ratio = 0 and 0.1, is large for both 4H- and 6H-SiC [Fig.3 (a), (c)] because ionized impurities scattering by compensating donors and compensated acceptors dominates the total mobility. In Fig.3 (b) and (d), the electron Hall mobilities of different compensation ratios converge to a constant value when the net-doping concentration becomes smaller than  $10^{14} \text{ cm}^{-3}$  because the contribution of the ionized impurity scattering to the total mobility becomes negligibly small.

## Conclusion

We have performed the theoretical calculation of the electron Hall mobility in both 4H- and

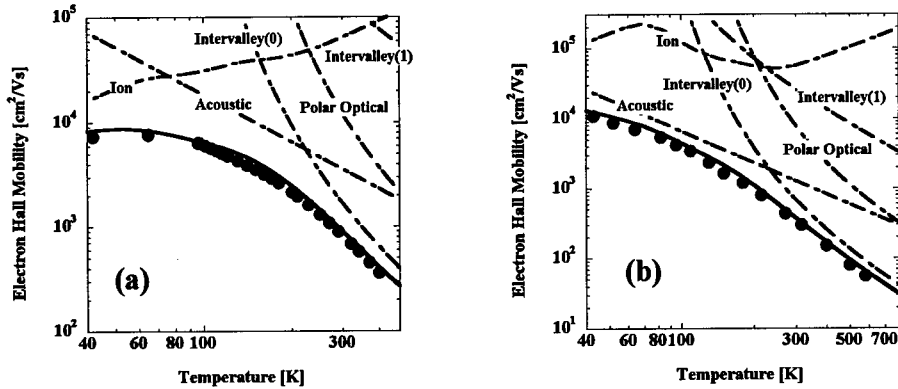


Fig.2. Direct comparison of our Hall mobility calculations (solid curve) with the Hall effect measurements (filled circles) in the configuration  $[j \perp c, B // c]$  for (a) 4H-SiC and (b) 6H-SiC. The contribution of various scattering mechanisms to the total electron Hall mobility is also shown. Experimental data of 4H-SiC and 6H-SiC are taken from Ref.10 and Ref.11, respectively.

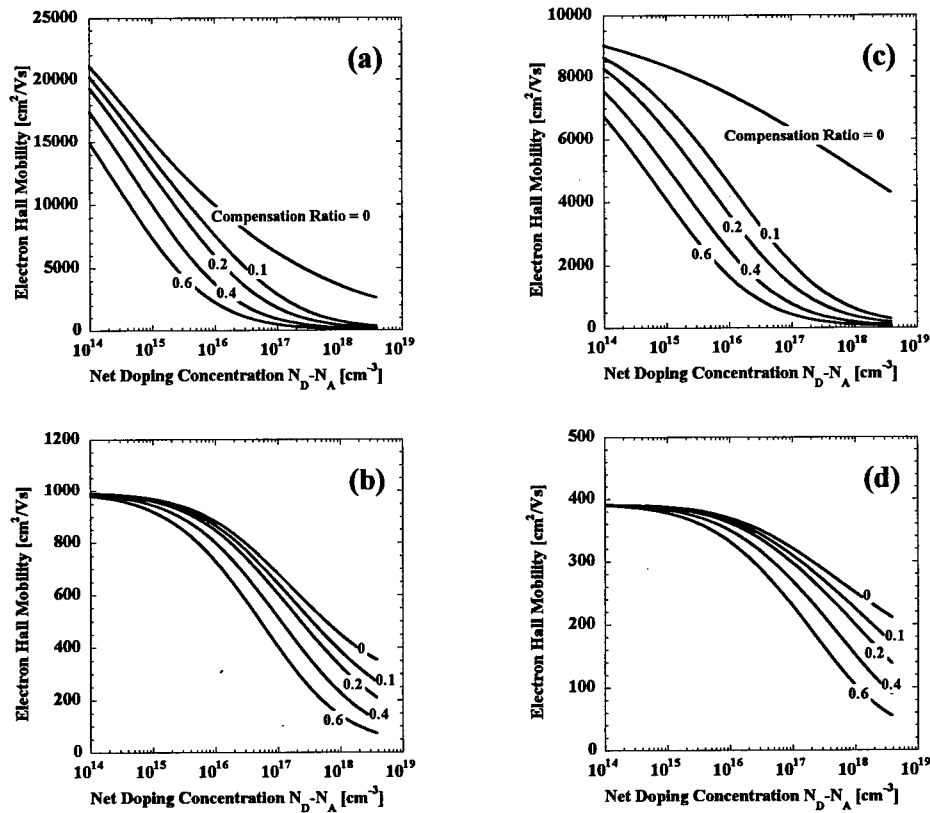


Fig.3. Electron Hall mobility in the configuration  $[j \perp c, B // c]$  as a function of the net-doping concentration and compensation ratio for (a) 4H-SiC at  $T=77\text{K}$ , (b) 4H-SiC at  $T=300\text{K}$ , (c) 6H-SiC at  $T=77\text{K}$ , and (d) 6H-SiC at  $T=300\text{K}$ .

6H-SiC in a wide range of temperature, net-doping concentration, and compensation ratio. The contribution of various scattering mechanisms to the total electron Hall mobility has been found for both 4H- and 6H-SiC.

#### Acknowledgement

The authors thank T. Kinoshita, G. Pensl, M. Schadt, W. J. Choyke, R. P. Devaty, H.-E. Nilsson, and E. Bellotti for fruitful discussions.

#### References

- [1] M. Schadt, G. Pensl, R. P. Devaty, W. J. Choyke, R. Stein, and D. Stephani, *Appl. Phys. Lett.* **65** (1994), p. 312.
- [2] T. Kinoshita, K. M. Itoh, J. Muto, M. Schadt, G. Pensl, and K. Takeda, in *Proc. Silicon Carbide, III-Nitrides and Related Materials*, ed. G. Pensl, H. Morkoç, B. Monemar, and E. Janzén, *Materials Science Forum* **264-268** (1998), p. 295.
- [3] T. Kinoshita, K. M. Itoh, M. Schadt, and G. Pensl, *J. Appl. Phys.* **85** (1999), p. 8193.
- [4] R. P. Joshi, *J. Appl. Phys.* **78** (1995), p. 5518.
- [5] R. P. Joshi and D. K. Ferry, *Solid-State Electron.* **38** (1995), p. 1911.
- [6] H.-E. Nilsson, U. Sannemo, and C. S. Petersson, *J. Appl. Phys.* **80** (1996), p. 3365.
- [7] R. Mickevičius and J. H. Zhao, *J. Appl. Phys.* **83** (1998), p. 3161.
- [8] C. Persson and U. Lindefelt, *Phys. Rev. B* **54** (1996), p. 10257.
- [9] W. R. L. Lambrecht and B. Segall, *Phys. Rev. B* **52** (1995), p. R2249.
- [10] G. Rutsch, R. P. Devaty, D. W. Langer, L. B. Rowland, and W. J. Choyke, in Ref. 2, p. 517.
- [11] S. Karmann, W. Suttrop, A. Schöner, M. Schadt, C. Haberstroh, F. Engelbrecht, R. Helbig, and G. Pensl, *J. Appl. Phys.* **72** (1992), p. 5437.

## Hall Scattering Factor and Electron Mobility of 4H SiC: Measurements and Numerical Simulation

G. Rutsch<sup>1</sup>, R.P. Devaty<sup>1</sup>, W.J. Choyke<sup>1</sup>, D.W. Langer<sup>2</sup>, L.B. Rowland<sup>3</sup>,  
E. Niemann<sup>4</sup> and F. Wischmeyer<sup>4</sup>

<sup>1</sup> Department of Physics and Astronomy, University of Pittsburgh, Pittsburgh, PA 15260, USA

<sup>2</sup> Department of Electrical Engineering, University of Pittsburgh, Pittsburgh, PA 15260, USA

<sup>3</sup> Northrop Grumman Science and Technology Center, Pittsburgh, PA 15235-5080, USA

<sup>4</sup> Research and Technology, DaimlerChrysler AG, Goldsteinstrasse 235,  
DE-60528 Frankfurt am Main, Germany

**Keywords:** Electron Mobility, Hall Effect, Hall Scattering Factor

**Abstract** Reliable values of the Hall scattering factor of 4H SiC are obtained by measurements on four n-type 4H SiC homoepitaxial films over the temperature range 40-290 K using magnetic fields up to 30 T. Good fits are obtained to the measured temperature dependent Hall mobility using a simulation that includes the inelastic process of polar optical phonon scattering without recourse to the relaxation time approximation. Two deformation potentials are the adjustable parameters. The model is tested by comparing calculated results, with no further adjustments of the parameters, with the measured temperature dependence of the Hall scattering factor.

### Introduction

The accurate determination of the charge transport properties of 4H SiC is a necessary step in the development of the knowledge base required for the design and fabrication of electronic devices. Several groups have measured [1-3] and modeled [3-8] electron transport properties in hexagonal SiC polytypes, mostly based on measurements using moderately to highly doped SiC boule samples grown by the Lely or the modified Lely methods. The Hall scattering factor  $r_H$ , where  $R_H = r_H/(en)$ , influences the donor activation energies extracted from temperature dependent Hall measurements. We [9,10] previously measured the Hall scattering factor of 4H and 6H SiC using magnetic fields up to 9 T, which proved to be inadequate to determine  $r_H$  accurately at temperatures above approximately 200 K. Here we present new measurements of the Hall scattering factor using magnetic fields up to 30 T using high mobility homoepitaxial layers of 4H SiC. Very good fits to the measured Hall mobility are obtained using a model based on the Rode iteration method [11,12], which is not based on the relaxation time approximation, for solving the Boltzmann equation for the chosen set of electron scattering mechanisms, which includes polar optical phonon scattering. Comparison of the simulation of  $r_H$  with the independently measured data allows one to test the model.

### Experiment

The four samples (A, B, C and D) used in this study are lightly nitrogen doped 3-8  $\mu\text{m}$  thick homoepitaxial layers grown on p-type substrates oriented  $8^\circ$  off the crystal c-axis. For the samples fabricated at Northrop Grumman, Ti/Ni electrical contacts are deposited, and clover leaf patterns are defined using reactive ion etching. The samples fabricated at DaimlerChrysler have annealed Ti contacts.

Low field ( $B = 0.741$  Tesla) temperature dependent Hall measurements are performed from 90 K to 410 K using a cold finger cryostat suspended in an iron core electromagnet. A cryostat with a 9 T superconducting solenoid is used to measure the Hall coefficient at magnetic fields ranging from 0.1 to 9 T at six temperatures ranging from about 40 K to 290 K. The temperature is measured using a Cernox<sup>®</sup> thermometer, which has a very low sensitivity to magnetic fields. Care is taken to

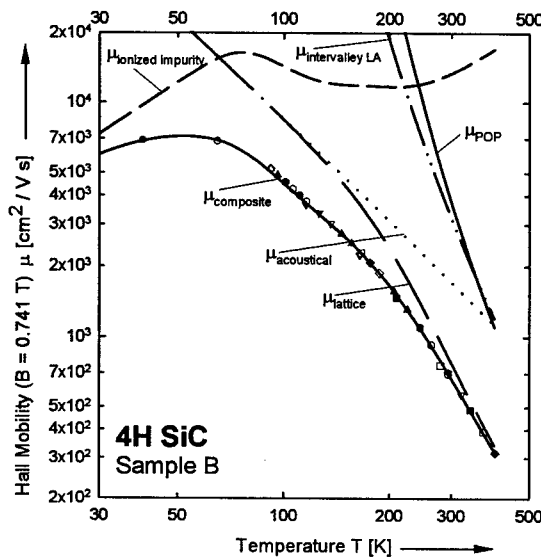


Fig. 1 Measured (symbols) and calculated (solid line) Hall mobility for Sample B, an n-type homoepitaxial 4H SiC layer grown on a p-type substrate. Also shown are the contributions of the various scattering mechanisms included in the calculation. The curve marked " $\mu_{\text{lattice}}$ " includes all the mechanisms but ionized impurity scattering.

to the correct expressions for the mass factors of 4H SiC applicable to the various Hall geometries. The density of states effective mass  $m^* = (m_1 m_2 m_3)^{1/3}$ , where the  $m_i$  ( $i = 1, 2, 3$ ) are the elements of the diagonal effective mass tensor [15], is used as the isotropic electron mass parameter in the numerical evaluations. The elements of the effective mass tensor also appear in the evaluation of the mobility. The temperature dependence of the electron mobility is modeled by choosing scattering mechanisms likely to be of importance: elastic deformation potential acoustic intravalley scattering [16], intervalley scattering [11], ionized impurity scattering (Brooks-Herring formula [13]), and inelastic polar optical phonon (POP) scattering [11]. Under the conditions discussed by Herring and Vogt [14], the first three scattering mechanisms are consistent with the relaxation time approximation. However, the relaxation time approximation does not apply to POP scattering. Two parameters, the intravalley acoustic deformation potential  $E_1$  and the intervalley deformation potential  $D_v$ , are adjusted to fit measured temperature dependent mobility data. For intervalley scattering a single phonon energy,  $\hbar\omega_{LA} = 76.6$  meV, is used. For POP scattering, we use  $\hbar\omega_{PO} = 120$  meV. We stress again that the formulae used to describe the scattering processes were derived for isotropic parabolic bands under nondegenerate (Maxwell-Boltzmann) conditions. Further details concerning the calculations, including all parameter values, will be provided in a separate publication.

### Results and Discussion

Fig. 1 shows the best fit of the model to the measured temperature dependence of the low field Hall mobility for Sample B. Based on a fit of the neutrality equation to the measured temperature dependence of the conduction electron concentration obtained from Hall data under the assumption  $r_H = 1$ , this 4H SiC homoepitaxial film has nitrogen donor concentrations  $N_{D1} = N_{D2} =$

maintain temperature stability to within  $\pm 50$  mK to keep the concentration of free electrons constant. Additional experiments in magnetic fields from 0.1 T to 30 T are performed using a Bitter magnet at the National High Magnetic Field Laboratory (NHMFL) in Tallahassee, Florida. All measurements are performed with the magnetic field oriented parallel to the crystal c-axis.

### Simulations

The temperature dependent electron mobility and Hall scattering factor are calculated numerically using a solution of the Boltzmann transport equation obtained using the Rode iteration method [11,12]. The effects of anisotropy of the electronic and vibrational properties of 4H SiC on the scattering processes are neglected in this solution. We partly account for the consequences of the anisotropy of the electron effective mass tensor by multiplying the calculated Hall scattering factor by a mass factor, based on an argument of Brooks [13]. The mass factor can be calculated using the method of Herring and Vogt [14]. Kinoshita et al. [4] recently published results that reduce

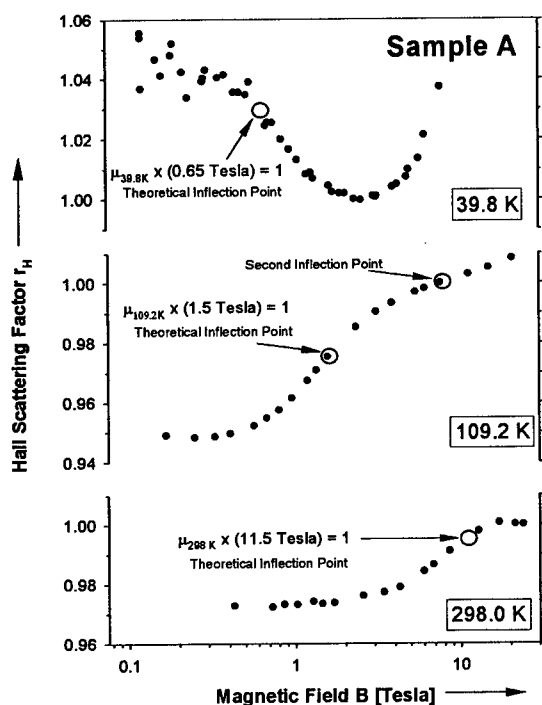
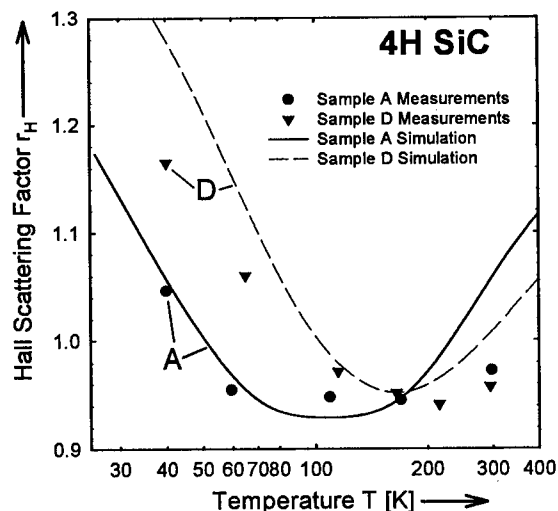


Fig. 2 Magnetic field dependence of the Hall scattering factor of an n-type 4H SiC homoepitaxial layer grown on a p-type substrate, measured at three temperatures. The "Theoretical Inflection Point" is discussed in the text.



$8.2 \times 10^{15} \text{ cm}^{-3}$  and a compensating acceptor concentration  $N_A = 6.4 \times 10^{14} \text{ cm}^{-3}$ . The contributions of the various scattering mechanisms are shown individually, as well as the contribution of "lattice scattering," neglecting ionized impurity scattering. As might be expected, ionized impurity scattering dominates at low temperatures, while lattice scattering takes over with increasing temperature. The values of the deformation potentials obtained from this fit are  $E_1 = 13.3 \text{ eV}$  and  $D_e = 1.46 \times 10^{11} \text{ eV/m}$ . Over the set of four samples, the nitrogen donor concentration ranges from  $3.3 \times 10^{15}$  to  $4.3 \times 10^{16} \text{ cm}^{-3}$ , the concentration of compensating acceptors from  $1.6 \times 10^{14}$  to  $7.1 \times 10^{15} \text{ cm}^{-3}$ ,  $E_1$  from 11.6 to 13.3 eV, and  $D_e$  from  $1.22 \times 10^{11}$  to  $1.54 \times 10^{11} \text{ eV/m}$ .

Fig. 2 shows the measured Hall scattering factor versus magnetic field at three selected temperatures for Sample A. Note the high field saturation at 298 K. There are theoretical arguments [17,18] that  $r_H$  tends to unity for large magnetic fields. Below room temperature, strong field induced electron freezeout occurs at high fields. Sample A is a 4H SiC homoepitaxial layer with nitrogen donor concentrations  $N_{D1} = 1.9 \times 10^{15} \text{ cm}^{-3}$  and  $N_{D2} = 1.4 \times 10^{15} \text{ cm}^{-3}$  for the hexagonal and quasicubic sites, respectively, and  $N_A = 1.6 \times 10^{14} \text{ cm}^{-3}$  for the concentration of compensating acceptors, all determined by fitting the neutrality equation to Hall data. An inflection point is expected at the field for which  $\mu_H(B)B = 1$ . This "Theoretical Inflection Point" [9,10] is estimated using the best estimate of  $R_H(\infty)$ , the high field limit of the Hall constant, and the measured dc resistivity. The "Theoretical Inflection Points" match the inflection points in the data quite well.

Fig. 3 shows the temperature

Fig. 3 Measured (symbols) and calculated (lines) temperature dependence of the Hall scattering factor for two n-type 4H SiC homoepitaxial layers, grown on p-type substrates.

dependence of the low field Hall scattering factor. The symbols indicate data points for Samples A and D.  $r_H$  is above unity below ~60 K and decreases with increasing temperature. Above 60-80 K, the measured  $r_H$  is less than unity and shows relatively little temperature dependence, although there is a slow increase as room temperature is approached. The lines are calculated using the simulation with the two deformation parameters set to the values obtained by fitting the Hall mobility data for each of the two samples. The calculated curves considerably exceed the data points for temperatures above 200 K. According to the model, lattice scattering dominates in this temperature range.

Reliable values of the Hall scattering factor, obtained using magnetic fields up to 30 T, can be applied to adjust the values of the electron concentration versus temperature obtained from low field Hall measurements. Fitting the neutrality equation to such corrected Hall data does not produce a sufficiently large change in the derived donor ionization energies to account for differences between values obtained by electrical and optical methods.

### Conclusion

Reliable values of the low field Hall scattering factor are obtained by performing high field measurements up to 30 T, which is sufficiently large to observe saturation, over the temperature range 40-290 K. The measured temperature dependence of the Hall mobility can be successfully modeled using the Rode iteration method with broad simplifying assumptions concerning the scattering mechanisms plus a mass factor to account for the anisotropy of the effective mass tensor. We stress that this success does not demonstrate conclusively the contributions of the various scattering mechanisms. Comparison between the calculated and measured temperature dependence of the Hall scattering factor provides a test of the model. A quantitative understanding of the electron scattering mechanisms in SiC polytypes remains a lofty goal for future work.

### Acknowledgements

We thank the Office of Naval Research for partial support of this work.

### References

- [1] M. Schadt, G. Pensl, R.P. Devaty, W.J. Choyke, R. Stein and D. Stephani, *Appl. Phys. Lett.* 65 (1994), p. 312.
- [2] W.J. Schaffer, G.H. Negley, K.G. Irvine and J.W. Palmour, *Mat. Res. Soc. Symp. Proc.* 337 (1994), p. 595.
- [3] St.G. Müller, D. Hofmann and A. Winnacker, *Mat. Res. Soc. Symp. Proc.* 572 (1999), p. 275.
- [4] T. Kinoshita, K.M. Itoh, M. Schadt and G. Pensl, *J. Appl. Phys.* 85 (1999), p. 8193.
- [5] R.P. Joshi, *J. Appl. Phys.* 78 (1995), p. 5518.
- [6] H.-E. Nilsson, U. Sannemo and C. Sture Petersson, *J. Appl. Phys.* 80 (1996), p. 3365.
- [7] H.-E. Nilsson, M. Hjelm, C. Fröjdth, C. Persson, U. Sannemo and C. Sture Petersson, *J. Appl. Phys.* 86 (1999), p. 965.
- [8] R. Mickevičius and J.H. Zhao, *J. Appl. Phys.* 83 (1998), p. 3161.
- [9] G. Rutsch, R.P. Devaty, W.J. Choyke, D.W. Langer and L.B. Rowland, *J. Appl. Phys.* 84 (1998), p. 2062.
- [10] G. Rutsch, R.P. Devaty and W.J. Choyke, *Mat. Sci. Forum* 264-268 (1998), p. 517.
- [11] D.L. Rode, in *Semiconductors and Semimetals*, Ed. R.K. Willardson and A.C. Beer (Academic Press, New York, 1975), Vol. 10.
- [12] D.L. Rode, *Phys. Stat. Sol. (b)* 55 (1973), p. 687.
- [13] H. Brooks, *Advances in Electronics and Electron Physics* 7 (1955), p. 85.
- [14] C. Herring and E. Vogt, *Phys. Rev.* 101 (1956), p. 944.
- [15] D. Volm, B.K. Meyer, D.M. Hofmann, W.M. Chen, N.T. Son, C. Persson, U. Lindefelt, O. Kordina, E. Sörman, A.O. Konstantinov, B. Monemar and E. Janzén, *Phys. Rev. B* 53 (1996), p. 15409.
- [16] J. Bardeen and W. Shockley, *Phys. Rev.* 80 (1950), p. 72.
- [17] P. Blood and J.W. Ornton, *The Electrical Characterization of Semiconductors: Majority Carriers and Electron States* (Academic Press, London, 1992), Chapter 3.
- [18] D.L. Rode, C.M. Wolfe and G.E. Stillman, *J. Appl. Phys.* 54 (1983), p. 10.



## Hall Mobility of the Electron Inversion Layer in 6H-SiC MOSFETs

N.S. Saks<sup>1</sup>, S.S. Mani<sup>2</sup>, A.K. Agarwal<sup>3</sup> and V.S. Hegde<sup>4</sup>

<sup>1</sup> Naval Research Laboratory, Code 6813, Washington, DC 20375, USA

<sup>2</sup> Northrop Grumman Corp., Pittsburgh, PA, USA now at Sandia National Laboratory,  
Albuquerque, NM, USA

<sup>3</sup> Northrop Grumman Corp., Pittsburgh, PA, USA now at CREE Research Inc., Durham, NC, USA

<sup>4</sup> Northrop Grumman Corp., Pittsburgh, PA, USA

**Keywords:** Charge-Sheet Model, Hall Effect, Interface Trap, Inversion Layer, Mobility, MOS

**Abstract:** Electron mobility and free carrier density have been measured in 6H-SiC MOS inversion layers using the Hall effect to study unexpectedly low transconductance in SiC MOSFETs. We find that the Hall mobility can be much larger than the effective mobility extracted from transconductance data. In addition, the actual free electron density is found to be smaller than predicted by the charge-sheet model, which is caused by substantial electron trapping at the SiC/SiO<sub>2</sub> interface.

**Introduction:** SiC MOSFETs with high current drive are needed for high power devices. SiC has a major potential advantage for MOS devices because an SiO<sub>2</sub> gate insulator can be grown by thermal oxidation of SiC. The MOS gate insulator must have a high quality SiC/SiO<sub>2</sub> interface with a high electron inversion layer mobility ( $\mu_e$ ) and a low interface trap density ( $D_{it}$ ). There has been significant recent progress in producing SiC MOS capacitors with low  $D_{it}$  [1]. However, reported inversion layer mobilities for SiC MOSFETs are typically much less than half of the bulk mobility, a ratio which is normally achieved in silicon MOS devices [2-4].

To investigate the possible causes of this low mobility, electron mobility  $\mu_e$  and free carrier density  $n_s$  have been measured in SiC MOS inversion layers using the Hall effect. Previous experiments use analysis of MOSFET transconductance (i.e., drain current  $I_{ds}$  vs. gate voltage  $V_g$  data) to determine "drift" mobility. In that approach, values for  $n_s$  are assumed based on the charge-sheet model [5]. In this work,  $\mu_e$  and  $n_s$  are measured independently using the Hall effect. Results here demonstrate that actual  $n_s$  values can be smaller than predicted by the charge-sheet model. Consequently, the calculated drift mobility underestimates the actual (Hall) inversion layer mobility.

**MOS devices:** N-channel, poly-silicon gate MOSFETs were fabricated on 6H-SiC wafers using a non-self-aligned process. The starting Si-face wafers (from CREE Research) have a 10  $\mu\text{m}$  thick, lightly doped ( $\sim 3 \times 10^{15} / \text{cm}^3$ ) p-type epi over a heavily doped P<sup>+</sup> substrate. After a standard RCA clean, a 32 nm wet gate oxide was grown at 1100°C for 3 hours, followed by a wet re-oxidation at 950°C for 2.5 hours to obtain a low mid-gap  $D_{it}$  ( $\sim 1\text{-}3 \times 10^{11} \text{ traps/cm}^2\text{-eV}$ ) [1]. A thick ( $\sim 900 \text{ nm}$ ) SiO<sub>2</sub> layer is used for field isolation. Other details of the fabrication process are described elsewhere [6]. A typical MOS-

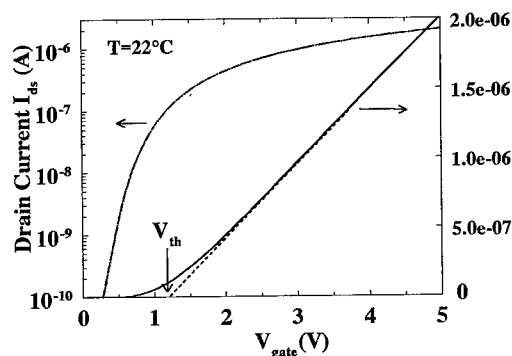


**Figure 1.** Drain current  $I_{ds}$  vs. gate voltage  $V_g$  for a typical large area ( $W/L=1$ ) 6H-SiC MOSFET.

FET drain current characteristic is shown in Fig. 1. The MOSFET threshold voltage  $V_{th}$  is low ( $\approx +0.5$  to  $+1.5$  V), junction leakage is negligible ( $<10$  pA), and the subthreshold slope is reasonably steep (100-150 mV/dec). Hall measurements were made on multiple wafers from three SiC MOS process lots. Hall parameters were measured as a function of  $V_g$  and temperature using MOS Hall bars. (Bar geometry is  $20\text{ }\mu\text{m} \times 162\text{ }\mu\text{m}$  with 2 voltage taps per side.) Values of the Hall mobility were extracted assuming a Hall scattering factor of 1.00 (supported by recent data [7]).

**Mobility and free carrier density:** Experimental mobility and free electron density data are shown in Fig. 2 as a function of  $V_g$  at 296K. To facilitate the mobility comparison, the "field effect" mobility (the incremental mobility associated with the change in electron density at each gate voltage) is shown for both Hall and drift data. The most striking feature of these data is that, for gate voltages just above threshold, the Hall mobility is substantially higher than the drift mobility. The maximum Hall mobility is  $\sim 100\text{ cm}^2/\text{V}\cdot\text{s}$ , which is  $\sim 50\%$  higher than the drift mobility for this particular sample. These results are representative of the best samples from several wafers. Although we have observed significant sample-to-sample variation in these values, the maximum Hall mobility was always considerably higher than the drift mobility.

The lower section in Fig. 2 shows the measured *change* in free electron density  $n_s$  (per volt change in  $V_g$ ) vs. the change predicted by the charge-sheet model [5]. These results show that at low  $V_g$  (i.e., just above threshold), the actual  $n_s$  is much smaller than predicted. Because the charge-sheet model is derived from electrostatics, the model correctly predicts the total number of electrons induced in the inversion layer. The difference between experiment and prediction is caused by electron trapping at the interface; i.e., many of the induced electrons are not free to contribute to the source-to-drain current. As  $V_g$  increases, Hall and drift mobilities gradually come into agreement, as does the experimental  $n_s$  with the charge-sheet model. This occurs because, in very strong inversion, the change in SiC surface potential with  $V_g$  becomes small, and so electron trapping tends to saturate.

**Trap density:** An estimate of the interface trap density  $D_{it}$  close to the conduction band edge  $E_c$  can be derived from the data in Fig. 2. The integral from  $V_g = V_{th}$  to  $+15$  V of the difference between the measured  $n_s$  and the predicted value gives the total number of trapped electrons. This equals  $1.56 \times 10^{12}\text{ e/cm}^2$ . We calculate that this change in  $V_g$  corresponds to a change in surface potential from  $-0.23$  to  $+0.06$  eV with respect to  $E_c$ . Thus the *average*  $D_{it}$  in this range is  $\sim 5.4 \times 10^{12}\text{ traps/cm}^2\cdot\text{eV}$ . This result is in good agreement with  $D_{it}$  values near  $E_c$  measured in the mid- $10^{12}$  range obtained using "low-frequency" C-V on a different chip from the same wafer [8].

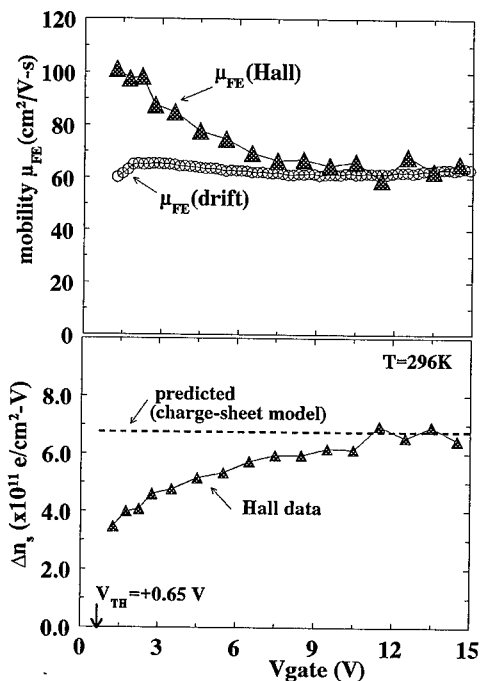


**Figure 2.** (upper) Comparison of field effect Hall and "drift" mobilities for a 6H-SiC MOS inversion layer vs. gate voltage. (lower) Change in Hall free electron density compared to predicted value from charge-sheet model.

**Temperature dependence:** The dependence of the free carrier density  $n_s$  on temperature and gate voltage above threshold is shown in Fig. 3. The predicted  $n_s$  from the charge-sheet model is shown by the dashed line. At low temperatures,  $n_s$  deviates most strongly from the model. At the highest temperature (473K), good agreement is obtained. This behavior can be understood from the fact that  $D_{it}$  has been shown to increase rapidly approaching  $E_c$  [8,9]. At low temperatures, inversion begins closer to  $E_c$  where  $D_{it}$  is high, causing a high level of electron trapping. Consequently,  $n_s$  is much lower than predicted by the model (which does not take trapping into account). On the other hand, at high temperatures, inversion begins closer to mid-gap where  $D_{it}$  is lower. Thus, electron trapping is reduced, and  $n_s$  is in better agreement with the model.

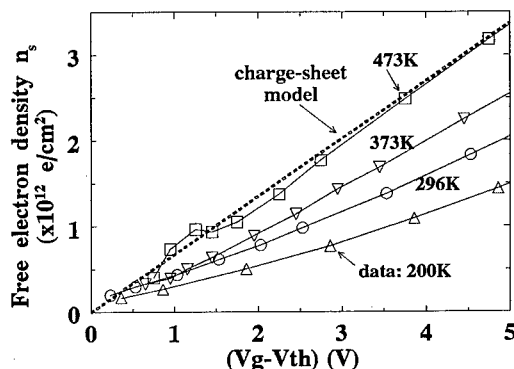


**Figure 3.** Dependence of free electron density (Hall data) on temperature and gate voltage above threshold.

The inversion layer mobility is also found to depend strongly on temperature. In Fig. 4, the maximum Hall mobility  $\mu_e$  (obtained at  $V_g \sim V_{th}$ ) is shown as a function of temperature for two samples: a "typical" sample (similar to the samples in Figs. 2-3), and a "high  $D_{it}$ " sample from a damaged wafer. For the "typical" sample at  $\sim 320K$  and above,  $\mu_e$  decreases approximately with  $T^{-2}$  (dashed line), which would be expected for lattice scattering. (The temperature dependence of the Hall mobility for an n-type epitaxial layer is  $\sim T^{-2.3}$  [10].) At low temperatures,  $\mu_e$  appears to saturate at  $\sim 110 \text{ cm}^2/\text{V-s}$ . The most likely cause of this saturation is increased scattering from trapped electrons, since more electrons are trapped at low temperatures. This interpretation is qualitatively supported by the results from the "high  $D_{it}$ " sample, where the saturation value for the Hall mobility is lower due to increased scattering from a higher density of trapped electrons.

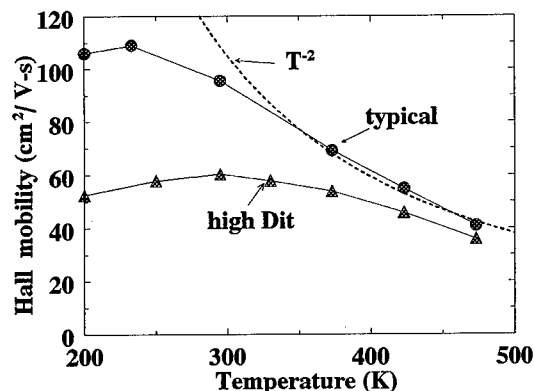


**Figure 4.** Temperature dependence of the Hall mobility for low and high  $D_{it}$  samples. Mobility values shown are the maximum values obtained just above threshold.

**Electric field dependence:** In Fig. 5, the effective Hall electron mobility at 295K of a typical 6H-SiC MOS sample is shown as a function of effective (average) electric field in the inversion layer. This is displayed as a ratio to the bulk mobility (using  $320 \text{ cm}^2/\text{V-s}$  [10]). For comparison, similar data from the literature is shown for silicon MOS devices [11,12]. The SiC data start at higher fields compared to the silicon data because the field at threshold is higher due to the wider bandgap of 6H-SiC (3.0 vs. 1.1 eV, respectively). For comparison, similar 6H-SiC MOSFET drift mobility data from the literature are also shown in Fig. 5 [1,3]. Results here show that the SiC mobility ratio approaches the ratio obtained in silicon at high fields, but the mobility is lower than expected (or hoped for) at lower fields.

In all MOS samples in Fig. 5, the mobility declines with increasing normal field due to surface (roughness) scattering. However, the SiC mobility appears less dependent on the field compared to silicon. The cause of this reduced field dependence in SiC is not clearly understood. However, this behavior does suggest that surface roughness scattering is not dominant even at high fields in the SiC samples, which would cause a stronger dependence of mobility on field strength [11]. Therefore, results in Figures 3 and 5 suggest that a higher mobility may be achieved in SiC if a lower interface trap density can be achieved.

**Summary:** In this paper, we report the first (to our knowledge) measurements of Hall mobility and free carrier density in 6H-SiC MOS inversion layers. The Hall mobility is typically found to be considerably larger than the mobility derived from the MOSFET transconductance. This occurs because the free carrier density in the inversion layer is lower than predicted by the charge-sheet model. This effect is almost certainly caused by trapping of inversion electrons at high densities of interface traps near the conduction band edge  $E_c$ . Electron trapping is found to increase at lower temperatures and decrease at higher temperatures. Both the high level of electron trapping, and its temperature dependence, are consistent with recent reports that  $D_{it}$  in SiC MOS devices increases rapidly as  $E_c$  is approached [7-9]. These results show that Hall experiments are clearly an invaluable tool to understand the behavior of inversion layers in SiC MOSFETs.

**Acknowledgements:** We thank the staff of the Northrop Grumman Corp. for sample fabrication and Dr. M. White and V. Vathulya (Lehigh U.) for growing the gate oxides. This work was partially supported by the Office of Naval Research.

#### References:

- [1] L. Lipkin and J. W. Palmour, *Mat. Sci. Forum* **264-4**, 853 (1998).
- [2] R. Schorner, P. Friedrichs, and D. Peters, *IEEE Trans. Electron Dev.* **46**, 533, Mar. (1999).
- [3] S. Srivedan and B. J. Baliga, *Mater. Sci. Forum*, **264-268(2)**, 997 (1998).
- [4] H. Yano, F. Katafuchi, T. Kimoto, and H. Matsunami, *IEEE Trans. Electron Dev.* **46**, 504, Mar. (1999).
- [5] E. Arnold, *IEEE Trans. Electron Dev.* **46**, 497, Mar. (1999).
- [6] N.S. Saks, S.S. Mani, A.K. Agarwal, and M.G. Ancona, *IEEE Electron Dev. Letts.* **20**, 431, Aug (1999).
- [7] G. Rutsch, R.P. Devaty, W.J. Choyke, D.W. Langer, and L.B. Rowland, *J. Appl. Phys.* **84**, 2062, Aug. (1998).
- [8] N. S. Saks, A. K. Agarwal, and S. S. Mani, presented at ICSCRM'99, p. 1113
- [9] V.V. Afanasev, M. Bassler, G. Pensl, and M. Schulz, *Phys. Stat. Sol. (a)* **162**, 321 (1997).
- [10] W. Suttrop, G. Pensl, W.J. Choyke, R. Stein, and S. Leibenzeder, *J. Appl. Phys.* **72**, 3708, Oct. (1992).
- [11] S.C. Sun and J.D. Plummer, *IEEE Trans. Electron Dev.* **ED-27**, 1497, Aug. (1980).
- [12] J.S. Cable and J. Woo, *IEEE Trans. Electron Dev.* **39**, 607, Mar. (1992).

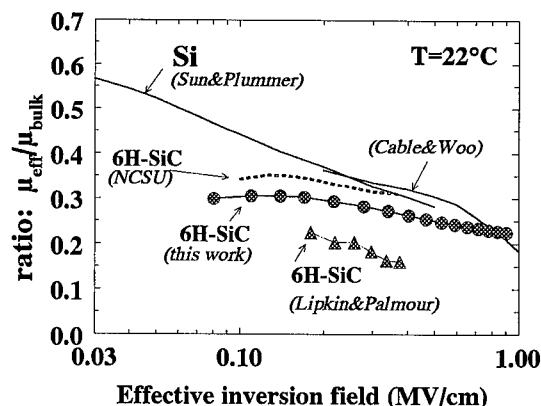


**Figure 5.** Ratio of SiC Hall electron inversion mobility to the bulk mobility, as a function of effective normal electric field in the inversion layer. Results here are compared with previous 6H-SiC and silicon data (for drift mobility).

## **Application and Improvement of the Spreading Resistance Method for p-type 6H-SiC**

T. Gebel<sup>1</sup>, D. Panknin<sup>1</sup>, R. Riehn<sup>1,2</sup>, S. Parascandola<sup>1</sup> and W. Skorupa<sup>1</sup>

<sup>1</sup> Institut für Ionenstrahlphysik und Materialforschung, Forschungszentrum Rossendorf,  
PO Box 510119, DE-01314 Dresden, Germany

<sup>2</sup> Cavendish Laboratory, University of Cambridge, Madingley Road, Cambridge, CB3 0HE, UK

**Keywords:** Contact Barrier, Ion Sputtering, Metal-Semiconductor Contact, Spreading Resistance, Surface States

### **Abstract**

Spreading resistance (SR) measurements on Al implanted 6H-SiC samples have been carried out after different surface treatments. Methods like polishing with diamond emulsion, annealing steps and ion sputtering of the surface have been used. After surface sputtering with 2 keV Ar<sup>+</sup> ions the measured resistance was reduced more than one order of magnitude compared to measurements after beveling. The measured profiles are discussed in correlation to SIMS profiles.

### **1. Introduction**

Since the end of the 1960's spreading resistance measurements have become a routinely used technique for determining charge carrier profiles in silicon. For wide band gap semiconductors however the application of this method is difficult because of the high contact barrier at the interface between the probe tips and the semiconductor surface. The measured resistance is strongly dominated by the contact resistance.

A strong dependence of the spreading resistance (SR) values on the material and its grain size used for beveling and polishing was reported for the wide band gap semiconductor GaAs [1]. For laser annealed 6H-SiC [2] and for 3C-SiC [3] SR measurements have been reported. The used measuring voltages were relatively high (1 to 5 V) compared to usual measurements on Si (10 mV). Ahmed et al. [2] found an electric activation of more than 100% which points to problems in the interpretation of the measurement.

If a SR system designed for measurements on silicon with a fixed voltage is used, two different approaches are possible in order to lower the contact barrier. First, the material of the tips could be changed with respect to its work function. However, this choice is limited because of the required mechanical properties of the tips concerning high hardness and low brittleness. The other way is to lower the barrier by influencing the surface states of the semiconductor material. This is actually more promising.

The present study is devoted to the use of several methods for surface treatment. The influence of polishing with diamond emulsion, further annealing of the bevel and finally sputter cleaning on the SR measurements was investigated.

## 2. Experimental

CREE 6H-SiC (n – type, epi – layer, 5  $\mu\text{m}$  thick) of research grade quality has been used. The samples were produced by implantation at RT and 400°C with  $\text{Al}^+$  ions at multiple energies of 450, 240, 115 and 50 keV to form a 500 nm thick homogeneously doped layer. The achieved plateau concentrations were in the range of  $5 \cdot 10^{19}$  to  $5 \cdot 10^{21} \text{ cm}^{-3}$ .

Various post annealing processes have been performed to cover a broad range of resistivities (0.01 .. 3  $\Omega\text{cm}$ ) with the samples. Furnace annealing was carried out at temperatures from 1500 to 1750°C for 10 min and flash lamp annealing at 2000°C for 20 ms. Resistivities were obtained from Hall measurements [4].

The 6H-SiC - surface was beveled with a diamond emulsion on a rotating glass plate. Grain sizes of 1.0  $\mu\text{m}$  and 0.1  $\mu\text{m}$  were used. The bevel angle was in the range 0.1 .. 0.5 °.

After beveling several of the samples were thermally treated or sputtered by means of  $\text{Ar}^+$  ions. Thermal treatment was carried out under vacuum for 5 min at temperatures of 1300 to 1400°C. Ion sputtering of the bevel was performed using  $\text{Ar}^+$  ions with an energy of 2 keV at a current density of  $50 \mu\text{Acm}^{-2}$  for 300 s. During the process the temperature of the sample was about 60 °C and the sputtering rate about 0.03 nm/s.

For SR profiling a SENTECH SR-210 device was used. The probe tips were made of sintered tungsten carbide with a tip radius of 5  $\mu\text{m}$ . The measuring voltage was kept constant at 10 mV allowing to measure resistance values up to 1 G $\Omega$ . The highest spatial resolution of the apparatus was 5 nm and the probe tip load during the measurements 0.09 N.

## 3. Results and Discussion

It was found that polishing with diamond emulsion of smaller grain size (0.1  $\mu\text{m}$ ) leads to lower resistances than for 1.0  $\mu\text{m}$  grains. This behavior is comparable to the results which are known for p-type GaAs with  $\text{Al}_2\text{O}_3$  emulsion from Ref. [1].

After thermal treatments following the polishing a thin graphite layer (about 1 nm thick) at the surface was detected by means of AES. This layer caused a decrease of the barrier resistance. The measured resistance was lowered up to a factor of three. Statistical variations however increased.

The influence of ion sputtering ( $\text{Ar}^+$ , 2 keV) on the bevel before the measuring procedure was studied. Compared to measurements after beveling SR measurements after sputtering showed a more than one order of magnitude lower resistance (Fig. 1). The shape of the preserved depth profile after sputtering remained comparable to that of polished surfaces. The statistical error of the measured resistances dropped significantly. For depth regions below 700 nm measurements on the beveled surface exceed the measuring range of 1 G $\Omega$ , whereas the sputtered samples give values of about  $10^8 \Omega$ .

In Fig. 1 also the Al – distribution measured by SIMS is presented. The range of the SR profile with lower resistances agrees with the plateau of the SIMS profile. Minimum resistance values occur at the maxima of the SIMS profile.

Samples with resistivities larger than 0.2  $\Omega\text{cm}$  had not been measurable after beveling but after subsequent sputtering. The resistivity range in which SR measurements can be carried out was extended to 3  $\Omega\text{cm}$ . Our investigations of SR depth profiles using this sputtering method show a very good reproducibility at remarkably small variations of the measured values.

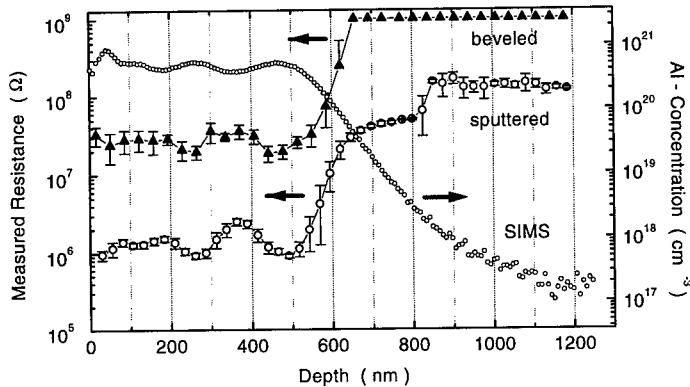


Fig. 1:

Depth profile of measured resistance after polishing and after sputtering compared to the Al - concentration determined by SIMS (plateau Al concentration  $5 \cdot 10^{20} \text{ cm}^{-3}$ ).

In Fig. 2 SR profiles of samples with a plateau Al concentration of  $5 \cdot 10^{20} \text{ cm}^{-3}$  are compared. Implantation and annealing conditions have been varied. Before the SR measurements a sputtering procedure of the surface was carried out. The sample implanted at RT shows a relatively smooth profile and no distinctive structures in contrary to those implanted at  $400^\circ\text{C}$ . This can be explained by the amorphization due to implantation at RT and the formation of a polycrystalline microstructure during the annealing process. This can lead on one hand to an enhanced diffusion of the dopants and hence to a smoothing of the profile. On the other hand the presence of semiconducting SiC grains separated by highly conductive Al-rich grain boundaries can induce different spreading conditions compared to monocrystalline material.

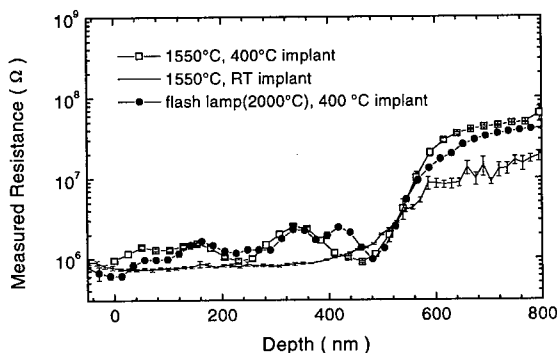


Fig. 2:

Depth profile of measured resistance after sputtering (for a plateau Al concentration of  $5 \cdot 10^{20} \text{ cm}^{-3}$  after different annealing of the samples)

The influence of the sputtering damage was tested with an ion beam which was focused to a diameter of about 2.5 mm. This size of the ion beam leads to a certain degrees of inhomogeneity of the sputtering damage. The bevel area was scanned by multiple SR depth profiling. Using a sample implanted with a mean concentration of  $5 \cdot 10^{19} \text{ cm}^{-3}$  after beveling the measured resistances were found to be above the limit of  $1 \text{ G}\Omega$ . Therefore no SR - profile could be determined. However, after sputtering the influenced area showed reduced resistances. In the upper part of Fig. 3 a two dimensional SR scan of the bevel is shown. The x - coordinate represents the length of the sample, the y - coordinate the length of the bevel which gives the information about depth. This experiment gives the evidence that this kind of surface treatment does only influence the barrier. If the measuring effect would only be caused by sputtering, the resistances in y - direction should be of the same value over the whole sputter crater because of the ratio between the x and y - scale which is about 40. The results however only show a profile up to the typical depth of about 600 nm.

The diagram in Fig. 3 below the scan shows a cross section through the sputtered region parallel to the edge of the bevel. One can see clearly the influenced region and the dependency of the sputtering damage on the edges of the sputtered area.

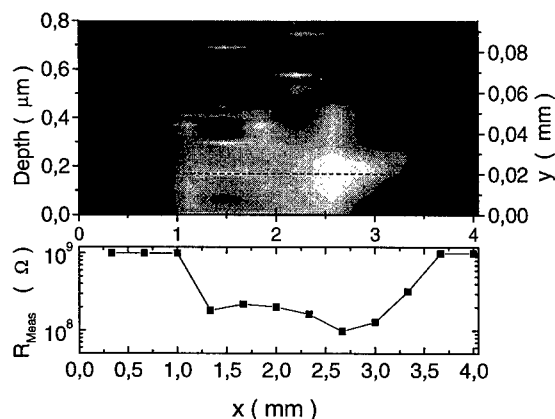


Fig. 3: Spreading resistance scan over sample with a sputter crater of about 2 mm diameter. Brighter colors are related to lower resistances. Areas around the sputter crater showed no measurable effect. The plot below the scan presents a cross-section of the profile parallel to the edge of the bevel.

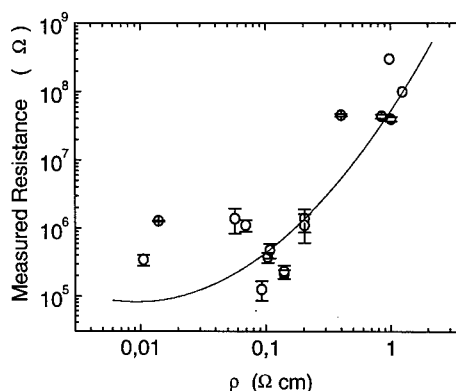


Fig. 4: Measured resistance after sputtering of the surface vs. resistivity. The  $\rho$  - values have been obtained by Hall measurements.

A first calibration of the measured resistance to the resistivity of the samples is plotted in Fig. 4. The used SR values characterize the mean resistance in the homogeneously doped layer. Resistivities of the doped layers have been determined by Hall measurements. The SR method combined with surface sputtering can cover a resistivity range up to 3  $\Omega\text{cm}$ . The variation of the calibration data could have been induced by the differences of the samples preparation concerning implantation and annealing conditions, which was also visible in Fig 2.

#### 4. Conclusion

SR depth profiles of  $\text{Al}^+$  implanted 6H-SiC have been obtained using a standard SR system for measurements on silicon. After surface polishing with diamond emulsion (0.1  $\mu\text{m}$ ) further thermal treatments of the surface lead to a decrease of the resistance of a factor of three. Ion sputtering of the surface using 2 keV  $\text{Ar}^+$  ions resulted in a lowering of the measured resistance of more than one order of magnitude. This can be explained by a lowering of the contact barrier due to the generation of surface states. Due to optimization of the sputtering process the measuring range should be extendible. Further measurements with well defined prepared samples are necessary to improve the calibration curve. To obtain charge carrier profiles calibration data from Hall measurements have to be used.

#### References

- [1] G. Queirolo, J. Electrochem. Soc., **125** (10) (1978), 1672.
- [2] S. Ahmed, C.J. Barbero and T.W. Sigmon, Appl. Phys. Lett. **66** (6) (1995), 712.
- [3] J. A. Edmond, S.P. Withrow, W. Wadlin, R.F. Davis, Mat. Res. Soc., **77** (1987), 193.
- [4] D. Panknin, H. Wirth, M. Mücklich, W. Skorupa, Mat. Sci. Engin. B61-62 (1999), 363.



## Theoretical Study of Carrier Freeze-Out Effects on Admittance Spectroscopy and Frequency-Dependent C-V Measurements in SiC

Andrei V. Los, Michael S. Mazzola and Stephen E. Saddow

Emerging Materials Research Laboratory, Department of Electrical & Computer Engineering,  
Mississippi State University, Mississippi State, MS 39762-9571, USA

**Keywords:** Differential Admittance, Frequency Dependence, Nitrogen Donor, Schottky Junction

### Abstract.

We present a theoretical model beyond the small-signal approximation for Schottky junction differential admittance for the general case of an arbitrary temperature, measurement signal frequency and amplitude, and doping occupation number. Shockley-Read-Hall statistics, an equilibrium nondegenerate free carrier distribution, a uniform impurity concentration, and a negligible minority carrier concentration are assumed. To show the influence of the carrier freeze-out effects we calculate the frequency dependence of a Schottky junction capacitance for the case of N-doped SiC. We compare results of calculations using the new model and models based on the truncated space charge approximation and small-signal approximation.

### Background.

It has been recognized for a while that deep levels can significantly affect the ac admittance of semiconductor junctions and introduce errors in the doping profiles extracted from capacitance-voltage data [1]. The reason for this is that the interpretation usually used with the differential admittance method relies on the assumption that the doping impurity is fully ionized throughout the semiconductor. The depletion region charge change in response to the applied ac measurement signal is then due only to the movement of free carriers at the depletion region boundary, and the concentration of free carriers in the semiconductor bulk is equal to the net doping concentration. If the semiconductor contains an impurity which is in a partial carrier freeze-out, not only the above assumption of the equality of the free carrier concentration and the net doping concentration becomes invalid, but also an additional error can be introduced in the measured junction admittance due to the impurity level occupation number change because of the level movement with respect to the Fermi level by the applied ac measurement signal. If the capture and emission rate of the impurity is low relative to the measurement signal frequency, its charging-discharging lags the ac signal and additional junction admittance contains a nonzero conduction component. This fact is the basis of the admittance spectroscopy technique. In SiC the common dopants, such as N, Al, and B, have energy levels which can be in a partial freeze-out even at room temperature, and therefore are subject to the investigation of their influence on the junction capacitance and conductance behavior.

The approaches commonly used to study the influence of deep levels on the semiconductor junction admittance are usually based on the truncated space charge approximation [2,3] and/or the small-signal approximation [4]. The former describes the situation adequately only if the Fermi level intersects the impurity level somewhere in the depletion region, but becomes inapplicable if the Fermi level is below the impurity level in the bulk. The latter can fail if the measurement signal amplitude is larger than  $k_B T/q$ , where  $k_B$  is the Boltzmann constant,  $T$  is temperature, and  $q$  is the electron charge. This may be true, for example, for a typical measurement signal of 30 mV rms, particularly for below room temperature measurements.

### Model.

The purpose of this study is to determine the influence of carrier freeze-out effects on Schottky junction differential admittance for the case of an arbitrary temperature, measurement signal frequency and amplitude, doping occupation number distribution, and constant doping concentration. The differential admittance of a Schottky junction per unit area is the ratio of ac current density to applied ac voltage. Taking into account that current is the same at all points of the circuit, that impedance meters filter out all harmonics of the current but the first one, and using Gauss's law we obtain the following expression for the junction admittance per unit area [4]

$$Y = -i\omega\epsilon \left( \frac{1}{\phi_1} \frac{d\phi_1}{dx} \right)_{x=0}, \quad (1)$$

where  $\omega$  is the measurement signal circular frequency,  $\epsilon$  is the semiconductor permittivity,  $\phi_1$  is the amplitude of the fundamental of the ac band potential with respect to the bulk potential, and the point  $x = 0$  corresponds to the semiconductor surface.

To find the band potential  $\phi(x)$  we need to solve the Poisson's equation  $\frac{d^2\phi}{dx^2} = -\frac{\rho}{\epsilon}$ , where  $\rho$  is the charge density. We assume a single Shockley-Read-Hall donor level. The relaxation time of the free carrier distribution is very short compared to the typical measurement frequency period [5], so we can assume that the free carriers are always in thermal equilibrium among themselves. Then for an ideal Schottky diode under a reverse or small forward bias the continuity equation contains only generation-recombination terms. For a wide-bandgap semiconductor we can neglect interaction of the donor level with the valence band. The generation-recombination equation then becomes

$$\frac{\partial N^+}{\partial t} = e_n(N - N^+) - C_n n N^+, \quad (2)$$

where  $e_n$  is the emission coefficient,  $C_n$  is the capture coefficient,  $N$  is the concentration of donors,  $N^+$  is the concentration of ionized donors, and  $n$  is the free carrier concentration. In a nondegenerate case  $n$  can be written as  $n = N_c e^{(\mu - E_c)/\beta} = n_0 e^{-\phi/\beta}$ , where  $\mu$  is the Fermi level,  $E_c$  is the conduction band edge energy,  $N_c$  is the effective density of states near the conduction band minimum,  $\beta = k_B T / q$ , and  $n_0$  is the free carrier concentration in the bulk.

We now note that for an arbitrary periodic potential  $\phi$  the junction will be in a steady state on average, and the free carrier concentration and the donor occupation number will be periodic. All these quantities can be expressed in a Fourier series form:  $N^+ = N_0^+ \sum_{k=-\infty}^{\infty} a_k e^{ik\omega t}$ ,  $\phi = \beta \sum_{k=-\infty}^{\infty} c_k e^{ik\omega t}$ ,

$n = n_0 \sum_{k=-\infty}^{\infty} b_k e^{ik\omega t}$ , where  $N_0^+$  is the concentration of ionized donors in the bulk. Substituting the

Fourier expansions in (2) and taking into account that exponential terms of different order are linearly independent, the generation-recombination equation is transformed into the system of linear equations for  $a_k$

$$\begin{cases} a_k (i\omega k + \tau^{-1}) + C_n n_0 \sum_{\substack{m=-\infty \\ m \neq k}}^{\infty} a_m b_{k-m} = 0, k \neq 0, \\ a_0 \tau^{-1} + C_n n_0 \sum_{\substack{m=-\infty \\ m \neq 0}}^{\infty} a_m b_{-m} = e_n \frac{N}{N_0^+} \end{cases} \quad (3)$$

where  $\tau^{-1} = e_n + C_n n_0 b_0$ . For a small sinusoidal measurement signal with amplitude  $V_M \ll \beta$  all  $a_k$  and  $b_k$  with  $|k| > 1$  vanish. In the limit  $|c_1| \rightarrow 0$ , we have  $|a_1| \rightarrow 0$ ,  $|b_1| \rightarrow 0$ , and the equation for  $a_0$  reduces to

$$e_n(N - a_0 N_0^+) - C_n b_0 n_0 a_0 N_0^+ = 0.$$

Here  $b_0 n_0$  is the steady state free carrier concentration,  $a_0 N_0^+$  is the steady state ionized donor concentration, and this equation expresses the fact that in the above limit the system must tend to the steady state with the capture and emission processes equalizing each other. In the small-signal case  $V_M \ll \beta$  the solution for the fundamental of the potential  $\phi$  reduces to the solution given in [4].

Using the Fourier expansions for  $N^+$ ,  $n$  and  $\phi$  the Poisson's equation can be transformed into the following system of differential equations for  $c_l$

$$\frac{d^2 c_l}{dx^2} = -\frac{q}{\epsilon \beta} (N_0^+ a_l - n_0 b_l), \quad l = 0, 1, 2, \dots \quad (4)$$

This is a two-point second order boundary-value problem for  $c_l$ , which should be solved numerically. The boundary conditions are

$$\begin{aligned} c_0(0) &= (V_B - V_A)/\beta, \quad c_1(0) = V_M/\beta, \\ c_l(0) &= 0, \quad |l| > 1, \\ c_l(\infty) &= 0, \quad l = 0, 1, 2, \dots \end{aligned} \quad (5)$$

where  $V_B$  is the junction built-in potential,  $V_A$  is the applied dc bias, and  $V_M$  is the ac measurement signal amplitude.

## Results and discussion.

We solve the system of equations (4) together with (3) and (5) to investigate the frequency dependence of SiC Schottky junction differential capacitance. The simulations were performed for room temperature, zero applied bias and the ac measurement signal amplitude of 42.4 mV (30 mV rms). In the simulations we used the values of activation energy  $E_A$  of 0.085 eV and 0.14 eV. The former approximately corresponds to the activation energy of nitrogen donor at the hexagonal site in 6H-SiC or at the quasicubic site in 4H-SiC. The latter corresponds to the N donor at two quasicubic sites in 6H-SiC [6]. Because of some uncertainty in the published values of the electron capture cross-section  $\sigma$  we used the values in the range  $5 \cdot 10^{-18}$ – $5 \cdot 10^{-17}$  cm<sup>2</sup> [7]. The following expressions were used for the capture and emission coefficients:  $C_n = \sigma v_{th}$ ,  $e_n = C_n N_c e^{-E_A/k_B T}$ , where  $v_{th}$  is the electron thermal velocity, and  $N_c = 4.06 \cdot 10^{15} T^{3/2}$  cm<sup>-3</sup> [6].

Fig. 1 (a) and (b) represent the calculated frequency dependencies. At low frequencies the change in depletion region charge is caused by the free carrier sweep-out and donor ionization at the space-charge region boundary. The concentration of free charge removed from the depletion region approximately equals the free carrier concentration in the bulk, and the concentration of additionally ionized charge approximately equals the non-ionized (neutral) impurity concentration in the bulk. Thus the low-frequency capacitance corresponds to the capacitance of a fully ionized semiconductor. At high frequencies the impurity occupation number changes little over one ac signal period, and thus the capacitance value principally carries information about the free carrier concentration in the semiconductor bulk.

Notice from the plots that the capacitance change is larger at higher doping levels, which is explained by the greater degree of donor freeze-out in a more heavily doped material. An increase in the donor capture and emission rates at higher values of the capture cross-section and higher doping levels (resulting in higher free carrier concentration) leads to the shift of the region of capacitance change to higher frequencies. For a more shallow level (Fig. 1 (b)) the degree of carrier freeze-out is smaller and the free carrier concentration is larger, so the capacitance change is smaller and occurs at higher frequencies. In the limit  $E_A \rightarrow 0$  the commonly used extrinsic semiconductor conditions are recovered.

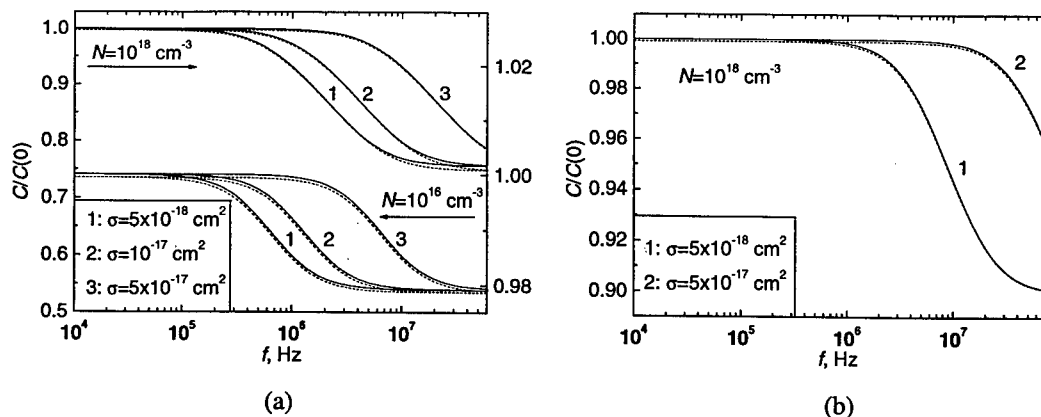


Fig. 1. Schottky junction capacitance as a function of measurement signal frequency normalized by the low frequency value. (a)  $E_A = 0.14 \text{ eV}$  and (b)  $E_A = 0.085 \text{ eV}$ . Dashed line is the small-signal capacitance.

For comparison we have calculated the capacitance frequency dependencies using the small-signal approximation based model [4] (dashed lines in Fig. 1). Since the applied ac signal amplitude used in the calculations was approximately equal to  $k_B T/q$ , the value of the fundamental of the potential  $\phi$  near the boundary of the space-charge region, where ionization of the impurity by the ac signal takes place, is small. Therefore in this case the small-signal approximation does not introduce large error in the calculated junction admittance. The error becomes noticeable for larger (with respect to  $k_B T/q$ ) ac signal amplitudes.

Another comparison was made with a simple truncated space charge approximation based model [3], which is commonly used for interpretation of the admittance spectroscopy data. Frequency dependencies calculated using this model exhibit capacitance changes of several orders of magnitude which occur at frequencies which differ somewhat from those predicted by more accurate models. Therefore using this model for accurate interpretation or simulation of the capacitance-frequency dependencies will lead to an error.

In conclusion we note that at some values of the semiconductor parameters and at typical measurement frequencies even nitrogen-doped silicon-carbide semiconductor materials (nitrogen is the most shallow of the commonly used SiC dopants) produce device capacitances from which incorrect doping information may be estimated due to carrier freeze-out effects. One can expect that for deeper dopants, such as aluminum and boron acceptors, this error will be even more pronounced.

### Acknowledgements

The authors thank Dr. Y. Koshka for stimulating discussions. This work was supported by the Office of Naval Research, Grant No. N0014-98-1-0824, Dr. C. Wood program manager.

### References

- [1] G. I. Roberts and C. R. Crowell, *J. Appl. Phys.*, **41** (1970), p. 1767, and references cited therein.
- [2] W. G. Oldham and S. S. Naik, *Solid-State Electron.*, **15** (1972), p. 1085.
- [3] G. Vincent, D. Bois, and P. Pinard, *J. Appl. Phys.*, **46** (1975), p. 5173.
- [4] D. L. Losee, *J. Appl. Phys.*, **46** (1975), p. 2204.
- [5] W. Shockley, *Bell System Tech. J.*, **28** (1949), p. 435.
- [6] S. R. Smith, A. O. Evwaraye, and W. C. Mitchel, *phys. stat. sol.*, **162** (1997), p. 227.
- [7] A. O. Evwaraye, S. R. Smith, and W. C. Mitchel, *J. Appl. Phys.*, **75** (1994), p. 3472.

## On the Existence of Deep Levels of the Acceptors Ga and In and of the Potential Double Acceptors Zn and Cd in SiC

N. Achtziger<sup>1</sup>, J. Grillenberger<sup>1</sup>, M. Uhrmacher<sup>2</sup> and W. Witthuhn<sup>1</sup>

<sup>1</sup> Institut für Festkörperphysik, Friedrich Schiller Universität Jena,  
Max-Wien-Platz 1, DE-07743 Jena, Germany

<sup>2</sup> II. Physikalisches Institut, Universität Göttingen, DE-37073 Göttingen, Germany

**Keywords:** Acceptors, D-Center, Deep Levels, Double Acceptor, Radiotracer

**Abstract:** Deep levels of the group II and III elements Zn, Ga, Cd, and In are investigated. By using radioactive impurities as a tracer, the assignment between a band gap state and a certain element is either established or ruled out definitely. By means of Deep Level Transient Spectroscopy on p-type SiC, one Zn- and two Cd-related band gap states are identified. In contrast to proposals based on magnetic resonance experiments, there is no deep level of the group III elements Ga and In in the lower part of the band gap. In particular, these elements do not contribute to the formation of the known D-center.

### Introduction

For the group-III acceptor boron, two sites in SiC are well established [1]: a Si-substitutional site acting as an acceptor and being used as p-type dopant [2] as well as a boron-vacancy complex creating a deep level, termed D-center. For other acceptors of this group, Al and Ga, magnetic resonance experiments [3] reveal many similarities to boron. Consequently, a scenario similar to boron has also been proposed for Al and Ga, but for these elements only the ordinary shallow acceptor state has been observed up to now. Eventually, the proposed, hypothetical deep level of these elements might roughly coincide with boron's D-center and might thus be misinterpreted as B-related since B is omnipresent in SiC.

To clarify the existence of deep states of group-III elements, we performed radiotracer-DLTS (Deep Level Transient Spectroscopy) experiments on group III-acceptors. Since there is no radioactive isotope of Al with a reasonable half-life ( $T_{1/2}$ ) available, we used the nuclear transmutations  $^{67}\text{Ga} \rightarrow ^{67}\text{Zn}$  ( $T_{1/2} = 3.25$  d) [4] and  $^{111}\text{In} \rightarrow ^{111}\text{Cd}$  ( $T_{1/2} = 2.83$  d). Due to the nuclear decay, the concentration of any level correlated with one of these elements will clearly be identified [5] by a characteristic decrease or increase of concentration in the course of subsequent measurements, no matter whether there is a chance coincidence with other levels or not.

We'd like to remark that we do not treat shallow levels here. The expected shallow acceptor levels of the group III elements are not detected in the present DLTS experiments due to the general restrictions of this technique. In contrast to In, the shallow Ga level is already known [6].

### Experiments

The experiments were done on commercial p-type epilayers of 4H and 6H-SiC on  $p^+$  substrates. Doping with  $^{67}\text{Ga}$  was done by recoil implantation [7] using the nuclear reaction  $^{66}\text{Zn}(d,n)^{67}\text{Ga}$ . This technique has already been used for radiotracer DLTS on other elements in SiC [8]. The radioactive isotope  $^{67}\text{Ga}$  is implanted with a broad energy distribution up to 0.7 MeV and a rather low fluence of  $3 \times 10^{10} \text{ cm}^{-2}$ . Inevitably, there is also a co-implantation of stable Zn with fluence and energy in similar order of magnitude. Because of the low fluence, experiments were done on lightly doped epitaxial layers with a net doping of  $3 \times 10^{15} \text{ cm}^{-3}$ . Though cut from a nominally 4H wafer, all samples turned out to be of the polytype 6H as determined by Raman Spectroscopy.

Doping with  $^{111}\text{In}$  was done by standard ion implantation (400 keV)[9] of commercially available  $^{111}\text{In}$ . Due to the much higher fluence ( $\approx 10^{12} \text{ cm}^{-2}$ ), more heavily doped samples with a p-type doping level of  $2 \times 10^{17} \text{ cm}^{-3}$  were used in addition to the doping level described above. In the case of  $^{111}\text{In}$ , all samples were of the polytype 4H.

The samples were annealed for 5 min. in argon at 1900 K and subsequently oxidized in  $\text{O}_2$  at 1600 K for 1-2 h. After oxide removal, Schottky diodes were prepared by evaporation of Ti dots (0.5 mm dia.) onto the epilayer and large area Al-contacts on the substrate. The number of radioactive isotopes remaining in the sample during the preparation process was checked by  $\gamma$ -ray spectroscopy. DLTS spectra were taken repeatedly on a time scale of several days.

The time zero is set to the annealing process. The DLTS system used is described elsewhere [8]; capacitance transients were digitally recorded within time windows of 5 ms, 100 ms, and 2 s. In the spectra shown, the peak positions correspond to a reference time constant of 44 ms.

#### Transmutation $^{67}\text{Ga} \rightarrow \text{Zn}$

The DLTS spectra of  $^{67}\text{Ga}$  doped samples (Fig. 1) exhibit one peak labeled Zn that is increasing during the elemental transmutation as shown in Fig. 1. This peak corresponds to a deep level at  $E_{\text{Zn}} = E_{\text{v}} + 1.16(2) \text{ eV}$  ( $E_{\text{v}}$  denotes the valence band edge) with a capture cross section of  $\sigma = 10^{-14} \text{ cm}^2$ . Further details, in particular the time dependence of the peak height, as well as spectra from similar samples can be found in Ref.[4]. The hole emission rate from this Zn level does not depend on the electrical field strength [4].

#### Transmutation $^{111}\text{In} \rightarrow \text{Cd}$

During this transmutation, the DLTS spectra exhibit two strongly increasing peaks labeled Cd1 and Cd2 as shown in Figs. 2 and 3. The sample shown in Fig. 2 has a rather high  $^{111}\text{In}$  concentration compared to the shallow doping level. As a consequence, the capacitance of the diode is changing as well, i.e. some of the changes observed are an indirect effect. This applies to the relatively small signal changes at 215 K, 280 K, and 430 K (Fig. 2) that are not correlated with the nuclear half life. The peak at 280 K corresponds to a deep level at  $E_{\text{v}} + 0.67 \text{ eV}$ ; it is present in as-grown samples as well and is interpreted as the known D-center. The peaks Cd1 and Cd2 are increasing with a time dependence expected for the Cd daughter element. The relative height of the two peaks strongly depends on DLTS measuring parameters (pulse bias, time window). This may be understood by the inhomogeneous depth distribution and the high concentration (maximum  $10^{17} \text{ cm}^{-3}$ ) of the implanted radiotracer isotope. These difficulties prevent a quantitative statement about the concentration ratio of the two Cd related levels. In the opposite case (Fig. 3) of a sample with higher initial p-type doping level and with smaller  $^{111}\text{In}$  concentration (due to out-diffusion during annealing), the capacitance remains constant and is hardly temperature dependent (not shown). Peak Cd2 is superimposed on a negative DLTS signal, whose origin is not understood. From the magnitude of the peak height changes, we derive a concentration ratio between Cd1 and Cd2 of 1:1 with an error of 30 %. The degree of electrical activation, i.e. concentration the ratio of

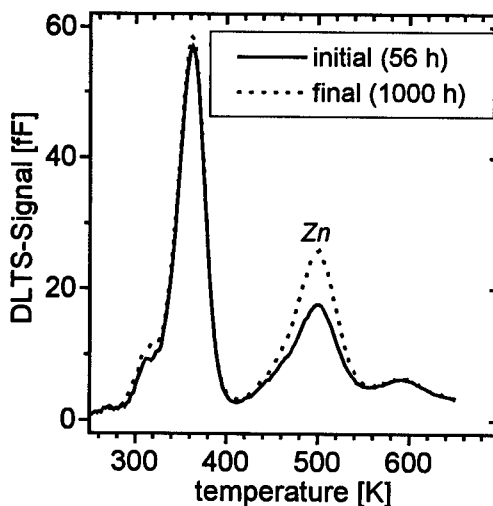


Fig.1: DLTS spectra of p-type 6H-SiC measured subsequently during the transmutation of  $^{67}\text{Ga}$  to Zn.

Cd-related gap states to Cd daughter atoms, is on the order of unity.

For both types of samples, the deep level parameters obtained for the Cd-related levels are the same:

$$\begin{array}{lll} \text{level Cd1} & E_{\text{Cd1}} = E_v + 0.90(3) \text{ eV} & \sigma = 2 \times 10^{-14} \text{ cm}^2 \\ \text{level Cd1} & E_{\text{Cd2}} = E_v + 1.19(4) \text{ eV} & \sigma = 2 \times 10^{-16} \text{ cm}^2 \end{array}$$

The dependence of the emission time constant on the electrical field strength was investigated by variation of the reverse bias voltage  $U_R$  (Fig. 4). To keep the probed depth region constant and to avoid non-exponential transients (due to the high Cd concentration, sample similar to the one shown in Fig. 2), we used isothermal Constant-Capacitance (CC-)DLTS. By forming differences between spectra taken with different pulse voltages, an identical depth interval is selected to rule out effects due to the inhomogeneous depth distribution. There is a small peak shift by less than a factor of 2 for the Cd1 peak and no effect for the Cd2 peak.

### Discussion

For both transmutations investigated, band gap states with a concentration increasing as expected for the daughter element are observed. Since we do not expect the production of decay induced defects because of the low recoil energies of the daughter elements (6.6 eV for  $^{67}\text{Zn}$ , 0.9 eV for  $^{111}\text{Cd}$ ) [10], this finding provides an unambiguous chemical identification of these states

with defects that either contain or are identical to one atom of Zn or Cd. Because of the identical concentration of the two Cd states, it is suggesting to interpret them as two charge states of one configuration. This possibility well corresponds to the expectation that a group II element in a group IV semiconductor should be a double acceptor. In this case, the center would be charged and the hole emission should become

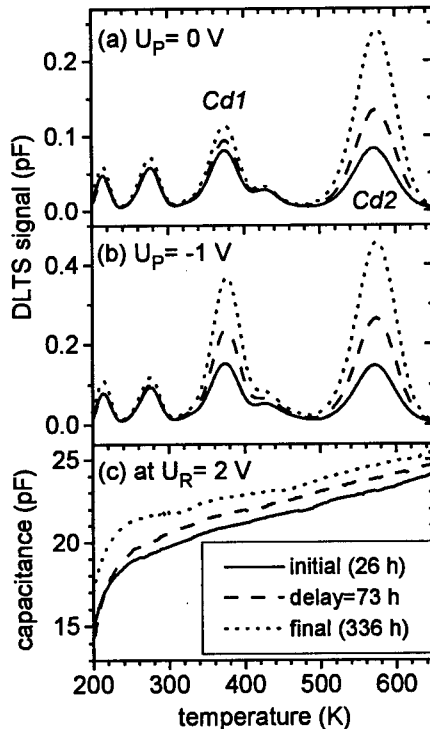


Fig.2: DLTS spectra (a,b) and capacitance (c) at a reverse bias of  $U_R = 2$  V measured during the transmutation of  $^{111}\text{In}$  to Cd in p-type SiC. Figs. (a) and (b) are measured with zero and forward pulse voltages ( $U_P$ ), respectively.

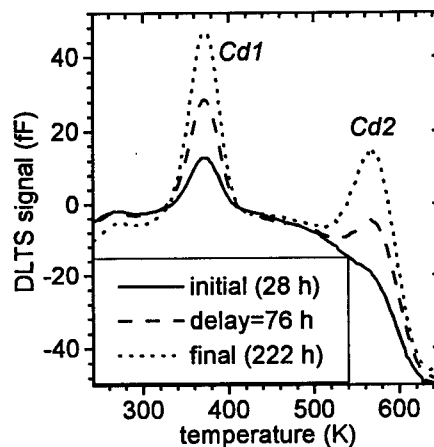


Fig.3: DLTS spectra of p-type SiC measured subsequently during the transmutation of  $^{111}\text{In}$  to Cd. Voltages are  $U_R = 2$  V and  $U_P = 0$  V.

faster (Poole-Frenkel effect) with increasing electric field strength. According to theory [11], the peaks Cd1 and Cd2 should shift by a factor of 3 and 2, respectively, in our experiments. The experimental effect, however, is either smaller or completely absent.

Concerning deep states of group III elements, our experiments do not provide any evidence for their existence. To make this statement meaningful, the experimental detection limits have to be discussed: Regarding the energy scale, our measurements are sensitive to any deep level emitting holes with a time constant between 1 ms and 2 s in the temperature range from about 250 K (freeze-out) and 650 K. Assuming a capture cross section in the range of  $[10^{-17}; 10^{-14}] \text{ cm}^2$ , this corresponds to an energy interval of, at least, [0.5; 1.4 eV] above  $E_V$ . Regarding concentration, the detection limit is 6% of all implanted radioisotopes for both Ga [4] and In.

### Conclusions

Band gap states of Ga, Zn, In and Cd are investigated by radiotracer DLTS. Within the limits discussed, there are no deep states of Ga or In after doping by ion implantation and annealing. For the group II elements, one band gap state of Zn at  $E_V + 1.16 \text{ eV}$  (polytype 6H) and two states of Cd with roughly identical concentration at  $E_V + 0.90(3) \text{ eV}$  and at  $E_V + 1.19(4) \text{ eV}$  (polytype 4H) are identified. For all of these group II related states, the influence of the electrical field strength on the hole emission is either missing or smaller than expected for (double) acceptor levels.

*We thank Dr. H. Hobert for polytype determination and C. Hülsen for technical assistance. The work was funded by the German BMBF and DFG.*

### References

- [1] J.Schmidt, T.Matsumoto, O.G.Poluekov, A.van Duijn-Arnold, T.Ikoma, P.G.Baranov, E.N.Mokhov, *Mat. Sci. For.* Vols 264-268 (1998), p. 587
- [2] T.Troffer, M.Schadt, T.Frank, H.Itoh, G.Pensl, J.Heindl, H.P.Strunk, M.Maier, *phys. stat. sol. (a)* **162** (1997) p. 277
- [3] P.G.Baranov, *Mat. Sci. For.* Vols 264-268 (1998), p.581
- [4] J.Grillenberger, N.Achtziger, F.Günther, W.Witthuhn, *Appl. Phys. Lett.* **73** (25), 3698 (1998)
- [5] N.Achtziger, *Mat. Sci. For.* Vols. 248-249 (1997), p.113
- [6] T. Troffer, G.Pensl, A.Schöner, C.Hallin, O.Kordina, E.Janzen, *Mat. Sci. For.* 264-268 (1998), p.557
- [7] N.Achtziger, H.Gottschalk, T.Licht, J.Meier and M.Rüb, U.Reislöhner and W.Witthuhn, *Appl. Phys. Lett.* **66** (1995) p. 2370
- [8] N.Achtziger, W.Witthuhn, *Phys. Rev. B* **57** (19) (1998) p. 12181
- [9] M.Uhrmacher, M.Neubauer, W.Bolse, L.Ziegeler, K.P.Lieb, *Nucl.Instr. and Meth. B139* (1998) p.306
- [10] N.Achtziger, J.Grillenberger, W.Witthuhn, *Hyperfine Interactions* **120/121** (1999) p.69
- [11] J.L. Hartke, *J.Appl.Phys.* **39** (1968) p. 4871

**Correspondence:** achtziger@pinet.uni-jena.de, Tel. ++49-3641-947313, Fax. ++49-3641-947302

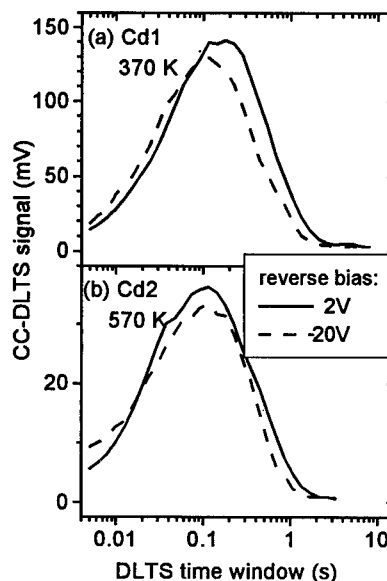


**Fig.4:** Isothermal CC-DLTS spectra of the two Cd-related levels. The spectra shown are differences of spectra measured with pulse voltages of -1 V (forward bias) and 0 V. The two different reverse bias voltages shown correspond to a mean electrical field strength of about 100 kV/cm and 250 kV/cm in the probed depth interval.



## Correlation between DLTS and Photoluminescence in He-implanted 6H-SiC

Th. Frank<sup>1</sup>, G. Pensl<sup>1</sup>, Song Bai<sup>2</sup>, R.P. Devaty<sup>2</sup> and W.J. Choyke<sup>2</sup>

<sup>1</sup> Institute of Applied Physics, University of Erlangen-Nürnberg,  
Staudtstr. 7/A3, DE-91058 Erlangen, Germany

<sup>2</sup> Department of Physics and Astronomy, University of Pittsburgh, Pittsburgh, PA 15260, USA

**Keywords:** DLTS, Implantation-Induced Defects, LTPL

**Abstract:** 6H-SiC samples were He<sup>+</sup>-implanted with different fluences and annealed at different temperatures (700°C to 1700°C) to generate intrinsic-related defect centers. Deep level transient spectroscopy (DLTS) and low temperature photoluminescence (LTPL) investigations were conducted on identical samples. The correlation of corresponding peak heights (defect concentrations) in DLTS and LTPL spectra as a function of the implanted He<sup>+</sup> fluence and of the annealing temperature leads to the conclusion that the E<sub>1</sub>/E<sub>2</sub>-center observed in DLTS spectra and the D<sub>1</sub> defect (L<sub>v</sub>-lines, v=1, 2, 3) observed in LTPL spectra are caused by the same defect center. A corresponding identity could be established for the Z<sub>1</sub>/Z<sub>2</sub>-center (DLTS) and the defect which is responsible for the PL line at 4349Å.

### Introduction

Ion implantation is an important technique to dope silicon carbide (SiC). In order to electrically activate the implanted donor or acceptor species and to largely remove the introduced lattice damage, an annealing step at elevated temperatures is required. As an unintentional side effect electrically active defect centers are generated by the implantation process, which partially survive temperatures up to 1700°C. The chemical composition and microscopic structure of all these defect centers are unknown; partially their electrical properties and thermal stability have been investigated. In 4H-SiC, e. g. Dalibor et al. [1] have demonstrated that the Z<sub>1</sub>/Z<sub>2</sub>-center and the D<sub>1</sub> defect observed in DLTS and in LTPL spectra, respectively, have the same origin. Based on detailed DLTS investigations, Hemmingsson et al. have shown that the Z<sub>1</sub>/Z<sub>2</sub>-center in 4H-SiC [3] and the E<sub>1</sub>/E<sub>2</sub>-center in 6H-SiC [4] are negative U-centers.

It is the aim of this work to elaborate correlations between DLTS and LTPL of implantation-induced defect centers observed in identical 6H-SiC samples.

### Experimental

For the investigations, we used samples cut from an n-type 6H-SiC wafer (CREE Research), which consisted of an n-type substrate overgrown by an n-type epitaxial layer (nitrogen concentration [N]=4×10<sup>15</sup> cm<sup>-3</sup>, thickness d=5µm). The defect centers under investigation are generated by implantation of He<sup>+</sup> ions. A sixfold He<sup>+</sup>-implantation with ion energies in the range between 30keV and 650keV was employed to form a box-shaped damage profile to a depth of 1.6 µm (see Fig.1). The damage is characterized by the total vacancy concentration [V<sub>Si</sub>]+[V<sub>C</sub>] calculated with the TRIM\_C Monte-Carlo simulation program of J. P. Biersack [5]. This concentration value is just an index and does not correspond to the real vacancy concentration, because the simulation program does not take into account more complicated processes like recombination or clustering. Three sets of samples (each set consisting of 5 samples) with different total vacancy concentration (2×10<sup>16</sup> cm<sup>-3</sup>, 8×10<sup>16</sup> cm<sup>-3</sup> and 2×10<sup>17</sup> cm<sup>-3</sup>, respectively) were prepared. Samples of each set received a single annealing step at a temperature T<sub>a</sub> equal to 700°C, 800°C, 1000°C, 1400°C and 1700°C, respectively, for 30 min.

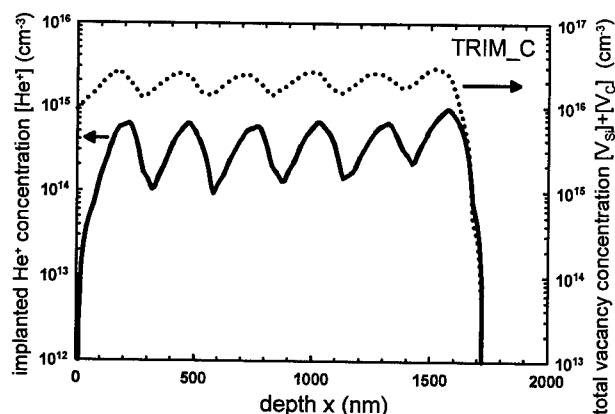


**Fig.1:** Implanted  $\text{He}^+$  concentration (left y-axis, solid curve) and total vacancy concentration  $[\text{V}_{\text{Si}}] + [\text{V}_{\text{C}}]$  (right y-axis, dotted curve), respectively, as a function of the depth  $x$ . The profiles are calculated with the TRIM\_C Monte-Carlo simulation program after [5].

Annealing steps with a temperature up to  $1000^\circ\text{C}$  were conducted in a rapid isothermal annealing system (RIA) under vacuum. Anneals at  $1400^\circ\text{C}$  and  $1700^\circ\text{C}$  were conducted in a graphite furnace; the samples were protected in a SiC crucible and kept in an argon ambient of 1atm. Subsequent to the annealing step, a top layer of 300nm was removed from each sample with reactive ion etching (RIE). Prior to the contact preparation a standard chemical cleaning process was performed using acetone, aqua regia and hydrofluoric acid. For the DLTS investigations, Schottky contacts with different diameters (0.6mm to 1mm) were fabricated by evaporation of nickel.

The DLTS spectra were taken in a temperature range between 100K and 550K; LTPL was conducted at 2K using a 50mW FreD laser at 244nm and a Fast-Fastie spectrometer.

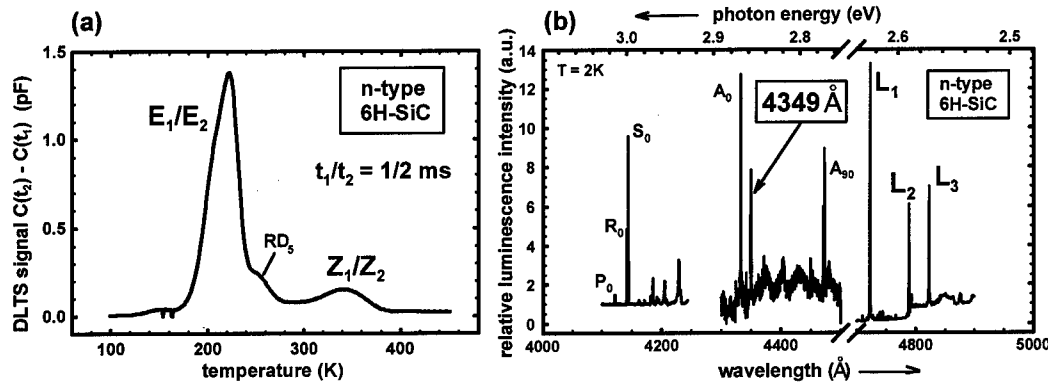
### Experimental results

Fig.2(a) displays the DLTS spectrum of a sample, which was annealed at  $1000^\circ\text{C}$ . A large DLTS peak appears at about 215K, which is caused by the  $\text{E}_1/\text{E}_2$ -center. Its ionization energy  $\Delta E_{\text{E}}$  obtained from an Arrhenius-Plot is  $\Delta E_{\text{E}/6\text{H}} = (420 \pm 20)\text{meV} / (460 \pm 20)\text{meV}$  depending on the temperature dependence of the capture cross section  $\sigma$  (see Table 1). These values correspond to mean values obtained from an average over DLTS data of all investigated samples. The second peak in Fig.2(a) at 350K belongs to the  $\text{Z}_1/\text{Z}_2$ -center; its ionization energy is  $\Delta E_{\text{Z}/6\text{H}} = (640 \pm 50)\text{meV} / (700 \pm 50)\text{meV}$ . A further peak appears as a shoulder on the trailing edge of the  $\text{E}_1/\text{E}_2$ -peak; it is termed  $\text{RD}_5$  according to the nomenclature in the literature [6]. The corresponding LTPL spectrum of this sample is displayed in Fig.2(b). Along with the nitrogen (N)- related lines  $\text{P}_0$ ,  $\text{R}_0$  and  $\text{S}_0$  and the titanium (Ti)-related lines  $\text{A}_0$  and  $\text{A}_{90}$  there appear three LTPL peaks  $\text{L}_v$  ( $v=1, 2, 3$ ), which are assigned to the  $\text{D}_1$ -defect. A further sharp LTPL peak is observed at a wavelength position at  $4349\text{\AA}$ . In Fig.3, the corresponding DLTS (a)- and LTPL (b)-spectrum is taken on a sample, which was processed in the same way, however, exposed to an annealing step at  $1400^\circ\text{C}$ . The DLTS spectrum is dominated by the  $\text{E}_1/\text{E}_2$ -peak; the  $\text{Z}_1/\text{Z}_2$ -center can no longer be observed. Its concentration is below the detection limit of the DLTS system ( $\leq 10^{12} \text{ cm}^{-3}$ ).

The LTPL spectrum of this sample is presented in Fig.3(b). Again the N- and Ti-related peaks and also the three peaks of the  $\text{D}_1$ -defect are visible. The LTPL-peak at  $4349\text{\AA}$  is annealed out; its amplitude is below the noise level.

**Table 1:** Average peak temperature and energy position of ground states of the prevailing peaks observed in DLTS spectra of  $\text{He}^+$ -implanted 6H-SiC samples.

Defect	Average peak temperature in DLTS spectra (K)	Energy position of the ground state (meV)	
		( $\sigma = \text{const.}$ )	( $\sigma \sim T^{-2}$ )
$\text{E}_1/\text{E}_2$	215	$\text{E}_{\text{C}} - (420 \pm 20)$	$\text{E}_{\text{C}} - (460 \pm 20)$
$\text{Z}_1/\text{Z}_2$	350	$\text{E}_{\text{C}} - (640 \pm 50)$	$\text{E}_{\text{C}} - (700 \pm 50)$



**Fig.2:** DLTS (a) and LTPL (b) spectrum taken on the same He<sup>+</sup>-implanted sample with a generated total vacancy concentration of  $2 \times 10^{16} \text{ cm}^{-3}$ ; the sample was exposed to an anneal at 1000°C for 30min.

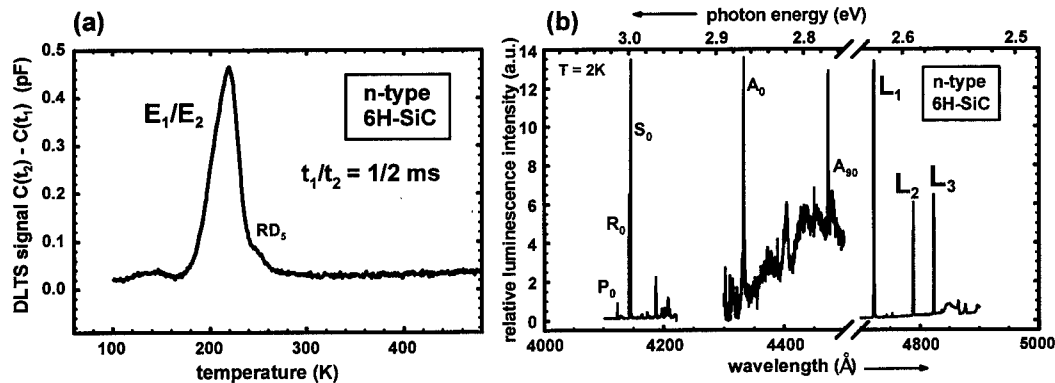


**Fig.3:** DLTS (a) and LTPL (b) spectrum taken on the same He<sup>+</sup>-implanted sample with a generated total vacancy concentration of  $2 \times 10^{16} \text{ cm}^{-3}$ ; the sample was exposed to an anneal at 1400°C for 30min.

It is the aim of this work to test whether any DLTS and LTPL peaks are caused by identical defect centers. We attempted to discover such an identification by comparing defect concentrations obtained from DLTS and LTPL peaks, respectively, as a function of the implanted He<sup>+</sup> fluence (or total generated vacancy concentration) and annealing temperature.  $E_1/E_2$  and  $Z_1/Z_2$  defect concentrations were calculated from the height of the DLTS peaks according to the standard evaluation procedure. A rough estimate for relative defect concentrations from LTPL spectra was obtained by taking the LTPL peak height at  $\lambda=4349\text{\AA}$  or in the case of the  $D_1$  defect by taking the sum of the LTPL peak heights over the three L-lines and by normalizing these quantities by either the height of the  $A_0$ - or  $S_0$ -line. Assuming that N and Ti are laterally homogeneously distributed over the investigated wafer, the quantities  $\sum_{v=1}^3 L_v/S_0$  and  $\zeta(4349\text{\AA})/A_0$  should provide a comparable relative concentration of corresponding defect centers.

### Discussion

In Fig.4(a) the  $E_1/E_2$  concentration obtained from DLTS (left y-axis) and the normalized relative  $D_1$ -defect concentration ( $\sum_{v=1}^3 L_v/S_0$ ) obtained from LTPL (right y-axis) are plotted as a function of the annealing temperature. The plot displays data for three sets of samples containing different vacancy

concentrations. A corresponding plot is determined for the  $E_1/E_2$  concentration and the normalized quantity  $\zeta(4349\text{\AA})/A_0$  in Fig.4(b). It turns out that both plots result in an one-to-one correlation of

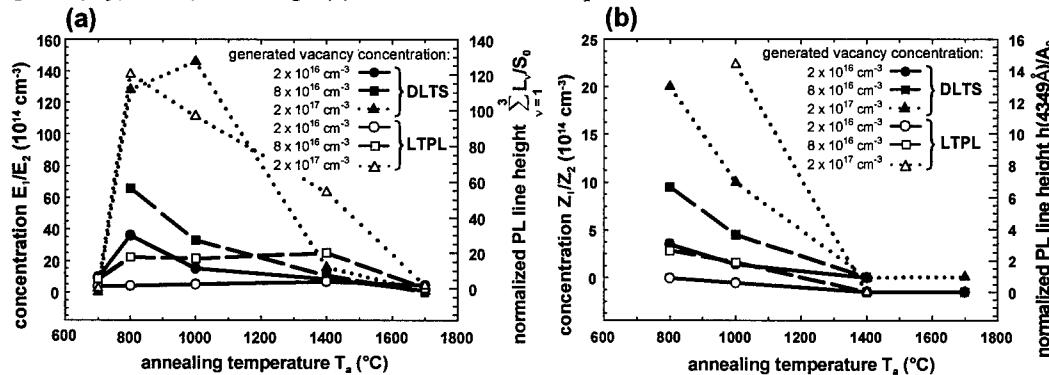


**Fig.4a:** Concentration  $E_1/E_2$  (determined by DLTS) and normalized LTPL peak height ( $\sum_{v=1}^3 L_v / S_0$ ) as a function of the annealing temperature  $T_a$  for three sets of samples containing a different vacancy concentration as indicated in the figure.

**Fig.4b:** Concentration  $Z_1/Z_2$  (determined by DLTS) as a function of the annealing temperature  $T_a$  for three sets of samples containing a different vacancy concentration as indicated in the figure.

corresponding DLTS and LTPL concentrations both as a function of the annealing temperature and as a function of the generated vacancy concentration. This observation clearly indicates, that the  $E_1/E_2$ -center and the  $D_1$  defect have the same origin. In analogy, we conclude, that the  $Z_1/Z_2$ -center and the center, which is responsible for the 4349Å LTPL line, are identical. This work and that of Ref.1 make it clear that in 4H-SiC the so-called  $Z_1/Z_2$ -center is to be associated with the  $D_1$  center observed in LTPL whereas in 6H-SiC we must associate the  $D_1$  center with the  $E_1/E_2$ -center. We conclude that  $Z_1/Z_2$  in 4H corresponds to  $E_1/E_2$  in 6H-SiC and what has been called  $Z_1/Z_2$  in 6H-SiC in reality is a different center associated with the LTPL line at 4349Å. This correlation is in agreement with the negative U-properties of the  $Z_1/Z_2(4H)$ - and  $E_1/E_2(6H)$ -center observed by Hemmingsson et al. [3, 4].

### Summary

DLTS and LTPL investigations were performed in  $\text{He}^+$ -implanted 6H-SiC. In identical samples, correlations between electrically and optically determined defect concentrations are observed as a function of the generated vacancy concentration and the annealing temperature. Based on these observations, it is very persuasive that the  $E_1/E_2$ -center and the  $D_1$  defect are caused by one and the same defect center; an analogous identity is obtained for the  $Z_1/Z_2$ -center and the center responsible for the 4349Å-line. Further analysis methods are required to also identify the chemical nature and the microscopic structure of both these defect centers.

### References:

- [1] T. Dalibor, C. Peppermüller, G. Pensl, S. Sridhara, R. P. Devaty, W. J. Choyke, A. Itoh, T. Kimoto, H. Matsunami, Inst. Phys. Conf. Ser. **142** (1996), p.517
- [2] W. J. Choyke, Inst. Phys. Conf. Ser. **31** (1977), p.58
- [3] C. G. Hemmingsson, N. T. Son, A. Ellison, J. Zhang, E. Janzén, Phys. Rev. B **58** (1998), p.10119
- [4] C. G. Hemmingsson, N. T. Son, E. Janzén, App. Phys. Lett. **74** (1999), p.839
- [5] J.P. Biersack Fortran Monte-Carlo program TRIM Cascade
- [6] T. Dalibor, G. Pensl, H. Matsunami, T. Kimoto, W. J. Choyke, A. Schöner, N. Nordell, phys. stat. sol. (a) **162** (1997), p.199

## Observation of Deep Levels in SiC by Optical-Isothermal Capacitance Transient Spectroscopy

Setsuko Kobayashi<sup>1,3</sup>, Seiji Imai<sup>1,3</sup>, Yasuaki Hayami<sup>1</sup>, Mitsuhiro Kushibe<sup>1,3</sup>,  
Takashi Shinohe<sup>1,3</sup> and Hideyo Okushi<sup>1,2</sup>

<sup>1</sup> UPR Ultra-Low-Loss Power Device Technology Research Body,  
1-1-4 Umezono, Tsukuba, Ibaraki, 305-8568, Japan

<sup>2</sup> Electrotechnical Laboratory, UPR Ultra-Low-Loss Power Device Technology Research Body,  
1-1-4 Umezono, Tsukuba, Ibaraki, 305-8568, Japan

<sup>3</sup> FED, on leave from, Toshiba Corporation, Corporate Research & Development Center,  
1 Komukai Tohisba-cho, Saiwai-ku, Kawasaki, 210-8582, Japan

**Keywords:** 4H-SiC, 6H-SiC, Deep Levels, Isothermal Capacitance Transient Spectroscopy

**Abstract.** Deep levels in bulk crystals of 6H- and 4H-SiC, and epilayers of 4H-SiC were studied using optical-isothermal transient spectroscopy (O-ICTS) and conventional dark ICTS methods, for the first time. For 6H-SiC bulk, E1 with  $3 \times 10^{15} \text{ cm}^{-3}$  ( $E_c - 0.32 \text{ eV}$ ), E2 with  $5 \times 10^{14} \text{ cm}^{-3}$  ( $E_c - 0.49 \text{ eV}$ ) and E3 with  $7 \times 10^{14} \text{ cm}^{-3}$  ( $E_c - 0.50 \text{ eV}$ ) were observed by dark ICTS. Further, E4 with  $1 \times 10^{15} \text{ cm}^{-3}$ , which was located between below E3 and above  $E_c - 1.96 \text{ eV}$ , was observed by O-ICTS. On the other hand, for 4H-SiC bulk, one dominant deep level (E5 with  $1 \times 10^{15} \text{ cm}^{-3}$  located at  $E_c - 1.15 \text{ eV}$ ) and one minor level (E6 with  $3 \times 10^{14} \text{ cm}^{-3}$  located at deeper than E5) were observed by both dark- and O- ICTS. However, for 4H-SiC epilayer, no significant levels were observed either by dark- or O-ICTS, which is consistent with the case of 6H-SiC epilayer reported previously.

### Introduction

Deep levels, and in particular the mid-gap states due to defects and impurities in semiconductors, act as trapping centers and/or recombination centers and greatly affect device performance. SiC has been viewed as a promising material for future high-power device applications, but the crystal growth technology is still immature and many kinds of defects are incorporated in SiC crystal. In order to realize SiC power devices, investigation of mid-gap states is essential. However, because of the wide band gap of SiC, little is known about mid-gap states in SiC<sup>[1,2]</sup>. The deep states located deeper than 1.0 eV from the conduction band edge ( $E_c$ ) are difficult to detect by conventional methods using thermal stimulation process of trapped carriers at the deep levels, such as deep level transient spectroscopy (DLTS)<sup>[3]</sup> or isothermal capacitance transient spectroscopy (ICTS).<sup>[4]</sup>

Recently, the optical-ICTS (O-ICTS) method based on the optical stimulation process, a powerful method for characterization of levels deeper than 1.0 eV from  $E_c$ , has been proposed and successfully demonstrated in the characterization of the mid-gap states in n-type GaN ( $E_g \sim 3.4 \text{ eV}$ ).<sup>[5,6]</sup> In this work, we have tried to observe the mid-gap states in SiC using O-ICTS.

### Experimental

The samples used in this study were n-type SiC wafers (4H, 6H polytypes) with or without epitaxially grown layers (10  $\mu\text{m}$  in thickness) which were purchased from Cree Research, Inc. The conditions of the samples are shown in Table 1.

Schottky barrier diodes were fabricated on each sample by forming Ni Schottky contacts with a diameter of 500 ~ 800  $\mu\text{m}$  on the (0001) Si face, tilted 3.5 and 8 degrees toward the (11-20) direction, and Ohmic contacts using Ni on the back side. Schottky contacts fabricated on each sample were 20 ~ 30 in number.

Table 1

Sample No.	Polytype	Bulk/Epilayer	Carrier density [ $\text{cm}^{-3}$ ]	RIE clean
#1	4H	Bulk	$1.3 \times 10^{17}$	No
#2	4H	Epilayer	$2.8 \times 10^{16}$	No
#3	4H	Epilayer	$6.5 \times 10^{15}$	No
#4	4H	Bulk	$1.3 \times 10^{17}$	Yes
#5	6H	Bulk	$2 \times 10^{17}$	No

Before forming the Ni Schottky contacts on sample #4, the surface was cleaned by reactive ion etching (RIE) followed by sacrificial oxidation. RIE conditions were as follows: rf power 300 W, pressure 0.2 Torr, gas flow rate  $\text{CF}_4(60 \text{ sccm}) + \text{O}_2(8 \text{ sccm})$ , etch rate  $4 \mu\text{m/hr}$ , and etch time 60 min.

A conventional (dark-) ICTS measurement was carried out in  $10^{-2}$  Torr vacuum.

In the O-ICTS measurement, the optical emission process from trapped carriers at mid-gap states was observed by stimulating the carriers using a He-Ne laser ( $h\nu = 1.96 \text{ eV}$ ). The ICTS measurement conditions were as follows: reverse voltage  $V_R = -3.0 \text{ V}$ , forward pulse voltage  $V_F = 3.0 \text{ V}$ , and pulse width  $W_F = 10 \text{ msec}$ .

## Results

### <Schottky diode characteristics>

In ICTS, high leakage current, higher than the order of  $\mu\text{A}$ , leads to inaccuracy. Current-Voltage (I-V) characteristics for each sample were measured before carrying out the ICTS measurement.

Typical I-V characteristics for sample #3 are shown in Fig. 1. I-V characteristics for the 2 epilayers, sample #2 and #3, were very good with low leakage current. The Schottky barrier height (SBH) was calculated to be  $\text{SBH} = 1.3 \sim 1.44 \text{ eV}$  for sample #2, and  $\text{SBH} = 1.4 \sim 1.52 \text{ eV}$  for sample #3. The difference in SBH is assumed to be caused by the doping density difference.

Samples #1, #4, and #5 showed leakage currents lower than  $1 \mu\text{A}$  @  $-3 \text{ V}$ , which is sufficient for carrying out the ICTS measurement.

However, I-V characteristics of sample #1 varied widely between electrodes. SBH versus ideality factors (n-factor) is indicated by black dots in Fig. 2. Sample #4 was diced from the same bulk wafer as sample #1, and its surface was cleaned using RIE prior to Schottky metallization. SBH versus n-factor of sample #4 is indicated by white dots in Fig. 2. I-V characteristics of sample #4 became more stable than those of sample #1. It is assumed that the damaged layer caused by the bulk-wafer-surface-polish may be removed by the RIE cleaning method, which leads to improvement of the Schottky diode I-V characteristics.

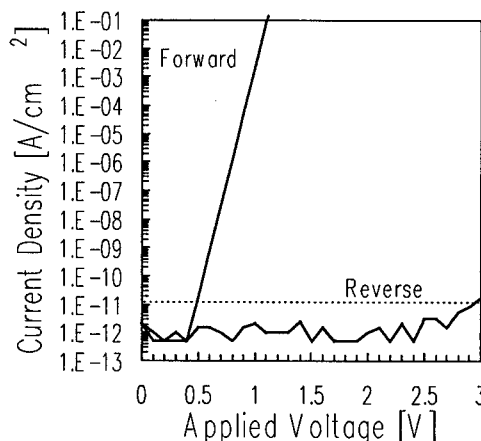


Fig.1 I-V characteristics of sample #3.

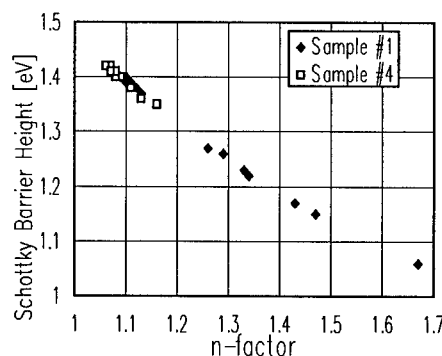


Fig.2 Schottky barrier height vs. n-factor of sample #1 and #4.

#### < 6H-SiC bulk >

ICTS measurement of sample #5 was carried out in the temperature range of 180 ~ 360 K. In dark-ICTS spectra at 190 K, carriers from level E1 with  $3 \times 10^{15} \text{ cm}^{-3}$  ( $E_c - 0.32 \text{ eV}$ ) are thermally emitted to the conduction band. Two dark-ICTS peaks due to levels E2 with  $5 \times 10^{14} \text{ cm}^{-3}$  ( $E_c - 0.49 \text{ eV}$ ) and E3 with  $7 \times 10^{14} \text{ cm}^{-3}$  ( $E_c - 0.50 \text{ eV}$ ) were observed at 297 K. In O-ICTS spectra at 360 K, a peak E4 with  $1 \times 10^{15} \text{ cm}^{-3}$  was observed in the longer time range than that of peak E3, indicating that E4 is located below E3 and above  $E_c - 1.96 \text{ eV}$ . Leakage current of the Schottky diodes at -3V did not exceed the order of  $\mu\text{A}$  up to 360 K. The O-ICTS signal of sample #5 at 360 K is shown in Fig. 3.

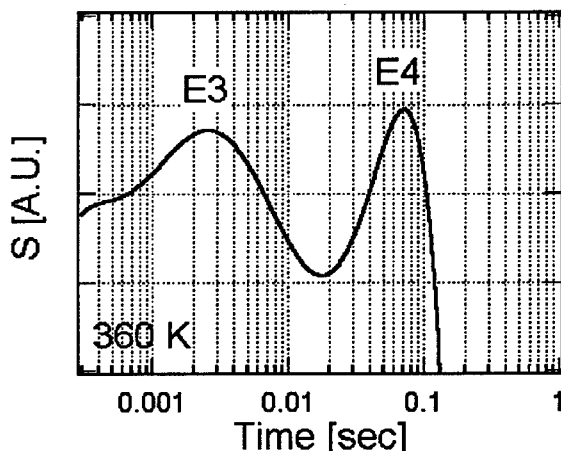


Fig.3 O-ICTS signal measured from sample #5, fabricated from 6H-SiC bulk wafer with carrier density of  $2 \times 10^{17} \text{ cm}^{-3}$ .

#### < 4H-SiC bulk >

Dark-ICTS measurement of sample #1, fabricated from 4H-SiC bulk wafer, was carried out in the temperature range of 200 ~ 460 K. The dark-ICTS spectra at 380 K, 420 K and 460 K are shown in Fig. 4. In the temperature range of 380 ~ 460 K, carriers from level E5 with  $1 \times 10^{15} \text{ cm}^{-3}$  ( $E_c - 1.15 \text{ eV}$ ) are thermally emitted to the conduction band. At temperatures 420 K and 460 K, a dark-ICTS peak due to level E6 is observed in the longer time range than that of peak E5.

However, enough data to determine the energy level of peak E6 could not be obtained at 460 K. Higher measurement temperature or O-ICTS is required to estimate the energy level. The electron trap concentration of E6 was estimated to be  $3 \times 10^{14} \text{ cm}^{-3}$ .

New peaks were not obtained by O-ICTS, but peaks E5 and E6 were observed even at the temperature as low as 200 K. This indicates that peak E6 is located below  $E_c - 1.15$  and above  $E_c - 1.96 \text{ eV}$ .

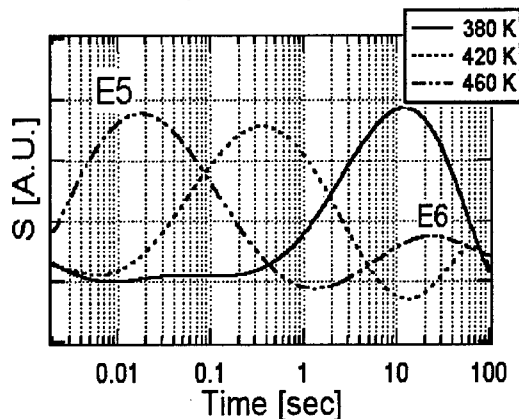


Fig.4 Dark-ICTS signal measured from sample #1, fabricated from bulk 4H-SiC with carrier density of  $1.3 \times 10^{17} \text{ cm}^{-3}$ .

#### < 4H-SiC epilayer >

ICTS measurement was carried out on the two samples fabricated from epilayers, sample #2 and #3, in the temperature range of 240 ~ 460 K; however, no peaks were observed either by dark- or O-ICTS.

### Discussion

Dark- and O-ICTS measurements of sample #4 were carried out, and the results were about the same as those for sample #1. Although the Schottky diode characteristics, which are mostly attributable to surface conditions, were improved by RIE, ICTS spectra were not changed by RIE. This indicates that ICTS spectra are attributable to the bulk condition of the sample. Therefore, the peaks observed for sample #1 are attributable to the deep levels in the bulk crystal, and not to the damaged layer caused by polishing the surface of the bulk wafer.

No peaks were observed either by dark- or O-ICTS from 4H-SiC epilayers, samples #2 and #3. Considering the measurement temperature and the time range, it is possible to measure deep levels located below  $E_c - 0.4$  and above  $E_c - 1.3$  eV with density of more than  $10^{13} \text{ cm}^{-3}$ . The present results indicate either that the 4H-SiC epilayers do not possess deep levels in the range of  $E_c - 0.4 \sim E_c - 1.3$  eV, or that the electron trap density is lower than our detection limit ( $10^{13} \text{ cm}^{-3}$ ). The fact that no significant deep levels were observed either by dark- or O-ICTS in the 4H-SiC epilayer is similar to the result for the 6H-SiC epilayer reported by Jang et al.<sup>[7]</sup>

The reason why no significant deep levels were observed in both 6H- and 4H-SiC is not clarified in the present work. However, the following two possible reasons are suggested: (1) The densities of deep levels due to defects and/or residual impurities in the epilayer are much less than those of the bulk. (2) Although deep levels exist below  $E_c - 1.3$  and above  $E_c - 1.96$  eV, the optical cross sections ( $\sigma_n$ ) are so small that the trapped carriers cannot be photoionized to the conduction band. In this case, the deep levels cannot be measured by O-ICTS.

### Conclusion

Deep levels including mid-gap states in SiC were studied using dark- and O-ICTS methods. The deep levels observed in this study are shown in Table 2. Deep levels from 4H-SiC epitaxial layers were not detected in the range of  $0.4 \sim 1.3$  eV below  $E_c$ , and in the detection limit of  $10^{13} \text{ cm}^{-3}$ .

Table 2 Deep levels observed in the present work.

	Energy levels [eV]	Electron Trap Density [ $\text{cm}^{-3}$ ]
6H-SiC bulk crystal	E1: $E_c - 0.32$	E1: $3 \times 10^{15}$
	E2: $E_c - 0.49$	E2: $5 \times 10^{14}$
	E3: $E_c - 0.50$	E3: $7 \times 10^{14}$
	E4: $E_c - 0.50 \sim E_c - 1.96$	E4: $1 \times 10^{15}$
4H-SiC bulk crystal	E5: $E_c - 1.15$	E5: $1 \times 10^{15}$
	E6: $E_c - 1.15 \sim E_c - 1.96$	E6: $3 \times 10^{14}$
4H-SiC epitaxial layer	-	-

**Acknowledgments.** This work was performed under the management of FED as a part of the MITI NSS Program (Ultra-Low Loss Power Device Technology Project) supported by NEDO.

### References

- [1] T. Dalibor, G. Pensl, H. Matsunami, T. Kimoto, W. J. Choyke, A. Schoner and N. Nordell, Phys. Stat. Sol. (a) **162** (1997), p. 199.
- [2] A. O. Evwaraye, S. R. Smith and W. C. Mitchel, J. Appl. Phys. **79** (1996), p. 7726.
- [3] D. V. Lang : J. Appl. Phys. **45** (1974), p. 3023.
- [4] H. Okushi and Y. Tokumaru: Jpn. J. Appl. Phys. **20**, Suppl. 20-1 (1980), p. 261.
- [5] P. Hacke and H. Okushi: Appl. Phys. Lett. **71** (1997), p. 524.
- [6] P. Hacke, H. Okushi and Y. Tokumaru: Inst. Phys. Conf. Ser. No.160 (IOP Publishing Ltd., 1997), p. 355.
- [7] S. Jang, T. Kimoto, and H. Matsunami: Appl. Phys. Lett., **65** (1994), p. 581.



## Improved Measurements of High-Field Drift Velocity in Silicon Carbide

I.A. Khan and James A. Cooper, Jr.

School of Electrical and Computer Engineering, Purdue University,  
1285 EE Building, West Lafayette, IN 47907-1285, USA

**Keywords:** Electron Mobility, Electron Transport, Velocity Saturation

### Abstract

We report improved measurements of the high-field drift velocity of electrons parallel to the basal plane in 4H and 6H-SiC as a function of temperature. The electron saturation drift velocity at room temperature is  $1.9(2.2) \times 10^7$  cm/s in 6H(4H) SiC. At 320 °C the electron saturation drift velocity is  $1.0(1.6) \times 10^7$  cm/s in 6H(4H) SiC.

### Introduction

Measurements of the high field drift velocity of electrons in 6H-SiC were first reported by v. Münch and Pettenpaul in 1977 [1], and more recent data on 6H and 4H-SiC was presented by us at this conference in 1997 [2]. Von Münch and Pettenpaul found a saturation drift velocity of  $2 \times 10^7$  cm/s for electrons in 6H-SiC. This value is about a factor of two higher than in most other semiconductors, and has long been quoted as one of the benefits of SiC as an emerging material for high performance devices. Our 1997 work [2] tended to confirm the results of v. Münch and Pettenpaul, but the highest velocities actually *measured* in [2] were only about  $1.5 \times 10^7$  cm/s. Moreover, a number of difficulties with the measurement procedure were identified, indicating the need for more careful and thorough experiments. In the present paper we report the results of additional experiments [3] that add a significant amount of new data and extend the measurement regime to higher fields and higher temperatures.

### Measurement Technique

The measurement technique employed by v. Münch and Pettenpaul, and also used here, consists of measuring the current-voltage relationship of a narrow constriction of n-type SiC material at high fields. The experimental device, illustrated in Fig. 1, consists of an n-type epilayer of doping  $1 \times 10^{17}$  cm<sup>-3</sup> grown on a lightly doped p-type epilayer on a heavily-doped p-type substrate. The n-type epilayer is patterned by reactive ion etching, forming a constriction of dimensions on the order of  $5 \times 5$  μm. Ohmic contacts are established on either side of the constriction by annealed Ni. Probe contact is made to the four ohmic contacts, and a pulsed bias is applied using the apparatus shown in Fig. 2. To prevent surface arcing, the samples are immersed in Fluorinert™. Bias pulses are applied to outer contacts  $L_1$  and  $L_4$  using a Directed Energy, Inc. GRX 1.5 K-E pulse generator, and the voltage drop across the inner contacts  $L_2$  and  $L_3$  is measured using the 1 MΩ inputs of a Tektronix 11401 digitizing oscilloscope. The current through the constriction is obtained from the voltage drop across the 50 Ω input of the oscilloscope in series with  $L_4$ . The electron drift velocity is calculated from the current using the relation

$$v = \frac{I}{q w n t} \quad (1)$$

where  $w$  is the width of the constriction,  $n$  is the electron density per unit volume, and  $t$  is the thickness of the undepleted portion of the n-type epilayer. The corresponding electric field is calculated from the voltage drop between the high impedance probes attached to  $L_2$  and  $L_3$ , with corrections for the end resistances between the inner ohmic contacts and the constriction.

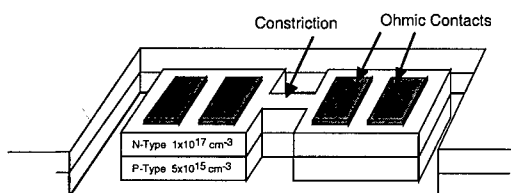


Figure 1. Isometric view of the experimental device. In most devices, the n-type epilayer is 4  $\mu\text{m}$  thick.

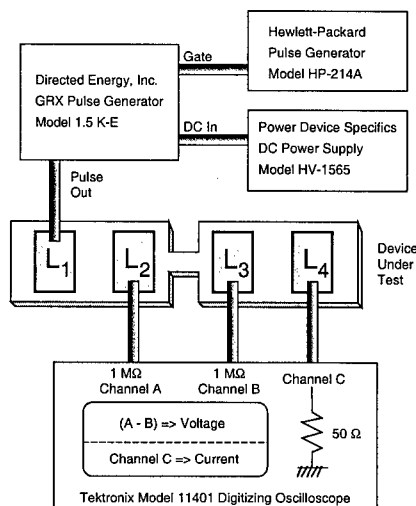


Figure 2. Schematic diagram of the test apparatus.

Figure 3 shows transient current waveforms for several different pulse conditions of increasing applied voltage. As seen, for electric fields above about 20 kV/cm the current decreases during the bias pulse due to transient heating at the constriction. To minimize this effect, we record the current at the earliest possible point in the bias pulse, typically within the first 50 ns. The transient response of the circuit becomes a limitation at the highest fields. The transient response is degraded by the parasitic capacitance of the probes, so at fields above 30 kV/cm we remove the two inner probes and calculate the voltage drop across the constriction using the equivalent circuit of Fig. 4. The elements in Fig. 4 represent the contact impedances and the spreading resistances of the n-type. Resistances ( $R_{C1} + R_1$ ) and ( $R_{C4} + R_4$ ) are obtained from four-probe measurements at low fields (no current flows through  $R_{C2}$  and  $R_{C3}$  due to the high impedance probes on L2 and L3). At high fields, the probes on L2 and L3 are removed and the voltage drops across ( $R_{C1} + R_1$ ) and ( $R_{C4} + R_4$ ) are calculated from the measured current and known resistances. These voltage drops are then subtracted from the voltage between probes L1 and L4 to obtain the equivalent inner probe voltage drop.

#### Device Details

In the experiments reported in 1997 [2], the n-type epilayer thickness was 1  $\mu\text{m}$ . This raised a concern about narrowing of the undepleted n-type channel due to the depletion region from the underlying pn junction. In the present experiments [3] we increased the thickness of the n-type epilayer to 4  $\mu\text{m}$  to minimize this effect, and we also included an analytical correction to the channel thickness  $t$  to account for the depletion. A variety of constriction sizes are also included, with dimensions (width x length) = 5x5, 5x10, 5x15, 10x10, and 10x15  $\mu\text{m}$ . To insure low resistance ohmic contacts, a high dose ( $1 \times 10^{19} \text{ cm}^{-3}$ ) nitrogen implant is performed in the contact regions and annealed at 1400°C for 18 minutes in argon. The doping-thickness ( $n \cdot t$ ) products for the n-type epilayers obtained from Hall measurements on each sample are 2.4 (3.6)  $\times 10^{13} \text{ cm}^{-2}$  for the 4H (6H) samples, respectively. In these calculations, the Hall scattering factor  $r_H$  is taken to be unity [4]. These ( $n \cdot t$ ) values agree well with separate TLM measurements on each sample. The lateral dimensions of the constrictions are determined within an accuracy of  $\pm 10\%$  from SEM photographs of the completed structures. Epilayer thickness and the uniformity of doping with depth are verified by SIMS.

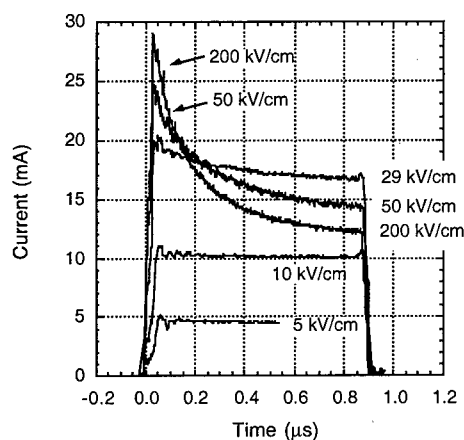


Figure 3. Transient current waveforms at various fields.

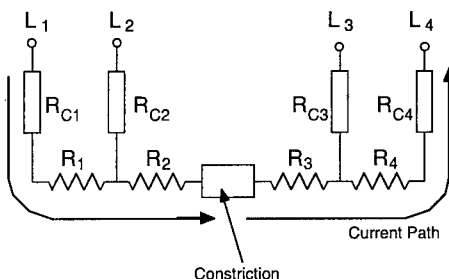


Figure 4. Equivalent circuit showing parasitic resistances.

### Experimental Results

Figures 5 and 6 show velocity-field data on the 4H and 6H samples at room temperature, 135, and 320 °C. Measurements on constrictions of various sizes are included at each temperature. The lines represent empirical fits to the equation

$$v(E) = \frac{\mu E}{\left[ 1 + \left( \frac{\mu E}{v_s} \right)^\alpha \right]^{\frac{1}{\alpha}}} \quad (2)$$

where  $\mu$  is the low field mobility,  $v_s$  is the saturation velocity, and  $\alpha$  is a shape parameter. Values of the fit parameters are listed in Table 1. Saturation velocities of  $2.2 (1.9) \times 10^7$  cm/s are obtained for 4H (6H) SiC at room temperature. These values decrease to  $1.6 (1.0) \times 10^7$  cm/s for 4H (6H) SiC at 320 °C.

### Summary

We have reported new measurements of high field drift velocity of electrons parallel to the basal plane in 4H and 6H-SiC at room temperature, 135, and 320 °C. The saturation drift velocity in 6H-SiC at room temperature is  $1.9 \times 10^7$  cm/s, very close to the value reported by v. Muench and Pettenpaul [1] in 1977. The saturation drift velocity in 4H-SiC is  $2.2 \times 10^7$  cm/s. Saturation velocities decrease with temperature, reaching  $1.6 (1.0) \times 10^7$  cm/s in 4H (6H) SiC at 320 °C.

### Acknowledgements

This work is supported by a grant from the Air Force Research Laboratories through the SiC Consortium, managed by the Auburn Space Power Institute, and by the Office of Naval Research under MURI grant No. N00014-95-1-1302. Experimental wafers are donated by Cree Research, Inc. The authors appreciate helpful comments from J. W. Palmour, Cree Research.

### References

- [1] W. v. Muench and E. Pettenpaul, J. Appl. Phys. 48 (1977), p. 4823.
- [2] I. A. Khan and J. A. Cooper, Jr., Silicon Carbide, III-Nitrides and Related Materials; G. Pensl, H. Morkoc, B. Monemar, and E. Janzen, Eds.; Trans. Tech. Publications (1998), p. 509.
- [3] I. A. Khan and J. A. Cooper, Jr., to appear in IEEE Trans. Electron Devices, February, 2000.
- [4] G. Rutsch, R. P. Devaty, D. W. Langer, L. B. Rowland, and W. J. Choyke, Mat'l's. Sci. Forum, 264-268 (1998), p. 517.

### Author's Contact Information

FAX: 1-765-494-6441, e-mail: [cooperj@ecn.purdue.edu](mailto:cooperj@ecn.purdue.edu), web: <http://www.ecn.purdue.edu/WBG/>

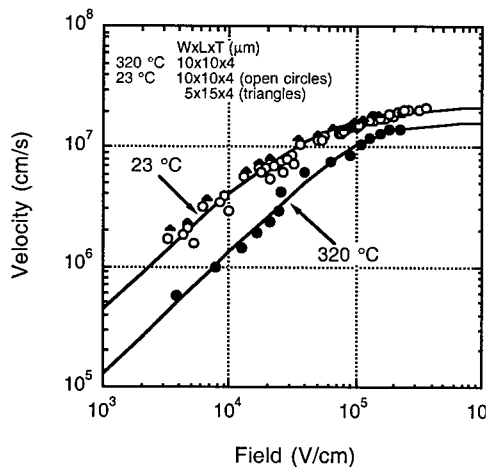


Figure 5. Velocity-field relation for electrons parallel to the basal plane in 4H-SiC. Constriction sizes for the various data points are given in the figure.

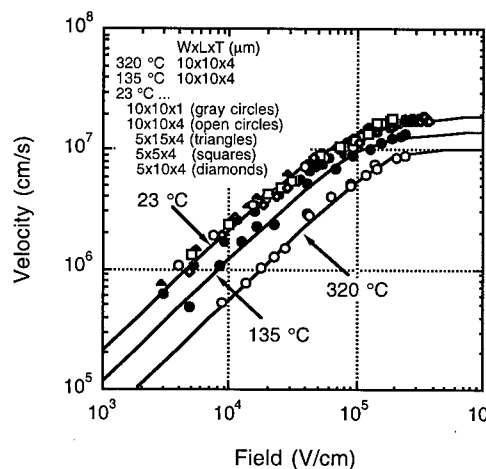


Figure 6. Velocity-field relation for electrons parallel to the basal plane in 6H-SiC. Constriction sizes for the various data points are given in the figure.

Temperature	Parameter	6H-SiC	4H-SiC	Units
23 °C	$\mu$	215	450	$\text{cm}^2/\text{Vs}$
	$v_s$	$1.9 \times 10^7$	$2.2 \times 10^7$	cm/s
	$\alpha$	1.7	1.2	--
135 °C	$\mu$	120	-	$\text{cm}^2/\text{Vs}$
	$v_s$	$1.4 \times 10^7$	-	cm/s
	$\alpha$	2.5	-	--
320 °C	$\mu$	56	130	$\text{cm}^2/\text{Vs}$
	$v_s$	$1.0 \times 10^7$	$1.6 \times 10^7$	cm/s
	$\alpha$	4.0	2.2	--

Table 1. Parameters used in (2) to fit the experimental velocity-field data.

## A Full Band Monte Carlo Study of High Field Carrier Transport in 4H-SiC

H.-E. Nilsson<sup>1</sup>, E. Bellotti<sup>2</sup>, K.F. Brennan<sup>2</sup> and M. Hjelm<sup>1</sup>

<sup>1</sup>Dept. of Information Technology, Mid-Sweden University, SE-851 70 Sundsvall, Sweden

<sup>2</sup>School of Electrical and Computer Engineering, Georgia Tech., Atlanta, GA 30332-0250, USA

**Keywords:** 4H-SiC, Charge Transport, Impact Ionization, Monte Carlo Simulation

**Abstract.** The high field transport properties of 4H-SiC have been studied using a bipolar full band ensemble Monte Carlo model. The impact ionization transition rates and the phonon scattering rates for both electrons and holes have been calculated numerically from the full band structure. The simulation results show a large anisotropy in the impact ionization coefficients for both electrons and holes.

### Introduction

Silicon Carbide has emerged as a very promising semiconductor for high power devices. The large band gap and thermal conductivity of silicon carbide are important advantages that can be utilized in power applications. Silicon carbide crystallizes in many different polytypes. Technologically, 3C-SiC, 4H-SiC and 6H-SiC are the most important. In this work we focus on the material properties of 4H-SiC. The 4H polytype has a higher mobility than 6H and is technologically more developed than 3C-SiC. The high field transport properties of 4H-SiC have not been studied very extensively and the knowledge regarding the impact ionization process in 4H is very limited. A technologically immature material such as 4H-SiC is plagued by a large amount of defects, which makes it difficult to obtain reliable experimental measurements of its intrinsic properties. Numerical studies can avoid all of these technological problems and directly focus on estimating the intrinsic properties such as the impact ionization coefficients, saturation velocity and energy relaxation time constants.

In this work we present a full band Monte Carlo study of the high field properties of 4H-SiC. Our goal is to present estimates of the electron and hole initiated impact ionization coefficients. This work should be regarded as a first step towards the understanding of the high field transport in 4H-SiC.

### The Monte Carlo model

The Monte Carlo model can be divided into three parts, the band model, the scattering model and the drift model.

**Band model.** The band model, presented in Fig. 1, has been obtained using a local empirical pseudo potential method (EPM). Twelve conduction bands and twelve valence bands have been used. The energy and energy gradient of each band has been stored for 11655 points in the irreducible wedge. These data are used to interpolate the energy and energy gradients for arbitrary k-points during the simulation.

**Scattering model.** The following scattering mechanisms are considered: acoustic phonon scattering, non-polar optical phonon scattering, polar optical phonon scattering, impact ionization and ionized impurity scattering. The phonon scattering rates and the impact ionization transition rate have been calculated directly from the band structure using available data on phonon modes and sound velocities [1]. The phonon coupling constants have been obtained by fitting the low field mobility to experimental data on mobility [2]. We have used completely  $k$ -dependent scattering rates instead of the standard formulation, where the  $k$ -dependent scattering rate is averaged over constant energy surfaces. The spread in the  $k$ -dependent scattering rate for points with the same energy is much larger in 4H-SiC than in 3C-SiC [3], due to the inherent asymmetry of the 4H unit cell. Averaging over constant energy surfaces filters away the high scattering rates present in certain parts of the Brillouin zone. Using  $k$ -dependent scattering rates reduces the carrier energy and gives lower impact

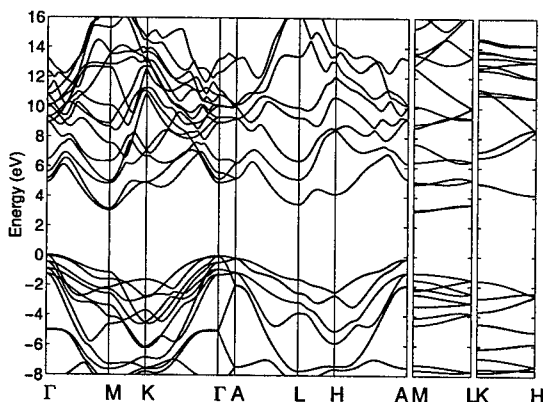


Fig. 1. The empirical pseudo potential (EPM) band structure used in this work.

ionization coefficients.

The selection of the final states after scattering is completely  $k$ -dependent, including the  $k$ -dependency of the overlap integral calculated using the pseudo wave functions. The final states after impact ionization are selected according to energy and momentum conservation. Secondary electrons and holes are dynamically created during runtime. This allows injection of secondary electrons and holes with high energy as a result of impact ionization. This injection is necessary in order to obtain a correct energy distribution at high fields.

**Drift model.** The electric field accelerates the carrier in  $k$ -space according to

Newton's laws. The 4H-SiC valence bands contain a large number of mixing and crossing points. In the presence of a crossing point, the particles group velocity changes abruptly in a nonphysical way. The conservation of the group velocity would require the particle's band index to change. In case of mixing points different bands are degenerate and have the same group velocity. To assign the correct path for the particle, the overlap integral between the starting and the final points is evaluated for different final bands after a short drift step. The assignment of final band index is based on a random selection weighted using the overlap values for different final bands.

The use of this simple tunneling model is justified by the fact, that the energy barrier that the carrier might tunnel over is small ( $<30$  meV). It is found that the inclusion of band crossing effects is essential in the Monte Carlo model in order to achieve agreement with experimental measurements of the impact ionization coefficients. Without band changes at these critical points, the impact ionization coefficients are calculated to be very low, orders of magnitude lower than the experimental values.

The conduction bands have a different structure than the valence bands. Along the  $c$ -axis the first and the second band are separated from all higher bands by an energy gap of approximately 1.5 eV. In perpendicular directions, the picture is more like that in the valence bands. Electrons that undergo impact ionization events for an electric field applied along the  $c$ -axis need to overcome the relatively large energy separation between bands 2 and 3. This can only happen through a

combination of scattering and drift. The scattering is limited by the interaction energy or phonon energy, which typically is very small compared to the energy separation. It is possible to surmount the energy separation if the right series of scattering events occurs. However, the probability for this is very low.

### Simulation results

In Fig. 2 the drift velocity as a function of electric field is presented for both electrons and holes. The electric field has been applied along  $\Gamma M$  and  $\Gamma A$ . At high fields the anisotropy of the Brillouin zone has a very large impact on the velocity. The peak velocities for holes with the field applied in the  $\Gamma M$  and  $\Gamma A$  directions are  $1.1 \times 10^7$  cm/s and  $6.5 \times 10^6$  cm/s respectively.

The electron saturation velocity for fields applied in the  $\Gamma A$  direction is  $1.64 \times 10^7$  cm/s and it is  $2.26 \times 10^7$  cm/s in the  $\Gamma M$  direction. The  $\Gamma M$  value is slightly higher than the experimental value  $2.1 \times 10^7$  cm/s obtained for 6H-SiC [4]. Other Monte Carlo studies on 4H-SiC presented in the literature [5,6] predict a lower saturation velocity, approximately  $2.0 \times 10^7$  cm/s. However, in these studies the formalism introduced by Ferry [7] on zero and first order intervalley scattering have been used. In our case, we are using a completely numerical formulation for the scattering and only the zero order mechanism has been included, since the first order mechanism is already considered by the numerical treatment of the acoustic phonons. The large scattering rate at high energies given by the analytical first order scattering model does not occur in the numerical formulation. The long  $q$ -vectors, responsible for the large scattering rate at high energies in the analytical first order scattering formulation, are mitigated by the overlap integral in the numerical model.

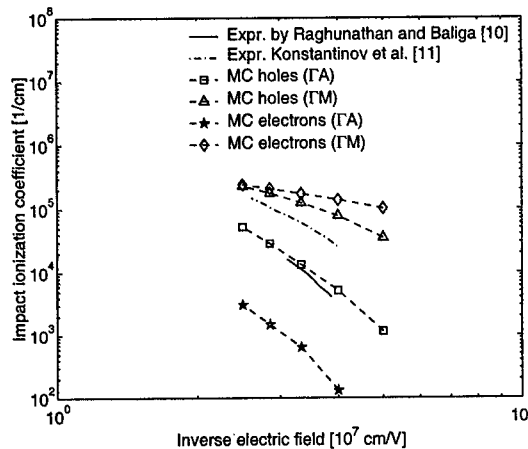
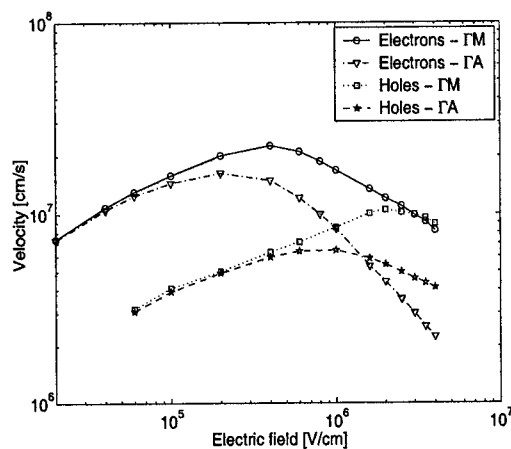


Fig. 2. Drift velocity as a function of electric field applied along  $\Gamma M$  and  $\Gamma A$  for electrons and holes.

Fig. 3. Impact ionization coefficients as function of inverse electric field.

The electron and hole impact ionization coefficients as a function of inverse electric field are presented in Fig. 3. Our simulation results are in good agreement with the experimental data obtained by R. Raghunathan and B.J. Baliga [8] along the  $c$ -axis direction. The experimental result by Konstantinov et al [9] is significantly higher than our result. The discrepancy between the two experiments is due to differences in the measurement techniques, where the technique used by R.

Raghunathan and B.J. Baliga [8] is considered to be more accurate. Konstantinov et al [9] has estimated the electron impact ionization coefficients to be substantially higher than what is calculated in this study, when tunneling over large energy separations is excluded. In a future work we will examine the consequences on the electron impact ionization coefficients of tunneling over large energy separations.

### Summary

The high field carrier transport in 4H-SiC has been studied, using a full band ensemble Monte Carlo technique. The peak velocity for holes (electrons) was found to be  $6.5 \times 10^6$  cm/s ( $1.64 \times 10^7$  cm/s) for an electric field applied along  $\Gamma A$  and  $1.1 \times 10^7$  cm/s ( $2.26 \times 10^7$  cm/s) for an electric field applied along  $\Gamma M$ . The anisotropy of the impact ionization coefficients for both electrons and holes was found to be very large. For electrons, the anisotropy is extremely large with a ratio in the coefficients of approximately 100. This phenomenon is related to the large energy separation between conduction bands 2 and 3 along the ML segment. There might be an additional mechanism of importance in the electron transport that has not been considered in this work, namely band to band tunneling over large energy separations. Band to band tunneling or the Zener effect is very well known in the case of a PN-junction. The temperature coefficient for Zener breakdown has an opposite sign compared to that of avalanche breakdown. The same characteristics have been observed for the electron impact ionization coefficients along the c-axis in 4H-SiC and 6H-SiC, with a temperature coefficient with opposite sign compared to a normal avalanche process [10]. The inclusion of band to band tunneling over large energy separations may be the key element to explain this peculiar behavior of the 4H and 6H polytypes.

### References

- [1] M. Hofmann, A. Zywiets, K. Karch and F. Bechstedt, Phys. Rev. B Vol. 50, (1994), p. 13401.
- [2] W.J. Schaffer, G.H. Negley, K.G. Irvine and J.W. Palmour, Mater. Res. Soc. Symp. Proc. 339 (1994), p. 595.
- [3] E. Bellotti, H-E. Nilsson, K.F. Brennan, P. P. Ruden, J. Appl. Phys. Vol. 85, (1999), p. 3211.
- [4] W. Von Münsch and E. Pettenpaul, J. Appl. Phys. Vol. 48, (1977), p. 4823.
- [5] R. Mickevicius and H. Zhao, J. Appl. Phys. Vol. 83, (1998), p. 3161.
- [6] H-E. Nilsson, U. Sannemo, C. S. Petersson, J. Appl. Phys. Vol. 80, (1996), p. 3365.
- [7] D.K. Ferry, Phys. Rev. B Vol. 14, (1976), p. 1605.
- [8] R. Raghunathan and B.J. Baliga, Solid-State Electronics Vol. 43, (1999), p. 199.
- [9] A. O. Konstantinov, Q. Wahab, N. Nordell and U. Lindefelt, Journal of Elec. Matls. Vol. 27, (1998), p. 335.
- [10] A. O. Konstantinov, N. Nordell, Q. Wahab and U. Lindefelt, Appl. Phys. Lett. Vol. 73, (1998), p. 1850.

Hans-Erik Nilsson@ite.mh.se



## Electron Saturated Vertical Velocities in Silicon Carbide Polytypes

V.I. Sankin and A.A. Lepneva

A.F. Ioffe Physico-Technical Institute, Russian Academy of Sciences,  
Polytekhnicheskaya st. 26, RU-194021 St.-Petersburg, Russia

**Keywords:** Miniband Transport, Natural Superlattice, Strong Electric Field, Superlattice

### Abstract

The most important device-related characteristic of a semiconductor crystal is its saturated drift velocity, which determines the frequency limits of semiconductor devices and consequently the range of their most efficient use. This remains true for the case of silicon carbide polytypes as well. At this time such velocities have been determined for two SiC polytypes (4H and 6H) for the direction perpendicular to the crystal c-axis [1]. As it was shown these values are equal. But there is anisotropy of electrical properties in silicon carbide polytypes for the direction along and perpendicular to the axis. The crystal axis is also the axis of the natural superlattice (NSL). It is well known that the drift velocities in artificial superlattices depend very strongly on parameters of the superlattice (SL), and change from  $10^6$  cm/s for a relatively wide [2] miniband to  $10^4$  cm/s for a narrow one [3]. In [4-6] it was shown that the NSL creates a miniband electron spectrum in silicon carbide polytypes that leads to the existence of such effects as Bloch oscillations, electro-phonon resonances, interminiband tunnelling and others. The miniband structure should affect the values of the vertical saturated drift velocities, i.e., a correlation should be observed between the velocities and the parameters of the miniband spectrum of different polytypes. Until now, such data have not been published. Probably some experimental difficulties did not allow one to carry out such experiments. But many devices, including high power high frequency transistors, are being designed to operate in this geometry so that the determination of vertical saturated drift velocities is an important problem both from fundamental and applied points of view.

### Experimental method

Our method is based on the following idea. When in an experimental structure with space charge limited current a drift current regime is realised the drift velocities may be obtained. This regime may be described by two equations for the one dimensional case:

$$d^2 V / dx^2 = \rho / \epsilon_s \quad (1)$$

$$J = \rho v \quad (2)$$

where  $V$ ,  $x$ ,  $\rho$ ,  $\epsilon_s$ ,  $J$ , and  $v$  are the voltage across the structure, the coordinate along the current direction, the space-charge density, the dielectric constant of the semiconductor, the current density, and the drift velocity, respectively. By some standard transformations we can show that a current-voltage characteristic consists of two regions: the first region where the drift velocity is changed with changing of an electrical field and the second one where velocity is saturated and does not vary with the field. If we consider the velocity equal to

$$v = \mu V / w, \quad (3)$$

then the  $I - V$  characteristic in the first region will be described by the expression

$$J = 2 \epsilon_s \mu V^2 / w^3 \quad (4)$$

Here,  $\mu$  and  $w$  are the mobility of the carriers and the length of the specimen, respectively. One should take into account that in (4)  $\mu$  may be a function of the field so that the I-V characteristic will not correspond to (4).

In the second region where  $v = \text{const}$  the I - V characteristic will be the following:

$$J = 2 \epsilon_S v_S V / w^2 \quad (5)$$

where  $v_S$  is the saturated velocity. Thus, when the drift velocity is saturated, we will observe the linear region in the I-V characteristic.

### Experimental structure

The original three-terminal  $N^+ - p - N^+$  structure has been used for these investigations. The structure consists of three regions, called the base, collector and emitter according to the transistor terminology. The middle region or base contains the silicon carbide polytype chosen for investigation. It is doped by the deep acceptor impurity scandium to obtain the minimal free hole concentration of about  $10^{10} \text{ cm}^{-3}$  at 300 K. The base is located between two n-regions, collector and emitter. The collector and emitter p-n junctions are the same, but they differ from the usual ones.

The forward biased junction can be opened only by a direct bias or by pulses with duration  $t_p > 10^{-2} \text{ sec}$ . Naturally, for lowering of the potential barrier, it is necessary to deionize the deep acceptor impurity in the space charge region. The characteristic time of this process is more than  $10^{-2} \text{ sec}$  at a hole concentration of about  $10^{10} \text{ cm}^{-3}$ . But when the potential barrier is lowered, injection, which is a noninertial process, can be accomplished by pulses with  $t_p \ll 10^{-2} \text{ sec}$ .

There is the following situation in the reversed biased junction. At the reversed direct bias, the field in the p-region is screened by ionised acceptor impurities with  $N_a - N_d \sim 10^{17} \text{ cm}^{-3}$ . For a voltage of about several tens of volts, the length of screening is less than  $10^{-4} \text{ cm}$  and the field in the p-region is nonuniform. However, the screening length is larger than  $10^{-1} \text{ cm}$  in accordance with the hole concentration of about  $p < 10^{10} \text{ cm}^{-3}$  at the reversed pulse bias with a duration  $t_p \ll t_i$ . Here  $t_i$  is the time of ionisation for the acceptor impurity. Therefore, the width of the p-region of about  $(5-10) \times 10^{-4} \text{ cm}$  allows one to obtain a practically uniform electric field. The field has to be directed parallel to the superlattice axis.

The working principle of the structure is the following: the collector junction is reversed biased by the pulse voltage with  $t_p \sim 10^{-7} \text{ sec}$ . The emitter junction is forward biased by direct voltage, which causes injection into the base. The electric scheme is analogous to the transistor with a common emitter.

The pulse field spreading through the base reaches the open emitter junction and causes injection into the base. The injected current increases with the pulse voltage, but it can be limited by the decrease of the bias between emitter and base.

Thus, there is the uniform electric field in the p-region and the current intensity is controlled independently on the field in the base region. Besides it is highly important that this experimental method allows one to conduct measurements with the electron current only without the current associated with the holes.

### Experimental results and discussion

The electronic transport in the experimental structure used for the measurements is determined by the transit time mechanism. It is known that the current-field characteristic inherent for the transit-time conduction mechanism includes the linear region associated with the space charge limited current. This region is observed when the concentration of the carriers injected is as large as an ionised impurity concentration in the base. In a usual situation such a condition is met at a very

large current density and a strong electric field when the carriers drift velocity reaches its saturation value.

The feature of the experimental structure used for the study is an ionised impurity concentration so low that the space charge limitation of the current takes place at low current density when the electric field is insufficient for the carriers velocity saturation.

In this paper we present the data of I-V characteristics investigation for the polytypes 4H, 6H, 8H, 15R and 21R SiC. The current-field characteristic of the experimental structure may include the following regions connected with the space charge limitation of the current injected: the region with  $j \sim V^2$  (4) and the region with  $j \sim V$  associated with electron velocity saturation (5). However, in real I-V characteristics (Fig.1) the current follows a power-law dependence  $J \sim V^{1.6}$ , probably because of the dependence  $\mu \sim V^{-0.4}$ , that was indicated above.

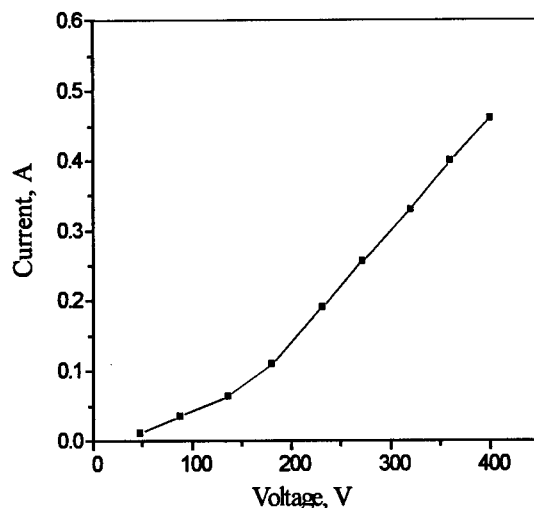


Fig 1. I-V characteristic of the 4H-SiC three terminal structure

From the analysis of the linear region of I - V characteristics the values of saturated electron drift velocities for 4H-, 6H-, 8H- and 21R-SiC (Fig.2) were obtained, which are approximately equal to  $3.3 \cdot 10^6$ ,  $2 \cdot 10^6$ ,  $10^6$  and  $4.4 \cdot 10^5$  cm/sec, respectively. The saturated electron drift velocity of 15R-SiC is approximately equal to  $\sim 1.2 \cdot 10^6$  cm/s. The low values of velocities, which are significantly smaller than the well known value  $v_s = 2 \cdot 10^7$  cm/sec for  $E \perp C$  [1] are of special interest. But these values qualitatively correspond to the analogous results for artificial SL's. Both for these SL and for the NSL of SiC polytypes the saturated drift velocity drops with a decrease of the miniband width. The NSL periods of 4H, 6H, and 8H SiC are equal to 5Å, 7.5Å, and 10Å, respectively, and their saturated electron drift velocities qualitatively confirms the relation  $v_s \sim 1/d^3$  for miniband transport in SL [7].

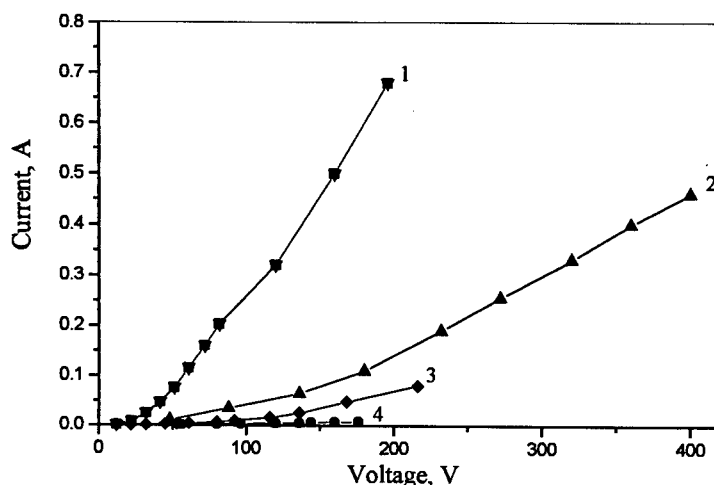


Fig. 2. I-V characteristics of 6H- (1), 4H- (2), 8H- (3), 21R-SiC (4) three terminal structures

The threshold fields at which the drift velocity is saturated for 4H, 6H, and 8H are equal to 155, 140, and 135 kV/cm, respectively. The obtained results do not allow one to determine accurate values of the threshold fields for 15R and 21R polytypes. However, because of the very narrow miniband for 21R-SiC the transport mechanism in strong field is probably a hopping one, which would explain the sharp drop of the saturated drift velocity in this polytype.

Thus, the presented results are new evidence of minizone structure of electron spectra in SiC polytypes and contribute to the data base for high power high frequency vertical transistors.

The partial financial support of Russian Foundation of Fundamental Research project 97-02-18295 and Russian Science Program «Physics of Solid State Nanostructures» project 97-1038 is gratefully acknowledged.

#### References

- [1] I. A. Khan and J. A. Cooper, Jr., Proceedings ICSCIII-N' 97, Stockholm, August 31-September 5, 1997, p. 57-58.
- [2] A. Sibille, J.F. Palmier, H. Wang, and F. Mollot, Phys. Rev. Lett. 6 (1990) p. 52.
- [3] H.T. Grahn, K. von Klitzing, K. Ploog, and G.H. Doler, Phys. Rev. B 43 (1997), p. 12094.
- [4] V.I. Sankin and I.A. Stolichnov, Semiconductors 31 (1996), p. 512.
- [5] V.I. Sankin and I.A. Stolichnov, JETP Lett. 64 (1996), p. 114.
- [6] V.I. Sankin and A. A. Lepneva, Nanostructures: Physics and Technology 97 St Petersburg 23-27 June 1997 p. 155.
- [7] L. Esaki and R. Tsu, IBM J. Res. Dev. 14 (1970), p. 61.

E-mail: <sankin@widegap.ioffe.rssi.ru>

Fax: (812) 247-10-17

## High Temperature Effects on the Terahertz Mobility of Hot Electrons in 3C-SiC and 6H-SiC

E.W.S. Caetano<sup>1</sup>, E.F. Bezerra<sup>1</sup>, V. Lemos<sup>1</sup>, V.N. Freire<sup>1\*</sup>, E.F. da Silva Jr.<sup>2</sup>  
and J.A.P. da Costa<sup>3</sup>

<sup>1</sup> Departamento de Física, Universidade Federal do Ceará, Campus do Pici,  
Caixa Postal 6030, BR-60455-760 Fortaleza, Ceará, Brazil

<sup>2</sup> Departamento de Física, Universidade Federal de Pernambuco, Cidade Universitária,  
BR-50760-901 Recife, Pernambuco, Brazil

<sup>3</sup> Departamento de Física, Universidade Federal do Rio Grande do Norte,  
Caixa Postal 1641, BR-59072-970 Natal, Rio Grande do Norte, Brazil

**Keywords:** Complex Mobility, High-Frequency Behavior, Transport ac+dc in 3C-SiC, Transport ac+dc in 6H-SiC

**Abstract** High temperature effects on the hot electron terahertz complex mobility in 3C-SiC and 6H-SiC subjected to *ac* (200 kV/cm) and *dc* (up to 800 kV/cm) electric field intensities are studied. A lattice temperature increase favors a strong reduction of both the frequency dependent electron mobility maxima and minima, and can even eliminate them when the *dc* electric field intensity is high enough.

**Introduction** Although silicon carbide polytypes are recognized as promising materials for high-power, high-temperature, and high-frequency operating devices, there is still a lack of results necessary for a better understanding of their properties, as for example in the carrier transport phenomena domain. Most of the investigations on the SiC polytypes transport properties were restricted to the steady-state response to constant electric fields  $E_{dc}$  [1-4]. In respect to the role of the lattice temperature, Monte Carlo simulations of electron transport in 4H-SiC indicated a decrease of the *dc* electron mobility with the raise of the lattice temperature in the 100 – 700 K range [5,6].

Recently, high temperature effects on the velocity overshoot of hot electrons in 6H- and 3C-SiC subjected to constant electric fields were shown to be very important [7]. It was demonstrated that an increase of the lattice temperature could reduce both the electron drift velocity and energy, being even possible to preclude the existence of the drift velocity overshoot effect. On the other hand, room temperature terahertz electron mobility in 3C-SiC under low ( $< 50$  kV/cm)  $E_{ac}+E_{dc}$  electric fields was studied by Weng and Lei [8]. They showed the possibility of the existence of a maximum (maximum and minimum) in the real (imaginary) mobility component in the 1–10 THz frequency range depending on the ratio of the electric field intensities  $E_{ac}$  and  $E_{dc}$ . However, the influence of the lattice temperature on the complex mobility of electrons in silicon carbides was disregarded up to now, even though it is fundamental for high-temperature operation of SiC-based devices.

The purpose of this work is to investigate the behavior of the terahertz electron mobility in 3C- and 6H-SiC at lattice temperatures 300 K, 673 K, and 1073 K. The focus on these silicon carbide polytypes is due to the potential applications associated with their higher saturation velocities, particularly in the domain of high-temperature, high-speed/high-field nanostructures and devices circuitry. Balance hydrodynamic equations for the electron drift velocity and energy are solved numerically, and the frequency dependent mobility is calculated through a Fourier transform of the electron drift velocity after its arrival at the steady state. It is shown that in both the silicon carbide polytypes the real part of the mobility presents a relative maximum  $\omega/2\pi \sim 12$  THz, while

the imaginary mobility can present a minimum (maximum) around  $\omega/2\pi \sim 2$  THz (12 THz). Their existence depends strongly on the lattice temperature, as well as on the ratio of the electric field intensities  $E_{ac}$  and  $E_{dc}$ .

**The Complex Electron Mobility** The electron drift velocity  $v(t, \omega)$  and mean energy  $\varepsilon(t, \omega)$  evolution towards the steady state is calculated through the numerical solution of Boltzmann-like transport equations within the energy  $\tau_\varepsilon(\varepsilon)$  and momentum  $\tau_p(\varepsilon)$  relaxation time approximations [7]. In this work,  $\tau_\varepsilon(\varepsilon)$  and  $\tau_p(\varepsilon)$  are obtained using the steady-state relations  $v \times E_{dc}$  and  $\varepsilon \times E_{dc}$  calculated by Weng and Cui [2] for 3C-SiC and 6H-SiC subjected to an electric field  $E_F(\omega, t) = E_{dc} + E_{ac}\cos(\omega t)$ , where  $\omega$  is the frequency of the oscillatory component of the electric field. The electrons are scattered through the acoustic-deformation-potential, the polar-optical and intervalley phonon, and ionized impurities.

The mobility  $\mu(t)$  at time  $t$  can be defined as the ratio between the drift velocity  $v(\omega, t)$  and the electric field  $E_F(\omega, t)$ . The complex Fourier spectrum  $\mu(\omega)$  of the time-dependent mobility may represent the dynamic mobility of the system under a  $dc$  plus  $ac$  electric field. It is calculated in the time period  $T$  by performing the following Fourier transform of the electron drift velocity after its arrival at the steady state at time  $\tau$ :

$$\mu(\omega) = \mu_R(\omega) + i\mu_I(\omega) = \frac{1}{T} \int_{\tau}^{\tau+T} \frac{v(t)}{E_{dc} + E_{ac} \cos(\omega t)} e^{+i\omega t} dt \quad (1)$$

A lattice temperature variation modifies the rate of change of the mean electron energy, which alters the time evolution of the electron drift velocity through the variation of the momentum relaxation time due to the electron scattering processes. Consequently, the complex mobility  $\mu(\omega)$  should also change with the variation of the lattice temperature, but depending highly on the frequency of the applied oscillatory electric field. The band structure characteristics of 3C-SiC and 6H-SiC are well established [9-12], but the numerical calculations are performed within the equivalent isotropic valley picture [1,2,7], in which the electron effective mass  $m_e$  in the conduction band is  $0.346 m_0$  ( $0.30 m_0$ ) for 3C-SiC (6H-SiC), where  $m_0$  is the free space electron mass. Band nonparabolicity is taken into account considering  $\hbar^2 k^2 / (2m_e) = \varepsilon (1 + \alpha\varepsilon)$ .  $\alpha$  is the nonparabolic band coefficient, which is  $0.323 \text{ eV}^{-1}$  for 3C-SiC, and  $(1 - m_e/m_0)^2/E_g$  for 6H-SiC, where  $E_g$  is the 6H-SiC gap energy [1,2,7].

**High Temperature Effects on the Terahertz Mobility** The terahertz frequency behavior of the components of the complex mobility of electrons in 3C-SiC and 6H-SiC subjected to a 200 kV/cm  $ac$  electric field intensity are presented in Fig. 1 and Fig. 2, respectively. For a given  $dc$  electric field intensity and frequency, the absolute value of both the real  $[\mu_R(\omega)]$  and imaginary  $[\mu_I(\omega)]$  components of the electron mobility in 3C-SiC is always bigger than in 6H-SiC, which is a consequence of the lower electron effective mass in the former than in the latter.

In both the silicon carbide polytypes,  $\mu_R(\omega)$  presents a maximum around  $\omega/2\pi \sim 7$  THz at low  $dc$  electric fields ( $< 450 \text{ kV/cm}$ ) and lattice temperature (300 K) depending on the ratio of the electric field intensities  $E_{ac}$  and  $E_{dc}$ . When the  $dc$  electric field intensity increases, the maximum becomes smoother up to its disappearance. The structure in the  $\mu_R(\omega)$  profile is considerably reduced for higher lattice temperatures, and an increase of about 300 K can preclude the existence of the maximum. At 300 K, the imaginary component  $\mu_I(\omega)$  of the electron mobility presents a minimum close to 2 THz, and a maximum around 12 THz for  $dc$  electric field intensities smaller than 550 kV/cm. However, both the maximum and the minimum disappear when  $E_{dc} > 550 \text{ kV/cm}$ . The minimum of  $\mu_I(\omega)$  is smoothed strongly when the lattice temperature is 673 K, disappearing completely at 1073 K. The maximum of  $\mu_I(\omega)$  is also smoothed strongly with the increase of the

lattice temperature, but does not disappear even at 1073 K. Comparison of the behavior of the 3C- and 6H-SiC mobilities reveals that the profiles are qualitatively the same, especially at the highest lattice temperature value. This is remarkable because the different polytypes have wide spread physical properties.

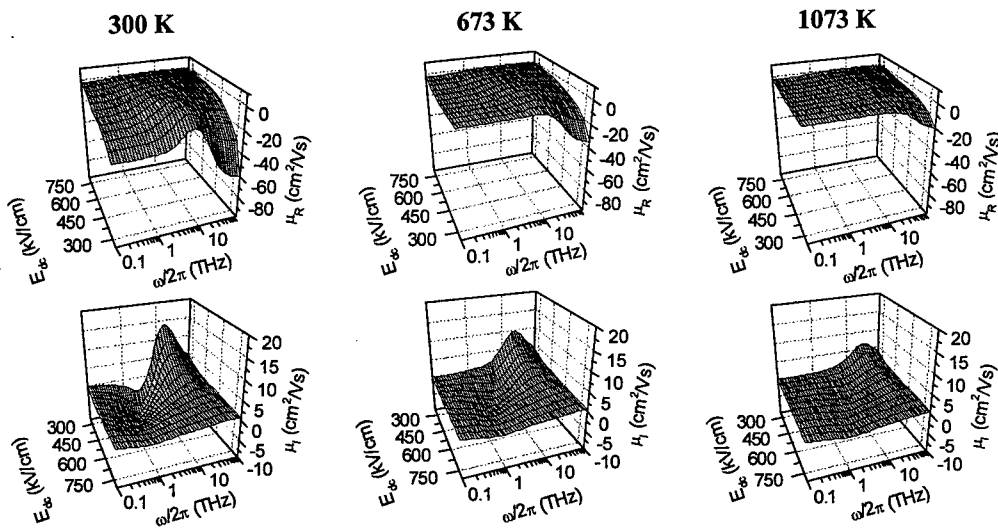


**Figure 1** Real (top) and imaginary (bottom) components of the complex mobility  $\mu(\omega)$  in 3C-SiC at 300 K (left panel), 673 K (central panel), and 1073 K (right panel). The ac electric field intensity is 200 KV/cm.

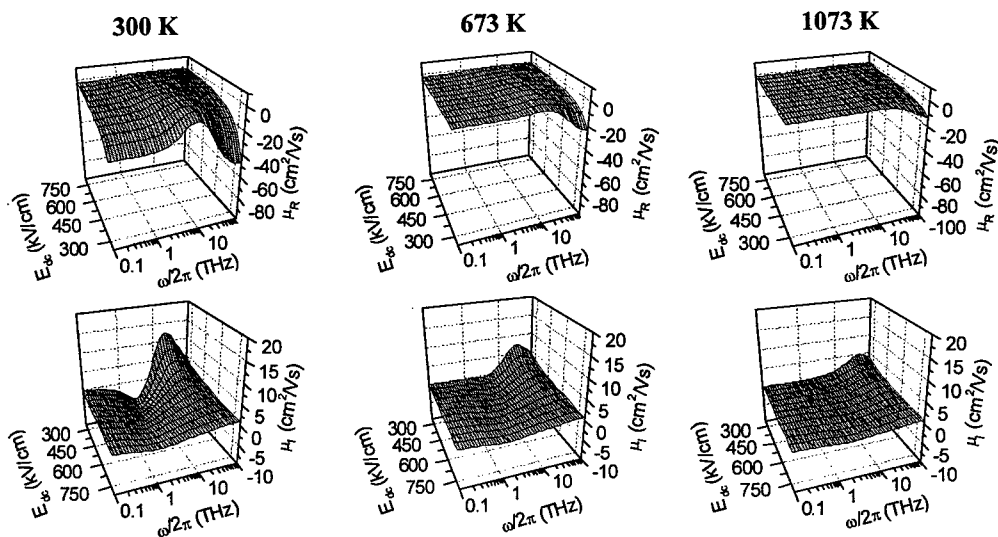


**Figure 2** Real (top) and imaginary (bottom) components of the complex mobility  $\mu(\omega)$  in 6H-SiC at 300 K (left panel), 673 K (central panel), and 1073 K (right panel). The ac electric field intensity is 200 KV/cm.

As stated previously, the hot electron high-frequency mobility calculations in 3C-SiC performed by Weng and Lei [2] have pointed out the existence of maxima and minima in the real and imaginary components of the mobility using the Lei-Ting balance equation theory [13,14], a completely different theoretical approach in comparison with the one considered in this work. It is interesting to remark that in both the works, the frequencies in which the maxima and minima of the components of the electron mobility occurs were shown to be very close. However, a direct comparison between their results with those presented in Fig. 1 and Fig. 2 is not possible since the highest *dc* electric field intensity used by Weng and Lei [8] was only 42 kV/cm, well below the values of the present work.

**Concluding Remarks** The results presented in this work indicate the important role of the lattice temperature on the terahertz mobility of hot electrons in 3C-SiC and 6H-SiC. The most remarkable effect is that an increase in the lattice temperature produces a striking smoothening of the structures in both the real and imaginary components of the hot electron mobility. The maxima and minima can even disappear for higher lattice temperatures resulting in a very similar profile for both polytypes investigated here. Since the approach used in this work for the solution of the transport equations underestimates (less than 10%) the peaks of the electron drift velocity [15], the variation of the terahertz electron mobility with the 3C-SiC and 6H-SiC lattice temperatures should be recognized as an indication of a behavior rather than offering accurate estimates.

**Acknowledgements** The authors would like to acknowledge the financial support received from the Brazilian National Research Council (CNPq), the Ministry of Planning through FINEP, the Science Funding Agency of the Ceará State in Brazil (FUNCAP), and the Banco do Nordeste S/A under contract BNB-FADE # 003/98.

## References

- [1] K. Tsukioka, D. Vasileska, and D. K. Ferry, *Physica B* **185** (1993), p. 466.
- [2] X. M. Weng and H. L. Cui, *Phys. Stat. Sol. (b)* **201** (1997), p. 161.
- [3] H.-E. Nilsson, M. Hjelm, C. Fröjdh, C. Persson, U. Sannemo, and C. S. Petersson, *J. Appl. Phys.* **86** (1999), p. 965.
- [4] E. Belloti, H.-E. Nilsson, K. Brennan, and P. P. Ruden, *J. Appl. Phys.* **85** (1999), p. 3211.
- [5] R. P. Joshi, *J. Appl. Phys.* **78** (1995), p. 5518.
- [6] H.-E. Nilsson, U. Sannemo, and C. S. Petersson, *J. Appl. Phys.* **80** (1996), p. 3365.
- [7] E. F. Bezerra, E. W. S. Caetano, V. N. Freire, E. F. da Silva Jr., and J. A. P. da Costa, *Semicond. Sci. Technol.* (1999), in press.
- [8] X. M. Weng and X. L. Lei, *Phys. Stat. Sol. (b)* **187** (1995), p. 579.
- [9] B. Wenzien, P. Käckell, F. Bechstedt, and G. Cappellini, *Phys. Rev. B* **52** (1995), p. 10897.
- [10] W. R. Lambrecht and B. Segall, *Phys. Rev. B* **52** (1995), p. R2249.
- [11] C. H. Park, B.-H. Cheong, K.-H. Lee, and K. J. Chang, *Phys. Rev. B* **49** (1994), p. 4485.
- [12] P. Käckell, B. Wenzien, and F. Bechstedt, *Phys. Rev. B* **50** (1994), p. 10761.
- [13] X. L. Lei and C. S. Ting, *Phys. Rev. B* **30** (1984), p. 4809.
- [14] X. L. Lei and C. S. Ting, *Phys. Rev. B* **32** (1985), p. 1112.
- [15] B. E. Foutz, S. K. O'Leary, M. S. Shur, and L. F. Eastman, *J. Appl. Phys.* **85** (1999), p. 7727.

**Author to whom correspondence should be sent:** V. N. Freire, Departamento de Física, Universidade Federal do Ceará, Caixa Postal 6030, Campus do Pici, 60455-760 Fortaleza, Ceará, Brazil, Email: [valder@fisica.ufc.br](mailto:valder@fisica.ufc.br), Fax: 55 (85) 2874138

(\*) Permanent Address: Instituto de Física Gleb Wataghin, Universidade Estadual de Campinas, 13083-970 Campinas, São Paulo, Brazil.



## Electron Beam Induced Current Investigation of High-Voltage 4H Silicon Carbide Diodes

John Österman<sup>1</sup>, Anders Hallén<sup>1</sup>, Mikael Jargelius<sup>1</sup>, Uwe Zimmermann<sup>1</sup>,  
Augustinas Galeckas<sup>1</sup> and Bo Breitholtz<sup>1,2</sup>

<sup>1</sup> Department of Electronics, Royal Institute of Technology,  
Electrum 229, SE-16440 Stockholm, Sweden

<sup>2</sup> ABB Corporate Research, SE-721 78 Västerås, Sweden

**Keywords:** Carrier Multiplication, CCD, Diffusion Length, EBIC, High Voltage

**Abstract:** High-voltage implanted 4H-SiC p<sup>+</sup>n diodes have been studied by means of electron beam induced current (EBIC) measurements for reverse voltages in the kV-range. Several EBIC investigating techniques were employed in different planar and cross-section geometries. A mapping of the multiplication coefficient revealed that the current through some defects saturates above a certain negative bias, causing a reduction in the multiplication of the electron beam generated charge carriers. By comparing EBIC images with optical images from CCD measurements, the presence of defects exhibiting an increased current without a corresponding increase in light emission can be detected. Finally, the diffusion length of holes in the low doped n-region close to the pn-junction was estimated to be 1.5 µm.

### Introduction

Due to recent improvements in growth technique, silicon carbide has emerged as a top-candidate among the wide bandgap semiconductor materials for high power, high frequency and high temperature applications. For further improvement of material quality and performance of SiC-based devices, techniques for measuring critical material as well as device parameters need to be developed.

Measuring the current through a pn-junction as a function of the position of a deliberately induced excess carrier distribution has traditionally been used as a valuable tool in determining such parameters [1,2]. The use of an electron beam as the source of excitation provides a non-destructive charge generation volume with a spatial resolution in the sub-micron range.

The object of this work is to show the potential of this technique using different sample geometries and to describe the benefits of combining EBIC measurements with optical CCD-images. Based on the experiments we will also try to explain the main results and to analyze some of the material properties.

### Experimental

The diodes consisted of aluminum- and boron implanted p<sup>+</sup>n junctions with a diameter of 0.8 mm surrounded by junction termination zones, on an epitaxial layer of CVD grown low n-doped 4H-SiC [3]. In figure 1 the different sample geometries are shown. The contact metallization was removed on the diodes intended for in-plane investigations (fig. 1a), but not on those subject to cross-section measurements (fig. 1b and c). The diodes were polished in a Phoenix Beta grinder/polisher using lapping film discs with a minimum surface roughness of 0.3 µm. During the entire process dummy pieces were attached tightly on each side of the selected diode, in order to reduce the induced surface damage at the edges.

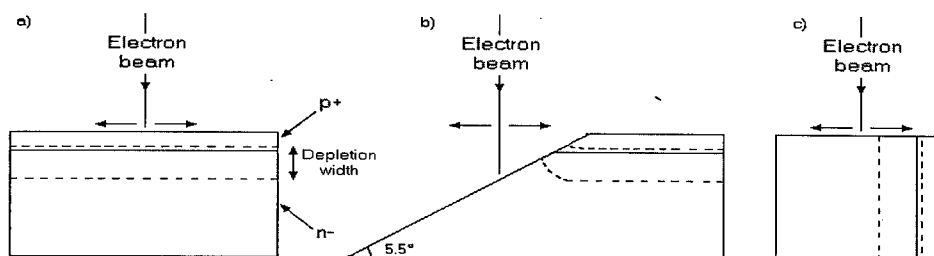


**Figure 1.** Scheme of the different EBIC scanning techniques. a) The diode is scanned across the surface parallel to the junction plane. b) The e-beam is incident at an angle of  $5.5^\circ$  to the plane normal, onto a polished cross-section through the junction (negative beveling angle). c) Scanning over an area perpendicular to the plane.

The EBIC measurements were conducted in a JEOL JSM-25S scanning electron microscope, using electron beam currents ranging from 5 pA to 3 nA and acceleration voltages of 5, 15 and 25 kV. A Keithley 237 high voltage source measure unit and a Stanford Research Systems high power supply model PS 305 were used for high-resolution and high-voltage (1–5 kV) measurements, respectively. Special sample holders were manufactured for planar and cross-sectional high-voltage measurements. The set-up was calibrated by measuring the extension of the depletion region as a function of reverse bias using high-voltage silicon diodes with well determined properties, and tested for applied voltages of up to 5 kV.

Three EBIC scanning modes were employed: (1) *Two-dimensional scanning* was used mainly for investigating surfaces and for locating defects. (2) *Line scans* were measured across the junction, both in order to determine the extension of the depletion region as a function of reverse bias and for evaluation of minority carrier diffusion length. (3) *Point measurements* of the EBIC current were performed at electrically active defects, during which the electron beam was kept at a constant position.

Details of the CCD- and I-V measurements can be found elsewhere [4].

## Discussion and results

### Qualitative analysis EBIC-/CCD measurements

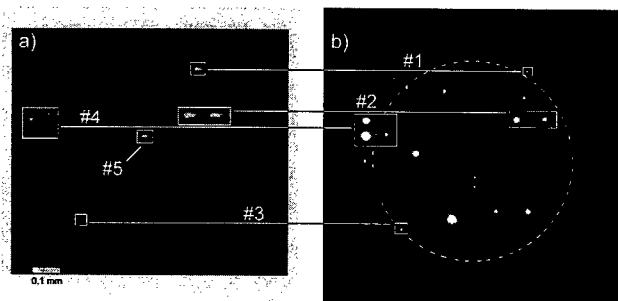


**Figure 2.** a) EBIC- and b) CCD image of a 4H-SiC  $p^+-n$  diode at a reverse bias of 500 V.

Figure 2 shows (a) the EBIC- and (b) the CCD image of one of the investigated diodes at a reverse bias of 500 V. The majority of the areas exhibiting an increased EBIC signal also show break down emission at similar positions (#1-4) - but not the opposite; the number of CCD-spots are clearly exceeding the number of EBIC-spots. This behavior was found to be in common for all investigated diodes.

The observed differences between the EBIC and CCD images are most likely related to different sensitivity and to the higher current flow during EBIC measurements due to the induced charge carriers. Moreover, the EBIC signal is generated only in the depletion region, whereas the light emission may originate from any depth. Consequently we cannot expect all CCD detected

variations in light intensity to be present as contrasts also in current distribution measured by EBIC. However, some of the bright EBIC spots (e.g. #5) can not be observed in the CCD-picture, suggesting increased current flow through the junction without the corresponding increase in light emission. This phenomenon was confirmed at defects on several of the investigated diodes.

Hence, an increase in breakdown emission without a similar EBIC contrast can be expected to correspond to a defect either situated outside the depletion region or not being electrically active, whereas a single EBIC contrast without CCD response may be related to the differences in current flow. Correlating images in this manner thus provides useful means to differentiate between electrically and/or optically active defects located within and/or outside the depletion region.

### Quantitative EBIC analysis

A mapping of the multiplication at electrically active defects was carried out over the junction area, employing the two-dimensional planar scanning EBIC technique in combination with point measurements of the current. Only defects not detectable in SEM mode were included in the investigation. Structural defects may influence the multiplication in several ways, for instance by containing generation centers or by having a smaller effective bandgap, which aids the ionization and thus enhance the creation of electron-hole pairs.

Figure 3 views the current ratio  $I_{\text{def}}/I_{\text{ref}}$  as a function of applied reverse bias at two electrically active defects, both showing CCD detectable breakdown emission.  $I_{\text{def}}$  is the *defect* current measured locally at the defect and  $I_{\text{ref}}$  is the *reference* current measured at an arbitrary defect free position. For both currents the leakage current (i.e. the current measured with no electron beam incident on the diode) is subtracted. Due to the subtraction,  $I_{\text{ref}}$  is assumed to be a constant as a function of reverse voltage up to the point where breakdown occurs, and equal to the current originating from the electron beam generation volume. The ratio  $I_{\text{def}}/I_{\text{ref}}$  then corresponds to the number of charge carriers created per initially induced electron-hole pair by the electron beam, and is a measure of the multiplication at defects.

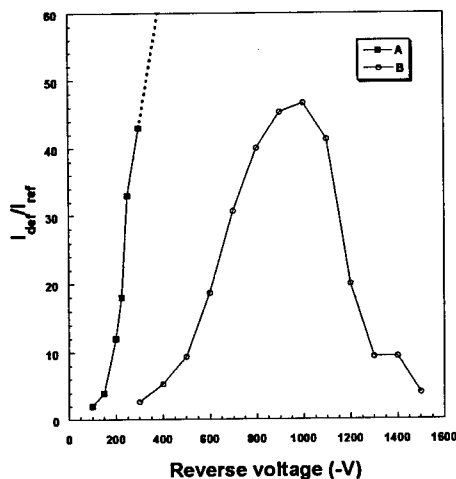


Figure 3. EBIC carrier multiplication

This ratio was generally found to exhibit the characteristic avalanche effect as a function of reverse bias, observed for defect A in fig. 3. Some defects however, were found to reach a saturated state after which the multiplication of the electron beam generated current was again reduced to zero, as characterized by defect B in fig. 3. This behavior indicates a limitation of current occurring at high current densities, which can be expected in the small region where  $I_{\text{def}}$  was measured. As the voltage is increased above a certain level corresponding to this saturation current, the multiplication of the electron beam generated carriers is reduced. The decrease may be explained by multiplication of the intrinsically present charge carriers so that the addition of the electron beam generated carriers no longer contributes to an increased current.

Furthermore, the in-depth extension of the depletion region was measured as a function of reverse bias up to -300V and was found to be about  $2 \times 10^{15} \text{ cm}^{-3}$ . The results suggest that the method is a useful tool for determining the concentration of electrically activated charge carriers in the low doped side of the pn-junction.

### Diffusion length measurements

The diffusion length was evaluated from EBIC line scans taken across the edge of the depletion region on polished cross-sections of the diode. Assuming pure diffusive transport of the generated minority charge carriers and neglecting surface recombination, the current decays exponentially as a function of distance  $x$  between the EBIC generation volume and the junction:

$$I = I_0 e^{-x/L} \Leftrightarrow -\ln(I/I_0) = x/L \quad (1)$$

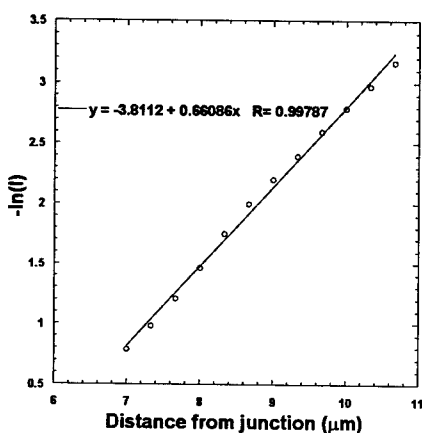


Figure 4.  $L_p$  in low doped n-region

The constant  $I_0$  is the maximum current corresponding to a complete collection of the generated charge carriers. The accuracy of such measurements is, however, strongly reduced close to the junction when the dimensions of the EBIC generation volume is of the same order of magnitude as the diffusion length. As deduced from Monte Carlo simulations [5], most of the EHP generated by a 15 keV electron beam extends less than 1 μm in 4H-SiC. For the extraction of diffusion length therefore, only the current measured more than 5-6 μm away from the junction was used. From the linear relation shown in fig. 4 for  $-\ln(I)$  as a function of  $x$ , an estimated diffusion length of  $L_p = 1.5$  μm could be obtained for holes in the low doped n-region.

### Conclusions

Correlating EBIC and CCD measurements has been proven efficient for differentiation between electrically and/or optically active defects located within and/or outside the depletion region of SiC p<sup>+</sup>n junctions.

The dominating mechanism governing the reverse I-V dependence at electrically active defects exhibits the characteristic avalanche behavior. However, EBIC measurements reveal that some defects reach a saturated state in which the multiplication of the electron beam generated carriers is prevented from avalanche.

### Acknowledgements

We gratefully acknowledge the ABB Silicon Carbide Research Project in Sweden for providing the material used in this work as well as for taking part in discussions.

Financial support was given by the Swedish Foundation for Strategic Research, within the SiCEP program.

### References:

- [1] M. Frischolz, Th. Mandel, R. Helbig, G. Schmidt, A. Hammerschmidt, *Applied Surface Science*, 65/66 (1993), p 784-88.
- [2] R. Raghunatan, B.J. Baliga, *Power Semiconductor Devices and ICs, ISPSD 96 Proceedings* (1996), p 111-14.
- [3] O.Kordina, C.Hallin, A. Henry, J.P. Bergman, I. Ivanov, A. Ellison, N.T. Son, E. Janzén, *Phys. Stat. Sol. B* 202 (1997), p 321.
- [4] U. Zimmermann, A. Hallén, A.O. Konstantinov, B. Breitholtz, *MRS Proc.* vol. 512 (1999), p151-156.
- [5] M. Jargelius, U. Gustafsson, M. Bakowski, *Microelectronics-Reliability*, vol.38, no.3 (1998), p.373-9

## Measurement of Charge Carrier Lifetime Temperature-Dependence in 4H-SiC Power Diodes

Andres Udál and Enn Velmre

Department of Electronics, Tallinn Technical University, Ehitajate tee 5, EE-19086 Tallinn, Estland

**Keywords:** Effective Lifetime Temperature-dependence, Reverse Recovery Charge Measurements

**Abstract** Charge carrier effective lifetimes in 4H-SiC power diode n-bases for wide temperature range  $-70 \div +180^\circ\text{C}$  were estimated by reverse recovery charge measurements and parallel simulations. At room temperature lifetime values in the  $50 \div 60\text{ ns}$  range were obtained. For lifetime temperature-dependence the power law behaviour  $\tau \sim T^\alpha$  was confirmed with exponent values  $\alpha \approx 2.0 \div 2.2$ .

### Introduction

To achieve accuracy in device simulation, especially in the case of relatively thick power structures, the minority carrier lifetime realistic temperature dependence  $\tau(T)$  is one of the most important physical submodels to be included. In particular, the increase of  $\tau$  at higher temperatures seems to be the main reason for forward voltage drop versus temperature negative coefficient  $dV_F/dT < 0$  often observed in the case of SiC-devices. On another hand, the theoretical reasoning for the  $\tau(T)$  dependence is very unclear.

The experience from Si power device simulations has shown that rather acceptable practical results in wide temperature range could be obtained by using power function approximation:

$$\tau(T) = T^\alpha \quad (1)$$

with exponent  $\alpha$  numerical values around 2 for Au-controlled lifetime and around 3 for Pt-controlled lifetime. For SiC there is only very limited experience of estimating  $\tau(T)$  dependence. For instance, in [1] the linear approximation

$$\tau(T) = \tau(300\text{K}) \cdot \left[ 1 + A \left( \frac{T}{300\text{K}} - 1 \right) \right], \quad A = 2.17 \quad (2)$$

was offered for 4H-SiC and temperature range  $300 \div 450\text{ K}$  by the measurements at Linköping University.

### Description of measurement and simulation techniques

In this paper, the inductive load reverse recovery (ramp recovery) charge measurements and parallel simulations with SiC-DYNAMIT-1DT simulator [2-4] are used to estimate the realistic  $\tau(T)$  dependence for 4H-SiC in temperature range  $-70 \div +180^\circ\text{C}$ . The investigated structures are

4H-SiC  $p^{++}p^{+}nn^{+}$  power diodes with  $(30\div40)\mu\text{m}$   $(0.9\div2.6)\cdot10^{15}\text{cm}^{-3}$  epitaxial n-base and with thin  $1.4\mu\text{m}$   $p^{++}p^{+}$ -emitters in the form of  $200\mu\text{m}$  diameter mesa islands [1], see Fig.1.

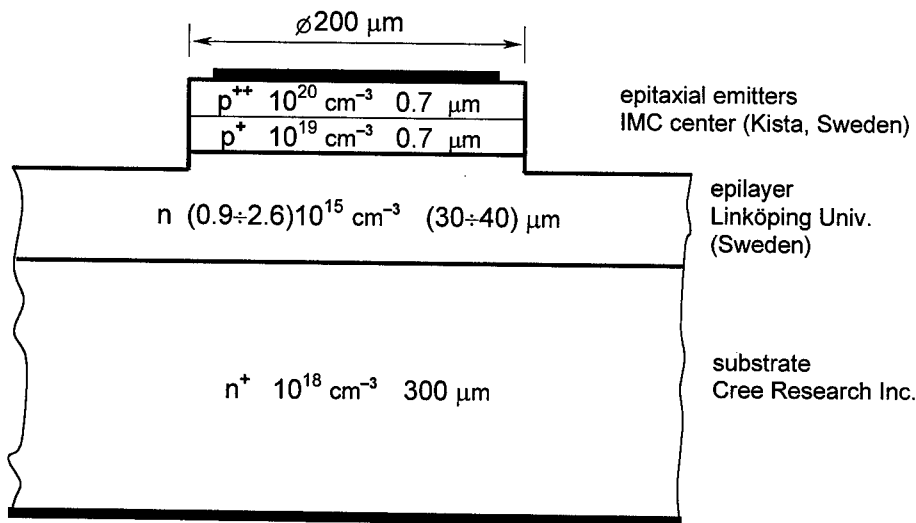


Fig.1. Schematic presentation of the investigated 4H-SiC structures.

Since initial on-state n-base over-equilibrium charge is directly proportional to effective n-base lifetime  $Q_F \approx \tau \cdot I_F$  (omitting some decrease due to emitters non-ideality) and the reverse recovery charge  $Q_{rr} = \int I_R dt$  forms rather definite fraction of  $Q_F$  (affected by reverse voltage level and recombination losses during transient process), the investigation of  $Q_{rr}$  behaviour gives rather direct characterization for  $\tau$  as well. At that influence of mentioned disturbing factors and effects may be minimized by use of numerical device simulator for experiment interpretation. Due to small n-base width in comparison to mesa island diameter, the one-dimensional simulation is assumed to be sufficiently accurate in the present case. Or in other words, the possible influences of surface recombination and nonuniform lateral current distribution are implicitly included within the obtained effective lifetime.

In simulations the room temperature (300K) lifetime was assumed to be  $\approx 50\text{ns}$  (52ns basic variant) in the n-base and 1ns in the  $p^{++}p^{+}$ -emitters and  $n^{+}$ -substrate. The lifetime injection-dependence was omitted and the same power law temperature-dependence (1) was applied in all device layers. The effective cross-section area was taken by  $p^{++}p^{+}$ - emitter island area  $S = 3.14 \cdot 10^{-4}\text{cm}^2$ .

Experiments were performed with pulse generator ( $\pm 10\text{V}$ ,  $R_{gen} = 50\Omega$ ) in inductive load circuit ( $L = 16\mu\text{H}$ ,  $R = 30\Omega$ ) which gave necessary control over the shape of current waveforms. Thus the typical current decreasing time from the forward current level 100mA ( $\approx 300\text{A/cm}^2$ ) was 70÷80ns and the duration of triangle-shaped reverse current pulse varied within 30÷100ns range.

### Results and conclusion

The main results of the present work are summarized by the Fig.2. below. Since the n-base remaining charge in the end of forward current linear ramp  $Q_0$  is related to initial on-state charge approximately as  $Q_0 = Q_F(\tau/t_{ramp})[1 - \exp(-t_{ramp}/\tau)]$ , in present case of relatively short lifetimes ( $\tau \ll t_{ramp}$ ), the relation between reverse recovery charge and lifetime approaches  $Q_{rr} \sim Q_0 \sim \tau^2$ , i.e. the exposed  $Q_{rr}(T)$  dependence actually amplifies the  $\tau(T)$  dependence.

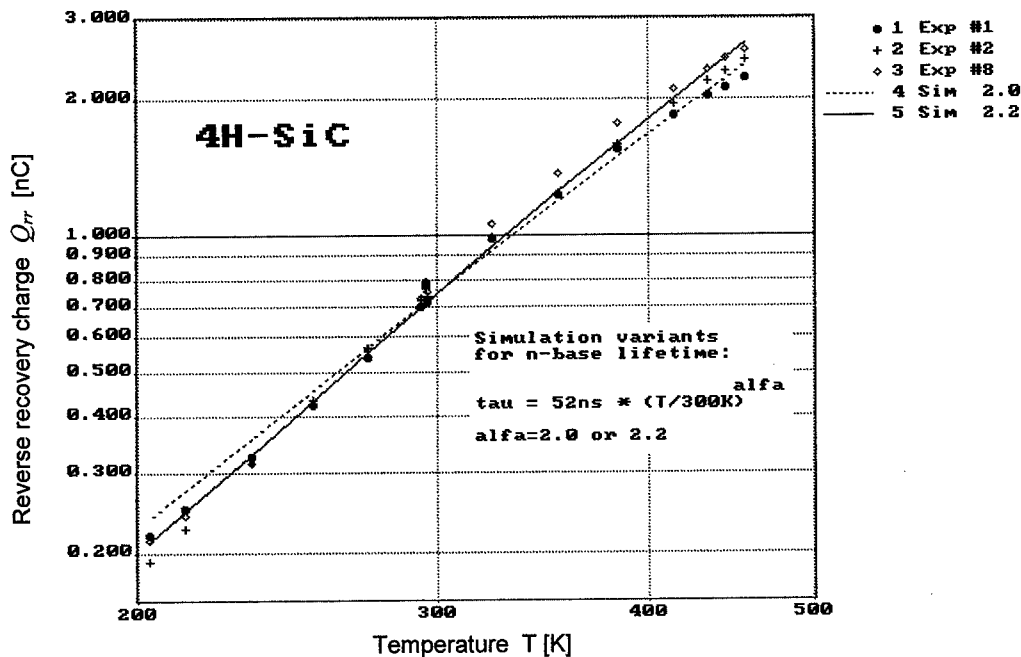


Fig.2. The comparison of temperature-dependences of measured and simulated reverse recovery charges. An acceptable accuracy of the n-base effective lifetime temperature dependence  $\tau \sim T^{2.2}$  is confirmed. Experimental data correspond to 3 different structures.

The main conclusions of the present study are:

1. The room temperature n-base minority carrier on-state lifetime range for the investigated 4H-SiC structures was 50÷60 ns.
2. In general lines the acceptable accuracy of power function dependence (1) was confirmed. In contrast, the linear approximation (2) was clearly incorrect in the present case.
3. For wide temperature range  $-70 \div +180^\circ\text{C}$  the numeric value  $\alpha=2.2$  for exponent in (1) may be recommended (see Fig.2).
4. At higher temperatures  $T > 100^\circ\text{C}$  the slope of the  $Q_{rr}(T)$  dependence becomes smaller so that lower exponent values  $\alpha \leq 2.0$  could be more adequate for that region (see Fig.2).

## Remarks:

1. In his recent experimental work [5] Neudeck observed remarkable rise of effective lifetimes in structures with larger diameter. He concluded that reason for that must be the decreasing role of strong surface recombination. To check his suggestion, we performed some control calculations with 2D-simulator, considering a rectangular structure with lateral size 200  $\mu\text{m}$ . However, even in the case of infinite surface recombination rates over all lateral boundary, the influence of surface recombination on reverse recovery charge remained within 5%. This gives us basis to assume that the reason for Neudeck's observations is probably not the surface recombination itself but decrease of n-epilayer bulk lifetime in structures with smaller p-emitter diameter, caused by some technological side-effect, e.g. by introduction of additional recombination centers in n-epilayer below p-emitter perimeter during p-emitter island processing.
2. Some signs like rather long backfront of the triangle-shaped reverse current pulse and transfer from oscillating reverse current behaviour at low temperatures to soft non-oscillating behaviour at higher temperatures showed that there is possible rather strong lifetime gradient  $\partial\tau/\partial x$  within n-base (higher  $\tau$  near the  $n^+$ -substrate). Anyway, the simulations with this gradient did not change remarkably the overall conclusions of the present work. For instance, if the 4-fold lifetime change within the n-base exists, instead the proposed  $\alpha=2.2$  the value 2.0 could be recommended.
3. A rather small uncertainty of the present results is associated with effective cross-section area selection in one-dimensional simulator. If, e.g. the cross-section area was doubled (to describe lateral current spreading) then fitting yields 49 ns instead 52 ns.

## Acknowledgement

This work has been supported by the Swedish Foundation for Strategic Research (SSF) and by the Swedish Institute through the joint SiCEP/Visby project and by the Estonian Science Foundation project 2828.

## References

- [1] K. Olsson: *Simulation and measurements of electrical properties of 4H-SiC power diodes*. ABB Technical report SECRC/G/TR-9/030E, (1997), 41p.
- [2] E. Velmre, A. Udal, F. Masszi and E. Nordlander: *Investigation of silicon carbide diode structures via numerical simulations including anisotropic effects*. Simulation of semiconductor devices and processes, Vol.6, Ed. by H. Ryssel and P. Pichler, Springer-Verlag, (Proc. of SISDEP'95, Erlangen, Germany, Sept. 6–8, 1995), (1995), pp.340–343.
- [3] E. Velmre and A. Udal: *Comparison of Si and SiC devices surge current capability by means of numerical simulations*. Proc. of the Baltic Electronic Conf. (BEC'96, Tallinn, Oct. 7–11, 1996), (1996), pp.77–80.
- [4] A. Udal and E. Velmre: *SiC-diodes forward surge current failure mechanisms: Experiment and simulation*. Microelectronics and Reliability, **37**, No.10/11 (1997), pp. 1671–1674.
- [5] P.G. Neudeck: *Perimeter Governed Minority Carrier Lifetimes in 4H-SiC  $p^+n$  Diodes Measured by Reverse Recovery Switching Transient Analysis*. Journal of Electronic Materials, **27**, No.4 (1998), pp. 317–323.

For correspondence with readers:

e-mail: audal@va.ttu.ee, FAX: +372 6 202 151, Phone: +372 6 202 150 / 153



## Donors and Acceptors in SiC-Studies with EPR and ENDOR

J.-M. Spaeth

Department of Physics, University of Paderborn, Warburgstr. 100, DE-33095 Paderborn, Germany

**Keywords:** Acceptors, Donors, ENDOR, EPR

**Abstract.** The results of EPR and ENDOR investigations of N donors in various SiC polytypes are critically reviewed. It is discussed whether N donors can be understood as shallow donors with the EMT (Effective Mass) theory. It is shown that only in 3C SiC they are adequately described as being shallow and by EMT. The EPR spectra of P donors are reviewed and reinterpreted to be due to B donors on SiC sites in analogy to the findings of N donors following a recent suggestion by Greulich-Weber. A brief discussion of the Al acceptors follows, which have shallow EMT character according to the present EPR data. Before discussing "shallow" B acceptors, the characteristic features of the deep Sc acceptors and their electronic structure is discussed. It is then shown that the shallow B acceptors clearly have a deep defect character when reviewing the EPR and ENDOR data, albeit being at a rather shallow ionisation level. A common feature between Sc and B acceptors is the fact that there are different EPR spectra and ionisation levels differing by a few meV depending on the localisation of the hole along the c-axis on other bond directions.

### 1. Introduction

Shallow defects are usually regarded as a type of defect well understood in terms of the so-called effective mass theory (EMT). The electronic structure is hydrogenic, the ionisation energy  $E_d$  and the Bohr radius are determined only by the effective mass  $m^*$  and the dielectric constant  $\epsilon_r$  of the material. The hydrogenic level is calculated by applying the factor  $m^* \cdot 1/\epsilon_r^2$  to the classical result of the hydrogen atom. This yields values of  $E_d$  of  $\sim 40$ -60 meV for typical semiconductors due to the large value of  $\epsilon_r$  and typical  $m^*$  values. It has largely been overlooked that this simple picture seems oversimplified. In a detailed study using electron nuclear double resonance (ENDOR) [1,2] of the shallow donors P, As and Sb in silicon, it was shown that the hyperfine (hf) and superhyperfine (shf) interactions cannot be explained using EMT theory, also not when including the so-called central cell corrections introduced to allow for the "chemical" nature of the various donors [1,2]. Since the donor EPR/ENDOR work in SiC, this problem has not been addressed anymore in detail. Now, in SiC one has the additional feature of the various inequivalent sites for the same donor in most polytypes, for example the two quasi-cubic and one hexagonal site in 6H-SiC. It is well known that N has different ionisation levels depending on the site which differ up to a factor of 4 compared to the "naive" EMT value calculated on the basis of  $m^*$  and  $\epsilon_r$  ( $\sim 40$  meV) for example in 6H SiC. No central cell correction due to the "chemical" nature is feasible there: it is always N, which would have the same central cell correction in all sites of the polytype. The question arises which theory is able to describe shallow donors quantitatively in SiC. In this paper the experimental results obtained

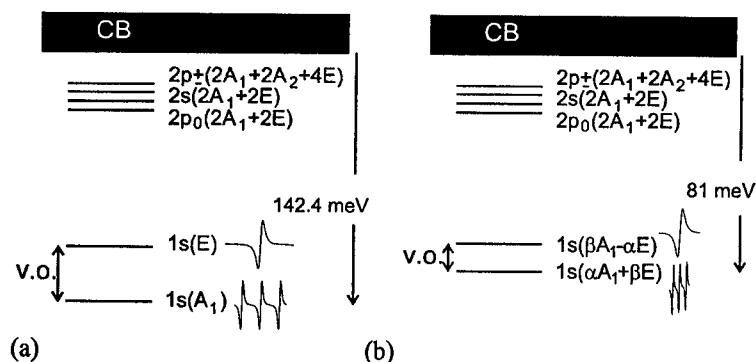


*Fig. 1: Proposed ground state energy levels of the quasi-cubic (a) and hexagonal (b) site nitrogen donors*

in recent years with EPR and ENDOR on N and P donors in various polytypes are critically reviewed and compared with theoretical predictions on the basis of EMT. The question is then addressed whether or not there are "shallow" acceptors, which can be understood by an EMT picture and in particular whether the most common acceptor B has shallow or deep character, having a not so shallow ionisation level at  $E_v+300$  meV. Before discussing the acceptors A1 and B, a brief account is given of the deep Sc acceptor which demonstrates a unique feature of acceptors in SiC, which is also present for the B acceptor: that there is one type of acceptor in various configurations depending on which of the bonds accommodates the hole. Thus, it is shown that defects in SiC have unique and interesting features which are not found in other compound semiconductors.

## 2. Donors

The EPR spectra of N donors in SiC usually show the N hf triplet structure ( $I(^{14}\text{N})=1$ ), in particular when measured at high microwave frequencies, where the various sites having only small g factor differences can be resolved [3]. In table 1 the main results of EPR and ENDOR experiments are summarised for three polytypes. It is apparent that the  $^{14}\text{N}$  hf interaction differs very much for different sites in the same polytype: in 6H-SiC the isotropic hf constant  $a/h$  differs by a factor of 14 between the cubic and the hexagonal sites, i.e. the spin density on the N nucleus differs very much. The hf interaction of the hexagonal site is anisotropic, that of the

polytype	3C	4H		6H		
band gap [eV]	2.40	3.28		3.10		
site	k	h	k	h	k <sub>1</sub>	k <sub>2</sub>
$E_D$ [meV]	54	52.1	91.8	81.0	137.6	142.4
v.o. splitting [meV]	8.37	7.6	45.5	12.6	60.3	62.6
$g_{  }$	2.0050	2.0055	2.0043	2.0048	2.0040	2.0037
$g_{\perp}$	2.0050	2.0010	2.0013	2.0028	2.0026	2.0030
$a/h$ [MHz]	3.500	2.900	50.970	2.468	33.221	33.564
$b/h$ [MHz]	0	0.080	0.004	0.137	0.004	0.009
$q/h$ [MHz]	0	0	0	0.017	0.007	0.007

*Table 1: Various properties of N donors in 6H-, 4H- and 3C-SiC:  $^{14}\text{N}$  hf and quadrupole interaction constants for SiC from analyses of ENDOR spectra. For the values of the "valley-orbit" splitting and the g tensors see [3].  $E_D$  is the experimental donor level.*

quasi-cubic sites isotropic. A qualitative explanation for this behaviour was given by Greulich-Weber [3] considering the valley orbit (v.o.) interactions (see fig. 1): the fully symmetric ground state  $1s(A_1)$  in the cubic site is 60 meV below that of the next site with  $1s(E)$  symmetry due to the v.o. splitting (fig. 1a), while for the hexagonal site the two states are only ~12 meV apart, which mixes E states into the  $A_1$  state causing an anisotropic hf interaction (fig. 1b) [3]. In the E state there is no spin density at the N nucleus. By comparison the hf results for various sites in various polytypes it was found that the isotropic hf interaction, i.e. the spin density at the N nucleus, is approximately proportional to the value of the v.o. splitting, when both values are normalised to the expectation of the simple EMT [3]. This explains qualitatively why  $a/h$  for the cubic sites in 3C is as small as that of the hexagonal sites in 6H- and 4H-SiC. Attempts to explain the shf interactions measured for numerous  $^{29}\text{Si}$  and  $^{13}\text{C}$  shells in 3C-, 4H- and 6H-SiC [3, 4] with EMT failed for all polytypes, except for 3C SiC, where the agreement is very good, which is surprising. The reason may be that the v.o. splitting is very small and that there is only one site. However, the ENDOR experiments yield that N must be on a C site, which was assumed but never really shown [3, 4]. However, there is no theory to explain the ENDOR data quantitatively. From experiment it is known that the wave function is very extended (more than a dozen of  $^{29}\text{Si}$  and  $^{13}\text{C}$  shells have been measured), such that the methods describing deep states (e.g. cluster methods etc.) are not adequate, while the EMT cannot be used either for a quantitative description.

N donors are present in all SiC samples. P donors can be produced by neutron transmutation of  $^{30}\text{Si}$ . There are at least two samples of 6H SiC available for  $^{31}\text{P}$ . Various  $^{31}\text{P}$  defects have been identified by EPR (see table 2): a low temperature defect with anisotropic hf interaction and two high temperature ( $> 60$  K) defects with almost isotropic hf interaction. Another P-related defect had been described by a P-vacancy pair defect, in which the vacancy should always lie along the c-axis [5]. All P defects have an axially symmetric hf interaction about the c-axis which is very similar to what was found for N [3]. It was proposed by Greulich-Weber [3] to reinterpret the origin of the three apparent different P donor-type defects: there is only one type of P donor on an Si site, analogous to the N donor on C site. The different spectra represent the two quasi-cubic sites at low temperature ( $P_2$ ) and high temperature ( $P_a, P_b$ ) and the hexagonal site at low temperature ( $P_1$ ) and high temperature ( $P-V$ ) (for details of the discussion on the hf interactions see [3]). This interpretation removes the old idea that there should be a P-V complex, where the vacancy is always only along the c-axis.

	temperature	$g_{\parallel}$	$g_{\perp}$	a [MHz]	b [MHz]
$P_a$	$T > 60$ K	2.0040	2.0029	156	0.7
$P_b$	$T > 60$ K	2.0040	2.0025	145	0
P-V	$T > 60$ K	2.0044	2.0025	22	1.9
$P_1$	$T \leq 10$ K	2.0049	2.0031	1.562	0.894
$P_2$	$T \leq 10$ K	2.0041	2.0028	8.7	4.2

**Table 2:**  $g$  values and hf interaction constants of three  $^{31}\text{P}$  defects in 6H-SiC doped by neutron transmutation. The defect  $P_{a,b}$  and P-V was observed by Veinger et al [5] and is observed only for  $T > 60\text{K}$ . The hf interaction constants were determined by EPR. The defect  $P_{1,2}$  is only observed at  $T < 10\text{K}$ . The hf interaction constants were determined by ENDOR [3]. All defects have axial symmetry above the  $\bar{c}$ -axis and thus only one centre orientation [3].

### 3. Acceptors

Al is an acceptor in SiC, which has characteristic features of a shallow defect with respect to the EPR data. From table 3 it is seen for 6H-SiC and 4H-SiC that the  $g$  factors deviate strongly from the free electron value 2.0, which, in this case, is characteristic for an electronic state built from valence band functions [6].  $g_{\perp} \approx 0$  is in agreement with theoretical expectations for a shallow state near the top of the valence band. See also Greulich-Weber [3]. From the hf interaction it can be concluded that only a small spin density is found on the  $^{27}\text{Al}$  nucleus (<5%), again characteristic for a shallow defect. There are no ENDOR data available yet. Thus, with the present knowledge, Al acceptors appear to be "shallow", maybe EMT-like (the ionisation level is at  $E_v + 200$  meV). Before discussing the B acceptors, the other "shallow" defects according to the common assumptions, the deep acceptor Sc is briefly discussed, because there are certain features similarly found in the B acceptors.

6H-SiC	sites I	II	III
$g_{\parallel}$	2.418(1)	2.404(1)	2.336(1)
$g_{\perp}$	$\sim 0$	$\sim 0$	$\sim 0$
$A_{\parallel}/h$ [MHz]	18.3(1)	18.9(1)	20.9(1)
4H-SiC	sites I	II	
$g_{\parallel}$		2.469(1)	2.451(1)
$g_{\perp}$		$\sim 0$	$\sim 0$
$A_{\parallel}/h$ [MHz]		17.3(1)	26.8(1)

**Table 3:** Principal values of  $g$  tensors and Al hf interactions for the shallow Al acceptors in 6H- and 4H-SiC as determined by the MCDA-EPR measurements. The hf interactions are given for  $A_{\parallel}$  only, since in other directions no hf interactions could be resolved. An assignment of  $g$  tensors and hf interactions to certain defect sites could not be made.

In 6H-SiC one finds at low temperature (4.2 K) an orthorhombic spectrum (spectrum A in table 4), where the hf and  $g$  tensor z-axis is in the connection line between the Sc site (C-site, see below) and one of the nearest three Si neighbours not along the c-axis. At higher temperature (> 20 K) the spectrum A disappears and two new axially symmetric spectra C and B appear (fig. 2). The hf and  $g$  matrix of spectrum C can be understood by a thermal averaging of the spectrum A about the c-axis, i.e. the hole at low temperature in the C-Si bond jumps rapidly between the three bond axes. The fact that Sc is on a C site is concluded from the resolved  $^{29}\text{Si}$  shf interactions [7, 8]. Thus, there are three different kinds of Sc acceptor EPR spectra, which all belong to Sc on a C site, but differ in the localisation of the hole: it is either on the C-Si bond on the c-axis or on other C-Si bonds at high temperature, the latter being delocalised by thermal activation. At low temperature the spectra of the three C sites for the hexagonal spectrum B could be resolved but not so for the orthorhombic spectrum A. An interesting behaviour is observed when monitoring the evolution of the EPR line intensities with temperature (fig. 2). The relative intensities do not follow the statistical expectations. It must rather be concluded that the ionisation level of centres A and B, i.e. for the hole along the C-Si bond in the c-axis (spectrum B) or in the other bond directions differ by a few meV (see fig. 4). In order to understand the temperature behaviour of the relative intensities of spectra B and C, it must be assumed that the level A is temperature dependent and lowered with increasing temperature, which is thought to be an effect of entropy ( $G = H - TS(T)$ ), because apparently a

soft vibrational mode is coupled to the defect that contains a large temperature depending entropy term [8,9]. Notably, as expected for a deep defect, the  $g$  factors are all very near to 2.0 and  $g_{\parallel} \approx g_{\perp}$  [8]. The whole spin density is about 40 %, also characteristic for a deeper state with a rather high spin localisation.

Boron, the other very common contamination and acceptor in SiC, behaves with respect to EPR/ENDOR very different from Al, but shows surprising similarities to the deep acceptor Sc. In 6H SiC, for example, there are two B-related levels known from DLTS: one at  $E_v + 0.3\text{eV}$ , which is commonly called the "shallow" B level, and one at  $E_v + 0.6\text{eV}$ , which is associated with a deep B defect. The EPR spectrum in a sample, where the Fermi level is pinned or near the shallow B level, shows the following characteristic features. At low temperature there is a B hf structure resolved in this EPR spectrum with low ( $C_{2h}$ ) symmetry, for the quasi-cubic sites the  $z$ -axis for  $g$ - and hf tensors being in a bond (C-Si) direction [11]. For the hexagonal sites there is an axially symmetric spectrum. The B hf interaction is very small: less than 1% hole spin density are at the B nucleus. This would be consistent with a shallow defect, if there were not the following additional features: there is a large hf interaction with one  $^{13}\text{C}$  neighbour representing 45% of the hole spin density, and the  $g$  factors are all very near to the free electron value  $g=2$ . Both the high spin density at one C neighbour as well as the  $g$  factors near  $g=2$  are very characteristic features for a deep defect and a shallow one. At higher temperature ( $>50\text{ K}$ ), the symmetry of

spectrum	tempe- rature	symmetry	$g_{xx}$	$g_{yy}$ ( $g_{\parallel}$ )	$g_{zz}$	$A_{xx}/h$ [MHz]	$A_{yy}/h$ [MHz]	$A_{zz}/h, (A_{\parallel}/h)$ [MHz]
A	$< 15\text{ K}$	monoclinic	1.999	1.996	2.002	0	17	106
I	4.2 - 70 K	axial	1.9976		2.0029	22.8		116.6
B II			1.9975		2.0026	22.3		116.5
III			1.9969		2.0020	22.7		116.4
C	$> 25\text{ K}$	axial	2.000		1.998	56		26

**Table 4:** Principal values of  $g$  tensors and hf tensors of Sc defects measured in 6H- and 4H-SiC at different temperatures.

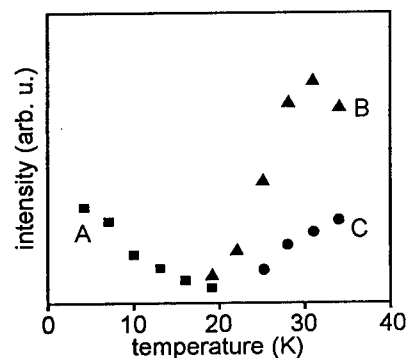


**Fig. 2:** Relative EPR line intensities of spectra A (■), B (▲) and C (●) at different temperatures. All spectra were measured with the same microwave power without illumination of the sample.

the spectra becomes axially symmetric for the quasi-cubic sites by thermal averaging similarly to what was found for Sc. The hexagonal site spectrum remains unchanged. With ENDOR the B hf structure was investigated in great detail in 3C, 4H and 6H SiC [3,11]. Table 5 shows as an example the results for the hexagonal site B in 6H SiC. Note, that the signs of the quadrupole interaction and the anisotropic hf interaction have the same sign while that of the isotropic interaction has the opposite sign. The structure models compatible with the EPR/ENDOR data are as follows: (for 6H-SiC) basically there is a hole at the C site next to  $B_{Si}$ . In the hexagonal site the hole is along the  $c$ -axis, for the quasi-cubic sites along the Si-C bond axis at low temperature, averaged about the  $c$ -axis at higher temperature. When studying the temperature dependence of the EPR intensities, it becomes apparent that the levels of the hexagonal site and

quasi-cubic sites are not identical: they are separated by about 3meV, and it is clear that the temperature dependence of the EPR signal intensities depend on the position of the Fermi level, i.e. the compensation and the sample. Thus, the behaviour of the B acceptors is very similar to what was observed in Sc, except that the hole is not mainly on B but on a C neighbour. The C neighbour is relaxed from its original lattice position. In a certain sense the B acceptor is a B-induced C acceptor. Although shallow ( $E_v + 0.3\text{eV}$ ), it has the character of a deep defect.

	a	b	q	sum of spin density $\eta$
$^{11}\text{B}$	$\mp 0.97\text{ MHz}$	$\pm 2.98\text{ MHz}$	$\pm 0.25\text{ MHz}$	
$\eta$	0.1 %	4.7 %		4.8 %
$^{13}\text{C}$	89.66 MHz	41.47 MHz		
$\eta$	3 %	39 %		42.0 %
$^{29}\text{Si}$	25.6 MHz	1.80 MHz		
$\eta$	1.5 %	4.5 %		6.0 %

*Table 5:  $^{11}\text{B}$  hf interaction constants determined by ENDOR and EPR [11] for the hexagonal site boron acceptor in 6H-SiC.*

#### 4. Conclusions

Although N and P donors are shallow donors, their quantitative understanding cannot be achieved with an EMT picture. A new theoretical approach is needed. N is on C sites, and there is only one P donor analogous to what is known for the N donors.

Al and B acceptors are both "shallow" with respect to their ionisation levels, but differ largely in character: Al seems EMT-like as far as knowledge is present, B is a deep defect in character. The Sc acceptor is characteristic for an acceptor in SiC: a hole on one lattice site in various configurations with respect to neighbours results in a number of different EPR spectra and in different ionisation levels.

- [1] E. B. Hale and R. L. Mieher, Phys. Rev. **184** (3) 739 (1969)
- [2] E. B. Hale, R. L. Mieher, Phys. Rev. **B184** (3) 751 (1969)
- [3] S. Greulich-Weber, phys. stat. sol. (a) **162** 95 (1997)
- [4] S. Greulich-Weber, M. März and J.-M. Spaeth, Proceedings of the ICDS 20 (Physica B), accepted
- [5] A.I. Veinger, A.G. Zabrodskii, G.A. Lomakina, and E.N. Mokhov, Soviet Phys. – Solid State **28**, 917 (1986)
- [6] Le Si Dang, K.M. Lee, G.d. Watkins and W.J. Choyke, Phys.Rev.Lett. **45**, 390 (1980)
- [7] M. März, J. Reinke, S. Greulich-Weber, J.-M. Spaeth, H. Overhof, E.N. Mokhov, A. D. Roenkov, E. N. Kalabukhova, Sol. Stat. Comm. **98** (5), 439 (1996)
- [8] J.-M. Spaeth, S. Greulich-Weber, M. März, E.N. Mokhov and E.N. Kalabukhova Proceedings of the ICDS 20 (Physica B), accepted
- [9] H. Söthe, J.-M. Spaeth and F. Luty, Radiation Effects and Defects in Solids, 119-121 269-274 (1991)
- [10] B. Hamilton, A.R. Peaker and S. S. Pantelides, Phys. Rev. Lett. **61** 1627 (1988)
- [11] S. Greulich-Weber, F. Feege, K.N. Kalabukhova, S.N. Lukin, J.-M. Spaeth and F. Adrian, Semicond. Science and Technology, **13**, 59 (1997)

## ESR Spectrum of Nitrogen in 6H SiC in the Ground and Excited States

E.N. Kalabukhova and S.N. Lukin

Institute of Semiconductor of Physics, National Academy of Science of Ukraine,  
 45 Pr. Nauki, Kiev, 252028, Ukraine

**Keywords:** Donors, Energy Characteristics, ESR, Photo-ESR, Temperature Dependence

**Abstract.** The temperature dependences of the ESR spectra of nitrogen in the  $1S(A_1)$  and  $1S(E)$  states were studied in n-type 6H SiC. The temperature dependencies of the line intensities and widths were used to determine ionization energies and the valley-orbit splitting of nitrogen on the cubic and hexagonal sites. The optical recharging of nitrogen in the paramagnetic  $1S(A_1)$  and  $1S(E)$  states was observed after cooling the 6H SiC samples under interband illumination.

### 1. Introduction.

It is well known that an additional broad line of unknown nature is observed in the ESR spectrum of nitrogen in SiC at high temperatures, coinciding with the resonance field of the nitrogen central triplet line [1]. The additional line has been interpreted alternatively as an exchange line in the nitrogen ESR spectrum due to non-localized electrons or as a structural defect.

In this work, we report the results of ESR investigations of bulk 6H SiC samples with uncompensated donor concentrations ( $N_D - N_A$ ) from  $2 \cdot 10^{18} \text{ cm}^{-3}$  to  $1 \cdot 10^{16} \text{ cm}^{-3}$  in the temperature interval from 20 K to 160 K at 9 and 37 GHz to establish the nature of this additional line in the nitrogen spectrum and the regularities of the temperature behavior of the nitrogen ESR spectra.

### 2. Temperature behavior of donor spectra in 6H SiC.

Fig. 1 displays donor ESR spectra in 6H SiC taken between 77 K to 145 K at a frequency of 37 GHz. At low temperature the spectrum consists of two triplets of hyperfine (hf) ESR lines  $I_{k1}$ ,  $I_{k2}$  due to nitrogen on the two cubic sites, and a single line  $I_h$  originating from nitrogen on the hexagonal site. A decrease in intensity and broadening of the hf lines of nitrogen ESR spectra are observed at higher temperature. At the same time the growth of the single  $I_{Nk}$  line coinciding with the center of gravity of the nitrogen ESR spectra is observed.

Fig. 2 displays the temperature dependencies of the relative integrated intensities of the nitrogen lines and the  $I_{Nk}$  line, obtained at 9 and 140 GHz [2]. The peaks observed in these intensities can be interpreted as due to successive redistribution of the relative population of the donor states due to thermal excitation. With increasing degree of compensation, the region of observation of the cubic nitrogen spectra shifts toward higher temperatures while that of the hexagonal site shifts toward lower temperatures, the maximum in intensity occurring at about  $T = 15 \text{ K}$  (Table 1).

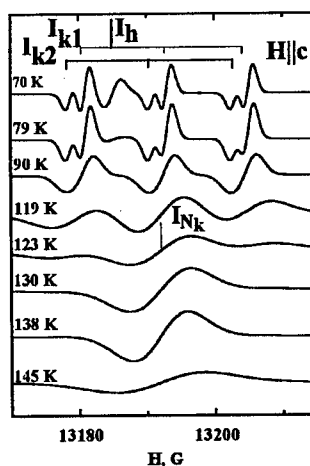


Fig. 1. The thermal evolution of donor ESR spectrum in the bulk 6H SiC with  $(N_D - N_A) \approx 2 \cdot 10^{18} \text{ cm}^{-3}$ .

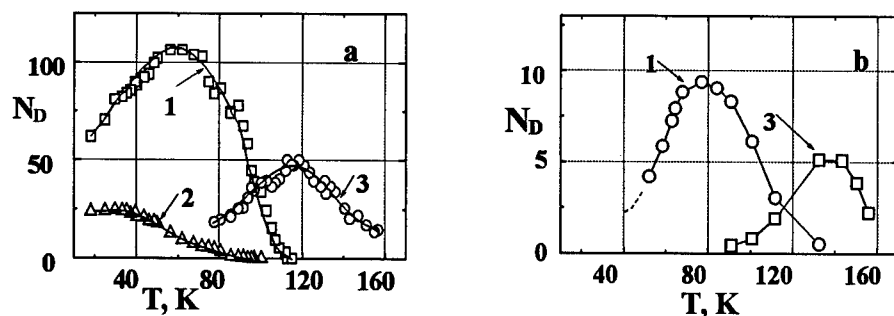


Fig. 2. Temperature dependence of the relative integrated ESR absorption line intensities of donors in 6H SiC with  $(N_D - N_A)$ : a -  $2 \cdot 10^{18} \text{ cm}^{-3}$ , b -  $8 \cdot 10^{17} \text{ cm}^{-3}$ . 1 -  $I_{k1}$ ,  $I_{k2}$ , 2 -  $I_h$ , 3 -  $I_{Nk}$ . (The range of saturation of the nitrogen ESR spectrum is indicated by a dashed line).

Table 1. Temperature characteristics of nitrogen ESR spectra in 6H SiC polytype.

$(N_D - N_A)$	$2 \cdot 10^{18} \text{ cm}^{-3}$	$8 \cdot 10^{17} \text{ cm}^{-3}$	$4 \cdot 10^{17} \text{ cm}^{-3}$	$1 \cdot 10^{16} \text{ cm}^{-3}$
$\Delta T_k, \text{ K}$	4.2 - 110	4.2 - 125	4.2 - 130	4.2 - 145
$T_k^{\text{max}}, \text{ K}$	60	78	82	92
$\Delta T_{Nk}, \text{ K}$	80 - 160	95 - 160	110 - 170	140 -
$T_{Nk}^{\text{max}}, \text{ K}$	110	135	140	
$\Delta T_h, \text{ K}$	4.2 - 85	4.2 - 70	4.2 - 60	4.2 - 30
$T_h^{\text{max}}, \text{ K}$	15	15		

$\Delta T_i$  - temperature interval of observation of the ESR spectra:  $I_k$ ,  $I_h$ ,  $I_{Nk}$ .

$T_i^{\text{max}}$  - the temperature at which the  $I_k$ ,  $I_h$ ,  $I_{Nk}$  ESR lines have maxima

The correlation between the temperature behavior of the donor spectra and degree of compensation of the samples can be explained as follows. The intensities of the donor lines decrease with increasing the temperature due to ionization of donor states. The free carrier concentration depends on the degree of compensation [3]:

$$n_0 \approx \beta \cdot N_C \left[ \frac{N_D - N_A}{N_A} \right] \exp\left(\frac{-E_D}{kT}\right) \quad (1),$$

where  $N_C$  and  $\beta$  are the conduction band density of states and degeneracy, respectively, and  $E_D$  is the ionization energy of the donors. It follows from (1) that equal free electron concentrations will occur at different temperatures for different compensation ratios,  $N_D/N_A$ .

The analysis of the temperature behavior of the ESR spectrum of nitrogen taken at 37 GHz indicates that a decrease of the hf splitting and a broadening of the lines are observed for the spectra of cubic nitrogen with increasing temperature (Fig. 3). This process is accompanied by the appearance of a single broad line,  $I_{Nk}$ , the intensity of which grows with increasing temperature while the line width decreases (Fig. 1). Such a decrease of the hf splitting and broadening of the triplet lines was also found for ESR spectrum of hexagonal nitrogen at 37 GHz between 30 and 60 K in [1] while the central triplet line at about 60 K was growing at the expense of the outer lines.

### 3. The nature of the high temperature ESR $I_{Nk}$ line.

The appearance of the  $I_{Nk}$  line and the temperature behavior of its line width, along with a decrease of the hf splitting of the nitrogen ESR spectra with increasing temperature can be explained by a thermally activated transition of donor electrons from the  $1S(A_1)$  state to the  $1S(E)$  state which has a node at the central N atom. The intensity of the  $I_{Nk}$  line increases with increasing temperature while the line width and hence the value of the unresolved hf interaction reaches a



minimum value and maximum anisotropy when the donor electrons occupy the  $1S(E)$  excited state. The minimum value of the  $I_{Nk}$  line width for two orientations of magnetic field obtained at 140 K for 6H SiC with  $(N_D - N_A) \approx 4 \cdot 10^{17} \text{ cm}^{-3}$  was given in Table 2.

The proposed interpretation is supported by the data concerning the optical recharging of nitrogen in the two paramagnetic states by ultraviolet (UV) light (Fig. 4). When the samples are cooled in the dark the ESR spectrum consists of two triplets of hf lines due to nitrogen on the two cubic sites at 77 K. With illumination present, one single  $I_{Nk}$  line with anisotropic width ( $\Delta H_{\parallel} = 6 \text{ Gs}$ ,  $\Delta H_{\perp} = 4.5 \text{ Gs}$ ) due to unresolved hf structure is observed in the donor ESR spectrum at 77 K with  $g_{\parallel} = 2.0038$  and  $g_{\perp} = 2.0028$  corresponding to the center of gravity of two ESR spectra of cubic nitrogen. The results obtained indicate that, as the temperature decreases, the nonequilibrium electrons created by the interband light at first are captured by the  $1S(E)$  level and are left there "freezing" as the temperature goes down. Only thermal excitation of electrons from  $1S(E)$  level would than change the distribution of donor electrons between the  $1S(A_1)$  and the  $1S(E)$  levels.

Table 2. Parameters of the nitrogen ESR spectra in 6H SiC.

	$I_h$	$I_{k1}$	$I_{k2}$	$I_{N,k}$
$g_{\parallel}$	2.0048	2.0040	2.0037	2.0038
$g_{\perp}$	2.0028	2.0026	2.0030	2.0028
A, $\Delta H$ , G	$\Delta H_{\parallel} = 2.5$ $\Delta H_{\perp} = 1.8$	11.8	12.0	$\Delta H_{\parallel} = 6.0$ $\Delta H_{\perp} = 4.5$

#### 4. Energy characteristics of donor centers.

An analysis of the temperature dependencies of the integrated ESR line intensities and line widths permitted the determination of the ionization energies of the donor centers. The temperature dependencies of the donor ESR line intensities, which are proportional to the concentration of paramagnetic donor centers  $N_D$ , are given by the expression:

$$N_D = \frac{I_D(T)}{I_{\text{ref}}(T)} \cdot \frac{1}{T} \cdot (\Delta H_D)^2 \approx \exp\left(-\frac{E_D}{kT}\right) \quad (2),$$

where  $I_D(T)$ ,  $I_{\text{ref}}(T)$  are the line intensities of the donor center and reference sample with a Curie Law temperature dependence.  $\Delta H_D$  is the peak-to-peak width of the first derivative of the absorption ESR line. As follows from (2), one can determine the donor energy from the slope of the  $\ln(N_D)$  vs.  $1/T$  curves (Fig. 2).

For the samples with  $(N_D - N_A) \geq 8 \cdot 10^{17} \text{ cm}^{-3}$  the high temperature slope gives ionization energies for the nitrogen levels which are in agreement with those obtained from Hall measurements [4, 5]

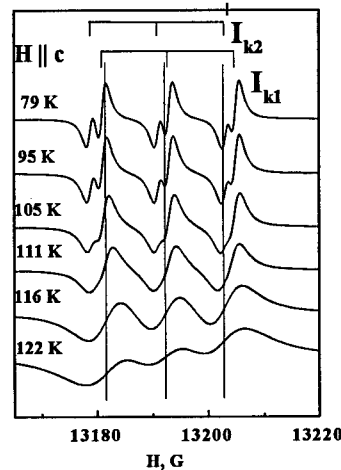


Fig. 3. Temperature behavior of hf splitting of ESR triplet lines of nitrogen on cubic sites.  $(N_D - N_A) \approx 4 \cdot 10^{17} \text{ cm}^{-3}$ .

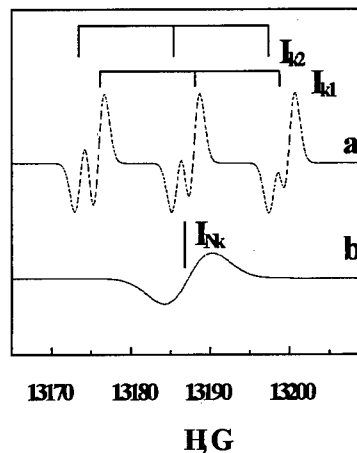


Fig. 4. Donor ESR spectrum of 6H SiC at  $T = 77 \text{ K}$  after cooling the sample a) in the dark; b) in the present of UV light.

and depend on the donor concentration, the higher the concentration the lower the energy. The ionization energy of the cubic site varied from 125 to 150 meV while that for the hexagon site varied between 80 and 85.5 meV. The valley orbit splitting was found to be 13 meV for the hexagonal site and 60.2 and 63.6 for the two cubic sites. For the samples with  $(N_D - N_A) \leq 4 \cdot 10^{17} \text{ cm}^{-3}$ , where the difference in the population of  $1S(A_1)$  and  $1S(E)$  levels becomes large, the high temperature slope of curve 1 (Fig. 2) yields an ionization energy coinciding with the value of valley-orbit splitting of cubic nitrogen [6].

In Fig. 5 the  $I_{Nk}$  line width ( $\ln \Delta H_{Nk}$ ) is plotted against inverse temperature, where one can separate three ranges between 100 K to 170 K. In the range from 100 K to 120 K the width increases due to the broadening of the unresolved  $1S(E)$  triplet lines while in the second range from 120 K to 140 K where the decrease of the hf splitting of the  $1S(E)$  triplet lines becomes noticeable, a narrowing of the line width is observed. At temperatures higher than 140 K the  $I_{Nk}$  line width increases due to both ionization electrons from  $1S(E)$  state to the conduction band and exchange interaction of donor electrons with the conduction electrons.

The three temperature slopes can be approximated with  $\exp(E_D/kT)$  where  $E_{D1} = 34 \text{ meV}$ ,  $E_{D2} = 21 \text{ meV}$ ,  $E_{D3} = 60 \text{ meV}$ .  $E_{D3}$  could be attributed to the ionization of electrons from the  $1S(E)$  level to the conduction band.

### 5. Conclusions.

The  $1S(E)$  paramagnetic state of nitrogen was found from an ESR study of the temperature behavior of donors in 6H SiC. The ESR spectrum of nitrogen in the excited  $1S(E)$  state consists of single lines with unresolved hf structure which appear in the donor ESR spectrum at high temperature when the donor electrons are excited from the  $1S(A_1)$  to the  $1S(E)$  level of nitrogen.

The authors are grateful to Dr. S. Greulich-Weber and Dr. W.C. Mitchel for valuable discussions of this work. The work was supported by Deutsche Forschungsgemeinschaft (Grant No FKZ:01 M 2971) and by the Air Force Research Laboratory (Contract SPC-98-4055).

### References

- [1] S. Greulich-Weber, Phys. Stat. Sol. (a), **162** (1997), p. 95.
- [2] E.N. Kalabukhova and S.N. Lukin, Phys. of the Solid. State **40** (1998), p. 1653; E. N. Kalabukhova and S. N. Lukin, Low Temp. Phys. **22** (1996), p. 808; E. N. Kalabukhova, V. S. Kiselev, and S. N. Lukin, Inst. Phys. Conf. Ser. **142** (1996), p. 405
- [3] J.S. Blakemore, "Semiconductor Statistics" (Dover Publications, Inc. New York, 1987).
- [4] W. Suttrop, G. Pensl, W.J. Choyke, R. Stein, S. Leibenzeder, J. Appl. Phys. **72** (1992), p. 3708.
- [5] A.O. Evwaraye, S.R. Smith, W.C. Mitchel, J. Appl. Phys. **75** (1994), p. 3472.
- [6] P.J. Colwell, M.V. Klein, Phys. Rev. B **6** (1972), p. 498.

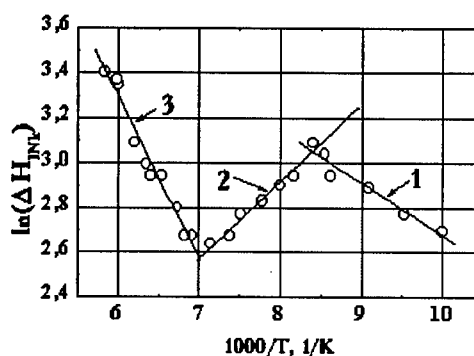


Fig. 5. Temperature dependence of ESR  $I_{Nk}$  - line width in 6H SiC for  $H \parallel c$ .

## Dopant-related Complexes in SiC

A. Gali<sup>1</sup>, J. Miró<sup>1</sup>, P. Deák<sup>1</sup>, R.P. Devaty<sup>2</sup> and W.J. Choyke<sup>2</sup>

<sup>1</sup>Dept. of Atomic Physics, Technical University of Budapest,  
Budafoki út 8, HU-1111 Budapest, Hungary

<sup>2</sup>Department of Physics and Astronomy, University of Pittsburgh, Pittsburgh, PA 15260, USA

**Keywords:** Boron, Occupancy Level, Phosphorus, Spin Distribution, Theory, Vacancy

**Abstract** Ab initio LDA calculations have been carried out for dopant-related complexes in silicon carbide. Cluster models with localized basis functions are used to calculate spin distributions while supercell calculations are used to determine the relative stabilities as the function of the chemical potential. We show that a divacancy capturing a P atom gives rise to a deep donor level and give an estimate for the occupancy level. Based on the calculated spin distribution on the phosphorus at the Si site next a carbon vacancy ( $P_{Si}+V_C$ ), such a complex can indeed be identified with the EPR center "P-V". We show that at high Si/C ratio the formation energy of P at the C site ( $P_C$ ) and at the Si site is about the same in thermal equilibrium.  $P_C$  is also an effective mass donor in 3C-SiC. We have established that the boron substitutional chooses the Si site in a divacancy in both the neutral and the negative charge state, i.e. no bistability occurs. The arising  $B_{Si}+V_C$  complex is a deep acceptor with spin distribution very close to that measured by ENDOR. The acceptor part of the complex is, however the  $V_C$ ! This explains why the PL spectra finds the acceptor on the same sublattice as  $N_C$ .

The development of SiC as device material for power electronics is making continuing progress. One key to the technology is the control of doping. Phosphorus is an n-type dopant while boron is an important p-type dopant in SiC. Phosphorus is expected to substitute preferentially on the silicon sublattice based on its size, and the shallow boron is suggested to be an off-center boron substituting for a Si atom ( $B_{Si}$ ) based on experiments [1]. Boron creates a shallow as well as a deep acceptor level [2]. The P implanted 6H-SiC epilayers have yielded two ionization energies below 110 meV associated with the  $P_{Si}$  donor [3]. Only one deep P-related donor level has been reported in neutron transmuted and subsequently annealed 6H-SiC samples [4]. In 6H material, the deep B acceptor has been recently identified with a B atom on a Si site next to a C vacancy ( $B_{Si}+V_C$ ) in electron spin resonance (EPR) and electron nuclear double resonance (ENDOR) experiments [5, 6]. Duijn-Arnold et al. [6] have shown that the spin density of the singly occupied orbital in the neutral charge state of the center is negligible on the boron atom and about 70-90% of it is localized on the three silicon atoms around the carbon vacancy. No significant difference was found between the  $k_{1,2}$  and  $h$  sites, although the corresponding signals have been resolved. Samples co-doped with N and B have shown a Type I PL spectrum for the deep B acceptors recombining with the shallow nitrogen donors in 3C-SiC [7], indicating that the ionized donor and acceptor occupy the same sublattice. Since the donor state is localized on  $N_C$ , the deep B center was associated with a complex containing B at a C site [7]. This is in clear contradiction with the ENDOR results above, which show B on the Si site. One aim of this paper to resolve this controversy.

Magnetic resonance studies have been performed on 6H-SiC crystals doped with P by neutron transmutation and subsequently annealed [4, 8]. Three distinct spectra were observed at 77K [4]. One (P-V) was interpreted as an axially symmetric phosphorus - vacancy complex. Differences between the hexagonal ( $h$ ) and cubic ( $k_{1,2}$ ) sites could not be resolved. The other two spectra ( $P_a$ ,  $P_b$ ) were interpreted as substitutional phosphorus on Si  $k_{1,2}$  sites.

Table 1: P-related hf constants measured in neutron-transmutation doped 6H-SiC. The corresponding molecular wave-function coefficients: localization ( $\eta^2$ ),  $s$  ( $\alpha^2$ ) and  $p$  ( $\beta^2$ ) character (in %) have been calculated.

signal	temperature	a/h [MHz]	b/h [MHz]	$\eta^2$	$\alpha^2$	$\beta^2$
$P_a$ <sup>1</sup>	T > 60 K	156	0.7	1.62	86	14
$P_b$ <sup>1</sup>	T > 60 K	145	0.0	1.32	100	0
P-V <sup>1</sup>	T > 60 K	22	1.9	0.81	24	76
$P_1$ <sup>2</sup>	T ≤ 10 K	1.562	0.894	0.30	5	95
$P_2$ <sup>2</sup>	T ≤ 10 K	8.7	4.2	1.43	5	95

<sup>1</sup>See Ref. [4]

<sup>2</sup>See Ref. [10]

Two other P-related signals ( $P_1$ ,  $P_2$ ), measured at 10 K, were also reported [9] and later interpreted [10] by analogy to N in SiC. Based on the very similar g-tensors of the  $P_a$ ,  $P_b$ , P-V and of the  $P_1$ ,  $P_2$  signals, all of them were assigned to the  $P_{Si}$  substitutional [10], despite the fact that the measured hyperfine (hf) constants for P were quite different (see Table 1). While  $P_{a,b}$  show strong s character for the orbital of the unpaired electron on phosphorus,  $P_{1,2}$  implied p-character. The reasoning of Ref. [10] was that for  $P_{Si}$  the effective mass E state might be lower in energy than the  $A_1$  state, and the increasing temperature causes mixing between them resulting in an increase in the isotropic hf constant (making the orbital more s-like). Therefore, the  $P_1$  signal (measured at 10 K) was identified with the P-V signal (measured at 77 K) and it was assumed that both originate from  $P_{Si}$  at a  $h$  site. Using the same argumentation, the  $P_2$  signal was interpreted as the low temperature, unresolved alterego of the  $P_{a,b}$  signals, all coming from  $P_{Si}$  at the  $k_{1,2}$  sites. In this paper the assignment of P related centers was investigated based on first principles calculations.

Ab initio calculations in the local density approximation of density functional theory [11] were performed using the AIMPRO code [12] which applies a Gaussian basis to expand the one-electron wave functions in a molecular cluster. (For details, see Ref. [13, 14].) For the EMT defects the 64 atom 3C and 72 atom 4H supercell calculations were also performed in  $K = 0$  approximations. Host atoms within the first and the second neighbor shell around defects were allowed to relax to obtain the minimum energy of the defects.

To investigate the P-related defects, first we wanted to check the assumption of Ref. [10]. Since  $P_{Si}$  is an effective mass donor, a supercell calculation was needed. The measurements were made on 6H-SiC but that would have required a supercell too big for our computer. However, the states around the conduction band minima are very similar, as far as their s/p character is concerned, in 4H and 6H polytypes [15]. Therefore, we have calculated  $P_{Si}$  in 4H-SiC.  $P_{Si}$  at the  $k$  site turned out to be more stable than at the  $h$  site by 0.26 eV. (This value should be checked later in better k-point sampling.) The occupied donor orbital in both cases belongs to the  $a_1$  irreducible representation of  $C_{3v}$  with dominantly s character, while the first excited state of the defect is a doubly degenerate  $e$  state with p character. This finding must be valid for 6H-SiC as well, contradicting the assumption of Ref. [10]. Since our calculation pertains to  $T = 0$  K, the  $P_{1,2}$  signals cannot correspond to  $P_{Si}$ . The assumption that  $P_{Si}$  is also more stable at the  $k$  sites than at the  $h$  site in 6H SiC, may explain why no signal could be assigned to  $P_{Si}$  at a  $h$  site in Ref. [4].

Unlike the effective mass donor  $P_{Si}$ ,  $P_{Si}+V_C$  is expected to give rise to a deep donor level, corresponding to a more localized orbital. In such a case the polytype differences are smaller. Therefore, in order to economize, we used a molecular cluster (5 complete host atom shells around  $V_C$ ) in 3C geometry for modeling the defect. As it has turned out, 85 % of the unpaired spin is localized within the second neighbor shell of  $V_C$ . The relaxed structure of  $P_{Si}+V_C$  is depicted in Figure 1, where the electronic structure is also marked. Due to the steric repulsion of the lone-pair electrons of P, the levels depicted in Figure 1 are pushed up in the gap relative to the donor level of  $V_C$ . Using the

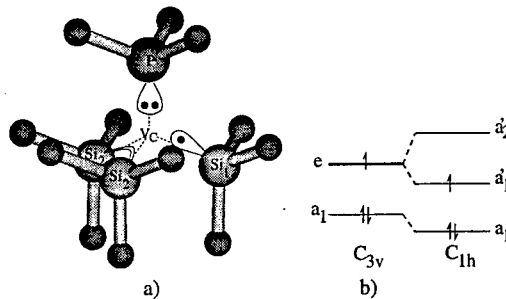


Figure 1: The relaxed  $P_{Si}+V_C$  complex in 3C SiC. Numbering refers to symmetry equivalent sites in the two sublattices. The electronic structure is shown a): in terms of localized orbitals, (normal, long and dangling bonds as well as lone pairs) and b): the energy levels of the canonical orbitals illustrating the Jahn-Teller effect

method described in Ref. [16], the (+/0) occupation level of  $P_{Si}+V_C$  can be estimated to be 0.22 eV farther from the valence band edge than that of  $V_C$  (i.e., about 2.2 eV above the valence band edge in 3C-SiC; the (0/+) occupation level of  $V_C$  is predicted to be about 2.0 eV above the valence band edge [17]). The calculated s/p ratio and the localization for the (singly occupied) donor orbital on P are 8/92 and 2% which should be compared to the values obtained from the measured hyperfine constants (Table 1). (See Ref. [14] for more detail.) The donor orbital of  $P_{Si}+V_C$  is dominantly p-like on P (in our T=0 K calculation), as is the case for the P-V center (measured at 77 K). This supports the assignment of the P-V center to the  $P_{Si}+V_C$  complex. The calculated s/p ratio is, however, closer to the one obtained for  $P_1$  (taken at 10 K). Using similar arguments as in Ref. [10], one could assume that at non-zero temperatures the many-electron wavefunction of the paramagnetic state has a more pronounced admixture of the s-like  $a_1$  state (see Figure 1) to the p-like  $a_1'$  state. If so, the P-V center could indeed be the 77 K manifestation of the  $P_1$  center – as assumed in Ref. [10] – but both being fingerprints of the same  $P_{Si}+V_C$  complex. In that case it would seem likely, that the  $P_1$  and  $P_2$  centers both come from this complex and correspond to  $h$  and  $k$  sites, which could have been resolved at low temperature.

We have also calculated the formation energies of  $P_{Si}$  and  $P_C$  as a function of chemical potential of Si in 3C-SiC supercell calculations. We have found that under extreme Si excess the formation of  $P_{Si}$  and  $P_C$  has about the same probability.  $P_C$  is also an EMT donor with deeper donor level than of  $P_{Si}$  which implies that new PL lines could be detected associated with this center in P-doped epitaxial grown SiC samples with high Si/C ratio. The calculation of  $P_C$  in 4H is in progress.

Returning to the problem of the deep boron center introduced at the beginning, an explanation for the contradicting PL and EPR/ENDOR results could be a possible bistability of the complex of a boron atom in a divacancy. In the neutral charge state, seen in EPR, the configuration could be  $(B_{Si}+V_C)^0$ . In the negatively charged state, observed in PL this could change to  $(V_{Si}+B_C)^-$ . To investigate this assumption the boron atom placed initially on the Si site of the divacancy results in the  $(B_{Si}+V_C)$  configuration like in Figure 1 replacing the P with lone pair to B with an empty orbital. Starting the calculation with the boron initially placed on the C site gives rise to the  $(V_{Si}+B_C)$  configuration. By comparing the total energies for the relaxed geometries, the  $B_{Si}+V_C$  complex turns out to be more stable by 3.78 eV in the neutral and by 2.22 eV in the negatively charged state than the  $V_{Si}+B_C$  configuration. The difference is caused mainly by the fact that the B-C bond is stronger than the B-Si bond, but also  $V_C$  somewhat more stable than  $V_{Si}$ . Based on the substantial energy difference in favor of the  $B_{Si}+V_C$  configuration in both charge states, bistability can safely be excluded.

The Jahn-Teller distortion in  $B_{Si}+V_C$  also occurs as in  $P_{Si}+V_C$ . The  $a_1'$  level lies close to the valence band edge, and serves an acceptor level. The electron distribution of  $B_{Si}+V_C$  was analyzed by means of Mulliken-analysis. For the acceptor level, 0.6, 68.3, and 0.5% of the spin density is

localized on the B atom, on the Si<sub>1</sub> and Si<sub>2</sub> atoms, and on the carbon neighbors of boron, respectively. The Si<sub>2</sub> atoms move closer and bond weakly while the third one has a dangling bond in which the acceptor level is mainly localized. Since about 70% of the acceptor orbital is localized on the first neighbors of the divacancy, it makes sense to compare the spin distribution calculated for 3C with experimental values obtained for the *k* sites of hexagonal polytypes. The values of the spin density of the singly occupied level measured by ENDOR in 6H-SiC [6] on B, on Si<sub>1</sub> and Si<sub>2</sub> atoms, and on the carbon neighbors of B were ~0, ~70-90, and ~0.6%, respectively. The similarity between the calculated 3C and measured 6H results corroborates the analysis in Ref. [6]. The strong localization explains why the difference is little between the two polytypes.

In the negatively charged state, the Si atoms around V<sub>C</sub> decrease their positive charge relative to that in the perfect lattice. This extra negative charge is again accommodated by the weak bond between the Si<sub>2</sub> atoms (9.5% on each) and the dangling bond of the Si<sub>1</sub> atom (43.3%), pointing toward the vacancy. Therefore, 62% of the trapped charge of the ionized acceptor is localized in V<sub>C</sub>. That means that in (B<sub>Si</sub>+V<sub>C</sub>)<sup>-</sup> complex, the acceptor part is, in fact, the V<sub>C</sub>, so the negative charge state can be noted as B<sub>Si</sub>+V<sub>C</sub><sup>-</sup>. The donor-acceptor recombination that gives rise to the PL spectrum occurs between centers in the same carbon sublattice resulting in a Type I spectrum. Still, B resides on the Si site as predicted by ENDOR. Thus, the contradiction of the PL and EPR results can be resolved without invoking bistability.

**Acknowledgement** Support by the Hungarian OTKA T-22139, FKFP 0289/97 and AKP 97-92 2,2/27 grants as well as the bilateral US-Hungarian (JFNo. 667) and Swedish-Hungarian (IVA-MTA No. 36) projects and the grant PHY970006P from the Pittsburgh Supercomputing Center are appreciated.

## References

- [1] S. Greulich-Weber, *phys. stat. sol. (a)*, **162** (1997) p. 95.
- [2] J. M. Blank, *Mat. Res. Bul.*, **4** (1969) p. 179.
- [3] T. Troffer *et al.*, *J. Appl. Phys.*, **80** (1996) p. 3739.
- [4] A. I. Veinger *et al.*, *Sov. Phys. Solid State*, **28** (1986) p. 917.
- [5] P. G. Baranov *et al.*, *Semicond. Sci. Technol.*, **11** (1996) p. 489.
- [6] A. Duijn-Arnold *et al.*, *Phys. Rev. B*, **57** (1998) p. 1607.
- [7] H. Kuwabara *et al.*, *Phys. Status Solidi A*, **30** (1975) p. 739.
- [8] S. Greulich-Weber *et al.*, *Solid State Commun.*, **93** (1995) p. 393.
- [9] J.-M. Spaeth *et al.*, *Materials Research Society, Boston Fall Meeting* (1996).
- [10] J.-M. Spaeth *et al.*, **vol. 442**, *Materials Research Society, Mat. Res. Soc. Symp.* (1997) p. 619-624.
- [11] W. Kohn *et al.*, *Phys. Rev. Lett.*, **140** (1965) p. A1133.
- [12] R. Jones, *Philos. Trans. R. Soc. London Ser. A*, **341** (1992) p. 351.
- [13] A. Gali *et al.*, *Phys. Rev. B*, **60** (1999) p. 10620.
- [14] A. Gali *et al.*, submitted to *Appl. Phys. Lett.* (1999).
- [15] W. R. L. Lambrecht *et al.*, *phys. stat. sol. (b)*, **202** (1997) p. 5.
- [16] A. Resende *et al.*, *Phys. Rev. Lett.*, **82** (1999) p. 2111.
- [17] A. Gali *et al.*, submitted to *Phys. Rev. Lett.* (1999).

## The Spatial Distribution of the Electronic Wave Function of the Shallow Boron Acceptor in 4H- and 6H-SiC

A. van Duijn-Arnold<sup>1</sup>, J. Mol<sup>1</sup>, R. Verberk<sup>1</sup>, J. Schmidt<sup>1</sup>, E.N. Mokhov<sup>2</sup>  
and P.G. Baranov<sup>2</sup>

<sup>1</sup> Huygens Laboratory, Leiden University, PO Box 9504, NL-2300 RA Leiden, The Netherlands

<sup>2</sup> A.F. Ioffe Physico-Technical Institute, Russian Academy of Sciences,  
Polytekhnicheskaya st. 26, RU-194021 St.-Petersburg, Russia

**Keywords:** B-Acceptor, Electronic Wave Function, ENDOR, Spatial Distribution

### Abstract

A high-frequency (95 GHz) pulsed electron paramagnetic resonance (EPR) and electron nuclear double resonance (ENDOR) study has been carried out on the shallow boron acceptor in <sup>13</sup>C-enriched 4H-SiC and 6H-SiC. From the hyperfine interaction of the unpaired electron spin with the <sup>13</sup>C (*I* = 1/2) nuclei the spatial distribution of the electronic wave function has been established, and turns out to be highly anisotropic. It is found that there are subtle differences in the degree of localization of this wave function between the different quasi-cubic sites in the polytypes 4H-SiC and 6H-SiC. For the hexagonal site no detailed analysis could be made of the ENDOR data, but the results indicate that here also the spatial distribution is highly anisotropic.

### I. Introduction

One of the intriguing problems in semiconductor physics is the nature of shallow impurities in the host-crystal lattice. The most critical test of the theoretical models describing the electronic wave function of the shallow donors and acceptors is provided by the hyperfine-interaction of the unpaired electron spin with the surrounding nuclear spins, obtained from electron-nuclear-double-resonance (ENDOR) spectroscopy. Calculations by Fukumoto[1] show that the unpaired electron connected to the sB acceptor center in 3C-SiC resides almost entirely on the C-atoms. To check this prediction we have performed a 95 GHz ENDOR study on a EPR/ENDOR spectrometer [2,3] on the <sup>13</sup>C (*I* = 1/2) nuclear spins in <sup>13</sup>C-enriched 4H- and 6H-SiC crystals. Both were free-standing epitaxial layers (with removed substrates) grown by the sublimation sandwich method. The first contained B in natural abundance, in the second B was diffused in at temperatures of 2000°C. It appears that, although the EPR properties of sB in 4H-SiC and 6H-SiC are very similar, a difference in behaviour can be observed in the ENDOR data. In particular it can be seen that for the *k*<sub>2</sub> site in 6H-SiC the electronic wave function is more localised than for the *k*<sub>1</sub> site in 6H-SiC and the *k* site in 4H-SiC.

### II. Results and Analysis

Figure 1 shows part of the <sup>13</sup>C ENDOR spectra of the sB *k*<sub>1</sub> and *k*<sub>2</sub> site in 6H-Si<sup>13</sup>C and the *k*-site in 4H-Si<sup>13</sup>C. The first thing to note is that the *k*<sub>1</sub> spectrum in 6H-SiC is roughly the same as that of the *k* site in 4H-SiC. This is the case for all measured orientations. The second thing to note is that the spectrum of *k*<sub>2</sub> contains less lines around the carbon nuclear Zeeman frequency than that of *k*<sub>1</sub> which, combined with the fact that we found one more line at 45 MHz for *k*<sub>2</sub>, suggests that for *k*<sub>2</sub> the spin density is more localised than for *k*<sub>1</sub>. Due to the overlap of the EPR lines of *k*<sub>1</sub> and *k*<sub>2</sub> in 6H-SiC "crosstalk" takes place, which complicates the assignment of the ENDOR lines. For all

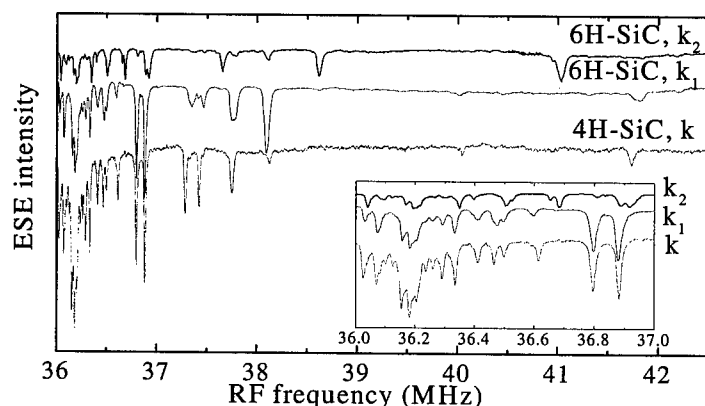


Fig. 1 : The  $^{13}\text{C}$  ENDOR spectrum of  $k_1$ - and  $k_2$ -sites of B in 6H-SiC and the k-site of B in 4H-SiC for  $\mathbf{B} \parallel \mathbf{c}$ .

orientations except  $\mathbf{B} \parallel \mathbf{c}$  and  $\mathbf{B} \perp \mathbf{c}$  the EPR lines lie too close together to clearly distinguish the two qc sites.

An important element in the assignment of the lines in the  $^{13}\text{C}$  ENDOR spectrum to specific  $^{13}\text{C}$  nuclei surrounding the B impurity is provided by the ab-initio cluster calculations of the hf interactions on the sB acceptor in

3C-SiC by Petrenko et. al.[4]. In this calculation, due to size problems, only nuclei up to two bond lengths away from the B atom could be taken into account. The results show that the largest isotropic hf interaction is with the C atom next to B. The next largest interaction is one order of magnitude smaller and with the three  $^{13}\text{C}$  atoms two bond lengths away along the direction of the B-main C bond. With all other  $^{13}\text{C}$  atoms (one or two bondlengths away from the B atom) the isotropic hf interaction is calculated to be again one order of magnitude smaller. It was proposed that the spin density distribution is cigar-like shaped oriented along the B-main C connection line away from the B atom.

With the help of this model we assigned orientational dependencies to groups of nuclei. Each group contains nuclei that have roughly the same distance to the B-nucleus and that are placed cylindrically symmetrical around the line going through the B-main C connection line. We assumed the anisotropic hf tensors to be oriented along the Si-C bonds. However, some orientational dependencies had extremes that clearly deviate from the natural bond angles and we concluded that in some cases linear combinations of two or more bonds directions are necessary to obtain the right angle. A more elaborate description of the assignments can be found in ref 5.

### III. Discussion

The results allow for an investigation of the difference in the electronic properties of the qc and hex sites in 4H-SiC and 6H-SiC. The EPR spectra indicate that the sB acceptor in 4H-SiC strongly resembles that in 6H-SiC. The g-tensors found are almost identical and the  $^{13}\text{C}$  hf splitting observed in the EPR spectra of the sB acceptor in 4H-SiC is similar to that in 6H-SiC. From the hf interaction with  $^{11}\text{B}$ , we find that there is no direct spin density on boron. Thus in both crystals ~30% of the spin density is located in a dangling bond  $p_z$  orbital on the C atom neighboring the B atom. B itself carries no spin density. The rest of the spin density is delocalized in the crystal.

The most remarkable result of our study is the assignment of lines in the  $^{13}\text{C}$  ENDOR spectra to specific C atoms up to 11 bond lengths away from the B atom. This allows for the determination of the spatial distribution of the unpaired spin density of the sB acceptor. It is found that this distribution is not spherically symmetric but is highly anisotropic and directed from B to the main C and beyond. This result is in striking agreement with the theoretical predictions of Petrenko et. al.[4].



The question arises whether the anisotropic distribution of the electronic wave function on the remote  $^{13}\text{C}$  nuclei as revealed by the  $^{13}\text{C}$  ENDOR data can be rationalised on the basis of Effective Mass Theory (EMT). sGa and sAl show a highly anisotropic g-tensor in agreement with the calculated g-anisotropy of the valence band hole. However the sB orbital angular momentum is quenched and one would not expect to see band structure properties reflected in the properties of the hole attached to the sB acceptor. Nevertheless we observe that the electronic wave function of the qc sB acceptor perpendicular to the c-axis extends considerably further than parallel to the c-axis in agreement with the anisotropy of the hole mass ( $m_{\text{hole}}^{\parallel} = 1.67 m_e$  and  $m_{\text{hole}}^{\perp} = 0.62 m_e$ )[6].

The fact that all three sB centers in 6H-SiC seem to have a different localization of the spin density and thus a different ionization energy supports the results of Evwaraye et.al.[7] who found three different levels for the sB acceptor at  $E_h = E_v + 0.27 \text{ eV}$ ,  $E_{k1} = E_v + 0.31 \text{ eV}$  and  $E_{k2} = E_v + 0.38 \text{ eV}$ . It seems probable that this lower lying  $k_2$  level leads partly to self-compensation in the crystal, which might explain the change in electrical characteristics found, when going from 4H-SiC to 6H-SiC.

To translate the observed and assigned  $^{13}\text{C}$  hf interactions into electron densities we take the point of view that the wave function of the sB acceptor consists mostly of 2s and 2p orbitals of the C atoms. We consider the wave function of the unpaired electron bound to the sB center as a LCAO-MO centered on C atoms near the defect,

$$\Psi = \sum_i \eta_i \psi_i, \quad \text{with} \quad \sum_i \eta_i^2 = 1 \quad (1)$$

and approximate the atomic function as a 2s-2p hybrid orbital at each C atom as

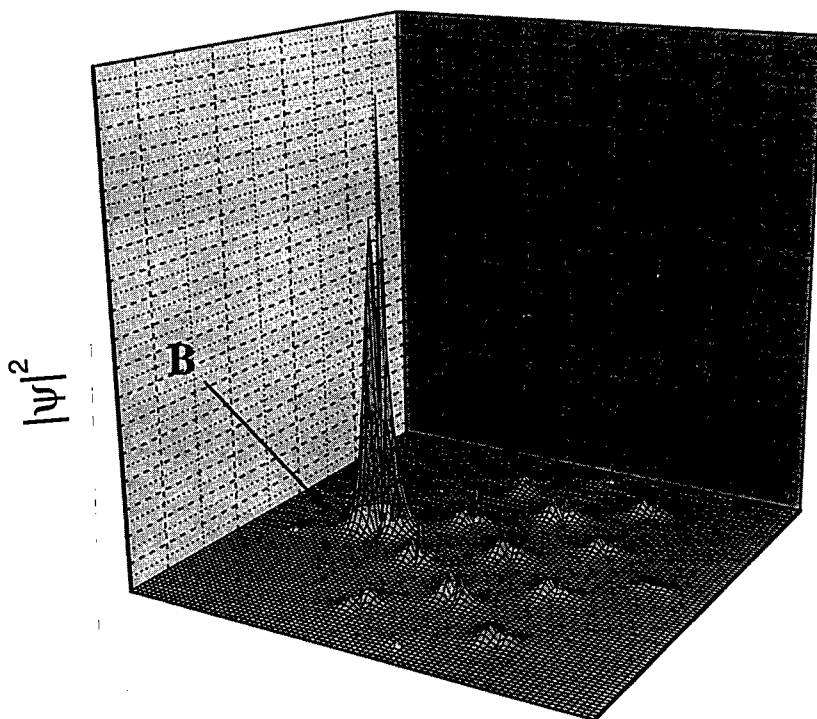


Fig. 2 : The electronic wave function distribution of  $k_1$ . The largest peak represents the main C atom. Boron is located just below the plane of the figure at the position indicated by the arrow.

$$\psi = \alpha_i(\psi_{2s})_i + \beta_i(\psi_{2p})_i, \quad \text{with} \quad \alpha_i^2 + \beta_i^2 = 1 \quad (2)$$

The 2p orbital is oriented along the four possible Si-C connection lines. By using eqs. 1 and 2, the experimental data, the table of Morton and Preston [8] and the Roothaan-Hartree-Fock wave functions [9] we can calculate the square of the total wave function of the electron at any point in space. In this we have assumed that spin density is the same as electron density (B is neutral).

To visualise the delocalisation of the electronic wave function connected to the  $k_1$  site we

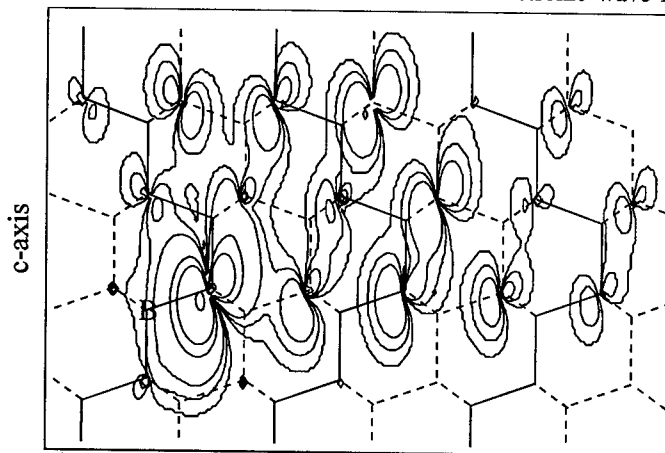


Fig. 3a : the electronic wave function distribution of  $k_1$ . The position of the boron atom is indicated with a B.

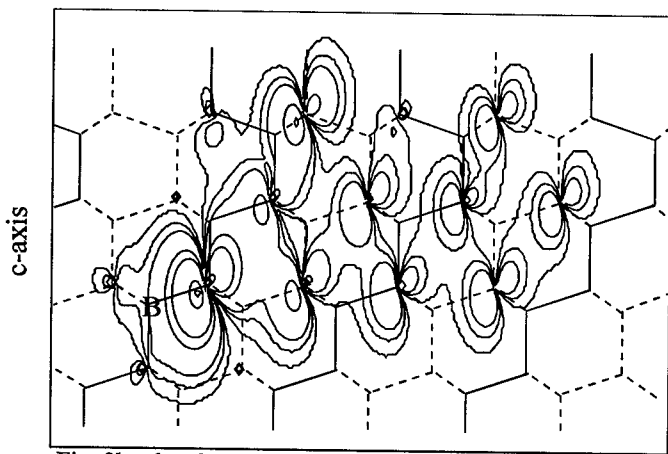


Fig. 3b : the electronic wave function distribution of  $k_2$ . The position of the boron atom is indicated with a B.

show in Fig. 2 its spin density at the C atoms in the plane perpendicular to the c-axis. The density on the main C atom dominates but there is an appreciable delocalisation of the wave function beyond this C atom, away from B. Figs 3a and 3b show the delocalisation of the wave function in the plane containing the c-axis for the  $k_1$  respectively the  $k_2$  site. The position with the largest amount of lines (to the right of the B atom), is the main C atom. From the figures it can be seen that the wave function is elongated along the B-C connection line and that the  $k_2$  site function is slightly more localized than the  $k_1$  site function.

Another important result of our findings is a reassignment of the ionization energy levels for sAl and sGa. We propose that the smaller ionization energy should be assigned to the hex and  $k_1$  site, with the  $k_2$  site having the larger one. This agrees with the ODMR results of K.M. Lee et. al.[10] and K. Maier et. al.[11] who find for the sAl acceptor in 4H-SiC two lines with  $g \sim 2.3$ . In 6H-SiC also a third line is found with  $g <$

2.3, which, as sAl and sGa obey effective mass theory, tells us that the third line belongs to a much deeper center. As explained the k-site in 4H-SiC is related to the  $k_1$  site in 6H-SiC and thus the third line should belong to the  $k_2$  site, in agreement with our results.

#### IV. Conclusion

We have been able to determine the spatial distribution of the electronic wave function of the shallow boron acceptor at the quasi-cubic sites in 4H-SiC and 6H-SiC up to 14 Å away from the B atom. It is found that the delocalization of this wave function is very anisotropic. Moreover, it is

found that the  $k_2$  site electronic wavefunction is slightly more localised than the  $k_1$  site wavefunction, suggesting that  $k_2$  has a larger ionization energy than  $k_1$ . The measurements also suggest that for the hex site the spatial distribution on the remote  $^{13}\text{C}$  nuclei is different from that at the qc sites in that it extends isotropically in the plane perpendicular to the c-axis. So, when comparing the qc sites with the hex site we conclude that the distribution of the spin density on the remote  $^{13}\text{C}$  is determined by two factors. The first one is the orientation of the core of the wavefunction, parallel c for the hex site and at  $70^\circ$  to the c-axis for the qc sites. The second one is the anisotropy of the effective mass in the crystal, which leads to a suppression of the distribution along the c-axis.

#### REFERENCES

- [1] A. Fukumoto, Phys. Stat. Sol. (b) **202** (1997), p. 125.
- [2] R.T.Weber, J.A.J.M.Disselhorst, L.J.Prevo, J.Schmidt, W.Th.Wenckebach, J. Magn. Res. **81** (1989), p.129
- [3] J.A.J.M.Disselhorst, H.van der Meer, O.G.Poluektov and J.Schmidt, J. Magn. Res. **115** (1995), p. 183.
- [4] T.L. Petrenko, V.V. Teslenko, A.A. Bugai, V.D. Khavryutchenko and A.A. Klimov, Semicond. Science Technol. **11** (1996), p. 1279.
- [5] A. v. Duijn-Arnold, J. Mol, R. Verberk, J. Schmidt, E.N. Mokhov, and P.G. Baranov, Phys Rev B **60** (1999), p. 15829.
- [6] W.R.L. Lambrecht, S. Limpijumnong, S.N. Rashkeev, B. Segall, Phys. Stat. Sol. (b) **202** (1997), p.5
- [7] A.O. Evwaraye, S.R. Smith, W.C. Mitchel, H. McD. Hobgood, G. Augustine, V. Balakrishna, Mat. Sc. Forum **258-263** (1997), p.691.
- [8] J.R.Morton and K.F.Preston, J. Magn. Res. **30** (1978), p. 377.
- [9] E. Clementi and C. Roetti, *Atomic data and Nuclear Data Tables* **14**, (Academic Press, New York,1974).
- [10] K.M.Lee, Le Si Dang, G.D.Watkins and W.J.Choyke, Phys. Rev. Lett. **45** (1980), p.390.
- [11] K.Maier, J.Schneider, W.Wilkening, S.Leibenzeder and R.Stein, Mat. Sc. and Engin. **B11** (1992), p.27.

e-mail to : [arnold@molphys.LeidenUniv.nl](mailto:arnold@molphys.LeidenUniv.nl)

## The Electronic Structure of the Be Acceptor Centers in 6H-SiC

A. van Duijn-Arnold<sup>1</sup>, J. Schmidt<sup>1</sup>, O.G. Poluektov<sup>2</sup>, P.G. Baranov<sup>3</sup>  
and E.N. Mokhov<sup>3</sup>

<sup>1</sup>Centre for the Study of the Excited States of Molecules, Leiden University,  
NL-2300 RA Leiden, The Netherlands

<sup>2</sup>Institute of Chemical Physics, Russian Academy of Sciences, RU- Moscow, Russia

<sup>3</sup>A.F. Ioffe Physico-Technical Institute, Russian Academy of Sciences,  
Polytekhnicheskaya st. 26, RU-194021 St.-Petersburg, Russia

**Keywords:** Be Acceptor Centers, Electronic Structure, EPR

**Abstract** In this paper we present an overview of the different shallow and deep acceptor centers in <sup>9</sup>Be-doped 6H-SiC. The g-, hyperfine and quadrupole tensors of up to eight different centers are identified. Their geometric and electronic structure resembles that of the B-related centers in 6H-SiC. Three of them showed the behavior characteristic of shallow B centers (sB), five of them that of deep centers (dB). Two of the deep centers have not been found in B-doped 6H-SiC.

### I. Introduction

Beryllium is an important double-charged acceptor and an electrically active impurity in silicon carbide. The electrical properties of SiC:Be have been studied by Maslakovets et. al. and Vodakov et. al.[1] and it was found that there are at least two acceptor levels,  $E_v + 0.42$  eV and  $E_v + 0.60$  eV. Alternatively, when Be is introduced into crystals that are highly doped with acceptor impurities (B, Al, Ga), Be acts as a donor, leading to an increase in the compensation of the sample by donor centers. Be is also a luminescence activator and the existence of several states of Be follows from an analysis of the luminescence parameters of 6H-SiC:Be[2]. Diffusion measurements confirm the existence of at least two states of Be with different activation energies[1,3].

The few EPR investigations on the Be acceptor that have been reported[4] were performed at 9.5 GHz (X-band) and suffer from poor resolution due to the very small g-anisotropy. Here we present EPR and ENDOR experiments that were performed at 95 GHz and 1.2 K on a pulsed EPR/ENDOR spectrometer[5] using as-grown and Be-diffusion doped 6H-SiC Lely type crystals.

### II. Results and Analysis

Figure 1 shows the EPR spectra of four different 6H-SiC:Be samples, for two characteristic orientations. The upper panel shows the spectra of the samples with **B** // **c** and the lower panel for the orientation **B** ⊥ **c**. Sample I and II are the as grown, sample III and IV are the Be diffusion doped crystals. The figure shows that the relative intensity of the different signals varies over the samples. It is seen that the two left-most signals, attributed to Be - C-vacancy pair centers, are more pronounced in sample III and IV, where they are more easily formed due to the high amount of vacancies.

From the orientational dependence of the EPR spectra it proved possible to assign the observed EPR lines to specific Be centers. In this way three shallow Be acceptor centers were identified with Be substituting for a Si atom in a hexagonal (hex) position ( $sBe_h$ ) and for a Si atom on a quasi-cubic (qc)  $k_1$  position ( $sBe_{k_1}$ ) or  $k_2$  position ( $sBe_{k_2}$ ). In addition three deep Be centers were found corresponding to a Be substituting for a Si on a hex,  $k_1$  or  $k_2$  position combined with a neighboring C vacancy along the c-axis ( $dBe_h$ ,  $dBe_{k_1'}$  and  $dBe_{k_2'}$ ). Remarkably we also found EPR lines related to Be atoms substituting for a Si on a qc site combined with a

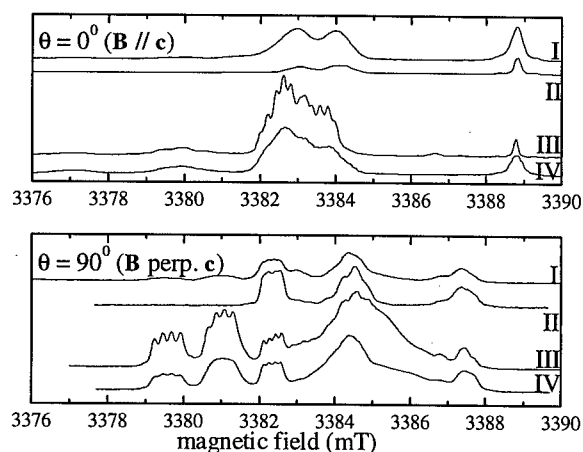


Fig. 1: The EPR spectra of samples I-IV for two different orientations. Samples I and II are as-grown-Be-doped, samples III and IV are Be-diffusion-doped 6H-SiC.

neighboring vacancy at  $70^\circ$  to the c-axis ( $dBe_{k1}''$  and  $dBe_{k2}''$ ).

The largest hyperfine (hf) interaction of the  $sBe_h$  concerns a  $^{13}C$  nuclear spin ( $I=1/2$ ), thus proving that Be substitutes for a Si. The second largest hf splitting was observed with  $^{29}Si$  ( $I=1/2$ ). The largest hf interaction of the  $dBe_{k1}''$  and  $dBe_{k2}''$  centers concerns the  $^{29}Si$  nuclei. Precise values for the  $^4Be$  hf interaction for all centers were found from Electron Nuclear Double Resonance (ENDOR) measurements[6]. The direction of the  $g_z$  axis and principal values of the g-tensors, the hf tensors of the  $^{13}C$  and  $^{29}Si$  nuclei and the hf- and

quadrupole tensors of  $^9Be$  are collected in Tables 1 and 2.

### III. Discussion

Figures 2a. to 2e. show the proposed models for the Be centers and the directions of their g-, hf- and quadrupole-tensors. They resemble the models for the shallow and deep B centers [7,8,9]. There it was found that the shallow (s) centers are characterized by a  $g_z$  value that is smaller than the  $g_x$  and  $g_y$  values, and the deep (d) centers by a  $g_z$  value that is larger than the  $g_x$  and  $g_y$  values. In the case of the shallow centers, the spin density is located on a dangling  $p_z$  orbital on the C atom next to B (Be) and parallel to the  $g_z$  axis[7]. In contrast, in case of the deep centers, the B (Be) is paired with a vacancy along the  $g_z$  axis direction (local symmetry axis) and thus the spin density is mainly distributed perpendicular to this  $g_z$  axis on the three Si atoms on the other side of the vacancy[10].

The  $sBe_h$  center can be described by the same model used for the  $sB_h$  center in 6H-SiC and is depicted in fig 2a. It is found that the g-tensor of the  $sBe_h$  site has its  $g_z$  axis parallel to the c-axis and

	$g_x$	$g_y$	$g_z$	$\angle(g_z, c)$	$^{13}C$ hf (mT)	$^{29}Si$ hf (mT)
$sBe_h$	2.00565(10)	2.00565(10)	2.00180(10)	$0^\circ$ [III]	$a = 4.2$ (5) $b = 1.1$ (5)	$a = 0.74$ (5) $b = 0.13$ (5)
$sBe_{k1}$	2.00505(10)	2.00498(10)	2.00210(10)	$70^\circ$ [III]	-	-
$sBe_{k2}$	2.00570(10)	2.00523(10)	2.00230(10)	$70^\circ$ [III]	-	-
$dBe_h$	2.0033	2.0033	2.0088	$0^\circ$ [III]	-	-
$dBe_{k1}', k2'$	2.0043	2.0043	2.0073	$0^\circ$ [III]	-	-
$dBe_{k1}''$	2.00500(10)	2.00300(10)	2.00764(10)	$68^\circ$ [III]	-	$A_{//c} = 7.5$
$dBe_{k2}''$	2.00435(10)	2.00360(10)	2.00700(10)	$63^\circ$ [III]	-	$A_{//c} = 7.5$

Table 1: The g- and hf tensors for sample III.  $\angle(g_z, c)$  gives the angle between the  $g_z$  axis and the c-axis. The  $g_z$  and  $g_x$  axis are both located in the (1 1 2 0) plane. All g-values are related to the  $sBe_h$  value 2.0018 found from ENDOR. We used the abbreviation  $dBe_{k1}', k2'$  to indicate  $dBe_{k1}'$  and  $dBe_{k2}'$ .

	a (MHz)	b(MHz)	b'(MHz)	q(kHz)	q'(kHz)	$\angle(z\text{-axis}, g_z)$
sBe <sub>k1</sub>	3.23(6)	-1.38(4)	-	338(30)	-	0°, 0°
sBe <sub>k2</sub>	3.37(8)	-2.41(6)	-	312(10)	-	0°, 0°
sBe <sub>h</sub>	2.92(4)	-1.44(3)	-	340(20)	-	0°, 0°
dBe <sub>k1</sub> "	6.33(1)	-0.45(3)	-0.05(1)	110(9)	-54(10)	103°, 61°
dBe <sub>k2</sub> "	6.31(1)	-0.49(3)	-0.13(1)	120(9)	-	100°, 63°

	A <sub>  c</sub> (MHz)	q(kHz)
dBe <sub>k1', k2'</sub>	6.6(1B)	36(1B)
	6.7(hB)	47.1(hB)
dBe <sub>h</sub>	6.78	46.5

Table 2: The Be hf- and quadrupole tensors for sample III (Be diffusion). The relative signs were determined using field-tagged[7] ENDOR, the absolute signs are based on the theoretical prediction that  $q > 0$ . The last column,  $\angle(z\text{-axis}, g_z)$  gives the angle between the principal symmetry (z) axis of the hf, quadrupole tensor and the  $g_z$  axis of the g-tensor of the site in question.

that  $g_z (\sim g_e) < g_x, g_y$ . The largest part of the unpaired spin density is located in a dangling bond  $p_z$  orbital on the nearest neighboring C along the c-axis. The largest Si hf interaction found is assigned to the three Si atoms neighbouring the main C. The hf and quadrupole interactions with Be were measured in ENDOR to be axially symmetric with their symmetry axes parallel to the  $g_z$  axis.

For the sBe<sub>k1</sub> and sBe<sub>k2</sub> sites, depicted in fig 2b, we find a similar behaviour and model as for

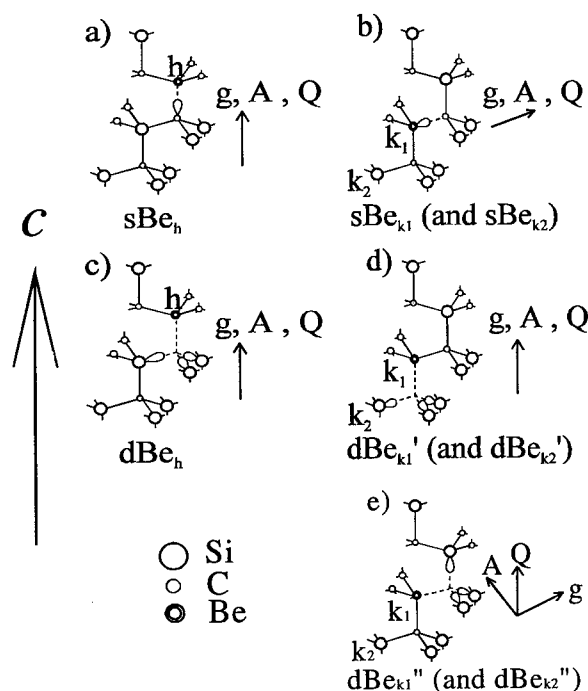


Fig. 2 : Models for the different Be centers and the z-directions of the g-, hf- and quadrupole tensors

the sBe<sub>h</sub> site, only this time the Be-main C bond makes an angle of 70° with the c-axis. Thus the Be  $g_z$ , hf and quadrupole tensor axes make an angle of 70° with c. For these sites no <sup>13</sup>C or <sup>29</sup>Si hf interactions were found.

The three deep Be centers with their  $g_z$  axis parallel to the c-axis, dBe<sub>h</sub>, dBe<sub>k1'</sub> and dBe<sub>k2'</sub>, resemble the deep acceptor centers found in B-doped 6H-SiC. Their model is depicted in fig. 2c and 2d. The Be atom substitutes on either a hex,  $k_1$  or  $k_2$  position and is accompanied by a C vacancy along the c-axis. The main part of the spin density, 75 % - 90 %, resides on the dangling bonds of the three Si atoms surrounding the vacancy (25 % - 30 % per Si). We expect the  $g_z$  axis to be oriented along c towards the vacancy. We assumed axial symmetry for the g-tensor, though it might be slightly non-axial. In ENDOR we measured one set of hf and quadrupole parameters on the hex site EPR line and two sets on the qc site EPR line for  $B \parallel c$ . The quadrupole principal values are an order of magnitude smaller

than those found for the sBe centers and are surprisingly small for an atom next to a vacancy, where a larger gradient would be expected. This effect was also measured for other impurity-vacancy complexes[9,10].

Two deep Be centers were found with their  $g_z$  axis at an angle of  $68 \pm 2$  degrees ( $dBe_{k1}$ ) and  $63 \pm 2$  degrees ( $dBe_{k2}$ ) to the c-axis (see model depicted in figure 2e). The model is the same as for the three deep centers discussed above but with the Be - C-vacancy axis making an angle of  $63^\circ$  or  $68^\circ$  with the c-axis. The largest hf interaction is with the  $^{29}\text{Si}$  nuclei. In contrast to the sBe<sub>k1</sub> and sBe<sub>k2</sub> centers the symmetry axes of the quadrupole and hf tensors of the  $dBe_{k1}$  and  $dBe_{k2}$  centers found in the ENDOR spectra are not collinear with each other nor with the g-tensor symmetry axis. The quadrupole principal values are three times smaller than for the sBe center.

#### IV. Conclusion

In this paper we present an overview of the different shallow and deep acceptor centers that are formed when 6H-SiC is doped with Be. It is found that three shallow acceptor centers and five deep acceptor centers are formed. It is also found that the Be centers can be described with a similar model as the B-related centers.

From our measurements it can be concluded that the two energy levels, at  $E_v + 0.42$  eV and  $E_v + 0.60$  eV, found by both electrical and diffusion measurements can be assigned to respectively, the three shallow centers and the five deep centers.

One of the most remarkable conclusions is that the electronic structure of the shallow and deep Be centers in *n*-type SiC strongly resemble those of B in *n*-type SiC, even though the charge states are different. Apparently their properties can be described in a satisfactory way by simple one-electron models. In particular the fact that both B and Be occupy off-center positions can be explained by their atomic radii, which are both much smaller than that of Si. For a detailed discussion of these results the reader is referred to our recent publication[6].

#### References

- [1] Yu.P. Maslakovets, E.N. Mokhov, Yu.A. Vodakov and G.A. Lomakina, *Sov. Phys. Sol. State* **10** (1968), p.634; Yu. A. Vodakov, G.A. Lomakina, E.N. Mokhov and V.G. Oding, *Sov. Phys. Sol. State* **20** (1978), p. 258.
- [2] V.I. Sokolov, V.V. Makarov, E.N. Mokhov and G.A. Lomakina, *Sov. Phys. Sol. State* **10** (1968), p. 2383.
- [3] E.N. Mokhov, Yu. A. Vodakov and G.A. Lomakina, *Problems in the Physics and Technology of Wide Band Semiconductors* (Leningrad, 1979), p. 136; Yu.A. Vodakov, E.N. Mokhov and V.G. Oding, *Neorgan. Materialy* **19** (1983), p. 1086.
- [4] A.Hofstaetter, B.K. Meyer, A. Scharmann, P.G. Baranov, I.V. Ilyin and E.N. Mokhov, *Materials Science Forum* **264-268** (1998), p.595; P.G.Baranov and E.N.Mokhov, *Phys. Solid State* **38** (1996), p.798.
- [5] R.T.Weber, J.A.J.M.Disselhorst, L.J. Prevo, J. Schmidt and W.Th. Wenckebach, *J. Magn. Res.* **81** (1989), p.129; J.A.J.M.Disselhorst, H.van der Meer, O.G.Poluektov, and J.Schmidt, *J. Magn. Res.* **115** (1995),p.183.
- [6] A. van Duijn-Arnold, O.G. Poluektov, P.G. Baranov, E.N. Mokhov and J. Schmidt, *Phys Rev B* **60** (1999), p. 15799.
- [7] T.Matsumoto, O.G.Poluektov, P.G. Baranov, E.N. Mokhov and J.Schmidt, *Phys. Rev. B* **55** (1997), p.2219.
- [8] P.G.Baranov, I.V.Ilyin, and E.N.Mokhov, *Solid state communications* **100** (1996), p.371; P.G.Baranov, *Defect and Diffusion Forum* **148-149** (1997), p.129.
- [9] A.v.Duijn-Arnold, T.Ikoma, O.G.Poluektov, P.G.Baranov, E.N.Mokhov, and J.Schmidt, *Phys. Rev. B* **57** (1998), p.1607.
- [10] G.D.Watkins, *Physical Review* **155** (1967), p.802.

## Electron Paramagnetic Resonance of the Scandium Acceptor in 4H and 6H Silicon Carbide

S. Greulich-Weber<sup>1</sup>, M. März<sup>1</sup>, J.-M. Spaeth<sup>1</sup>, E.N. Mokhov<sup>2</sup>  
and E.N. Kalabukhova<sup>3</sup>

<sup>1</sup> Department of Physics, University of Paderborn, DE-33095 Paderborn, Germany

<sup>2</sup> Ioffe Physico-Technical Institute, Russian Academy of Sciences,  
Polytekhnicheskaya st. 26, RU-194021 St.-Petersburg, Russia

<sup>3</sup> Institute Semiconductors, National Academy of Science of Ukraine, Kiev, 252028, Ukraine

**Keywords:** Acceptors, EPR, Scandium

**Abstract.** In Sc-doped 6H-SiC epitaxial layers we observed several different electron paramagnetic resonance (EPR) spectra with a  $^{45}\text{Sc}$  hyperfine interaction pattern. The spectra are explained as being due to the isolated  $\text{Sc}^0$  ( $S = 1/2$ ) acceptor on carbon sites but with different microscopic configurations. The spectra show a pronounced temperature dependence. At low temperatures the hole of the  $\text{Sc}^0$  acceptor is located in a  $\text{Sc}^0$ -Si bond either along the  $\bar{c}$ -axis forming an axial centre or along one of the 3 other C-Si bonds giving rise to a monoclinic centre. At higher temperature the hole changes place rapidly between the three Sc-Si bonds resulting in an axial centre. All three  $\text{Sc}^0$  hole configurations have different ionisation levels. The ionization level of the low temperature monoclinic – high temperature axial centre is significantly influenced by an entropy term. In 4H-SiC spectra were only observed from a single  $\text{Sc}^0$  centre with monoclinic symmetry.

### Introduction.

Recently the microscopic and electronic structure of the Sc impurity in SiC has been a controversial issue [1-3]. Sc is expected to act as an acceptor in SiC [4]. 6H-SiC doped with Sc shows a photoluminescence band with an onset at about 2.55 eV and a maximum at about 2.2 eV [4]. With electron paramagnetic resonance (EPR) detected via the photoluminescence (PL-EPR) several EPR lines were observed, but no hyperfine (hf) structure was resolved [1,3], leaving the origin of the observed lines open. With conventional EPR up to four different EPR spectra were reported for 6H-SiC, measured at different temperatures, all having the typical  $^{45}\text{Sc}$  hf splitting of octets [2,3]. It was argued that these spectra have to be explained assuming two Sc defects [3]. In one EPR spectrum a resolved  $^{29}\text{Si}$  superhyperfine (shf) interaction was found, from which it was concluded that Sc replaces C [2] in contrast to other speculations that Sc occupies a Si site [3]. In order to further clarify the structure of the Sc acceptors, we present a new EPR investigation of the Sc acceptor at various temperatures, mainly in 6H-SiC.

### Experimental

6H- and 4H-SiC epitaxial layers were grown on 6H- and 4H-SiC single crystal substrates, respectively, by a sublimation sandwich method [1, 2] and doped with Sc during the growth. The measured sample contained the epitaxial layer with a Sc concentration of the order of  $(1 - 3) \times 10^{17} \text{ cm}^{-3}$  and an unknown degree of compensation with N. The n-type substrate contains N donors, which were seen in the EPR spectra.

### Experimental Results

In 6H-SiC an X-band EPR spectrum with axial symmetry about the c-axis was measured, published previously by the authors [2, figs. 1 and 2]. It was reinvestigated in this study because of the controversial discussions about the microscopic structure of the Sc acceptor [2,3]. The spectrum could be observed between 4.2 and 70 K with signal intensities depending on temperature and illumination. In K-band three sets of eightfold split spectra were resolved (fig. 1 in [2]), while in X-band only one octet was resolved at slightly lower temperature under the same conditions otherwise (fig. 2 in [2], fig. 3). The eightfold split EPR lines were explained with an effective spin of  $S=1/2$  and an anisotropic hf interaction of a 100% abundant nucleus with  $I=7/2$  such as  $^{45}\text{Sc}$ . The 3 octets observed in K-band were assigned to the 3 inequivalent defect sites in 6H-SiC (two quasi-cubic sites ( $k_1, k_2$ ), one



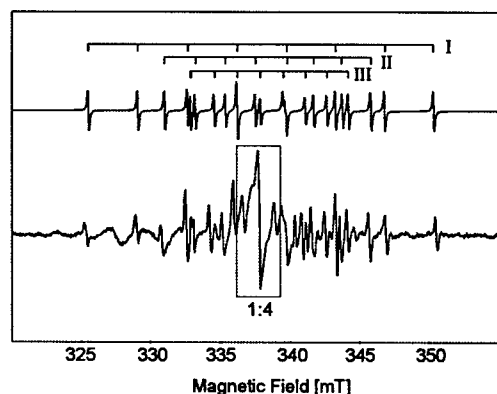


Fig. 1: Upper curve: EPR spectrum of defect A for  $B \parallel \bar{c}$  calculated with the parameters given in table 1. Lower curve: EPR spectrum of Sc-doped 6H-SiC (X-band,  $T=4.5$  K) measured in the dark for  $B \parallel \bar{c}$ . The central part of the spectrum shows the triplets of the N donors (reduced by a factor of 4).

hexagonal site (h)). The hf parameters and g tensors are given in table 1 (spectrum B, sites I, II, III). The 3 octets of sites I, II and III show only slightly different g tensors and very similar hf parameters indicating that Sc is in a very similar configuration on all 3 sites. An assignment to the specific sites  $k_1$ ,  $k_2$  and h could not be made. The axial Sc centre is not seen at low temperature ( $T < 15$  K) in the dark, but appears upon illumination with above-band-gap light.

Two small satellite lines symmetrically about the  $^{45}\text{Sc}$  hf EPR lines (fig. 1 and 2 in [2], fig. 3) were previously analysed by März et al [2]. It was concluded that these satellite lines are due to four equivalent nearest neighbour Si nuclei (equivalent within the line width) and that therefore Sc is on a C site, in contrast to recent speculations that Sc resides on a Si site [3]. The analysis of März et al [2] was checked again on the basis of new measurements confirming the previous results.

Below 15 K the axial spectrum B disappears in the dark and can only be measured under above-band-gap illumination. Yet another EPR spectrum is measured (fig. 1, lower curve), which shows six octets corresponding to six defect orientations with different splittings. The eightfold splitting of each spectrum is again associated with Sc. Fig. 1 shows 3 octets which are seen for  $B_0 \parallel \bar{c}$ . The symmetry observed is monoclinic, which made it necessary to measure the angular dependence in two planes ( $(11\bar{2}0)$  and  $(0001)$ ) in order to determine the spin Hamiltonian parameters. Fig. 1 (upper curve) shows the calculated spectrum for  $S=1/2$  and for the parameters given in table 1 for spectrum "A". The principal axis of the hf tensor with the largest interaction (z-axis) is oriented along the bond axis between Sc on the C site and a nearest Si neighbour in the plane perpendicular to the  $\bar{c}$ -axis. The three inequivalent sites (h,  $k_1$ ,  $k_2$ ) were not resolved in X-band.

Upon increasing the temperature the line intensities of the monoclinic spectra A decrease until above about 15 K they vanish (see fig. 2, squares). Until above 25 K a new octet spectrum appears having axial symmetry about the  $\bar{c}$ -axis, which is also attributed to Sc. The intensity of the spectrum increases with temperature (see fig. 2, circles). The g and hf tensors are collected in table 1 (spectrum C). The  $^{45}\text{Sc}$  hf splitting of the axial spectrum C is largest when  $B \perp \bar{c}$ . In contrast to this in spectrum B it is largest for  $B \parallel \bar{c}$ . At low temperature the EPR line intensity of spectrum B (measured under illumination) depends on the microwave power due to saturation effects. The line intensity increases with temperature above about 20 K (fig. 2, triangles). Above 40 K the intensity does not change under illumination with above-band-gap light any more.

In 4H-SiC doped with Sc we observed an EPR spectrum only at low temperature ( $T < 15$  K) with the g and hf tensors given in table 1. The symmetry is monoclinic and six octets were observed for an arbitrary orientation in the dark similarly to what was observed in 6H-SiC at low temperature.

poly-type	spectrum	tempe- rature	symmetry	$g_{xx}$	$g_{yy}$ ( $g_{\parallel}$ )	$g_{zz}$	$A_{xx}/h$ [MHz]	$A_{yy}/h$ [MHz]	$A_{zz}(A_{\parallel})/h$ [MHz]
6H	A	< 15 K	mono- clinic	1.999 (0.001)	1.996 (0.001)	2.002 (0.001)	0 (15)	17 (15)	106 (1)
	B II III	4.2 - 70 K	axial	1.9976 (0.0003)	2.0029 (0.0003)	22.8 (0.4)	116.6 (0.2)		
				1.9975 (0.0003)	2.0026 (0.0003)	22.3 (0.4)	116.5 (0.2)		
				1.9969 (0.0003)	2.0020 (0.0003)	22.7 (0.4)	116.4 (0.2)		
	C	> 25 K	axial	2.000 (0.001)	1.998 (0.001)	56 (1)	26 (1)		
4H	D	< 15 K	mono- clinic	1.995 (0.001)	1.993 (0.001)	1.9976 (0.001)	13 (15)	0 (15)	104 (1)

Table 1: Principal values of g and hf tensors of Sc defects measured in 6H- and 4H-SiC.

### Discussion

We observed three different types of EPR spectra in Sc doped 6H-SiC, all showing a pronounced temperature dependence. They all exhibit the Sc hf interaction pattern, however with different hf splittings, indicating Sc to be present in different configurations. The EPR spectrum type A observed at low temperature ( $<15$  K) has almost the same value of  $A_{zz}$  as that observed in the axial spectrum B. Furthermore,  $A_{yy}$  of spectrum type A is much smaller than  $A_{zz}$  as is  $A_{\perp}$  of spectrum type B compared to  $A_{zz}$  ( $A_{\parallel}$ ). Unfortunately,  $A_{xx}$  and  $A_{yy}$  of spectrum type A could not be determined precisely enough to check whether their average is close to  $A_{\perp}$  of spectrum type B. Similarly we observed for the g values that both the monoclinic spectrum A and the axial spectrum B show very similar values of  $g_{zz}$  (although different orientations). Furthermore,  $g_{\perp}$  of the spectrum type B is the average of  $g_{xx}$  and  $g_{yy}$  of the spectrum type A. If one calculates an average of the g and hf tensors of the spectrum type A such that the orientations of the principal axes for the average tensors are parallel and perpendicular to the  $\bar{c}$ -axis, one finds approximately the hf tensors of the observed axial spectrum type C: About 55 MHz for  $A_{\perp}$  and about 12 MHz for  $A_{\parallel}$ , in fair agreement with the experiment.

From these observations the following Sc defect model is proposed:  $\text{Sc}^0$  ( $4s^2 3d^1$ ) resides in a carbon vacancy ( $V_C$ ). All three types of Sc EPR spectra (A, B, C) are due to the isolated  $\text{Sc}^0$  acceptor only. The EPR spectra observed originate from different configurations of the Sc hole which is located in a bond to one of the four nearest silicon neighbours.

At low temperature the hole is in one of the C-Si bonds as shown in fig. 3 (a). There are six orientations for this configuration in the crystal: two groups of three in a  $C_{3v}$  arrangement, twisted with respect to each other by  $60^\circ$ . In this configuration one measures the monoclinic spectrum type A. Upon raising the temperature the hole starts to hop between the bonds of the 3 next neighbour Si in the plane perpendicular to the  $\bar{c}$ -axis (fig. 3 (b)). Due to this thermally induced motion, the low temperature g and hf tensors with monoclinic symmetry are averaged such that an EPR spectrum with axial symmetry about the  $\bar{c}$ -axis (type C) is observed with  $A_{\parallel} < A_{\perp}$  and with  $g_{\parallel} < g_{\perp}$ . In the case of the axial spectrum type B with  $A_{\parallel} > A_{\perp}$  (fig. 3 (c)) and  $g_{\parallel}$  parallel to the  $\bar{c}$ -axis the bond direction is along the  $\bar{c}$ -axis. There is no hopping process for center B, since the spectral positions of the EPR lines of spectra B do not change in the whole temperature range investigated.

The different hole configurations leading to spectra of types A, B or C lead to three different defect levels in the gap which is probably caused by different lattice relaxations and lattice vibrations. Their position relative to the Fermi level determines whether the EPR spectrum is observable in the dark or not. From the measured EPR line intensities as a function of temperature and illumination we propose that at low temperature (4.2 K) the ionization level of defect A is above that of defect B (see fig. 4). At 4.2 K the Fermi level is near (slightly above) the ionization level of center A, which is then (at least partly) in the paramagnetic  $A^0$  state, while center B remains in the diamagnetic  $A^-$  state. Upon above band gap illumination level B can catch holes to convert to the  $A^0$  state and becomes visible in the EPR as observed. Upon raising the temperature above 4.2 K the Fermi level drops and moves

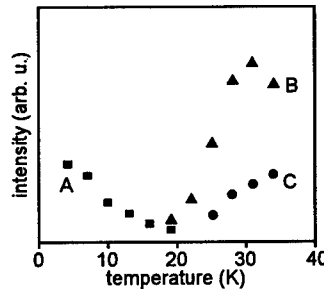


Fig. 2: Relative EPR line intensities of one Sc hf line of spectra A (full squares), B (full triangles) and C (full circles) at different temperatures (same microwave power, without illumination).

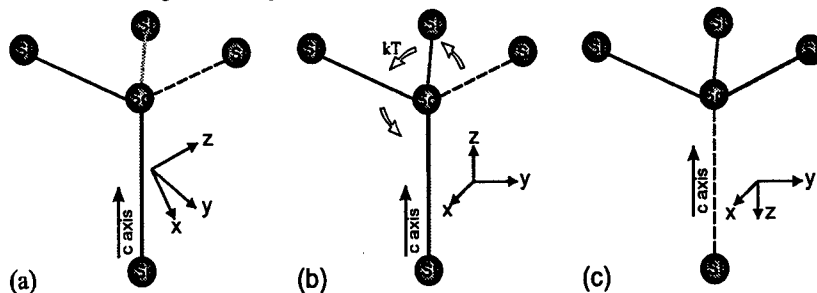


Fig. 3: Models of the  $\text{Sc}_C$  impurity in 6H-SiC explaining all EPR spectra observed (A to C). (a) At low temperature ( $T < 15$  K) the hole is oriented along one of the nearest neighbour Si bonds in a plane  $\perp \bar{c}$  (spectrum A) or  $\parallel \bar{c}$  (spectrum B). (b) At higher temperature the hole starts jumping about the 3 nearest neighbour Si bonds and the axial spectrum C is observed. (c) The axial orientation of the hole ( $\parallel \bar{c}$ -axis) shows no change in spectral position of EPR lines as a function of temperature (spectrum B).

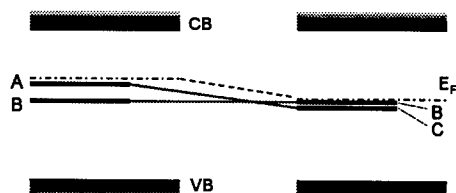


Fig. 4: Proposed ionisation level scheme for defects A, B and C. The low temperature case is shown qualitatively on the left with centre A observed by EPR in the dark. With increasing temperature the Fermi level moves downwards towards level B. In the high temperature case on the right, the level of defect C is below that of defect B. Therefore the intensity of lines of defect C is lower than that of defect B. Had it full hole occupancy the lines of defect C should have 3 times the intensity of those of defect B.

towards the ionization level of B (see fig. 4) increasing more and more the hole occupancy there ( $A^0$  occupancy). Therefore the line intensity of center B increases with increasing temperature (fig. 2, triangles) until a maximum is reached at about 40 K. Had the Fermi level been such that all centres B had been in the paramagnetic state at 4.2 K then the signal intensity would have been decreasing with increasing temperature due to the Boltzmann factor ( $\propto 1/T$ ). The decrease of the signal intensity of the center A with increasing temperature is probably not due to the Boltzmann factor, but due to the thermal hopping of the hole resulting in the axial center C and disappearance of the ionization level A. It is proposed that the centre C has a level below that of B, certainly below the assigned position of the monoclinic centre A. It is probably near that of B. The reason is that because of the thermally activated hole hopping associated with soft local lattice modes the ionization level is

determined by a larger entropy term compared to the low temperature monoclinic configuration A. The importance of an entropy term has been demonstrated for two bistable defect configurations, where the bistability was thermally driven [10,11]. If we consider the Gibbs free energy ( $G = H - TS(T)$ ,  $H$  = configuration enthalpy,  $T$  = temperature and  $S(T)$  = entropy of defect) the defect level is shifted downwards when raising the temperature. The entropy is thought to be associated with rather soft local lattice modes which also enable the thermal hopping of the hole. The negative entropy term in the Gibbs free energy increases in magnitude rapidly with increasing temperature. For soft modes the entropy increases significantly with increasing temperature [10]. Whether also the level of B has an appreciable entropy term, we do not know. We think that relative to B the center C has the larger entropy term. Upon increasing the temperature above 20 K the Fermi level is lowered and moves nearer to the C level resulting in an increase of its line intensities, which at 40 K has not yet reached a maximum.

In contrast to our measurements Baranov et al. [3] claimed that they found in total four types of Sc EPR spectra instead of three as we have observed. A closer inspection of [3] shows that their EPR spectra were not analysed satisfactorily. In fact, Baranov et al. measured the same low temperature EPR spectrum as we did (spectrum type A in our notation). The interaction parameters given in ref. [3] seem doubtful, since the largest hf splitting should occur at  $B \parallel \bar{c} + 70^\circ$  (along the Si-C bond direction) and not for  $B \perp c$  as stated in ref. [3]. Furthermore, the two spectra labelled  $Sc_{\alpha 1}(LT)$  and  $Sc_{\alpha}(LT)$  in ref. [3] are not due to two different centres as assumed there but are due to two different orientations of the low temperature Sc configuration (labelled type A by us). The spectra shown in ref. [3] are the same as those measured here (spectra types B and C (table 1)). We could explain the lines of fig. 4 in [3] with the data presented in table 1. However, the  $g$  and hf values given in ref. [3] differ significantly from ours (table 1) by about 15%. In both investigations the EPR of the shallow N donor was observed simultaneously, which could be used as an independent field marker for the determination of the  $g$  and hf values [9]. Probably the field calibration used in ref. [3] was erroneous.

- [1] P. G. Baranov, N. G. Romanov, V. A. Vetrov and V. G. Oding, 20<sup>th</sup> Int. Conf. Phys. Semicond. (3), World Scientific, Singapore (1990), pp. 1855-1858
- [2] M. März, J. Reinke, S. Greulich-Weber, J.-M. Spaeth, H. Overhof, E.N. Mokhov, A. D. Roenkov, E. N. Kalabukhova, Sol. Stat. Comm. 98 (1996), 439
- [3] P. G. Baranov, I. V. Il'in, E. N. Mokhov, A. D. Roenkov, V. A. Khramtsov, Phys. Solid State 39 (1997), 44
- [4] V. S. Ballandovich, Sov. Phys. Semicond. 25 (1991), 174
- [5] Yu. A. Vodakov, E. N. Mokhov, M. G. Ramm, A. D. Roenkov, Kristall und Technik 14 (1979), 6
- [6] Yu. A. Vodakov and E. N. Mokhov, USA Patent No. 4147572
- [7] Yu. M. Tairov, I. I. Khlebnikov, V. F. Tsvetkov, phys. stat. sol. (a) 25 (1974), 349
- [8] J.-M. Spaeth, J.R. Niklas and R.H. Bartram, *Structural Analysis of Point Defects in Solids: Introduction to Multiple Magnetic Resonance Spectroscopy*, Springer 1992 (Heidelberg)
- [9] E. N. Kalabukhova, N. N. Kabin, S. N. Lukin, Sov. Phys. Solid State 29 (1987), 1461
- [10] H. Söthe, J.-M. Spaeth and F. Luty, Radiation Effects and Defects in Solids, 119-121 (1991), 269-274
- [11] B. Hamilton, A.R. Peaker and S. S. Pantelides, Phys. Rev. Lett. 61 (1988), 1627

## ESR Study of Delamination in H<sup>+</sup> Implanted Silicon Carbide

Ershad Ali Chowdhury<sup>1</sup>, Toshihide Seki<sup>1</sup>, Tomio Izumi<sup>1</sup>, Hisao Tanaka<sup>2</sup>  
and Tohru Hara<sup>2</sup>

<sup>1</sup>Department of Electronics, Tokai University,  
1117 Kitakaname, Hiratsuka, Kanagawa 257-1292, Japan

<sup>2</sup>Electrical Engineering, Hosei University, 3-7-2 Kajinocho, Koganei, Tokyo 184-8584, Japan

**Keywords:** Defects, Delamination, Electron Spin Resonance, Hydrogen Ion Implantation, SiC On Insulator

**Abstract:** Electron spin resonance (ESR) and scanning electron microscope (SEM) methods were used to investigate the delamination phenomena in silicon carbide. 3C-SiC substrate was implanted with a high dose H<sup>+</sup>. An ESR signal with a  $g = 2.0031$  and a spin density of  $6.1 \times 10^{15}$  spins/cm<sup>2</sup> was observed in the as-implanted layer. The  $g$ -value of this signal shifted to 2.0028 after annealing over 650 °C. Changes in  $g$ -value and signal intensity during annealing were caused by desorption of hydrogen during delamination. Another ESR measurement of a high dose H<sup>+</sup> implanted Si was also performed to compare with the 3C-SiC.

### 1. Introduction

Cubic silicon carbide (3C-SiC) has been regarded as a potential material for advanced electronic devices because of its outstanding and unique properties like thermal stability, high electron mobility, high saturation electron drift velocity, and large band gap [1]. Unlike conventional semiconductor materials, devices that work under high temperature and high radiation can be achieved by 3C-SiC. Another large potential application will probably be microwave metal semiconductor field effect transistor (MESFET), due to the high electron mobility of 3C-SiC. Silicon carbide on insulator (SiCOI) structures is suitable for achieving the MESFET [2]. Delamination of SiC by hydrogen ion implantation, presently, attracts a great deal of attention as a fabrication process of this substrate [3]. This is a process by which a thin and uniform SiC layer can be obtained through delamination of the SiC layer by the implantation of high dose hydrogen ions followed by annealing. Some interesting work related to defects and hydrogen behaviors during delamination have been reported [4,5]. However, only a few have so far been revealed on radiation-induced defect structure and mechanism of the delamination. In the present study, we have performed measurements with electron spin resonance (ESR) and scanning electron microscope (SEM) to investigate the defect structure during the delamination.

### 2. Experimental

3C-SiC was implanted with a dose of  $2 \times 10^{17}$  H<sup>+</sup> ions/cm<sup>2</sup> at 100 keV and, for the comparison of the defect structure, another Si substrate was also implanted with a dose of  $6 \times 10^{16}$  H<sup>+</sup> ions/cm<sup>2</sup> at 100 keV. Damage density and hydrogen ion concentration for the implantation were determined by the Monte Carlo simulation using TRIM-95. Annealing was performed in Ar ambient up to 1100 °C for 30 min. ESR measurements were performed at room temperature using X-band microwave spectroscopy and delamination stages were observed by SEM.

### 3. Results

Figure 1 shows a cross-sectional SEM micrograph for  $H^+$  implanted SiC after annealing at 1050 °C. Delamination took place uniformly at the depth of nearly 600 nm from the ion-implanted surface. The depth peak of ion-induced defects obtained by Monte Carlo simulation coincides well with this result.

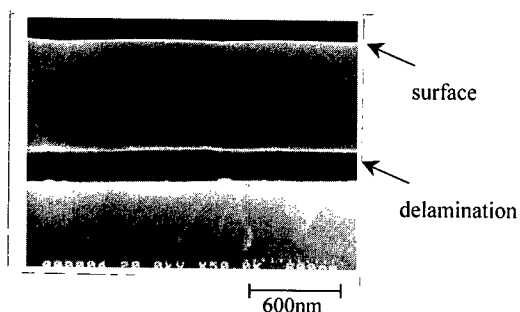


Fig.1 X-SEM micrograph for  $H^+$  implanted SiC.

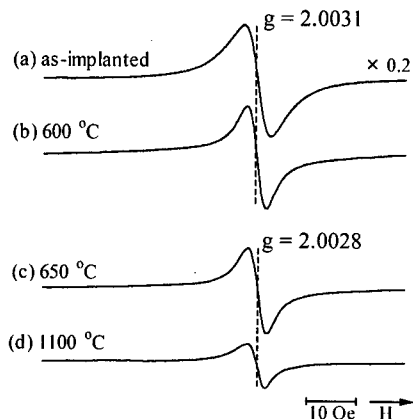


Fig.2 Typical example of the ESR spectra created in SiC by  $H^+$  implantation with a dose of  $2 \times 10^{17}$  ions/cm<sup>2</sup> at 100 keV.

Figure 2 shows the ESR spectra for the 3C-SiC implanted with a dose of  $2 \times 10^{17}$   $H^+$  ions/cm<sup>2</sup> at 100 keV. An ESR signal with a  $g = 2.0031$ ,  $\Delta H_{pp} = 5.4$  Oe, and a spin density of  $6.1 \times 10^{15}$  spins/cm<sup>2</sup> from the as-implanted layer is shown in Fig. 2 (a). This signal is identical to Si dangling bonds with C atom neighbor at the damaged as-implanted SiC region (generally known as  $P_{SiC}$ -center) [6]. The  $g$ -value of this signal shifted to 2.0028 after annealing over 650 °C.

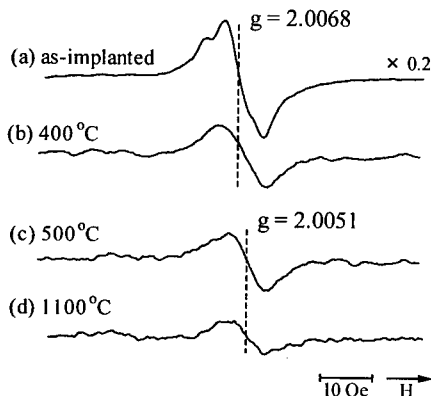


Fig.3 Typical example of the ESR spectra created in Si by  $H^+$  implantation with a dose of  $6 \times 10^{16}$  ions/cm<sup>2</sup> at 100 keV.

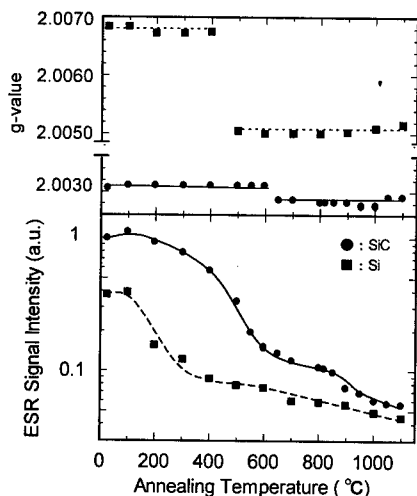


Fig.4 Annealing properties of  $g$  value and signal intensity for  $H^+$  implanted SiC and Si substrates.

We also have performed ESR measurements of high dose  $H^+$  implanted Si, in order to compare it with the SiC. Fig. 3 shows the ESR spectra for the Si substrate implanted with a dose of  $6 \times 10^{16}$   $H^+$  ions/cm<sup>2</sup> at 100 keV. Fig. 3 (a) shows the ESR signal observed from the as-implanted layer, practically found anisotropic with a g-value of 2.0068 and a spin density of  $3.2 \times 10^{14}$  spins/cm<sup>2</sup>. This ESR signal probably arises from Si dangling bonds of different vacancy-type defects such as Si-Si center [7]. Seemingly hydrogen atoms can occupy the part of the dangling bonds of these vacancy-type defects. The g-value of this signal shifted to 2.0051 after annealing over 500 °C.

Figure 4 shows the isochronal annealing curves of the g-value and the signal intensity for the paramagnetic defects, which were observed for SiC and Si substrates used in Fig. 2 and Fig. 3, respectively. The signal intensity decreased for both the samples when annealing temperature increased. However, defects remained stable even after annealing at the temperature of 1100 °C.

#### 4. Discussion

During the implantation, most of the H atoms interact immediately with the implantation induced or pre-existing dangling bonds in Si to form a variety of types of Si-H complexes such as interstitial-H, multivacancy-H, multyhdrogen monovacancy; some of the H atoms form  $H_2$  pairs and the rest remain as atomic H [8,9]. It has been suggested that the delamination phenomena is closely related to the formation of Si-H defect bonds and also to the release of these bonds [10]. This release of H atoms occurs gradually and shows time variations. Usually only 30% of the implanted hydrogen is actually involved in splitting. The annealing kinetics of  $H^+$  implanted silicon can be found elsewhere [11].

Atmospheric pressure ionization mass spectrometer (APIMS) measurement [12] for Si showed that ion implanted H is tied strongly to the defective Si and is stable up to 400 °C so that no out-diffusion of H occurs. However, the intensity increased rapidly above this temperature and reached a first peak at 450 °C due to a change in complex defects of Si-H configurations. Extra H, formed by these configuration changes, leads to the deposition of H at 450 °C. Our ESR measurement also obtained a similar result with the above-mentioned discussion. The ESR line shape changes gradually as annealing temperature increases (Fig. 3 (b)), although no noticeable change in g-value appears up to 400 °C. Changes in ESR line shapes can be explained as passivation of dangling bonds by remaining H atoms (Fig. 3). Changes in signal intensity for Si also agrees with passivation that takes place due to annealing (Fig. 4). However, g-value suddenly decreases to 2.0051 at the annealing temperature over 500 °C. APIMS measurement showed a second peak near 650 °C, due to desorption of H. However, our ESR measurement does not show any noticeable change (neither in g-value nor in signal intensity). This is due to the fact that 40% of the implanted H atom still exists in the Si layer [12].

Similar formation of defective Si-H bonds in other Si compounds such as SiC and SiN can be presumed [4] and similar kinds of results are also obtained for SiC. However, for that case, the temperature for delamination is relatively very high. Secondary ion mass spectrometry (SIMS) studies showed for SiC that hydrogen starts to diffuse between 700 °C to 900 °C [2] that plays important role for delamination.

In the case of SiC, there is no change in the observed g-value except a sharp decrease in signal intensity at the annealing temperature up to 600 °C. The g-value shifts up to 2.0028 from 2.0031 at a annealing temperature above 650 °C (Fig. 2). However, no noticeable change is observed except a gentle decrease in the signal intensity.

The above discussion shows that the ESR method can be a useful analytical tool to study the delamination mechanism. However, further studies are required to reveal the delamination phenomena in detail.

## 5. Conclusion

High dose H<sup>+</sup> was implanted to 3C-SiC and Si with an implantation energy of 100 keV with a dose of  $2 \times 10^{17}$  and  $6 \times 10^{16}$  ions/cm<sup>2</sup>, respectively, to study the delamination phenomena. The as-implanted 3C-SiC showed an ESR signal, due to Si dangling bonds with C atom neighbor with a g-value of 2.0031 and a spin density of  $6.1 \times 10^{15}$  spins/cm<sup>2</sup>. The g-value shifted to 2.0028 after annealing at 650 °C. In the case of Si, an anisotropic ESR signal with a g-value of 2.0068 and a spin density of  $3.2 \times 10^{14}$  spins/cm<sup>2</sup> was observed, due to hydrogen induced Si dangling bonds. The g-value shifted to around 2.0051 after annealing over 500 °C. Changes in g-value and signal intensity during annealing were caused by desorption of hydrogen during delamination.

## References

- [1] J. W. Palmour, H. S. Kong and R.F. Davis, Appl. Phys. Lett. **51** (1987), p. 2028.
- [2] L. Di Cioccio, F. Letertre, Y. Le Tiec, A. M. Papon, C. Jaussaud and M. Bruel, Mat. Sci. Eng. **B46** (1997), p. 349.
- [3] L. Di Cioccio, Y. Le Tiec, F. Letertre, C. Jaussaud and M. Bruel, Elec. Letts. **32** (1996), p. 1144.
- [4] T. Hara, Y. Kakizaki, H. Tanaka, M. Inoue, K. Kajiyama, T. Yoneda and K. Masao, Jpn. J. Appl. Phys. **36** (1997), p. L1142.
- [5] Q.-Y. Tong, K. Gutjahr, S. Hopfe, U. Gösele and T. -H. Lee, Appl. Phys. Lett. **70** (1997), p. 1390.
- [6] T. Izumi, K. Kobayashi, E. Hirose, T. Kawahara and H. Nagasawa, Mater. Sci. Forum **264-268** (1998), p. 619.
- [7] Yu. V. Gorelkinskii and N.N. Nevinnyi, Physica B **170** (1991), p. 155.
- [8] Q-Y. Tong and R.W. Bower, MRS BULLETIN **23** (1998), p. 40.
- [9] Michel Bruel, MRS BULLETIN **23** (1998), p. 35.
- [10] B. Bech Nielsen, J. Olajos and H. G. Grimmeiss, *Defects in Semiconductors*, Editor G. Ferenczi, (Trans. Tech. Aedermannsdorf, 1989), p. 1003.
- [11] J. Zeigler, J. P. Biersack and U. Litmark, *The Stopping and Ranging of Ions in Solid*, (Permagon Press, New York, 1985).
- [12] T. Hara, Y. Kakizaki, T. Kihana, S. Oshima and T. Kitamura, J. Electrochem. Soc. **144** (1997), p. L78.

## Vacancies and their Complexes with H in SiC

P. Deák<sup>1</sup>, A. Gali<sup>1</sup>, B. Aradi<sup>1</sup>, N.T. Son<sup>2</sup>, E. Janzén<sup>2</sup> and W.J. Choyke<sup>3</sup>

<sup>1</sup> Dept. of Atomic Physics, Technical University of Budapest,  
Budafoki út 8, HU-1111 Budapest, Hungary

<sup>3</sup> Dept. of Physics and Measurement Technology, Linköping University,  
SE-581 83 Linköping, Sweden

<sup>4</sup> Department of Physics and Astronomy, University of Pittsburgh, Pittsburgh, PA 15260, USA

**Keywords:** Hydrogen, Local Vibration Mode, Occupation Level, Spin Distribution, Stability, Theory, Vacancy

**Abstract:** Ab initio calculations (LDA and MCSF) have been carried out for vacancies ( $V_{\text{Si}}$  and  $V_{\text{C}}$ ) and interstitial H, as well as for V+H complexes in 3C SiC. Relative stability of different charge-states/configurations and occupation levels were determined in supercells with plane wave basis sets while vibration frequencies and spin distributions were calculated in clusters with localized basis functions. Both types of vacancies show amphoteric electrical activity. In equilibrium, atomic  $H^+$  is at the  $AB_{\text{C}}$ , and  $H^-$  is at the  $T_{\text{Si}}$  site, while  $H^0$  does not appear to be stable with respect to them, so H can also act both as a deep donor and an electron trap. Hydrogen can passivate the  $V_{\text{Si}}$  acceptor but not the  $V_{\text{C}}$  donor. Conditions for the formation of the possible V+H centers and their properties are given and used to discuss experimental information (or the lack of them) about H in SiC.

### 1. Introduction

A key to successful application of semiconducting materials in electronics technology is defect engineering, which is based on the knowledge about the behavior and interaction of intrinsic and extrinsic point defects. The data base necessary to that is still in the making for SiC. The present paper tries to contribute to this process with results of first-principles model calculations on the interaction of vacancies with hydrogen impurities. Vacancies are thermodynamically stable in any crystal and, in addition, can be created by irradiation. Many technological steps (e.g. etching) may lead to hydrogen contamination and in epitaxial SiC layers, grown from hydrogen-rich precursor molecules, the presence of H is inevitable. Usually vacancies are the most common traps for hydrogen — the latter significantly influencing the electrical and chemical activity, as well as the diffusion characteristics of the former. Since doping in SiC often utilizes the competition of dopants and host atoms for a given site in the crystal, hydrogen entering the race for the free valences of a vacancy may influence doping efficiencies.

Relatively few papers have been published on H in SiC, and the experimental fingerprints of its main forms have not yet been established. Photoluminescence bands arising as phonon replica due to modes at 2988, 2962, and 2977  $\text{cm}^{-1}$  were interpreted as indication of the presence of H in a silicon vacancy (C—H stretch modes) [1]. These bands were observed only in epitaxial layers grown under Si-poor conditions and were not always present even then.  $H^+$  implants into Lely-platelets only very rarely showed these C-H centers. Vibrations which could be assigned to Si—H stretching modes ( $\sim 2100 \text{ cm}^{-1}$ ) have not yet been observed. No DLTS peaks could be related to hydrogen in electron-irradiated and deuterium implanted 6H SiC [2]. As yet no EPR signals related to H has been observed either, but  $\mu\text{SR}$  experiments indicate Mu (an analogue of the H atom made of a muon and an electron) at tetrahedral interstitial sites (see ref. [3] and references therein). Due to this general lack of information about H in SiC, *a priori* knowledge about its various forms and about the conditions under which those are formed could be helpful — even if the data supplied by model calculations are only approximate. The only theoretical study we are aware of considered hydrogen only as an isolated interstitial in the neutral charge state [4].



## 2. Methods

We have carried out first principles calculations for supercell models (SCM) as well as for hydrogen saturated molecular cluster models (MCM) of SiC. Local Density Approximation (LDA) to Density Functional Theory has been used both with a plane wave basis up to a cut-off of 64 Ry for SCMs (FHI96MD code [6]) and with a basis of uncontracted Gaussian-type orbitals with preoptimized exponents (AIMPRO code [5]) for MCMs. Suitable forms of norm-conserving pseudopotentials were applied. Details are given elsewhere including matters of convergence [7,8]. Stability and occupation levels have been calculated in SCM, correcting the formation energies for the LDA gap error and for defect level dispersion. The general uncertainties of these calculated values are about  $\pm 0.15$  eV. No spin polarization was, however, allowed which may influence the relative stability of systems with even and odd number of electrons. Spin densities and local vibration modes were calculated in spin polarized MCM calculations. Localization values may be too high by a factor of 2, due to size limitations. Vibration frequencies are accurate within about  $\pm 40$  cm<sup>-1</sup>. The spin state of the neutral silicon vacancy was obtained with the Multi-Configurational Self-Consistent-Field (MC-SCF) method on an MCM, in order to take into account many-body effects in an appropriate way [9]. Our calculations (if not otherwise noted) pertain to 3C SiC. At present we assume stoichiometric conditions.

## 3. Results

### 3.1. Carbon vacancy ( $V_C$ )

In the neutral charge state of  $V_C$  our SCM calculation [8] resulted in a formation energy of  $E_{\text{form}} = 6.7$  eV at 2.6 % inward breathing and 7.7 % pairing distortion in  $D_{2d}$  symmetry. ( $E_{\text{form}}$  refers to creating  $V_C$  and an additional C atom in the SiC host. If C is removed from the crystal  $4.7 = E'_{\text{form}}(\mu_C) = 5.3$  eV.) We find a doubly occupied one-electron level at  $E_V + 1.5$  eV. These results are in good agreement with earlier theoretical results ([10,11] and references therein). Comparing different charge states we find  $V_C^{2+}$  to be the most stable for Fermi-level positions  $E_F = E_V + 2.0$  eV, and  $V_C^-$  for  $E_F = E_V + 2.4$  eV. The lack of spin polarization may have caused the underestimation of the relative stability of the latter (spin-half) system by 0.1 - 0.3 eV. So the (0/-) occupation level is somewhere between 2.1 - 2.3 eV above  $E_V$ . For Fermi-level positions lower than that but above  $E_V + 2.0$  eV, the calculation predicts  $V_C^0$  to be stable. Even allowing for the aforementioned error,  $V_C^+$  can only be marginally stable around  $E_V + 2.0$  eV. In fact,  $V_C^+$  has been observed in EPR [12], although it is not clear whether the experiments were carried out under equilibrium conditions. The  $\pm 0$  occupation level was expected to be around midgap [12] but no DLTS data are available in 3C SiC. (In 6H SiC a donor at  $E_C - 0.51$  eV and an acceptor at  $E_C - 0.34/0.41$  eV were assigned to  $V_C$  [2].) We have calculated the spin distribution for  $V_C^+$  in an MCM. We found 16 % of the orbital with the unpaired spin localized on each of the Si neighbors with an s/p ratio of 16/84. Regarding the limiting effect of the cluster size to delocalization, these compare well with the values deduced from the hyperfine constants in ref. [12]: 7% and 19/81, respectively. Based on our calculated occupation levels,  $V_C$  may also act as an electron trap (hyper-deep acceptor), not just as a deep double donor. The trapped electron in  $V_C^-$  occupies an orbital which is antibonding between two Si neighbors of the vacancy ( $C_{2v}$  symmetry). On each of these two atoms the calculated localization of the spin is 30 %, with an s/p ratio of 25/75. On the other two Si neighbors and on all twelve C second neighbors together the localizations are 6 % and 17 %, respectively.

### 3.2. Silicon vacancy ( $V_{Si}$ )

$V_{Si}$  in SiC is unique among vacancies of tetrahedral crystals because it doesn't show significant distortion from  $T_d$  symmetry in the Jahn-Teller unstable charge states. Our SCM calculation gives 9 % outward relaxation and  $E_{\text{form}} = 7.5$  eV ( $8.9 = E'_{\text{form}}(\mu_C) = 9.5$  eV), in agreement with previous studies [10,11,13]. The relative stability of all charge states of  $V_{Si}$  have already been reported from a high level LDA-SCM calculation [13].  $V_{Si}^-$  may act as a deep acceptor as well as a hole trap (hyper-deep donor). Using the data of ref. [13],  $V_{Si}^0$  is stable above about  $E_V + 0.56$  eV. A stability window of  $\sim 0.07$  eV was calculated below that for  $V_{Si}^+$ . It has to be noted, however, that a one-electron theory, like LDA, necessarily predicts a triplet spin state for  $V_{Si}^0$ . Our MC-SCF calculations on MCM-s of various sizes showed that the singlet state is more than 0.1 eV lower in energy than the triplet one [9]. Therefore, the

stability window for  $^1V_{si}^0$  can be twice as wide around  $E_v + 0.5$  eV (using Fig. 1 of ref. [13]). Regarding the small energy difference between the singlet and triplet states of  $V_{si}$ , the latter could still, in principle, be detected in EPR at higher temperatures. The small stability window of the triplet state makes that, however, unlikely. So the primary EPR active form of the silicon vacancy must be  $V_{si}^-$ . It is interesting to note that a larger stability window for the neutral state can be expected in hexagonal polytypes, offering better chances to see  $^3V_{si}^0$ . Spin density calculations for these cases are under way.

### 3.3. Interstitial hydrogen

We have calculated the relative stability of an isolated interstitial hydrogen atom at various sites, in the  $-0/+$  charge states, under conditions identical to those used for the vacancies. Atomic H turns out to be stable near the tetrahedral interstitial sites ( $T_C$  and  $T_{si}$  denote the ones with four C and Si neighbors, respectively). In the neutral charge state H is about equally stable (within 0.2 eV) near to  $T_C$  and  $T_{si}$ . In the slightly more stable case H is 0.69 Å away from  $T_C$  along [111], in a so-called antibonding ( $AB_C$ ) position. It forms a bond (1.14 Å) with the nearest C neighbor and the C-Si bond further along that direction is weakened ( $d_{C-Si} = 1.95$  Å). The unpaired electron occupies an effective-mass-like state. (This is the reason why our result contradicts that of the MCM calculation of ref. [4], where the unpaired electron goes to a localized antibonding orbital due to the larger width of the MCM gap. Our MCM calculation also predicts H near  $T_{si}$  to be significantly more stable than near  $T_C$ .) In the slightly less stable case H is almost on the  $T_{si}$  site (0.08 Å away along [111]) and the nearest Si-C bond is only slightly perturbed. The unpaired electron is on a localized orbital. H at the bond center (BC) site is 0.62 eV less stable than at  $AB_C$ . Changing the charge state we find that  $H^+$  prefers the  $AB_C$  and H the  $T_{si}$  position (0.7 eV over BC in the former case, 1.3 eV over  $T_C$  in the latter one). Considering the  $- (+)$  charge on C(Si) in the host lattice, this situation seems to be natural. Our results indicate negative U behavior for H by a wide margin (0.6 eV) placing the  $\pm$  occupation level at  $E_v + 2.3$  eV. So H may act both as a donor and an electron trap but, in equilibrium, it is not EPR active. ( $\mu$ SR is usually recorded under non-equilibrium conditions and the small mass and large zero point energy of the muon makes for a dynamically averaged tetrahedral symmetry even if the energy minimum is somewhat off the T site.) It is important to note that this high lying  $\pm$  favors the compensation/passivation of shallow acceptors but not donors. Calculations of characteristic vibration modes are under way.

### 3.4. Vacancy-hydrogen centers

$V_{si}$  captures a H impurity the way one expects it intuitively: one of the dangling bonds is saturated by H, two others form a long bond, and there remains one dangling bond. The system reconstructs to  $C_{1h}$  symmetry.  $V_{si} + H$  has a  $(0/-)$  acceptor level at about  $E_v + 0.3$  eV, i.e. significantly lower than that of  $V_{si}$ . Capture of subsequent H atoms into  $V_{si}$  is energetically less and less favorable if  $[V_{si}] > [H]$ . However, two H atoms passivate  $V_{si}$  completely. So if  $[V_{si}] < [H]$ ,  $V_{si} + nH$  complexes may form without new DLTS peaks appearing — at least in 3C SiC. Preliminary calculations show that the C-H vibrations in  $V_{si} + H$  are in the range given by ref. [1]. The calculated frequency for  $V_{si} + H$  is 2961  $cm^{-1}$  (preliminary results with forces calculated for first neighbors only). Regarding the occupation levels of  $V_{si}$  and H, as mentioned in Sections 3.2-3, a complex between them can form under equilibrium conditions if  $E_v + 0.6$  eV =  $E_F = E_v + 2.3$  eV, i.e. when H is positive and  $V_{si}$  is neutral or negative. Since the range is wide, the complex formation is likely. The binding energy is 3.5 (4.0) eV between neutral (negative)  $V_{si}$  and positive H.

Even though  $V_C$  is more stable than  $V_{si}$ , it is less effective in capturing H. For one thing, the occupation levels of  $V_C$  and H leave only a narrow window for the Fermi-level where H and  $V_C$  is not in the same charge state. For  $E_v + 2.0$  eV =  $E_F = E_v + 2.3$  eV, under equilibrium conditions,  $V_C$  is neutral and H is positive. They do not repel each other but there is no attraction either. In addition, the binding energy is only 2.4 eV. It has to be noted, however, that the formation of  $V_C + H$  (from standard states) is 0.67 - 1.95 eV more favorable (depending on  $\mu_C$ ) than that of  $V_{si} + H$ . If  $V_C + H$  complexes arise, they may be very interesting [8]. Instead of showing the analogue of  $V_{si} + H$  with  $C_{1h}$  symmetry, the bonding combination of the  $sp^3$  hybrids of two Si-neighbors of  $V_C$  "envelope" the nucleus of the H atom, forming a so-called *three-center bond*, and the complex has  $C_{2v}$  symmetry (see Fig. 1). In the neutral charge state the unpaired electron goes to the antibonding combination of these hybrids, which has a node at H. The  $C_{1h}$  configuration with the single Si-H bond is metastable with energy higher by 0.5 eV

in the neutral and by 0.2 eV in the singly positive charge state. (We find a similar situation in MCM calculations for 4H SiC as well!) The  $+/0$  occupation level is between 1.8 - 2.0 eV above  $E_v$ , i.e.,  $V_C + H$  is a donor with the  $+/0$  occupation level close to the  $+(+)/0$  one of  $V_C$ . (Even though the singly occupied one-electron level of neutral  $V_C + H$  is at  $E_v + 0.9$  eV, i.e. lower than the doubly occupied one of neutral  $V_C$ .) We do not find the  $2+$  charge state stable at any position of the Fermi level (even if the possible spin polarization error is considered). Still, there is another (donor) occupation level,  $3+/+$ , at  $E_v + 1.4$  eV (which might be inaccessible to DLTS). In the  $3+$  charge state a configuration with  $C_{3v}$  symmetry becomes more stable, H being closer to one of the Si neighbors along  $[111]$ , but this bond is already very weak. So the  $V_C + H$  complex is a bistable, negative U, triple donor system.  $V_C$  can capture two hydrogens at most: both forming three-center bonds with two Si-neighbors. The Si-H-Si bonds are in this case puckered ( $\theta = 156^\circ$ ,  $d_{HH} = 1.62$  Å). The  $V_C + 2H$  system is a double donor. Therefore, the carbon vacancy cannot be passivated by hydrogen, even if it succeeds capturing one or two of them! ( $V_C + H$ )<sup>0</sup> has the same symmetry and very similar spin distribution to  $V_C$ . On each of the two Si atoms next to H the localization of the orbital with the unpaired spin is 32 %, with an s/p ratio of 18/82. On the other two Si neighbors and on all twelve C second neighbors together the localizations are 4 % and 18 %, respectively. Accordingly, both  $V_C$  and ( $V_C + H$ )<sup>0</sup> qualify as the origin of the E1 center [14]. We have also calculated the frequencies of the Si-H-Si vibrations. The asymmetric and the symmetric stretch modes for neutral (singly positive)  $V_C + H$  are 1570 (1770) and 991 (1189)  $\text{cm}^{-1}$ , respectively. (All these modes are both Raman- and IR-active.) In case of  $V_C + 2H$ , the two Si-H-Si units give rise to a pair of degenerate (both Raman/IR-active) asymmetric stretch modes, and to a symmetric (Raman-active) and an antisymmetric (IR-active) combination of the symmetric ones. These latter have low frequencies, close to the continuum. The rest are given (also for partial and full D  $\rightarrow$  H substitution) in Table 1.

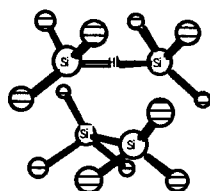


Figure 1. The geometry of the  $V_C + H$  complex.

Table 1. Isotope shifts of the Si-H-Si related vibration frequencies for  $V_C + 2H$  in  $\text{cm}^{-1}$ .

charge state	band	HH	HD	DD
$(V_C + 2H)^0$	Raman/IR	976	797	730
	Raman/IR	976	975	730
	Raman	1332	1177	952
$(V_C + 2H)^{2+}$	Raman/IR	1132	909	900
	Raman/IR	1132	1125	900
	Raman	1205	1067	884

**Acknowledgment** Support by the Hungarian OTKA T-22139, FKFP 0289/97 and AKP 97-92 2,2/27 grants, as well as the bilateral US - Hungarian (JFNo. 667) and Swedish-Hungarian (IVA-MTA No. 36) projects and the grant PHY970006P from the Pittsburgh Supercomputing Center are appreciated.

## References

- [1] W. J. Choyke and L. Patrick, Phys. Rev. Lett. 29 (1972) p. 355.
- [2] M. O. Aboelfotoh and J. P. Doyle, Phys. Rev. B 59 (1999) p. 10823.
- [3] S. K. Estreicher, Mater. Sci. Forum 148-149 (1994) p. 349.
- [4] M. A. Roberson and S. K. Estreicher, Phys. Rev. B 44 (1991) p. 10578.
- [5] R. Jones, Philos. Trans. R. Soc. London Ser. A 341 (1992) p. 351.
- [6] M. Bockstedte, A. Kley, J. Neugebauer, and M. Scheffler, Comp. Phys. Comm. 107 (1997) p. 187.
- [7] A. Gali, P. Deák, R. P. Devaty and W. J. Choyke, Phys. Rev. B 60 (1999) p. 10620.
- [8] A. Gali, B. Aradi, P. Deák, W. J. Choyke and N. T. Son, Phys. Rev. Lett. *submitted*
- [9] P. Deák, J. Miró, A. Gali, L. Udvardi and H. Overhof, Appl. Phys. Lett. 75 (1999) p. 2103.
- [10] A. Zywiets, J. Furthmüller and F. Bechstedt, Phys. Stat. Sol. (b) 210 (1998) p. 13.
- [11] P. Deák et al., Mater. Sci. Forum 264-268 (1998) p. 279.
- [12] H. Itoh, et al., Phys. Stat. Sol. (b) 162 (1997) p. 173.
- [13] L. Torpo, R. M. Nieminen, K. E. Laasonen and S. Pöykkö, Appl. Phys. Lett. 74 (1999) p. 221.
- [14] N. T. Son, W. M. Chen, J. L. Lindström, B. Monemar, and E. Janzén, Mater. Sci. Eng. B 61-62 (1999) p. 202.

## The Carbon Vacancy Pair in 4H and 6H SiC

N.T. Son<sup>1</sup>, P.N. Hai<sup>1,2</sup>, A. Shuja<sup>1</sup>, W.M. Chen<sup>1</sup>, J.L. Lindström<sup>3</sup>, B. Monemar<sup>1</sup>  
and E. Janzén<sup>1</sup>

<sup>1</sup> Department of Physics and Measurement Technology, Linköping University,  
SE-581 83 Linköping, Sweden

<sup>2</sup> Permanent address: Department of Physics, Hanoi University, 90 Nguyen Trai, Hanoi, Vietnam

<sup>3</sup> Department of Solid State Physics, Lund University, Box 118, SE-221 00 Lund, Sweden

**Keywords:** Carbon Vacancy, Electron Irradiation, Electron Paramagnetic Resonance

**Abstract:** Electron paramagnetic resonance (EPR) was used to study defects in p-type 4H and 6H SiC irradiated with 2.5 MeV electrons at elevated temperatures (400 °C). After irradiation, an anisotropic EPR spectrum, labeled EI4, having monoclinic symmetry ( $C_{1h}$ ) and an effective spin  $S=1$  was observed in both 4H and 6H SiC. The same  $g$ -tensor with the principal values,  $g_x=2.0051$ ,  $g_y=2.0038$  and  $g_z=2.0029$  was determined for the spectra in both polytypes. Here the  $z$ - and  $x$ -axis lie in the  $(11\bar{2}0)$  plane and the  $y$ -axis perpendicular to this plane. The angle between the principal  $z$ -axis and the  $c$ -axis is  $54^\circ$ . The fine structure parameters were determined as  $D=3.28\times 10^{-2} \text{ cm}^{-1}$  and  $3.44\times 10^{-2} \text{ cm}^{-1}$  for 6H and 4H SiC, respectively;  $E=0.67\times 10^{-2} \text{ cm}^{-1}$  for both polytypes. From the obtained  $^{29}\text{Si}$  hyperfine structure and spin Hamiltonian parameters, the defect can be identified as the pair of two carbon vacancies in the  $(11\bar{2}0)$  or equivalent planes.

### 1. Introduction

Vacancies created during growth of SiC can move around and interact with each other to form associated complexes when cooling down the crystal after growth. During ion implantation, which is often used for making contact or isolation layers for SiC electronics, or electron irradiation used for lifetime control, a large amount of vacancies can also be introduced. At high annealing temperatures or at elevated working temperatures for SiC based high-temperature electronics, single vacancies become mobile and interact with each other to form vacancy pairs or with other defects to form vacancy-related complexes. As shown from electron paramagnetic resonance (EPR) studies of heat-treated 6H SiC by Vainer and Ilin [1], the coupling between the vacancies leads to the formation of different vacancy pairs with an electron spin  $S=1$ . As known from other semiconductors, vacancy pairs can be stable at very high temperatures. The study of such defects is therefore important for defect engineering.

In this work, we use EPR to study defects in p-type 4H and 6H SiC irradiated with electrons. Since the carbon vacancy becomes mobile at rather low temperatures (150-200 °C) [2], while the silicon vacancy is stable up to 750 °C [2], the electron irradiation was performed at ~400 °C in order to preferentially introduce carbon vacancy-related complexes. An EPR spectrum with monoclinic symmetry ( $C_{1h}$ ) and an electron spin  $S=1$  was observed in 4H and 6H SiC right after irradiation. From the observed  $^{29}\text{Si}$  hyperfine structure and spin Hamiltonian parameters, this spectrum is concluded to be related to a carbon vacancy pair in 4H and 6H SiC.

### 2. Experiment

The starting materials used in this work were p-type, Al-doped 4H and 6H SiC substrates. The concentration of Al in both polytypes is about  $5\times 10^{17} \text{ cm}^{-3}$ . Substrates are off-axis wafers with the planes inclined an angle ( $\sim 3.5^\circ$  for 6H and  $\sim 8^\circ$  for 4H polytypes) with respect to the  $c$  axis towards the  $[11\bar{2}0]$  direction. The samples were irradiated by 2.5 MeV electrons at 400 °C with a dose of

$10^{18} \text{ cm}^{-2}$ . EPR measurements were performed on a Bruker ER-300 X-band ( $\sim 9.5 \text{ GHz}$ ) EPR spectrometer. Most of the EPR measurements were performed at 77 K with samples immersed in liquid nitrogen. Special sample holders were used for 4H and 6H SiC samples to compensate the off-axis angles of the wafers in order to have the magnetic field rotating in the  $(11\bar{2}0)$  plane for the angular dependence studies of the EPR spectra.

### 3. Results and discussion

In the 4H and 6H SiC samples irradiated at  $400^\circ\text{C}$ , several EPR spectra were detected. Fig.1 shows one of these spectra, labeled EI4, observed in 4H SiC for the magnetic field  $B$  parallel to the  $c$  axis. The spectrum in the 6H polytype is very similar. The EI4 spectrum was not detected in the samples irradiated at room temperature. At this direction of the magnetic field the spectrum consists of two lines, each accompanied by two weak satellites as indicated by arrows in Fig.1. The total intensity of these two satellites is about 19% of the main line. This corresponds to the natural abundance of four  $^{29}\text{Si}$  atoms (4.7%), which has a nuclear spin  $I=1/2$ . These satellite lines are therefore attributed to the hyperfine structure (HFS) due to the interaction between the electron spin and the nuclear spin of four equivalent  $^{29}\text{Si}$  atoms in the nearest neighbor shell. From this HFS it can be concluded that the spectrum is related to a defect occupying a carbon site in the lattice. Details of this hyperfine structure will be discussed later.

The angular dependencies of the spectrum in 4H and 6H SiC are shown in Figs. 2(a) and 2(b), respectively. The positions of the EPR lines are plotted versus the angle between the  $c$  axis and the direction of the magnetic field  $B$  rotating in the  $(11\bar{2}0)$  plane. The plot in Fig. 2(a) shows a typical variation pattern of a low-symmetry EPR center having  $S=1$  in a hexagonal lattice. In the case of the 6H SiC, however, two of the four loops split due to sample misalignment and all twelve transitions of a spin  $S=1$  center corresponding to six possible EPR orientations can be separately observed [Fig. 2(b)]. Such a misalignment is typical in cases of using off-axis substrates and has been described elsewhere [3]. These angular dependencies can be described by the following spin Hamiltonian

$$H = \mu_B B \cdot g \cdot S + S \cdot D \cdot S \quad (1)$$

with the effective electron spin  $S=1$  and  $g$  tensor is constrained to monoclinic symmetry ( $C_{1h}$ ). Here  $\mu_B$  is the Bohr magneton and the  $D$  tensor represents the spin-spin interaction. The  $g$  and  $D$  tensors are diagonalized in the principal coordinate system with  $x$  and  $z$ -axes lie in the  $(11\bar{2}0)$  plane and the  $y$ -axis perpendicular to this plane [3]. The best fits gave the same principal  $g$  values:  $g_x=2.0051$ ,  $g_y=2.0038$  and  $g_z=2.0029$  for both spectra in 4H and 6H SiC. The error in the determination of the  $g$

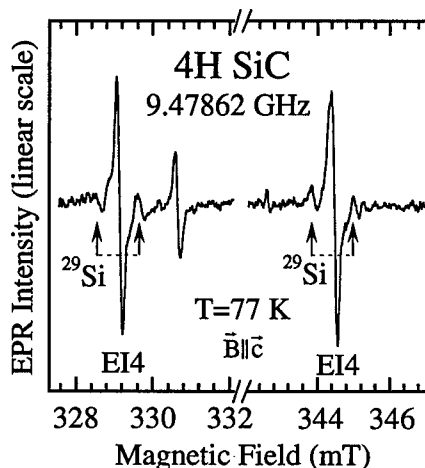


Fig.1. EPR spectrum observed in p-type 4H SiC irradiated by 2.5 MeV electrons at  $400^\circ\text{C}$ , with a dose of  $10^{18} \text{ cm}^{-2}$  for  $B$  along the direction of the  $c$  axis. Two strong lines, each accompanied by two weak  $^{29}\text{Si}$  hyperfine lines (indicated by arrows), belong to the pair of two carbon vacancies. The weak line at around 330.6 mT belongs to another EPR center. For clarity, strong EPR signals from the Si vacancy related defects in the range 332–342 mT are not shown in the figure.

values is  $\pm 0.0002$ . The angle between the principal z-axis and the c-axis is  $\alpha = 54^\circ$ . The parameters D and E describing the trigonal and orthorhombic crystal fields, respectively, were determined as:  $D = (3/2)D_z = 3.28 \times 10^{-2} \text{ cm}^{-1}$  for 6H SiC and  $D = 3.44 \times 10^{-2} \text{ cm}^{-1}$  for 4H polytype;  $E = (1/2)(D_x - D_y) = 0.67 \times 10^{-2} \text{ cm}^{-1}$  for both polytypes. The principal z-axis of the D-tensor lies in the  $(11\bar{2}0)$  or equivalent planes and inclines an angle of  $54^\circ$  with the c-axis. The simulated angular dependencies using the obtained parameters and the spin-Hamiltonian Eq (1) were also plotted as dashed curves in Figs. 2(a) and 2(b). The splitting in the case 6H SiC [Fig. 2(b)] can be accounted for by including a misalignment angle of  $5.1^\circ$  in the fit.

The obtained parameters of the EI4 center are very similar to those of the P4 center observed in heat-treated 6H SiC [1]. It is difficult to compare since in their work the angular dependence was not presented and the P4 spectrum appeared quite different from ours in the line shape. The angular dependence presented in their earlier work [4] is very similar to what we observed, but the g value was determined as isotropic  $g = 2.004$ . It is possible that our spectrum and the P4 spectrum in 6H SiC are the same. The HFS of the P4 center was concluded to be due to the interaction with four equivalent Si atoms and the hyperfine constant is isotropic,  $A = 6 \times 10^{-4} \text{ cm}^{-1}$  (or 6.4 G) [1]. We could not determine the  $^{29}\text{Si}$  hyperfine tensor for the EI4 center due to a weak intensity and severe overlapping, but from the complicated angular dependence partly observed the symmetry of the A-tensor must be lower than trigonal. For  $\vec{B} \parallel \vec{c}$  we observed a hyperfine splitting of 11.3 G, which is different from that given in Ref 1.

As shown from the observed HFS, the defect is related to the carbon vacancy. Since the irradiation was performed at temperatures much higher than the anneal-out temperature for the carbon vacancy [2], this defect must be a complex or paired center involving a carbon vacancy. From the direction of the symmetry axis of the D tensor, it can be concluded that both components of the pair lie in the  $(11\bar{2}0)$  or equivalent planes and the axis connecting them inclines an angle of  $54^\circ$  with the c-axis. Assuming that the main contribution to the fine structure parameter D comes from the spin-spin interaction, and using the point dipole approximation [5], a distance of about 4.3 Å between the two spins was estimated. In this case,  $E \neq 0$  and hence the interaction is not pure dipole-dipole interaction and the point-dipole model is, in principle, not valid. The real distance between the two spins could be smaller but may be not so much different from the estimated value (4.3 Å). In 4H and 6H SiC, the distance between two carbon sites in the  $(11\bar{2}0)$  plane as indicated

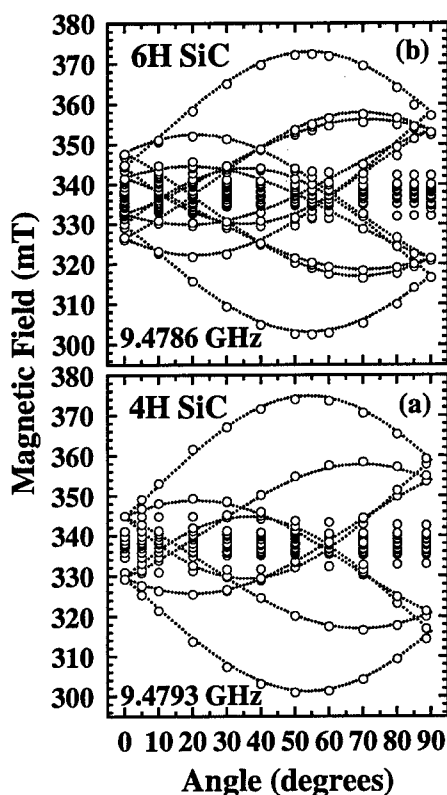


Fig.2. Angular dependence of the spectrum in (a) 4H and (b) 6H SiC with  $\vec{B}$  rotating in the  $(11\bar{2}0)$  plane. Open circles represent data points and dashed curves are simulated ones using the obtained parameters and Eq (1). In (b), the splitting is caused by a misalignment angle of  $5.1^\circ$ . Some of the data points in the region 330-345 mT belong to other EPR centers. The zero angle corresponds to  $\vec{B} \parallel \vec{c}$  while  $90^\circ$  corresponds to  $\vec{B} \perp \vec{c}$  and  $\vec{B} \parallel [\bar{1}100]$ .

in Fig.3 is  $4.36 \text{ \AA}$ , and the axis connecting these two sites also makes an angle of  $54^\circ$  with the c-axis. This configuration of the carbon vacancy pair appears to be the only model that could explain the observed HFS and D tensor. These two vacancies should have the same charge state and hence relax in the same way to keep the direction ( $54^\circ$  off the c-axis) unchanged compared to the perfect lattice. Models with both the vacancies either negatively ( $V_c^- - V_c^-$ ) or positively ( $V_c^+ - V_c^+$ ) charged can form a spin triplet ( $S=1$ ) state. However, these models can be distinguished from their hyperfine interaction with Si atoms in the nearest neighbor shell. In the case of the  $V_c^+$  in 3C SiC [2], hyperfine interaction with four nearest Si neighbors has been detected. For the V in Si [6] or the  $V_c^-$  in SiC [7], the hyperfine interaction is only with two nearest neighboring Si atoms. In the case of interaction with four Si neighbors then for the direction of  $B$  parallel to the c-axis, all the four Si atoms cannot be equivalent and this will result in more than two hyperfine lines. In our case we observed only two lines. This HFS can only be explained by the interaction with two Si atoms. The electron spin located at each carbon vacancy interacts with nuclear spins of two equivalent Si neighbors. The contribution from both vacancies then gives rise to two hyperfine lines with the same total intensity as expected for the case of interaction with four Si atoms. The EI4 center in 4H and 6H SiC is therefore concluded to be a pair of two negatively charged carbon vacancies lying in the  $(11\bar{2}0)$  or equivalent planes.

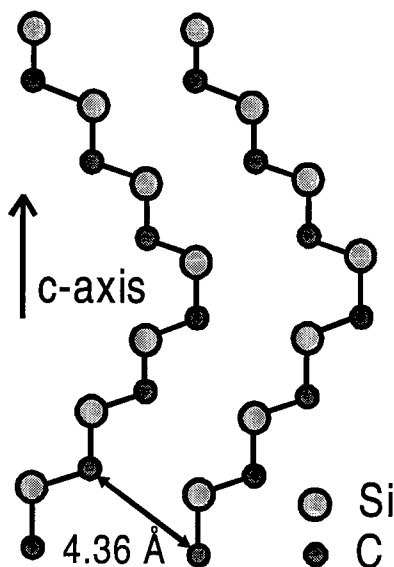


Fig.3. The  $(11\bar{2}0)$  plane in the 6H SiC lattice. The arrow indicates the configuration of the carbon vacancy pair. The distance between the two carbon sites is  $4.36 \text{ \AA}$  and the angle between this direction and the c-axis is  $54^\circ$ . The configuration of the carbon vacancy pair in the 4H polytype is similar.

**Acknowledgements:** Support for this work was provided by the Swedish Research Council for Engineering Sciences (TFR), the Swedish Natural Science Research Council (NFR), the SSF program SiCEP and ABB Corporate Research.

#### References

- [1] V.S. Vainer and V.A. Ilin, Sov. Phys. Solid State **23**, (1981) 2126.
- [2] H. Itoh, A. Kawasuso, T. Ohshima, M. Yoshikawa, I. Nashiyama, S. Tanigawa, S. Misawa, H. Okumura and S. Yoshida, Phys. Stat. Sol. (a) **162**, (1997) 173, and reference therein.
- [3] N.T. Son, W.M. Chen, J.L. Lindström, B. Monemar, and E. Janzén, Physica Scripta **T79**, (1999) 46.
- [4] V.S. Vainer, V.I. Veinger, V.A. Ilin, and V.F. Tsvetkov, Sov. Phys. Solid State **22**, (1980) 2011.
- [5] A. Abragam and B. Bleaney, *Electron Paramagnetic Resonance of Transition Ions* (Clarendon Press-Oxford, 1970), p.502.
- [6] G.D. Watkins, *Radiation Damage in Semiconductors* (Paris-Royaumont, 1964), p.97.
- [7] N. T. Son, W. M. Chen, J. L. Lindström, B. Monemar, and E. Janzén, Mater. Sci. Eng. B **61-62**, (1999) 202.

Author for correspondence: N.T. Son, tel: 46-13-282531, fax: 46-13-142337, e-mail: son@ifm.liu.se

## Electron Spin Resonance in Neutron-Irradiated n-type 6H-Silicon Carbide

S. Kanazawa<sup>1</sup>, I. Kimura<sup>1</sup>, M. Okada<sup>2</sup>, T. Nozaki<sup>1</sup>, I. Kanno<sup>1</sup>, S. Ishihara<sup>2</sup>  
and M. Watanabe<sup>3</sup>

<sup>1</sup>Department of Nuclear Engineering, Kyoto University,  
Yoshidahonmachi, Sakyo, Kyoto, 606-8501, Japan

<sup>3</sup>Research Reactor Institute, Kyoto University, Noda, Kumatori, Osaka, 590-0494, Japan

<sup>4</sup>Ion Engineering Research Institute Corporation, Hirakata, Osaka, 573-0128, Japan

**Keywords:** Annealing, Electron Spin Resonance, Neutron Irradiation, Radiation Defect, Silicon Vacancy

**Abstract.** In order to investigate the defects in n-type 6H-SiC single crystals caused by neutron irradiation, electron spin resonance (ESR) measurement was carried out for neutron irradiated samples during annealing up to 1,400°C. Six centers arising from radiation induced defects were observed in ESR spectra at liquid nitrogen temperature. The angular dependences and isochronal annealing behaviors of these centers are also described. On the basis of the results, we discuss the structural models for these defects.

### Introduction

Single crystalline silicon carbide (SiC) is expected to be an excellent material for making high power electronic devices used under severe environment such as intense ionizing radiation field with high temperature atmosphere. For the fabrication of high-power semiconductor devices, SiC wafers must have excellent homogeneity in resistivity. The neutron transmutation doping (NTD) technique[1] can be applicable for producing n-type SiC wafers as well as n-type Si wafers. During the NTD process, however, fast neutrons induce radiation damage in SiC crystal and cause serious problems such as carrier trapping. The radiation damage problems should be studied intensively, however, not many works on this subject have been carried out so far.

In previous works, electron spin resonance (ESR) was applied for the investigation of point defects in 3C- and 6H-SiC irradiated by electrons, neutrons and protons[2-5]. However the structures and annealing kinetics of the defects in neutron irradiated SiC are still unclear.

Previously, we reported the optical absorption centers in neutron irradiated SiC and the annealing behaviors of these absorption spectra[6]. In this study, ESR measurements have been performed for nitrogen doped n-type 6H-SiC irradiated by reactor neutrons and annealing behaviors of several centers in the ESR spectra have been investigated up to 1,400°C.

### Experimental Arrangement

The nitrogen doped n-type 6H-SiC samples (manufactured by Nippon Steel Corporation) were approximately 7mm×6mm×0.4mm in dimension and had the carrier density in the order of  $10^{17}/\text{cm}^3$ . The neutron irradiation was carried out at 350K using the low temperature irradiation-loop facility of the Kyoto University Reactor(KUR) at the Research Reactor Institute, Kyoto University (KURRI). The fast neutron fluence was monitored by the activation method using a Ni foil, and was nearly  $6 \times 10^{16} \text{ n/cm}^2 (>0.1 \text{ MeV})$ . Isochronal annealing was performed for 5 minutes in helium atmosphere in the temperature range between 100 and 1,400°C. The ESR measurements were carried out at room temperature(RT) and at liquid nitrogen temperature(LNT) with a type JES-TE200 spectrometer of JEOL which used X-band (9GHz) microwave incident on a TE<sub>110</sub> cylindrical cavity. By rotating the c axis of



the crystal round the the a axis, which was kept perpendicular to the magnetic field, the angular dependence of the absorption lines was measured.

### Results and Discussion

It is found that the three-line nitrogen donor spectrum observed at LNT before irradiation had disappeared after neutron irradiation. Figure 1 shows typical ESR spectra for the neutron-irradiated n-type 6H-SiC obtained at (a)RT and (b)LNT. In the ESR signals, distinct lines or centers named K1, K2, K3, K4, K5 and K6 are observed at LNT. The K1,K2,K5 and K6 are also observed at RT, but K3 and K4 are not observed. The K5 and K6 signals are concealed in the K1 before annealing, but they become clear after annealing above 600°C. The ESR absorption spectra after isochronal annealing are shown in Fig.2. It is seen that the K5 and K6 centers become clear after the K1 center disappears by annealing.

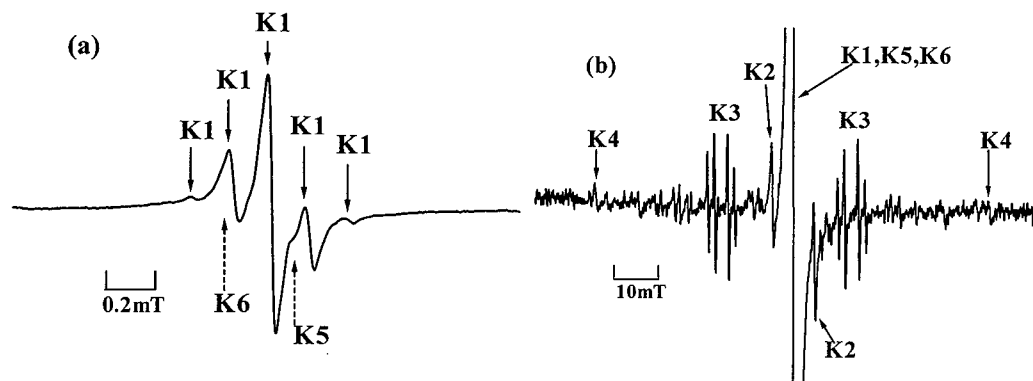


Fig. 1 ESR spectra observed at (a) RT and (b) LNT for the neutron-irradiated n-type 6H-SiC.

The number and the intensity ratio of the ESR lines and the g-value(2.0032) of the K1 signals are similar to those of single-negative silicon vacancies which were found in electron-irradiated 3C-SiC(T1 center)[3,4] and 6H-SiC(NA center)[5]. Figure 3 shows the angular dependence of the K2 center when the magnetic field was rotated in a plane approximately perpendicular to the c axis. The angular dependences of the K2,K3 and K4 centers with an effective spin  $S=1$  are described by the two electron spins interacting each other. The g-value and D tensors are found  $g=2.0032$  and  $|D|=4.26 \times 10^{-3} \text{ cm}^{-1}$

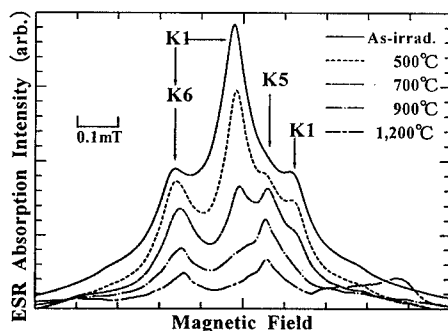


Fig. 2 ESR absorption spectra after isochronal annealing.

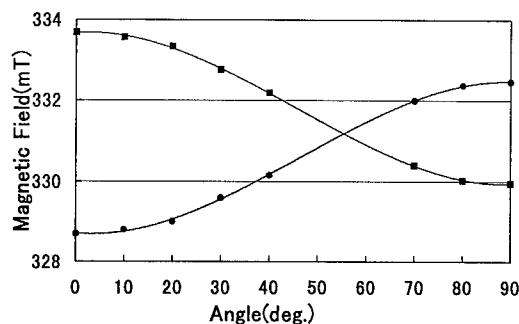


Fig. 3 Angular dependence of the K2 center.

for the K2 center,  $g=2.013$  and  $|D|=5.58 \times 10^{-2} \text{cm}^{-1}$  for the K3 center, and  $g_{\parallel}=2.0036$ ,  $g_{\perp}=2.0071$  and  $|D|=4.02 \times 10^{-2} \text{cm}^{-1}$  for the K4 center. The average distances of two electron spins for these centers are estimated to be  $8.49 \text{ \AA}$  (K2),  $3.60 \text{ \AA}$  (K3) and  $4.01 \text{ \AA}$  (K4), respectively. These results suggest that these centers originate in complexes. Since the average distance ( $8.49 \text{ \AA}$ ) of two electron spins for the K2 center is approximately half as long as the lattice constant ( $a=15.12 \text{ \AA}$ ), divacancies (V<sub>Si</sub>-V<sub>Si</sub>) are considered as a possible structure of the K2 center. The K3 and K4 centers are similar to the NC and NB centers observed in electron-irradiated 6H-SiC, respectively [5].

Figure 4 shows the angular dependence of the K5 center when the magnetic field was rotated in a plane approximately perpendicular to the *c* axis. The K5 and K6 centers with an effective spin  $S=1/2$  exhibit to have  $g_{\parallel}=2.0028$ ,  $g_{\perp}=2.0045$  and a nearly isotropic  $g$ -value of  $2.0041$ , respectively.

Isochronal annealing behaviors of the K1, K2, K3, K4, K5 and K6 centers are shown in Fig. 5. The K3 center anneals out at  $200^{\circ}\text{C}$ , while the K1 and K2 centers at around  $800^{\circ}\text{C}$ . The K5 and K6 centers grow up after the K1 center is annealed, and they disappear at around  $1,300^{\circ}\text{C}$ . After annealing of the crystal at  $1,400^{\circ}\text{C}$ , the three-nitrogen donors ESR spectrum recovered drastically.

These results suggest that these grown defects after annealing at  $800^{\circ}\text{C}$  are related to silicon vacancies and impurities. Probably, the residual defects above  $800^{\circ}\text{C}$  are arising from the complexes between silicon vacancies and impurities and they breakup at around  $1,300^{\circ}\text{C}$  [5].

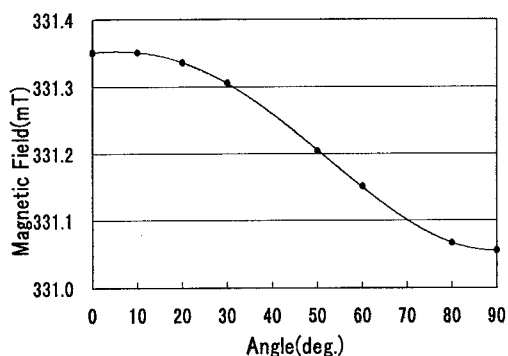


Fig. 4 Angular dependence of the K5 center.

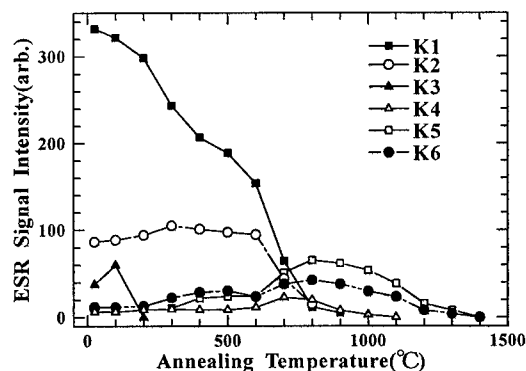


Fig. 5 Isochronal annealing behavior of the ESR centers.

The characteristics of the ESR centers found in neutron irradiated SiC are summarized in the Table 1. In this table it is also shown the results of the neutron irradiated 4H-SiC obtained by our ESR measurements.

### Summary

In order to investigate the defects in nitrogen doped n-type 6H-SiC induced by reactor neutron irradiation, ESR measurements were carried out for neutron irradiated samples during annealing up to  $1,400^{\circ}\text{C}$ . In the ESR signals, the K1, K2, K3, K4, K5 and K6 centers are observed after neutron irradiation. The main K1 center originates from silicon vacancy. The angular dependences of the K2, K3 and K4 centers with an effective spin  $S=1$  can be described by the two electron spins interacting each other. These results suggest that the K2, K3 and K4 centers originate in complexes related to silicon vacancy. These centers show different isochronal annealing behaviors; the K3 center is annealed out at  $200^{\circ}\text{C}$ , while the K1 and K2 centers at around  $800^{\circ}\text{C}$ . The K5 and K6 centers with an effective spin  $S=1/2$  grow up after the

K1 center is annealed, and they disappear at around 1,300°C.

Table 1. The characteristics of the ESR centers in the neutron irradiated SiC.

Center	Spin:S	g-value	Polytype	D (10 <sup>2</sup> cm <sup>-1</sup> )	r <sub>spin</sub> (Å)	Ta (°C)	Model	Electron- irradiated SiC[3-5]
K1	3/2	2.0032	4H,6H			~800	V <sub>Si</sub>	TI(3C),NA
K2	1	2.0032	4H 6H	0.232 0.426	10.04 8.49	~800	V <sub>Si</sub> -V <sub>Si</sub> ?	
K3	1	2.013	4H, 6H	4.39 5.58	3.90 3.60	~200	V <sub>Si</sub> -I?	NC(6H) Divacancy
K4	1	2.0050 ⊥ 2.0083	4H	3.60	4.16	~900	V <sub>Si</sub> -V <sub>C</sub> ?	NB(6H) V-I pairs
		2.0036 ⊥ 2.0071	6H	4.02	4.01			
K5	1/2	2.0028 ⊥ 2.0045	4H,6H			~1,300	V <sub>Si</sub> -N?	
K6	1/2	2.0041	4H,6H			~1,300	?	

r<sub>spin</sub>: average distance of two spins. Ta: annealing temperature.

### Acknowledgements

The authors would like to thank Professor T.Yoshiie and Dr.Q.Xu of KURRI for their assistance in operation of the low temperature irradiation facility. The authors would like to thank Professor H.Hase and Dr.T.Warashina of KURRI for their guidance in the ESR measurements. This work was done under the Visiting Researchers Program of the KURRI. The authors would like to express their thanks to the staffs of KURRI and the joint research group for their support in the experiment. The present work was also supported by the Grant-in-Aid for Scientific Research from the Ministry of Education, Science, Sports and Culture and the New Energy and Industrial Technology Development Organization (NEDO), Japan.

### References

- [1] S.Tamura, T.Kimoto, H.Matsunami, M.Okada, S.Kanazawa, I.Kimura, in this proceeding, p. 849
- [2] L.A. de S. Balona and J.H.N.Loubser, J.Phys.C:Solid St.Phys.3(1970),p.2344.
- [3] H.Itoh, N.Hayakawa, I.Nashiyama and E.Sakuma, J.Appl.Phys.66 (1989), p.4529.
- [4] H.Itoh, M.Yoshikawa, I.Nashiyama, S.Misawa, H.Okumura and S.Yoshida, IEEE Trans.Nucl.Sci.37 (1990), p.1732.
- [5] A.Kawasuso, H.Itoh, D.Cha and S.Okuda, Mater. Forum 264-268(1998), p.611.
- [6] M.Okada, I.Kimura, T.Nakata, M.Watanabe, S.Kanazawa, I.Kanno, K.Kamitani, K.Atohe and Nakagawa, Inst.Phys.Conf.Ser.No.142(1996),p.469.

### For Correspondence with readers:

S.Kanazawa(E-mail:kanazawa@nucleng.kyoto-u.ac.jp, Fax +81-75-753-5845)

## Author Index

- A**
- Abe, Koji..... 857
- Åberg, D..... 1327
- Aboughé-Nzé, P..... 599, 1467
- Aboujja, S. .... 691
- Acero, M.C..... 309
- Achtziger, N..... 639, 749, 929, 933
- Adachi, K. .... 1419
- Adås, C..... 1255
- Adivarahan, V. .... 1603
- Afanas'ev, V.V..... 831, 1065
- Agarwal, A.K. .... 737, 1113, 1307, 1387
- Ahn, Sang Hyun..... 1553
- Ahnoff, M. .... 1117
- Aigo, T. .... 379, 493
- Akahane, T..... 1511
- Akasaki, I. .... 1571
- Alexandrov, P. .... 1375, 1399
- Alfred, Cheng Hon Huan ..... 325
- Allen, S.T..... 1643
- Alok, Dev..... 1077
- Alsina, F..... 663
- Amano, H..... 1571
- Amekura, H..... 977
- Amy, F. .... 395
- Androjna, D..... 1439
- Anikin, M..... 13, 25, 47, 91
- Anthony, C.J..... 655
- Anwand, W. .... 877
- Aradi, B..... 817
- Arai, Kazuo ..... 75, 83, 99, 103, 169, 233, 457, 461, 865, 1037, 1073, 1283
- Arita, M..... 297
- Arnodo, C..... 1247
- Arnold, Emil ..... 1077
- Arwin, H. .... 537, 575, 1085
- As, D.J..... 1591, 1595
- Asai, R..... 1195
- Asami, S..... 269
- Asano, Katsunori..... 1105, 1183, 1371
- Aspnes, D.E. .... 1033
- Åstrand, B. .... 1423
- Attenberger, W..... 285
- Averous, M. .... 289, 1527
- Avrov, D.D..... 1515
- B**
- Baba, M..... 587
- Babanin, A.I..... 1017
- Badila, M. .... 1219, 1355
- Bahng, Wook ..... 83, 99, 103, 233, 461
- Bai, Song ..... 551, 567, 753
- Bailey, S.G..... 489
- Balkas, Cengiz M..... 79
- Balogh, A.G. .... 965, 969
- Banc, C. .... 695
- Banerjee, S..... 1279
- Bano, E. .... 695
- Banu, V. .... 1219, 1355
- Baranov, P.G..... 799, 805
- Bardwell, J.A. .... 1647
- Barrett, D.L..... 9, 111
- Bartsch, Wolfgang ..... 1167, 1243
- Baski, A. .... 1453
- Basset, G. .... 13, 47
- Bassler, M. .... 831, 1065, 1109
- Bauman, D. .... 229
- Baumvol, I. .... 1133
- Beaumont, B. .... 1487
- Bechstedt, F. .... 427, 643
- Beck, D. .... 181
- Bellitto, V.J..... 1533, 1537, 1541
- Bellotti, E..... 765
- Bentoumi, G..... 1467
- Benz, K.W. .... 1549
- Berberich, S. .... 1303
- Bergman, J.P..... 131, 575, 675, 687, 1327, 1571
- Bernard, C..... 13, 25, 91
- Bernhardt, J..... 341, 345, 383
- Bertke, R. .... 841
- Bertram, F. .... 1483, 1575
- Bevilacqua, P. .... 1363
- Bezerra, E.F. .... 773
- Bhatnagar, M. .... 1287
- Bickermann, Matthias..... 39, 71, 445
- Billon, T..... 715, 885, 1041, 1215, 1267
- Birch, J..... 1519
- Blanquet, Elisabeth..... 25, 91, 1041, 1507
- Bluet, J.M. .... 885, 1507
- Bockstedte, Michel ..... 949
- Bogdanova, E.V..... 221, 973

- 
- |                       |                            |                             |  |
|-----------------------|----------------------------|-----------------------------|--|
| Bonds, J.....         | 1149                       | Chaix, O.....               | 13                                       |
| Bousquet, V.....      | 1487                       | Chandler, Jr., T.C.....     | 845                                      |
| Boutros, K.S.....     | 1627                       | Chante, J.P. ....           | 921, 1219, 1355, 1363                    |
| Bowen, W.R.....       | 403                        | Charles, J.-P.....          | 691                                      |
| Bozack, M.J. ....     | 335, 423, 997              | Chartier, E.....            | 1247                                     |
| Brady, M. ....        | 3, 21                      | Chassagne, T.....           | 599, 1467                                |
| Brandes, G.R.....     | 185, 437                   | Chatillon, Christian.....   | 91                                       |
| Bratus', V. Ya.....   | 497                        | Chatty, K.....              | 1211, 1279, 1331                         |
| Brauer, G.....        | 877                        | Chaudhuri, J.....           | 1045, 1599                               |
| Breitholtz, B.....    | 683, 777, 1179, 1323, 1327 | Chaussende, D. ....         | 1467                                     |
| Brémond, G.....       | 635                        | Chen, C.Q. ....             | 611                                      |
| Brenn, R.....         | 1549                       | Chen, J. ....               | 273                                      |
| Brennan, K.F.....     | 765                        | Chen, Liang-Yu .....        | 1439                                     |
| Brezeanu, G.....      | 1219, 1355                 | Chen, W.M.....              | 559, 563, 821                            |
| Brixius, W.....       | 3                          | Chen, Y.....                | 197, 257, 711                            |
| Broser, I.....        | 1575                       | Chen, Z.Y.....              | 189                                      |
| Brown, April S.....   | 1499                       | Cherednichenko, D.I.....    | 35, 59                                   |
| Brown, Dale .....     | 1291                       | Cherenkov, A.....           | 225                                      |
| Brown, J.....         | 841                        | Chévrier, V. ....           | 119                                      |
| Bryant, K.W.....      | 335, 423, 997              | Chi, G.C.....               | 1631                                     |
| Brylinski, C.....     | 395, 411, 1247, 1651       | Cho, S.-H. ....             | 1545                                     |
| Buckanan, D.....      | 841                        | Chourou, K. ....            | 635                                      |
| Buczko, R.....        | 1133                       | Chow, T.P.....              | 1155, 1211, 1279, 1331, 1367, 1391, 1415 |
| Buhay, H.....         | 1053                       | Chowdhury, Ershad Ali ..... | 813                                      |
| Bulman, G.....        | 1477                       | Choyke, W.J.....            | 551, 567, 639, 679, 733, 753, 795, 817   |
| Burger, A.....        | 415                        | Chriss, M.F.....            | 1627                                     |
| Burk, Jr., A.A.....   | 173                        | Christen, J.....            | 1483, 1575, 1591                         |
| Burton, J.C.....      | 615                        | Christiansen, K. ....       | 193                                      |
| Bustarret, E. ....    | 1467                       | Christiansen, S.....        | 193                                      |
| <b>C</b>              |                            | Chu, S.N.G.....             | 1631                                     |
| Cabon, B.....         | 1267                       | Chua, Soo Jin.....          | 325, 659, 1619                           |
| Caetano, E.W.S.....   | 773                        | Chung, G.....               | 1097, 1133                               |
| Camassel, J.....      | 301, 599, 885, 1041        | Chung, Juyong .....         | 249, 525                                 |
| Campos, F.J.....      | 663, 893                   | Chung, Ki Woong.....        | 1639                                     |
| Cantin, J.L.....      | 715                        | Chuo, C.-C.....             | 1631                                     |
| Canut, B. ....        | 921                        | Chuvilin, A. ....           | 533                                      |
| Cao, L.....           | 1399                       | Chyi, J.-I. ....            | 1631                                     |
| Cao, Li Hui.....      | 1375                       | Cimalla, V.....             | 285, 321                                 |
| Cao, X.A.....         | 1631                       | Ciplys, D.....              | 1583                                     |
| Capano, M.A.....      | 703, 901                   | Clemens, S.....             | 1029                                     |
| Carlin, C.....        | 313                        | Clerjaud, B.....            | 635                                      |
| Carlone, C. ....      | 691                        | Coatney, S.E.....           | 1599                                     |
| Carlson, Eric P.....  | 1491                       | Cobet, C.....               | 1033                                     |
| Carlsson, F.H.C.....  | 687                        | Collins, W.E.....           | 415                                      |
| Carter, G.E.....      | 245, 1149                  | Constantinidis, G. ....     | 1017                                     |
| Carter, Jr., C.H..... | 3, 21                      | Contreras, S.....           | 599, 885                                 |
| Casady, J.B.....      | 901, 1053, 1149, 1203      | Cooper, Jr., James A.....   | 703, 761, 901, 1069                      |
| Cauwet, F.....        | 1467                       | Couchaud, M.....            | 47                                       |
| Chafai, M.....        | 707                        |                             |  |

Crean, G.M.	571
Crenshaw, T.R.	415
Cressler, J.D.	1053, 1339
Crofton, John	997, 1013

**D**

da Costa, J.A.P.	773
Dahlquist, F.	1179
Dang, G.T.	1631
Danielsson, E.	1049
da Silva Jr., E.F.	773
Das, Mrinal K.	1069
Daudin, B.	1467
Davis, R.F.	353, 1049, 1315, 1471, 1491, 1615
Davydov, D.V.	221, 973, 1447
De Graef, M.	477
Deák, P.	365, 795, 817
Dedulle, Jean-Marc	25
Defives, D.	411
Demenet, J.L.	517
Deneuville, A.	1467
Derenge, M.	245, 1395
de Sousa, J.S.	1567
Desouza, M.M.	1359, 1411
Devaty, R.P.	551, 567, 639, 679, 733, 753, 795
Diagne, N. Fama	157
Di Cioccio, L.	715, 1041
Dieringer, H.	1477
di Forte-Poisson, M.A.	1651
Dimitrijević, S.	399
Di Persio, J.	1175
Di Ventra, S.	1133
Dmitriev, V.A.	225, 229, 237, 453, 505, 1203
Dohnke, Karl Otto	1243
Dolle, J.	87
Domeij, M.	1327
Doolittle, W. Alan	1499
Dorozhkin, S.I.	1515
Doverspike, K.	1477, 1643
Doyle, R.	1463
Dries, Chris	1383
Dua, C.	1247
Dudley, Michael	431, 453, 465, 469, 473, 489
Duffar, Th.	119
Dunne, G.T.	161
Dunstan, P.R.	403, 1025, 1081

Durand, O.	411
Duranova, E.	1171
Durst, F.	31
Duscher, G.	1133
Dyakonova, N.V.	1319

**E**

Ebling, D.G.	1549
Ecke, G.	289
Edgar, J.H.	1045, 1599
Edmond, J.	1477
Edwards, N.V.	1033
Egilsson, T.	647, 651
Egloff, Richard	1077
Eickhoff, M.	301, 529
Eiserbeck, W.	87
Ekedahl, Lars-G.	937, 1435
Elasser, A.	1367
Ellis, E.C.	1053, 1339
Ellison, A.	131, 137, 1171, 1175
Emerson, D.	1477
Enck, R.	1503
Endo, T.	265
Engelbrecht, F.	611
Epelbaum, B.M.	107
Eriksson, Joakim	1207, 1255, 1259
Erlandsson, R.	981
Ervin, M.	245
Eryu, O.	873, 1005
Eshun, Ebenezer	157
Esser, N.	1033
Esteve, J.	309
Everson, W.J.	9, 837
Evwaraye, A.O.	21

**F**

Faik, A.	313
Falk, Fritz	1523
Falkovski, L.	301
Fantini, M.C.A.	329
Farias, G.A.	1567
Faure, C.	13, 25, 47
Fechko, G.	3
Fedison, J.B.	1367, 1391
Feenstra, R.M.	353
Fejes, P.	1463
Feng, Zhe Chuan	325, 501, 659
Feldman, L.C.	1133
Fenstermaker, S.T.	407
Ferdos, Fariba	1207

Ferguson, I.T.	157, 1623
Ferrand, B.	47
Ferraria, Ana Maria	91
Ferro, G.	481
Feuillet, G.	1467
Filho, J. Ribeiro	1567
Fischer, P.	1575
Fissel, A.	205, 209
Flament, O.	1215
Flank, A.M.	329
Flynn, J.S.	1627
Forsberg, U.	575, 619, 1171
Fraisse, B.	599
Frank, Thomas	753, 831, 857
Frauenheim, Th.	365
Freire, V.N.	773, 1567, 1579
Freitas, Jr., J.A.	161
Frey, T.	1595
Fricke, J.	43
Friedrichs, Peter	1089, 1243, 1295
Frischholz, M.	1423
Fukuda, Kenji	861, 865, 1073, 1283
Füllmann, M.	1407
Fursin, Leonid	1375, 1399
Furthmüller, J.	427, 643
Furusho, T.	217
Fuyuki, T.	201, 361

**G**

Galeckas, Augustinas	555, 683, 777
Gali, A.	795, 817
Ganser, D.	1029
Gao, Y.	945
Gaska, R.	1583
Gaspar, C.	1651
Gebel, T.	741
Gehoski, T.	1029
Gehrke, T.	1471, 1491, 1615
Geil, B.R.	245, 1137, 1395
George, J.T.	1045
Ghezzi, Mario	1291, 1367, 1391
Gibart, P.	1487
Glass, R.	3
Godignon, P.	663, 889, 1219, 1303, 1355
Gold, J.S.	293
Goldstein, Jonathan	21
Goto, Motoki	627
Grange, Y.	13
Grau, M.	39
Gray, M.	1439

Greulich-Weber, S.	809
Griebel, Erich	1167
Griffin, James	157
Griffin, T.E.	1395
Grillenberger, J.	749
Grivickas, Paulius	555, 671
Grivickas, Vytautas	555, 671
Grosse, P.	13, 25, 47
Grossner, Ulrike	427
Gruzinskis, V.	1379, 1635
Gu, Chun-Yuan	149, 153
Guest, J.J.	1251
Guillot, G.	635, 715
Guiot, E.	1527
Guo, S.	1141
Gurary, Alex	157
Gustafsson, U.	1255
Gutmann, R.J.	1211, 1279, 1331

**H**

Ha, S.	67, 477
Haberern, K.	1477
Hai, P.N.	563, 821
Hajnal, Z.	365
Hall, W.B.	1403
Hallen, A.	505, 777, 869, 889, 893, 1323
Hallin, C.	149, 153, 563, 981, 1175
Han, J.	1631
Handy, E.M.	925
Hansson, G.V.	981
Hara, S.	1459
Hara, Tohru	813
Harada, S.	297
Harima, Hiroshi	115, 217, 485, 591, 603, 607, 711
Harris, C.I.	1255, 1431
Harrison, H.B.	399
Hartman, J.D.	353
Hartung, Wolfgang	445
Hasan, M.-A.	313
Hasegawa, M.	909, 917
Hatayama, Tomoaki	201, 361
Hayami, Yasuaki	757
Hayes, D.G.	1251
Hecht, Christian	1243
Heera, V.	881, 897
Hegde, V.S.	737, 1307
Heinz, K.	341, 345, 383
Heissenstein, Hans	853
Helbig, Reinhard	193, 611, 623, 853

Held, R. ....	1407
Hemmingsson, C. ....	131, 675, 687
Henkel, T. ....	481, 953
Henry, A. ....	131, 165, 237, 619, 647, 651, 1171, 1175
Henry, R.L. ....	1533, 1537, 1541
Henshall, D. ....	3
Hensley, D.K. ....	667, 1443
Heydemann, V.D. ....	9, 55, 63, 67, 837
Hilfiker, J.N. ....	537
Hilton, K.P. ....	1199, 1251
Hinrichsen, P.F. ....	691
Hirai, M. ....	419
Hiramatsu, K. ....	1483, 1575
Hirao, T. ....	1105
Hishida, Y. ....	873, 1347
Hishita, S. ....	953
Hjelm, M. ....	765
Hobert, H. ....	205
Hobgood, D. ....	3
Hoffman, Jr., Richard W. ....	1439
Hoffmann, A. ....	1483, 1575
Höfgen, A. ....	897
Hofmann, Dieter ..... 31, 39, 43, 71, 107, 229, 445	
Hofmann, D.M. ....	559
Holland, O.W. ....	925
Hollering, M. ....	387, 391
Holloway, P.H. ....	407
Holst, J. ....	1575
Holtz, P.O. ....	1571
Hong, Moon-Hi ..... 249, 513, 517, 525	
Horn, R. ....	43
Hoshino, S. ....	1511
Hosoda, Toru ..... 603, 607	
Houdayer, A. ....	691
Hsieh, A.J. ....	901
Hunag, M.B. ....	1133
Huang, W. ....	465, 469
Huang, Xianrong ..... 431	
Hugonnard-Bruyère, E. ....	715
Hülßen, C. ....	929, 933
Hultman, L. ....	537, 869, 1519
Hundhausen, M. ....	579, 583, 587, 595
Hunn, J. ....	1615
Hunter, Gary W. ....	1439
Hwu, Y.-K. ....	395

**I**

Iakimov, T. ....	95, 375
Ide, T. ....	1459
Ignatiev, K. ....	1599
Ikoma, Y. ....	265, 297
Ila, D. ....	667, 1443
Imai, Seiji ..... 757, 861, 865	
Imaizumi, M. ....	1057
Irmscher, K. ....	87
Isaacs-Smith, T. ....	901
Isberg, P. ....	1423
Ishida, Y. ....	169, 253, 917, 1545
Ishida, Yuuki ..... 1037, 1129, 1235	
Ishihara, S. ....	825
Isoird, K. ....	1363
Ito, Hirokazu ..... 1557	
Ito, Hitoshi ..... 1227	
Itoh, Hisayoshi ..... 857, 1129, 1239, 1299	
Itoh, Kenji ..... 1495	
Itoh, Kohei M. ....	729
Ivanov, A.M. ....	1447
Ivanov, I.G. ....	647, 651
Ivanov, P.A. ....	1319
Ivantsov, V. ....	229
Iwami, M. ....	419
Iwase, Mitsuo ..... 1557	
Iwata, Hisaomi ..... 729	
Izumi, K. ....	145
Izumi, Tomio ..... 813, 1557	

**J**

Jacob, Chacko ..... 197, 249, 257	
Jacobsson, H. ....	165
Jamison, K.D. ....	181
Jang, T. ....	1001
Janson, M.S. ....	889, 933, 937
Janzén, E. .... 95, 131, 137, 165, 237, 375, 559, 563, 619, 631, 647, 651, 675, 687, 817, 821, 1171, 1175	
Jargelius, Mikael ..... 777	
Järrendahl, K. .... 575, 1033, 1519	
Jemander, S.T. ....	981
Jenkins, M. ....	313
Jenny, J. ....	3
Ji, Wei ..... 149, 153	
Jiang, W. ....	957
Jikimoto, T. ....	145
Jiménez, J. ....	707
Jin, Li. ....	453
Jinschek, J. ....	521



- Johansson, N. .... 1423  
 Johnson, C.M. .... 1199, 1419  
 Johnson, G.M. .... 1275  
 Johnson, H.K. .... 1251  
 Jones, K.A. .... 245, 277, 925, 1395, 1503  
 Jonsson, Rolf. .... 1263  
 Jordà, X. .... 1303
- K**
- Kachi, Tetsu .... 1495  
 Kadinski, L. .... 31, 39, 71  
 Kaiser, U. .... 205, 521, 533  
 Kakanakov, Roumen .... 1009  
 Kalabukhova, E.N. .... 791, 809  
 Kalinina, E.V. .... 497, 505  
 Kaltschmidt, Rainer .... 1243  
 Kamata, I. .... 145  
 Kamimura, Kiichi .... 1227  
 Kamiya, N. .... 441  
 Kanaya, M. .... 379, 493  
 Kanazawa, S. .... 825, 849  
 Kang, Sangbeom .... 1499  
 Kang, Soo Chang .... 993  
 Kanno, I. .... 825  
 Karlsson, S. .... 309, 505, 937, 1255  
 Karlsteen, M. .... 313  
 Kaschner, A. .... 1483, 1575  
 Kassamakov, Ivan .... 1009  
 Kassamakova, Liliana .... 1009  
 Kato, Tomohisa. .... 75, 449, 457, 461  
 Katsuno, M. .... 379, 493  
 Kayambaki, M. .... 1061  
 Kelly, P.V. .... 571  
 Kempel, M.L. .... 181  
 Keogh, D.M. .... 1627  
 Keskar, N. .... 1343, 1351  
 Kestle, A. .... 403, 1025, 1081  
 Key, P.H. .... 655  
 Khan, I.A. .... 761  
 Khan, M. Asif .... 1583, 1603  
 Khan, Muhammad Nasir .... 99, 103, 233  
 Khemka, V. .... 1211, 1331, 1367  
 Khlebnikov, I.I. .... 35, 59, 615, 945  
 Khlebnikov, Y. .... 59, 615  
 Khlebnikov, Y.I. .... 35  
 Kildemo, M. .... 571  
 Kim, Kwang Chul .... 317  
 Kim, Yunsoo .... 177  
 Kimoto, Tsunenobu. .... 189, 201, 361, 627, 849, 1105, 1109, 1315, 1347
- Kimura, I. .... 825, 849  
 Kirste, L. .... 1549  
 Kishimoto, N. .... 977  
 Kitabatake, Makoto. .... 141, 357  
 Kitou, Yasuo .... 83, 99, 103  
 Klettke, O. .... 961  
 Kobayashi, N. .... 481, 861, 865, 909, 913, 917, 953  
 Kobayashi, Setsuko. .... 757, 861  
 Kögler, R. .... 309  
 Koh, A. .... 403, 1025, 1081  
 Koizumi, T. .... 1545  
 Kojima, Kazutoshi .... 857, 1129, 1239, 1299  
 Koleske, D.D. .... 1533, 1537, 1541  
 Kompan, M.E. .... 1587  
 Kong, H.S. .... 1477  
 Kono, K. .... 977  
 Konstantinov, A. .... 505, 1255, 1431  
 Kordes, M.E. .... 181  
 Kordina, Olle .... 1387  
 Koshka, Y. .... 699  
 Kosugi, R. .... 1283  
 Kotousova, I. .... 225  
 Kotvas, J.C. .... 1403  
 Kozlov, V.A. .... 1319  
 Kozlovski, V.V. .... 221, 973  
 Krasnobaev, L.Ya. .... 1615  
 Kräußlich, J. .... 205  
 Kretschmer, James W. .... 1291, 1367, 1391  
 Krishnamurthy, Nicole .... 1291  
 Krötz, G. .... 301, 529  
 Krtischil, A. .... 1591  
 Krüger, Peter. .... 349, 369  
 Kryganovski, A. .... 225  
 Kuhr, T.A. .... 473  
 Kuriyama, K. .... 905  
 Kurobe, K. .... 361  
 Kusaka, M. .... 419  
 Kushibe, Mitsuhiro .... 169, 757, 1037  
 Kuznetsov, A.N. .... 221, 973  
 Kuznetsov, A.Yu. .... 869, 889, 893  
 Kuznetsov, N. .... 229  
 Kuznetsov, N.I. .... 497, 505, 1655
- L**
- Lahrière, H. .... 1487, 1651  
 Lambrecht, Walter R.L. .... 545  
 Lampert, W.V. .... 407  
 Landini, B.E. .... 185  
 Lane, W.A. .... 1191

Langer, D.W.....	733
Lannon, Jr., J.S.....	293
Lari, M.B.....	845
Laridjani, M. Rouhani.....	289, 1527
Larkin, David J.....	667, 1443
Laube, Michael .....	623, 831, 941
Lauer, V. ....	635
Laügt, M.....	1487
Lazar, M.....	921
Leamy, H.J.....	313
Lebedev, A.A.....	221, 225, 509, 973, 1219, 1355, 1447
Lebedev, A.O.....	1515
Leckey, R.C.G.....	387
Lee, C.-M.....	1631
Lee, Kyung-Won.....	177
Lee, S.K. ....	1049
Lee, Sung Yong .....	177
Lee, Won Sang.....	1639
Leisenberger, F. ....	387
Leite, J.R.....	1595
Leis, A.J.....	1121, 1137, 1503
Lemos, V.....	773, 1567, 1579, 1595
Lendenmann, H.....	1179, 1423
Leonard, M.....	1643
Leonard, R.....	3
Lepneva, A.A.....	769
Letertre, F.....	715
Leveugle, C.....	1191
Levinshtein, M.E.....	1319, 1603
Ley, L.....	387, 391, 579, 583, 595
Leycuras, André.....	241
Li, H.-F.....	399
Li, Q.....	181
Li, Xueqing .....	1375
Li, Z.....	1367
Liaw, H.M.....	1463
Lieu, D. ....	313
Lim, S.L.....	1619
Limpijumnong, Sukit .....	545
Lin, Jianyi .....	325
Lin, N.....	981
Lindelfelt, U.....	719, 1335
Lindner, J.K.N.....	285
Lindquist, O.P.A.....	575
Lindström, J.L.....	821
Linnarsson, M.K.....	165, 619, 889, 893, 933, 937
Linnros, Jan.....	555, 671, 683
Linthicum, K.J.....	1049, 1315, 1471, 1491

Lipkin, Lori A.....	1093, 1275
Lischka, K.....	1591, 1595
Lisker, M.....	1591
Liu, C.C. ....	1439
Liu, L. ....	1599
Liu, Sam.....	1021
Lo, Y.-H.....	305
Loboda, M.J.....	273, 1463
Locatelli, M.L.....	921, 1219, 1355, 1363
Lofgren, Peter M.....	149, 153
Long, F.H.....	615, 1623
Look, D.C.....	1603
Los, Andrei V. ....	745
Lu, W.J.....	415
Lu, Wenchang.....	349, 369
Luckowski, E.....	1029
Lukin, S.N.....	791
Lundström, Ingemar .....	937, 1085, 1435
Lungu, P.....	1355
Luo, Yanbin.....	1013, 1379, 1383, 1399
Luzzi, R.....	1579

## M

Ma, T.P. ....	1311
MacElwee, T.W.....	1647
Macfarlane, P.J.....	1125
MacMillan, M.F.....	173
Madangarli, V.....	1223, 1231
Madar, Roland .....	13, 25, 47, 91, 635, 1507
Madathil, Shankar E.....	1359, 1411
Madsen, Lynnette D....	981, 1009, 1033, 1171
Magnusson, B. ....	631
Magnusson, W.....	131
Maier, F.....	387
Malalingham, K.....	841
Malta, D.....	3
Maltsev, Andrei A.....	79
Mani, S.S.....	737, 1113, 1307
Martin, E.....	707
Martinez, A.....	1327, 1335
Martinez, G.....	611
Martinez, R.....	1175
Martinez-Guerrero, E.....	1467
März, M.....	809
Masahara, K.....	169, 1037
Mascher, P.....	965, 969
Masri, P.....	229, 289, 1527
Masuda, Y.....	197, 257, 711
Matsukawa, Toshikazu .....	1557
Matsumoto, K.....	217

- Matsunami, Hiroyuki ..... 125, 189, 201, 361,  
 627, 849, 1105, 1109, 1315, 1347  
 Matsuura, H. .... 711  
 Mauder, Anton ..... 1167  
 Mawby, P.A. .... 403, 1025, 1081  
 Mazzola, Michael S. .... 245, 305, 699, 745,  
 901, 1203  
 McDaniel, G.Y. .... 407  
 McDonald, K. .... 1133  
 McGrath, Don ..... 1291  
 McLean, F.B. .... 1121, 1137, 1503  
 Mehregany, Mehran ..... 541, 595, 1141, 1145  
 Meinschien, Jens ..... 1523  
 Melloch, M.R. .... 703, 1463  
 Melnik, Yu.V. .... 1655  
 Melnychuck, G. .... 245  
 Merrett, J.N. .... 1339  
 Mestres, N. .... 663, 893  
 Meyer, B.K. .... 559  
 Michaud, J.F. .... 885  
 Mihara, I. .... 419  
 Millan, J. .... 663, 1219, 1355  
 Ming, Bin ..... 1503  
 Miró, J. .... 795  
 Mitchel, W.C. .... 21, 703, 707, 841  
 Mittlehner, Heinz ..... 1243, 1295  
 Miyamoto, N. .... 1347  
 Mokhov, E.N. .... 799, 805, 809  
 Mol, J. .... 799  
 Möller, H. .... 301, 529  
 Molnar, R.J. .... 1603  
 Monemar, B. .... 563, 821, 1571  
 Monteil, Y. .... 599, 1467  
 Monteiro, T. .... 1651  
 Montserrat, J. .... 1303  
 Mooney, M.B. .... 571, 1191  
 Moore, K. .... 1029  
 Moore, V. .... 1199  
 Morante, J.R. .... 309  
 Morii, T. .... 419  
 Morkoç, Hadis ..... 1453  
 Morozov, A. .... 229  
 Morrison, D.J. .... 1199  
 Mortet, V. .... 1527  
 Morvan, E. .... 663, 889, 893  
 Motooka, T. .... 265, 297  
 Mou, D. .... 1423  
 Moulin, C. .... 13, 47  
 Mücklich, A. .... 897  
 Mukhopadhyay, S.M. .... 407  
 Müller, M. .... 107  
 Müller, St.G. .... 3, 39, 43  
 Müller, T. .... 87  
 Muntele, C.I. .... 1443  
 Muntele, Iulia ..... 1443  
 Musseau, O. .... 1215  
 Mynbaev, K. .... 225  
 Mynbaeva, M. .... 225  
  
**N**  
 Nagai, Kiyoko ..... 1073, 1283  
 Nahm, Kee Suk ..... 317, 1553  
 Nakaïke, Y. .... 905  
 Nakamura, Shuji ..... 1609  
 Nakamura, Shun-ichi ..... 201, 361  
 Nakamura, Tomonori ..... 985  
 Nakao, Masato ..... 1227  
 Nakashima, K. .... 873, 1005  
 Nakashima, Shin-ichi ..... 587, 591, 603, 607  
 Nakazawa, H. .... 269  
 Nam, O.-H. .... 1049, 1471  
 Namavar, F. .... 525  
 Naniwae, K. .... 353  
 Nashiyama, Isamu ..... 857, 1299  
 Nathan, M.I. .... 1453  
 Nemanich, R.J. .... 353  
 Nemoto, T. .... 1459  
 Nerding, M. .... 345  
 Netzer, F. .... 387  
 Neudeck, P. .... 465, 469  
 Neudeck, P.G. .... 489, 1343  
 Neudeck, Philip G. .... 1161, 1351, 1439  
 Neyret, E. .... 1041  
 Ng, K.M. .... 1619  
 Nielsen, M.C. .... 1391  
 Nielsen, Matthew ..... 1291  
 Niemann, E. .... 695, 733, 1407  
 Nieminen, R. .... 95  
 Nikitina, I. .... 229  
 Nikitina, I.P. .... 497, 1017, 1655  
 Nikolaev, A.E. .... 1655  
 Nilsson, H.-E. .... 765  
 Nilsson, O. .... 43  
 Nilsson, P.Å. .... 1255  
 Nishiguchi, T. .... 51, 115  
 Nishino, S. .... 51, 115, 197, 217, 257, 485,  
 711  
 Nishino, Shigehiro ..... 83, 103, 249  
 Nishio, Y. .... 197  
 Nishizawa, S. .... 481, 953

Nishizawa, Shin-ichi ..... 75, 83, 99, 103, 233,  
457, 461

Niu, G. .... 1339

Noblanc, O. .... 411, 1247

Nordby, Jr., H.D. .... 173

Nordell, Nils. .... 309, 1009

Nozaki, T. .... 825

Nuhfer, N.T. .... 477

## O

Obermeier, E. .... 529

O'Brien, J. .... 1191

Odekirk, B. .... 1001

Oder, T.N. .... 997

Ogino, Shinji ..... 1101, 1195

Ogura, M. .... 909, 917

Ohba, Takaomi ..... 261

Ohdaira, T. .... 909

Ohno, T. .... 169, 913, 1037

Ohsato, Hitoshi ..... 449

Ohshima, Takeshi ..... 857, 1129, 1239, 1299

Ohtani, N. .... 379, 493

Oikawa, Tadaaki ..... 1101

Okada, M. .... 825, 849

Okada, S. .... 51, 115

Okada, Shinsuke ..... 1227

Okada, Sohei ..... 857, 1129, 1239, 1299

Okamoto, A. .... 441

Okhuysen, M.E. .... 245, 305, 1149

Okuda, Takashi ..... 449

Okumura, H. .... 169, 253, 909, 917, 1037,

1235, 1459, 1545

Okushi, Hideyo ..... 757, 861, 865, 1073, 1283

Ólafsson, H.Ö. .... 1117

Oliver, Jr., J.D. .... 173

Olivier, J. .... 411

O'Loughlin, M.J. .... 173

Olsen, Gregory ..... 1383

O'Neill, A.G. .... 1419

Onuma, Yoshiharu ..... 1227

Opfermann, Th. .... 639

Orazio, Jr., Fred D. .... 841

Ortolland, S. .... 1419

Oshima, S. .... 51

Österman, John ..... 777

Östling, M. .... 309, 1049, 1179, 1315

Ottaviani, L. .... 921, 1303, 1363

Ouisse, T. .... 695, 715, 1267

Ovren, C. .... 1423

Oyanagi, Naoki ..... 75, 99, 103, 457, 461

Ozeki, T. .... 1057

## P

Palmer, P. .... 1231

Palmour, John W. .... 1093, 1271, 1275, 1319,

1371, 1387, 1427, 1643

Pan, M. .... 1187, 1379, 1399, 1635

Panknin, D. .... 741, 877

Pankratov, Oleg ..... 949

Pantelides, S.T. .... 1133

Papanicolaou, N. .... 925, 1017

Parascandola, S. .... 741

Parikh, N. .... 1615

Park, Chan Il ..... 317

Parker, M. .... 615

Pascual, J. .... 663, 893

Patel, A. .... 1503

Pearson, S.J. .... 1631

Pécz, B. .... 881, 961

Pelissier, B. .... 13, 47

Pennycook, S.J. .... 1133

Pensl, Gerhard ..... 111, 579, 623, 753, 831,

857, 941, 961, 1065, 1109

Peppermüller, Christian ..... 611, 623, 853

Pereira, E. .... 1651

Pereyra, I. .... 329

Pérez-Rodríguez, A. .... 309

Pernot, E. .... 13, 47, 1507

Pernot, J. .... 885

Perrin, Ronald ..... 21, 707

Persson, C. .... 719

Persson, P.O.Å. .... 537, 869, 1519

Peters, Dethard ..... 1295

Petrich, C. .... 353

Pezoldt, J. .... 281, 285, 289, 321

Pidduck, A.J. .... 1199

Pieterwas, R. .... 289

Piner, Eddie ..... 17

Pirouz, Pirouz ..... 249, 513, 517, 525, 841

Pisch, A. .... 13, 25, 91

Planes, N. .... 301, 599

Planson, D. .... 921, 1363

Poker, D.B. .... 667, 1443

Pollmann, Johannes ..... 349, 369

Poluektov, O.G. .... 805

Pons, Michel ..... 13, 25, 91

Pope, G. .... 403, 1025, 1081

Pophristic, M. .... 1623

Porter, L.M. .... 1001

Portmann, J. .... 1549

- 
- |                          |                          |                            |                                |
|--------------------------|--------------------------|----------------------------|--------------------------------|
| Potts, Gregory .....     | 1021                     | Ristein, J. ....           | 387, 391                       |
| Powell, Adrian .....     | 17, 437                  | Robbie, K. ....            | 981, 1033                      |
| Powell, G.D. ....        | 1033                     | Robert, J.L. ....          | 885                            |
| Powell, J.A. ....        | 465, 469                 | Robin, Brian M. ....       | 1491                           |
| Pozina, G. ....          | 675, 1571                | Robins, L.H. ....          | 1599                           |
| Prado, R.J. ....         | 329                      | Rodrigues, C.G. ....       | 1579                           |
| Prakash, S. ....         | 1619                     | Rohmfeld, S. ....          | 579, 583, 595                  |
| Preble, Edward A. ....   | 1491                     | Rohrer, G.S. ....          | 55, 63, 67, 477                |
| Pressler, H. ....        | 481                      | Romano-Rodríguez, A. ....  | 309                            |
| Pribble, W.L. ....       | 1643                     | Rorsman, Niklas ....       | 1207, 1255, 1259               |
| Pritchard, M. ....       | 403, 1025, 1081          | Rost, H.-J. ....           | 87                             |
| Pudda, C. ....           | 1041                     | Roth, Matthew D. ....      | 79                             |
| Puff, W. ....            | 965, 969                 | Roughani, Bahram ....      | 841                            |
| Purser, D. ....          | 313                      | Rouhani Laridjani, M. .... | 289, 1527                      |
| Püsche, R. ....          | 583                      | Rowland, L.B. ....         | 161, 733                       |
| <b>R</b>                 |                          | Royet, A.S. ....           | 1267                           |
| Råback, P. ....          | 95                       | Rudloff, D. ....           | 1483                           |
| Radtke, C. ....          | 1133                     | Rudner, Staffan ....       | 1263                           |
| Raevki, S.D. ....        | 1587                     | Rumyantsev, S.L. ....      | 1319, 1603                     |
| Raffaëlle, R.P. ....     | 489                      | Rupp, R. ....              | 1089, 1167                     |
| Raffy, C. ....           | 1041                     | Rushworth, S. ....         | 599                            |
| Rajagopal, P. ....       | 1471, 1491               | Rutsch, G. ....            | 733, 1001                      |
| Rajan, N. ....           | 1145                     | Ryssel, H. ....            | 1089                           |
| Ramabadran, Uma B. ....  | 841                      | Ryu, Sei-Hyung ....        | 1271, 1387, 1427               |
| Ramachandran, V. ....    | 353                      | <b>S</b>                   |                                |
| Raman, A. ....           | 1619                     | Saddow, Stephen E. ....    | 245, 453, 745, 901, 1149, 1203 |
| Ramberg, E. ....         | 1507                     | Sadowski, Horst ....       | 623, 853                       |
| Ramungul, Nudjarin. .... | 1367, 1415               | Safronov, I.N. ....        | 1587                           |
| Rao, Mulpuri V. ....     | 925                      | Saito, Ryuichi ....        | 1183                           |
| Rashkeev, Sergey ....    | 545                      | Saito, S. ....             | 587                            |
| Rastegaev, V.P. ....     | 1515                     | Saito, T. ....             | 419                            |
| Rattunde, M. ....        | 1549                     | Saitoh, A. ....            | 1347                           |
| Rauls, E. ....           | 365                      | Saks, N.S. ....            | 737, 1113, 1307                |
| Ravetz, M. ....          | 599                      | Salamanca-Riba, L. ....    | 277                            |
| Raynaud, C. ....         | 1363                     | Samant, A.V. ....          | 513                            |
| Redwing, Joan ....       | 17                       | Sanchez, E.K. ....         | 55, 63                         |
| Reislöhner, U. ....      | 929                      | Sands, D. ....             | 655                            |
| Rek, Z. ....             | 1045, 1599               | Sanger, P.A. ....          | 1307, 1403                     |
| Ren, F. ....             | 1631                     | Sankin, V.I. ....          | 769                            |
| Rendakova, S. ....       | 229, 237, 453, 505, 1203 | Saraie, Junji. ....        | 627                            |
| Reshchikov, M.A. ....    | 1453                     | Sardela, Jr., M.R. ....    | 313                            |
| Resnick, D. ....         | 1029                     | Sarney, W.L. ....          | 277                            |
| Rexer, B. ....           | 43                       | Saroukhan, A.M. ....       | 1255, 1431                     |
| Ribeiro Filho, J. ....   | 1567                     | Sasaki, M. ....            | 51, 115, 485                   |
| Richter, W. ....         | 205, 521, 533, 1033      | Satoh, Masataka ....       | 905, 985                       |
| Riehn, R. ....           | 741                      | Savage, Susan ....         | 1009, 1431                     |
| Riemann, T. ....         | 1483, 1575               | Savkina, N.S. ....         | 225, 509, 973, 1447            |
| Riley, J.D. ....         | 387                      | Sawada, Minoru ....        | 989                            |
| Rimeika, R. ....         | 1583                     |                            |                                |

Sawaki, N. ....	1575	Shimizu, T. ....	51
Saxler, Adam.....	17, 21, 703, 707	Shin, Moo Whan.....	993, 1639
Schaefer, J.A. ....	281, 289	Shinohe, Takashi.....	757, 861
Schardt, J. ....	341, 383	Shiomi, H. ....	485
Scharnholz, S. ....	695	Shirafuji, T. ....	257
Schattner, T.E.....	453, 1203	Shishkin, Y. ....	639, 679
Scheglov, M.P. ....	225, 509	Shovlin, J.D. ....	181
Schikora, D. ....	1595	Show, Yoshiyuki .....	1557
Schlaf, M. ....	655	Shuja, A. ....	821
Schmid, U. ....	695	Shur, M.S. ....	1583, 1603
Schmidt, J. ....	799, 805	Siche, D. ....	87, 119
Schnabel, C.M. ....	489	Sieber, N. ....	387, 391
Schöner, A. ....	937	Siergiej, R.R. ....	1053, 1339
Schörner, Reinhold .....	1089, 1295	Silveira, E. ....	1595
Schöttker, B. ....	1591	Simin, G. ....	1603
Schröter, B. ....	205	Singh, Ranbir .....	1271, 1275, 1319, 1371, 1387, 1427
Schulz, D. ....	87	Skorupa, W. ....	309, 529, 741, 877, 897
Schulz, M. ....	1065	Skowronski, M. ....	55, 63, 67, 473, 477
Schulze, Norbert .....	111, 579, 623	Skromme, B.J. ....	1029
Scofield, J.D. ....	1021, 1149	Slater, D. ....	1477
Scozzie, C.J. ....	1121, 1137, 1503	Smith, B.H. ....	1251
Segall, Benjamin .....	545	Smith, G.M. ....	1627
Seiler, C.F. ....	1053	Smith, M.C.D. ....	1203
Seki, Toshihide .....	813	Smith, S.R. ....	21
Sekigawa, T. ....	1235, 1283	Snyder, D.W. ....	9, 55, 63, 67, 837
Sekigawa, Toshihiro .....	253, 1073	Solomon, J.S. ....	21
Selder, M. ....	31, 39, 71	Solov'ev, V. ....	505
Senzaki, Junji .....	861, 865, 1283	Soloviev, S.I. ....	35, 945
Seredova, N. ....	225	Son, N.T. ....	131, 559, 563, 631, 817, 821
Sernelius, B.E. ....	1571	Song, X. ....	1141
Serre, C. ....	309	Souifi, A. ....	635
Seshadri, S. ....	1403	Soukiassian, P. ....	395
Seubert, A. ....	341, 345	Spaeth, J.-M. ....	785, 809
Shabanov, I.Yu. ....	1587	Spencer, M.G. ....	157, 277
Shah, P.B. ....	1395	Spetz, Anita Lloyd.....	937, 1085, 1435
Shamsuzzoha, M. ....	453	Spieß, L. ....	289
Sharma, R.P. ....	1503	Sridhara, S.G. ....	551, 567
Shcheglov, M.P. ....	497	Stafast, Herbert .....	1523
Shen, X.-Q. ....	1459, 1545	Stall, Rick .....	157
Shen, Z.X. ....	659	Starikov, E. ....	1379, 1635
Shenai, K. ....	1343, 1351	Starke, U. ....	341, 345, 383
Sheppard, S.T. ....	1643	Stauden, Th. ....	281, 289
Sheridan, D.C. ....	1053, 1339	Steckl, A.J. ....	273
Shi, D.T. ....	415	Stedile, F.C. ....	1133
Shibata, T. ....	1575	Stepanov, S. ....	225
Shigiltchhoff, O. ....	551, 567	Stephani, Dietrich .....	1089, 1167, 1243, 1295
Shiktorov, P. ....	1379, 1635	Stinespring, C.D. ....	293
Shimada, Hisanori .....	985	Stock, Stuart R. ....	1499
Shimizu, Hideki .....	261	Stoemenos, J. ....	529, 881, 961
Shimizu, M. ....	1459		

Stoemenos, Y. ....	301	Tanaka, Yasunori .....	861, 865, 909, 917
Storasta, L. ....	687	Tang, H. ....	1647
Stout, Phillip J. ....	213	Tang, Yi .....	1415
Straubinger, T.L. ....	31, 39, 71	Tani, T. ....	441
Strel'chuk, A.M. ....	973	Tanigawa, Shoichiro .....	857
Stritzker, B. ....	285	Tanimura, J. ....	1057
Strokan, N.B. ....	1447	Tanoue, Hisao .....	481, 861, 865, 909, 917
Strong, R.M. ....	1053	Tarplee, M. ....	1223, 1231
Strunk, H.P. ....	193	Tarui, Y. ....	1057
Su, H.B. ....	489	Taylor, Crawford .....	157, 277
Sudarshan, T.S. ....	35, 59, 615, 845, 945, 1223, 1231	Thoms, B.D. ....	1533, 1537, 1541
Sudre, C. ....	571, 1191	Thomson, D. ....	1049, 1615
Suemitsu, M. ....	269	Tillmann, K. ....	1549
Suemoto, T. ....	587, 591	Tin, C.C. ....	1097, 1133, 1339
Sugawara, Yoshitaka .....	1105, 1183, 1371	Titkov, A. ....	225
Sugimoto, H. ....	1057	Tobias, Peter .....	1435
Sugiyama, N. ....	441	Toda, Tadao .....	989
Suh, Eun-Kyung. ....	317, 1553	Tolani, V.L. ....	293
Sukhoveev, V. ....	229	Tomita, Kazuyoshi .....	1495
Suvkhanov, A. ....	1615	Tomita, T. ....	587, 591
Suvorov, A.V. ....	1275	Tone, Kiyoshi ...	659, 1013, 1187, 1375, 1399
Suzuki, R. ....	909	Torres, A. ....	1215
Suzuki, Seiji .....	1073, 1283	Tottereau, O. ....	1487
Suzuki, T. ....	169, 1037	Tran, C. ....	1623
Svedberg, Erik B. ....	1009	Tregubova, A.S. ....	221, 225, 497, 509
Svedberg, J.-O. ....	1179, 1255	Trentin, R. ....	1595
Sveinbjörnsson, E.Ö. ....	1117	Treu, M. ....	1089, 1167
Svenningstorp, Henrik .....	1435	Tseng, Huang-Ju R. ....	841
Svensson, B.G. ....	869, 889, 933, 937	Tsuchida, H. ....	145
Sweatman, D. ....	399	Tsuji, T. ....	1195
Syvjäärvi, M. ....	95, 165, 237, 375	Tsvetkov, D. ....	225
<b>T</b>		Tsvetkov, V. ....	3, 21
Tabacniks, M.H. ....	329	Tucker, J.B. ....	925
Tabata, A. ....	1595	Tungasmita, S. ....	1519
Tabib-Azar, M. ....	489	<b>U</b>	
Tada, T. ....	265	Uchida, Masao .....	141, 357
Tadano, Hiroshi .....	1495	Uchimura, K. ....	905
Tairov, Yu.M. ....	1515	Udal, Andres .....	725, 781
Takahashi, Kunimasa .....	141, 357	Ueda, Yasuhiro .....	989
Takahashi, T. ....	169, 253, 1037, 1235	Uedono, Akira .....	857
Takami, T. ....	1057	Ueno, Katsunori .....	1101, 1195
Takano, Yukio .....	457, 461	Uenoyama, Takeshi .....	141
Tamura, S. ....	849	Uhrmacher, M. ....	749
Tamweber, F.D. ....	1627	Ukai, S. ....	1005
Tan, L.S. ....	1619	Um, Benjamin S. ....	1069
Tanaka, Hisao .....	813	Unéus, Lars .....	1435
Tanaka, T. ....	169, 1037, 1073, 1283	Urban, W.M. ....	1053
Tanaka, Y. ....	481, 953	Uren, M.J. ....	655, 1199, 1251
		Usov, I. ....	1615

**V**

Vacas, J. ....	1651
Vaccaro, F. ....	313
Valek, W.F. ....	1053
Van de Walle, Chris G. ....	1561
van Duijn-Arnold, A. ....	799, 805
Van Landuyt, J. ....	309
Vasconcellos, A.R. ....	1579
Vassilevski, K.V. ....	1017
Vellvehi, M. ....	1303
Velmre, Enn. ....	725, 781
Venkatesan, T. ....	1137, 1503
Vennéguès, P. ....	1487
Venugopal, R. ....	1463
Verberk, R. ....	799
Vetter, W.M. ....	465, 469, 473
Vicente, P. ....	599
Vispute, R.D. ....	245, 277, 1137, 1503
Volm, D. ....	559
von Bardeleben, H.J. ....	715

**W**

Wagner, G. ....	87
Wagner, Mt. ....	631
Wahab, Q. ....	131, 537, 1171, 1175, 1263
Walker Jr., D.E. ....	407
Walton, C.D. ....	655
Wan, J. ....	1463
Wang, Jue. ....	1359, 1411
Wang, Shaoping. ....	17, 437
Wang, X.W. ....	1311
Wang, Y. ....	1287
Wang, Yihua. ....	325
Watanabe, F. ....	265
Watanabe, M. ....	419, 825, 873, 1005, 1347
Webb, J.B. ....	1647
Weber, W.J. ....	957
Wee, A.T.S. ....	1619
Weidner, Michael. ....	111, 831
Weiner, M. ....	1187, 1379, 1399, 1635
Weinert, Ulrich. ....	1243
Weis, Benno. ....	1243, 1295
Weitzel, C. ....	1287
Weller, R.A. ....	1133
Wellmann, P.J. ....	31, 39, 71
Werner, Wolfgang. ....	1167
Wickenden, A.E. ....	1533, 1537, 1541
Wiedenhofer, A. ....	1089
Wilding, P.J. ....	1199, 1251
Wilks, S.P. ....	403, 1025, 1081

Willander, Magnus. ....	313
Williams, B.W. ....	1359, 1411
Williams, E.K. ....	667, 1443
Williams, J.R. ....	901, 997, 1097, 1133
Williams, V. ....	1507
Wilson, R.G. ....	1631
Winnacker, Albrecht. ....	39, 71, 107, 445
Wirth, H. ....	877
Wischmeyer, F. ....	733
Withrow, S. ....	1615
Witte, H. ....	1591
Witthuhn, W. ....	639, 749, 929, 933
Wöhner, T. ....	281, 289, 321
Wollweber, J. ....	87, 119
Won, J.H. ....	1097, 1133
Wondrak, W. ....	695
Woodin, R.L. ....	181
Wright, C.J. ....	403
Wright, N.G. ....	1419
Wu, Chien-Hung. ....	541, 1141
Wu, Q.H. ....	1439
Wyczisk, F. ....	411

**X**

Xie, Z.Y. ....	1045
Xu, G. ....	501

**Y**

Yakimova, R. ....	95, 165, 237, 375
Yamaguchi, Hirotaka. ....	75, 103, 457, 461
Yamaguchi, M. ....	419
Yamamoto, T. ....	189
Yan, Feng. ....	1013, 1383
Yang, J.W. ....	1583
Yang, Seung Hyun. ....	1553
Yang, Y. ....	1533, 1541
Yano, H. ....	189, 1105, 1109, 1315
Yashiro, H. ....	379, 493
Yasseen, A.A. ....	1141
Yasui, K. ....	1511
Yoshida, K. ....	1005
Yoshida, S. ....	461, 917, 1037, 1235, 1283, 1545
Yoshida, Sadafumi. ....	169, 253, 909, 1073
Yoshikawa, Masahito. ....	857, 1129, 1239, 1299
Yoshimoto, Masahiro. ....	627
Yushin, Nikolay K. ....	79

**Z**

Zangooie, S. ....	537, 1085
-------------------	-----------



Zappe, S. ....	529
Zekentes, K. ....	1017, 1061
Zeman, J. ....	611
Zetterling, C.-M. ....	1049, 1179, 1315
Zhang, A.P. ....	1631
Zhang, J. ....	131, 137, 1171
Zhang, Q. ....	1223, 1231
Zhao, J. ....	1399
Zhao, J.H. ....	1635
Zhao, Jian H. ....	659, 1013, 1187, 1375, 1379, 1383
Zhao, Qingxiang ....	313
Zheleva, T. ....	245, 1503
Zheleva, T.S. ....	1471
Zhilyaev, Yu. ....	1587
Zhou, P. ....	277
Zhu, W.J. ....	1311
Ziemer, K.S. ....	293
Zimmermann, Uwe ....	777, 1323
Zirath, Herbert ....	1207, 1255, 1259
Zorman, Christian A. ....	541, 595, 1141, 1145
Zubrilov, A. ....	225, 229, 497, 505
Zvanut, M.E. ....	1125
Zywietz, A. ....	643

## Keyword Index

( $\sqrt{3} \times \sqrt{3}$ )R30° Reconstructed 6H-SiC(0001) Si-Face..... 357  
 (001) Surface..... 349  
 (10 $\bar{1}$ 0)..... 365, 905  
 (11 $\bar{2}$ 0)..... 189, 365, 1105  
 {01 $\bar{1}$ 4} Face..... 201  
<sup>13</sup>C..... 579, 623

**1**  
 1.54  $\mu$ m Luminescence..... 639  
 1/f Noise..... 1603  
 15R-SiC..... 111, 115, 1109

**2**  
 2-D Simulations..... 1351  
 2H-SiC..... 465

**3**  
 3C-SiC..... 119, 245, 253, 277, 313, 525, 529, 599, 711, 1129, 1149, 1235, 1239  
 3C-SiC / Silicon-On-Insulator..... 529  
 3C-SiC Deposition..... 301  
 3C-SiC/6H-SiC..... 1045  
 3C-SiC/Si..... 257  
 3C-SiC/Si/3C-SiC/Si(100)..... 265

**4**  
 4H and 6H-SiC Sublimation Growth..... 13  
 4H-SiC..... 13, 21, 341, 365, 497, 513, 517, 571, 695, 707, 757, 765, 841, 861, 1017, 1065, 1211, 1279, 1331, 1419

**6**  
 6H-SiC..... 87, 197, 341, 365, 481, 497, 513, 659, 695, 757, 953, 989, 1065, 1359, 1519  
 6H-SiC Reliability..... 1215

**A**  
 Ab Initio Defect-Energetics..... 949  
 Absorption..... 3, 551, 567  
 Acceptors..... 749, 785, 809, 929, 933  
 Accumulation Layer..... 1271

Accumulation Mode..... 1057, 1287  
 Activation..... 1615  
 Activation Energy..... 79  
 Adatom Structure..... 345  
 Adhesion..... 993  
 Admittance Spectroscopy..... 21, 1065  
 Adsorption..... 427, 1541  
 Adsorption Kinetics..... 407  
 Adstructures..... 365  
 AFM..... 257, 861, 1467, 1487, 1549  
 Al and Al/C Implantation..... 885  
 Al<sub>4</sub>C<sub>3</sub> precipitates..... 881  
 Al<sub>x</sub>Ga<sub>1-x</sub>N..... 1491  
 AlN..... 313, 1137, 1315, 1511, 1519  
 AlN Encapsulation..... 1503  
 AlN High Temperature Dielectrics..... 1503  
 Alpha Particles Spectroscopy..... 1447  
 Aluminum..... 83, 497, 687, 877, 909, 1005, 1013  
 Aluminum implantation in 6H-SiC..... 881  
 Ambipolar Diffusivity..... 671  
 Amorphization..... 897, 957  
 Amorphous Phase..... 537  
 Amorphous Silicon Carbide..... 325, 329  
 Amplitude Spectrum..... 1447  
 Angle Resolved Photoelectron Spectroscopy..... 387  
 Anisotropic Etching..... 537  
 Anisotropic Scattering..... 725  
 Anisotropy..... 375, 571, 1105  
 Anneal..... 901  
 Annealing..... 411, 659, 825, 837, 849, 869, 877, 921, 925, 953, 1009, 1017, 1029, 1615  
 ANNNI Spin Model..... 513  
 Antiphase Domain..... 257, 305  
 APCVD..... 253, 595  
 APD Annihilation Mechanism..... 253  
 Arsenic..... 865  
 ATLAS..... 1231  
 Atomic Force Microscopy..... 415, 841, 1499  
 Auger Electron Spectroscopy..... 335, 407, 411, 423, 981  
 Auger Lineshape..... 981

Auger Spectroscopy .....	1491	Carrier Multiplication .....	777
Avalanche Breakdown .....	1161, 1295	Carrier Removal .....	977
Avalanche Breakdown Emission .....	691	Carrier Scattering .....	559
Avalanche Photodiodes .....	1383	Carrier Trapping .....	603
<b>B</b>		Carrier Traps .....	1327
Background Doping .....	157	Catalytic Metal .....	1435
Background Doping Concentration .....	229	Cathodoluminescence .....	945, 1519, 1599
Band Edge Distortions .....	719	Cavities .....	529
Band Gap Narrowing .....	719	c-BN Phase Control .....	1527
Band Structure .....	545, 551, 559, 567	CCD .....	777
Band-to-Band .....	1603	Cellular Structure .....	1355
Barrier Height .....	1029, 1227	CH <sub>3</sub> SiH <sub>3</sub> .....	265
Be Acceptor Centers .....	805	Channel Mobility .....	1101, 1109, 1299
Beryllium .....	953	Channeling .....	869, 889, 893
Beyond SRH .....	1335	Charge Carrier Concentration .....	725
Biaxial Strain .....	595	Charge Transport .....	765
Biomedical Probe .....	1149	Charge Trapping .....	1089
Bipolar Junction Transistor .....	1391	Charge-Sheet Model .....	737
Bipolar Transistor .....	1419	Chemomechanical Polish .....	841
Birefringence .....	571	Chimney .....	131
Bond Polarizability Model .....	591	Chimney CVD .....	137
Bond-Raman-Polarizability Model .....	587	Chloride-Transport Process .....	1515
Boron .....	687, 795, 909, 949	Cleaning .....	1033
Boron Acceptor .....	111, 799	Cleavage Surface .....	441
Boron Diffusion .....	831	CMP .....	837
Bound Excitons .....	647, 675	Coimplantation .....	917
Breakdown .....	1231, 1339, 1363	Colloids .....	667
Breakdown Voltage ..	1211, 1287, 1359, 1631	Compensation .....	973
Buck-Converter .....	1343	Complex Mobility .....	773
Buffer Layers .....	1463	Compliant Substrate .....	313, 525
<b>C</b>		Computational Modeling .....	213
C/Si Ratio .....	83	Conductance Spectroscopy .....	1117
CAICISS .....	1459	Conduction Bands .....	551
Capacitance-Voltage Measurements .....	853, 1113, 1117, 1283	Contact Annealing .....	1219
Capacitive Contact .....	699	Contact Barrier .....	741
Capacitive Loss .....	1255	Contact Formation .....	981
Capping .....	1615	Contact Preparation .....	655
Carbon .....	917	Contact Resistance .....	1323
Carbon Vacancy .....	221, 821	Contact Resistivity .....	1009
Carbon/Boron-Coimplantation .....	941	Controller .....	1403
Carbonization .....	261, 281, 285, 297, 321	Converter .....	1403
Carbon-Related Defects .....	1125	Coplanar Waveguides .....	1267
Carrier Concentration .....	711	Core Level Photoemission .....	395
Carrier Diffusion .....	1623	Coupled Mode .....	603, 607, 711
Carrier Diffusion Length .....	683	Crack .....	1495
Carrier Lifetime .....	675	Crystal Bending .....	145
Carrier Mobility .....	1303	Crystal Defect .....	83, 1161
		Crystal Field Splitting .....	567
		Crystal Shape .....	13, 99
		Cubic III Nitrides .....	1545

Current Gain.....	1391
Current Spreading .....	1223
C-V Characteristics .....	853,
1113, 1117, 1283	
CVD .....	131, 149, 153, 157, 177, 189, 193,
197, 241, 273, 297, 525, 1507	
CVD growth.....	309
Cyclotron Resonance .....	559

## D

D <sub>1</sub> Center.....	909
Damage .....	481, 845, 893, 953
Dangling Bond .....	1073
DC .....	1207, 1259
DC Breakdown Voltage.....	1215
D-Center.....	749
Deep Centers .....	221, 973
Deep Level .....	1651
Deep Level Analysis .....	849
Deep Levels ....	189, 639, 687, 715, 749, 757,
1591	
Defect.....	603, 627, 643, 683, 853, 1203
Defect Centers.....	111
Defect Complexes.....	949
Defect Density .....	131, 225
"Defect" Diode .....	1351
Defect Formation .....	1515
Defect Kinetics.....	869
Defect Selective Etching.....	493
Defect Structure .....	1557
Defects ....	3, 13, 51, 431, 449, 457, 489, 497,
647, 687, 813, 957, 965, 969	
Deformation .....	513, 1587
Degradation.....	1089
Degradation of SiC MOS Capacitors.....	831
Delamination.....	813
Dendrite.....	59
Deposition Rate.....	169
Depth Profile .....	865
Depth Profiling.....	1017
Desorption.....	261
Deuterium .....	937, 1533
Device Simulation.....	1243
Dielectric Function.....	571, 575
Dielectrics .....	1093, 1303
Differential Admittance .....	745
Diffusion .....	933, 937, 945, 949, 1275
Diffusion Coefficients.....	321
Diffusion Length.....	489, 777, 1319, 1447

Diode.....	925, 1161, 1203, 1331, 1339, 1363,
1375, 1403	
Dislocation. ....	441, 485, 509, 1175, 1495, 1499,
1609, 1647	
Dislocation Arrays .....	473
Dislocation Density .....	1627
Dislocation Loop .....	913
Disorder .....	1623
Dissociation .....	929
Dissociation Width .....	513
Di-Vacancy.....	909
DLOS .....	635
DLTS .....	111, 221, 639, 753, 973
DMOSFET.....	1275
Donor-Acceptor Pairs .....	627
Donors.....	551, 785, 791
Doping ....	125, 165, 181, 719, 925, 953, 1561
Doping by Ion Implantation.....	831
Doping Concentration.....	575
Doping Profile .....	1061
Dose Dependence .....	869
Double Acceptor.....	749
DRIE .....	1145
Drive .....	1403
Dry Heat-Treatment.....	1125
Dynamic Avalanche.....	1327
Dynamic Trapping .....	1335

## E

Edge Emission .....	1587
Edge Termination ....	1223, 1231, 1287, 1339,
1399	
Effective Lifetime Temperature-	
dependence .....	781
Effective Mass .....	559
Electric Carrier Diffusion Length.....	229
Electrical Activation.....	877, 921, 1347
Electrical Characterisation.....	1199
Electrical Characteristics .....	849
Electrical Conductivity .....	873
Electrical Properties.....	317, 1167, 1655
Electrical Resistivity.....	537
Electroluminescence ....	683, 687, 1323, 1651
Electrolytic Etching .....	1061
Electron Beam Induced Current	
(EBIC).....	489, 777
Electron Concentration .....	857
Electron Cyclotron Resonance Plasma...	1511
Electron Density .....	501
Electron Emission.....	1557

- 
- |  |  |   |                        |
|--|--|---|------------------------|
| Electron Energy Loss Spectroscopy .....                                | 1537   | $f_t$ .....                             | 1255                   |
| Electron Gas .....   | 719  | Failure Mechanisms .....                | 1167                   |
| Electron Irradiation .....   | 821  | Fano Interference .....                 | 607                    |
| Electron Mobility .....  | 703, 725, 733, 761                                 | FBSOA .....                             | 1415                   |
| Electron Spin Resonance .....  | 715, 785, 791, 805, 813, 809, 821, 825, 1125, 1557 | Fermi Level Pinning .....               | 1029                   |
| Electron Stimulated Desorption .....                                   | 1537   | Field-Effect Mobility .....             | 1077                   |
| Electron Transport .....   | 729, 761   | Field-Plate .....                       | 1223, 1231             |
| Electron Trap .....  | 1105   | Filament Lifetime .....                 | 157                    |
| Electron-Hole Transport .....  | 1379   | First Principles Calculations .....     | 1561                   |
| Electron-Hole-Plasma .....   | 719  | Folded Longitudinal Phonon Modes .....  | 587, 591               |
| Electronic Nose .....  | 1439   | Folded Phonon Modes .....               | 583                    |
| Electronic Raman Scattering .....                                      | 615  | Forced Convection .....                 | 119                    |
| Electronic Structure .....   | 369, 631, 643, 805                                 | Forward Current Density .....           | 1223                   |
| Ellipsometry .....   | 571, 575   | Forward I-V Characteristics .....       | 1351                   |
| ELOG .....   | 1575   | Free Carrier Absorption .....           | 555, 671               |
| Emitter Injection Coefficient .....                                    | 1319   | Free Electron Laser .....               | 353                    |
| Encapsulation .....  | 1615   | Free Excitons .....                     | 675, 679               |
| Encapsulation Technique .....  | 1355   | Frequency Dependence .....              | 745                    |
| ENDOR .....  | 785, 799   | FTIR .....                              | 309, 611, 1467         |
| Energy Level Shifts .....  | 1567   | <b>G</b>                                |                        |
| Energy Loss Spectroscopy .....   | 335, 1541  | Ga-Al-N Alloys .....                    | 1503                   |
| Energy of Electron-Hole Pair Formation .....                           | 1447   | Gain .....                              | 1291                   |
| Epilayer Growth Pits .....   | 489, 1161  | Gallium .....                           | 917                    |
| Epitaxial Defects .....  | 1175   | GaN .....                               | 1155, 1459, 1477       |
| Epitaxial Guard Ring .....   | 1375   | GaN Device on Si-SiC .....              | 17                     |
| EPR .. 715, 785, 791, 805, 813, 809, 821, 825, 1125, 1557              |  | GaN/GaAs-Heterostructure .....          | 1591                   |
| Equilibrium Energy-Band Diagram .....                                  | 1655   | Gas Sensors .....                       | 1085, 1431, 1435       |
| Equivalent Circuit .....   | 1259   | Gas Source Molecular Beam Epitaxy ..... | 269, 313, 361          |
| Erbium .....   | 639  | Gas Switching .....                     | 1049                   |
| Eshelby Twist .....  | 465  | Gaseous Etching .....                   | 469                    |
| ESR .. 715, 785, 791, 805, 813, 809, 821, 825, 1125, 1557              |  | Gate Dielectrics .....                  | 1137, 1315             |
| Etch Pit .....   | 1061   | Gate Turn-Off Thyristor .....           | 1395, 1403             |
| Etching .....  | 481, 845, 1041, 1053                               | Germanium .....                         | 281, 289               |
| Evaporation Coefficient .....  | 91   | Global Heat Transfer .....              | 31                     |
| Excess Current .....   | 1323   | Graphite Intercalation .....            | 981                    |
| Excimer Laser .....  | 873, 1005  | Graphite Mask .....                     | 945                    |
| Excitonic Emission .....   | 627  | Growth Anisotropy .....                 | 193                    |
| Excitonic Luminescence .....   | 1575   | Growth Conditions .....                 | 205, 209               |
| Excitons in GaN/Al <sub>x</sub> Ga <sub>1-x</sub> N Quantum Dots ..... | 1567   | Growth Mode .....                       | 253                    |
| Ex-Situ Seed Preparation .....   | 47   | Growth Model .....                      | 285, 321               |
| Extended Defects .....   | 961  | Growth Pressure .....                   | 83                     |
| <b>F</b>   |  | Growth Rate .....                       | 75, 79, 83, 173, 233   |
| $f_{\max}$ .....   | 1255   | Growth Surface Morphology .....         | 379                    |
|  |  | GSMBE .....                             | 201                    |
|  |  | GTO .....                               | 1375, 1387, 1399, 1403 |
|  |  | GTO Thyristor .....                     | 1391                   |
|  |  | Guard Rings .....                       | 1339, 1399             |

Guided Optical Mode..... 1583

## H

Hall Effect..... 21, 111, 707, 711, 729, 733,  
737, 853

Hall Effect Measurement ..... 273, 715, 861,  
885, 909, 917

Hall Mobility..... 711

Hall Scattering Factor ..... 733

Hard Switching ..... 1343

HBT..... 1049

HCDS..... 249

Heat Transfer ..... 39

Heat Treatment..... 419

HEMT ..... 1643

Heterointerface..... 1545

Heterointerface Control ..... 289

Heterojunction..... 1647

Heterojunction Diode..... 313, 1651

Heterostructures ..... 205, 341

Hexagonal Stacking ..... 213

Hexagonal Surfaces ..... 341, 345, 383

Hexagonal Voids..... 437

High Blocking Voltage ..... 1371

High Current Switching ..... 1423

High Efficiency..... 1643

High Power ..... 1271, 1427

High Resistivity ..... 131

High Resolution Electron Energy-

Loss Spectroscopy ..... 357

High Temperature .... 1271, 1315, 1387, 1427,  
1431, 1435, 1439

High Temperature Annealing ..... 981

High Temperature Ion-Implantation ..... 865

High Temperature Mass Spectrometry ..... 91

High Voltage..... 777, 1323

High Voltage Switching..... 1423

High-Frequency Behavior..... 773

High-Level Lifetime ..... 1367

High-Level Mixer ..... 1207

High-Power Device..... 1171

High-Resolution X-Ray Mapping..... 473

High-Temperature Electronics..... 1311

High-Temperature Topography ..... 461

High-Voltage Power Device ..... 1367

HMDS..... 599

Hole Concentration..... 607

Hole Effective Masses ..... 563

Homojunction Diodes ..... 1651

Hot Carriers..... 691

Hot Wall Resistive Heating Reactor..... 241

Hot-Implantation..... 857, 861

Hot-Wall ..... 149, 153

HREELS ..... 357, 1533

HRXRD ..... 493

HTCVD..... 131

Hydride Vapor Phase Epitaxy ..... 1655

Hydrocarbon ..... 1439

Hydrogen ..... 651, 817, 929, 933, 1537

Hydrogen Annealing..... 1073

Hydrogen Etching..... 185, 353, 981, 1037

Hydrogen Ion Implantation..... 813

Hydrogen Sensors..... 1443

## I

ICP ..... 1049

Ideal Electrical Characteristics ..... 1219

Ideality Factor..... 1029, 1227

IGBT ..... 1415

Image Simulation..... 533

Impact Ionization..... 695, 765, 1327, 1379

Implantation.... 639, 687, 889, 933, 989, 1275

Implantation Temperature ..... 869

Implantation-Induced Defect Centers..... 831

Implantation-Induced Defects ..... 753

Impurity Incorporation..... 83

In Exposure..... 1459

In Situ Etching ..... 13

In Situ Monitoring ..... 281

In Situ Observation..... 75, 457, 461

In Situ Sublimation Etching ..... 47

In Situ Surface Treatment..... 1045

Incomplete Ionization ..... 1335, 1411

In-Doping..... 1495

Inductive Half-Bridge Switching..... 1187

Inductively Coupled Etching..... 1471

Infrared ..... 655

InGaN MQW ..... 1571

Instability ..... 95

Insulated Gate Bipolar Transistor..... 1427

Intensity Profiles ..... 591

Interband Optical Transitions ..... 555

Interface ..... 395, 399, 403, 521, 993, 1081,  
1101, 1133

Interface Silicides ..... 419

Interface States..... 1069, 1077, 1093, 1109,  
1117, 1655

Interface State Density..... 1073

Interface Trap..... 737, 1113, 1121, 1129,  
1133, 1307

Interface Trap Density .....	1097	Laser Processing .....	1005
Interface Trap Profiles .....	1113	Lateral Epitaxial Overgrowth .....	245, 615, 1471
Interfaces .....	957	Lateral Growth .....	103, 375, 1491
Interfacial Energy .....	237	Lateral Overgrowth .....	249, 1609
Interfacial Layer .....	411	Lattice Recovery .....	655
Interfacial Structures .....	415, 1133	Lattice Relaxation .....	1545
Internal Stresses .....	449	Layer Growth Kinetics .....	321
Inversion Channel Mobility .....	1105	Layer Thickness .....	1583
Inversion Layer .....	737	LDMOS .....	1307
Inverter .....	1403	Leakage Current .....	1029, 1195, 1211, 1323
Ion Beam Synthesis .....	309	Leakage Mechanism .....	1137
Ion Channeling .....	957	LEDs .....	1477, 1609
Ion Drift .....	929	LEO .....	245, 615, 1471
Ion Implantation .....	481, 659, 663, 667, 873, 877, 893, 897, 901, 905, 909, 913, 921, 925, 953, 1101, 1347, 1443, 1615	Lifetime .....	679, 691, 1319, 1609
Ion Irradiation .....	977	LiGaO <sub>2</sub> .....	1499
Ion Sputtering .....	741	LO Phonon .....	607, 711
Ionization Energies .....	703	Load-Pull .....	1259
Irradiation .....	965, 973	Local Density Theory .....	369
Isolation .....	1053	Local Spin Density Approximation .....	349
Isothermal Capacitance Transient Spectroscopy .....	757	Local Vibrational Mode .....	817
Isotype n-n Heterojunction .....	1655	Long-Repeat Polytype .....	469
I-V Characteristics .....	1025, 1323	Low Angle Grain Boundaries .....	493
<b>J</b>		Low Defect Density .....	525
JBS .....	1323	Low Pressure CVD .....	1239
JBS Rectifier .....	1179	Low Temperature Annealing .....	1619
JCT .....	1403	Low Temperature Epitaxy .....	249
Jet Vapor Deposition .....	1311	Low-Energy Electron Diffraction .....	341, 345, 383
JFET .....	1243, 1403	Low-Frequency Noise .....	1603
JTE .....	1363, 1387	Low-Pressure CVD .....	313
Junction Barrier Controlled Schottky Diode .....	1183	LPCVD .....	145, 253, 1129, 1235
Junction Barrier Schottky .....	1179	LPE .....	229, 233, 237, 1203
Junction Controlled Thyristor .....	1403	LPE Reactor for SiC .....	241
Junction Impedance .....	699	LTPL .....	753, 853
Junction Rectifiers .....	1331	Luminescence .....	643
<b>K</b>		<b>M</b>	
Kick-Out Mechanism .....	941	Macrodefects .....	445
KOH Etching .....	837, 1195	Magnetospectroscopy .....	611
<b>L</b>		Masking .....	1053
Lapping .....	845	Mass Transport .....	31, 39, 79, 95
Large Area Devices .....	1423	Maximum Frequency .....	1639
Laser Annealing .....	655, 873	MBE .....	205, 209, 289, 313, 521, 533, 1315, 1453, 1459, 1647
Laser Diode .....	1609	MEDICI .....	1339
		MEMS .....	1053, 1141, 1145, 1149
		Mesa JTE .....	1371
		Mesa pn Diode .....	1355
		MESFET .....	1247, 1251, 1255, 1259, 1263, 1639

Metal Growth Modes .....	423	Mott Transition .....	619, 719
Metal/SiC .....	411	MOVPE .....	1471, 1487
Metallic Ga.....	1553	MPS Diode .....	1187
Metallization .....	419	Multilayer SiC Substrate.....	1267
Metal-Oxide-Semiconductor (MOS)		Multi-Wafer Reactor.....	173
Devices.....	1069, 1299		
Metal-Semiconductor Interfaces.....	1001	<b>N</b>	
Metal-Semiconductor Contact .....	741	Nanoclusters .....	667
Metastability .....	651	Nanopipes .....	1549
Methyl Radicals .....	293	Nanostructure.....	305
Micro Raman .....	841	Natural Superlattice .....	769
Microelectromechanical.....	1149	Near-Interface Traps.....	1065, 1109
Micromachining.....	1145	Negative-Bias-Temperature Instability ....	831
Micromolding .....	1141, 1145	Neutron .....	853
Micropipe.....	3, 9, 51, 59, 217, 431, 437, 441, 445, 449, 453, 485, 505, 603, 1161, 1203, 1355	Neutron Irradiation .....	825
Micropipe Filling .....	237, 505	n-GaN .....	1619
Microplasmas .....	1161	Nickel.....	989, 1025, 1029
Micro-Raman Spectroscopy.....	1575	Nickel Silicide .....	981, 985
Microwave .....	1247, 1647	Niobium .....	997
Microwave Characterization.....	1267	NiSi <sub>2</sub> .....	981, 985
Microwave Generation.....	1635	Nitridation.....	317, 399
Microwave Power .....	1251, 1643	Nitrided Stainless Steel.....	1515
Microwave Power Transistor .....	1263	Nitrogen .....	551, 877, 1133, 1279, 1331
Millimeter Wave Generation .....	1379	Nitrogen Concentration .....	87
Miniband Transport .....	769	Nitrogen Donor.....	745
Minority Carriers .....	679	Nitrogen Doping .....	273, 615
Mirror Field.....	1511	Nitrogen Implantation.....	703
MISFET .....	1315	N <sup>+</sup> P.....	989
Mobility.....	729, 737, 1069, 1093, 1243, 1307	Noise.....	1259
Mobility Degradation Coefficient.....	1121	Nonabrupt Interface .....	1567
MOCVD.....	1511	Non-Contact Characterization .....	699
Modeling.....	25, 1259, 1267, 1351	Non-Planar Substrates .....	193
Modified Junction Termination		Nonpolar Surfaces .....	365
Extension.....	1375	Non-Radiative Recombination .....	627
Modified Lely Method.....	457, 579, 623	'non-reacted' Ohmic Contact.....	997
Molecular Growth Species.....	293	Nonuniformity of Lifetime .....	1447
Molybdenum Target.....	501	n-Type.....	545
Monomethylsilane.....	269	n-Type Doping.....	619
Monte Carlo Simulation..	213, 765, 889, 1635	Nuclear Transmutation Doping .....	849
Morphology.....	137, 197	Nucleation.....	63, 209
MOS.....	737, 1065, 1073, 1089, 1113, 1129	Numerical Modelling.....	31, 43
MOS Structure .....	1283	Numerical Simulation.....	25, 99, 149, 153
MOSFET.....	695, 1057, 1069, 1077, 1093, 1101, 1105, 1109, 1121, 1271, 1279, 1287, 1291, 1303, 1431, 1435	<b>O</b>	
MOS-Gated Bipolar Transistor.....	1415	OBIC.....	1363
Motor.....	1403	OBIC Images .....	1195
		Occupation Level.....	795, 817
		Off-Angle.....	1283



- 
- |  |  |
|--|--|
| Ohmic Contacts.....                          | 981, 985, 989, 993, 1001, 1005, 1013, 1017, 1021, 1025, 1503, 1619                       |
| ONO Dielectric .....                         | 1093, 1311   |
| Operational Amplifier .....                  | 1291   |
| Optical Absorption.....                      | 545, 635   |
| Optical Anisotropy.....                      | 555  |
| Optical Emission Microscopy.....             | 683  |
| Optical Microscopy.....                      | 509  |
| Optical Properties.....                      | 1553   |
| Optical Wave Guide.....                      | 1523   |
| Optically Detected Cyclotron Resonance ..... | 563  |
| Outdiffusion .....                           | 941  |
| Overcurrent Limitations.....                 | 1167   |
| Oxidation.....                               | 395, 403, 1081, 1133   |
| Oxide.....                                   | 383, 399   |
| Oxide Charge .....                           | 1121   |
| Oxide Layers .....                           | 1129   |
| Oxide Ramp Profile .....                     | 1219   |
| Oxide-Trapped Charges .....                  | 1129   |
| Oxygen.....                                  | 349, 1561  |
| Oxygen Implantation .....                    | 961  |
| Oxygen Precipitates .....                    | 961  |
| Ozone Cleaning.....                          | 1085   |
| <b>P</b>                                     |  |
| Packaging.....                               | 1439   |
| Palladium .....                              | 415, 1013  |
| Partial Dislocation.....                     | 517  |
| Passivation .....                            | 929, 933   |
| Passivation Films .....                      | 1137   |
| P-Channel.....                               | 1427   |
| PECDV .....                                  | 325  |
| PEEM.....                                    | 353  |
| Pendellosung .....                           | 465  |
| Pendeo-Epitaxy.....                          | 245, 1471, 1491  |
| Perfect Dislocation.....                     | 517  |
| Peripheral Protection.....                   | 1363   |
| Phonon Dispersion.....                       | 579  |
| Phonons.....                                 | 707  |
| Phosphorus.....                              | 795, 849, 853, 861, 1279, 1331   |
| Phosphorus Implantation .....                | 703  |
| Photo Emission Electron Microscopy.....      | 353  |
| Photoconductivity .....                      | 977  |
| Photodiodes.....                             | 1627   |
| Photoelasticity.....                         | 449  |
| Photoelectrochemical Etching .....           | 1639   |
| Photoelectron Spectroscopy.....              | 391  |
| Photo-ESR.....                               | 791  |
| Photoexcited Zincblende GaN.....             | 1579   |
| Photoluminescence ..                         | 325, 619, 623, 631, 647, 651, 659, 679, 849, 873, 909, 945, 1453, 1463, 1487, 1571, 1615 |
| Photoluminescence Image .....                | 627  |
| Photoluminescence in c-InGaN.....            | 1595   |
| Photon Backscattering .....                  | 841  |
| Photon Emission .....                        | 695  |
| Photoresponsivity .....                      | 1383   |
| Photovoltage .....                           | 699  |
| Physical Vapor Transport Growth...           | 9, 21, 31, 55, 63, 67, 71, 103, 477  |
| PiN Diode .....                              | 1371, 1399, 1423   |
| Pin Rectifier.....                           | 1367   |
| Pinholes .....                               | 55   |
| Pipes.....                                   | 509  |
| PL see "Photoluminescence"                   |  |
| Planar Defects.....                          | 59, 445, 485   |
| Plasma-Assisted CVD .....                    | 261  |
| Plasmon .....                                | 607, 707, 711  |
| Plastic Deformation .....                    | 67   |
| Plasticity .....                             | 517  |
| Platinum.....                                | 1029   |
| pn Diode.....                                | 687, 885, 1161, 1183, 1323, 1343, 1347, 1351   |
| Point Defects.....                           | 949  |
| Polar Faces.....                             | 335  |
| Polarity.....                                | 1459, 1499   |
| Polarization .....                           | 1453   |
| Polarized Light.....                         | 1587   |
| Polishing .....                              | 837, 845   |
| Polycrystalline SiC .....                    | 541, 1141  |
| Polycrystals.....                            | 103  |
| Polygonization .....                         | 477  |
| Polytypism .....                             | 209, 277, 427, 627   |
| Porous Si.....                               | 313  |
| Porous SiC .....                             | 537  |
| Porous Substrate .....                       | 225  |
| Positron Annihilation Spectroscopy .....     | 857, 909, 965, 969   |
| Post-Oxidation Annealing .....               | 1299   |
| Power Conditioning .....                     | 1395   |
| Power Devices .....                          | 1275, 1335, 1387   |
| Power Diode .....                            | 1187   |
| Power Modules .....                          | 1423   |
| Power MOSFETs.....                           | 1295, 1307   |
| Power Rectifier .....                        | 1179   |
| Power Switching Device.....                  | 1391   |
| Pressure Dependence .....                    | 1037   |
| Prism-Coupling Method .....                  | 1583   |

Processing .....	1077
Production .....	173
Proton Irradiation .....	221, 969
Protons .....	973
PTIS .....	611
p-Type .....	497, 1017, 1239
p-Type SiC .....	607
Power Devices .....	1407
Pulse Doping .....	141
Pulse Valve .....	141
Pulse Width Modulated .....	1403
Pulsed Laser Deposition .....	1137, 1503, 1523
Punch-Through .....	1359
Purity .....	3, 9, 131, 165
PVT see "Physical Vapor Transport Growth"	
PWM .....	1403
Pyrogenic Oxidation .....	1129

## Q

Quantum Dots .....	1453
Quantum Dots in c-InGaN .....	1595

## R

Radiation Damage .....	663
Radiation Defect .....	825
Radiation Effects .....	977
Radiation-Induced Conductivity .....	977
Radiotracer .....	749
Raman .....	659, 707, 893, 1467
Raman Imaging .....	603
Raman Polarizability .....	583
Raman Scattering .....	591, 607, 663, 711
Raman Scattering in c-InGaN .....	1595
Raman Spectroscopy .....	217, 325, 579, 583, 595, 1599
RBS .....	849, 869, 873, 997, 1615
RBS/Channeling .....	921, 1549
RBS-C .....	917
RBSOA .....	1415
Reactive Ion Etching .....	1029, 1049, 1053, 1057, 1149, 1199
Recombination Centers .....	489
Recombination Lifetime .....	683
Reconstruction .....	341, 345, 383
Recrystallization .....	897
Rectifier diode .....	1319
Rectifiers .....	1161, 1407
Reflectivity .....	411, 655
Refractive Index .....	1583

Reliability .....	1089, 1093, 1161, 1167, 1311, 1343
Re-Oxidation .....	1117
Re-Oxidation Anneal .....	1097
Residual Stress .....	595
Resistive Heating .....	157
Resistivity .....	3, 17, 933
Residual Stresses .....	67
Resonances .....	587
Response Speed .....	1383
Responsivity .....	989
Reststrahlen Band .....	655
RESURF .....	1279, 1307
Reverse Recovery .....	1327, 1367
Reverse Recovery Charge Measurements .....	781
Reverse Recovery Time .....	1371
RF 1639	
RF Atomic Source .....	313
RF Measurements .....	1207
Rf-Plasma Nitrogen Source .....	1499
RHEED .....	201, 361, 1467, 1545
RIE .....	1029, 1049, 1053, 1057, 1149, 1199
RIE Rate .....	1057
Rocking Curve .....	145
Rutherford Backscattering Spectrometry .....	849, 869, 873, 997, 1615

## S

Sacrificial Oxidation .....	1199
Sacrificial Silicon .....	1081
Sapphire Substrate .....	1603
Saturation .....	695
Saw-Damage .....	51
Scaling .....	1203
Scandium .....	809
Scanning Electron Microscopy .....	509, 1471
Scanning Tunneling Microscopy .....	341, 345
Scattering Mechanisms .....	1105
Schottky .....	1203, 1323
Schottky Barrier .....	505, 1025, 1029
Schottky Barrier Characteristics .....	1235
Schottky Barrier Height .....	1239
Schottky Contacts .....	1227, 1239
Schottky Diodes .....	145, 1085, 1161, 1167, 1171, 1175, 1183, 1199, 1207, 1219, 1223, 1231, 1407, 1631
Schottky Emission .....	1137
Schottky Junction .....	745
Schottky Rectifiers .....	1195, 1211

Scratch Test.....	993	Simulation....	95, 253, 893, 1171, 1263, 1287, 1339, 1419
Screw Dislocation .....	63, 431, 453, 489, 1161	Single Precursors .....	177
Secondary Defect .....	913	Singly Balanced Mixer .....	1207
Secondary Ion Mass Spectrometry .....	937	SiN <sub>x</sub> /Si Structure.....	317
Seed Orientation.....	87	SiO <sub>2</sub> .....	541
Seeded Supersonic Molecular Beam .....	181	SiO <sub>2</sub> /SiC Interface .....	383, 1097
Selective Doping.....	945	Site Preference.....	917
Selective Epitaxy .....	249	Slip Bands.....	477
Selective Growth.....	1491	Small Angle Grain Boundaries.....	217
Self-Interstitial .....	869	Smart-Cut.....	715
Semi-Insulating Material .....	21, 165, 965	SOI.....	301, 305, 1467
Semi-Insulating SiC .....	1643	SOI Substrates .....	599
Semi-Insulating Substrate .....	1247	Solution Growth .....	107, 119
Sensor.....	1439	S-Parameter.....	1259
SF <sub>6</sub> .....	1149	Specific Contact Resistance.....	997
Shallow Nitrogen Donor.....	611	Spectral Measurements.....	691
Shape Evolution.....	95	Spectroscopic Ellipsometry ..	281, 1033, 1085
Sheet Resistance.....	885	Spin Distribution.....	795, 817
Shockley-Read-Hall.....	1335	Spin Polarization.....	643
Shunt .....	1323	Spin-Orbit Splitting .....	567
Si Outdiffusion.....	269, 521	Spiral Growth.....	1549
Si/3C-SiC/Si(100).....	265	Spreading Resistance .....	741
Si/C Ratio.....	1097	Sputtering.....	1519
Si <sub>2</sub> (CH <sub>3</sub> ) <sub>6</sub> (Hexamethyldisilane) .....	711	SRH .....	1335
Si <sub>3</sub> H <sub>8</sub> .....	265	Stability.....	817
Si <sub>3</sub> N <sub>4</sub> .....	541	Stacking .....	427
SiC N-Channel IGBT.....	1411	Stacking Fault Energy.....	513
SiC on Insulator .....	297, 715, 813	Stacking Sequence .....	341, 345
SiC P-Channel IGBT .....	1411	Stark Effect .....	1453
SiC Powder .....	71	Static Induction.....	1183
SiC Substrates .....	17, 1549	Steam Annealing.....	1129
SiC Wafers .....	237	Step Bunching.....	125, 137, 213, 375, 379
SiC/Si/Si <sub>3</sub> N <sub>4</sub> /Si System .....	529	Step Flow Growth.....	47, 1499
Si/3C-SiC/Si(100).....	265	Step Height .....	185
Si/C Ratio.....	1097	Step Kinetics.....	379
Si <sub>2</sub> (CH <sub>3</sub> ) <sub>6</sub> (Hexamethyldisilane) .....	711	Step Repulsive Interaction.....	379
Si <sub>3</sub> H <sub>8</sub> .....	265	Step-Controlled Epitaxy .....	125
Si <sub>3</sub> N <sub>4</sub> .....	541	Stoichiometry.....	111
Silane overpressure .....	901	Strain Relaxation .....	301
Silane Starving Plasma Regime .....	329	Stress Effects .....	1121
Silicate Adlayer.....	391	Si Outdiffusion .....	269, 521
Silicon .....	917	Stress Reduction .....	225
Silicon Dioxide .....	391	Strong Electric Field.....	769
Silicon Nitride Mask.....	1471	Structural Properties .....	1553
Silicon Oxide .....	387	Structure Factor .....	501
Silicon Processing Techniques .....	1191	Structured Overshoot.....	1579
Silicon Vacancy .....	825	Sublimation.....	79, 209, 335, 485, 1507
SIMOX.....	297	Sublimation Bulk Growth.....	87
SIMS ...	83, 623, 861, 889, 893, 921, 941, 953	Sublimation Epitaxy .....	217, 1447

Sublimation Growth.....	9, 25, 47, 55, 63, 75, 83, 99, 111, 1515
Sublimation Heteropolytype Epitaxy.....	221
Sublimation Method.....	51, 115, 217
Sub-Micron Resolution.....	627
Substrate Bias.....	261
Substrate Effect.....	1627
Substrate Engineering.....	1491
Substrate Flatness.....	837
Substrate Growth.....	277
Substrate Orientation.....	185
Substrate Temperature.....	261
Substrates.....	3, 9
Sub-Surface Damage.....	845
Super Screw Dislocations.....	437
Superlattice.....	769
Supersonic free jet CVD.....	265
Surface.....	369, 395, 427, 1541
Surface Acoustic Waves.....	1523
Surface Defects.....	261
Surface Etching.....	1507
Surface Hydrogen.....	269
Surface Kinetics.....	213, 407
Surface Micromachining.....	1141
Surface Modification.....	169
Surface Morphology.....	233, 257, 481, 865, 1037, 1283, 1499
Surface Preparation.....	353, 1033
Surface Reactions.....	293
Surface Reconstruction.....	353, 357
Surface Roughness.....	137, 837, 1057, 1571
Surface States.....	387, 391, 741
Surface Stoichiometry.....	921
Surface Structure.....	341, 345, 361, 383, 415, 419
Surface Topography.....	403
Surface Traps.....	1251
SWBXT.....	453
Switch.....	1387
Switching.....	1303, 1407
Switching Characteristics.....	1243, 1295
Switching Devices.....	1155
Synchrotron.....	1033
Synchrotron Radiation.....	395
Synchrotron Topography.....	431
Synchrotron White-Beam X-Ray Topography (SWBXT).....	489
Synchrotron X-ray Topography.....	1045

## T

Tantalum Carbide.....	161
Taper Angle.....	103
TEM.....	193, 245, 249, 285, 297, 309, 411, 453, 521, 533, 841, 869, 913, 1463, 1487, 1519, 1647
Temperature Dependence.....	169, 791, 1243, 1631
Temperature Distribution.....	79
Temperature Gradient.....	99, 233
Temperature Phonon Shift.....	707
Temperature Stability.....	1009
Theory.....	43, 795, 817
Thermal Conductivity.....	3, 43
Thermal Oxidation.....	1125
Thermal Stability.....	1021
Thermodynamic Study.....	1041
Thermodynamics.....	209
Thermoelastic Stress.....	67
Thick GaN.....	1553
Thick Layers.....	145
Thin Film Growth.....	293
Thin Film Morphology.....	1471
Thin Oxide.....	1085
Thin SIMOX.....	525
Thinning Process.....	301
Threading Dislocation Array.....	477
Threading Dislocations.....	63, 1463
Threshold Voltage.....	1105, 1109, 1299
Thyristors.....	1387, 1503
Ti Schottky Contact.....	1191
Ti/Al.....	1619
Time-Resolved.....	1571
Time-Resolved Micro-PL.....	1575
Time-Resolved Photoluminescence.....	675, 1623
TiN.....	1503
Titanium.....	1005, 1013, 1029
TLM.....	1323
TMA.....	249
Top-seeded Growth Method.....	107
TPD.....	1533
Transferred Electron Devices.....	1635
Transient Grating.....	671
Transition Layer.....	59
Transmission Electron Microscopy.....	193, 245, 249, 285, 297, 309, 411, 453, 521, 533, 841, 869, 913, 1463, 1487, 1519, 1647
Transmission X-Ray Technique.....	75

Transport ac+dc in 3C-SiC .....	773
Transport ac+dc in 6H-SiC .....	773
Trimethylsilane .....	273, 313
Tungsten.....	1005
Twin .....	305

## U

Ultrafast Transport Transient.....	1579
Universal Compliant .....	305
UV Detectors .....	1383, 1591
UV Sensor.....	989

## V

V <sub>F</sub> .....	1371
Vacancy.....	643, 795, 817, 869, 909, 1561
Vacancy-Type Defects.....	857
Vacuum Sublimation Epitaxy.....	509
Valence Bands .....	567
Vanadium .....	631, 635
Vaporization.....	91
Velocity of Growth .....	35
Velocity Saturation .....	761
Vertical Hot-Wall Reactor .....	131
Vertical Hot-Wall Type CVD.....	141
Vickers Indenter.....	441
Visible-Blind.....	1383
Void.....	521
Volatility .....	335

## X

X-Band.....	1643
XPS .....	399, 997, 1025, 1057, 1199
X-Ray.....	79
X-Ray Diffractometry.....	189, 217
X-Ray Diffraction .....	501, 1045, 1463, 1499
X-Ray Emission Analysis.....	419
X-Ray Imaging.....	71
X-Ray Induced Photoelectron Spectroscopy.....	387
X-Ray Photoelectron Spectroscopy .....	415
X-Ray Scattering.....	993
X-Ray Topography .....	221, 457, 461, 469, 473, 509, 1599
XRC .....	1495
XRD .....	309, 411, 1519, 1549
XTEM .....	201

## Y

Yield.....	1291
Yield Stress .....	517

## Z

ZVS Switching .....	1343
---------------------	------

## **Carbon-Containing Layers on Silicon**

### **Growth, Properties and Applications**

**H.J. Osten**

Materials Science Foundations Vol. 7

ISBN 0-87849-834-6

Publication Date: September 1999

88 pages, CHF72.00/US\$48.00

The addition of supersaturated carbon to silicon or silicon-germanium thin films leads to a new class of semiconducting materials. This new material can alleviate some of the constraints on strained  $\text{Si}_{1-x}\text{Ge}_x$  and may help to open up new fields of device applications for heteroepitaxial Si-based systems. Basic growth problems, as well as the mechanical and electrical properties of  $\text{Si}_{1-y}\text{C}_y$  and  $\text{Si}_{1-x-y}\text{Ge}_x\text{C}_y$  layers grown pseudomorphically onto Si(001), have been reviewed. The incorporation of carbon can be used (i) to enhance SiGe layer properties, (ii) to obtain layers with new properties, or (iii) to control dopant diffusion in microelectronic devices. The phenomenon of suppressed boron diffusion in carbon-rich epitaxial layers can be used to increase the performance of SiGe heterojunction bipolar transistors (HBTs). When compared with SiGe technologies, the addition of carbon offers a significantly greater flexibility in process design and a greater latitude in processing margins.

#### **CONTENTS**

1. Introduction. 2. Growth of epitaxial  $\text{Si}_{1-y}\text{C}_y$  and  $\text{Si}_{1-x-y}\text{Ge}_x\text{C}_y$ . 3. Mechanical and structural properties. 4. Electrical properties of C containing alloys on Si(001). 5. Highly concentrated pseudomorphic  $\text{Si}_{1-y}\text{C}_y$  layers. 6. Application of SiGe:C in heterojunction bipolar transistors. 7. Summary and outlook.

Detailed information on this title – including the full table of contents – is available on the internet at <http://www.ttp.net>

---

**ttp Trans Tech Publications Ltd**

Brandrain 6  
CH-8707 Uetikon-Zuerich  
Switzerland

Fax: +41 (1) 922 10 33  
e-mail: [ttp@ttp.net](mailto:ttp@ttp.net)  
Web: <http://www.ttp.net>

## **Silicon Carbide, III-Nitrides and Related Materials**

**Eds. G. Pensl, H. Morkoç, B. Monemar and E. Janzén**

Proceedings of the 7th International Conference on Silicon Carbide, III-Nitrides and Related Materials,  
Stockholm, Sweden, September 1997

Materials Science Forum Vols. 264-268

ISBN 0-87849-790-0

Publication Date: April 1998

1606 pages, 2-Vol. Set, CHF520.00/US\$398.00

The two-volume set documents our present understanding of the many topics of interest, such as the growth of bulk crystals, the growth of epitaxial layers, theoretical approaches, the characterization of the grown material, the development of suitable processes and electronic devices operating under extreme conditions and providing outstanding properties.

Presented are 348 articles which describe the depth and breadth of the activity in this field. An exciting publication for anyone working with wide bandgap materials.

### **CONTENTS**

**PART 1:** 1. SiC BULK GROWTH. 2. SiC EPITAXY. 2.1 Homoepitaxial Growth. 2.2 Heteroepitaxial Growth. 3. THEORY. 4. CHARACTERISATION OF SiC. 4.1 Surfaces and Interfaces. 4.2 Structural Characterisation. 4.3 Optical Characterisation. 4.4 Electrical Characterisation. 4.5 Magnetic Resonance Characterisation. 4.6 Thermal and Mechanical Properties. 5. MEASUREMENT TECHNIQUES.

**PART 2:** 6. PROCESSING OF SiC. 6. 1 Doping

Detailed information on this title – including the full table of contents – is available on the internet at  
<http://www.ttp.net>

---

 **Trans Tech Publications Ltd**

Brandrain 6  
CH-8707 Uetikon-Zuerich  
Switzerland

Fax: +41 (1) 922 10 33  
e-mail: [ttp@ttp.ch](mailto:ttp@ttp.ch)  
Web: <http://www.ttp.ch>

## **Defects and Diffusion in Semiconductors**

### **An Annual Retrospective II**

**Ed. D.J. Fisher**

Defect and Diffusion Forum Vols. 171-172

ISBN 3-908450-46-2

Publication Date: September 1999

336 pages, CHF240.00/US\$176.00

This second volume in the new-format coverage of the latest results in the field covers abstracts from the approximate period of mid-1998 to mid-1999. As always, due to the vagaries of some journal publication dates, abstracts of earlier work may be included in order that the present contents merge seamlessly with those of volumes 162-163; the previous issue in this sub-series.

The original works in the present volume concern diffusion phenomena and defects in the two most important semiconductors, with C.A.Londos et al's major paper on infra-red experimental studies of oxygen-vacancy related defects that result from the irradiation of silicon, plus shorter theoretical papers on the calculation of Cd diffusion profiles in GaAs (E.Antoncik), on the enhancement or retardation of donor/acceptor dopants in pre-doped silicon (Antoncik) and self-diffusion in GaAs (P.Murugan and K.Ramachandran).

As to the abstract section of the present volumes, this again reflects the increasing interest in ceramic-type semiconductors such as GaN which, before volumes 162-163, had been covered under 'nitride' or 'carbide' headings; without reference to their semiconducting properties.

The original papers and abstracts together provide an invaluable and up-to-date insight into current understanding of, and future prospects, in the field of semiconductors.

#### **CONTENTS**

1. Original Papers (70 pp). 2. Abstracts (224 pp). 3. Indexes (22 pp)

Detailed information on this title – including the full table of contents – is available on the internet at <http://www.ttp.net>

---

**ttp Trans Tech Publications Ltd**

Brandrain 6  
CH-8707 Uetikon-Zuerich  
Switzerland

Fax: +41 (1) 922 10 33  
e-mail: [ttp@ttp.net](mailto:ttp@ttp.net)  
Web: <http://www.ttp.net>



---

## *Advanced Reading*

---

# **Diffusion in Silicon - 10 Years of Research**

**Ed. D.J. Fisher**

Defect and Diffusion Forum Vols. 153-155

ISBN 3-908450-29-2

Publication Date: March 1998

560 pages, CHF360.00/US\$272.00

The present book presents a thorough treatment of the subject, covering a full decade of progress in the understanding of Diffusion in Silicon.

In its first section, thirteen in-depth reviews provide the reader with a concentrated yet comprehensive update in all of the most important areas.

The second section is made up by a 300-page collection of extended abstracts. However, the information has not only been abstracted but also organized and analyzed, and presented it in a readily accessible form. For example, each item in this section of the volume begins with a graphical compilation of relevant diffusion data which have been reported during the past decade. The plotted data are also tabulated as indicated on the graph.

A must for any library holding with an interest in the field!

### ***CONTENTS***

Section 1: Original and Review Papers.

Section 2: Abstracts of Papers on Experiment and Theory.

Detailed information on this title – including the full table of contents – is available on the internet at <http://www.ttp.net>

---

** Trans Tech Publications Ltd**

Brandrain 6  
CH-8707 Uetikon-Zuerich  
Switzerland

Fax: +41 (1) 922 10 33  
e-mail: [ttp@ttp.ch](mailto:ttp@ttp.ch)  
Web: <http://www.ttp.ch>